ASM INTERNATIONAL

HUBERTUS COLPAERT

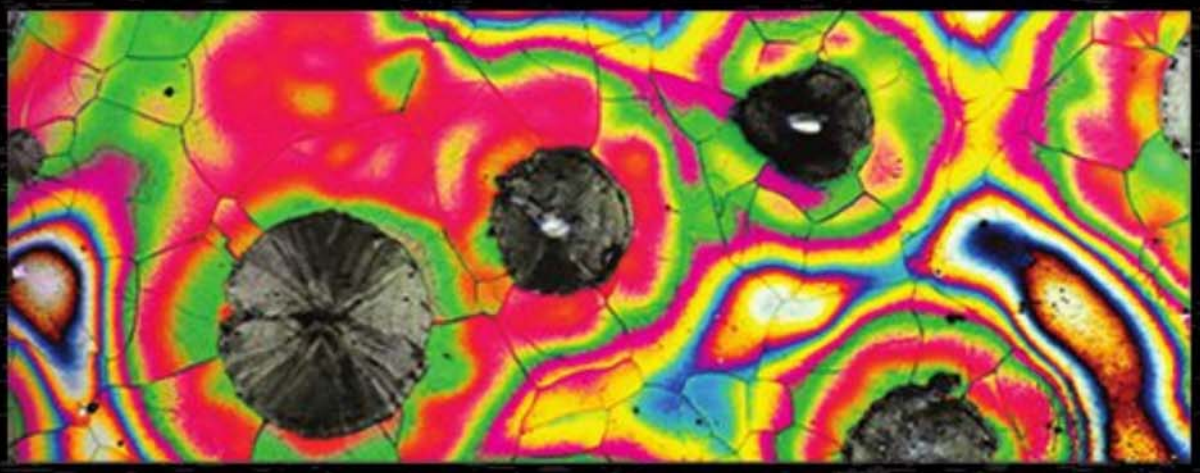

METALLOGRAPHY OF STEELS

Interpretation of Structures and the Effects of Processing

Updated and Translated by André Luiz V. da Costa e Silva

HUBERTUS COLPAERT

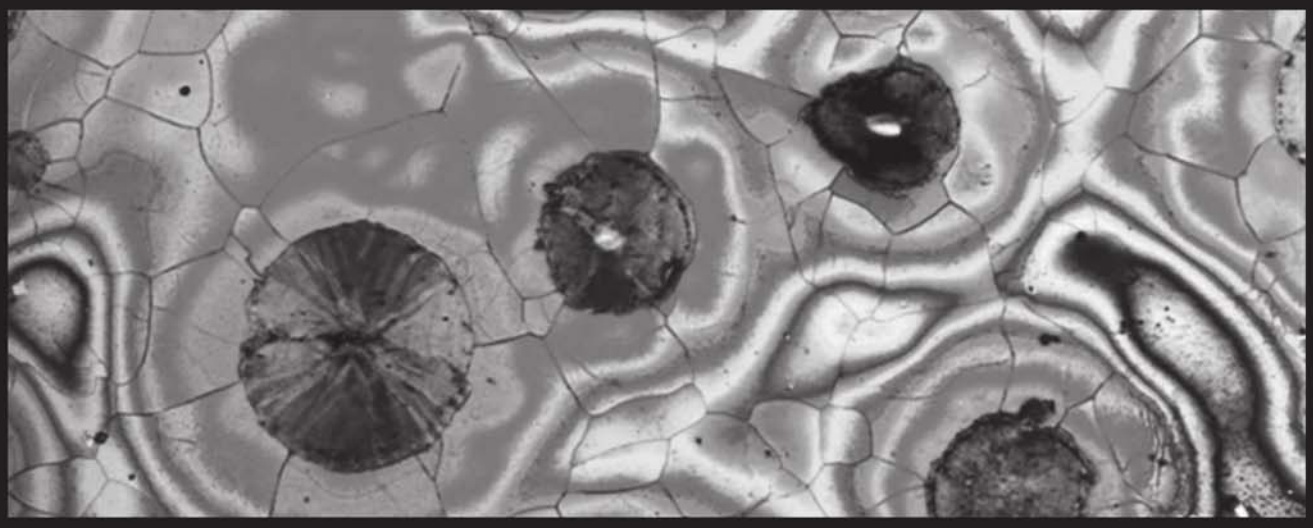

METALLOGRAPHY OF STEELS

Interpretation of Structure and the Effects of Processing

Updated and Translated by André Luiz V. da Costa e Silva

ASM International®
Materials Park, Ohio 44073-002
www.asminternational.org

Originally published and authorized translation from the
Portugese language edition as Metalografia dos Produtos Siderúrgicos Comuns, 4ª Edição,
© 2008 by Editora Blucher

First printing, August 2018

Comments, criticisms, and suggestions are invited, and should be forwarded to ASM International.

Prepared under the direction of the ASM International Technical Book Committee (2017–2018), Steve Yue, Chair.

ASM International staff who worked on this project include Scott Henry, Senior Manager; Karen Marken, Senior Managing Editor; Amy Nolan, Content Developer; Madrid Tramble, Manager of Production; Jennifer Kelly, Production Coordinator

Editorial assistance by Scott Ryan and Lilla Ryan

Library of Congress Control Number: 2017950638
ISBN-13: 978-1-62708-148-1 (print)
ISBN-10: 1-62708-148-8
ISBN: 978-1-62708-149-8 (pdf)
SAN: 204-7586

ASM International®
Materials Park, OH 44073-0002
www.asminternational.org

Printed in the United States of America

ON THE COVER: Ductile cast iron, annealed. The etchant reveals silicon segregation. Silicon content decreases as the distance from the graphite nodule increases. Etched with sodium hydroxide (NaOH), picric acid, and potassium metabisulfite in 100 ml distilled water. Courtesy of J. Radzikowska, Foundry Research Institute, Krakow, Poland.

Contents

Foreword

The names of three archaeological eras are described by their dominant structural materials: the stone age, the bronze age, and the iron age. While the metals in the bronze age were obtained by smelting, early use of iron relied on finding the metallic form, mostly from meteorites. Its scarcity, together with its softness and tendency to corrode, limited its application. With time, however, extraction methods from ores and techniques such as surface hardening to improve the properties, broadened the application of iron. The first steel was made in the early iron ages but did not become a significant commodity until the middle of the nineteenth century when Henry Bessemer invented a new steelmaking process, which started the second phase of the industrial revolution. Around the same time, the introduction of microscopic investigation of materials led to a better understanding of steel properties and soon thereafter books on the metallography of steel were being published.

Metallography has a long tradition in Brazil going back to the early twentieth century. Metallography became a pillar in quality control of the construction materials used in the rapid expansion of the Brazilian railway system in the late 1920s. At this time, Hubertus Colpaert, at the Institute of Technological Research in São Paulo, began systematic work on the study of the metallographic characteristics of ferrous metals. In 1951, this work resulted in the publication of the book *Macrographic and Micrographic Metallography of Common Steel Products*. This book offered a unique combination of a metallography atlas, manual of metallographic techniques, and introduction to the fundamentals of phase transformations and thermal treatment of these alloys, and quickly became the most important Brazilian reference book for those working on processing and treatment of ferrous alloys. A second and third editions of this book was published in 1959 and 1969, respectively.

Since the publication of the third edition, advanced microscopy techniques became widely available and a significant number of new steel products have been developed. These developments are reflected in the fourth edition of the book while maintaining the spirit of the original edition, being a unique

combination of a metallography atlas, manual and textbook. For publication of the English edition, the title of the book was changed from the Portuguese original *Metallography of Common Steel Products* to *Metallography of Steels: Interpretation of Structure and the Effect of Processing*. Although this title better indicates that the book offers much more than metallography alone, it still does not fully reflect the rich content of the book.

The editor of the fourth edition, André Costa e Silva, is a professor at the Universidade Federal Fluminense in the Rio de Janeiro area, Brazil. He is an expert in the processing-properties-performance relations in steel with a focus on computational thermodynamics and its applications to steelmaking and advanced steel processing. He is also experienced in specification, inspection and failure analysis of metallic materials.

Ursula R. Kattner
National Institute of Standards and Technology
Materials Science and Engineering Division,
Thermodynamics and Kinetics Group

Preface to the Fourth Edition

During one semester in 1975, my Tuesday mornings were devoted to preparing, observing, and recording macrographs and micrographs of steels and cast irons under the guidance of Edil Patury Monteiro, with support of the book *Metalografia dos produtos siderúrgicos comuns* by Hubertus Colpaert. At the same time, I was being exposed to the theory of the kinetics of phase transformations with José Roberto Costa Guimarães. From this time on, Colpaert's book became to me—as to many Brazilian students, technicians, and engineers—a fundamental reference in academic and professional life. A very well-balanced mix of textbook and atlas of metallographic structures, for decades the book has been the companion of Brazilian metallographers, metallurgists, and steelmakers. At the end of 2006, when Paulo Mei and I concluded the second edition of *Steels and Specialty Alloys*, I was honored by the invitation from our editor, Edgard Blücher, to consider updating the text and images of the Colpaert's book. The opportunity to collaborate on incorporating technological developments to this outstanding book was an irresistible challenge.

Globally the steel industry is enjoying a time of rare expansion and vigor, with more than 1,400 Mt of steel produced each year and several years of significant increases in production. Furthermore, the production and processing of these iron-based alloys has reached an admirable degree of sophistication and control. In average quality steels, many elements are controlled to the level of parts per million in mass (1 ppm in mass is 1 g in 1 mt!) and the structure of the steels is controlled to a degree of precision never before experienced.

Metallography is one of the essential tools that made it possible to attain this degree of sophistication. It is a tool widely used in the whole field of metallurgy, in particular, for the whole spectrum of iron and steel products, from steel used in nails, springs, nuclear reactors and packaging and to cast irons used in engines, fittings, railroad parts, and so on. Metallographic techniques have evolved along with the steel industry. Besides the use of visible light, techniques that use other types of interactions with matter and in special in-

teractions between electrons and matter have become common. Techniques aimed at quantifying structural features have also greatly evolved, and the past decade has seen a dramatic advance in the techniques of three-dimensional reconstruction of material structures. If during Colpaert's time the breadth of knowledge and experience needed to write such a book were already rare—this being one reason for my respect for his work—in these days it is almost impossible for a single person to have all of the knowledge needed to bring this work up to date. Thus, the help and collaboration of many have been essential to creating an updated version with a depth and breadth comparable to the original work. Luckily the same fascination Colpaert's work exerted over me is present in a whole generation of renowned metallurgists in our country. I met enthusiastic collaboration in companies, universities, and laboratories where people volunteered to help. This has certainly been one of the most interesting technical experiences of my career. A remarkable brotherhood of people interested in steel seems to exist all over the world; indeed, the willingness of people to help me, in Brazil and abroad, was outstanding.

To all of these collaborators, who have given essential contributions to this project, I offer my thanks in the next section.

Due to the difficult decision that had to be made regarding which images of the previous editions should be replaced or removed, Editora Blucher kept all of the old images available at their website.

I hope this revised and updated edition may be as useful to today's metallurgists as the previous editions have been to me, and to a whole generation of enthusiasts of steel and cast iron development.

Acknowledgments

It is extremely difficult to decide the proper order for acknowledging all who helped me on this project. Each of the groups or individuals have in some way contributed to the success of this work. Some helped with images, some with encouragement, and others with discussions and suggestions.

In the first place, I must thank Edgard Blücher and Hubertus Colpaert's family for trusting me with this task and staying with me along the way.

The support of colleagues from the steel industry in Brazil and other countries, with images and enlightening discussions, has been essential to this project. I present them by alphabetical order of the companies (using the company names in 2008).

In Brazil: Sergio Augusto de Almeida Ferreira, ArcelorMittal Aços Longos—Juiz de Fora; Francisco Boratto, ArcelorMittal Monlevade; Jardel Prata Ferreira and João Batista Ribeiro Martins, ArcelorMittal Brasil (Tubarão); Carlos Henrique Lopes, BR Metals Fundições Ltda.; Fátima Cunha, CBV-FMC—Rio de Janeiro; Walter da Costa Reis, Antonio Augusto Martins, Nilza Cristina S.B. Zwirman and Simone Pereira Santos, CSN—Volta Redonda; Luiz Antonio Iapichini and Cícero Tavares, FIBAM Cia. Industrial Ltda.—São Bernardo do Campo; Henrique Aché Pillar, MRS Logística—Rio de Janeiro; Mauro Souza, Neumayer-Tekfor—Jundiaí; Marcelo M. Moraes, NUCLEP—Itaguaí; Gerson Ronelli, PL Fundição e Serviços Ltda.; Marcelo Martins, Sulzer-Fundinox—Jundiaí; Wilson Guesser, Tupy Fundições S.A.—Joinville; Antonio Sérgio Fonseca, Alfredo Figueiredo, Ricardo Nolasco and Osvaldo Neto, V&M Tubes do Brasil—

Belo Horizonte; Marcos Stuart, Edson Mendes Vieira, Celso Barbosa, Leonardo Sandor, Ismael Polidori, and Cristiane S. Gonçalves, Villares Metals S.A.—Sumaré.

Outside of Brazil: M. Nishimura, Daido-Steel Co., Japan; James Casey, Dofasco, Canada; Giorgio Polonioli, Metalcam, Italy (Breno); Tooru Matsumiya and Masaaki Sugiyama, Nippon Steel, Japan; Carlos Cicutti, Tenaris, CINI, Argentina.

Laboratories: Research institutes and academia in Brazil and abroad have been very generous, sharing images, clarifying points, and showing great patience with my many urgings and requests.

Following is the alphabetical order of countries.

Belgium: Frans Mampaey, Sirris.

Brazil: André Pinto, Instituto Militar de Engenharia—Rio de Janeiro; Annelise Zeemann, Tecmetal—Rio de Janeiro; Antonio Gorni; Antonio Jorge Abdala, IEAv, CTA—São José dos Campos; Antonio Ramirez, LNLS—Campinas; Carlos de Moura Neto, CTA—São José dos Campos; Carlos Sérgio da Costa Viana, Paulo Rangel Rios, Tânia Nogueira, and Carlos Xavier, EEIMVR-UFF—Volta Redonda; Fernando Rizzo, PUC-Rio; Fernando Landgraf and Hélio Goldenstein, USP—São Paulo; Luiz Henrique Dias Alves; Margareth Spangler Andrade, CETEC—Belo Horizonte; Hans-Jurgen Kestenbach, UFSCar—São Carlos; Ibrahim Cerqueira Abud, INT—Rio de Janeiro; Ronaldo Antônio Neves Barbosa and Dagoberto Santos, UFMG—Belo Horizonte.

Canada: Alec Mitchell, University of British Columbia, Vancouver.

England: Graham Thewlis, South Yorkshire; H.K.D.H. Bhadeshia and Bill Clyne, University of Cambridge.

France: Bernard Marini and Caroline Toffolon, CEA; Jacques Lacaze, CIRIMAT, NSIACET, Toulouse.

Germany: Dietmar Lober; H.W. Viehrig, FZD, Dresden; Frank Mücklich and Alexandra Velichko, Universitaet des Saarlandes, Saarbruecken.

Italy: Paolo Emilio Di Nunzio, CSM, Roma; Stefania Bruschi, Università degli Studi di Padova, Padova.

Japan: S. Mizoguchi; Toshi Emi, IRIS, Sha-Steel; Fujio Abe, National Institute for Materials Science (NIMS); Kiyohito Ishida, Tohoku University.

Netherlands: Jilt Sietsma, Technische Universiteit Delft.

New Zealand: Milo Kral, University of Canterbury, Christchurch.

Poland: Leszek Zabdyr; Janina Radzikowska, Polish Foundry Research Institute, —Krakow.

South Korea: Sunghak Lee, Pohang University.

Spain, Tomas Gómez-Acebo, San Sebastian; Jon Sertucha, AZTERLAN—Durango; Carlos García de Andrés, Carlos Garcia-Mateo, Carlos Capdevila Montes, and Francisca G. Caballero, Materialia Research Group, CENIM-CSIC—Madrid.

Sweden: Mats Hillert and Malin Seleby, KTH, Stockholm.

United States: Sridhar Seetharaman and Eric Schmidt, Carnegie Mellon University, Pittsburgh; George Krauss, John Speer, Michael (Mike) Kaufman, John Chandler, Colorado School of Mines, Golden; Scott Chumbley, Iowa State University, Ames; Stephen W. Banovic and Ursula Kattner, NIST, Gaithersburg; Doru M. Stefanescu, Ohio State University, Columbus; Donald Koss and Zi-Kui Liu, Penn State University, State College; Alan Cramb, Rensselaer Polytechnic Institute, Troy; Donald Susan, Sandia National Laboratories, Al-

buquerque; Robert DeHoff, University of Florida, Gainesville; Christoph Beckermann, University of Iowa, Iowa City; Roger K. Pabian, University of Nebraska, Lincoln.

I thank all of you for the friendship, support, encouragement, suggestions, advice, patience, and interest in sharing your remarkable knowledge about metallography and iron and steel products. This has made a tremendous difference in this new edition. To anyone I might have forgotten, my apologies and my thanks!

Whenever possible, I have tried to give the proper credit in all images and refer to the proper texts used as the basis of this publication. There will likely be mistakes, for which I apologize in advance.

Finally, I thank my family for the support, patience, and encouragement over the long nights and weekends dedicated to this project.

André Luiz V. da Costa e Silva
Rio de Janeiro, August 2008

Preface to the Second Edition

Published in mid-1951 by the *Instituto de Pesquisas Tecnológias (IPT-SP)* [Technological Research Institute of São Paulo State], Bulletin no. 40 about the metallography of common iron and steel products has helped fulfill an important demand in the mechanical and metallurgical sectors, which needed a technical book that could serve as a manual for solving problems related to the properties and applications of iron and steel products.

Notwithstanding the fact that it has been solely distributed by *IPT-SP*, the first edition went out of stock in a few years, due to its high technical and scientific quality and the excellent documentation, all in a very didactic presentation format.

Although the guidelines to be adopted for the second edition had already been defined, the sudden passing away of the author in January 1957 rendered impossible the satisfactory conclusion of the revised work.

Having had the opportunity to collaborate with Colpaert for more than 12 years, having followed the lecture notes prepared by him that led to Bulletin no. 40, and being familiar with the use of this publication as a textbook, I was honored with the task of performing the revisions needed for this second edition.

In the first edition, some of the fundamental principles were presented in a simplified manner or even omitted. During use as a textbook, it was noted that this simplification in some chapters, such as the one on micrography and heat treatment, ended up creating barriers to the best understanding. This classroom experience suggested a complete revision of these chapters, particularly the one focused on heat treatments. The simplified presentation of transformation diagrams in the austenite decomposition processes that in the first edition was made in the form of a "critical segment" was replaced with the presentation of isothermal and continuous cooling transformation diagrams. The atomic mechanisms involved in these processes were discussed in more detail so that the changes observed by the metallographic examination could be better understood.

The chapter on cast irons could not be further improved because due to the complexity of the subject, from a didactic point of view, a simplified pre-

sentation that would offer a first view acting as a basis for further studies was preferred to a detailed discussion of the graphitization processes, which could make the text almost inaccessible to those being introduced to the subject.

Alberto Albuquerque Arantes
São Paulo, November 1959

Preface to the First Edition

During the recent and solemn commemoration of the 50th anniversary of this Instituto de Pesquisas Tecnológicas [Technological Research Institute], the beginning and the further development of various technological sectors of the institute were remembered. Among these, the field of microscopic metallography has received deserved attention; having started almost at the same time as this field was developed in Europe, it is one of the oldest in the institute.

It is an important fact that in 1910, the head of the Office of Strength of Materials, Hippolyto Pujol Jr., was already teaching and applying in the country such a novel science, far in advance of our industrial development. In 1926, it was up to Ary Frederico Torres to give further drive to these studies, creating strong interest and promoting the specialization of many students from the Polytechnic School [today the Polytechnic School of the University of São Paulo]. The author of this volume was among those and in 1928 was raised to the position of head of the Metallography Section.

In the past 25 years, the application and research work performed in the Metallography Section of IPT has resulted in a very refined technique and precise documentation with more than 10,000 macrographs and micrographs.

In addition to these activities, focused on the industrial segment, the Metallography Section has paid special attention to education, either teaching the students in various courses of the Polytechnic School or opening opportunities for interns who come here in search of deeper knowledge.

Among the educational resources, one that has been extremely successful is the distribution of illustrated pamphlets condensing the subjects presented in class. The simple and accessible presentation, not only of the metallographic technique but also of the laws and basic metallurgical facts—indispensable to the understanding of metallography and useful to the steel industry—quickly garnered great interest. This intertwining of steelmaking and processing concepts with specialized metallographic concepts may seem

strange at first, but at least in our community and for the time being, this is the orientation that has proven most efficient for the desired objectives.

After various successive editions of these pamphlets, and faced with an ever-increasing demand and the growing collection of experiments, the institute has decided to publish its material in a more permanent form and in more copies, asking the author himself to collect them, after revision and considerable expansion of the illustrations, in a printed volume that came to be the present bulletin.

Maintaining the initial aim, certain theoretical concepts are presented in a simplified way while others are omitted, not because they are useless but because they can be dispensed of in view of the character and aim of this publication.

To those wishing to research the problem more deeply, the cited bibliography, however small, offers additional information. After the bibliography, the conference proceedings and the specialized journals are yet additional sources which the reader can make use of to get properly familiarized with this constantly evolving science.

The macrographs and micrographs that were reprinted in Bulletin no. 40 were selected as among the most significant cases studied in the section. For each type of occurrence, many examples were presented to illustrate the variability that certain aspects may present and to warn the less experienced metallographer about the risk of possible confusion. In the choice and presentation of this vast documentation, it was our intention to offer to those interested a real atlas of "standard aspects" that could help in interpreting cases one might face in practice. Furthermore, there was always the aim of presenting the original documents in the best way possible, without reduction and with maximum sharpness, to make it easier for the reader to properly appreciate the features in the structures.

In the course of the text, the main errors related to technique and interpretation are discussed, along with their consequences and how to avoid them.

With the goals above described, the Instituto de Pesquisas Tecnológicas hopes to have extended the usefulness of this publication to all, whether in the plant or in the laboratory, who apply metallography.

Hubertus Colpaert
São Paulo, June 1951

About the Editor

André Luiz V. da Costa e Silva graduated as a metallurgical engineer from the Military Institute of Engineering (IME), Rio de Janeiro, in 1976. He earned his M.A.Sc. from the University of British Columbia, Vancouver, in 1979 and his Ph.D. from the University of Florida, Gainesvile, in 1994. His career started as an engineer in Eletrometal Aços Finos S.A. (currently Villares Metals S.A.). He was the materials engineering manager at CBV Industria Mecanica S.A. (Currently TechnipFMC plc) and took part in pioneer projects on deepwater oilfield completion and production. He was technical director of the Brazilian Institute for Nuclear Quality, where he was certified as a Level III Inspector and a Level III Expert in the Engineering Materials area. He is currently professor at the Metallurgical Engineering School in Volta Redonda, Universidade Federal Fluminense.

His main professional interests are the processing–properties relationships in materials and the application of computational thermodynamics to the processing and development of materials in special steels and superalloys, areas in which he consults for many organizations. He has published three books on steels and has more than 205 publications. André was the chair of the Alloy Phase Diagram International Commission (APDIC) from 2008 to 2013. He was awarded the 2014 Hume Rothery Award, for distinguished achievements in relation to phase transformations by IOM^3, England, and in 2017 became the fifteenth recipient of the triennial Hubertus Colpaert Silver Medal for his contribution in metallography and physical metallurgy by ABM, Brazil. He is a member of ASM International, ABM, and TMS. André is married and has one daughter and two grandchildren.

Metallography of Steels—Interpretation of Structure and the Effects of Processing
Hubertus Colpaert
Updated and Translated by André Luiz V. da Costa e Silva

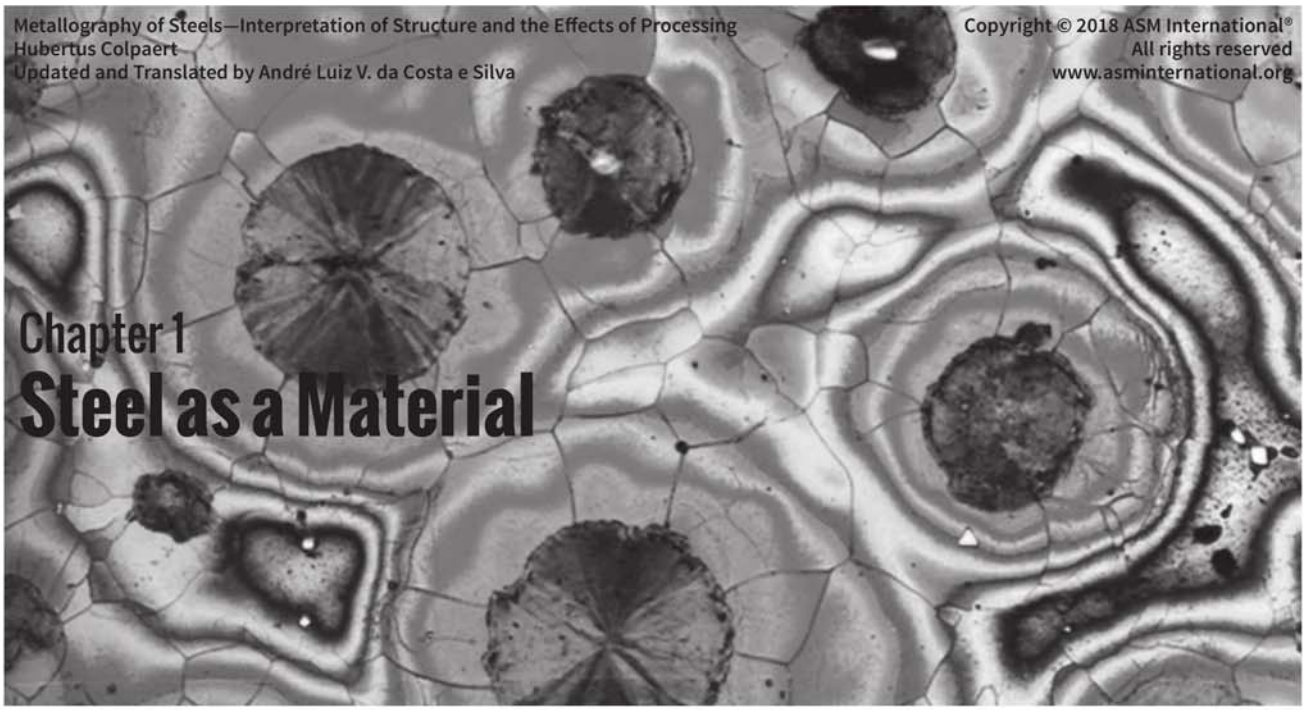

Chapter 1
Steel as a Material

Humankind has used iron products since at least 1200 B.C. Even though iron is one of the five most abundant elements in the Earth's crust by weight, occurrences of metallic iron in nature are scarce and normally associated with meteorites. Thus, to make iron products, humanity has developed processes to extract it from iron oxides, the most common iron ores. As the most common fuels in nature are rich in carbon, which under the right conditions can reduce iron oxides to metallic iron, carbon has played a decisive role in the development of products made of iron and its alloys.

The presence of carbon in the steps to manufacture iron-based products probably led to the observation that this element has important effects on the properties of iron alloys. This observation gave rise to the main iron-based alloys: steels and cast irons. Iron and its alloys have been produced for many centuries by artisanal methods that have comprised many different processes for *reducing* iron (i.e. converting it from an oxidized state) from its naturally occurring ores together with some mechanical work and some control of heating and cooling conditions (see Chapter 2, "Processes in Steel Production," in this book). A turning point came when it was noticed that substantial alloying with carbon significantly lowered the alloy melting point: this made possible, around the 18th century, the production of liquid iron alloys on an industrial scale and thus of large quantities of iron-based alloys. Thus, from around 40,000 t/yr in 1856, humankind entered the 21st century regularly producing 1,000 Mt/yr of steel. (Unless otherwise noted, the units of the International System, SI, are used in this book. Here, in particular, steel production is given in millions of metric tons.)

The evolution of steel usage as an engineering material is related to many technical and economic aspects. In particular, in the last decades of the 20th century, the accumulated knowledge of the relations between chemical composition, structures, properties, and performance, together with the effect of processing on these features, has reached a level that allows continuous scientific development of new alloys and improvement of available ones.

One of the important tools in this development has been (and still is) metallography. The understanding of the relationships between properties and structure in the scale of micrometers (μm, 10^{-6} m) to millimeters (mm, 10^{-3} m) depends largely on metallography, a science established on the basis of the initial research of Henry Clifton Sorby in Sheffield, England, around 1860. Together with a variety of other important tools for characterizing metals, metallography has become so essential to the understanding of the behavior of steels that almost all materials engineering courses dedicate a significant amount of time to teaching this topic. Furthermore, it is essentially impossible to find an industrial establishment producing or processing steel that does not rely on metallographic techniques at some stage of development, quality control, or failure analysis.

1.1 Steels and Cast Irons

For at least the last two centuries, iron-based *alloys* (mixtures of metals, or of a metal and another element that exhibit metallic behavior or have a metallic bonding character) have occupied an important position among industrial materials. The two main families of iron alloys are steels and cast irons. Steels are the most widely used iron-based alloys. One of the most important differences between steels and cast irons is the ability of steels to deform plastically.

Many factors contribute to the importance of steel as an industrial material. Iron ores are abundant, and modern steel plants have achieved low production costs. Furthermore, steels can achieve remarkable combinations of physical and mechanical properties. Today steels are also valued for their ability to be recycled. When steels are discarded, they degrade quickly to oxides that are not harmful; moreover, they require relatively low amounts of energy to be produced and even less to be recycled. Because most steels are magnetic, they are easy to separate from other materials during recycling. Thus, steel is a highly sustainable material.

The ability to properly manipulate steel characteristics to obtain the right combination of chemical composition and structure (at various scales) for a given application allows one to achieve extraordinary performance with steel, combined with outstanding combinations of physical and mechanical properties.

1.2 Structure

Structure is a fundamental concept in materials science, materials engineering, and metallurgy. Although the atomic structure is important in defining some aspects of material behavior, the classical study of structures begins at the crystalline structure level. Most metals and industrial alloys, including the vast majority of steels, are used in conditions under which the atoms are regularly organized in a lattice, forming a crystal. The way the atoms are organized in a metal or in an alloy determines several properties of the metal. Ferrous alloys having the face-centered cubic (FCC) structure, for instance, are nonmagnetic, whereas alloys with the body-centered cubic (BCC) structure are ferromagnetic at room temperature.

Structure—from the crystalline structure level (nm, 10^{-9} m)—plays a role in determining steel performance. However, steel items seldom are composed of a single crystal or even of a single phase. The way different crystals organize themselves in a polycrystalline material, their size and shape, as well as the amount of each phase that might be present in the material are the characteristics normally occurring in the range of dimensions conventionally referred to as *microstructural* (μm scale).

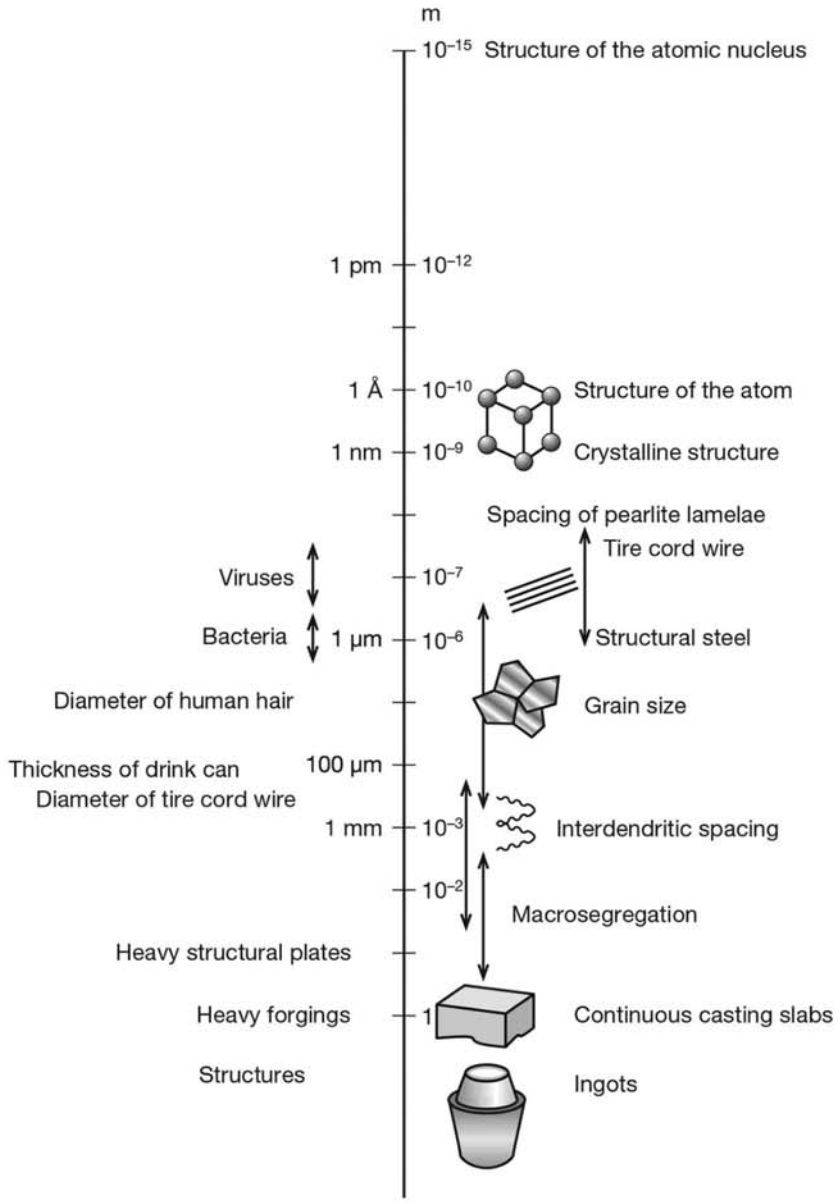

Fig. 1.1 Scales relevant to the structure of materials. On the left, the approximate dimensions of some objects are given as reference

The mass production of steel at rates compatible with a world production on the order of 1000 Mt/yr (1649 Mt in 2013) results in heterogeneities in chemical composition and properties in larger dimensions, at a scale conventionally called *macrostructural* (mm scale). Figure 1.1 schematically depicts steel structural features in the ranges discussed. Properly controlling structure (at all scales) is one of the most important tools for producing steels with proper properties and performance.

1.3 Crystal Structure of Iron-Based Alloys

Almost every metal exhibits, at ambient pressure (1 atm or 1.013×10^5 Pa), a single stable crystal structure from room temperature to its melting point. The most common metal structures are the FCC and hexagonal close-packed (HCP), both compact structures, and the BCC structure, which is not compact. In this respect, iron is exceptional in exhibiting polymorphism. Depending on temperature, iron can have two different crystal structures at ambient

pressure. At low temperatures (up to 910 °C, or 1670 °F) iron is BCC. Above this temperature, FCC becomes more stable. At temperatures above 1394 °C BCC becomes stable again, up to the melting point of iron at 1535 °C (2795 °F). Thus, different *phases* (regions of a material that are chemically uniform and physically distinct) of iron are stable at different ranges of temperature and pressure (Fig. 1.2).

Causing and controlling the transformations between these two structures is one of the most important and most widely used tools in the control of steel product microstructure. How atoms are arranged in a given crystal structure depends on how these atoms interact. When other elements are mixed with the iron atoms, forming an alloy, the relative stability of the different phases is changed. Carbon addition to iron, for instance, causes important changes in the relative stability of iron phases and introduces the possibility of new phases forming. One of the ways of representing these changes is through a *phase equilibrium diagram*, as shown in Fig. 1.3. This diagram shows that carbon additions of up to around 4.2% (mass percent, as are all compositions in this book unless otherwise noted) lower the melting point and that additions up to around 0.8% C increase the stability of the FCC phase with respect to the BCC phase. Thus, adding alloying elements to iron allows one to tailor the relative stability of the phases and affect the structure that will be formed in a steel. These elements have other important effects, which are discussed in more detail later.

1.4 Steel Characterization

The combination of chemical composition and structure defines steel properties. Many analytical chemistry methods and techniques can be used to characterize chemical composition. Structure can also be characterized by a

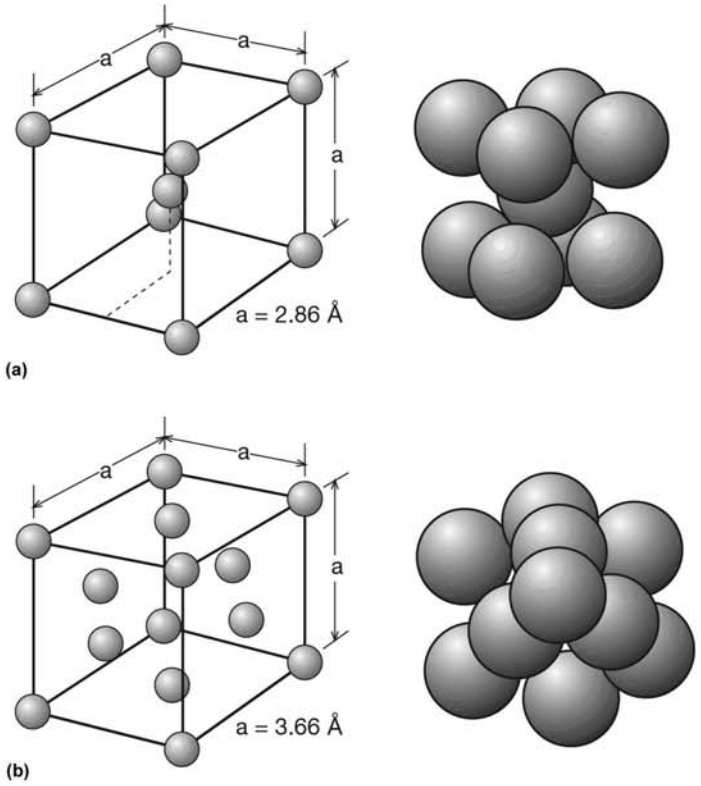

Fig. 1.2 (a) Body-centered cubic (BCC) structure. The lattice parameter for pure iron at room temperature is 2.86 Å. (b) Face-centered cubic (FCC) structure. The lattice parameter for pure Fe at room temperature is approximately 3.66 Å.

wide range of techniques, depending, among other factors, on the scale of the structure. Table 1.1 presents some structural characterization techniques related to the dimensional scale at which they are applicable. Metallographic techniques (both micro- and macrographic) are applied to the structure characterization at the microscopic and macroscopic scales, respectively. The structural characteristics that are most relevant to the development and control of steel features are in the range of 10 nm to 1 mm. For this reason, metallography has a paramount role in steel characterization. The various metallographic characterization techniques are discussed in more detail in Chapter 4, "Metallographic Technique: Macrography," Chapter 5, "Metallographic Technique: Micrography," and Chapter 6, "Metallographic Technique: Electron Miscroscopy and Other Advanced Techniques," all in this book.

1.5 Chemical Composition of Steels

Besides carbon, which is not always a desirable alloying element, many chemical elements may be present in a steel. Elements not intentionally added are called *residuals*. Elements added to steel to affect its behavior are usually called *alloying elements*. However, many elements that are not classified as residuals or alloying elements are critical to the behavior of steels and are frequently omitted from discussions on steel chemical compositions. Figure 1.4 lists the main functions of alloying elements as normally accepted. Besides these, elements coming from scrap (such as copper, arsenic, antimony, zinc, and lead) and those coming from the atmosphere (such as nitro-

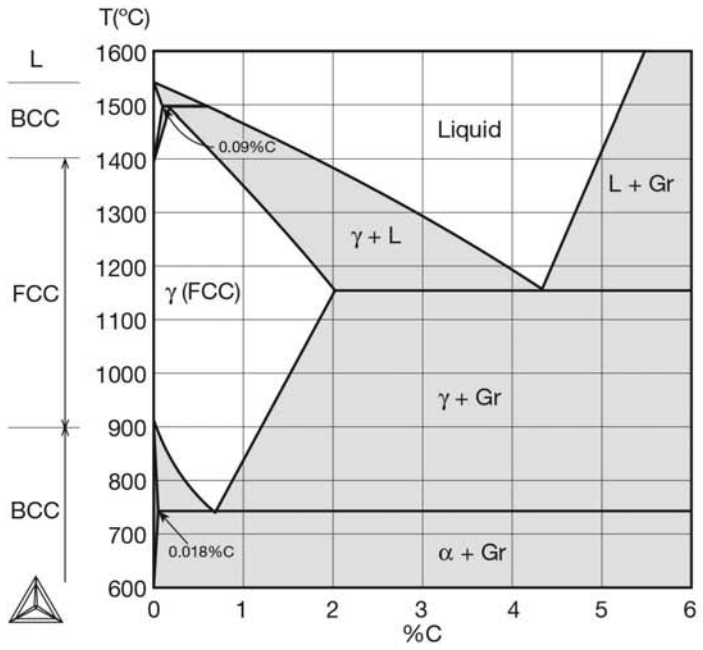

Fig. 1.3 The Fe-C phase equilibrium diagram at 1 atm. The phase transformations of Fe are indicated on the vertical axis (0% C), corresponding to pure Fe. The range of temperatures in which FCC (called γ, or austenite) is stable increases with the addition of C up to around 0.8%, and then decreases. The BCC phase (called ferrite) is able to dissolve only 0.018% C in its low-temperature range (α). Above this limit, other phases are more stable and are formed. The metastable Fe-C phase diagram is frequently used and is discussed in Chapter 7, "Equilibrium Phases and Constituents in the Fe-C System," in this book.

Table 1.1 Structural characterization techniques usually employed for metals

Scale (approximate dimensions)	Characterization techniques
Crystalline structure (Å)	X-ray diffraction Transmission electron microscopy (electron diffraction)
Structural features in the range of 10–100 nm (dislocations, stacking faults, ultrafine grains, etc.)	Transmission electron microscopy
100 nm–1000 μm	Scanning electron microscopy Atom force microscopy
1–1000 μm	Optical microscopy Confocal laser microscopy
1–1000 mm	Macrography

gen, hydrogen, and oxygen, the last of which is the main refining agent in steelmaking and dissolves significantly in liquid steel; see Chapter 2, "Processes in Steel Production") also must be considered when discussing residuals in steels. Several elements can be residuals in some steels and deliberate additions in others. For instance, copper is added to weathering steels to promote the formation of a patina. Also, lead can be used to promote machinability, although this use is declining because of its environmental impact.

The main effects of elements added to steel, summarized in Fig. 1.4, are discussed in detail in the following chapters.

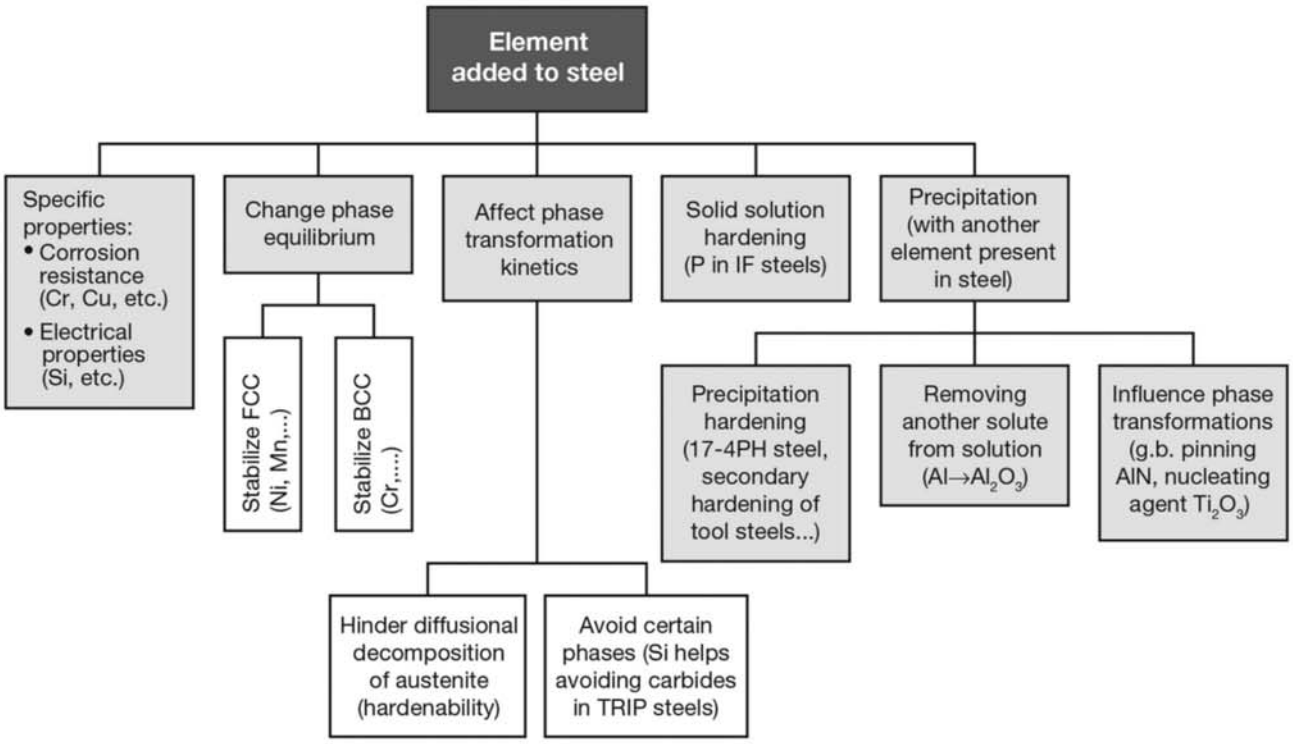

Fig. 1.4 Schematic presentation of the main effects and functions of chemical elements added to steel. In parentheses, some specific examples of each function are presented. Evidently, some elements have more than one function in the alloy design of a given steel.

Metallography of Steels—Interpretation of Structure and the Effects of Processing
Hubertus Colpaert
Updated and Translated by André Luiz V. da Costa e Silva

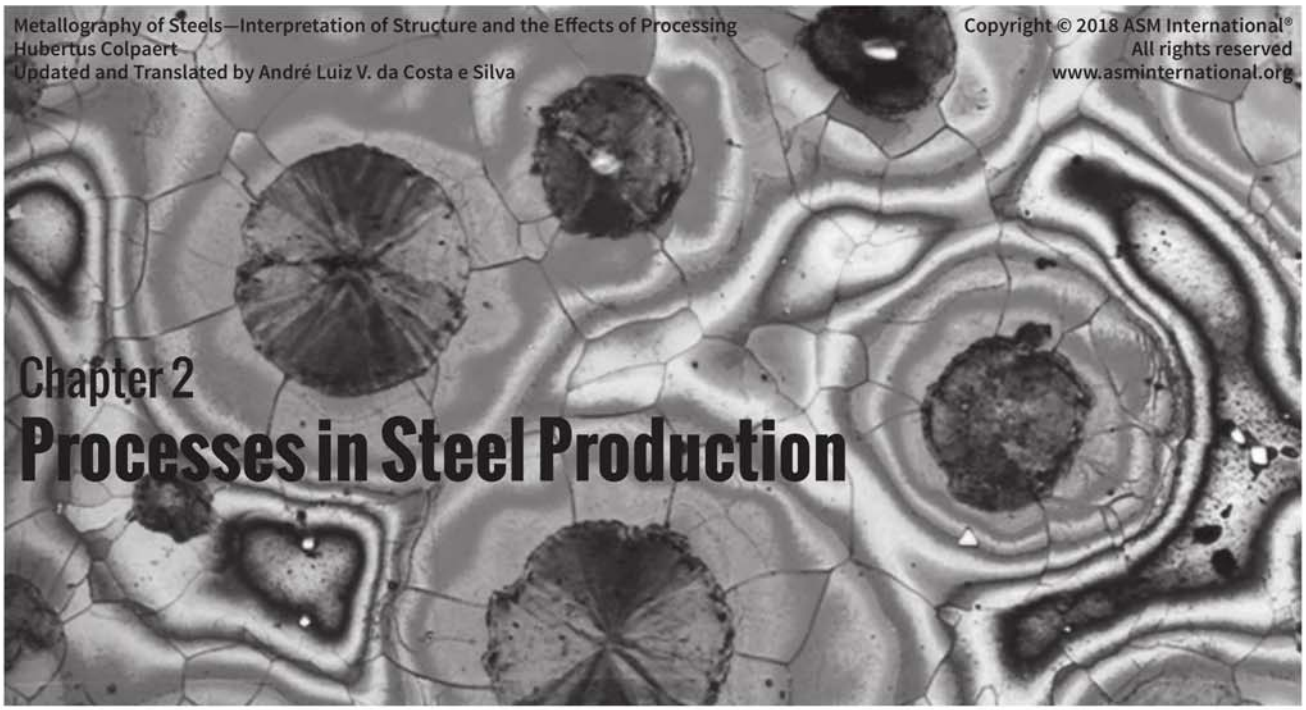

Chapter 2
Processes in Steel Production

The classical definition of *steel* is "an iron-carbon alloy with up to [about] 2% carbon" (Ref 1). This limit is taken from the maximum solubility of carbon in the FCC structure (austenite, refer to Fig. 1.3). Iron-carbon alloys with higher carbon content will have a lower melting point, are adequate to casting processes, and normally are called *cast irons*. The addition of other alloying elements affects this limit. For this reason, the definition of steel based on this chemical composition limit should be restricted to the so-called *carbon steels*.

In the past, alloys with low carbon content used to be known as irons. In recent decades, the ability of refining processes to systematically attain very low carbon contents has led to the development of the interstitial-free (IF) steels, in which maximum carbon content is in the range of tens of parts per million in mass. This evidently challenges the definition presented above because carbon is almost a residual element in these steels. On the other hand, the traditional view that steels are alloys that can be formed in a plastic way (Ref 2) is also questioned by the evolution of cast irons: nodular cast iron, for instance, can have outstanding combinations of strength and ductility (see Chapter 17, "Cast Irons," in this book).

This discussion is relevant because of the importance of iron-based alloys (steels and cast irons) as engineering materials and their constant evolution. While steels are the most widely used iron-based alloys, about 70% of all cast metal production consists of cast irons (Ref 3).

Although iron artifacts have been produced on a small scale from meteorites, it was only the ability to extract iron from its ores and, more important, the ability to obtain a liquid product that made viable the production of iron and later steel on a significant scale. Large furnaces able to reduce iron ore to metallic iron in the liquid state were developed starting around the 14th century. This made possible the easy removal of the metallic product from the furnace and, at the same time, the casting of the product in the desired shape.

Two factors made liquid metal production possible in these furnaces:

- The larger size of the reduction furnaces and the use of coal or coke (instead of wood) as fuel and reducing agent dramatically increased thermal efficiency, resulting in a higher temperature inside the furnace.
- Excess carbon (i.e., beyond that needed to burn with injected air and react with the oxygen in the ore) and reducing conditions inside the furnace made it possible for the iron to dissolve a large amount of that element (Ref 4), significantly lowering the metal melting point (refer to Fig. 1.3).

Liquid iron produced this way is rich in carbon and contains undesirable impurities, leading to a product with somewhat limited properties. These developments, however, were decisive in making iron casting viable and triggering the development of refining processes for steelmaking.

2.1 Reduction Processes

The combination of an iron ore reducing process with metal refining processes has created the modern concept of a steel mill, schematically presented in Fig. 2.1.

Presently, there are two main routes to make iron from iron ores: the blast furnace and the direct reduction processes. As iron in the ores is in an oxidized state (Fe^{+3}, Fe^{+2}), the chemical reaction that transforms it into metallic

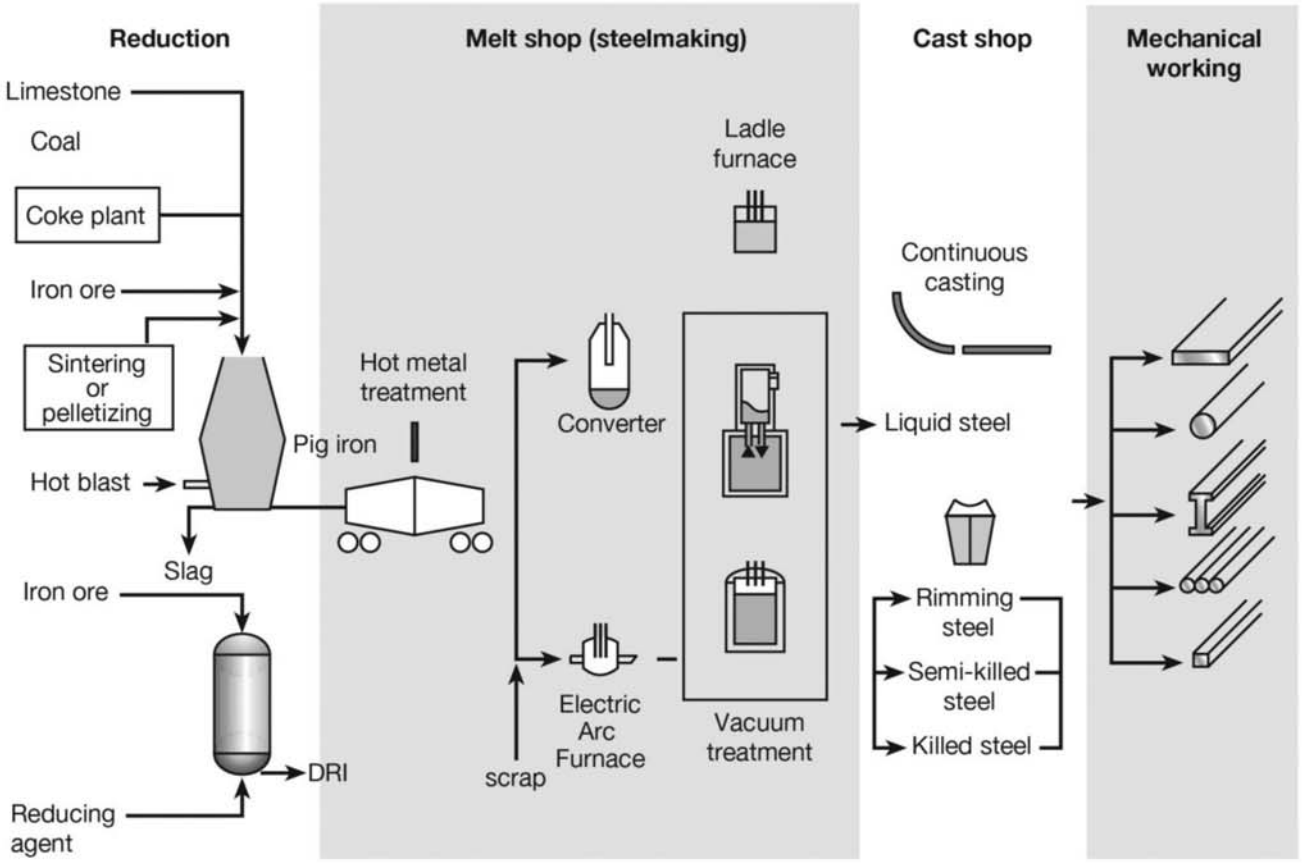

Fig. 2.1 Flowchart of steel production including the various options for each step. Evidently, not all steel plants have all the listed equipment or processes.

iron (Fe^0) is a reduction reaction, and such processes are therefore called reduction processes.

2.1.1 The Blast Furnace

The classical process for reduction of iron ores takes place in the blast furnace, which is the result of more than 500 years of technical development. In a blast furnace, iron oxide is reduced by gases generated from coke (a product of the controlled distillation of coals) or charcoal and additions of powdered coal. Injecting air (or oxygen-enriched air) through tuyeres in the lower part of the furnace oxidizes part of the carbon introduced in the furnace, thus promoting an increase in temperature. A mixture of reducing gases is formed and rises to react with the oxides. The result of the reduction process is collected in liquid form in a crucible (for a detailed description, see Ref 4). The highly reducing conditions prevailing inside the furnace are such that a large part of the phosphorus in the iron ore and the sulfur from the coke and coals is incorporated in the liquid metal, pig iron. Several other impurities are collected in a slag with a chemical composition properly adjusted by careful additions.

Depending on the operating conditions of the blast furnace, silicon and manganese recovery into the pig iron can vary. In large steel mills, a balance must be reached to optimize the economics of the pig iron production and the needs for further refining in the steelmaking processes. Generally the pig iron produced in large steel mills is used only as an intermediate product for steelmaking, not as a material for the direct production of cast parts.

Figure 2.2 shows the scheme of a blast furnace and an approximate mass balance for this process. Temperature gets sufficiently high for liquid metal to drop through the lower part of the furnace, where it is collected in the hearth. A mixture of the nonreduced impurities and fluxes added to the charge leads to the formation of a liquid slag. Density difference and surface tension between the liquid metal and the slag favor phase separation, making it possible to tap the metal and the slag out of the furnace independently, through different openings designed for these purposes.

The actual sequence of processes taking place inside a blast furnace is complex. Only since the 1960s has there been a good understanding of these processes. Coke gasification, combustion, solid-state reduction of the iron ore followed by liquid-state reactions, and the interactions between liquid metal and slag are some of the complex processes affecting the overall result of a blast furnace process. Thus, the chemical reactions presented in Fig. 2.2 are a representation of the macroscopic thermodynamic equilibria driving the system and not an exact description of the processes occurring inside the furnace. Metal residence time can reach values of up to 12 hr, so the response time of the furnace adds to the process complexity.

2.1.2 Direct Reduction Processes

In contrast to blast furnace processes, reduction also can occur when the metal is produced in the solid state. These are called direct reduction processes. Historically, direct reduction was developed before blast furnaces and the production of liquid pig iron. However, it took a long time for these

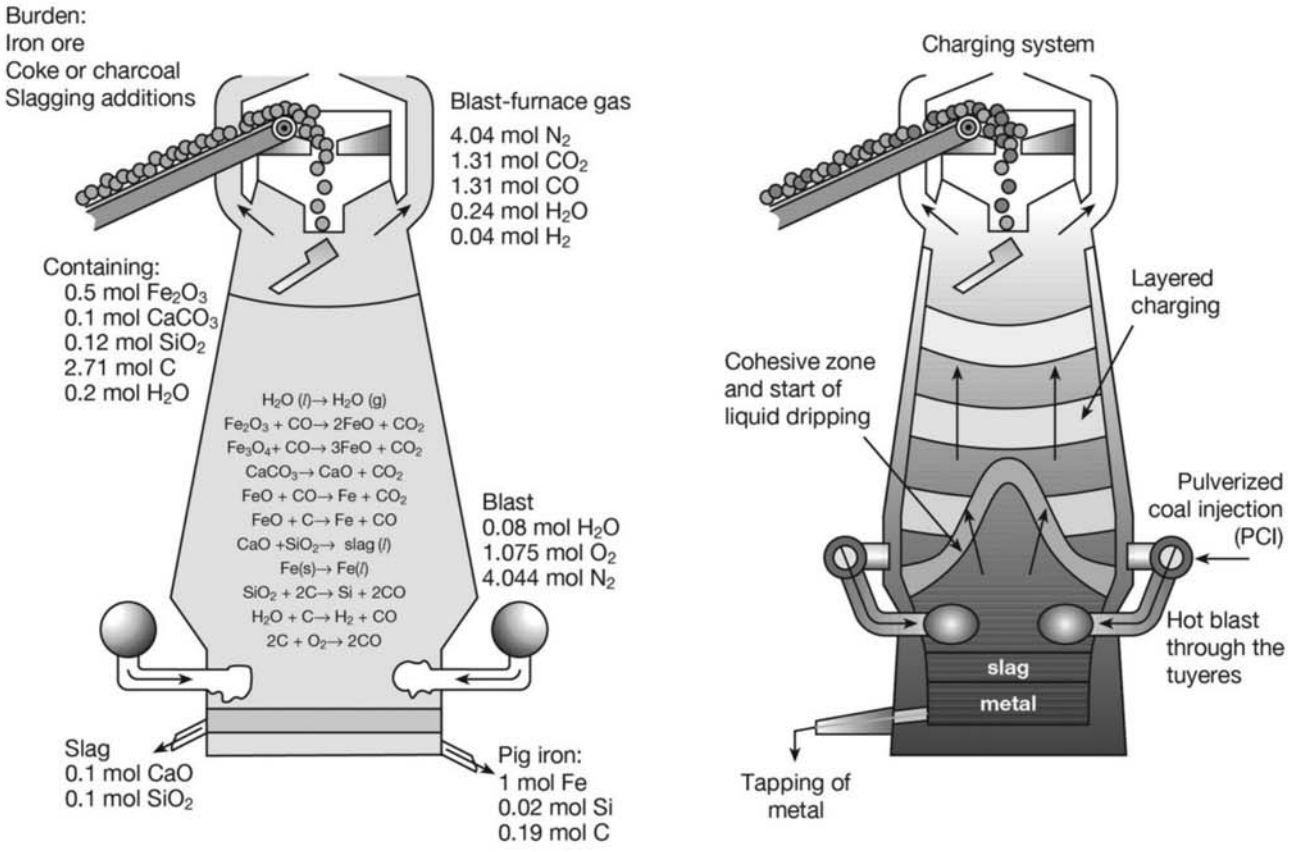

Fig. 2.2 The iron blast furnace process. Left: typical mass balance for the production of 1 mol of iron contained in the tapped pig iron. Right: physical arrangement of the process.

processes to evolve to the level needed for large-scale production and they were overtaken by the blast furnace.

The product of direct reduction is a porous solid mass with the approximate shape of the iron source charged in the reactor. This product is called direct-reduced iron (DRI) or, more true to its physical aspect, sponge iron. Recently direct reduction processes have benefited from carburizing the produced iron, so that a certain fraction of Fe_3C (cementite) is formed. This carbide has a lower melting point than the metallic iron. When charged to electric furnaces (see the section "The Electric Arc Furnace" in this chapter), the usual refining process of choice for DRI, it enhances DRI melting and brings important carbon to the energy balance. This improvement in melting behavior and the additional fuel incorporated as carbon improve the performance of DRI in electric furnaces. A drawback of direct reduction is that because DRI is solid, a significant portion of the impurities in the iron source for the process (ore, pellet, etc.) is retained in the final product. Currently, DRI is used as a charge for steelmaking (or refining) processes, mostly in electric furnaces.

Historical Direct Reduction Products

Steelmaking and steel refining processes encompass not only decreasing the content of undesirable solutes, such as carbon, sulfur, phosphorous, and

silicon, but also increasing the metal temperature to be able to keep it liquid as the carbon content is decreased, as shown in Fig. 2.3.

Until the end of the 19th century and the beginning of the 20th, before the melt shops and refining processes that are today ubiquitous, lower-carbon iron products were commonly manufactured through forging or roughing. (This sort of forging was performed in a forge, an open furnace for heating metal ore and/or metal for working and forming; confusingly, the term "forging" also is used to refer to a metal-forming process.) In these forges (such as the *Catalan forge*, sometimes called the Spanish forge), the charge was made of iron ore, charcoal, and a fluxing agent such as limestone. The fluxing agent was added to try to lower the melting point of the ore impurities and hopefully make it fluid (or at least more plastic) so it would separate from the metal. Iron produced this way had a low carbon content and a significant amount of slag inclusions, but also had very high plasticity compared with the carbon-saturated variety. This made possible the hot working of the iron in a forge, the product so obtained being called wrought iron.

Later, the process was improved when decarburization of cast iron was developed. Probably the most remarkable was the invention of Henry Cort in the 18th century (Ref 5), although it apparently had existed in 1st-century China. In reverberatory furnaces (in which the metal was heated from above; also called puddling furnaces), iron ore, iron scale, or iron scrap was added to liquid pig iron, together with fluxes. The oxidizing additions would decrease silicon, manganese, and carbon content. The reverberatory furnaces did not reach high enough temperatures, however. Thus, as carbon content was decreased, the product would become more viscous or even solid. This product, a mixture of decarburized iron containing some oxide inclusions, was taken

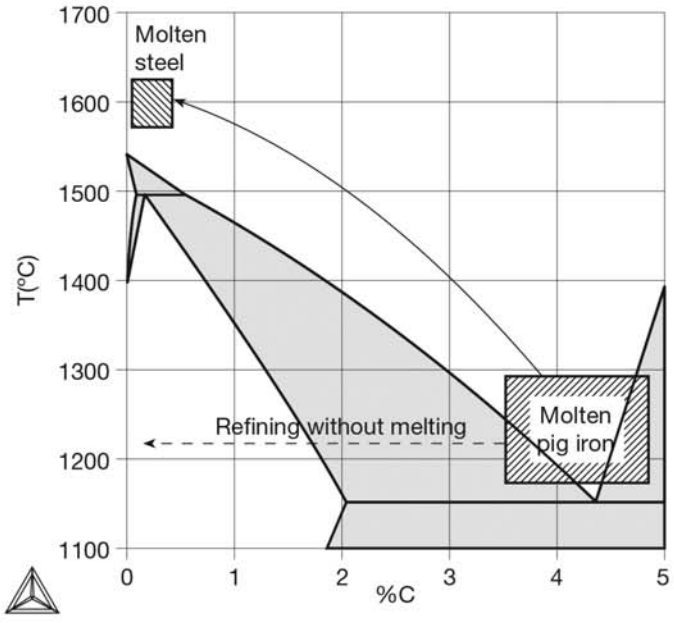

Fig. 2.3 Steelmaking, in the melt shop, involves chemical composition changes and increase in temperature to keep the charge in the liquid state. In older ironmaking processes, refining was conducted without reaching the liquid state. Residues such as slags were retained in the product.

to a forging shop and formed to the desired shapes (Ref 6). Figures 2.4 and 2.5 show the microstructure of the products obtained this way.

2.2 Steelmaking

In the mid-19th century, Sir Henry Bessemer developed and patented a process that could "convert" pig iron in steel by injecting air at room temperature through molten pig iron, without the addition of fuel of any sort (Ref 9).

The process took place in a cylindrical vessel, similar to modern converters. Air was blown through tuyeres at the bottom of the furnace. To keep these tuyeres unobstructed at all times, Bessemer devised the rotating furnace, which could lower its opening during charging in such a way that a constant air flow could be kept through the tuyeres at all times. Later the process was further developed by introducing basic refractories, making possible the dephosphorization and limited desulfurization of the metal. (With some ores, phosphorous oxidation made an important contribution to the converter energy balance.)

Air blowing had two important drawbacks. First, because of nitrogen's solubility in liquid iron, the refined metal absorbed a significant amount of nitrogen during the process, with undesirable effects on the mechanical properties of the steel (Ref 1). Second, a significant heat loss was associated with heating the nitrogen gas that left the furnace unreacted. This drawback limited the use of scrap in the charge of the Bessemer furnace and similar converters using air as an oxidant.

At about the same time, William Siemens, in England, was able to develop a furnace that used the heat from burned gases for preheating the incoming

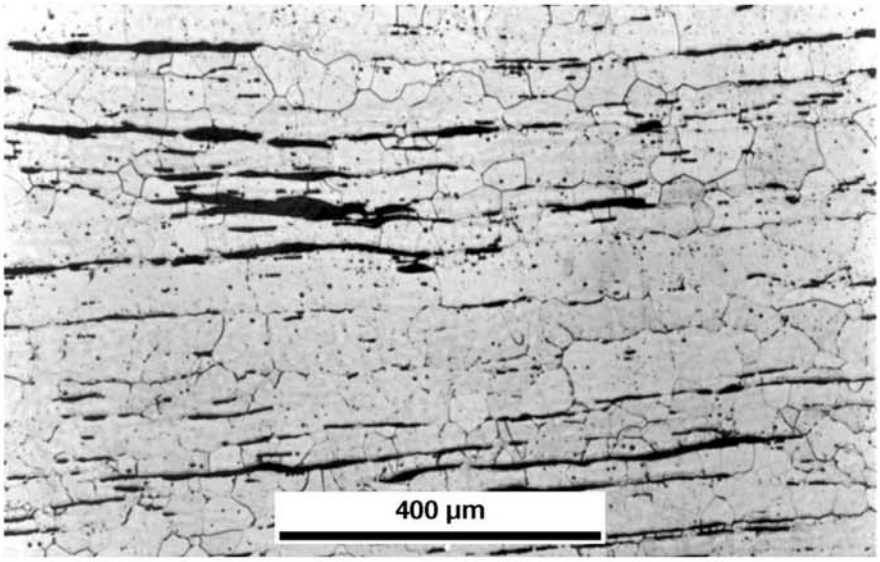

Fig. 2.4 An example of wrought iron. The matrix is ferrite with very low C content. A large amount of silicate-based nonmetallic inclusions (the slag of the refining process) can be seen. The inclusions are elongated in the major working direction (see Chapter 11, "Hot Working," in this book) as they were plastic at the work temperature. Etchant: 2% nital. Courtesy of DoITPoMS, Department of Materials Science and Metallurgy, University of Cambridge. Source: Ref 7

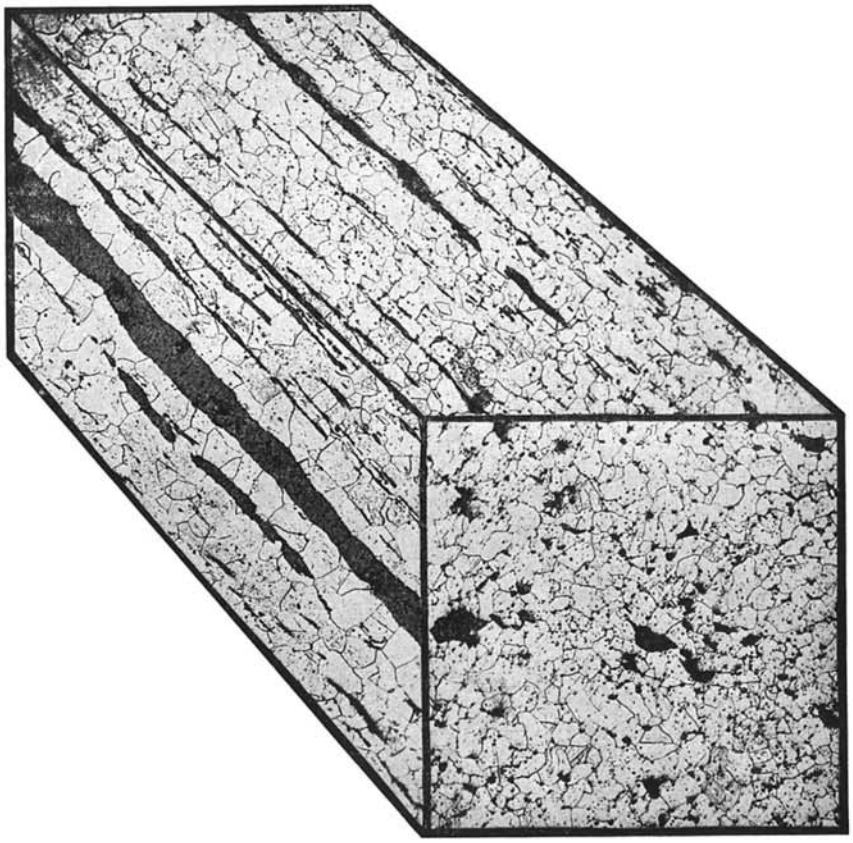

Fig. 2.5 Wrought iron. Tridimensional reconstruction using three mutually perpendicular micrographs. The elongation of the nonmetallic inclusions in the major working direction can be seen. Source: Ref 8

air to the burners. This design significantly increased the flame temperatures in these furnaces. It involved regenerator chambers, with checker brick assemblies inside them, through which, alternately, hot combustion gases or air to be preheated would flow. The same concept was being developed simultaneously aiming at the use of "hot blast" in blast furnaces, an invention that Edward Cowper patented in 1857 (Ref 10). With the same technology as Siemens, Pierre-Émile Martin, in France, developed a furnace that was able to reach liquid steel temperatures. In Europe, this became known as the Siemens-Martin furnace and in the United States, as the open hearth or basic open hearth furnace (BOH).

The development of large-scale oxygen production (that could be blown economically in converters (see the section "Oxygen Converters," next) and the price increase of the fuels usually employed in the BOH led to its almost complete disappearance by the 1970s.

2.2.1 Oxygen Converters

Oxygen started to be separated from air in an economical way in the 1930s and 1940s. The first industrial converter able to use the large-scale "industrial" oxygen that become available after World War II (around the 1940s) was

the LD converter (known in English as the basic oxygen furnace, BOF), named after Linz and Donawitz, the two Austrian cities where it was developed by Vöest-Alpine (Ref 11). In these converters, oxygen is blown on top of the liquid metal using a water-cooled lance. When the blow is properly controlled (via adjustments of lance height and oxygen flow) an iron oxide–rich slag is produced, which is followed by the formation of an emulsion comprising liquid metal, slag, and gas. The refining reactions take place extremely rapidly in the emulsion. Blow times of around 20 min and a tap-to-tap time in the range of 35–40 min are standard in the industry. (Tap-to-tap time is an important indicator of furnace productivity. It encompasses the time from tapping one heat from the furnace until the tapping of the next heat from the same furnace, so that all relevant operations—charging, analysis, refractory repair, etc.—are properly accounted for.)

When oxygen converters were first introduced, it was not feasible to use the bottom-blow technique developed by Bessemer, which otherwise would have been the obvious next evolutionary step. The rapid exothermic reactions at the region of injection, very close to the tuyere, created a harmful condition for the furnace refractories: the combination of high temperature and high FeO content, an excellent flux to basic oxides like those used as refractories. This difficulty has delayed the development of bottom-blown oxygen converters. Only with the development of concentric tuyeres, which made possible localized cooling using hydrocarbons, have bottom-blown converters (Fig. 2.6) become commercial. The most popular of these is the quick basic oxygen process (Q-BOP) converter.

Figure 2.7 summarizes the evolution of refining reactions in a typical oxygen converter. The main reactions taking place are oxidation reactions, which

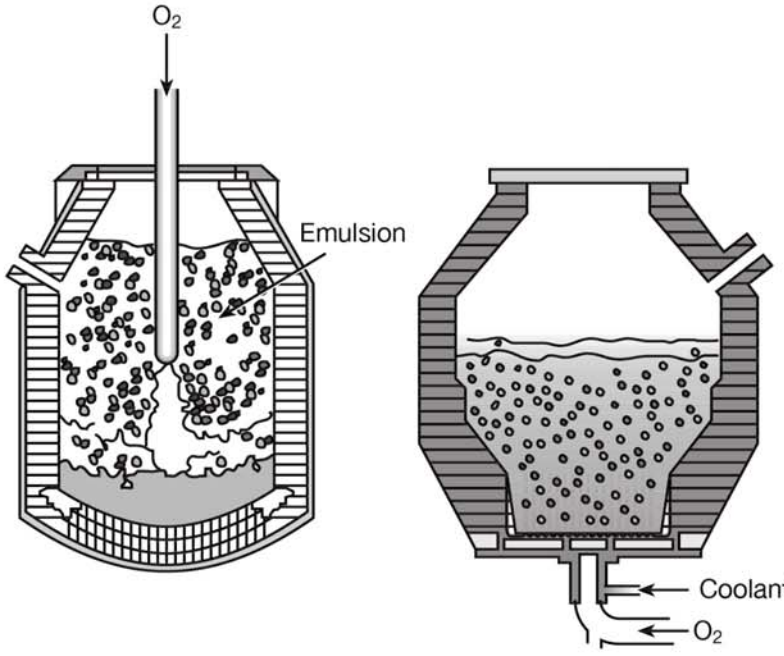

Fig. 2.6 Oxygen converters. BOF (LD) converter with top blowing of oxygen, and Q-BOP converter where oxygen is injected through the bottom of the converter.

occur because of the oxygen blow, and those involving the slag, formed by lime added to the charge, in combination with oxidation products.

Because the main refining reactions are oxidation reaction, the significant solubility of oxygen in liquid iron is one of the most important factors in making possible the very high rates at which the refining processes take place.

In the Fe-O phase equilibrium diagram in Fig. 2.8, it is evident that liquid iron can dissolve up to around 0.2% oxygen at 1600 °C (2910 °F), a typical temperature in the range of steelmaking processes. The very low solubility of oxygen in solid iron, however, requires special attention to the deoxidation processe to avoid important defects in the steel produced (see the section "2.2.2 The Electric Arc Furnace" in this chapter).

Conversion processes approach the thermodynamic equilibria described in Table 2.1 but do not reach them. In particular, the equilibrium between carbon and oxygen dissolved in the steel (with CO) and the dissolved oxygen and iron oxide (mostly FeO) have significant consequences for the efficiency of the process: higher FeO contents in the slag, for instance, will result in higher iron losses in the process. In this respect, the Q-BOP process has a significant advantage over the LD (BOF) process as shown in Fig. 2.9, where typical ranges of "end-of-blow" states are presented. On the other hand, higher metal oxidation and higher FeO favor early slag formation and good dephosphorization observed in the LD (BOF). Once the reasons for these differences became evident (Ref 12), mixed (or combined) blow processes (in which some inert gas is blown through the bottom of BOF furnaces) became the rule, improving their metallic yield and the approach to the C + O = CO equilibrium, approaching the results of Q-BOP in these aspects.

Le Chatelier's principle, or the law of mass action, can be stated as follows: when a system in equilibrium is subjected to a change the position of equilibrium will move in such a way as to counteract the change. (The term "mass action" can lead to some confusion because, in most cases, it will be the chemical potential or the activity that will cause changes in the equilibrium.

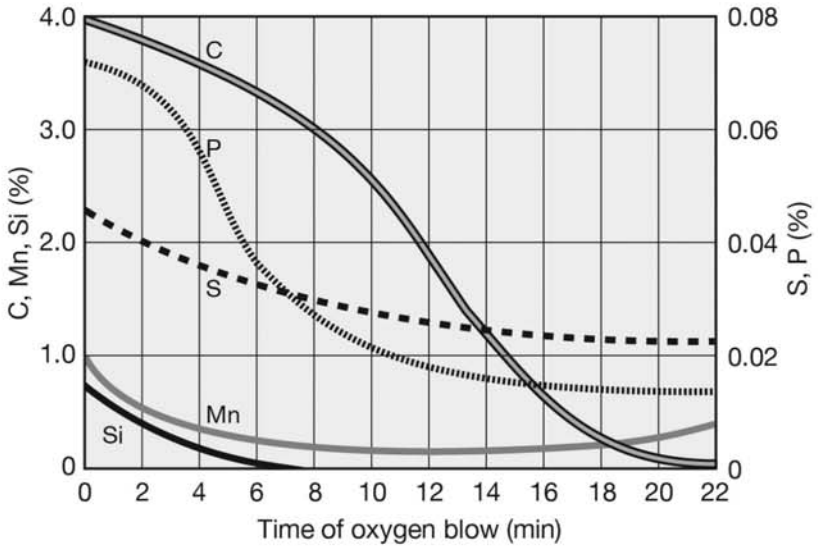

Fig. 2.7 Evolution of liquid metal chemical composition during refining in a converter.

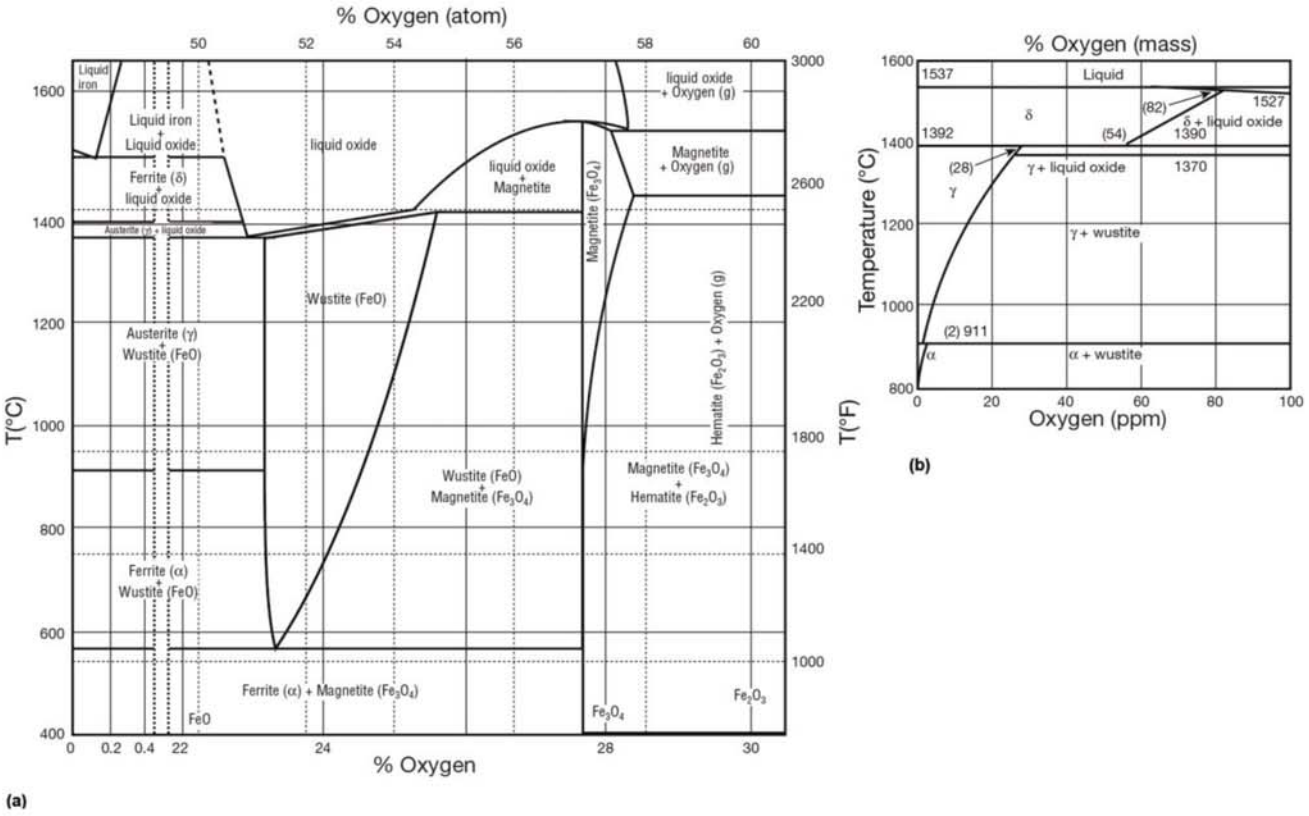

Fig. 2.8 Fe-O equilibrium phase diagram. (a) Solubility of oxygen in liquid iron and the various oxides formed. (b) Magnification of the iron-rich corner, between 0 and 0.01% (100 ppm) oxygen. The very low solubility of oxygen in all solid phases of Fe is evident. Source: Ref 13, 14

Table 2.1 Main reactions in steelmaking processes

$\underline{Si} + 2\,\underline{O} \leftrightarrow (SiO_2)$ (1)	
$Fe + \underline{O} \leftrightarrow (FeO)$ (2a)	$Fe + CO \leftrightarrow (FeO) + \underline{C}$ (2b)
$\underline{P} + 2\,\underline{O} + 3\,(O^{-2}) \leftrightarrow (PO_4^{-3})$ (3a)[a]	$2\,\underline{P} + 5(FeO) + 3\,(CaO) \leftrightarrow (CaO)_3(P_2O_5) + 5\,Fe$ (3b)
$\underline{C} + \underline{O} \leftrightarrow CO\,(g)$ (4)	
$\underline{S} + (O^{-2}) \leftrightarrow \underline{O} + S^{-2}$ (5a)[a]	$\underline{S} + (CaO) \leftrightarrow \underline{O} + (CaS)$ (5b)

Note: Underlined elements are dissolved in the liquid metals. Species in parentheses are dissolved in slag. (a) Reactions based on the ionic theory of slags.

See Ref 13, 14 for a more accurate discussion.) This principle can be used for a semi-quantitative understanding of the progress of refining reactions. Thus, when the products of a given reaction dissolve in slag, lowering their activities of chemical potential, the chemical reaction will change in the direction of forming more of the products (to increase the activity) to minimize the ef-

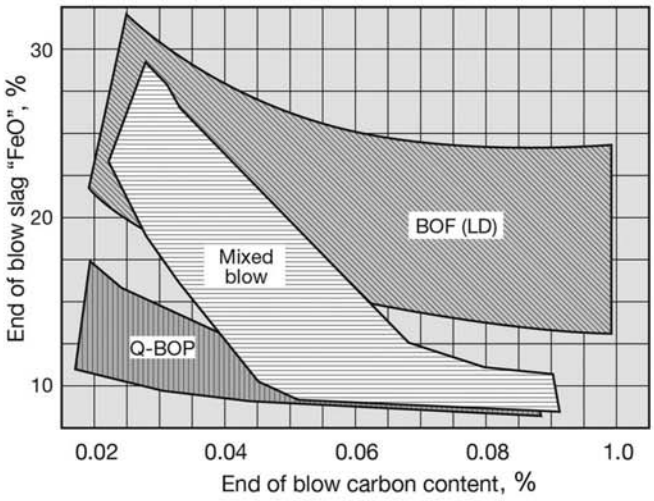

Fig. 2.9 Relationship between FeO in slag and end-of-blow C for different types of converters (different converters approach in different degrees the equilibrium of reactions 2a and 2b in Table 2.1). Source: Ref 11

fects of the change. Conversely, when the chemical potential or activity of a reactant is increased (by dissolving more oxygen in the steel, for instance) the reactions will change in the direction associated with the consumption of the reactant (to reduce the activity). Thus, basic slags (with high CaO contents) are used, because they have high solubility for the species listed in Table 2.1. Furthermore, basic slags contain the O^{-2} ion, a critical reactant both in usual dephosphorization and desulfurization reactions.

Another example is the examination of the effect of dissolved oxygen on the desulfurization reaction (reactions 5a or 5b, Table 2.1). Because a high content of dissolved oxygen is encountered in steel in the converter and is a reaction product in reactions 5a or 5b, desulfurization will not be favored in converter steelmaking.

2.2.2 The Electric Arc Furnace

The electric arc furnace (EAF) is arguably the most versatile steelmaking tool presently in use. In recent decades, it also has become one of the most efficient. Some of the main advantages of the electric arc furnace are:

- High energy efficiency.
- Almost any type of steel can be produced in this furnace, because heating can be controlled largely independently from chemical reactions.
- It is extremely versatile concerning its charge. While it is nomral to operate it with 100% solid charge (scrap, solid pig iron, DRI, etc.), some EAFs operate with a substantial portion of liquid pig iron in their charge.
- Interruptions in the production schedule are not exceedingly complicated and production schedules can be changed without dramatic impact on the rest of the plant.

- EAFs are commercially viable from tens to hundreds of tons of capacity, depending mostly on local economic variables and product mix.

The continuous growth of the number of EAF melt shops and its share of world steel production in the past decades as well as the introduction of bigger furnaces (200–250 t) are evidence of the relevance of this process.

The flexibility of the arc furnace combined with the possibility of controlling temperature without resorting to chemical reactions (as oxidation in the converter) have, over decades, made the EAF the furnace of choice for steels that required careful refining (such as low P and low S steel) and alloying (such as medium- and high-alloy steel).

As these furnaces evolved toward the end of the 20th century, however, they were optimized as melting instruments. Tap-to-tap times shorter than 50 min were reached by the end of the 1980s with 100% solid charge. When optimizing the heat balance and the energy cost of these furnaces, the contribution of oxidation reactions has reached around 35% of the total energy input, and oxygen usage came very close to that of converters (40 Nm^3/t metal, where the quantity of oxygen is given by volume and the "N" represents not Newtons but "normal – STP- (conditions)").

These developments made the EAF less than economical for refining a liquid steel bath, as was the practice until the 1960s and 1970s. To keep these very powerful furnaces "idling," waiting for metal–slag reactions (which are limited mostly by transport kinetics) to happen became economically inviable. This led to transferring a part of the refining operations to other equipment prepared to receive and process liquid steel. These are called secondary metallurgy operations. Particularly important was the development of "ladle furnaces" that could receive liquid steel from the primary processes and perform the refining operations, freeing the primary furnaces for more efficient melting, decarburization, and dephosphorization.

Electric arc furnaces are the largest consumers of steel scrap. Converters have a heat balance limit to the maximum amount of scrap they can melt and refine; this limitation is not present in EAFs. Two additional factors limit converter scrap usage to around 15% of the charge: (a) as integrated steel plants (which start from ore and proceed all the way to final product) become more efficient, less internal scrap is generated; and (b) since scrap cost and availability are critical considerations for EAF operators, they try to include the complete scrap cycle in their supply chain.

Scrap quality has a considerable effect on final steel residuals. Because scrap separation is never perfect, and iron/steel scrap is one of the cheapest metallic scraps, it is common to find other metals present in steel scrap, contaminating it. Typical cases are the scrap of coated steel products (tin foil and galvanized products, which will bring tin, zinc, and eventually aluminum into the charge). Furthermore, copper electrical conductors in cars and appliances are an important source of contamination of the scrap with this metal. Several of these residuals can be undesirable in certain products. Presently, there are no viable processes to remove tin, zinc, copper, and the metallic impurities associated with them (lead, antimony, arsenic, etc.) from liquid steel. Because these elements can have negative effects on the properties of some steels, it is up to the EAF operators to take care in their charge prepara-

tion to develop a proper balance for achieving dilution of the residuals to acceptable levels. Converter steelmakers are less affected by this problem, because they operate mostly with their internal scrap and there is significant dilution by pig iron. The main concern, in this case, is the segregation of coated steel scrap and judicious use of this scrap in grades that will tolerate these residuals.

2.2.3 Deoxidation

After the oxidation refining of steel, the oxygen content in the liquid metal must be reduced to acceptable levels in the solid product. Keeping the oxygen content below the solubility limit in solid iron is essential for avoiding the formation of low-melting iron oxide, as shown in the phase diagram of Fig. 2.8.

Many elements have more affinity for oxygen than iron does. The most common deoxidants are aluminum, silicon, manganese, and a combination of silicon and manganese. One important consequence of the use of deoxidants is the formation of solid or liquid products from the deoxidation reaction. (Vacuum carbon deoxidation is an exception but is of limited application.) During further processing of the steel, care should be exercised to remove as much of these products as possible. Deoxidation products that remain in the steel become nonmetallic inclusions and affect the properties of the steel to various extents.

In addition, the solubilities of the oxides formed during deoxidation decrease with the reduction of temperature. Thus, even if it was possible to completely remove all deoxidation products formed in the liquid steel, it would be almost impossible to produce a steel completely free of nonmetallic inclusions. Nonetheless, steelmaking technology is constantly improving and making possible the production of steels with reduced amounts of nonmetallic particles (see Chapter 8, “Solidification, Segregation, and Nonmetallic Inclusions,” in this book).

Because converters operate in highly oxidizing conditions, deoxidation usually is performed during or after tapping of steel to the ladle. Although it is possible to perform deoxidation as a part of the EAF process, this method is used less and less in steelmaking as the EAF process relies significantly on oxidation reactions, and furnace time is more efficiently used for melting and decarburization operations. Thus, deoxidation in EAFs frequently starts during tapping, too.

2.2.4 Secondary Steelmaking Processes

Achieving proper thermodynamic conditions for some of the important steel refining reactions can be difficult in converters and EAFs operating in oxidizing conditions. Furthermore, some of the important conditions and operations in steelmaking, such as chemical composition and temperature homogenization, as well as nonmetallic inclusion removal, involve the need for some holding time. To avoid tying the primary steelmaking processes (converters and EAFs) to the performance of these operations in nonefficient ways, steelmaking has developed split processes, introducing the aforemen-

tioned secondary metallurgy. In these processes, liquid steel from primary processes is subjected mostly to refining operations and to adjustments of chemical composition and temperature.

The first large-scale secondary process developed was vacuum degassing. Because of the problems caused by hydrogen absorbed during the steelmaking process (see Chapter 10, "Conventional Heat Treatment: Basic Concepts," in this book), vacuum processes have been developed. When carbon and oxygen dissolved in steel react, they form a gas, mostly CO at steelmaking temperatures. This reaction also is sensitive to pressure. Once vacuum treatment of steel became a reality, the possibility of vacuum carbon deoxidation began to be explored.

The main types of vacuum treatment of liquid steel are ladle degassing and circulation degassing. Casting under vacuum can be used especially for large ingots (Fig. 2.10).

Decades after the development of vacuum treatment, with the dramatic increase in power of modern electric furnaces from around 300–400 kVA/t in the 1960s to 1000 kVA/t from the 1980s on, processes were developed with the goal of transferring the time-consuming, low-power refining activities from the EAF to other reactors. Thus, deoxidation, desulfurization, temperature and composition homogenization, and inclusion removal ("rinsing") were transferred to lower-electrical-power heating equipment called ladle furnaces (Fig. 2.11). Evidently, introducing the ladle furnace was most welcome to converter steelmakers: this advance made it possible for them to produce very low-sulfur, very clean steel and high-alloyed steel with a modest investment, a benefit that was probably unexpected by its developers.

The advantage of the lower pressure in vacuum treatment (or inert gas dilution) on the carbon oxidation reaction has had a tremendous impact on stainless steel and high-silicon electric steel processing. The development of

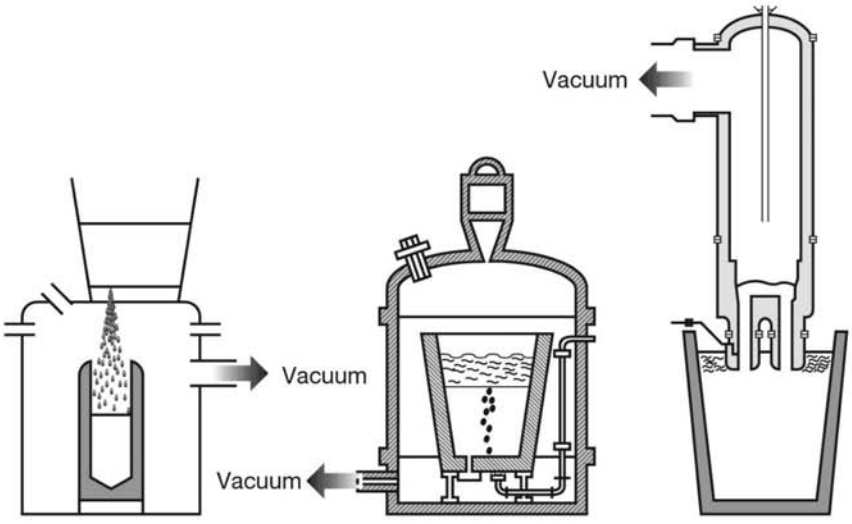

Fig. 2.10 Most usual vacuum degassing processes used in steelmaking. Left to right: stream (or ladle-to-mold) degassing; ladle degassing; circulation degassing in RH reactor.

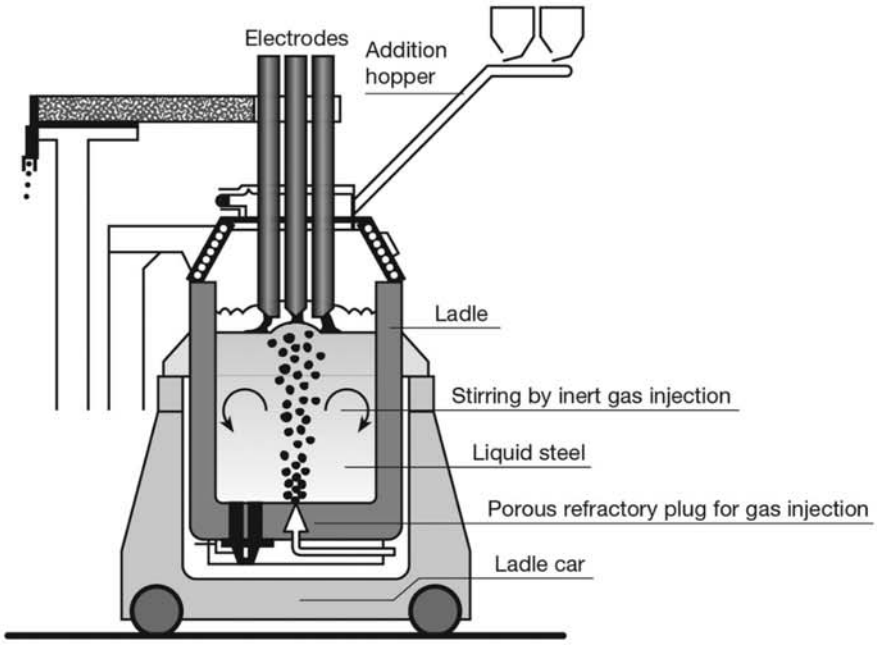

Fig. 2.11 Schematic presentation of a ladle furnace. (Large ladles are frequently moved from tapping to the ladle furnace using cars. The use of cranes is also common, depending on melt shop layout.)

vacuum oxygen decarburization (VOD) and argon oxygen decarburization (AOD) processes, favoring carbon over chromium or silicon oxidation because of the low effective CO pressure, was the main reason for the change. This also has made possible the production of extra-low-carbon steels (such as 20 ppm C IF steels). In this case, carbon oxidation is favored over iron oxidation, which limits the minimum carbon content that can be reached in the converter or the EAF.

2.3 Secondary Remelting Processes

An additional class of secondary refining processes starts from solid steel, as opposed to having a charge of liquid steel as most of the "conventional" secondary processes. One of the main objectives in these processes is to affect how steel solidifies. These processes are discussed in more detail in Chapter 8, "Solidification, Segregation, and Nonmetallic Inclusions."

REFERENCES

1. G. Krauss, *Steels: Processing, Structure and Performance*, ASM International, 2005
2. F. Oeters, *Metallurgy of Steelmaking*, Stahleisen, 1989
3. D.M. Stefanescu, Solidification and Modeling of Cast Iron—A Short History of the Defining Moments, *Mat. Sci. Engin. A*, Vol 413–14, 2005, p 322–33
4. D.H. Wakelin, ed., *Making, Shaping and Treating of Steel—Ironmaking Book*, 11th ed., AIST, 1999

5. Wikipedia, Henry Cort, https://en.wikipedia.org/wiki/Henry_Cort (accessed October 2015)
6. Wikipedia, Puddling (metallurgy), http://en.wikipedia.org/wiki/Puddling_%28metallurgy%29 (accessed October 2015)
7. DoITPoMS, Dissemination of IT for the Promotion of Materials Science, University of Cambridge, http://www.doitpoms.ac.uk/miclib/index.html (accessed October 2007)
8. A. Sauveur, *Metallography and Heat Treatment of Iron and Steel*, 4th ed., McGraw-Hill, 1935
9. H. Bessemer, *F.R.S.*, *An Autobiography*, Offices of "Engineering," 1905, http://babel.hathitrust.org/cgi/pt?id=nyp.33433000048458;view=1up;seq=1 (accessed October 2015)
10. Great Britain Patent Office, Chronological Index of Patents Applied for and Patents granted for the year 1857, Great Seal Patent Office, https://books.google.co.uk/books?printsec=frontcover&dq=index+of+patents&ei=A6cpU7vGKM3xhQef5ICIAg&id=zXMyAQAAIAAJ&hl=pt-BR&output=text (accessed October 2015)
11. R.D. Pehlke, C.W. Porter, and R.F. Urban, *BOF Steelmaking*, Iron and Steel Society-AIME, 1982
12. P.E. Niles, New Techniques in Basic Oxygen Steelmaking, *Mixed Gas Blowing in Steelmaking*, ed. P.E. Niles, ISS-AIME, 1982, p 3–13
13. L. Darken and R. Gurry, *Physical Chemistry of Metals*, McGraw-Hill, 1953
14. E. Turkdogan, *Principles of Steelmaking*, Institute of Materials, 1996

Metallography of Steels—Interpretation of Structure and the Effects of Processing
Hubertus Colpaert
Updated and Translated by André Luiz V. da Costa e Silva

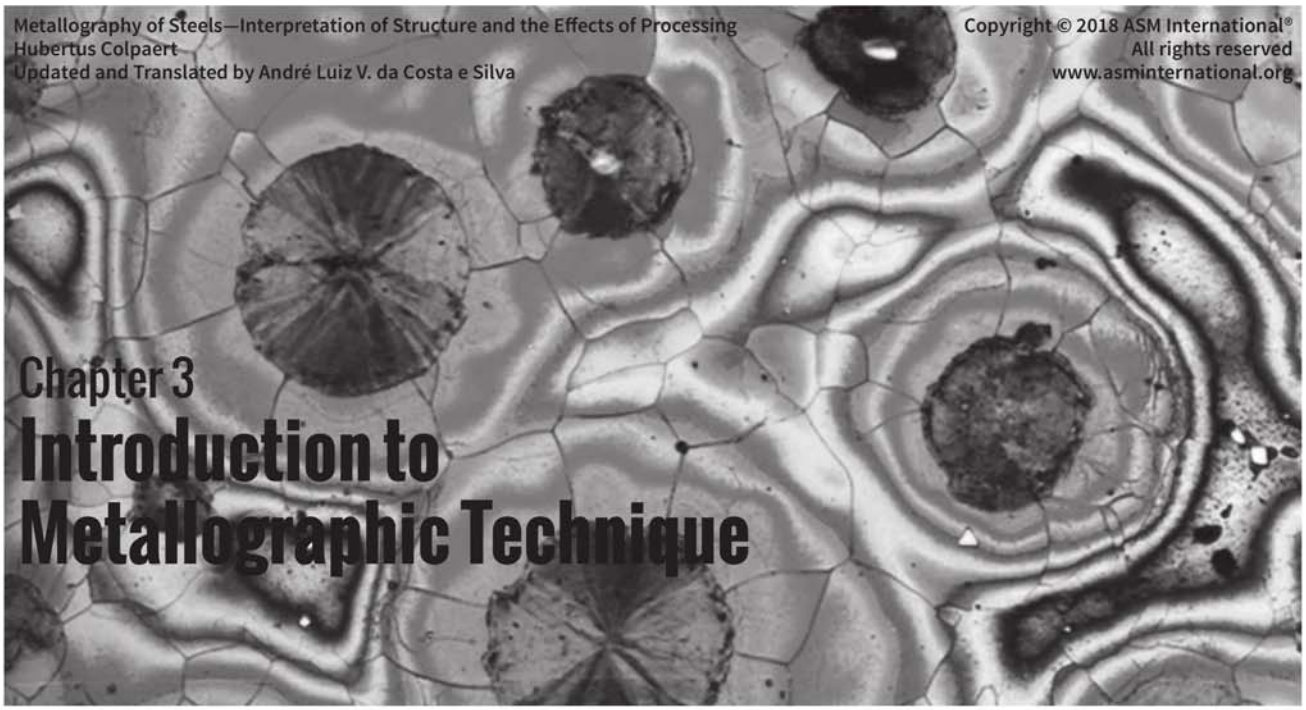

Chapter 3
Introduction to Metallographic Technique

One of the most interesting problems in evaluating micro- and macrostructures of metals is the fact that most available analytical techniques make it possible to observe two-dimensional sections of three-dimensional structures.

This transformation, which may seem simple at first glance, requires extraordinary care in the study of metallography. Thus, for instance, care must be taken from the start, when the cross sections to be examined are selected, and continue through to the evaluation of these sections and the idealization of the three-dimensional features of the structure.

While three-dimensional reconstruction techniques are available and are being used more often, they still require a considerable investment of time and material resources. The first attempt at three-dimensional reconstruction involved the metallographic preparation and examination of successive planes and manual reconstruction (Ref 1). Today automatic reconstruction of three-dimensional tomography is available. Some of these techniques already are employed with steels and cast irons (Ref 2, 3). Chapter 9, "Conventional Heat Treatments: Usual Constituents and Their Formation" and Chapter 17, "Cast Irons," in this book present examples of the reconstruction of some of the microstructural constituents of steels and cast irons. These techniques expand significantly the understanding of the material structure and, in some cases, make possible much better correlations between structure and properties.

3.1 Grains in Metals

The structures observed in steel products are directly dependent on the phase transformations that occur during processing, starting with solidification—in which the liquid phase transforms, for instance, into the solid body-centered cubic (BCC) phase—and including many solid-state transformations during thermomechanical treatment. In general, these transformations take place with the formation of many nuclei of the new phase(s) that is (are) formed in the volume of material undergoing the transformation. Most often

the phases formed are crystalline (i.e., composed of atoms in regular, repetitive arrangements). It is almost impossible that all nuclei in a volume of metal form with exactly the same crystallographic orientation. Thus, when the crystals formed in a transformation reach each other, there will be regions where the atoms cannot exactly fit the structure of either of the growing crystals, as shown in Fig. 3.1.

Each continuous crystalline region with a single crystallographic orientation is called a grain. The transition region between two grains is called a grain boundary. Material that is composed of many grains (or crystals) is called polycrystalline.

Many relevant phenomena that occur in crystalline materials can be represented or simulated in two dimensions. (The DoITPoMS Project at the University of Cambridge has excellent examples of structure modeling using bubble rafts to simulate atomic arrangements in 2D, which can be found at http://www.doitpoms.ac.uk/tlplib/dislocations/index.php.)

However, the real metal structure is three-dimensional, and great errors can be made when this is not properly considered. In rare cases, some metallic structures indeed develop in approximately two dimensions. Zinc coating applied to steel plate is an example. During immersion galvanizing, different zinc crystals (or crystals of a zinc alloy) nucleate over the steel plate after immersion in the liquid zinc–rich bath. As the metal is extracted from the bath, a thin layer of liquid remains over the plate surface and solidifies, reacting with the steel substrate to some extent. These crystals of solid alloy start to grow on the steel plate surface. When different grains meet each other, the crystal growth is interrupted and grain boundaries are formed (Fig. 3.2). In the case in which the growth of each crystal is significant in three dimensions, each individual crystal will occupy a certain volume, and the surfaces that separate these crystals will be the grain boundaries.

Figure 3.3 presents a three-dimensional image of a polycrystalline material and a model of such a material using bubbles in a foam. Figure 3.1 could represent a plane section through a polycrystalline structure of the kind shown in Fig. 3.3.

The conditions that define the shape of grains in a metal have been the subject of study for a long time. Cyril Stanley Smith (Ref 4) summarized these conditions in various publications. Two basic forces act to define the shape of the grains (as in the case of the shape of bubbles in a foam):

- The balance between the forces related to interfacial energy, frequently called surface tension. If surface tension is the same in all interfaces, they will meet at 120° angles.
- Grains (or bubbles) must fill the space so all of their surfaces (the interfaces) belong simultaneously to two grains.

Among the regular polyhedra, the tetrakaidecahedron (or tetradecahedron), presented in Fig. 3.4 is the closest to fulfilling these conditions and is frequently used as a model for the grain shape of single-phase materials. Thompson (Ref 6), however, called attention to the fact that in real situations grains or bubbles seldom take exactly these regular shapes. Surfaces have curvature, becoming nonplanar, and similar or distorted polyhedra are formed. The fundamental fact as stated by Thompson and by Smith, how-

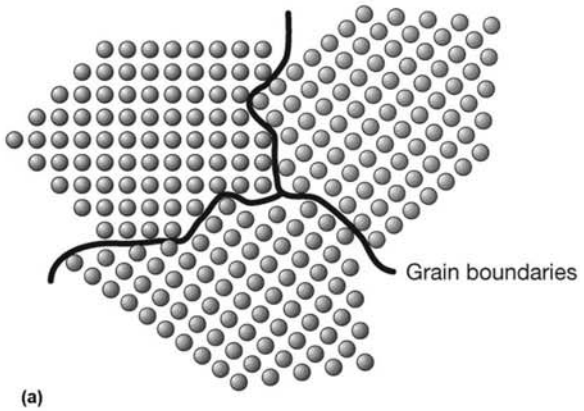

(a)

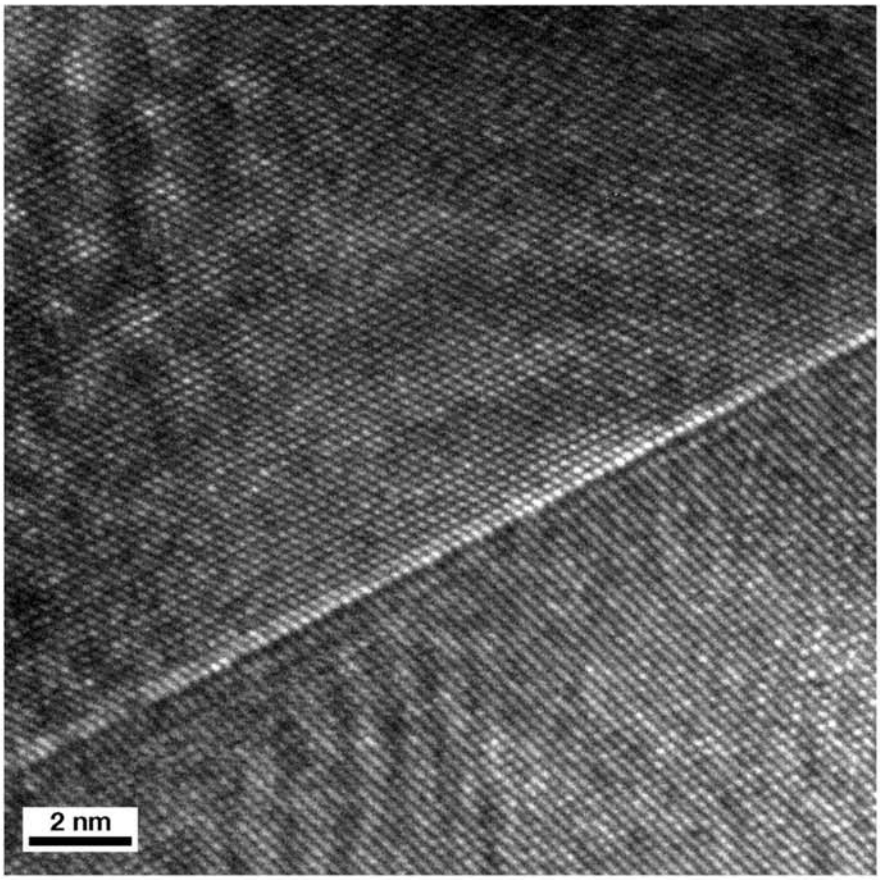

(b)

Fig 3.1 (a) Two-dimensional representation of the boundary between two crystals with different crystalline orientations. The regions indicated by the lines are called grain boundaries, regions where the atoms are somewhere between the two crystalline lattices. The two-dimensional representation is a simplification, as real crystals are three-dimensional. (b) Image of a twin interface in copper. The two crystals have different orientations, and the interface can be clearly observed. (The two crystals separated by a twin interface bear a symmetry relationship, frequently a reflection operation ("mirror" element). This special interface can be observed in a high-resolution transmission electron microscope (TEM) image (see Chapter 6, "Metallographic Technique: Electron Microscopy and Other Advanced Techniques," in this book). There is no orientation condition that allows the formation of a high-resolution image of the two grains, simultaneously at the more common high-angle grain boundaries.) High-resolution TEM image. Each point represents a column of atoms aligned with the observation direction. Courtesy of M.J. Kaufman, Colorado School of Mines.

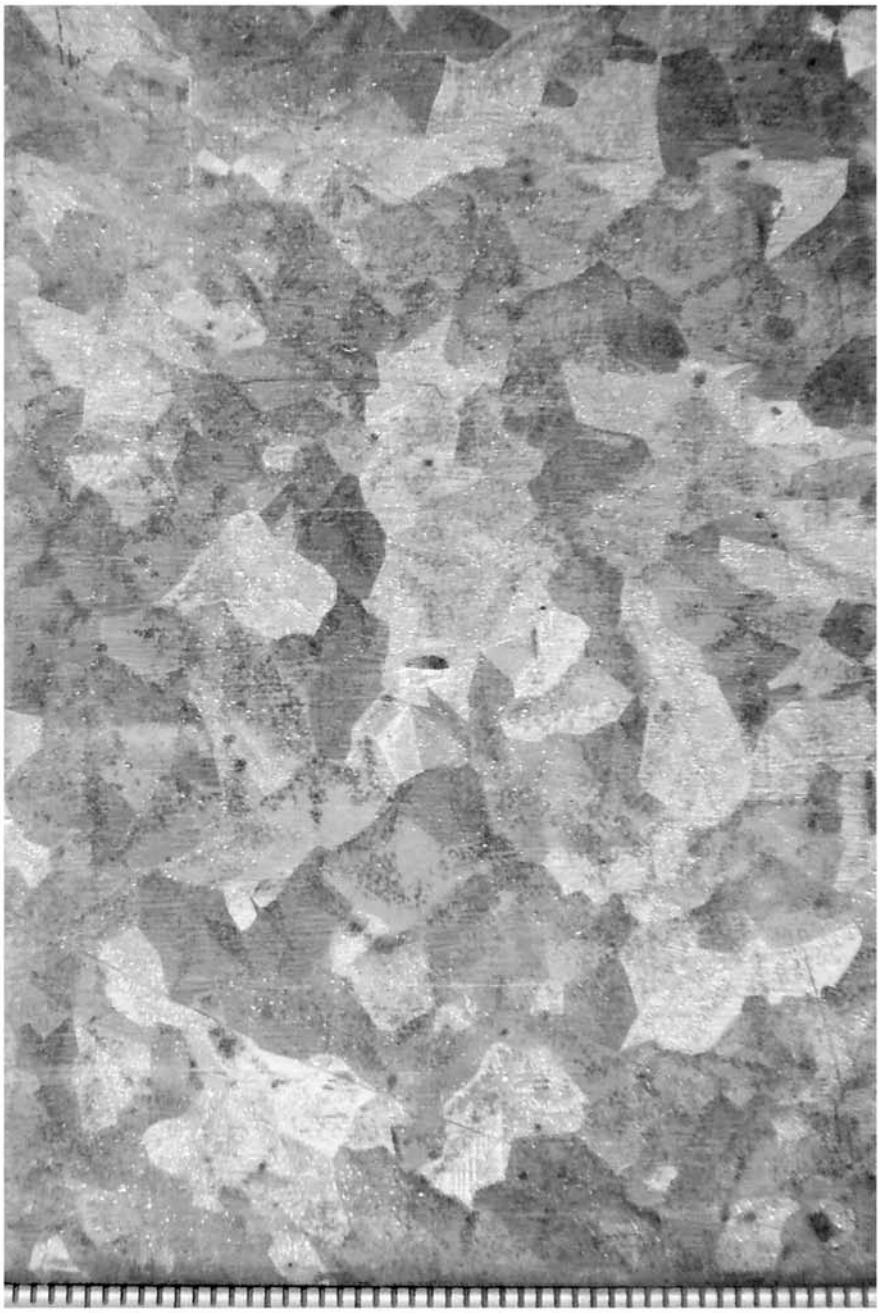

Fig. 3.2 Galvanized steel plate. The grains of zinc that solidified on the plate surface can be observed. The structure is almost two-dimensional. Each division in the ruler at the lower part of the image corresponds to 1 mm. No etching.

3.2 Stereology

ever, is that structure is dominated by the space-filling limitations and by surface energies. This information is essential in the understanding of the macro- and the microstructure of metals, particularly steels.

Steel microstructures are three-dimensional. Most microscopy techniques generate information on two dimensions. Stereology allows one to infer the

(a)

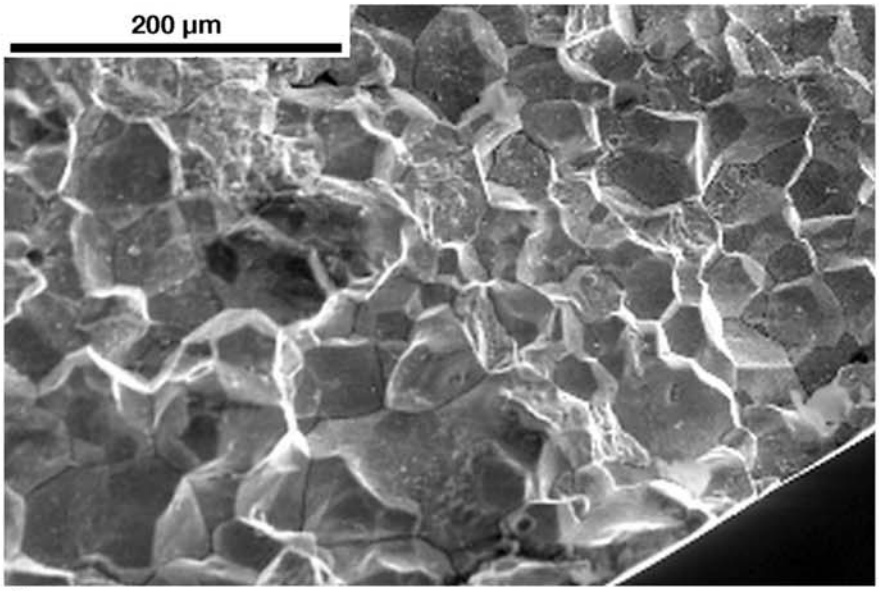

(b)

Fig. 3.3 (a) Three-dimensional visualization of structure composed of space-filling grains, using bubbles. The interior of each bubble would be a crystal (grain), and the bubble walls would be the grain boundaries. (b) Intergranular fracture. The fracture path follows the embrittled previous austenite grain boundaries. The shape of the grains can be observed (scanning electron microscope (SEM), imaging with secondary electrons (SE)). The real shape of grains in metals is very close to the shapes generated with the bubble model. The bubble model is reproduced here with permission from DoITPoMS, University of Cambridge.

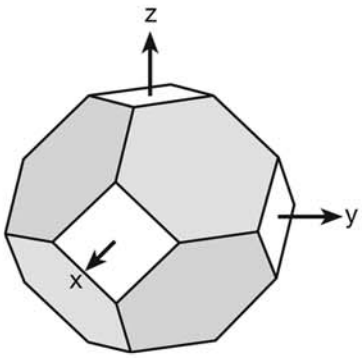

Fig. 3.4 A tetrakaidecahedron, or Thomson or Kelvin polyhedron (William Thomson (1824–1907) was the first Baron Kelvin and is cited in scientific texts as both Thomson and Kelvin. He discussed this geometrical shape in Ref 5). This polyhedron is a truncated octahedron where the corner or vertices along the directions indicated as x, y, and z in the figure have been cut (truncated). In each vertex (or corner), there are one 90° and two 120° angles. (More at www.steeluniversity.org under grain size strengthening.)

three-dimensional geometry of a structure from two-dimensional observations (Ref 7). Although it is not the object of this book to present the stereological techniques used in quantitative metallography, it is important to highlight some of the problems and difficulties associated with this inference process about the three-dimensional micro- and macrostructural state of a material from the information contained in two-dimensional sections. There are excellent texts that discuss these problems in depth (Ref 8, 9). Figure 3.5 presents some examples of the information acquired when arbitrary planes section different three-dimensional geometrical shapes. When performing metallographic analysis, one always should keep these transformations in mind.

Two of the most important descriptions of the microstructural state of a material are the qualitative and the quantitative descriptions of the geometric state.

3.2.1 Qualitative Description

From the geometrical point of view, microstructures have one-dimensional, two-dimensional, and three-dimensional features. Most of these features are the result of grain contact. Two three-dimensional grains will meet in a two-dimensional interface. Three grains will meet in a single line; four grains touching will define a quadruple point. The qualitative description of a system encompasses a list of features that are present as well as some sort of qualification of these features. This description can be very complex at times. Table 3.1 lists the features that could be present in structures containing one, two, or three phases. The sections of grains, interfaces, and lines will appear in two-dimensional images, in a microscope, as areas, lines, and points. Quadruple points are not seen in metallographic sections, and their features must be inferred from the other available information. Table 3.2 presents the correspondence between three-dimensional features of the real structure and how they are seen in two-dimensional sections.

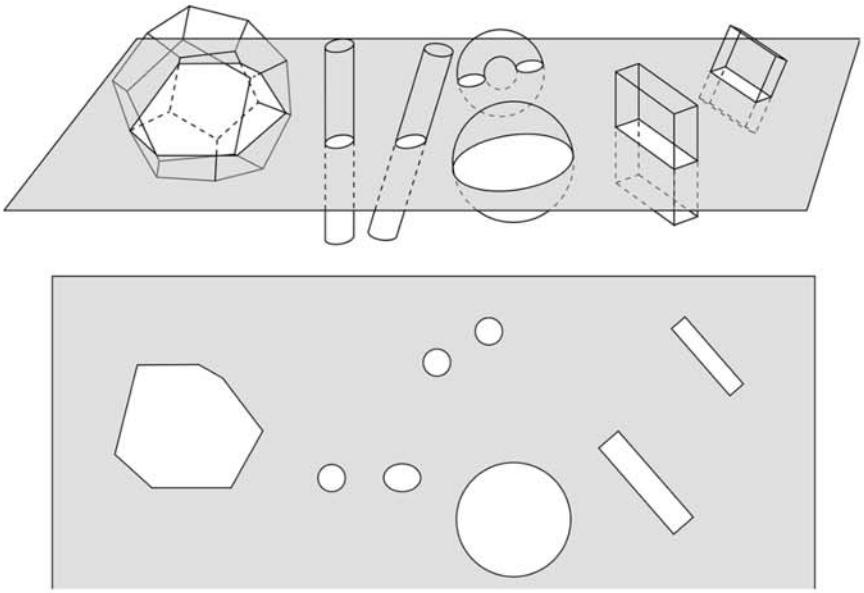

Fig. 3.5 When three-dimensional bodies (top) are sectioned, two-dimensional shapes result (bottom). These two-dimensional shapes supply incomplete information about the geometrical features of the sectioned bodies.

Table 3.1 A list of qualitative features of the microstructural state. When observed in a microscope, in 2D images, all features have one dimension less (see Table 3.2)

Dimensions	Feature	Phases		
		One	Two	Three
3	Volume, grains	α	α, β	α, β, γ
2	Surfaces, interfaces	$\alpha\alpha$	$\alpha\alpha$, $\alpha\beta$, $\beta\beta$	$\alpha\alpha$, $\alpha\beta$, $\alpha\gamma$, $\beta\beta$, $\beta\gamma$, $\gamma\gamma$
1	Lines (triple lines)	$\alpha\alpha\alpha$	$\alpha\alpha\alpha$, $\alpha\alpha\beta$, $\alpha\beta\beta$, $\beta\beta\beta$	$\alpha\alpha\alpha$, $\alpha\alpha\beta$, $\alpha\beta\beta$, $\alpha\alpha\gamma$, $\alpha\gamma\gamma$, $\alpha\beta\gamma$, $\beta\beta\beta$, $\beta\beta\gamma$, $\beta\gamma\gamma$, $\gamma\gamma\gamma$
0	Points (quadruple points)	$\alpha\alpha\alpha\alpha$	$\alpha\alpha\alpha\alpha$, $\alpha\alpha\alpha\beta$, $\alpha\alpha\beta\beta$, $\alpha\beta\beta\beta$, $\beta\beta\beta\beta$	15 possible combinations

Source: Adapted from Ref 7, 8

According to Ref 7, the major importance of the evaluation of the qualitative state of a structure is to determine which features are absent from the list of possible features. If, for instance, $\alpha\alpha\beta$ triple point (lines in three dimensions) are not observed, this would indicate that β particles avoid the $\alpha\alpha$ grain boundaries.

Table 3.2 Features observed in a cross section of material constituted of an α matrix phase and β phase particles

Feature in 3D	Phases	Feature in 2D	Feature in 3D	Phases	Feature in 2D
Volume		**Area**	**Line** (space curve)		**Point**
Grain	α	Grain (section)	Grain edge (triple line)	ααα	Triple point
Particle	β	Particle (section)	Triple lines	ααβ,αββ	Triple point
Surface		**Line**	**Point**		
Grain boundary	αα, ββ	Grain boundary (trace)	Quadruple point	αααα	Not observed
Interface	αβ	Phase boundary (trace)	Quadruple points	αααβ	Not observed
				ααββ	Not observed
				αβββ	Not observed
				ββββ	Not observed

Source: Adapted from Ref 7, 8

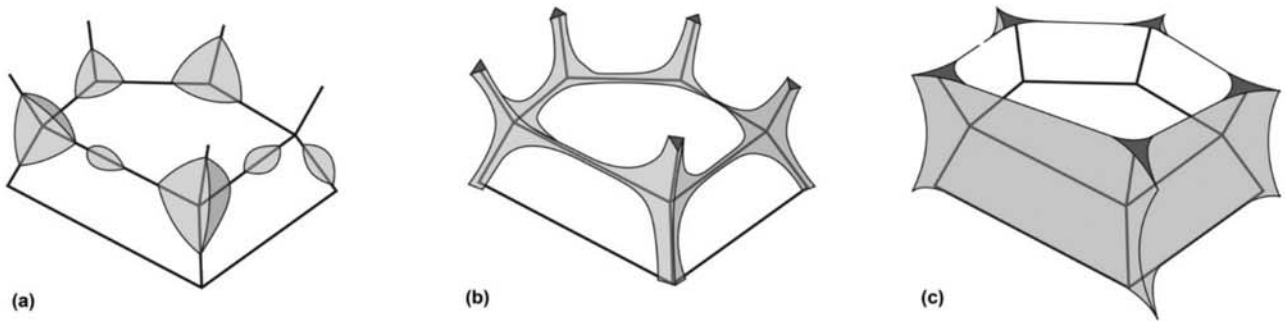

Fig. 3.6 Three possible spatial arrangements of a second phase, β (gray), in an α-phase (white) matrix. The dihedral angle θ between the phases (defined by the interfacial energies) defines the three-dimensional morphology. (a) θ > 60°, (b) θ < 60°, (c) θ = 0°. A careful analysis of two-dimensional sections of this structure is needed to determine which of the features described in Table 3.2 are present or absent from the microstructure and thus to understand the microstructural state.

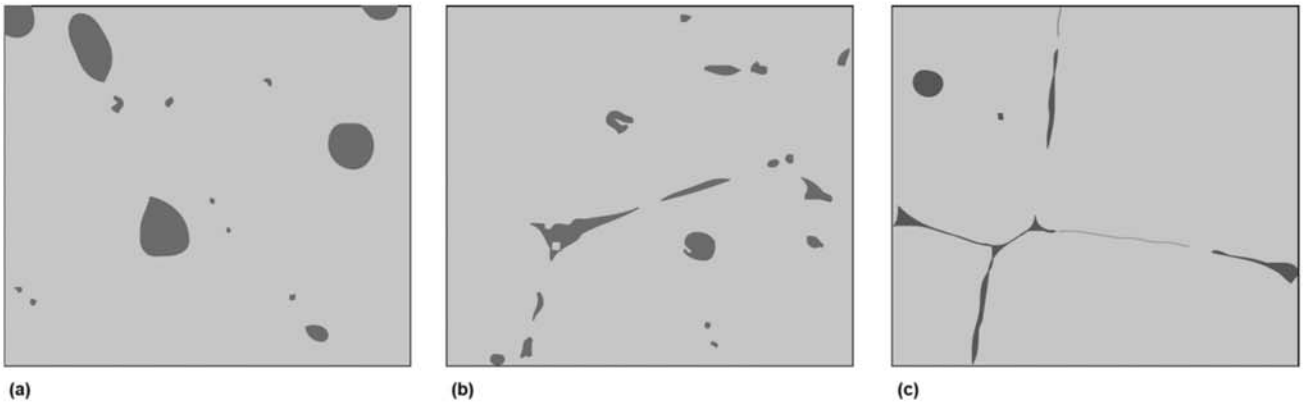

Fig. 3.7 Micrographs corresponding to the second-phase distributions presented in Fig. 3.6.

Figure 3.6 presents some possible structural variations when a phase β occurs in a smaller volume fraction than the matrix phase. Figure 3.7 shows corresponding visualizations in two-dimensional planar sections (micrographs).

3.2.2 Quantitative Description

The qualitative features listed in Table 3.1 can be measured and quantified metrically and topologically. In the following, only the metrical aspects will be discussed, highlighting some of the important variables useful in quantifying the microstructural state. For three-dimensional features, volume V is the important variable. Volume is frequently discussed in terms of volumetric fraction V_V. (In stereology, the subscript is used to represent the normalizing factor. Thus, volume fraction is the volume of a phase divided by the total volume sampled.) The extent or amount of two-dimensional features is its area, in general presented as areal density S_V. For linear features, length density L_V is used. These are the most basic measurements that can be used to quantify a microstructure. Connectivity, curvature, and so on are more complex measurements that also are used to quantify the microstructural state. Some variables usually measured in stereology are presented in Table 3.3.

Volumetric Fraction

If measurements are performed with statistical uniformity (i.e., randomly) it can be shown that:

$$V_V = A_A = P_P$$

Thus, the volume fraction of a phase can be estimated using the area fraction on a cross section or the fraction of points falling in the phase to be measured. Details about the manual performance of point count for measurement of volume fraction can be found in Ref 10. When automated measurements are used, area fraction normally is used in connection with image analysis, in accordance with Ref 11.

Table 3.3 Some typical stereological measures

Symbol	Units	Description
V_V	mm^3/mm^3	Volume fraction. Volume of the feature per unit volume
N_L	mm^{-1}	Number of intersections of a feature with a line, per unit length of the line
A_A	mm^2/mm^2	Area fraction. Area of the feature per unit area
P_P		Point count. Number of points in a feature per total number of sampling points

Source: Adapted from Ref 7, 8

Grain Size

Almost all mechanical properties of steels are affected by grain size. For this reason, grain size measurements are among the most important in quantitative metallography. This fact has been recognized since well before stereology was established as a field in science and before the geometrical relationships in microstructures were well understood (Ref 9).

To measure grain size manually, three procedures were standardized by ASTM E112 (Ref 12). The first uses a comparison procedure with graded images presented in charts or in eyepiece reticles. The results are given in ASTM grain size number *G*, originally defined by Eq 1, where *n* is the number of grains per square inch at 100× magnification:

$$n = 2^{G-1} \quad \text{(Eq 1)}$$

The second method is the so-called planimetric procedure, based on a proposal in Ref 13 that simplified the planimetric methods used at the time and was initially developed in Ref 14. The method involves counting the number of grains in a given area of a metallography, usually defined by a circle of known radius (see Fig. 3.8). Grains that are intercepted by the circle are counted as half. This method gives a value of the length of triple line where three grains meet in the sample volume (Ref 9). The value of *G* then is obtained using the formula or the table given in the standard. Automated image processing equipment (Ref 15) frequently employ the planimetric method to determine the grain size, as shown in Figure 3.8.

The third method, the intercept procedure, initially was based on the work of Heyn, but there are several developments possible. In this method, the number of grains intercepted by a line of given length superimposed on a metallographic specimen is counted. This makes it possible to determine the mean lineal intercept length ($\bar{l}$); from this measurement, the value of *G* can be determined. This method is a measure related to the surface area per unit

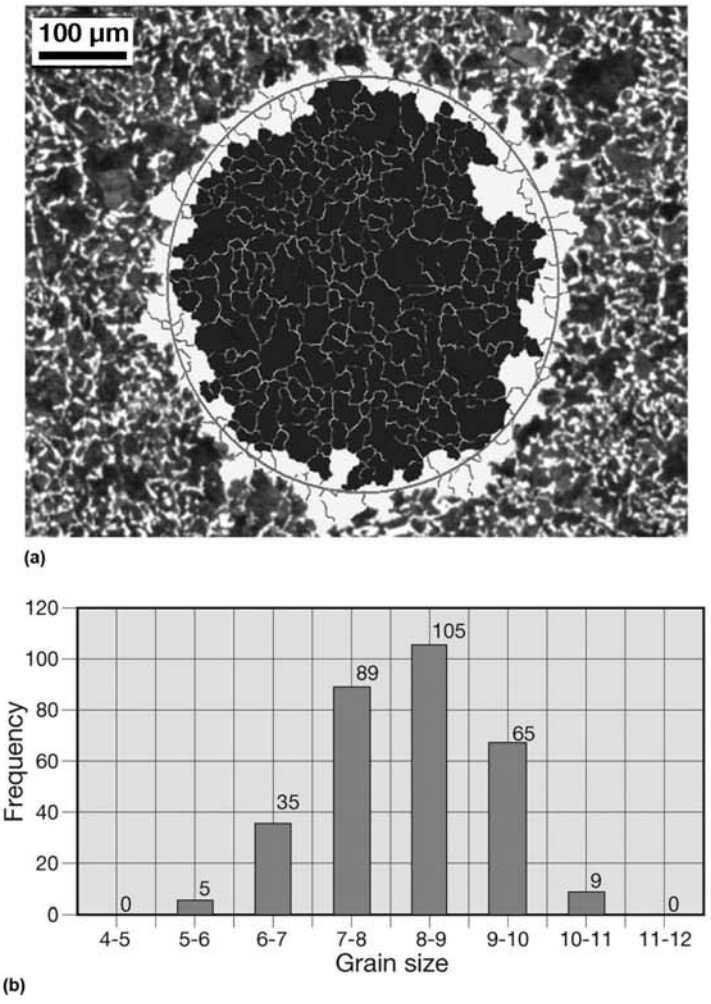

Fig. 3.8 Automated planimetric method in image processing system. (a) The system can identify the grain boundaries and marks with different colors the grains completely inside the circle and those intercepted by it. (b) A grain size distribution as well as the average grain size can then be determined automatically. Courtesy of Neumayer-Tekfor, Brazil.

volume, S_v (Jeffries and Sauver Ref 9). To ensure a random orientation of the line with respect to the grains, a circle frequently is used.

In the planimetric method, to guarantee accuracy, a minimum number of grains must be sampled; likewise, in the intercept procedure, a minimum number of intercepts must be sampled (Ref 12). Experimental results confirm that samples that are too small may lead to incorrect grain size estimates (Ref 15).

Some of these methods are used in other standards such as ISO643 (Ref 16), which adopts the charts of ASTM 112 (Ref 12) for the comparison method.

The three methods give equivalent values of *G*. Evidently, the repeatability and reproducibility of the methods are not the same, and the ASTM standard establishes that in case of dispute, the planimetric procedure should be used.

The standard makes it clear that the test method deals with the determination of "planar grain size," that is, a measure related to the two-dimensional grain sections in the sectioning plane and not a "spatial" (or volumetric) grain size.

Estimation of the actual "size" of grains in three dimensions depends first on which parameter is taken to define "size." Volume, intercept, or more complex linear dimensions such as the mean perpendicular distance between two parallel tangent planes to the grain (this would be the diameter, if the grains were spherical) are possible choices. Second, the grain size distribution is relevant, if one attempts to characterize grain size with a single variable. In ASTM 112, for instance, the grain size distributions are approximately log normal and must be unimodal; duplex grain size should not be measured using ASTM 112. Many authors have derived relationships between a given distribution of grain shapes and sizes and planar grain sizes. A complete review of the work in this area is beyond the objective of this text, but a simple summary can be found in Ref 17. Mendelson summarized relations derived between a three-dimensional average grain size (expressed as an averaged spatial "diameter" $\overline{D}$) and the mean lineal intercept in two dimensions ($\overline{l}$). He also derived a relation between these variables for grains with the tetrakaidecahedron shape and a size distribution proposed in Ref 18, given in Eq 2.

$$\overline{D} = 1.57\overline{l} \qquad \text{(Eq 2)}$$

When automated image analysis is used, the applicable standard is ASTM EI382 (Ref 19). The techniques described in this standard make it possible to calculate the average area of the two-dimensional grain sections in the sectioning plane. It is clear that this is not an estimate of the average of the maximum cross section of the three-dimensional grains because the sectioning plane will seldom section a grain through its maximum cross section. (In the case of a spherical grain, the maximum cross section in three dimensions would be a circle with the grain diameter.)

Other Important Measurements

Well-defined stereological methods are available for the measurement of the mean spacing between particles in a structure or of the mean free path in a given phase. In many cases, mechanical properties of steels present clear correlations with these structural features (Ref 20–23). As the quantification of the structure–properties relationships becomes more important in steel metallurgy, one must rely more on these quantitative characterization tools and abandon the simple qualitative or semi-quantitative analysis that are able to show only trends.

REFERENCES

1. G. Krauss and A.R. Marder, The Morphology of Martensite in Iron Alloys, *Metall. Trans.*, Vol 2, 1971, p 2343–58
2. M.V. Kral, M.A. Mangan, G. Spanos, R.O. Rosenberg, Three-Dimensional Analysis of Microstructures, *Mat. Charact.*, Vol 45, (No. 1), 2000, p 17–23
3. G. Spanos, A.W. Wilson, and M.V. Kral, New Insights into the Widmanstätten Proeutectoid Ferrite Transformation: Integration of Crystallographic and Three-Dimensional Morphological Observations, *Metall. Mat. Trans. A*, Vol 36A, 2005, p 1209–18

4. C.S. Smith, Microstructure, *Trans. ASM*, Vol 45, 1953, p 533–75
5. W. Thomson (Lord Kelvin), On the Division of Space with Minimum Partitional Area, *Phil. Mag*., Vol 24, 1887, p 503–24, available at http://zapatopi.net/kelvin/papers/on_the_division_of_space.html (accessed November 20, 2015)
6. S.D.A.W. Thompson, *On Growth and Form*, Dover, 1992
7. R.T. DeHoff, Stereology and Metallurgy, *Metals Forum*, Vol 5, (No. 1), 1982, p 4–12
8. R.T. DeHoff and F.N. Rhines, *Quantitative Microscopy*, McGraw-Hill, 1968
9. J. Russ and R.T. DeHoff, *Practical Stereology*, Springer, 2000
10. "Standard Test Method for Determining Volume Fraction by Systematic Manual Point Count," E562-02, ASTM, 2002
11. "Standard Practice for Determining the Inclusion or Second-Phase Constituent Content of Metals by Automatic Image Analysis," E1245-03, ASTM, 2003
12. "Standard Test Methods for Determining Average Grain Size," E112-13, ASTM, 2013
13. Z. Jeffries, A.H. Kline, and E.B. Zimmer, The Determination of the Average Grain Size in Metals, *Trans. AIME*, Vol 54, 1916, p 594–607
14. G. Vander Voort, Committee E-4 and Grain Size Measurements: 75 Years of Progress, *ASTM Stand. News,* 1991, available at http://www.metallography.com/grain.htm (accessed November 20, 2015)
15. J. Klansky, Grain Size Measurement—Variables to Consider, *Microsc. Microanal*., Vol 8, Suppl 2 (2202), p 348–49
16. "Steels—Micrographic Determination of the Apparent Grain Size," ISO 643:2012
17. M.I. Mendelson, Average Grain Size in Polycrystalline Ceramics, *J. Am. Cer. Soc*., Vol 52, (No. 8), 1969, p 443–6
18. M. Hillert, Theory of Normal and Abnormal Grain Growth, *Acta Metall.,* Vol 13, (No. 3) 1965, p 227–38
19. "Standard Test Methods for Determining Average Grain Size Using Semiautomatic and Automatic Image Analysis," E1382-97, ASTM, 2010
20. W.L. Roberts, *Cold Rolling of Steel*, CRC Press—Marcel Dekker, 1978
21. J. Gurland, Correlation Between Yield Strength and Microstructure of Some Carbon Steels, STP 504, *Stereology and Quantitative Metallography*, ASTM, 1972, p 108–18
22. R. W. Armstrong, The Hardness and Strength Properties of WC-Co Composites, *Materials*, Vol 4, (No. 12), 2011, p 1287–308
23. A. Velichko and F. Muecklich, Quantitative 3D Characterization of Graphite Morphology in Cast Iron—Correlation Between Processing, Microstructure and Properties, *Int. J. Mat. Res*., Vol 100, (No. 8), 2009, p 1031–7

Metallography of Steels—Interpretation of Structure and the Effects of Processing
Hubertus Colpaert
Updated and Translated by André Luiz V. da Costa e Silva

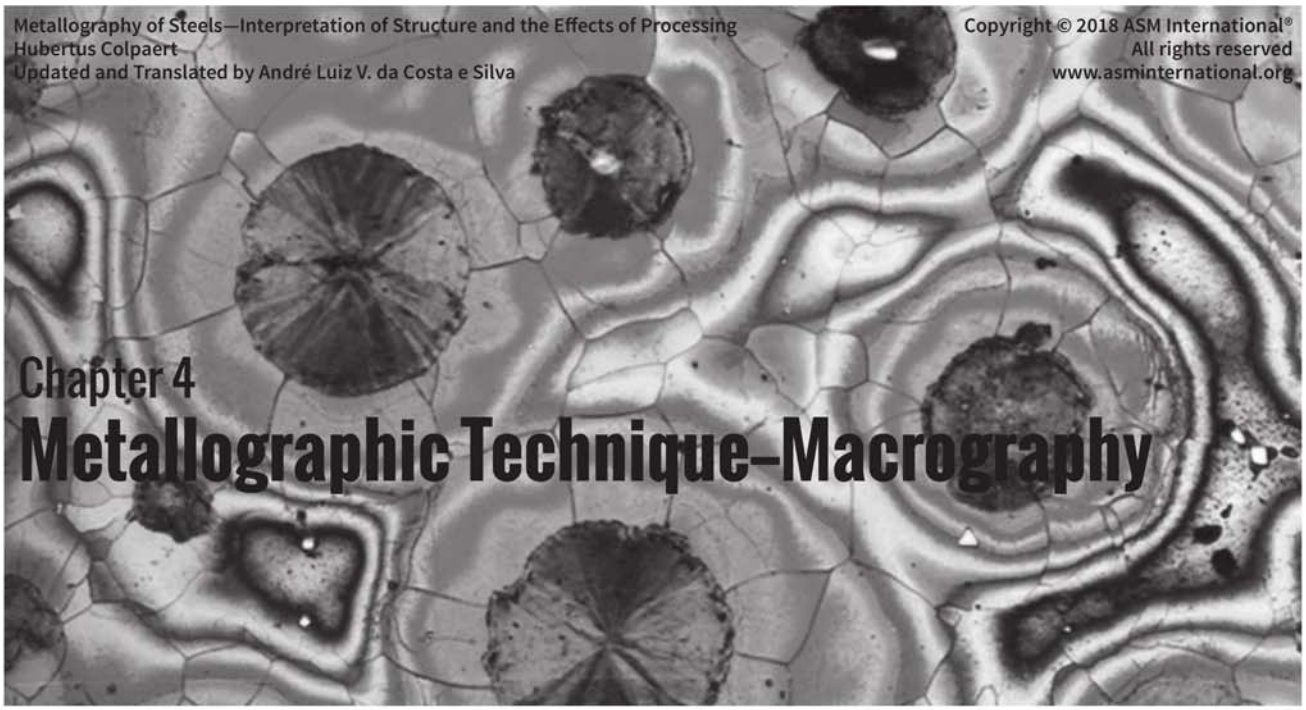

Chapter 4
Metallographic Technique–Macrography

Macrographic examination is the examination under low or no magnification of a polished plane section of a part or a metallic sample, usually subjected to etching with an appropriate reactant. The features observed in the macrographic examination are part of the macrostructure of the material. The sample usually is examined with the unaided eye or with a magnifying glass or loupe. A macrograph is a document that reproduces the macrostructure of the material, either in real size, slightly reduced, or with a maximum magnification of 10 times (Ref 1). When an enlargement greater this size is used, the technique is called micrographic and generally a microscope is used.

4.1 Sample Preparation for Macrographic Examination

Attention: Sample preparation and etching involves occupational and environmental risks. It is not the purpose of this text to discuss these risks, but the reader is cautioned not to start any metallographic preparation before completely familiarizing him- or herself with the risks, required safety equipment, proper protection measures, and correct measures to dispose of the products used during the preparation.

Sample preparation for macrographic examination normally comprises:

- Choosing the sample location and orientation.
- Preparing a flat and ground surface in the selected location and orientation. Reference 2 recommends that "polishing" be used to designate operations in which loose abrasive (≤ 6 μm) is used. For macrographic preparation, the required finish normally does not require the use of abrasive finer than grit 600 (14.5 μm).
- Etching the ground surface with the proper etchant.

4.1.1 Choice of Sample Location and Orientation

When the material section to be examined is not defined by a standard applicable to the evaluation in question, the part shape and the information

desired from the examination are the main factors defining the selection of the location and orientation of the sample plane to be prepared for the macrographic examination. For semi-finished products and regular-shaped products, the usual sampling orientations are related to shape and major working direction and are frequently longitudinal and transverse sections. (There is often confusion between orientations based on major working direction and on geometrical shape in a semi-finished product. This is discussed in Chapter 11, "Hot Working," and Chapter 12, "Mechanical Work of Steels: Cold Working," in this book). Some macrostructural features are easier to observe when the proper sample orientation is used (Ref 2).

Transverse sections are preferred when observing macrostructural features such as:

- Evaluation of material homogeneity along the cross section
- Characterization of segregation mode and intensity
- Evaluation of position, shape, and dimensions of cracks and pores
- Evaluation of the presence of pipe, residual pipe, or shrinkage cavities
- Evaluation of the presence, depth, and homogeneity of surface heat treatments or thermochemical treatments (carburizing, nitriding, etc.)
- Evaluation of hardening depth
- Investigation of the manufacturing process of tubes and pipes (seamless, welded, and, in this case, welding process)
- Evaluation of the extension of the heat-affected zone in a weld (in this case the macrograph orientation is transverse to the welding direction)
- In the case of cutting tools with inserts, evaluation of brazing or welding thickness and uniformity
- Evaluation of depth and uniformity of chilled layers in chilled cast iron parts

This list is not exhaustive, and the features described are discussed in detail in other chapters in this book.

Longitudinal sections are preferred mostly to determine:

- Whether a part has been cast, forged, or rolled
- Whether the part shape has resulted from casting, machining, or forming
- Whether wires, bars, or rebars have been welded
- The features of conventional friction welds
- The extent of surface heat or thermochemical treatments, and so on.

Because the macrostructural features of a material do not always relate directly to the external shape of a part to be examined, care must be taken when evaluating the structural features of the material based on the observa-

tion of few sections, either longitudinal or transverse. For example, the extent of the segregation observed in a cylindrical bar rolled or forged from a square or rectangular billet or ingot may depend on how the longitudinal section intercepts this feature, as shown schematically in Fig. 4.1.

Thus, in this case, the evaluation of the extent of this feature cannot be correctly performed using a single longitudinal section. In Fig. 4.2 and in the macrographs in Fig. 4.3, one can observe the different aspects of nuts subjected to sectioning transverse or longitudinal to the rolling direction of the bar from which they were machined. The bar presents heavy central segregation, which enhances the differences visible in the macrographs. One would expect that nuts would be machined from cylindrical bars, with their axis coinciding with the bar axis. Expectations and assumptions, however, can frequently lead to mistakes in metallographic investigations.

When examining castings, that is, parts that are cast directly in their final shape, the sectioning planes are normally selected based on part geometry. One must try to choose sections that include the critical locations of the part, such as regions subjected to higher loads or regions in which casting defects are more likely to occur because of the design of the casting process.

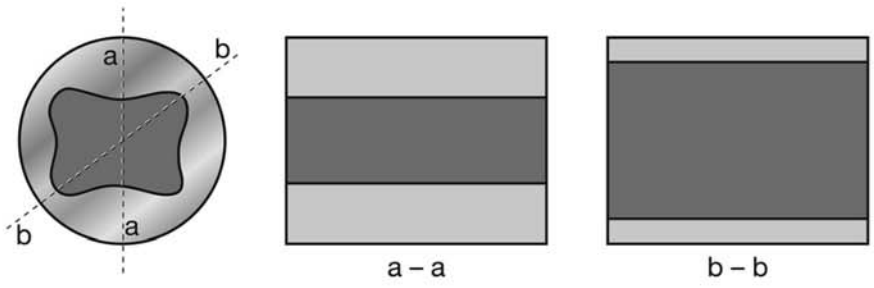

Fig. 4.1 Example of the influence of the orientation of a longitudinal cut on the segregation aspect in macrographs of a cylindrical part. Effect also may occur in other shapes of semi-finished products.

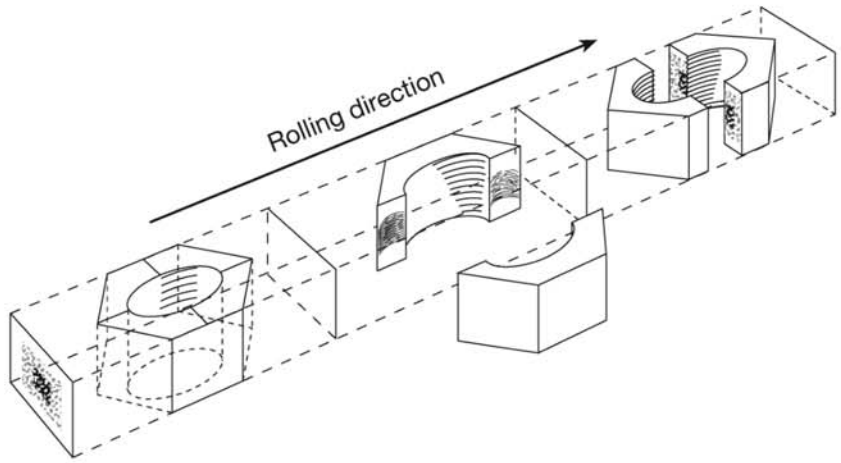

Fig. 4.2 Example of how the selection of the macrographic section influences the result of the examination.

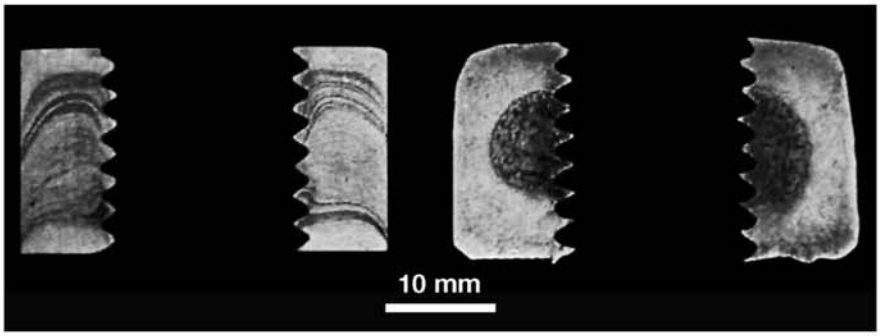

Fig. 4.3 Macrographic aspect of two sections performed in nuts produced by forming, from a rolled cylindrical bar. Sections have been made as identified in Fig. 4.2. Strong segregation in the original bar makes the differences clearer.

Frequently the macrographic examination of a steel casting is aimed at locating pipe and other shrinkage defects, bubbles and pores, and cracks, as well as evaluating the dendritic structure and sometimes qualitatively evaluating the extent of segregation.

Among cast irons, normally chilled irons and mottled irons are the only ones subjected to macrographic evaluation. In mottled irons one can evaluate the size and distribution of the graphite nuclei, whereas in chilled irons the depth of the chilled layer and its transition to the core structure can be evaluated. Evidently, selecting the proper section depends on the geometry of the part and the feature to be evaluated.

4.1.2 Surface Preparation

Achieving a proper surface for the macrographic examination comprises two steps: cutting and grinding. Sometimes a sample requires cleaning before its preparation (to remove oxidation, etc.). If the underlying surface is of interest (e.g., fracture surfaces), cleaning should be performed with special care. ASTM E3 (Ref 2) gives guidelines about surface cleaning.

Cutting usually is done with a saw or an abrasive disk cutter ("cut-off" saw). The cut defines the surface to be examined. In some cases, cutting is not viable, and machining or grinding can be used to remove sufficient material to reach the plane to be examined. When large parts must be examined and flame cutting is unavoidable as the first sectioning stage, one must make sure that sufficient material is left between the flame-cut surface and the surface of interest so that the volume of material thermally affected by the cutting process (the heat-affected zone, or HAZ) is completely eliminated. This way, flame or plasma cutting can be used to reduce part dimensions and make possible the proper preparation of the surface. Automated grinding equipment or a machining process (milling, for instance) is used to finish this first stage, aimed at achieving a flat surface, with reasonably low rugosity and at the proper orientation and position in the part.

In general, no less than 10 mm of material from the flame-cut surface must be removed. The surface oxidation caused by the flame-cutting operation is an indication of the minimum extent of material to be removed. ASTM E340 (Ref 3), for instance, presents as an example the removal of a sample for mac-

rograph 100–130 mm (4–5 in.) away from the torch-cut edge. In any case, extreme care must be exercised when examining the macrograph (and eventually the micrographs). Should any doubt remain, the discard should be increased to determine that the heat-affected region has been completely removed and the unaffected structure of the material is being examined.

One of the difficulties in this step is achieving a truly flat surface. Larger macrographs, materials with nonuniform hardness, and parts with complex geometry make it harder to achieve flat surfaces in this preparation step.

All of these preparation operations must be performed with care to avoid localized work hardening and heating above around 100 °C (210 °F). Both can be evidenced later by etching, leading to artifacts and incorrect evaluation of the features of the macrograph.

The pressure applied during grinding as well as the feed in the case of machining operations must be carefully controlled and should take into consideration the part hardness. Soft materials should not be subjected to high pressures or feeds, and too coarse a grinding grit should be avoided.

The ideal sample surface rugosity depends on the etchant to be used and the features to be observed. In some cases, surfaces directly produced by cutting with saws or by facing by machining can produce acceptable macrographs.

Final preparation for macrographic examination involves grinding. Silicon carbide grinding papers are the most commonly used grinding materials. Grinding is started in a direction perpendicular to the coarse grinding marks or machining marks on the sample surface. This is performed at least until these marks are removed. Preparation proceeds by changing to a finer grit material and changing the grinding direction by 90°. The new stage continues until all the previous grinding marks have been removed. The procedure is repeated using, typically 100 or 120, 220, and 320 grit paper. In general, the part is moved over the grinding paper. If the macrograph is sufficiently small, automatic grinding machines, in which the grinding paper moves and the sample is fixed (usually manually held) can be used. For large macrographs, it may be necessary to fix the part in a vise and perform the grinding by moving the grinding paper over the part. In this case, it is convenient to have a flat support for the grinding paper (Fig. 4.4). Care must be exercised to avoid rounding the edges of the sample when the region close to the surface is to be examined. Important information about the material is often located at or

Fig. 4.4 Alternative way for sanding larger parts for macrographic examination. Grinding paper is held flat in contact with a piece of wood or plastic; sample is held fixed in a vise.

close to the part surface: rounding the edges makes it impossible to properly examine these regions.

In manual grinding, only proper training will lead to good sample preparation practices and to the absence of rounded corners. To avoid rounded corners, force must be applied normal to the contact surface. It is a natural response to increase the pressure on the edge that faces the grinding paper movement, for instance, but this leads to rounding of edges.

Grinding (or polishing) to an excessively low roughness ("mirror-like") finish should be avoided when preparing macrographs. First, this can cause difficulties in wetting by the etchant, and second, photographic recording difficulties increase as a result of reflections.

When changing from one grit to the next, the part should be cleaned carefully to avoid contaminating the finer grinding paper with coarser fragments that would scratch the sample. In all cleaning steps, washing with water and carefully drying with alcohol and hot-blown air are permissible. When pores and cavities are present, the risk of staining the surface must be considered. Once the grinding is finished, the surface should be cleaned carefully again with a piece of clean cloth or cotton ball.

At this point of the preparation, some important features can be observed: porosity, bubbles, pipe, large nonmetallic inclusions, and some weld defects are already evident without etching. Another important reason to examine the as-polished surface carefully is that etching frequently hides defects of sample preparation. As a rule, even if someone else prepares the sample, the person responsible for evaluating the material should observe the sample quality before etching and then witness the etching process. Only after recording all relevant features (or the absence of recordable features) on the unetched sample and evaluating the overall sample preparation and cleanness should etching be performed.

Etching is important to show other heterogeneities or features of the structure, as well as the relationship between the features that can be observed before and after etching.

4.1.3 Surface Etching

Safety precautions are of paramount importance when dealing with etchants. As mentioned before, it is not the objective of this text to discuss these precautions, but the reader is cautioned about the need to fully understand the risks associated with the operations he or she will perform and the chemicals that will be handled. Protective equipment, adequate laboratory organization, and proper disposal procedures are essential in metallographic preparation. The reader is cautioned to procure the proper information on performing these tasks with adequate safety and protection and without harming the environment.

Normally, when a ground or polished sample surface is subjected to the uniform action of an etchant, some regions will be etched to a greater or lesser extent than others. This difference in response results mostly from two sources: differences in chemical composition and differences in crystal structure. This subject is discussed in more detail in subsequent sections. The different etching responses are responsible for showing the macrostructural features of the material.

Etching (the contact between the sample surface and the reagents) can be performed in three different ways:

- *Immersion or dipping:* the polished surface is immersed in a container that is resistant to the reagent used. This is the most common method and is the only applicable method when etching is not performed at room temperature. If the part is too large for immersion in a proper container, it can be cut into reasonably sized pieces. Alternatively, if observing the region close to the edges is not important, very large sections that cannot be properly immersed in a container can be covered with the etchant if plasticine barriers are built over the edges of the sample and the reagent is carefully poured over the surface with proper care not to overflow the barriers. When attempting this alternative, one should first check the compatibility of the plasticine with the reagent and observe all safety precautions.
- *Brushing or swabbing:* a thin layer of the reagent is spread over the surface to be etched with either a brush or a swab (cotton, usually). Achieving uniform etching requires constant observation of the sample and correction of the reagent application.
- *Direct print:* in the case of sulfur prints (Ref 4), a sheet of photographic paper soaked in the proper etchant is placed on the ground surface of the specimen. A print of the sulfur and sulfides distribution in the steel is revealed as a mirror image in the photographic paper.

Reagents for Macrographic Etching

Table 4.1 presents the most commonly used reagents for etching ferrous products and their basic indications (Ref 3, 5–7).

In the following sections, the applications of selected macrographic etchants are discussed. Beginning in Chapter 7, "Equilibrium Phases and Constituents in the Fe-C System," in this book, examples of the application of various reagents are presented.

Iodine and Potassium Iodine (or Simply Iodine) Etchant. Although this reagent is not listed in ASTM E340 (Ref 3) or E381 (Ref 6), it is one of the recommended macroetchants for steel welds in Section IX of the ASME Code (Ref 7). It is quite easy to use and, in addition to its classical use, can produce very interesting results when associated with light regrinding and eventually a short second etching.

Along with the classical results, etching with an iodine reagent can produce two other types of results that can greatly help in understanding sample macrostructure: some of the results that show after etching can be almost completely removed when a light regrinding is performed afterward. This is the case with HAZs, carbon- and phosphorous-rich segregated areas, and surface-hardened zones, among others. Segregation, dendritic structure, banding, and structural changes associated with these features, on the other hand, can be shown in an enhanced way after a light regrinding followed by a very short time (around 2 s) of etching, followed by cleaning with a copious water flow on the sample surface or by immersion and agitation of the sample in water. It is possible, then, when using iodine to study macrostructures, to tailor the etching-grinding sequence to get the most out of the evaluation.

Table 4.1 Reagents for macrographic etching

Etching reagent	Composition and remarks	Application
Iodine and potassium iodide	Powdered iodine (solid): 10 g Powdered potassium iodide: 20 g Water: 100 mL	General application, welds according to ASME IX
Mixed acids	Hydrochloric acid (conc.): 38 mL Sulfuric acid (conc.): 12 mL Water: 50 mL Use hot: 70–80 °C	Highlights segregation and fiber structure
Heyn	Ammonium tetrachlorocuprate II: 9 g Water: 100 mL Deposited copper must be removed by slight abrasion after etching	Defines phosphorous segregation Highlights segregation
Hydrochloric acid	Hydrochloric acid (conc.): 50 mL Water: 50 mL Use hot: 70–80 °C	Segregation, depth of hardening in tool steels. General macroetching of steel (ASTM E381) Macroetching austenitic stainless steel (AISI 300 series)
Oberhoffer	Distilled water: 500 mL Ethyl alcohol: 500 mL $FeCl_3$: 30 g $SnCl_3$: 0.5 g $CuCl_2$: 1 g Use at room temperature, 20s immersion, approx.	Segregation. Dendritic structure. Iron rich areas are normally darker.
Fry	Distilled water: 100 mL Hydrochloric acid 32%: 120–180 mL $CuCl_2$: 90–45 g	Deformation bands. Lüders bands in cold worked steel
Ammonium persulfate	Distilled water: 100 mL $(NH_4)_2S_2O_8$ (ammonium persulfate): 10 g Swabbing or immersion	Welds, segregation, dendritic structure
Humfrey	Distilled water: 500 mL Hydrochloric acid: 25ml $Cu(NH_3)_4Cl_2$: 60 g Deposited copper must be removed by slight abrasion after etching	Segregation. Dendritic structure
Two-stage Humfrey	First stage: neutral Humfrey Distilled water: 500 mL $Cu(NH_3)_4Cl_2$: 60 g Second stage: acid Humfrey Distilled water: 500 mL $Cu(NH_3)_4Cl_2$: 60 g Hydrochloric acid: 25 mL	Dendritic segregation, continuous cast products structure, high cleanness steel

Of course, when performing macrographic examination according to codes or standards, the practice defined by the code or standard must be followed strictly.

Sulfuric Acid and Mixed-Acid Reagent. Sulfuric acid and mixed-acid reagents are used hot, close to boiling. They result in rapid and deep etching in a few minutes, especially if the material has a high number of nonmetallic inclusions. Etching at room temperature with these reagents takes several hours. These reagents are especially useful to show material "fibers" (see Chapter 11, "Hot Working," beginning with the section "11.2.3 Change of Shape and Distribution of Segregates").

Heyn's Reagent. Heyn's reagent is one of a group of reagents that contain copper in their formulation. When the specimen emerges from the etching, it is covered by a red layer of powdered copper. This layer should be removed by lightly swabbing with a piece of cotton under flowing water. Should the layer adhere too strongly to the surface, the sample can be washed with a solution of ammonium citrate in water with a little ammonia in solution.

Like other cupric reagents, it is especially suited to reveal phosphorous-rich zones.

Humfrey's Reagent (and Two-Stage Humfrey Etching). Like Heyn's reagent, Humfrey's reagent contains copper. Reference 8 reports outstanding results with this reagent when observing the macrostructure of low-carbon, low-residual (P and S), high-cleanness steels produced by continuous casting. Reagents in this group do not react with nonmetallic inclusions. When macrograph etching is used to locate segregated areas to focus the investigation on nonmetallic inclusions, this is a significant advantage over sulfuric, mixed, or hydrochloric acid reagents. Because inclusions are not etched away, it is possible to cut a sample from the macrograph and directly start the preparation for micrographic examination of the nonmetallic inclusions. When a more aggressive reagent is used and the nonmetallic inclusions are corroded, a significant portion of material must be removed from the surface before starting micrograph preparation on sound material. This may lead to the complete removal of areas of inclusion concentration and compromise the investigation.

Hydrochloric Acid. This reagent is used in hot etching. It is widely used in the observation of the macrostructure of billets, blooms, and other semi-finished products, in accordance with ASTM E381 (Ref 6). It also can be used to macro-etch some stainless steels of the AISI 300 (austenitic) series.

Fry's Reagent. This reagent is recommended to highlight deformation lines in material that has been subjected to light work hardening (Lüders bands, see Fig. 12.3 and 12.4)

Sulfur Print (or Baumann Print)

Sulfur prints (Ref 4) use plain black-and-white photographic paper (silver bromide paper). Matte finish paper is preferred. The paper is immersed for about 1 min in an aqueous solution of sulfuric acid (1–5%) when the print is ready to be made. The soaked paper sheet is drained to remove excess solution and laid over the sample surface. It is especially important to lay the paper carefully to guarantee perfect paper–sample contact, without trapping air bubbles or sliding the paper over the surface, once contact is started. A rubber roller or manual pressure can help in this task.

ASTM recommends the sample surface roughness, R_a, should be greater than 0.4 μm to reduce the chances of the paper sliding over the sample. Up to 1.6 μm may be necessary to avoid sliding. Other standards suggest that a R_a of 3.2 μm may be a safer value for this purpose (Ref 9). Proper surface finish can be achieved by grinding with 60-grit abrasive or grinding paper.

After about 5 min the paper is carefully lifted from the sample, washed in clean water, and immersed in photographic fixer solution (sodium thiosulfate, or sodium hyposulfite, or "hypo") for about 15–20 min. The exact time required for a good sulfur print must be determined experimentally. If prints of different materials or different heats of a steel are to be compared, the time must be standardized. After fixing, wash the paper in running water for about 1 h. Although all of these operations can be performed under normal lighting conditions, one should be careful to avoid excessive exposure of photographic paper to light (either for a long time or to very intense light sources).

Regions rich in sulfides show up as brown or dark brown to black areas because sulfuric acid can decompose these inclusions. The product of this reaction (H_2S) reacts with the silver bromide in the photosensitive layer of the photographic paper. The final product of the reaction is silver sulfide that impregnates the paper emulsion. The hyposulfite fixer eliminates the unreacted silver bromide from the paper emulsion and preserves the reacted regions. For high-sulfur (e.g., 0.1 wt% S) free-cutting steels, the sulfuric acid solution must be significantly diluted to achieve acceptable results.

The results from sulfur prints are similar to those achieved with the iodine reagent with respect to segregation, bubbles and pores, and "fiber" orientation and distribution. However, the sulfur print will not show regions where segregation of carbon, manganese, silicon, or phosphorous is present but not associated with sulfur segregation. In general, the segregation of sulfur accompanies the segregation of these elements (see Chapter 8, "Solidification, Segregation, and Nonmetallic Inclusions," in this book). The reader is cautioned to the fact that very low sulfur steel is produced for many applications (e.g., hydrogen-induced cracking or HIC-resistant steel, high-toughness plates, and forgings for nuclear vessels) and although segregation will be present, it may not be revealed by the sulfur print because of the very low sulfur contents (in the ppm range) of these steels. Furthermore, although etching with iodine reagent, for instance, will clearly show structural changes caused by thermal cycles, these will not be revealed in a sulfur print.

One would expect a clear relationship between the steel sulfur content and the intensity of the images produced in a sulfur print, but the correlation is not well defined even when all test conditions are kept constant: solution concentration, temperature, duration of application, paper type and quality, and so on. As a general rule, if all conditions are kept constant, darker prints are associated with higher sulfur content while very light prints indicate low to very low sulfur content.

One must keep in mind that several metallurgical factors besides sulfur concentration in the nonmetallic inclusions will play a role in the intensity of the print. One example that demonstrates this is the examination of rolled products. In these products, manganese and iron-manganese sulfides become elongated during hot working (see Chapter 11, "Hot Working" in this book). The sulfur print from a transverse section normally is darker than the corresponding print from the longitudinal section. Figure 4.5 illustrates the

reason for this difference: in the transverse section, the reagent will find the elongated inclusions normal to the surface and will penetrate to a significant depth, as compared with the longitudinal sample. Thus, in the transverse sample, more H_2S is generated in the reaction between inclusions and reagent than in the case of the longitudinal section. For this reason, comparing the intensity of sulfur prints from different orientations with respect to the working direction of the material can be misleading.

Care must be exercised when a second sulfur print from the same surface is needed or when it is desired to further investigate findings from a sulfur print with another technique, for example, micrography. Because the reagent corrodes the sulfides, new machining is needed and sufficient material should be removed to eliminate the corroded region (Fig. 4.6). As discussed already, the amount of material to be removed in a transverse section is larger than in a longitudinal section. This precaution is applicable to all deep etching techniques (such as hydrochloric reagent). When a dye penetrant examination is performed on a macrograph that has been subjected to etching with hydrochloric acid or to a sulfur print, it is not uncommon to find indications that would not be present in the as-ground surface. These "pores" are deeply corroded regions. When several examination techniques are going to be used on

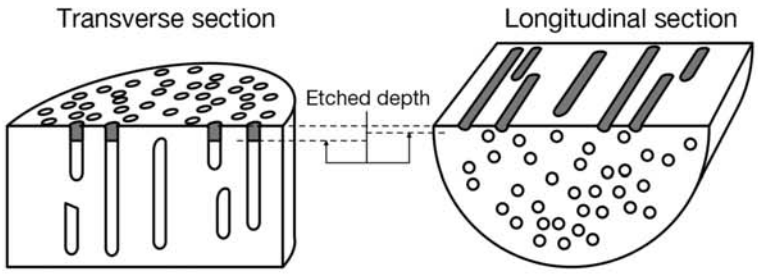

Fig. 4.5 Influence of macrographic section orientation with respect to nonmetallic anisotropy in hot-worked products (rolled, forged, etc.). In sulfur prints, the differences in etching depth result in different intensities in the print.

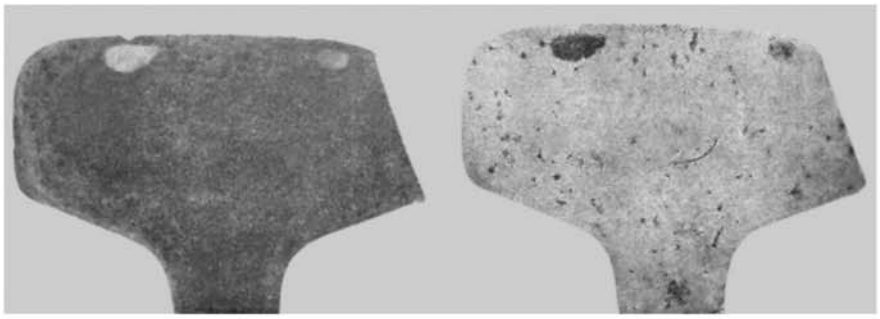

Fig. 4.6 When bubbles are retained between the sample and the paper in a sulfur print (see also Chapter 8, "Solidification, Segregation, and Nonmetallic Inclusions," in this book) regrinding is required before performing a new sulfur print. Otherwise, as the nonreacted regions under the bubble are etched in the second print, they will appear much darker.

the same sample, the sequence of performance should be carefully studied to avoid misleading results.

While in the past the sulfur print has been a powerful tool helping in failure analysis, its use has been reduced in the past few decades. Presently it is used almost only in quality control for steel rolled and forged products and monitoring continuous casting processes. As discussed, the test results depend on the sulfur present in the steel and its segregation. As the industry's quality requirements have increased, lower sulfur contents and stringent segregation control have become the norm (Chapter 8, "Solidification, Segregation, and Nonmetallic Inclusions"). This sometimes limit the possibility of producing relevant sulfur prints. The technique still is widely used in many plants for the quality control of rolled and forged products, and to control, in close to real time, the adjustment of continuous casting machines (see Chapter 8).

Artifacts and Precautions

It is important to keep in mind that lack of proper care during grinding or etching may lead to mistakes in the evaluation of macrographs. Grinding, sanding, and sample cutting with abrasive disks may lead to thermal cycles that can induce structural changes or excessive work hardening. In this respect, surface work hardening and distortion are widely recognized as a pervasive problem in sample preparation for many metallographic techniques. The effects of thermal cycles and/or work hardening will show during etching and are artifacts, that is, not part of the original material structure.

Figures 4.7 to 4.9 show some examples of these problems. Drying the specimens is a delicate operation, especially when porosity, cracks, pipes, and other cavities open to the surface are present. These cavities will retain washing water or reagent that will slowly exude from them, spreading around the cavity, causing stains of different shapes, especially if tissue or grinding paper is applied to the surface afterward. In some cases, the liquid may, as a result of capillarity, take long times to exude at the surface, producing marks that can be judged as stains (in the most favorable scenario) or artifacts that influence the evaluation (see Fig. 8.54a).

Failure to immediately rinse, clean, and regrind a sample that was subjected to a sulfur print and will be examined through macroetching can lead to stains. The sulfuric acid held in the cavities resulting from the corrosion of the specimen or in pores or pipes will cause stains when the sample is in contact with the new etchant.

In all cases, a surface to be etched should be as clean as possible: not even fingers, even when they are apparently clean, should come in contact with the surface. The natural oils in the skin will interfere with the homogeneity of the etching behavior over the surface.

Grease and oily substances left on the side surfaces of the sample should be carefully removed to avoid their making contact with the reactant and causing contamination of etching surfaces.

When performing long acid etchings, the possibility of electrochemical corrosion should be considered when metallic supports, tweezers, and similar accessories made from metal different from the alloy being etched are in contact with the bath or the specimen. Electrolysis can lead to chemical deposits forming on the sample surface.

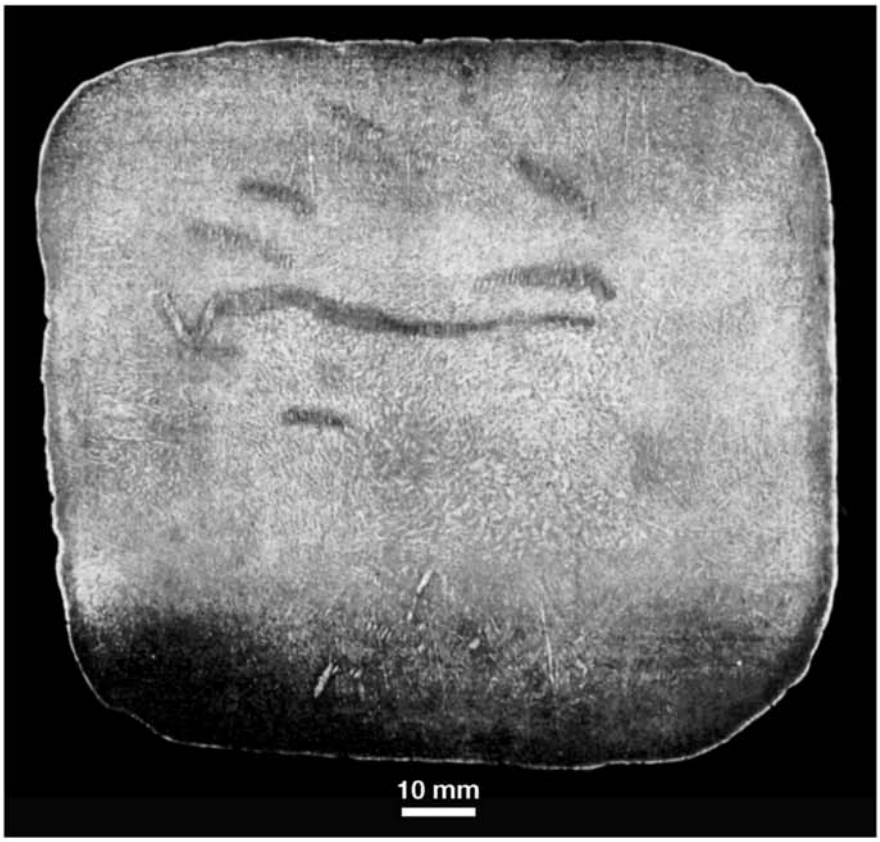

Fig. 4.7 False indications (artifacts) in a macrograph. Dark bands are the result of local hardening due to excessive heating during the sample preparation with a grinding wheel. Etchant: iodine reagent.

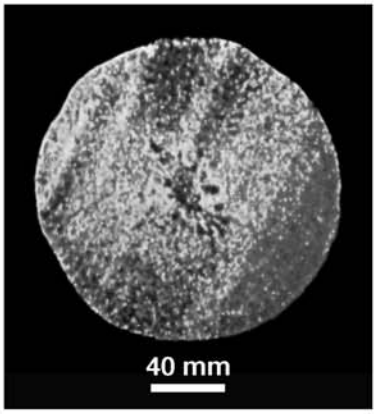

Fig. 4.8 False indications (artifacts) in a macrograph. Dark and light bands are the result of local hardening due to excessive heating during the sample preparation with a cut-off wheel. Either excessive pressure or insufficient refrigeration was used. Etchant: iodine reagent.

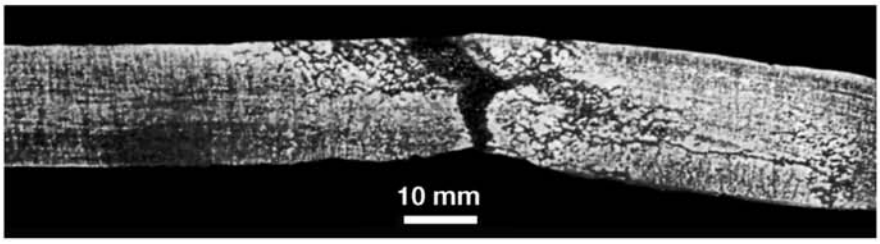

Fig. 4.9 False indications (artifacts) in a macrograph. Transverse scratches left from coarse sanding that were not completely removed on the finer sanding stages. Dark stain at the left is the camera lens reflection on the sample surface (see the section "Reflections and Glare"). Etchant: iodine reagent.

When etching, frequent agitation of the specimen (or of the reagent) is recommended to eliminate gas bubbles. Several of the reactions associated with etching result in the formation of gases. If bubbles adhere to the specimen surface, they prevent etchant–sample contact, leading to stains or discolorations. Similarly, if air bubbles are mechanically entrained in the solution and trapped in contact with the sample, circular regions that are lighter or not

etched at all will be produced. When immersing the sample in the solution, care should be taken to make sure all bubbles that might adhere to the specimen surface are removed via agitation.

Too shiny a grinding (or a polishing) will make a good etching harder, because the reagent will not be able to "wet" the sample surface properly and homogeneously. Then, when the specimen is removed from the reagent or when one tries to uniformly wipe the reagent with a cotton swab, the liquid surface tension will make it collapse into isolated droplets; the etching occurs under the droplets while the rest of the sample surface is not etched. The result is staining and nonuniform etching.

4.1.4 Evaluation and Interpretation of Results

Macrographic etching produces contrasts related to areas with differences in chemical composition or different metallographic structure (due to the presence of different phases, different volume fraction of the phases, or even differences in size and distribution of phases). The observed contrast is because different regions react differently and darken more or less under the action of the reagent.

Specific standards used to perform macrographic evaluation frequently define evaluation criteria. This is the case, for instance, with ASTM E381 (Ref 6), which defines rating criteria for conventional ingot products and continuous cast products. If the macrograph evaluation is not performed according to a given standard, the results must be evaluated and interpreted considering the information revealed by the macrograph.

Results from Iodine Reagent Etching

In this section, the main results of etching with iodine as reagent are discussed.

With respect to chemical composition, it generally is observed that the following areas darken more when etched:

- Areas with higher carbon content
- Areas with higher phosphorous content
- Areas with higher concentration of nonmetallic inclusions, especially those rich in sulfides

Thus, in general, areas presenting positive segregation and carburized areas will appear darker than the rest of the sample.

Regrinding after Etching with Iodine Reagent. When not otherwise defined by the macrographic standard being used, interesting additional information may be gained by lightly regrinding the sample after etching to highlight the contrast developed by etching.

Darker regions caused by carbon or phosphorous segregation will become lighter after light regrinding, whereas those containing higher concentration of sulfide inclusions will remain darker as a result of the reaction that occurs around the inclusions. As the regions around them with lower concentration of sulfides become lighter after light regrinding, those rich in sulfides will be

further highlighted, and the image contrast will increase. For this reason, dendritic structure is highlighted after light regrinding. The axis of the dendrite arms will become lighter, whereas the interdendritic regions, richer in inclusions and more segregated (see Chapter 8, "Solidification, Segregation, and Nonmetallic Inclusions") and thus more actively etched, will remain darker.

A similar phenomenon is observed when examining the longitudinal section of rolled parts. In this case, light regrinding will highlight the "fibrous" structure caused by the significant elongation that inclusions, especially manganese sulfides, suffer during rolling (see Chapter 11, "Hot Working," specifically the section "11.3.1 Closed Die Forging"). Further forming (e.g., closed die forging, thread rolling; see Chapter 11 and Chapter 12, "Mechanical Work of Steels: Cold Working") will deform the fibers, altering their orientation and spacing. How fibers are oriented with respect to part mechanical loading is very important, and macrographic examination is essential to perform this evaluation (See Chapter 11, specifically the section "11.4 Defects in Hot Working").

Conversely, grain size heterogeneity ("coarse" structure) is associated with a shallower reaction region during etching. Thus, when light regrinding is performed, this indication will disappear from the macrograph, and more deeply etched regions will become more evident. Similarly, quenched and tempered regions are very sensitive to this etchant and will darken significantly. However, these darker regions will disappear from the macrograph after light regrinding. Because they are harder, they may become even "shinier" than the surrounding regions. Finally, the darkening of cold-worked regions caused by this etchant will disappear after light regrinding.

In summary, light regrinding may be used to highlight the structural features that result in deeper etching and might be less visible because of the simultaneous appearance of other features that are, however, associated with a shallower reaction volume. Light regrinding is an operation that must be performed with care and in a progressive way. As the metallographer practices this technique, he or she will gain experience in judging which cases the technique can be applied to with good results.

As an example, if coarse grain size is to be highlighted, regrinding is not recommended. If, however, one wants to emphasize the dendritic structure, it is possible that it will clearly appear only after light regrinding. Figures 4.10, 4.11, 4.12, and 4.13 illustrate some of the effects that can be expected when light regrinding is applied after etching with iodine reagent.

4.1.5 Photographic Record

Sulfur prints are produced directly on photographic paper, and these images can be reproduced by digitizing or photographing the print. However, when a specimen is etched with the usual macrographic etchants or even when an "as-ground" surface is to be recorded, the sample must be photographed.

Size and Resolution

For macrographs, natural size (1:1) reproduction is usually preferred. Small samples or important details may be enlarged when taking the photograph.

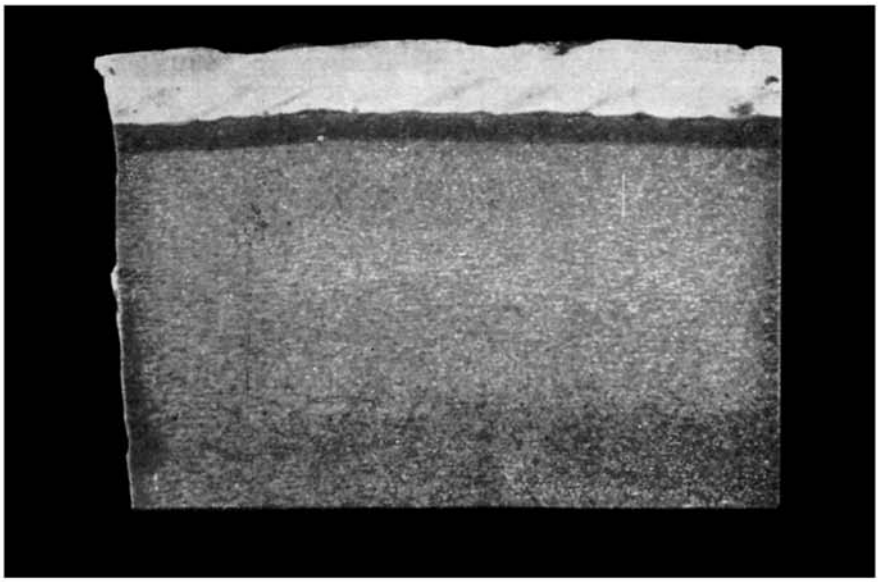

Fig. 4.10 Macrograph of a radial section of a tram wheel that was repaired by welding. Deposited metal appears light while the heat affected zone (HAZ) (see Chapter 14, "Structural Steels and Steels for Pressure Vessels, Piping, and Boilers," in this book) appears dark. Etchant: iodine reagent.

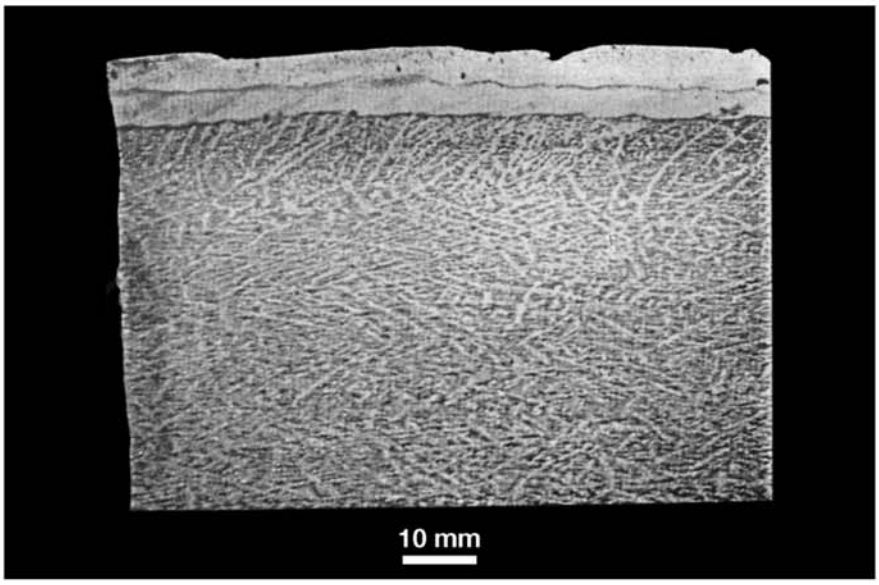

Fig. 4.11 Macrograph of Fig. 4.10 after light regrinding. Transition zone between the two weld layers and the dendritic structure of the cast wheel can be observed. Etchant: iodine reagent, followed by light regrinding.

In this case, macro lenses, common in many cameras, including digital cameras, can be used.

When the surface to be photographed is very large, it can be recorded in multiple images that can be assembled as a mosaic, or the record can be reduced to a practical size, as long as the important features are still visible.

One should be aware that conventional photographic techniques (using films for negatives or slides) in general have high resolution. When digital imaging is used, one should consider a minimum of 75 dots per inch (dpi) when preparing images for observation on a computer screen or 300 dpi for prints. When making images of large samples, it is convenient to evaluate the approximate number of pixels in the final image. This makes it possible to deter-

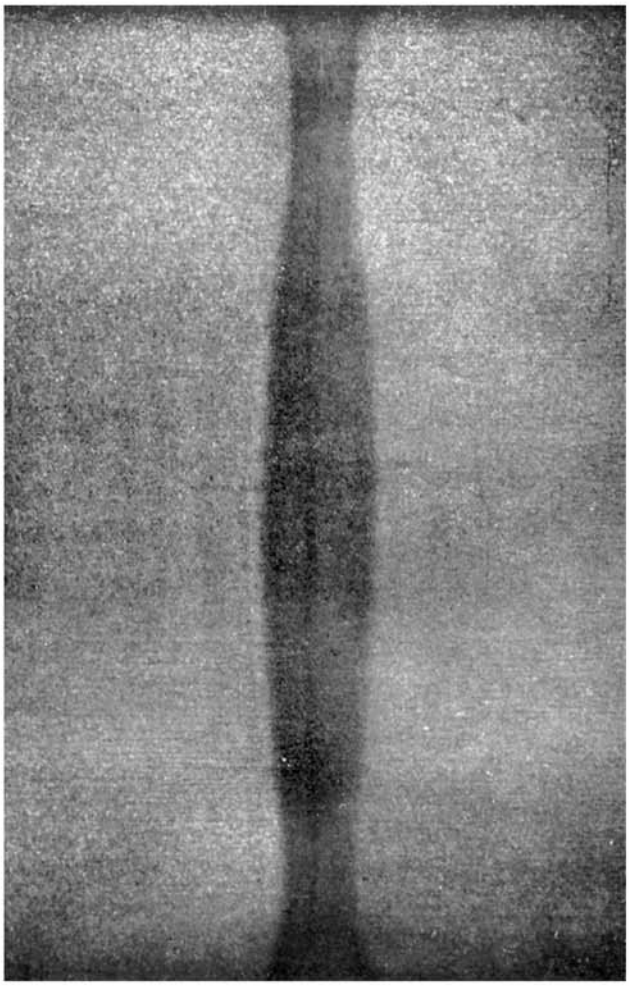

Fig. 4.12 Macrograph of the longitudinal section of two rails that were forge welded (joined by heat and pressure). The HAZ can be seen. The width of the HAZ is not uniform because the rail has a variable cross section. Etchant: iodine reagent.

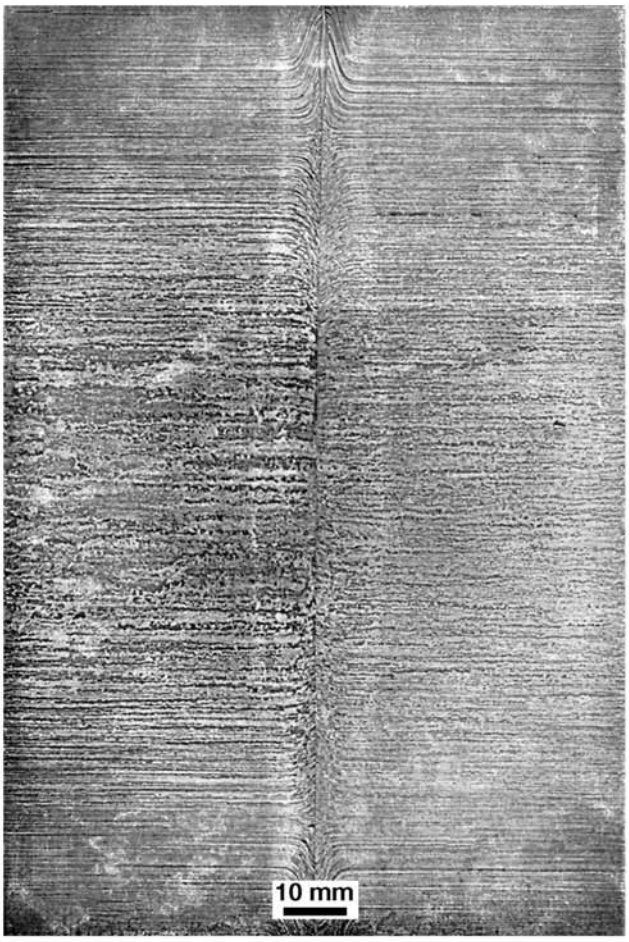

Fig. 4.13 Macrograph of Fig. 4.12 after light regrinding. Material "fibers" in the longitudinal direction of the rails are visible. Fibers have been distorted in the welding region by the applied pressure. HAZ appears as a lighter "halo." Etchant: iodine reagent, followed by light regrinding.

mine the largest sample that can be photographed with appropriate quality and the highest magnification (in print) that can be produced. For digital cameras, it is common to have information on the number of pixels in an image. Once the number of pixels in each direction of the image and the size of the part are known, one can calculate the number of pixels used to record a given dimension. Converting to pixels per inch will give an approximate dpi value for the photograph. If the camera manual does not give information about the number of pixels in each direction, the total number of pixels in an image can be used to estimate the value in each direction. One needs to know or assume the horizontal/vertical size ratio of the picture; 4/3 and 3/2 are typical ratios.

For example: consider a camera with 7.2 megapixels, and suppose that all of the pixels are used to compose the image. If the image ratio is $h/v = 4/3$,

what is the largest horizontal dimension that still will be compatible with 300 dpi? The number of pixels in the horizontal direction can be estimated as:

$$h \times \tfrac{3}{4} h = 7.2 \times 10^6 \, pixels$$

Hence,

$$h = \sqrt{\frac{4}{3}} \times 7.2 \times 10^6 \, pixels \cong 3100$$

Thus, if there are approximately 3,100 pixels in the horizontal direction of the camera sensor, the maximum width that still will retain a 300 dpi or better image is about 10 in. (254 mm).

In any case, it is convenient to maintain a simple ratio between the original size and the photographic image, so that size estimations can be performed without difficulty. It is also good practice to include a ruler or a size reference in the photographic field to guarantee that the information on the object size is preserved. If this simple procedure is used, considerable time will be saved in the future. Furthermore, it is convenient to include in the image field some sort of identification of the part or the sample to guarantee traceability.

Lighting

Whichever photographic technique is used, three aspects related to sample lighting are especially important to ensure good quality photographic images:

- Uniform lighting and properly oriented light sources
- Adequate control of reflections and shadows (caused by lighting) over the sample surface
- Sufficient light intensity

Usually the image created on the sample surface by the etching process is due to different reflection behavior: areas where the etchant reacts less with the sample will reflect with more intensity, whereas those areas that react more with the reagent will become corroded or dull, dispersing the light that reaches them.

When an etched surface is observed, it is possible that certain incident light orientations will make certain features of the etching more evident. When one wants to record this feature, it is necessary to make sure that the camera lens "sees" the sample surface to be recorded under the same illumination.

There basically are two lighting angles when macrographs are to be photographically recorded. This is illustrated in Fig. 4.14. In the arrangement of Fig. 4.14(a), the light reflected by the less etched (shinier) region of the sample is directed to the camera lens and will reach the film or the camera sensor. The dull or dark region (more etched) will disperse the incident light and thus not reflect light toward the camera lens. In the second arrangement, light reaches

the etched surface under a greater angle so that the rays reflected by the shinier regions will not reach the camera lens. These areas now will become darker. The reflection from the deeply etched regions is not significantly altered. These areas will look lighter in the photograph.

Lighting uniformity and homogeneity are essential for a successful photographic reproduction of a macrograph. When proper equipment is not available to produce uniform and controlled lighting, one of the best options is an "open shade," or using ambient solar light. Evidence shows controlled lighting techniques will lead to better results than lighting that is not controlled.

One good way of achieving uniform and homogeneous lighting is using reflectors (or bounce boards or board reflectors). Because using reflectors may result in loss of light intensity, the light sources should be properly dimensioned to achieve sufficient contrast. There are a number of light diffusers and light sources used in general photography that also can be useful when photographing macrographs. When reflectors are used, the light source area should be in accordance with the conditions presented in Fig. 4.15 to guarantee that all reflecting surfaces to be photographed have their reflected rays captured by the camera lens. These conditions are easier to fulfill when using cameras in which the lens plane can move parallel to the film plane. Unfortunately, this type of conventional camera, using bellows, is becoming less available. When the sample to be photographed has low contrast, the quality and size of the reflector are especially important. Too large a reflector for a given sample (Fig. 4.15b) will result in loss of light intensity because part of the light that bounces from the reflector, when reflected by the sample, does not reach the camera lens. The loss of light intensity will result in loss of contrast in the photograph.

Reflections and Glare

Surfaces that are too bright can pose a special problem. Moving the sample or the camera lens with respect to the axis of the camera will avoid mirroring the camera by the sample (Fig. 4.16). Additional information on how to deal with reflections and glare can be found in photographic technique books (Ref 10).

Surface Relief

When surface relief must be recorded in a photograph, the combination of light and shadows is of special importance. In general, surface relief is easier to interpret in a photograph if the lighting is done either from top to bottom, left to right, or front to back. For this reason, the main lighting source or the single light source (when only one source is used) should be in one of these positions. However, when the shadows caused by the relief in a fracture surface, for instance, are too intense and preclude recording the regions covered by them, it is convenient to use another light source of less intensity from the opposite direction. This fill-in light will improve the visibility of the details in the shade.

As important as the lighting orientation is how the final photograph is presented to the observer (Fig. 4.17). This care extends to micrographs when some constituents are observed in relief, as a result of either etching or relief

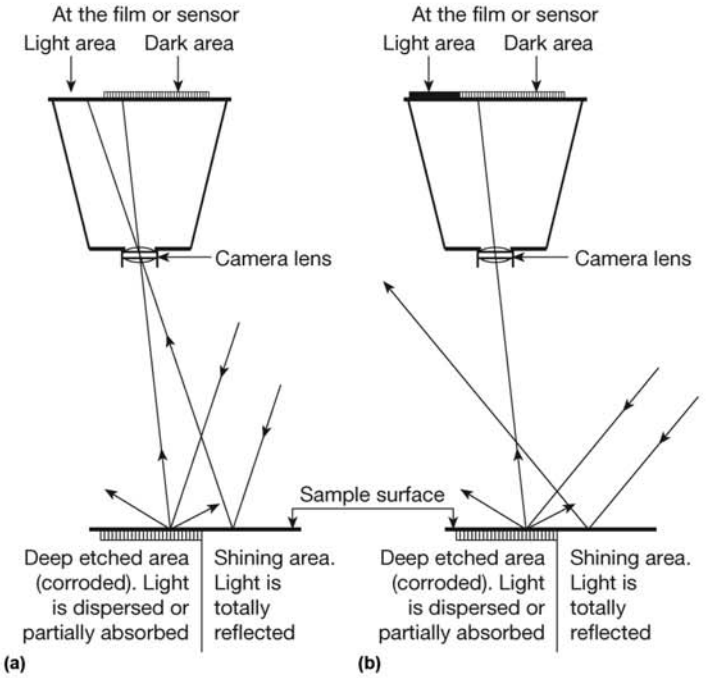

Fig. 4.14 Schematic presentation of two basic illumination arrangements used for photographing macrographs. (a) Illumination arranged so that the reflected light rays from the lighter etched regions ("shiny" regions) reach the film or the camera sensor. (b) Light rays reflected from the lighter etched regions ("shiny" regions) do not reach the film or the camera sensor.

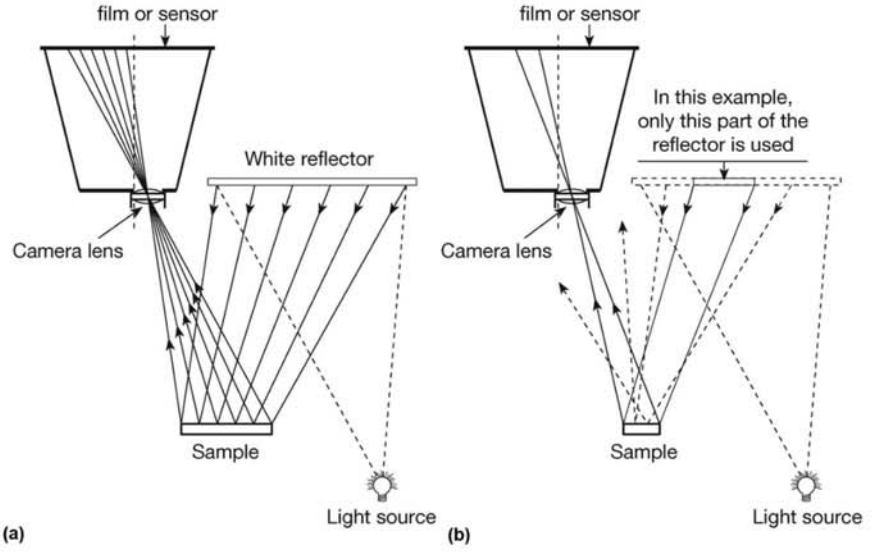

Fig. 4.15 (a) Illumination scheme using reflector to diffuse and homogenize light reaching the sample. (b) Poorly dimensioned reflectors result in loss of lighting and less contrast.

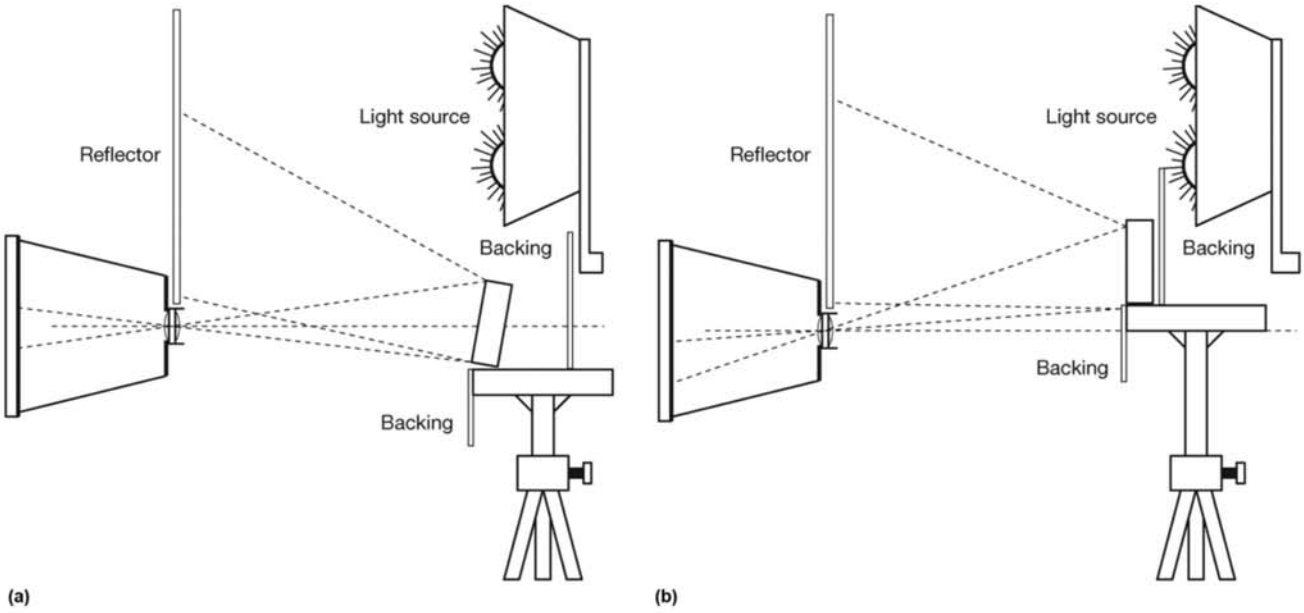

Fig. 4.16 Illumination arrangement to avoid reflections. (a) Sample is tilted to avoid the camera reflection on the sample surface. This arrangement will lead to some distortion. (b) Camera axis is dislocated with respect to the sample.

polishing. Figure 4.18(a) and (b) show how carbides in a micrograph can look as if they are depressions or protrusions from the average level of the surface. In general, to avoid confusion, misinterpretation, and optical illusions, it is convenient to present images from samples with relief in a way that the shadows are oriented as if the lighting had been performed as described in the previous paragraph.

Depth of Field

Depth of field or depth of focus is the distance between the nearest and farthest objects in a scene that still appear acceptably sharp (in focus) in an image. This distance is controlled by the lens aperture (f-stop or diaphragm opening) and the object to lens distance. In general, depth of field increases with a smaller lens aperture (larger f-stop). This, however, implies less light is reaching the film or camera sensor and may require longer exposure times and thus, camera support to avoid movement during the exposure. Increasing the distance between the object and the camera also will increase depth of field. The effect of the lens focal length is normally a consequence of the combination of f-stop and camera-to-object distance that will be used. When a sample is photographed slightly tilted or when a fracture is recorded, stopping down the lens will ensure a sharper image by making possible that parts closer and away from the camera remain in focus. Some cameras have selectors for depth of field preview, and with a digital camera, the image can be inspected immediately.

Lighting Arrangements

Digital photography has made possible almost instantaneous observation and evaluation of captured images. This is an enormous advantage that

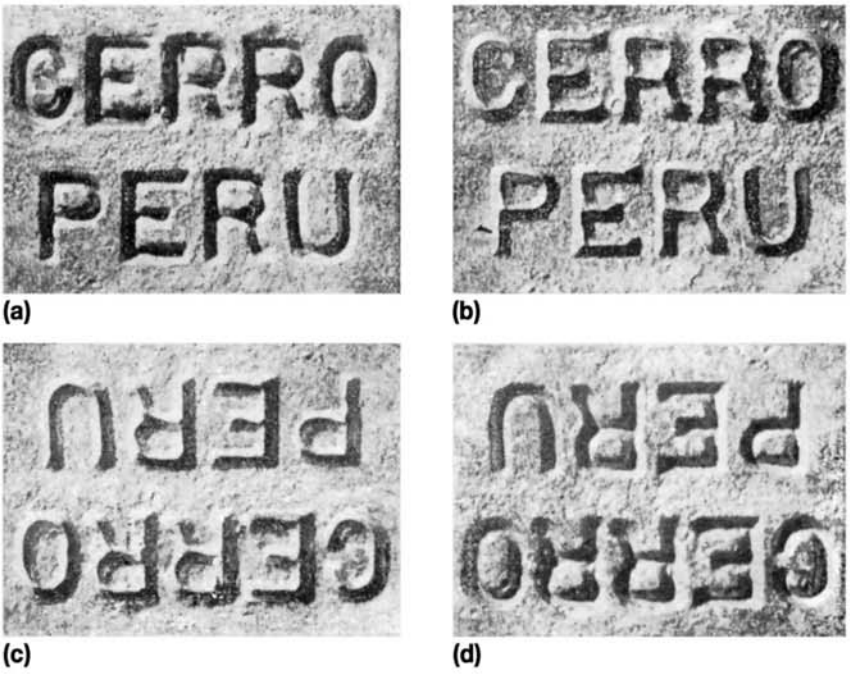

Fig. 4.17 The direction from which light reaches a sample has a great influence on how surface relief looks. (a) Light comes from the correct direction, upper left corner, giving the appearance that the letters are engraved in the sample surface (which indeed they are). (b) Light source is at the lower right corner, and the letters appear to be above the sample surface. Images (c) and (d) are images (a) and (b) inverted. This shows that how the way images are presented can be important to their ability to convey the right information.

makes it possible to avoid creating defective records compared with conventional pictures using film. However, it also has a bad side effect: the ease with which digital pictures can be captured frequently leads to careless procedure. Thus, careless lighting, lack of traceability and measurement reference, and undesired reflections became more common after the introduction of digital photography. Many digital camera sensors will introduce noise to the image when light sensitivity is set to ISO 400 or higher. Thus, even if the light

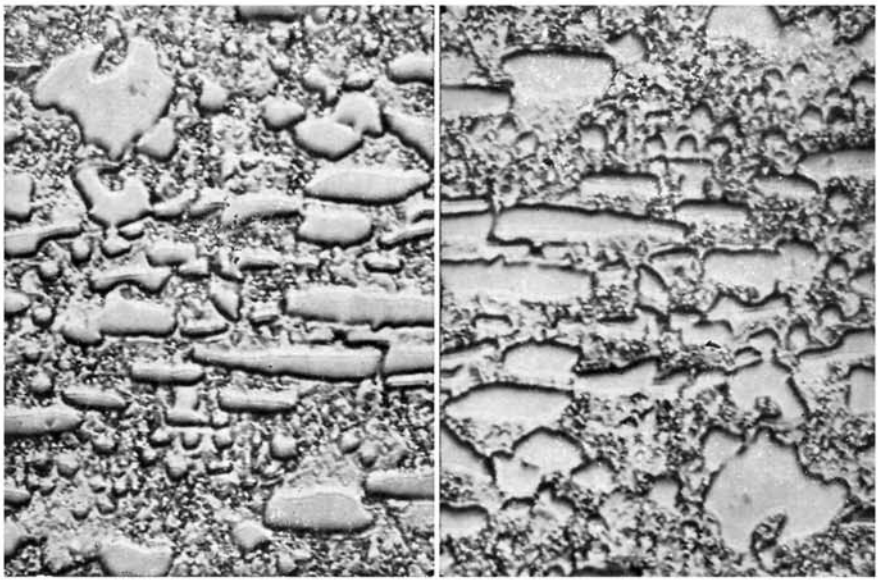

Fig. 4.18 Two positions (inverted) of the same micrograph. (a) Lighter areas appear to be above the overall surface (which indeed they are); (b) lighter areas look like depressions.

meter can find an exposure solution without the need for the use of a stand or a tripod for camera stabilization, the final result may be compromised by noise. Likewise, as automatic exposure may lead to large lens openings, and depth of field may be lost. The reader is cautioned to use, whenever possible, low ISO settings and moderate to high f-stops to ensure good image quality even if a stand or tripod becomes necessary for stabilization. (The manuals for some cameras and lenses also provide information on the f-stop that produces the best optical quality.) Because the sample is a static object, there normally is no reason to rely on automatic camera stabilization instead of using more intense lighting and/or a camera stand or a tripod.

In any event, there is no substitute for proper lighting as a critical element of a good photograph.

The instructions and ideas presented in the next sections, together with the quality that can be achieved with digital photography, should make possible an extraordinary quality of macrographic or photographic records. When studying the proposed lighting arrangements, the reader will notice that built-in flashes are normally improperly placed for good macrographs, notwithstanding the fact that their intensity is normally adequate for good contrast. Therefore, in most cases, using a camera flash should be avoided.

Arrangement A (Direct, Diffuse Lighting). The lighting arrangement schematically presented in Fig. 4.16 and 4.19 is specially indicated to highlight, in the photograph, those features of the macrograph associated with deeper etching, such as dendritic structure, "fibers," segregation, bubbles, and pores. The light sources are disposed either on one side (as indicated in the figure) or on both sides of the sample, when needed. Care should be exercised so that the light source neither faces the camera lens directly nor illuminates the sample directly. The specimen is indirectly illuminated with light coming from one or more sources bouncing on a reflector. (Although commercial reflectors are ideal, white matte cardboard usually gives good results.)

The lightly etched regions will be more reflective and will result in lighter surfaces in the photograph. The deeply etched regions will reflect less light, appearing as dark surfaces in the photograph. The arrangement in the figure is deliberately off-axis to avoid reflections. Narrow and long samples should be photographed with their largest dimension normal to the lens axis and parallel to the camera sensor or film. When the sample is tilted slightly or the arrangement is a little off-axis, small distortions are introduced. Generally this is not important. Excessive tilting should be avoided, however, because this will produce distortions that can lead to asymmetric images of symmetric objects.

When digital photography is used, many image processing software packages can correct these distortions without difficulty. GIMP is a free, open-source image editor that can perform these transformations. They also are easily done with commercial image processing software. See also Chapter 18, "Metallographic Evaluation: Guidelines for Performing and Reporting," in this book.

Arrangement B (Direct, Simple, Inclined Lighting). This arrangement (Fig. 4.20) should be used when features that are differentiated only by superficial corrosion are to be recorded, as already discussed. The surface to be recorded can be placed centered and normal to the camera axis because the camera is subjected to very little illumination and so, should there be any reflection

from the lens, it will be very faint. When arrangement B is used for macrographs that would give better results under arrangement A, the dark and light tonal differences are inverted.

Arrangement C (Mixed Lighting). When both types of features mentioned above must be recorded, arrangements A and B can be combined in a balanced way to achieve an adequate illumination. This combined arrangement is illustrated in Fig. 4.21.

Arrangement D (Direct Lighting, Normal to the Surface to Photograph). Small, planar samples (in general, up to 25 mm, or 1 in. diameter) normally can be photographed with light perpendicular to its surface, as shown in Fig. 4.22. This illumination arrangement is very similar to that used in optical metallographic microscopy. In this arrangement a piece of transparent glass (or a half-mirrored surface) with plane and parallel surfaces is placed between the camera and the object, inclined 45° with respect to the camera axis. The light source is placed in a way that the light reflected by the glass surface falls normally on the surface to register.

It is advisable to add a light condenser with one or two lenses, between the light source and the glass. Part of the light is lost (not reflected by the glass), but part of it is reflected by the glass surface, reaches the sample, and is reflected back—through the glass—into the camera. This arrangement will result in the same type of contrast as arrangement A. This is limited to small samples because large condenser lenses would be required for large samples. This arrangement is recommended especially when one wishes to photograph planar surfaces with magnifications above 3:1. In these cases, an appropriate lens that for macrofocusing is needed, and it becomes almost impossible to prevent camera reflections on the sample surface if arrangement A is used.

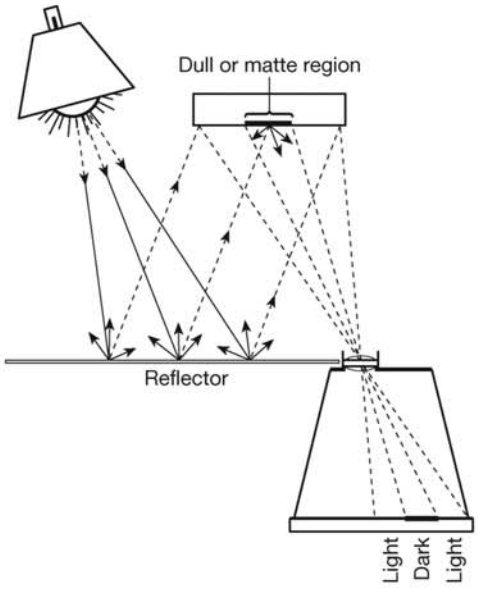

Fig. 4.19 Lighting arrangement using a reflector (arrangement A in the text).

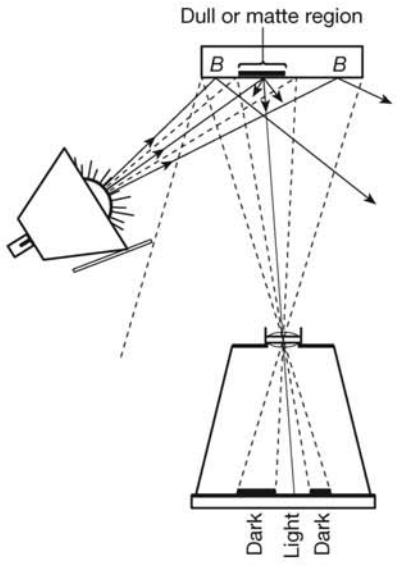

Fig. 4.20 Direct lighting arrangement (arrangement B in the text).

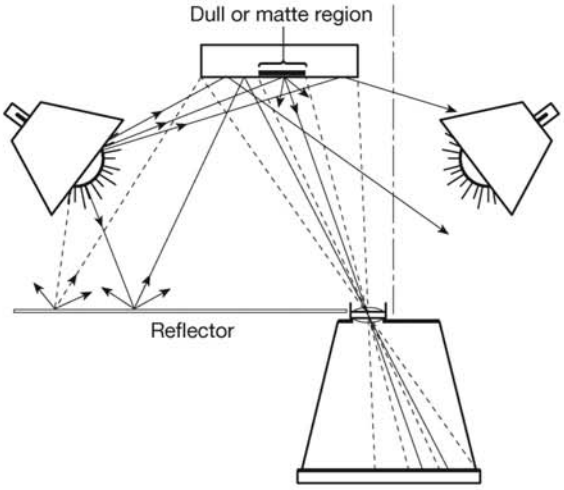

Fig. 4.21 Mixed lighting scheme (arrangement C in the text).

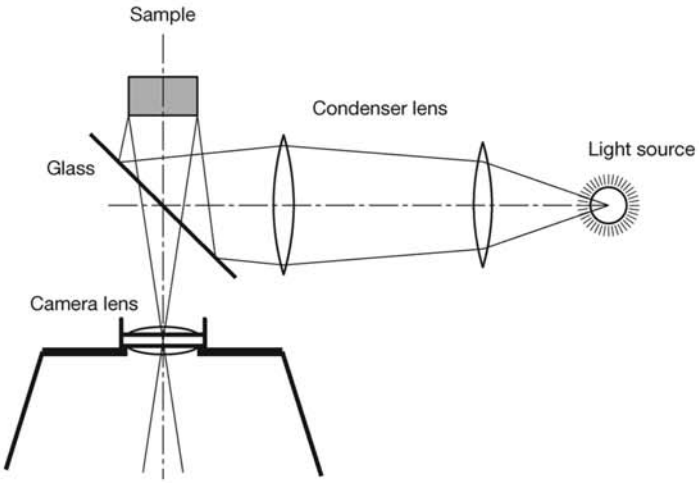

Fig. 4.22 Flat glass at 45° makes possible illumination normal to the surface of small samples (arrangement D in the text).

Arrangement E (Direct Illumination, Inclined and from Two Sources). Arrangement E is recommended especially for recording fracture surfaces. It is based on arrangement B but with the addition of a second light source as a fill light.

In this arrangement, the fracture surface is illuminated directly by two light sources. The first one, which is stronger, is placed closer to the fracture, to the left and a little above the camera. The second one is placed to the right of the camera, to make the shadows less harsh and to make possible the recording of detail in the shaded areas (Fig. 4.23).

Arrangement F (Direct Illumination, Inclined, Oriented). When surfaces with coarse machining marks are photographed, the direction of illumination might help reduce the effect of the marks in the photograph. Maximum and minimum visibility of the machining marks are obtained, respectively, with the illumination arrangements (a) and (b) in Fig. 4.24. Although this is a particular case of arrangement B, it is useful for recording surfaces in which the features to be recorded are just porosity, pipes, and other casting defects. These surfaces need not be ground to a good finish, provided the proper illumination is used.

Arrangement G (Indirect Illumination, Peripheral). Ground or polished cylindrical surfaces that contain details of metallographic interest require good lighting to guarantee the proper recording of these details. Arrangement G (Fig. 4.25) is recommended in this case. The direct incidence of light on the sample is avoided with this arrangement.

Arrangement H (Glass Base with Backlighting). If the objects to be photographed create undesirable shadows, this arrangement is a good alternative. The objects are placed on top of a glass plate covered with translucent paper. Under the glass, the light sources, if possible with diffusers, are disposed. The illumination from under the paper lightens the shadows produced by the top illumination and may even make the shadows disappear completely (Fig. 4.26).

In addition to the illumination techniques exemplified, the background plays an important role. Dark images normally are better reproduced when placed on a light background and vice versa.

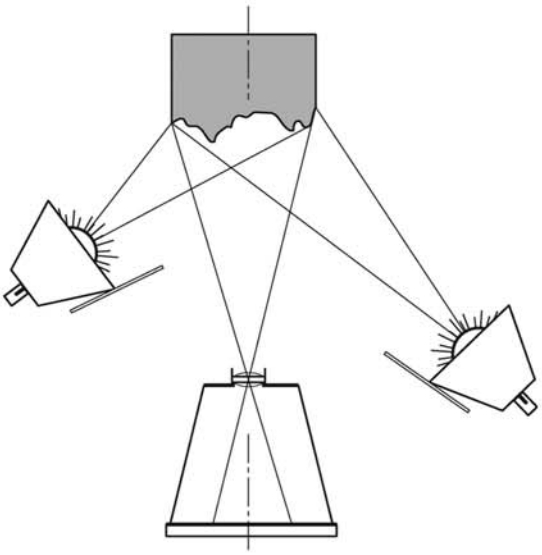

Fig. 4.23 Illumination arrangement recommended for fracture surfaces and other nonplanar surfaces (arrangement E in the text).

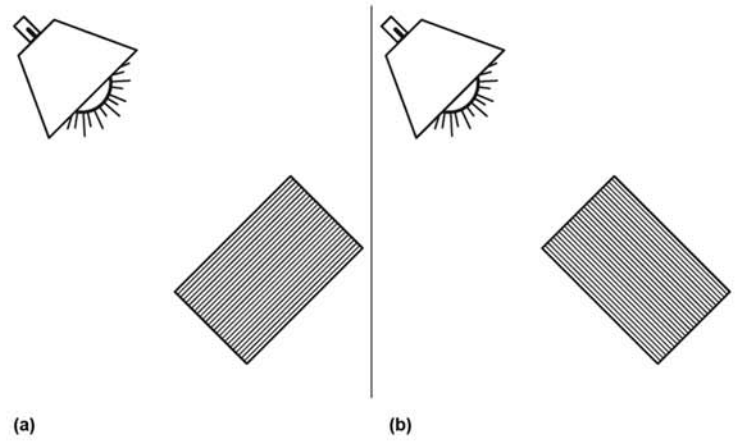

Fig. 4.24 Illumination arrangements: (a) machining marks will be most visible; (b) machining marks will be least visible (arrangement F in the text).

4.1.6 Techniques for Enhancing Macrographic Observations

Extremely clean and low residual steels can be very hard to etch with a sufficient intensity to produce a good macrograph. Furthermore, very low sulfur steels frequently do not produce useful sulfur prints. Casey (Ref 8) and (Ref 11) developed some techniques to improve the observation of the macrographs taken from these steels.

Use of Printing Ink (Ink Highlighting)

The simplest technique developed by Ref 11 involves highlighting the relief generated by etching with the use of printing ink. This process encompasses four steps:

1. Perform a careful and light regrinding with 500 or 600 grit paper.
2. Apply a layer of printing ink over the etched and reground surface.
3. Remove the excess of ink with clean cotton rags embedded with mineral solvent.
4. Visually evaluate and photographically record the surface as needed.

Printing in Cellophane Tape ("Taping") or Paper

This technique is ideal for recording coarse structures obtained with hot hydrochloric acid reagent. Normally this will lead to a better photographic record than the previous technique. Of the techniques described in this section, however, this is not the best to record finer details of the structure. When transparent tape is used, the following stages are involved:

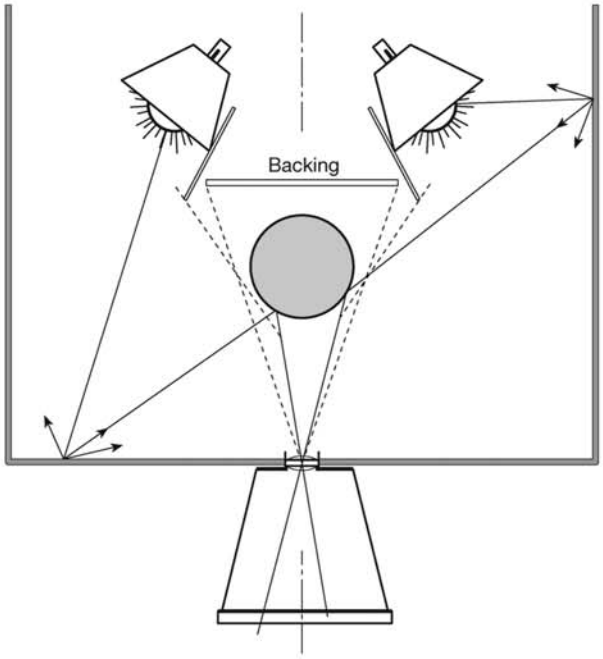

Fig. 4.25 Illumination arrangement for cylindrical parts when the surface aspects are to be recorded (arrangement G in the text).

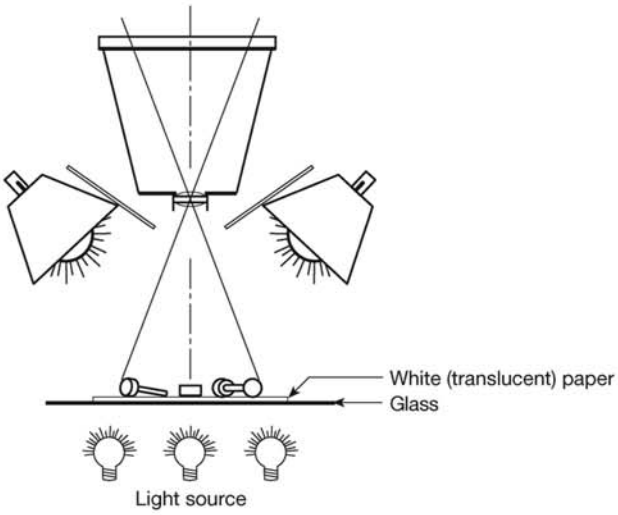

Fig. 4.26 When objects to be photographed cast inconvenient shadows, a glass base with backlighting may lessen their presence (arrangement H in the text).

1. A thin layer of printing ink is applied to the etched surface using a hard rubber roll.
2. Wide transparent tape is applied over the region where the ink was applied (Fig. 4.27).
3. The tape is carefully removed from the macrograph and then applied over a piece of high-quality heavy white paper (Fig. 4.28).
4. The resulting image in the tape is a "replica," visible through the tape, of the etched surface. This image can be used directly as a record, photographed, or digitized.

Alternatively, a piece of thick, good-quality white paper can be applied directly to the surface to which the ink was applied. Then this paper sheet is pressed over the sample with a rubber roll press, using a pressure in the range of 0.7–1.4 MPa (100–200 psi). This technique is called "relief printing" and is similar to some methods using in graphic arts to produce prints.

Intaglio Ink Printing (Using Macrograph Relief to Make Intaglio Prints)

In this technique, the macrograph, after etching, is used as a plate for producing an intaglio print. This method is ideal for macrographs obtained with the two-stage etching with Humfrey's reagent. These steps are performed to achieve this technique:

1. Printer ink is applied liberally to the macrograph, making sure all depressions, pores, and so on are completely filled with ink.

2. Excess ink is removed by the successive application and removal of cellophane tape.
3. Paper is brought into contact with the macrograph after all excess ink is removed and is pressed into contact with the sample using a manual graphic arts press with a pressure in the range of 7–14 MPa (1000–2000 psi) (Fig. 4.29). Cotton paper should be used if the best prints are to be produced. Examples of the results of the application of this technique are presented in Chapter 8, "Solidification, Segregation, and Nonmetallic Inclusions."

Other Highlighting Contrasting Media

Contrast in macrographs also can be highlighted for recording using other media such as aniline dyes or rubber-stamp ink (refer to Fig. 11.54). India ink is an option to highlight small pores and similar features (Ref 12).

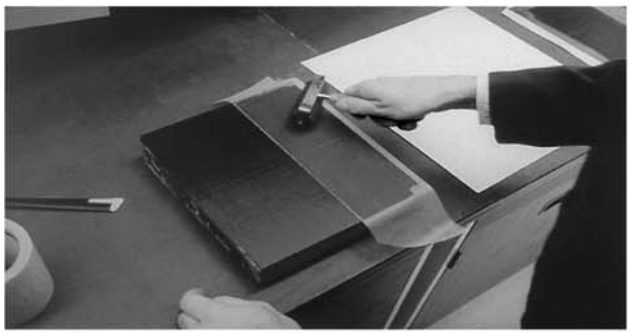

Fig. 4.27 Application of cellophane tape over a macrograph to which printing ink has been previously applied. Courtesy of J. Casey, Dofasco, Canada.

Fig. 4.28 Transferring the image from tape to paper, using a rubber roll. Courtesy of J. Casey, Dofasco, Canada.

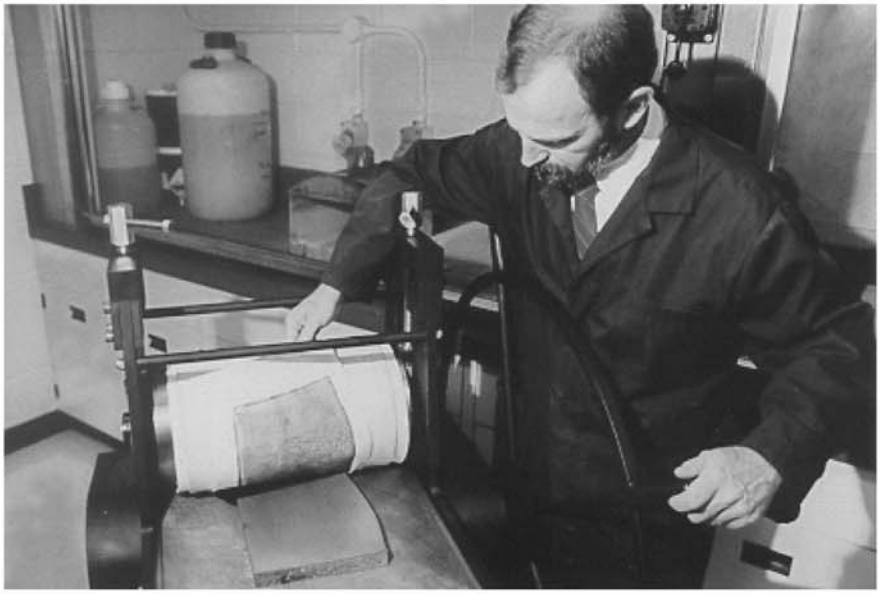

Fig. 4.29 The making of an intaglio print from a macrograph, using a graphics art press. Courtesy of J. Casey, Dofasco, Canada.

REFERENCES

1. "Standard Terminology Relating to Metallography," E7-15, ASTM, 2015
2. "Guide for Preparation of Metallographic Specimens," E3-11, ASTM, 2011
3. "Standard Practice for Macroetching Metals and Alloys," E340-15, ASTM, 2015
4. "Standard Practice for Preparing Sulfur Prints for Macrostructural Evaluation," E1180-08 (Reapproved 2014), ASTM, 2014
5. B.L. Bramfitt and A.O. Benscoter, Common Etchants for Irons and Steels, *Adv. Mat. Proc.*, June 2002, p 42–43
6. "Method of Macroetch Testing Steel Bars, Billets, Blooms, and Forgings," E381-01 (Reapproved 2012), ASTM, 2012
7. ASME Boiler and Pressure Vessel Code Section IX, "Welding and Brazing Qualifications," QW-472, ASME, 2010
8. J. Casey, Macro-Etching of Continuous Cast Steel, *Microsc. Microanal.*, Vol 8, (Suppl. 2), 2002, p 362–63
9. "Steel—Macrographic Examination by Sulfur Print (Baumann Method), 4968:1979, ISO, 1979 (same as BS 6285:1982, BSI Group, 1982)
10. J. McKenzie and D. Overturf, *Artificial Lighting for Photography*, Delmar Cengage Learning, 2009
11. J. Casey, Revealing Primary Solidification Structures in Low Residual Continuously Cast Steels, In: *Summary of Macroscopy Methods*, ASM Fall Meeting, October 1991, ASM International, 1991
12. M. Scal, Private communication, 2007

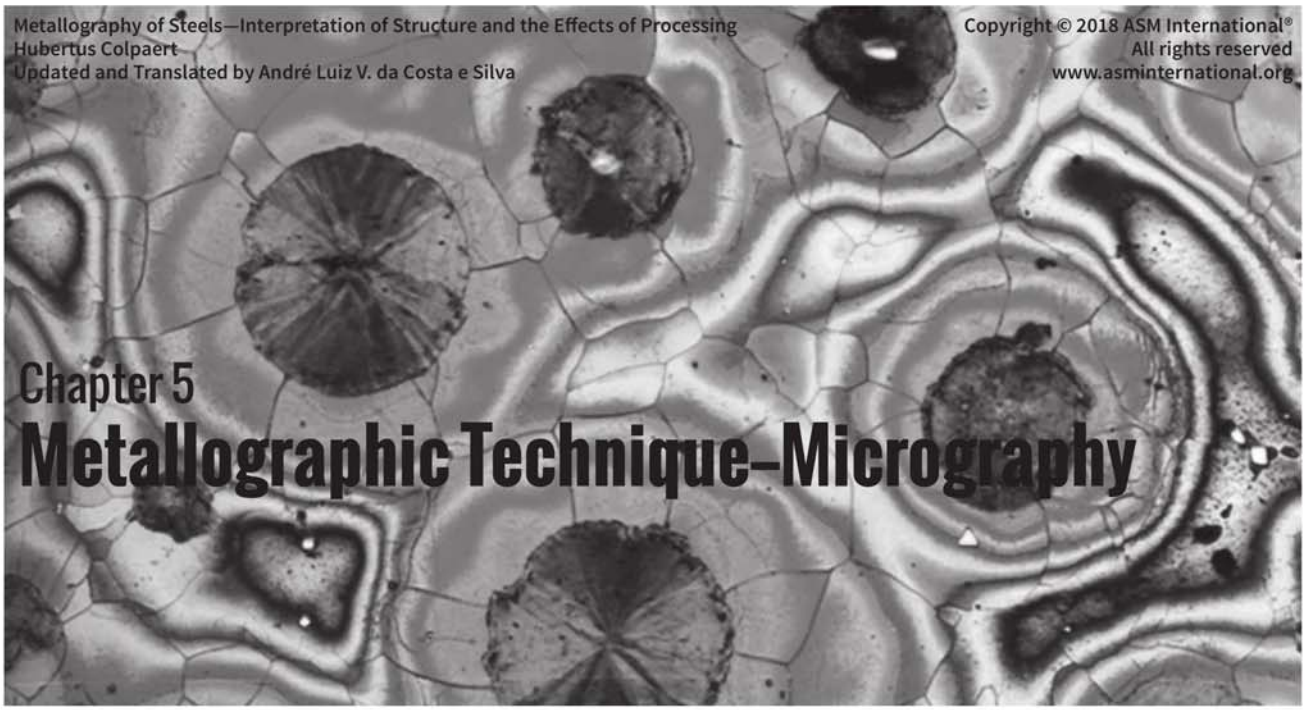

Chapter 5
Metallographic Technique–Micrography

Several techniques are used to observe the structure of steels and cast irons in the microscopic scale. For many of these techniques, sampling and sample preparation techniques are very similar. Some techniques, such as scanning electron microscopy (SEM), make it possible to observe samples with little or no preparation. (See the discussion on SEM in Chapter 6, "Metallographic Technique— Electron Microscopy and Other Advanced Techniques," in this book.) This is especially useful in failure analysis. On the other hand, techniques such as transmission electron microscopy (TEM) require specific sample preparation techniques, quite different from those required for the majority of micrographic techniques, because it relies on the analysis of an electron beam crossing the sample thickness. (See the discussion on TEM in Chapter 6.) The major micrographic techniques are discussed in the following sections, highlighting advantages and limitations, possible sources of artifacts and errors in sample evaluation, and specific care required for sample preparation. Because the field is very wide, supplementary readings and references are given and the reader is encouraged to peruse them before starting on a new technique.

5.1 Optical Microscopy

Among the various techniques used to characterize steel and cast iron microstructure, the most common is optical microscopy. In this technique, the sample is illuminated properly with visible light and the reflected light reaches the observer, as schematically shown in Fig. 5.1. The resolution that can be achieved depends on the wavelength of the radiation used. For visible light with green color, the resulting resolution is in the range of 220 to 250 nm corresponding to a maximum magnification of about 1400 times (1400x) (Ref 1). Although optical microscopes that can provide magnifications higher than this are available on the market, the results are called "empty" magnifications, because they will not provide additional information when compared with the maximum magnification of around 1400x (Ref 1).

On the other hand, depth of field (see the section "Depth of Field," in Chapter 4, "Metallographic Technique—Macrography," in this book) is dependent

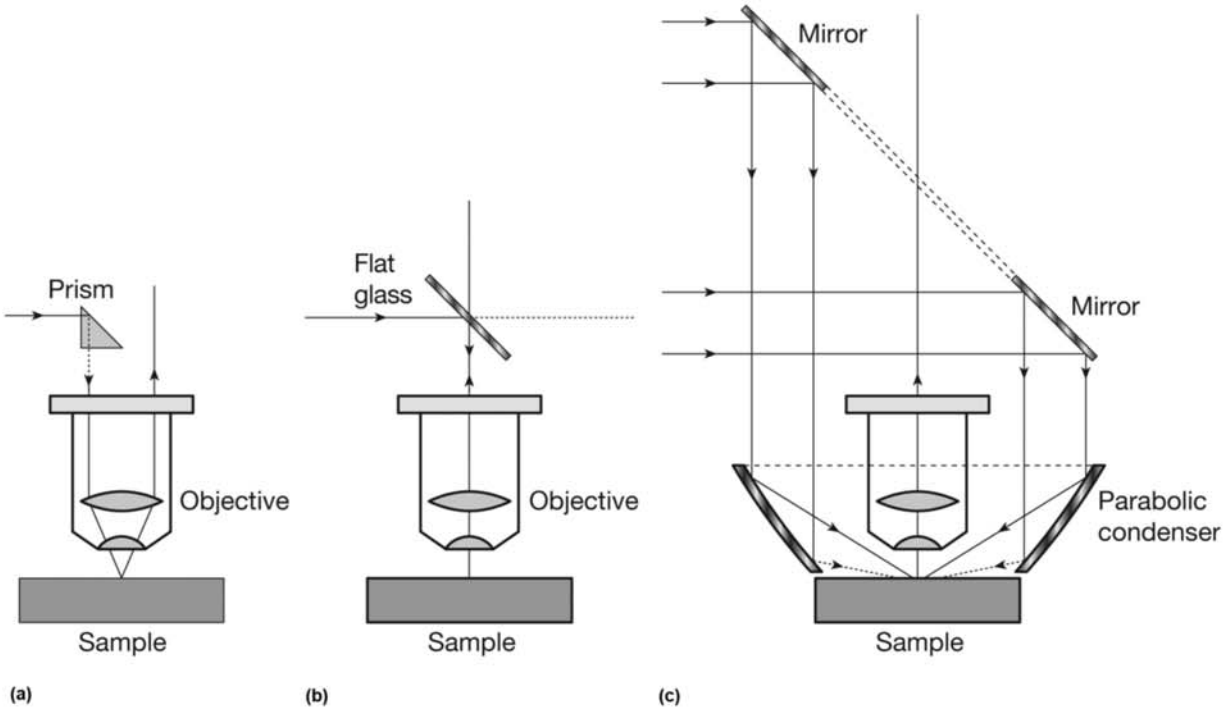

Fig. 5.1 Schematic illustration of lighting methods in metallographic optical microscopes: (a) oblique or inclined illumination; (b) normal illumination or illumination parallel to the optical axis—the most common method; (c) dark field illumination.

on the wavelength of the radiation used in observing the sample and on the lens focal distance—besides lens aperture (which also is discussed in Chapter 4). When an optical microscope is used, depth of field is quite low (typically in the 200 nm to 8 mm range, depending on the magnification—the higher the magnification, the lower the depth of field. Thus, if one wishes to observe the whole sample surface in focus, it is essential that the sample be quite flat and the surface perpendicular to the optical axis of the microscope. Thus, sample preparation procedures for optical microscopy must dedicate special attention to sample flatness or planicity and avoid edge rounding during polishing.

Different observation techniques may be used in optical microscopy (oblique lighting, polarized light, dark field imaging, etc.). Detailed information on these techniques can usually be found in equipment manuals or in texts specifically about microscopy.

The different illumination techniques that can be used in optical microscopy of opaque samples, such as metals, are shown in Fig. 5.1. Oblique (or inclined) illumination may be used to highlight some aspects of the microstructure or to change the way contrast is perceived (see Fig. 8.38 in Chapter 8, "Solidification, Segregation, and Nonmetallic Inclusions," in this book). The most common form of illumination, however, is parallel to the optical axis of the microscope. In general this type of illumination will result in lighter images of flat or nonetched regions of the sample and darker images of the nonflat regions such as cracks and pores and etched regions. In some special cases, objectives that can illuminate the specimen surface in an oblique way

with a conical light beam can be used—this is called dark field illumination. Light beams that reach the flat regions of the sample are not reflected into the observation path of the microscope. These areas will appear dark. Etched regions and the edges of pores, cracks, and other irregularities can reflect the oblique beam into the optical path and appear bright in the image.

5.1.1 Sample Preparation for Optical Microscopy

The technique for sample preparation for microscopic examination by an optical microscope can be divided into six steps:

1. Selection of the section to be examined
2. Preparation of a flat, polished surface in the plane of the section to be examined
3. Examination of the flat, polished surface of the sample in the optical microscope to record the features visible without etching (and to evaluate the quality of the sample preparation for flatness, scratches, etc.)
4. Etching of the surface with an adequate etchant
5. Examination of the etched surface to evaluate the microstructure
6. Recording of the microstructure (photographic)

Selection of a Section to Be Examined

The dimensions of samples for microscopic evaluation may be limited by different reasons, including:

- The difficulties in achieving a good flatness in the complete surface, in the case of optical microscopy
- The maximum weight that can be handled by the sample holder (in optical microscopes and SEM)
- The dimensions of the chamber entrance port in the case of SEM
- The distance between sample holder and lenses in conventional optical microscopes (as opposed to inverted microscopes)

The decision regarding the exact location to remove specimens for micrographs for larger parts or samples frequently depends on the results of a previous macrograph. When the macroscopic aspect is homogeneous, there is considerable freedom as to the exact region from where the sample for micrographic examination will be removed. If, however, the macrograph indicated heterogeneities, it might be advisable to increase the number of samples for micrographic examination to include all areas in which a detailed exam might bring important information. When examining small parts, it is frequently possible to examine the complete cross section of the part in a single micrograph.

In cases where anisotropy is expected (forgings, rolled products, formed parts, etc.), section orientation is critical and must be recorded. When samples are cut for metallographic preparation, it is highly advisable that mark-

ing is properly made and kept at all times and reference to the longitudinal direction of the part is preserved. Sketches of the sample removal scheme are very useful. Also, with the low cost of digital imaging, photographically recording each step of sectioning and preparation, in addition to using reliable and permanent marking or stamping, is a good idea for keeping traceability and make sense of the results. Losing information on sample location or orientation may require resampling and repetition of the complete process, if reliable results are expected. In castings, orientation is less important. Even in this case, recording the sample position and orientation cannot be neglected.

In all cases, the sample distance to part surfaces is an important variable that must be considered and registered. Because samples have thicknesses that are not negligible, it is important to record which of the sample faces has been prepared and observed. Sometimes the use of nondestructive metallography or a metallographic replica technique may be required (see section "Metallographic Replication" later in this chapter). In these cases, one must keep in mind that the part surface may have suffered changes with respect to the bulk; that is, the surface may have decarburized, may have been cold worked, and so on. Thus, when a small region of a part surface is prepared for metallography, one must not forget that the results of the observations may be affected by these changes.

Preparation of a Flat, Polished Surface in the Plane of the Section to Be Examined

In addition to the points highlighted with respect to the preparation of the sample surface for macrographic examination, some other points must be considered as microscopic features will be observed.

In the "classical" sample preparation route, after cutting the sample either by saw or by machining, there are two main options:

- The sample is mounted in some polymer that will give better support and make it easier to hold, besides making it possible to use additional measures to retain the sample edges during grinding and polishing. (Bakelite, polyester resins, and epoxies are some of the common materials used. If the sample will be examined later in SEM, due consideration must be given to the mounting material's potential to emit volatile species under vacuum. This would result in contaminating the SEM working environment.)
- The sample is directly subjected to grinding and polishing. Surface preparation includes grinding in automatic grinders using an appropriate sequence of grinding papers. Usually the material of choice is silicon carbide with water cooling and lubrication. A usual sequence is 100 (or 120) (or 180), 240, 320, 400, and 600 grit. Eventually 1200 grit paper also may be used. For softer materials such as stainless steels and low carbon ferritic steels, and for some carburized parts when deformation during grinding and polishing must be carefully controlled, the sequence of grinding papers may be 240, 320, 400, 600, (800), and 1200. In these cases, the use of grit 120 (or 180) is not recommended. The grinding direction should be rotated by 90° when changing to a finer grit

paper. A practical rule of thumb is to grind in each grit at least twice the time required to remove the grinding marks from the previous grit size. When the samples are not mounted in polymer, it is advisable to chamfer the sample edges before the start of grinding and polishing. This will reduce the chance of damaging the grinding paper and polishing cloths and reduce the risk of the specimen being caught at the paper or cloth and being ejected at high speed from the equipment.

Grinding media and water or other lubricating media used in polishing are extremely deleterious to the microscope, so before any attempt to examine the sample is made, careful washing and drying (sample and hands!) should be performed. This should be a rule even if only a brief look at the sample surface is desired to check for the progress of the grinding and polishing operation. The usual practice is to wash under clean water, gently swabbing with a clean piece of cotton. After washing, drying should be performed immediately using a small amount of alcohol and gently swabbing with another clean piece of cotton. Blowing hot or warm air (a hair dryer works well) at an angle to the sample surface helps in drying and preventing drying stains.

After grinding in silicon carbide paper, polishing follows. A piece of cloth or felt is mounted on a rotating disk. The cloth is impregnated with a small amount of the polishing media. Usual media are alumina suspensions, diamond paste, and colloidal silica suspensions.

Polishing can be performed in manual or automatic polishing machines. When repetitive sample preparation is needed (for instance, quality control metallography, in industry) automatic polishing machines can be very convenient. In all cases, one must determine, mostly by trial and error, the ideal pressure (load on the sample) and disk rotating speed (or vibration conditions in some polishing machines) for each material to be prepared. Usually grinding in 600 grit paper is followed by alumina suspensions in the sequence 1, 0.3, and 0.05 μm or diamond paste of 3 μm followed by 1 μm paste (Ref 2).

Table 5.1 presents rugosity values measured in two different materials after different polishing routes. Values obtained in different materials and using different polishing techniques can be used only as rough guidelines for the expected rugosities after polishing. Companies specializing in metallography supplies make available much information that can help with these choices. (Some examples are Buehler, Struers, and Leco. Citing some suppliers is neither an endorsement nor a recommendation of their products. Many suppliers are available, and readers are advised to locate one that best fits their needs.) This normally is a good starting point for optimizing the sample preparation process. When the sample surface reaches a “mirrorlike” finish, without visible scratches under a magnification of 100–200x, it already is possible to evaluate the sample for nonmetallic inclusions in normal steels, cracks, graphite distribution in cast iron, porosity, and other features that can be observed without etching. In any case, the guarantee of a good polishing procedure is obtained only after a successful etching. The abrasive material used in polishing not only scratches the surface but, in combination with the pressure applied during polishing, will cause cold deformation in the layer immediately under the polished surface. (See discussion on work hardening in Chapter 12, “Mechanical Work of Steels: Cold Working,” in this book.) The

Table 5.1 Average rugosity after polishing

Stainless steel samples[a]		
Silicon carbide grinding paper	Rugosity, average (R_a)	
	Manual, µm	Automatic, µm
120	0.23	0.18
180	0.13	0.08
240	0.10	0.10
320	0.10	0.05
400	0.05	0.03
600	0.05	0.03

Titanium alloy, manual[b]	
Polishing until	R_a, µm
1200 grit grinding paper	0.130
6 µm diamond paste	0.125
3 µm diamond paste	0.060
0.7 µm diamond paste	0.056

Note: Values are only for reference. (a) Source: Adapted from Ref 3. (b) Source: Adapted from Ref 4

depth of deformation is directly dependent on the grain size of the grinding or polishing material and the pressure used for polishing or grinding. On the other hand, the depth of deformation is inversely proportional to the material hardness, as schematically indicated in Fig. 5.2.

When the subsequent polishing steps are able to remove the scratches or depressions caused by the coarser previous material without removing the work hardened layer in the material, the surface may look properly polished (mirrorlike finish, no visible scratches). However, when this specimen is etched, the results lack uniformity: the work hardened regions will be more reactive and more etched by the reagent than the rest of the surface. Thus, darker lines may appear in regions that were previously scratched. The roughness aspect in the interior of ferrite grains as well as an appearance of a "smeared" surface are other possible effects in samples that have residual work hardening from the polishing operations. Figure 5.3 presents a schematic representation of how these remains of deep scratches may persist in the material.

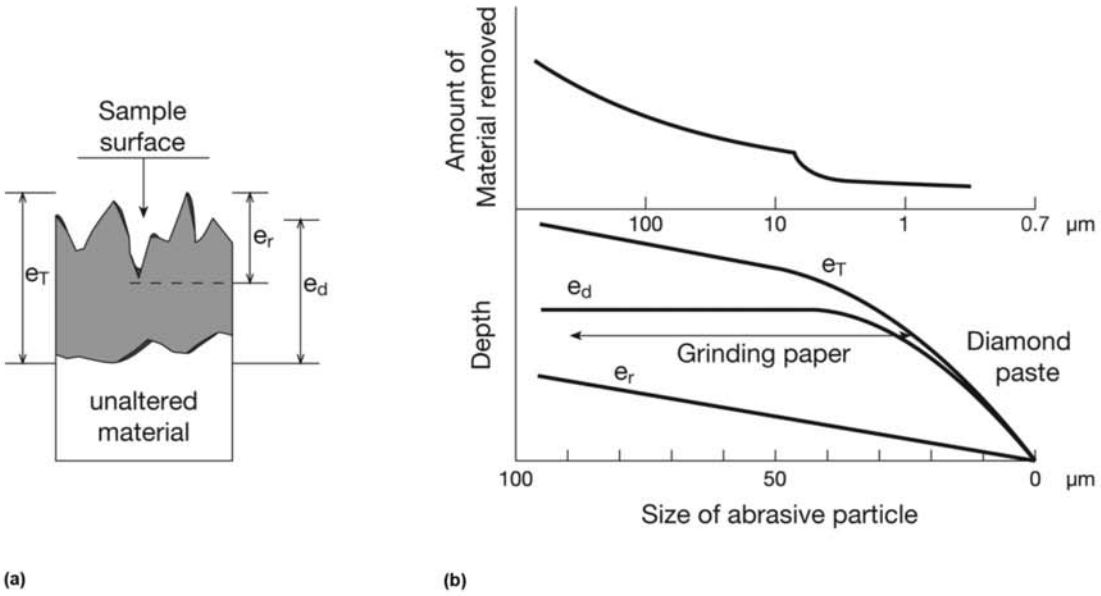

Fig. 5.2 (a) Schematic cross section through a sample subjected to polishing, indicating the three most relevant thicknesses, related to the surface quality: e_r—rugosity, e_d—deformed thickness, and e_t—total thickness affected by the polishing process. (b) Evolution of the three variables defined in (a) as a function of abrasive grain size. Source: Ref 4

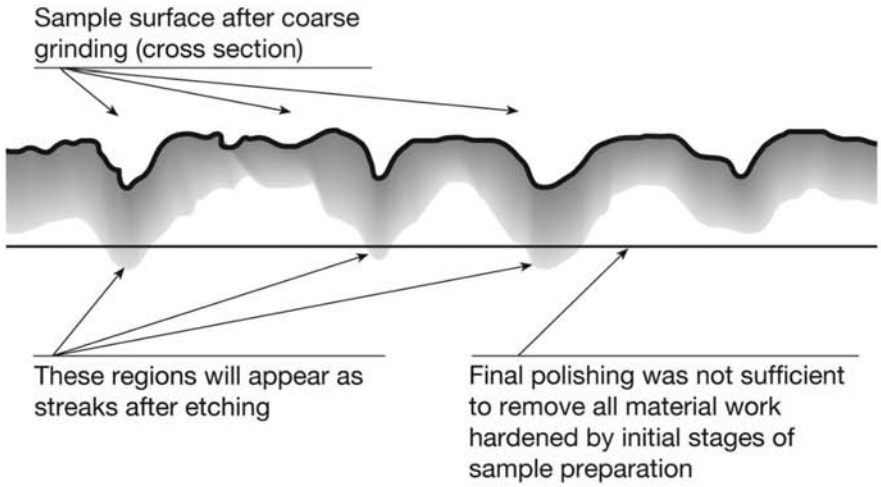

Fig. 5.3 Schematic presentation of subsurface work hardening caused by grinding.

The proper preparation of transverse or longitudinal sections of wires, cables, and thin plates may require the material to be properly fixed in a support, as indicated in the examples shown in Fig. 5.4. In some cases these arrangements can be good alternatives to the procedure of mounting the samples in polymers.

These arrangements also are advisable when the region very close to the surface of the sample must be examined. It is extremely difficult to prevent

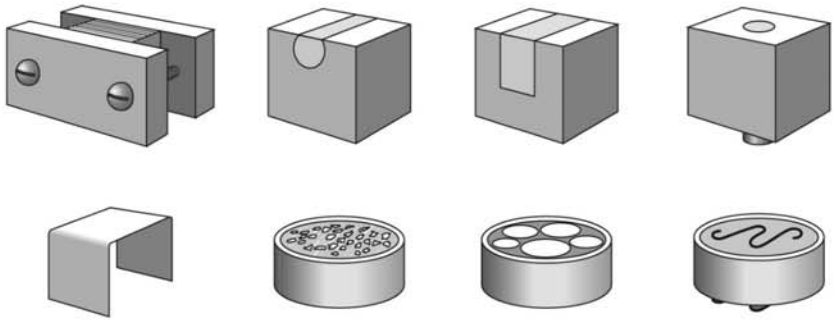

Fig. 5.4 Some ways of holding small parts to facilitate proper polishing for micrographic examination. These are practical ways of avoiding mounting samples in polymers.

rounding the edges of samples during grinding and polishing unless something is included in the mounting or support to protect these regions and guarantee flat polishing. Without attention to this detail, it is almost impossible to get good focus close to the sample edges, and one frequently finds a concentration of scratches in these areas. This procedure is especially important when examining samples from fractured material, surface decarburization, depth of carburization or other thermochemical treatments, coatings, and so on. In the case of mounting in polymer or plastic, the best option typically is the application of a coating on the specimen surface that one wishes to protect for observation (for instance, a layer of nickel deposited by chemical processes; see Fig. 14.21 in Chapter 14, "Structural Steels and Steels for Pressure Vessels, Piping, and Boilers," in this book). Another option is mounting, together with the part to be prepared, pieces of the same or similar material that will support the pressure during polishing, preventing the sample from being inclined during the polishing operation and reducing the chances of rounding edges (see Fig. 12.32). When vibrating polishing is used, the problem of rounded corners is frequently minimized.

As in the case of macrographic preparation, it is very important to avoid heating the sample during grinding and polishing to avoid changing the structures one wishes to observe. When a manual saw is used and the grinding is done manually on a flat grinding table, it is difficult to cause overheating. Furthermore, an attentive operator will notice the heating and can manage the process. If however, mechanical saws or cutoff wheels are used, special care must be taken. It is not enough just to turn the cooling fluid on; it is important to make sure the cutting conditions are compatible with the heat extraction provided.

Mounting specimens in phenolic resins (such as Bakelite) should be employed only if one is sure that the heating (temperatures on the order of 150 °C, or 300 °F) will not influence the material structure. If even this low of heating is to be avoided, cold polymerization materials should be selected for the sample mounting. It is common to perform grinding operations with running water, which not only cools but lubricates the sample and helps remove the grinding products and residues continuously created during the operation.

Figures 5.5 to 5.13 present a properly polished surface, several defects of polishing and drying, and some degradation that might occur if the sample surface is not properly protected after polishing and cleaning.

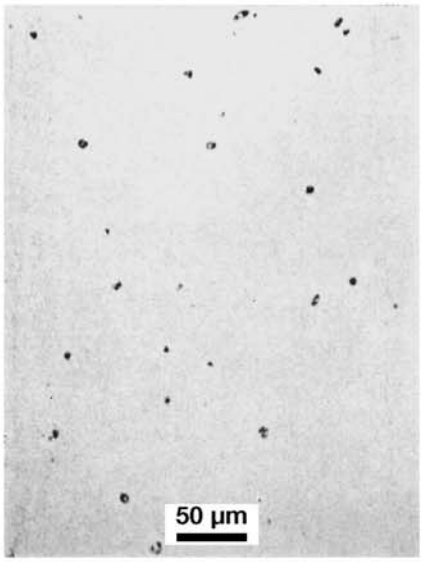

Fig. 5.5 Properly polished steel sample, not etched. Many globular nonmetallic inclusions are visible.

Fig. 5.6 Poorly polished sample. Many scratches from grinding or from previous polishing steps are visible.

Fig. 5.7 Properly polished sample of eutectic cast iron (see Chapter 17, "Cast Irons," in this book). The patterns visible on the surface result from the relief created by polishing a material with constituents having large differences in hardness.

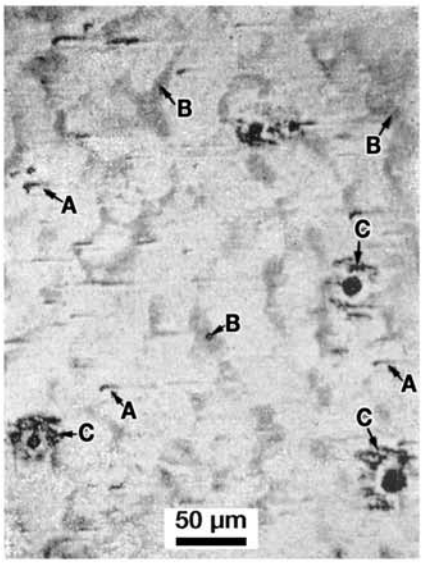

Fig. 5.8 Polishing defects: A—comets; B—brown stains; C—halos surrounding small pores in the sample.

Fig. 5.9 Filiform (filament-shaped) rusting that can occur during improper sample storage after polishing.

Fig. 5.10 Drying marks. The small spots are drying marks from water droplets. Material is "rough iron" (See "Historical Direct Reduction Products" section of Chapter 2, "Processes in Steel Production," in this book) with many large nonmetallic inclusions.

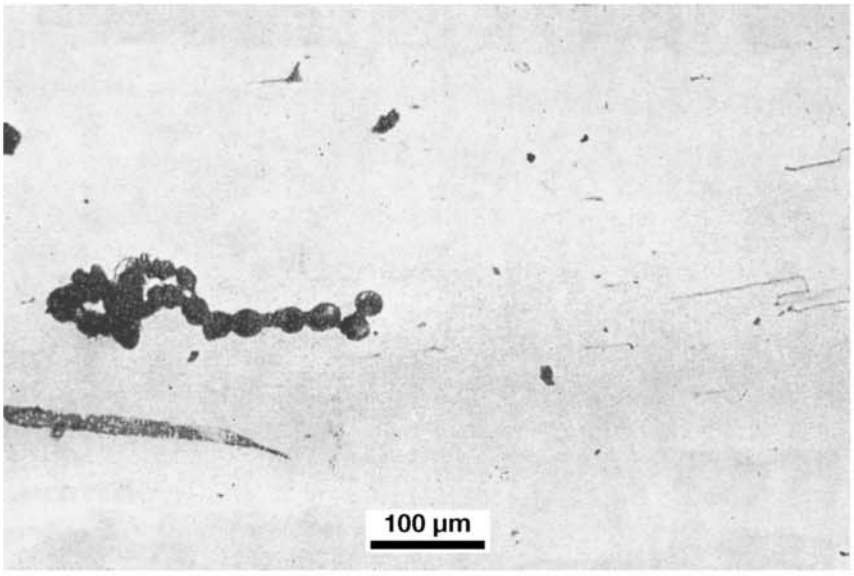

Fig. 5.11 Some problems that may occur on polished sample surfaces: cotton threads (from the drying swab material), dust particles, filiform rust, rust in the shape of a rosary.

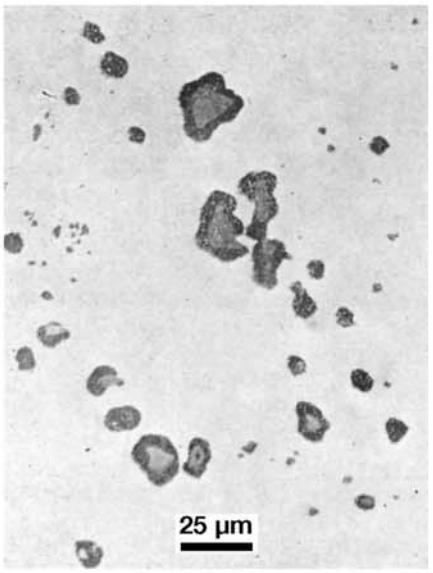

Fig. 5.12 Surface that was previously subjected to macroetching with iodine etchant and was not sufficiently ground and polished afterward. Regions around nonmetallic inclusions still are corroded.

In Fig. 5.8 some of the most common defects related to polishing are presented. Comets are due to excessive pressure during polishing and or pieces that break apart from hard, brittle nonmetallic inclusions (alumina, for instance). Brown stains are present when too low pressure is used in the final steps of polishing. More frequent in higher phosphorous steels, dark and heterogeneous rings (or aureoles) are frequently associated with a long duration of water washing after polishing and delays the start of the sample drying after polishing. When the polished surface is not immediately etched, oxidation must be prevented. Although this is not easy or simple, a desiccator with silica gel or other drying agent can preserve polished samples waiting to be etched. In any case, the time between the completion of the polishing, cleaning, and drying operations and the start of etching should be as short as possible. Handling samples in desiccators should be done only with clean and dry hands.

Microscopic Examination Prior to Etching. The microscopic examination of a sample before any etching has two purposes. The first purpose is to make possible an evaluation of the quality of the polishing and overall sample preparation. Many polishing defects may influence the results of etching and make metallographic evaluation difficult or confused. It is of paramount importance that before any etching, the polishing quality should be evaluated and confirmed as satisfactory. (This is especially important for professionals responsible for evaluating micrographs but not preparing the samples themselves. Only when one is completely satisfied that the sample has been properly prepared can etching be performed.) The second important purpose is to evaluate those structural features that are visible at this stage, such as non-

metallic inclusions, graphite, cracks, and porosity. Whereas in many cases it also is important to observe these features after etching (especially when it is desired to relate their position to the material structure), observing these features without any etching provides much clearer and more objective results. Furthermore, the absence of the structure information given by the etching reduces clutter and avoids confusion during evaluation. When optical microscopy is used, the low depth of focus can be useful in distinguishing between small pores and nonmetallic inclusions. When the microscope focusing is altered forward or backward with respect to the sample surface, it is possible to focus on points inside cavities and remove the cavity border from focus. In the case of nonmetallic inclusions, this is not observed because they are in the same plane as the metallographic section.

Fig. 5.13 Stains caused by water retained between the metallic matrix and the graphite in an oxidized cast iron. Sometimes it can take a few seconds or minutes for water to leave cavities. Inverted optical microscopes help accelerate the water exudation. This contributes to damaging the microscope lenses. In the case of SEM observation, time to achieve a sufficiently low pressure (vacuum) for the SEM operation increases and environmental contamination may occur.

Etching the Surface

The first step in etching is deciding which etchant should be used. Then one should become familiar with all safety precautions related to using and discarding the reagent and its constituents. Finally, one must evaluate the stability and durability of the etchant, as some reagents lose effectiveness with time, exposure to air, and so on, while others can be stored, provided ambient conditions are properly controlled.

Etching is normally performed by immersing the face of the specimen to be etched in the reagent. Care must be exercised to avoid the formation of air bubbles and stagnant solution areas; moving the specimen to keep the solution in contact with the surface is a common agitation method. A small dish is often used for etching. (Concave dishes are frequently used to avoid the risk of scratching the sample surface on the bottom of the dish.) For typical reagents and standard steels and cast irons, 5–15 seconds is usually a sufficient etching time. After etching, the specimen surface is immediately washed with alcohol, and drying is performed as previously described. (After etching with a reagent that uses an alcohol as a solvent, washing should be performed with alcohol.) A piece of cotton is often used for swabbing with alcohol, and the specimen is placed under a jet of hot or warm air, taking care to prevent drying stains. Generally it is better to underetch than to overetch; if additional etching is needed, it can be performed after the first observation. Some features of the structure are better observed with a lighter etching, whereas others might take a longer time to be properly observed. As a general rule, lighter etching is better for higher magnification observation. Once the operator has sufficient experience with an etchant/material combination, observing the surface during etching may give sufficient information to determine when etching should be stopped. Figure 5.14 shows the effects the reagents can produce on the sample surface. Table 5.2 presents the most common etchants used in steel metallography and their main features.

5.1.2 Metallographic Replication

When the structure of a part must be evaluated without removing a piece, the technique of replicating the part surface on a different medium may be very useful. The region to be observed must be prepared in accordance with good metallographic practice. This frequently is a challenge and represents a quality limitation of replica metallography. The surface preparation sequence

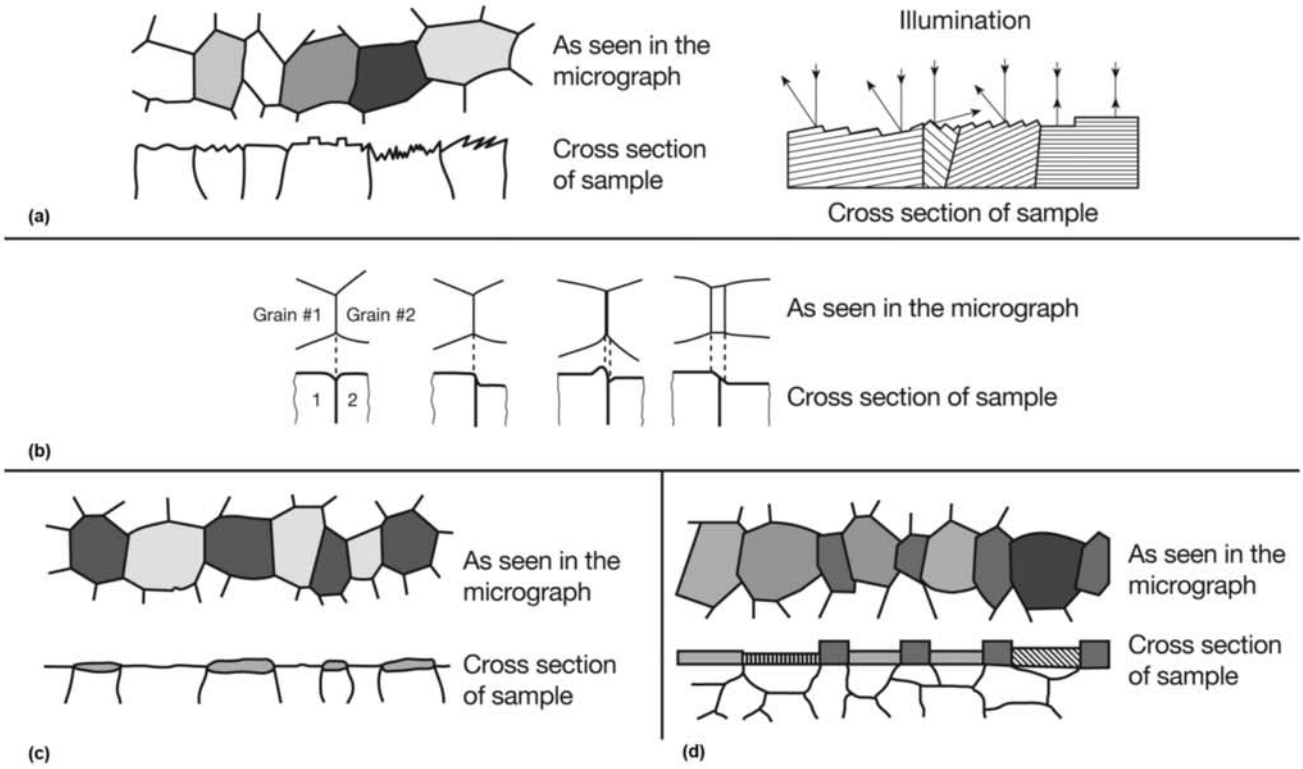

Fig. 5.14 Different effects on sample surface produced by reagents. (a) Contrast between different grains in a sample due to different reflectivities after etching (associated with different crystallographic orientation of the grains). (b) Differential contrast between grains, causing depressions in grain boundaries and thus image contrast. (c) and (d) Contrast generated by the deposition of layers on top of certain phases or with different thicknesses depending on phases etched. Source: Ref 4, 5

depends on the state of the original surface. For parts that have a machined finish, it is normally acceptable to start the grinding with 120 grit paper. For rougher surfaces or those that have suffered oxidation, it may be necessary to start with a coarser grit. After all grinding steps up to 600 grit are completed, it is typical to employ 6 μm diamond paste, followed by 1 μm paste and a final polish with 0.05 μm alumina suspension (Ref 10).

Many metallographic supply companies sell replication media. Cellophane is probably the most commonly used replication medium. Other materials such as silicone base elastomers are available and can produce high-quality replicas (Ref 11). When cellophane is used, after polishing, etching, and drying the position to be observed, a piece of cellophane (cellulose acetate, 3–5 mils thick) is used to replicate the surface relief. One of the surfaces of the cellophane film is softened by the application of some drops of acetone for about 30 sec. Excess acetone is removed and the softened face of the film is carefully pressed over the surface to be replicated. Usually 10–15 min are required for the cellophane to become hard again and record, as a replica, the surface relief, as indicated in Fig. 5.15. It is critical that the film is not moved during the replication period; both the application and removal of the film from the surface are delicate operations. Once the film is removed, it is fixed to a glass

Table 5.2 Reagents for micrographic etching

Reagent	Chemical composition and remarks on application technique	Indication
Nital (1–5%)	1–5 mL HNO_3, nitric acid 99–95 mL ethanol, ethyl alcohol	For steel microscopic examination 2% is the usual upper limit. Etches grain boundaries. Albeit it is considered a "general use" reagent, it is not ideal for pearlite, since it does not etch uniformly this constituent (see examples in Chapter 14 of the use of nital and picral in sequence). Excessive etching of pearlite or etching very fine pearlite results in dark or black pearlitic areas and in the confusion of the lamellae.
Picral 4%	4 g picric acid 96 mL ethanol, ethyl alcohol (3–5 drops of benzalkonium chloride at 15–17% can be added as a "wetting" agent)[(a)]	Recommended for pearlite and other carbide containing microstructures, such as tempered martensite. According to Bramfitt and Benscotter (Ref 7) picral is one of the few reagents that improve with use. These authors suggest "ageing" the reagent by introducing steel pieces or turnings inside the solution until it becomes dark green (the usual color is yellowish). For samples containing more than 0.5% Cr, the addition of 5 drops of hydrochloric acid per 100mL of solution is suggested (Ref 7).
Sodium picrate alkaline solution	100 mL water 25 g de NaOH (or Sodium hydroxide at 36° Baumé) 2 g picric acid	Pearlite is revealed through coloring cementite. Also colors several carbides. Does not color carbides containing more than 10%Cr (Ref 7). Etches sulfides and will show the grain boundaries of slow cooled steels. Solution is prepares by dissolving picric acid in boiling water and progressively adding the sodium hydroxide at 36° Baumé. Etching is performed with the solution boiling. It will react with Bakelite. Mounting in epoxy is recommended. The solution should not be left to boil until dry. Etching times range from 5–15 minutes.
Oxidizing etching (heat tinting)		Grain boundaries may be revealed by differential oxidation. In alloy steel oxidation of different grains and different constituents can be explored by this technique. The oxide layers are usually thin and have colors that are dependent on their thickness. It is common to pre-etch with nital or picral. There are several examples in the literature to use of this etching technique for alloy steels (heat tinting). Etching at around 250–300 °C may be useful to develop the grain structure in low carbon steel, too. Not to be confused with high temperature oxidation used, for instance in austenitic grain size determination.
Klemm or Klemm I	Saturated aqueous solution of sodium thiosulfate: 50 mL (solubility of anhydrous sulfate, $Na_2S_2O_3$ at 20 °C, is 50 g/100 mL Solubility of hydrated sulfate is 291.1 g/100 mL at 45 °C) 1 g potassium metabisulfite	Colors ferrite (40–100s). Shows phosphorous segregation and overheating. Useful to highlight carbides in a ferritic matrix.

(a) There are antiseptics and disinfectants in the commercial market with concentrations in this range that fulfill the function listed here.

Table 5.2 Continued

Reagent	Chemical composition and remarks on application technique	Indication
Beraha	100 mL H_2O 10 g $Na_2S_2O_3$ 3 g $K_2S_2O_5$	One of the many etchants developed by Beraha, will color marteniste, ferrite and bainite. There are many reagents that produce results in colors and were developed by Beraha.
Beraha II	Solution I: 800 mL water 400 mL HCl 48 g ammonium bifluoride Before using, add 1–2 g potassium metabisulfite to solution I before etching.	Stainless steels. Duplex stainless steels (Chapter 16)
Oberhoffer	30 g $FeCl_3$ 1 g $CuCl_2$ 0.5 g $SnCl_3$ 50 mL HCl 500 mL ethanol 500 mL H_2O	Shows phosphorous segregation
Béchet-Beaujard	2g picric acid 100 mL water 20mL neutral soap	Shows "fibers" (Chapter 14)
Potassium metabisulfite	800 mg Potassium metabisulfite 100 mL water	Will color differently ferrite and pearlite. Used in dual phase and multiphase steels (Chapter 13)
Sodium metabisulfite (Datta and Gokhale)	20 g sodium metabisulfite 100 mL water	In multiphase steels (Chapter 13), will differentiate between ferrite and martensite (Ref 8)
LePera	Solution I: 1 g sodium metabisulfite 100 mL water Solution II: 4 g picric acid 100 mL ethanol Mix solutions in 1:1 ratio	Many applications in dual phase, multiphase and TRIP steels (Chapters 11 and 13). Many variations are available, most related to the different proportions of solution I and solution II in the final etchant (Ref 9)
Kalling	2 g cupric chloride 40–80 mL methanol 40 mL H_2O 40 mL HCl	Stainless steels. Darkens ferrite and martensite. Austenite remains light color. Carbides are not affected (Chapter 16)
Vilela	1 g picric acid 5 mL HCl 100 mL ethanol	General use in carbon steels. May be used to develop previous austenitic grain boundaries. Applications to stainless steels (Chapter 16)

(a) There are antiseptics and disinfectants in the commercial market with concentrations in this range that fulfill the function listed here.

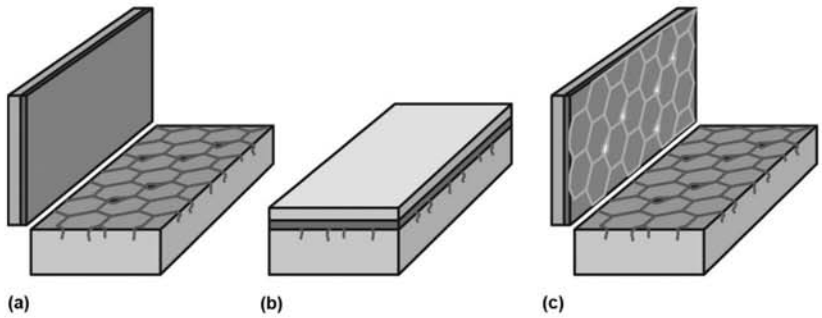

Fig. 5.15 Three steps of the replication process. (a) Part is ground, polished, and etched in the region of interest, and the material for producing the replica is prepared. (b) Replica material is carefully pressed over the region to replicate—and kept in place, without movement, for sufficient time for the material to harden. (c) Replica is carefully removed and taken for microscopic examination.

slide to be taken to the microscope. Carbon deposition on the replica surface can be useful to enhance contrast but is not essential.

Replication allows on to observe relatively large curved surfaces (such as portions of pressure vessel shells) in focus, on an optical microscope, because the curvature, if not too great, can be eliminated when fixing the replica to the gas slide. Standards ASTM E1351 (Ref 12) and ISO 3057 (Ref 13) give guidance about metallographic replication.

REFERENCES

1. J.G. Delly, Light Microscopy, *Encyclopedia of Materials Characterization*, C.R. Brunde, C.A. Evans Jr., and S. Wilson, eds., Butterworth-Heinemann, 1992
2. I.C. Abud, Instituto Nacional de Tecnologia-INT, Brazilian National Institute of Technology, private communication, 2007
3. L. Dillinger, Met Tip: Surface Roughness (016), LECO Corporation, 2002
4. T. Kuníková, L. Caplovic, M. Vojs, P. Grgac, and M. Vesely, Influence of Ti6Al4V Alloy Surface Preparation on Formation of DLC Layers, https://www.mtf.stuba.sk/docs/internetovy_casopis/2006/2/kunikova.pdf (accessed March 27, 2016)
5. H. Schummann, K. Cyrener, W. Molle, H. Oettel, J. Ohser, and L. Steyer, *Metallographie*, Deutscher Verlag fur Grunstoffindustrie—Wiley-VCH, 1990
6. G.A. Chadwick, *Metallography of Phase Transformations*, Crane, Russak, 1972
7. B.L. Bramfitt and A.O. Benscoter, Common Etchants for Irons and Steels, *Adv. Mat. Proc.*, June 2002, p 42–43
8. D.P. Datta and A.M. Gokhale, Austenitization Kinetics of Pearlite and Ferrite Aggregates in a Low Carbon Steel Containing 0.15 wt% C, *Metall. Trans. A*, Vol 12, (No. 3) 1981, p 443–50

9. F.S. Lepera, Improved Etching Technique for the Determination of Percent Martensite in High-Strength Dual-Phase Steels, *Metallography*, Vol 12, 1979, p 263–68
10. L. Dillinger, Met Tip: In-Situ Metallography (03), LECO Corporation, 2007
11. D. Zuljan and J. Grum, Non-Destructive Metallographic Analysis of Surfaces and Microstructures by Means of Replicas, *8th International Conference of the Slovenian Society for Non-Destructive Testing*, "Application of Contemporary Non-Destructive Testing in Engineering," September 1–3, 2005, Portorož, Slovenia, p 359–68
12. "Standard Practice for Production and Evaluation of Field Metallographic Replicas," E1351-01, ASTM, 2006
13. "Nondestructive Testing—Metallographic Replica Techniques of Surface Examination," 3057, ISO, 1998

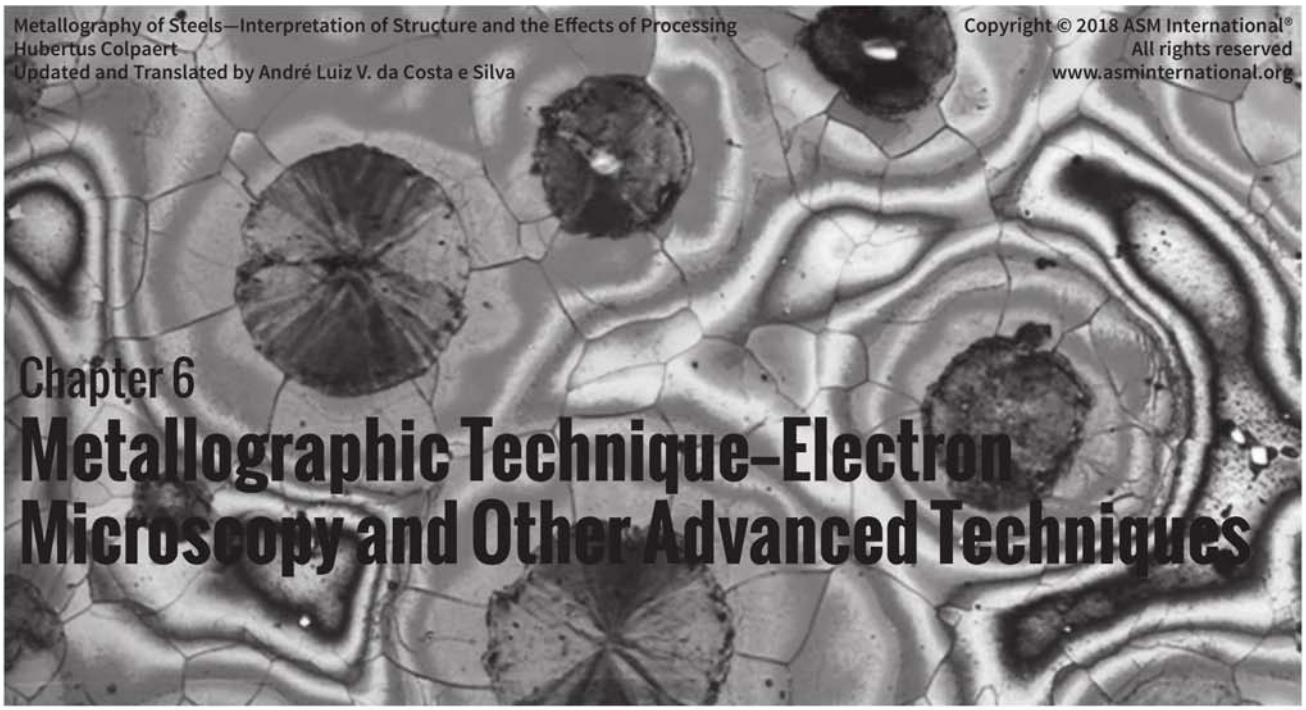

Chapter 6
Metallographic Technique–Electron Microscopy and Other Advanced Techniques

Although optical microscopy is based on the interaction of light (mostly visible light) with a sample, making possible primarily the observation of color, relief, and polarization, electron microscopy makes use of a variety of metal–electron interaction phenomena to provide valuable information from the sample observation. In many phenomena, electron behavior is described in terms of radiation (Ref 1). Table 6.1 compares some characteristics of visible light and electrons.

The most important electron–metal interactions are summarized in Fig. 6.1. When the sample is thin enough and the electron beam energy and current are sufficiently high, information is obtained from signals originating from electrons and radiation transmitted through the sample. These are the signals typically analyzed in a transmission electron microscope (TEM). Images observed result from the interaction of a very large number of electrons with the sample. Mathematical methods make possible the simulation of these interactions and can be especially useful in understanding the com-

Table 6.1 Some features of visible light compared to x-rays and electrons

Feature	Visible light	X-rays	Electrons
Wavelength, nm	400–700	0.05–0.3	0.001–0.01 100 kV = 0.0037 nm 20 kV = 0.0085 nm
Energy, eV	1	1×10^4	1×10^5
Mass at rest, g	0	0	9.11×10^{-28}

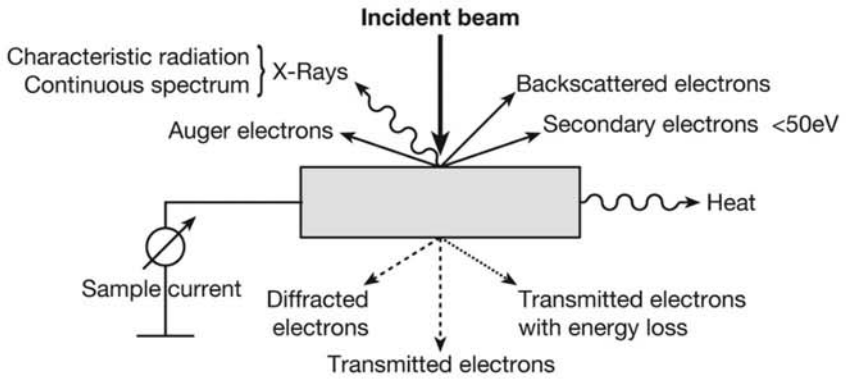

Fig. 6.1 Summary of main interactions as an electron beam reaches a sample. Many results of these interactions can be used to acquire useful information about the sample.

bined effect of sample material, sample thickness, and acceleration voltage applied to the electrons. The simulator available at Ref 2 provides a good visualization of electron scattering, which results in backscattered, secondary, and transmitted electrons.

Radiation that does not go through the sample is used in scanning electron microscopes (SEMs). Some of this radiation, which may also be referred to as signals (the usual generic term), is also used in the TEM. As a result of the interactions of electrons with the sample material, a volume significantly larger than the area where the electron beam impinges the sample surface is excited by the beam. This is a key concept in electron microscopy and should be kept in mind. The sample volume excited by an impinging electron beam depends on the electron energy (measured by the acceleration voltage) and the atomic number of the sample material (Z), as indicated in Fig. 6.2. The different signals generated by the various electron–sample interactions may or may not have enough energy to leave the sample and reach one of the microscope detectors. In any case, it is essential to remember that the signals recorded by the different detectors may represent more than the area of the sample where the electron beam impinged, and may originate from a significantly larger volume than would be preferred. All electron microscopes (transmission and scanning) have in common some basic features: a source, which is able to generate an electron beam with energy and intensity compatible with the interactions to be produced, and a set of lenses to focus and guide the electron beam over the sample. Furthermore, SEMs have an additional set of lenses that make it possible for the electron beam to scan the sample surface (discussed later in this book). TEMs have a set of lens that can properly process the transmitted and diffracted beams in order to create the desired images. The optics used in these instruments are discussed in detail in texts such as Ref 1. Readers interested in using these microscopes should search for additional information in specific texts to understand the advantages and limitations associated with different electron sources and lens configurations as well as apertures and detectors. This book presents only the basic information needed to understand and interpret the usual image modes of electron microscopes, in particular SEMs.

6.1 The Scanning Electron Microscope

The main feature of the scanning electron microscope (SEM) is that although the sample illumination is done with a focused electron beam (typical beam diameters are in the range of 1 nm to 1 μm, depending on operating mode and microscope features), a relatively large area of the sample can be observed as the beam scans the sample surface. As the beam scans the sample surface (Fig. 6.3), signals are generated, acquired by one of the detectors, and presented on a screen, which is scanned in synchrony with the beam scanning the sample. The ratio between the distance on the sample surface scanned by the beam and the dimension scanned on the screen is the magnification of this microscope. Each one of the signals presented in Fig. 6.1 provides a different type of information about the sample, as described in the following items.

6.1.1 Secondary Electrons

The cut-off energy value that separates secondary electrons (SEs) from backscattered electrons (BEs) is arbitrary. Secondary electrons are low-energy electrons (<50 eV) emitted by the sample. Because they have low energies, they can only escape from a narrow region very close to the sample surface. The SE detector is usually positioned to the side and above the sample and is polarized to select the electrons that will be collected based on their energy. Figure 6.4 presents a schematic of the location of an SE detector with

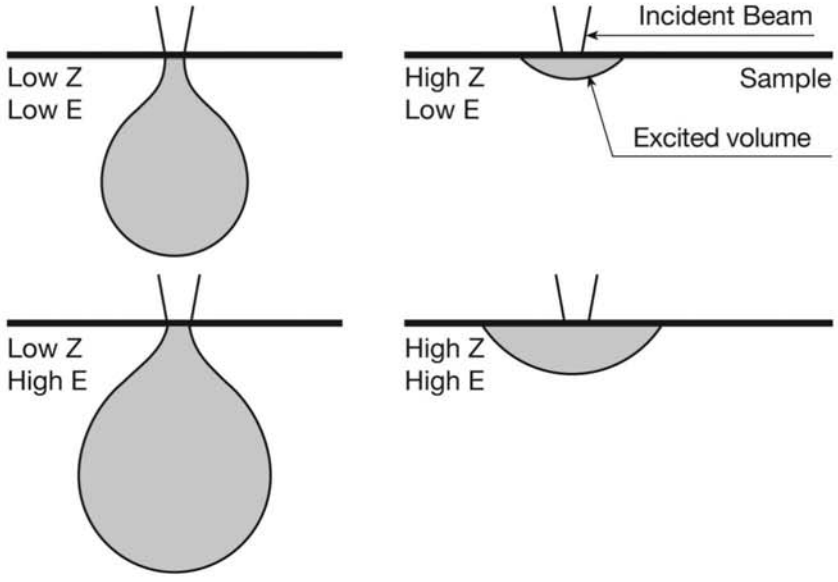

Fig. 6.2 Schematic presentation of the volume in a sample that is excited by the incident electron beam, as a function of material atomic number (Z) and beam acceleration voltage (V), and thus energy (E). In some cases, the sampled volume may have a much larger diameter than the incident beam diameter, particularly with signals other than secondary electrons. Besides having an effect on image resolution, the effective sampled volume influences the results of chemical analysis made using the x-rays emitted by the sample.

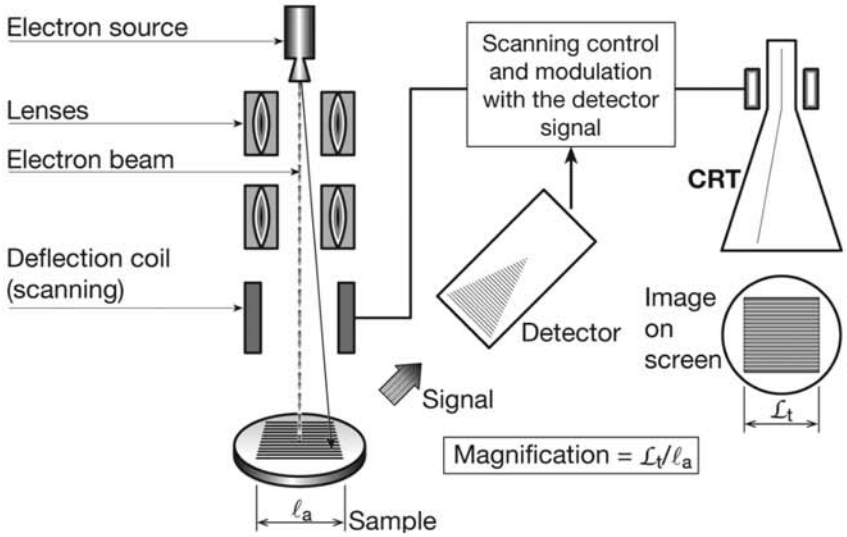

Fig. 6.3 Simplified schematic of an SEM. A source generates a flow of electrons that are collimated and focused using a series of lenses and apertures. The magnetic field in the deflection coils will cause the electron beam to scan the sample (it is also possible to keep the beam on a single spot on the sample, i.e., when a local analysis is required). As the beam scans the image, several signals are generated (see Fig. 6.1). The signal chosen to generate the image is used to modulate a scanning system synchronized with the sample scanning, creating an image on a monitor. The ratio between the dimension scanned (l_a) and the image size (L_t) defines the image magnification.

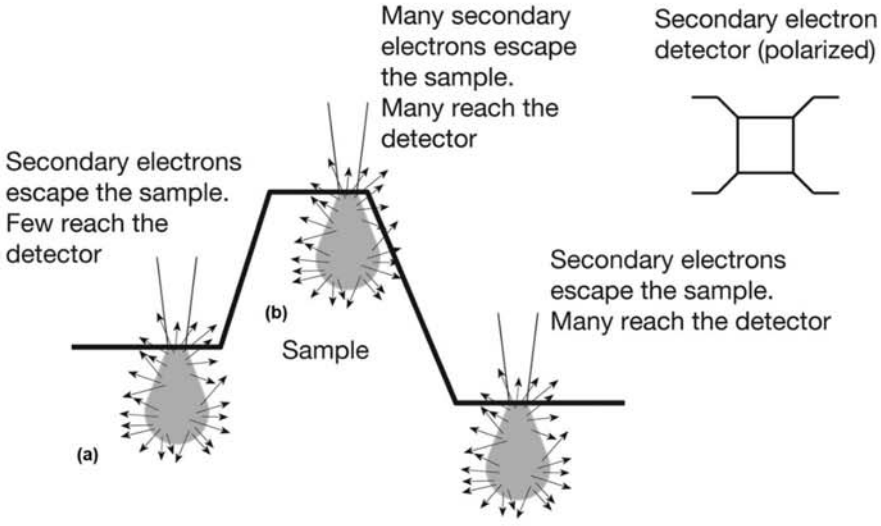

Fig. 6.4 Schematic presentation of the source of topographic contrast in SE operation. (a) Topographic features of the sample (such as etching relief or fracture topography) are significant obstacles to the low-energy SEs. Thus, they cannot reach the SE detector. (b) Edges produce stronger SE signals. Thus, sample inclination with respect to incident beam and the detector have a significant effect on contrast in this image mode.

respect to the sample position. Sample topography greatly influences the electrons' ability to reach the detector. For this reason, this is the most common imaging mode when fracture surfaces and surfaces of etched samples, in which topography is important, are observed.

Sample tilting with respect to the incident electron beam has also an important effect on the ability of SEs to reach the SE detector.

Even though SEM construction is relatively complex, images from this microscope are normally easy to interpret, using the optical analogy presented in Fig. 6.5. The SE image is analogous to the optical image that would be obtained had the specimen been illuminated (with visible light) from the position of the SE detector and observed from the position of the source of the electron beam. This analogy is especially good when the image formation/scanning is oriented in a way that the "lighting" (that is, the position of the SE detector) corresponds to the top of the observation screen in the SEM (see the section, "Relief," in Chapter 4, "Metallographic Technique—Macrography," in this book). Images created with SE signals are especially good for observing topographic details. For microstructures in which etchants are used to produce the relief, as a rule much lighter etching than that used for optical observation should be employed when classical reagents are used. The highest magnifications and best resolutions in SEM are generally obtained with SE images. One must keep in mind that the SEM operation conditions (accelerating voltage, spot size, and working distance, among others) must be optimized for each kind of signal that is used to generate an image.

For many years, the depth-of-field associated with SE observation has been a tremendous advantage of the SEM in the observation of surfaces with significant relief, such as fracture surfaces. As seen in earlier chapters of this book, conventional light microscopes are not able to produce focused images of surfaces with this feature. Some digital microscopes currently offer the

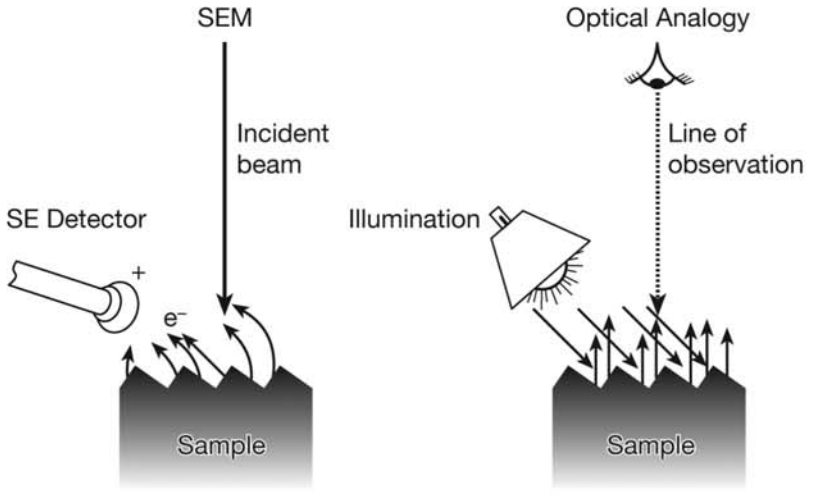

Fig. 6.5 Optical analogy useful for the interpretation of an SE image in an SEM. The resulting image is analogous to an optical image that would be obtained if the sample were illuminated with a light source positioned at the SE detector and observed from the top of the microscope column, the position of the electron source.

ability of generating three-dimensional (3D) imaging and measuring by using image stacking and digital processing. These microscopes are commercially called "three-dimensional microscopes." They use step motors to take images from a range of focal planes in the field of view and reconstruct them in a 3D color image of the sample that is presented in a monitor instead of in an eyepiece. The accuracy and quality of the images depend on the quality of the lenses, the step motor system, and the software used. Figure 6.6 is an example of a 3D image of a Charpy-V specimen.

6.1.2 Backscattered Electrons

Some electrons, as they interact with atoms in the sample, have their trajectories changed by nearly 180° without significant loss of energy, a mechanism similar to an elastic collision. These electrons return toward the sample surface and, when they manage to escape from the sample, can be captured in a detector located in a plane perpendicular to the incident electron beam (i.e., the detector is parallel to the sample). Because backscattering is extremely dependent on the atomic number of the atoms in the sample, the signal intensity depends on this variable, and the resulting image carries this information. The formation of images using backscattered electrons (BEs) is especially interesting when evaluating differences in atomic number (and hence in chemical composition) as shown in Chapter 8, "Solidification, Segregation, and Nonmetallic Inclusions," specifically Fig. 8.73 and 8.74, in this book.

Scanning electron microscope (SEM) design and construction aims at optimizing the ability to capture the desired electrons at the correct detector. Thus, one tries to prevent SEs from reaching the BE detector and BEs from reaching the SE detector (through the physical arrangement of the detectors, for instance). This is not always possible, and it is common for some contrast

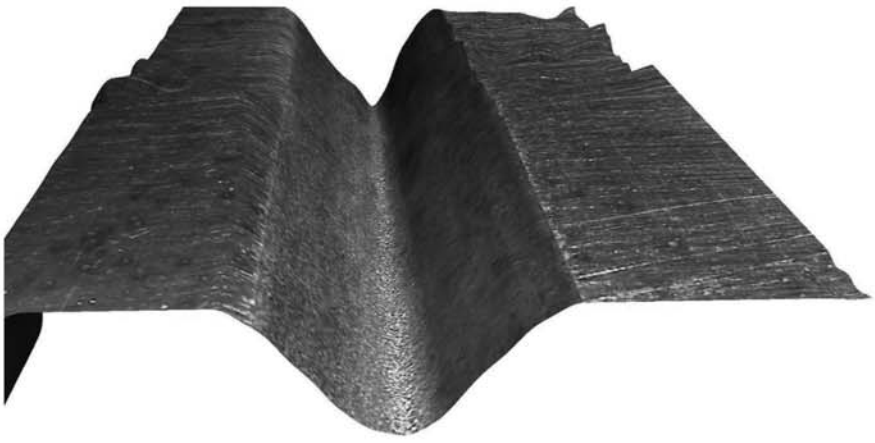

Fig. 6.6 Portion of a Charpy-V specimen machined to meet ASTM E23 requirements. The notch is specified to be 2 mm deep and 10 mm long (0.08 in. deep and 0.4 in. long). The specimen cross section should be 10 × 10 mm ± 0.075 mm (±0.003 in.). The surface where the notch is machined should have a surface roughness better than 2 μm. Image taken with "3D optical microscope" is ideal to check the quality of specimen preparation.

associated with the atomic number to be perceived in the SE images and for some relief to be seen on BE images (even when split BE detectors, which favor the capture of relief information, are not used). In some microscopes, it is possible to subtract the signals acquired by one detector from the signals acquired by another and hopefully produce images that would be less subject to this type of influence. However, this is not a very common practice, even when the feature is available.

In a crystalline sample, as the BEs travel back to the surface, they are also diffracted. In recent decades, with the improvement in detectors and computational power, the diffraction information from the BE has turned into an important source of complementary structural information. Crystallographic texture, relative orientation of grains, crystal structure, phase identification, structure stresses, and deformation are some of the data that can be gained using the technique known as electron backscattering diffraction (EBSD). Some additional examples are given in Chapter 12, "Mechanical Work of Steels: Cold Working," in this book .)

6.1.3 X-Rays

The interaction of an electron beam with a sample also generates radiation in the wavelength of x-rays. Part of this radiation is simply the continuous radiation spectrum (*Brehmstrahlung*, in German) that contains little or no information about the material. However, when the incident electron energy is sufficiently high, it can remove bound electrons from some energy levels of the sample material. When an electron from a higher energy level "decays" to the empty lower level, the energy released in the transition corresponds to the difference in energy of the two levels. As the energy levels of the electrons in the material are quantized, so is this energy difference, which is then characteristic for any given element. Hence, should it be possible to collect and analyze the x-rays emitted by the sample, either by their energy or by wavelength, it should also be possible to identify the chemical elements present in the sample and even perform chemical analysis of points or regions of the sample.

Two methods are widely used to analyze the energy spectrum of the x-rays. The first one is a method called wavelength dispersion spectroscopy (WDS), in which the spectrum of emitted x-rays is directed toward a crystal of known plane spacing. The angle at which diffraction occurs depends on the radiation wavelength (and thus its energy) according to Bragg's law. This makes it possible to construct a spectrum of x-ray intensity versus x-ray wavelength (or energy). Wavelength dispersion spectroscopy is used in SEMs known as electron microprobes. These SEMs are optimized to work in conditions that generate high x-ray intensity for WDS under stable conditions. This was the first equipment able to perform reliable quantitative microanalysis. The second method consists of separating the energies of the x-ray signals that reach the detector using electronic methods. This method is called energy dispersive spectroscopy (EDS). Detectors are normally based on semi-conducting materials that create an electron-hole pair when absorbing the x-ray. This charge pair is converted into a voltage pulse proportional to the energy of the absorbed x-ray and processed by a multiple channel analyzer. This processing is done to present the number of counts as a function of energy of the x-rays

reaching the detector. Although EDS requires a lower intensity of the x-ray beam reaching the detector than does WDS and is much faster, because all energies are sampled at the same time, in many cases WDS analysis is still much more precise and reliable. In particular, calibration methods require special attention by the operator. Even when "standardless" methods are used, it may be advisable to check the results using materials of known composition, so as to avoid errors. Chapter 11, "Hot Working," in this book, particularly Fig. 11.24 and 11.29, present some examples of the use of EDS to identify the composition of nonmetallic inclusions.

Besides acquiring complete spectra of the observed energies, the x-ray signal (EDS or WDS) can be used to generate an image that shows the regions where there is a larger generation of a given x-ray energy, and hence where a higher concentration of a given element is expected. In Chapter 8, "Solidification, Segregration, and Nonmetallic Inclusions," particularly Fig. 8.34 and 8.35, are examples of this type of image, also called x-ray mapping. One must be aware, when using these techniques that, in order to a given characteristic x-ray to be emitted, the electrons reaching the sample must have sufficient energy to remove an electron from the energy level to which an electron will decay. If the accelerating voltage is not adequate, certain characteristic radiations of elements may not be present in the x-ray spectrum collected, notwithstanding the fact that the element is present in the sample.

6.2 The Transmission Electron Microscope

The transmission electron microscope (TEM) uses electron beams that are able to go through the sample thickness for image formation. For this reason, sample preparation for TEM involves producing very thin regions. As it is normal to use very large magnifications in the TEM (this is one of the most important abilities of this microscope), the total volume of metal that is examined in the TEM is very small. Thus, this microscope is usually used to observe general characteristics of the material, not localized particularities, because it is difficult to guarantee that areas of specific interest will be effectively analyzed. In recent years, there has been a significant improvement in the ability to locate and sample specific regions of a material. Probably the most relevant contribution to this has come from the development of the focused ion beam (FIB) technique, which is briefly discussed in the section "6.3.1 FIB in Localized Sample Preparation," later in this chapter.

Besides creating images, TEMs also perform chemical analysis via EDS (normally EDS detectors in TEMs are located above the sample), or evaluate the energy loss on the transmitted electrons in a technique known as electron energy loss spectroscopy (EELS). The technique is reviewed in detail in Ref 3 and 4. Examples of the application to the characterization of nanoparticles in steel can be found in Ref 5 and 6. One significant aspect of EELS, relevant to iron and steel products, is its suitability to detect light elements, significantly better than that of x-ray analysis methods (Ref 3). More detailed information on the TEM is found in Ref 7 and 8.

Even the simplest images obtained by TEM require knowledge of phase crystallography and of the TEM technique to be properly interpreted. Important aspects of TEM technique are:

- It is possible to obtain diffraction patterns from extremely small particles in the sample. The identification of the crystal structure and the spacing of the crystallographic planes are often enough to completely

identify the phase in question. This information is frequently complemented by the spectrometric data acquired in TEM itself.

- It is possible to identify the crystallographic orientation of each grain and study the crystallographic relations between the phases. EBSD is increasingly used for this because (a) it can measure the features for a large number of grains and (b) acquiring information is becoming less time consuming due to the improvement in hardware and software. However, TEM is still the most appropriate approach for fine precipitates and fine phase dispersions.
- Dislocations and their orientations in a crystal can be observed and identified.

6.3 Scanning Transmission Electron Microscopy

Like a SEM, scanning transmission electron microscopy (STEM) uses a finely focused electron beam to scan the sample surface and synchronize the signals collected from the sample to generate an image in a screen (Ref 9). Like a TEM, STEM looks primarily at electrons that are transmitted by the sample. STEM are constructed and have developed in recent years to provide tremendous spatial resolution.

In a "conventional" TEM, a large area of the sample is illuminated by electrons, and the significant magnification is performed by the lens system after the specimen (Ref 10). Very seldom, a convergent electron beam is used to probe the sample. In the STEM, the electron beam is finely focused before it reaches the sample and generates signals from precise locations in the sample. A variety of signals can be acquired and treated to generate images with high spatial resolution.

Figure 6.7 (Shigesato et al. Ref 11) shows a previous austenitic grain boundary in a boron-containing low alloy steel. Using EELS in an aberration corrected STEM, Ref 11 was able to quantify the boron segregation in a few atomic layers close to the previous austenitic grain boundary, as shown in Fig. 6.8.

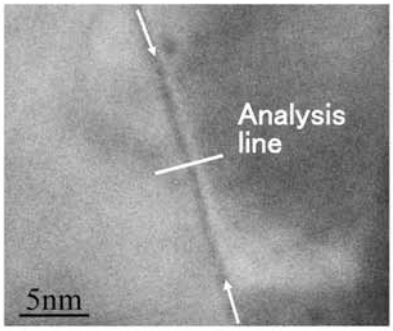

Fig. 6.7 STEM dark field images of the prior austenite grain boundary in B added steel (0.05%C, 1.5%Mn, 3%Ni, 0.5%Mo, 11 ppm B). Courtesy of Nippon Steel & Sumitomo Metals Corporation. Source: Ref 11

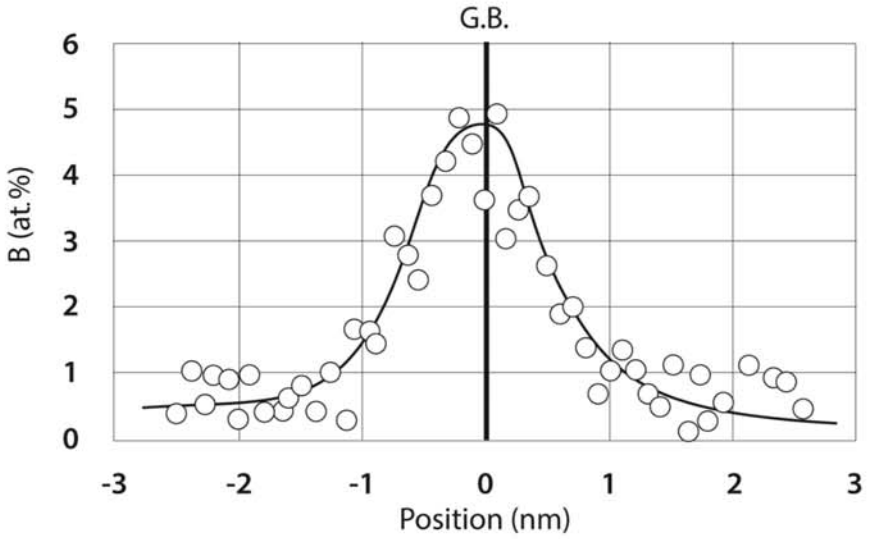

Fig. 6.8 Example of boron profile measured using EELS in STEM around the prior austenite grain boundary marked in Fig. 6.7. Adapted from Ref 11 with permission of Nippon Steel & Sumitomo Metals Corporation.

6.3.1 FIB in Localized Sample Preparation

Preparing samples for observation in TEM and in STEM is not an easy task. The samples must have a significant area thin enough to be transparent to electrons (10–200 nm thickness being a typical range for steels). This involves several steps encompassing mechanical preparation, erosion by an ion bombardment (ion milling), electrolytic methods, and so on. These methods have the potential to introduce artifacts in the sample due to mechanical deformation (it is easy to deform very thin samples) or the effect of heat (it is easy to overheat a very small sample). Furthermore, although one can try to start with a sample from the general area of interest in the material, it is extremely difficult to ensure that the thinning will be properly localized on the features to be examined. In general, TEM and STEM are particularly useful for observing features that are present in the whole material and not localized characteristics and features. This was a significant disadvantage of these techniques, until FIB "machining" techniques became available. With the FIB technique, once an area of interest is selected (for instance using a SEM equipped with FIB) a TEM or STEM sample can be precisely removed and thinned with mostly automated manipulation.

Figure 6.9 shows the sequence of steps in obtaining a thin sample from a defined location in a specimen. This technique has its own difficulties and requires constant care. Some recommended publications for the beginner to advanced user are included in Refs 12 to 14.

Practical examples of use of this technique to specific problems in steels are now common in the literature. The application to austenite decomposition (Ref 14), galvannealed steel (Ref 15), and welding and solidification (Ref 16) are some interesting examples.

6.4 Atom Probe Tomography

Atom probe tomography is a technique that makes possible 3D image reconstruction and chemical composition measurements at the atomic scale (Ref 17–19). This technique relies on the evaporation of individual atoms (ions) from the tip of a very sharp, fine needle of the material to be examined. The evaporation is normally produced by high voltage pulsing or by laser. The time-of-flight is directly related to the ratio of mass to charge of the ion, and the x-y position information makes it possible to determine the position of the atom (ion) on the original specimen. Thus, it is possible to reconstruct the individual position of atoms in the sample and identify the element in question. As the procedure of evaporating atoms in subsequent layers is repeated, a 3D reconstruction of the specimen on the atomic scale is then possible. The atoms reach a two-dimensional detector that precisely records the x-y position of the ion impact and the time-of-flight from the specimen to the detector. The instrument is quite complex because it is important to closely control the pulsing, so as to evaporate individual atoms and detect their signals on the detectors. Performing an analysis in a reasonable time is closely connected to this ability.

The typical atom probe specimen is a sharp needle with an apex radius between 50 and 150 nm (Ref 17). The needle normally has a very small taper of approximately 10°.

During the examination the needle evaporates, and thus its tip geometry suffers changes that must be accounted for in the reconstruction process.

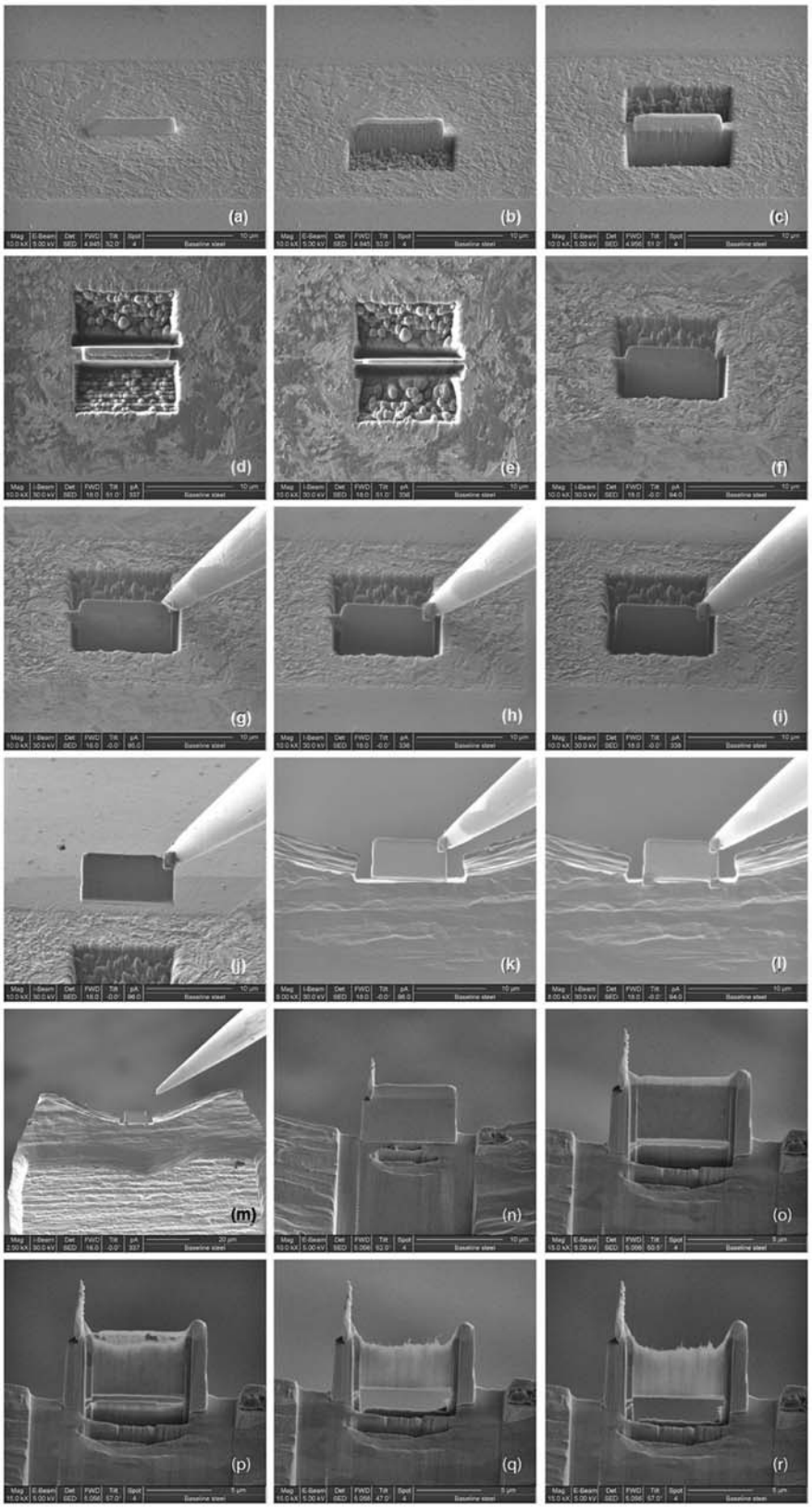

Fig. 6.9 Sample removal and thinning using FIB. In a sample where the microstructure was revealed by FIB sputtering/cleaning of the surface, the location of the thin sample to be removed is selected and an ion beam–assisted platinum deposition is done on location (a). A trench is dug on each side of the region to be sampled by sputtering using a high-energy ion beam (b–e). Images (d) and (e) are top views. The sample is separated from one edge using the ion beam, welded to a needle using an ion beam–assisted platinum deposition, separated from the other edge (f–i), and lifted out (j). The sample is then welded using the same platinum deposition technique to a substrate for thinning and the needle weld is removed so the needle itself can be removed (k–m). (n) is a view from the opposite side of previous views of the sample ready for thinning. In (o–r) the sample is progressively thinned via sputtering with the ion beam. All images are SE images from a dual-beam (electron, FIB) microscope. Images (d) to (m) were generated using an incident ion beam. Images (a) to (c) and (n) to (r) were generated using an incident electron beam. Courtesy of N. Rudawski and A. Dempere, University of Florida.

Proper modeling of these changes is essential to ensure accurate analysis; understanding and progress in this area is ongoing (Ref 20). When the technique is properly used, the amount of information gained and the insights provided are impressive. Figure 6.10 shows results related to the deformation-driven decomposition of the carbides in heavily cold worked pearlitic wire.

For more examples of the application of this technique to steel, see Refs 19 and 22.

6.5 Atomic Force Microscopy

Recent decades have seen the development of instruments that can measure and present the results of the interactions of a fine sensor and the surface of a sample. The technique, called atomic force microscopy (AFM), encompasses a vast array of instruments and resolving powers (Ref 23). When observing steel microstructures, these microscopes usually operate in very simple environmental conditions and produce interesting information. In general, these microscopes are classified as mechanical scanning probe microscopes. Unlike other microscopes, light or electrons are not used to generate the image. Instead, signals deriving from the interaction from moving a fine "stylus" over the sample surface is used to generate images, as shown schematically in Fig. 6.11. The most common information obtained from analyzing microstructures is relief information, and relief in the order of angstroms can be mea-

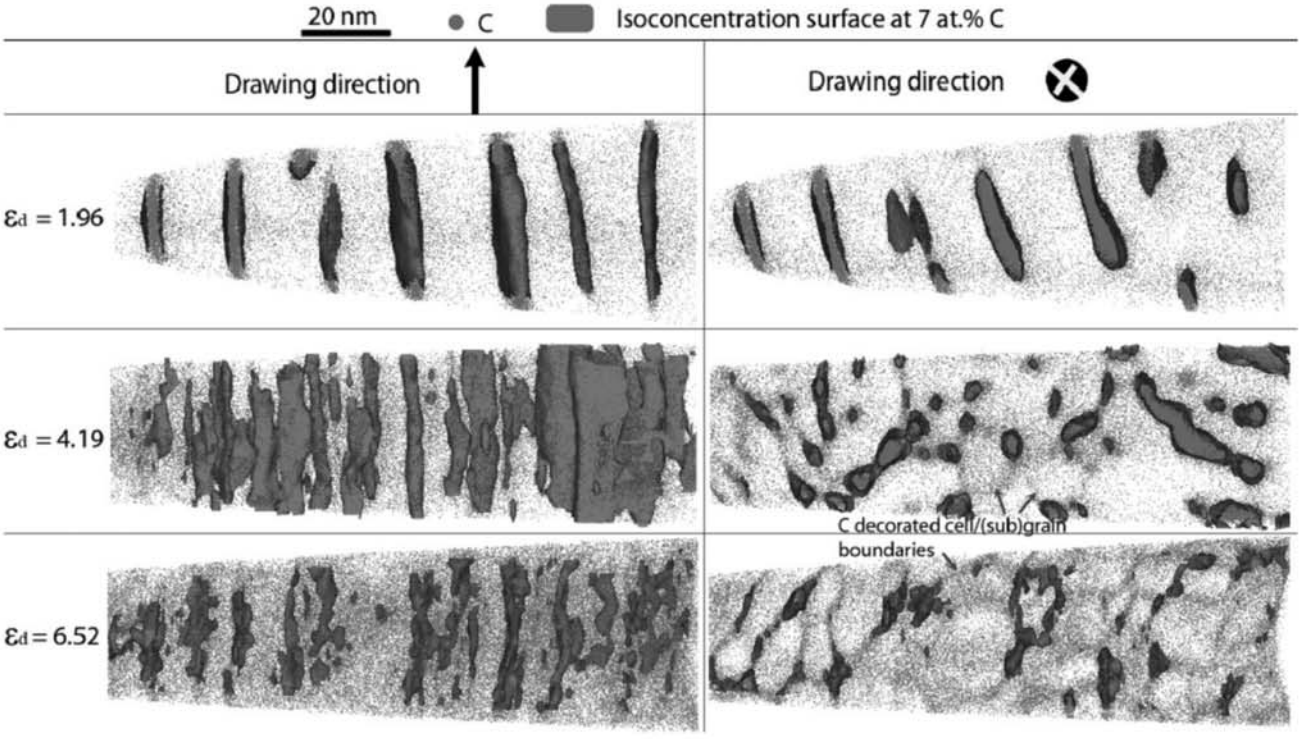

Fig. 6.10 Atom probe tomography results of pearlitic steel wires cold drawn to different strains (indicated in the pictures). 3D carbon atom maps parallel and transverse to the wire drawing direction are shown. Dots are carbon atoms. Carbon iso-concentration surfaces 7 at.% are shown. Figure reprinted with permission from Ref 21, Copyright 2014, by the American Physics Society. Source: Ref 21

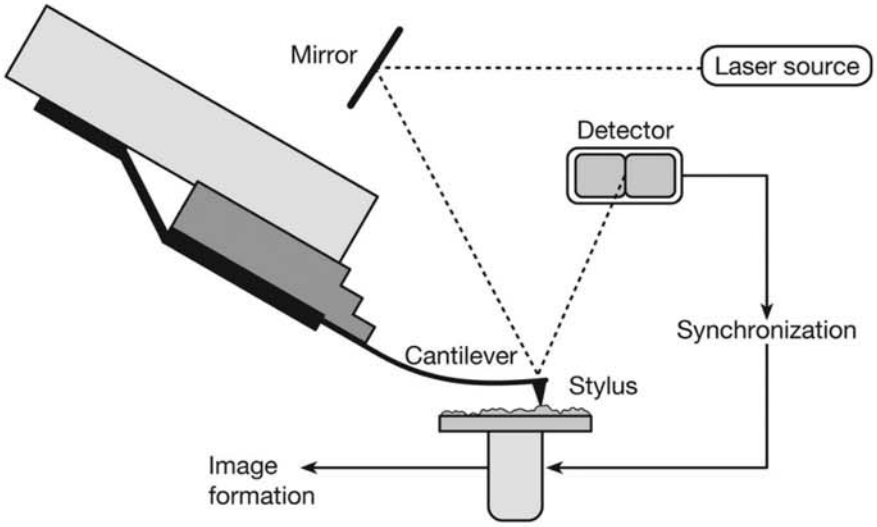

Fig. 6.11 Simplified schematic representation of an atomic force microscope. The "stylus" at the end of the sensor scans the sample surface. Its deflection is measured by the position of the reflection of a laser beam pointed at the cantilever holding the stylus. The positional information of the cantilever makes it possible to derive the sample relief at a given point. This signal is synchronized to the stylus scanning of the sample so that a sample image with the collected signals can be presented.

sured. Important features of the technique are that (a) it is possible to acquire quantitative information about dimensions in the vertical direction on the sample (relief) and (b) samples do not need to be electrical conductors (as in electron microscopes) (Ref 24). Magnetic information, for instance, can be acquired with the proper stylus and signal treatment (Ref 25).

6.6 Laser Scanning Confocal Microscopy

Laser scanning confocal microscopy (LSCM) was initially developed for applications in biology. It combines the advantages of confocal optics and the use of laser. A detailed discussion of the technique is given in Ref 26. The combination of confocal optics and laser makes it possible to evaluate samples at high temperatures with high resolution. Confocal optics makes it possible to select the signal coming from the plane under focus and reduce the intensity of signals coming from regions out of this plane. By scanning the sample through various focusing planes, it is possible to reconstruct a 3D image with high resolution. Images of irregular surfaces, as well as images of samples with relief, can thus be obtained, even with wavelengths of light (laser). Because the laser intensity is much higher that the radiation from high-temperature samples, it is possible to observe the material without undue interference from the radiation. According to Ref 27, the technique is extremely useful for the in-situ observation of liquid metal, chemical reactions, phase transformations, and so on. Examples of the application of the technique are presented in Chapter 8, "Solidification, Segregation, and Nonmetallic Inclusions." Orrling et al. (Ref 27) also made available a number of images and videos. A collection of examples of applications to steels is presented in Ref 28.

REFERENCES

1. J. Goldstein, D.E. Newbury, D.C. Joy, C.E. Lyman, P. Echlin, E. Lifshin, L.C. Sawyer, and J.R. Michael, *Scanning Electron Microscopy and X-Ray Microanalysis*, Springer Science and Business Media, 2003
2. http://www.matter.org.uk/tem/electron_scattering.htm (Java is required)
3. K.J. Keast, Application of EELS in Materials Science, *Materials Characterization*, Vol 73, Nov 2012, p 1–7.1
4. R.F. Egerton and M. Malac, EELS in the TEM, *J. Electron Spectr. Rel. Phen.*, Vol 143, (No. 2–3), May 2005, p 43–50
5. A. Hirata, T. Fujita, Y.R. Wen, J.H. Schneibel, C.T. Liu, and M.W. Chen, Atomic Structure of Nanoclusters in Oxide-Dispersion-Strengthened Steels, *Nature Mater.*, Vol 10, (No. 12), Oct 23, 2011, p 922–26
6. G. Shigesato, S. Taniguchi, M. Sugiyama, and M. Ikematsu, Nano-Characterization Technique for Steel Research by Using Aberration-Corrected Scanning Transmission Electron Microscopy, *Nippon Steel Tech. Rep.*, Vol 100, 2011, p 8–13; available from: http://www.nssmc.com/en/tech/report/nsc /pdf/n10003.pdf
7. D.B. Williams and C.B. Carter, *Transmission Electron Microscopy: A Textbook for Materials Science*, Plenum Press. 1996
8. M.H. Loretto, *Electron Beam Analysis of Materials*, Springer, 1994
9. S.J. Pennycook, A.R. Lupini, M. Varela, A.Y. Borisevich, Y. Peng, M.P. Oxley, et al., Scanning Transmission Electron Microscopy for Nanostructure Characterization, *Scanning Microscopy for Nanotechnology*, Springer, 2006, p 152–91; available from: http://link.springer.com /content/pdf/10.1007/978-0-387-39620-0_6.pdf
10. M. Varela, A.R. Lupini, K. van Benthem, A.Y. Borisevich, M.F. Chisholm, N. Shibata, et al., Materials Characterization in the Aberration-Corrected Scanning Transmission Electron Microscope, *Annu. Rev. Mat. Res.*, Vol 35, (No. 1), Aug 4, 2005, p 539–69
11. G. Shigesato, S. Taniguchi, M. Sugiyama, and Y. Ikematsu, Nano-Characterization Technique for Steel Research by Using Aberration-Corrected Scanning Transmission Electron Microscopy, *Nippon Steel Tec. Rep.*, Vol 100, 2011, p 8–13
12. B.L. Peterson, *TEM Sample Preparation Tips*, FEI, https://www.fei.com /WorkArea/DownloadAsset.aspx?id=21474838571
13. Steps in TEM Specimen Preparation by "Lift-Out" Method, Fibics, http://www.fibics.com/fib/application/steps-in-tem-specimens-preparation-by-lift-out-method-/24/
14. M. Gouné, F. Danoix, J. Ågren, Y. Bréchet, C.R. Hutchinson, M. Militzer, et al., Overview of the Current Issues in Austenite to Ferrite Transformation and the Role of Migrating Interfaces therein for Low-Alloyed Steels, *Mat. Sci. Engin. Rep.*, Vol 92, June 2015, p 1–38
15. T. Kato, M.H. Hong, K. Nunome, K. Sasaki, K. Kuroda, H. Saka,

Cross-Sectional TEM Observation of Multilayer Structure of a Galvannealed Steel, *Thin Solid Films*, Vol 319, (No. 1–2), 1998, p 132–39

16. M.J. Perricone, Advanced Milling Technology Helps Identify Phase Transformations, *Welding J.*, Vol 84, (No. 10), 2005, p 44–49
17. T.F. Kelly and M.K. Miller, Invited Review Article: Atom Probe Tomography, *Rev. Sci. Instr.*, Vol 78, (No. 3), 2007, p 31101
18. A. Cerezo, P.H. Clifton, M.J. Galtrey, C.J. Humphreys, T.F. Kelly, D.J. Larson, et al., Atom Probe Tomography Today, *Mat. Today*, Vol 10, (No. 12), 2007, p 36–42
19. D. Raabe, Tomographic Atom Probe Analysis, http://www.dierk-raabe.com/atom-probe-tomography/
20. F. Vurpillot, B. Gault, B.P. Geiser, and D.J. Larson, Reconstructing Atom Probe Data: A Review, *Ultramicroscopy*, Vol 132, Sept 2013, p 19–30
21. Y. Li, D. Raabe, M. Herbig, P.-P. Choi, S. Goto, A. Kostka, et al., Segregation Stabilizes Nanocrystalline Bulk Steel with Near Theoretical Strength, *Phys. Rev. Lett.*, Vol 113, (No. 10), September 5, 2014; available at: http://link.aps.org/doi/10.1103/PhysRevLett.113.106104
22. J. Takahashi , K. Kawakami K., and M. Ueda, Atom Probe Tomography Analysis of the White Etching Layer in a Rail Track Surface, *Acta Materialia*, Vol 58, (No. 10), June 2010, p 3602–12
23. P. Eaton and P. West, *Atomic Force Microscopy*, Oxford University Press, 2010
24. M.S. Andrade, J.M.C. Vilela, and O.A. Gomes, Microscopia de Varredura por Sonda Mecânica: Ampliando as Fronteiras da Análise Metalográfica, *Metalurgia & Materiais*, Vol 58, (No. 518), 2002, p 123–25
25. A. Dias and M.S. Andrade, Atomic Force and Magnetic Force Microscopies Applied to Duplex Stainless Steels, *Appl. Surf. Sci.*, Vol 161, (No. 1), 2000, p 109–14
26. R.H. Webb, Confocal Optical Microscopy, *Rep. Prog. Phys.*, Vol 59, 1996, p 427–71
27. C. Orrling, Y. Fang, N. Phinichka, S. Sridhar, and A.W. Cramb, Observing and Measuring Solidification Phenomena at High Temperatures, *JOM*-e, Vol 51, (No. 7), July 1999; available at: http://www.tms.org/pubs/journals/JOM/9907/Orrling/Orrling-9907.html
28. Y. Komizo and H. Terasaki, Optical Observation of Real Materials Using Laser Scanning Confocal Microscopy, Part 1—Techniques and Observed Examples of Microstructural Changes, *Sci. Technol. Welding Joining*, Vol 16, (No. 1), Jan 2011, p 56–60

Metallography of Steels—Interpretation of Structure and the Effects of Processing
Hubertus Colpaert
Updated and Translated by André Luiz V. da Costa e Silva

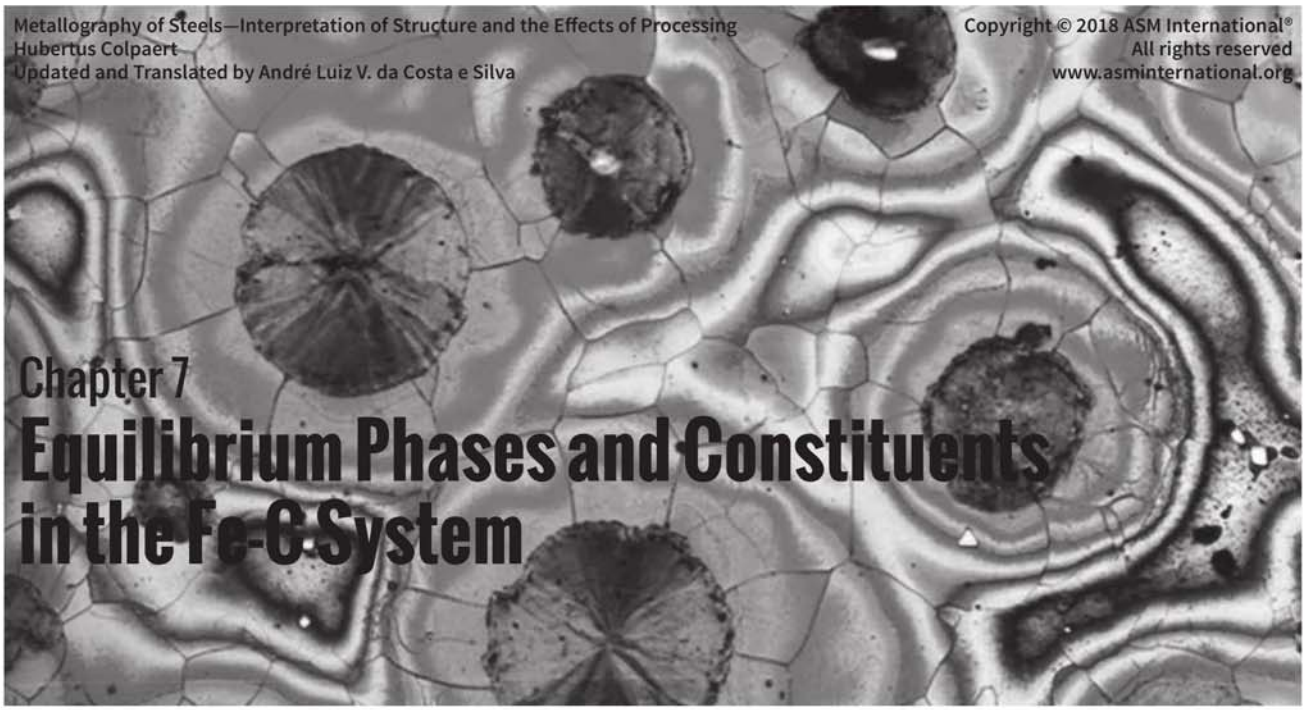

Chapter 7
Equilibrium Phases and Constituents in the Fe-C System

This chapter introduces the basic concepts of the phases and constituents present in the simpler steels in conditions near equilibrium. The discussion focuses on the iron-carbon (Fe-C) system. Understanding these concepts is fundamental for a proper understanding of the transformations that occur during steel solidification, heat treatments, and thermomechanical processing. Discussion of the Fe-C system is of paramount importance to understanding many phenomena that also occur in complex alloy steels.

The combination of chemical composition and structure (in its various scales, as discussed in Chapter 1, "Steel as Material," in this book), defines the properties and hence the performance of steels. Chemical composition is controlled essentially during the steelmaking processes, although the composition close to the part surface can be affected by thermochemical treatments in the solid state. Structure, on the other hand, is altered by the combination of deformation and temperature change, normally grouped under the name of thermomechanical treatments.

Producing phase transformations between the two main crystal structures of iron, body-centered cubic (BCC) and face-centered cubic (FCC) (presented in Chapter 1) and forming structures other than equilibrium structures (see Chapter 9, "Conventional Heat Treatments—Usual Constituents and Their Formation," in this book) with interesting properties in terms of application and with reasonable stability are possibly the two main reasons that explain the wide use of steels as industrial materials.

A main objective of this book is to present the structures that result from applying different thermomechanical treatments of steels with various chemical compositions, in particular at the size scale evaluated through metallography. Underlying the effect of these treatments on steels with different chemical compositions is the concept of phase transformation. The way steel undergoes phase transformations in the different stages of its processing is a critical factor in defining the features and properties of the structures formed. While the object of this book is not the in-depth study of phase transformations, the reader should be familiar with the concepts that control these

transformations. Here, only the fundamental aspects essential to understanding the features presented are discussed; excellent literature is available on the subject at different levels of complexity in Ref 1 to 4.

7.1 The Phases of Iron and Its Alloys

At atmospheric pressure, iron can have two solid crystal structures (BCC or FCC), depending on temperature, and is able to transform into the liquid state (the conditions under which iron is present as a vapor are less interesting to metallurgy).

Alloying elements added to iron may help make one or the other structures more stable. They may also form new, important phases in steel. For this reason, the first important information related to the possible structures of an iron-base alloy is to understand the equilibrium state of the alloy at different temperatures. In metallurgy this information is classically presented in the equilibrium phase diagrams. These diagrams are constructed directly from the collection and consolidation of the results of experiments. Alternatively, when thermodynamic data are available, phase diagrams can be calculated from these data (Ref 5, 6).

Hence, the first classification of the effect alloying elements can have on steel (as seen in Chapter 1) is based on the stability of the crystalline phases of iron: (a) ferrite (BCC) stabilizers and (b) austenite (FCC) stabilizers. More complex classifications of the effect of alloying elements exist. One example can be found in Ref 7.

Traditionally, simpler structural analysis of steels employ the Fe-C equilibrium phase diagram. This is due to two reasons: 1. for a long time there was a relative scarcity of accurate data on the phase equilibrium in more complex steels, and 2. the difficulties associated with graphically representing the equilibrium information of higher order systems and interpreting the associated diagrams. In any case, the Fe-C diagram is a good starting point for analysis, because it is quite instructive and can help describe many families of steels that are widely employed in industry. The Fe-C equilibrium in Chapter 1, "Steel as Material," Fig. 1.3, is usually not fully established in steels in the solid state, and graphite is usually not present. Instead of graphite, a metastable iron-carbide Fe_3C (with 25 atomic % or 6.67% C) is observed. The carbide is called "metastable" (with respect to one or more phases) when it is in equilibrium except for the absence of the more stable phase(s) in question (graphite, in the present case).

Figure 7.1 presents the metastable Fe-C equilibrium phase diagram. The typical transformation path of a steel along its processing history is shown in a simplified manner beginning with solidification starting from the single phase field where the liquid phase is present (L), passing through the field where FCC (γ) exists, and then passing to the field where BCC(α) + Fe_3C are present.

The equilibrium phase diagram indicates that when a line that separates two fields is reached, the energy (in the case of a system at constant pressure, the Gibbs free energy, see Ref 1, for instance) of the phases in equilibrium at this line are equal. Thus, there is no reason for any transformation to occur, as nature has no energy to gain with this transformation. As a given phase is taken into thermodynamic conditions where other phase or other phase combinations are stable, a nonzero difference in energy begins to exist between the two possible configurations. This energy difference is interpreted as the "driving force" for the transformation.

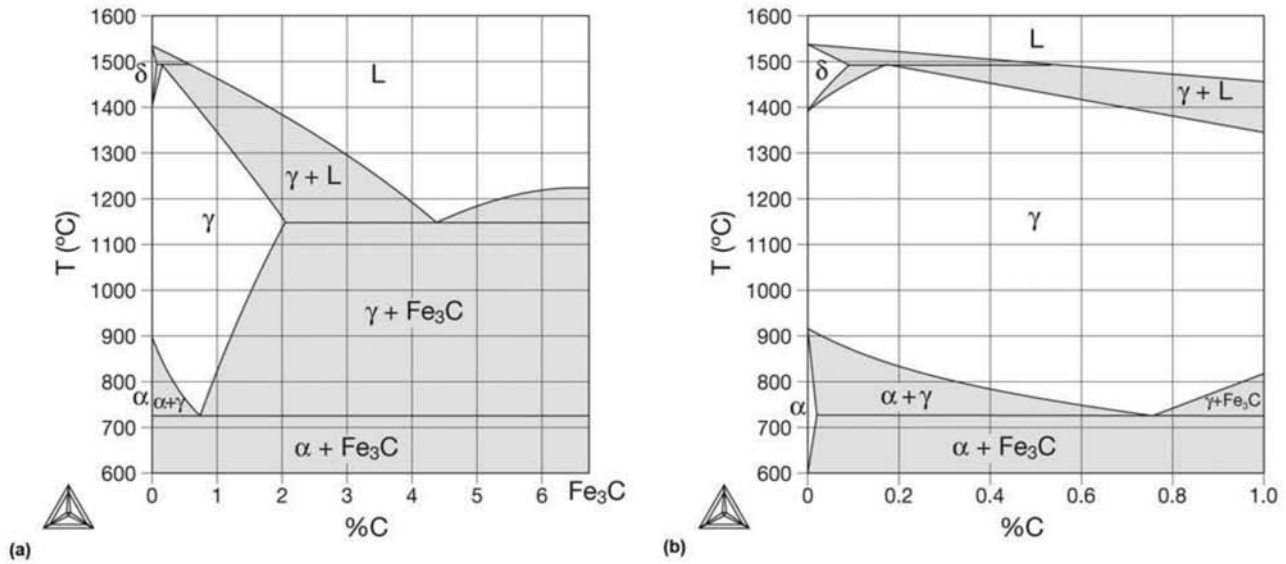

Fig. 7.1 Metastable equilibrium phase diagram for the system Fe-C, presented in two composition ranges. The diagram is metastable with respect to graphite, which is not formed. The diagram indicates the equilibrium phases in each region but it does not inform (a) if equilibrium will be reached and (b) the microstructural features (shape, phase distribution) in each field. Calculated diagram. Source: Ref 8, 9

For a transformation to occur, two steps are needed:

1. The new phase or phase combination must appear (nucleate), and once nucleated it needs to
2. Grow.

The "driving force" is "spent" to make these two processes happen.

For the nucleation to occur, it is necessary to "spend" energy to form new interfaces between the original phase and the new phase as atoms organize in the new crystal structure. This requires the atoms to be sufficiently mobile. It is also necessary to use energy to counteract forces associated, for instance, with the volume differences between the new phase nuclei and the previously existing phase.

For growth to occur, it is usually necessary for atoms to move. If the phases growing have chemical compositions that are not the same as that of the vanishing phase , solute will have to move and redistribute between the phases.

Thus, on a qualitative basis, phase transformations are dominated by the balance among the driving force available to create interfaces, counteracting forces (e.g., elastic), and atomic mobility. Describing the phases in steel and how they form from other phases is simpler when this transformation occurs in conditions near to equilibrium. This means a situation in which this balance is such that as we move into a new field in the phase diagram, (a) the new phases predicted are able to surpass the nucleation barriers; and (b) the atomic mobility conditions are such that the solute atoms will have time to redistribute properly between the phases. These conditions are normally – called—in an inexact way— "slow cooling" conditions. In this chapter the dis-

cussion is limited to transformations that do not involve the liquid phase (see Chapter 8, "Solidification, Segregation, and Nonmetallic Inclusions," in this book). Thus, we are only concerned with BCC, FCC, and the iron carbide Fe_3C, called cementite. In this situation, the constituents present in steel are those described below.

7.2 Ferrite

Pure iron or steel containing carbon below the solubility limit of cementite in the BCC phase is essentially a single phase, at room temperature, containing only the BCC phase, called *ferrite*. Ferrite formation from austenite (FCC, γ) in conditions close to equilibrium is shown schematically in Fig. 7.2.

Figure 7.3 presents a sample of Armco® iron with extremely low carbon content in which the microstructure is essentially composed of ferrite grains. Steels in which ferrite is formed via relatively slow cooling from the austenitic phase field normally have equiaxed ferrite grains (grains with approximately the same dimension in all directions or axis).

Should this material be cold formed, the grain shape will change (see Chapter 12, "Mechanical Work of Steels: Cold Working," in this book) as a result of deformation. This type of material normally has very low hardness. When the grain size is sufficiently large, it can be used in applications such as metal-to-metal sealing rings in the oil industry, where the ring is required to deform during the closing of the connection to achieve proper sealing. Figures 7.4 and 7.5 present an annealed interstitial free (IF) steel. IF steels have a

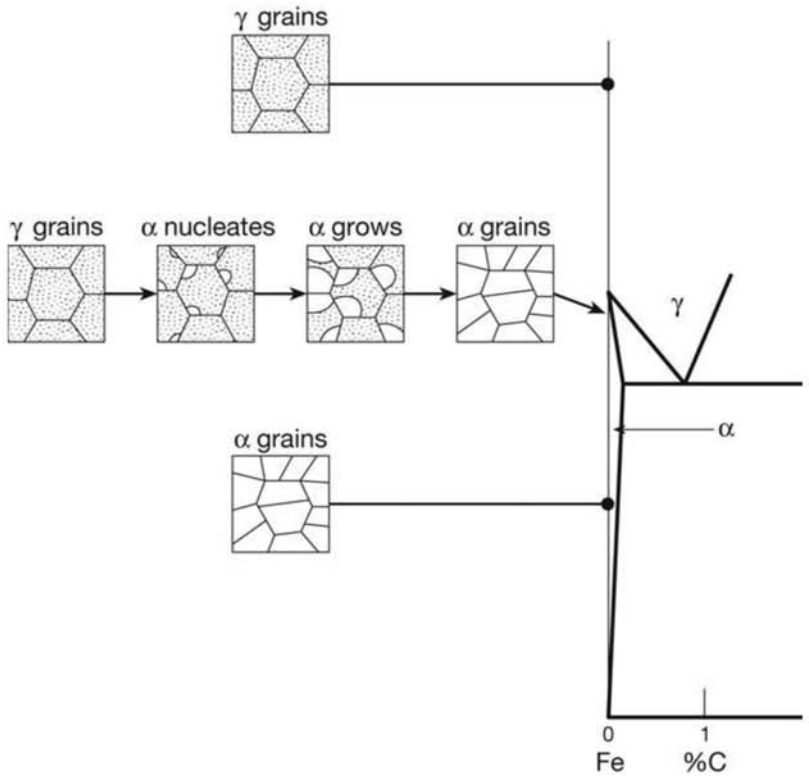

Fig. 7.2 Schematic presentation of the transformation of austenite in ferrite in conditions close to equilibrium. Adapted from: Ref 10

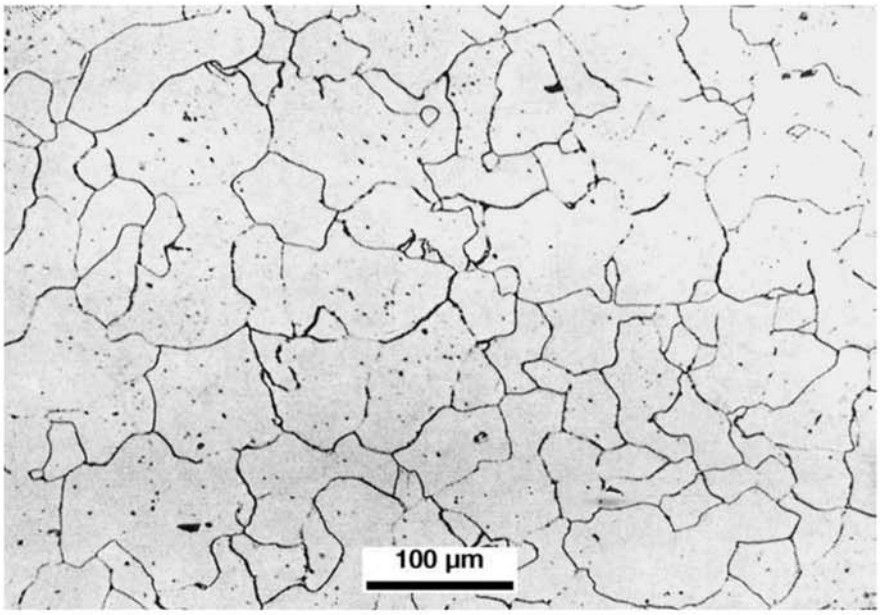

Fig. 7.3 Extra low-carbon steel (Armco® iron). Ferrite grains and small nonmetallic inclusions. Etchant: aqua regia.

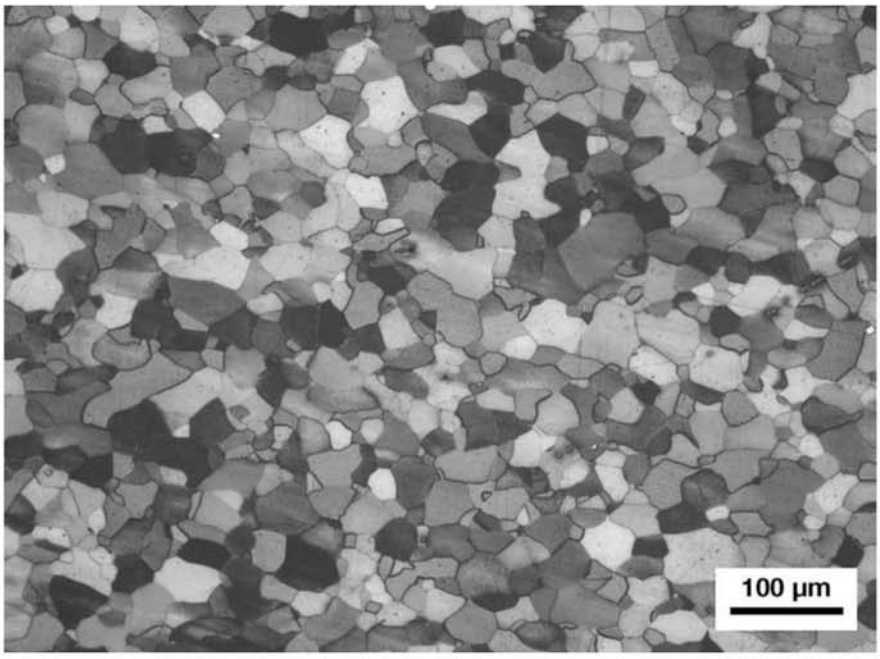

Fig. 7.4 IF steel (C = 26 ppm, N = 30 ppm, Ti = 600 ppm) annealed. Polygonal (equiaxed) ferrite grains. Etchant: Klemm.

composition and processing designed to minimize the content of interstitials C and N in ferrite (Ref 11). This sample has a hardness of 33–36 HRB, yield strength around 150 MPa (22 ksi), and tensile strength close to 315 MPa (46 ksi). The carbon content of these steels is usually sufficiently low to prevent cementite formation. Furthermore, titanium and/or niobium are usually

added to form carbides or carbonitrides that further scavenge interstitials from dissolving in the BCC matrix. These carbides or carbonitrides are usually formed in the solid state and are sufficiently small as to not be visible with optical microscopy techniques. Other chemical compositions, such as high-silicon steels for electrical applications, as discussed in Chapter 12, also have a fully ferritic microstructure, as shown in Fig. 7.6.

Ferrite (BCC) Stabilizing Alloying Elements

Some elements, when dissolved in iron, have a tendency to stabilize the BCC structure with respect to the FCC structure (e.g., chromium; Fig. 7.7). This frequently happens with elements that, when pure, are stable in the BCC structure. This is not a perfect rule, however. The main ferrite stabilizing elements are silicon, chromium, phosphorous, molybdenum, vanadium, titanium, niobium, and aluminum (pure aluminum, for instance, is FCC in the solid state).

7.3 Austenite

When ferrite in Fe-C steels is heated, the FCC phase, called austenite, is formed. Austenite is named after Sir William Chandler Roberts-Austen (1843–1902), professor of the Royal School of Mines (later the Imperial College) and a pioneer in metallography and the study of iron alloys. The direct observation of austenite in pure iron and Fe-C alloys can only be done with microscopes that operate at high temperatures, at which point this phase is stable. Figure 7.8 presents an example of austenite formation from ferrite in an IF steel (containing 40 ppm C). Because the steel has a very low carbon content,

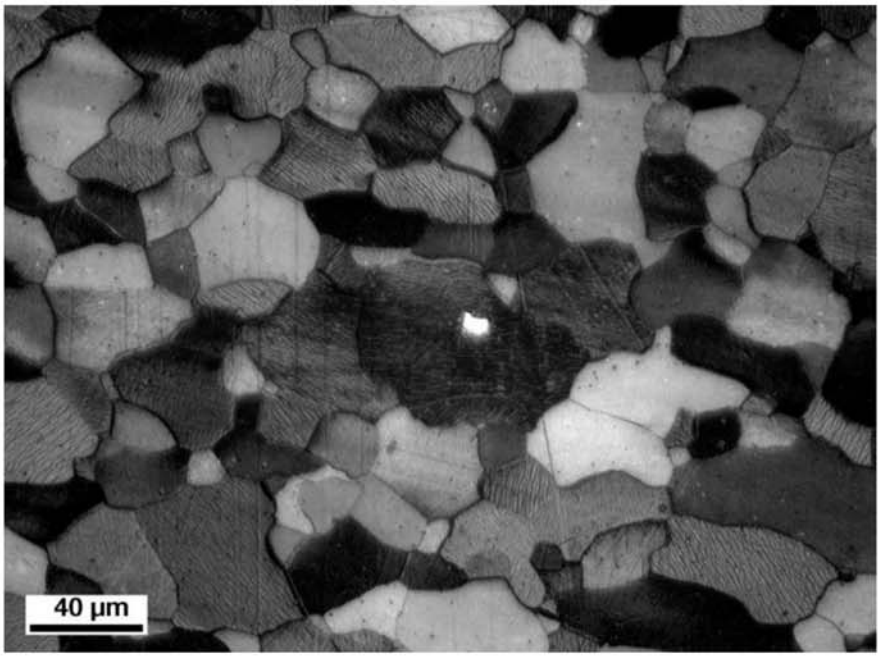

Fig. 7.5 IF steel (C = 26 ppm, N = 30 ppm, Ti = 600 ppm) annealed. Polygonal (equiaxed) ferrite grains. In the center of the image, a small nonmetallic inclusion is present. Possibly TiN. Etchant: Klemm.

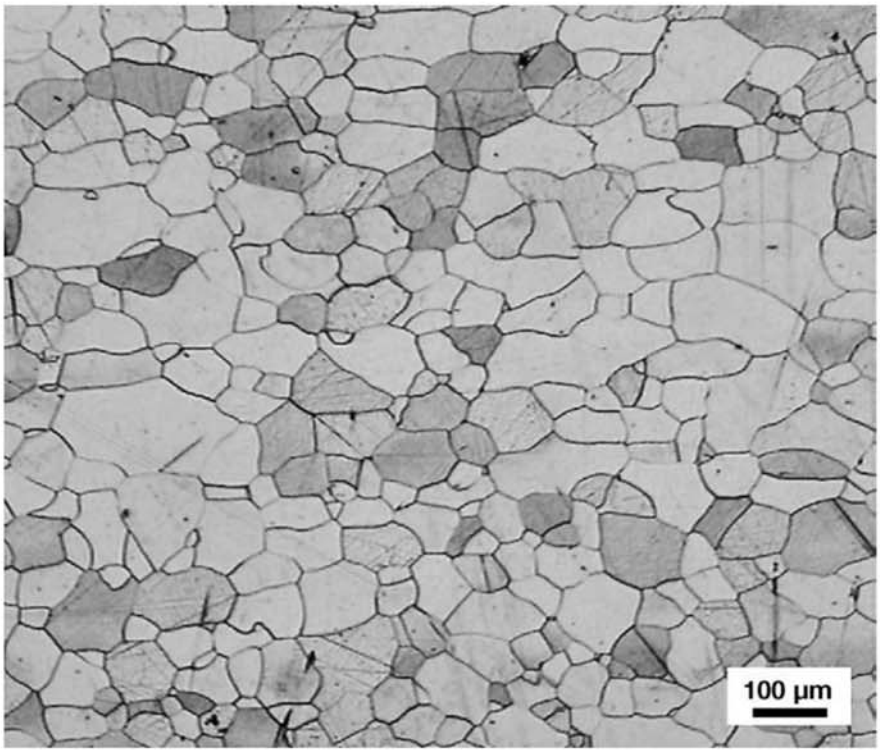

Fig. 7.6 Polygonal ferrite in electric steel, annealed. Courtesy of C. Capdevila Montes, Centro Nacional de Investigaciones Metalúrgicas—CENIM-CSIC, grupo Materialia, Madrid, Spain.

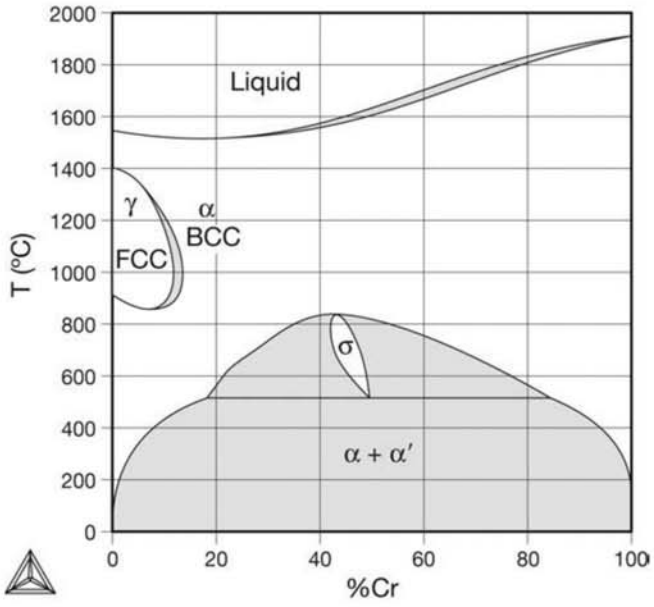

Fig. 7.7 Fe-Cr equilibrium phase diagram. Adding chromium to iron reduces the range of temperatures in which the FCC phase is stable until around 13% Cr, when this phase is not stable anymore. Calculated diagram. Source: Refs 8, 9

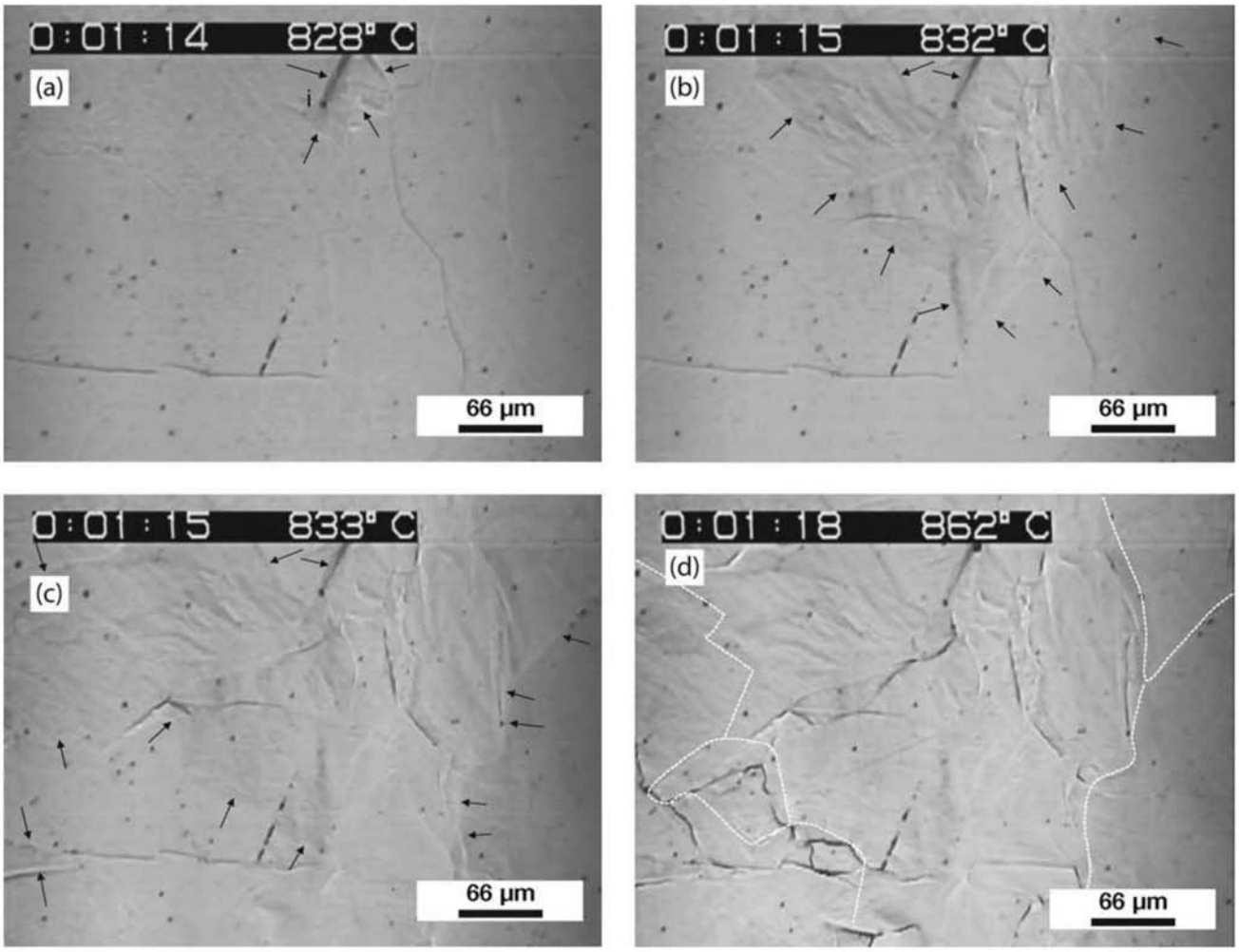

Fig. 7.8 IF steel heated at 10 K/s from a ferritic microstructure. Frames of a video made with a confocal laser microscope. On the upper corner of the picture are indicated time (hours:minutes:seconds) and temperature in degrees Celsius. In (a), the grain boundaries of an austenitic grain just nucleated inside the ferrite are indicated. The letter *i* indicates a nonmetallic inclusion that prevents movement of that region of the grain boundary (see b and c). In (c) another nucleus starts forming in the lower left region of the image. In (d) transformation is complete and the approximate positions of the austenitic grain boundaries are indicated with white lines superimposed on the picture. Courtesy of S. Sridhar and E. Schmidt, Carnegie Melon University, Pittsburgh, PA. Source: Ref 12

its redistribution between austenite and ferrite does not significantly slow the transformation. There are also situations in which it is possible that this transformation happens without solute redistribution, in a mechanism called massive transformation. Alternatives to high-temperature microscopy are techniques that reveal indirect information about the austenite grain size in a room-temperature sample. In most cases, the interest is in knowing the austenitic grain size before the steel transformed to ferrite. These techniques are discussed in more detail in Chapter 9, "Conventional Heat Treatments: Usual Constituents and Their Formation," in this book. Figure 7.9 presents the austenitic grain boundaries that existed in a steel before it was cooled and transformed.

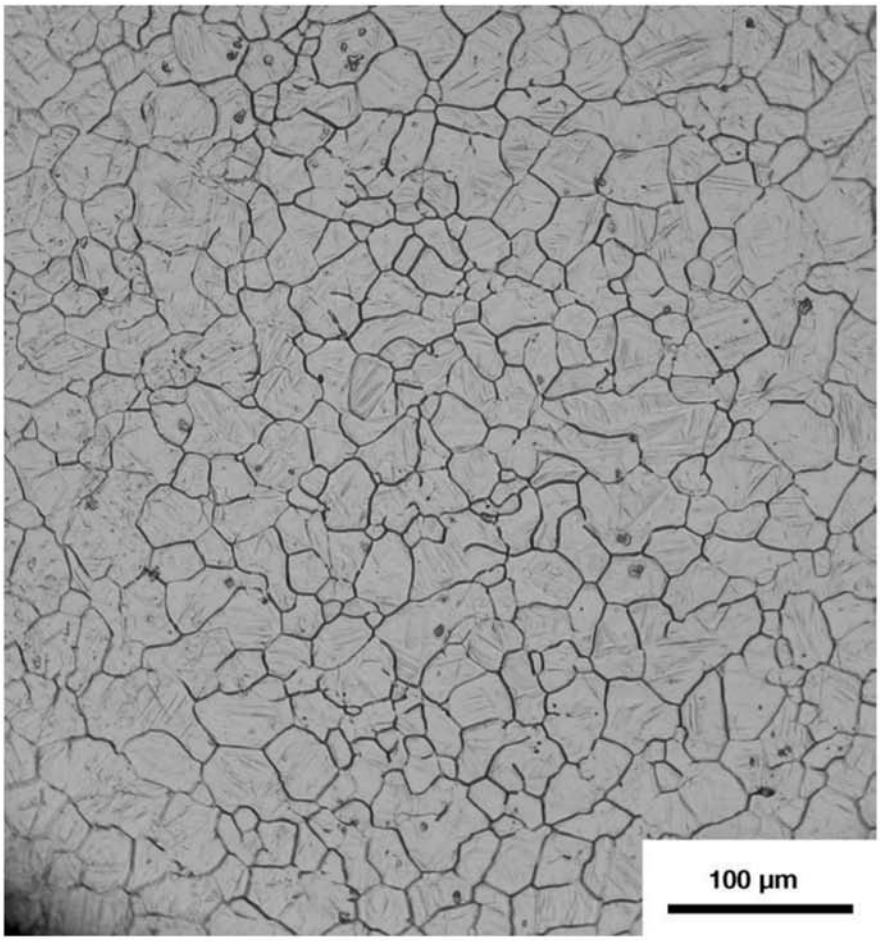

Fig. 7.9 Austenitic grain boundaries in a steel containing C = 0.08%, Mn = 0.7%. The grain boundaries were revealed by thermal oxidation etching (see Chapter 9, "Conventional Heat Treatments: Usual Constitutents and Their Formation," in this book). Courtesy of C. Garcia-Mateo, Centro Nacional de Investigaciones Metalúrgicas—CENIM-CSIC, grupo Materialia, Madrid, Spain.

Austenite (FCC) Stabilizing Alloying Elements

Some elements, when dissolved in iron, have a tendency to stabilize the FCC structure over the BCC structure (e.g., manganese; Fig. 7.10). This effect is more common with alloying elements that have the FCC structure when they are pure. Like the case of BCC stabilizing elements, this is not a general rule. The main FCC stabilizing elements are nickel, manganese, carbon, cobalt, copper, and nitrogen.

7.4 Cementite

When carbon solubility in ferrite is exceeded, cementite becomes a part of the steel structure at room temperature. Low-carbon steels for cold forming usually present cementite distributed over the product as a dispersed second phase, as shown in Fig. 7.11. In these steels, it is important that the heat cycles facilitate the precipitation of cementite as much as possible, to scavenge

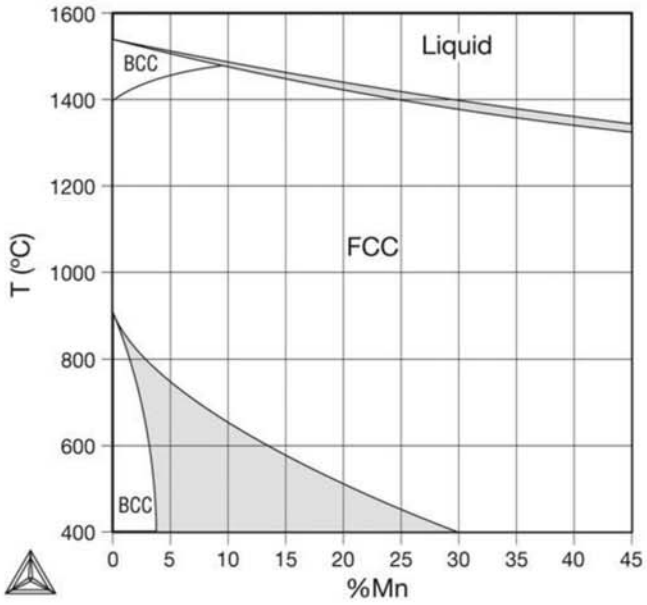

Fig. 7.10 Fe-Mn equilibrium phase diagram. Adding manganese to iron increases the range of temperatures in which the FCC phase is stable. Calculated diagram. Source: Refs 8, 9

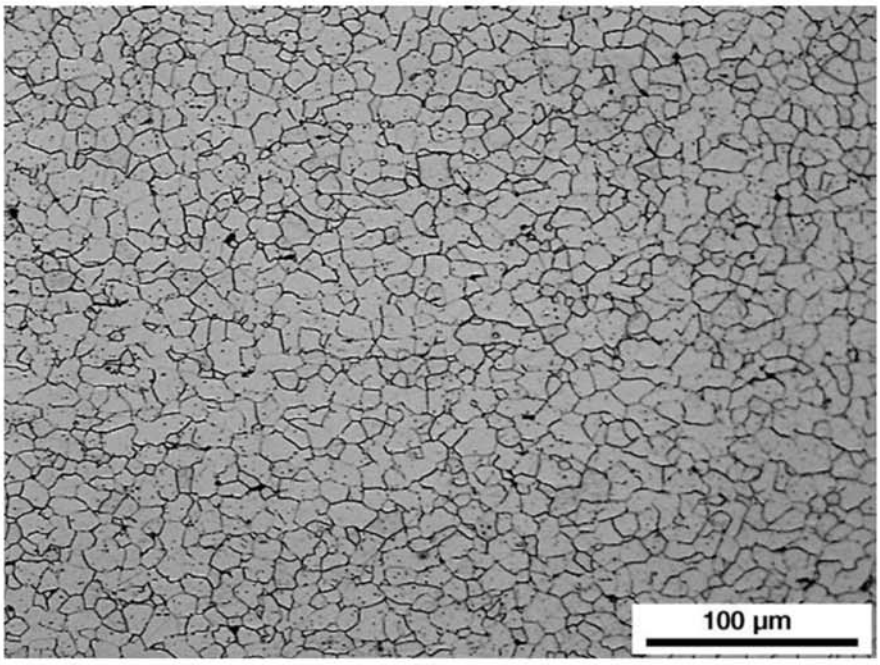

Fig. 7.11 Highly formable hot-rolled steel (C = 0.042%, Mn = 0.2%) used for demanding forming, such as hermetic compressor shells. Microstructure composed of polygonal ferrite and fine globular grains of cementite. Etchant: nital 2%.

as much carbon as is attainable from the ferrite matrix to enhance formability (Ref 11).

During heat treatment, cementite particles nucleate in structural heterogeneities and grow by the diffusion of carbon to these nuclei. Because the carbon concentration in cementite is high, a significant movement of carbon in the steel is needed to make sure cementite will form and grow.

Carbide-Forming Elements

Many elements have a high affinity for carbon and may form stable carbides in the steel or dissolve in cementite. Chromium, tungsten, vanadium, titanium, niobium, and molybdenum are some important carbide formers. Although silicon does form a stable carbide (SiC), this carbide does not occur in steels; furthermore, silicon has almost no solubility in cementite and can hinder its formation if partitioning is required.

7.5 Pearlite

The Fe-C phase diagram presents an eutectoid equilibrium, which is discussed in Chapter 8, "Solidification, Segregation, and Nonmetallic Inclusions," in this book. (In Greek, "eutectoid" means "eutectic-like".) This eutectoid equilibrium is a three-phase equilibrium between ferrite, cementite, and austenite; at atmospheric pressure, it occurs at 723 °C (1335 °F). When steels containing higher carbon contents transform from the austenite field to the field below the eutectoid temperature, ferrite and cementite are the expected phases. Examining the phase diagram, it is clear that as discussed earlier because these two phases have significantly different carbon contents, carbon atoms will be required to move a considerable amount. For this reason, and in the same way that will be seen when eutectic transformations are discussed in Chapter 8, nature finds mechanisms that makes the transformation more efficient, minimizing the distances carbon will have to diffuse. In this case, this happens through cooperative growth of ferrite and cementite. Because some combinations of crystallographic orientations of ferrite and cementite result in interfaces with relatively low energies (Ref 13), cooperative growth happens with the formation of parallel plates of the two phases, as indicated in Fig. 7.12(a). It is believed that as cementite nucleates, it impoverishes the surrounding austenite in carbon, making it easier for ferrite to nucleate. From this point on, the nuclei advances as indicated in Fig. 7.12(b) while the nucleation of other plates (called *lamellae*) with the same orientation continue, giving rise to what is called a pearlite colony: a set of lamellae of cementite and ferrite with the same crystallographic orientation.

Steel compositions corresponding to the composition of austenite in the eutectoid point (C = 0.77% in the Fe-C system) will transform completely from austenite to pearlite when the cooling conditions are adequate for carbon to redistribute (slow cooling). Figure 7.13 is a schematic presentation of the transformation of austenite with a eutectoid composition into pearlite, when the transformation happens in conditions close to equilibrium.

Figures 7.14 to 7.19 present examples of pearlitic microstructure. As the metallography plane sections the different pearlite colonies at different angles to the lamellae, the lamellae spacing varies within the micrograph, as shown in Fig. 7.14. Lamellae spacing depends on both the cooling rate and the

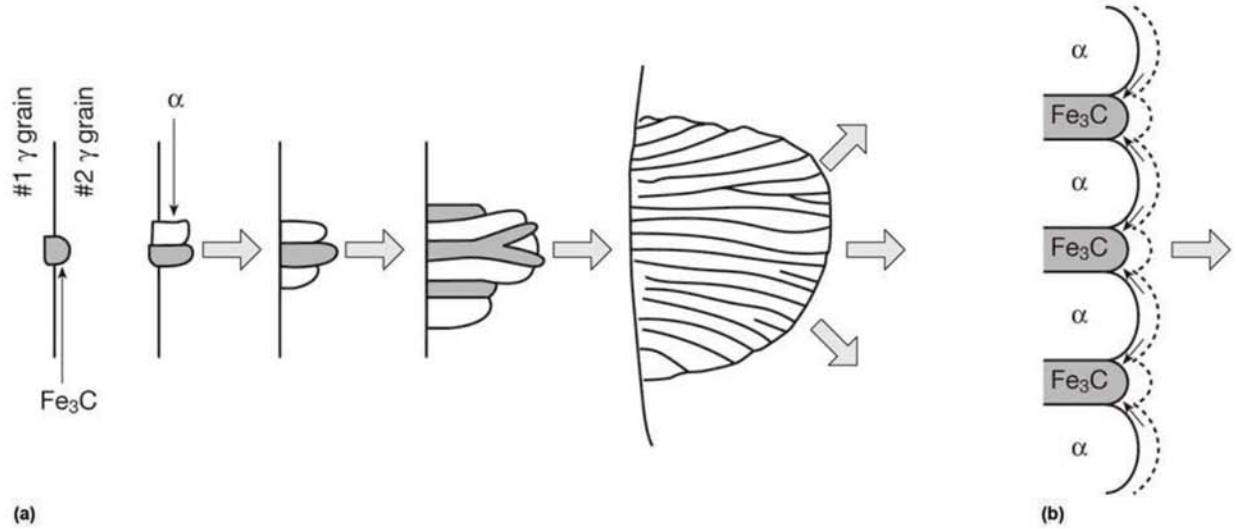

Fig. 7.12 Simplified scheme of the nucleation and growth mechanism of pearlite. Transverse section to the ferrite and cementite plates (lamellae). (a) Carbide nucleates in an austenitic grain boundary. The surrounding region becomes carbon depleted, favoring the nucleation of ferrite. Nucleation occurs, forming a low-energy ferrite–cementite interface. The nucleation process is repeated. (b) Ahead of the lamellae, carbon diffuses a short distance in austenite, leaving the regions in front of ferrite toward the regions where the carbides will grow, as indicated by the small arrows. Broad arrows indicate the direction of growth of the pearlite colony.

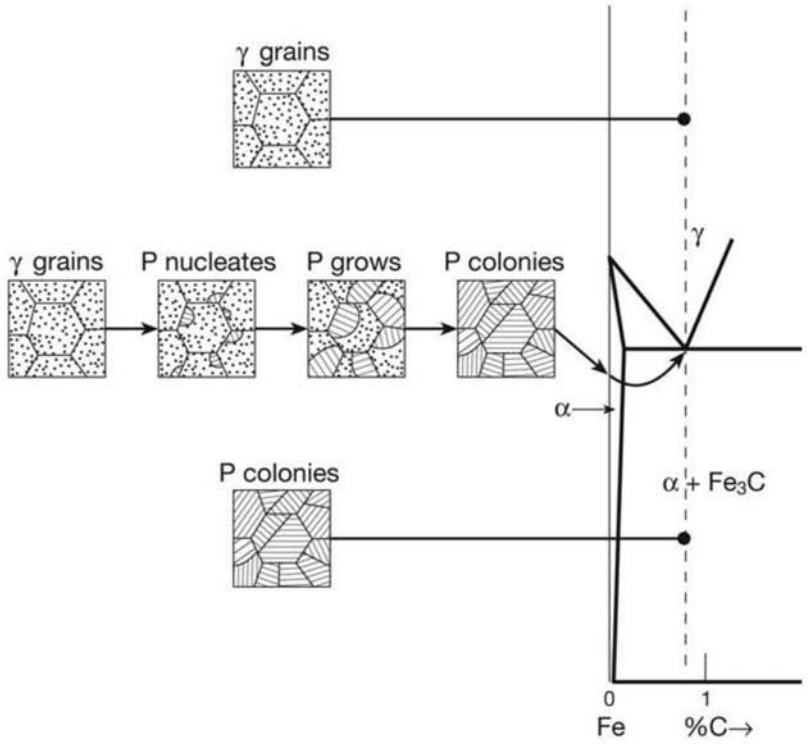

Fig. 7.13 Schematic presentation of the transformation of austenite in pearlite in conditions close to equilibrium. Steel has a eutectoid composition. P = pearlite. Source: Ref 10

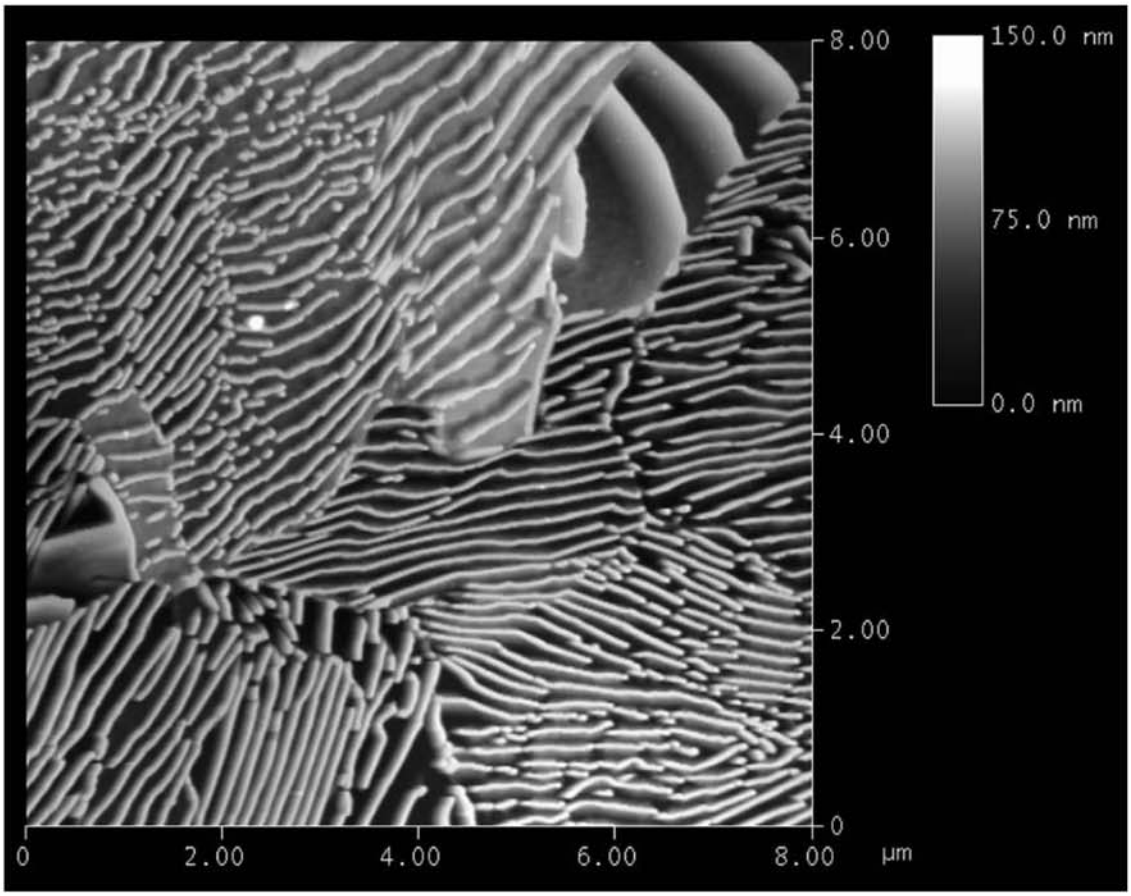

Fig. 7.14 Pearlite in a eutectoid steel. The etching relief is such that cementite is higher than ferrite. As the different pearlite colonies are intercepted at different angles by the metallography plane, the lamellar spacing observed in the image varies considerably. For instance, in the top right corner, a colony in which the lamellae are almost parallel to the metallography plane can be observed. Atomic force microscopy. The scale on the top right refers to the vertical dimensions in the sample. Etchant: nital 2%. Courtesy of M. S. Andrade, CETEC-MG, Brazil.

temperature at which pearlite formation starts. Slow cooling (and hence transformation starting at higher temperatures) results in larger interlamellar spacing, whereas faster cooling (lower transformation temperature) results in "finer" pearlite (Fig. 7.15–7.19).

From the standpoint of properties, pearlite is one of the most interesting natural composite materials. It brings together a ductile matrix (ferrite) and an aligned reinforcing phase with high hardness (cementite). Although it is not a high toughness structure (due to the presence of brittle cementite), it has high hardness, wear resistance, and fatigue resistance and reasonable fracture toughness. Railcar wheels, rails (see Chapter 15, "Engineered Special Bar Quality Steel," in this book) and high-strength wires (see Fig. 12.13 in Chapter 12, "Mechanical Work of Steel: Cold Working," in this book) are examples of applications in which the pearlitic structure is still one of the best solutions.

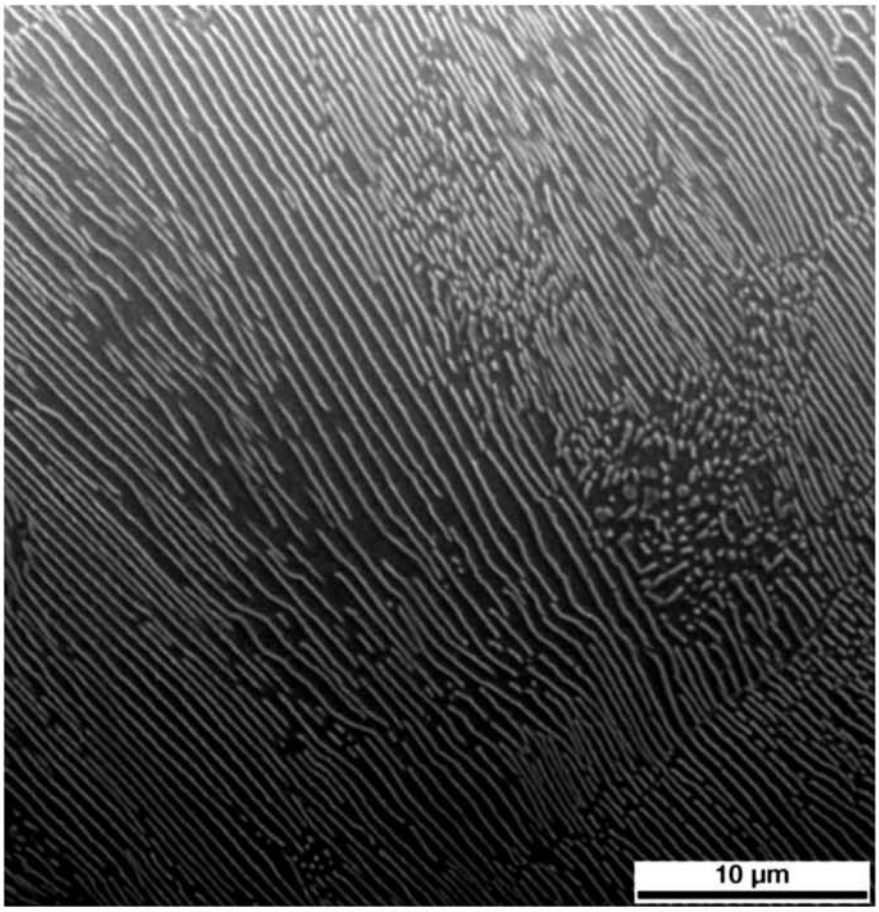

Fig. 7.15 Detail of pearlite structure in an engineering steel. Pearlitic portion of the microstructure of a steel containing C = 0.5%, Mn = 1.5% isothermally treated at 688 °C (1270 °F). SEM, SE. Etchant: nital 2%. Courtesy of C. Capdevila Montes, Centro Nacional de Investigaciones Metalúrgicas—CENIM-CSIC, grupo Materialia, Madrid, Spain.

The constituent received this name due to the aspect of etched samples of eutectoid pearlitic steels. These samples, normally etched with nital, have the characteristic shine of mother of pearl or nacre, the carbonate common in shells (which is also lamellar).

7.5.1 Volumetric Fraction of Phases and the "Lever Rule"

When the composition of phases in equilibrium is known (from the phase diagram) it is possible to estimate the fraction of each phase that should be present in equilibrium. The basis for this estimation is mass conservation. In the case of the Fe-C system, because all the carbon must be in one of the phases present, it is possible to calculate the amount of each phase that must exist in the steel to reach the correct composition. If one considers a steel with the eutectoid composition C_e (0.77%), as indicated in Fig. 7.20, at room temperature two phases will be present: ferrite and cementite. Ferrite has a

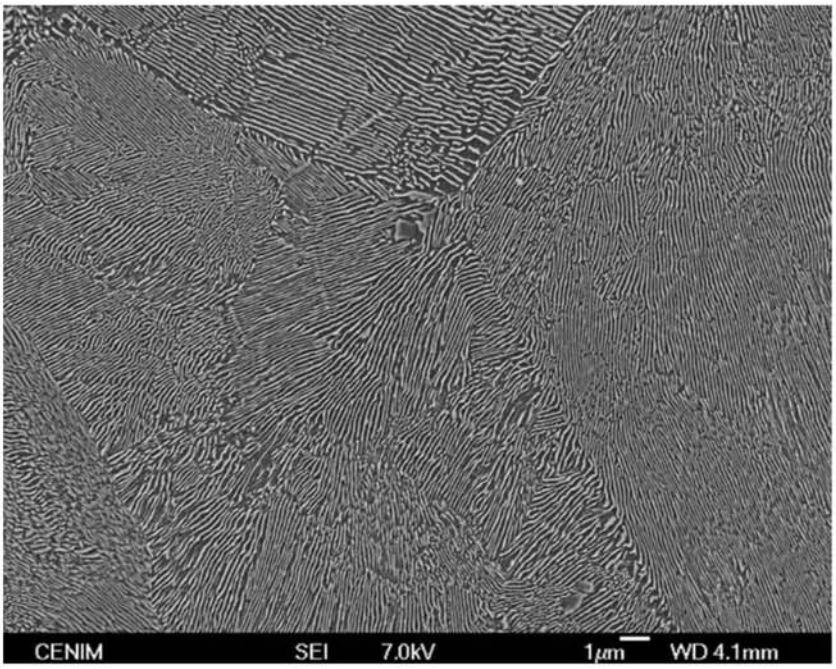

Fig. 7.16 Pearlite colonies in a steel containing C = 0.78% cooled from the austenitic field at 0.1 K/s. SEM, SE. Etchant: nital 2%. Courtesy of C. Garcia-Mateo, Centro Nacional de Investigaciones Metalúrgicas—CENIM-CSIC, grupo Materialia, Madrid, Spain.

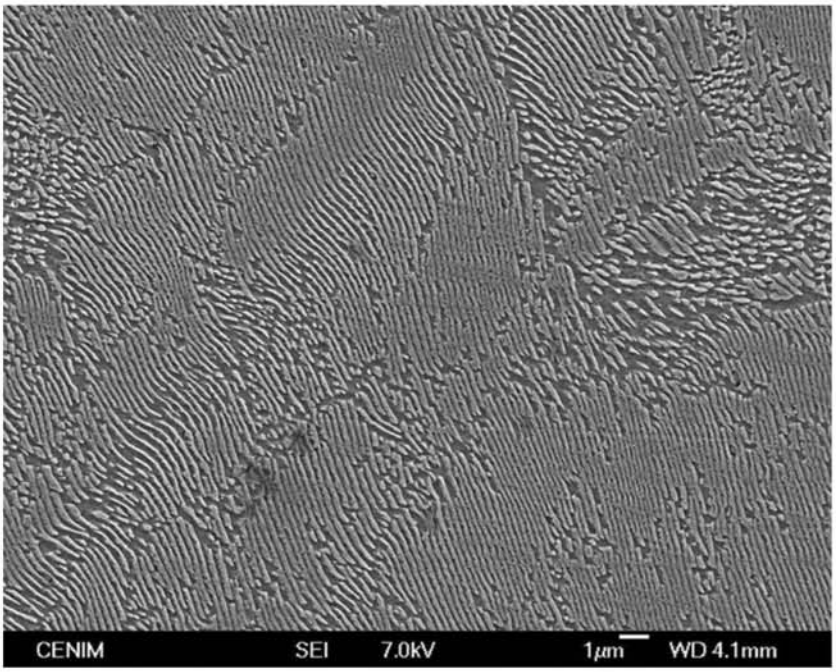

Fig. 7.17 Pearlite colonies in a steel containing C = 0.78% (same steel as in Fig. 7.16) cooled from the austenitic field at 0.005 K/s. SEM, SE. Etchant: nital 2%. Courtesy of C. Garcia-Mateo, Centro Nacional de Investigaciones Metalúrgicas—CENIM-CSIC, grupo Materialia, Madrid, Spain.

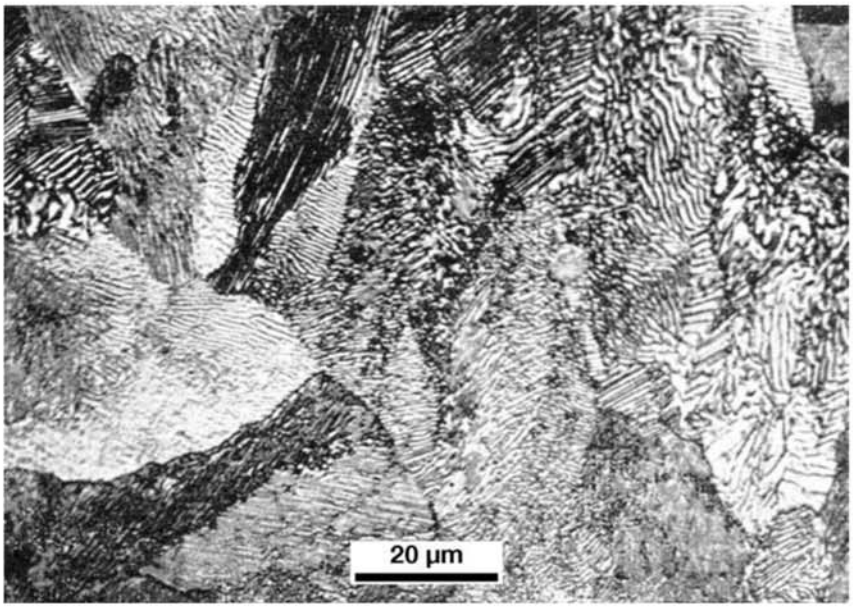

Fig. 7.18 Pearlite colonies in eutectoid steel. Areas where the colonies do not appear to be well defined have their lamellar more clearly observed if the sample is rotated 90° under the microscope. Etchant: nital.

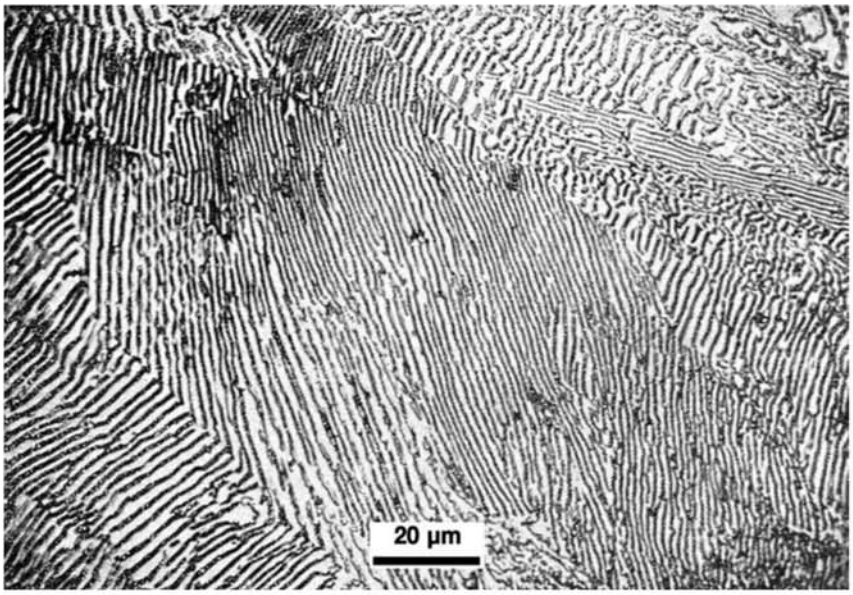

Fig. 7.19 Eutectoid steel cooled very slowly from the austenitic field. Etchant: nital.

composition of C_α and the carbon content of cementite is given by C_{Fe_3C}. The mass conservation of carbon in a given mass of steel is expressed as:

$$\frac{\%C_{steel} \cdot \text{mass of steel}}{100} = \frac{\%C_\alpha \cdot \text{mass of ferrite}}{100} + \frac{\%C_{Fe_3C} \cdot \text{mass of } Fe_3C}{100} \qquad \text{(Eq 1)}$$

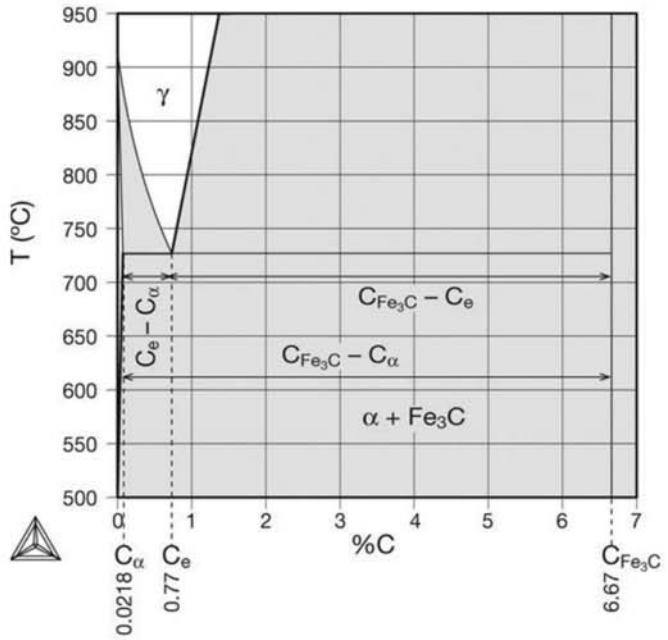

Fig. 7.20 Metastable Fe-C phase equilibrium diagram (graphite is not present). The ferrite field at lower temperatures was exaggerated (out of scale) to be visualized.

The mass fraction of each phase can be expressed as:

$$f_\alpha = \frac{\text{mass of ferrite}}{\text{mass of steel}}$$

and

$$f_{Fe_3C} = \frac{\text{mass of } Fe_3C}{\text{mass of steel}}$$

Dividing Eq 1 by the mass of steel, substituting the mass fractions, and multiplying by 100, Eq 2 is derived:

$$\%C_{steel} = \%C_\alpha \cdot f_\alpha + \%C_{Fe_3C} \cdot f_{Fe_3C} \qquad \text{(Eq 2)}$$

Noticing that $f_\alpha + f_{Fe3C} = 1$, one can derive equations for the mass fractions of both phases from Eq 2.

$$f_\alpha = \frac{\%C_{Fe_3C} - \%C_{steel}}{\%C_{Fe_3C} - \%C_\alpha}$$

$$f_{Fe_3C} = \frac{\%C_{steel} - \%C_\alpha}{\%C_{Fe_3C} - \%C_\alpha} \qquad \text{(Eq 3a)}$$

When these fractions are calculated for the compositions in a steel with the eutectoid composition C_e, as indicated in Fig. 7.20,

$$f_{\alpha} = \frac{\%C_{Fe_3C} - \%C_{steel}}{\%C_{Fe_3C} - \%C_{\alpha}} = \frac{6.67 - 0.77}{6.67 - 0.0218} = 0.89$$

$$f_{Fe_3C} = \frac{\%C_{steel} - \%C_{\alpha}}{\%C_{Fe_3C} - \%C_{\alpha}} = \frac{6.77 - 0.0218}{6.67 - 0.0218} = 0.11 \quad \text{(Eq 3b)}$$

Because the density of cementite is 7.66–7.68 g/cm^3 (Ref 14) and that of ferrite is 7.87 g/cm^3, the volumetric fractions are approximately equal to the calculated mass fractions (the exact volumetric fraction of cementite in pearlite is 0.12, or 12%).

The "Lever Rule"

When one observes the relationships expressed by Eq 3(a) and 3(b), it can be seen that in the fractions, the numerators and denominators are segments that can be directly computed from the phase diagram, as indicated in Fig. 7.20. Thus, it is common to calculate the mass fractions of phases using the "Lever Rule" as indicated in Fig. 7.20. In the case of the Fe-C system, it is also common to directly interpret the mass fractions thus obtained as volume fractions. This rule can be applied to any steel composition and any two phase fields in a true phase diagram. There are many tutorials about the application of the lever rule in Ref 15.

However, this rule can only be applied in true phase diagrams. A simple rule to make sure a diagram is a true phase diagram is to check if the tie-lines are in the plane of the diagram. That is, the steel composition and the composition of the phases in equilibrium are in the same plane. Although this is true for isothermal sections of ternary diagrams, for instance, it is not true in most other plane sections of ternary or higher order phase diagrams, so-called isopleths. Care should be exercised when attempting to apply the lever rule in complex diagrams.

In general the lever rule can be used to determine the fraction of phases or constituents (such as pearlite) present in equilibrium in a microstructure. There is no restriction to use the rule for constituents and it applies the same way. However, the rule is based on mass conservation. In metallography, what is normally quantified is volume fraction, not mass fraction. The two fractions are approximately equal only when the phases in question have similar densities.

Figure 7.21 presents the fraction of equilibrium phases and constituents calculated in accordance with the lever rule in the Fe-C system. The lever rule can be applied to any solute, subject to the limitation that the calculated fraction is always the mass fraction and not the volume fraction.

7.6 Intermediate Structures—Hypo-Eutectoid and Hyper-Eutectoid

Carbon steels (or low alloy steels) containing less than 0.77% C are called hypo-eutectoid steels. (In Greek, "hypo" means "under" and "hyper" means "over.") Carbon steels with more than 0.77% C are called hyper-eutectoid steels.

When austenite is cooled into a two-phase field, when the solute redistribution is essentially complete, a phase is formed before pearlite. This phase is called pro-eutectoid. In hypo-eutectoid steels, the pro-eutectoid phase is ferrite; in hyper-eutectoid steels, it is cementite.

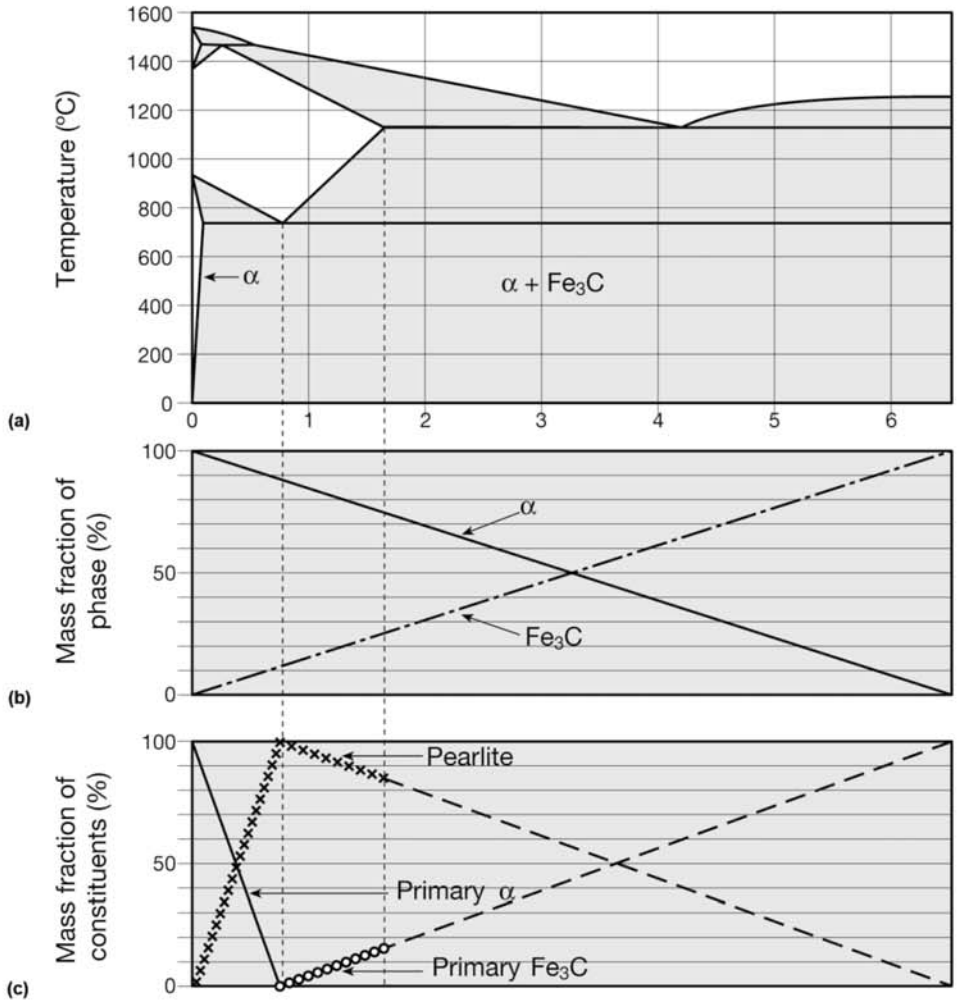

Fig. 7.21 (a) Metastable Fe-Fe3C equilibrium diagram for the system Fe-C. (b) Mass fraction of the phases present in equilibrium in Fe-C alloys. (c) Mass fraction of the constituents present in equilibrium in Fe-C alloys. The fraction of cementite that precipitates in ferrite due to the decrease of carbon solubility below the eutectoid temperature was neglected, as it is quite small. Adapted from: Ref 10

7.6.1 Hypo-Eutectoid Steels

When slowly cooled close to the equilibrium conditions dictated by the metastable Fe-C phase diagram, hypo-eutectoid steel microstructure can have a range of pearlite volume fraction between 0% and 100% (very low-carbon steel frequently has cementite in such a low fraction that dispersed cementite may be formed instead of pearlite).

As discussed earlier, the volume fraction of pearlite and ferrite can be estimated from the steel carbon content. Conversely, the carbon content can be estimated based on the volume fraction observation in metallographic examination. This estimation will only be valid, however, if the steel has been processed close to equilibrium (examples of out-of-equilibrium structures in

hypo-eutectoid steel can be seen in Chapter 14, "Structural Steels and Steels for Pressure Vessels, Piping, and Boilers," esp. Fig. 14.17, in this book). Figure 7.22 presents the schematic structure evolution of hypo-eutectoid steels transformed from the austenite field in conditions close to equilibrium. Figures 7.23 to 7.30 present typical microstructures of hypo-eutectoid steels slow cooled or at most normalized (cooled in still air; see Chapter 10, "Convention Heat Treatment: Basic Concepts" in this book).

7.6.2 Hyper-Eutectoid Steels

When hyper-eutectoid steels are slowly cooled, a network of pro-eutectoid cementite can be formed on the previous austenitic grain boundaries. For this reason, austenitization of these steels is frequently performed at a temperature at which the dissolution of carbides is not complete, avoiding the formation of this brittle network of cementite. Figure 7.31 presents a schematic sequence of the formation of these structures in hyper-eutectoid steels.

Figures 7.32 and 7.33 present examples of the microstructure of hyper-eutectoid steels. With nital etching it may be difficult to distinguish pro-eutectoid cementite in these steels from pro-eutectoid ferrite in hypo-eutectoid steels. There are specific etchants that highlight cementite in the micrograph, as shown in Fig. 7.33.

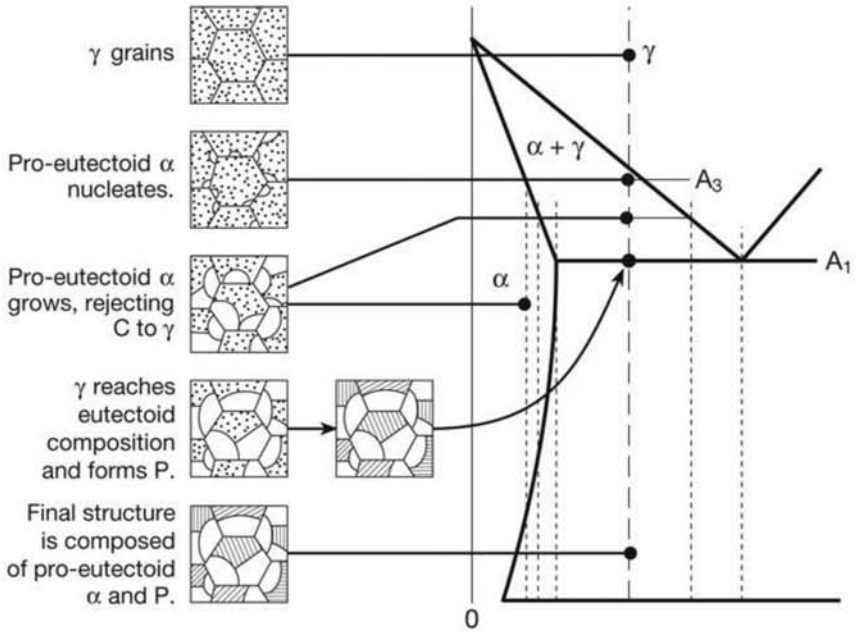

Fig. 7.22 Schematic presentation of the transformation of austenite in pro-eutectoid ferrite and pearlite (P) in conditions close to equilibrium. Steel has hypo-eutectoid composition. Adapted from: Ref 10

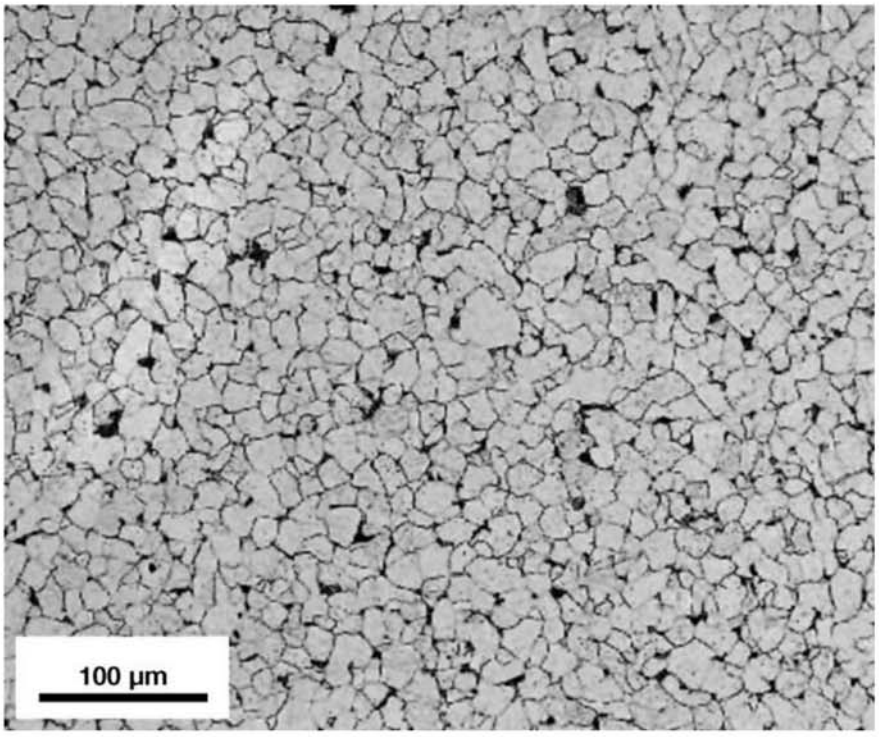

Fig. 7.23 Cross section of AISI 1005 wire rod, normalized. Ferrite and pearlite (approx. volume fraction 5%). Ferritic grain size ASTM 9 (according to ASTM E112 (Ref 16), Chapter 3). Etchant: nital 2%. Courtesy of ArcelorMittal Aços Longos, Juiz de Fora, MG, Brazil.

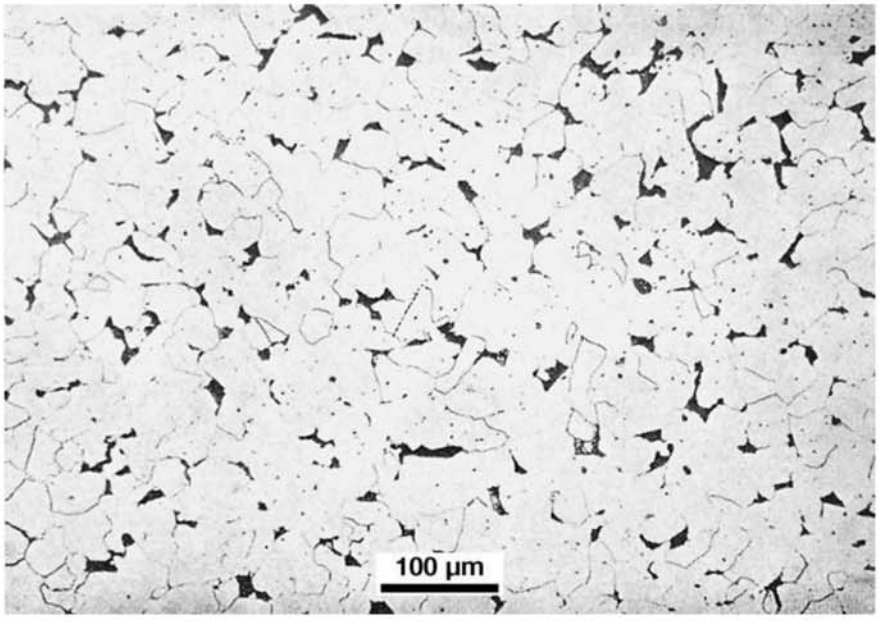

Fig. 7.24 Steel containing approximately 0.1% C, slowly cooled from the austenitic field. Pearlite (dark regions) and ferrite with numerous nonmetallic inclusions. Etchant: picral.

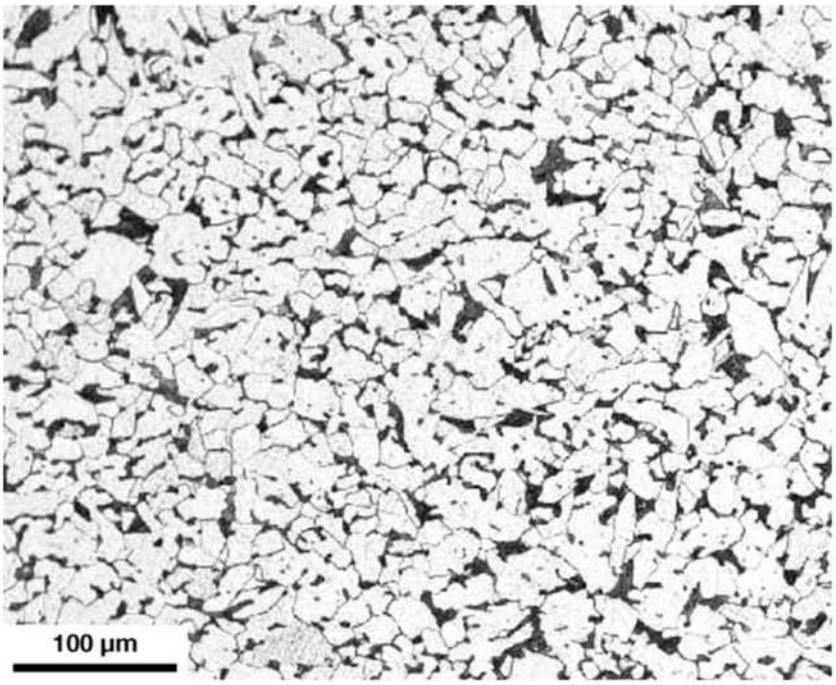

Fig. 7.25 Cross section of AISI 1010 wire rod, normalized. Ferrite and pearlite (approx. volume fraction 10%). Ferritic grain size ASTM 8-9 (according to ASTM E112 (Ref 16)). Etchant: nital 2%. Courtesy of ArcelorMittal Aços Longos, Juiz de Fora, MG, Brazil.

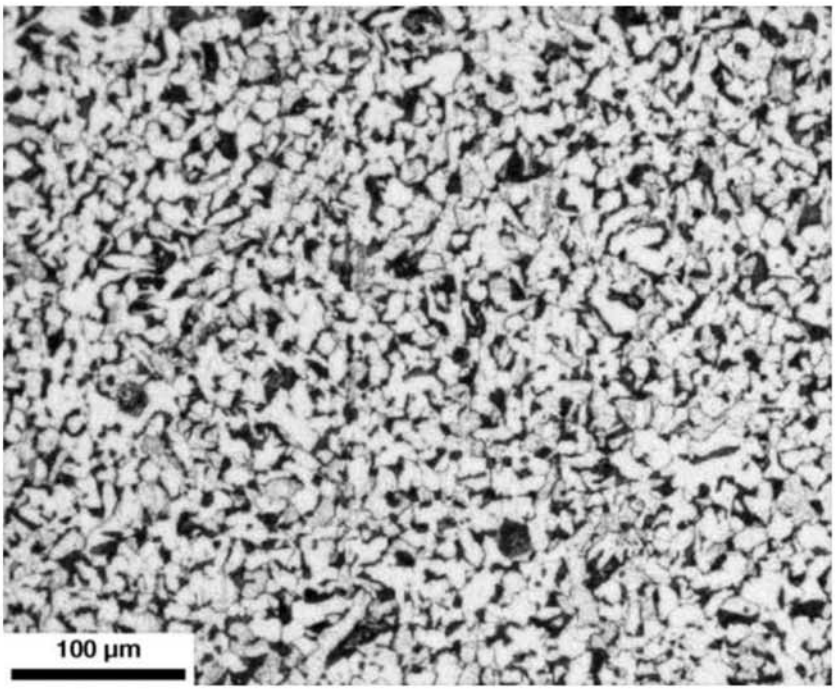

Fig. 7.26 Cross section of AISI 1015 wire rod, normalized. Ferrite and pearlite (approx. volume fraction 15%). Ferritic grain size ASTM 9 (according to ASTM E112, Ref 16). Etchant: nital 2%. Courtesy of ArcelorMittal Aços Longos, Juiz de Fora, MG, Brazil.

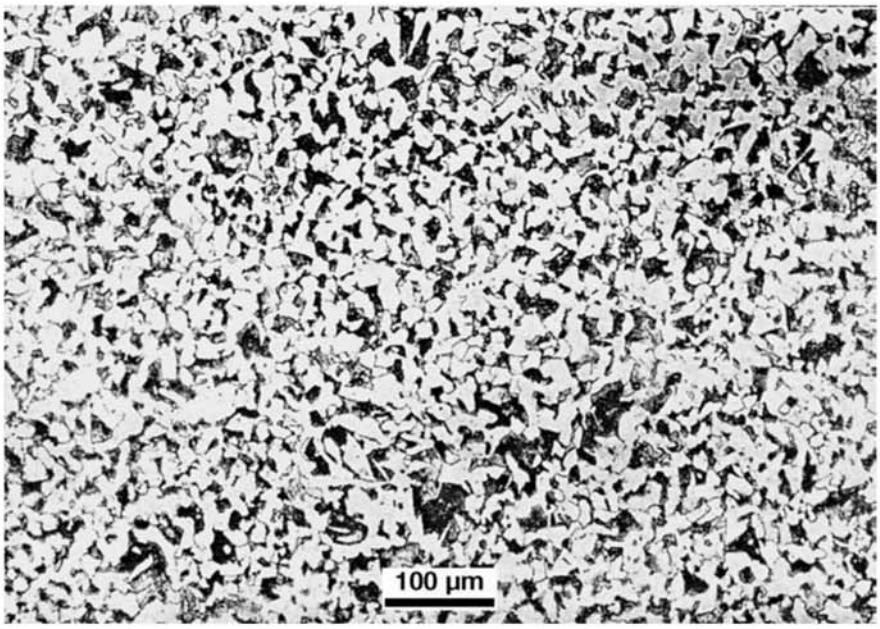

Fig. 7.27 Steel containing approximately 0.3% C, slowly cooled from the austenitic field. Ferrite and pearlite. Etchant: nital.

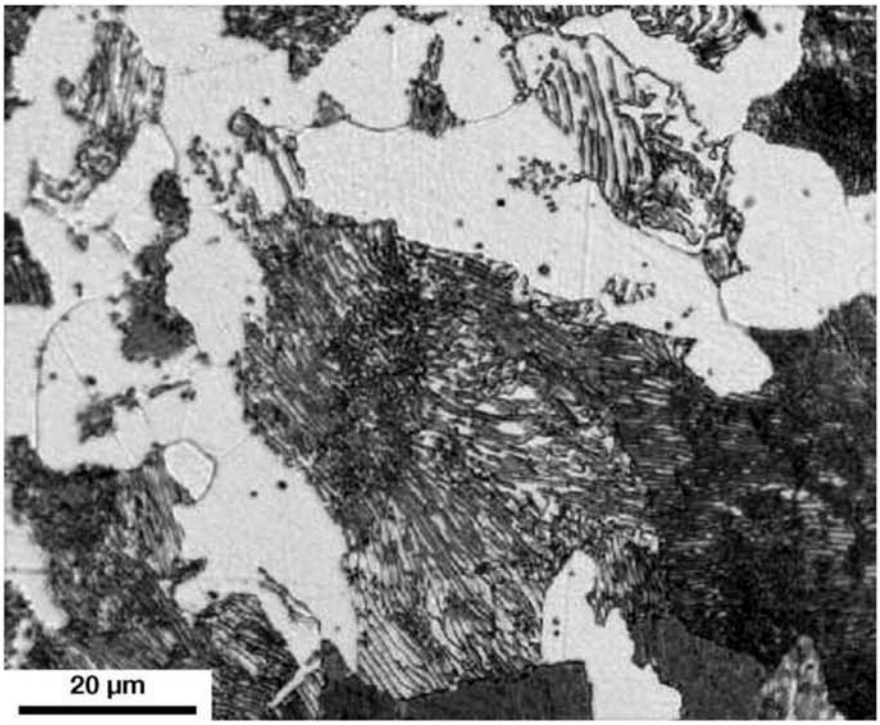

Fig. 7.28 Cross section of AISI 1045 wire rod, fully annealed. Ferrite and pearlite. Etchant: nital 2%. Courtesy of ArcelorMittal Aços Longos, Juiz de Fora, MG, Brazil.

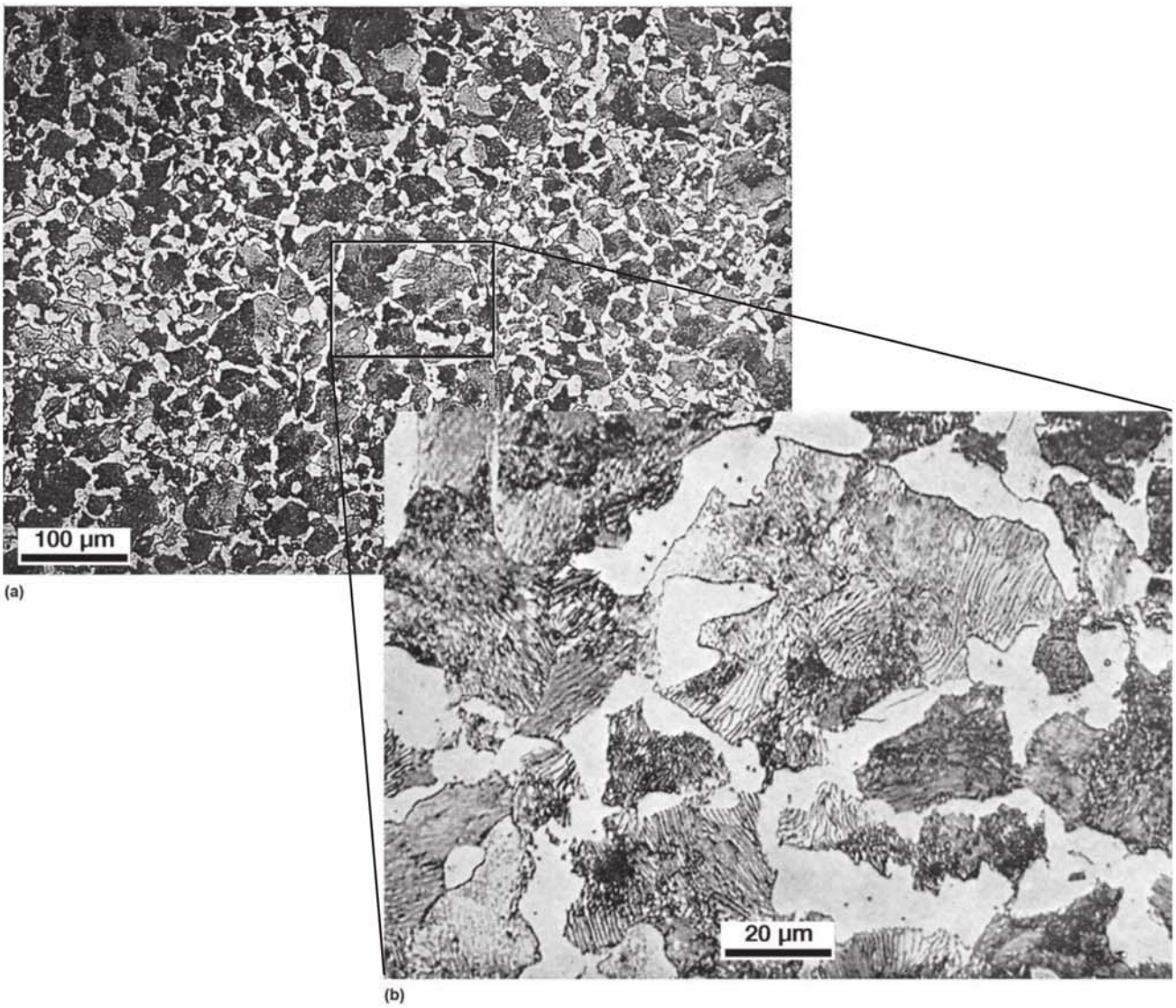

Fig. 7.29 (a) Steel containing approximately 0.5% C, slowly cooled from the austenitic field. Pearlite and pro-eutectoid ferrite grains in a network. (b) Higher magnification of the region. Etchant: nital.

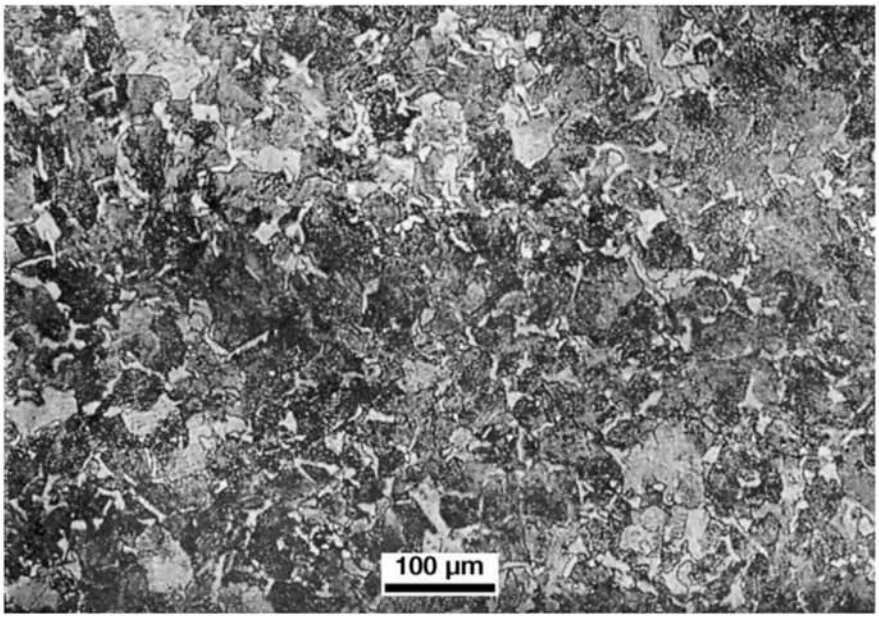

Fig. 7.30 Steel containing approximately 0.7% C, slowly cooled from the austenitic field. Pearlite and few areas of ferrite. Etchant: nital.

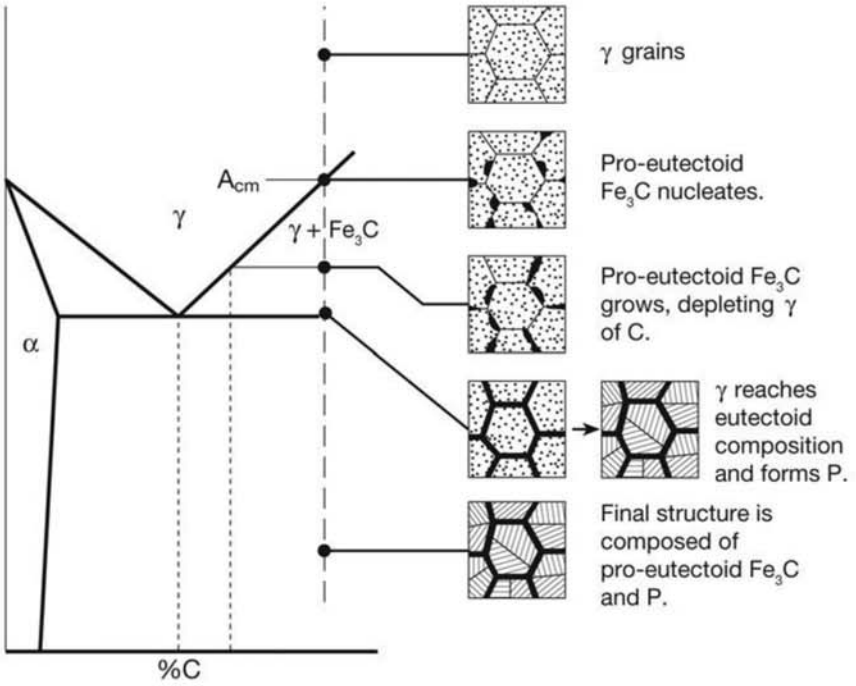

Fig. 7.31 Schematic presentation of the transformation of austenite in pro-eutectoid cementite and pearlite (P) in conditions close to equilibrium. Steel has hyper-eutectoid composition. Adapted from: Ref 10

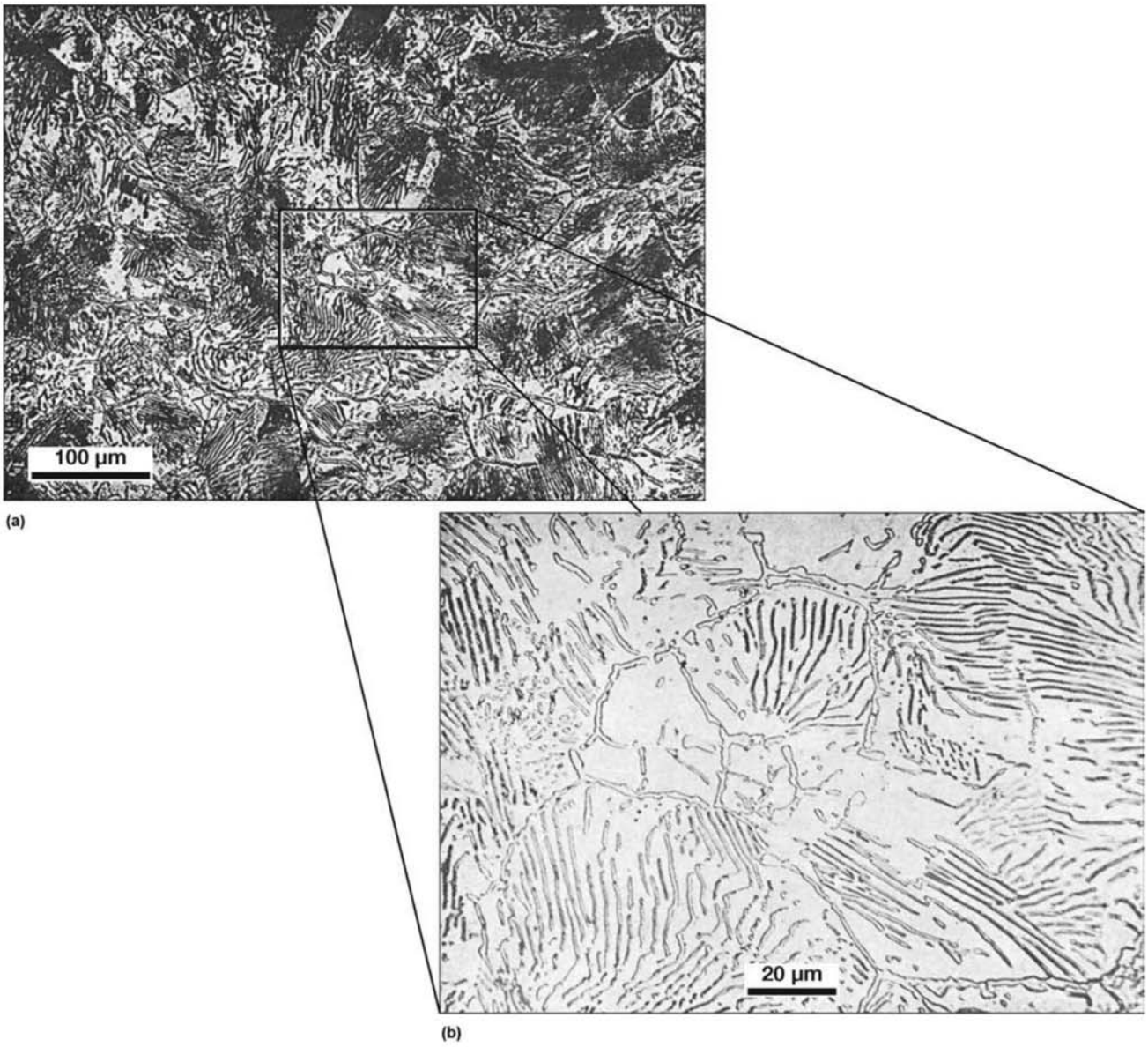

Fig. 7.32 (a) Cementite network in hyper-eutectoid steel. Etchant: nital. (b) Higher magnification of area.

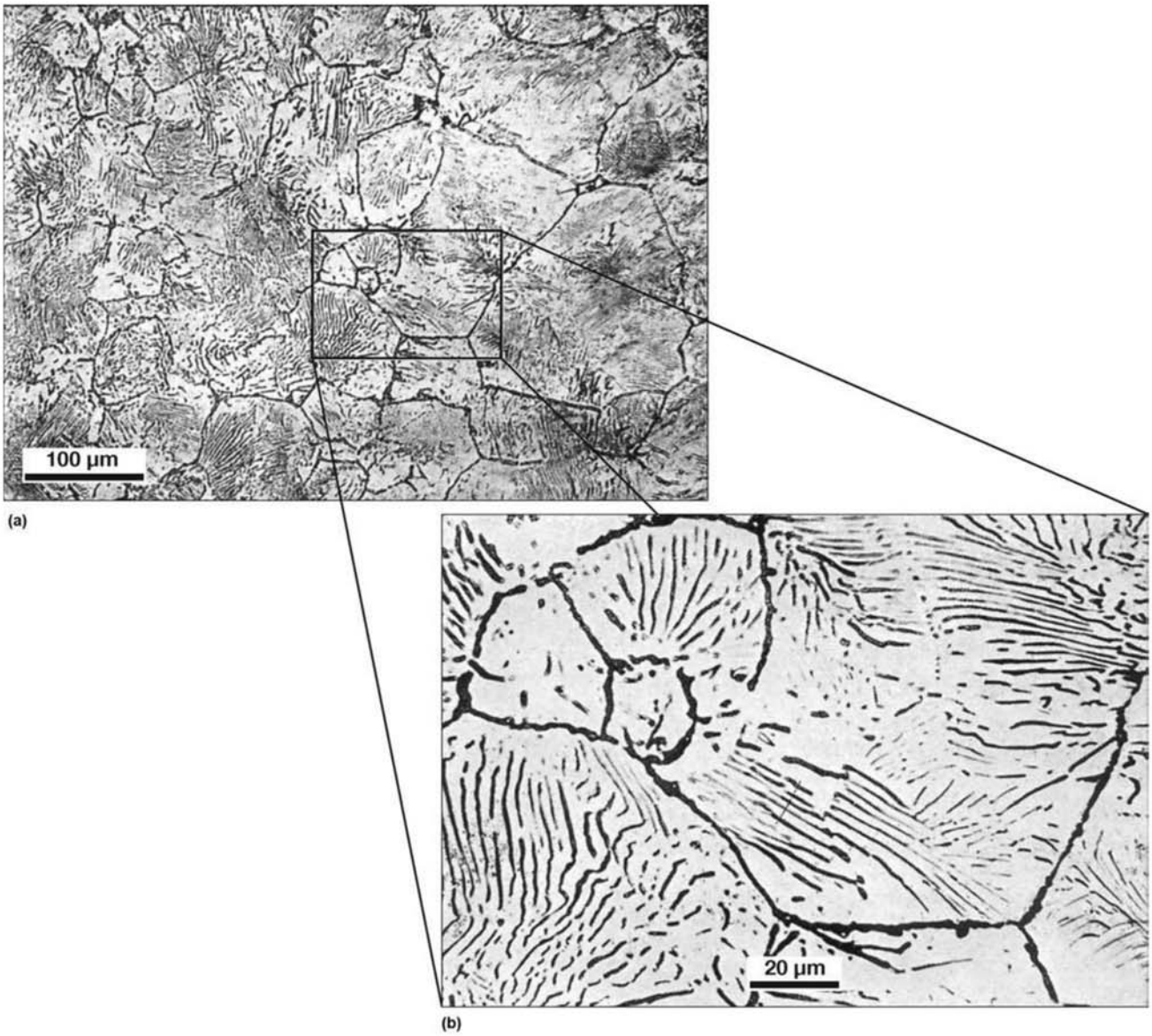

Fig. 7.33 (a) Hyper-eutectoid steel, same region as in Fig. 7.32(a). Pro-eutectoid cementite (forming a network) and the coarser cementite lamellae in pearlite show dark with this etching. Etchant: sodium picrate. (b) Higher magnification of area.

REFERENCES

1. D.A. Porterand K.E. Easterling, *Phase Transformations in Metals and Alloys*, 2nd ed., Chapman & Hall, 1992
2. P.R. Rios and A.F. Padilha, *Transformações de Fase*, Artliber, 2007
3. G.A. Chadwick, *Metallography of Phase Transformations*, Crane, Russak, 1972
4. J.W. Christian, *The Theory of Phase Transformations in Metals and Alloys*, 3rd ed., Pergamon Press, 2002
5. A. Costa E Silva, J. Agren, M.T. Clavaguera-Mora, D. Durojvic, T. Gomez-Acebo, B.-J. Lee, Z.-K. Liu, P. Miodownik, and H.J. Seifert, Applications of Computational Thermodynamics the Extension from Phase Equilibrium to Phase Transformations and Other Properties, CALPHAD, Vol 31, 2007, p 53–74
6. N. Sauders and P. Miodownik, *CALPHAD*: *A Comprehensive Guide*, Pergamon Press, 1998
7. H. Bhadeshia and R. Honeycombe, *Steels: Microstructure and Properties*, 3rd ed., Elsevier, 2006
8. B. Sundman, B. Jansson, and J.O. Andersson, The Thermo-Calc Databank System, CALPHAD, Vol 9, 1985, p 153–90
9. TCAB, TCFE7 Iron Based Alloy Thermodynamics Database, v7, Stockholm, 2012
10. M.F. Ashby and D.R.H. Jones, *Engineering Materials*, 2nd ed., Pergamon Press, 1986
11. I. Kosazu, Processing: Thermomechanical Controlled Processing, *Materials Science and Technology: Constitution and Properties of Steels*, F.B. Pickering, ed., Wiley-VCH, 1996
12. E. Schmidt, D. Soltesz, S. Roberts, A. Bednar, and S. Sridar, The Austenite/Ferrite Front Migration Rate during Heating of IF Steel, *ISIJ International*, Vol 46 (No. 10), 2006, p 1500–1509
13. R.J. Dippenaar and R. Honeycombe, The Crystallography and Nucleation of Pearlite, *Proc. R. Soc. Lond. A*, Vol 333, 1973, p 455–67
14. T. Ishigaki, Determination of the Density of Cementite, *Sci. Repts. Tôhoku Imp. Univ.*, Vol 16, 1927, p 295–302
15. Lever Rule tutorials are available at http://www.soton.ac.uk/~pasr1/tielines.htm#page1 (accessed August 8, 2016); and http://www.doitpoms.ac.uk/tlplib/phase-diagrams/lever.php (accessed August 8, 2016)
16. "Standard Test Methods for Determining Average Grain Size," E112-96, ASTM International, 2004

Metallography of Steels—Interpretation of Structure and the Effects of Processing
Hubertus Colpaert
Updated and Translated by André Luiz V. da Costa e Silva

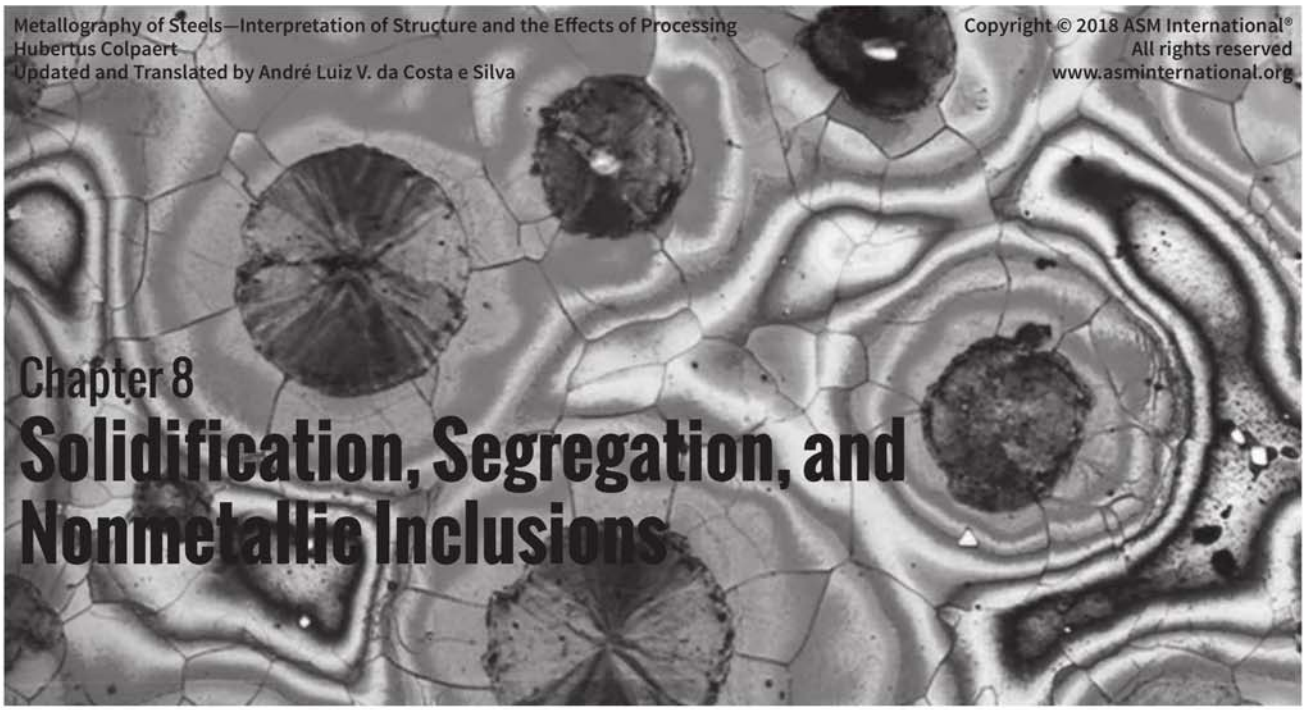

Chapter 8
Solidification, Segregation, and Nonmetallic Inclusions

Modern steelmaking and refining processes are capable of producing large masses of highly homogeneous steel, both chemically and thermally. However, these liquid steel masses must be transformed into solid products with the required shapes and dimensions.

Three main process families are responsible for the majority of the transformation of liquid steel into the required shapes and dimensions: foundry casting, ingot casting, and continuous casting. Atomization, spray casting, and other processes that lead to the formation of steel droplets are used for important products such as tools and intricate parts, particularly through powder metallurgy, but these processes are responsible for only a small fraction of the total steel produced in the world. A significant portion of the structural characteristics of steel products are directly linked to the changes that occur during solidification. These features suffer relatively little change during further processing of the cast products. In the case of wrought products subjected to forming, in particular hot working (rolling, forging, etc.), some of these features are modified, but as discussed later in this chapter, they are largely preserved in the final product.

The main solidification phenomena that give rise to the features of steel products are volume contractions associated with phase change and solute redistribution, called segregation.

Because the atomic arrangement in the liquid phase is less compact than in the solid phases of iron (BCC or FCC), a significant change of volume (contraction) occurs during solidification. (In the case of cast irons, see Chapter 17, “Cast Irons,” in this book; this contraction or shrinkage is largely counteracted by the formation of graphite, which has low density.) This change of volume may induce the formation of different shrinkage defects, such as porosity and pipe, and may contribute to liquid movement during solidification. These movements, in turn, might influence solute redistribution, creating segregation on the macroscopic scale.

Steels are iron-based alloys, thus several solute (alloying, residuals, etc.) elements are also present. As a rule, the solubilities of the various elements

are not the same in the liquid and solid phases formed from this liquid. This difference in solubility leads to the redistribution of solutes during the solidification process. Because industrial solidification is not slow enough to allow phase equilibrium to be restored at the end of the process, a portion of this solute redistribution remains in the solid product in the form of segregation. On the other hand, the single viable mechanism to produce homogenization in the solid state is diffusion. The low mobility of the substitutional elements in iron in the solid state and the size scale in which solidification segregation usually occurs make it almost impossible to completely eliminate segregation from steel products.

In addition, other problems may occur during solidification, giving rise to important structural features and defects.

8.1 Continuous Casting and Ingot Casting

The vast majority of steel produced around the world is processed through continuous casting. In this process, solidification begins in a water-cooled copper mold and, after a solid steel shell of sufficient thickness is formed, the material is taken from the mold and directly cooled by water sprays. For specialty steels that are produced in smaller quantities, for large forgings, and for some steels that require special solidification conditions, casting is performed in ingots using static molds. In this process, steel is poured in molds (usually made of cast iron) and solidifies statically. The final solid product is called an ingot. Finally, parts can be produced in their final shape using various foundry casting processes in which the liquid steel is poured into molds made with different materials and processes. Parts ranging in size from grams (e.g., small parts for guns and machinery) to tons (e.g., hydroelectric turbine rotors) can be produced this way. Cast iron, as the name implies, is always produced via foundry casting.

The ideal product from ingot making or continuous casting would be physical and chemically homogeneous, with a fine, equiaxial structure and free of segregation, porosity, pipe, and nonmetallic inclusions. However, the laws governing the solidification process prevent obtaining such homogeneous material. Furthermore, solidification shrinkage is an important source of problems in solidification. Besides these internal quality problems, surface quality can be an important issue when defects such as surface cracks, folds, and other irregularities occur.

8.2 Solidification Shrinkage

When steel solidifies, shrinkage of about 4% in volume occurs due to the different densities of solid and liquid steel. In rimmed steels cast in ingots, shrinkage used to be balanced by pores caused by the evolution of CO gas (associated to the C + O = CO reaction) during solidification (Fig. 8.1 and 8.2). Rimmed steel took advantage of this reaction to generate gas that would "push" the segregated liquid to central region of the ingots, forming a "rim" of purer steel in the ingot. Rimmed steels were extensively used for flat products in which good surface quality was the main requirement. These steels stopped being produced because they were not amenable to continuous casting, requiring conventional ingot casting, which rendered them economically inviable.

In killed (fully deoxidized) steel there is no gas evolution during solidification. To avoid the presence of internal shrinkage cavities in castings or ingots (pipe, porosity, etc.), it is necessary to take measures to concentrate this con-

Fig. 8.1 Macrograph of the longitudinal plane of an ingot of rimming steel. The CO bubbles formed during solidification offset the solidification shrinkage. No etching. Copyright © Wiley-VCH Verlag GmbH & Co. KGaA. Reprinted with permission. Source: Ref 1

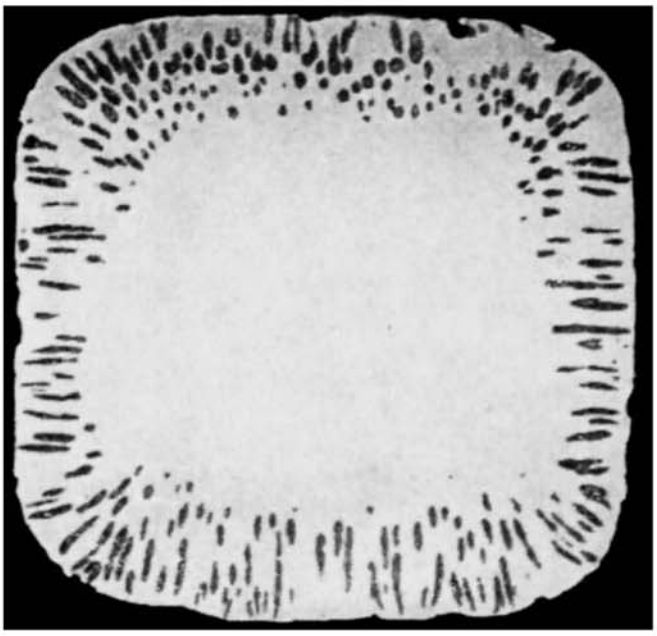

Fig. 8.2 Macrograph of the transverse section of an ingot with bubbles close to the surface. The aspect is typical of a rimmed steel ingot. Bubbles nucleate after the start of solidification and grow in the direction of solidification. No etching.

traction in a certain portion of the ingot or the cast piece. This is done by properly controlling solidification in the vertical and horizontal direction, making sure directional solidification occurs. In cast pieces, directional solidification is controlled via proper design of the feeding channels (through which the liquid steel enters the mold), risers, and sometimes coolers. Risers are added to the piece design to guarantee that solidification advances toward them. Their dimensions and positions are designed to make sure they are the last portion of the liquid mass to solidify, providing a permanent supply of liquid metal to "feed" the part as shrinkage occurs. A simple indicator of solidification time is the volume/area ratio and, for simple shapes, Chvorinov's rule (Fig. 8.3) gives good results in the design of cast pieces.

Chvorinov's rule is based on the condition that the heat flux extracted by all surfaces of the part is the same. When heat is extracted preferentially through the sides and bottom of the mold, solidification advances as shown schematically in Fig. 8.4.

Figures 8.5 and 8.6 present pipes (shrinkage cavities) in ingots that solidified in conditions similar to those shown in Fig. 8.4. The liquid metal surface in the top of these ingots cools rapidly due to radiation heat losses, and a "bridge" forms that hides the pipe from external observation of the ingot. The use of thermal insulating material in feeders makes it possible to increase their solidification time without increasing the amount (volume) of these

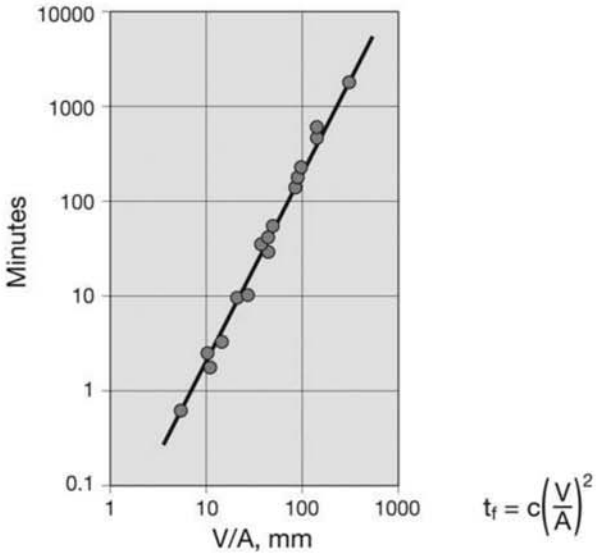

Fig. 8.3 Experimental results from Chvorinov: solidification time of castings as a function of the volume/area ratio of the part. Source: Ref 2

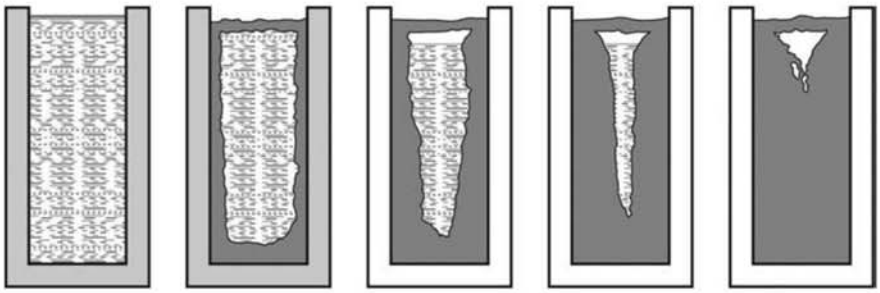

Fig. 8.4 Solidification progress in a metallic mold, when heat extraction occurs preferentially by the sides and bottom of the mold. Heat extraction by the top is less important.

feeders. Feeders with insulating walls are frequently used in foundries, as shown in Fig. 8.7. Sometimes exothermic material may also be used.

Thicker regions and changes in part of the cross section deserve special care during the design of castings to avoid forming voids caused by solidification shrinkage, as shown in Fig. 8.8 and 8.9.

In conventional ingot casting, solidification is basically controlled via the thermal aspects of the phenomenon. Proper design of the mold (taper, height/diameter ratio, etc.) and the use of insulating or eventually exothermic "hot-top" are the main measures available to achieve this control.

8.3 Segregation

8.3.1 Solute Redistribution during Solidification

Solute redistribution phenomena during solidification are part of day-to-day observations. When a cola solidifies inside a freezer, it is easy to observe that the solid is lighter in color than the liquid. This indicates that the solutes

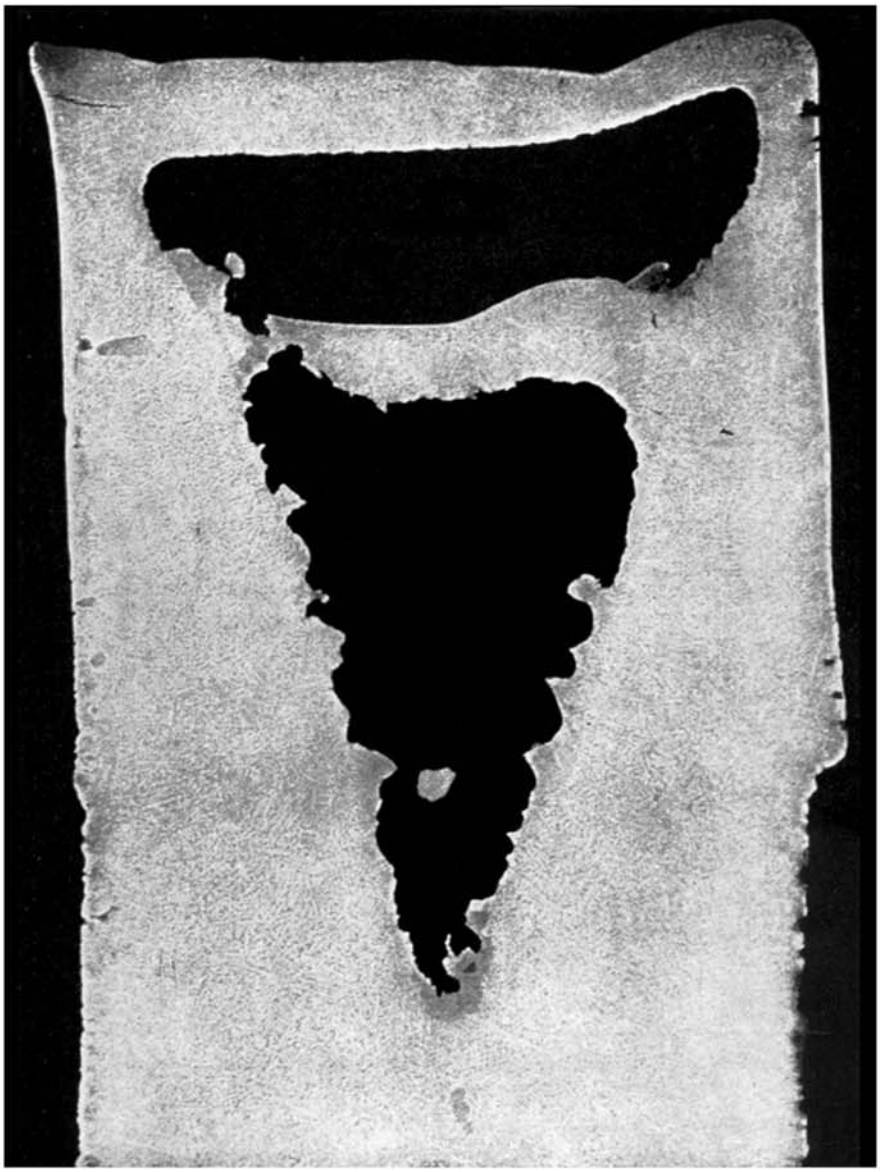

Fig. 8.5 Pipe or shrinkage cavity in the top of an ingot. Longitudinal section.

in the soda are more soluble in liquid water than in solid water (ice). In addition, the solubility of carbon dioxide is much higher in liquid water than in the solid; it concentrates in the liquid, and opening the container can have catastrophic results.

Ice cubes formed from water with dissolved air contain small tube-like pores (in a shape similar to those pores in Fig. 8.2, but farther away from the cube surface). This region solidifies as an ice-air eutectic (the liquid transforms to ice and air, at a given temperature). Machine-made ice cubes are normally free from these pores because of the use of flowing water over a chilled surface, in such a way that the liquid enriched with dissolved gas is constantly removed from the system (for a complete discussion see Ref 3).

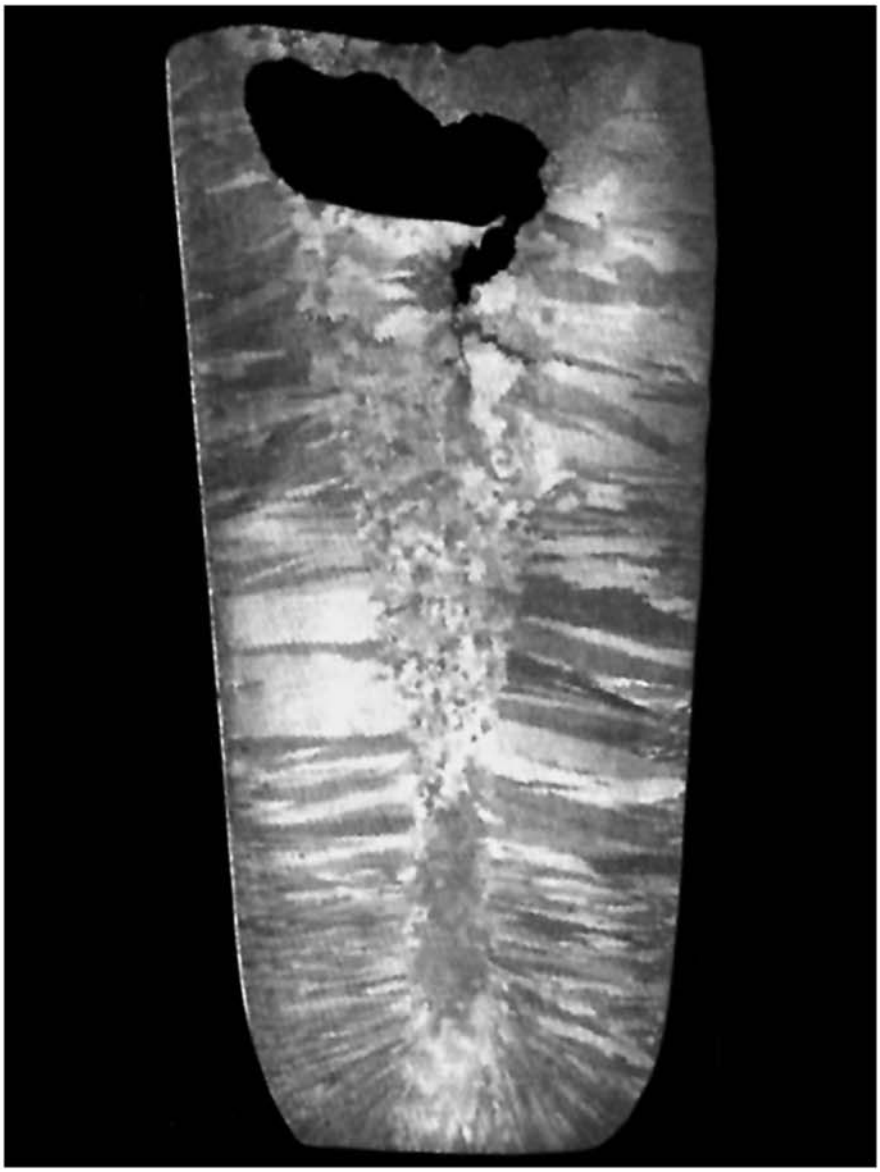

Fig. 8.6 Pipe in a small ingot. Etched. A hot crack starting at the bottom of the pipe and propagating between two grains can be seen. Copyright © Wiley-VCH Verlag GmbH & Co. KGaA. Reprinted with permission. Source: Ref 1

Usually when steel solidifies, the composition of the solid and liquid in thermodynamic equilibrium vary continuously with temperature. Solutes are less soluble in the solid phase, as mentioned already. Thus, a solute must redistribute between the forming solid and the remaining liquid. Figure 8.10 presents a schematic portion of a hypothetical binary equilibrium phase diagram between A and B, where the phase boundaries are straight lines. An alloy with an initial composition given by C_0 will then start to solidify forming a solid with kC_0 content of solute (where k is the solute distribution coefficient for B in this alloy).

Fig. 8.7 Transverse section of a casting and its feeder showing the region where the solidification shrinkage was concentrated. Courtesy of G. Ronelli.

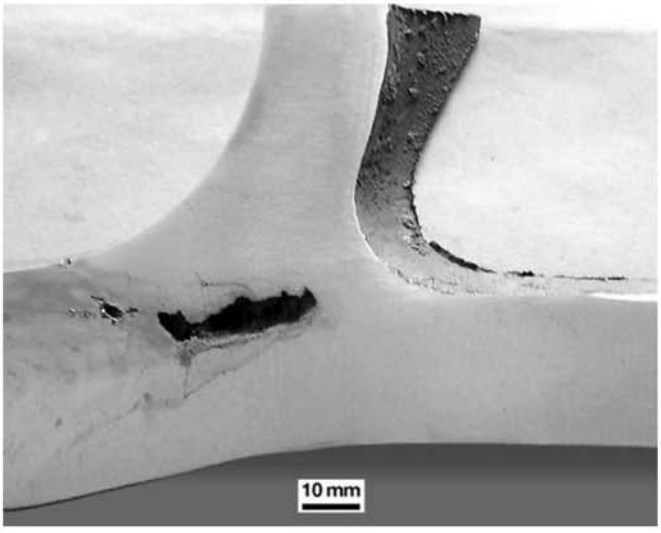

Fig. 8.8 Macrograph of the transverse section of a steel casting for railway application. Solidification shrinkage can be observed at the region of cross section change. Etched with HCl (stains close to the pores are caused by poor drying practice after etching). When only shrinkage observation and recording is necessary, macrograph without etching is preferred. Courtesy of MRS Logistica S.A. Rio de Janeiro, Brazil.

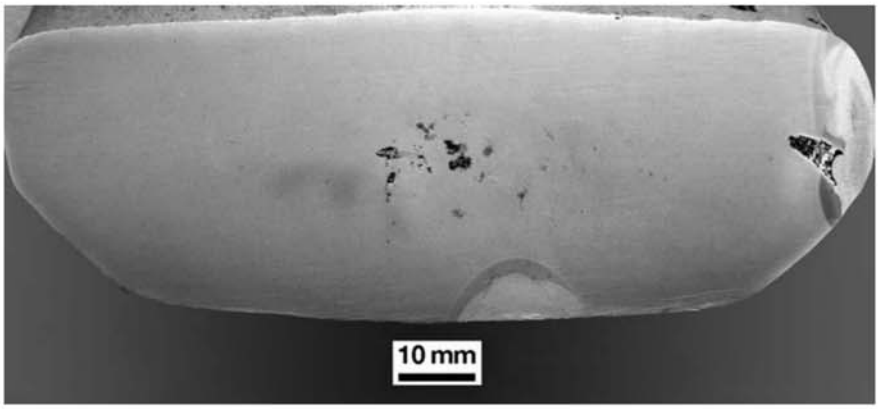

Fig. 8.9 Macrograph of the transverse section of a steel casting for railway application. Presence of porosity in the thickest section of the part. A weld repair region can also be seen at the bottom and to the right of the figure. (see Chapter 14, "Structural Steels and Steels for Pressure Vessels, Piping, and Boilers," in this book). The welding preparation for the repair at right was insufficient to completely remove the casting defect. Courtesy of MRS Logistica S.A. Rio de Janeiro, Brazil.

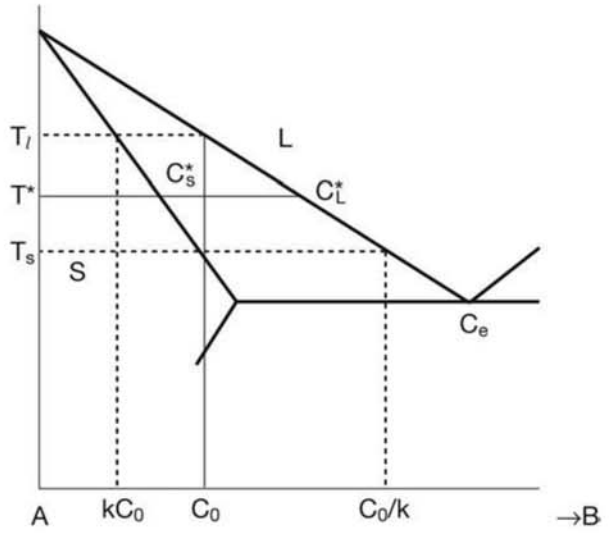

Fig. 8.10 Portion of a binary phase equilibrium diagram of a hypothetical system A-B, indicating the partition coefficient k for B as a solute. C_L^* and C_S^* are the equilibrium compositions of the liquid and the solid, respectively, at any given temperature, T*.

If solidification progresses in equilibrium, in accordance with the phase diagram of Fig. 8.10, the solid and the liquid would be completely homogeneous during the process and have the compositions indicated by the boundaries of the two-phase field in the diagram as the temperature decreases, as presented schematically in Fig. 8.11.

Two conditions are necessary for the final solid to be completely homogeneous with composition C_0. The liquid would have to reach the end of solidifi-

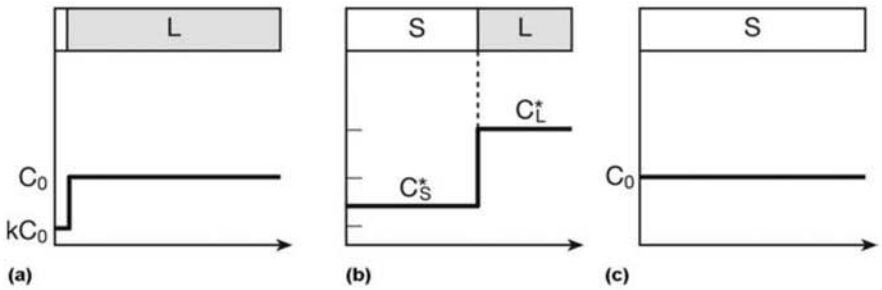

Fig. 8.11 Composition profile of a sample that solidifies unidirectionally (from left to right in the sketches) in accordance with the phase diagram presented in Fig. 8.10. (a) Indicates the situation immediately below T_f, (b) the conditions at T*. (c) The end of solidification. It is important to observe that the composition of the solid phase already formed must vary as solidification progresses. This can only happen by solid-state diffusion.

cation completely homogeneous with composition C_0/k. Furthermore, the solidification should have proceeded for a very long time or at an extremely small scale, so that solid-state diffusion could homogenize the solid during the process. The result would then be as indicated in Figs. 8.10 and 8.11.

In normal steelmaking solidification, this transformation happens in minutes or at the most hours. Neither is the size scale extremely small (see section "Dendritic Growth" in this chapter). Under these conditions, solid and liquid cannot keep homogeneous compositions because this would involve solid-state diffusion that requires much longer times. In general, thermodynamic equilibrium prevails only at the interface, where solid and liquid phases are in contact.

Figure 8.12 indicates qualitatively how the average solid composition deviates from the equilibrium composition due to the lack of complete homogenization of the solid during the process. The solid phase so obtained has a nonuniform composition and is described as being "cored." Clearly at the end of the solidification the average solid composition must be C_0 because of mass conservation. On a microscopic scale, the composition of the solid varies, however.

In nature, segregation is important in many processes. Agates, for instance, are formed from a liquid solution trapped inside rocks. As the solid crystalizes (precipitates) on the rock walls, changes in the liquid phase composition happen, and this causes changes in the characteristics of the formed solid, creating an aspect of a cored solid, as presented in Fig. 8.13. (Chemical composition, the process by which crystallization occurs, and crystal orientation change as the solid forms in a very complex process.)

If no homogenization happens in the solid and the liquid is fully homogeneous during the process (a reasonable approximation because liquids can move by convection) the Scheil model (Ref 4, 5) can predict the solute redistribution as depicted schematically in Fig. 8.14.

The heterogeneities in chemical composition generated by solidification—segregation—can be detected using chemical etchants, localized chemical analysis, and techniques such as SEM with EDS or WDS or microprobes and through the observation of the changes in microstructure associated to the variation of chemical composition.

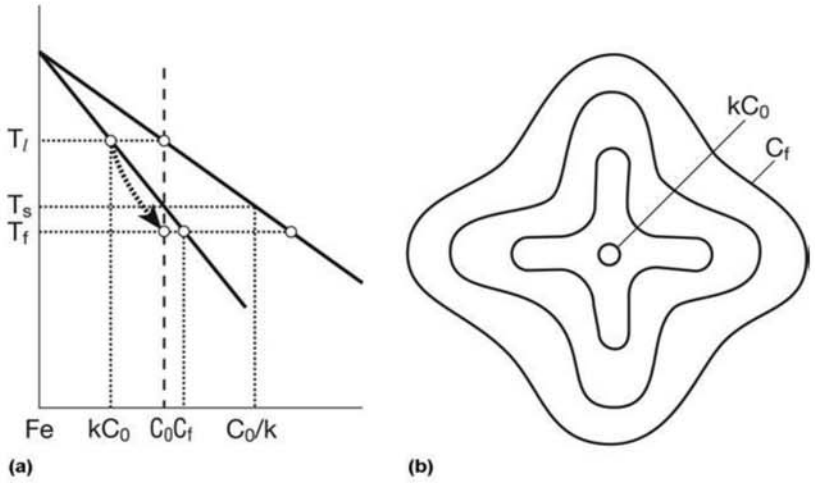

Fig. 8.12 Schematic progress of solidification when equilibrium occurs only at the solid-liquid interface and the solid phase composition does not homogenize during the process. Solidification starts at T *liquidus* (T_l) with the appearance of a solid with kC_0 composition. The "liquidus" line is where the solid phase fraction is zero, that is, the line that defines the temperatures and compositions where the solid phase starts to appear in equilibrium. As solidification progresses, solute has no time to diffuse into the previously formed solid and the solid average composition (dashed line) deviates from the composition of the "solidus" line. As the *equilibrium solidus temperature* (T_s) for this alloy is reached, solidification has not been completed, since the average composition of the solid formed does not yet reach the effective "solidus" line. The effective "solidus" line is where, in equilibrium, the last portion of liquid vanishes.

8.3.2 Dendritic Growth

When the structure of solidified metals is observed, it is frequently found that the solid grows with a nonplanar interface, in contrast with the simple examples presented in the earlier sections of this chapter. Furthermore, in some cases the solid nuclei transported ahead of the solid-liquid interface find thermal conditions in which they can survive and grow. In the solid crystals there are crystallographic planes in which the process of atom attachment and organization in the liquid-solid transformation is easier, so it is not surprising that not all crystallographic orientations of the solid will grow into the liquid with the same velocity for the same thermal conditions. What defines if the solid-liquid interface will be planar is whether instabilities in the interface can survive. In other words, are the conditions ahead of a planar interface such that a solid grain, growing faster than the others, will survive and continue growing? In the case of pure metals, this phenomenon can only happen in the presence of a negative temperature gradient in the liquid ahead of the interface (undercooling), something that is not extremely common. For alloys, phenomena such as constitutional undercooling (Ref 5–7) caused by solute redistribution ahead of the interface may make stable solid growth with a nonplanar interface. This condition is exemplified schematically in Fig. 8.15, where its relationship with the equilibrium phase diagram is highlighted.

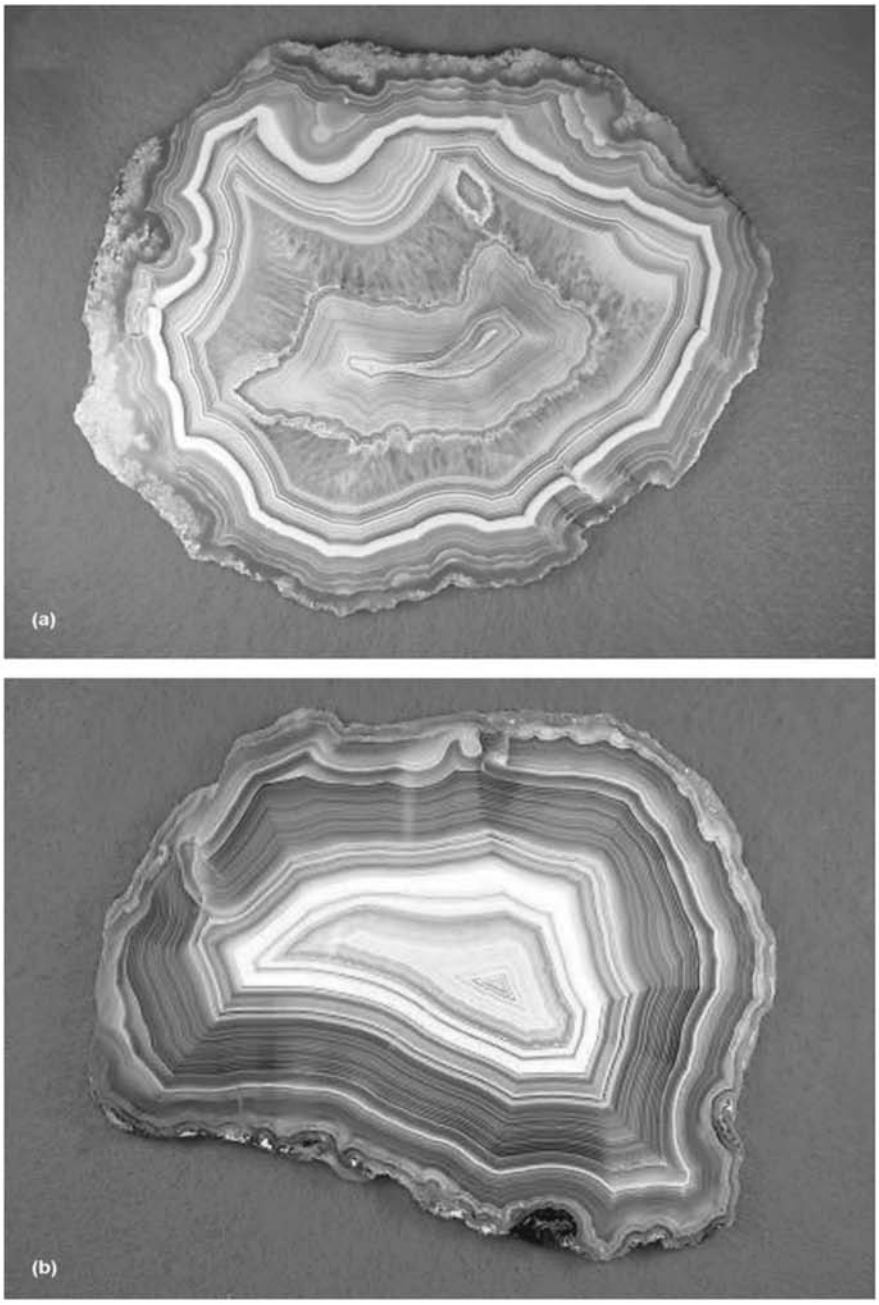

Fig. 8.13 Polished cross sections of agate. Agate forms with the initial formation of an external rock with an internal cavity (probably caused by gas). Later, the cavity is filled with a liquid from which solids precipitate from the outside to the inside. The changes in liquid composition as the solids precipitate lead to the formation of "layered" solids with variable structure and/or composition. When the retained liquid volume is small, cavities remain inside the agate. Courtesy of R. Pabian, University of Nebraska–Lincoln, EUA.

The resemblance of the solid metal formed this way (Fig. 8.16 to 8.18) to tree branches is responsible for this shape being called "dendrites" (Greek: *dendron* = tree). Because the solid metal has a crystalline structure, growth in some crystallographic directions is faster, as discussed earlier, and solidifica-

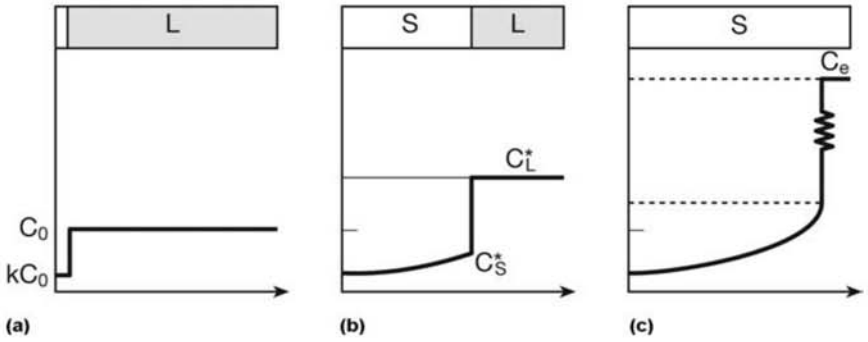

Fig. 8.14 Composition profile of a sample that solidifies unidirectionally (from left to right in the sketches) without any homogenization in the solid, complete homogenization in the liquid and thermodynamic equilibrium between solid and liquid at the interface, according to the phase diagram of Fig. 8.10. (a) Composition and phase distribution immediately below T_l. (b) Composition and phase distribution at T*. (c) Composition and phase distribution at the end of solidification. Under these circumstances, it is not possible to use the lever rule on a equilibrium phase diagram to calculate the phase fractions of solid and liquid. (Chapter 7, "Equilibrium Phases and Constituents in the Fe-C System," section 7.6.1, "Hypo-Eutectoid Steels," in this book)

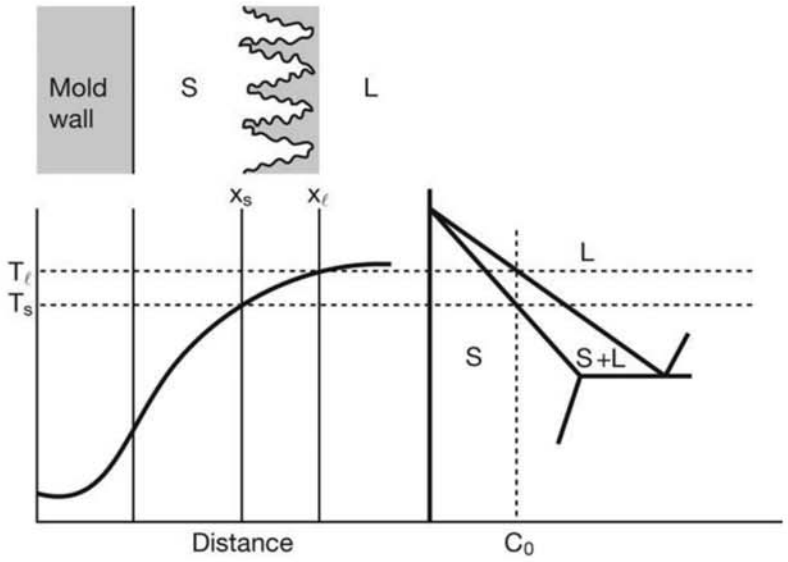

Fig. 8.15 Simplified scheme showing directional solidification of an alloy from the mold surface. In the region between x_s and x_l, temperatures are between T_s and T_l, and the solid phase fraction varies from 1 to 0. When the temperatures associated with the actual temperature gradient are below the equilibrium liquidus temperatures, solid interface instabilities grow until they reach the position corresponding to x_l.

tion evolves in a way that the structures formed in this "solid-liquid" region have well-defined shapes. Though it is usual to call the solid-liquid region a "mushy zone" due to its rheological behavior, there is no mushy state of matter; the behavior of this region is due to the presence of material in two different physical states, solid and liquid, and their physical distribution.

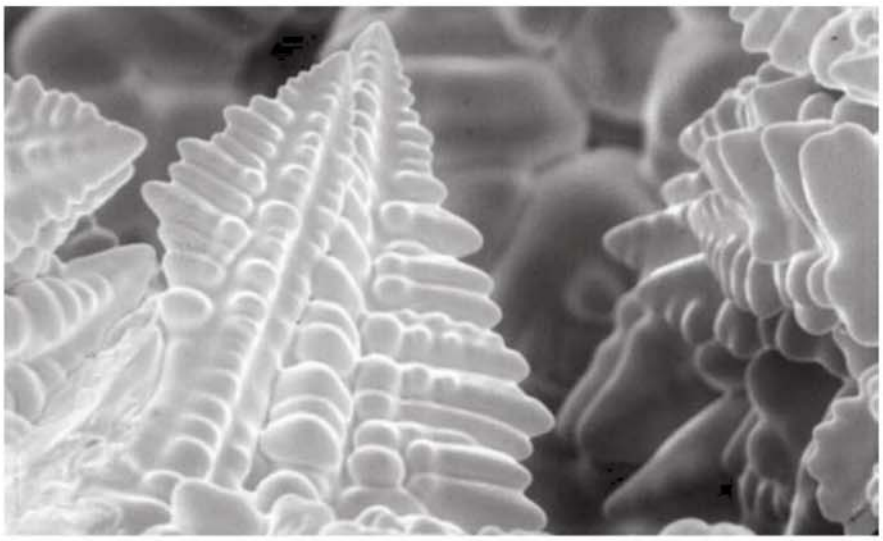

(a)

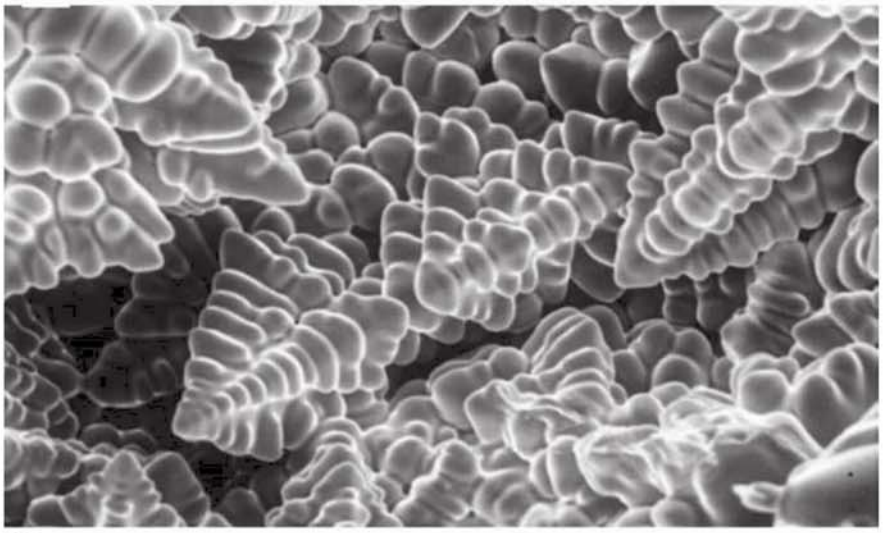

(b)

Fig. 8.16 Dendrites formed during the solidification of a metallic alloy. The spacing between the dendrite "branches" or arms in steel solidified in industrial processes range from hundreds of micrometers to millimeters. The most common measurement to characterize dendrite spacing is the spacing between secondary arms. SEM, SE, no etching. Nb-rich, Nb-Cu alloy, arc melted. The two metals have very limited miscibility in the solid state; after solidification is complete, copper is selectively dissolved by chemical etching, leaving behind only the primary niobium dendrites. Courtesy S. Chumbley, Iowa State University. Reprinted with permission. Source: Ref 8

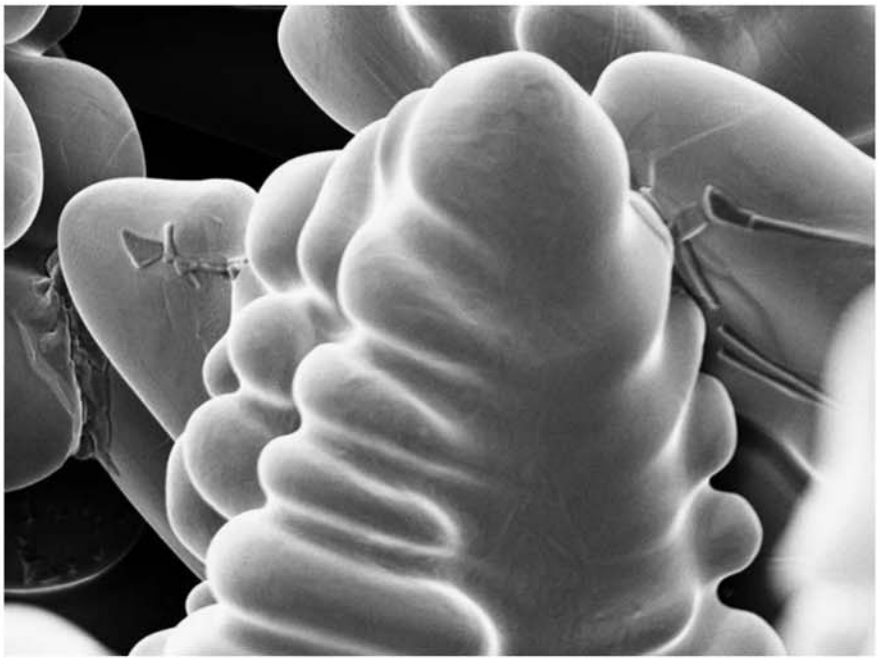

Fig. 8.17 Dendrite in low-carbon steel. SEM, SE, no etching. Courtesy of ArcelorMittal Tubarão, Brazil.

Thus, the solid dendrite branches advancing into the liquid in search of ideal growth conditions (segregated liquid where constitutional undercooling is present) need to balance the crystallographic conditions of the solid with the direction of heat extraction. In the case of tree growth and branching, where the branches seek light and aeration conditions adequate for growth, the limitations for the growth and branching directions are more evident in conifers (such as fir and pine trees) than in hardwood (broad-leaved) trees, where the visual similarities to metallic dendrites are more limited.

A clear relationship is observed between the secondary arm spacing (those that grow transverse to the main growth direction) and the cooling rate imposed on the metal, as shown in Fig. 8.19. This relationship is frequently used to derive cooling rates from metallographic observations.

In Fig. 8.20 it is possible to see the effect of changing the cooling rate during an experiment simulating an ingot solidification. The change in dendrite arm spacing is evident.

8.3.3 Reactions during Solidification

When a reaction happens simultaneously with solidification, the growth morphology (form) can be altered. Figure 8.18, for instance, presents some characteristic aspects of the solidification of a ductile cast iron containing approximately 3.27% C and 4.38% Si. When austenite is formed as the primary phase from the liquid, dendritic growth is well defined. However, when the conditions are such that graphite and austenite must grow simultaneously from the liquid, austenite surrounds the spherical graphite nuclei (see

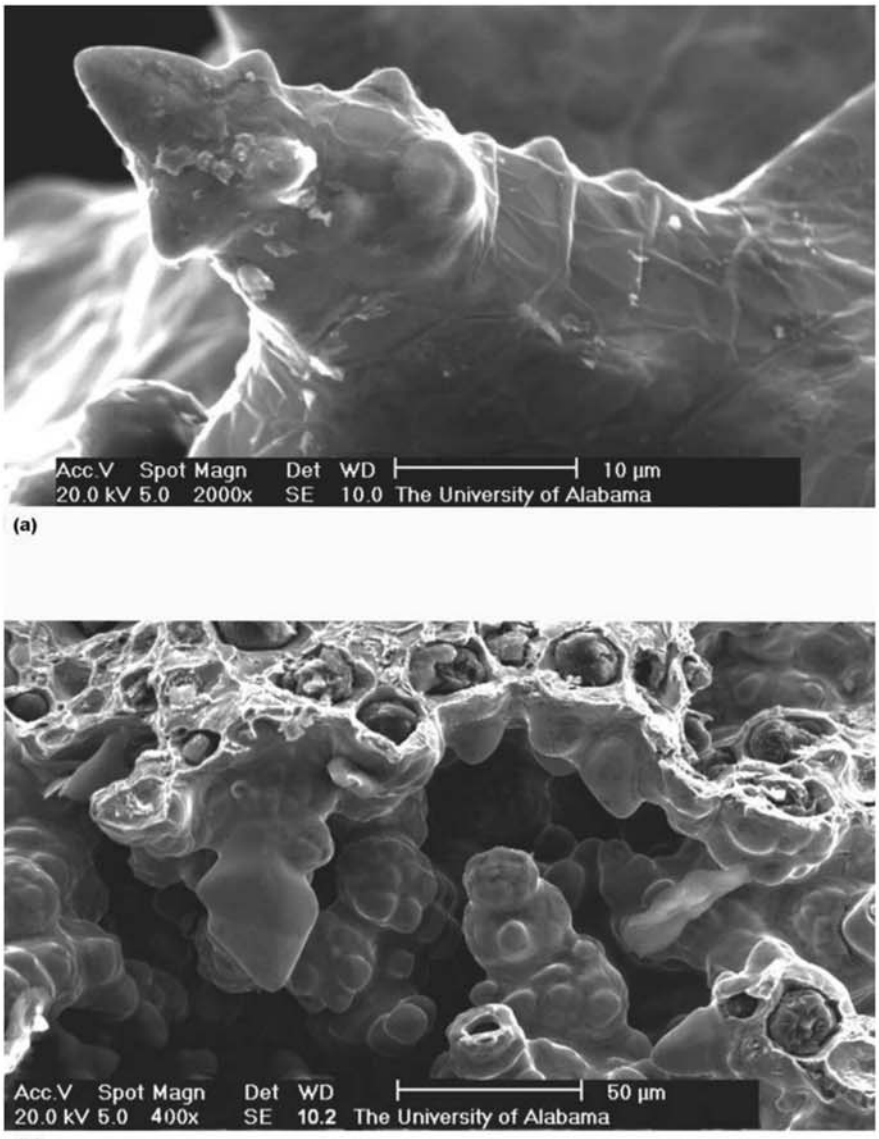

Fig. 8.18 (a) Primary austenite dendrites in a pore of a sample of ductile cast iron. (b) Grains of the austenite-spheroidal graphite in the same pore. Some regions show graphite not completely surrounded by austenite. SEM, SE, no etching. (See also Chapter 17, "Cast Irons," in this book). Courtesy of D. Stefanescu, University of Alabama. Copyright American Foundry Society. Reproduction authorized by courtesy by AFS. Source: Ref 9

Chapter 17, "Cast Irons"). The solidification progress now depends on carbon diffusion through austenite so it can reach the graphite nodules. This influences the morphology of the solid phases.

The two most common reactions that happen during solidification are discussed here: the peritectic and the eutectic reactions. The reactions involving precipitation of nonmetallic inclusions are discussed in section 8.10 in this chapter.

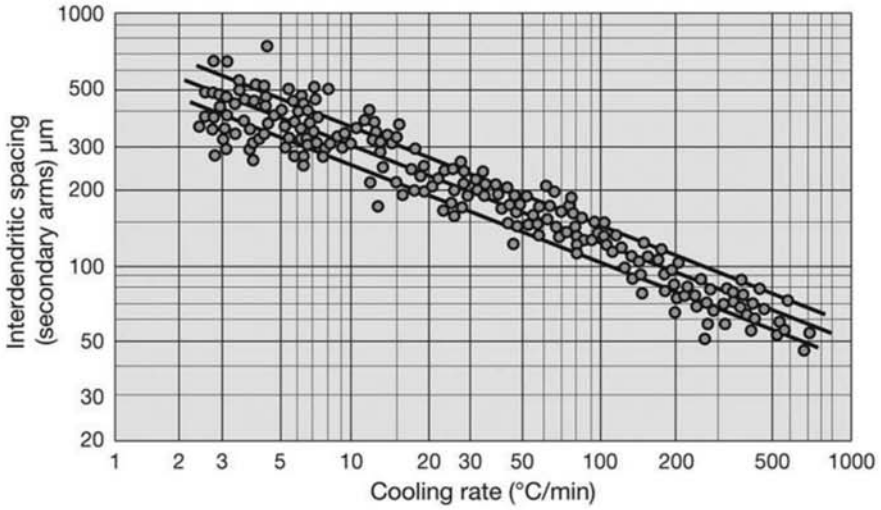

Fig. 8.19 Secondary dendrite arm spacing as a function of cooling rate in steels (experimental data). Source: Ref 4, 10

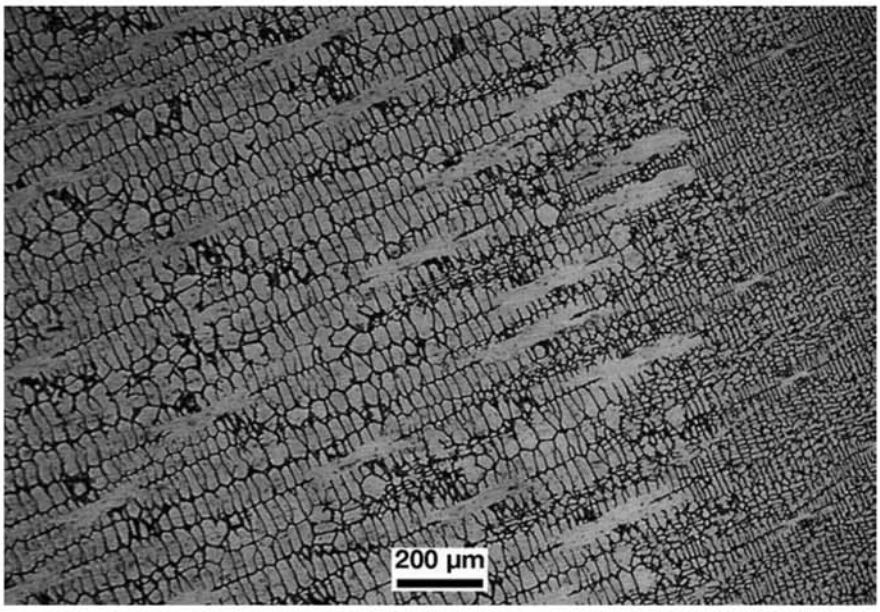

Fig. 8.20 Macrograph of an experiment simulating an ingot of alloy 718. The left region has solidified in conditions similar to the center of an ESR ingot (see the section "Remelting Processes" in this chapter) with a diameter of 550 mm (22 in.). The sample was then quenched, when solidification was concluded swiftly, with fine dendrite arm spacing (right side region). The processing (melting, solidification, and working) of nickel-based alloys (such as alloy 718) is similar to that of steels. The similarity is present in many macrostructural features. Courtesy of A. Mitchell, University of British Columbia, Canada.

The Peritectic Reaction

The peritectic reaction is important in the solidification of steels with relatively low carbon content. This reaction has been extensively studied because of its importance to the formation of hot cracks during continuous casting and ingot casting. Figure 8.21 presents the region of the peritectic reaction L + δ = γ in the Fe-C phase diagram. A line through the common composition of 0.14% C is included in this figure. The peritectic reaction involves the liquid reacting with the already formed solid to form a new solid. This process normally requires a layer of the new solid to surround the initial solid. For the peritectic reaction between the liquid and the first solid to proceed, diffusion through this layer of the new solid must occur. The peritectic reaction gets its name from the Greek language: *peri* = "around" and *tektos* = "able to dissolve" (from *tēkein* = to melt), due to the layer of solid formed around the previously formed solid.

Figures 8.22 and 8.23 present the evolution of the structure as the steel solidifies. The fast transformation of ferrite in austenite, as well as the volume change, results in deformation of the free surface of the solid, as can be seen.

The Eutectic Reaction

In a binary system, the eutectic reaction involves the decomposition of the liquid into two different solids. As the solids grow from the liquid, cooperative growth mechanisms are common. Depending on the crystal structure of the solid forms, there may be preferred orientations between the two solids, and aesthetically interesting structures may be formed. In the stable Fe-C system, there is one eutectic reaction: L = γ + graphite. In the metastable Fe-C (or Fe-Fe_3C) system, where graphite formation is suppressed, there is also one eu-

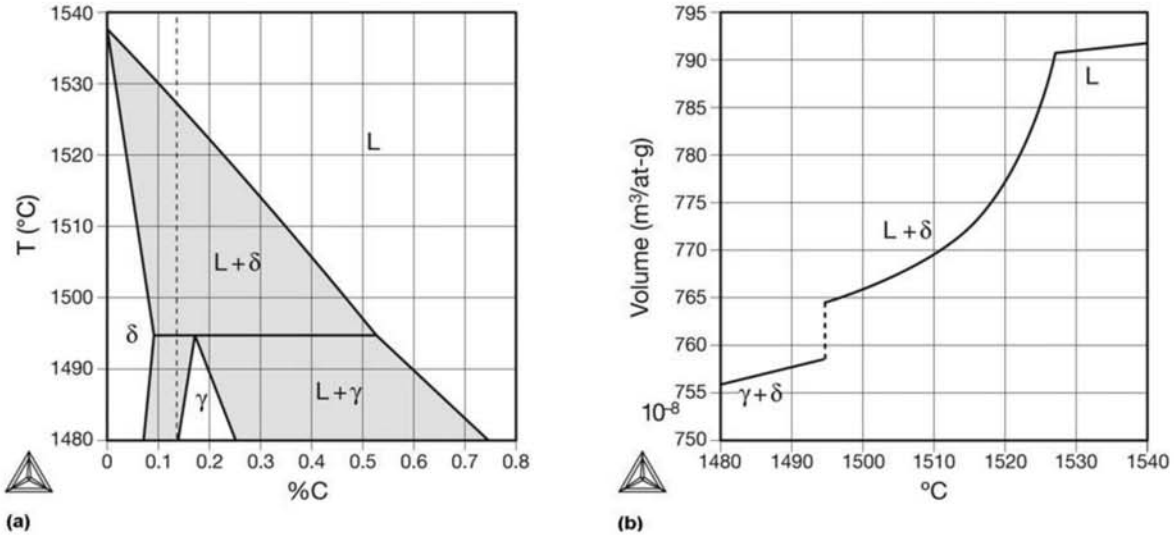

Fig. 8.21 (a) Equilibrium phase diagram Fe-C in the region of the peritectic reaction. The dashed line indicates the composition of 0.14% C. The two-phase field without identification in this diagram is δ + γ. (b) Volume change during equilibrium solidification (without segregation) of a steel containing 0.14% C. The discontinuity in volume change corresponds to the shrinkage during the peritectic reaction. Calculated. Source: Ref 11, 12

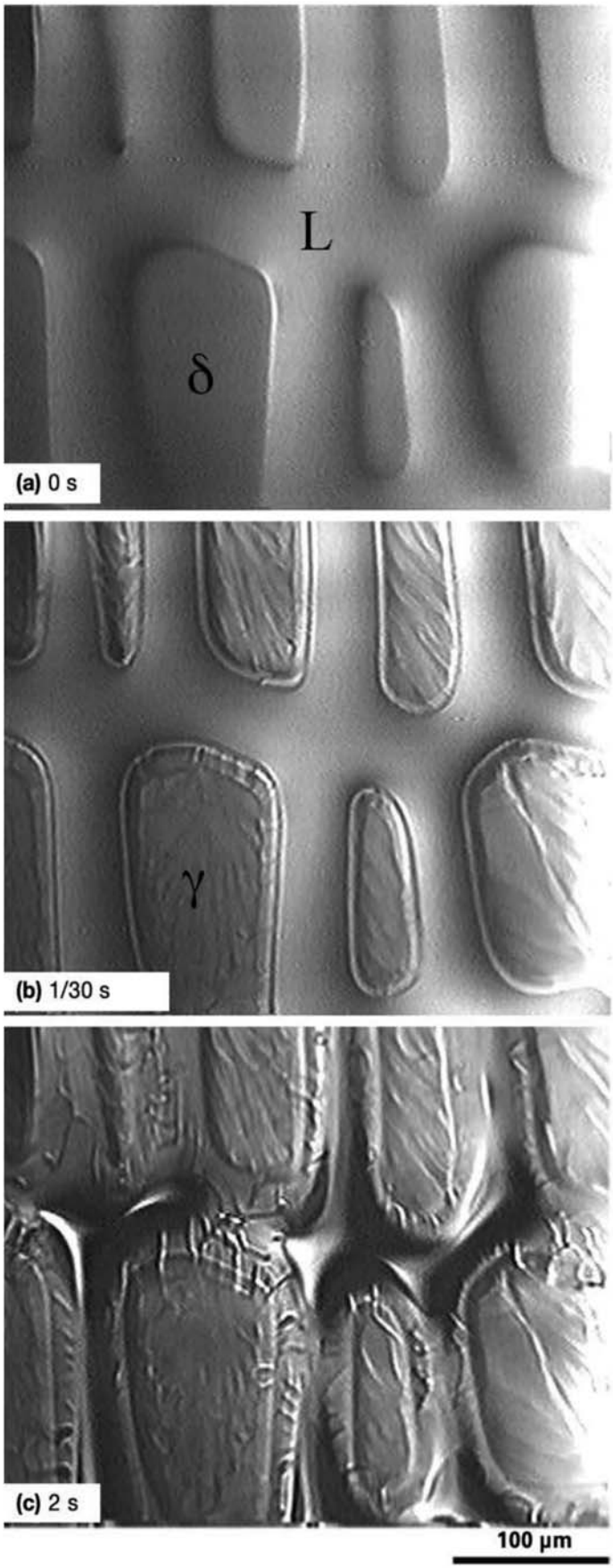

Fig. 8.22 A steel with 0.14% C subjected to a temperature gradient of 4 K/mm and cooled through its solidification range with a rate of 20 K/min. Confocal laser microscopy. Between times (a) t = 0 and (b) t = 1/30 s, corresponding to 1495 °C (2725 °F), the peritectic reaction was completed. The temperature gradient causes the solidification front of the sample to move normal to the plane of the image. The interval between frames when filming the experiment is 1/30 s. After (c) 2 s solidification is complete. Courtesy of T. Emi, Institute of Research of Iron and Steel (IRIS), Sha-Steel. Copyright © Springer Science and Business Media. Reprinted by courtesy of Springer. Source: Ref 13

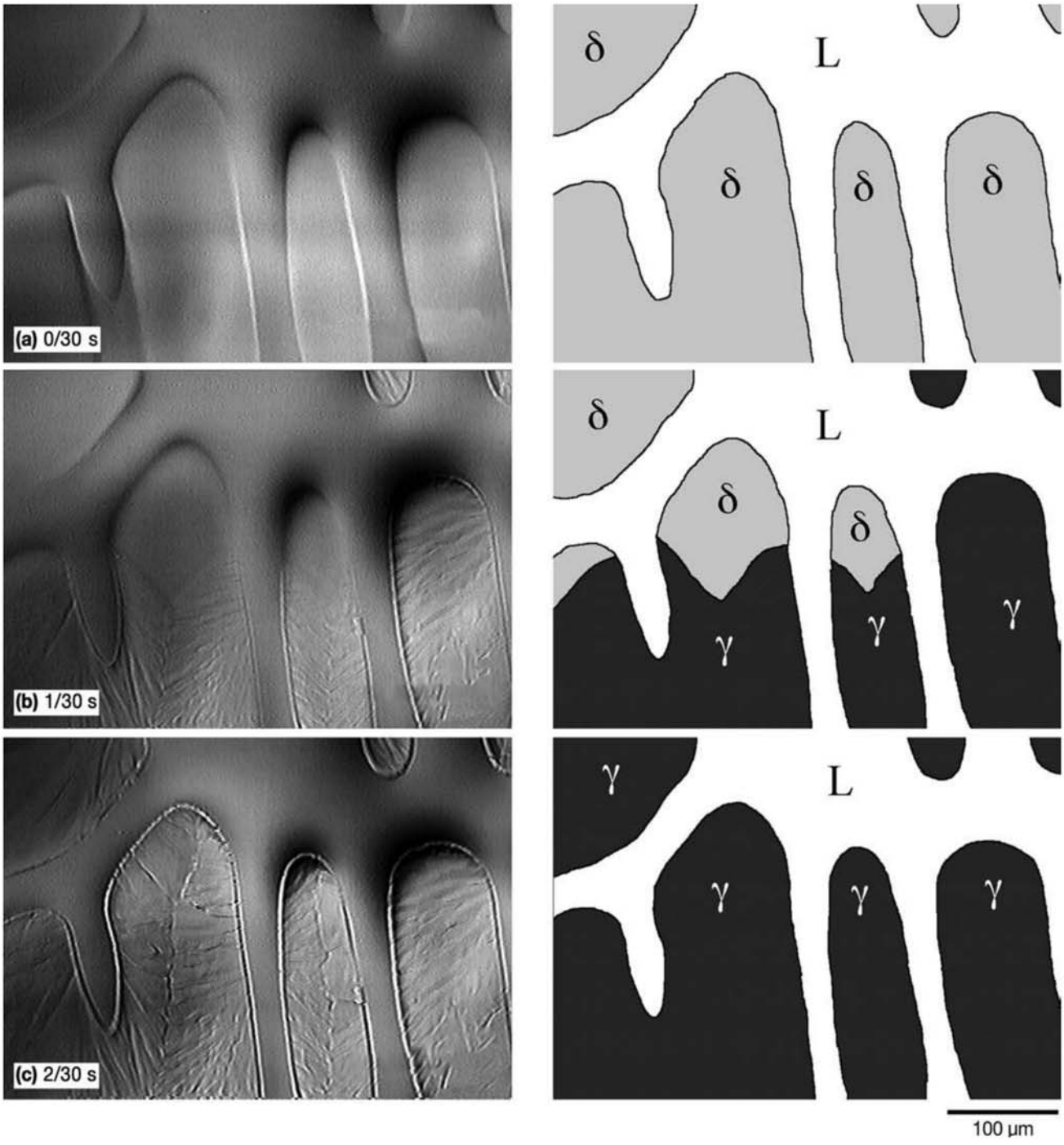

Fig. 8.23 A steel with 0.14% C subjected to a temperature gradient of 4 K/mm and cooled through its solidification range with a rate of 10 K/min. Confocal laser microscopy. Between times (a) t = 0 and (b) t = 1/30 s, it is possible to follow the peritectic reaction. At (c) 2/30 s the reaction is already complete with the associated deformation covering the solid. The temperature gradient causes the solidification front of the sample to move normal to the plane of the image. The interval between frames when filming the experiment is 1/30 s. Courtesy of T. Emi, Institute of Research of Iron and Steel (IRIS), Sha-Steel. Copyright © Springer Science and Business Media. Reprinted by courtesy of Springer. Source: Ref 8

tectic reaction: L = γ + Fe_3C. The eutectic constituent involving austenite and cementite is called ledeburite after Karl H.A. Ledebur (1837–1906), professor at Freiberg, who studied this constituent in 1882 (Ref 14). These two eutectic reactions are very important in cast iron metallurgy (see Chapter 17, "Cast Irons"). The first is most important in cast irons that contain graphite, and the second one in white cast irons. The eutectic reaction is named after the Greek word *eutektos*, meaning easy melting.

When the alloy composition is not exactly equal to the eutectic composition, a pro-eutectic phase is formed, as shown in the scheme presented in Fig. 8.24. Figures 8.25 and 8.26 present cast-iron microstructures in which the pro-eutectic phase can be seen.

During the solidification of some tool steels, the liquid may reach eutectic compositions close to the end of the solidification process. Generally these are high carbon steels and contain significant additions of carbide-forming alloying elements. Thus, eutectics in these cases are frequently formed between austenite and alloy carbides. Figure 8.27 presents the microstructure of D2 tool steel. During further hot working of this cast structure, it is essential to try to homogenize the carbide distribution as much as possible, homogenizing and improving the tool properties (see Chapter 11, "Hot Working," in this book).

As briefly discussed in connection with Fig. 8.18, an important and complex case of eutectic solidification is the solidification of cast irons in which

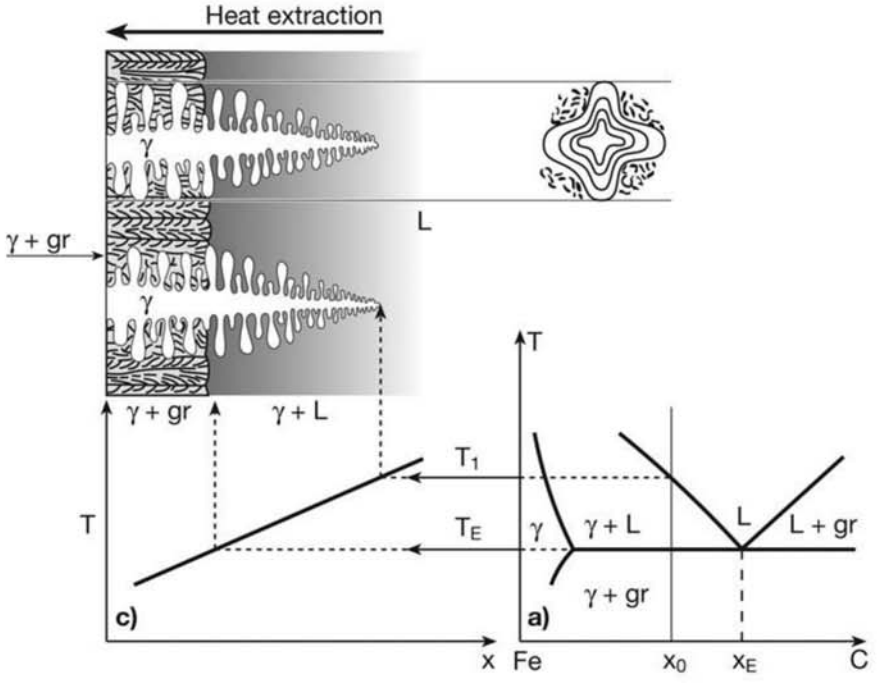

Fig. 8.24 The solidification of an alloy with a hypo-eutectic composition X_0 begins with the formation of austenite in accordance with the schematic phase diagram. As austenite forms, the interdendritic liquid gets richer in carbon until the composition of the eutectic, X_E, is reached. At this point, austenite and graphite grow in a cooperative way from the liquid. Fig. 8.25 presents the corresponding microstructure. Source: Ref 15

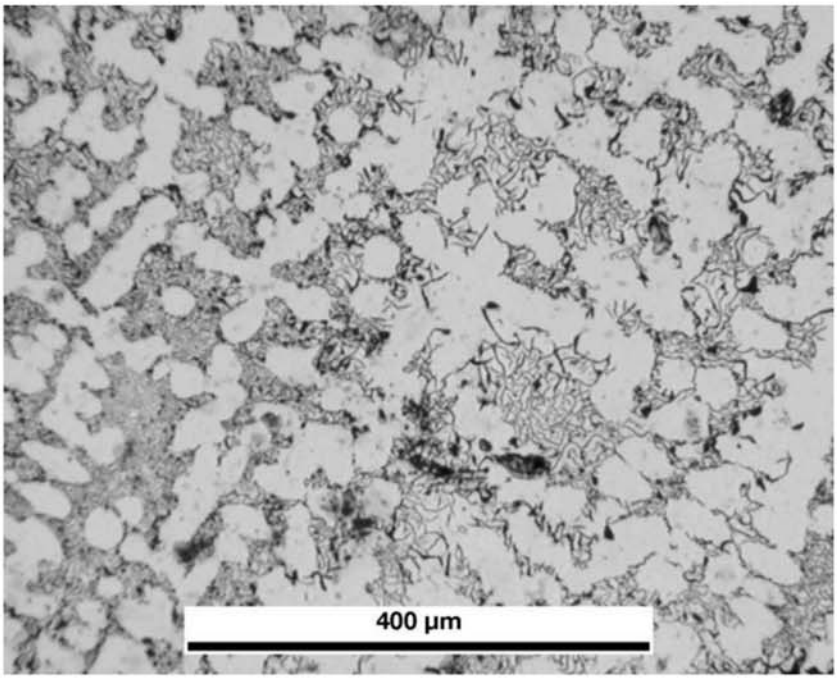

Fig. 8.25 Cast iron. White regions are dendrites of pro-eutectic austenite. Between the dendrites the austenite-graphite eutectic can be seen. Optical micrograph; picral etchant. Reproduced with permission from DoITPoMS, University of Cambridge.

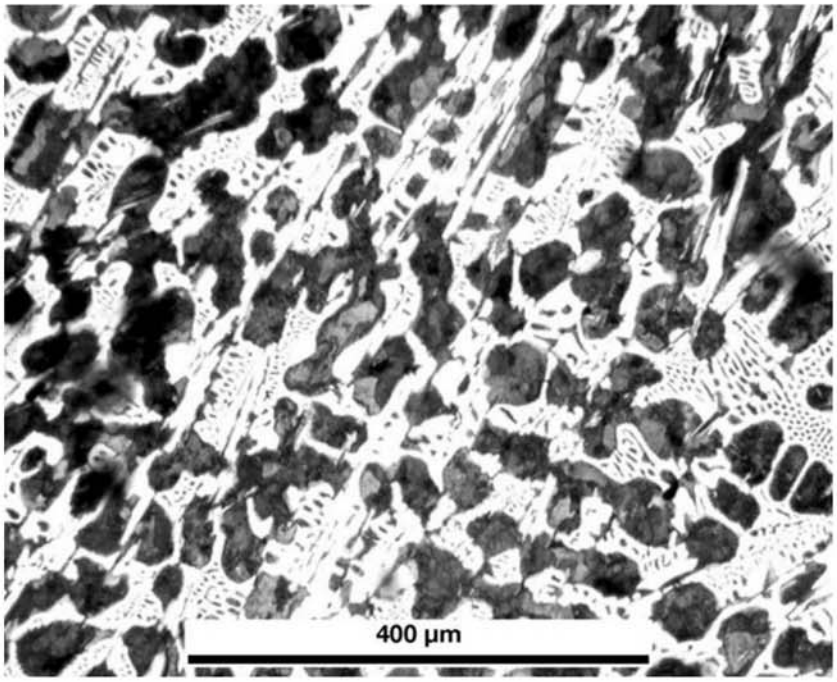

Fig. 8.26 White cast iron. Dark regions are dendrites of pro-eutectoid austenite that transformed to pearlite on cooling. In the regions between the dendrites, the austenite-cementite eutectic (ledeburite) can be seen. In the eutectic, austenite has transformed to pearlite (dark) and the iron carbide is the light-colored phase. Optical micrograph, picral etching. Reproduced with permission from DoITPoMS, University of Cambridge.

nodular graphite is formed. One theory (Ref 9) proposes that austenite and graphite can grow independently from the liquid phase until the solid volume fraction reaches a value of about 30%, a fraction sufficient to significantly hinder liquid convection. From this point on, the graphite particles are trapped by the austenite and their growth becomes controlled by carbon diffusion through austenite, as shown schematically in Fig. 8.28.

8.4 Microporosity

When a region containing solid and liquid is formed, liquid flow may be hindered. This may cause difficulties to the liquid flow necessary to compensate for solidification shrinkage. Figure 8.29 presents a sketch of the liquid flow needed to compensate for shrinkage, and the location of an eventual micro-

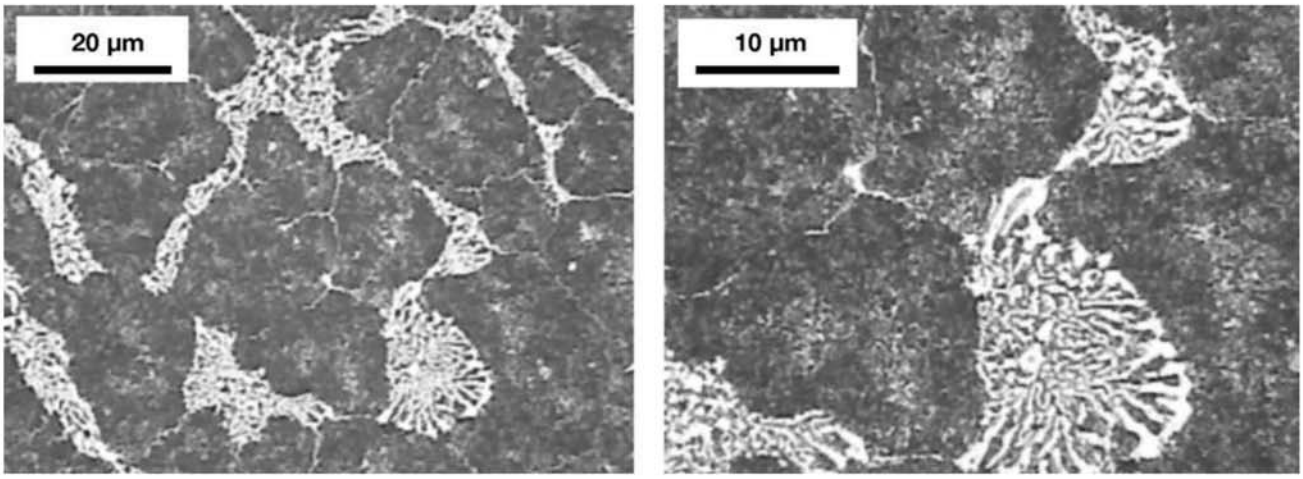

Fig. 8.27 As cast structure of ASTM A681 D2 cold work tool steel. A eutectic constituent composed of carbides (white) and austenite can be observed. The austenite has decomposed after cooling in both images, leading to dark regions of ferrite carbide agglomerates or tempered martensite. This eutectic is formed close to the end of the solidification process, as discussed in Ref 5 and 16. Optical micrograph. 4% nital etching. Courtesy of Villares Metals, Sumaré, Brazil.

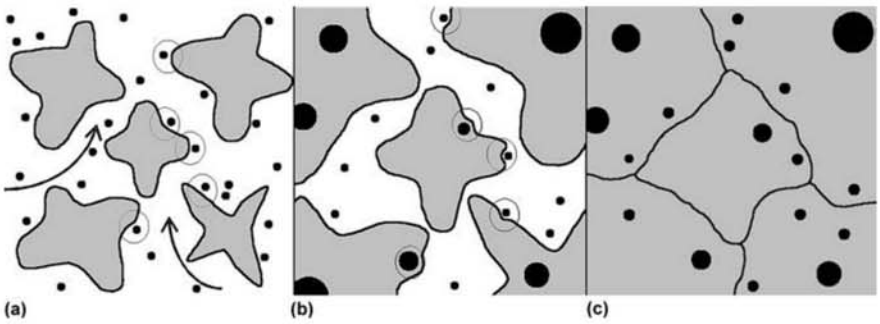

Fig. 8.28 Schematic presentation of the evolution of solidification in a eutectic cast iron with spheroidal graphite. Initially (a) austenite dendrites and graphite particles can grow independently, from the liquid. (b) From about 30% volume fraction of solid phase, graphite particles begin to be trapped by austenite (see also Fig. 8.18b). (c) From this point, graphite particles have their growth controlled by carbon diffusion through austenite. Source: Ref 9

pore (indicated by P), should flow be insufficient, for instance, due to a very long mushy zone. Figures 8.30 to 8.32 present examples of microporosity in a steel casting.

8.5 Segregation in Steel Products

8.5.1 Microsegregation or Dendritic Segregation

When solute redistributes during solidification, segregation can occur. If this is combined with solid growth with a non-planar solid-liquid interface (cellular or, most commonly, dendritic) the resulting solid structure shows chemical composition variations in accordance with the shape that represents the solid-liquid interfaces of the dendrites at each point in the solidification process, as shown in Figure 8.33. Segregation produced in columnar solidification in controlled conditions, in laboratory is shown in Figures 8.34 and 8.35. The difference between cellular and dendritic growth is explained in solidification texts such as Ref 7 and 16. The "cellular" solidification mode in which individual grains may look like "columns" (see Fig. 8.36) because there is no side branching as in the case of dendrites, should not be confused with the columnar structure that is usually a result of directional heat extraction (see the section "The Structure of Ingots and Continuous Casting Products") during dendritic growth.

Two techniques are especially useful for observing dendritic structure in solid metals: chemical etching that preferentially etches segregating elements, and mapping characteristic x-rays of these elements using a properly

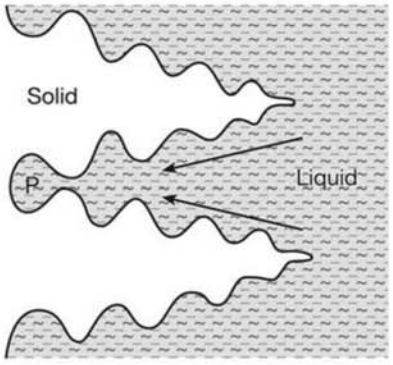

Fig. 8.29 Schematic illustration of the liquid flow needed to compensate solidification shrinkage and the eventual formation of a micropore in the point marked P.

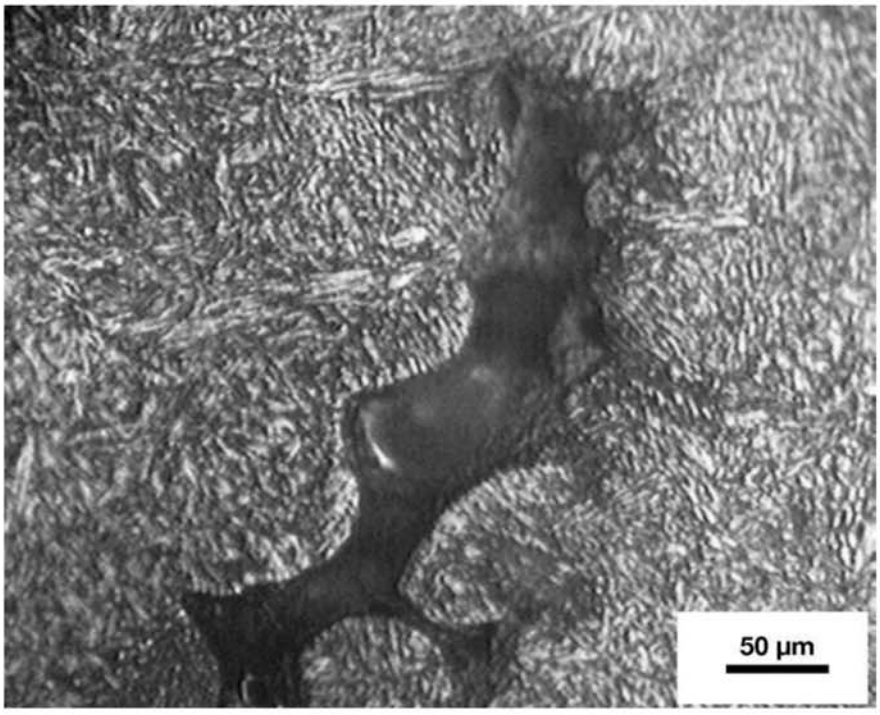

Fig. 8.30 Interdendritic porosity (microporosity) in a steel casting containing 0.28% C, quenched and tempered. The shape of porosity in castings is very similar to the shape of the interdendritic spaces. Optical micrograph. 2% nital etching (porosity is visible without etching).

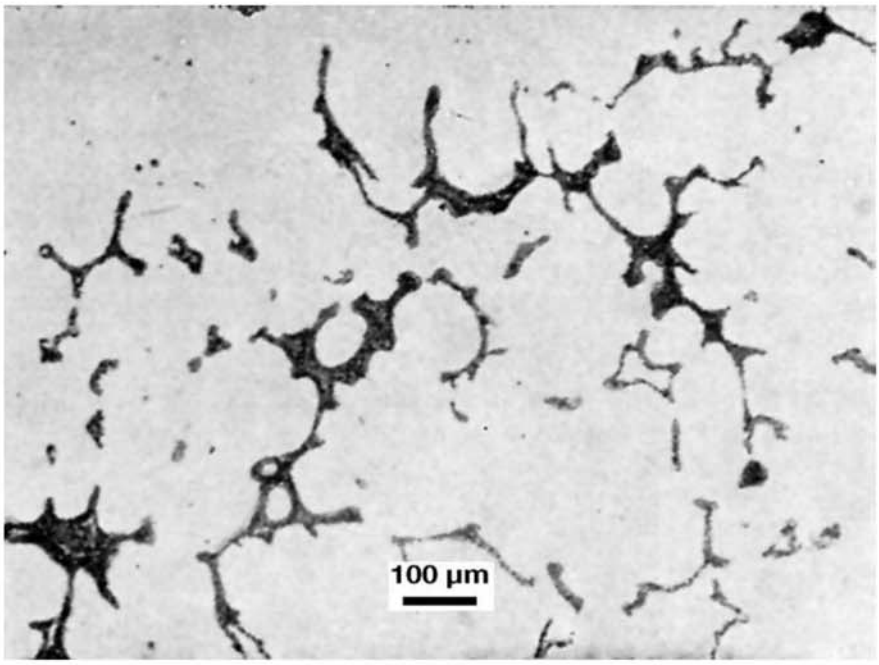

Fig. 8.31 Severe porosity in a steel casting. Optical micrograph. No etching.

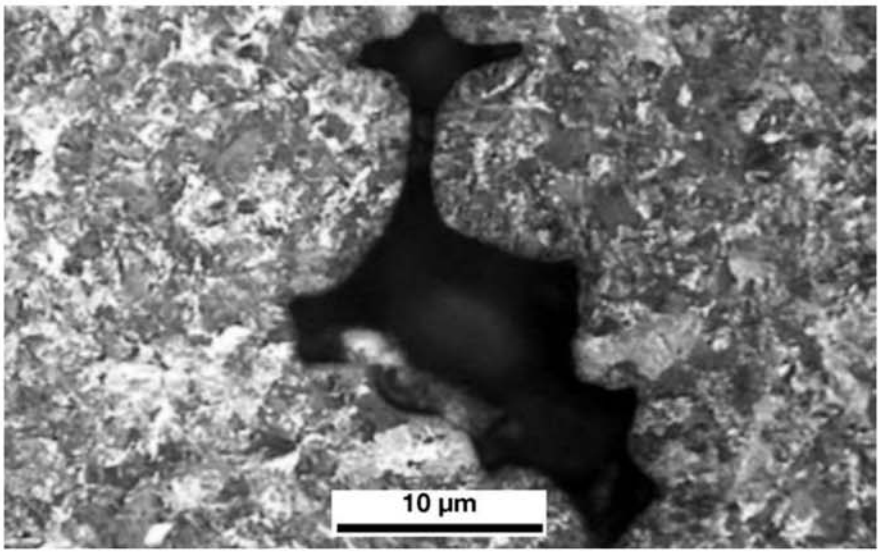

Fig. 8.32 Porosity in cast eutectoid steel. The shape of porosity in castings is very similar to the shape of the interdendritic spaces. Optical micrograph. 2% nital etching (porosity is visible without etching).

equipped SEM or microprobe (see Chapter 6, "Metallographic Technique: Electron Microscopy and Other Advanced Techniques," in this book). When solidification occurs in a controlled way, it is easier to observe and measure the results of solute redistribution. Mizoguchi (Ref 19) performed unidirectional solidification experiments with low alloy steels under conditions that

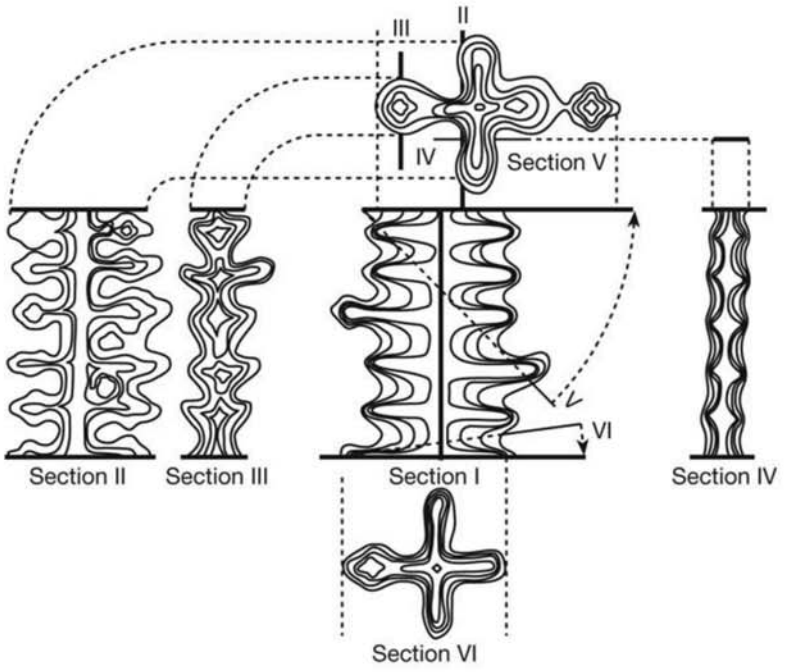

Fig. 8.33 Projections of iso-concentration surfaces (surfaces with the same concentration of solute) in a dendrite in low alloy steel. If the position of these surfaces (or lines, in a plane section) are determined via chemical etching or an analytical method, the dendritic structure is more or less evident. Source: Ref 16

led to nonplanar solid-liquid interface, mostly "cellular." In these experiments a cylindrical steel sample is placed in a tubular furnace that imposes a thermal gradient. The sample is completely melted and then cooled in a controlled way. Finally, the sample is quenched from its final condition. This way, each point in the specimen has a well-defined thermal history, and it is possible to examine the extension of segregation and the structures obtained for each of the thermal cycles, starting with fully liquid steel at 1560 °C (2840 °F) (see Fig. 8.34 and 8.35).

Observing segregation through metallography requires careful technique. The choice of etchant is essential to reveal segregation clearly. In low residual steels, special etching and development techniques may be necessary (Ref 20), as the example in Fig. 8.37 shows.

Conversely, there are cases in which etching a steel sample does not reveal the primary solidification structure. There are different etchants more appropriate for this task, whereas others are more effective at revealing the different phases present in a steel or cast-iron sample, as indicated in Fig. 8.38 to 8.40.

The changes in chemical composition resulting from segregation often result in variations in the microstructure, including changes in the phase fractions and even in the phases present in each region of the material.

In many cases, the composition of the center (or axis) of the dendrites is so different from the composition of the last liquid to solidify that the idea of two different steels juxtaposed is not far from reality.

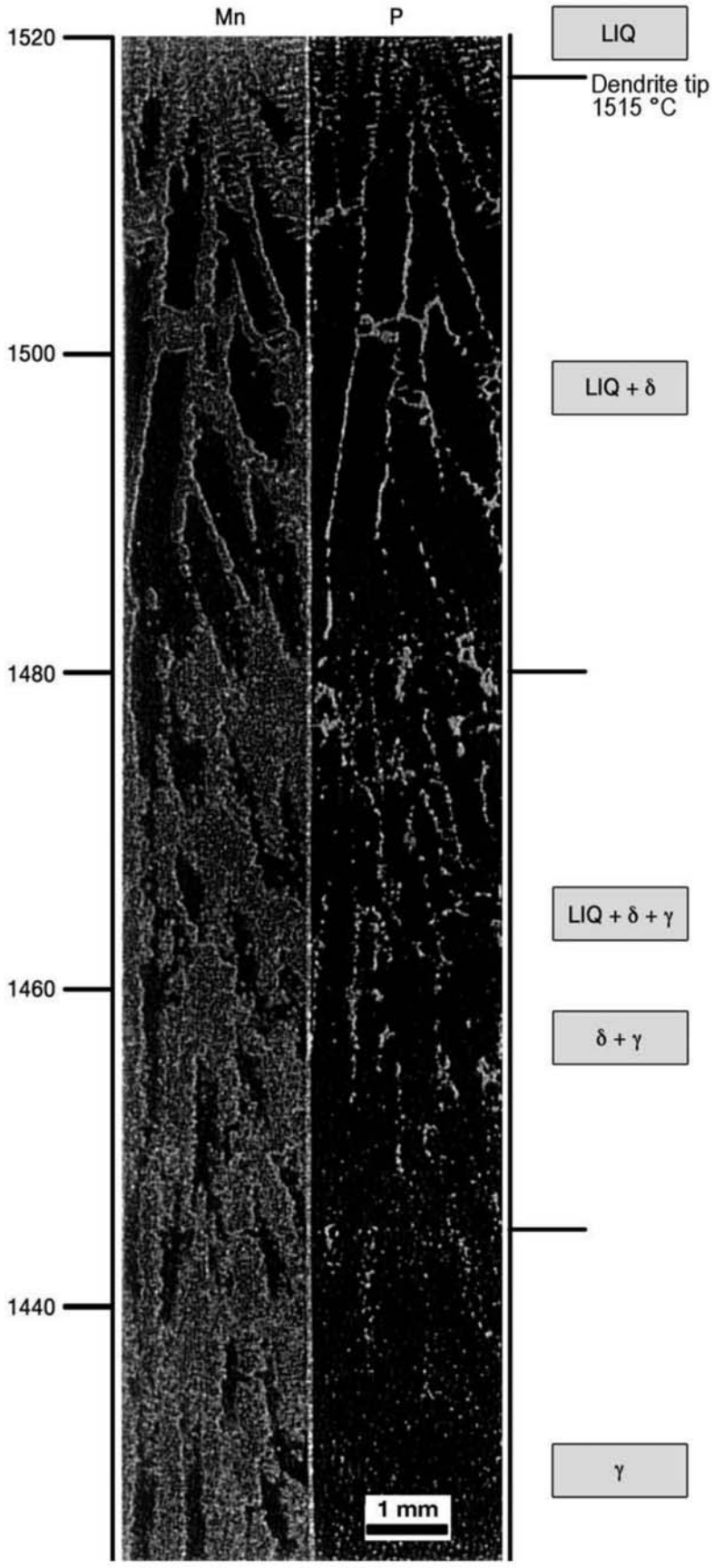

Fig. 8.34 Mapping of characteristic x-rays for elements manganese (varying from 1.3% to 1.6%) and phosphorus (from 0% to 0.03%) in the longitudinal section of a sample that was subjected to controlled cooling followed by quenching. Lighter regions indicate higher concentrations of these elements. The temperature scale to the left indicates the sample temperature at this point when the sample was quenched. The right-side caption indicates the phases present in the sample at the time of quenching. The redistribution of phosphorus and manganese during solidification is evident. Experiments performed with cooling rate of 27 °C/min (48 °F/min) and a steel containing 0.13% C, 1.52% Mn, 0.018% P, 0.35% Si, 0.002% S). Courtesy of S. Mizoguchi.

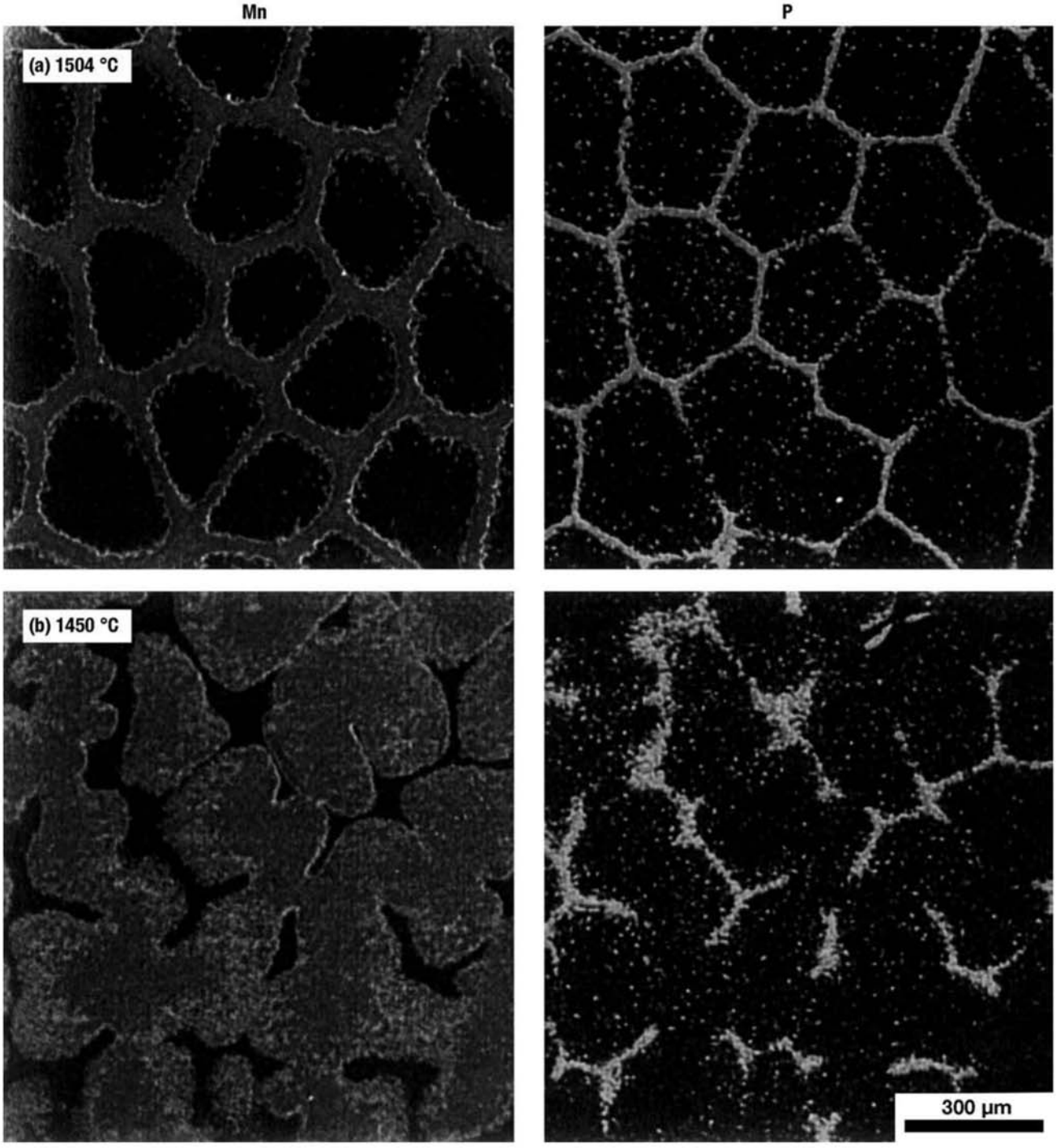

Fig. 8.35 Mapping of characteristic x-rays for elements manganese (varying from 1.3% to 1.6%) and phosphorus (from 0% to 0.03%) in the transverse section of a sample that was subjected to controlled cooling followed by quenching. Lighter regions indicate higher concentrations of these elements. (a) Quenched from 1504 °C (2740 °F). (b) Quenched from 1450 °C (2640 °F). The redistribution of P and Mn during solidification is evident. Experiments performed with cooling rate of 2.7 °C/min (5 °F/min) and a steel containing 0.13% C, 1.52% Mn, 0.018% P, 0.35% Si, 0.002% S. Notice the similarity to the columnar (cellular) structure presented in Fig. 8.36. Courtesy of S. Mizoguchi.

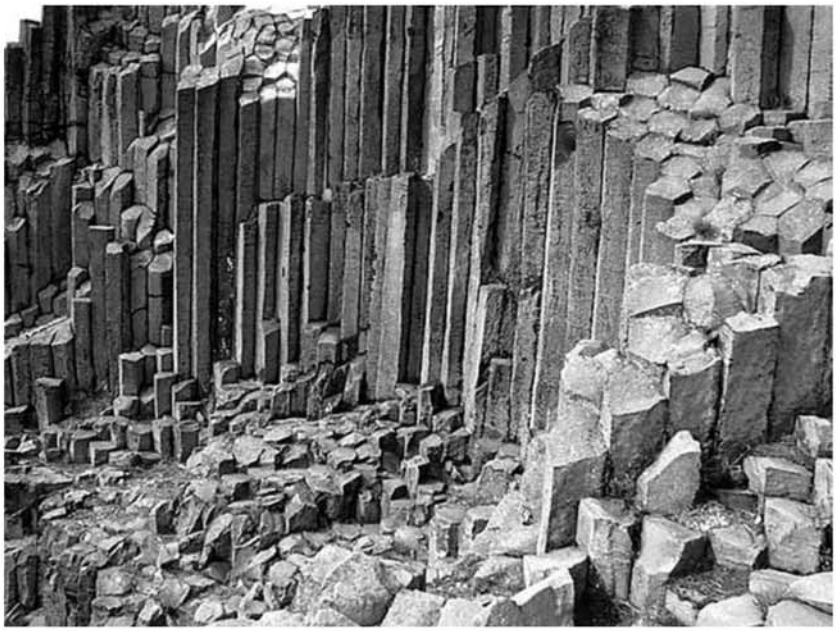

Fig. 8.36 Basalt with columnar structure near the city of Kamenický Šenov, north of Bohemia. Similarity to the morphology of the cellular solidification presented in Fig. 8.35 is evident. Source: Ref 17, 18

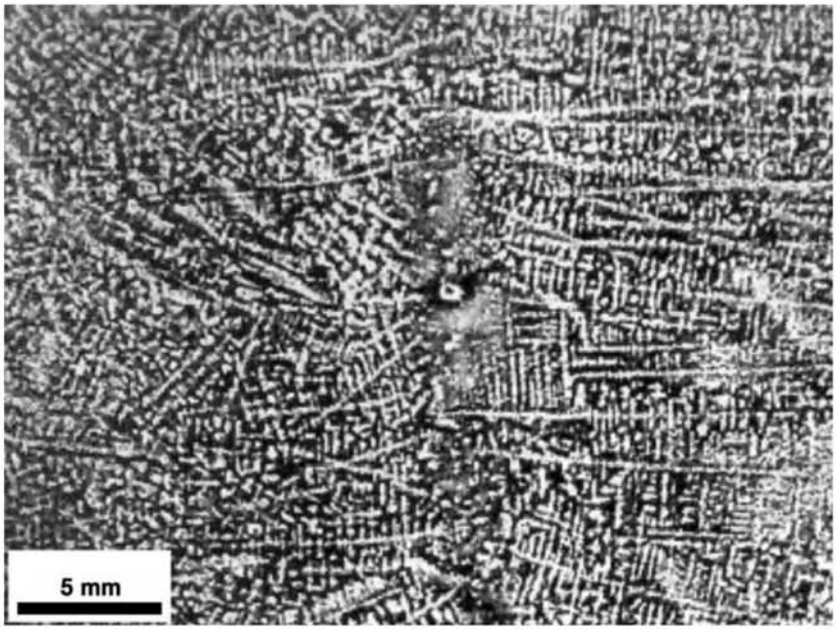

Fig. 8.37 Transverse section of the center of a continuous cast slab. Steel containing 0.08% C, 0.61% Mn, 0.0018% S, 0.005% P. Etching: Humfrey's reagent in two stages (neutral copper ammonium chloride at 12%, followed by immersion in acidified solution of the same chloride, containing 4% vol. of HCl. Etch at room temperature). Intaglio print using ink and press (see Chapter 4, "Metallographic Technique—Macrography," in this book). The morphological similarity to the iso-concentration profiles presented in Fig. 8.33 is evident. Courtesy of J. Casey, DOFASCO, Canada.

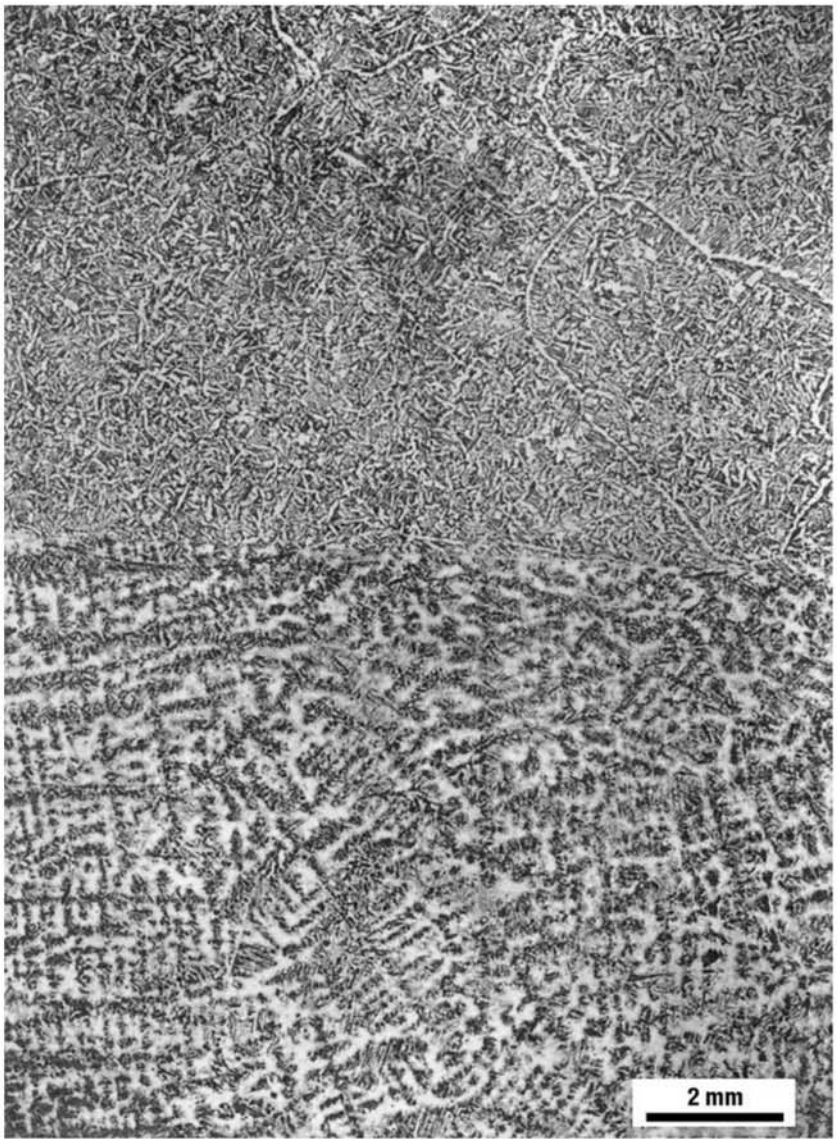

Fig. 8.38 Cast steel with 0.25% C. The sample was etched in two steps using two different etchants. The top part of the sample was etched with 1% nital and shows the ferrite-pearlite microstructure, characteristic of this steel at room temperature in the "as cast" condition, without further heat treatment. Pro-eutectoid ferrite delineates the previous austenite grain boundaries. Inside the grains, ferrite, Widmänstatten ferrite, and pearlite are present. (See Chapter 9, "Conventional Heat Treatments—Usual Constituents and Their Formation," in this book for a detailed discussion of this type of structure). The bottom part of the sample was etched with Oberhoffer reactant, which reveals the primary solidification structure. The low phosphorous regions, corresponding to the center or the axis of the dendrites, are darker while the regions richer in phosphorus are lighter. (The use of oblique illumination after etching with Oberhoffer reactant can change this contrast.) Source: Ref 1

Fig. 8.39 Macrograph of a large (14 t) steel casting. The large interdendritic spacing indicates slow cooling. The straight axes of the dendrites indicate that no mechanical work was performed on the part (i.e., that this is not a wrought steel part: see Chapter 11, "Hot Working," in this book). Etchant: iodine. With this etchant the dendrite axes are lighter the richer they are in ferrite. (Compare with Fig. 8.37.)

Fig. 8.40 Macrograph of a white cast iron. Dendrites are clearly visible. The dendrite axes are dark, as the austenite in these regions has decomposed into ferrite and cementite, probably pearlite. Etchant: Nitric acid (nital). (Compare with Fig. 8.39.)

8.6 Hot Cracking

While steel undergoes solidification, its tensile strength is almost negligible due to the presence of the liquid phase in the structure. Once solidified, the mechanical properties of steel at a high temperature are still relatively low. Appropriate solidification processes must be chosen to minimize significant tensile stresses on the solidified shell to avoid hot cracking. It must be considered that shrinkage in itself is already a source of tensile stress in a solidifying mass. As long as the liquid phase is continuously present in the interdendritic spaces, tensile ductility will be null. Any situation that might result in a decrease of the liquidus temperature will also favor the occurrence of hot cracks (Fig. 8.41).

All phenomena related to shrinkage solidification are present during welding, where restrictions to deformation, and hence the associated stresses, may be more severe.

Figures 8.42 and 8.43 show the interior aspect of cracks in steel subjected to continuous casting. The smooth surfaces of the dendrites indicate that they were covered by liquid at the time of the fracture. Many second-phase particles can be seen on the surface of the dendrites. These particles in many cases have the aspect of films, indicating that they were covering the interfaces between dendrites.

8.7 The Structure of Castings, Ingots, and Continuous Casting Products

8.7.1 Conventional Ingot Casting

Types of Molds—Ingot Casting Techniques

The combined design of ingot and ingot mold is done with the aim of optimizing the ingot solidification variables and considering further hot working after solidification. Ingot molds are normally box-shaped, made of cast iron, and weigh about 1–1.5 times the weight of the desired ingot. A variety of transverse sections are used: square, cylindrical, octagonal (or faceted), and, less frequently, rectangular. Normally ingots are tapered (the cross sec-

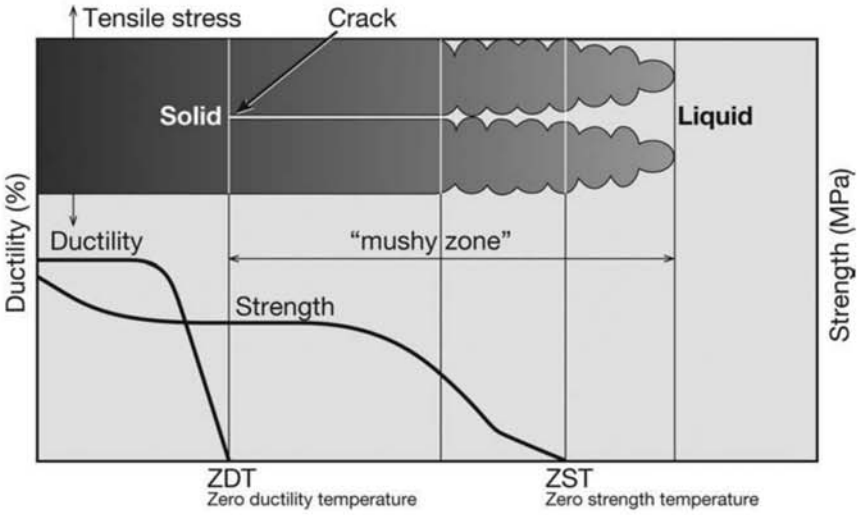

Fig. 8.41 Proposed mechanism for the formation of hot cracks during solidification. Tensile stresses, if applied above the zero ductility temperature (TDZ) will cause separations and cracks. This temperature can be further reduced by impurity segregation, low melting eutectics, and so on. These factors favor the occurrence of hot cracking. Source: Ref 17

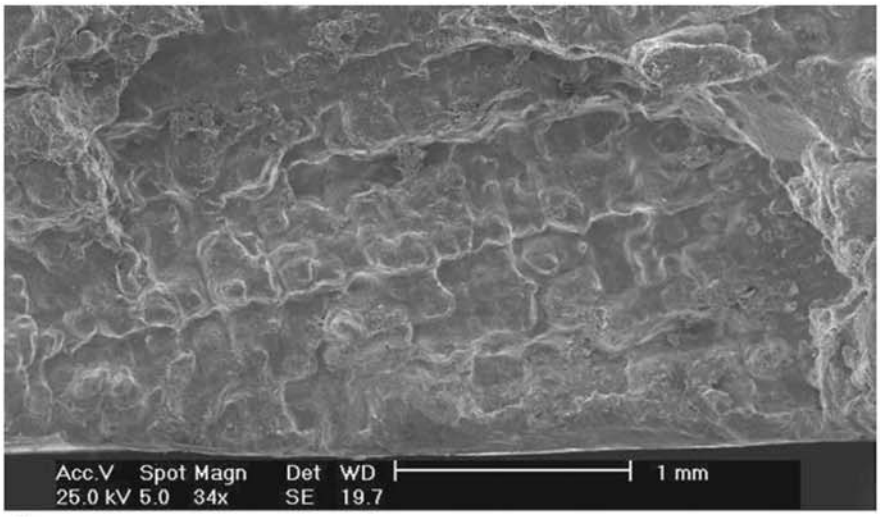

(a)

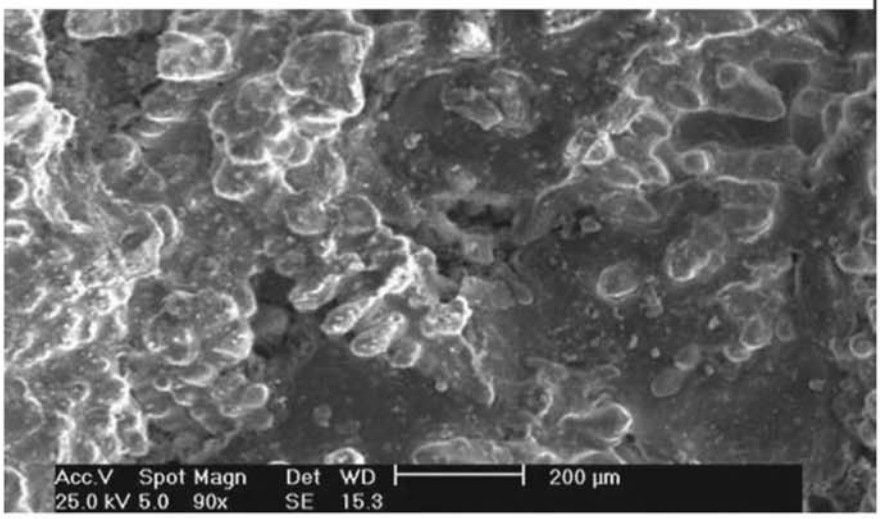

(b)

Fig. 8.42 Surface of hot cracks formed during continuous casting of steel. SEM, ES. The dendritic morphology is evident, even in the low-magnification image at the top. Copyright © 2007 Tenaris. Courtesy of C. Ciccuti, CINI, Argentina.

tion dimensions vary along the ingot height) which favors directional solidification and makes it much easier to extract the solid ingot from the mold once solidification is finished. Concerning the taper, there are two types of ingots: "big end up" and "big end down." Currently, big end up ingots are much more common. Beside the ingot mold design, the main tool used to prevent shrinkage cavities in ingots (pipes) is the use of thermal insulation on the top of the ingot, the so-called hot top (Fig. 8.44 and 8.45). A combination of insulating and exothermic materials can be used, as discussed earlier in this chapter.

When insufficient discard is made from the hot-top region, or when a secondary pipe is present, residual pipe can be found in the wrought products

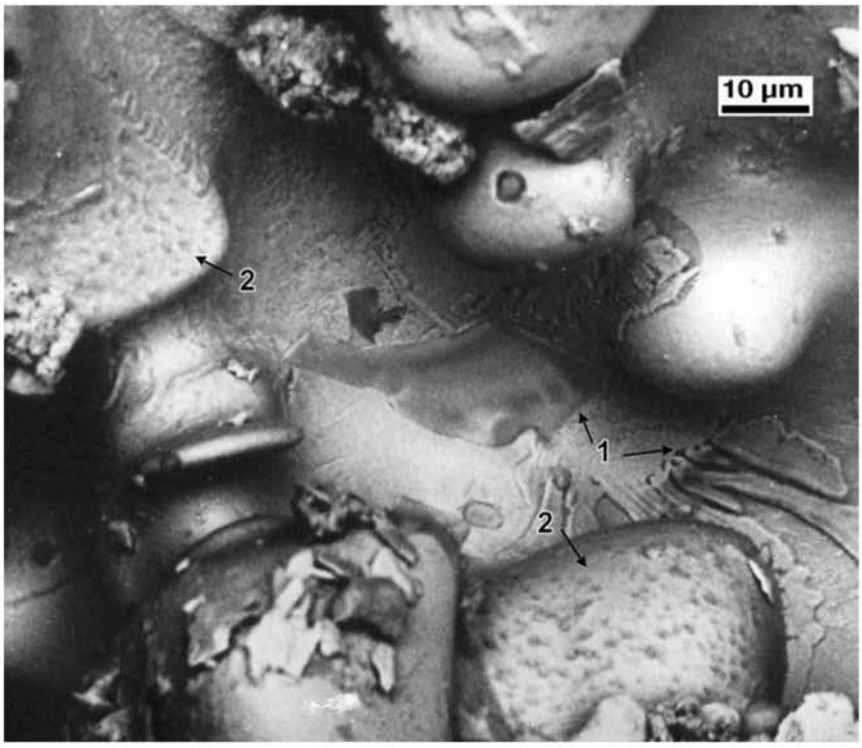

Fig. 8.43 Surface of hot cracks formed during continuous casting of steels. SEM, BE. Points marked as 1 present second-phase particles spread as films over the dendrite surfaces. The small second-phase particles marked as 2 in the fracture surface are probably manganese sulfide (or a manganese sulfide–containing eutectic) that was liquid during solidification and, due to surface tension, compacted to droplets as it solidified over the dendrites (mechanism proposed in Ref 18).

manufactured from these ingots (see Chapter 11, "Hot Working"). These defects are normally identified by ultrasonic inspection.

When cross sections close to circular are needed, in particular for forging ingots, it is common to use a corrugated polygonal transverse section as a better solution, as shown in Fig. 8.46.

8.7.2 Rimming Steels

In the old process of making rimming steel, the nucleation and growth of bubbles (containing mostly CO formed by the C + O = CO reaction) transported the interdendritic segregated liquid to the center of the ingot, as shown in Fig. 8.47. The first steel that solidified close to the mold was subjected to strong cooling from the mold and had fine structure and little segregation. Then the "rim" region was very low in residual elements, because they were pushed to the center. Provided the rimming process was properly controlled and the CO "boiling" started only after a solid continuous shell was formed, the gas bubbles could be welded during hot rolling, resulting in a product with good surface quality (and no need for hot topping, because the gas formation counteracted the shrinkage). This is one example of "macrosegregation" caused by the movement of liquid during solidification inside the ingot.

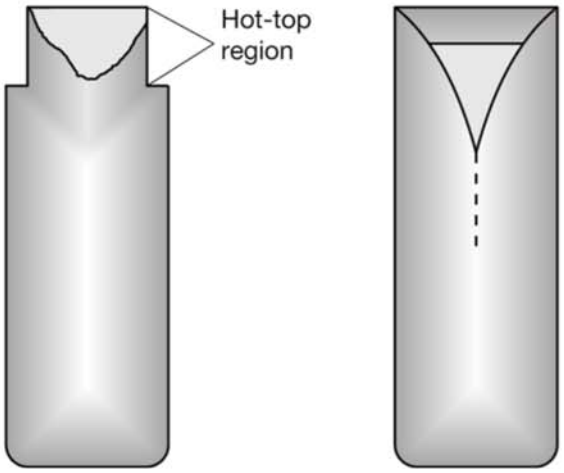

Fig. 8.44 Solidification shrinkage in ingots. Right, an ingot without hot topping. Solidification progresses uniformly along the walls of the mold and a large primary pipe and secondary pipe can be the result of the process. Insulating and/or exothermic materials in the hot top slow down its solidification. The liquid metal contained in the hot top can feed the ingot during the whole solidification process, compensating for shrinkage. All shrinkage volume is concentrated in the hot top. A combination of proper mold taper and mold design with an adequate hot top prevents formation of a secondary pipe. (See Fig. 8.45)

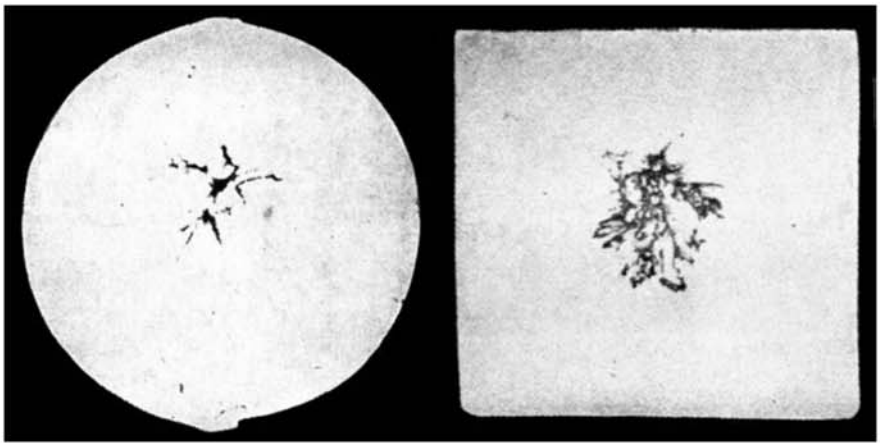

Fig. 8.45 Macrographs showing examples of residual pipe and/or secondary pipe in hot formed bars produced from conventional ingots. No etching.

8.7.3 Continuous Casting (Ref 21, 22)

More than 90% of world steel production is cast with continuous casting. In this system, liquid steel is poured into a water-cooled copper mold. Inside this mold, the first solid shell of the cast strand is formed, and the product is extracted using a mechanical system of traction and supporting rolls. The mold has a slight amplitude oscillation during the casting process to prevent solidifying steel from adhering to it and to make extraction of the solid product easier. Once the formed solid shell is thick enough to resist the pressure exerted by the liquid steel inside it, the strand leaves the mold, and cooling continues by water aspersion in jets or sprays and by radiation until solidification is finished (Fig. 8.48). Different cross sections can be produced via continuous casting. Steelmakers making flat steels produce slabs, usually with a thickness around 250 mm (10 in.), and widths that exceed 1 m (39 in.). The so-called thin slab casting casts slabs with thickness in the range of 80–100 mm (3–4 in.) and can eliminate the first stage of hot rolling. Billets (square or round) are produced by steelmakers making long products and seamless tubes. The casting machine is normally equipped with a tundish that allows

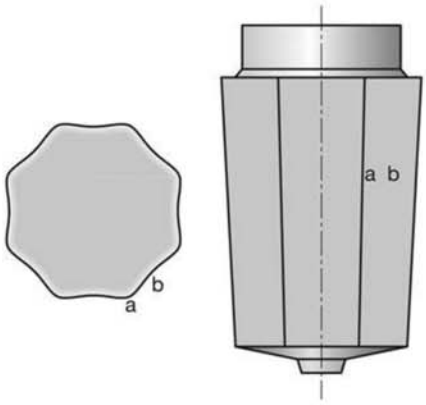

Fig. 8.46 A typical forging ingot. The region marked as "a" solidifies faster than the region marked as "b". Due to its concave shape, region "b" does not suffer tensile stresses from the liquid metal pressure inside the solid shell. Region "a" being thicker earlier in the process is able to resist the stress occurring once the ingot shrinks away from the mold. This type of ingot design greatly reduces the chance of surface hot cracks called "panel cracks".

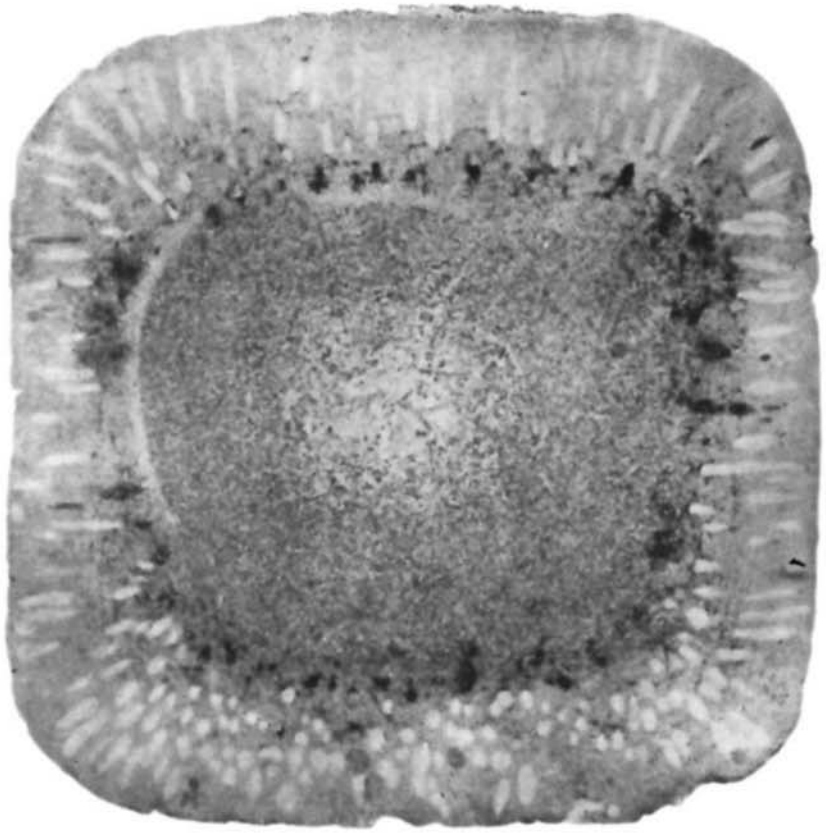

Fig. 8.47 Sulfur print of the transverse section of a steel ingot with many bubbles close to the surface (the border or "rim" of the print). In this steel, sulfides are formed in a region closer to the ingot center, because the segregated liquid has been pushed from the interdendritic regions in the rim by the bubbles. This causes the darker center of the sulfur print. Typical aspect of a rimming steel ingot. Compare to Fig. 8.2

changing ladles without interrupting the casting sequence, so that 10 or more heats can be cast in sequence without interruption in some plants. However, this does impose significant synchronization challenges to the melt shop.

8.7.4 The Structure of Ingots and Continuous Casting Products (Ref 16, 21)

As already discussed, ingots are castings that are designed to optimize their solidification structure, taking into consideration the hot working steps that follow the casting operation. Commercial ingots normally present three zones with different characteristic structures, as indicated in Fig. 8.49.

- Fine equiaxial zone in the surface: this zone is formed due to the copious nucleation that occurs once the metal is poured and makes contact with the cold walls of the mold. Crystals in this zone are dendritic and equiaxial. Their growth is limited by the presence of other nuclei and impingement from the growing crystals.

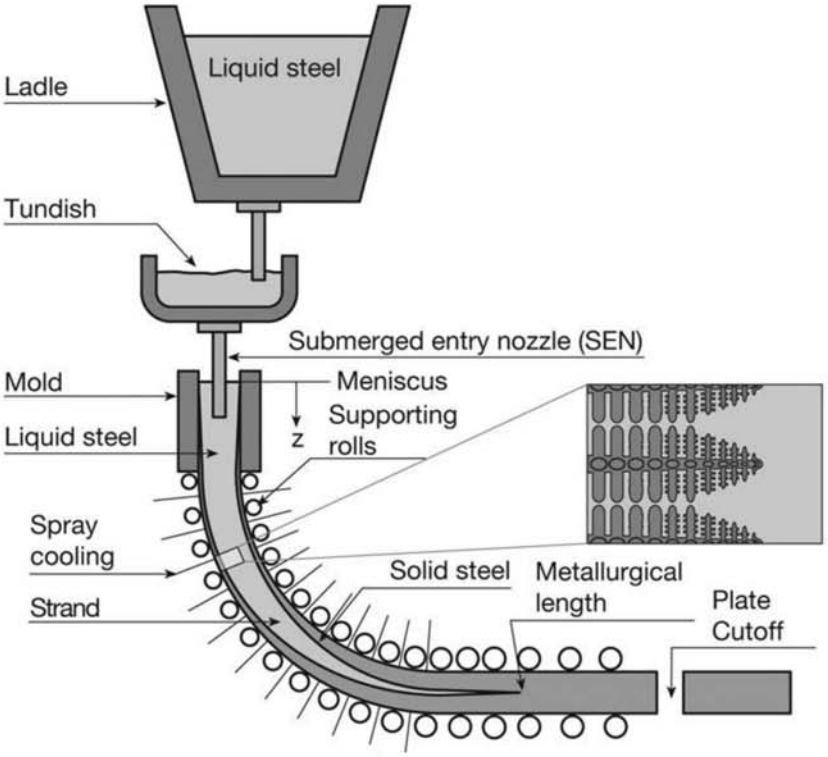

Fig. 8.48 Schematic presentation of a continuous casting machine. Solidification is concluded several meters away from the level of the meniscus formed inside the mold. (This distance is called the "metallurgical length" of the caster). Typical casting (or strand) velocities are in the range of 1 m/min. With the large metallurgical length of modern caster, almost all continuous casting machines have curve strands. For this reason, the solidified structure is not perfectly symmetric. (See Fig. 8.52)

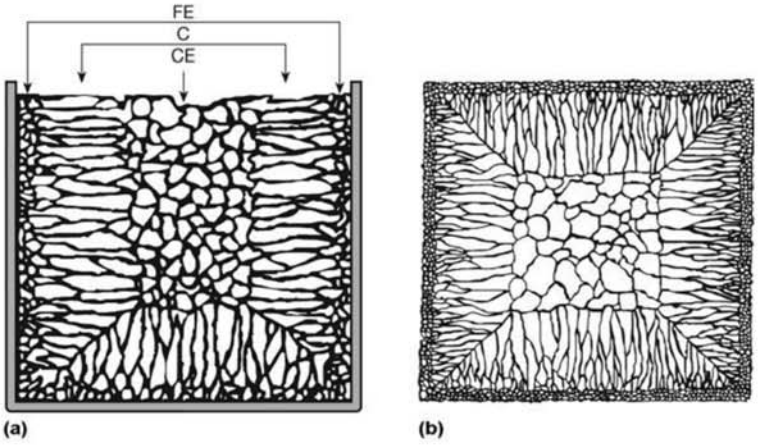

Fig. 8.49 The different structural areas that may occur in an ingot, (a) longitudinal and (b), transverse section. Fine equiaxial zone (FE), columnar zone (C) and central equiaxial zone (CE). The extension of each zone depends on the alloy being cast and on the casting conditions. The same structures are present in continuous casting products. Adapted from Ref 5

- Columnar zone: as the equiaxial zone grows toward the center of the volume of poured steel (opposite to the heat extraction direction), crystals with directions favorably oriented with respect to the heat flux will grow faster than the others, limiting their further growth, as presented schematically in Fig. 8.50.
- Central equiaxial zone: should the liquid inside the mold get undercooled, central equiaxial growth may occur. This growth can be nucleated by nuclei formed in the central region or dendrite tips that may be broken and transported by convection in the liquid metal.

It must be kept in mind that the three zones may not always be present in commercial ingots. The formation and extension of each zone may be promoted or not depending on several factors, such as casting variables and alloy composition.

Continuous casting products present the same evolution of possible structures along their cross sections. Close to the mold, a fine equiaxial zone is formed, followed by a columnar zone. A central zone of equiaxial crystals is also frequently observed, as shown in Fig. 8.51. The most important variable influencing the relative extension of the columnar and central equiaxial zones

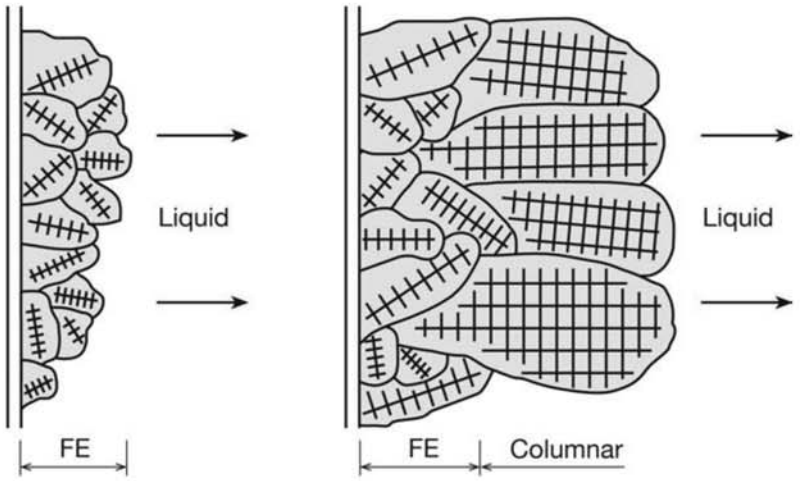

Fig. 8.50 Transition from fine equiaxial zone (FE) to columnar growth zone. Grains with favorable crystallographic orientation with respect to the heat extraction directions will grow faster and dominate the structure. Adapted from Ref 5

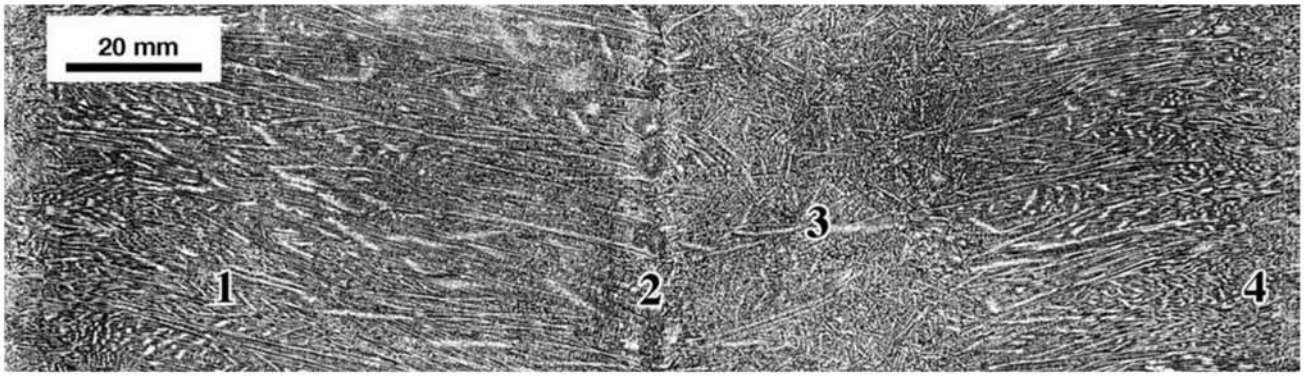

Fig. 8.51 Macrograph of the longitudinal plane of a continuous cast plate of pipeline steel (0.08%C, 0.61%Mn, 0.21%Si, 0.0018%S, 0.005%P). (1) Columnar region (2) Center line, (3) Equiaxed "central" region, (4) Fine equiaxial region. As solid steel sinks in liquid steel, the equiaxed crystals will show a tendency to sink in the strand. Thus, in a curved strand, the exterior region of the strand (larger radius) will show a trend of concentrating the larger extent of the equiaxial region. This region, thus, is not symmetric in curved strand machines. Etching: two-stage Humfrey (see Chapter 4, "Metallographic Technique—Macrography," in this book). Intaglio print. The low sulfur content of this steel makes a sulfur print impossible. The low contents of phosphorus and carbon make a conventional macrograph very difficult to evaluate, due to low etching contrast. The technique used improves contrast and makes possible the photographic record. Courtesy of J. Casey, DOFASCO, Canada.

is casting superheat (the difference between the casting temperature and the liquidus temperature of the steel being cast) (Ref 5, 23, 24). Figure 8.52 shows the effect of the superheating in continuous casting on the extension of the columnar and central equiaxed zones.

It is important to understand how different structures develop in steel from the start of solidification until the end of complete cooling and finally during thermomechanical treatment. As the columnar grains are formed, with the same crystallographic orientation, they can create grains of the first solid phase, or during cooling, they can suffer solid state transformation, masking the grain boundaries that originate in solidification. Figure 8.53 presents an example in which different scales of the formed structure can be observed. In this low-magnification image, columnar crystals are clearly visi-

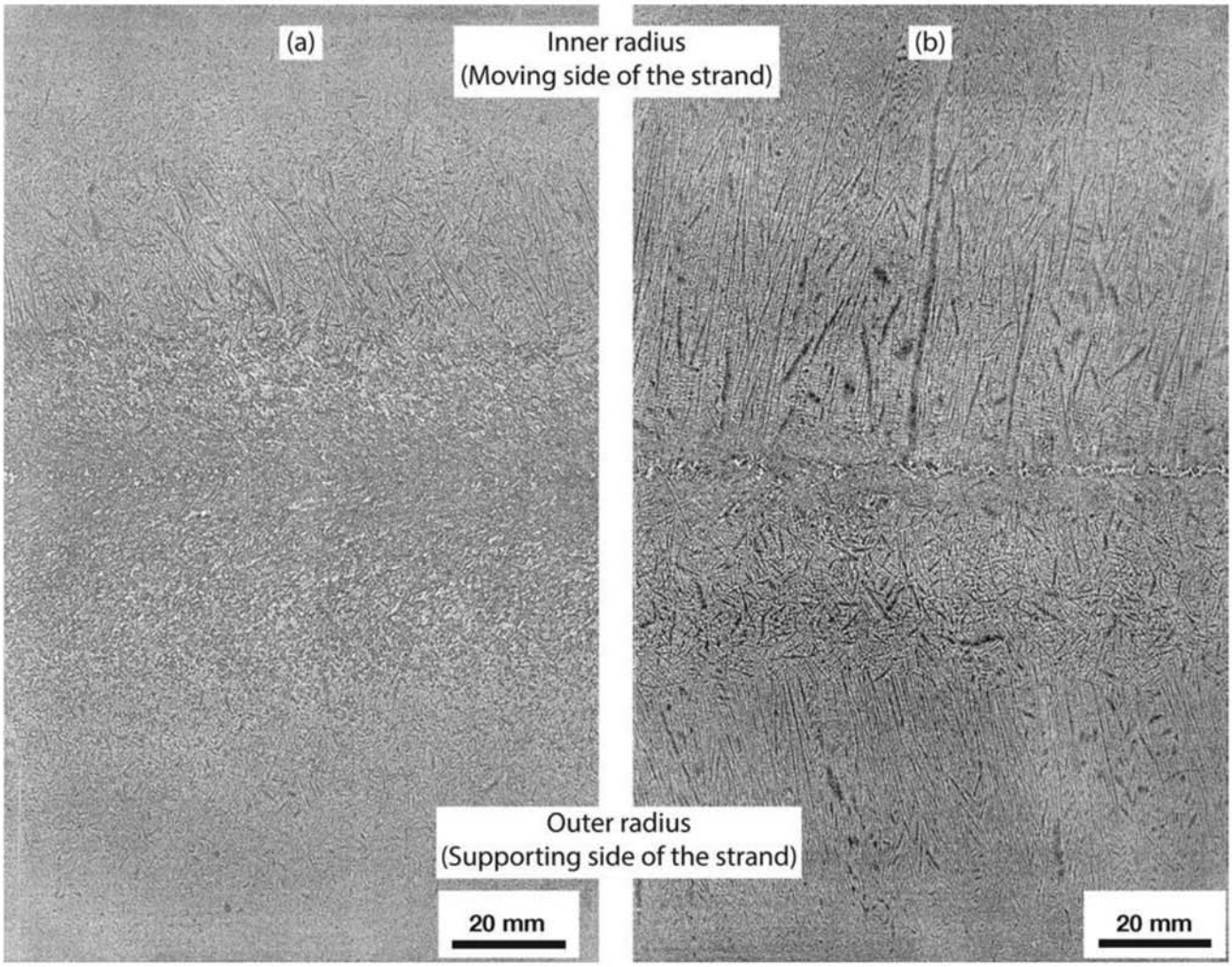

Fig. 8.52 Macrograph of the longitudinal plane of a continuous cast plate of pipeline steel resistant to hydrogen induced cracking (HIC). (a) low superheat. (b) high superheat. All other casting and compositional parameters kept constant. The larger extension of the columnar zone and the coarser structure of the dendrites is clear in the product with higher superheat. Etching: two stage Humfrey (Chapter 4, "Metallographic Technique—Macrography," in this book). Intaglio print. The low sulfur content of this steel makes a sulfur print impossible. The technique improves contrast and makes possible the photographic record. Courtesy J. Casey, DOFASCO, Canada.

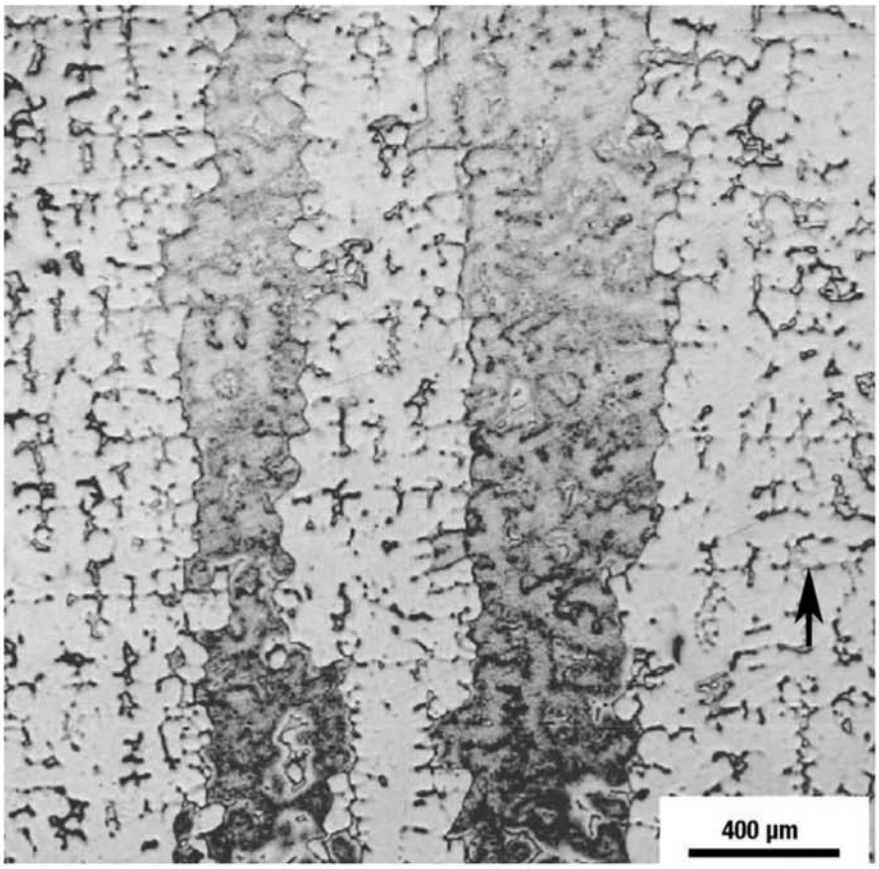

Fig. 8.53 Micrograph of a sample of stainless steel AISI 316 subjected to unidirectional solidification in the direction indicated by the arrow. Columnar grains from solidification are evident. Dendrite images are clearly visible because this steel initially solidifies as austenite, and ferrite precipitates during the final stages of solidification. The ferrite grain, in this case, indicates the shape of the dendrites while the austenitic grains, the columnar crystals. Etching: Electrolytic with 60 ml HNO_3 mixed with 40 ml H_2O at 1.1 V. With permission from Springer Science and Business Media. Source: Ref 25

ble. The characteristic phase distribution associated with dendritic solidification can also be observed. The microstructure of stainless steels is discussed in detail in Chapter 16, "Stainless Steels," in this book. Figure 8.38 is also a good example of the wealth of information accessible to a careful metallographer.

The different macrostructures of a continuous cast slab of low carbon steel and of high-purity steel are shown in Fig. 8.51 and 8.52. The asymmetry of the equiaxial central zone, typical of curved strands, can also be seen.

Another way of altering the ratio between the zones of columnar and central equiaxial structure is by using electromagnetic agitation of the liquid during solidification. The agitation favors the fracture of the dendrite ends that can act as nuclei of equiaxial crystals. It also enhances heat transfer and the removal of the casting superheat (Ref 22). Figure 8.54 presents the effect of electromagnetic stirring in a cylindrical mold. Another example of the effect of this technique can be seen in Fig. 15.38.

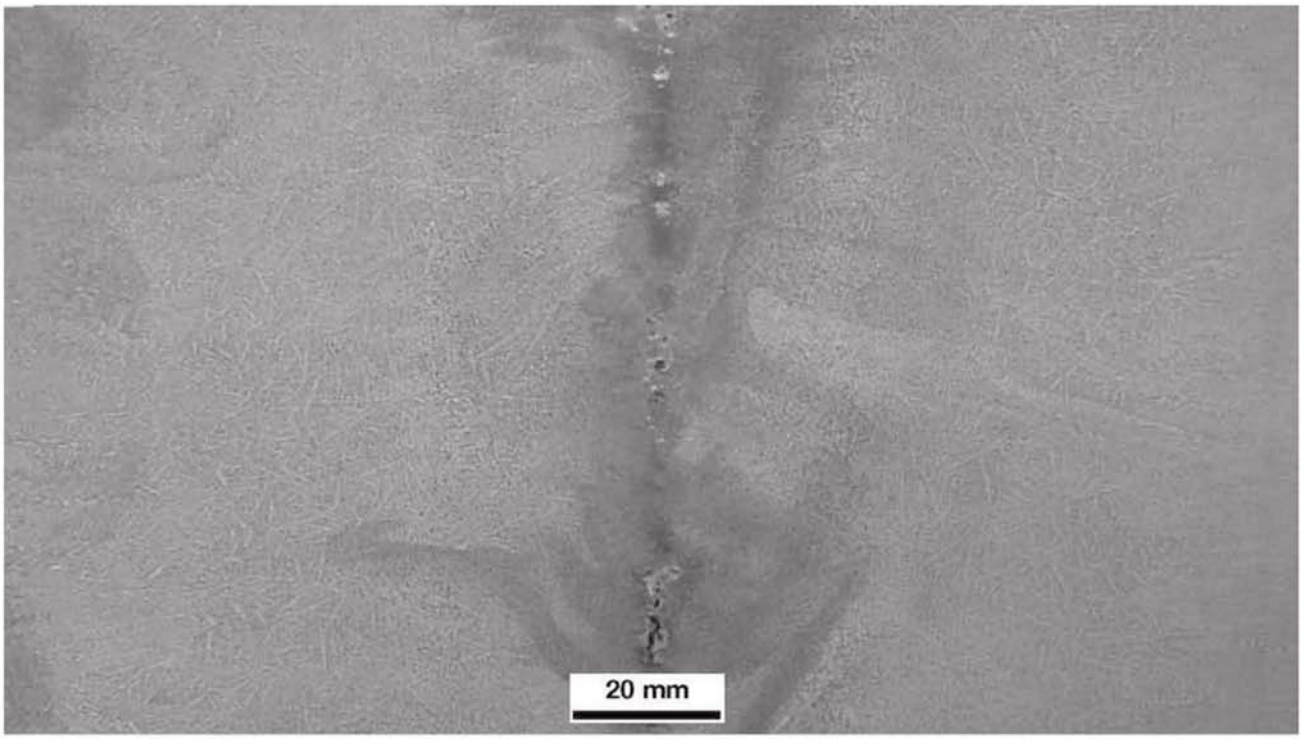

(a)

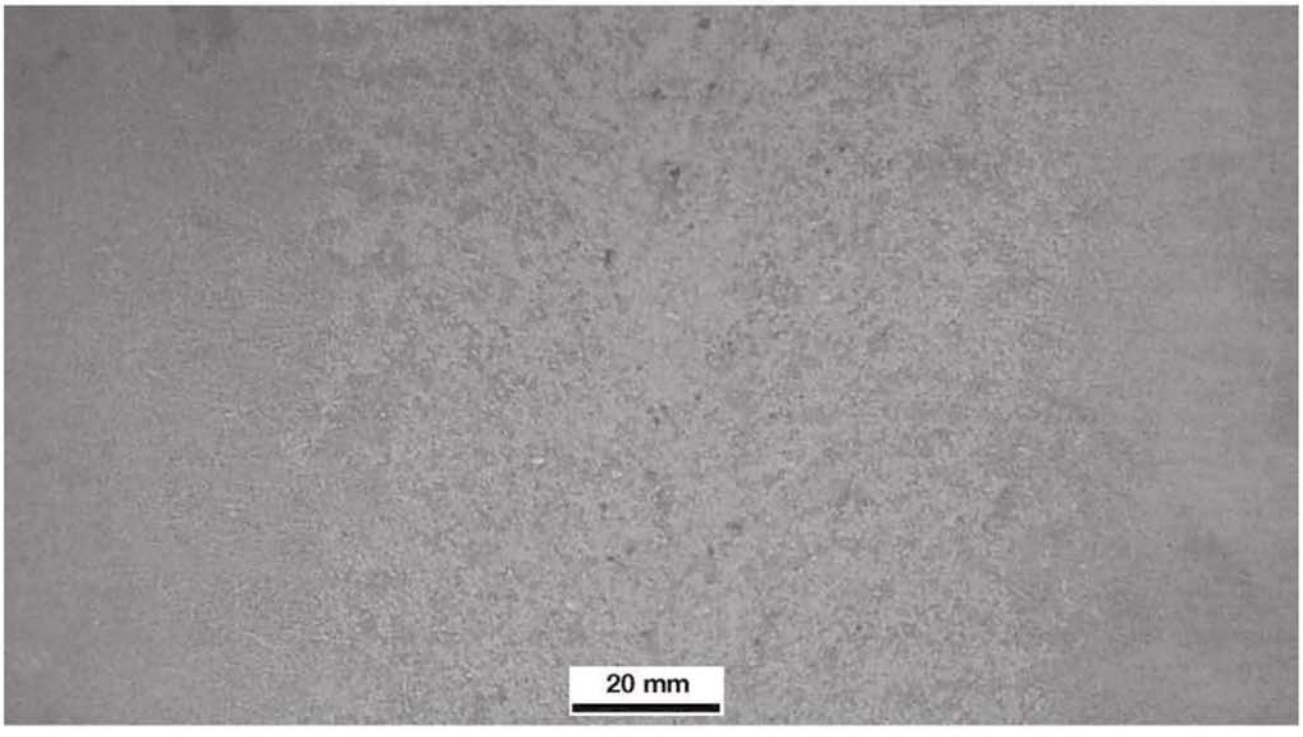

(b)

Fig. 8.54 Macrograph of the longitudinal plane of a cylindrical billet of N80 steel for pipelines, produced in continuous casting. (a) No magnetic stirring. Columnar structure and centerline porosity are evident (drying marks can also be seen in the macrograph). (b) With magnetic stirring. Finer structure, ample central equiaxial zone. Etchant: hot hydrochloric acid etchant. Courtesy of Vallourec Tubes do Brasil.

8.8 Macrosegregation

Besides the segregation that happens at the interdendritic scale, segregation can also occur at a larger dimensional scale, in particular due to movements of the interdendritic liquid (Ref 26). There are two main causes of this movement: (a) density differences between the segregated interdendritic liquid and the nonsegregated liquid, ahead of the solidification front, and (b) other forces that may cause interdendritic liquid movement.

"A" Segregates or "Freckles"

When the density difference between the interdendritic liquid and the liquid ahead of the solidifying front is sufficiently large, convection currents may appear. This convection normally happens preferentially through "channels" in the mushy zone. These channels are created and enlarged by the flow of liquid and the liquid characteristics. Phosphorous and sulfur are two elements with a large effect over the liquid density when segregated (Ref 5, 27). In ingots the channels formed by liquids of lower density (such as those enriched in phosphorus) transfer liquid up, enriching the region close to the top of conventional ingots in the segregating elements. Evidently, the density differences are small, and these phenomena show themselves with more intensity either in large ingots or in steels that have a composition especially prone to causing these changes in density. Figures 8.55 and 8.56 show the main features of conventional ingots, and "A" segregates (sometimes also called "inverted V" segregates) are indicated.

8.8.1 Remelting Processes

In conventional ingot casting processes, the total mass of the ingot is poured at approximately the same time inside the mold and left to solidify. In continuous casting, the solidification conditions are frequently limited by the requirements of productivity and operational stability. These processes can generate conditions to the occurrence of segregation such as "A" segregates discussed above, and "V" segregates, which will be discussed later. It is clear that these heterogeneities are acceptable in most steels in normal applications. However, as requirements increase, failures are commonly caused by or originated in these segregates. An alternative, in this case, is the use of a remelting process, which, by controlling the heat input and extraction, makes it possible to have a progressive solidification, as shown in the scheme in Fig. 8.57, while performing additional refining of the steel.

There are two processes most commonly used for remelting steels: electroslag remelting (ESR) and vacuum arc remelting (VAR). The specific characteristics of these processes are compared elsewhere (Ref 5, 29). Their solidification characteristics are somewhat similar.

Figure 8.58 presents a typical macrograph of the longitudinal section of a remelted ingot. However, to achieve proper quality, remelting must be controlled and the solidification parameters kept within the desired ranges. If the solid-liquid zone becomes too wide in the remelting process, "A" segregates can be formed. As the most common observation involves macrographs of transverse sections, when these segregates appear as segregated channels with approximately circumferential cross sections that etch with significantly different shades from the matrix, they are commonly called "freckles." In the

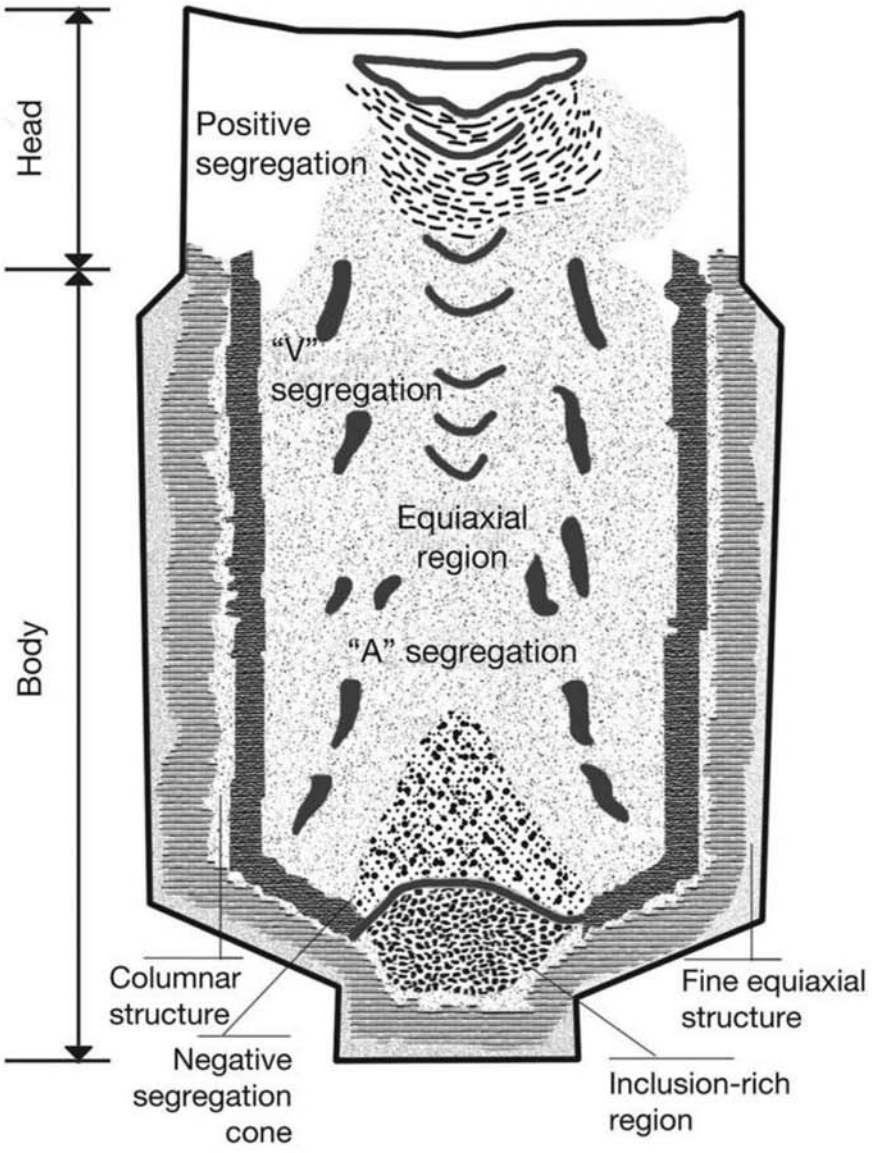

Fig. 8.55 Main structural features of a killed steel conventional ingot. Source: Ref 5

longitudinal section of the ingot, these segregates show as typical "A segregates" as shown in Fig. 8.59 and 8.60.

"V" Segregates

During the final stages of solidification, the central region of the ingot or the casting may already contain a significant fraction of solid phase. Conditions that force the liquid phase to move through this region can appear, for instance, when "feeding" regions that are separated from the hot top or from the feeders by a considerable extension of this solid-liquid mixture with relatively low permeability to the liquid. In these cases, the stresses caused by "suction" associated with the shrinkage may be such that this

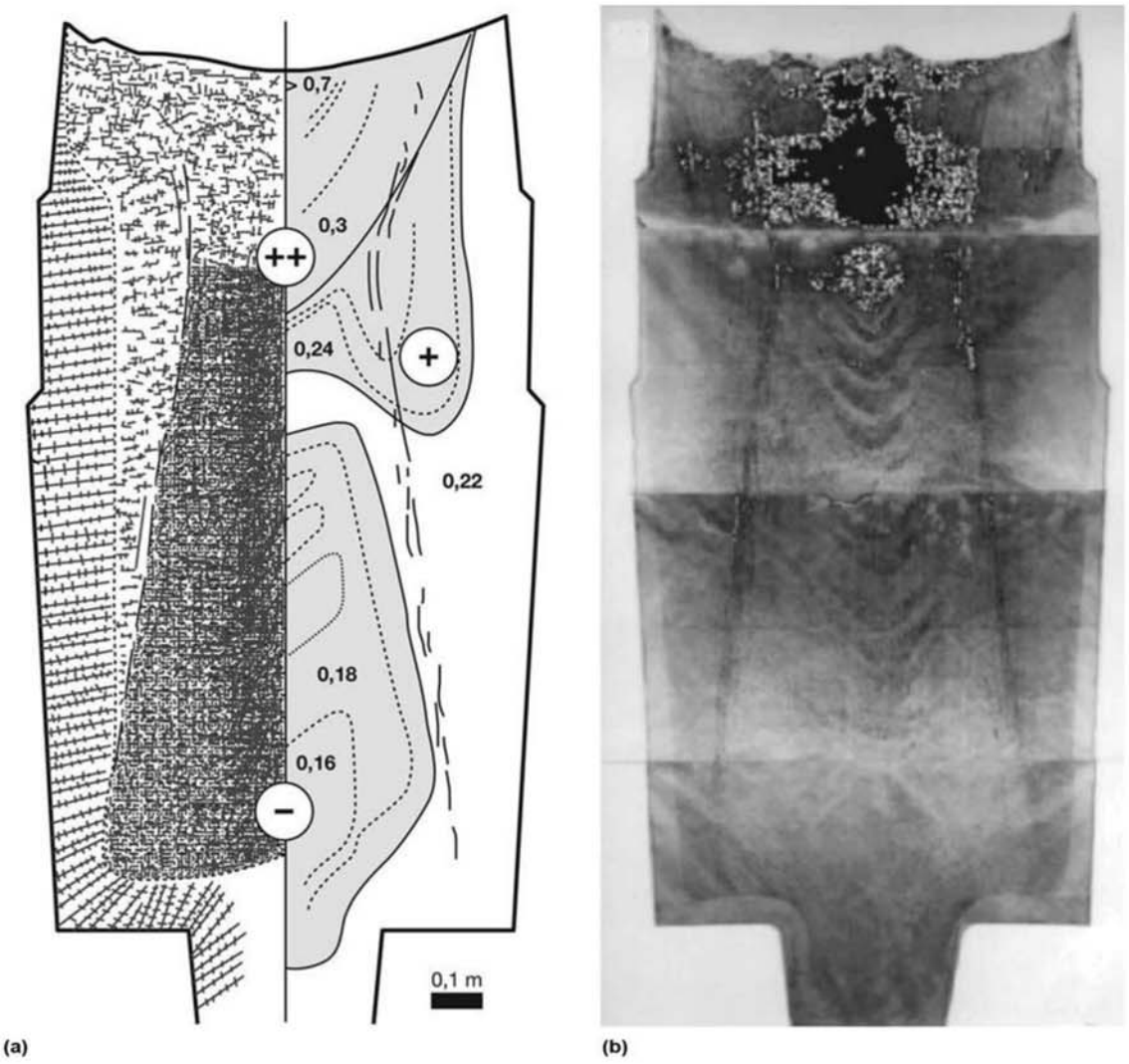

Fig. 8.56 (a) Carbon content mapping in the longitudinal section of a 65 t conventional ingot of killed steel containing 0.22% C. Positive and negative segregation regions are evident. (b) Sulfur print of the longitudinal section of the same ingot. "A" and "V" segregates, schematically presented in Fig. 8.55, can be seen, as well as the positive segregation of sulfur to the top of the ingot. Reprinted with permission from Elsevier. Source: Ref 28

two-phase region may shear in planes at about 45°, with the suction direction forming feeding channels, called "V" segregation. These segregates can be clearly seen in the sulfur print of Fig. 8.56. Figure 8.61 shows the occurrence of these segregates in a steel casting.

8.9 Monitoring the Quality of Continuous Casting Products

In conventional ingot casting, significant movements are absent after pouring, and in the remelting process, the solidification front slowly advances through the continuous but slow addition of liquid metal (from the melting electrode). Continuous casting processes are characterized both by high rates of addition of liquid metal and by the need to move the solidifying product as it is formed. These two features introduce significant stresses in the

strand, while the occurrence of movements in the liquid phase during the casting process may give rise to specific problems.

Figure 8.62 illustrates the "bulging" mechanism that originates movement of the interdendritic liquid in continuous casting. Besides the bulging mechanism, other similar mechanisms, mostly related to the alignment and positioning of the supporting rolls, are responsible for stresses that can cause cracking, for instance. It is important to notice that the correct positioning of the rolls is not a trivial question, because as the steel travels along the caster, it suffers shrinkage, thermal contraction, and possibly solid-state phase transformations. The rolls are responsible for properly supporting the strand

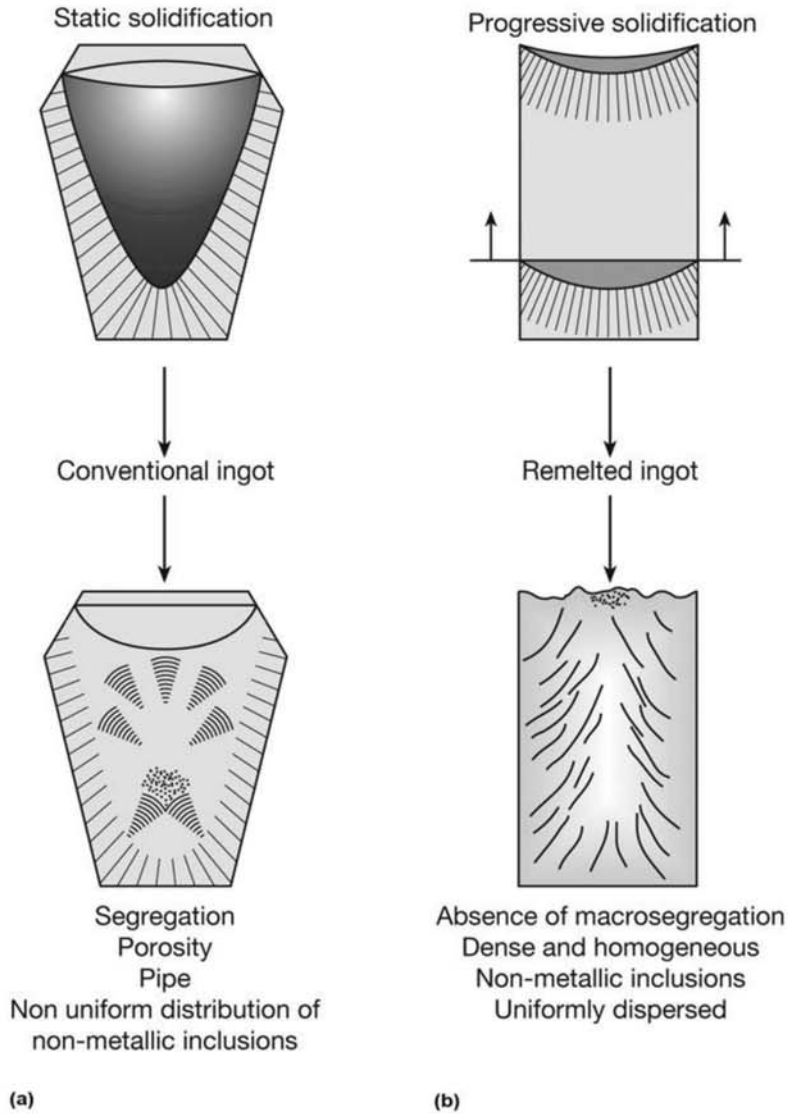

Fig. 8.57 Schematic progress of solidification in a conventional ingot (a) and in a remelted ingot (b). For approximately the same ingot size, the amount of liquid metal present at each moment is much smaller in the remelting process, which results in a more homogeneous structure.

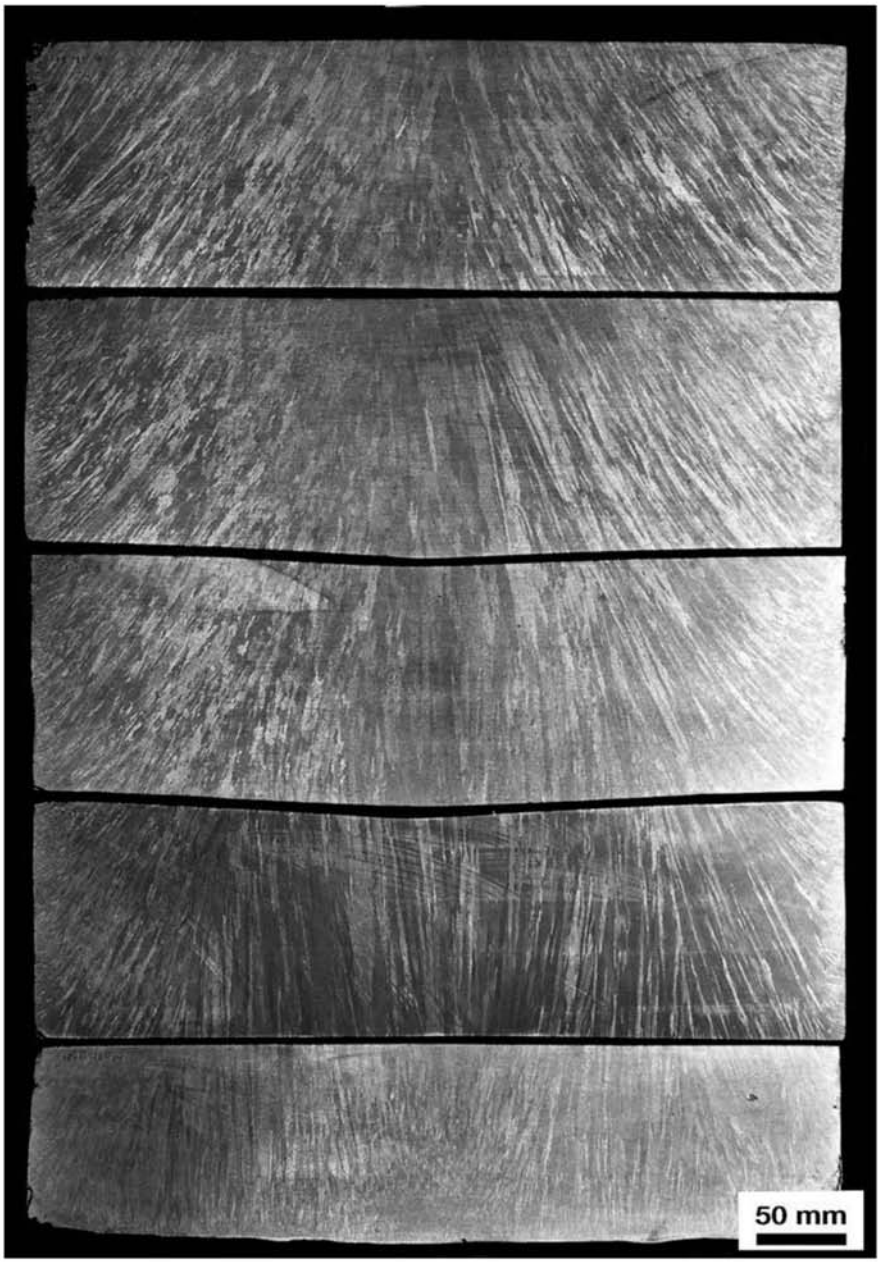

Fig. 8.58 Macrograph of the longitudinal section of an INVAR (iron-nickel alloy) VAR ingot with 550 mm (22 in.) diameter. Structure is extremely homogeneous. The orientation of the columnar crystals makes it possible to estimate the contour of the liquid pool at each moment of the remelting process since the columnar crystals grow essentially perpendicular to the solidification front. Courtesy of A. Mitchell, University of British Columbia, Canada.

while not causing additional stresses. One usual way of controlling the quality of the as-cast product is to perform macrographs and sulfur prints during the casting sequence.

Because the continuous casters are long and have many supporting rolls and independent cooling regions, it is very important to be able to properly

Fig. 8.59 Macrograph of the longitudinal plane of 18% Cr 18% Mn steel remelted via electroslag (ESR). "A" segregates or "freckles" are visible. Courtesy of A. Mitchell, University of British Columbia.

identify in the macrograph or the sulfur print the approximate region of the caster where the problems might have originated. For this purpose, correlations between solidification time and solid thickness (Fig. 8.63) are normally used.

Figures 8.64 to 8.67 present typical sulfur prints and macrographs made during continuous casting of industrial flat products.

8.10 Nonmetallic Inclusions

Liquid steels contain many nonmetallic elements in solution. In particular, oxygen, sulfur, and nitrogen are common solutes. Oxygen and sulfur can form low melting point compounds (see, for instance, the Fe-O phase diagram, Fig. 2.9, Chapter 2, "Processes in Steel Production," in this book). Thus, the basic strategy for controlling oxygen and sulfur in steel involves reducing their contents as much as possible and then retaining the remaining quantities in the

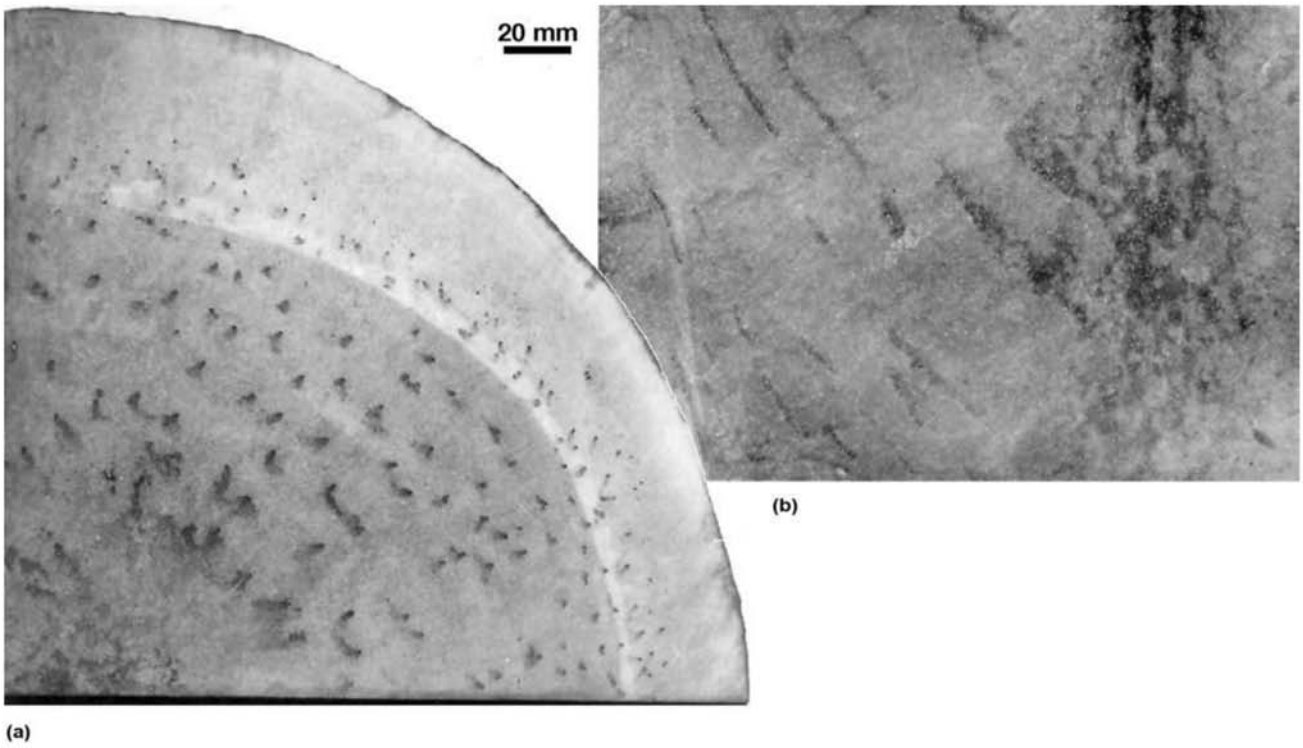

Fig. 8.60 "Freckles" in an ESR remelted ingot made of Ni-Fe-Cr alloy IN718. (a) Ingot transverse section. (b) Ingot longitudinal section. Courtesy of A. Mitchell, University of British Columbia.

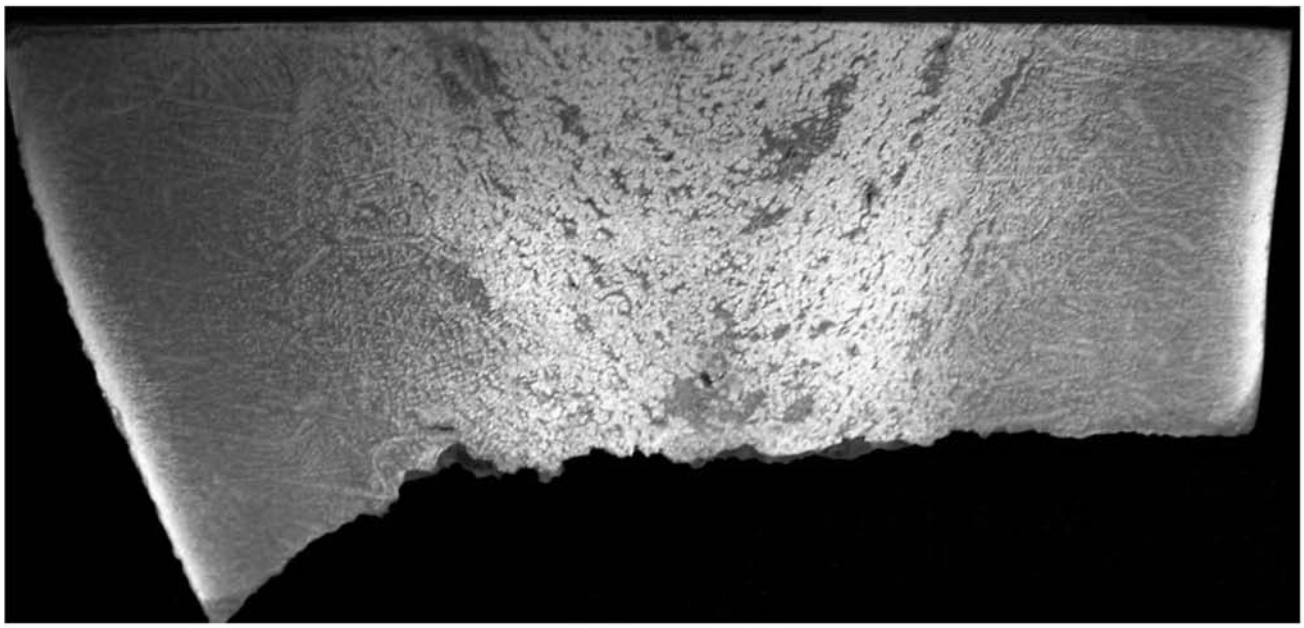

Fig. 8.61 Macrograph of a plane transverse to a fracture in a steel casting. (The fracture surface is at the bottom of the image.) The central region of the casting presents strong "V" segregation and some porosity. Etchant: hot hydrochloric acid

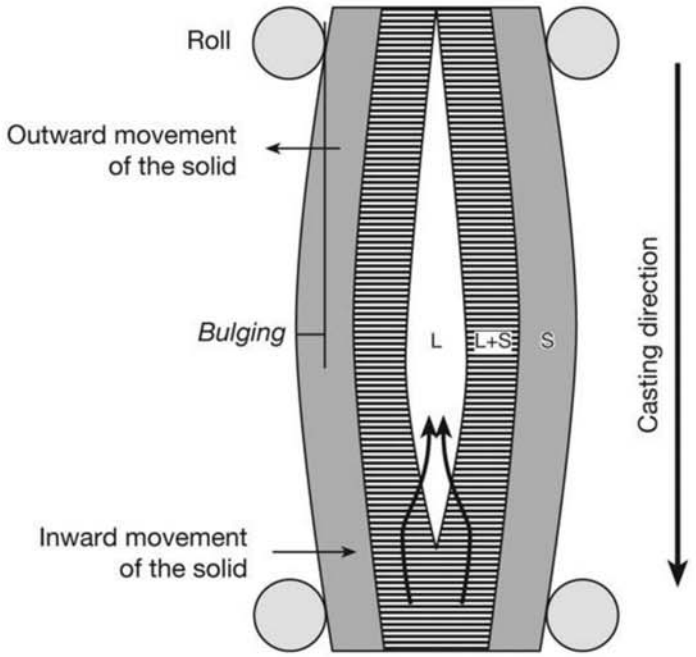

Fig. 8.62 "Bulging" mechanism that originates movement of the interdendritic liquid in continuous casting. Source: Ref 5

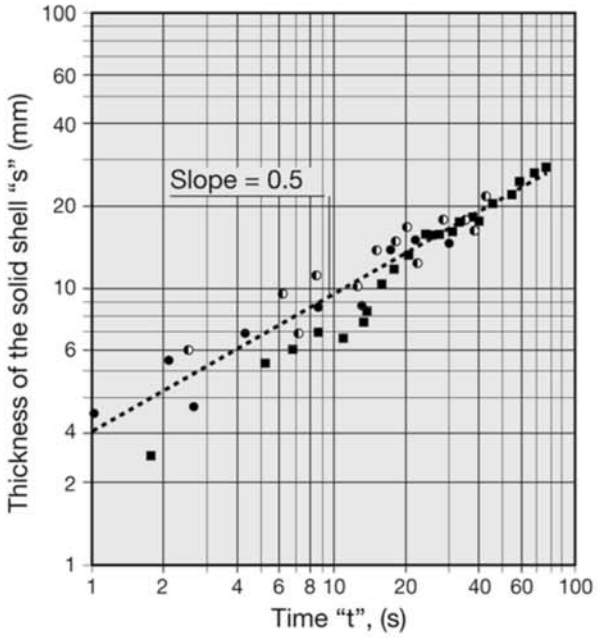

Fig. 8.63 Example of the fitted correlation between the solid thickness, and time from the steel entering the caster mold, for AISI 304 stainless steel. The slope of 0.5 in the log thickness versus log time graph corresponds to a square root of time dependence of the solid thickness. Source: Ref 22

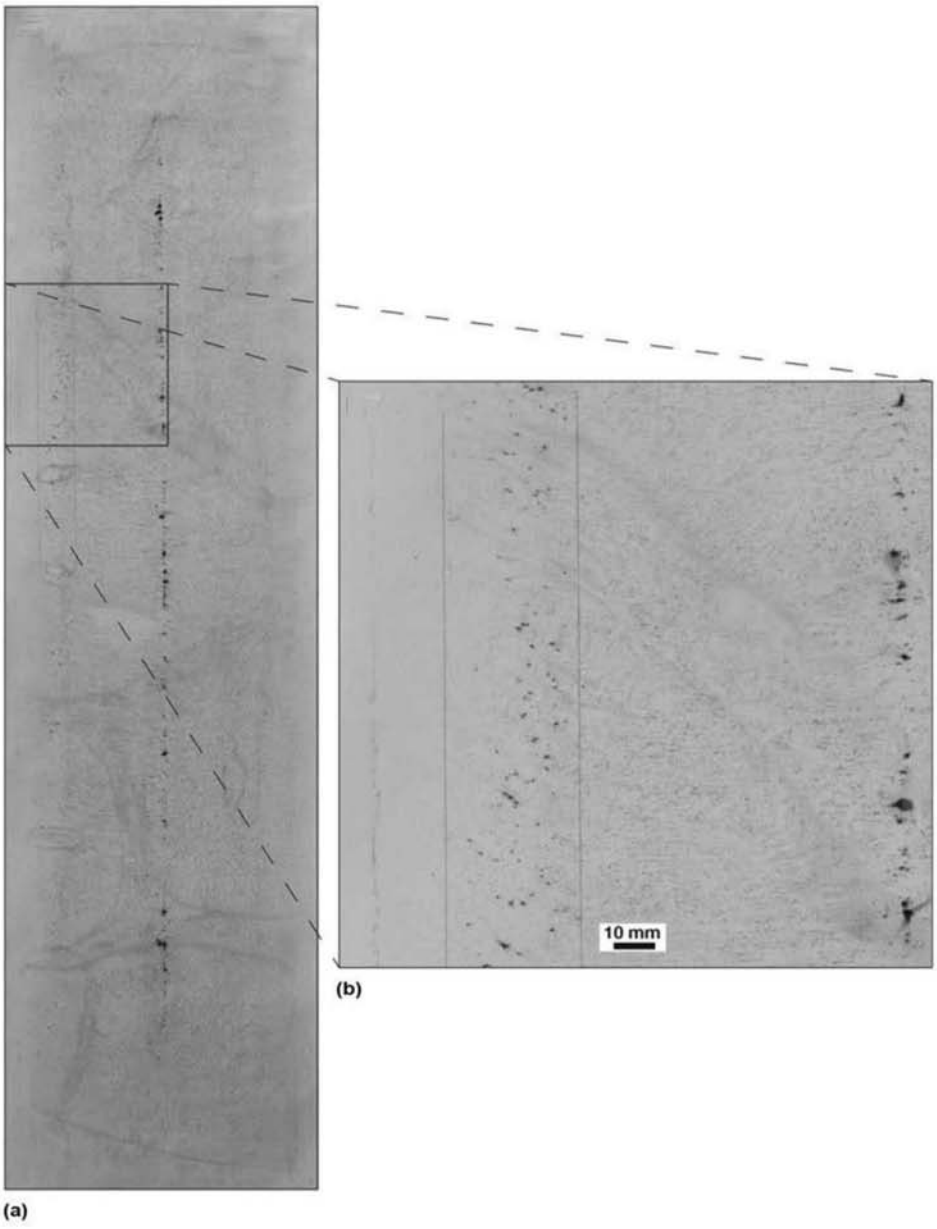

Fig. 8.64 (a) Sulfur print of the transverse plane of a continuous cast low-carbon steel plate, with chemical composition close to the peritectic point (C = 0.13%, Mn = 0.65%, S = 0.010%, P = 0.017%). Discontinuous central segregation as well as small defects indicated by the lines drawn over the print can be seen. Slab thickness, 250 mm (10 in.). (b) Detail of the region with small nonmetallic inclusions and "pinholes" (small bubbles) marked by the lines penciled over the print. The columnar structure can also be observed. The inclusions are in the small radius side of the curved strand (inner side) since they "float" during the solidification. Note: this print is typical of those made during process control. The print is produced in a very short time, so the results can be used to correct and adjust the casting process. For this reason, there are some stains caused by relative movement between paper and sample—a piece of the slab with approximately 1400 × 250 mm (55 × 10 in. by 50 mm 2 in.) thick!—as well as some "bubbles" of trapped air between the paper and the sample.

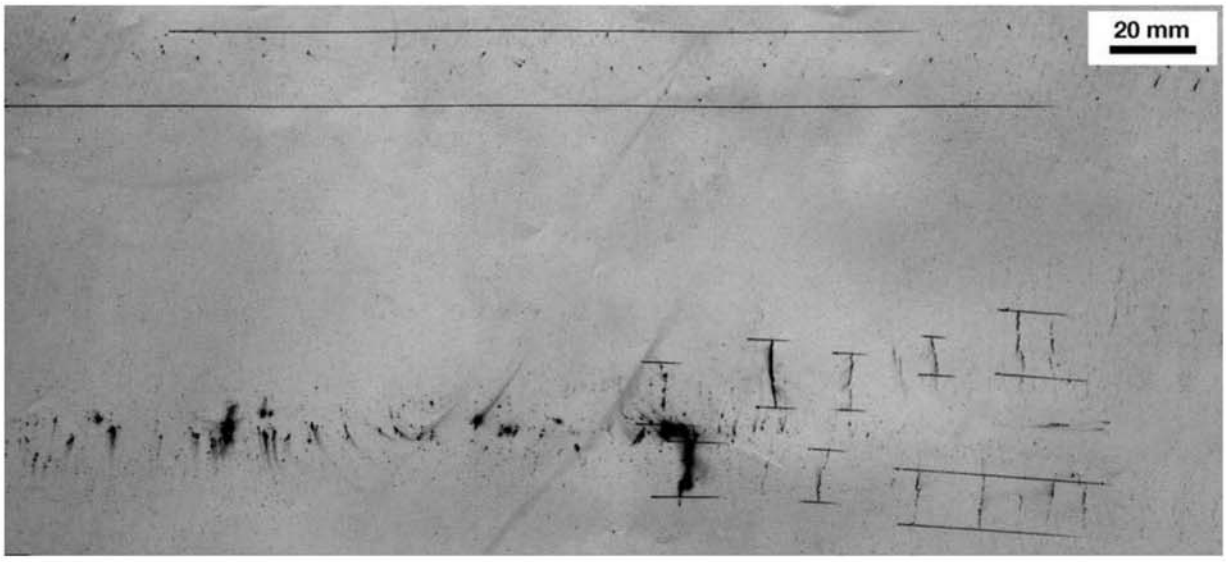

Fig. 8.65 Portion of a sulfur print taken from the transverse section of a continuous cast slab of low-carbon steel, with the chemical composition close to the peritectic. Small nonmetallic inclusions and "pinholes" (small bubbles) in the small radius of the curved strand (inner side). Cracks can be seen close to the central segregation region. The lines penciled over the print were used to measure the position of the indications and correlate them with the position they probably occurred along the length of the caster.

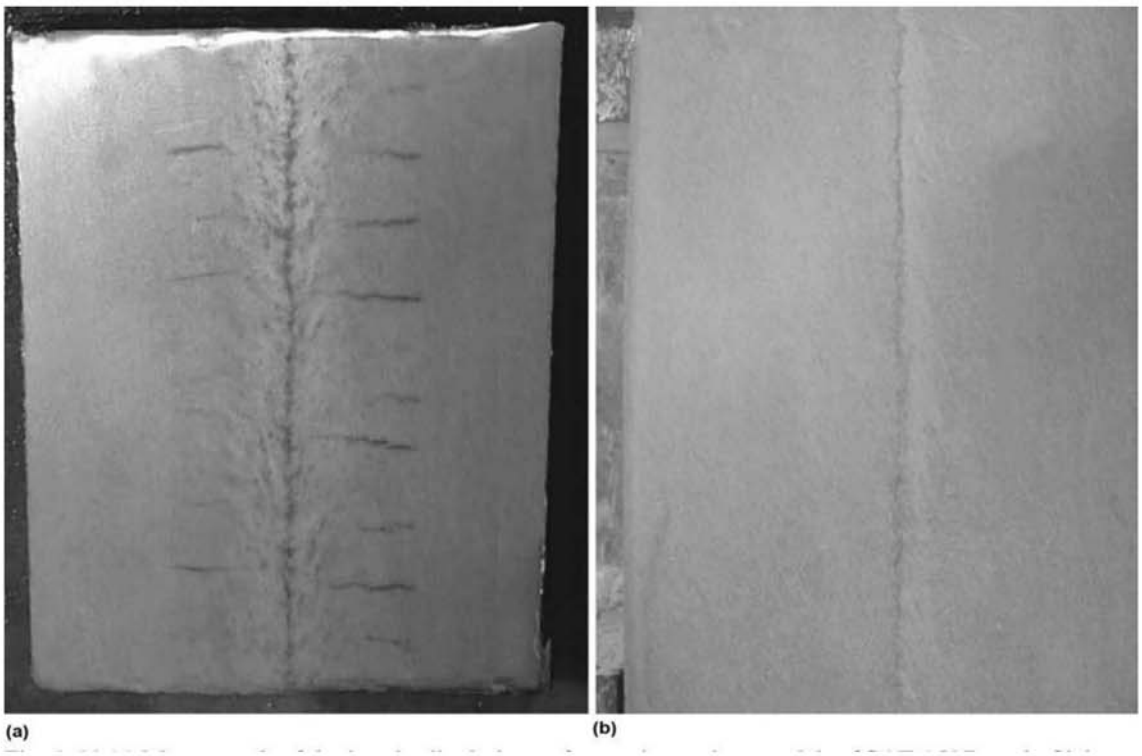

Fig. 8.66 (a) Macrograph of the longitudinal plane of a continuously cast slab of SAE 1527 steel. Slab thickness, 225 mm (9 in.). Cracks and central segregation. The "V" shape of the central segregation can also be seen. (b) Macrograph of the longitudinal plane of a continuously cast slab. Slab thickness, 225 mm (9 in.). Central line crack. The top right corner of these macrographs have been subjected to digital editing to eliminate traceability marks from the steelmaker.

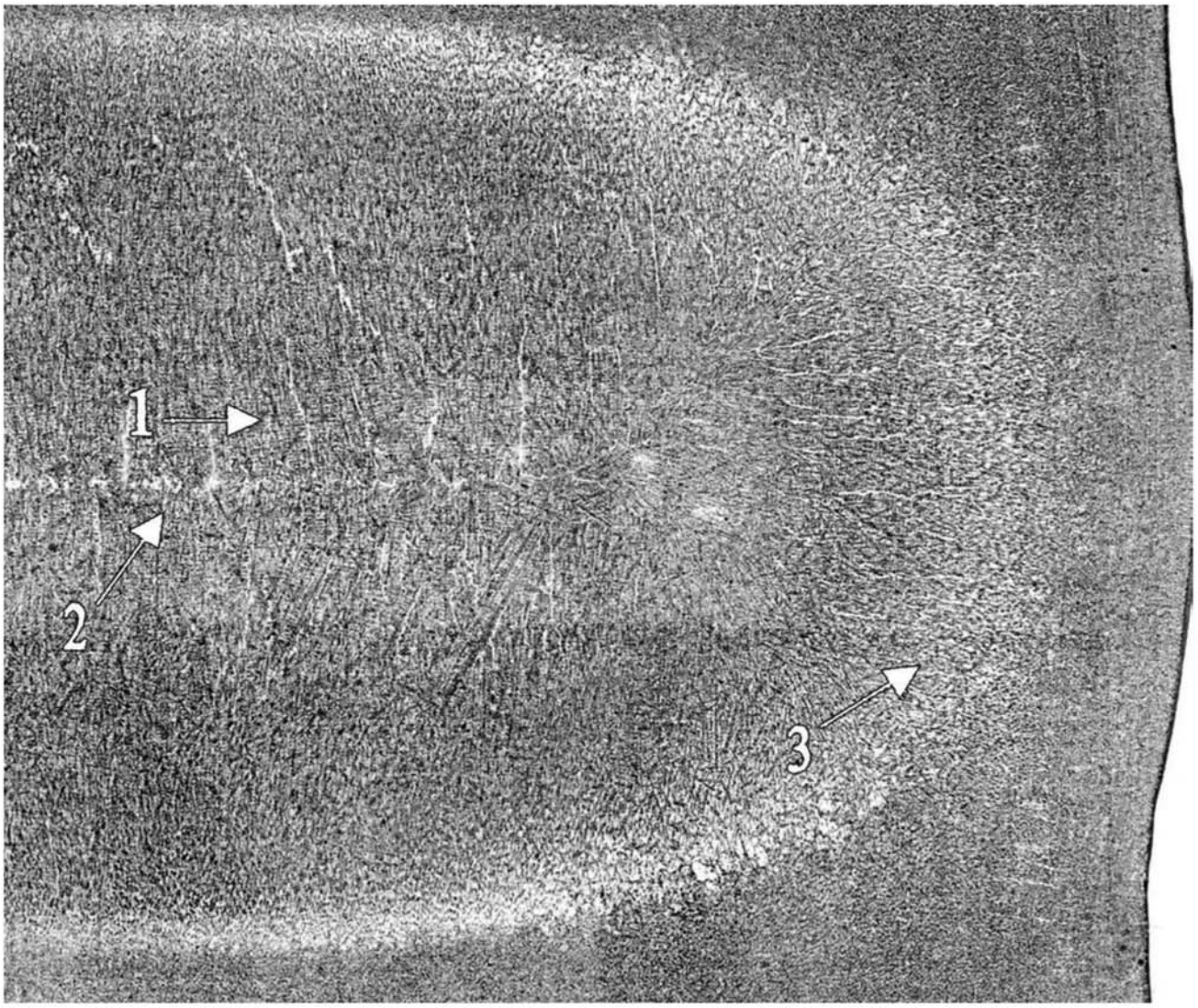

Fig. 8.67 Macrograph of the longitudinal plane of a continuously cast slab of steel with C = 0.30%, Mn = 0.53%, Si = 0.23%, S = 0.003%, P = 0.0012%). Slab thickness, 125 mm (5 in.). To the right is the side surface of the slab. (1) Midway cracks, (2) central segregation, (3) triple point cracks (corner of the slab). Macrograph produced using "engraving" technique, for publication (see Chapter 4, "Metallographic Technique—Macrography," in this book). Courtesy of J. Casey, DOFASCO Canada.

form of precipitate particles (nonmetallic inclusions) with a sufficiently high melting point to avoid compromising the steel quality. Sometimes the same strategy is used for nitrogen, although it is more common for this interstitial to have its content controlled to remain in solution in the steel. The solubility of sulfur in solid iron is also very low (similar to the solubility of oxygen). When this solubility is exceeded, low melting iron sulfide can be formed. Figures 8.68 and 8.69 present images in which a network of iron sulfide is present in the steel: when sulfur solubility is exceeded, this sulfide may precipitate at the end of the solidification process. This structure cannot sustain hot working because the presence of this low melting phase and is sometimes called "hot short" (see Fig. 8.70) Adding sufficient manganese to the steel will result

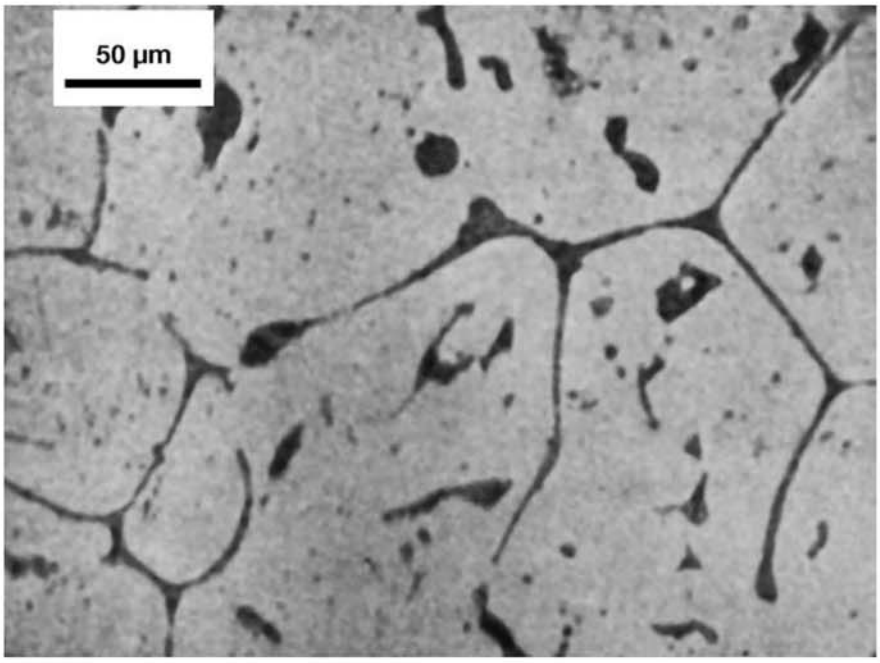

Fig. 8.68 Micrograph of as-cast steel containing a network of iron sulfide. The low melting point of the sulfide makes it the last to solidify, forming the network (or continuous "films") on the grain boundaries. The material is then brittle at high temperature ("hot shortness") (see Fig. 8.70). No etching. Source: Ref 30

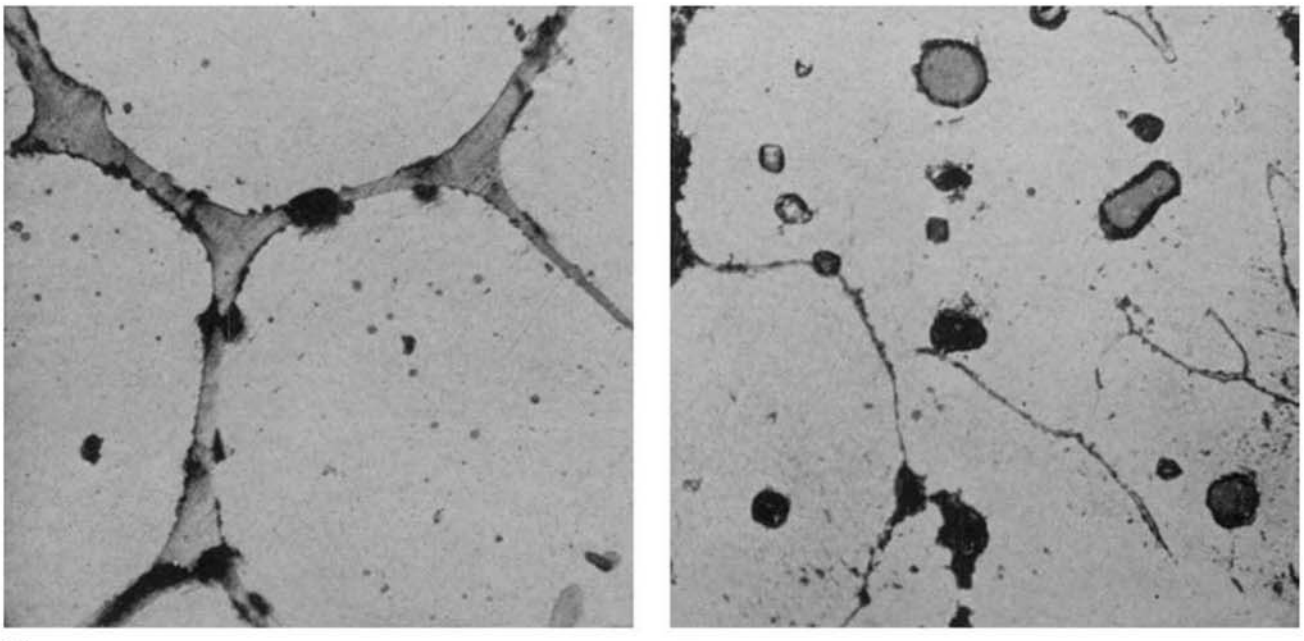

Fig. 8.69 Micrographs of as-cast steel containing iron sulfide network (a) and globular manganese sulfide (b). No etching. The amount and size of the nonmetallic inclusions shown in this and Fig. 8.68 are almost impossible to find in modern steels produced with current refining processes. The educational value of the figure is very important. Source: Ref 30

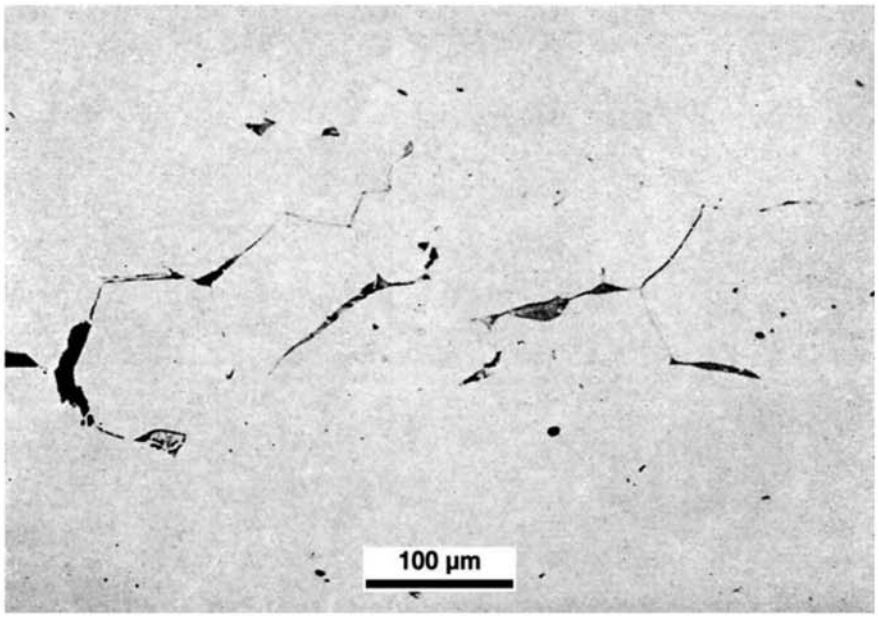

Fig. 8.70 Micrograph of steel containing iron sulfide, hot worked. The presence of the sulfide in the grain boundaries has caused hot shortness (cracks are evident). No etching.

in the formation of a more stable sulfide with a higher melting point, manganese sulfide, which also precipitates at temperatures somewhat higher.

As the origin and formation of nonmetallic inclusions is quite complex (see, for instance, Ref 5, 31, 32), several classification methods have been proposed (and are used) for these particles. Unfortunately, these classification schemes do not use the same criteria, so there is significant superposition of the classifications and this can be the cause of misunderstanding. Inclusions can suffer changes in their chemical composition and shape from the moment they are formed in the steel and in particular can undergo significant shape changes during hot working. Besides the evident classification method based on their composition (oxides, sulfides, nitrides, etc.) it is common to attempt to classify nonmetallic inclusions based on whether they are external to the process, that is, exogenous (*exo* = external) or endogenous. A large portion of the inclusions that might be formed outside of the process (entrapped pieces refractories, slag, etc.) react with the steel and have their composition changed, frequently in such a way that tracing them to their original source may be difficult. Modern steelmaking processes, when properly controlled, can almost completely eliminate this type of inclusion. Figure 8.71 presents a large oxide inclusion (frequently called a macro-inclusion) in a casting that demonstrates some of the problems associated with tracing the origin of these particles.

8.10.1 Deoxidation

Aluminum is the most common steel deoxidizer. When aluminum is used in sufficient amounts, the oxide formed is aluminum oxide or alumina. Nor-

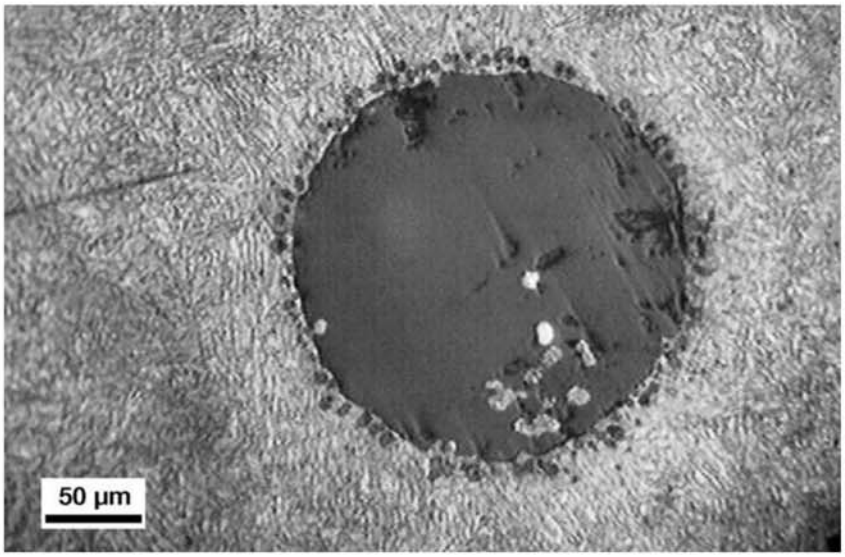

Fig. 8.71 A large oxide nonmetallic inclusion in a cast steel, quenched and tempered. Clearly the reaction between the inclusion and the steel has been stopped by the end of the part solidification. There is a "crown" of small oxide particles around the inclusion. This probably results from the reaction between the steel and the "original" inclusion that could be either an exogenous particle or a reoxidation product. The inclusion is not composed of a single phase: there are small particles that look like entrapped metal and darker particles, where "comet tails" formed during polishing, are present. Optical micrograph. Etchant: nital 2%. For more examples of nonmetallic inclusions in steel castings, see the AFS Non-metallic Inclusions Atlas. Source: Ref 33

mally, most of the alumina formed during deoxidation precipitates before solidification starts, in the liquid steel (frequently classified as "primary"), and a small residual part precipitates does so during and after solidification, due to the decrease of alumina solubility in steel with the decrease in temperature and phase changes. Most of the "secondary" alumina precipitates during solidification. Due to its high melting point, alumina is formed as a solid phase inside the liquid. Alumina can form in several morphologies and this can influence steel processing and properties. Figure 8.72 shows a polygonal alumina inclusion, extracted from an ESR ingot through a dissolution technique that completely dissolves the surrounding steel.

In some cases, the steel deoxidation can be performed in such a way that more complex composition nonmetallic inclusions are formed (Fig. 8.73 and 8.74). This is the case when, for instance, deformable inclusions are desired during further working of the steel.

8.10.2 Sulfides

The most common sulfide in steel is manganese sulfide. It has a sufficiently high stability and melting point to prevent the formation of films at the end of solidification, avoiding the hot shortness associated to iron sulfide. Even so, the stability of this sulfide is such that this compound only precipitates after solidification starts, at lower temperatures, and when manganese

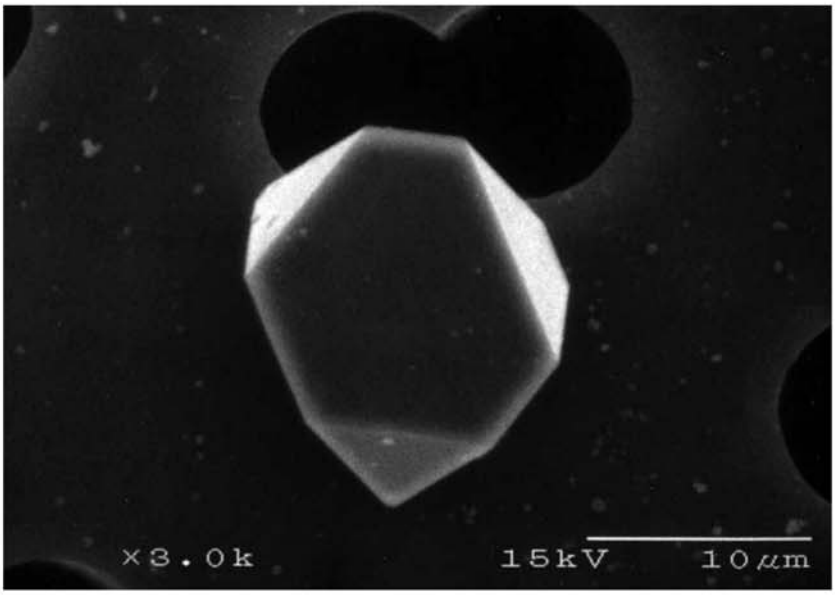

Fig. 8.72 Alumina inclusion from a steel ingot produced via electroslag remelting. The polygonal shape indicates that the inclusion has formed as a solid phase. These inclusions are frequently classified as type D according to ASTM E45 methods. SEM, SE. The steel was completely dissolved via etching, and the inclusion was retained in a substrate for observation. Courtesy of A. Mitchell, University of British Columbia.

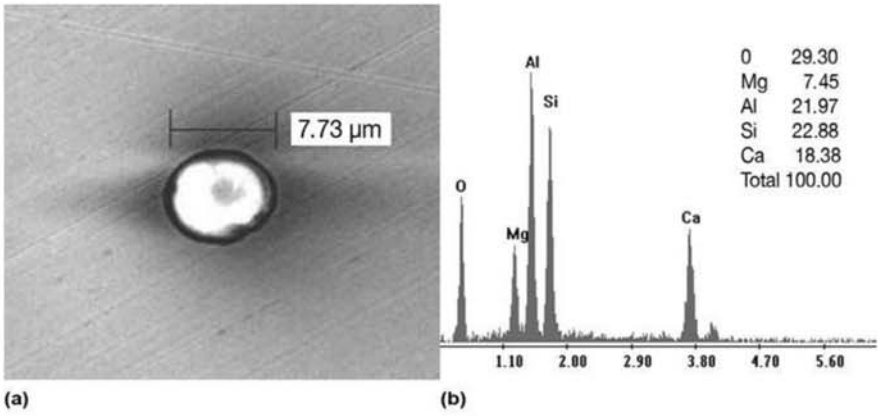

Fig. 8.73 (a) Oxide inclusion in as-cast steel. The sperical shape of the inclusion may indicate that it precipitated in the liquid state of the steel. SEM, SE. (b) EDS spectrum from the nonmetallic inclusion. The calculated quantitative analysis from the EDS data is listed on the right. No etching. Note: the inclusion appears light, possibly due to electrical charging during the time it was held under the electron beam for the performance of the EDS analysis. The nonmetallic inclusion is not a good conductor of electricity, and the sample has not been coated with a conducting material to avoid affecting the EDS results, so there is a charging (electrons are accumulated) of the inclusion. This charge caused the electron beam to be repealed (deflected) from the inclusion, resulting in a lighter image. This is a common artifact when doing analytical work in SEM

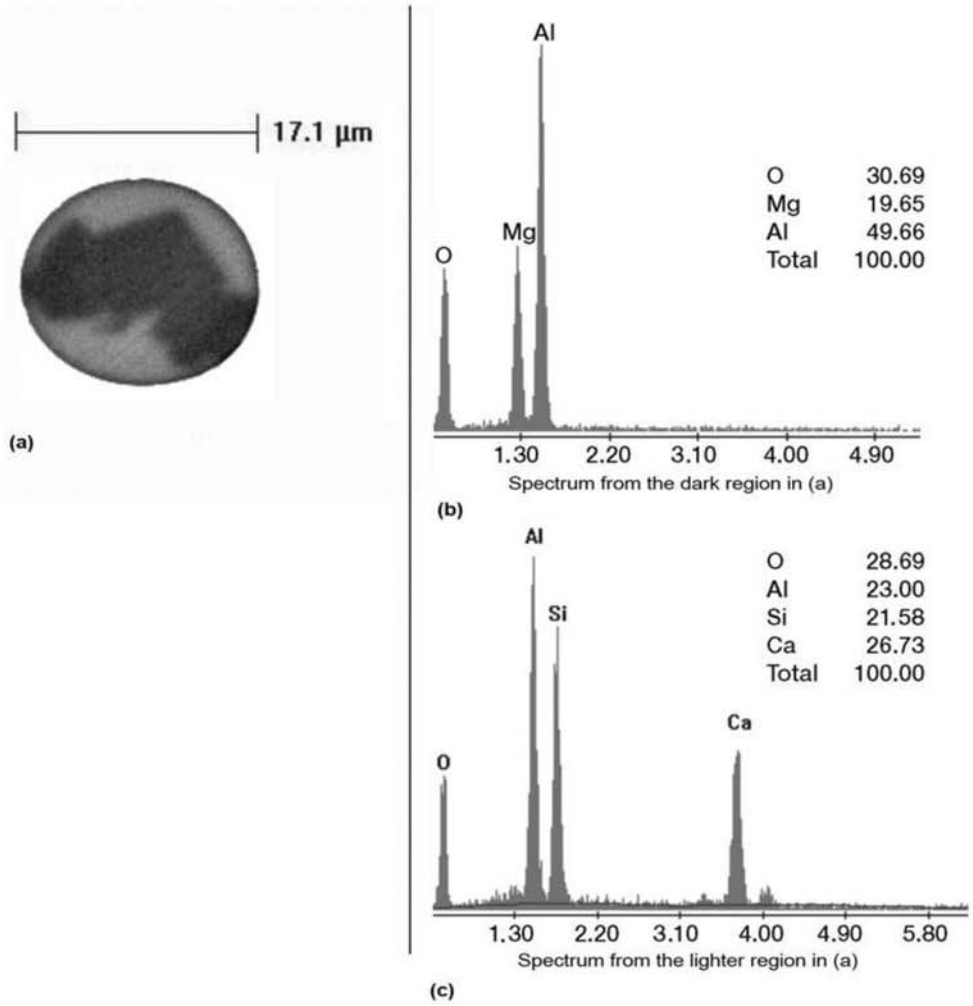

Fig. 8.74 (a) Oxide inclusion in as-cast steel. The inclusion is composed of two phases with different chemical compositions. SEM, BE. (b) The dark, polygonal phase is an oxide containing magnesium and aluminum, probably high melting point spinel ($MgAl_2O_4$). Its shape indicates it has probably formed as a solid from the liquid steel. The lighter phase that covers it has a spherical shape, which might indicate it has precipitated as liquid in the liquid steel, nucleating from the spinel particle. (c) This second phase is a complex oxide, mixture of CaO, Al_2O_3, and SiO_2. Spectra in (b) and (c) are EDS. The quantitative analyses listed on the right are calculated from the EDS analysis. No etching.

and sulfur are segregated to the interdendritic spaces. Mizoguchi (Ref 19) performed directional solidification experiments in which a cylindrical sample of steel starting fully in the liquid stated was control cooled in a tubular furnace and subjected to a thermal gradient. At the end of each experiment, the sample was quenched from the temperature it was at that moment. This way, each position of the sample had a well-defined thermal history, and it was possible to observe the extension of segregation as well as the structure formed for each thermal cycle, all starting at 1520 °C (2770 °F). Figure 8.75 presents the results for the segregation of manganese and sulfur, and the associated precipitation of manganese sulfide.

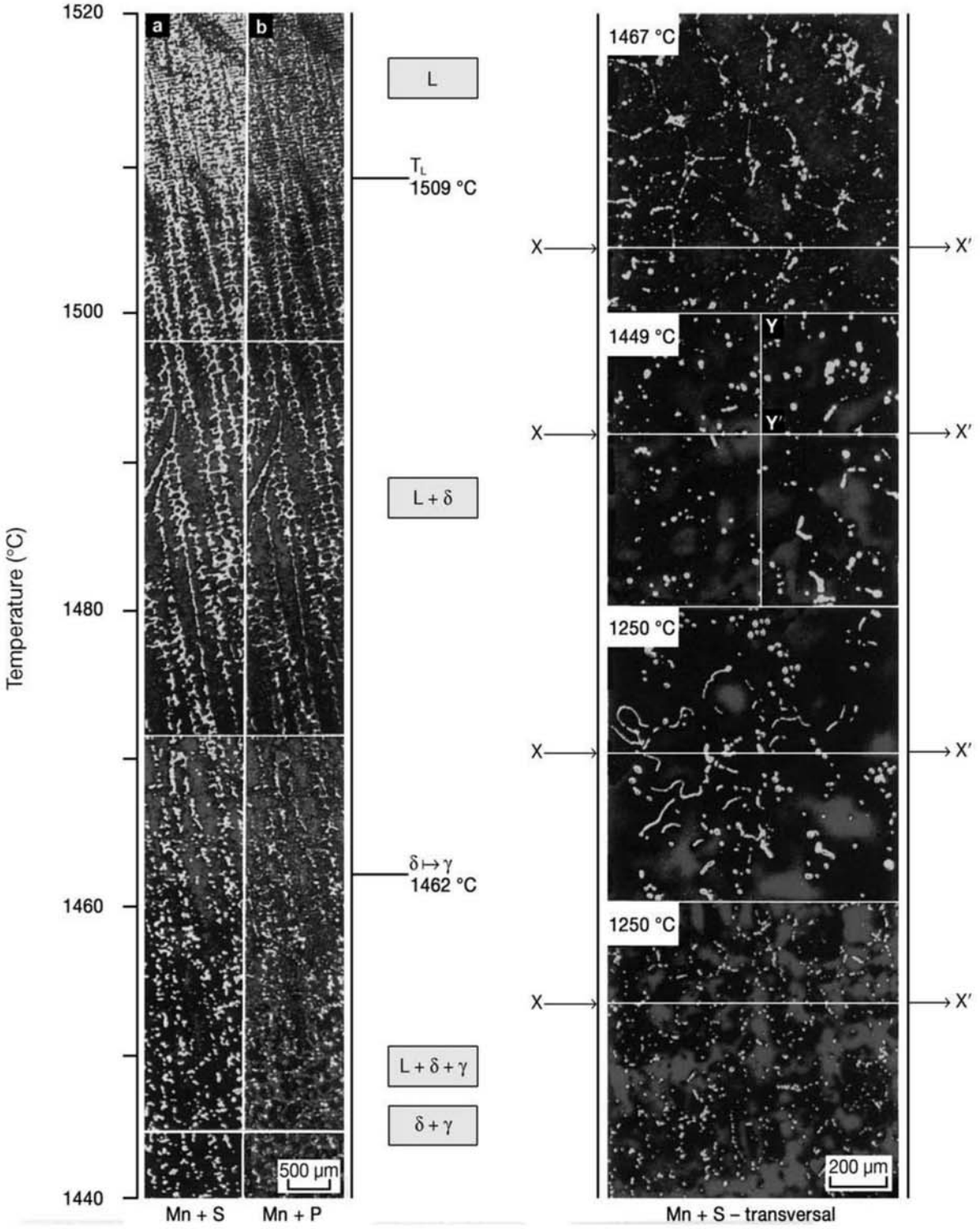

Fig. 8.75 (a) Manganese and sulfur and (b) manganese and phosphorus characteristic x-ray mapping in longitudinal section of samples subjected to controlled cooling and quenched. Lighter regions indicate higher concentration of these elements and the formation of manganese sulfide in (a). The temperature scale (to the left) indicates the temperature at this position of sample when it was quenched. The caption in the right hand side indicates the phases present at this position when the sample was quenched. The redistribution of manganese and sulfur during solidification and the consequent nonuniform distribution of manganese sulfide in the solid structure is evident. Experiments performed with cooling rate of 5.4 °C/min (9.7 °F/min) and steel with 0.08% C, 1.04% Mn, 0.075% P, 0.351% S. Courtesy of S. Mizoguchi.

Sulfides are frequently used to improve steel machinability (Chapter 11, "Hot Working"). For this reason, it has become common in recent years, particularly in steels for the automotive industry, to specify sulfur composition ranges between 0.015% and 0.030%, instead of just a maximum sulfur content, as was usual until the 1990s. These are not "free-cutting" steels, but have improved machinability when compared to low-sulfur steels.

Although localized analysis techniques in SEM or microprobe are the most reliable techniques to identify the chemical composition of nonmetallic inclusions, particularly in as-cast steels, when the effects associated with the relative plasticity of the inclusions during hot working are still absent (Fig. 8.76), there are some indications in optical metallography that might be helpful, specifically, its color. Manganese sulfide, even without etching, has a dark gray color. Iron sulfide, on the other hand, presents a light yellow color in samples without etching.

In as-cast steel, manganese sulfide may present different morphologies depending mostly on the sulfur, manganese and oxygen contents of the steel

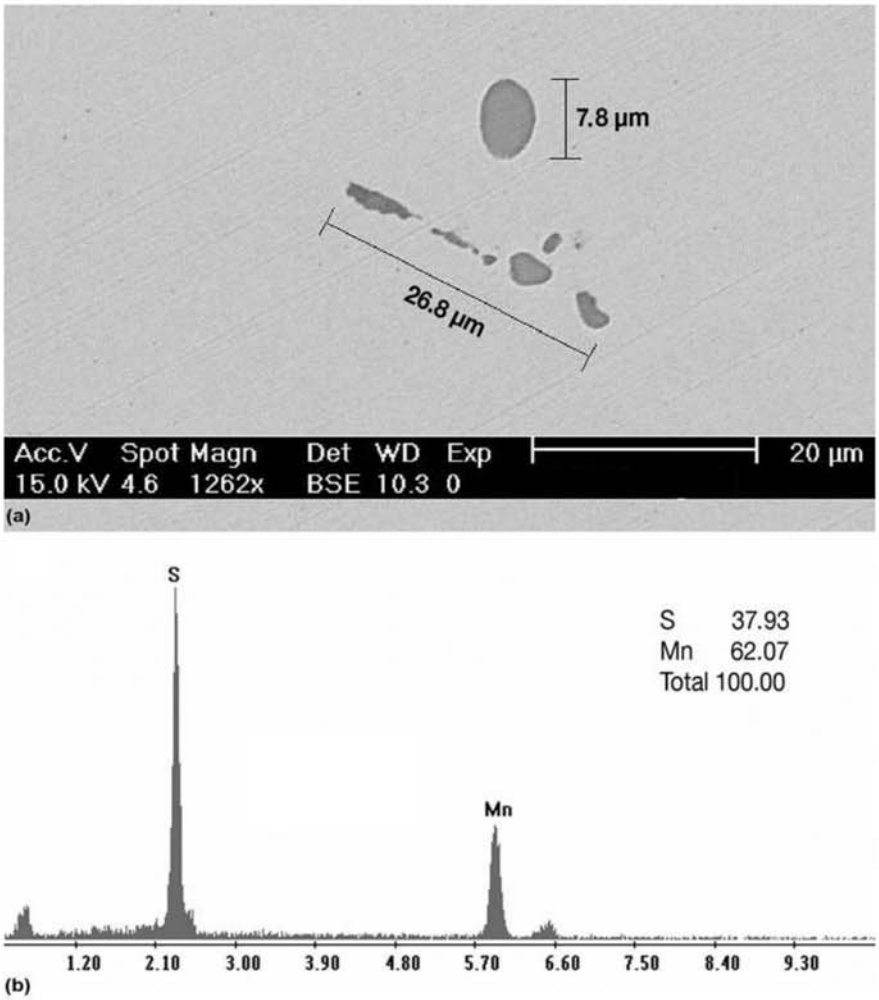

Fig. 8.76 (a) Sulfide nonmetallic inclusion in as-cast steel. SEM, BE. No etching (b) EDS spectrum of the inclusion. Quantitative analysis calculated from EDS results. Manganese sulfide.

(Ref 34–37). Sulfide morphology after hot working is discussed in Chapter 11, "Hot Working." Figures 8.77 and 8.78 present other morphologies of manganese sulfide in as-cast steel. The sulfide contents in Fig. 8.77 and 8.78, as in Fig. 8.69 and 8.70, are very high and would rarely be found in a modern steel. The figures do illustrate well extreme cases and possible morphologies.

In high silicon electric steels, manganese sulfide can have an important role in grain size control during heat treatment (see Fig. 8.79).

8.10.3 Nitrides

Although nitrides can be considered structural constituents in steels (in particular in microalloyed steels), when they are formed from the liquid phase, they are normally classified as nonmetallic inclusions. The most common nitride observed in steels as an inclusion is titanium nitride (TiN) which shows a light gold color when observed without etching (Fig. 8.80).

Aluminum nitride has an important role in controlling austenitic grain size in heat-treated steels (Chapter 9, "Conventional Heat Treatments: Usual Constituents and Their Formation"), as well as in the control of texture of steels for cold forming (Ref 38) (Chapter 12, "Mechanical Work of Steels—Cold Working"). However, excessive levels of aluminum and nitrogen in steel can lead to the precipitation of this nitride in a eutectic reaction during the end of the solidification (Ref 38 and 39). This kind of precipitation leads to the embrittlement of the as-cast grain boundaries as shown in Fig. 8.81 and 8.82. Even after the steel is heat-treated and "new" grain boundaries are formed, the nitride network remains, as does the embrittlement.

Fig. 8.77 Micrograph of as-cast steel with a high concentration of polygonal manganese sulfide inclusions (sometimes called type III sulfide). Etchant: nitric acid.

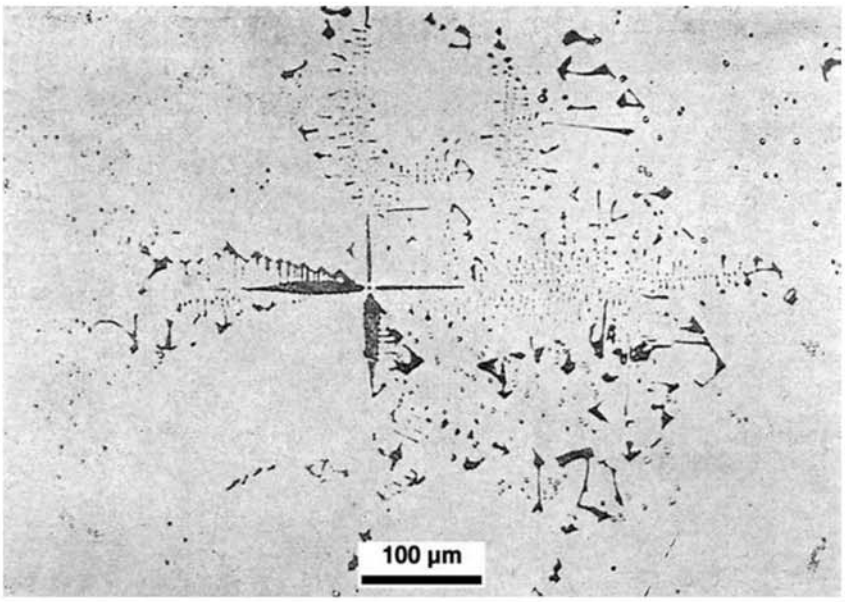

Fig. 8.78 Micrograph of as-cast steel. High concentration of dendritic manganese sulfide (sometimes called type II sulfide). No etching.

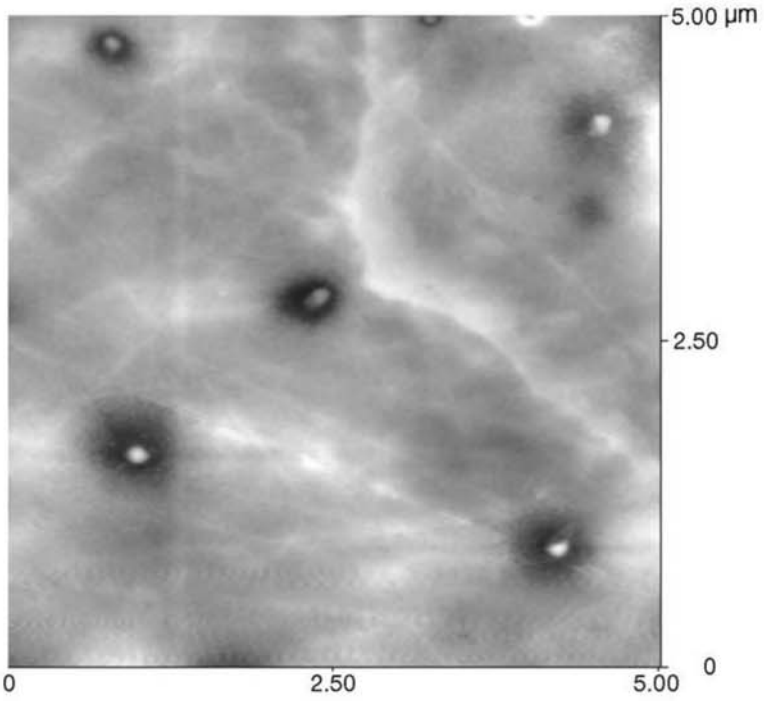

Fig. 8.79 Atom force micrograph of silicon steel for electrical applications, indicating size, shape and distribution of manganese sulfide. Manganese sulfide precipitates are under 250 nm. Courtesy of M. Spangler, CETEC- MG, Brazil.

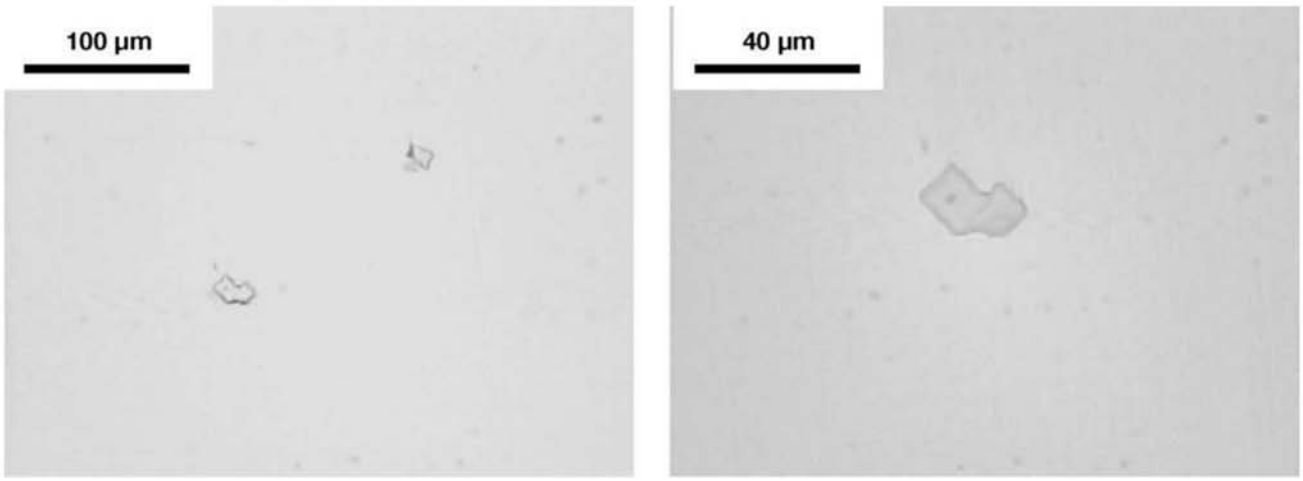

Fig. 8.80 Micrograph of AISI 321 stainless steel showing titanium carbonitride inclusions. No etching. Polygonal shape and golden color are typical of titanium nitrides and carbonitrides. Courtesy of Villares Metals, Sumaré, Brazil.

Fig. 8.81 "Rock candy" fracture surface in cast steel, embrittled by the precipitation of aluminum nitride on the grain boundaries during solidification. Source: Ref 31, 39

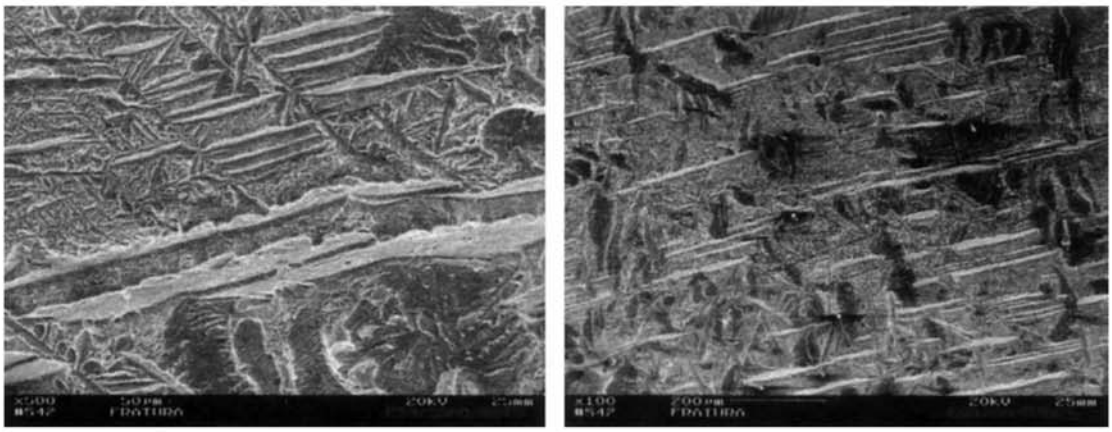

Fig. 8.82 "Rock candy" fracture surface in cast steel, embrittled by the precipitation of aluminum nitride on the grain boundaries during solidification. SEM, SE. Source: Ref 31, 39

REFERENCES

1. H. Schummann, K. Cyrener, W. Molle, H. Oettel, J. Ohser, and L. Steyer, *Metallographie*, Deutscher Verlag fur Grunstoffindustrie, Wiley-VCH, 1990
2. N. Chvorinov, *Giesserei*, Vol 27, 1940, p 177
3. M.F. Ashby and D.R.H. Jones, *Engineering Materials, 2*, Pergamon Press, 1986
4. M.C.Flemings, , Solidification, *Advanced Physical Chemistry for Process Metallurgy*, N. Sano et al., eds., Academic Press, 1997, p 151–82
5. A.L.V. Costa e Silva and P.R. Mei, *Aços e Ligas Especiais*, 3rd ed., Editora Edgard Blucher, 2010
6. W.C. Winegard, *An Introduction to the Solidification of Metals*, Institute of Metals, 1964
7. W. Kurz and D.J. Fisher, *Fundamentals of Solidification*, Trans Tech Publications, 1984
8. S. Chumbley, Method to Make Dendrites, Iowa State University, private communication
9. R. Ruxanda, L. Beltran-Sanchez, J. Massone, and D.M. Stefanescu, On the eutectic Solidification of Spheroidal Graphite Iron—An Experimental and Mathematical Modeling Approach, *Proceedings of Cast Iron Division, AFS 105th Casting Congress, Dallas, Texas*, American Foundry Society, 2001
10. A. Suzuki, T. Suzuki, Y. Nagaoka, and Y. Iwata, On Secondary Dendrite Arm Spacing in Commercial Carbon Steels with Different Carbon Content, *J. Japan Inst Metals*, Vol 32 (No. 12), 1968, p 1301–5
11. B. Sundman, B. Jansson, J.O. Andersson, *The Thermo-Calc Databank System*, CALPHAD, Vol 9, 1985, p 153–90
12. TCAB, TCFE7 *Iron Based Alloy Thermodynamics Database*, v7, Stockholm, 2012
13. H. Shibata, Y. Arai, M. Suzuki, and T. Emi, Kinetics of Peritectic Reaction and Transformation in Fe-C Alloys. *Metallur. Mat. Trans. B*, Vol 31B, October 2000, p 981–91
14. Wikipedia, *Adolf Ledebur*, 2007, http://de.wikipedia.org/wiki/Adolf_Ledebur (accessed January 4, 2015)
15. D.A. Porter and K.E. Easterling, *Phase Transformations in Metals and Alloys*, 2nd ed., Chapman & Hall, 1992
16. M.C. Flemings, *Solidification Processing*, McGraw-Hill, 1974
17. Basalt, Wikipedia, 2005, http://commons.wikimedia.org/wiki/Image:Basalt-tschechien.jpg (accessed January 4, 2015)
18. J.J. Gilman, Basalt Columns: Large Scale Constitutional Supercooling?, *J. Volcanol. Geotherm. Res.*, Vol 184 (No. 3–4), 2009, p 347–50
19. S. Mizoguchi, *A Study on Segregation and Oxide Inclusions for the Control of Steel Properties*, Ph.D. thesis, University of Tokyo, 1996, p 97

20. J. Casey, Macro-Etching of Continuous Cast Steel, *Microsc. Microanal.*, Vol 8, Suppl. 2, 2002, p 362–63

21. A. Cramb, Ed., *The Making, Shaping and Treating of Steel, Casting Volume*, 11th ed., AISE, 2003

22. S. Mizoguchi, T. Ohashi, and T. Saeki. Continuous Casting of Steel, *Annu. Rev. Mat. Sci.*, Vol 11, 1981, p 151–69

23. G. Vandrunen, J.K. Brimacombe, and F. Weinberg, Internal Cracks in Strand-Cast Billets, *Ironmak. Steelmak.*, Vol 2, 1975, p 125–47

24. G. Krauss, Solidification, Segregation, and Banding in Carbon and Alloy Steels. *Metallurg. Mat. Trans. B*, Vol 34B (No. 6), 2003, p 781

25. M.C. Mataya, E.R. Nilsson, E.L. Brown, and G. Krauss, Hot Working and Recrystallization of As-Cast 316L, *Metallurg. Mat. Trans. A*, Vol 34A, August 2003, p 1683–703

26. J.J. Moore and N.A. Shah, Mechanisms of Formation of A- and V-Segregation in Cast Steel, *Int. Metals Rev.*, Vol 28 (No. 6), 19836, p 338

27. M.C. Flemings, Principles of Control of Soundness and Homogeneity of Large Ingots, *Scand. J. Metallurg.*, Vol 5, 1976, p 1–15

28. G. Lesoult, Macro Segregation in Steel Strands and Ingots: Characterisation, Formation and Consequences, *Mat. Sci. Engin. A*, Vol 413, 2005, p 19–29

29. K.O. Yu, J.A. Domingue, G.E. Maurer, and H.D. Flanders, Macrosegregation in ESR and VAR Processes, *JOM*, Vol 38 (No. 1), October 26, 2012, p 46–50

30. A. Sauveur, *Metallography and Heat Treatment of Iron and Steel*, 4th ed., McGraw-Hill, 1935

31. R. Kiessling, *Non-Metallic Inclusions in Steels*, Iron and Steel Institute, 1968

32. IISI, *IISI Study on Clean Steel*, International Iron and Steel Institute, 2004

33. A. Cramb, *AFS Inclusion Atlas*, 1998, http://neon.mems.cmu.edu/afs/afs2/window2.html (accessed January 4, 2015)

34. E. Steinmetz, H.U. Lindenberg, and F.J. Wahlers, *Morphologie der Oxide und Sulfide bei der Desoxidation von Eisenschmelzen mit Mangan und Silicium*, Vol. 106 (No. 11), 1986

35. E.T. Turkdogan and G.J.W. Kor, Sulfides and Oxides in Fe-Mn Alloys: Part I. Phase Relations in Fe-Mn-S-O System, *Metallurg. Trans.*, Vol 2, June 1971, p 1561–70

36. K. Oikawa, H. Ohtani, K. Ishida, and T. Nishizawa, The Control of the Morphology of MnS Inclusions in Steel during Solidification, *ISIJ Int.*, Vol 35 (No. 4), 1995, p 402–8

37. K. Oikawa, S. Sumi, and K. Ishida, Morphology Control of MnS Inclusions in Steel during Solidification by the Addition of Ti and Al, *Zeits. Metallkunde*, Vol 90 (No. 1), 1999, p 13–18

38. F.G. Wilson and T. Gladman, Aluminum Nitride in Steel, *Int. Mat. Rev.*, Vol 33 (No. 5), 1988, p 221–88

39. A. Costa e Silva, F. Rizzo, and J.G. Speer, Thermodynamic Study of Aluminum Oxide and Nitride Precipitation in Ferrous Alloys, *CALPHAD XXX: Calculation of Phase Diagrams and its Applications*, 2001

Metallography of Steels—Interpretation of Structure and the Effects of Processing
Hubertus Colpaert
Updated and Translated by André Luiz V. da Costa e Silva

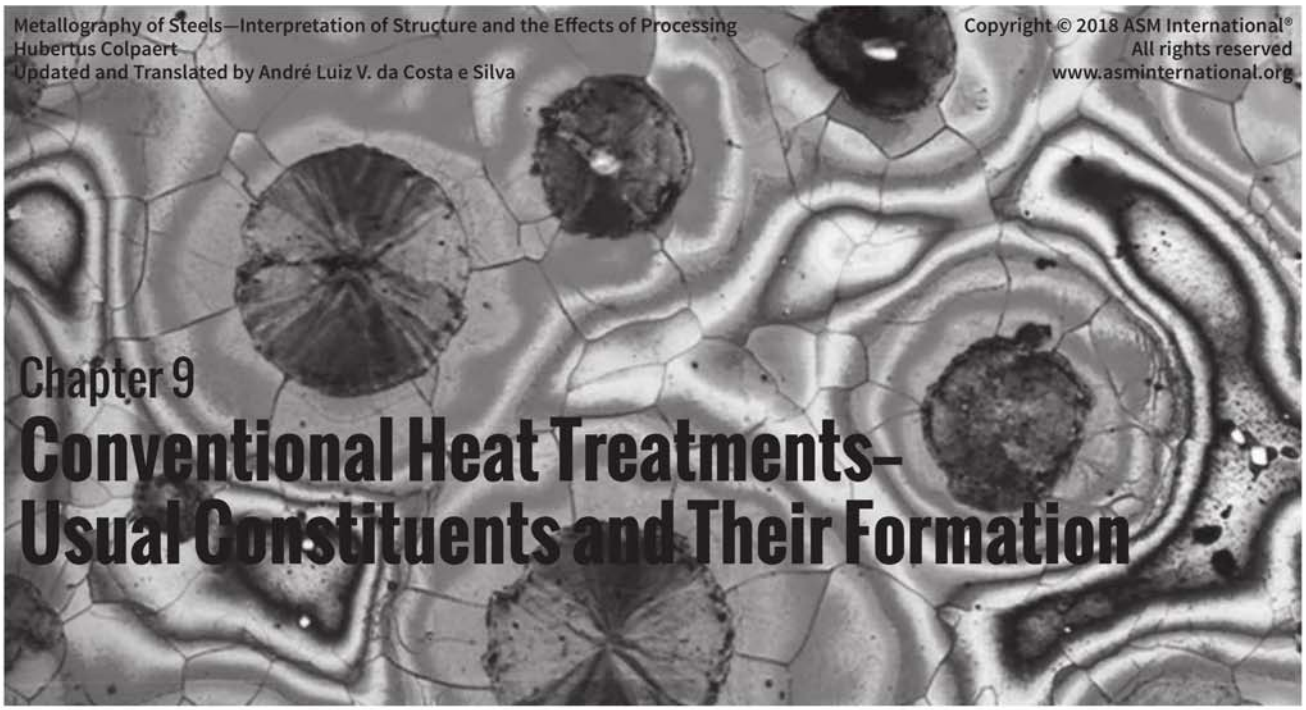

Chapter 9
Conventional Heat Treatments–Usual Constituents and Their Formation

Heat treatment is the most common way of altering the mechanical, physical, and even chemical properties of steels. In this chapter, conventional heat treatments, primarily those applied to carbon and low alloy steels, are discussed. In general, conventional heat treatments involve heating and cooling and include annealing, normalizing, and quenching and tempering. Treatments involving chemical changes to the part surface, usually classified as thermochemical treatments, are discussed in Chapter 10, "Conventional Heat Treatments—Basic Concepts," in this book. In general, they comprise carburizing, nitriding, and carbonitriding. These treatments normally involve changes in carbon and nitrogen content , interstitial solutes in iron that have high mobility. Treatments in which mechanical forming is performed together with phase transformations normally envisaged during heat treatment are classified as thermomechanical treatments and are discussed in Chapter 11, "Hot Working," in this book. The temperatures at which phase transformations between ferrite, austenite, and cementite occur are normally called "critical temperatures" in the discussion of heat treatments. Because transformations do not happen at exactly the equilibrium temperatures (as discussed later), it is common to include the subscripts "c" (for the French, "chauffage" = heating) and "r" (for the French "refroidisement" = cooling) to indicate the temperatures at which transformation starts on heating and cooling, as indicated in Fig. 9.1.

Most conventional heat treatments involve a first step of heating the steel from room temperature to the single-phase austenitic field in the equilibrium diagram. This involves crossing the so-called critical region. Treatments that do not go over the A_1 temperature are called subcritical. Treatments involving holding at temperatures between A_1 and A_3 are normally called intercritical

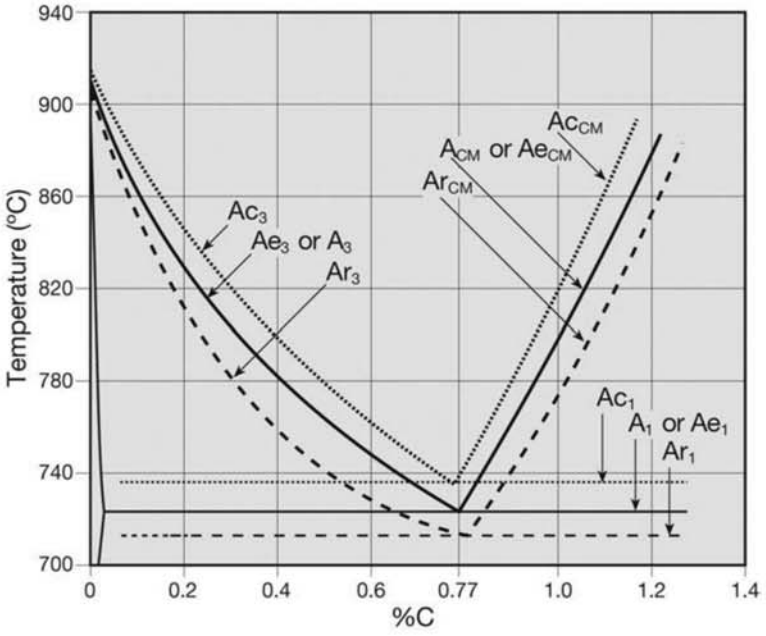

Fig. 9.1 Two and three-phase equilibrium lines in the metastable Fe-C equilibrium diagram. Equilibrium lines either have no subscript or have the e subscript. Transformation lines on cooling are indicated with r and on heating with c.

and usually are not classified as conventional heat treatments (see Chapter 10). Although it is possible to accurately determine the phase equilibria temperature using computational thermodynamics, there are a large number of empirical relations for the calculation of A_1 and A_3 temperatures as a function of steel chemical composition (Ref 1). These relationships must be used with care and within the interpolation range they were established.

All heat treatments that involve heating steel into the austenitic field have, as the first important phase transformation, austenite formation. Frequently this transformation receives less attention than it should in the study of heat treatments and in their performance. Not giving proper attention and care to the heating and austenite formation stage of a heat treatment may have serious consequences and can lead to unsatisfactory results. This transformation is discussed in detail in the section 9.2.1 "Austenite Formation" in this chapter.

In the following section, the discussion is based on the premise that the treatment starts with a steel that is single-phase austenitic and chemically and microstructurally uniform (e.g., grain size and shape) .

9.1 Austenite Decomposition

The way austenite decomposes during conventional heat treatments largely defines the final result, from the microstructural aspect. Phase transformations during austenite decomposition happen via nucleation and growth.

The nucleation and growth processes that control the formation of ferrite, cementite, and pearlite from austenite are essentially diffusional. These processes are extremely important for two reasons:

- They define morphology (shape), size, and volumetric fraction of these phases when they form. Thus, they largely define the physical and mechanical properties resulting from heat treatments in which these phases are the final product.
- When the diffusional transformations that lead to equilibrium phases (including metastable cementite) do not happen, the stage is set for nonequilibrium phases that form through mechanisms more complex than diffusional nucleation and growth. These phases are largely responsible for the outstanding physical and mechanical properties steels can attain.

9.1.1 Nucleation

Nucleation—the appearance of the "nuclei" of a new phase inside an existing phase—plays an important role in phase transformations and the rate at which they occur. Some everyday examples highlight the importance of nucleation of phase transformations and are very instructive for understanding phase transformations in materials and, particularly in steels.

It is well known that it is possible to "undercool" water (or beer or soda) below the solidification temperature without solidification (liquid → solid) occurring until some instability causes the ice to nucleate. Bottles that are forgotten in the freezer and are thus at a temperature in which liquid is unstable, are generally handled with care to prevent the onset of the liquid → solid transformation. On the other hand, when nucleation is promoted, through agitation associated with opening or hitting the bottle or the undercooled liquid, transformation takes place at a very high rate (videos are available; Ref 2). From the thermodynamic point of view, water should be solid, but the transformation does not happen for the lack of one (or more) starting nuclei.

Although less common, overheated water can be obtained if steam is not nucleated when the boiling point is reached. When heating water in a pan on a stove, the pan walls are normally much hotter than the water and have surface heterogeneities that make steam bubble nucleation very easy at the water–pan interface. In this case overheating cannot be observed because there is no nucleation barrier. When water is heated in a microwave oven that does not heat the ceramic or glass cup, it is possible to create conditions to reach overheated water (above 100 °C, or 210 °F) inside the cup or glass without steam being nucleated. Adding a nucleating agent such as soluble coffee (this is a dangerous experiment, video is available; Ref 3) or sugar may have catastrophic consequences with the sudden nucleation of a large amount of steam.

Finally, liquids that are supersaturated in carbon dioxide with respect to air (beer, soda, champagne) are kept in equilibrium in closed bottles due to the high pressure inside the containers. When exposed to air, where the carbon dioxide partial pressure is much lower than the previous equilibrium, carbon dioxide elimination will depend on bubble nucleation. When a glass containing one of these liquids is observed, one can see that the bubbles nucleate in preferential sites in the liquid–glass interface, possible sites of small defects in the glass (video is available; Ref 4). Conversely, nucleating agents such as sugar, salt, or gas bubbling (e.g., through a straw) will promote copi-

ous nucleation and the rapid elimination of the carbon dioxide from the liquid, usually with dire consequences to the taste of the resulting liquid. These experiments highlight the importance of heterogeneities on the nucleation of a thermodynamically more stable phase. In the absence of nucleation, it is possible to keep systems away from the stable thermodynamic equilibrium.

In a classical work, Turnbull (Ref 5) was able, through the almost complete elimination of heterogeneities that could act as nuclei for iron solidification, to undercool liquid iron 295 °C (565 °F) below its melting point. More recently, Ref 6 showed that it is possible to control the action of alumina as a nucleating agent for steel solidification and reproduce the undercooling from Ref 5. The researchers used a steel drop over an alumina support and avoided the nucleation by controlling oxygen partial pressure in the experimental environment.

In the case of solid state phase transformations in steels and cast irons, structural heterogeneities play an important role as nucleating agents (or sites); grain boundaries, highly deformed regions (with more stored energy), and interfaces with nonmetallic inclusions are some examples of sites that may favor the nucleation of new phases. A simplified interpretation of this effect is to associate these locations with an energetic advantage: when comparing these regions with defect-free homogeneous regions in the material, these regions have higher energy, and their elimination through substitution by a new phase or a new interface between phases will contribute favorably (from the energy point of view) to the system.

Nucleation Theory

When applied to phase transformations, classical nucleation theory shows that a nucleus of a new phase cannot be formed at the exact conditions of equilibrium between the phases. Creating a nucleus involves an "expenditure" of energy to form an interface between the existing phase (matrix) and the new phase (nucleus). In equilibrium, the phase transformation produces no energy change, hence the total energy balance will not favor the transformation.

As the system deviates from equilibrium, the change from the less stable to the more stable phase is associated with an energy gain. Part of this energy can be used to create an interface between matrix and nucleus. Because the energy gain depends on the transformed volume, and the interfacial energy depends on the interfacial area, these two energy terms depend in different ways on the nucleus size, as illustrated schematically for a spherical nucleus at a given temperature in Fig. 9.2. One observes that the total nucleus energy goes through a maximum: nuclei that are smaller than the size associated with the maximum can decrease the system energy by decreasing in size and disappearing. Nuclei larger than this critical radius can reduce the system energy by growing. Classical nucleation theory calculations indicate that the further out of equilibrium, the smaller the critical nucleus. Under this single aspect, nucleation would be more favorable the farther from equilibrium the system is. Another factor must be taken in consideration, however. Although a criterion for nuclei survival has been defined, the question "how do nuclei form?" remains to be answered. According to classical nucleation theory, atomic oscillations may create nuclei of the new structure at any point in time

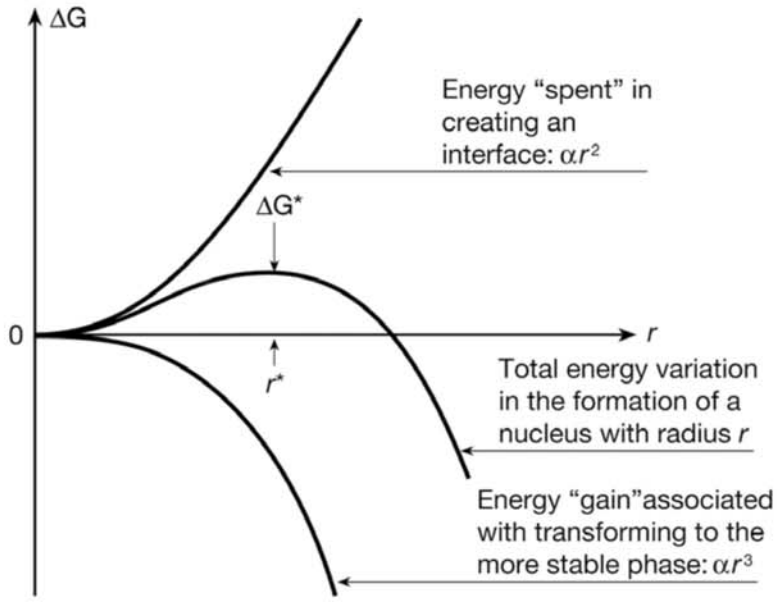

Fig. 9.2 Different terms of the energy change (ΔG) associated to formation of a spherical nucleus of a less stable phase from a more stable phase as a function of the nucleus radius (r) at a given temperature. One term corresponds to the energy expenditure associated with creating an interfacial area between the two phases. The other term corresponds to the energy gain associated with the formation of a volume of the more stable phase starting with the less stable phase. The total energy change goes through a maximum at a radius called the critical radius (r^*). Nuclei reaching this size can decrease their energy by further growth and hence are viable. Smaller nuclei will probably decrease their energy by shrinking and disappearing. The nucleus total energy goes through a maximum at r^*. This value is known as the nucleation barrier. Complete discussion of this topic can be found at different levels in Ref 7, 8, and 9.

for brief moments. If these nuclei are not stable, they will return to their initial configuration. Two points must be considered. First, if the critical nucleus is large, it is difficult to imagine that nature can generate a random oscillation of so many atoms, and it is reasonable to assume that the rate of formation of these prenuclei that have survival conditions will be low. Second, the chance of forming prenuclei via atomic-scale oscillations must decrease with temperature decrease (and less atomic mobility). If the phase to be nucleated becomes more stable as temperature is decreased (as is the case for ferrite or cementite from austenite), this becomes an especially interesting problem, which is discussed next. On one hand, the energy difference between the phases (the driving force for the transformation) increases with lower temperatures and the critical nucleus size also decreases with decreasing temperatures—both factors favoring nucleation. On the other hand, atomic mobility decreases as temperature is lowered, making oscillations and nucleation harder. It can be expected that the nucleation rate may go through a maximum as a result of the combination of these two opposed effects of temperature, schematically presented in Fig. 9.3. While the discussion and most of the usual mathematical formalism is focused on homogeneous nucleation, the same

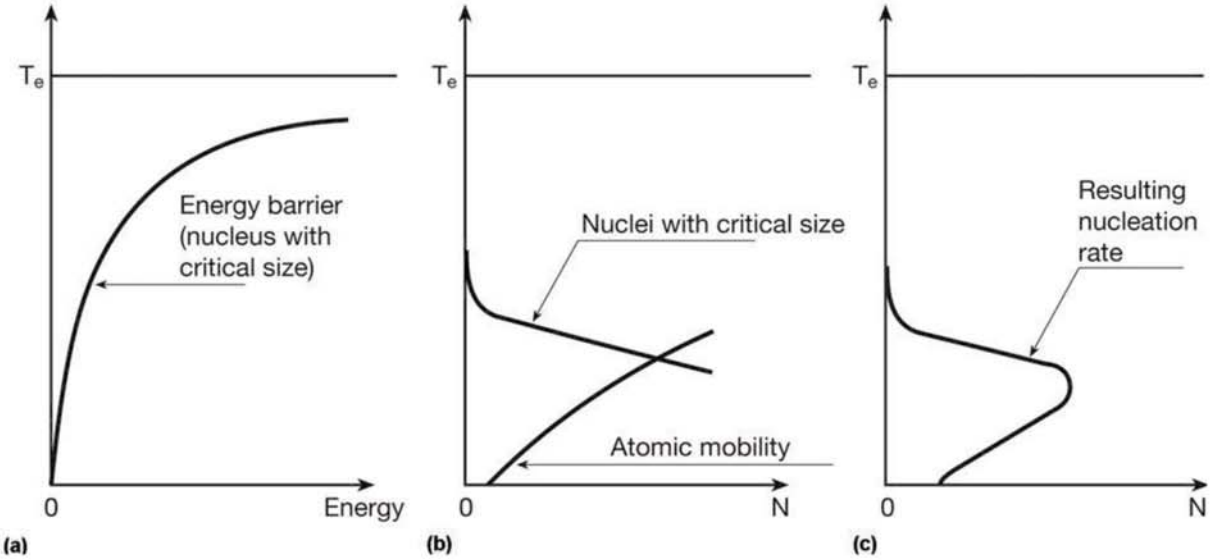

Fig. 9.3 (a) If the matrix and the phase to be nucleated are in equilibrium at T_e, according to classic nucleation theory the nucleation barrier will decrease with the undercooling below the equilibrium temperature. (b) As the critical nucleus size decreases along with the nucleation barrier, it is easier to have prenuclei with the critical size. For a prenucleus to become active, atoms must have sufficient mobility to grow the nucleus beyond the critical size and the mobility decreases as temperature decreases. (c) The resulting effect is that nucleation rate should go through a maximum at a certain intermediate temperature. For a complete discussion, including the applicable equations, see Ref 7 and 8.

applies to heterogeneous (happening at special sites) nucleation. The main quantitative difference is that the maximum of the nucleation rate for heterogeneous nucleation will happen closer to the equilibrium temperature.

An additional variable not mentioned during this simplified discussion is the effect of stresses caused by the volume difference between the phase forming and the phase being consumed. This represents an additional barrier to nucleation from a quantitative point of view. Qualitatively it is interesting to notice that if the phases are anisotropic, there may exist orientation conditions more favorable for nucleation, minimizing induced stresses. Finally, this simplified discussion ignores the fact that the interfacial energy between two crystals has a very strong dependency on the relative orientation between them.

Essentially, in all phase transformations involving austenite decomposition, the orientation relationships between austenite and the phases being formed is important, at least at the nucleation stage.

9.1.2 Diffusive Growth

In most transformations occurring during austenite decomposition in steels and cast irons, solutes must redistribute between austenite and the phases formed, ferrite and cementite. Considering simply the formation of ferrite from austenite in a Fe-C alloy, as shown in Fig. 9.4, the main aspects of diffusive growth may be analyzed, at least qualitatively.

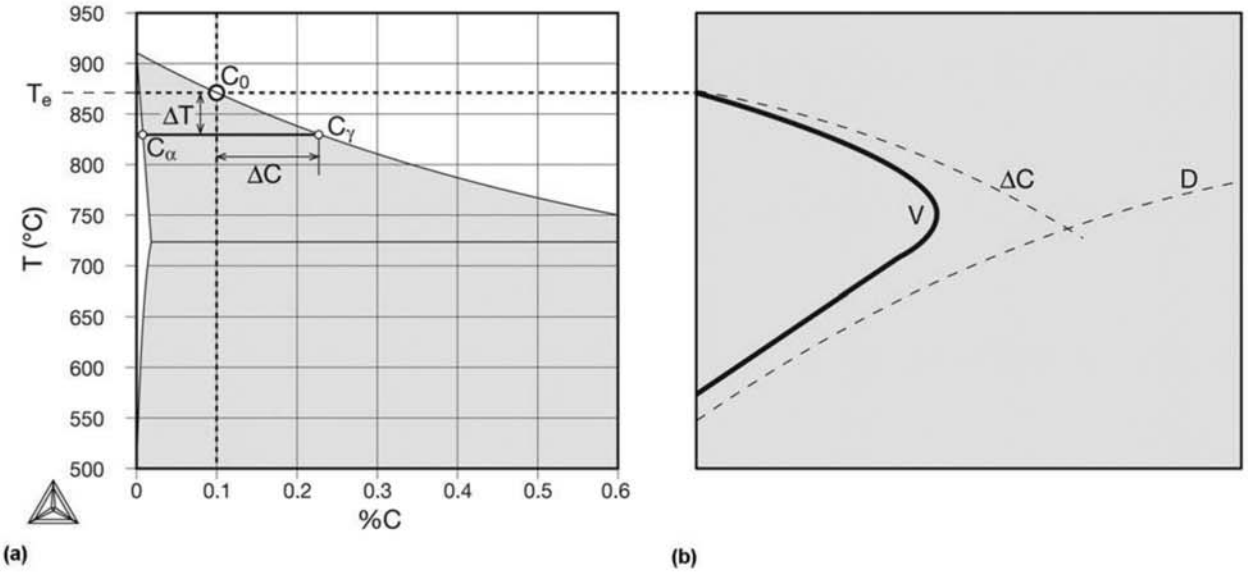

Fig. 9.4 Conditions influencing the growth of ferrite from austenite of C_o composition, in accordance with the Fe-C phase diagram (a). Below T_e, thermodynamic conditions for growth are present. The carbon flux in austenite will define the growth velocity. Two factors contribute to the carbon flux in austenite: the difference between the carbon content at the austenite-ferrite interface (C_γ) and the average carbon content of austenite (C_0), ΔC, and the diffusion coefficient of carbon (D) in austenite. (b) ΔC increases as temperature decreases. Conversely, the diffusion coefficient decreases with temperature reduction. The two opposing effects result in a maximum in the growth velocity (V) curve.

Diffusive flux will depend on two factors:

- the diffusion coefficient, directly dependent on temperature (Ref 7), and
- the chemical composition gradient, responsible for diffusion

Although Fick's law of diffusion (Ref 7) expresses the flux as a function of the chemical composition gradient, in most cases it is more correct to express the flux as resulting from chemical potential gradients. For the current discussion, the simplified approach of Fick's law is acceptable. For more details see Ref 10, 11.

Figure 9.4(a) presents schematically, on a Fe-C phase diagram, the conditions associated with the transformation of austenite to ferrite in a steel containing 0.1% C (C_o). Should equilibrium at interface prevail (an assumption normally accepted), the composition difference associated with carbon diffusion in austenite at a given temperature T – ΔT will be $\Delta C = C\gamma - C_0$.

Contrary to the diffusion coefficient, ΔC increases as the temperature decreases below the equilibrium temperature between the initial austenite and ferrite. Thus Fig. 9.4(b) schematically illustrates the variation of D and ΔC with ΔT. It is also clear that in this case, there will be a maximum in the growth rate, due to the balance between the decreasing diffusion coefficient and increasing driving force for diffusion.

Time-Temperature-Transformation Curves

The combination of nucleation and growth rates make possible the evaluation of transformation rates in isothermal conditions, for each value of ΔT under the equilibrium temperature. If we start with a steel with a very low carbon content (such as an IF steel), it is possible to measure, for each temperature (or ΔT), curves that will show the volume fraction of transformed phase as a function of time elapsed, as shown in Fig. 9.5(b). These curves are

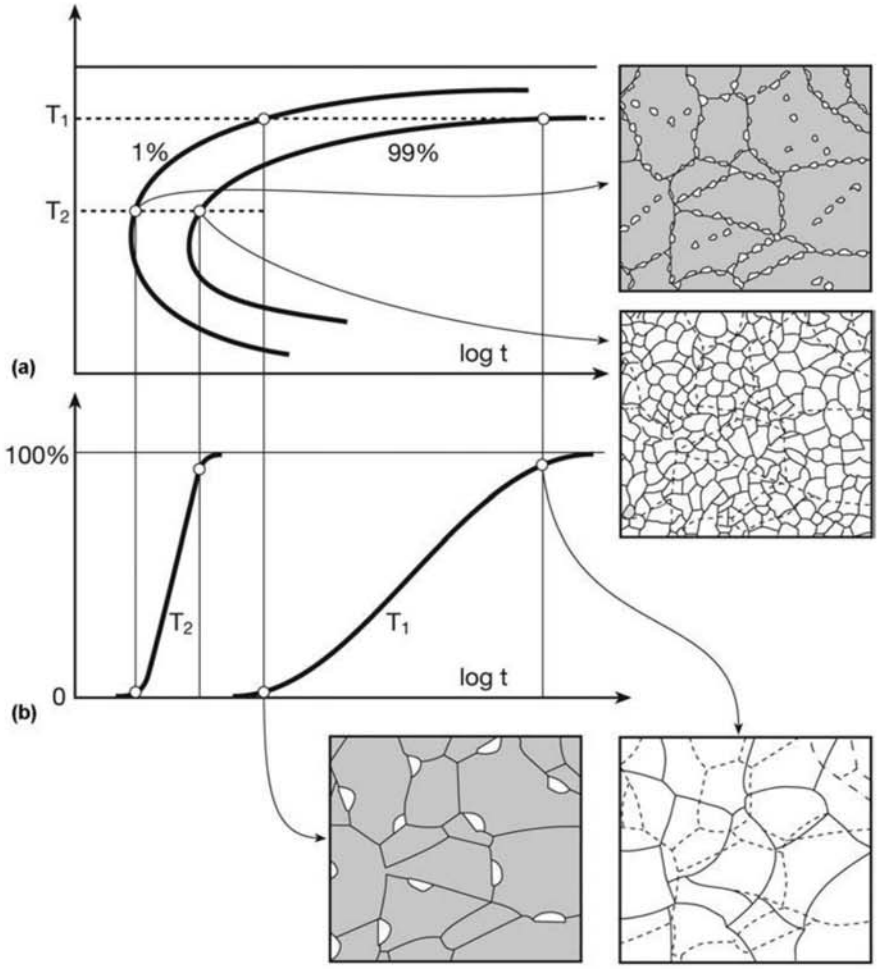

Fig. 9.5 (a) A TTT (time-temperature-transformation) curve for an extra low carbon steel that transforms from austenite to ferrite, without the formation of cementite. The line indicated as 1% is the locus of the points at which 1% of austenite (indicated as gray in the accompanying sketches) has transformed to ferrite (indicated as white). The 99% line is the locus of points in which 99% of austenite has been converted to ferrite (end of transformation). (c) Transformed fraction versus time curves for two temperatures T_1 and T_2. The schematic micrographs indicate that for the same initial austenitic microstructure, there will be more nucleation at temperature T_2, close to the "nose" of the curve than at T_1, as discussed in the text. More copious nucleation in a transformation like this one that consumes the whole of the matrix phase, will lead to a finer ferritic grain size.

the result of the combination of the nucleation and growth rate behavior discussed already (Ref 7, 8).

If one defines a certain fraction transformed as the conventional starting point of the transformation (e.g., 1%) and 99% as the end of the transformation, the information in Fig. 9.5(b) maps to a curve showing the time progress of transformation at each temperature, the so-called time-temperature-transformation or TTT curve of Fig. 9.5(a). Although the concept of a TTT curve is always the same, as the possibilities of microstructural evolution of steels become more complex, the TTT curves become less simple.

Time-Temperature-Transformation Curves—Eutectoid Steel. In Fig. 9.6, a schematic TTT curve for an Fe-C steel with eutectoid composition is presented in the region where only pearlite is formed.

When pearlite is formed, two important aspects related to nucleation and growth must be considered. First, as nucleation increases, the final size of the colonies of pearlite will be smaller because of an impingement phenomenon, as described in the discussion of ferrite formation in Fig. 9.5. The second aspect is related to the fact that pearlite spacing adjusts itself to optimize growth conditions: at relatively low temperatures and thus high driving force for transformation, it is convenient to have a short diffusion path (Fig. 9.7), even at the cost of increasing the interfacial area inside pearlite. Conversely, at temperatures close to the eutectoid temperature where the atomic mobility is high, the lamellae can be further spaced, saving on interfacial energy. Figure 7.14 in Chapter 7, "Equilibrium Phases and Constituents in the Fe-C System," in this book, presents isothermally formed pearlite in a steel with eutectoid composition. Figures 7.15 to 7.17 in Chapter 7, as well as Fig. 9.7 il-

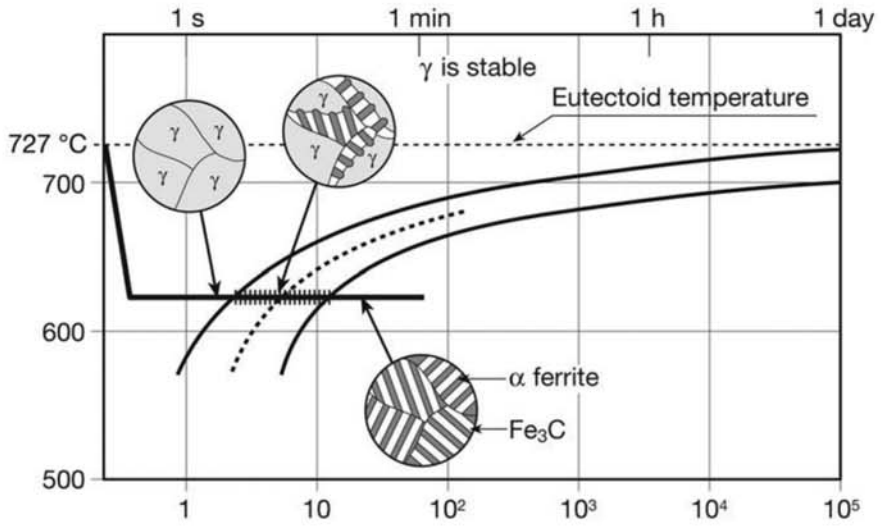

Fig. 9.6 Schematic TTT curve for a Fe-C steel with eutectoid composition. The overall kinetics of pearlite formation is similar to that discussed in Fig. 9.4 for single-phase ferrite. As cementite and ferrite must nucleate (Chapter 7, "Equilibrium Phases and Constituents in the Fe-C System," in this book) lowering the temperature to the temperature of maximum transformation rate has two effects in the formation of pearlite: (i) the lamellae spacing in pearlite is reduced, leading to finer pearlite and (ii) the size of pearlite colonies is also reduced.

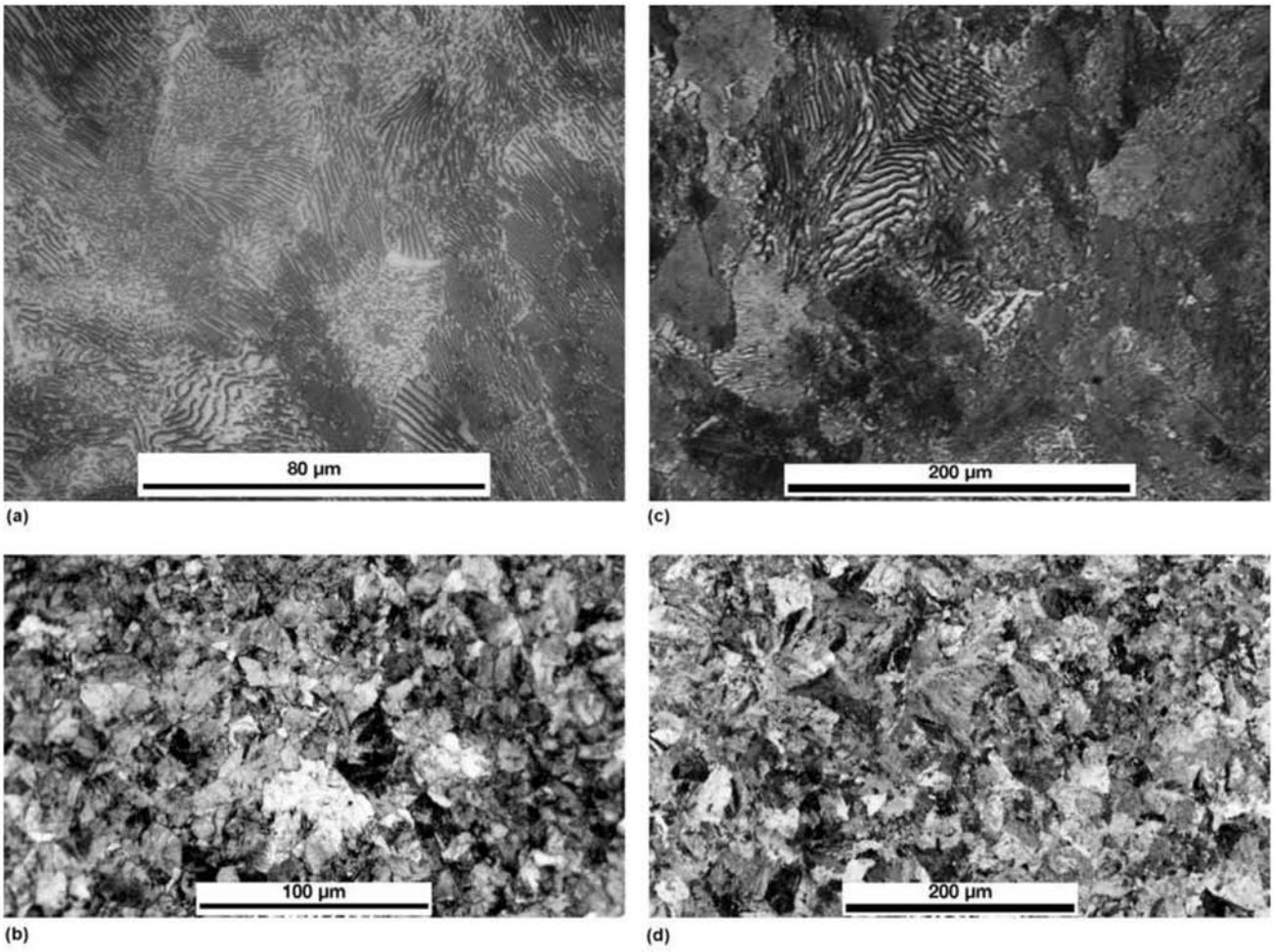

Fig. 9.7 (a) and (c) Steel with eutectoid composition cooled slowly from the single-phase austenitic field. Pearlite. (b) and (d) Steel with eutectoid composition air cooled from the single-phase austenitic field. The difference in lamellar spacing and colony size can be seen. Nital 2%. Courtesy of DoITPoMS, Cambridge University, England.

lustrate the effect of the cooling rate on the lamellar spacing and the size of the pearlite colonies formed.

9.1.3 Martensite—Diffusionless Growth

Phase transformations involving the formation of ferrite and cementite—and hence pearlite—require atomic movement by diffusion. Even in the cases when no significant solute redistribution is required, these transformations are characterized, in terms of individual atom behavior as "civilian" transformations (as opposed to "military" transformations), in which atoms cross the interface between the phases individually and in a noncoordinated way, reorganizing themselves according to the new crystal structure. These transformations are also classified as reconstructive because as they cross the interface, the atoms construct a new phase with movements exceeding the average atomic distances. As austenite is cooled, the atomic mobility is progressively reduced and transformations requiring diffusion and long-range

atomic movement become harder. Even in these cases, when the conditions are adverse to atomic reorganization through diffusion and significant atomic movements across an interface, it is not impossible for ferrous alloys to reorganize into structures that have lower energy than austenite. These transformations normally occur under conditions in which diffusion is not significant any more (low temperatures) and are not associated with changes in chemical composition, only with changes in crystal structure. For these transformations to happen under conditions where the atoms have low mobility, it is common for coordinated movement of atoms to occur, in what is then called a "military" transformation. The most important example of a diffusionless phase formed through a military transformation in steel is martensite. This transformation is also called a displacive transformation due to the coordinated movement (or displacement) of the atoms.

Martensite is named after Adolf Martens, a German scientist (1850–1914) and one of the pioneers of metallography (Ref 12). Martensite has a body-centered tetragonal (BCT) crystal structure. Among the various ways of visualizing displacive transformations that may change austenite, face-centered cubic (FCC) into a BCT structure, the most widely accepted is the Bain distortion, shown in Fig. 9.8. The BCT structure can be visualized as a distortion of body-centered cubic (BCC) in which the lattice parameter in the [001] direc-

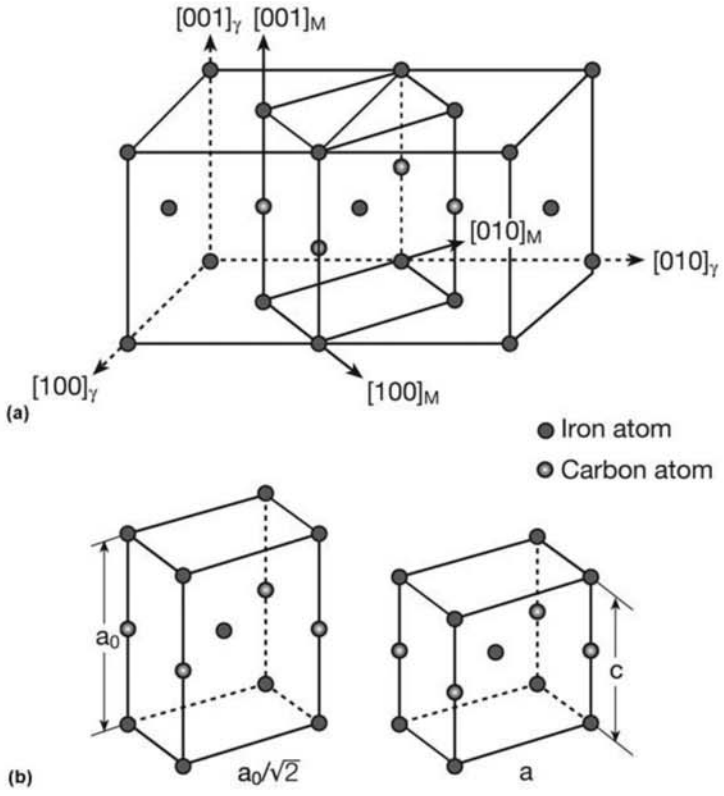

Fig. 9.8 Bain distortion. (a) Two austenite (FCC) unit cells side by side and a BCT cell highlighted from the two FCC cells (some of the atoms in the FCC cell have been removed to enhance visualization of the BCT cell). (b) For the BCT cell to change into BCC, a compression in the "vertical" ($[001]_m$) direction and an expansion in the sides of the cell base $[010]_m$ and $[100]_m$ would be required.

tion is not the same as in the [010] and [100] directions. Martensite lattice parameters are directly dependent on carbon content since, as an interstitial solute, it is mainly responsible for the lattice distortion, as indicated in Fig. 9.8(b). Figure 9.9 shows the effect of carbon content on martensite lattice parameters and hardness. The theories that describe the formation of martensite can be quite complex and are not discussed in detail here. More detailed discussions may be found in Ref 7, 8, and 13. Some important fundamental aspects of these transformations that differentiate them from diffusive transformation and which are relevant to microstructural analysis are:

- Martensite chemical composition is the same as that of the parent austenite from which it has formed.
- The transformation is essentially athermal, that is, the amount of martensite formed depends on the temperature reached and not on the time the material is held at this temperature. Although there are examples of isothermal formation of martensite (Ref 14), the amounts and frequency of occurrence are not of much relevance for the heat treatment of commercial steels.
- The transformation is associated with a significant volume change. This, together with its displacive character, leads to a high level of residual stresses.

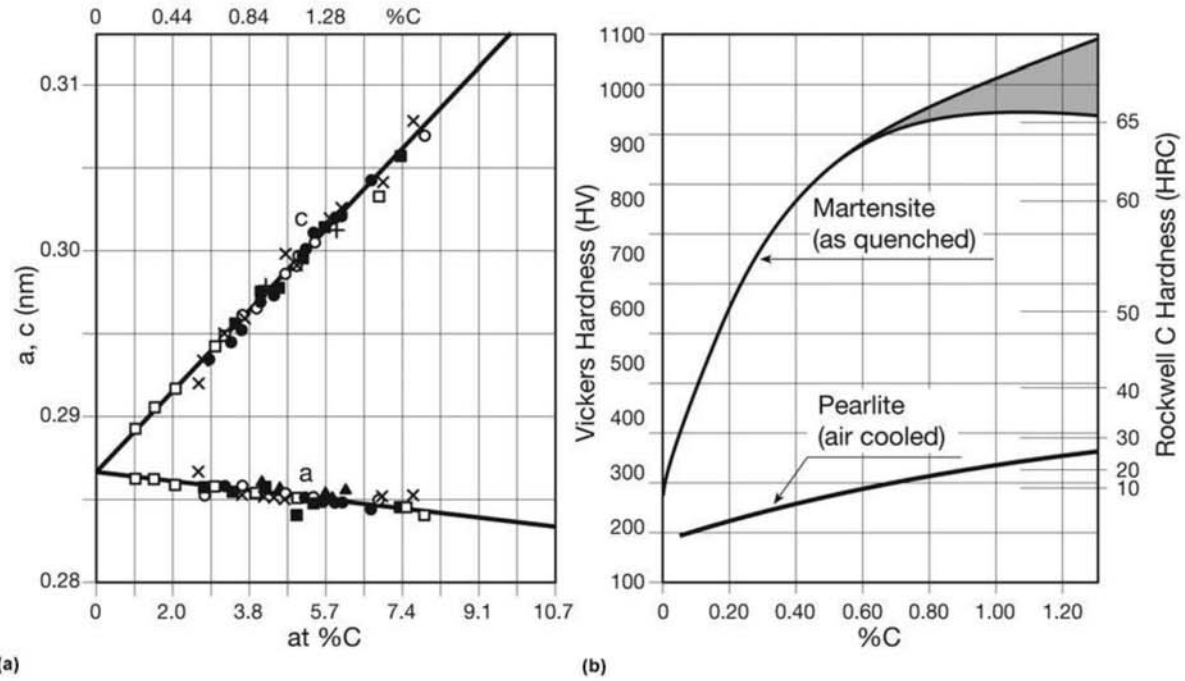

Fig. 9.9 (a) Martensite lattice parameters as a function of carbon content. (b) The hardness of martensite as a function of the carbon content. In the gray region, untransformed (retained) austenite may be present. The upper limit of the region corresponds to the real hardness of martensitic structures. The lower limit corresponds to structures containing retained austenite. The hardness of pearlite formed during air-cooling for the same compositions is also presented, for comparison. Source: Adapted from Ref 13

It is easy to observe (Fig. 9.9a) that the higher the carbon content in the steel, the higher the distortion associated with the formation of martensite. To be able to transform austenite into martensite, increasingly larger amounts of available energy (driving forces) will be needed for the transformation to happen. Thus, it is reasonable to imagine that as the carbon content of austenite increases, a larger undercooling will be needed to make the formation of the metastable martensite phase viable, the alternative the system is left with when it is not possible to transform through diffusional processes anymore.

The temperature at which the martensitic transformation starts is called M_s (s = start). Figure 9.10 presents the M_s temperatures for Fe-C alloys superimposed on the Fe-C equilibrium diagram. This figure demonstrates that the increase in the carbon content of the steel leads to the lowering of the start of the martensitic transformation (M_s). Because M_s is difficult to predict through thermodynamics (Ref 16), empirical relationships are commonly used, as listed in Table 9.1, and recently reviewed in Ref 21. On the other hand, in many steels, the transformation is completed at approximately 130–150 °C (265–300 °F) below the transformation start temperature (Ref 22), and the martensite volumetric fraction $V_{\alpha'}$ transformed at a given temperature T can be estimated using the Koistinen and Marburger equation (Ref 17):

$$V_{\alpha'} = 1 - \exp[-0.011(M_s - T)] \quad \text{(Eq 1)}$$

There is considerable controversy around the value of M_s for pure iron and values significantly different from that presented in Fig. 9.10 have been proposed (Ref 14, 21). Starting at around 0.6% C in Fe-C alloys, M_f (f = finish) the temperature at which the martensitic transformation is concluded is lower than 0 °C (32 °F). Thus, in normal heat treatments, the microstructure may

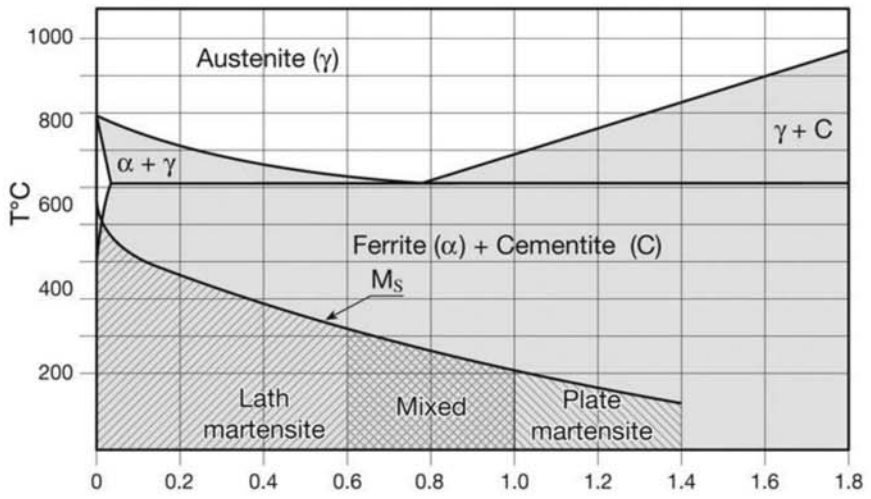

Fig. 9.10 Start temperatures for the martensitic transformation in Fe-C alloys, superimposed on the equilibrium phase diagram for this system. The range in which each of the martensite morphologies is predominant is indicated. Source: Adapted from Ref 15

still present austenite at the end of the treatment. This austenite is commonly referred to as retained austenite.

Martensite forms at very high velocities (the velocity of the martensitic transformation is close to the velocity of sound in the material; Ref 7) and in elongated shapes, either "laths" or "plates." In either case, in the two-dimensional cross-section they look elongated, "needle-like," or acicular. Figure 9.11 presents a phenomenological scheme of the martensitic transformation (in two dimensions). Once nucleated, plates will grow rapidly, becoming longer rather than thicker. Growth is interrupted by obstacles, initially austenitic grain boundaries and later previously formed plates. Careful observation of the steel surface during transformation can supply interesting information, as shown in Fig. 9.12. The interfaces between the parent austenite and the formed martensite are macroscopically coherent. During the transformation, previously existing surface scratches are deviated, but there is no discontinuity in the lines. Significant distortion happens during the transformation, as indicated by the relief, and by the lines deviating from their initial straightness. These observations support a schematic visualization of the

Table 9.1 Some equations used for M_s prediction in steels

All concentrations are in wt%

Equation	Ref
Andrews equation M_S (°C) = 539 – 423 (%C) – 30.4 (%Mn) – 17.7 (%Ni) – 12.1 (%Cr) – 7.5 (%Mo)	17
M_S (°C) = 545 – 470.4 (%C) – 37.7 (%Mn) – 3.96 (%Si) – 21.5 (%Cr) + 38.9 (%Mo)	18
For stainless steel around 12% Cr: M_S (°C) = 300 – 474 (%C) – 33 (%Mn) – 17 (%Ni) – 17 (%Cr-12) – 21 (%Mo) – 11 (%Si) – 11 (%W)	19
For steel with 10–18% Cr and 0–7% Ni: M_S (°C) = 540 – 497 (%C) – 6.3 (%Mn) – 36.3 (%Ni) – 10.8 (%Cr) – 46.6 (%Mo)	20

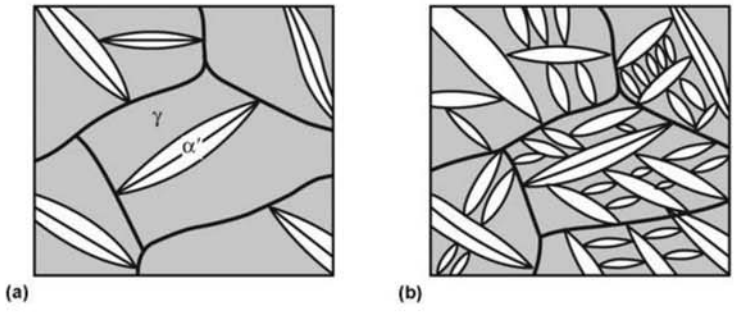

Fig. 9.11 A schematic presentation (in a two-dimensional section) of the growth of martensite (α′) plates with the reduction of temperature below M_s.

transformation, presented in Fig. 9.13. One important conclusion derived from these observations is that martensite cannot form at just any orientation in a given austenite grain: it must form in the right orientations and with the interfaces on well-defined crystallographic planes. This leads to an im-

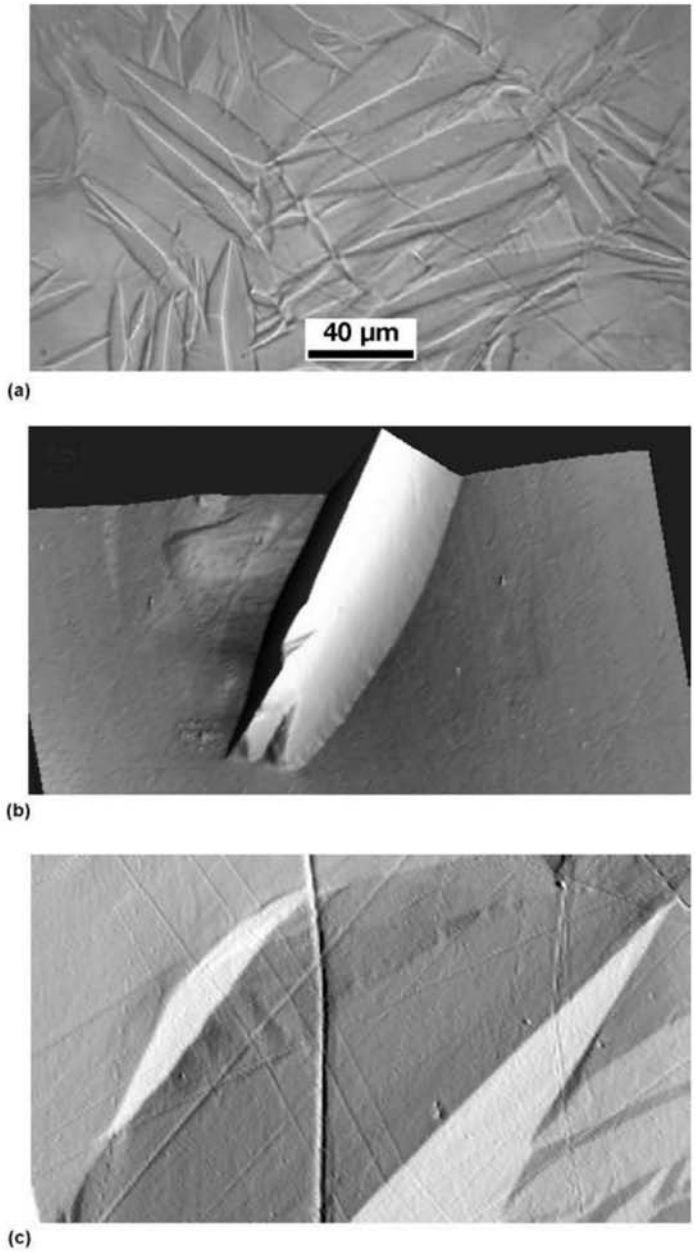

Fig. 9.12 Sample of an iron-based alloy containing C = 0.31% and Ni = 30.5% subjected to metallographic preparation while fully austenitic and transformed to martensite. (a) Optical microscopy showing the initially straight lines on the austenitic sample surface distorted by the transformation. (b) and (c) Atomic force microscopy showing the relief of the martensite plates and the absence of any discontinuity when the lines cross the austenite-martensite interface. Courtesy of H.K.D.H. Bhadeshia, Cambridge University, England. More information in Ref 23.

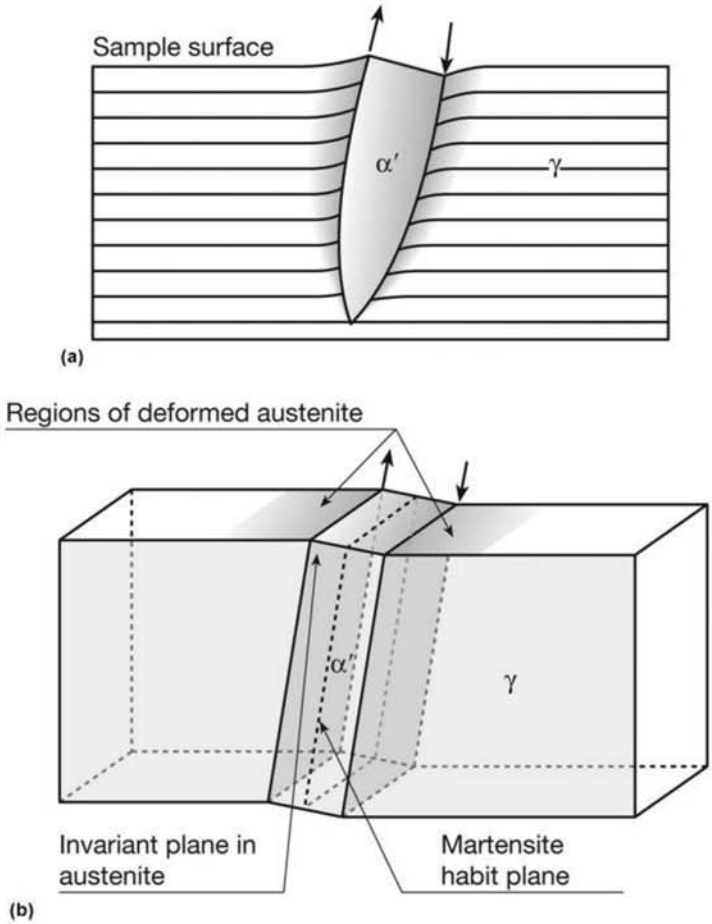

Fig. 9.13 A schematic representation illustrating how it is possible for martensite (α') to maintain macroscopic coherency with the surrounding austenite (γ). For this to happen, martensite must form with well-defined crystallography in relation to the parent austenite, as discussed, for instance in Ref 7. Micrographic evaluation indicates that the orientation of the martensite "needles" are not random in a single austenite grain.

portant micrographic feature, which can be observed even with optical microscopy. Each austenitic grain has a limited number of martensite orientations. Another important observation is that some deformation must happen in both the parent austenite and the formed martensite.

Martensite Morphology

Martensite morphology is mainly affected by carbon content. The usual engineering steels (with carbon contents up to around 0.6%) have martensite formed in laths aligned in groups most often called packages. Many packages can be found in a given previous austenite grain, and the laths are visible, in optical microscopy, as a substructure of the packages. Steel richer in carbon (and Fe-Ni), on the other hand, presents plate martensite. The morphology of martensite laths in the packages was first clarified in the 1960s and 1970s (Ref

24, 25). The problem is especially complex because the laths are generally too fine for detailed observation with optical microscopy and too large for analysis with TEM. The classical work of Krauss (Ref 24 and 25) used a Fe–0.2% C alloy in which two laths were initially marked and identified in one micrograph. Then a series of metallographic sections parallel to the original micrograph were performed, removing about 1.5 μm of material each time via electrolytic polishing. Using this method, it was possible to perform a three-dimensional reconstruction of the isolated laths, as indicated in Fig. 9.14. More recently, the relationships between laths, the blocks formed by them, and the packages, have been further clarified (Ref 26, 27) using a combination of optical microscopy, EBSD/SEM, and TEM. Martensite is usually subjected to a tempering heat treatment (Chapter 10, "Conventional Heat Treatment: Basic Concepts," in this book) in which part of the carbon leaves the supersaturated solution, precipitating carbides and other changes occur, generally reducing residual stresses and increasing ductility.

Figures 9.15 to 9.20 present various morphological aspects of martensite in different steels.

9.1.4 Bainite—An Intermediate Constituent

In the intermediate temperature range, between the temperatures at which the eutectoid transformation will happen, forming pearlite (around 550–720 °C, or 1020–1330 °F) (Ref 17), and the temperature at which martensite transformation starts, a series of specific microstructures can form in carbon steel that is either isothermally treated or continuously cooled. These

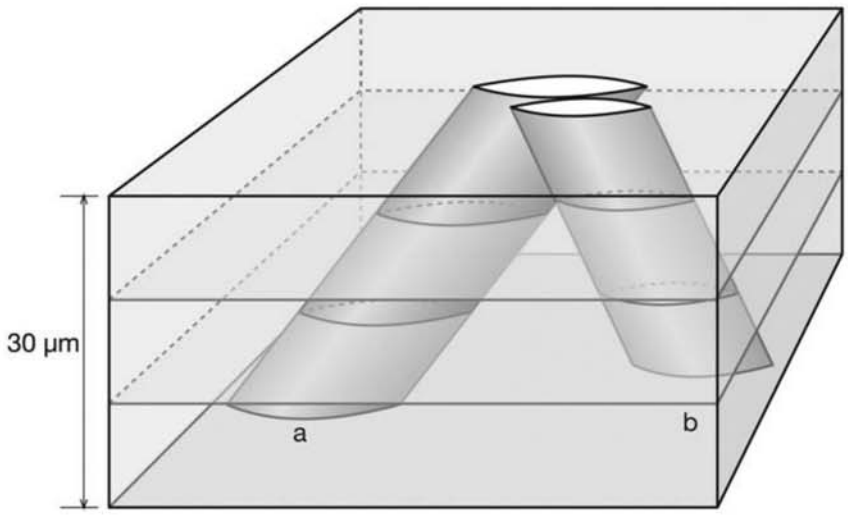

Fig. 9.14 Three-dimensional reconstruction of two laths in the martensite package in a Fe-0.2% C alloy. A series of micrographs 1.5 μm spaced in depth were made to create a reconstruction such as this one. A significant portion of the laths have a cross section that is approximately rectangular and not lenticular, as indicated in this figure. A package is evidently composed of many laths side by side, filling the volume (see Fig. 9.8a). In the figure, only two laths are represented to make possible a complete visualization. Source: Adapted from Ref 24 and 25

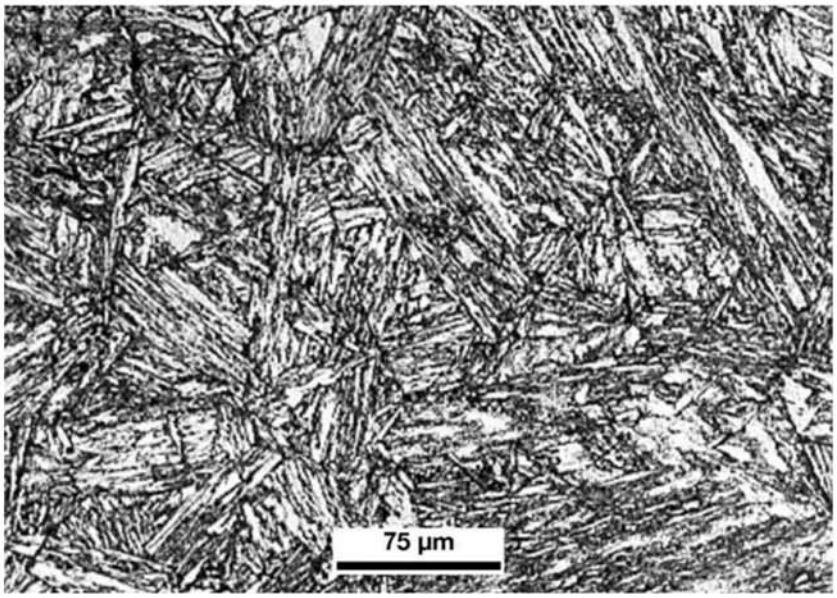

Fig. 9.15 Martensite in low alloy steel ASTM A533 Cl.1 (ASME SA 533 Cl 1 or 20MnMoNi55) with C = 0.2%, Mn = 1.38%, Si = 0.25%, Ni = 0.83%, Mo = 0.49% continuously cooled at 50 °C/s (90 °F/s). Transformation start temperature: 415 °C (780 °F). Etchant: Nital 2%. Courtesy of B. Marini, CEA, France. Source: Ref 28

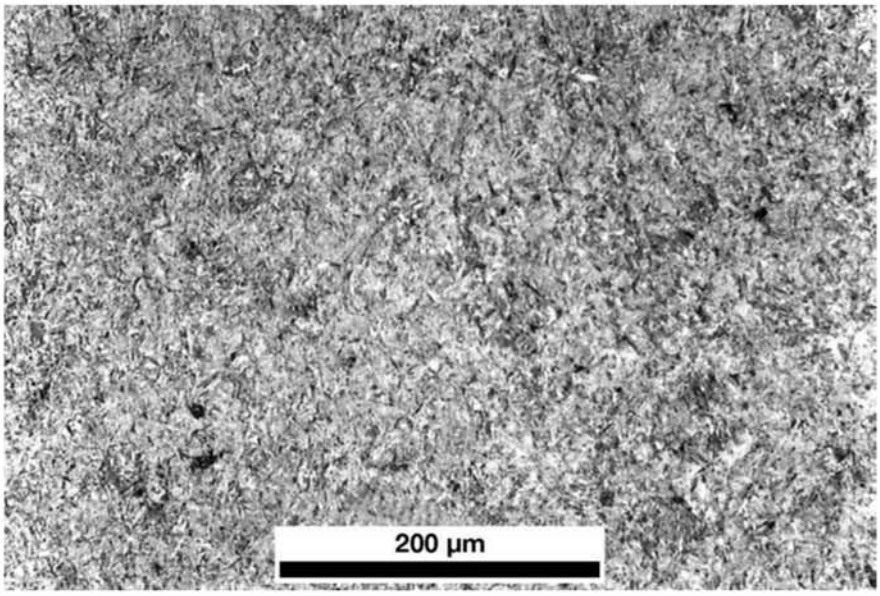

Fig. 9.16 Rapidly cooled steel containing 0.55% C and 0.65% Mn. Martensite. Etchant: nital. Courtesy of DoITPoMs, Cambridge University, England.

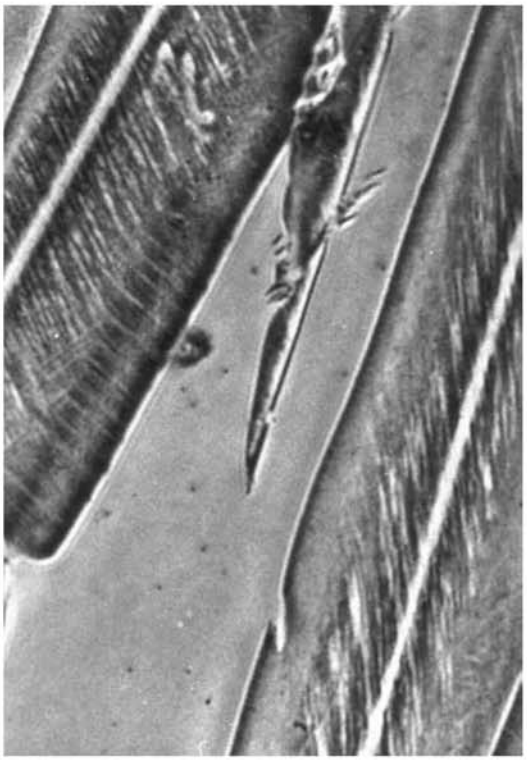

Fig. 9.17 Martensite plates in an experimental steel containing C = 0.1%, Ni = 30%. The central line, called "midrib" associated in the martensite formation theory to nucleation (Ref 7), can be seen. Image by J.R.C. Guimarães, Courtesy of H.-J. Kestenbach, UFSCar, Brazil.

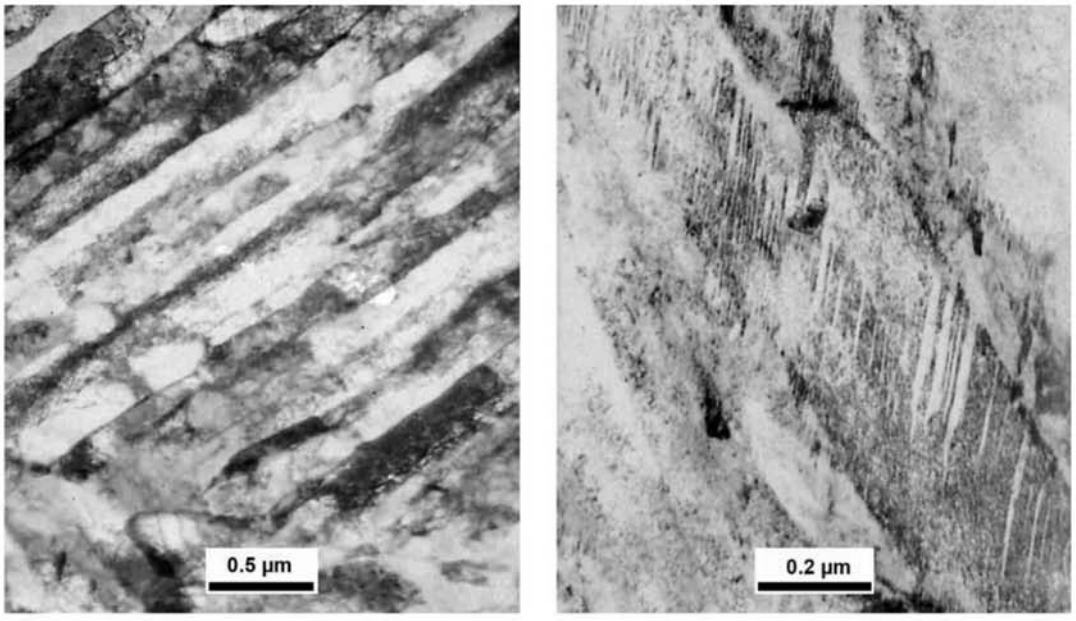

Fig. 9.18 (a) Lath martensite in a steel with C < 0.16%, Mo = 0.3–0.6%, Cr = 0.6–1.2%, Cu 0.2–0.5% V ≤ 0.1%V. (b) Plate martensite (with twins) in the high carbon layer of a carburized AISI 4118 steel. TEM. Courtesy of H.-J. Kestenbach, UFSCar, Brazil.

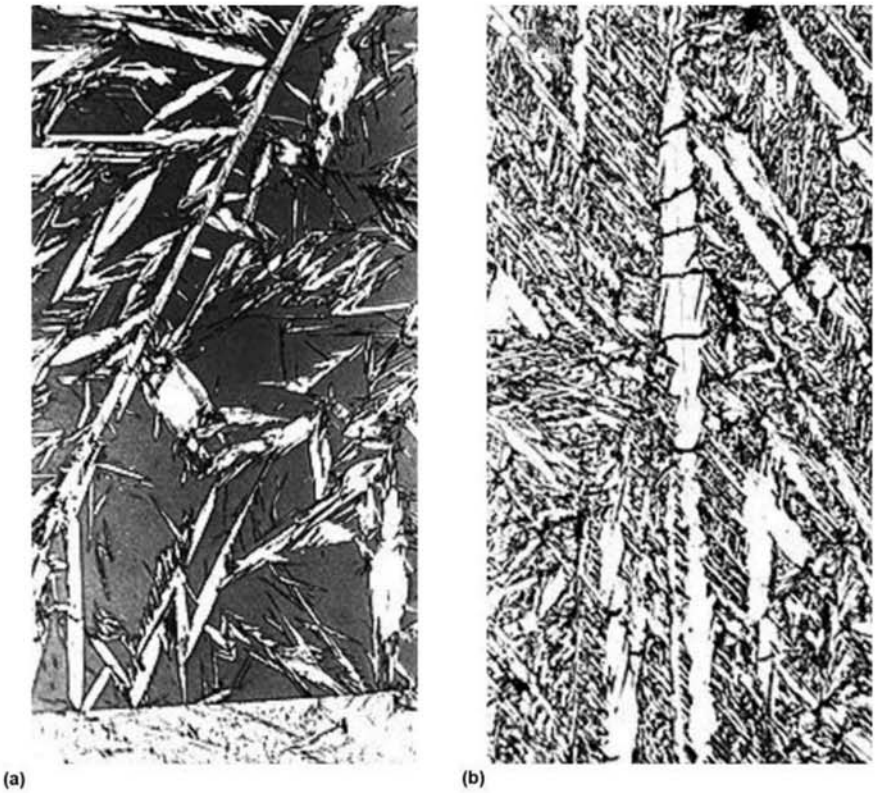

Fig. 9.19 (a) Martensite plates in a retained austenite matrix in a steel containing 1.7% C, rapidly cooled to room temperature. (b) The same sample subjected to cooling in liquid air. Martensite volume fraction has increased significantly and retained austenite has been almost completely eliminated. The central martensite plate presents cracks transverse to its major axis. Compare with Fig. 9.11. Courtesy M. Hillert. Source: Ref 29

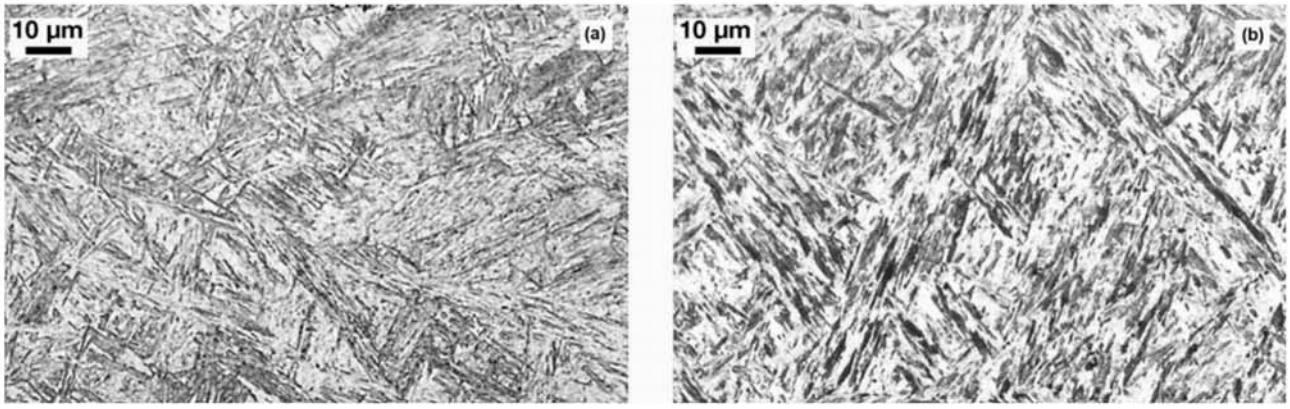

Fig. 9.20 Martensite (a) in laths, in a laser-welded steel containing 0.13% C and (b) in plates (or twined) in laser welded steel containing 0.27% C. Courtesy G .Thewlis, reprinted with permission from Maney Publishing. Source: Ref 30

microstructures are frequently ferrite-cementite (or other carbides, in alloy steels) aggregates with very fine characteristic dimensions. The studies of Bain and Davenport (Ref 31) have led to the identification of a "constituent … which was neither … pearlite nor … martensite, but a novel constituent" Bain (Ref 32) formed in this intermediate range of temperatures. Edgard Bain lead a small important research group in the 1920s–1930s in what was then one of the largest steelmakers in the world, US Steel. In 1934 his colleagues named this "new" constituent after him (Ref 33). It is interesting that the name that prevailed in Germany for this constituent was *Zwischenstufengefüge*, "intermediate structures." This was an especially interesting discovery because in carbon steel, the nucleation and growth curves (C-shaped curves) for pearlite and bainite formation are essentially superimposed, as indicated in Fig. 9.21. Thus, bainite can be characterized as a transformation product formed in an intermediate temperature range between the eutectoid transformation (pearlite formation) and the martensitic transformation. This constituent is formed by ferrite-cementite aggregates. There is considerable discussion and controversy on the mechanisms of formation of bainite and on the application of the term bainite (Ref 33, 34, 35). Bhadeshia (Ref 33) suggests that the "microstructural" definition of bainite proposed by Aaronson of a nonlamellar aggregate of ferrite and carbides in which the phases form consecutively, continues to be adequate. Furthermore, these microstructures can be classically classified in two types, depending on the temperature range in which they are formed and on their microstructural features: upper and lower bainite. This is an important classification in view of the significant differences in properties that these two types of bainite exhibit. The main difference between the two microstructures is related to the way carbides precipitate. Unfortunately, these differences are not observable in the scale of optical microscopy. Even the distinction between bainite and martensite

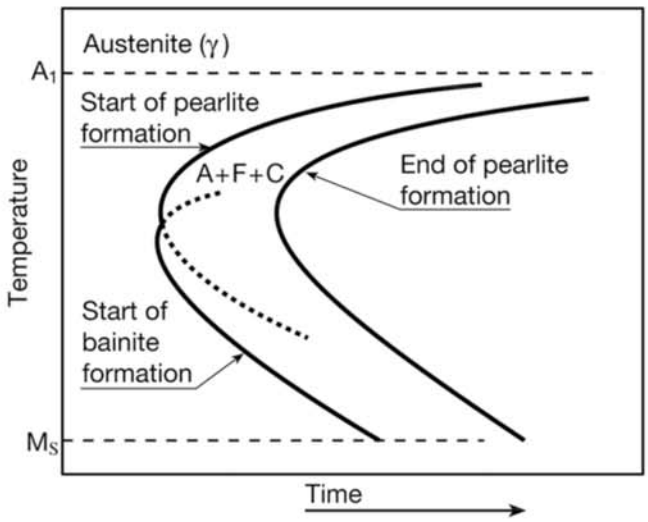

Fig. 9.21 Schematic TTT curve for a eutectoid steel. The pearlite transformation curve is essentially superimposed on the bainitic transformation curve. The diagram also illustrates schematically the temperature at which martensite formation starts. A = austenite, F = ferrite, C = carbide.

using optical microscopy is not always an easy task, because features of these structures are usually in the resolution limit of the technique. Martensite usually looks finer than bainite in the optical microscope, because all martensite crystals are usually smaller than the resolving power of the optical microscope. Furthermore, there may be some evidence of the crystallographic habit planes of the martensite laths in a martensite package (Ref 36). In the absence of cementite in the microstructure, the intermediate constituents are better classified as ferrites (Ref 13), including "bainitic ferrite" (see 9.3 "Ferritic Microstructure" in this chapter).

Upper and Lower Bainite

Upper bainite is formed in the temperature ranges immediately below the range of formation of pearlite. In a TTT diagram, the curves representing the formation of upper bainite and pearlite become more distinct as alloying elements are added to the steel. A classical explanation for this effect is the fact that in a diffusion-controlled transformation, alloying elements have to be redistributed between the phases (austenite and ferrite). The effect of this partition on the kinetics of formation of ferrite and pearlite is quite different from its effect on the bainitic transformation, so that in TTT curves of alloy steels, it is normally possible to clearly distinguish the curve describing the formation of bainite, as shown schematically in Fig. 9.22. Figure 9.23 presents two of the most common morphologies of bainite. If one follows Hillert´s point of view (Ref 37), supported by other classical viewpoints (Ref 38), bainite is the product of the nonlamellar eutectoid decomposition of austenite. Other microstructures should be classified as ferrites or as tempered martensite. (Within this point of view, there are many other bainite morphologies, as described in Ref 39). Upper bainite is composed of sheaves of ferrite crystals. These ferrite crystals are most frequently laths or plates parallel to each other

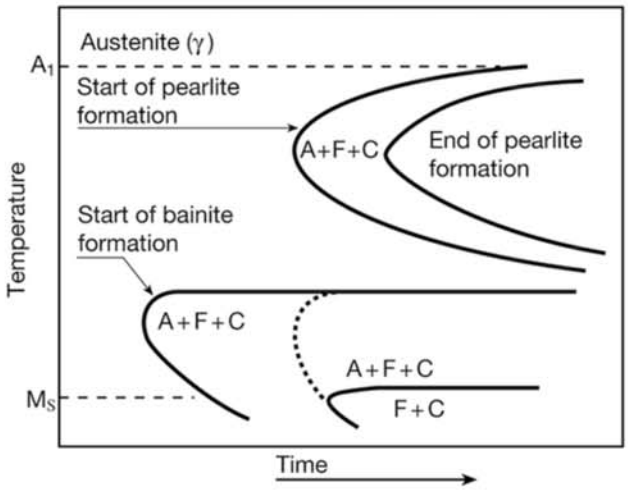

Fig. 9.22 Schematic TTT curve for a steel in which the bainitic transformation is not superimposed on the pearlitic transformation. The diagram also illustrates the temperature at which martensite formation starts. The bainitic transformation may not go to completion in a range of temperatures. A = austenite, F = ferrite, C = carbide.

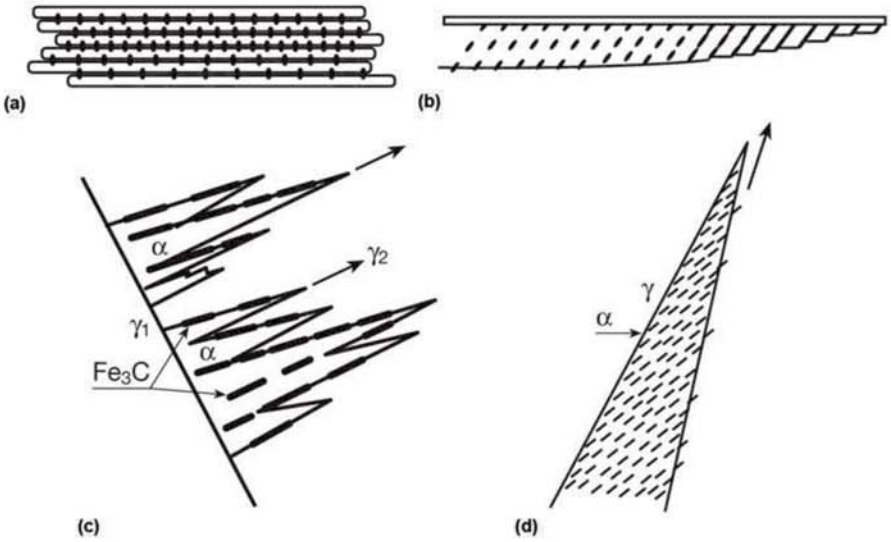

Fig. 9.23 Schematic representation of the two most common bainite morphologies. (a) Upper bainite and (b) lower bainite. The dark particles represent cementite, and the white regions represent ferrite. Simplified growth schemes are indicated for upper bainite (c) with carbide precipitation between the ferrite plates and for lower bainite (d) in which carbides precipitate in the ferrite after its formation from austenite. In lower bainite, carbides can also occur between the ferrite plates. Source: (a) and (b) adapted from Ref 39; (c) and (d) adapted from Ref 7

that grow through the austenite grains. Carbides are present between the ferrite crystals. Many studies have analyzed the crystallographic orientation between the ferrite crystals (which have very close orientations among them in the same sheaf) and those between ferrite and the parent austenite from which they were formed. This can be measured using EBSD (Ref 40). The carbides in upper bainite are larger than those in lower bainite, but they are still not visible in optical microscopy. Upper bainite normally shows dark in optical metallography due to the rugosity caused by the etching around the cementite particles. Packages may be formed by laths (Ref 40). Lower bainite, on the other hand, presents long ferrite plates in a microstructure somewhat similar to plate martensite (Ref 13). This morphology leads to the common classification as acicular. Distinguishing this structure from martensite with optical microscopy is difficult, as mentioned earlier. Color etching that tints phases differently (Fig. 9.24) is very useful in uncertain cases. Recently EBSD has been shown to be successful in identifying and quantifying bainite and ferrite and distinguishing them from martensite in a TRIP steel. The challenge is that the structures are very similar, and EBSD relies on the diffraction of the electrons backscattered from the sample surface region. Thus, complete removal of any deformation caused during preparation is essential for the success of the technique. The proper treatment of the diffracted signals also is a critical aspect (Ref 42). Figures 9.25 to 9.28 present different metallographic aspects of bainite. In isothermal treatments, it is frequently possible to produce structures with the characteristic features of upper and lower bainite. In continuous cooling, however, the observed morphologies are not easily characterized as either upper or lower bainite (Ref 43). Hence, the effect of cooling

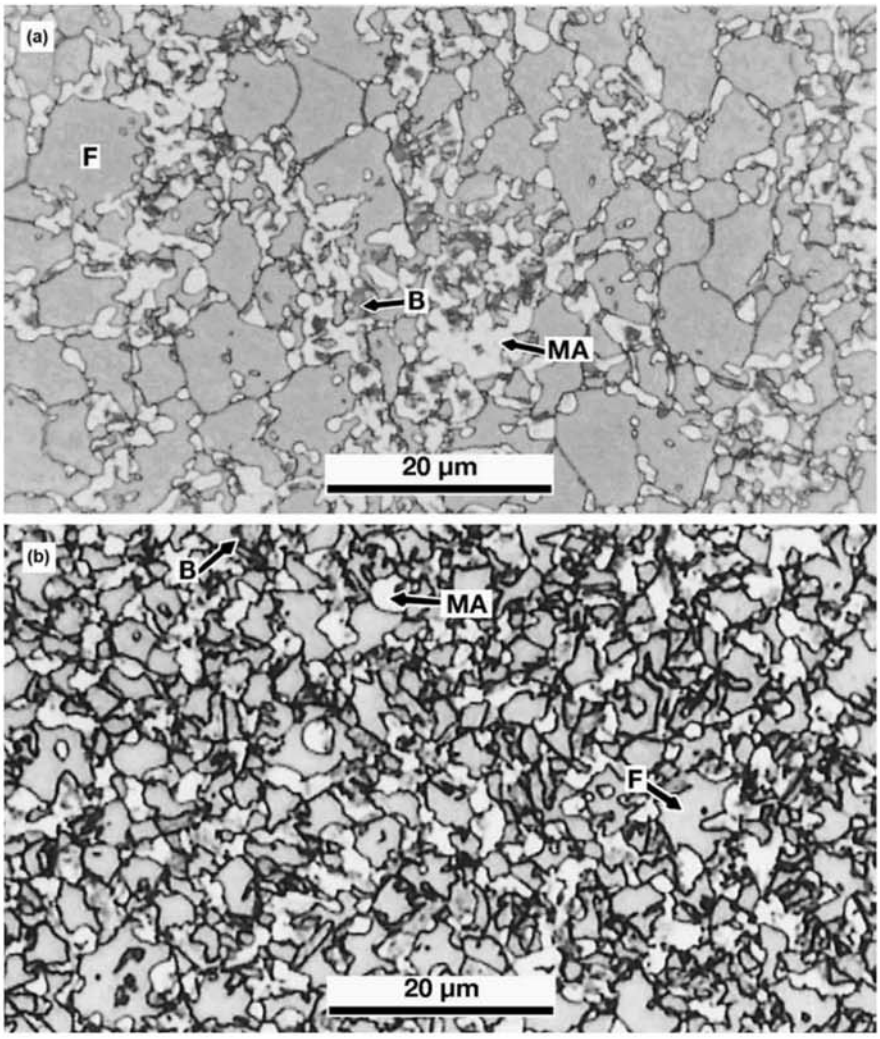

Fig. 9.24 Etchants such as LePera and their modifications can selectively color tint phases. In the photographs (here reproduced in grayscale), (a) and (b) F = ferrite, bluish green in the original, here intermediate gray tone; B = bainite (brown, darker gray tone); M-A, white. TRIP steels (see Chapter 13, "Advanced Steels for Forming Operations," in this book) (a) (C = 0.11%, Si = 1.5%, Mn = 1.53%) and (b) (C = 0.7%, Si = 1.4%, Mn = 1.4%) after intercritical treatment followed by isothermal treatment. Etchant: modified LePera: two fresh solutions must be mixed immediately before etching. 30 ± 2 ml of solution (#1) (1 g $Na_2S_2O_5$ (sodium metabisulfite) + 100 ml distilled water and 30 ± 2 ml of solution (#2) (4 g dry picric acid + 100 ml ethanol). Immerse for 10 to 20 s, wash with ethanol, and dry with fresh air. More details in the original reference. Reproduced with permission from Elsevier. Source: Ref 41

speed on bainite morphology is evident (compare Fig. 9.27 and 9.28). Other bainite morphologies can be seen in Fig. 9.29–9.31.

A constituent that has been the subject of some controversy for some time is also present in Fig. 9.24. Habraken and Economopuoulos (Ref 43) observed that under some transformation conditions, regions of the steel may be sufficiently enriched in carbon to partially transform into martensite and retain a

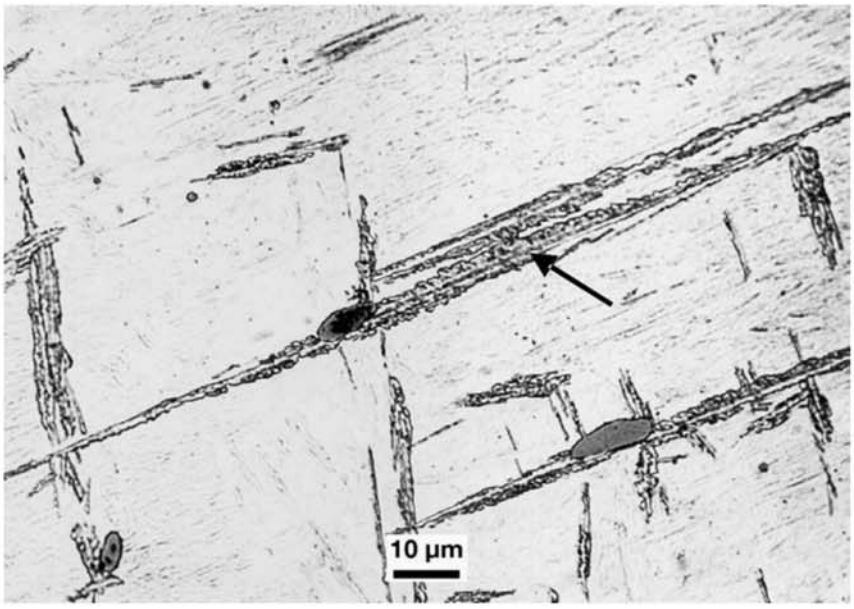

Fig. 9.25 Growth of bainite plates from intragranular nonmetallic inclusions in a steel containing C = 0.38%, Mn = 1.39%, S = 0.039%, V = 0.09%, N = 130 ppm isothermally treated for 38 s at 450 °C (842 °F). Arrow indicates bainite plates with carbides in between the plates as well as inside them. The untransformed portion of the matrix has transformed to martensite on cooling after the isothermal treatment. Courtesy G. Thewlis, reprinted with permission from Maney Publishing. Source: Ref 30

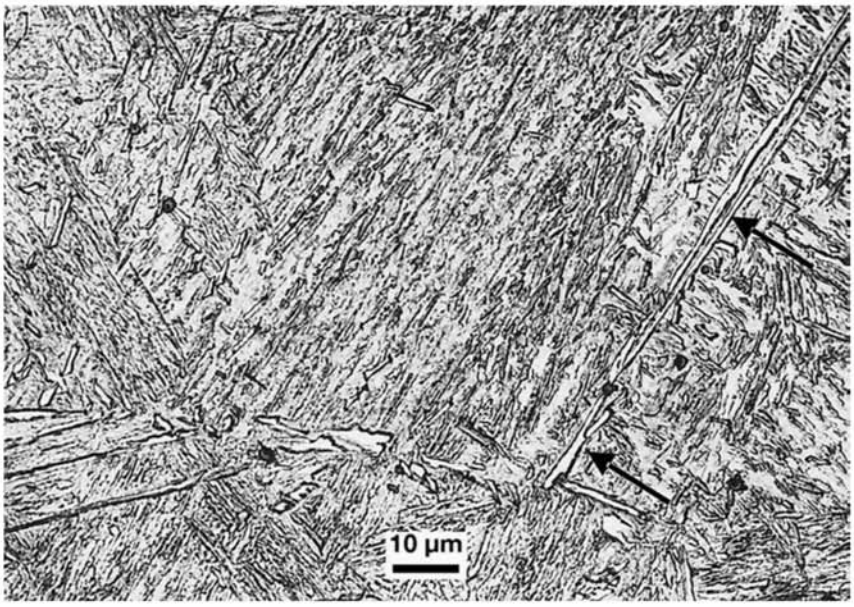

Fig. 9.26 Growth of intragranular plates of granular bainite in a steel containing C = 0.38%, Mn = 1.39%, S = 0.039%, V = 0.09%, N = 130 ppm isothermally treated for 38 s at 500 °C (930 °F). Arrow indicates individual plates of bainitic ferrite nucleated in a nonmetallic inclusion. Courtesy G. Thewlis, reprinted with permission from Maney Publishing. Source: Ref 30

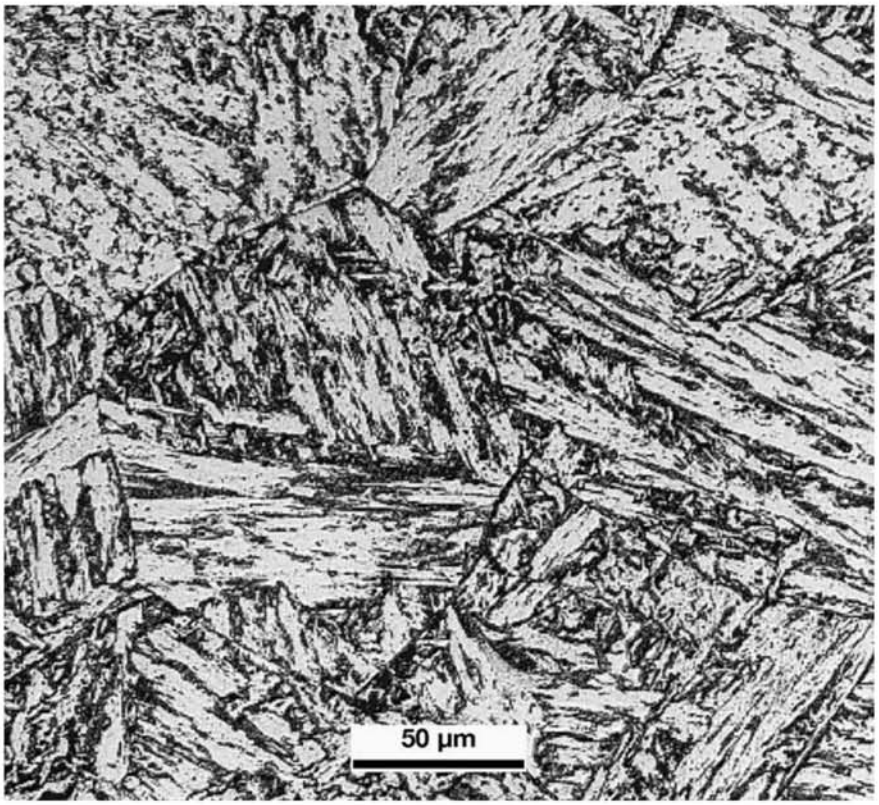

Fig. 9.27 Bainite in low alloy steel ASTM A 533 Cl.1 (ASME SA 533 Cl 1 or 20MnMoNi55) containing C = 0.2%, Mn = 1.38%, Si = 0.25%, Ni = 0.83%, Mo = 0.49% (same steel as in Fig. 9.15) continuously cooled at 0.1 °C/s (0.18 °F/s). Transformation start at 590 °C (1094 °F). Etchant: nital 2%. Prior austenite grain boundaries are visible. Courtesy of B. Marini, CEA, France. Source: Ref 28

fraction of untransformed (retained) austenite. These regions generally present a uniform response to most etchants, which can make it difficult to resolve the martensite from the retained austenite. They have been named MA areas. This is a constituent that plays an important role in certain properties, including toughness. On many occasions the increase of its volume fraction has been associated with a decrease in steel toughness (Ref 44).

9.1.5 Time-Temperature-Transformation Curves and Continuous Cooling Transformation Curves

Time-Temperature-Transformation Curves

Time temperature transformation curves, sometimes also called isothermal-time-transformation (ITT), discussed in the section "Time-Temperature-Transformation Curves" earlier in this chapter, can be determined experimentally in two ways. The first way involves dilatometry techniques. When one follows the change in volume over time of a sample rapidly cooled to the transformation temperature to be studied, the start and end of the transformations can be observed by noticing the volume changes. Because austenite

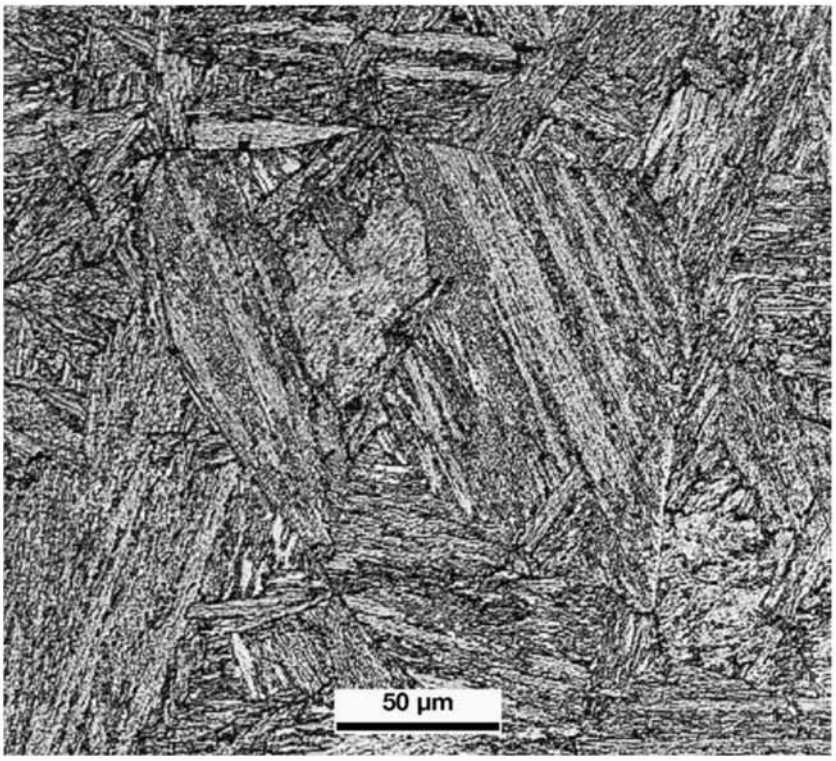

Fig. 9.28 Bainite in low alloy steel ASTM A 533 Cl.1 (ASME SA 533 Cl 1 or 20MnMoNi55) containing C = 0.2%, Mn = 1.38%, Si = 0.25%, Ni = 0.83%, Mo = 0.49% (same steel as in Fig. 9.15) continuously cooled at 2 °C/s (3.5 °F/s). Transformation start at 590 °C (1094 °F). Etchant: nital 2%. Prior austenite grain boundaries are visible. Courtesy of B. Marini, CEA, France. Source: Ref 28

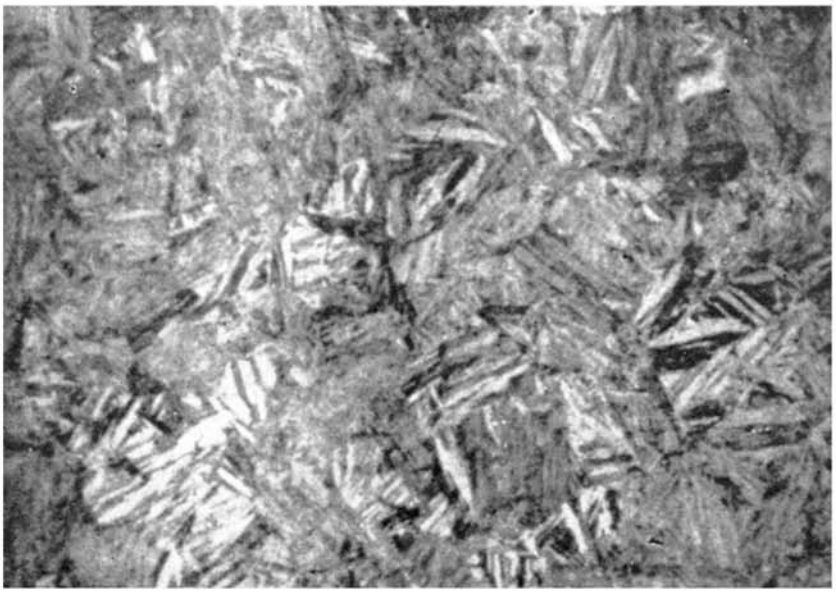

Fig. 9.29 Bainite formed in isothermal heat treatment at 400 °C (750 °F) (austempering in liquid lead bath). Etchant: nital.

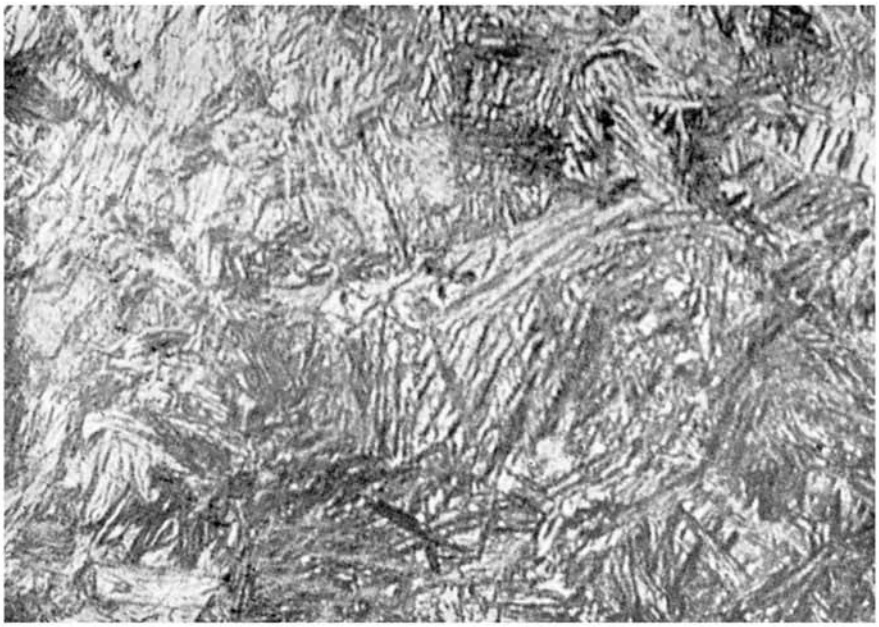

Fig. 9.30 Bainite formed in isothermal heat treatment at 250 °C (480 °F) (austempering in a salt bath). Etchant: nital.

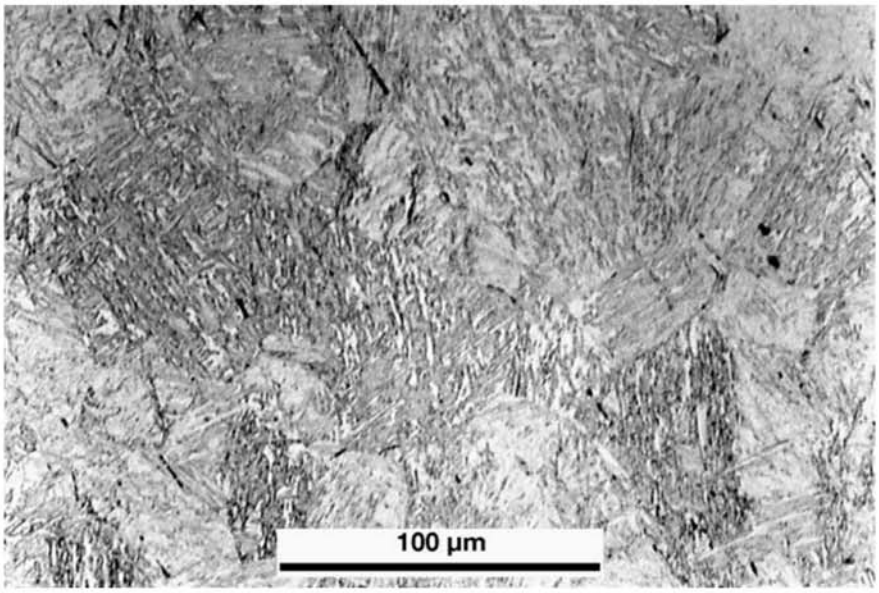

Fig. 9.31 Bainite in steel containing 0.4% C. Etchant: nital 2%. Courtesy of DoITPoMS, Cambridge University, England.

and the phases into which it decomposes have different densities, the transformations cause measurable changes in volume.

The second technique is metallography. When following this method, various specimens of the steel are simultaneously austenitized for the same time at the same temperature. Once austenitization is complete, the specimens are simultaneously and rapidly cooled to the temperature at which the phase

transformation is to be studied. They are held at this temperature and removed from the furnace one by one and quenched (rapidly cooled) at defined time intervals. If the time for which the specimen has been held at the study temperature has not been sufficient for the transformation to start, austenite will transform completely to martensite on quenching. Otherwise, the sample will present a certain area (volume fraction) that is isothermally transformed, and the rest will be transformed to martensite during the ensuing quenching. Metallographic examination of this series of specimens (Fig. 9.32) makes it possible to follow the transformation. The data can be used to graphically present the percentage of phase isothermally transformed as a function of holding temperature, as shown schematically in Fig. 9.33. Because the transformation time varies several orders of magnitude (between seconds and days) when the transformation temperature changes, the time

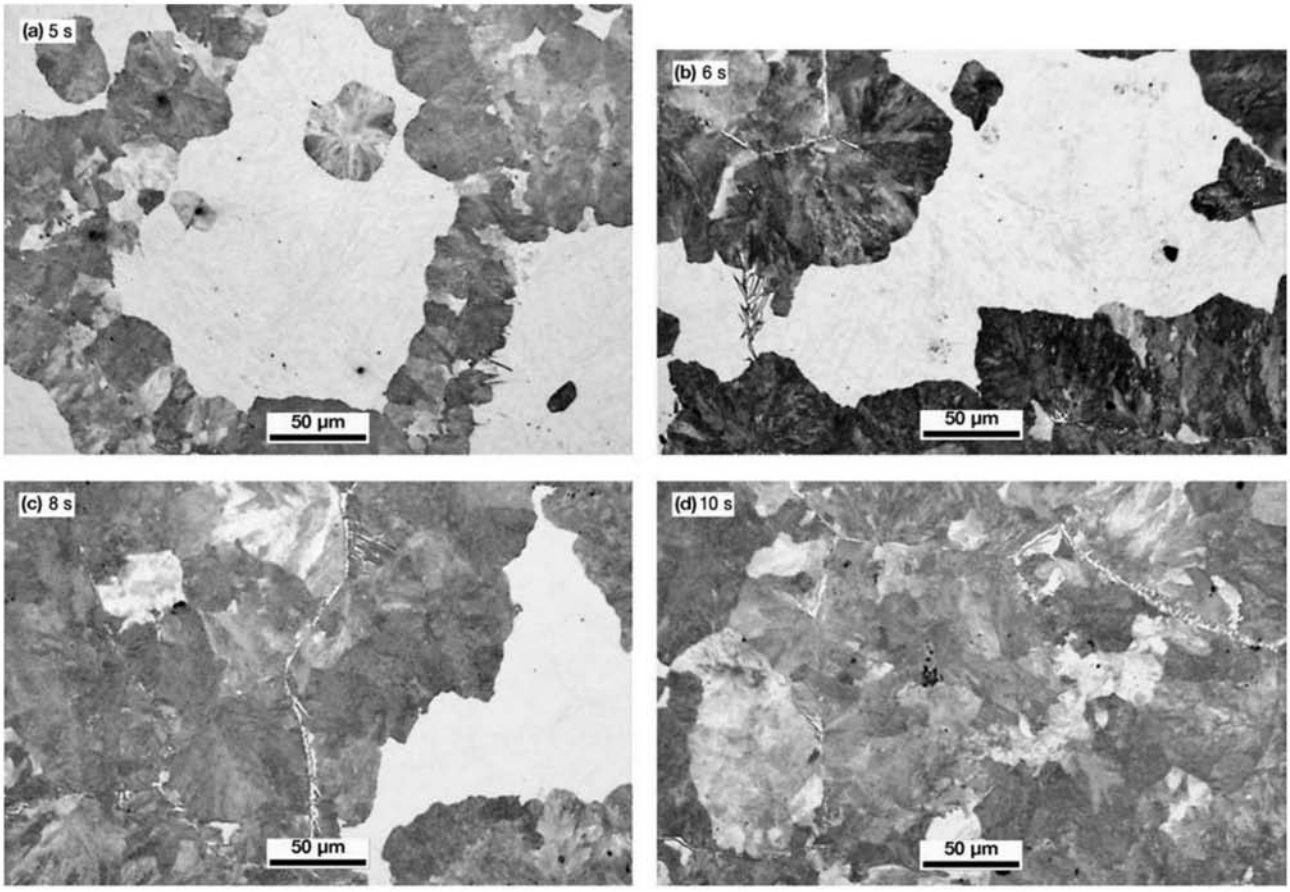

Fig. 9.32 Isothermal transformation in a steel containing C = 0.5%, Mn = 1.5% at 538 °C (1000 °F). The specimens are rapidly cooled from the austenitization temperature to the isothermal heat treatment temperature. They are then maintained at this temperature for the times indicated in each figure. Afterward, they are quenched to room temperature to interrupt the transformation. The fraction of nontransformed austenite appears as martensite (light) in the images. The transformation starts at the austenitic grain boundaries, where the transformation has already been completed in (a) and (b). A few pearlite colonies nucleate inside the austenitic grain, as can be seen in (a). From (b) to (d) pro-eutectoid ferrite can be observed. The region of sample (a) may present slight segregation or heterogeneity so that the pro-eutectoid constituent is absent. With 10 s of isothermal treatment at 538 °C (1000 °F), transformation is completed, as can be seen in (d). Etchant: nital 2%. Courtesy of C. Capdevila Montes, Grupo Materialia, Spain.

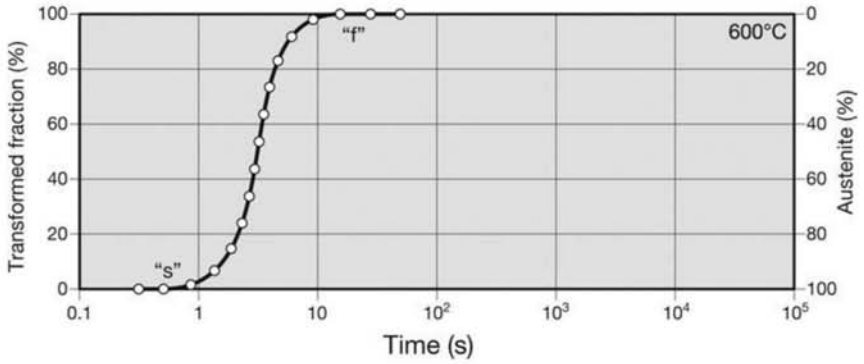

Fig. 9.33 Fraction transformed curve in an isothermal transformation of an eutectoid steel at 600 °C (1110 °F). The start and the end of the transformation (s and f) are normally characterized by volume fractions that can be measured via quantitative metallography.

scale is usually plotted on a log scale. This graph supplies, as information, the start and finish times (points s and f) of the transformation of austenite at the chosen temperature. When the same experiment is repeated with the same material, subjected to austenitization at the same conditions, but cooled to different isothermal transformation temperatures, similar results are obtained. The various results can then be combined in a temperature-time diagram, similar to the one presented in Fig. 9.34. This diagram is called an ITT or a TTT diagram (see the section "Time-Temperature-Transformation Curves" earlier in this chapter) or sometimes C or S curves. Although TTT curves are very important tools for studying phase transformations in steels and cast irons and are very common in the literature, generally real heat treatments involve continuous cooling instead of isothermal holdings at a constant temperature. (Important exceptions involving austenite decomposition are isothermal annealing, patenting, and austempering, covered in Chapter 10, "Conventional Heat Treatment: Basic Concepts," in this book). Thus, it is important to know the effect of imposing a cooling rate on austenite, instead of keeping it at a constant temperature. The direct application of cooling curves on top of TTT diagrams may lead to significant errors, as discussed in the next section.

Continuous Cooling Transformation Curves

Processes in which austenite is subjected to continuous cooling are represented in continuous cooling transformation (CCT) curves. These curves are usually determined by dilatometry (Ref 45). Figure 9.35 shows the two most common presentations of these curves. It is important to clearly identify the axis in the graph before analyzing the data. Figure 9.35(a) presents an example of a curve in which the horizontal axis is time, whereas the graph in Fig. 9.35(b) uses the cooling rate for the horizontal axis. Comparing TTT and CCT curves for a steel can be especially instructive and can show some of the risks associated with attempting to use TTT curves to make predictions about the results of continuous cooling treatments. As Fig. 9.36 indicates, the cooling rate to avoid diffusive transformations (if one erroneously plots a cooling rate

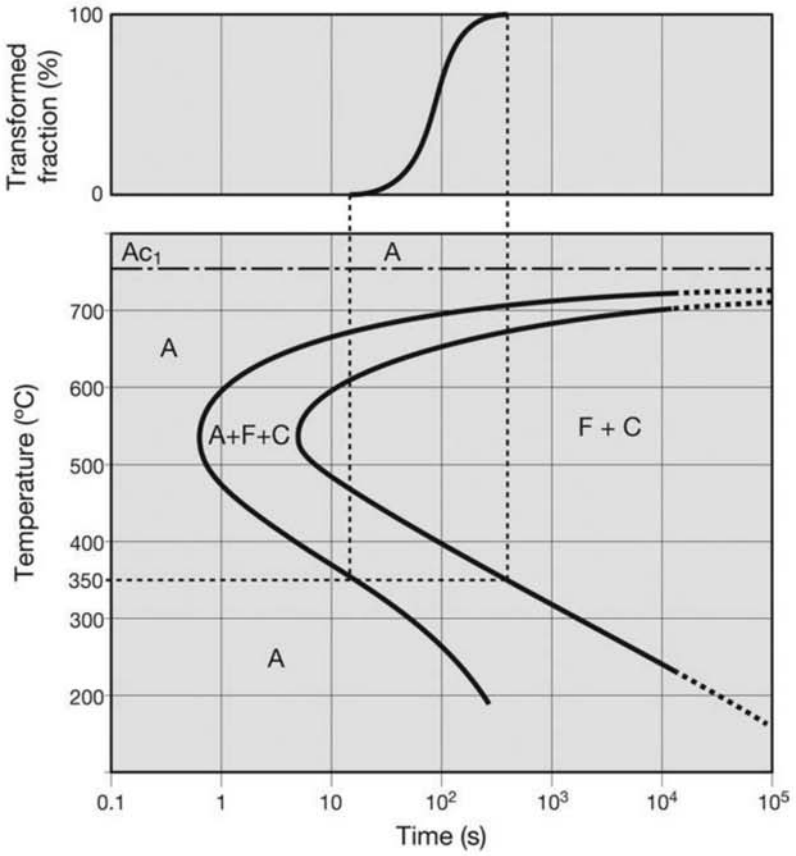

Fig. 9.34 Schematic relationship between the isothermal transformation fractions and the TTT diagram (see also Fig. 9.5 and 9.6)

over the TTT diagram), indicated as V_{crit}TTT, is the critical quenching rate, required to guarantee martensite formation. As a matter of fact, because of the way TTT curves are determined, by holding temperature constant and measuring transformation progress, cooling rates plotted in this type of curve have no meaning. Furthermore, the critical cooling rate for bainite formation can be read from the CCT curve (dashed lines), while a casual observation of the TTT curve could lead one to believe incorrectly that bainite cannot be formed in this steel without first forming pearlite (solid lines in the graph). Figure 9.37 presents a CCT curve determined using dilatometry with the hardness values corresponding to each cooling rate (specimen) indicated. Figure 9.38 presents the micrographs for the specimens.

9.2 Austenite and the Measurement of the Austenitic Grain Size

In most steels one has no access to austenite except by indirect observations from metallographic examination; however, the features of the austenitic structure have a decisive influence on the results of most heat treatments and thermomechanical treatments of steels. This discussion does not apply to steels that have an austenitic microstructure at room temperature, such as some stainless steels (see Chapter 16, "Stainless Steels," in this book).

The transformations during austenite decomposition are influenced by the occurrence of nucleation and by the frequency and location of the nuclei formed. These features depend directly on the austenitic grain size (and

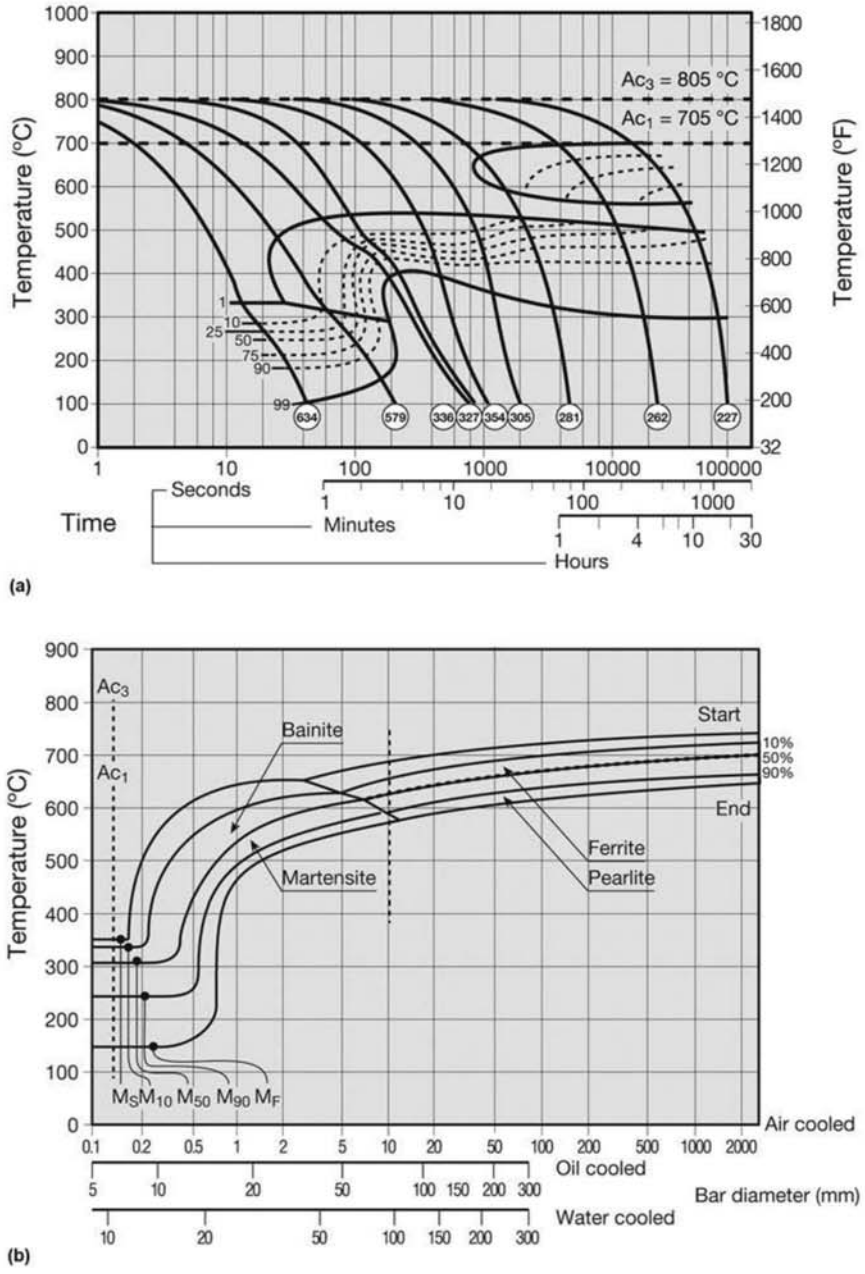

Fig. 9.35 (a) CCT curve in time-temperature axis for a steel containing C = 0.39%, Mn = 1.45% and Mo = 0.49%. Each cooling rate is represented by a curve superimposed on the T versus t graph. Frequently the final hardness values are indicated for each cooling rate. (b) CCT in cooling rate- temperature axis for a steel containing C = 0.38%, Mn = 0.6%. Each cooling rate is shown as a vertical line on the *T* vs *dT/dt* curve. Source: Adapted from Ref 46 and 47

hence of the interfacial area density, because nucleation at interfaces is normally preferred) and its size distribution, on the chemical homogeneity of austenite, and on the presence or absence of second phases (such as undissolved carbides). Understanding the mechanisms of austenite formation, a

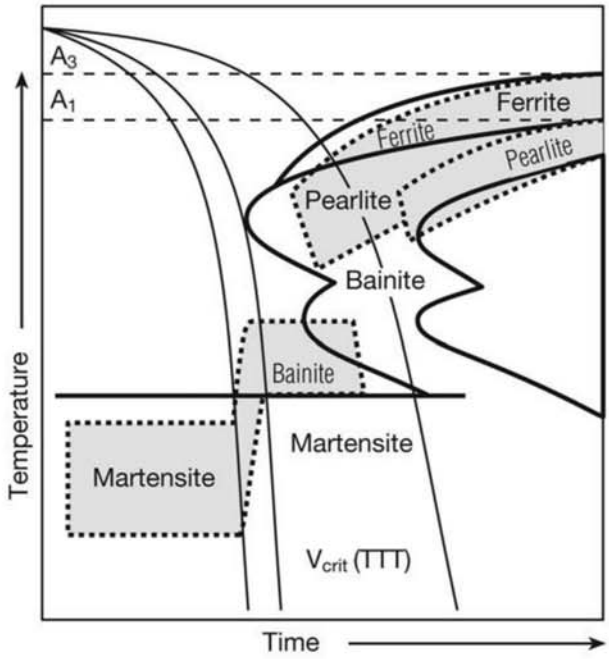

Fig. 9.36 Schematic presentation of a CCT curve (dashed) superimposed on the TTT curve (solid lines) for the same steel. The cooling rate required to avoid the "nose" of the TTT curve is not the same as the critical cooling rate to guarantee martensite formation. Some of the points of the TTT diagram are inaccessible via continuous cooling. Source: Adapted from Ref 14

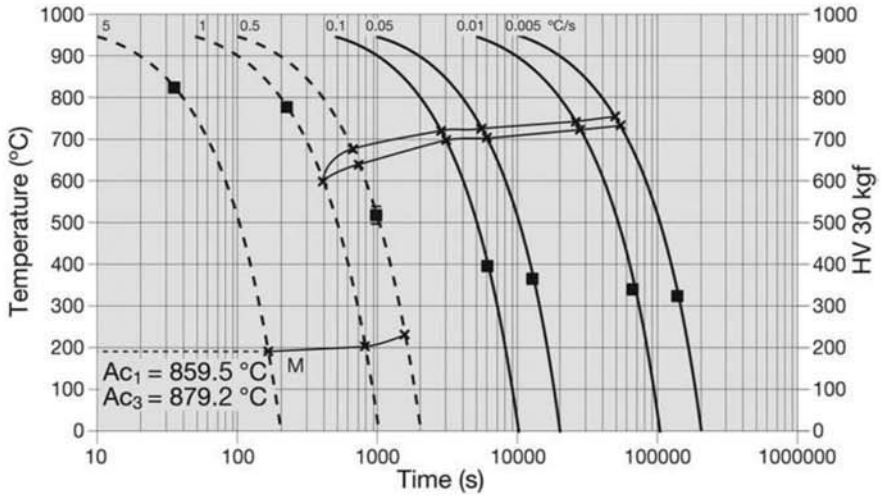

Fig. 9.37 CCT curve for an experimental steel containing C = 0.78%, Si = 1.6%, Mn = 2.02%, Mo = 0.24%, Cr = 1.01%, Co = 3.87%, and Al = 1.37%, determined using dilatometry. The black dots indicate the hardness (on the right side scale) for each cooling rate. The crosses indicate start and end of transformation, as measured with the dilatometer (see corresponding micrographs in Fig. 9.38). The cooling rates are indicated in °C/s, for each curve, on the top portion of the graph. Courtesy of C. Garcia-Mateo, Grupo Materialia, Spain.

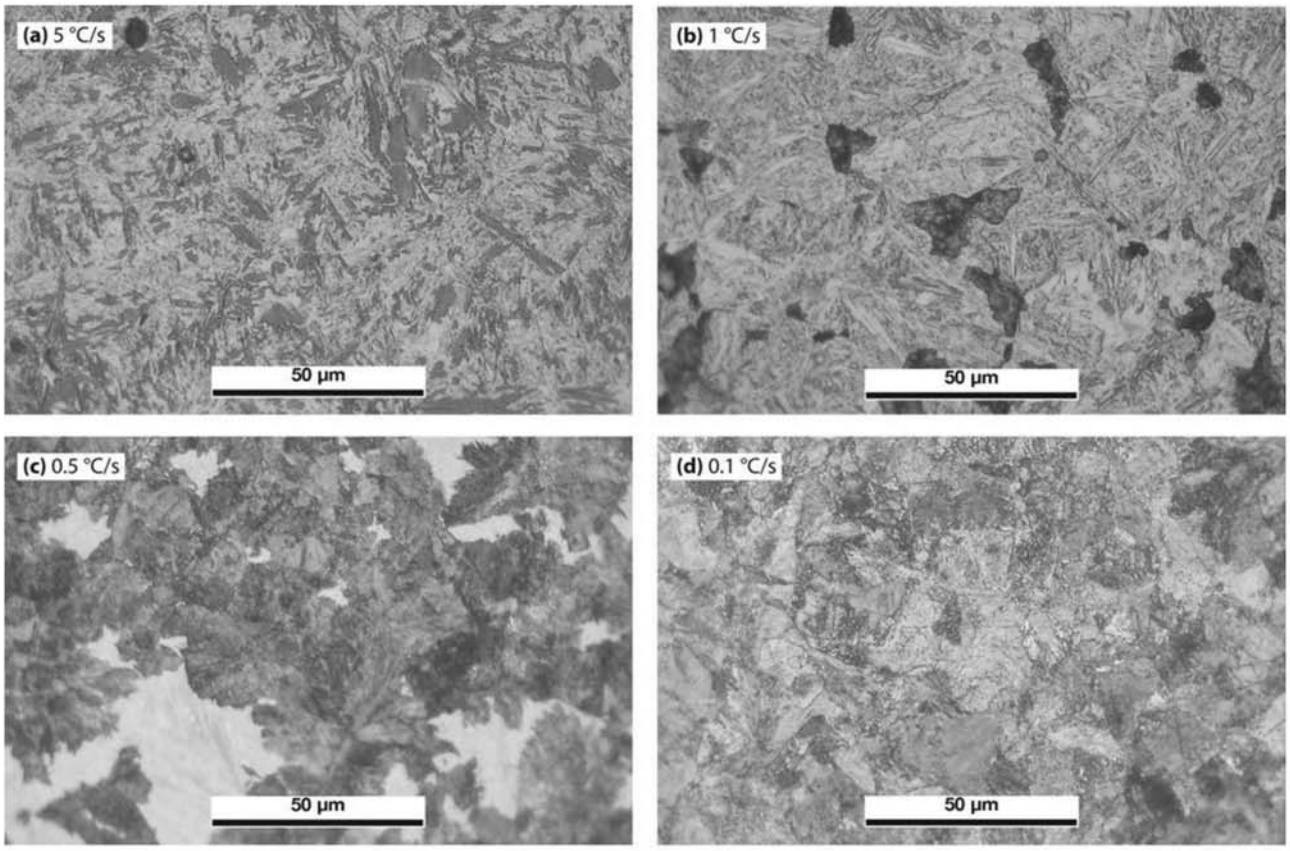

Fig. 9.38 Selected micrographs from the specimens used to determine the CCT curve of Fig. 9.37. Sample (a) presents only martensite (and possibly some retained austenite, in view of the measured M_s temperature). Samples (b) and (c) show pearlite (in the past, some of the very fine pearlites have been misnamed troostite) and martensite (retained austenite is possibly also present). Pearlite has nucleated from the austenite mostly in grain boundaries. The nodular shape of the pearlite colonies can be observed. Austenite that has not transformed in pearlite has transformed into martensite when M_s was reached. With cooling rates lower than 0.1 °C/s (0.18 °F/s) only pearlite is observed, that is, all austenite has transformed to pearlite. The pearlite lamellar spacing is finer with the higher cooling rates as shown in samples (e) and (h). Pearlite darkens much faster than martensite during etching (b and c). Etchant: nital 2%. Courtesy of C. Garcia-Mateo, Grupo Materialia, Spain.

process that in most conventional treatments occurs during heating and holding the steel at a certain temperature for a given time (see also Chapter 10, "Conventional Heat Treatment: Basic Concepts," in this book), is thus of great importance.

9.2.1 Austenite Formation

Austenite is formed by nucleation and growth from whatever microstructure the steel has when it is heated for the heat treatment. The most remarkable difference in the austenite formation kinetics when compared to the decomposition kinetics is that while decomposition happens during cooling and is normally finished at room temperature, austenite formation happens with heating and is concluded at a stage in which the atoms have great mobility. For this reason, some processes that do not happen during austenite decomposition are extremely important during its formation. The main one is grain growth.

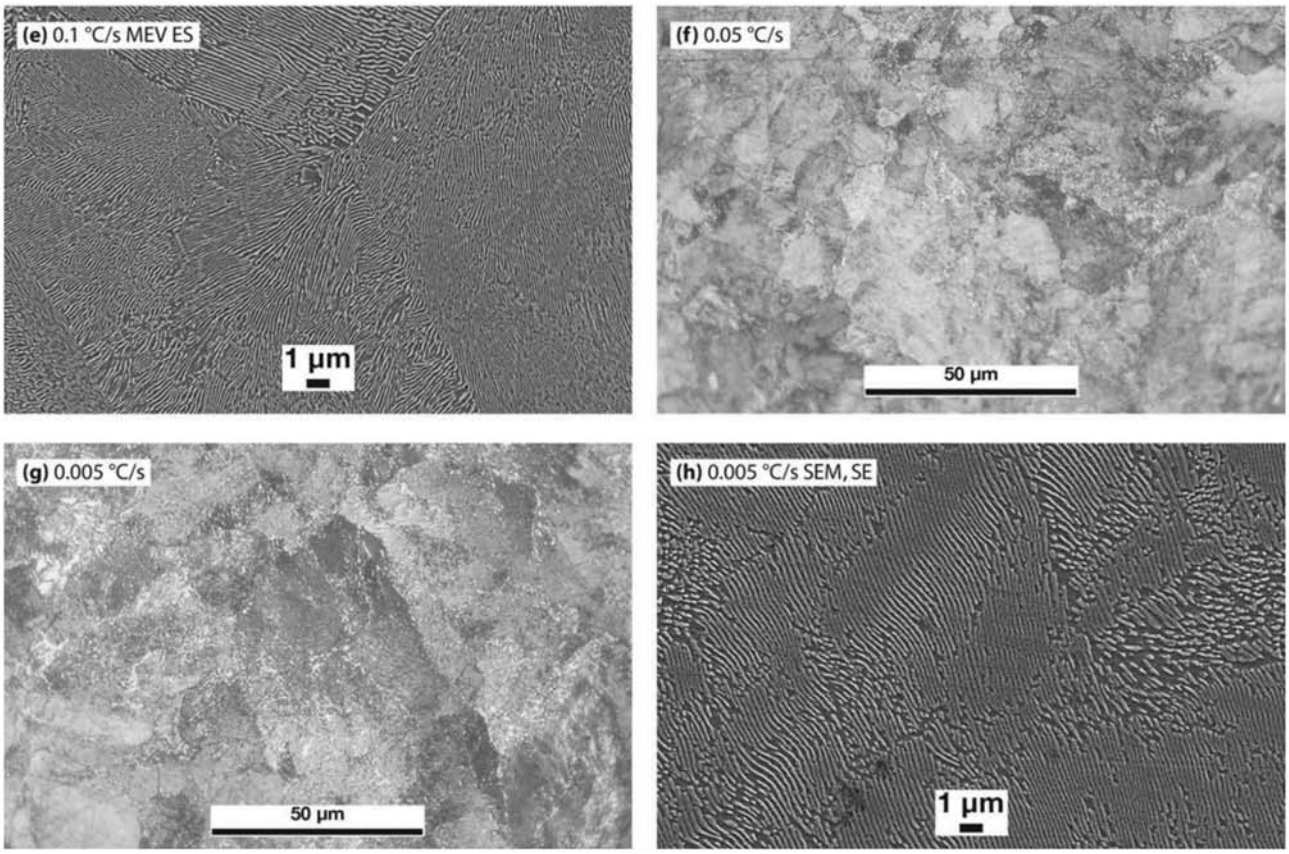

Fig. 9.38 (continued) Selected micrographs from the specimens used to determine the CCT curve of Fig. 9.37. Sample (a) presents only martensite (and possibly some retained austenite, in view of the measured M_s temperature). Samples (b) and (c) show pearlite (in the past, some of the very fine pearlites have been misnamed troostite) and martensite (retained austenite is possibly also present). Pearlite has nucleated from the austenite mostly in grain boundaries. The nodular shape of the pearlite colonies can be observed. Austenite that has not transformed in pearlite has transformed into martensite when M_s was reached. With cooling rates lower than 0.1 °C/s (0.18 °F/s) only pearlite is observed, that is, all austenite has transformed to pearlite. The pearlite lamellar spacing is finer with the higher cooling rates as shown in samples (e) and (h). Pearlite darkens much faster than martensite during etching (b and c). Etchant: nital 2%. Courtesy of C. Garcia-Mateo, Grupo Materialia, Spain.

Schmidt, Soltesz et al. (Ref 48) used high-temperature confocal microscopy and confirmed that the triple points of the ferritic microstructure of IF steels are preferential regions for the nucleation of austenite (see Fig. 7.8, in Chapter 7, "Equilibrium Phases and Constituents in the Fe-C System" in this book). Savran, Leeuwen et al. (Ref 49) performed interrupted austenitizing treatments in C35 and C45 steels (similar to AISI 1035 and 1045). As the samples reached a given temperature, they were quenched, transforming the austenite present at high temperature into martensite. They observed that austenite nucleates predominantly in pearlite. Significant nucleation also occurred in ferrite triple points: these are the preferential nucleation points (Fig. 9.39 to 9.42). There is a superposition in time of two transformations: ferrite to austenite and pearlite to austenite. The transformation of pearlite to austenite follows two distinct mechanisms, depending on the heating rate. During slow heating the plates of cementite and ferrite transform to austenite at the same time. With rapid heating, however, ferrite is first transformed into austenite, and then cementite dissolves on the new formed phase.

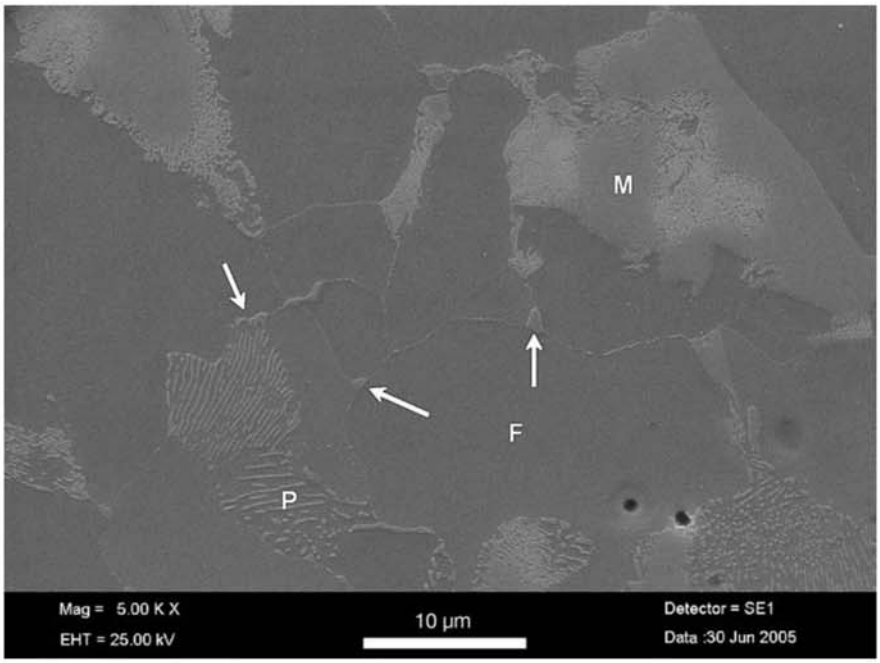

Fig. 9.39 C35 steel (similar to AISI 1035) heated at 0.05 °C/s (0.09 °F/s). Treatment interrupted by quenching from 745 °C (1375 °F). F = ferrite, P = pearlite, and M = martensite. The martensite regions were austenite at the moment the heat treatment was interrupted and the sample quenched. Arrows indicate nucleation of austenite in triple points of the microstructure, and the start of the formation of austenite from a pearlite colony (arrow at the left of the image). SEM, SE. Courtesy of V. Savran and J. Sietsma, Delft University of Technology, Delft, Netherlands.

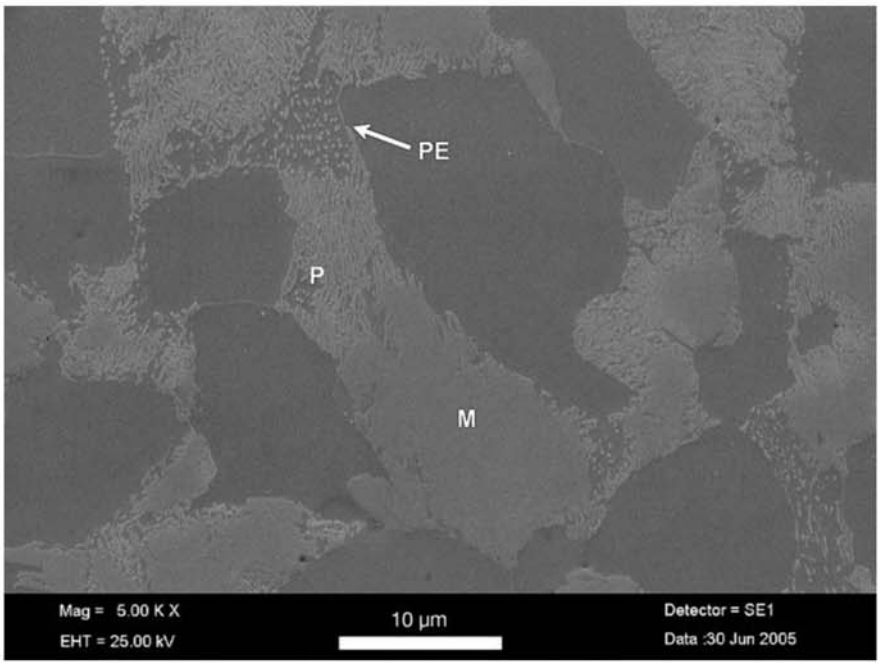

Fig. 9.40 Same steel and same treatment conditions as Fig. 9.39. Some of the cementite of the pearlite has spheroidized (PE). SEM, SE. Courtesy of V. Savran and J. Sietsma, Delft University of Technology, Delft, Netherlands

9.2.2 Time-Temperature-Austenitization Curves

Using a methodology similar to that used to record austenite decomposition kinetics, it is possible to construct curves to record the transformations happening on heating and austenitizing steels. Because austenite formation happens through nucleation and growth, it is natural that these time-temperature-austenitization (TTA) curves bear a resemblance to upside-down

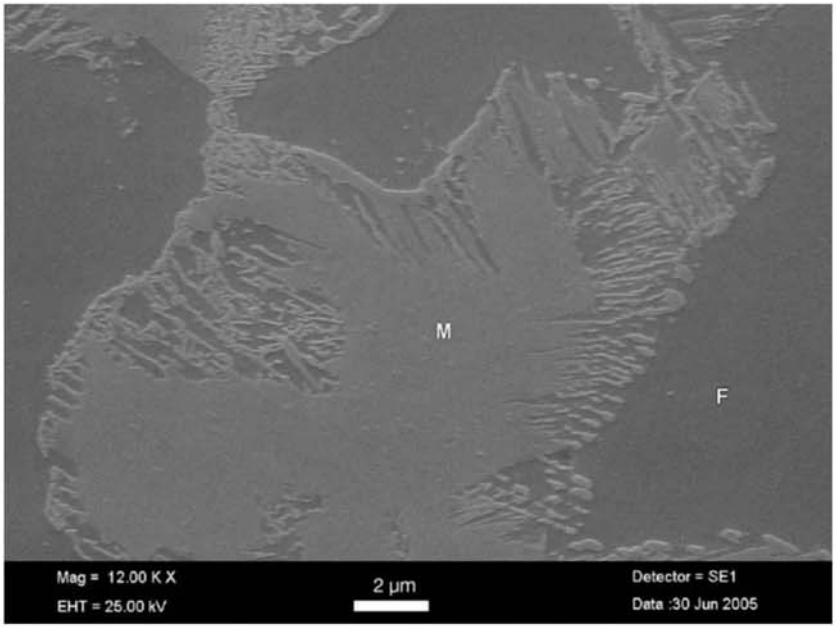

Fig. 9.41 Same steel and same treatment conditions as Fig. 9.39. The austenite (already transformed to martensite) can be observed along the ferrite lamellae of pearlite. Cementite dissolution lags a little in time. SEM, SE. Courtesy of V. Savran and J. Sietsma, Delft University of Technology, Delft, Netherlands.

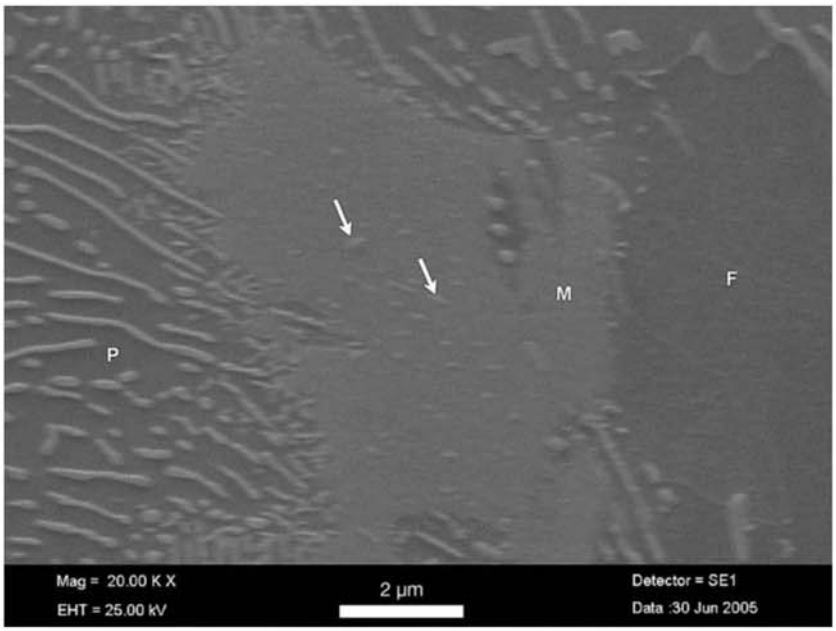

Fig. 9.42 C45 steel (similar to AISI 1045) heated at 20 °C/s (35 °F/s). Treatment interrupted by quenching from 765 °C (1410 °F). F = ferrite, P = pearlite, and M = martensite. The martensite regions were austenite at the moment the heat treatment was interrupted and the sample quenched. Arrows indicate undissolved carbides in the austenite formed from a pearlite colony. SEM, SE. Courtesy of V. Savran and J. Sietsma, Delft University of Technology, Delft, Netherlands.

CCT curves, as shown in Fig. 9.43. Figure 9.44 presents transformation on austenitization for steels AISI 4140 and 52100. The different behavior of the two steels is significant. The different carbon (0.4% and 1.00%) and chromium (1% and 1.5%, respectively) contents are the main causes for these differences. Because AISI 52100 is a hyper-eutectoid steel, there is a range of temperatures in which carbides and austenite coexist in equilibrium, whereas in AISI 4140 (as in the scheme presented in Fig. 9.43), carbides and austenite coexist mostly for kinetic reasons. Analyzing Fig. 9.44(b) highlights another critical problem in the heat treatment of alloy steels, which is particularly evident in

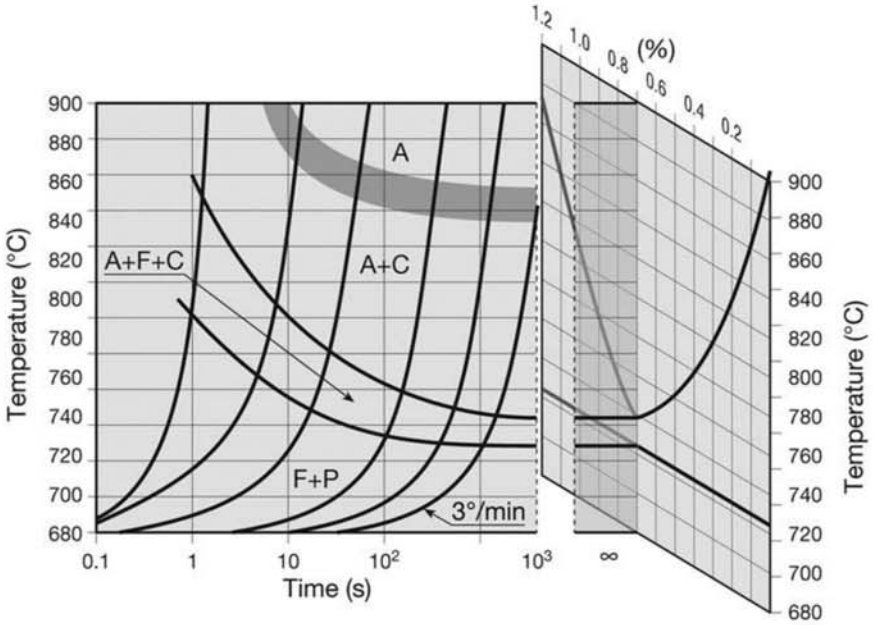

Fig. 9.43 The relationship between continuous transformation curves on heating for a steel containing C = 0.7% and the Fe-C equilibrium diagram. The delay on the carbide dissolution, discussed in the text, is represented by the different regions indicated in the diagram (A = austenite F = ferrite, C = carbide, P = pearlite).

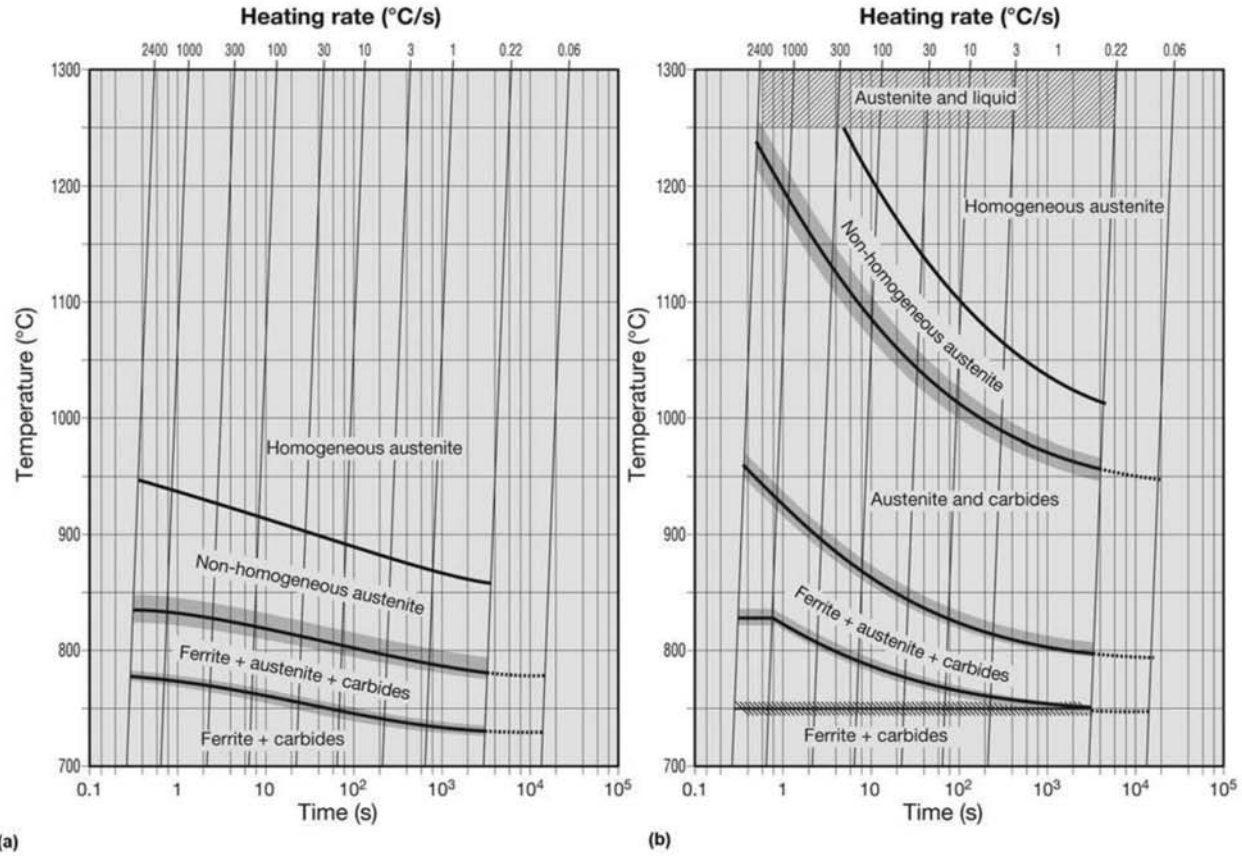

Fig. 9.44 Austenitization curves for the steels (a) 42CrMo4 (AISI 4140) and (b) 100Cr6 (AISI 52100). Source: Ref 13, 50

high-alloy steels. As the alloying element content increases, the austenitizition kinetics slows down, generally because of the need to dissolve alloy carbides and homogenize the substitutional solutes through diffusion. On the other hand, there is a trend toward the reduction of the solidus temperature with the increase in carbon and alloy content. This narrows the range of temperatures in which it is viable to perform austenitizing heat treatments, either for hot working (see Chapter 11, "Hot Working," in this book) or for normal heat treatments (see Fig. 9.45). Austenite heterogeneity and the presence of undissolved constituents favor the nucleation of diffusion-formed constituents. The effect on TTT curves is schematically indicated in Fig. 9.46.

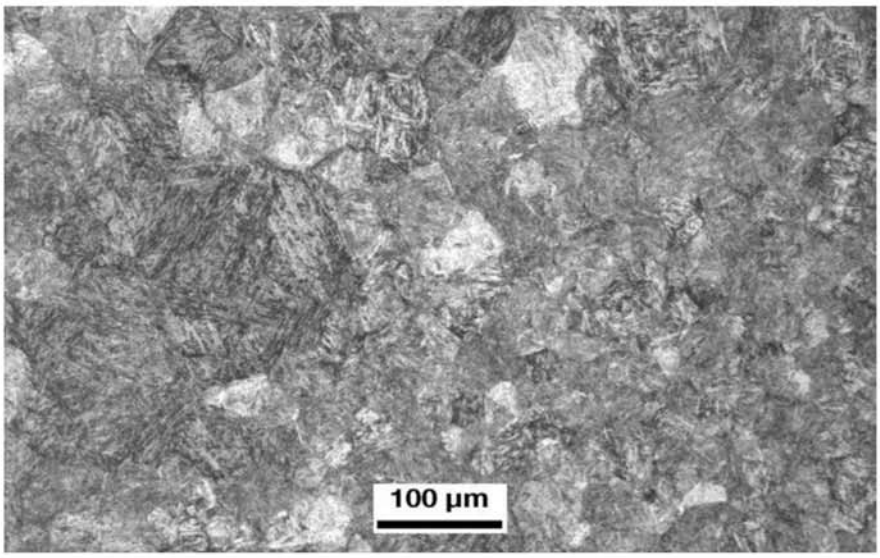

Fig. 9.45 Steel for hot working tools W.Nr 1.2365 (similar to AISI H10) with heterogeneous austenitic grain size. Martensitic structure with carbides, formed via heating to 1020 °C (1870 °F) for 0.5 h, transferred to another furnace at 700 °C (1290 °F) for 1 h air-cooled. Etchant: Villela. Courtesy of Villares Metals S.A., Sumaré, SP, Brazil.

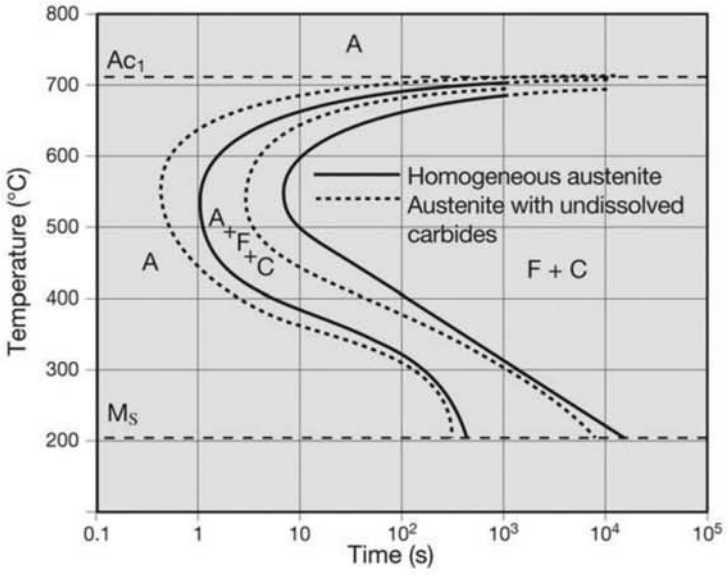

Fig. 9.46 The influence of austenite homogeneity on the TTT curve of a steel containing C = 0.87%, Mn = 0.3%, and V = 0.27%. A = austenite, F = ferrite, C = carbide. Source: Adapted from Ref 51

9.2.3 Austenitic Grain Growth

Distinct from the transformations on cooling, there is significant atomic mobility during the austenitization heat treatment, even when the "end" time of the treatment is reached. This can lead to a process of austenitic grain growth. Generally austenitic grain growth can have two important effects. First, embrittling elements can segregate to the austenitic grain boundaries. The larger the grain size, the less grain boundary area will be available per volume, and hence, for a given concentration of segregating element in the steel, the grain boundary concentration will be higher. Second, the nucleation of constituents in grain boundaries will be less favored, as indicated in Fig. 9.47. Figure 9.48 presents the effect of austenitization temperature on the austenitic grain size for a silicon deoxidized steel. The higher the heat treatment holding temperature, the larger the grain size at the end of the treatment. Controlling austenitizing temperature (and to a lesser extent, time) is thus extremely critical for guaranteeing heat treatment reproducibility and, hence, systematic response to the heat treatment. The effect of time on grain size at a constant temperature for a given steel can be approximated using a relationship of the type $D = k\sqrt{t}$ where D is the grain size (in length units), t is time, and k is a constant that depends on the steel and the temperature of treatment (Ref 13). Figure 9.49 presents the effect of time and temperature of austenitization on the steel microstructure.

Controlling Austenitic Grain Size with Second Phase Particles

To achieve a uniform austenite, essential for obtaining reproducible results from heat treatments and thermomechanical treatment, it is evident from the discussion in the section "TTA Curves" earlier that time and temperature in austenitization are very important. Thus, simple rules for defining

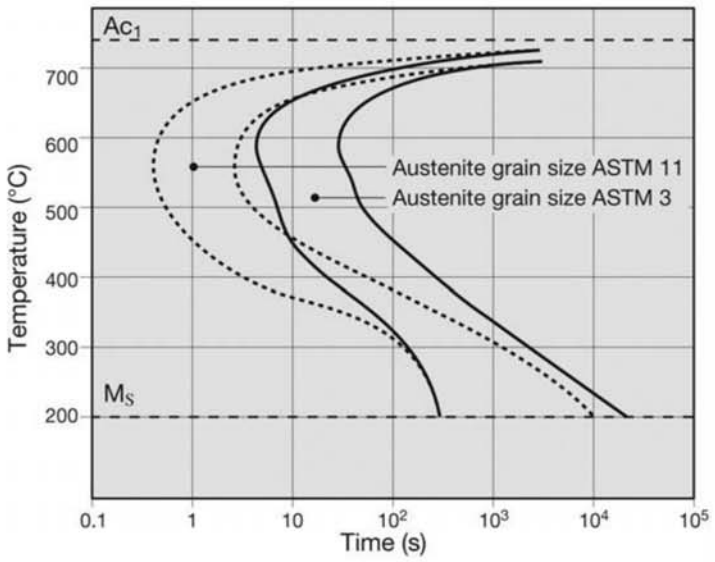

Fig. 9.47 The influence of austenitic grain size on the TTT curve of a steel containing C = 0.87%, Mn = 0.3%, and V = 0.27%. Source: Adapted from Ref 51

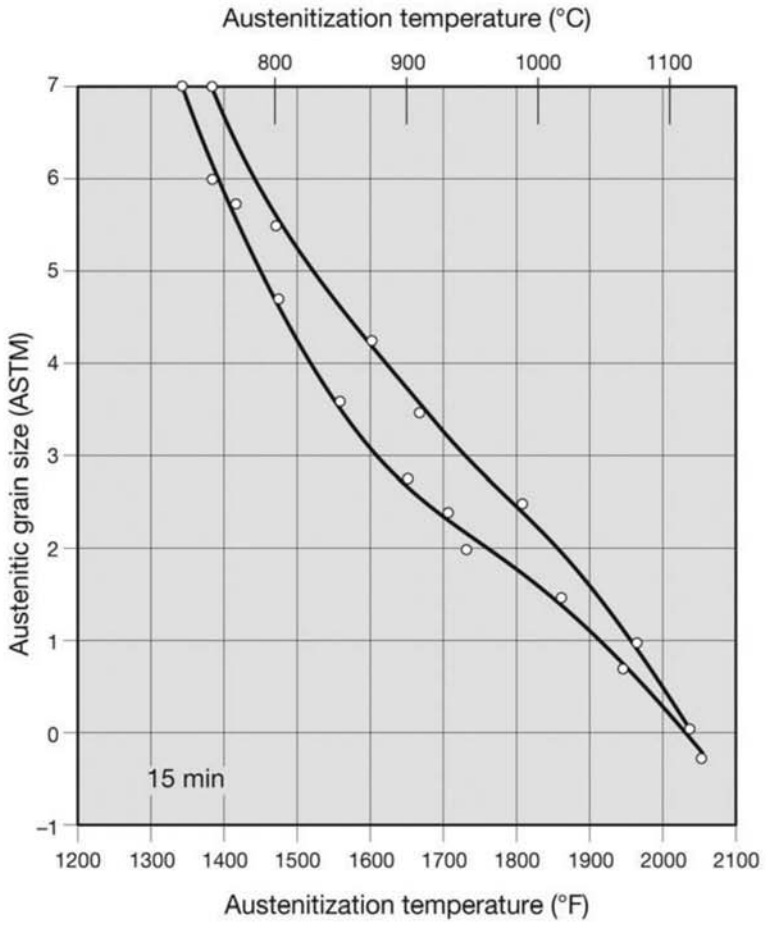

Fig. 9.48 The effect of austenitization temperature on the austenitic grain size for the same holding time at temperature for a silicon-deoxidized steel. Source: Adapted from Ref 52

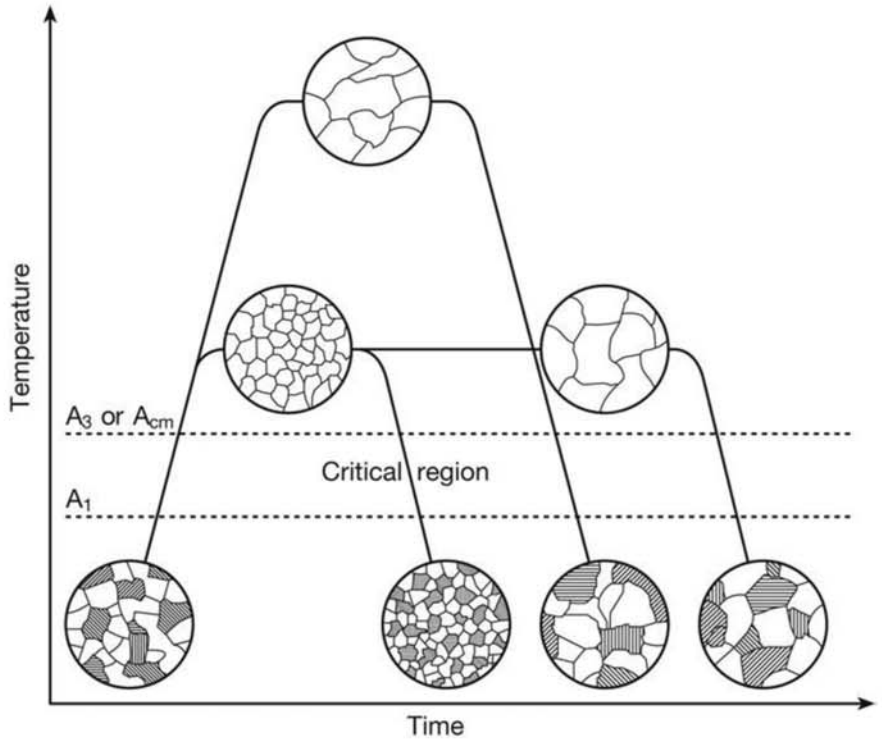

Fig. 9.49 Schematic representation of the effect of austenitization time and temperature on the austenitic grain size and the effect on the structure in a Fe-C steel, air-cooled. The scheme supposes that austenite is homogeneous in grain size and chemical composition.

holding times, such as "one hour per inch of part thickness," should only be used as a rough starting point for developing the ideal heat treatment cycle and in the complete absence of more precise information about the steel to be treated. On the other hand, once the ideal time and temperature are defined for the austenitization temperature, in terms of austenite homogeneity, it may be impossible to get the austenitic grain size needed to achieve the desired results. For this reason, it is common to use measures to control the austenitic grain size, particularly when small ("fine") grain size is desired as an outcome of the heat treatment. This is not a general rule: in high-temperature steels, for instance, it may be preferred to have a larger grain size, sacrificing toughness to improve high-temperature strength and creep resistance (e.g., comparing ASTM A515 and A516 steels). In any case, many applications benefit from fine austenitic grain size. The most efficient way to control the grain size is to have a fine dispersion of second-phase particles. The interaction between these particles and the grain boundaries creates a reaction to the grain growth driving force, as presented schematically in Fig. 9.50. For this dispersion to be effective, it is essential that the average size of the particles ($2r$ in the figure) and its volume fraction (f in the figure) are such that the pinning force compensates the driving force for grain boundary movement. The theories that deal with this phenomenon are discussed in detail in Ref 7, 53, and 54. Figure 9.51 shows an example of in situ observation of this phenomenon.

Not all particle dispersions in steel satisfy the conditions needed to effectively control the austenitic grain size, as indicated in Fig. 9.52 and experimentally confirmed in Ref 56. Figure 9.53 shows the effect of different austenitization temperatures in an aluminum killed steel in which the precipitation of aluminum nitride creates a fine dispersion that controls the austenitic grain growth. For a wide range of temperatures in which the dispersion is stable, homogeneous, and relatively constant, grain size is observed because of the dispersion presence. At a certain temperature range there is a transition

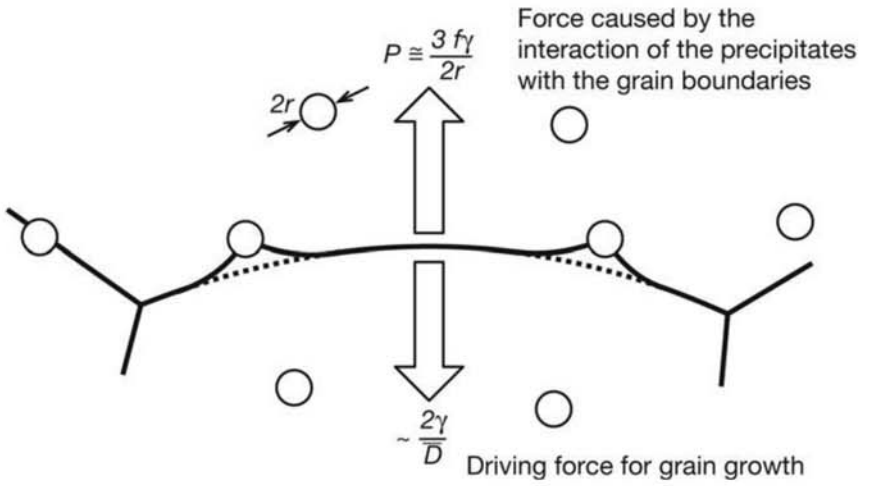

Fig. 9.50 Interaction between grain boundaries and second-phase particles. This interaction may be sufficient to balance the driving force for grain growth, stabilizing the grain size D is the diffusion coefficient and γ is the interfacial energy. Source: Adapted from Ref 7

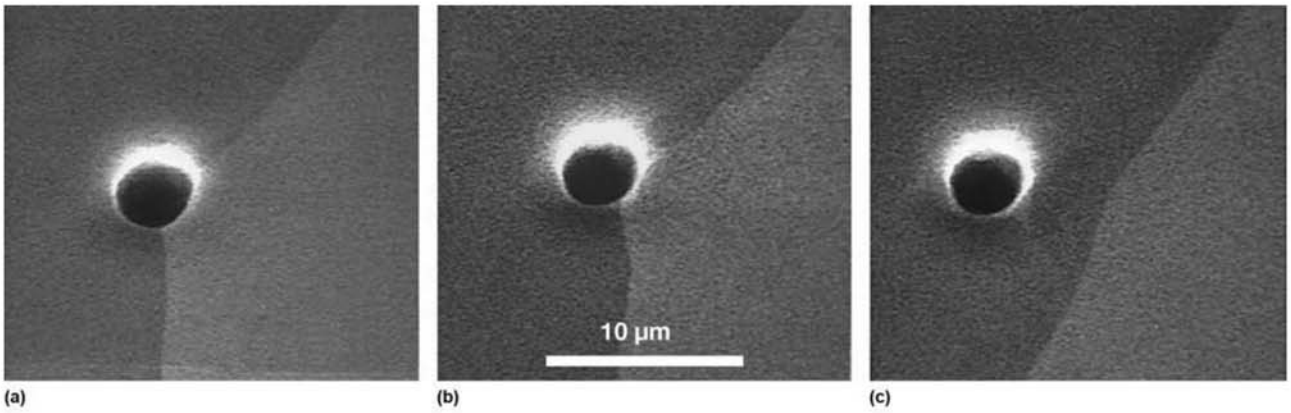

Fig. 9.51 In situ observation of the interaction of a precipitate with an austenitic grain boundary at 1100 °C (2010 °F). (a) Grain movement is interrupted—pinning. (b) Grain boundary still held by the precipitate. (c) Grain boundary has freed itself from the precipitate. As a result of the precipitate size and spacing, the pinning force has not been sufficient to stop the grain boundary movement at this point. Compare to Fig. 9.50. SIM, FIB (SEM with focused ion beam). Reproduced courtesy of Nippon Steel Corporation. Source: Ref 55

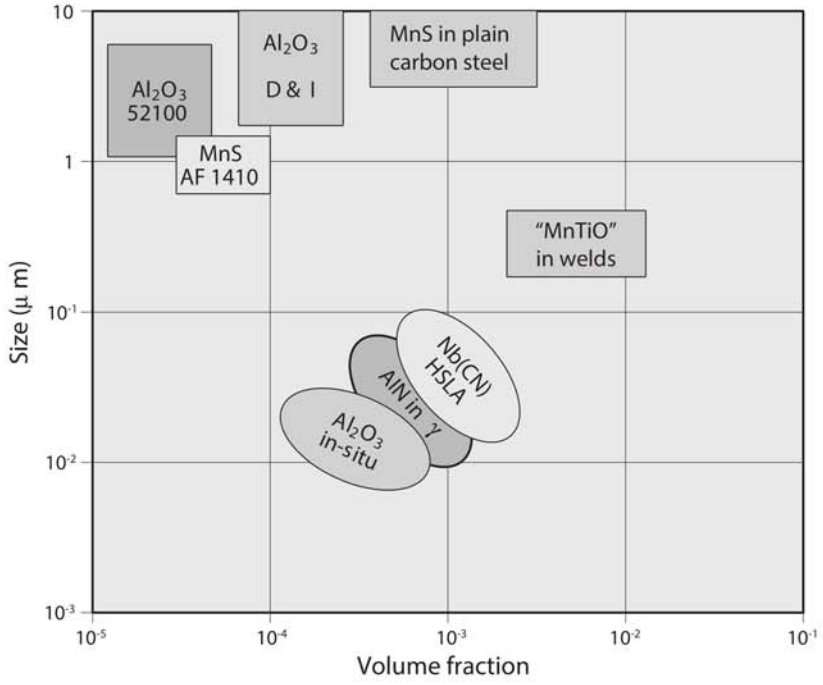

Fig. 9.52 Volume fraction and size for typical second-phase particles in steels. Nonmetallic inclusions (see Chapter 8, "Solidification, Segregation, and Nonmetallic Inclusions," in this book) normally have a combination of size and distribution out of the region where second phase hardening or austenitic grain size control can be achieved. This region is indicated by the range where one finds the niobium carbonitrides Nb(C,N) in HSLA steels, aluminum nitride (AlN) in engineering steels, and the results of a synthetic dispersion of alumina in steel prepared in Ref 56 (indicated in the figure as Al_2O_3 in situ) that resulted in effective austenitic grain size control.

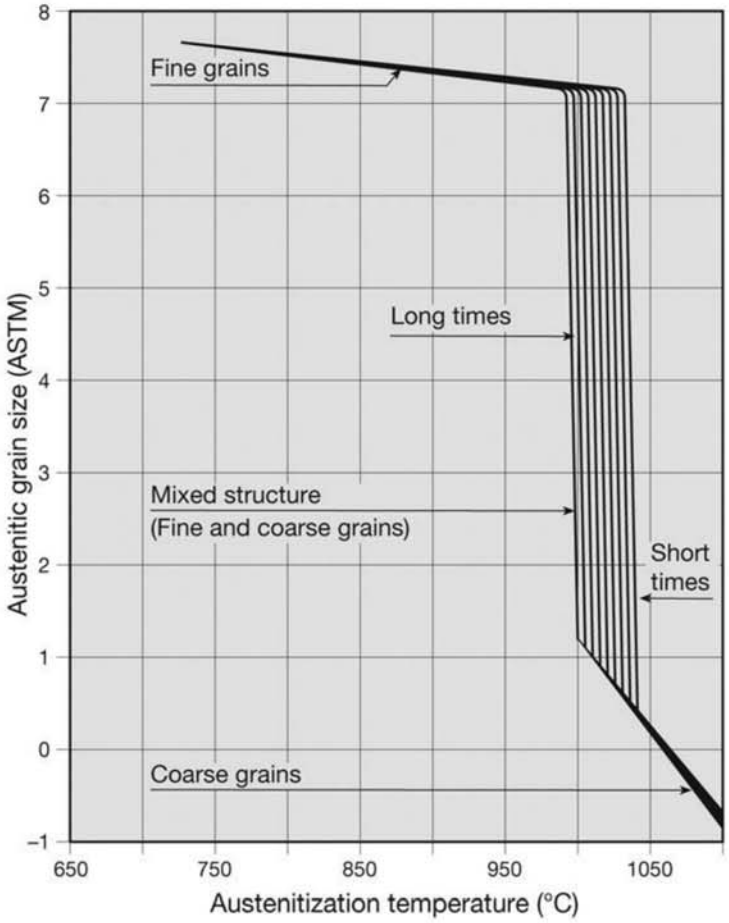

Fig. 9.53 Schematic representation of the effect of the austenitization temperature on the austenitic grain size of aluminum killed steel (where AlN precipitates). Source: Adapted from Ref 52

to coarse grains, caused by the dissolution of the precipitates. Dissolution depends on temperature and on how homogeneous the particle distribution is. Thus, it happens along a range of temperatures. Figure 9.54 presents a schematic representation of the sequence of transformations occurring when a hypo-eutectoid steel with a dispersion of fine precipitates is present. The temperature at which the dissolution of the precipitates is complete depends on the steel composition and can be calculated from thermodynamic data. For some simple precipitates, it is possible to express these temperatures in the form of simple equations called solubility products. Some of these are presented in Table 9.2. For more complex precipitates, accurately calculating the dissolution (or precipitation) temperature is better done using computational thermodynamics. As precipitates dissolve, the grain size control effect disappears and grain growth starts. Especially deleterious is the fact that in the temperature range in which dissolution happens, the spread of the distribution of grain sizes increases dramatically, as shown in Fig. 9.55 resulting in microstructures like those shown in Fig. 9.56. Furthermore, conditions are set for the phenomenon called abnormal grain growth, in which some grains grow significantly more than others. Figures 9.57 and 9.58 present other ex-

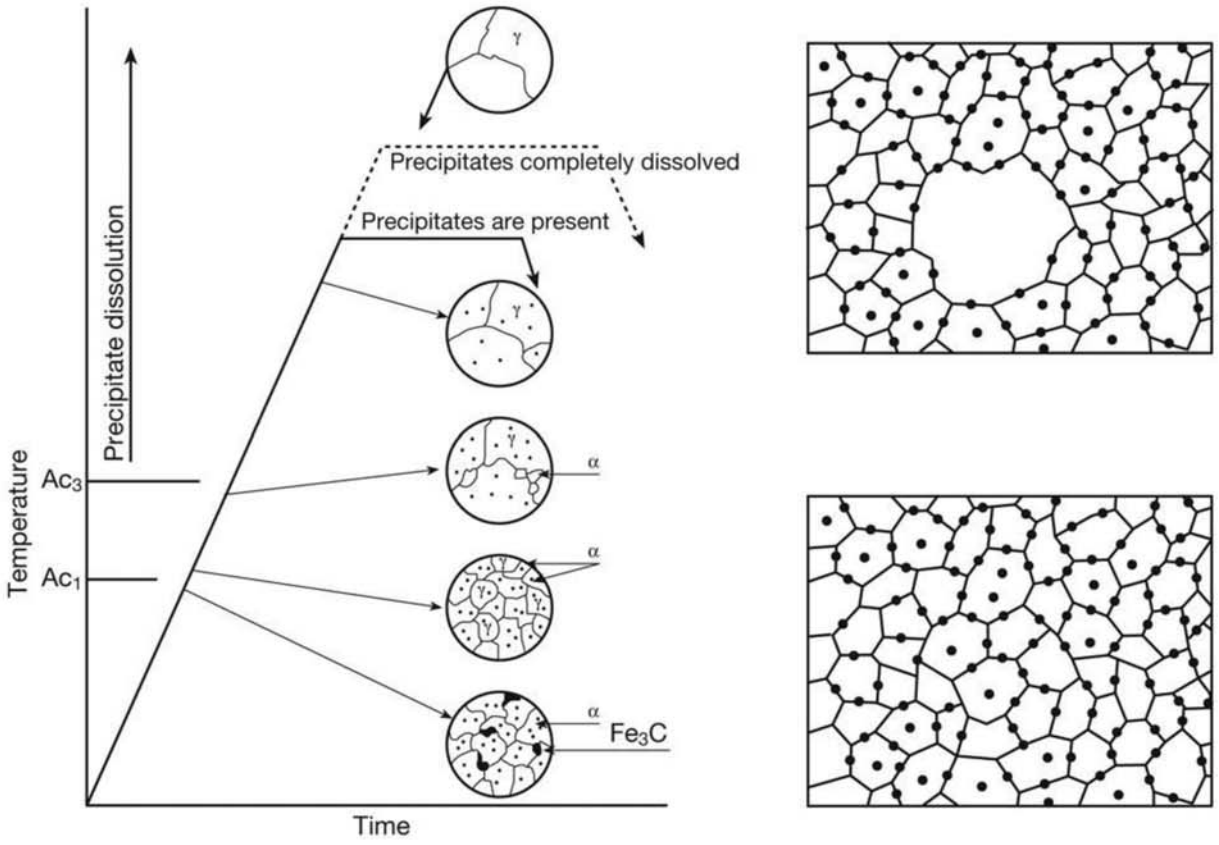

Fig. 9.54 Schematic representation of the austenitization of a hypo-eutectoid steel containing a dispersion of fine precipitates (the particle sizes are exaggerated so they can be visualized). If the austenitization is performed above the temperature at which the precipitates dissolve, austenitic grain growth will happen (the formation of austenite of heterogeneous grain size is schematically presented on the right side of the figure).

amples of significant microstructural heterogeneity caused by austenite lack of homogeneity. Although grain size heterogeneity is a frequent cause, other types of heterogeneity (such as chemical composition heterogeneity due to segregation) may also lead to this type of microstructure.

9.2.4 Austenitic Grain Size Measurement

Knowledge of the austenitic grain size can be important for the development and control of heat treatment or thermomechanical treatment processes and in the analysis of failures and deviations. However, metallographic techniques used to reveal the austenitic grain size in a material in which this phase has already decomposed are neither easy to perform nor always lead to good results.

There are basically two types of techniques to determine the austenitic grain size:

- Techniques that reveal the grain boundaries that existed before the material underwent the phase transformations that led to the presently existing phases, or
- Techniques that involve forming new austenitic grains

Table 9.2 Solubility products for several compounds in austenite. For a steel containing known amounts of aluminum and nitrogen, for instance, AlN will dissolve above the temperature calculated as log_{10} (%*Al*%*N*) = (-6770)/(T(*K*))+1.033. These equations do not take in consideration the presence of other elements. Thus, in a steel containing titanium, for instance, a portion of the nitrogen may be combined as TiN and would not be available for the formation of AlN. Computational thermodynamics makes it possible to circumvent these problems (For instance Ref 57 and 58).

Solubility product	$log_{10}k$	Solubility product	$log_{10}k$
%B%N	–13970/T + 5.24	%V%N	–7700/T + 2.86
%Nb%N	–10150/T + 3.79	%V%C	–6500/T + 4.45
$\%Nb\%C^{0.87}$	–7020/T + 2.81	%Ti%S	–16550/T + 6.92
$\%Nb\%C^{0.7}\%N^{0.2}$	–9480/T + 4.12	$\%Ti\%C^{0.5}\%S^{0.5}$	–15350/T + 6.32
%Ti%N	–15790/T + 5.40	%Mn%S	–9020/T + 2.93
%Ti%C	–7000/T + 2.75	%Al%N	–6770/T + 1.033

Source: Ref 17 and 46

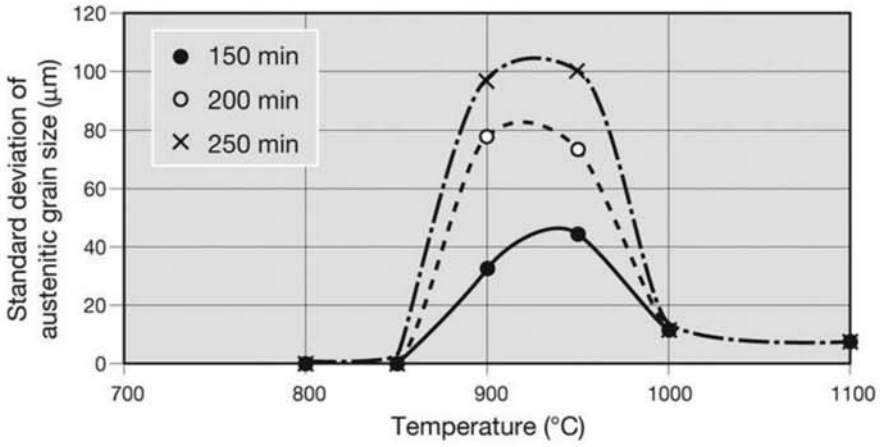

Fig. 9.55 Standard deviation of the measured austenitic grain size in different combinations of time and temperature for austenitization. Steel containing C = 0.46%, Mn = 0.7%, Al = 0.02%, and N = 32 ppm. The spread in the grain size distribution increases in the temperature range where aluminum nitride dissolution occurs. Source: Adapted from Ref 59

The techniques involving reaustenitization provide information about the behavior of the material when exposed to well-defined austenitization cycles and are useful for the development and control of processes and in quality control. For failure analysis, however, they may be of limited application, because they will not allow the observation of possible structural problems caused by unrecorded deviations during the treatment of the part.

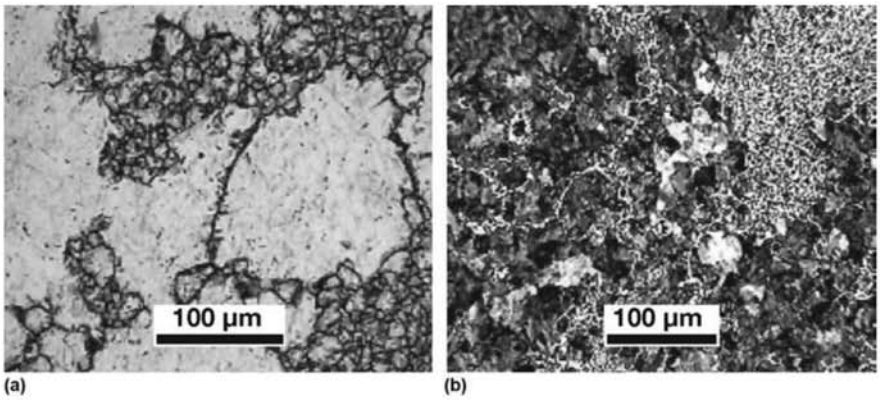

Fig. 9.56 Steel with the composition indicated in Fig. 9.55 austenitized at 900 °C (1650 °F) for 200 min (a) heterogeneous austenitic grain size revealed with etchant based on picric acid (75 ml distilled water, 55 ml teepol [industrial detergent], and 3 g picric acid). (b) After air-cooling, microstructure composed of ferrite and pearlite with heterogeneous size and distributions.

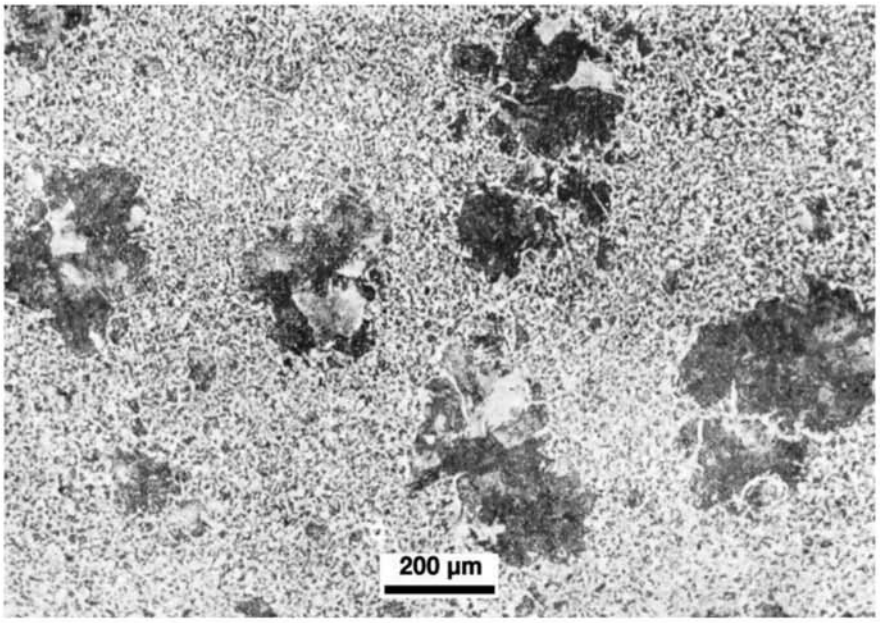

Fig. 9.57 Steel containing C = 0.38%, normalized. Heterogeneous microstructure containing ferrite and pearlite. Large pearlite colonies are present due to austenite lack of homogeneity. Etchant: nital.

Table 9.3 presents a summary compilation of the most common techniques used for austenitic grain size evaluation. Results of the McQuaid-Ehn technique of revealing austenitic grain boundaries after reaustenitization are presented in Fig. 9.59. Recently Ref 63 compared different methods when applied to steels alloyed with vanadium, titanium and combinations of these elements, and have determined the reliability and general applicability of the thermal etching method. The technique is schematically presented in Fig. 9.60 and results of thermal etching are shown in Fig. 9.61.

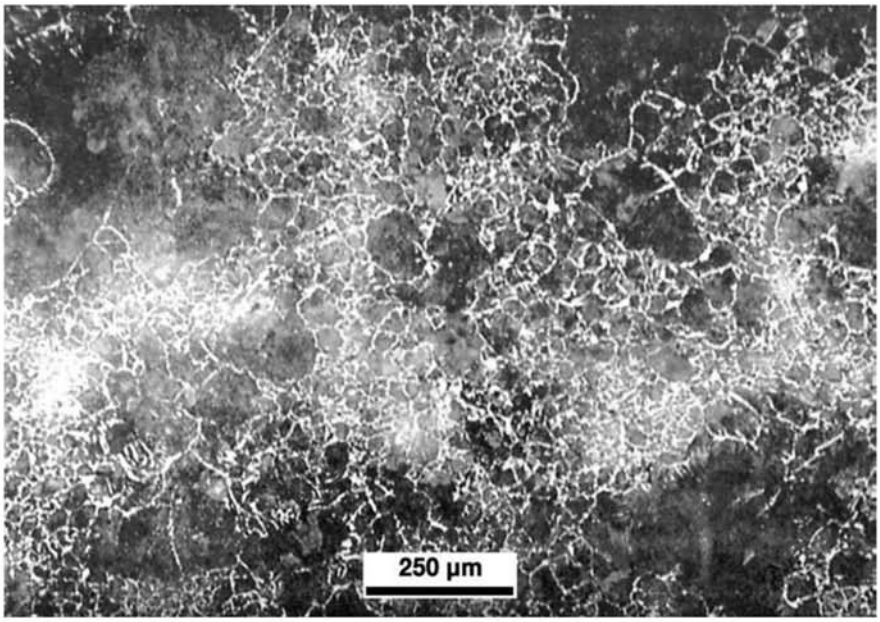

Fig. 9.58 Cast steel containing C = 0.43%, Cu = 0.13%, and P = 0.085%. Normalized after 2 h austenitization at 950 °C (1740 °F). Heterogeneous microstructure containing ferrite and pearlite, indicating heterogeneous austenite. The difference in response to etching (lighter regions) is caused by phosphorous segregation during solidification (Chapter 8, "Solidification, Segregation, and Nonmetallic Inclusions," in this book). Etchant: nital.

9.3 Ferritic Microstructures

In Chapter 7, "Equilibrium Phases and Constituents in the Fe-C System," in this book, the body centered cubic (BCC) phase of iron, ferrite, is presented. Many images of low carbon steels in which ferrite appears with the shape of equiaxed grains are presented. Images in which pro-eutectoid ferrite also has equiaxed shapes are shown for steels with different carbon contents. Furthermore, in the sections 9.1.3 "Martensite" and 9.1.4 "Bainite" in this chapter, bainite and martensite—out of equilibrium (or metastable) constituents—as well as the controversy on bainite formation mechanisms and its microstructural classification are briefly presented. It is important to know that depending on the conditions under which austenite transforms, ferrite can be formed with other morphologies (different from "equiaxial"). Many of these morphologies are not the result of a martensitic transformation and cannot be classified as bainites (Ref 30, 37), as discussed later. One of the most common and well known of these morphologies is Widdmanstätten ferrite, named after Austrian researcher Alois Widmanstätten (1753–1849), who first characterized it, when etching iron-rich meteorites.

As technology evolved during the second half of the 20th century, there was an intense search for steel compositions that could guarantee good toughness and high strength and would be easy to weld (requiring neither preheat nor postweld heat treatment (see the section 7.6 "Intermediate Structures—Hypo-Eutectoid and Hyper-Eutectoid Steels" in Chapter 7, "Equilibrium Phases and Constituents in the Fe-C System," in this book). One of the most important routes that made this development possible was reducing the carbon content of the steel and using other alloying elements to achieve

Table 9.3 Summary of the most common techniques for the metallographic evaluation of austenitic grain size

Technique	Details	Applications
Picric acid solutions	Room temperature etching. Many compositions can be used, for instance a. 75ml Hp, 55ml teepol (industrial detergent) and 3g picric acid (Ref 59) b. Saturated solution of picric acid in water, 1%HCI and tensoactive agent (detergent) (Ref 61)	Employed for a wide range of steel, in special with martensitic or bainitic structure. Technique may give information about the prior austenitic grain size (without new austenitization (see Fig. 9.56)
Carburizing Mc-Quaid-Ehn (Ref 62)	Carburizing at 925 °C (1670 °F) for 5 h. Polishing and etching (Nital, for instance) to highlight and reveal the cementite that will decorate the austenitic grain boundaries .	Used mostly for hypo-eutectoid. Does not reflect the "as received" austenitic grain size. The measured grain size is reasonable information for carburizing steels. For other steels, it is an upper limit of the possible austenitic grain sizes to be expected during heat treatment (see Fig. 9.59).
Oxidation	A polished surface of the steel is exposed to an oxidizing atmosphere at 855 °C (1570 °F) for 1 h. The steel is quenched in brine or water and lightly repolished to observe the austenitic grain boundaries which are revealed by preferential oxidation.	Applicable in particular to hypo-eutectoid steels. Does not reflect the "as received" austenitic grain size.
Thermal etching or vacuum treatment (Ref 62)	Vacuum treatment at 900 °C (1650 °F) for 1 h or less (see details in Ref 63)	Applicable to a wide range of steels. Does not reflect the "as received" austenitic grain size (see Fig. 9.61)
Highlighting with pro-eutectoid ferrite or cementite	Full austenitization, followed by controlled cooling to precipitate the pro-eutectoid phase in a network along the austenitic grain boundaries.	Applicable to a wide range of hypo- and hyper-eutectoid steels. In some cases, the treatment may not be needed since the network may already be present.

Source: Adapted from Ref 60

adequate control of the microstructure. As the volume fraction of ferrite has increased in steel microstructures (in particular for structural steels), it has become more important to have a better understanding of the mechanisms that lead to the different ferrite morphologies and of the mechanical properties they have. The first area where a need to correlate ferrite morphologies in the microstructure with properties was observed in weld-deposited metal. Most compositions employed for weld-deposited metal in structural steels and low-alloy steels rely on the proper ferrite morphology to achieve the desired properties with low carbon contents. Thus, the importance of quantify-

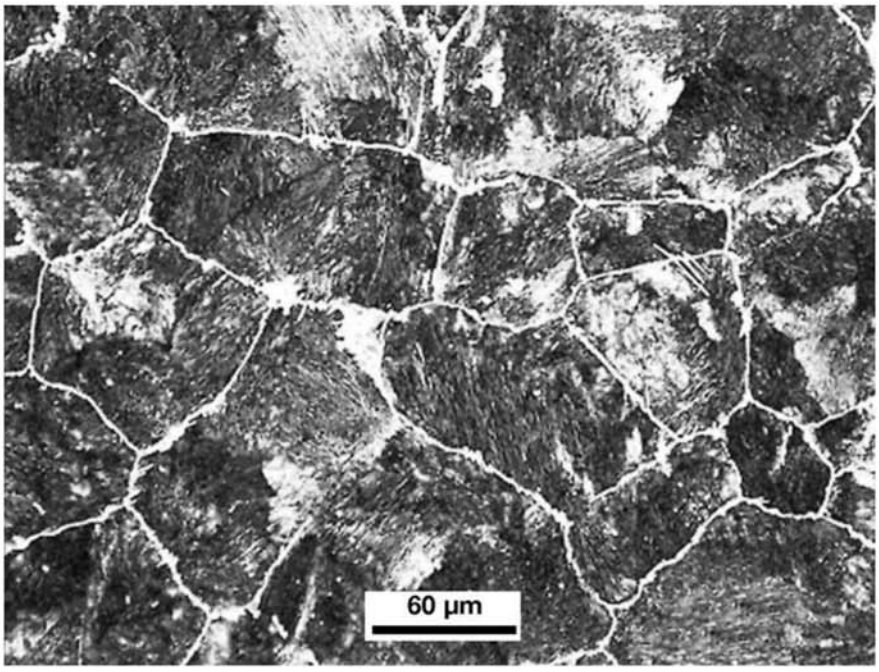

Fig. 9.59 McQuaid-Ehn test sample with austenitic grain boundaries marked by a network of cementite produced by carburization of the specimen surface. Courtesy of S. Bruschi, Universitá degli Studi di Padova, Padova, Italy.

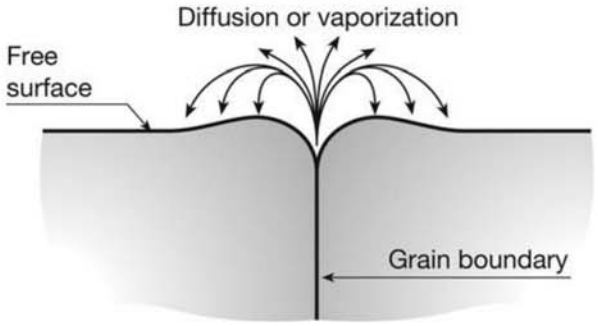

Fig. 9.60 Schematic cross section of two grains and their grain boundary, illustrating the diffusion or selective evaporation mechanism at the grain boundary that leads to the formation of a groove in this region. Source: Adapted from Ref 63

ing the relationships between properties and structure (and hence properly classify the structures) soon became evident.

As discussed in the section, 9.1, "Austenite Decomposition," as the atomic mobility decreases with lower austenite decomposition temperatures, products like bainite and martensite may become easier to form than ferrite and pearlite. However, in the same way that pearlitic lamellar spacing can adjust to the reduction of mobility, the modes of ferrite formation can also change, resulting in different morphologies, *before* bainite and martensite start to dominate the microstructure. As undercooling increases (either due to higher cooling rates or lower isothermal holding temperatures), important changes in the ferrite formation mechanism may occur. One of the main reasons that

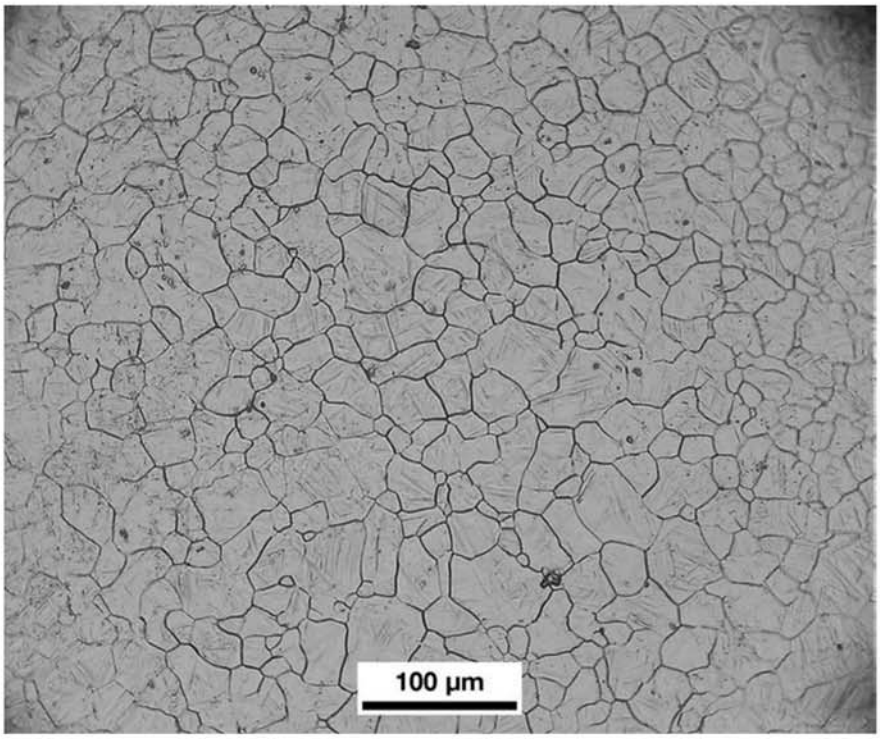

Fig. 9.61 Steel containing C = 0.08%, Mn = 0.73%, V = 0.26%, N = 33 ppm, and Al = 0.021%, thermally etched at 1200 °C (2190 °F) for 120 s (pressure < 1 Pa). The austenitic grain boundaries are visible. The grain interior is probably composed of martensite. Courtesy of C. Garcia, Mateo, Grupo Materialia CENIM-CSIC, Madrid, Spain.

makes this possible is the large difference in diffusion mobility between carbon, an interstitial solute, and that of the usual alloying elements, substitutional solutes, that have lower diffusion mobilities and thus diffuse at a much lower rate than carbon. The main mechanisms that may happen in these transformations are:

- Significant partition of the solutes, with thermodynamic equilibrium at the interface (PLE, partition, local equilibrium). In this case, it is possible that ferrite reconstruction from austenite can occur with the diffusion of all solutes from one phase to the other, maintaining the complete equilibrium indicated by the high-order Fe-C-alloying elements phase diagram.
- Negligible partition (of the substitutional solutes) with thermodynamic equilibrium at the interface (NPLE, negligible partition, local equilibrium). In this case, reconstruction happens without a significant redistribution of the substitutional solutes between the phases, just with the partition of carbon, which is a fast-diffusing species.
- Para-equilibrium (Ref 64, 65, 66), with no change in the concentration of the substitutional elements, but carbon redistribution. This mechanism is different from NPLE because there is no complete thermodynamic equilibrium at the interface between the phases but an equilibrium only with respect to carbon chemical potential.

- Massive transformation (Ref 7), where the structure is reconstructed without changes in composition. For the case of an austenite-ferrite transformation, this is normally only possible for steels with low carbon contents.
- Bainitic transformations (see the section 9.1.4, "Bainite—An Intermediate Constituent,") are considered by some authors to be a displacive transformation from the point of view of iron and substitutional elements atoms (Ref 67) with diffusive movement of carbon.
- Martensitic transformations (see the section 9.1.3, "Martensite—Diffusionless Growth") are displacive transformations in which the atoms rearrange without any diffusion and thus no change in chemical composition between parent and final phase.

For a more complete discussion, see Ref 7 and 68, and the recent review in Ref 66.

When the cooling rates vary, different transformation kinetics can be observed, even for relatively simple alloys, as shown in Fig. 9.62. The main objective here is to present and discuss the microstructures resulting from steel processing. It is therefore essential to present and discuss the classification methodologies for the varying morphologies that can result from the different possible transformation mechanisms. Some of these classifications are extremely useful, because they make it possible to establish quantitative correlations between properties and microstructure. This is of paramount importance: as we attempt to better characterize property-structure relationships and develop microstructural evolution models, we must be able to describe the different microstructural features in a uniform and standardized way. Otherwise, there will be little hope of achieving correlations between

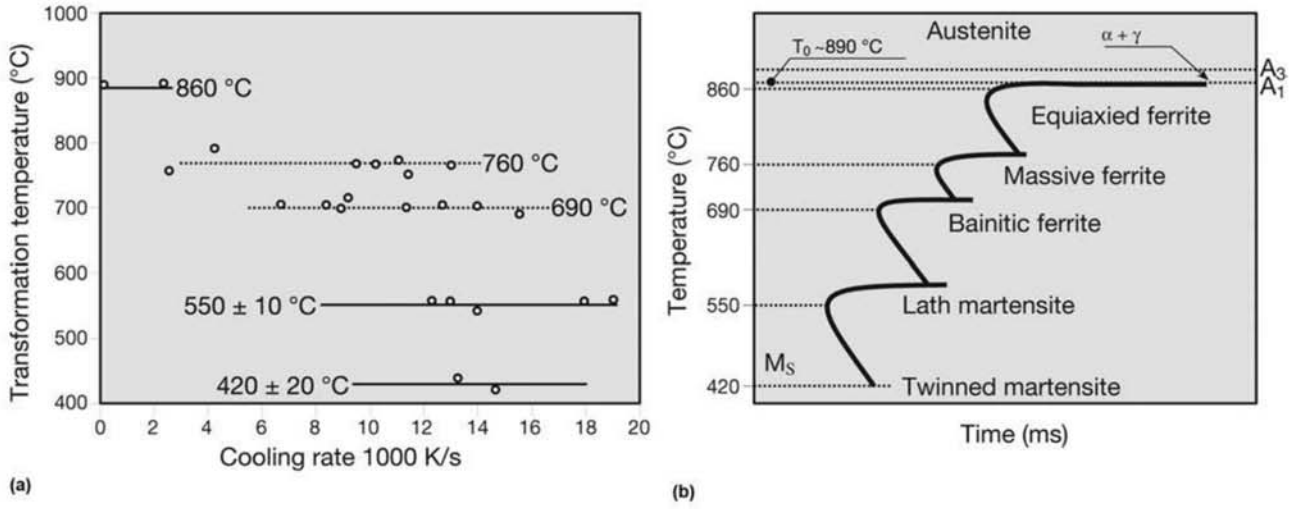

Fig. 9.62 (a) Experimental results of transformation temperatures as a function of cooling rates for a Fe-0.011% C alloy. (Note that these are extremely high cooling rates, only feasible in small scale). (b) Schematic TTT curve derived from the measurements indicated in (a), showing the different transformation curves for some of the transformation product morphologies, as classified by Wilson in his original work. Source: Adapted from Ref 69

measured properties, microstructural features, and the results forecasted by models.

9.3.2 Metallographic Classifications of Ferrite

There are at least five important methods of classifying ferrite morphologies. The Dubé classification, modified by Ref 70 and 71, is the oldest. The classification methods proposed by the IIW (International Institute of Welding) and the ISIJ (Iron Steel Institute of Japan) were devised mostly to handle microstructures resulting from welding and are relatively similar, although using different nomenclature. The classification by Ref 72 was developed having low carbon steel semi-finished products in mind, while Ref 30 proposes a classification aimed at weld-deposited metal and semi-finished products.

Dubé and Aaronson Classification

The classical classification of ferrite morphologies is the one in Ref 70, modified by Ref 71, presented in Fig. 9.63.

Allotriomorphs and Idiomorphs. Allotriomorphic (Greek: *allotrio*: different, *morph*: shape) is an expression used to indicate crystal which has its external shape defined by the environment and not by its crystallography. Idiomorphic (Greek: *idio*: own) crystals have a shape that reflect their own crystalline symmetry. Figure 9.63(a) schematically shows crystals (grains) of ferrite that have nucleated and grown along a previous austenitic grain boundary. This type of crystal is called a grain boundary allotriomorph and corresponds to equiaxial ferrite and pro-eutectoid ferrite, shown in Chapter 7, "Equilibrium Phases and Constituents in the Fe-C System" in this book. In Fig. 9.63(d), an idiomorphic crystal is shown schematically. This crystal has its shape defined

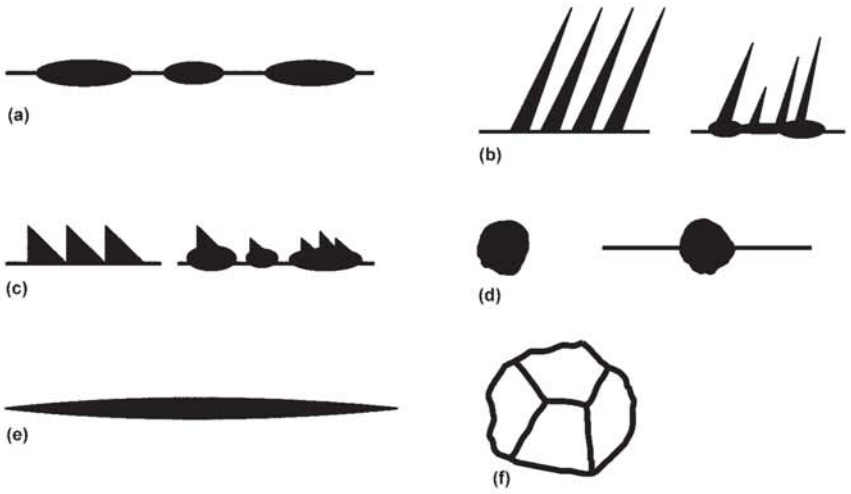

Fig. 9.63 Schematic representation of the Dubé classification modified by Aaronsson for the shape of ferrite in steels: (a) grain boundary allotriomorphs, (b) primary and secondary Widmanstätten side plates, (c) primary and secondary Widmanstätten sawteeth, (d) idiomorphs, (e) intergranular Widmanstätten plates (or needles), and (f) massive ferrite. Source: Adapted from Ref 73

by the crystal symmetry of ferrite and its relation to austenite. Idiomorphic crystals frequently nucleate in nonmetallic inclusions, without being influenced by austenitic grain boundaries. Figures 9.64 and 9.65 present examples of allotriomorphic ferrite in grain boundaries and of idiomorphic ferrite. In the final product, idiomorphic ferrite will also result normally in equiaxial ferrite.

Allotriomorphic crystals nucleate in grain boundaries and normally establish a preferential (low-energy) crystallographic relationship with respect to one of the grains and a random orientation with respect to the other. This leads to a low-energy configuration. The growth of the allotriomorphs happens by reconstruction with a high-mobility "incoherent" interface (the interface with random orientation). Thus the crystal normally grows toward one of the austenite grains only. This can be clearly seen in the allotriomorphs indicated in Fig. 9.64 to 9.66.

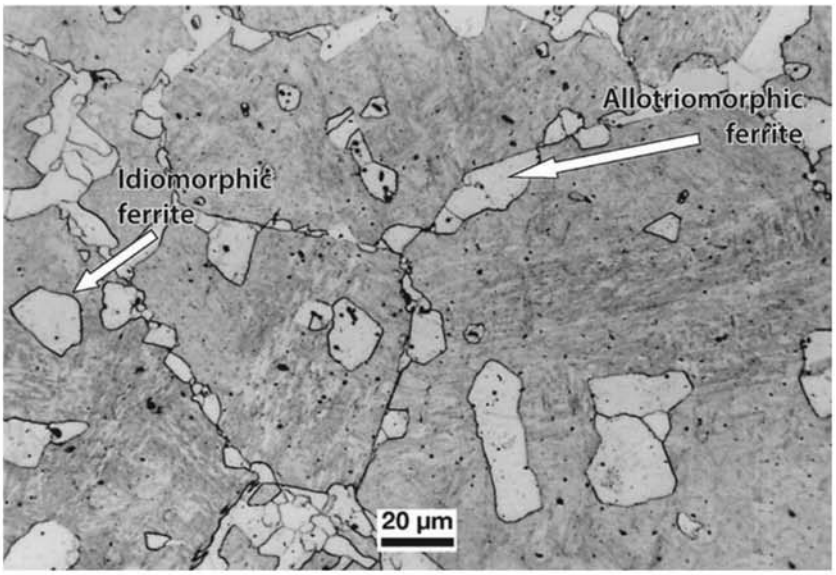

Fig. 9.64 Different morphologies of pro-eutectoid ferrite in a steel containing C = 0.37%, Mn = 1.5%, and V = 0.11% isothermally transformed at 700 °C (1290 °F). Allotriomorphic ferrite nucleated in austenitic grain boundaries and idiomorphic ferrite can be observed. Matrix has transformed to martensite on quenching after the isothermal treatment. Courtesy of C. Capdevila Montes, Grupo Materialia (CENIM-CSIC), Madrid, Spain.

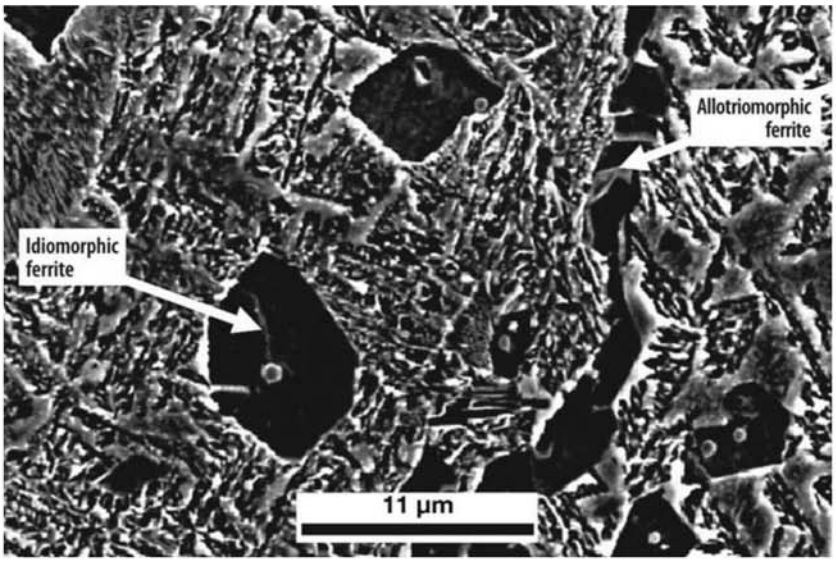

Fig. 9.65 Different morphologies of pro-eutectoid ferrite in a steel containing C = 0.37%, Mn = 1.5%, and V = 0.11% isothermally transformed at 640 °C (1185 °F). Allotriomorphic ferrite nucleated in austenitic grain boundaries and idiomorphic ferrite can be observed. Matrix has transformed to martensite on quenching after the isothermal treatment. A nonmetallic inclusion can be clearly seen inside the marked idiomorphic crystal. SEM, SE. Courtesy of C. Capdevila Montes, Grupo Materialia (CENIM-CSIC), Madrid, Spain.

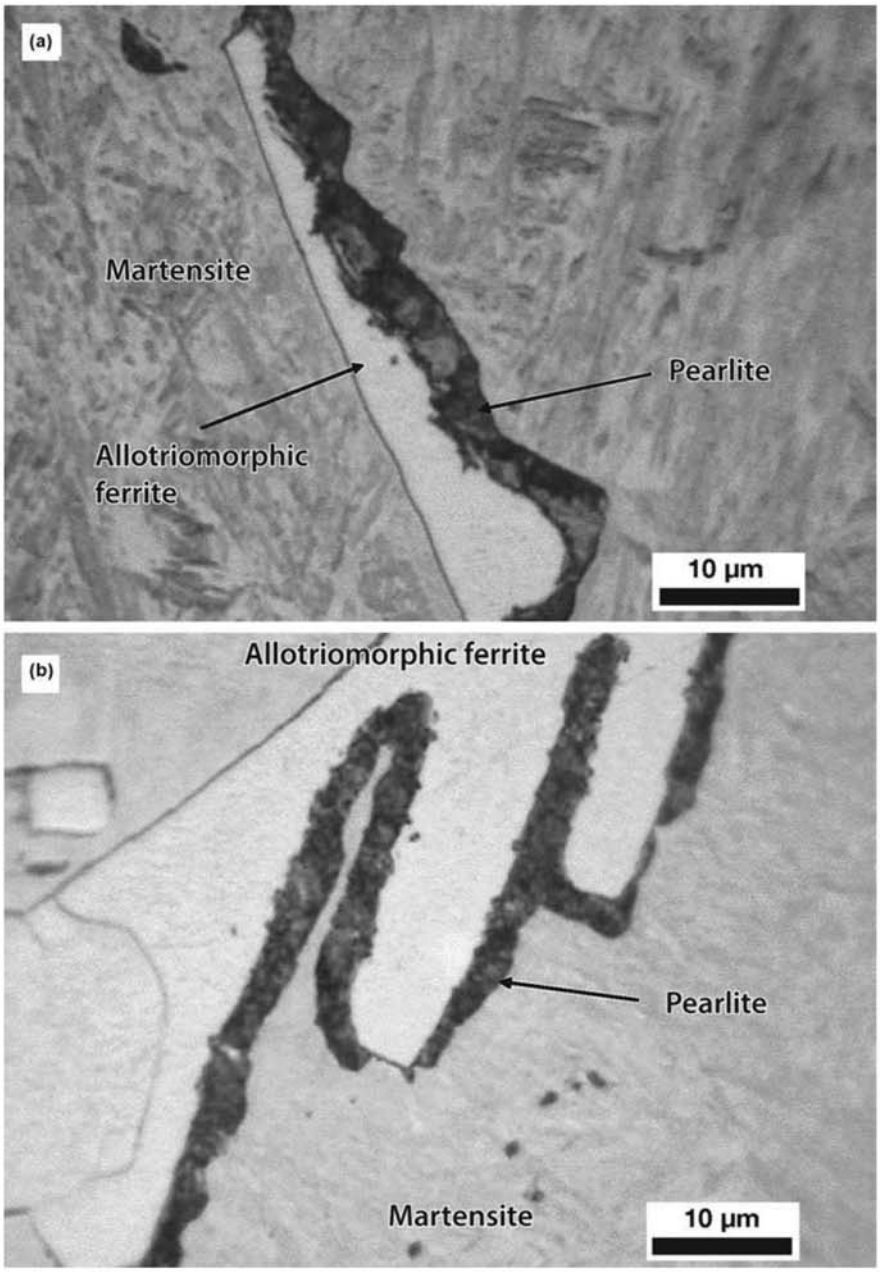

Fig. 9.66 Formation of pro-eutectoid allotriomorphic ferrite in medium carbon steel containing C = 0.5% and Mn = 1.5% isothermally transformed at (a) 723 °C (1335 °F), (b) 688 °C (1270 °F), followed by quenching. Quenching was not sufficiently rapid to avoid the formation of a thin layer of very fine pearlite, before the M_s temperature was reached. The growth of the allotriomorph toward the center of only one of the prior austenite grains can be observed. As-quenched martensite (not tempered, see Chapter 10, "Conventional Heat Treatment—Basic Concepts," in this book) is essentially not etched. Etchant: nital 2%. Courtesy of C. Capdevila Montes, Grupo Materialia (CENIM-CSIC), Madrid, Spain.

Widmanstätten Ferrite. Figure 9.63(b) schematically presents Widmanstätten ferrite plates. In three dimensions this type of ferrite has a shape somewhere between laths and plates. In transverse sections, these ferrites appear elongated and are called acicular (needle-like, even though they are not needles in three dimensions!). These plates may nucleate directly from the austenitic grain boundary or develop from allotriomorphs already nucleated in the grain boundary, as shown schematically in Fig. 9.63. Although the appearance in optical microscopy is that these plates are extensions of the grain boundary ferrite, Ref 74 showed that the plates of ferrite growing in this case do not have the same crystallographic orientation, nor do they keep the same orientation as the ferrite initially formed in the grain boundaries. Figures 9.67 to 9.69 show examples of Widmanstätten ferrite. Figure 9.70 presents three-dimensional reconstructions of primary and secondary Widmanstätten ferrite. This analysis is especially interesting because it shows many important features of the growth of ferrite with this morphology. One of the most remarkable is that the ferrite plates have a larger extension in the direction parallel to the grain boundary plane than in the direction towards the grain interior, contrary to the belief held until some years ago (Ref 74). Recent results suggest that different crystals forming a secondary Widmanstätten ferrite package grow via sympathetic nucleation on the allotriomorphs and do not form a single crystal, as indicated in Fig. 9.71 (Ref 74). It is common to refer to all types of plates and lath ferrite microstructural as "acicular ferrite" as a generic term. Figures 9.72 and 9.73 present various ferrite morphologies.

9.3.3 International Institute of Welding Classification

The International Institute of Welding (IIW) developed a classification system for the constituents in weld-deposited metal (in the fusion zone of a weld) based on observations with an optical microscope that has become ac-

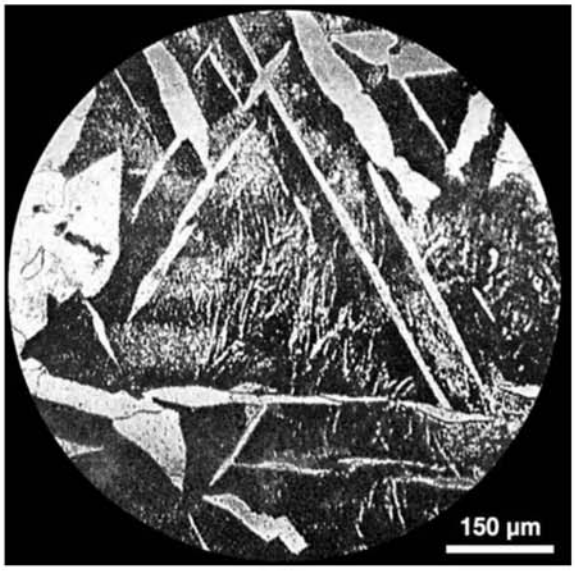

Fig. 9.67 Widmanstätten ferrite in a medium carbon steel. The ferrite plates in this case are disposed at an angle of 60° in the prior austenitic grain. Etchant: aqua regia.

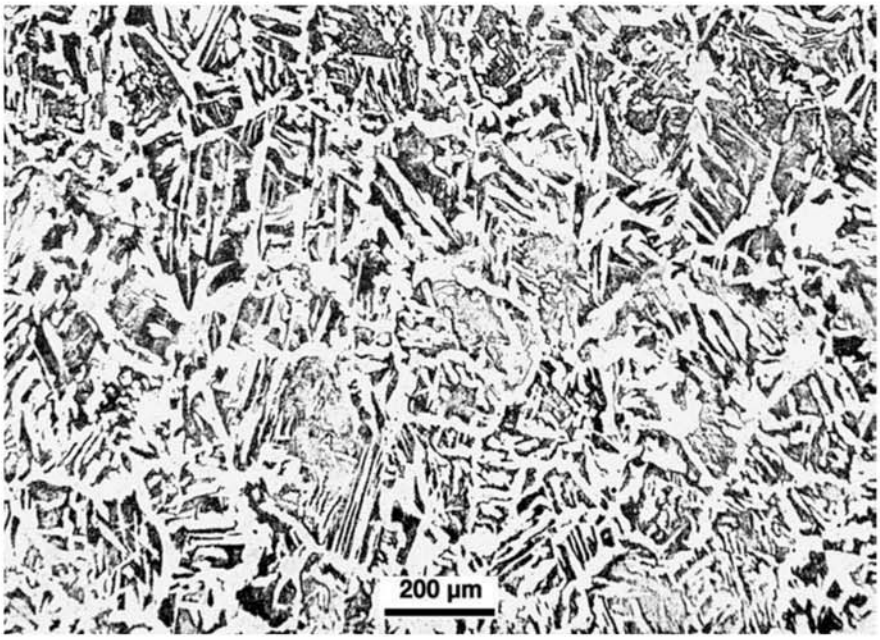

Fig. 9.68 Medium carbon steel. Pro-eutectoid ferrite and pearlite. Allotriomorphic ferrite in the prior austenite grain boundaries, Widmanstätten ferrite in primary and secondary plates. Mostly "acicular" structure. Steel with a large prior austenitic grain size, probably due to overheating (see Chapter 10, "Conventional Heat Treatment—Basic Concepts"). Etchant: nital.

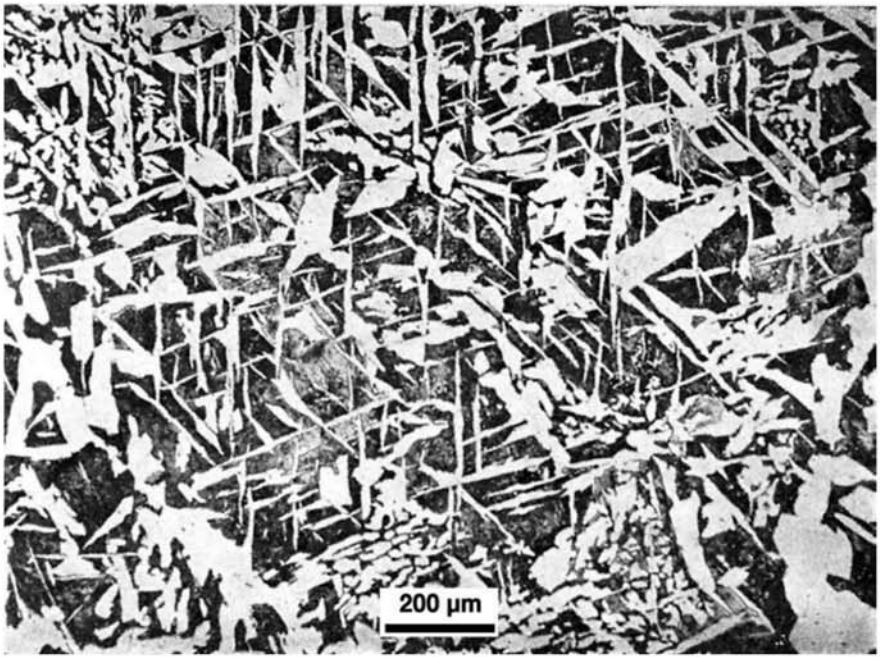

Fig. 9.69 Medium carbon steel containing Cr = 0.3%, as cast. Ferrite and pearlite. Widmanstätten ferrite. Etchant: nital.

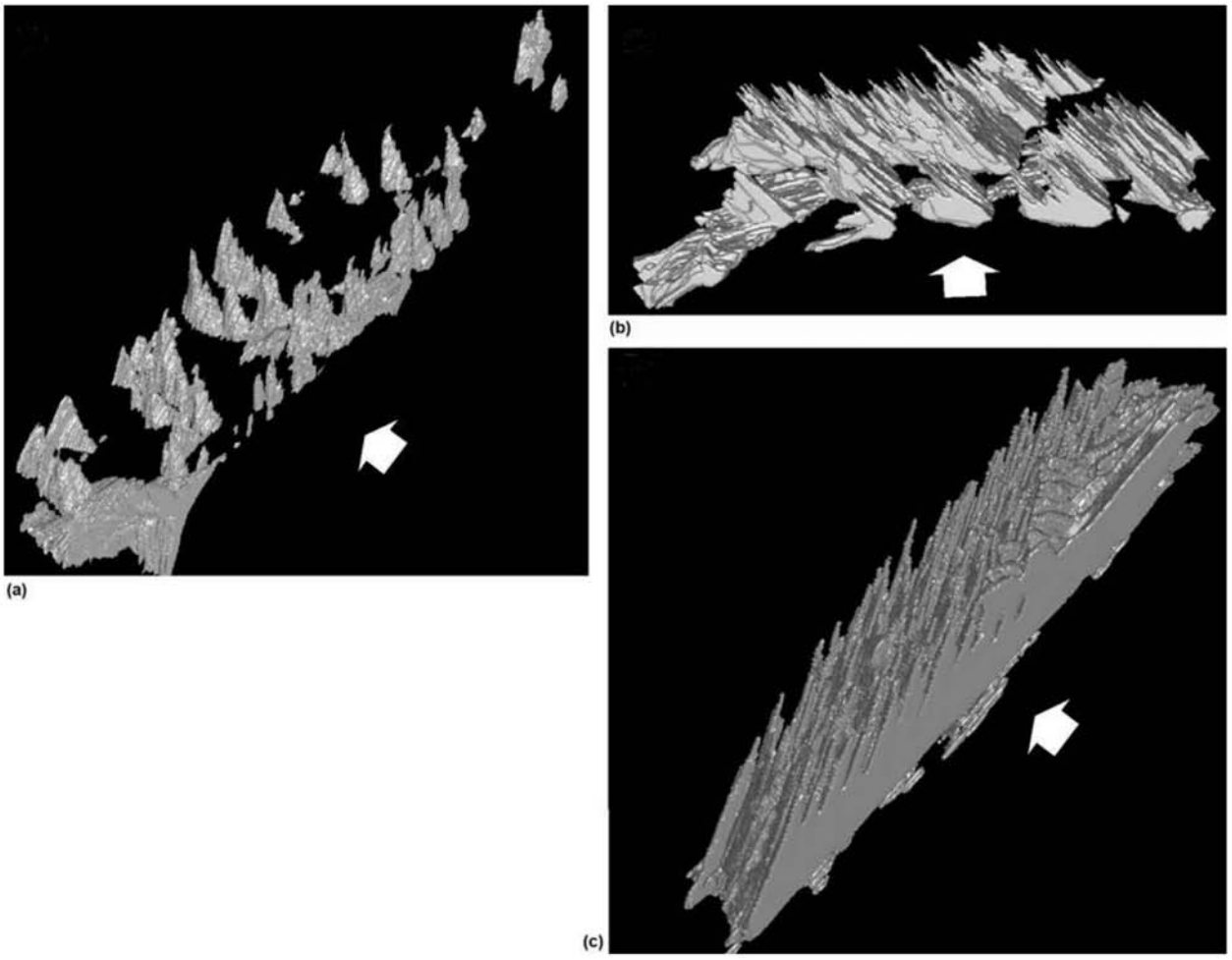

Fig. 9.70 Three dimensional reconstruction of Widmanstätten ferrite (a) primary (spikes), (b) and (c) secondary. Arrows indicate the plane where the sectioning has started, and the direction of the successive sections to create the reconstruction. The sections advance in a direction parallel to the plane of the austenitic grain boundary. Courtesy of M. Kral, University of Canterbury, Christchurch, New Zealand.

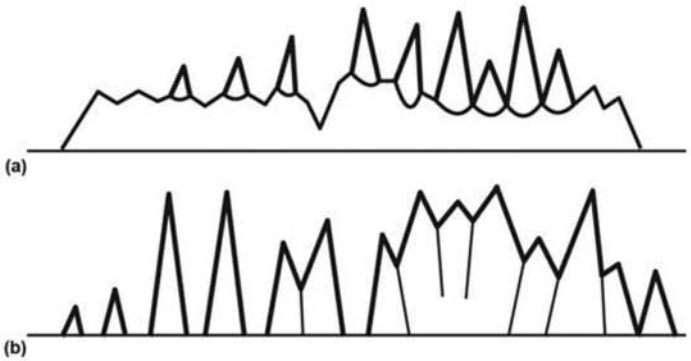

Fig. 9.71 Schematic representation (in two dimensions) of the proposed mechanisms for (a) formation of secondary Widmanstätten ferrite (sideplates) with sympathetic nucleation on the allotriomorphs and (b) independent growth of primary Widmanstätten ferrite (spikes) until they impinge adjacent crystals. Source: Adapted from Ref 74

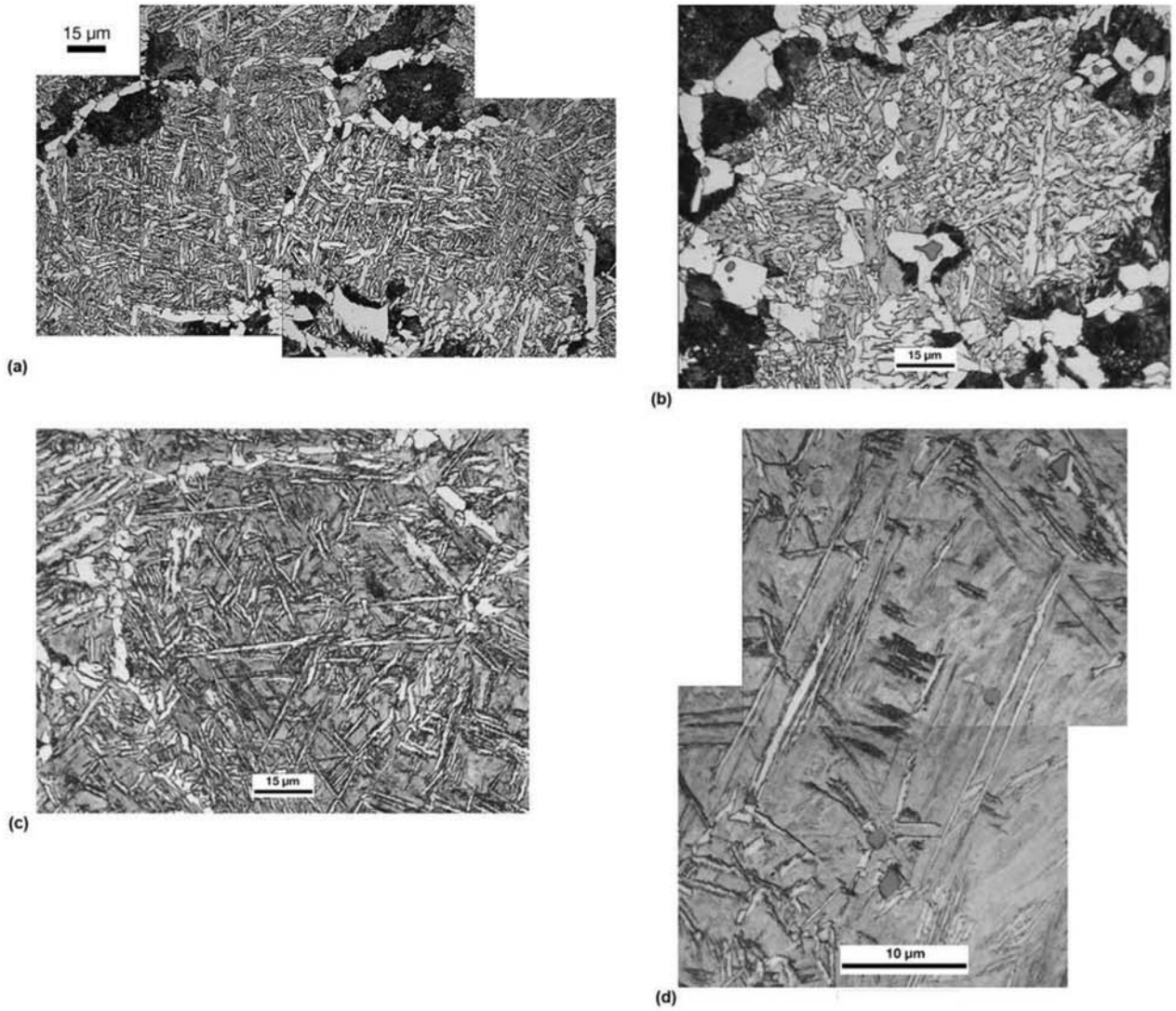

Fig. 9.72 (a) Microstructure of a medium carbon steel containing C = 0.37%, Mn = 1.5%, V = 0.11% subjected to accelerated cooling from the austenitic field. Acicular ferrite, idiomorphic ferrite, allotriomorphic ferrite (in the prior austenitic grain boundaries) and pearlite. The areas between the ferrite plates are martensite. (b) Microstructure of the medium carbon steel in (a). Acicular ferrite, idiomorphic ferrite (gray MnS inclusions can be observed inside this constituent) allotriomorphic ferrite and pearlite. The areas between the ferrite plates are martensite. Etchant: nital. (c) Microstructure of the medium carbon steel in (a). Acicular ferrite, allotriomorphic ferrite in the prior austenitic grain boundaries. The areas between the ferrite plates are martensite. Etchant: nital. (d) Microstructure of the medium carbon steel in (a). Acicular ferrite in a martensitic matrix. MnS inclusions can be seen. The ferritic transformation progressed to a lesser extent than in (a) to (c). There is indication of start of ferrite nucleation in some inclusions. Etchant: nital. Courtesy of C. Capdevila Montes, Grupo Materialia, CENIM-CSIC, Madrid, Spain.

cepted worldwide. According to this system, the most common constituents can be classified as shown in Table 9.4. (For a detailed discussion of this system applied to weld metal, the reader should consult Ref 75 and 76.) The classification scheme proposed by the IIW is quite direct and objective and is aimed at avoiding doubts when using optical microscopy. In the method, a grid is applied over the optical metallography, and the constituent found

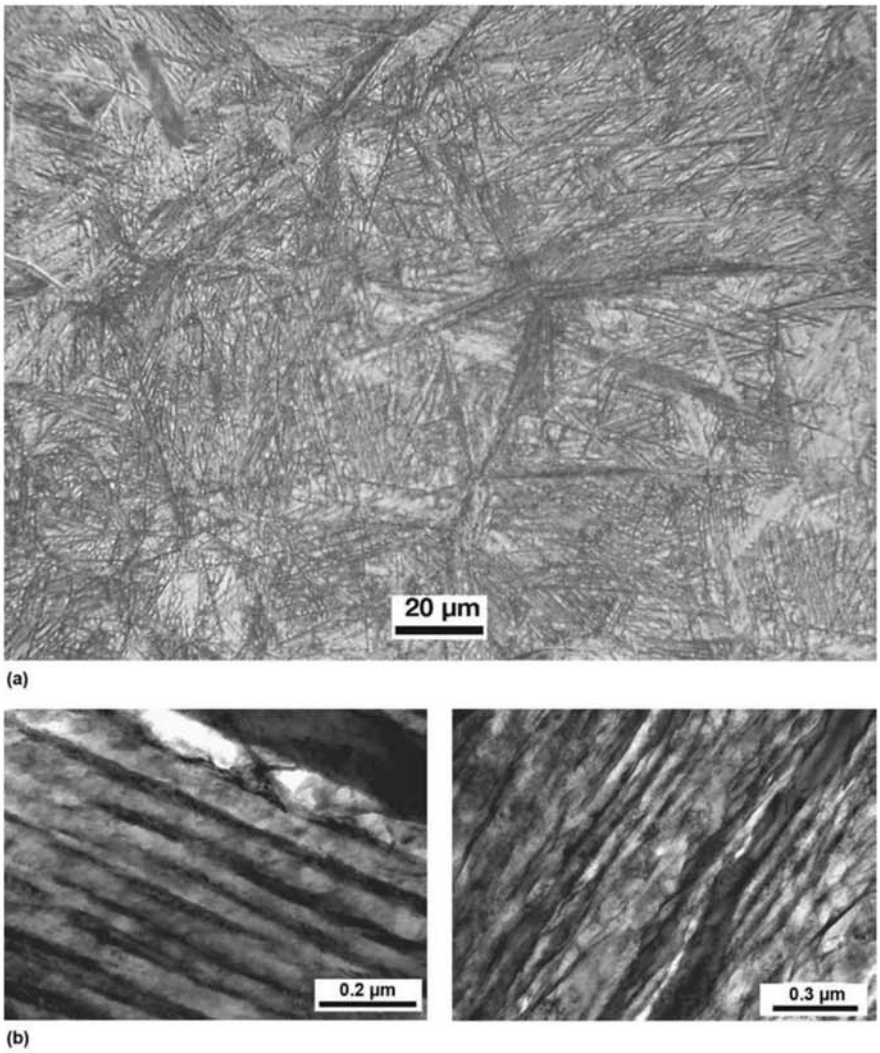

Fig. 9.73 (a) Steel containing C = 0.78%, Si = 1.6%, Mn = 2.02%, Co = 3.87%, Al = 1.37% isothermally treated at 200 °C (390 °F) for 3 days, 6 hours. Bainitic ferrite and retained austenite. (The creator of the image classifies the constituent as "bainitic ferrite" in accordance with the proposal of Ref 37 when ferrite has a morphology similar to bainite but there are no precipitated carbides.) (b) TEM image of the steel. In the diffraction condition of the image, the light areas are bainitic ferrite, intercalated with fine layers of retained austenite (dark). Courtesy of C. Garcia-Mateo, Grupo Materialia, CENIM-CSIS, Madrid, Spain.

under each grid point is identified in accordance with a flowchart that essentially eliminates confusion and misinterpretations (see Fig. 9.74 and 9.75). The microstructure is defined by the volumetric fraction of each constituent, inferred from the point fraction measured.

9.3.4 Classification by Anelli and Di Nunzio

In a project sponsored by the European Community to enhance flat steel product development, a collaboration of many organizations has resulted in

Table 9.4 The constituents in the IIW scheme for low-carbon weld metal microstructure classification (see also Fig. 9.77)

Constituent main category	Constituent sub-category	Abbreviation
Primary ferrite		PF
	Grain boundary ferrite	PF(G)
	Intragranular polygonal ferrite	PF(I)
Ferrite with second phase		FS
	Ferrite with nonaligned second phase	FS(NA)
	Ferrite with aligned second phase	FS(A)
	Ferrite side plates	FS(SP)
	Bainite	FS(B)
	Upper bainite	FS (UB)
	Lower bainite	FS (LB)
Acicular Ferrite		AF
Ferrite-carbide aggregate		FC
	Pearlite	FC (P)
Martensite	Lath martensite	M (L)
	Twin martensite	M (T)

the classification scheme proposed by Anelli and Di Nunzio (Ref 72). The evaluation system also involves classifying constituents that are found on points of a grid superimposed on the microstructure. In this case, there is a branch in the flowchart that depends on the ability to observe the microstructure with higher magnification (Fig. 9.76). Some examples of microstructures classified according to this scheme are presented in Fig. 9.77.

Harmonizing this system with other classifications is naturally not an easy task because not all correspondences are one-to-one. Thewlis, Whiteman and Senogles (Ref 77) and Ref 78 compared the usual classifications, as presented in Table 9.5. This table offers an overview of the various classification

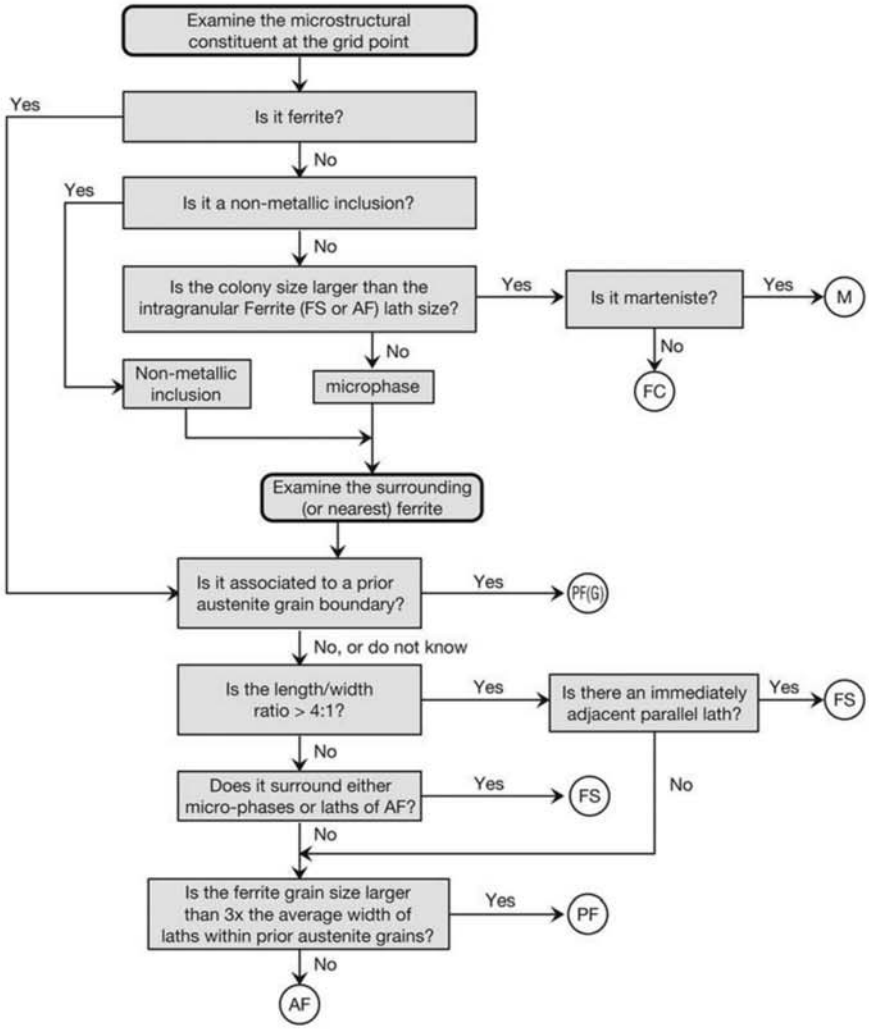

Fig. 9.74 Flowchart for the classification of constituents in weld metal, adapted from Ref 76 in a classification very similar to the one defined by the IIW (this flowchart should not be used for evaluations and classification in which compliance with the IIW practice is required. In these cases, use Ref 75.) The definition of the constituents is given in Table 9.4 (see also Fig. 9.77).

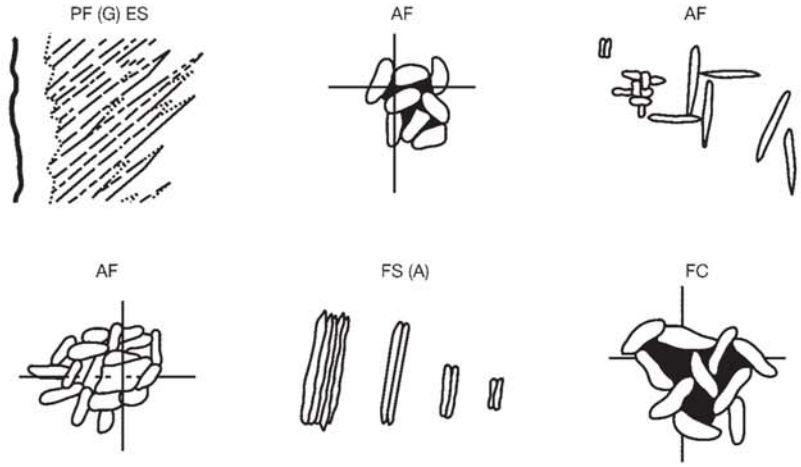

Fig. 9.75 Schematic presentation of some constituent morphologies according to the classification presented in Fig. 9.76. The IIW supplies "standard" micrographs to be used as reference for comparison. Source: Adapted from Ref 76

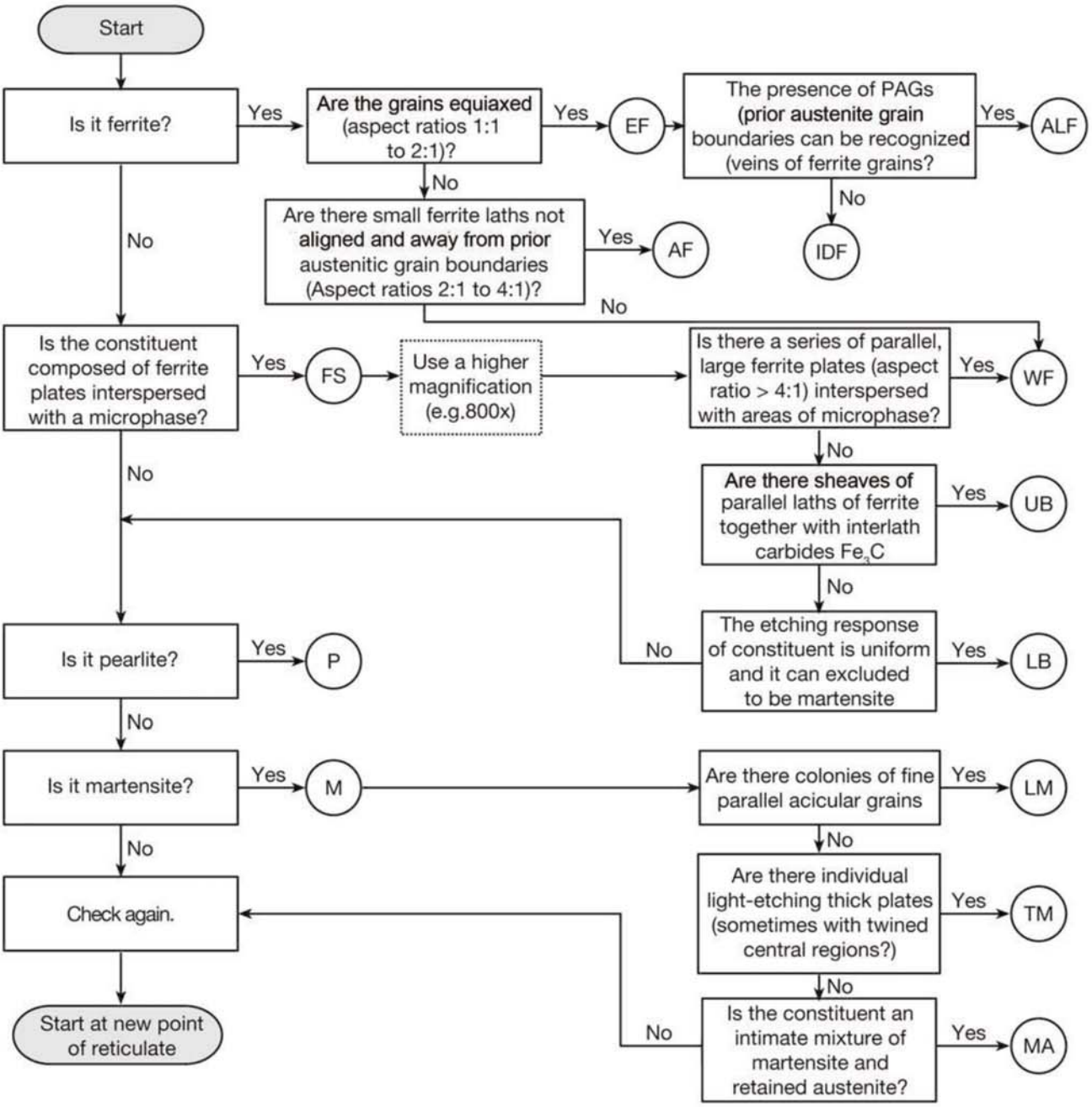

Fig. 9.76 Flowchart for the classification of constituents in low-carbon steel. The constituents are defined according to Table 9.4. Source: Adapted from Ref 72

schemes and a comparison of the different constituent nomenclatures. Evidently, depending on the classification scheme used, different views of the system may be reached. An excellent summary of the different classifications can be found in Ref 80.

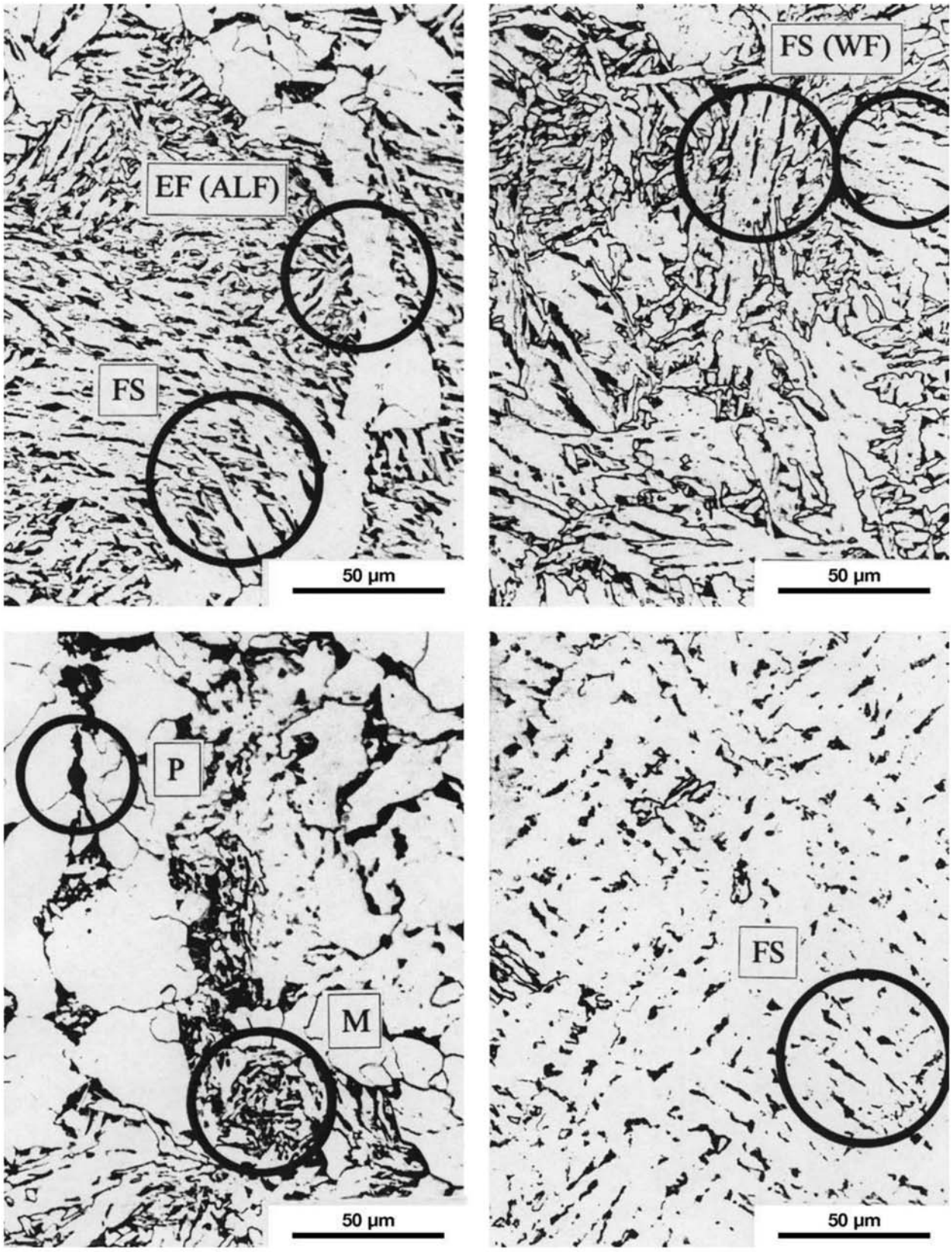

Fig. 9.77 Some examples of microstructures classified in accordance with the scheme proposed by Anelli and Di Nunzio (Fig. 9.76). Courtesy of P. E. Di Nunzio, CSM, Roma, Italy.

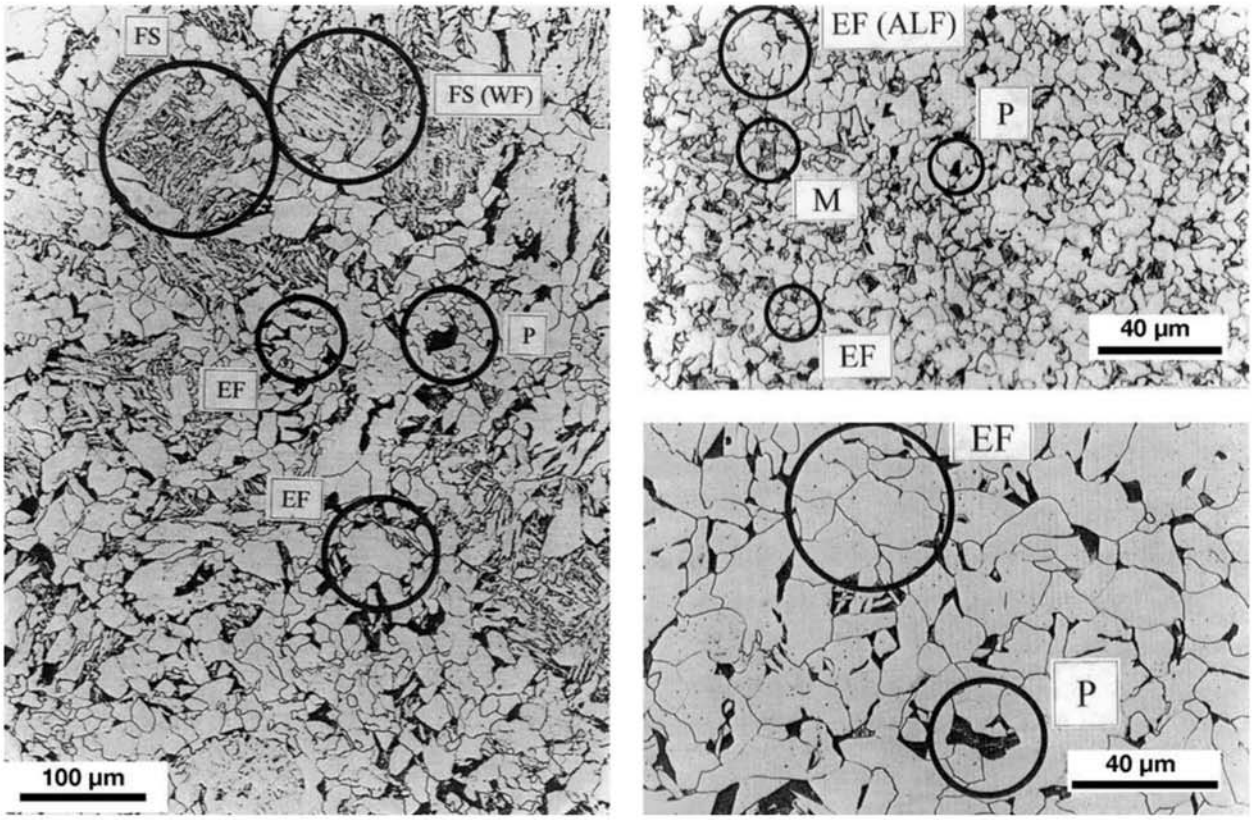

Fig. 9.77 (continued) Some examples of microstructures classified in accordance with the scheme proposed by Anelli and Di Nunzio (Fig. 9.76). Courtesy of P. E. Di Nunzio, CSM, Roma, Italy.

More recently, Thewlis proposed an interesting improvement in the IIW method and in the Anelli and DiNunzio scheme, aimed at applications with structural steels (Ref 30).

Although growth conditions play a role in the formation of these structures, the important role of nonmetallic inclusions in the nucleation of ferrite in weld-deposited metal is well established. Recently, particularly in connection with the continuous casting of thin flat products, the possibility of transferring this technique to cast and formed steels has received significant attention. The possibility of achieving fine grained structures without the need for extensive hot working is being explored (Chapter 11, "Hot Working," in this book). Many theories attempt to explain the effect of non-metallic inclusions on nucleation. The simplest theories of heterogeneous nucleation are not always successful, since some inclusions are effective in nucleating ferrite, while others are not. There are theories which propose that nucleation is favored by a compatible crystal structure (see Ref 81, 82) that would make possible the epitaxial nucleation of ferrite. Other theories propose that the formation of nonmetallic inclusions can locally deplete the matrix surrounding the inclusion in certain alloying elements and thus stabilize ferrite in this region. This would be the cause of the action of manganese sulfide as a nucleation agent, as shown in Fig. 9.78, 9.79, 9.80, and 9.81. The example given in Fig. 9.81 supports this hypothesis.

Table 9.5 Comparison of the main classification schemes for ferrite and constituents in steel and weld metal

Transformation regime	Principal structure classification	Component structure description	Abbreviation		
			Dube (Ref 70)	Annelli (Ref 72)	Abson (Ref 79)
Reconstructive	Ferrite	Grain boundary ferrite; allotriomorphic ferrite; grain boundary polygonal ferrite; primary ferrite	GBF	GBF	PF(G)
		lntragranular polygonal ferrite; idiomorphic ferrite	…	IPF	PF(I)
	Pearlite	Lamellar pearlite Degenerate pearlite Fine colony pearlite	…	p	FC(P)
Increasingly displacive, at least for the substitutional elements. Growth requires some sort of cooperative movement.	Ferrite sideplate	Grain boundary primary and secondary Widmanstätten ferrite	FS	Wf	FS(A) FS(SP)
		lntragranular primary and secondary Widmanstätten ferrite	IFP	…	FS(NA)
		Acicular ferrite	IFP	AF	AF
		Upper bainite	FS	UB	FS(A) FS(UB)
		lntragranular bainite; intragranular ferrite plates	IFP	…	Ver (AF)
		Granular bainite	…	GB	FS (NA)
		Lower bainite	…	LB	FS(A)
Displacive	Martensite	Lath martensite	…	LM	M M(L)
		Twinned martensite , plate martensite	…	MA	M M(T}

Abbreviation	
Thewlis (Ref 68)	Comments
GB(PF)	Ferrite veins or polygonal ferrite grains associated with previous austenite grain boundaries
I (PF)	Polygonal ferrite grains found within previous austenite grains of a size approximately three times greater than the surrounding ferrite grains—may be GBF seen from the end; ferrite idiomorphs associated with intragranular nucleation sites (oxide or sulfide inclusions).
…	Alternated lamellae of ferrite and cementite. Pearlite is often unresolvable in optical metallography; pearlite may be present as a microphase.
GB (Wf)	Parallel laths of ferrite with microphases between the laths, ranging from pearlite to martensite. Primary ferrite sideplates grow directly from previous austenitic grain boundaries, whereas secondary ferrite sideplates grow from allotriomorphic ferrite at the boundaries.
I(Wf)	Ferrite within the previous austenitic grains completely surrounding microphases—may be ferrite sideplates seen from their end. Ferrite plates with an aspect ratio >4:1 growing from intragranular nucleation sites (oxide or sulfide inclusions). Primary ferrite sideplates grow directly from inclusions, whereas secondary ferrite sideplates grow from the ferrite idiomorphs nucleated on the inclusions.
AF	Very fine ferrite within previous austenite grains interspersed with microphases, ranging from pearlite to MA. Acicular ferrite originally believed to be intragranularly nucleated bainite.
GB(B)	Fine parallel laths of ferrite with interlath cementite. Grows directly from the prior austenitic grain boundaries. Upper bainite has higher dislocation density than primary Widmanstatten ferrite.
I(B)	Bainite may nucleate directly from small intragranular nonmetallic inclusions (oxide or sulfide).
…	Aggregate of bainitic ferrite and twinned martensite microphase islands.
…	Presents fine dispersion of cementite particles.
…	Low-carbon martensite with internal lath substructure. Colonies of martensite may form which are larger than adjacent ferrite laths within the previous austenite grains. Smaller colonies may be treated as microphases. Hardness less than 350HV.
…	High carbon martensite with retained austenite. Light brown color. Hardness greater than 400HV.

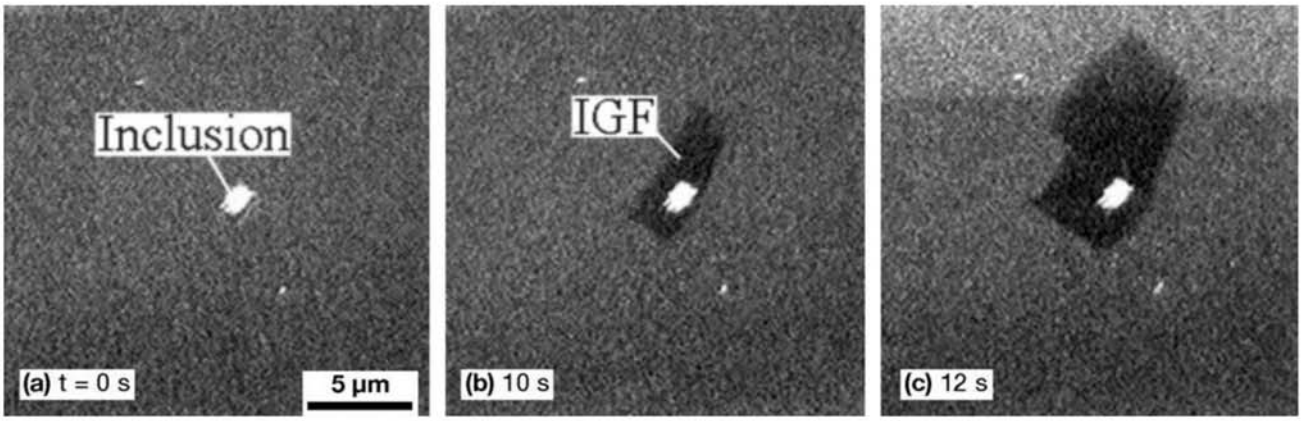

Fig. 9.78 Nucleation of a grain of idiomorphic ferrite (IGF) in a nonmetallic inclusion during isothermal transformation at 600 °C (1110 °F). The sample was heated at 1,400 °C (2550 °F) and then held at 1100 °C (2010 °F) to precipitate and grow MnS inclusions. To avoid the effects of fast diffusion on surfaces, the sample was prepared in situ using FIB for sectioning after austenitization at 800 °C (1470 °F), and then cooled from the austenitic field reaching the isothermal transformation temperature at the time indicated as t = 0 (a). According to the authors, the region surrounding the MnS inclusion is depleted in manganese, which in terms of thermodynamics favors ferrite formation. SIM. Steel containing C = 0.08%, Si = 0.2%, Mn = 1.47%, S = 0.004%, Al = 0.03%, Ti = 0.01%, N = 0.0040%. See Ref 55 and 83 for details. Reprinted courtesy of Nippon Steel Corporation. Source: Ref 55

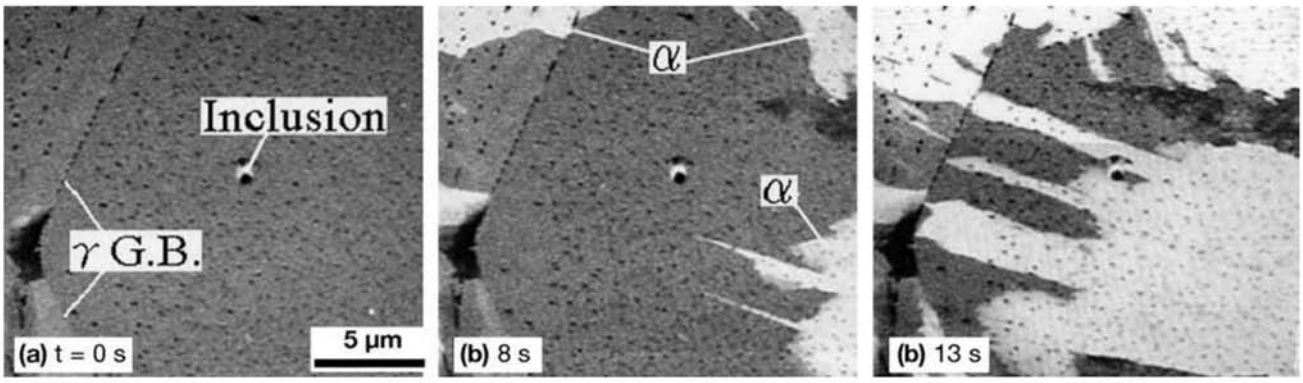

Fig. 9.79 Ferrite growth in a steel containing C = 0.08%, Si = 0.2%, Mn = 1.47%, S = 0.004%, Al = 0.03%, Ti = 0.01%, N = 0.0040%. The nonmetallic inclusion marked in the figure was not an effective nucleus for idiomorphic ferrite (see Fig. 9.78), since it was already at the sample surface during the heating performed at 1400 °C (2550 °F) and during the holding at 1100 °C (2010 °F) (to precipitate and grow MnS inclusions). The rapid diffusion at the surface has rapidly eliminated the manganese depletion around the inclusion. The sample has been quenched from the austenitic field reaching the isothermal heat treatment temperature at t = 0 (a). SIM. See Ref 55 and 83 for details. Source: Ref 55

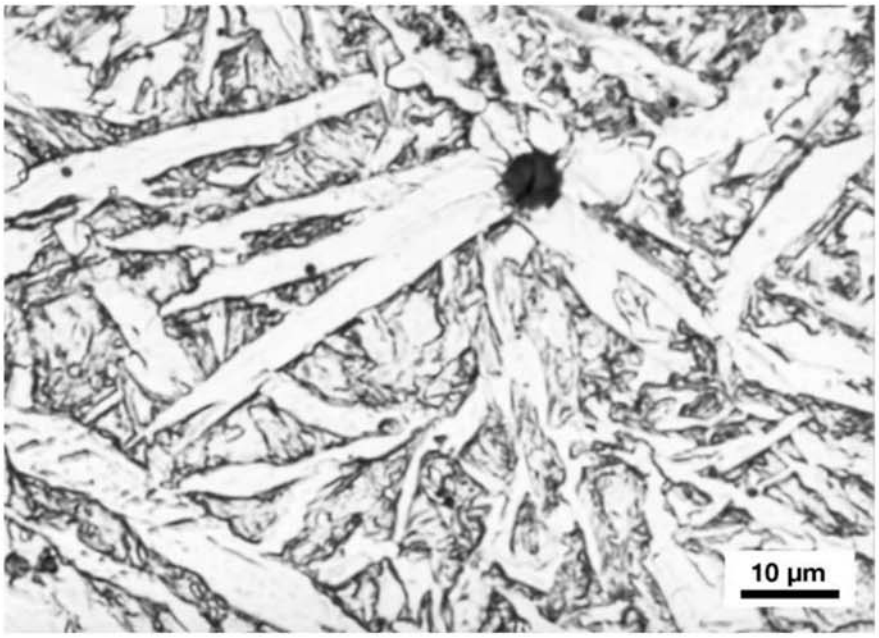

Fig. 9.80 Widmanstätten ferrite plates nucleated in a nonmetallic inclusion in a low-carbon steel. The variety of orientations of the plates indicates that the nucleation mechanism does not involve epitaxy. Courtesy of G. Thewlis.

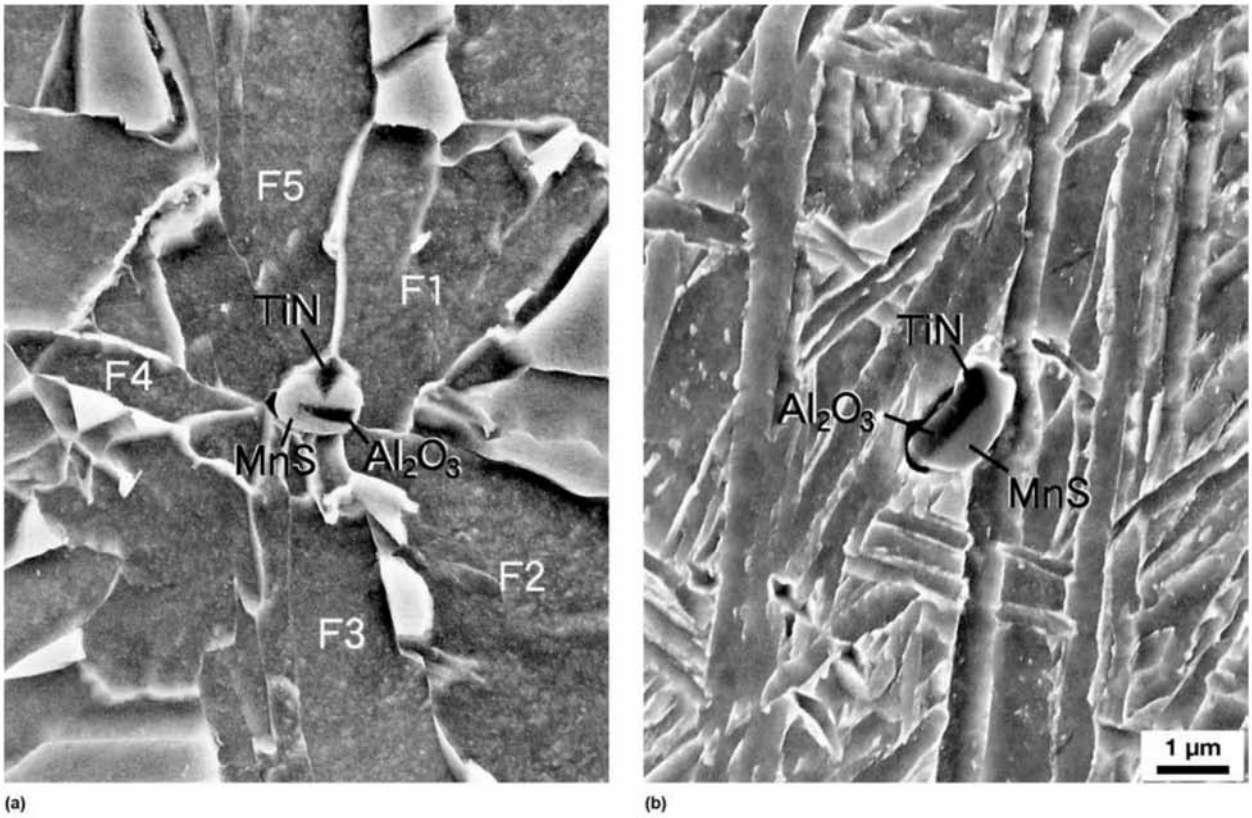

Fig. 9.81 Structural steel containing C = 0.08%, Si = 0.19%, Mn = 1.47%, S = 0.004%, Ti = 0.012%. Determining the nucleation conditions for intragranular ferrite (acicular) in a complex nonmetallic inclusion. Simulated welding thermal cycle: heating to 1440 °C (2625 °F) for 4 s followed by holding at (a) 1100 °C (2010 °F) for 100 s and (b) 1250 °C (2280 °F) for 100 s followed by rapid cooling. In (a) many grains of acicular ferrite have nucleated (F1 to F5) on the inclusion. In (b) there was no ferrite nucleation and only martensite was formed, without nucleation relations to the inclusion. Local analysis close to the inclusion indicated that in case (a) there was manganese depletion around the inclusion, whereas this did not happen in case (b). Reproduced courtesy of Nippon Steel Corporation. Source: Ref 84 and 85

Figure 9.82 presents an example of the importance of ferrite morphology on the mechanical behavior of the material. The welding parameters (current, speed, etc.) strongly influence microstructure (see Chapter 14, "Structural Steels and Steels for Pressure Vessels, Piping, and Boilers," in this book) as can be seen in Fig. 9.83.

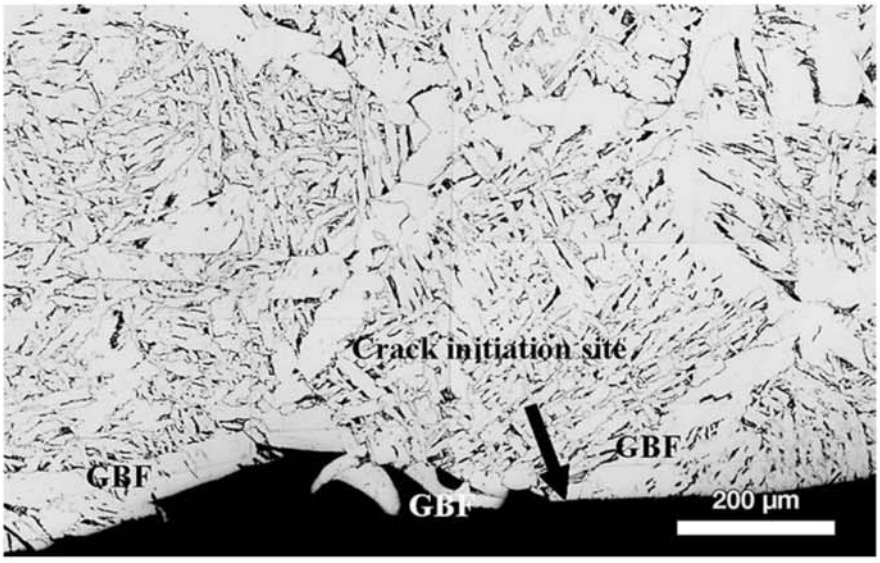

Fig. 9.82 Cross section through the brittle fracture region of the heat-affected zone of a weld in a structural steel with 490 MPa (71 ksi) strength. Fracture close to the fusion line in an electrogas (high heat-input) weld. The large austenitic grain size and the layer of pro-eutectoid ferrite in the prior austenitic grain boundaries (GBF) lower the material toughness. The arrow indicatesd the crack initiation site. Reproduced courtesy of Nippon Steel Corporation. Source: Ref 86

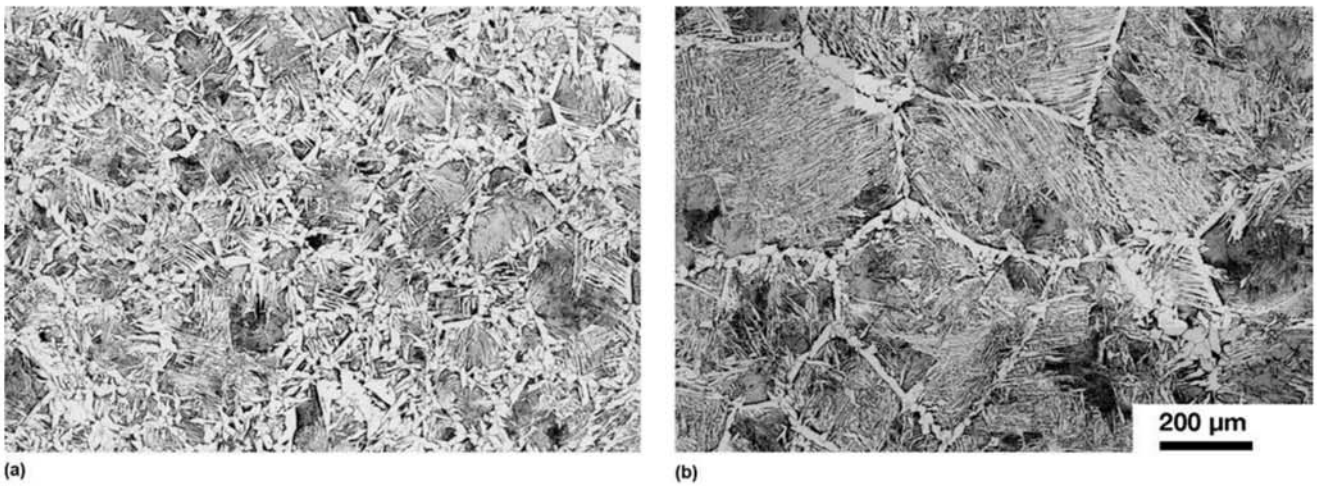

Fig. 9.83 Different welding conditions (heat cycles) can lead to significantly different microstructures. Here shown for (a) and (b) a structural steel with 490 MPa (71 ksi) strength. The austenitic grain growth in (b) is significantly larger than in (a). Network ferrite in the grain boundaries and acicular ferrite. Reproduced courtesy of Nippon Steel Corporation. Source: Ref 86

Furthermore, the different microstructures in low carbon steels can be produced when the cooling rate is varied. In this case, the effect of increasing the cooling rate is the increase in the volume fraction of acicular constituents. Microstructures formed by slow cooling are generally composed of ferrite and pearlite; as the cooling rate increases, the fraction of ferrite formed via fully reconstructructive transformation decreases (see the CCT curve presented in Fig. 9.84). Conversely, the fraction of constituents that are more acicular increases, up to the point where martensite forms, as shown in the sequence of images of Fig. 9.85, which correspond to the microstructures formed with the different cooling rates shown in the CCT curve Fig. 9.84.

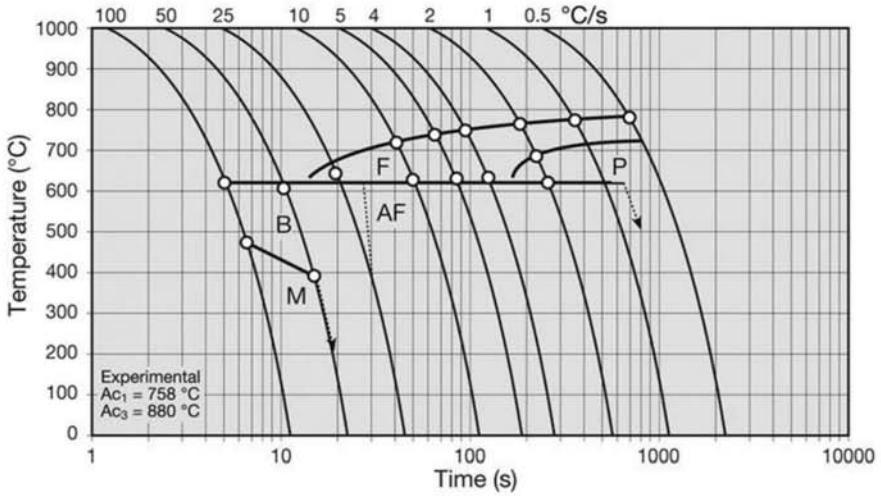

Fig. 9.84 CCT curve for an experimental steel containing C = 0.08%, Mn = 1.46%, V = 0.25%. F = equiaxial ferrite, P = pearlite, B = bainite, AF = acicular ferrite, M = martensite. The cooling rates are indicated for each cooling curve on the figure top, in °C/s. The steel has been austenitized at 1125 °C (2055 °F) for 120 s. Fig. 9.85 presents the corresponding microstructures. Courtesy of C. Garcia- Mateo, Grupo Materialia, CENIM-CSIC, Madrid, Spain

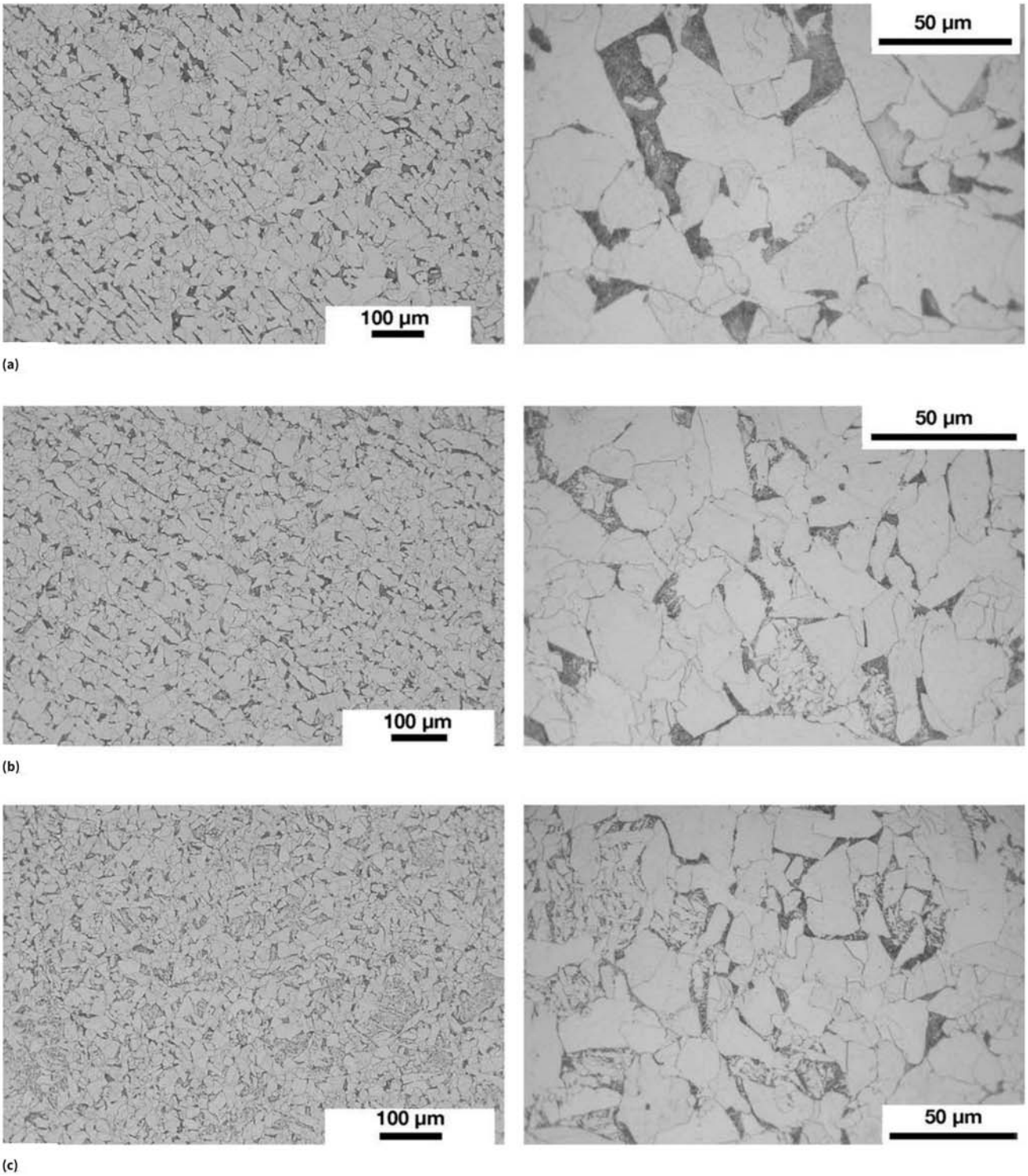

Fig. 9.85 Microstructures corresponding to the samples subjected to different cooling rates in Fig. 9.84. (a) Sample cooled at 0.5 °C/s (1 °F/s) presents a structure close to equilibrium. Equiaxial ferrite and pearlite. (b) The sample cooled at 1 °C/s (2 °F/s) starts to show the presence of acicular constituents. The classification "degenerated pearlite" sometimes employed, can be applied to some of the pearlite present. Acicular ferrite starts to appear in the structure. (c) This is the last sample in which pearlite is still formed. The progressive reduction of the volume fraction of equiaxial ferrite is remarkable. Courtesy of C. Garcia-Mateo, Grupo Materialia, CENIM-CSIC, Madrid, Spain.

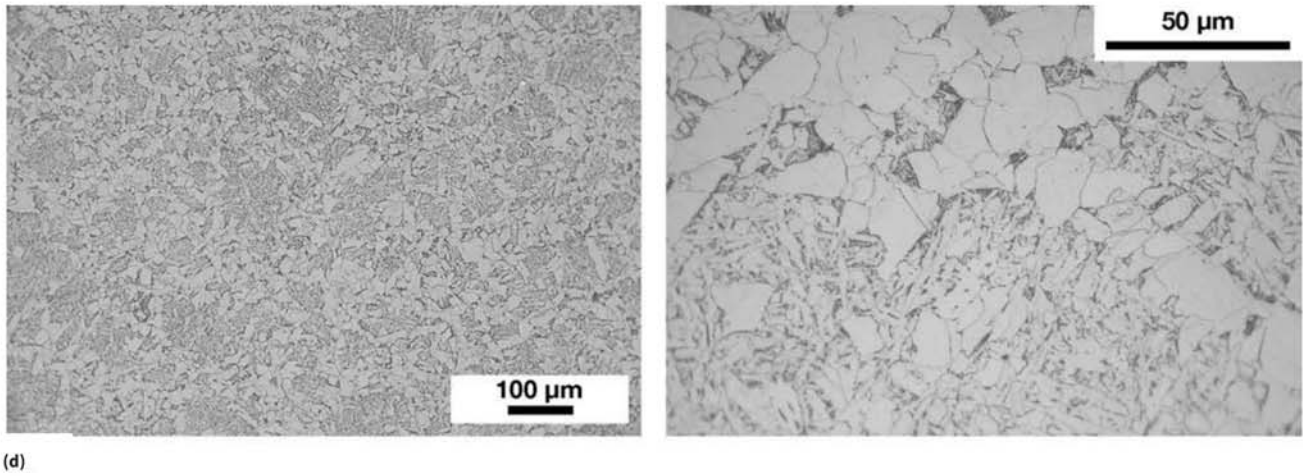

(d)

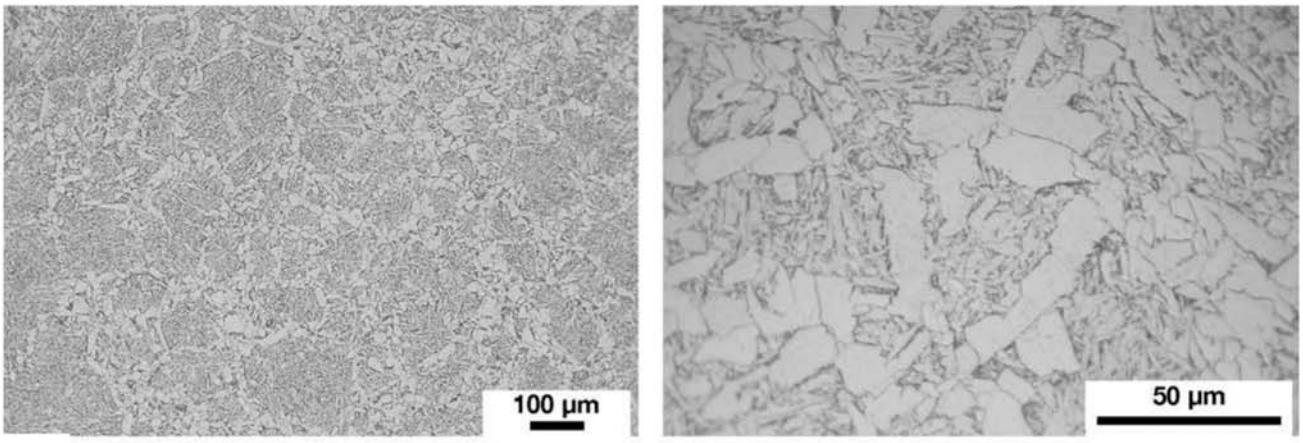

(e).

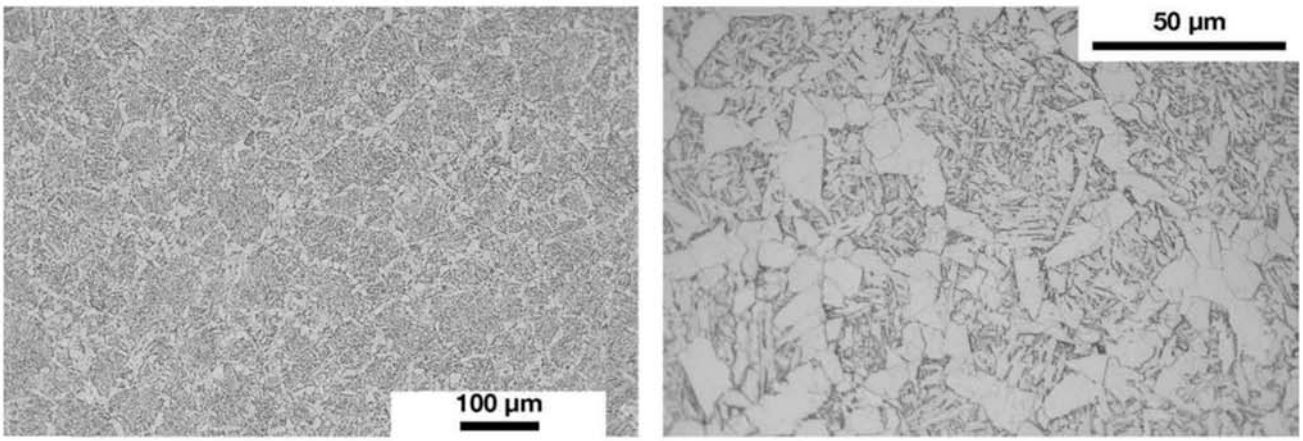

(f)

Fig. 9.85 (continued) Microstructures corresponding to the samples subjected to different cooling rates in Fig. 9.84. (d) Equiaxial ferrite and acicular ferrite. (e) and (f) The samples cooled between 5 and 10 °C/s (10 and 20 °F/s) present decreasing amounts of equiaxial ferrite and acicular ferrite. The sample cooled at 10 °C/s (20 °F/s) is the last to show acicular ferrite. Courtesy of C. Garcia-Mateo, Grupo Materialia, CENIM-CSIC, Madrid, Spain.

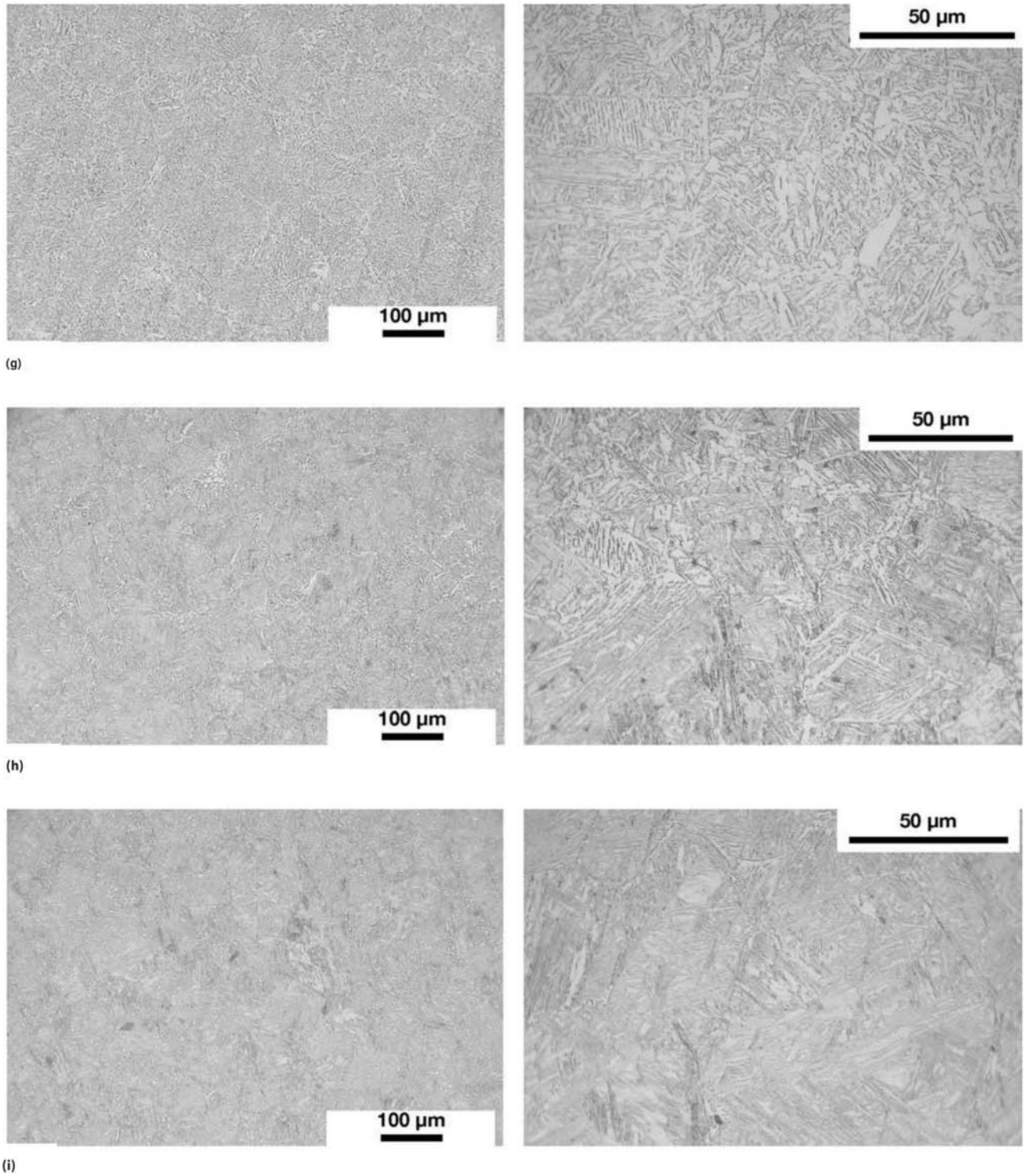

Fig. 9.85 (continued) Microstructures corresponding to the samples subjected to different cooling rates in Fig. 9.84. (g) At 25 °C/s (45 °F/s) reconstructive transformation is essentially impossible for formation of equiaxial ferrite. Bainite is the predominant constituent. (h) At 50 °C/s (90 °F/s) bainite and martensite are formed (i) At 100 °C/s (180 °F/s) the sample is almost completely formed of lath martensite. Courtesy of C. Garcia-Mateo, Grupo Materialia, CENIM-CSIC, Madrid, Spain.

REFERENCES

1. H. Ohtani, Processing—Conventional Heat Treatments, F.B. Pickering, Ed., *Materials Science and Technology—Constitution and Properties of Steels*, Wiley-VCH, 1996
2. *Supercooled Water*. Video. https://youtu.be/DpiUZI_3o8s (accessed August 14, 2016) or *Corona Freeze*. Video. https://youtu.be/4i11h VEVPdM (accessed August 14, 2016)
3. *Do Not Boil Water into Microwave Oven!* Video, https://youtu.be/nkM 8XpY3ItA (accessed August 14, 2016)
4. *Bubbles Champ*. Video, https://youtu.be/ZQgMjXqlKQc (acessed August 14, 2016)
5. D. Turnbull, R.E. Cech, *J. Appl. Phy.*, Vol 21, 1950, p 804–10
6. M.E.Valdez, P. Uranga, K. Fuchigami, H. Shibata, and A.W. Cramb, Controlled Undercooling of Liquid Iron in Contact with Al_2O_3 Substrates under Varying Oxygen Partial Pressures, *Metall. Mat. Trans. B*, Vol 37B, October 2006, p 811–21
7. D.A. Porter and K.E. Easterling, *Phase Transformations in Metals and Alloys*, 2nd ed., Chapman & Hall, 1992
8. G. Kostorz, Ed., *Phase Transformations in Materials*, Wiley-VCH, 2001
9. E. Pereloma and D.V. Edmonds, *Phase Transformations in Steels: Fundamentals and Diffusion-Controlled Transformations*, Woodhead Publishing, Elsevier, 2012
10. J. Agren, Computer Simulations of the Austenite/Ferrite Diffusional Transformation in Low-Alloyed Steels, *Acta Metall.*, 1982, Vol 30, 1982, p 841–51
11. J.O. Andersson and J. Agren, Models for the Numerical Treatment of Multicomponent Diffusion in Simple Phases, *J. Appl. Phys.*, Vol 72 (No. 4), 1992, p 1350–55
12. P.D. Portella, Adolf Martens—And His Contributions to Materials Engineering. http://www.phase-trans.msm.cam.ac.uk/2002/Martens.pdf (accesssed April 2 2018)
13. G. Krauss, *Steels: Processing, Structure and Performance*, ASM International, 2005
14. J.C. Zhao and M.R. Notis, Continuous Cooling Transformation Kinetics Versus Isothermal Transformation Kinetics of Steels: A Phenomenological Rationalization of Experimental Observations, *Mat. Sci. Engin.*, Vol 15, 1995, p 135–208
15. A.R. Marder and G. Krauss, The Morphology of Martensite in Iron-Carbon Alloys, *Trans. ASM*, Vol 60, 1967, p 1
16. A. Stormvinter, A. Borgenstam, and J. Ågren, Thermodynamically Based Prediction of the Martensite Start Temperature for Commercial Steels, *Metall. Mat. Trans.* A, Vol 43 (No. 10), 2012, p 3870–79
17. R.W.K. Honeycombe, *Steels: Microstructure and Properties*, Edward Arnold, 1981

18. J. Wang, P.J. VanderWolk, and S. VanderZwaag, Determination of Martensite Start Temperature in Engineering Steels Part I. Empirical Relations Describing the Effect of Steel Chemistry, *Mat. Trans. JIM*, Vol 41 (No. 7), 2000, p 761–68

19. K. Irvine, D. Crowe, and F. Pickering, The Physical Metallurgy of 12% Cr Steels, *J. Iron Steel Inst.*, Vol 195, 1960, p 386

20. T.G. Gooch, P. Woollin, A.G. Haynes, Welding Metallurgy of Low Carbon 13% Chromium Martensitic Steels, *Supermartensitic Stainless Steels 99 Proceedings*, Belgian Welding Institute, Belgium, May 27–28, 1999

21. M. Peet, Prediction of Martensite Start Temperature, *Mat. Sci. Technol.*, Vol 31 (No. 11), 2015, p 1370–75

22. O.M. Akselsen, G. Rorvik, P.E. Kvaale, and C. VanderEijk, Microstructure-Property Relationships in HAZ of New 13% Cr Martensitic Stainless Steels, *Weld. Res. Suppl.*, May 2004, p 160s–167s

23. http://www.phase-trans.msm.cam.ac.uk/2004/CMisc/scratch/scratch.html (accessed April 2, 2018)

24. G. Krauss and A.R. Marder, The Morphology of Martensite in Iron Alloys, *Metall. Trans.*, Vol 2, 1971, p 2343–58

25. R.N. Caron, Ph.D. dissertation, Lehigh University, 1970

26. S. Morito, X. Huang, T. Furuhara, T. Maki, and N. Hansen, The Morphology and Crystallography of Lath Martensite in Alloy Steels, *Acta Mater.*, Vol 54 (No. 19), 2006, p 5323–31

27. S. Morito, H. Tanaka, R. Konishi, T. Furuhara, and T. Maki, The Morphology and Crystallography of Lath Martensite in Fe-C Alloys, *Acta Mater.*, Vol 51 (No. 6), 2003, p 1789–99

28. S. Raoul, Rupture Intergranular Brittle Fracture of a Low-Alloy Steel Induced by Grain Boundary Segregation of Impurities: Influence of the Microstructure, Rapport CEA-R-5874, Université Paris-Sud XI, 1999

29. M. Hillert, *Metallographic Atlas*, Materials Education Council, Pennsylvania State University, 1991

30. G. Thewlis, Classification and Quantification of Microstructures in Steels, *Mat. Sci. Technol.*, Vol 20, February 2004, p 143–60

31. E.S. Davenport and E.C. Bain, Transformation of Austenite at Constant Subcritical Temperatures, *Trans. AIME*, Vol 90, 1930, p 117–44

32. E.C. Bain, Some Recollections, Early Observations of Phase Transformations—Micromorphology, *Metall. Trans.*, Vol 3, 1972, p 1031–34

33. H.K.D.H. Bhadeshia, *Bainite in Steels*, 2nd ed., Institute of Materials, 2001, http://www.phase-trans.msm.cam.ac.uk/2018/Bainite_2.pdf (accessed on March 29, 2018)

34. M. Hillert and G.R. Purdy, On the misuse of the term bainite, *Acta Metall.*, Vol 43, 2000, p 831–33

35. A. Borgenstam, M. Hillert, and J. Ågren, Metallographic Evidence of Carbon Diffusion in the Growth of Bainite, *Acta Mater.*, Vol 57 (No. 11), 2009, p 3242–52

36. G. Krauss, Private communication, 2007

37. M. Hillert, Paradigm Shift for Bainite, *Scripta Mater.*, Vol 47, 2002, p 175–80

38. H.I Aaronson, G. Spanos, and W.T. Reynolds Jr., A Progress Report on the Definitions of Bainite, *Scripta Mater.*, Vol 47 (No. 3), 2002, p 139–44

39. W.T. Reynolds Jr., H.I. Aaronson, and G. Spanos, Development of Bainite-Austenite Steel by Air, *Mat. Trans. JIM*, Vol 32 (No. 8), 1991, p 737

40. A.F. Gourgues, H.M. Flower, and T.C. Lindley, Electron Backscattering Diffraction Study of Acicular Ferrite, Bainite and Martensite Steel Microstructures, *Mat. Sci. Technol.*, Vol 16, January 2000, p 26–40

41. E. Girault, P. Jacques, P. Harlet, K. Mols, J.V. Humbeeck, E. Aernoudt, and F. Delannay, Metallographic Methods for Revealing the Multiphase Microstructure of TRIP-Assisted Steels, *Mat. Charact.*, Vol 40, 1998, p 111–18

42. S. Zaefferer, P. Romano, and F. Friedel, EBSD as a Tool to Identify and Quantify Bainite and Ferrite in Low-Alloyed Al-TRIP Steels, *J. Microsc.*, Vol 230, (No. 3), 2008, p 499–508

43. L.J. Habraken and M. Economopuoulos, Bainitic Microstructures in Low-Carbon Alloy Steels and Their Mechanical Properties, *Transformation and Hardenability in Steels*, Climax Molybdenum, 1967

44. A. Kojima, K. Yoshii, T. Hada, O. Sarki, K. Ichikawa, Y. Yoshida, Y. Simura, and K. Azuma, Development of High HAZ Toughness Steel Plates for Box Columns with High Heat Input Welding, *Nippon Steel Tech. Rep.*, Vol 90, July 2004, p 39–44

45. C.G. Andrés, F.G. Caballero, C. Capdevila, and L.F. Álvarez, Application of Dilatometric Analysis to the Study of Solid–Solid Phase Transformations in Steels, *Mat. Charact.*, Vol 48, 2002, p 101–11

46. D.T. Llewellyn and R.C. Hudd, *Steels: Metallurgy and Applications*, Butterworth-Heinemann, 1998

47. M. Atkins, *Atlas of Continuous Cooling Transformation Diagrams for Engineering Steels*, American Society for Metals, 1980

48. E. Schmidt, D. Soltesz, S. Roberts, A. Bednar, and S. Sridhar, The Austenite/Ferrite Front Migration Rate during Heating of IF Steel, *ISIJ Int.*, Vol 46 (No. 10), 2006, p 1500–1509

49. V.I. Savran, Y.V. Leeuwen, D.N. Hanlon, C. Kwakernaak, W.G. Sloof, and J. Sietsma, Microstructural Features of Austenite Formation in C35 and C45 Alloys, *Metall. Mat. Trans. A*, Vol 38A, 2007, p 946–55

50. VDEh, *Atlas von Wärmebehandlung der Stähle*, Vol 3: *Zeit Temperatur Austenitizierung Schaubilder*, VDEh, 1973

51. USS, *Atlas of Isothermal Transformation Diagrams*, 3rd ed., United States Steel, 1963

52. E.C. Bain and H.W. Paxton, *Alloying Elements in Steel*, ASM, 1966

53. P.A. Manohar, M. Ferry, and T. Chandra, Five Decades of the Zener Equation, *ISIJ Int.*, Vol 38 (No. 9), 1998, p 913–24

54. P.R. Rios, Overview No-62—A Theory for Grain-Boundary Pinning by Particles, *Acta Metall.*, Vol 35 (No. 12). 1987, p 2805–14

55. M. Sugiyama, and G. Shigesato, Development of In Situ Microstructure Observation Technique in Steel, *Nippon Steel Tech. Rep.*, Vol 91, 2005, p 13–17

56. T. Gladman, G. Fourlaris, and M. Talafi-Noghani, Grain Refinement of Steel by Oxidic Second Phase Particles, *Mat. Sci. Technol.*, Vol 15, 1999, p 1414–24

57. A. Costa e Silva and R.R. Avillez, Um banco de dados termodinâmicos para aços IF, *Rev. Tecnol. Metal. Mat.*, Vol 1 (No. 1), 2004, p 64–68

58. S. Akamatsu, M. Hasebe, T. Senuma, Y. Matsumura, and O. Akisue, Thermodynamic Calculation of Solute Carbon and Nitrogen in Nb and Ti Added Extra-Low Carbon Steel, *ISIJ Int.*, Vol 34 (No. 1), 1994, p 9–16

59. R.C. Botelho, F.J.M. Boratto, and D.B. Santos, Influência das condições de processamento na ocorrência de crescimento anormal de grão em aços médio carbono, *Anais do 62.º Congresso Anual da ABM*, ABM, 1997, p 3254–61

60. R. Millsop, A Survey of Austenite Grain Size Measurements, *Hardenability Concepts with Applications to Steel*, TMS-AIME, 1977

61. R. Schreiman and W. Bolton, Estimation of Prior-Austenite Grain Size in Heat-Treated Martensitic Carbon and Low-Alloy Steels, *Microsc. Microanal.*, Vol 9, 2003, p 732–33

62. ASTM, ASTM E112-96 (2004) E2 Standard Test Methods for Determining Average Grain Size, 2004

63. C.G. Andrés, F.G. Caballero, C. Capdevila, and D.S. Martin, Revealing Austenite Grain Boundaries by Thermal Etching: Advantages and Disadvantages, *Mat. Charact.*, Vol 49, 2003, p 121–27

64. M. Gouné, F. Danoix, J. Ågren, Y. Bréchet, C.R. Hutchinson, M. Militzer, et al., Overview of the Current Issues in Austenite to Ferrite Transformation and the Role of Migrating Interfaces therein for Low-Alloyed Steels, *Mat. Scie. Engin. Rep.*, Vol 92, June 2015, p 1–38

65. A. Hultgren, Isothermal Transformation of Austenite, *Transactions ASM*, 1947, p 915

66. M. Hillert and J. Agren, On the Definitions of Para-Equilibrium and Ortho-Equilibrium, *Scripta Mater.*, Vol 50, 2004, p 697–99

67. J.G. Speer, D.V. Edmonds, F.C. Rizzo, and D.K. Matlock, Partitioning of Carbon from Supersaturated Plates of Ferrite, with Application to Steel Processing and Fundamentals of the Bainite Transformation, *Curr. Opin. Solid State Mat. Sci.*, Vol 8, 2004, p 219–37

68. H.K.D.H. Bhadeshia, Deffusonal Formation of Ferrite in Iron and Its Alloys, *Prog. Mat. Sci.*, Vol 29, 1985, p 321–86

69. E.A. Wilson, The γ->α Transformation in Low-Carbon Irons, *ISIJ Int.*, Vol 34 (No. 8), 1994, p 615–30

70. C.A. Dubé, H.I. Aaronson, and R.F. Mehl, *Rev. Metall.*, Vol 55 (No. 3), 1958, p 201

71. H.I. Aaronson, The Proeutectoid Ferrite and the Proeutectoid Cementite Reactions, V.F. Zackaye and H.I. Aaronson, Eds., *Decomposition of Austenite by Diffusional Processes*, Interscience, 1962, p 387–542

72. E. Anelli and P.E. DiNunzio, Classification of Microstructures of Low Carbon Steels: Preparation of a Set of Standard Micrographs, ECSC Agreement 7210—EC/405 (94–D3.02a), CSM, 1996

73. M.V. Kral and G. Spanos, Three-Dimensional Analysis and Classification of Grain Boundary–Nucleated Proeutectoid Ferrite Precipitates, *Metall. Mat. Trans. A*, Vol 36A, May 2005, p 1199–207

74. G. Spanos, A.W. Wilson, and M.V. Kral, New Insights into the Widmanstätten Proeutectoid Ferrite Transformation: Integration of Crystallographic and Three-Dimensional Morphological Observations, *Metall. Mat. Trans. A*, Vol 36A, May 2005, p 1209–18

75. IIW, *International Institute of Welding Guidelines for the Classification of Ferrite Steel Weld Metal Microstructure Constituents Using the Light Microscopy*, International Institute of Welding, IIW DOC. IX-1533-88

76. A. Duncan, Further Development of a Scheme for the Classification of Ferritic Weld Metal Microstructures, *Welding Inst. Res. Bull.*, August 1986, p 260–65

77. G. Thewlis, J. Whiteman, and D. Senogles, Dynamics of Austenite to Ferrite Phase Transformation in Ferrous Weld Metals, *Mat. Sci. Technol.*, Vol 13 (No. 3), 1997, p 257–74

78. G. Thewlis, Private communication, 2007

79. D.J. Abson and R.E. Dolby, *Welding Inst. Res. Bull.*, Vol 21 (No. 4), 1980, p 100

80. R.M. Alé, J.C.M. Jorge, and J.M.A. Rebelo, Constituintes Microestruturais de Soldas de Aço C-Mn Baixa Liga. Parte II: Metal de Solda, Soldagem e Materiais, *Arquivo Técnico*, Vol 1 (No. 2), 1993, p 18–25

81. A.G. Fox and D.G. Brothers, The Role of Titanium in the Nonmetallic Inclusions Which Nucleate Acicular Ferrite in the Submerged Arc Weld (SAW) Fusion Zone of Navy HY-100 Steel, *Scripa Metall. Mater.*, Vol 32 (No. 7), 1995, p 1061–66

82. S.S. Babu and S.A. David, Inclusion Formation and Microstructure Evolution in Low-Alloy Steel Welds, *ISIJ Int.*, Vol 42 (No. 12), 2002, p 1344–53

83. G. Shigesato and M. Sugiyama, Development of In Situ Observation Technique Using Scanning Ion Microscopy and Demonstration of Mn

Depletion Effect on Intragranular Ferrite Transformation in Low-Alloy Steel, *J. Electron Microsc.*, Vol 51, 2002, p 359

84. S. Aihara, G. Shigesato, M. Sugiyama, and R. Uemori, Microstructural Control of Weld Heat-Affected Zone of Steel by Mn Depletion Around Nonmetallic Inclusions, *Nippon Steel Tech. Rep.*, Vol 91, 2005
85. G. Shigesato, M. Sugiyama, S. Aihara, R. Uemori, and Y. Tomita, *Tetsu-to-Hagane*, Vol 87 (No. 2), 2001, p 23–30
86. A. Kojima, A. Kiyose, R. Uemori, M. Minagawa, M. Hoshino, T. Nakasima, K. Ishida, and H. Yasui, Super High HAZ Toughness Technology with Fine Microstructure Imparted by Fine Particles, *Nippon Steel Tech. Rep.*, Vol 90, 2004, p 2–6

Metallography of Steels—Interpretation of Structure and the Effects of Processing
Hubertus Colpaert
Updated and Translated by André Luiz V. da Costa e Silva

Chapter 10
Conventional Heat Treatment–Basic Concepts

The aim of this chapter is to discuss the main conventional heat treatments of steels and cast irons and the structures resulting from them.

Before discussing the heat treatments from the materials point of view, it is important to call attention to the fact that thermal metrology is a fundamental tool for the success of any heat treatment. The equipment, instruments, transducers, and cables used in the measurement and control of heat treatment temperatures should be subject to a consistent and well-organized maintenance and calibration program. This is of paramount importance if consistent, reliable results from heat treatments are to be achieved.

On the other hand, the survey of heat treatment furnaces to determine temperature homogeneity is frequently overlooked, or is only done when explicitly required by a client or a standard. For the whole volume of the furnace to maintain reasonable variations of temperature with respect to that measured by the control or recording thermocouple is never an easy task. To have stability along the heat treatment time and in the whole furnace volume is even more complex. Performing furnace surveys to evaluate temperature homogeneity (along the furnace dimensions and along the heating and holding times) is an essential part of quality assurance of heat treatment operations. The heat transfer mechanisms operating at the different temperature ranges in which heat treatments are performed are not the same. In the range of temperatures of tempering and stress relief (around 300–650 °C, or 570–1200 °F), for instance, convection is dominant, whereas in treatments that involve austenitizing (typically those above about 800 °C, or 1470 °F), radiation is the most important mechanism of heat transfer. Thus, if the furnace is to be used in both temperature ranges, one survey is required for each range. Some standards present methods and requirements for heat treatment furnace surveys (Ref 1) and may be used as a guideline when no specific requirement can be found. Furthermore, some industries (such as nuclear) require that the temperature be measured by thermocouples in direct contact to the part be treated, for parts that are safety-related.

10.1 Annealing

ASTM A941 (Ref 2) defines *annealing* as "a generic term covering any of several heat treatments." Indeed, although several industries use the word with a defined meaning, one has to define clearly what exact type of annealing is being discussed.

10.1.1 Full Annealing

Frequently, full annealing is meant when the word "annealing" is used to define a heat treatment. Annealing involves heating the steel above the critical range, or sometimes in the intercritical range, when it is called "intercritical annealing," followed by slow cooling (inside the furnace, for instance).

This heat treatment is normally used with goals to:

- Recover material properties that have been altered by a previous mechanical or heat treatment
- Refine or homogenize "as-cast" structures (see Chapter 8, "Solidification, Segregation, and Nonmetallic Inclusions," in this book)

Annealing usually "erases" the structures resulting from heat or mechanical treatment to which the material has been previously subjected because, as the material crosses the intercritical range, new crystals (or grains) of austenite nucleate and grow, regardless of which microstructure was previously present. Later, this austenite will decompose in slow cooling conditions, approximating the equilibrium structures discussed in Chapter 7, "Equilibrium Phases and Constituents in the Fe-C System," in this book.

10.1.2 Important Points During the Annealing Thermal Cycle

The aspects important for the performance of a proper annealing cycle are heating, annealing or holding temperature, holding time at temperature, furnace atmosphere, and slow cooling.

Heating

The heating cycle should be uniform and the heating rate compatible with the part dimensions and the envisaged holding temperature. The holding temperature should be kept as constant as possible during the holding time. A nonuniform heating or holding temperature can result in part distortion and, in extreme cases, in the fracture of the part. This is especially important in view of some of the usual structures present before annealing cycles, such as cold worked, with residual stresses, and as-cast, with significant structure and chemical composition heterogeneity.

Annealing (or Holding) Temperature

For each chemical composition, there is an ideal temperature for full annealing. This is usually 20–50 °C (35–90 °F) above the upper limit of the intercritical range, for hypo-eutectoid steels. The diagram in Fig. 10.1 indicates the temperatures recommended for carbon steels and which can normally be used for low alloy steels, too. For hyper-eutectoid steels, it is common prac-

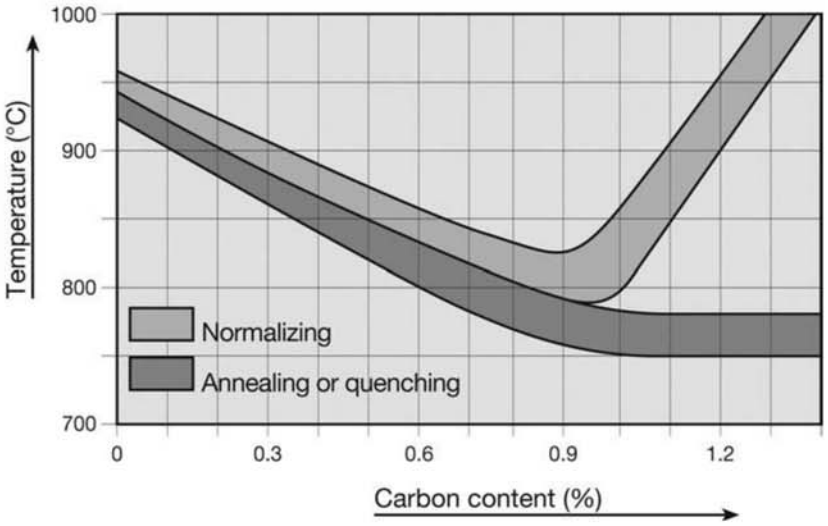

Fig. 10.1 Recommended temperatures for austenization for full annealing, normalizing, and quenching of carbon steels. For alloy steels, the temperatures can be different in view of the changes in phase equilibria caused by alloying elements (see Ref 3).

tice to avoid the formation of pro-eutectoid cementite as a network in the austenitic grain boundaries, which could lead to brittleness. In this case, the full annealing is performed between the A_1 and A_{cm} temperatures.

Holding Time at Temperature

The holding time at temperature should be enough for austenite to form and homogenize as much as possible (see Chapter 9, "Conventional Heat Treatments: Usual Constituents and Their Formation," in this book). In any case, the heating rate and the holding time should be adjusted to guarantee that the center of the part reaches the desired temperature and will be held at this temperature for a time sufficient for the transformation to occur. In small or thin parts, the usual rule of thumb is a holding time of at least some minutes at temperature. For thicker parts, a common rule is holding at temperature for 20 min for each 10 mm (1 h/in.) of part thickness to guarantee temperature homogeneity along the cross section and sufficient time for austenite to form and homogenize. (Although interstitials will dissolve fast at the usual temperatures of annealing, diffusion of substitutional elements will be slower, and if strong segregation is present along significant distances, little homogenization of these elements is to be expected.)

Furnace Atmosphere

In furnaces with an oxidizing atmosphere, it is advisable at least to minimize air intake to reduce the formation of scale. This is especially important in the case of larger parts that may have to remain inside the furnace for longer times. In the case of parts in which surface decarburization must be avoided, special care with the furnace atmosphere must be taken. This is especially important in the treatment of tools and parts in which surface hard-

ness is important (gears, fasteners, etc.) and in springs and other parts in which fatigue resistance is important. Surface decarburization has a strong effect on the fatigue resistance.

Slow Cooling

It is common practice to cool the parts—at least until a temperature in which one can be sure that austentite decomposition has taken place completely—inside the furnace. Should the cost of using the furnace for the time required for the cooling be incompatible with the part costs, alternative cooling methods can be employed. This is usually only possible for parts that are sufficiently large that they can be removed from the furnace and transferred to adequate cooling places without being subjected to substantial cooling and thus, being sure that the decomposition of austenite only happens under the desired, slow cooling conditions. These parts can be cooled under insulated campanulas or boxes, buried in thermal insulating minerals such as vermiculite, powdered lime, dry sand, ashes, or other media. It is essential to guarantee slow cooling from the moment the parts leave the furnace. In Chapter 7, "Equilibrium Phases and Constituents in the Fe-C System," several microstructures resulting from full annealing are presented.

10.1.3 Annealing Treatment in which the Maximum Temperature Is Lower than the Critical Temperature (A_1)

Many annealing treatments do not involve heating above or inside the intercritical zone. The main annealing treatments are spheroidizing, stress-relieving, annealing for hydrogen diffusion, and annealing for recovery and recrystallization.

Spheroidizing (or Spheroidizing Annealing)

The objective of spheroidizing is usually to alter the distribution and morphology of carbides in the microstructure (particularly those present in pearlite), changing them in spheroidal or globular form, dispersed in the matrix. This treatment is usually not accompanied by phase transformation. The driving force for the microstructure change is the reduction of interfacial area. A sphere is the geometrical shape with minimum area to volume ratio. In many cases, particularly in medium and high carbon steels, this microstructure is the most favorable for machinability (Ref 3). Figure 10.2 presents the evolution of the microstructure of structural steels subjected to a simulated heat treatment below the critical A_1 temperature. The shape change of the carbides is evident, even for relatively short times.

Figure 10.3 presents the microstructure of a hyper-eutectoid steel after a spheroidization treatment.

Many different heat cycle practices can be used to achieve spheroidization (Ref 3), such as holding for long time at temperatures below Ae_1, heating and cooling alternately between temperatures just above and just below Ae_1. Figure 10.4 shows the effectiveness of this alternating cycle for the spheroidization of some steels.

Some examples of microstructures resulting from deviations during annealing heat treatments are presented in Fig. 10.5 and 10.6. Because the an-

nealed microstructures are very close to the (meta-stable) equilibrium condition, it is almost impossible to identify the microstructure present before the annealing treatment, when this is performed correctly. Spheroidizing treatments, particularly heating pearlite, bainite, or martensite for a sufficiently long time at the requisite heat treatment temperature, will result in microstructures that are not distinguishable from one another.

Stress-Relieving Annealing

This heat treatment is usually called "stress-relieving heat treatment." Although frequently used to reduce or eliminate residual stresses in parts or welds, it is important to consider that in the case of welded joints of structural steels (see Chapter 14, "Structural Steels and Steels for Pressure Ves-

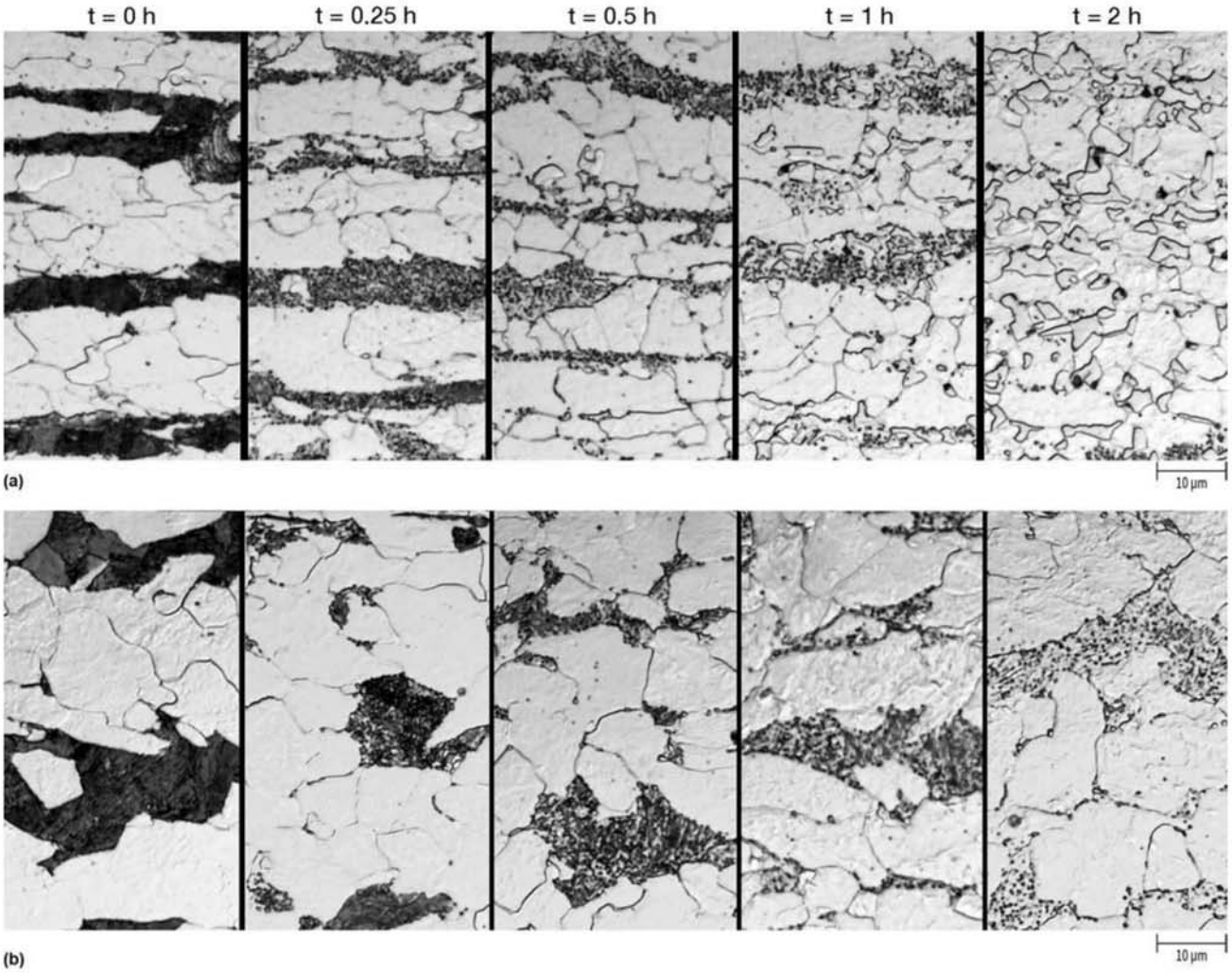

Fig. 10.2 Structural steel subjected to heat treatment at 625 °C (1155 °F) for different times. The spheroidization of the carbides with increasing holding times is evident. (a) Specified strength of 413 MPa (60 ksi), with a starting microstructure of ferrite and fine pearlite. (b) Specified strength of 290 MPa (42 ksi), with a starting microstructure of ferrite and fine pearlite. Etchant: nital 2% + picral 4%. Courtesy of the National Institute of Standards and Technology (NIST), USA. Source: Ref 4. Figure 10.2 continued next page

sels, Piping, and Boilers," in this book) a stress-relieving heat treatment may have the additional objective of producing metallurgical changes similar to tempering (see the section "Transformations on Tempering" later in this chapter). In these cases, even if it can be proved that the residual stresses in the weld are negligible or acceptable, the heat treatment cannot be skipped because the metallurgical effect is essential for the weld joint properties. Stress relieving is also used after solidification (for some types of castings) and after machining.

Some specific points require special attention in the stress relieving heat treatment:

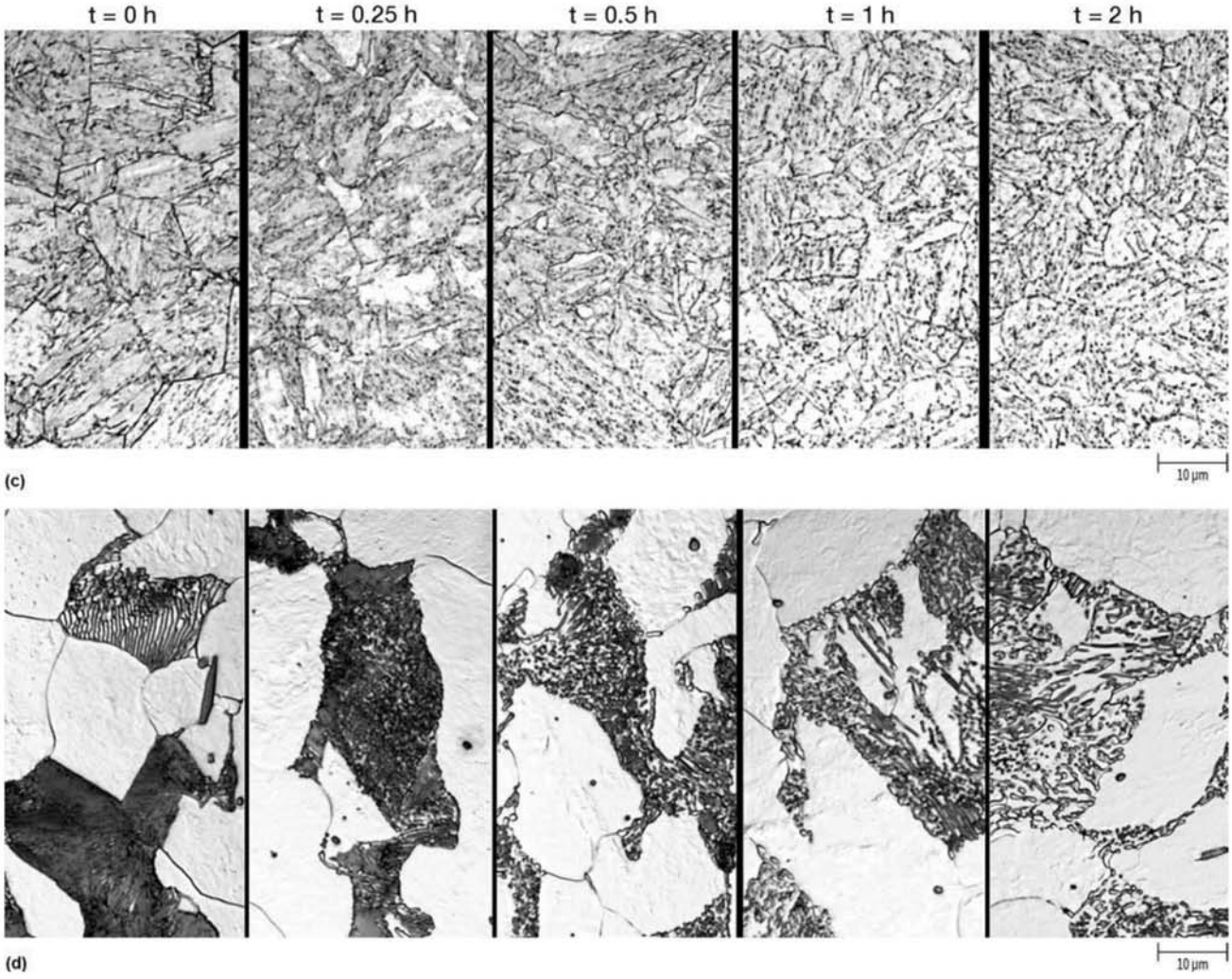

Fig. 10.2 (continued) Structural steel subjected to heat treatment at 625 °C (1155 °F) for different times. (c) Specified strength of 690 MPa (100 ksi), produced using quenching and tempering heat treatment (see the sections "Quenching and Tempering" and "Tempering" in this chapter) with a starting microstructure of tempered martensite, acicular ferrite, and carbides (cementite). The prior austenitic grain boundaries are clearly visible after etching. There is some carbide precipitation in these boundaries. The final microstructure after long heat treatments is composed of ferrite and carbides. (d) Specified strength of 290 MPa (42 ksi), with starting microstructure of ferrite and pearlite. Etchant: nital 2% + picral 4%. Courtesy of the National Institute of Standards and Technology. Source: Ref 4

- Heating, and in particular cooling after the treatment, must be performed in a slow, uniform, and controlled way to avoid introducing additional stresses. Special care is required when localized heat treat-

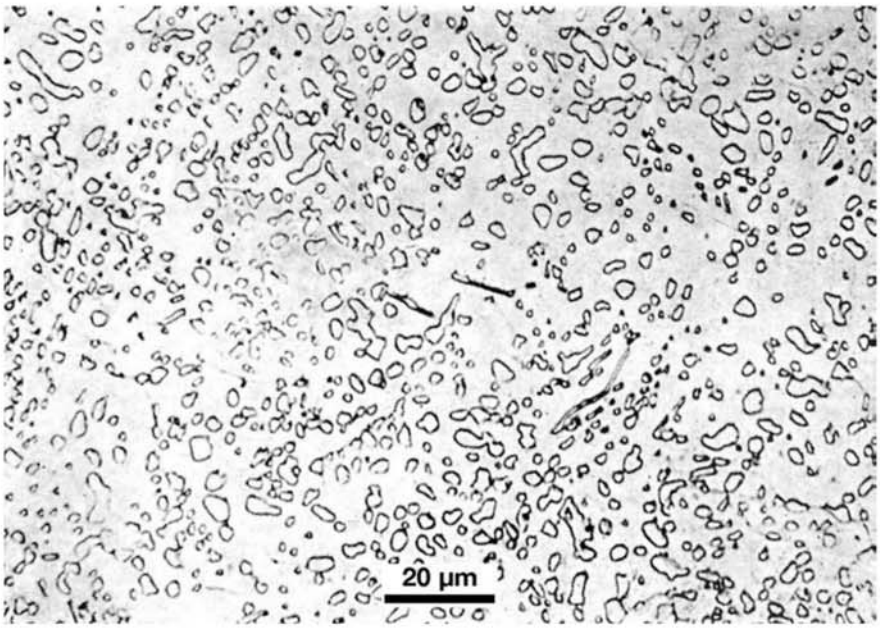

Fig. 10.3 Hyper-eutectoid steel subjected to spheroidizing annealing. Cementite in globules in a ferritic matrix. Etchant: nital.

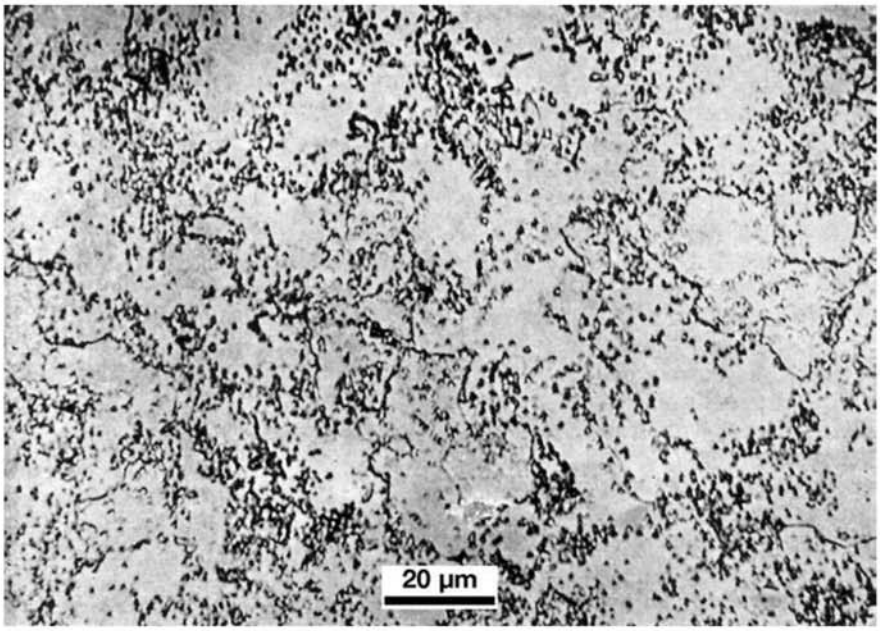

Fig. 10.4 Steel containing C = 0.5% spheroidized for 15 cycles between 650 and 750 °C (1200 and 1380 °F), in 85 min. Spheroidized cementite in small globules in a ferritic matrix. Etchant: nital.

ment is used (see Ref 5). When localized heat treatments are performed without the proper care, additional stresses or even deformation can be caused. Recommendations concerning localized heating are given in standards and in Ref 5.

Fig. 10.5 Hyper-eutectoid steel containing C = 1%, improperly annealed. Cementite is present partially in lamellae and partially in globules. Etchant: nital.

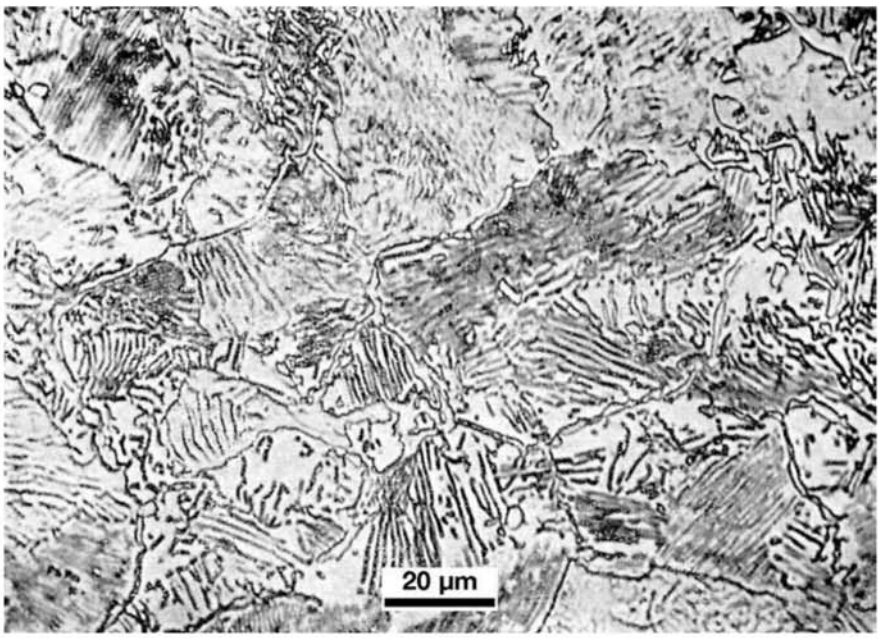

Fig. 10.6 Same steel presented in Fig. 10.5 subjected to another improper annealing cycle. Cementite in grain boundary network and coarse pearlite. Etchant: nital.

- One must keep in mind that the stress-relieving heat treatment may cause changes in the material microstructure. For instance, it can behave as an additional tempering cycle, in quenched and tempered steels, or even result in partial spheroidization if the temperature is not correctly selected. For quenched and tempered steels, it is usual to adopt, as a guarantee, that the stress-relieving treatment be at least 30 °C (55 °F) below the lowest tempering temperature to which the material has been subjected. For very important items, performing mechanical tests after simulating the stress-relieving cycle may be recommended to guarantee compliance with the specified mechanical properties.

Annealing for Hydrogen Diffusion

Hydrogen embrittles steel (Ref 6). Excessive hydrogen content in the steel may cause porosity ("bubbles") and blisters. Hydrogen may also cause the formation of cracks called flakes (Fig. 10.7). The changes in hydrogen solubility in the different phases of iron (Fig. 10.8) have a central role in the occurrence of these phenomena. Extensive studies by Troiano and colleagues in the 1950s clearly established that flakes are formed by a combination of hydrogen and stresses (caused by phase transformation, for instance), further enhanced by segregation, as shown in Fig. 10.9 and 10.10. The typical aspect of flakes on transverse macrographs, is shown in Fig. 10.9(b) and (d). The cracks in Fig. 10.9(a) have the macroscopic aspect of quench cracks.

The results of Ref 10 in Fig. 10.9 indicate that when austenite decomposition is complete at relatively high temperatures without martensite formation, there is no occurrence of flaking, even in material with a high concentration of hydrogen. This does not mean that the hydrogen has been removed from the steel. These results are summarized in Fig. 10.11. The flaking mechanism is summarized in the next paragraphs.

To investigate the effects of segregation on the formation of flakes, Scott and Troiano (Ref 11) prepared bars of AISI 4140 steel with inserts of AISI 8640 steel. The difference in composition of the two steels simulates the presence

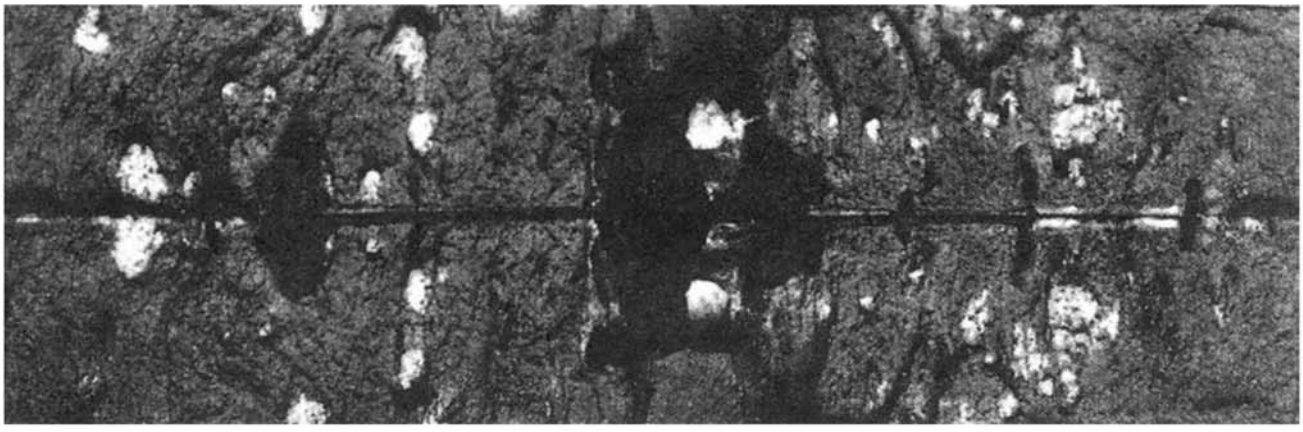

Fig. 10.7 Specimen broken according to the blue fracture technique (Ref 7) used for measurement of nonmetallic inclusions. The fracture surface presents regions that have a metallic, bright aspect that are called "flakes." These are cracks caused by hydrogen in steel. Magnification not informed. Copyright Wiley-VCH Verlag GmbH & Co. KGaA, reproduced with permission. Source: Ref 8

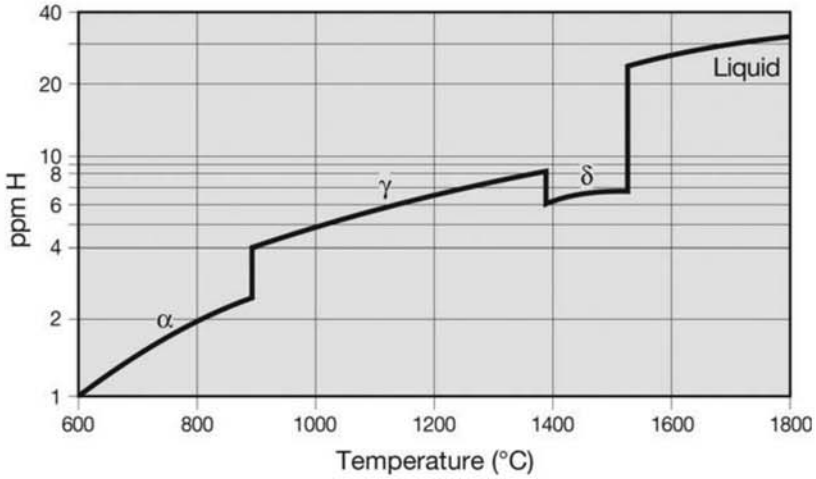

Fig. 10.8 Hydrogen solubility in iron at 1 atm as a function of temperature. Solubility in austenite is substantially higher than in ferrite. The maximum solubility happens in the liquid phase. Source: Ref 9

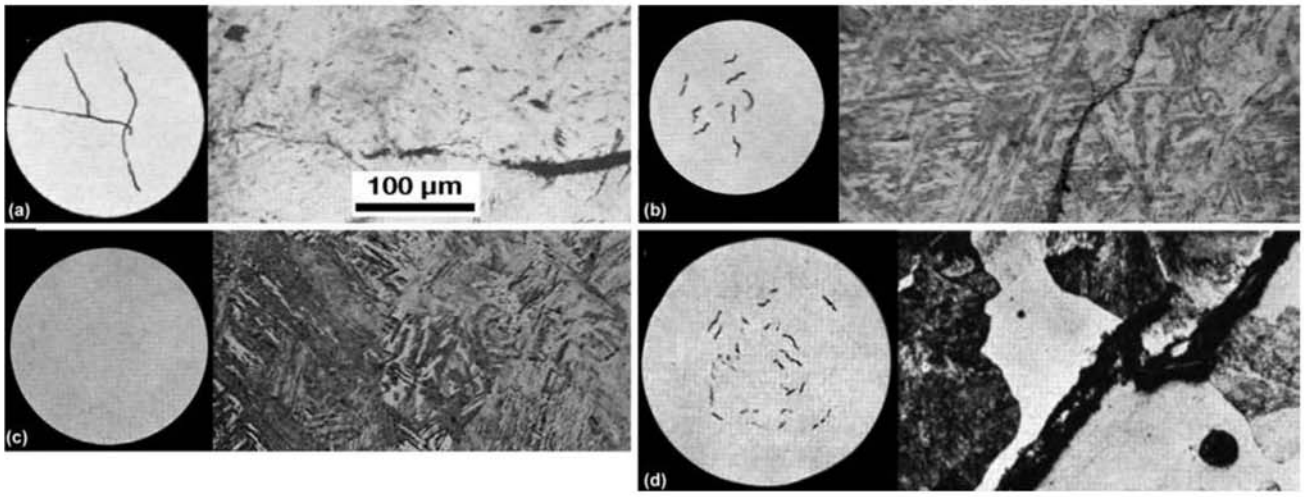

Fig. 10.9 Cylindrical bars of AISI 4340 steel. Each figure presents the macrograph (no etching) and the corresponding micrograph. (a)–(c): Bars with 25 mm (1 in.) diameter, austenitized in a hydrogen atmosphere at 1120 °C (2050 °F) and subjected to isothermal heat treatment at 338 °C (640 °F) for (a) 2 min (b) 6 min (c) 22 min, followed by rapid cooling. (d) Bar with 45 mm (1.7 in.) diameter, austenitized in a hydrogen atmosphere at 1120 °C and subjected to isothermal heat treatment at 630 °C (1165 °F), followed by rapid cooling. In (a), (b), and (d), where the bars were rapidly cooled before the end of the isothermal transformation, flakes were formed. In (c), where austenite was completely transformed before the bar was cooled, no flakes were formed. Etchant: nital 3%. Reprinted with authorization of TMS, The Minerals, Metals, & Materials Society. Source: Ref 10

of a segregated region (the insert). These bars were subjected to various isothermal heat treatments, followed by quenching, to produce different microstructure combinations in the two steels. Figure 10.12 presents the difference in the kinetics of austenite decomposition in the two steels at the temperature studies. When sufficient time was given for the bar and the insert to transform to ferrite and pearlite, flakes were not observed. In some of the treatments resulting in the formation of martensite in both steels, some

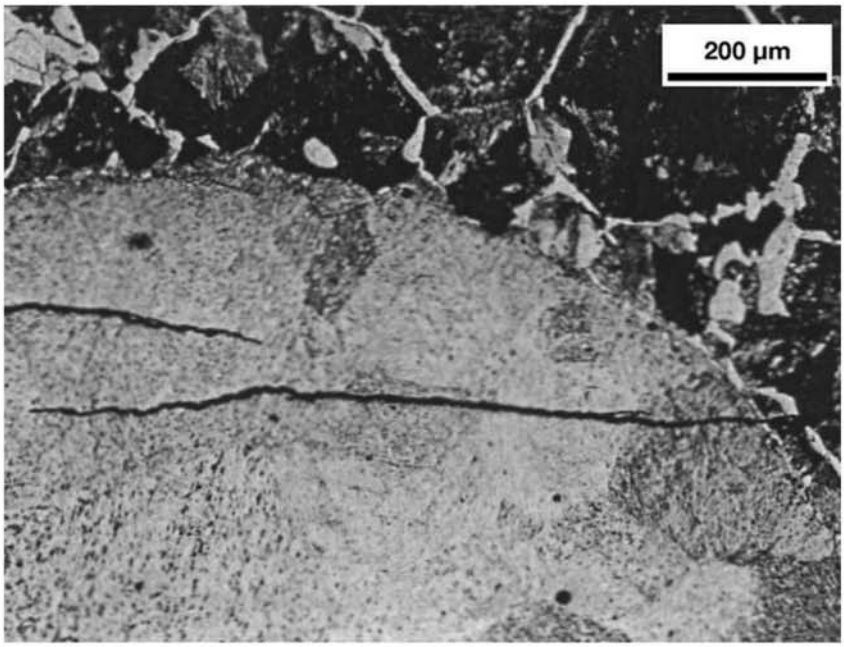

Fig. 10.10 AISI 4140 steel bar with a cylindrical insert of AISI 8640 steel subjected to austenitization in hydrogen atmosphere at 1120 °C (2050 °F) and isothermally treated at 650 °C (1200 °F). Treatment was sufficiently long to transform the steel AISI 4140 to ferrite and pearlite, followed by quenching, transforming the AISI 8640 insert into martensite. Hydrogen cracks ("flakes") can be seen in the martensitic region (Ref 11). Etchant: nital 3%. Reprinted with permission from TMS, The Minerals, Metals, & Materials Society.

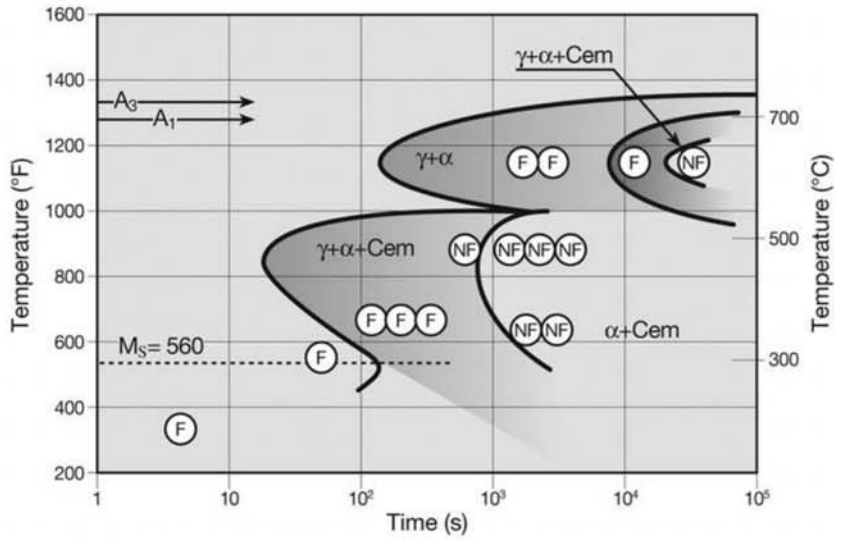

Fig. 10.11 Results of the heat treatment of samples of steel AISI 4340 charged with a high content of hydrogen, superimposed on the TTT curve. The samples have suffered isothermal heat treatment at the indicated temperatures and times, and were then quenched. "F" indicates the occurrence of flakes. "NF" indicates absence of flakes. Source: Ref 10

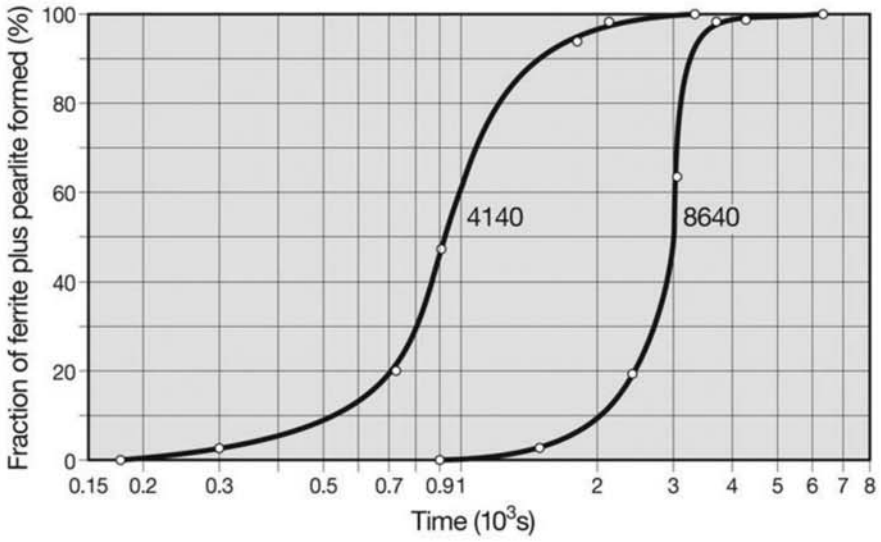

Fig. 10.12 Austenite fraction transformed in ferrite and pearlite during the isothermal treatment of steels AISI 4140 and 8640 at 650 °C (1200 °F). Source: Ref 11

cracks were observed, but without the clear aspect of flakes. The characteristic appearance of flakes has only been observed in samples in which the AISI 4140 steel ("matrix") completely transformed to ferrite and pearlite and the AISI 8640 steel ("the segregate") transformed, on quenching, to martensite (even if the percentage of martensite in the microstructure was not 100%) as shown in Fig. 10.10.

The accepted mechanism for flake formation can be summarized as follows: when the matrix (4140) transforms from austenite to ferrite and pearlite, and the simulated segregate (8640) is still fully austenitic, hydrogen diffuses to the austenite due to the large solubility difference in these phases (see Fig. 10.8). Because the 8640 region is enriched in hydrogen and subjected to stresses during quenching and martensitic transformation, it is very susceptible to cracking (flaking) due to the embrittlement effect of the hydrogen. During steelmaking, the main source of hydrogen is moisture: humidity in the air, moisture in ferro-alloys, slag-forming additives, casting pit refractories, and so on. Vacuum degassing of liquid steel is the most effective way of removing hydrogen from steel. However, some considerations must be made: introducing an extra vacuum degassing step in the steelmaking process is not always the most cost-effective measure to control the effects of hydrogen; in some cases, in particular in high nickel steels, vacuum degassing alone may not be sufficient to prevent the occurrence of hydrogen defects.

Because hydrogen diffusivity is extremely high, even in the solid state and at relatively low temperatures, high-temperature annealing treatments are not always enough to eliminate hydrogen from the steel. The most favorable combination for removing hydrogen from steel using heat treatments is high diffusivity with low solubility, conditions that can be achieved with a ferritic microstructure. Heat treatments in the austenitic range are frequently ineffective in view of the high solubility of hydrogen (Fig. 10.8) and comparatively lower diffusivity (Ref 12) in this phase. Isothermal heat treatments are effi-

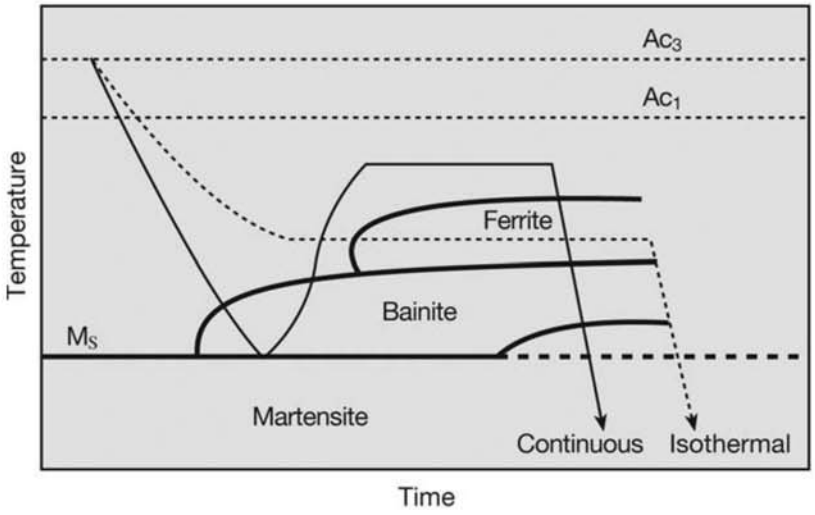

Fig. 10.13 Heat treatment cycles for preventing hydrogen cracks superimposed on a hypothetical CCT curve. The "isothermal" cycle is the most commonly used. For steels in which diffusive decomposition of austenite is too slow, the "continuous cooling" heat treatment leads to good results in shorter times. Source: Ref 13

cient and the most common. However, for high alloy steels such as Ni-Cr-Mo, forgings for generator and turbine rotors (normally the largest section forgings in production), more complex treatments are advisable. A treatment that will ensure the transformation of austenite to bainite, followed by an isothermal diffusion holding time, as shown in Fig. 10.13, is effective to further reduce hydrogen content (beyond the values of liquid steel degassing) and eliminate the risk of the incidence of flakes (Ref 13).

There are also sources of hydrogen after steelmaking: chemical processes that generate H^+ ions, such as pickling, electrolytic deposition, corrosion processes, and cathodic protection, are some processes that can introduce hydrogen in solid steel and lead to embrittlement, defects, and failure.

Annealing for Recovery and Recrystallization

After cold work, subcritical heat treatments may be advisable to recover (completely or partially) the physical and mechanical properties of the material or to cause other structural changes, as will be discussed in Chapter 12, "Mechanical Work of Steels: Cold Working," in this book.

10.2 Normalizing

Although steels subjected to controlled thermomechanical treatments usually have uniform structures at the end of the treatment (see Chapter 11, "Hot Working," in this book), conventional hot-worked steels usually have structures that are not homogeneous and may have large grain sizes. Normalizing is the indicated heat treatment to achieve a homogeneous and refined structure and improve the properties of steels subjected to conventional hot-working. Furthermore, in many cases, consistent and uniform response to heat treatments such as quenching and tempering can only be obtained with a uniform starting structure, obtained via normalizing. Normalizing can also

be used as a homogenization annealing. Thus normalizing is frequently the treatment of choice for:

- Microstructural homogenization of casting and forgings, particularly large parts. Normalizing is also frequently used as a first homogenization before any other heat treatment, such as quenching and tempering.
- Microstructural homogenization of parts subjected to incorrect or faulted heat treatments, in particular before repeating quenching treatments.
- Achieving homogeneous and "fine" microstructure aiming at final properties, in particular when good balance between strength and toughness are needed in conventional structural steels, and when the use of a quenching and tempering treatment is not economical. (This may occur not only due to the cost of the heat treatment but also, in the case of large parts produced in large quantities, where the cost of alloying to achieve hardenability (see the section 10.3.1 "Steels for Quenching and Tempering" in this chapter) and form martensite, may be excessive.

The normalizing thermal cycle involves heating for the complete transformation in austenite, followed by air cooling, as indicated in Fig. 10.14. Two features of this treatment must be kept in mind:

- Some steels, particularly those that have high hardenability (see the section "Hardenability" in this chapter) as do some tool steels, cannot (or should not) be normalized, if the result of this treatment is the formation of martensite and,

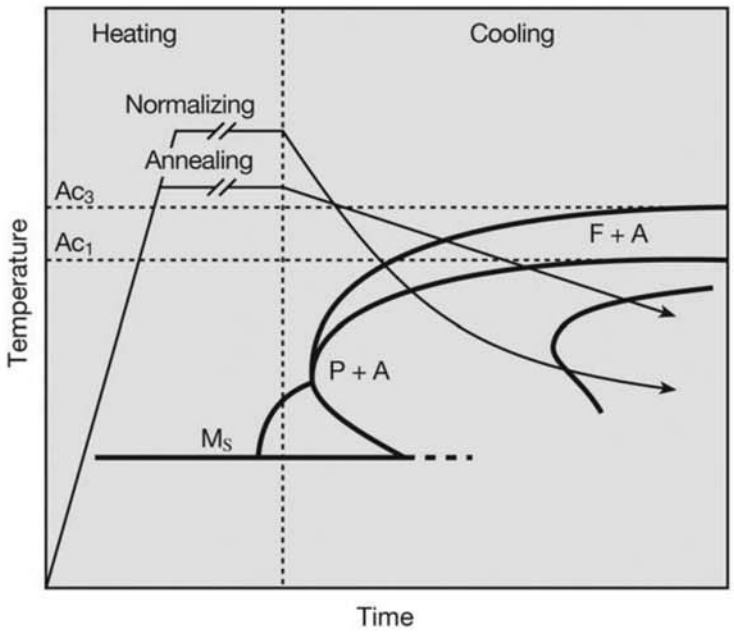

Fig. 10.14 Schematic presentation of the heat treatment cycles for annealing (full) and normalizing, superimposed on a CCT curve of a hypothetical steel. A = austenite, P = pearlite, F = ferrite.

- The microstructure resulting from normalizing is sensitive to part dimensions, because once the cooling medium is fixed, the part's geometrical characteristics will define the cooling rate. Some examples of the microstructures of normalized AISI 1005 to 1015 steels are presented in Chapter 7, "Equilibrium Phases and Constituents in the Fe-C System." Figures 10.15 to 10.19 present other examples of microstructures produced by normalizing heat treatment. Successive normalizing cycles may have a favorable effect on the austenitic grain size. Figure

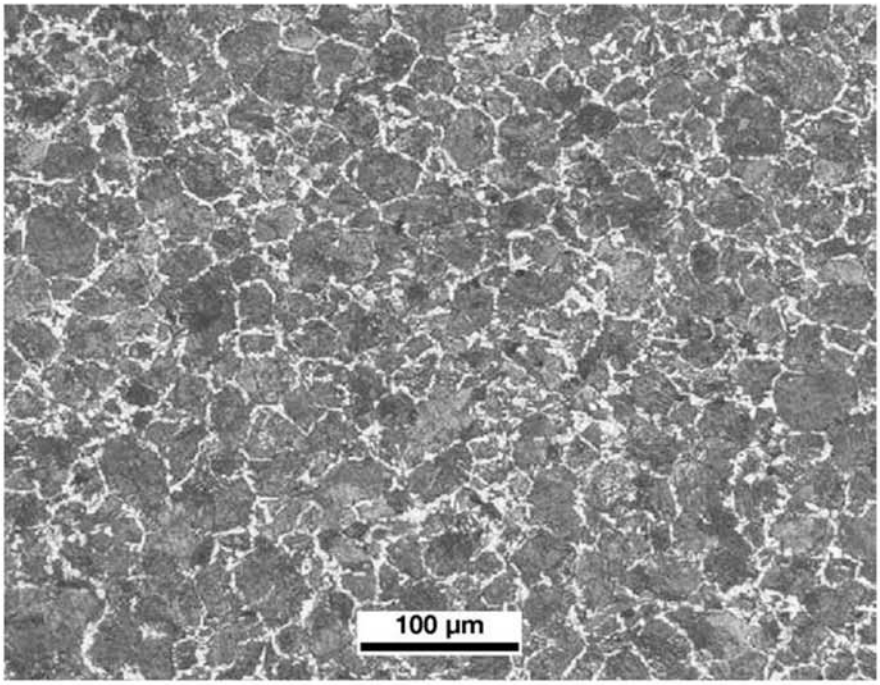

Fig. 10.15 AISI 1045 wire rod normalized. Pro-eutectoid ferrite and pearlite. Etchant: nital 2%. Courtesy of ArcelorMittal Aços Longos, Juiz de Fora, MG, Brazil.

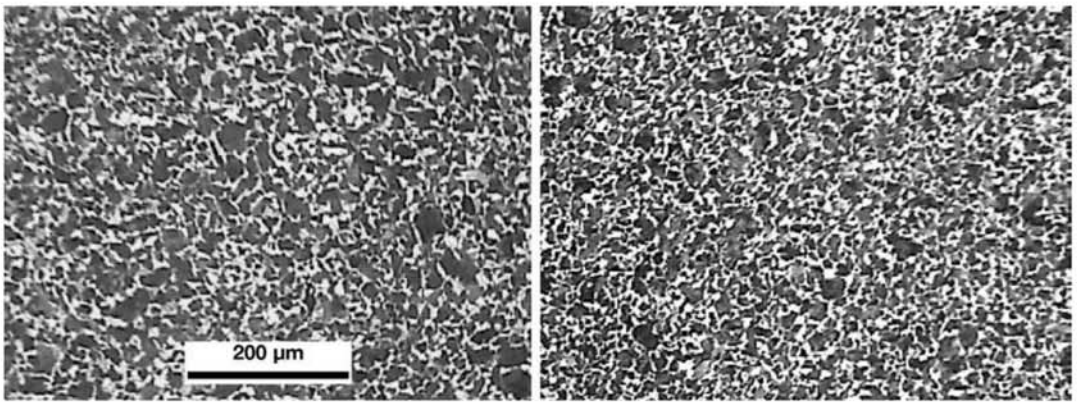

Fig. 10.16 AISI 1045 forging, normalized. Pro-eutectoid ferrite and pearlite. Etchant: nital 2%. Courtesy of Villares Metals S.A., Sumaré, SP, Brazil.

10.20 presents results from Ref 14, where a series of normalizing cycles were performed on a low alloy steel used for tubes. The results shown in Fig. 10.21 indicate that the austenitic grain size measured after each normalizing heat treatment decreased.

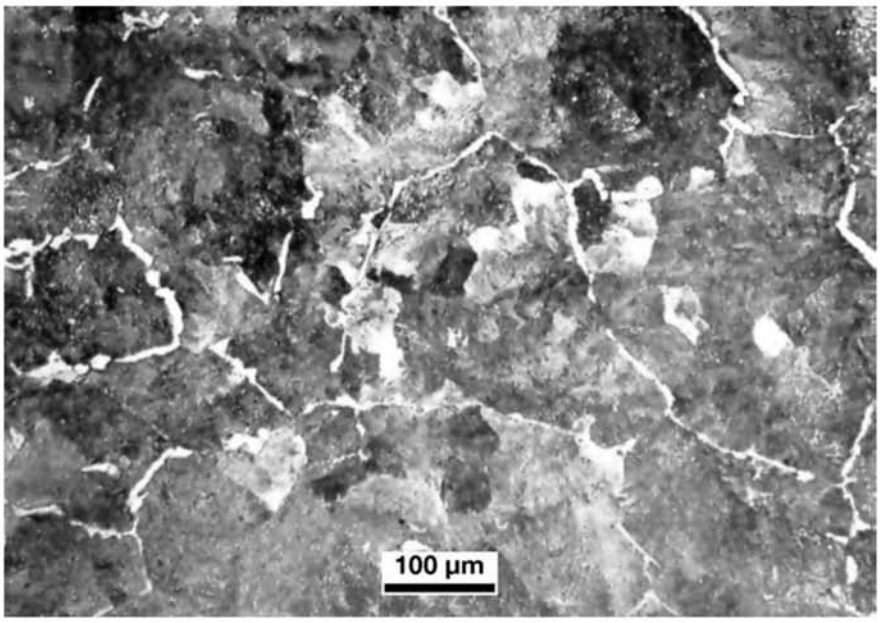

Fig. 10.17 Steel containing C = 0.45% and Mn = 0.77% normalized. Pro-eutectoid ferrite in a network at the prior-austenitic grain boundaries and fine pearlite. Etchant: nital.

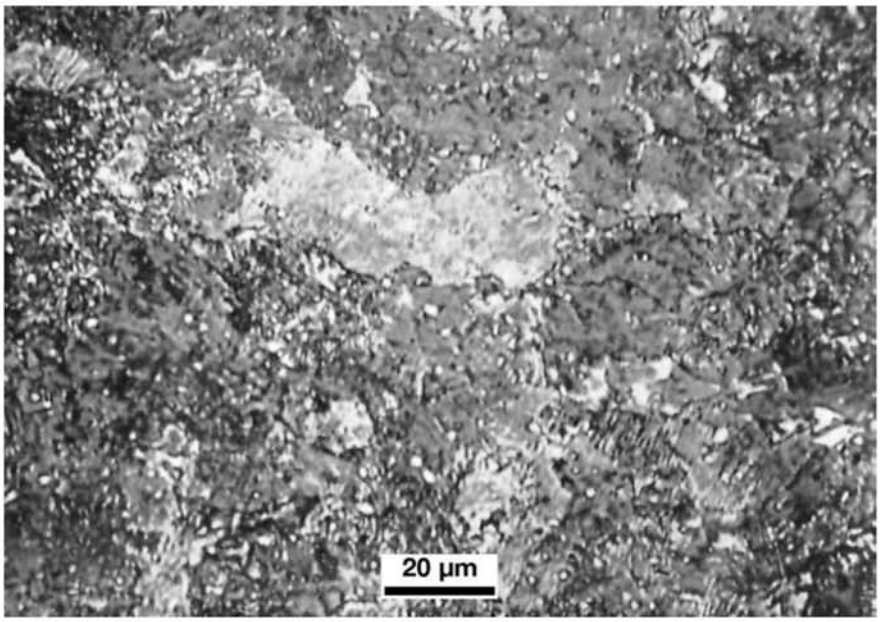

Fig. 10.18 Hyper-eutectoid steel spheroidized and normalized. Cementite globules in a ferritic matrix. The austenitizing cycle in the normalizing treatment was not sufficient to completely dissolve the globular cementite. Etchant: nital.

10.2.1 Deviations During Heating for Heat Treatment and Hot Working

The conditions required for the formation of homogeneous austenite with uniform grain size are discussed in the section "Austenite and the Measurement of the Austenitic Grain Size," in Chapter 9, "Conventional

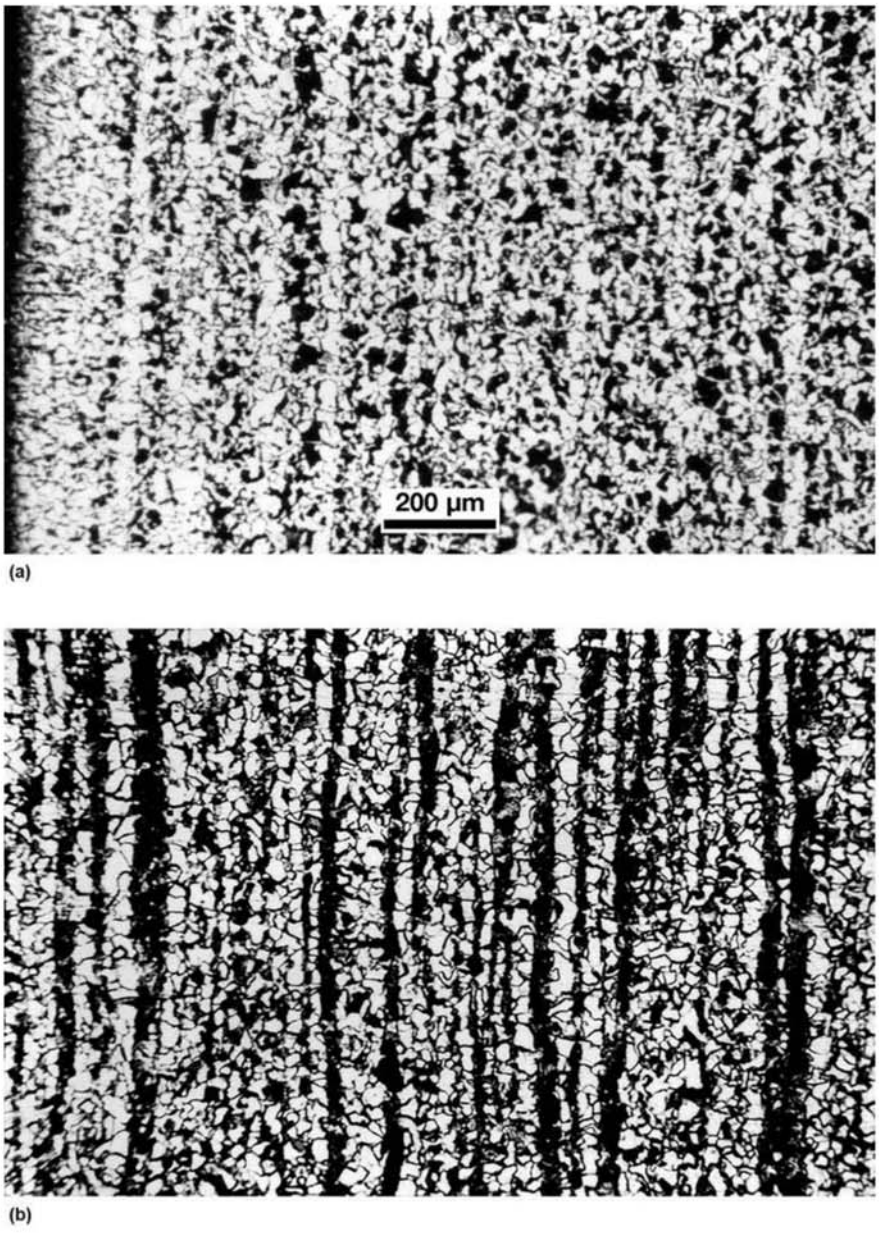

Fig. 10.19 Longitudinal cross section of a thick plate of structural steel WStE355 (C = 0.19%, Mn = 1.2%) 38 mm (1.5 in.) thick, normalized. In this figure, the longitudinal direction of the plate is along the vertical direction. (a) Surface region of the plate (on the left side, slight decarburization can be observed). Ferrite and pearlite. (b) Midthickness of the plate. Ferrite and pearlite. Banding is present (see Chapter 11, "Hot Working," in this book). Etchant: nital.

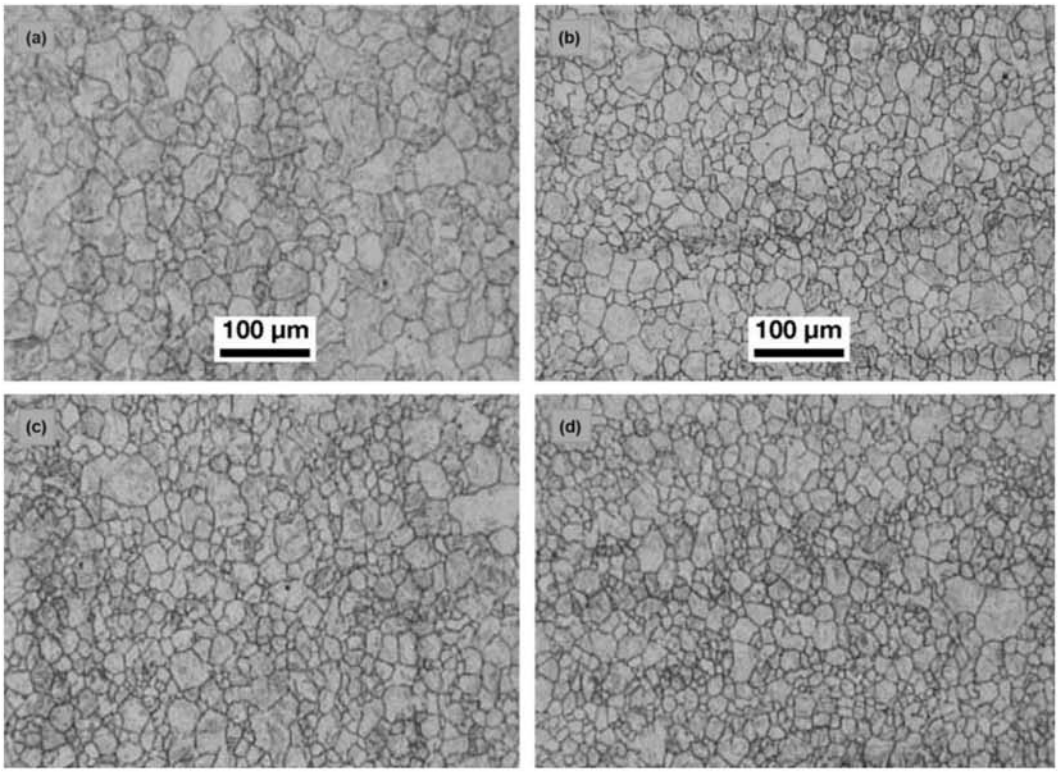

Fig. 10.20 Samples of a tube with 117.8 mm (4.6 in.) diameter and 12.7 mm thickness (½ in. nominal) containing C = 0.29%, Mn = 0.86%, Si = 0.27%, Cr = 0.94%, Mo = 0.40%, Al = 0.025%, N = 0.005% after normalizing at 900 °C (1650 °F) for 5 min holding time. The samples have been etched to reveal the prior austenitic grain boundaries. (a) Single normalizing cycle. (b) Two normalizing cycles. (c) Three normalizing cycles. (d) Four normalizing cycles. Etchant: picric acid. Courtesy of A.L.L. Figueiredo, V&M Tubes do Brasil. Source: Ref 14

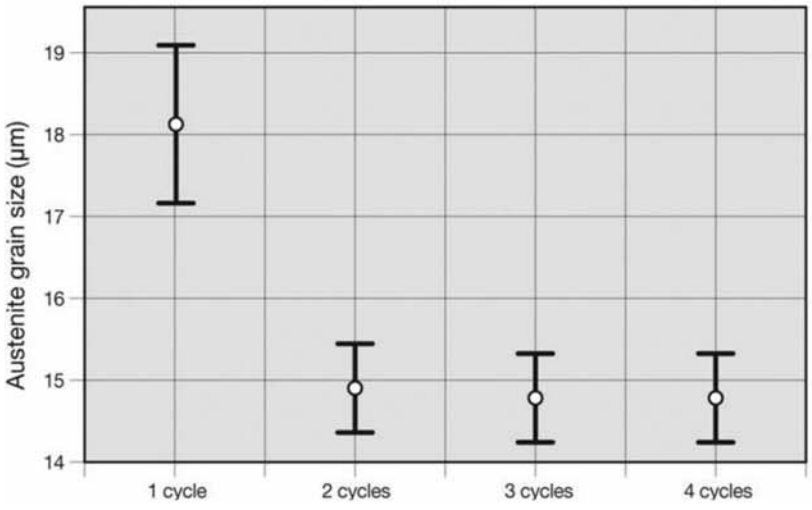

Fig. 10.21 Austenitic grain size as a function of the number of normalizing cycles for the steel in Fig. 10.20. Average of approximately 500 measurements per sample. 95% confidence intervals for the average are plotted. Source: Ref 14

Heat Treatments: Usual Constituents and Their Formation." The important points related to a heat treatment involving heating to form austenite were also discussed previously, when full annealing was presented (see the earlier section 10.1.2 "Important Points During the Annealing Thermal Cycle"). Often, when planning a heat treatment cycle, great emphasis is placed on achieving homogenization. In addition, in the heating for hot working, one may want to use higher starting temperatures so that all envisaged hot working operations can be performed without the need for more heating, with an increase in processing time and costs. However, excessive heating can lead to important deviations, some of which can cause irrecoverable structural changes. The two most important deviations are overheating and burning. "Burning" (resulting in "burnt" or "burned" microstructures) is discussed in Chapter 11, "Hot Working." Conversely, insufficient heating, in normalizing and annealing may result in inadequate microstructures (see the sections "Insufficient Heating (Resulting in Intercritical Treatment)" and 10.3.4 "Deviations During Heating and Austenitizing" in this chapter).

Overheating

When a part is heated to overly high temperatures, excessive austenitic grain growth may happen. The resulting microstructure frequently fulfils the specified requirements for strength (and hardness) but does not reach adequate values of ductility (measured by elongation and reduction or area in tensile test, for instance) or toughness (Fig. 10.22 to 10.26).

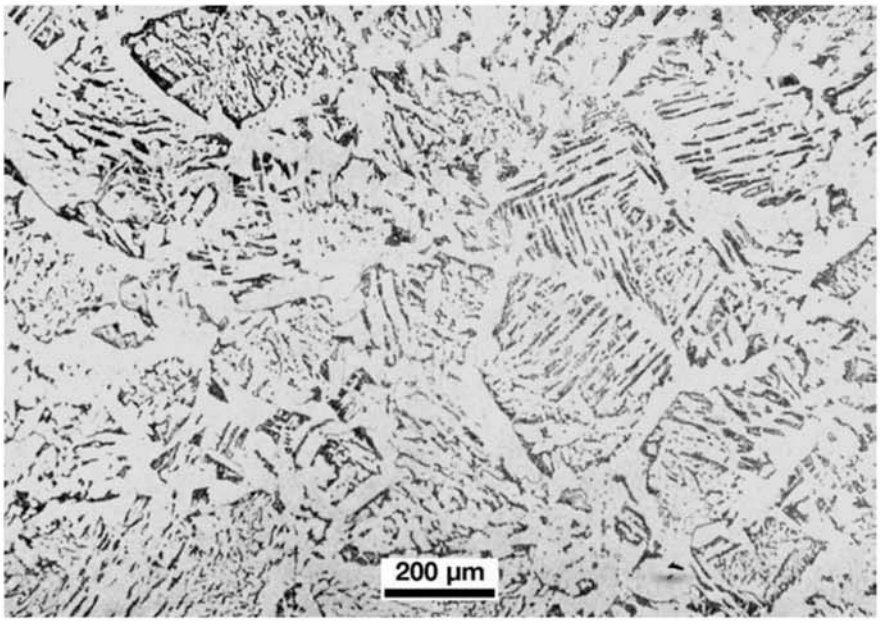

Fig. 10.22 Low carbon steel overheated in the austenitic single-phase field. Ferrite in an incomplete network and acicular ferrite. The incomplete ferrite network makes it possible to estimate the austenitic grain size prior to cooling (≅ 290 µm). This indicates the possibility of overheating. Etchant: nital.

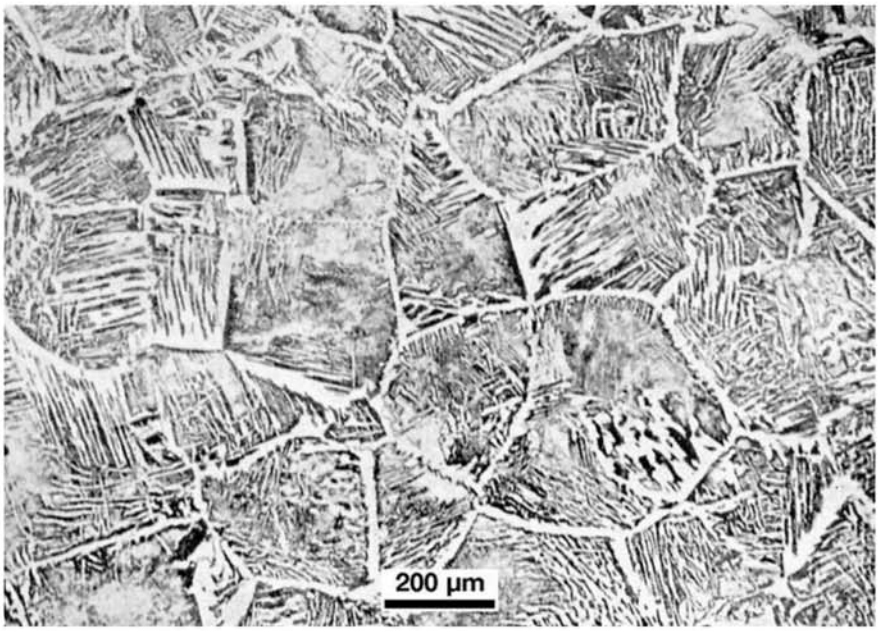

Fig. 10.23 Steel containing C = 0.24%, overheated in the austenitic single-phase field. Ferrite in network and acicular ferrite. The ferrite network makes it possible to estimate the grain size prior to cooling (≅ 340 µm). This indicates the possibility of overheating. Etchant: nital.

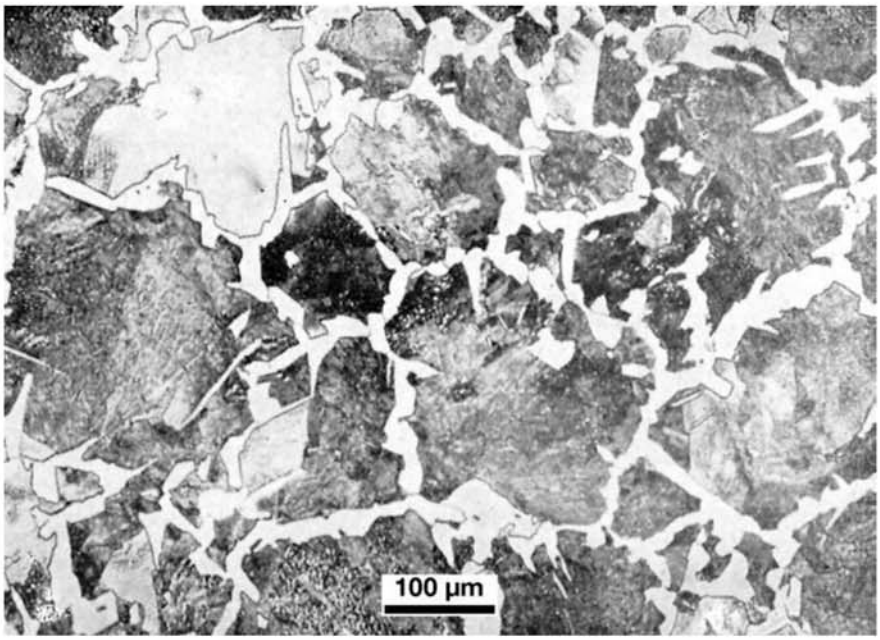

Fig. 10.24 Steel containing C = 0.5%, overheated in the austenitic single-phase field. Ferrite in network and acicular ferrite, fine pearlite. The ferrite network makes it possible to estimate the grain size prior to cooling (≅ 200 µm). This indicates the possibility of overheating.

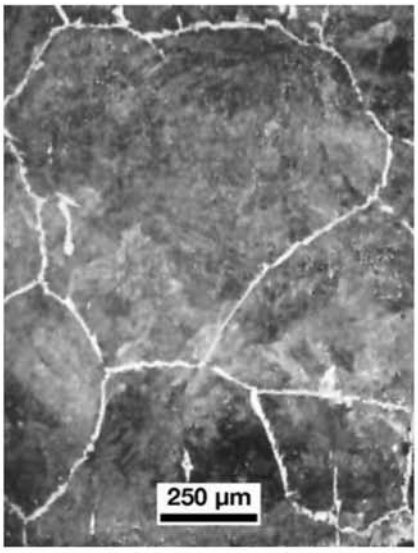

Fig. 10.25 Steel containing C = 0.53% overheated in the austenitic single-phase field. Pro-eutectoid ferrite network and fine pearlite colonies. Etchant: nital.

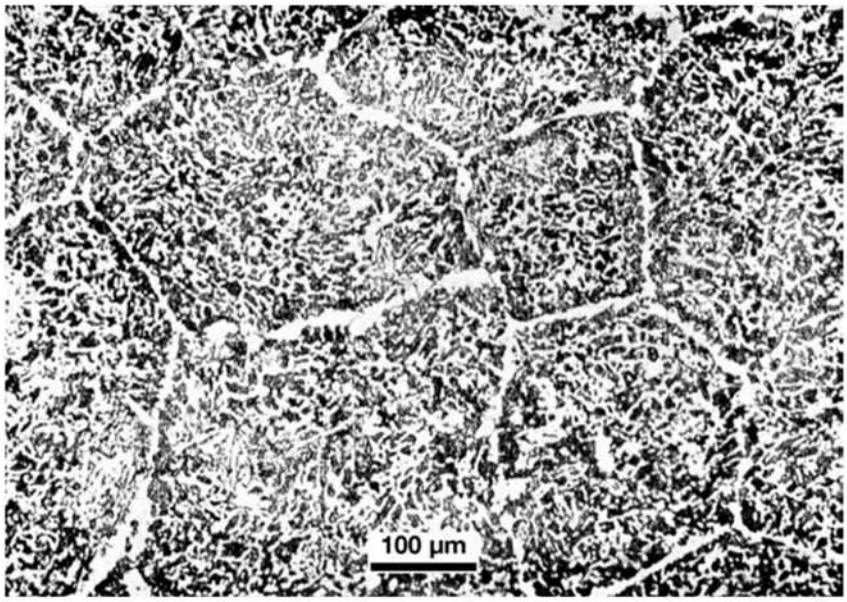

Fig. 10.26 Medium carbon steel, with a microstructure originally similar to the one in Fig. 10.23 (overheated). The steel has been subjected to a new austenitization for normalizing, in the intercritical region (temperature was too low for complete austenitization). The pro-eutectoid in the previous austenitic grain boundaries did not dissolve. Austenite began forming in the pearlite areas (see Chapter 9, "Conventional Heat Treatments: Usual Constituents and Their Formation," in this book) as expected but transformation was not complete. The regions that did transform to austenite in this intercritical treatment transformed on cooling to ferrite and pearlite, which are finer than that initially present in the overheated material.

Insufficient Heating (Resulting in Intercritical Treatment)

(Also see the section "Deviations During Heating and Austenitizing" in this chapter). While intercritical heat treatments are becoming more important for some families of structural steels (such as *dual-phase s*teels and TRIP steels, see Chapter 13, "Advanced Steels for Forming Operations," in this book), austenitizing inside the intercritical temperature range in conventional heat treatments may result in inadequate microstructures (Fig. 10.27).

Decarburization

At the temperatures in which austenite forms, carbon is highly mobile in steels. Unless special care is taken, most heat treatment atmospheres will cause decarburization of steel. To avoid this, the best solution in industrial heat treatments is either the use of atmospheres in which the chemical potential of carbon is adjusted to be in equilibrium with the steel or the use of salt baths. When salt baths are used, the part is immersed in a molten salt bath held at the desired austenitizing temperature (see Ref 3, for instance). Alternative measures are protecting the part surface with special paints or

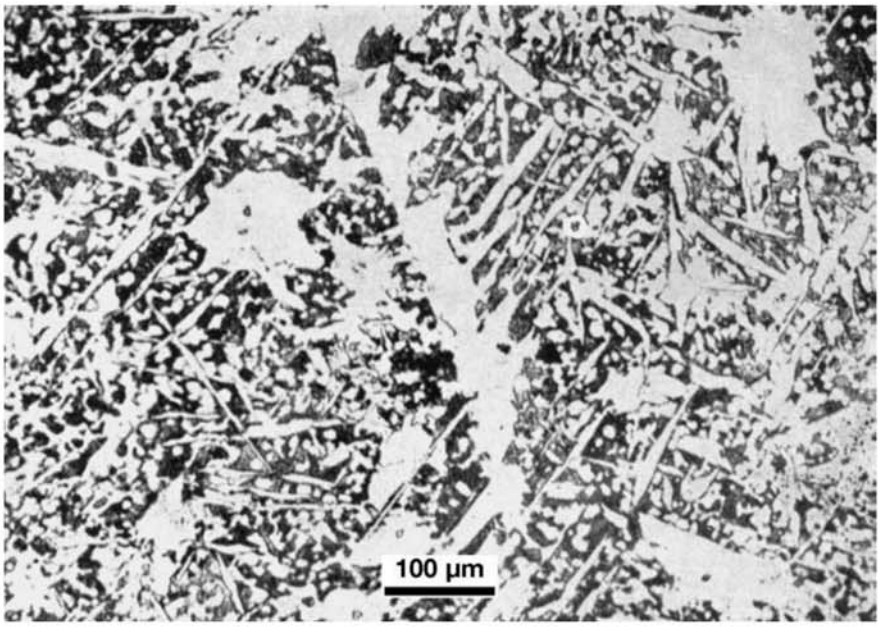

Fig. 10.27 Cast medium carbon steel annealed in the intercritical region (temperature was too low for complete austenitization). Pearlite areas transformed to austenite, but pro-eutectoid allotriomorphic and acicular ferrite regions did not. The region where austenite did form has transformed to fine ferrite grains and small pearlite colonies. Etchant: nital.

other adequate coatings or the use of solid packing materials. Decarburization is especially important in parts subjected to high surface stresses, and when fatigue is a consideration. SAE J419 standard (Ref 15), for instance, defines typical decarburization profiles and defines a methodology for the measurement of the decarburized layer in steel parts. Figure 10.28 presents examples of two usual decarburization profiles in wire rods. Figure 10.29 presents decarburization at the surface of a thick plate of structural steel hot rolled and normalized. In this case, decarburization is not important for product performance. Figures 10.29 to 10.32 show examples of decarburization. In some cases, a slightly oxidizing atmosphere may be beneficial for treatment of semi-finished products, if oxidation can be slightly faster than decarburization, and the decarburized layer may disappear as part of the oxide scale.

When evaluating part failures, particularly when cracks are observed, the presence of decarburization around the crack or fracture is an indication that it was present in the part when the material was exposed to high temperatures, possibly during hot working or annealing, normalizing, or quenching heat treatments, as shown in Fig. 10.33 and 10.34.

10.3 Quenching and Tempering

10.3.1 Steels for Quenching and Tempering (or "Engineering" Steels)

The microstructure that usually leads to the best combination of strength and toughness in steels is tempered martensite. In general this microstructure cannot be consistently achieved in as-cast or wrought steels (as forged

or as rolled) or after annealing or normalizing. It is necessary to use quenching and tempering heat treatments. Furthermore, parts that can be produced in the normalized condition can be redesigned to be lighter (due to the increased strength) if quenched and tempered steels are used.

Although structural steels are normally supplied to meet mechanical property requirements (frequently including toughness), and some chemical composition restrictions to ensure weldability, "engineering" steels are usually supplied to meet a specified chemical composition. The reason is that these steels do not receive their final heat treatment at the steelmaking plant. Usually they are heat treated to meet properties after machining (and sometimes forging) at the part manufacturer. The main goal when chemical composition of these steels is specified is hardenability, which is discussed in more detail in the section 10.3.3 "Hardenability" later in this chapter. This is the most important property when selecting engineering steels for quenching and tempering. It is important not to confuse hardenability with maximum hardness after quenching, which is essentially a function of the steel carbon content

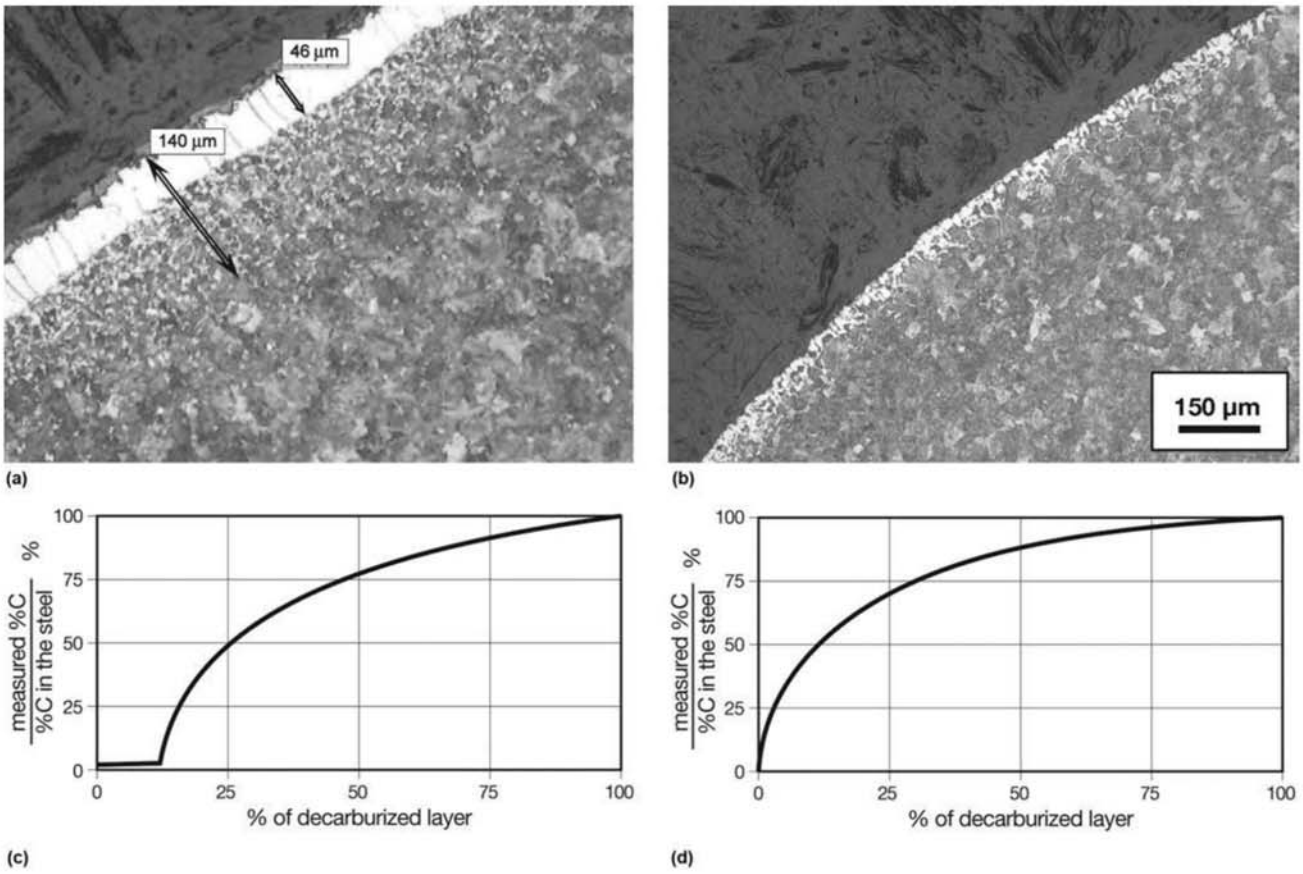

Fig. 10.28 Some examples of decarburized wire rod (cross sections). (a) Type 1 decarburization profile (schematically presented in c). (b) Type 2 decarburization profile (schematically presented in d). Inside the material, the microstructure is mostly composed of pearlite. In the decarburized region, the volume fraction of ferrite increases. In the case of the type 1 profile (a), there is a region of pure ferrite with coarse, columnar, grains. A layer of oxide (gray) can be seen between the ferrite and the polymer used to mount the sample (darker region). Decarburization classified according to SAE J419 standard. Etchant: nital. Source: Ref 15

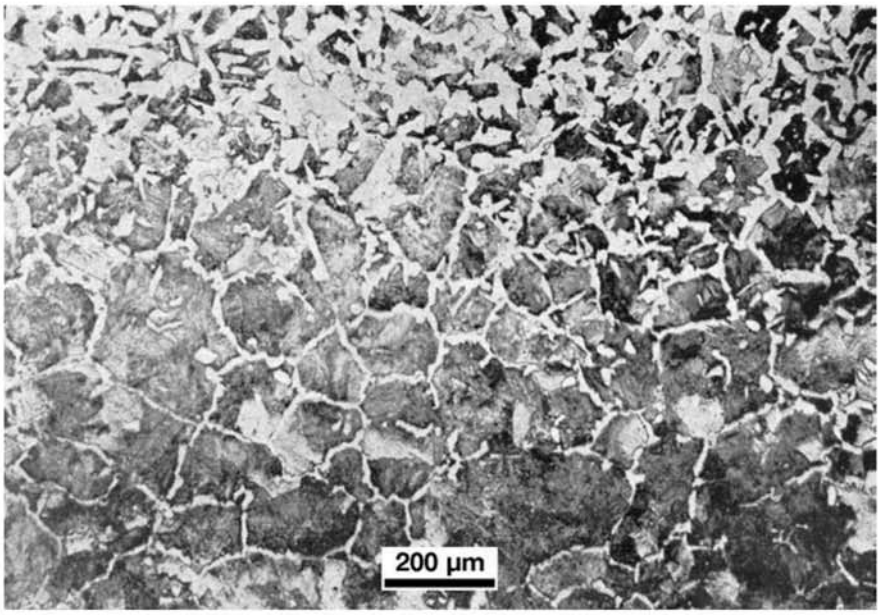

Fig. 10.29 Detailed view of a decarburized zone with profile type 2 according to SAE J419 standard (Ref 15) in a normalized medium carbon steel. The pearlite volume fraction decreases as the distance to the part surface increases (top of the image). Etchant: nital.

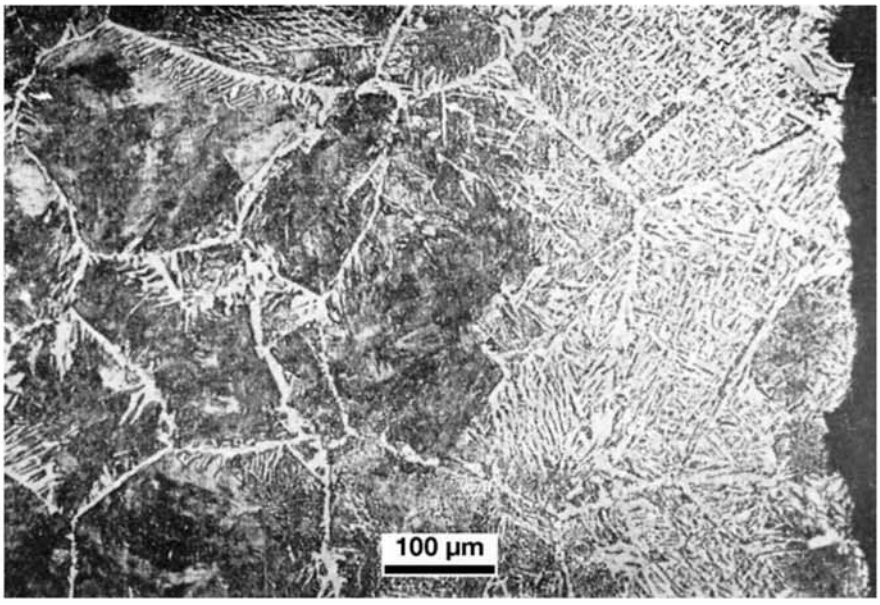

Fig. 10.30 Microstructure close to the surface of a medium carbon steel overheated. Ferrite delineating the prior austenite grain boundaries, acicular ferrite, and pearlite. Superficial decarburization is also present. The surface region is rich in acicular ferrite. Etchant: nital.

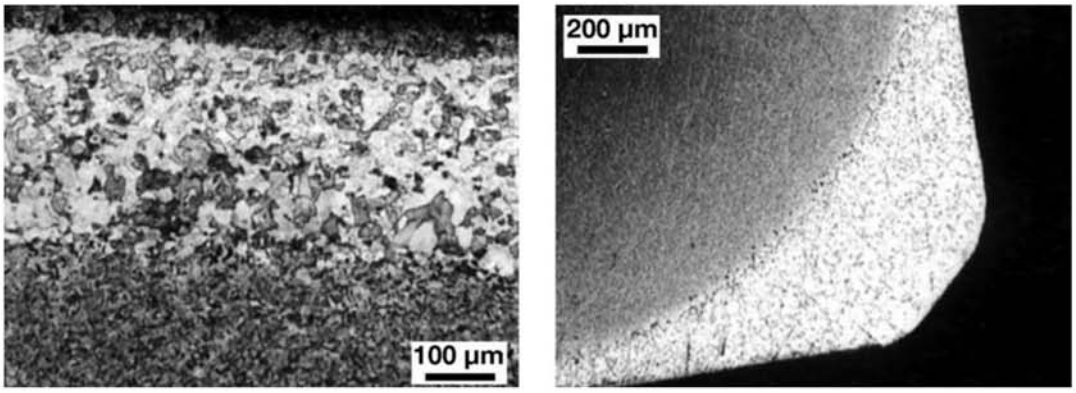

Fig. 10.31 AISI 4340 steel heated in an oxidizing atmosphere at 850 °C (1560 °F). Severe surface decarburization. Etchant: nital. Courtesy of Villares Metals S.A., Sumaré, SP, Brazil.

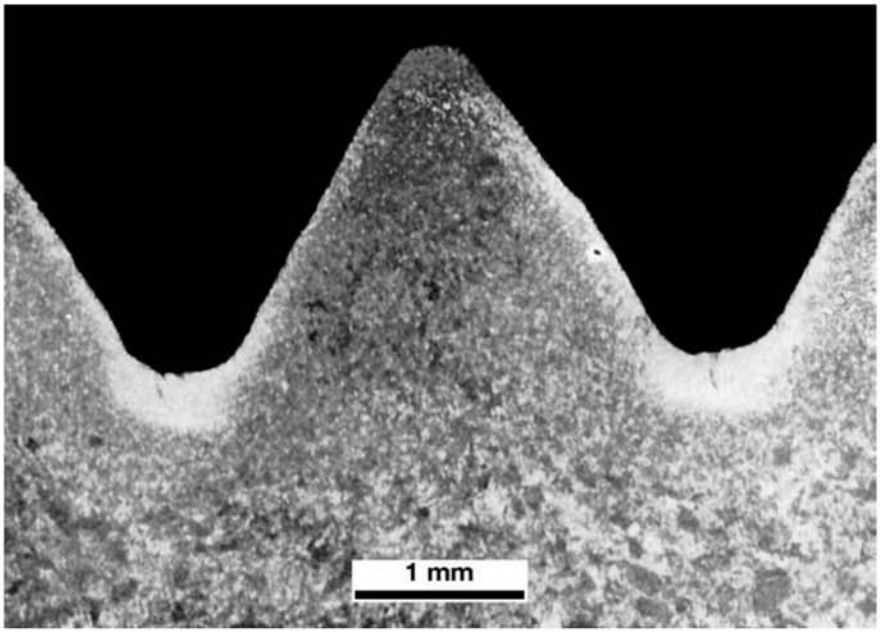

Fig. 10.32 Longitudinal section of a high strength bolt heat treated after the threading process. (See also Chapter 12, "Mechanical Work of Steels: Cold Working," in this book). Intense decarburization and cracks at the roots of the thread. Etchant: nital.

(see Chapter 9, "Conventional Heat Treatments—Usual Constituents and Their Formation," Fig. 9.9) and of the volume fraction of martensite in the microstructure (Fig. 10.35).

Frequently when designing, quenched and tempered hardness is used as an indirect indicator of mechanical strength, as indicated in Fig. 10.36, or using the following approximate empirical relationships:

$$\text{UTS (MPa)} = 3.55 \times \text{HB} \quad \text{HB} \leq 175$$

$$\text{UTS (MPa)} = 3.38 \times \text{HB} \quad \text{HB} > 175$$

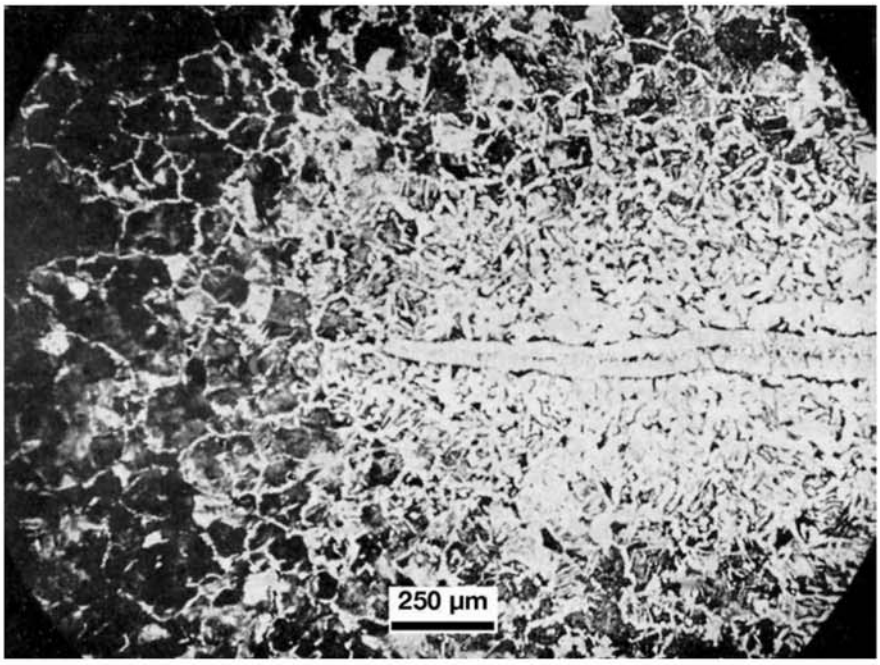

Fig. 10.33 Cross section of a defect close to the surface of a steel part. The defect may be a pore or a gas bubble that was open to the part surface, making possible the severe decarburization of this region. The defect is partially closed, probably due to further hot working. In these cases, it is normal to find a large incidence of oxide particles inside the defect. Etchant: aqua regia.

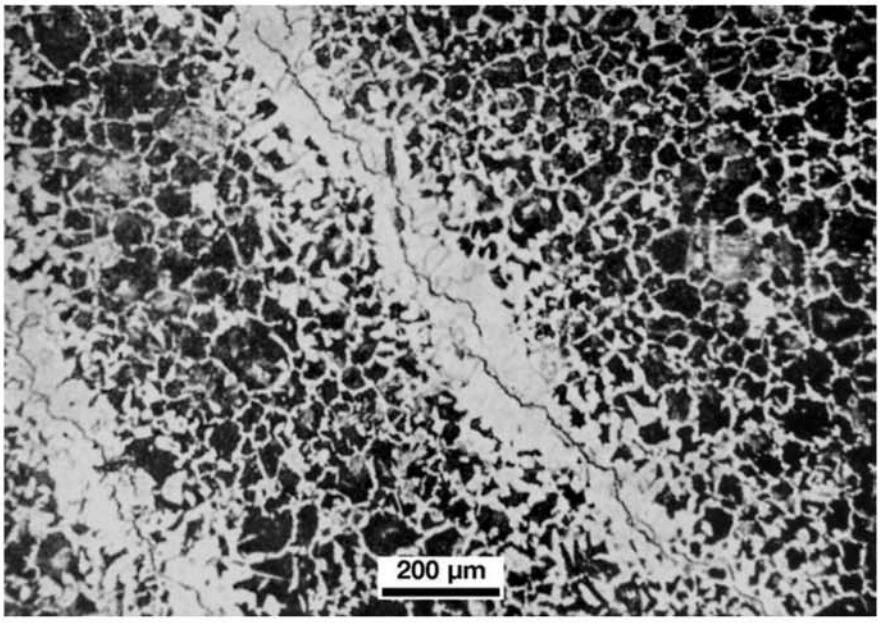

Fig. 10.34 Cracks showing decarburized edges. The crack shape suggests these can be quench cracks from a previous heat treatment (see the section 10.3.5 "Quench Cracks" in this chapter). Decarburization happened during an annealing or normalizing heat treatment that resulted in the observed ferrite and pearlite microstructure. Etchant: aqua regia.

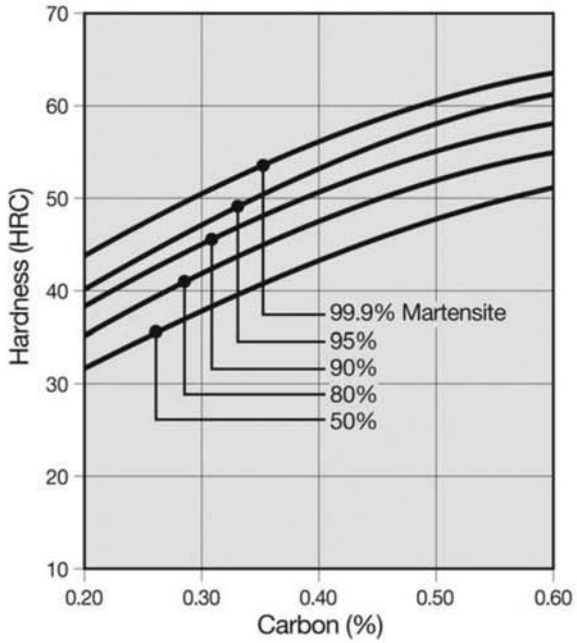

Fig. 10.35 Hardness reached by steels after quenching as a function of their carbon content and the percentage of martensite in the microstructure. Martensite hardness depends only on carbon content. Source: Ref 16

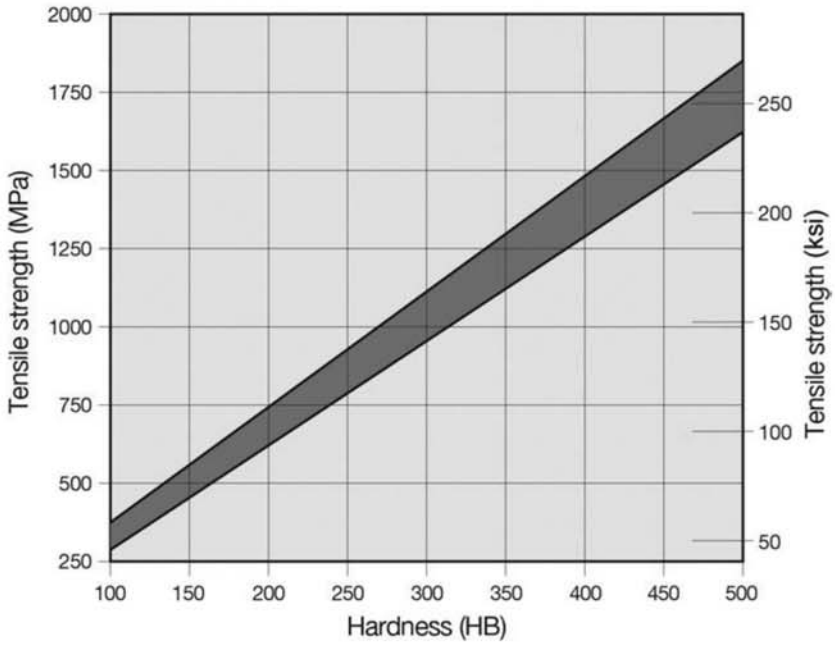

Fig. 10.36 Approximate relationship between ultimate tensile strength and hardness (HB) for steels in the quenched and tempered, normalized, and "as hot-worked" condition.

where HB is the Brinell hardness measured with a 10 mm (0.4 in.) diameter sphere and a load of 3000 kgf. Hardness is only required as a design property when wear is an important issue in the part design. In this case, steels that are able to transform to 100% martensite at the surface and with the highest possible hardness should be selected.

AISI Classification System for "Engineering Steels"

The classification system created by the American Iron and Steel Institute (AISI) and Society of Automotive Engineers (SAE, SAE J404) has been basically the same since the 1940s. In this system, the steels are divided into groups according to their general chemical composition and, within these groups, into families with similar features. The grades are indicated, in general, by a set of usually four digits. This is illustrated by:

YY	XX
Steel family	Carbon content in hundredths of a percent (0.01%)

Thus, a 4340 steel, for instance, belongs to the 43 family with 1.8% Ni, 0.8% Cr, and 0.25% Mo nominal contents and 40 hundredths of a percent of carbon, that is, 0.40%. Besides the numbers, letters can be used to designate special aspects in the classification. An "H" after the digits indicates that the hardenability of the steel is guaranteed according to a given specification, whereas a "B" between the digits representing the steel family and the carbon content means that the steel has a deliberate addition of boron to increase hardenability. Thus, an 8620H steel has a more consistent response to the quenching and tempering treatment than does an 8620 steel. Its hardness response will be more reproducible and in the upper region of the usual range for an 8620 steel. A 10B46 steel is essentially a 1046 steel (carbon steel with 0.46% nominal carbon content) to which an addition of boron of at least 5 ppm is made to improve hardenability (see Table 10.1).

10.3.2 Quenching

Heat treatment nomenclature varies around the world. In some countries, the heat treatment used to promote the formation of martensite has a specific name (*Vergütung*, in German, encompasses quenching and tempering to form martensite), independent of the cooling rate. In English, accelerated cooling is called quenching. According to ASTM A941, quenching is the "rapid cooling in a fluid at a rate sufficient to preserve or produce desired material characteristics." The standard also proposes the use of "quench hardening" to designate the operation of "hardening a steel object by austenitizing it, and then cooling it rapidly enough that some or all of the austenite transforms to martensite" which is closer to the terminology adopted in other countries.

Quench hardening thus consists of:

- Heating the part to a temperature that is sufficient to produce an austenitic microstructure; guidelines for this temperature and that of other heat treatment of these steels are given in Figure 10.37

- Holding the part at this temperature for the correct time
- Cooling the part in a fluid medium that will cause a cooling rate sufficient to result in the formation of martensite

The depth of hardening and the distribution of hardness through the part cross section after quenching will depend on the steel hardenability, on the size and shape of the part, the austenitizing temperature and time, and the quench medium.

Table 10.1 Main steel families according to AISI and SAE classification

Carbon steels	10xx	Carbon steels
	11xx	Carbon steels (resulfurized) "free machining"
	12xx	Carbon steels (resulfurized and (rephosphorized) "free machining"
Low alloy steels (engineering steels)	13xx	Mn 1.75%
	23xx	Ni 3.5%
	25xx	Ni 5.0%
	31xx	Ni 1.25%, Cr 0.65%
	33xx	Ni 3.50%, Cr 1.55%
	40xx	Mo 0.25%
	41xx	Cr 0.50% or 0.95%, Mo 1.12% or 0.20%
	43xx	Ni 1.80%, Cr 0.50% or 0.80%, Mo 0.25%
	46xx	Ni 1.55% or 1.80%, Mo 0.20% or 0.25%
	47xx	Ni 1.05%, Cr 0.45%, Mo 0.20%
	48xx	Ni 3.50%, Mo 0.25%
	50xx	Cr 0.80% or 0.40%
	51xx	Cr 0.80% to 1.05%
	5xxxx	Cr 0.50% or 1.00% or 1.45%, C 1.00%
	61xx	Cr 0.80% or 0.95%, V 0.10% or 0.15% minimum
	86xx	Ni 0.55%, Cr 0.50% or 0.65%, Mo 0.20%
	87xx	Ni 0.55%, Cr 0.50%, Mo 0.25%
	92xx	Mn 0.85%, Si 2.00%
	93xx	Ni 3.25%, Cr 1.20%, Mo 0.12%
	98xx	Ni 1.00%, Cr 0.80%, Mo 0.25%

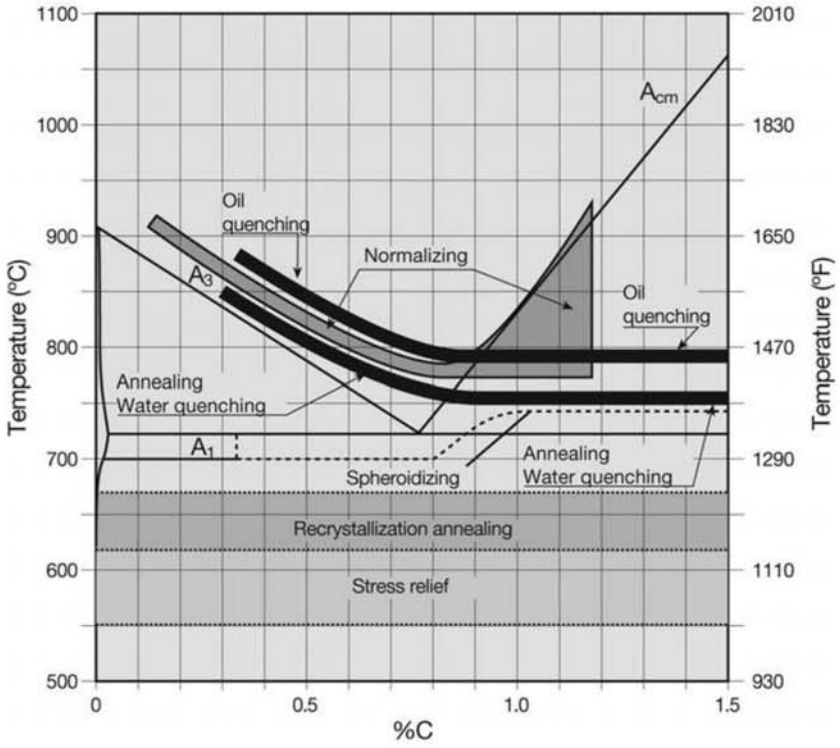

Fig. 10.37 Recommended temperature ranges for the heat treatment of carbon steels, superimposed on the Fe-C metastable equilibrium diagram. Source: Ref 17

10.3.3 Hardenability

Hardenability is the feature of a steel that defines the variation of hardness from the surface to the center of a part when it is quenched, or as defined in ASTM A941 (Ref 2), the property that determines the depth and distribution of hardness induced by quenching a steel object. This property is associated with the ability of a steel to form martensite and thus to the critical quenching rate (see Chapter 9, "Conventional Heat Treatments: Usual Constituents and Their Formation"). The austenitic grain size before quenching and the homogeneity of austenite at this stage influence the steel hardenability.

Although carbon has a strong effect on martensite hardness besides affecting hardenability, most alloying elements added to steel delay diffusional decomposition of austenite, increasing its hardenability. Thus, the critical cooling rate for martensite formation is lower for steel with a greater content of alloying elements, as shown in the example of Fig. 10.38 and the scheme presented in Fig. 10.39. Cobalt is frequently considered an exception among the alloying elements, as it reduces hardenability (Ref 20).

When a part is quenched, two factors influence the rate at which different positions of the part will cool.

- The rate at which heat is extracted from the part surface, which is a function of the quenching medium used
- Heat transfer, by conduction, inside the part

The combination of these factors causes different positions inside a part to cool with different rates, as indicated in Fig. 10.40. When the cooling curves are superimposed on the steel CCT diagrams, it is possible to determine the expected microstructures in the part after quenching, as shown in Fig. 10.41. During materials selection, however, the problem is the inverse: it involves defining which steel, quenched in which medium, will reach a predetermined microstructure (and thus properties) at a given position in the part that is to be produced. To solve this problem, efficient methods of microstructure prediction for quenched steels were developed around the middle of the 20th

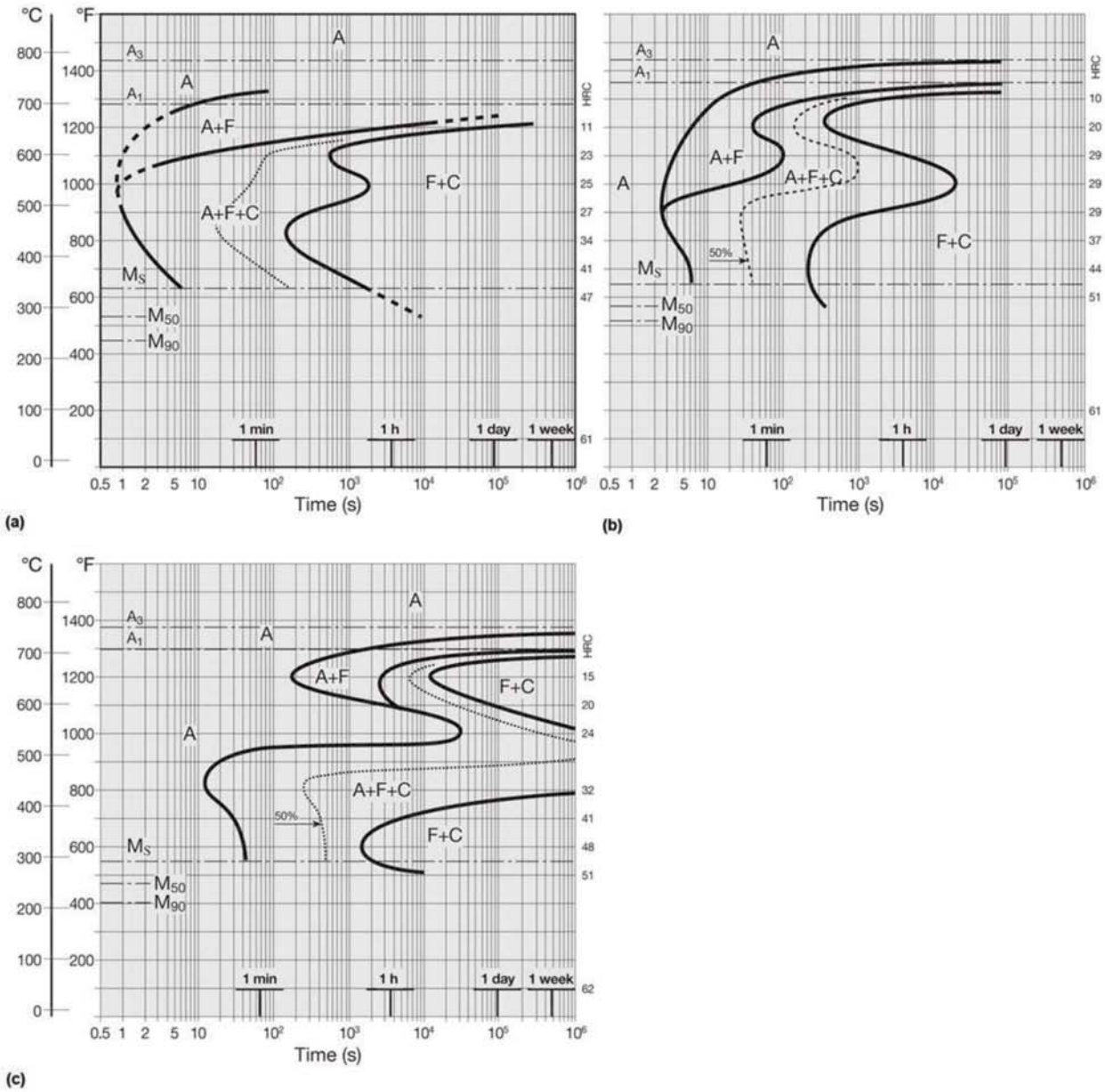

Fig. 10.38 TTT diagrams for three steels containing approximately (a) C = 0.4% and Mn = 1%. In (b) also Cr = 1%, Mo = 0.2%, and in (c) also Cr = 0.8%, Mo = 0.3%, and Ni = 1.8%. Increasing the content of alloying elements will generally displace the curves for ferrite and bainite formation toward longer times and will lower the M_s temperature. A = austenite, P = pearlite, F = ferrite. Source: Ref 18

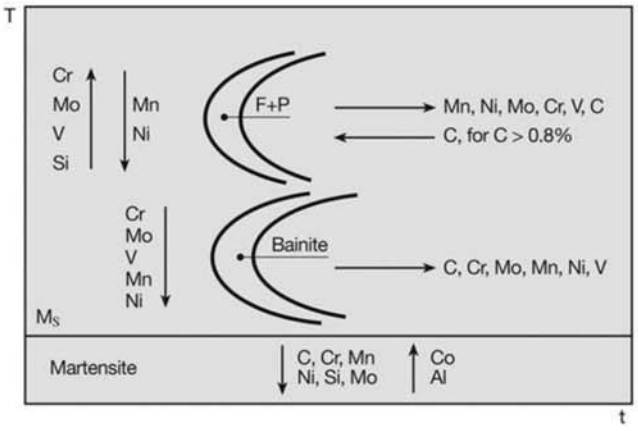

Fig. 10.39 Schematic presentation of the effect of various solute elements in steel on the position of the curves representing the main phase transformations on a TTT diagram. Although this scheme presents commonly observed trends, one is cautioned against generalization about the effects of alloying elements in view of the complexity of the phenomena involved. F = ferrite, P = pearlite. Source: Ref 19

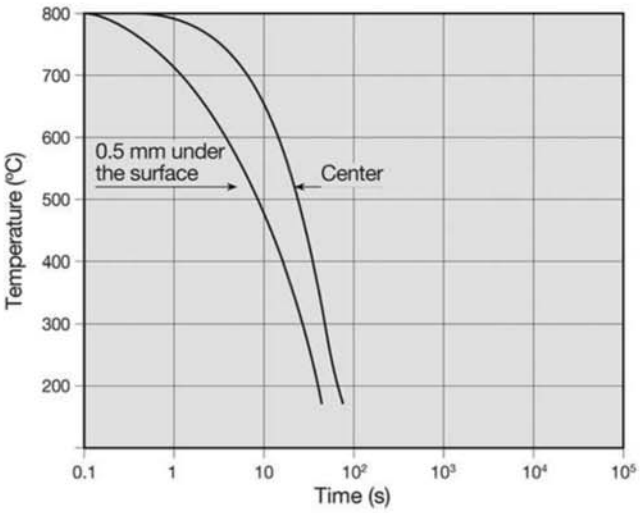

Fig. 10.40 Cooling curves for the surface and for the center of a cylindrical steel bar with diameter of 28 mm (1.1 in.) cooled in water.

century. In the latter decades of the 20th century, efficient mathematical models were developed to perform this prediction (e.g., Ref 21).

Two important methods have been established to measure and quantify steel hardenability: the Jominy method (Ref 22) and the Grossmann critical diameter method (Ref 20). The Jominy method is simpler and more widely used.

The Critical Diameter

The Grossmann method involves quenching bars of increasing diameter to determine the diameter at which 50% volume fraction of martensite is formed at the center of the bar. This is called the "critical diameter." This evaluation can be performed either by metallography or through hardness measurements. Although the hardness for structures containing 50% martensite can be obtained from data such as that presented in Fig. 10.35, it is common to adopt the value of 50 HRC as the threshold to define the critical diameter. For this method, it is normal to present the hardenability measurements in graphs in which several curves, such as the ones shown in Fig. 10.42(a), are superimposed on a single graph, called "U" curves, as shown in Fig. 10.43. Because the quenching medium is a defining variable in the result, the Grossmann method makes it possible to consider the effect of the quenching medium via a factor "H" called "quench severity." The way the quench severity in a given medium is determined according to the Grossmann method is described in detail in Ref 23.

Macrographic examination can supply an indication of hardening depth as shown in Fig. 10.44. However, the limits of the "hardened region" determined using macrographic technique, micrographic examination, or hardness measurements seldom coincide.

Quenching Media and Quench Severity

Table 10.2 presents the H factor determined for different quench media, adopting water quenching as a reference (H = 1). Higher quench severity corresponds to faster cooling. One must keep in mind that the potential for cracking and distortion on quenching also increases with the increase of quench severity. As a general guideline for the selection of quenching medium, one should consider that water can be used for parts with simple and symmetrical geometry, in which some distortion can be tolerated (for instance, when final machining is performed after the heat treatment). Less dramatic quenching media will promote shallower temperature gradients in the parts and should be preferred when the prevention of distortion and cracking are important. In general, the trend to the formation of quench cracks will depend on the M_s temperature and of the carbon equivalent (C_{eq}) (see the section 10.3.5 "Quench Cracks" in this chapter) of the steel selected.

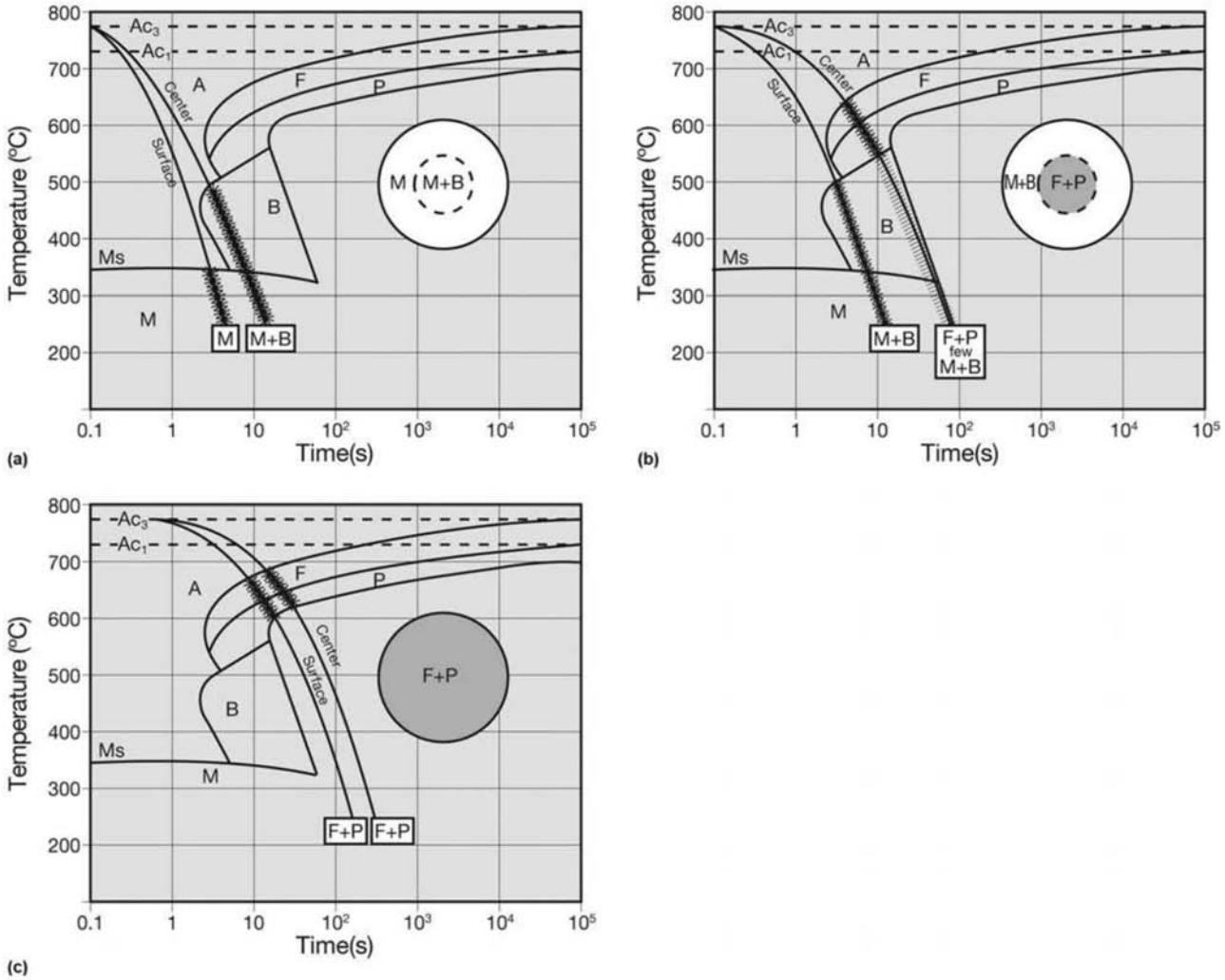

Fig. 10.41 Different cooling conditions applied to a bar of a given steel will result in different microstructure distributions along the bar cross section, depending on the steel hardenability, the bar dimensions, and on the quenching medium selected. A = austenite, F = ferrite, B = bainite, M = martensite.

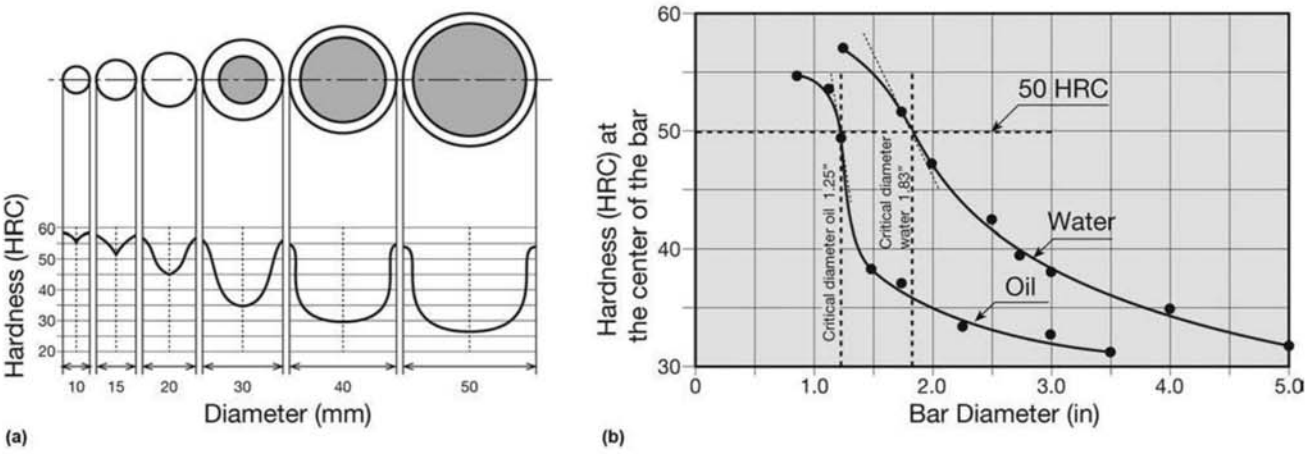

Fig. 10.42 Determination of the critical diameter according to Grossmann. (a) Bars with different diameters are quenched and the hardness profile is measured along the bar diameter. (b) The results of hardness measurements on the center of the bars may be presented in a single plot where the critical Grossmann diameter can be determined for a given quenching medium. The example in the figure shows results for AISI 3140 steel. Source: Ref 23 and 20

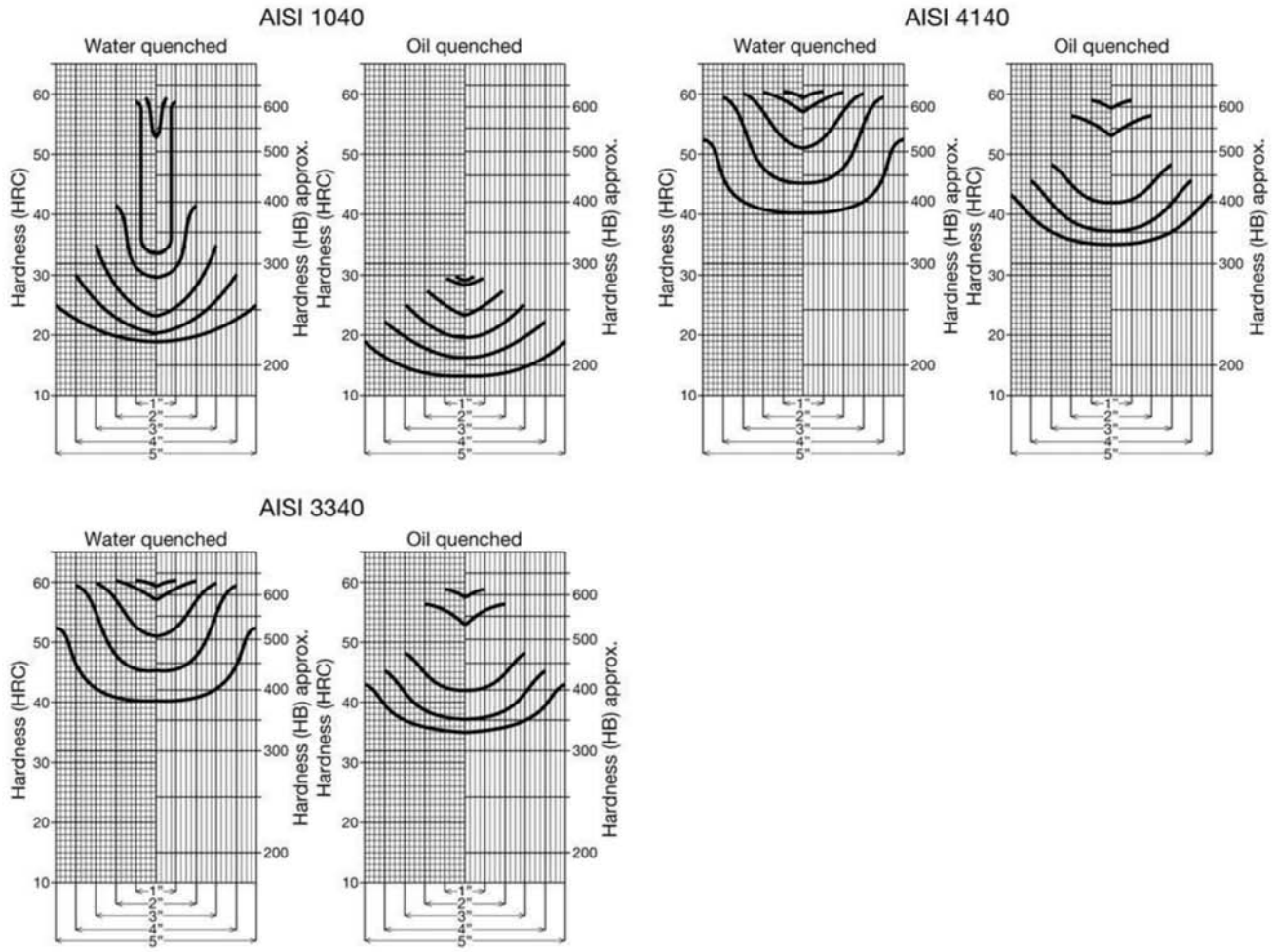

Fig. 10.43 Hardness along bar diameter for bars of three different steels containing C = 0.4% (see Table 10.1 for the rest of the relevant chemical composition). Bars quenched in oil and quenched in water. The effect of the alloying elements on hardenability is evident. The bar diameters are indicated in the horizontal axis (1 to 5 in., or 25 to 125 mm).

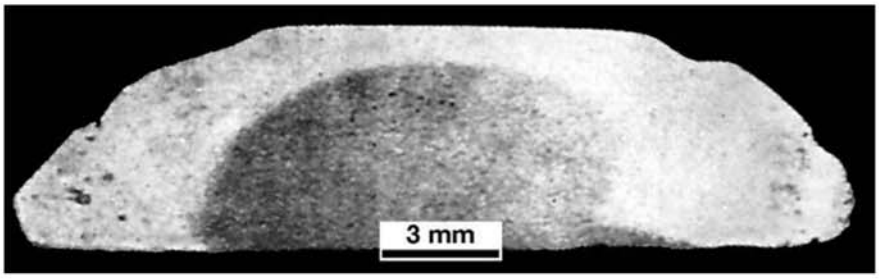

Fig. 10.44 Cross section of a hand file. The white, external region corresponds to the area that transformed to martensite on quenching. The gray central area corresponds to the region where the cooling rate was not sufficiently high to form 100% martensite. Etchant: nital.

Table 10.2 Quenching severity for different quenchants compared to water

Quenching medium	Severity of quench (H)	
Oil, no agitation	0.2	
Oil, moderate agitation	0.5	
Oil, vigorous agitation	0.7	
Still water	1.0	↓ Increasing: Cooling rate, Possibility of cracks, Possibility of distortion
Water, vigorous agitation	1.5	
Brine, no agitation	2.0	
Brine, vigorous agitation	5.0	

Cooling in a liquid medium is not a simple process and has been the subject of extensive studies aimed at improving the quenching processes. Figure 10.45 presents the main phenomena that occur during water quenching and their effects on the part cooling rate. The first stage happens when a continuous layer of steam is formed over the part, significantly hindering heat extraction and thus the cooling rate. Thus it is common to use surface-active additions to the water to reduce the extent of this stage by enhancing breakage of the steam film by the liquid. This first stage happens exactly in the range of temperatures at which a high cooling rate would be beneficial to the quenching efficiency. At somewhat lower temperatures, heat extraction is controlled by the formation and separation of isolated steam bubbles on the part surface. In this stage, the cooling rate of water is at its maximum. This maximum rate happens below the temperature range where diffusional transformations are faster. Thus, it contributes mostly to the creation of re-

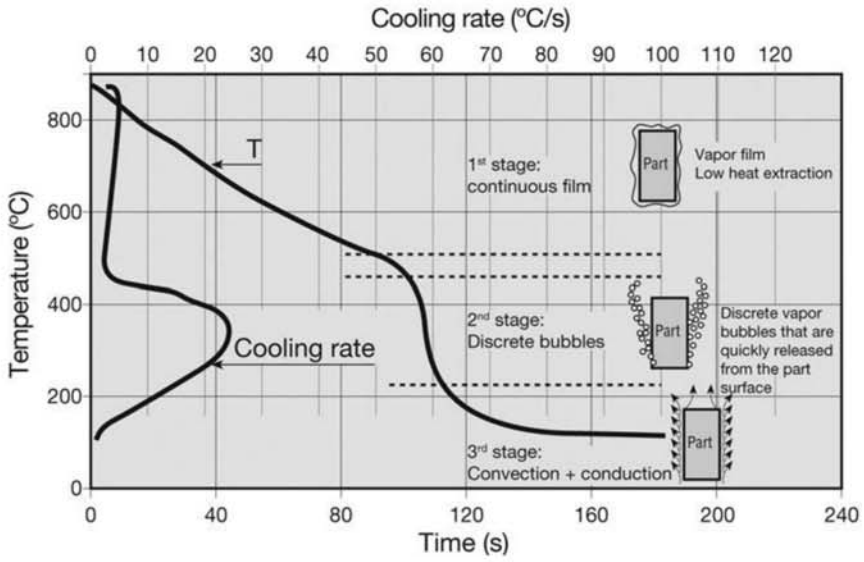

Fig. 10.45 Evolution of the temperature and corresponding cooling rate in the center of a steel round bar of 25 mm (1 in.) diameter during water quenching. The three stages of cooling on quenching and the dominant heat extraction mechanisms are indicated in the figure. Source: Ref 3

sidual stresses. Finally, cooling happens without steam formation via conduction and convection. Analyzing the experience with quenching processes and cooling rate graphs, such as the one presented in Fig. 10.45, makes it possible to define some basic recommendations for any quenching treatment:

- The quenching tank volume must be sufficiently large that during the whole process of heat removal the average temperature of the quenchant is little changed. Should the quenchant temperature increase, the cooling rate of the part decreases. It is common to circulate the quenchant in cooling systems to guarantee this condition.
- The initial temperature of the quenchant should be sufficiently low. In some standards, limits such as 40 °C (105 °F) for the maximum water temperature during the whole quenching process are defined. Again, the increase of quenchant temperature reduces the cooling rate of the part. In the case of water, for a comparison, at temperatures close to 100 °C (210 °F), its cooling power is reduced to around 1/10 of that when the water is at room temperature.
- Nonuniform cooling is regarded as one of the main reasons for faulty quenching and quenching distortion. It is even more relevant than quenchant severity as a cause of cracks and distortion. Sufficient agitation during the quenching process is essential. Among other advantages, vigorous agitation reduces the first stage (continuous film) of quenching to a minimum.
- The time taken to transfer the part from the furnace it is austenitized in to the tank in which it will be quenched is critical for quality of the heat treatment, particularly for small parts that lose heat at high rates and

may suffer partial transformation (diffusive) during the cooling between furnace and tank.

The formulas derived from the Grossmann method are still used today, and this pioneer work has been decisive in defining methodologies for the selection of steels based on hardenability. However, the Jominy test, which is discussed in the next section, is considerably cheaper and makes it possible to tabulate the information on each steel in a more compact form. For these reasons, it is the preferred method for measuring hardenability.

Jominy Test

The most usual method for the measurement and quantification of hardenability of engineering steels is the Jominy test (Ref 22). In this test, also called the "end quench hardenability test," a wide range of cooling rates are generated in a single specimen. After austenitization in conditions defined by the test standard (Ref 22), a water jet in controlled and standardized conditions (Fig. 10.46) cools the end of the specimen. This causes different cooling rates in different positions along the cylindrical surface of the specimen. Thus, each position undergoes different transformations, resulting in different values of hardness, as presented in Fig. 10.47.

There are well-established methods to correlate the cooling rates in actual parts with the cooling rates of a Jominy specimen. Thus, for steels for which the Jominy hardness curve is known, it is possible to estimate, for a given position in a part of given dimensions and known geometry, what its hardness would be in the "as quenched" condition (see, for instance, Ref 3). Lober (Ref 26) shows micrographs of Jominy specimens for different steels, at various distances for the quenched end of the specimen, available online.

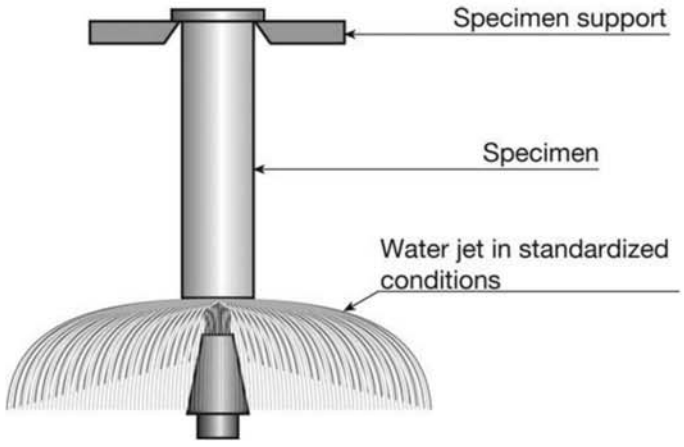

Fig. 10.46 Arrangement for the Jominy end-quench hardenability test according to SAE J406 or ASTM A255 (Ref 22) standards. Specimen dimensions and all other relevant testing conditions are fixed in the standard so that the cooling rates obtained along the surface of the specimen are consistent. A video of the Jominy test can be seen in Ref 24. A Jominy test can be simulated by accessing Ref 25.

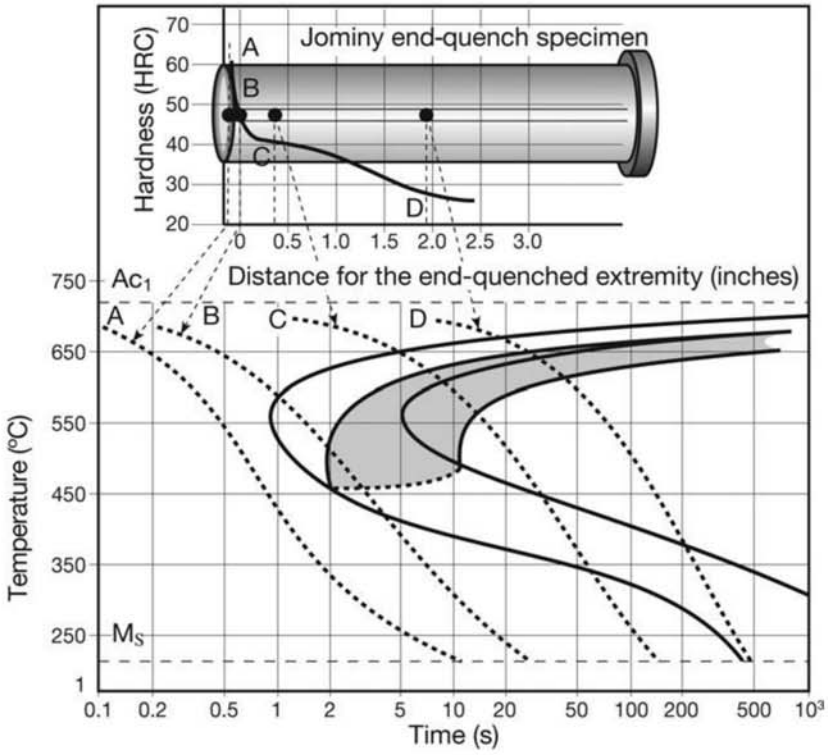

Fig. 10.47 The Jominy end-quench hardenability test makes it possible to achieve a large range of cooling rates in a single specimen. In the lower part of the figure, the different cooling rates in a Jominy specimen are superimposed on a TTT diagram (and a CCT diagram, gray). In the upper part, a schematic "Jominy curve" (hardness versus distance along the surface of the Jominy specimen, measured from the quenched end) is presented for the steel for which the transformation curves apply. Source: Ref 3 and 23

These micrographs are excellent references for the evaluation of quenched microstructures.

Predicting Microstructure via Computer Software

There are many techniques for predicting hardenability using mathematical models. Two main approaches can be used:

- Modeling phase transformations
- Fitting empirical formulas to data related to phase transformations (Ref 13, 16)

Among the methods that use empirical formulas, those using correlations between chemical composition and the critical transformation rates or the critical diameter are especially interesting and efficient. Methods that correlate chemical composition and the critical cooling rates use variations around the flow chart presented in Fig. 10.48. The critical rates used for the predicted microstructure are usually those indicated in the diagram presented in Fig. 10.49.

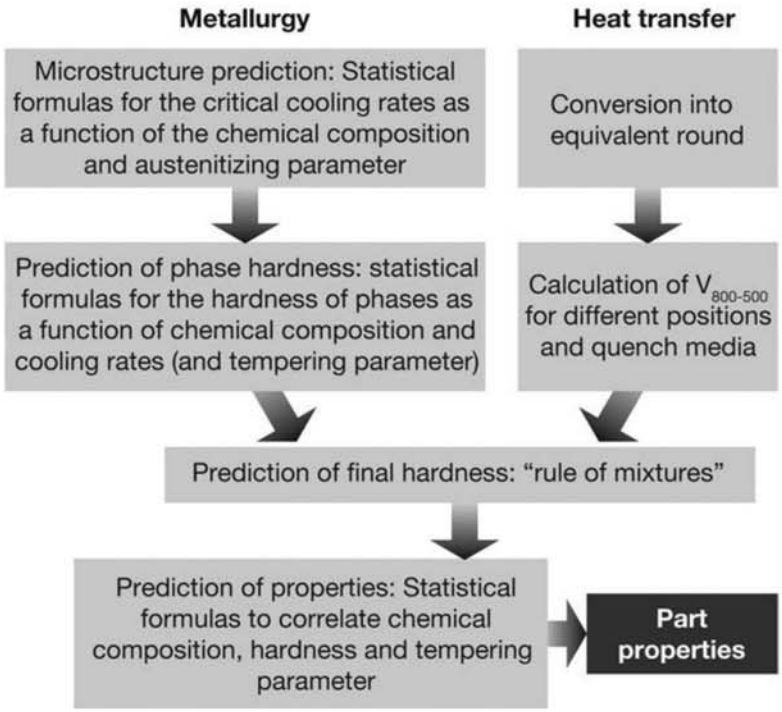

Fig. 10.48 Basic flowchart of a computer program used to calculate mechanical properties of steels as a function of chemical composition (and its relation to hardenability). ($V_{800-500}$ is the average cooling rate in the range 800–500 °C, or 1470–930 °F.)

One example of the formula for calculating the critical cooling rate for martensite formation (indicated as V_1 in Fig. 10.49) is given in Ref 13:

$$\log V_1 = 3.274\,(\%C) + 0.046\,(\%Si) + 0.626\,(\%Mn) + 0.026\,(\%Ni) + 0.706\,(\%Cr) + 0.675\,(\%Cu) + 0.520\,(\%Mo) - 1.818$$

Empirical formulas that take into account the effect of the austenitic grain size must also be included in the model. Many commercial and proprietary software to perform calculations with these techniques are available (e.g., Ref 27).

The results of a significant microstructural modeling effort, initially focused on welds but applicable to steels in general (Ref 28), are publicly available online (Ref 29) to calculate CCT curves.

Metallographic examination after quenching is unusual for two reasons:

- Almost all applications of steels subjected to quenching involve the subsequent tempering treatment
- Parts that are only quenched have high levels of residual stresses and are susceptible to cracking

It is standard and recommended practice to start the tempering treatment as soon as possible after quenching is concluded. Figures 9.25, 9.32, and 9.38(a) in Chapter 9, "Conventional Heat Treatments—Usual Constituents and

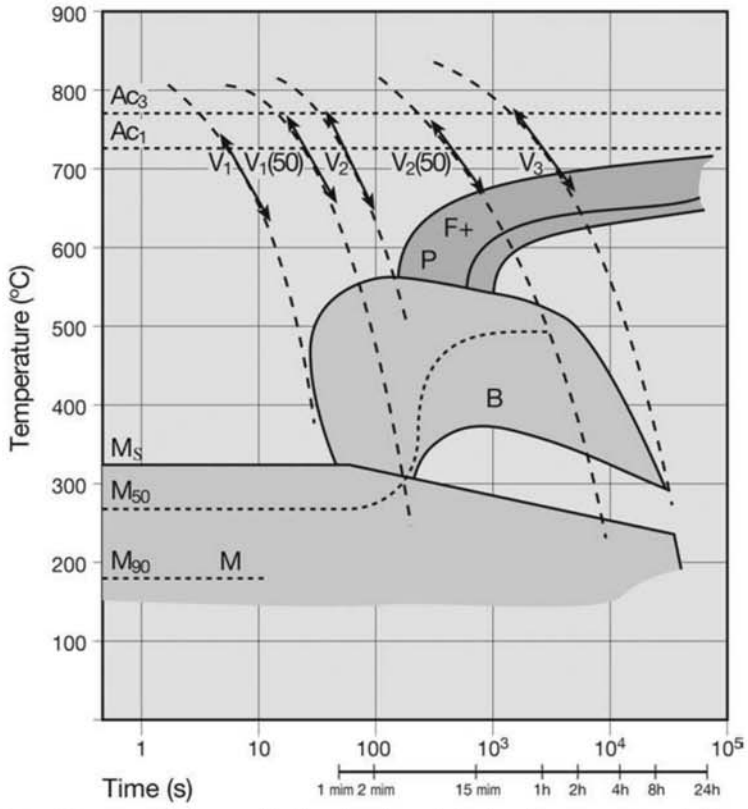

Fig. 10.49 CCT curve for a steel indicating the critical cooling rates for which empirical statistical regressions with the chemical composition are made. V = cooling rate, F = ferrite, B = bainite, P = pearlite, M = martensite. See also Ref 3 and 27.

Their Formation," in this book, are typical micrographs of nontempered (as quenched) martensite. In general, as-quenched martensite is resistant to usual etchants, such as nital and picral, and is etched lightly and slowly by these reactants.

10.3.4 Deviations During Quenching

The most common source of deviations in the quenching heat treatment occur during the austenitization step and during the cooling step (some of which were already discussed).

Deviations During the Cooling Step of the Quenching Heat Treatment

One important point in quenching treatments is to effectively reach the expected (or desired) quenching rates. Small parts quenched in tanks that are not close to the austenitization furnace, and the case of furnaces in which the complete charge is removed from the interior of the furnace and then quenched in groups of parts (e.g., when many parts are located on a movable platform that exits the furnace but does not move into the quenching tank) are two situations where the parts may enter the quenching tank at a temperature significantly lower than the austenitization temperature.

Figure 10.50 compares the simulated effect of some of these conditions on the resulting microstructure. When nonsatisfactory results are obtained, evaluating the microstructures can give important indications about the possible sources of the deviations in the heat treatment.

Figure 10.51 presents a case similar to cycle (b) in Fig. 10.50 for a steel with higher carbon content. While austenitization was performed in a proper way, holding the part for a short time at 700 °C (1290 °F) was sufficient to make possible the transformation of austenite into ferrite, as discussed in Chapter 9, "Conventional Heat Treatments—Usual Constituents and Their Formation," in this book. When the conditions are not adequate to guarantee cooling rates higher than the critical rate for martensite formation, other constituents will form. Usually these constituents will nucleate on prior austenitic grain boundaries. Quenching in these conditions is usually called "slack quenching." In carbon steel, ferrite can form in many different morphologies, as discussed in Chapter 9.

In medium and high carbon steels, when the cooling rate is high but not sufficient to guarantee martensite formation, fine pearlite and bainite may be formed, as shown in Fig. 10.52 to 10.54. In the past, these constituents were misnamed "troostite" (Ref 30, 31). At the time, the difficulties with resolving the fine microstructures of these constituents in optical microscopy led to naming all constituents resulting from austenite decomposition with cooling rates between the rate for forming martensite and the rate for forming ferrite either "troostite" or "sorbite" (Ref 30). It is sad that the constituent named after the pioneer of metallography Henry Clifton Sorby (1826–1908) turned out not be a single constituent. In 1953 C. S. Smith (Ref 32) proposed (without success) that pearlite be renamed sorbite to correct this injustice.

The problem was further aggravated due to confusion of the constituents resulting from austenite decomposition at intermediate cooling rates with those resulting from the tempering of martensite (Ref 30, 33). What is known as bainite today was designated either troostite or sorbite, despite the fact that very fine pearlite and tempered martensite were also classified with these terms (Ref 33). As discussed in Chapter 9, the morphologies of isothermal bainites can be significantly different from those of bainites obtained via continuous cooling, which further aggravated the confusion. Presently, sorbite and troostite are not to be used any more to identify constituents or phases in steels (Ref 31–33) .

Deviations During Heating and Austenitizing for the Quenching Stage

Further to the problems discussed in the section "Overheating," an example of which is presented in Fig. 10.55 for a quenching treatment, it is not uncommon to find insufficient heating (rate, time or temperature), as discussed in Chapter 9.

Inhomogeneous austenite and, in extreme cases, incomplete dissolution of previous phases in the austenite may occur. Figure 10.56 presents the result of intercritical heating of the same steel presented in Fig. 10.51. This kind of problem may happen due to temperature measurement errors, furnace inhomogeneity, or, in the case of more complex chemical composition steels, lack of proper knowledge of the correct A_1 and A_3 temperatures of the steel to be treated.

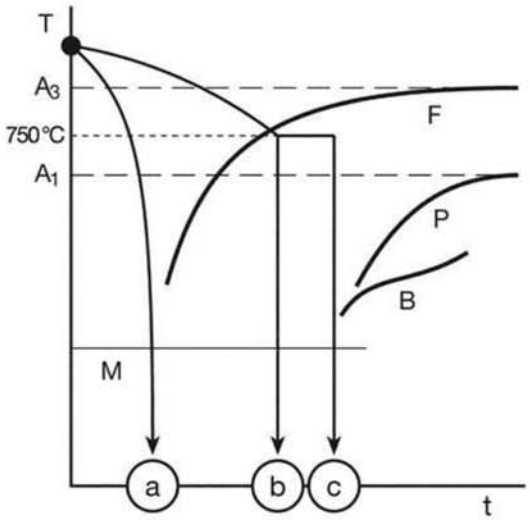

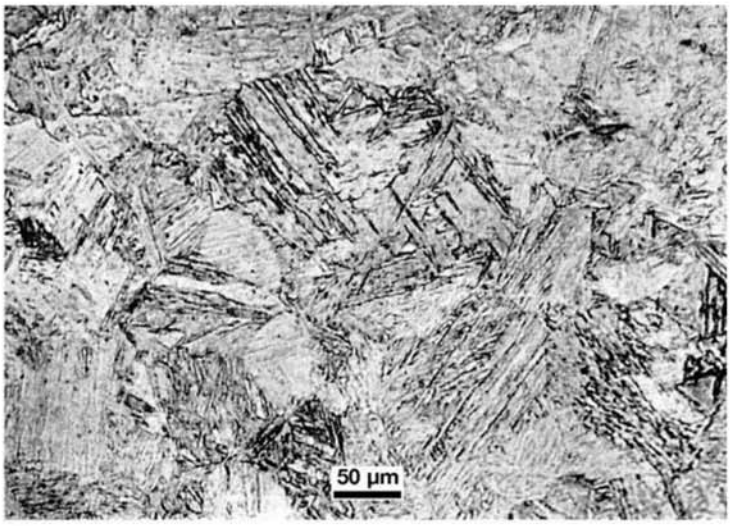

(a)

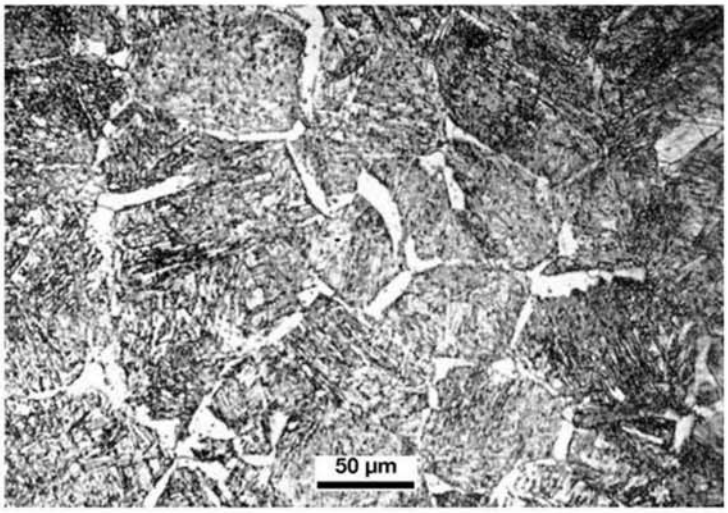

(b)

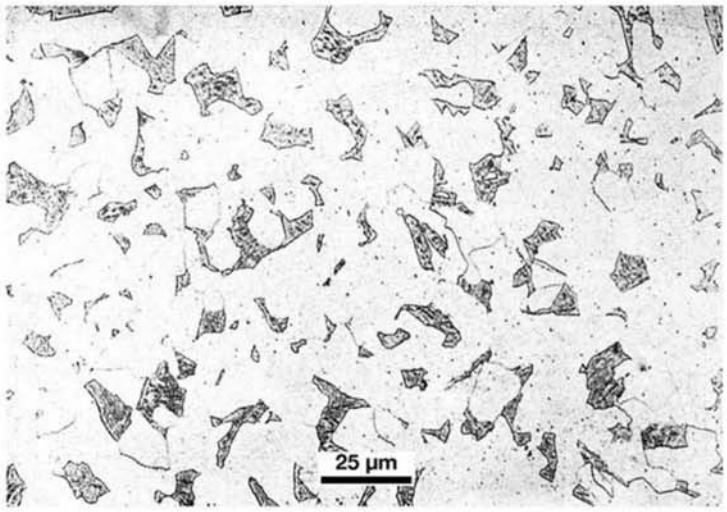

(c)

Fig. 10.50 Different microstructures observed in a steel containing C = 0.2% after the heat treatments summarized in the schematic CCT diagram shown on the top left. (a) Drastic quenching in water containing NaOH. Martensite with a small amount of acicular ferrite (b) cooled to 750 °C (1380 °F) (intercritical region) followed by drastic quenching. Proeutectoid ferrite network, in the prior austenite grain boundaries, and martensite. (c) Cooled to 750 °C (1380 °F) (intercritical zone), held for some minutes at this temperature, followed by drastic quenching. Equiaxial ferrite and martensite—some bainite may also be present. The ferritic transformation advanced during the holding time and the untransformed austenite regions (richer in carbon due to the formation of ferrite) transformed to martensite during the quenching. Etchant: nital.

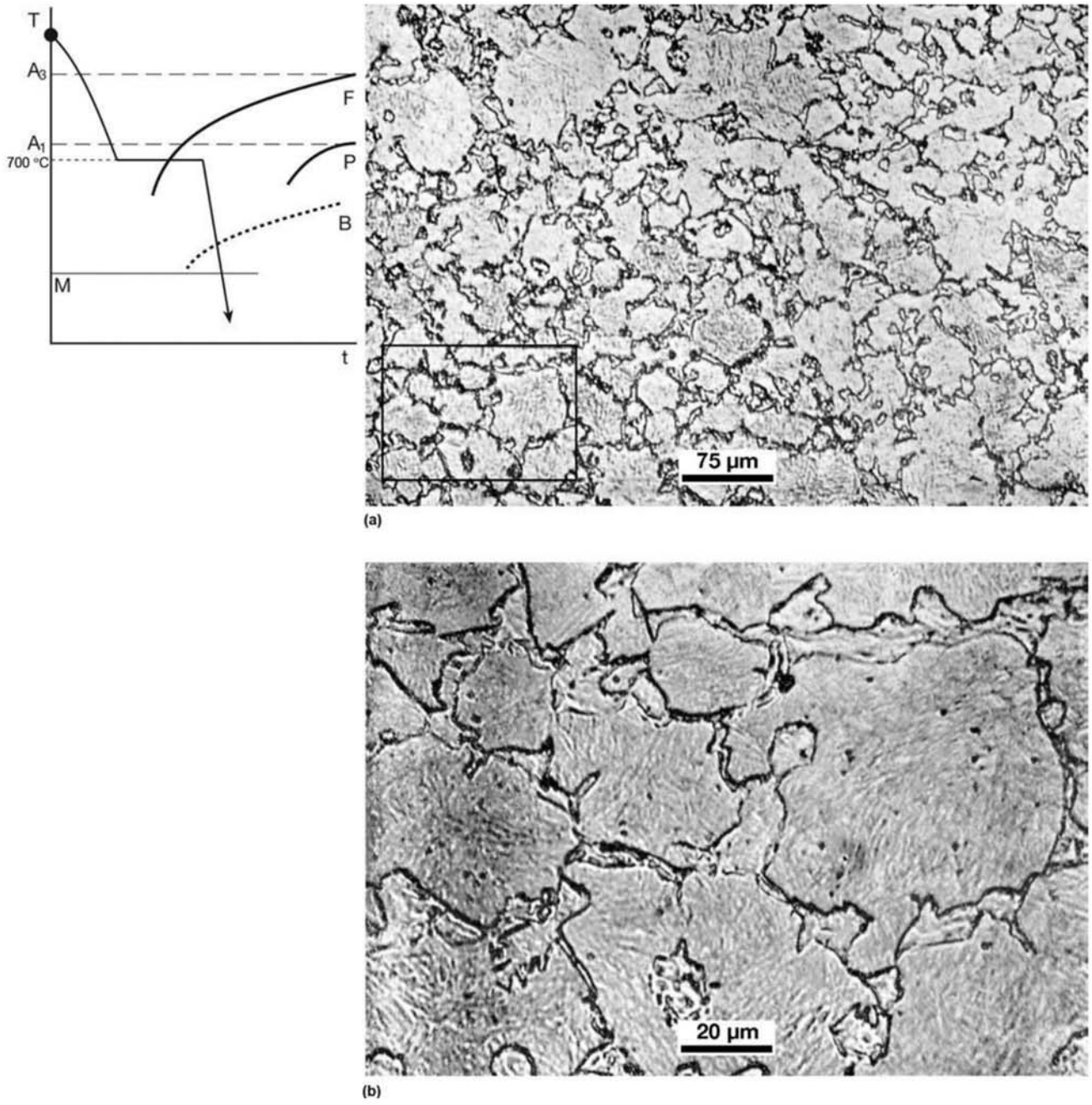

Fig. 10.51 Microstructure of a steel containing C = 0.5% after the heat treatments summarized in the schematic CCT diagram shown on the top left. Despite the fact that the steel was correctly austenitized, the part was cooled to 700 °C (1290 °F) (below A_1) and held at this temperature for some seconds before quenching. (a) Pro-eutectoid ferrite in a network along the prior austenite grain boundaries and martensite. (b) A higher magnification of the region indicated in (a). Compare the ferrite morphology with the allotriomorphic ferrite presented in Chapter 9, "Conventional Heat Treatments—Usual Constituents and Their Formation." Etchant: nital.

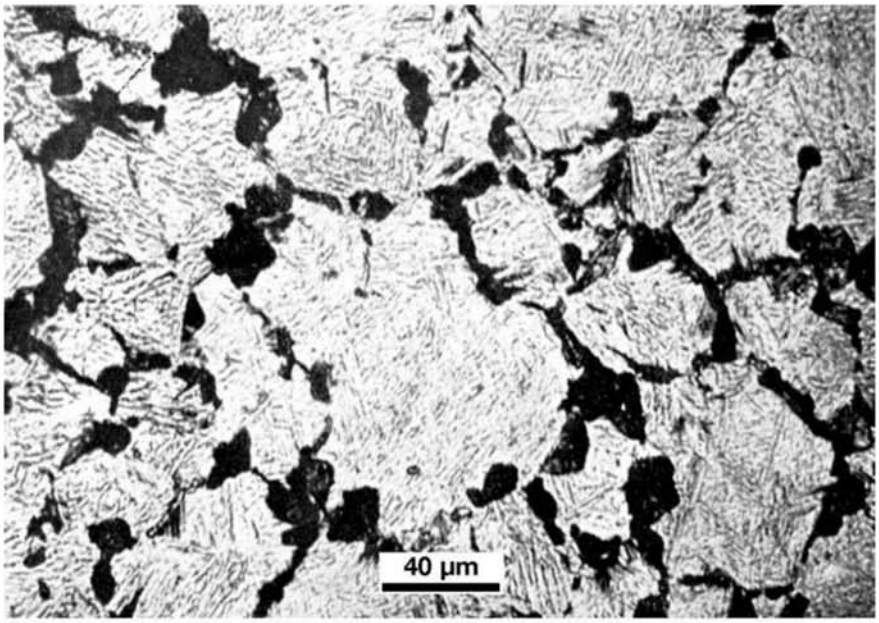

(a)

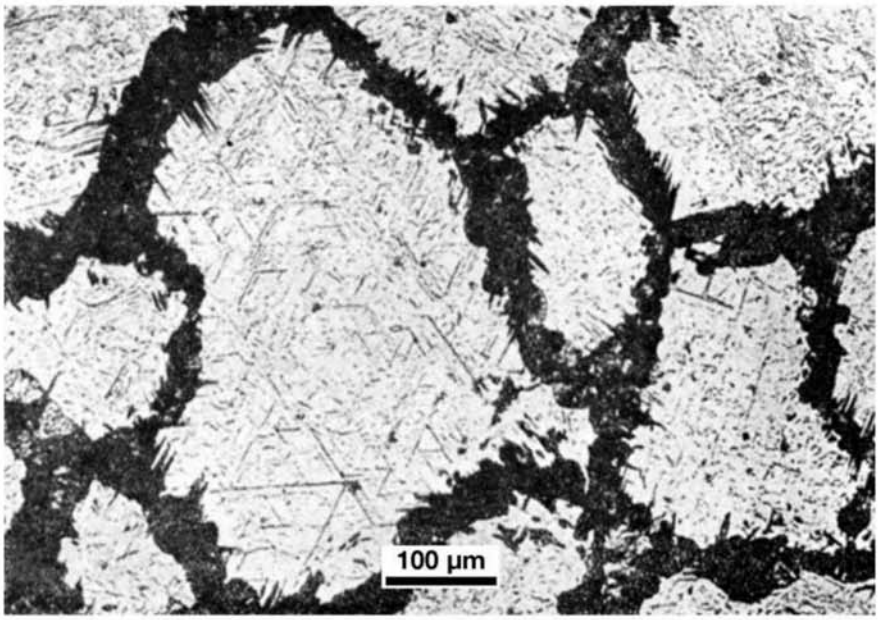

(b)

Fig. 10.52 Medium carbon steels quenched at a rate insufficient to guarantee complete transformation to martensite. (a) Steel containing C = 0.5%. Fine pearlite and bainite (elongated) formed from the prior-austenitic grain boundaries, in a martensitic matrix. Etchant: nital. (b) Fine pearlite and bainite formed from the prior austenitic grain boundaries, in a martensitic matrix. The prior austenitic grain size (delineated by the pearlite) suggests overheating during the austenitizing stage of the quenching treatment.

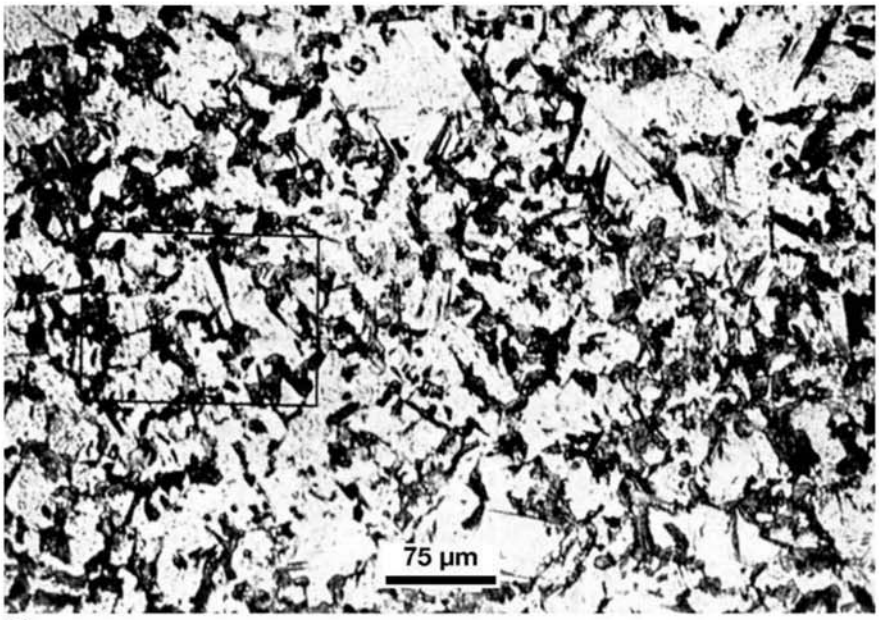

(a)

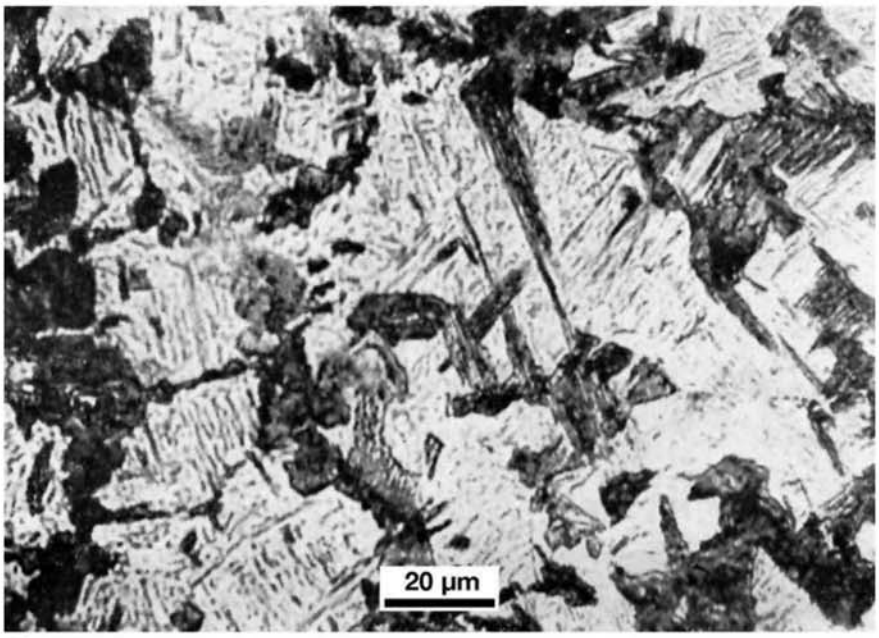

(b)

Fig. 10.53 (a) Steel containing C = 0.5% (cylindrical bar with 10 mm, or 0.4 in. diameter, quenched in oil at 200 °C, or 390 °F). Fine pearlite and bainite in the prior austenitic grain boundaries in a martensitic matrix. (b) Higher magnification of the area marked in (a). The etching difference between bainite and untempered martensite is not clear. Etchant: nital.

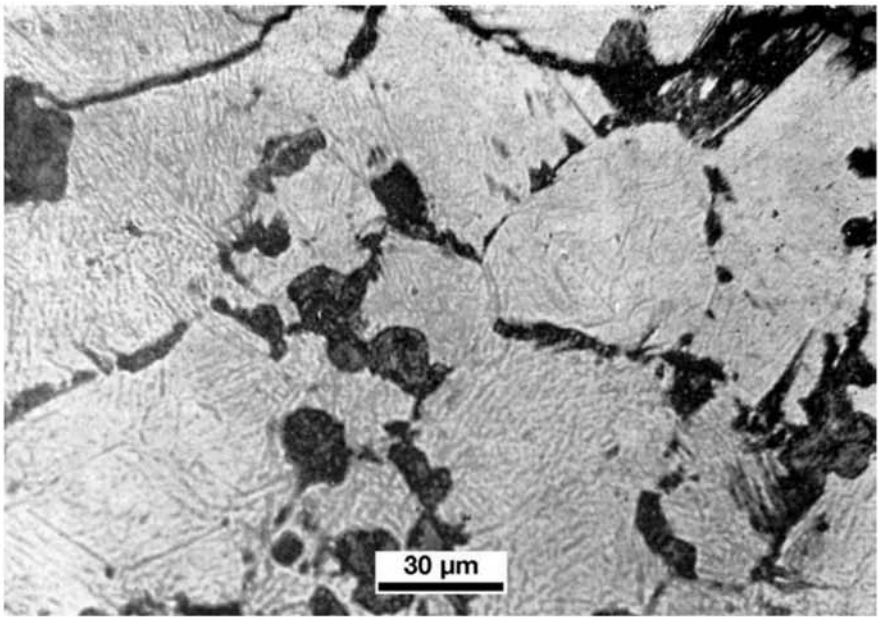

Fig. 10.54 Steel containing C = 0.5% slack quenched. Fine pearlite and bainite in a martensitic matrix. In the top left region of the image is a quench crack. Bainite shows dark and acicular. The pearlite colonies are equiaxed (or granular). Etchant: picral 4% for 30 s.

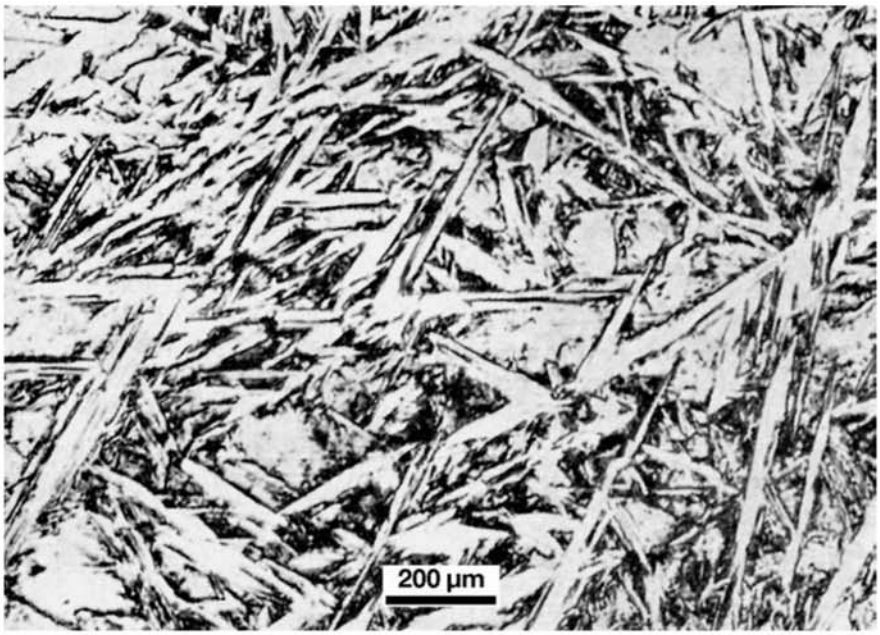

Fig. 10.55 High carbon steel quenched after overheating in the austenitic single phase field. Very coarse martensite. Etchant: nital.

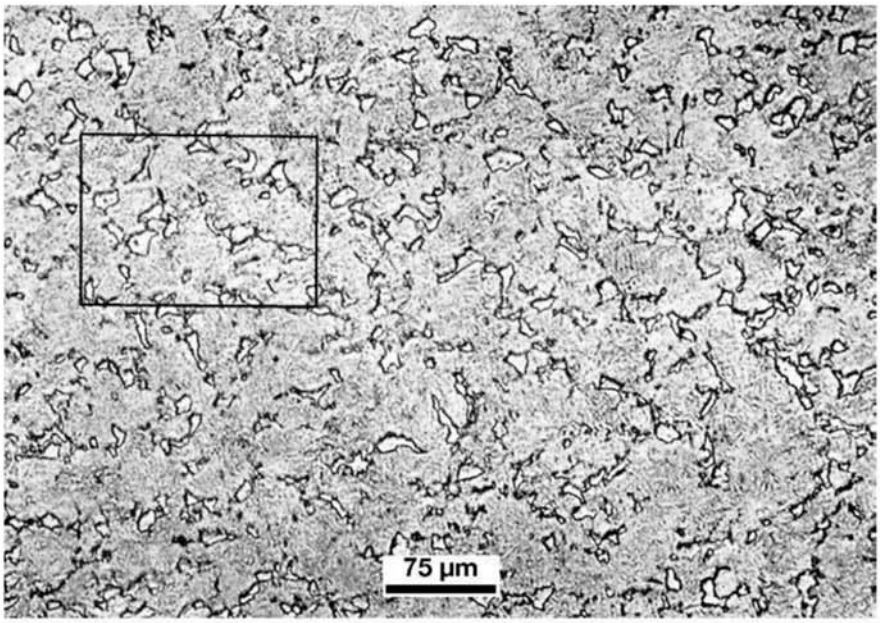

(a)

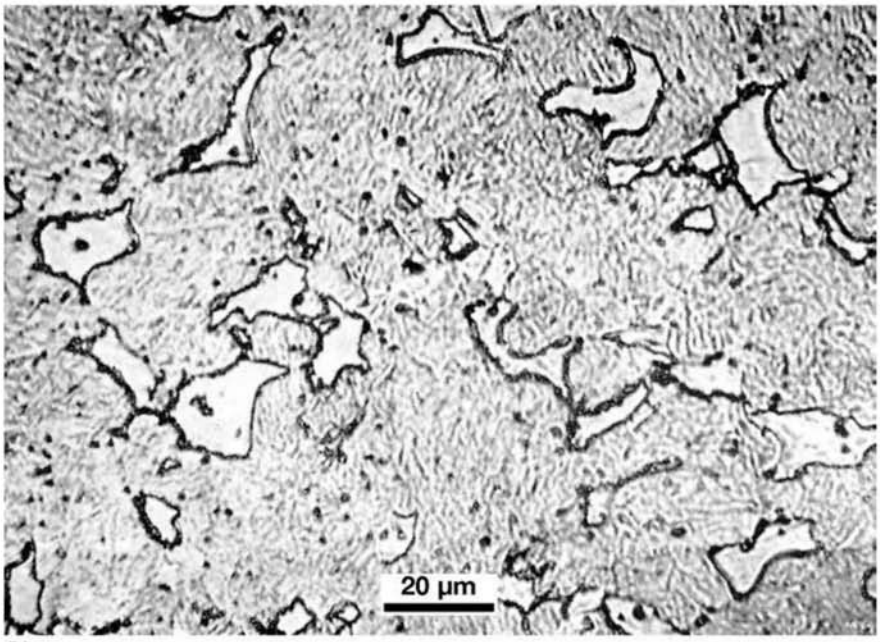

(b)

Fig. 10.56 Same steel as in Fig. 10.51 austenitized in the intercritical region (735 °C, or 1355 °F). At this temperature, in equilibrium, the steel would have 25% volume fraction of ferrite and 75% of austenite. (a) As-quenched steels. Ferrite islands in a martensitic matrix. (b) Higher magnification of the region marked in (a). Ferrite in islands, undissolved, and martensite. The ferrite grain boundaries are concave (compare with Fig. 10.51b), suggesting that ferrite is undergoing dissolution in austenite instead of growing from it. Etchant: nital.

10.3.5 Quench Cracks

During cooling or heating of any steel part, internal stresses are generated because of the temperature heterogeneity in the part combined to thermal expansion. In the case of the rapid cooling associated with quenching, this is further compounded by the combination of two factors:

- A large temperature heterogeneity associated with rapid cooling introduces steep temperature gradients in the part. Thus, larger stresses and stress variations appear inside the part associated with the restrictions to thermal expansion (or contraction).
- The martensitic transformation is associated to a dramatic volume change that occurs as the different regions of the part reach the M_s temperature.

Figure 10.57 shows dilatometry measurements for slow cooling and quenching of a single steel. The expansion on martensite formation is evident. Figure 10.58 schematically presents the superposition of thermal and martensitic transformation stresses in a part with simple geometry. It is evident that the quenching process, with martensite formation, will introduce a significant level of internal stresses in the material. These stresses may cause distortion or cracking if preventive measures are not considered. Figure 10.59 presents the correlation between chemical composition and the tendency to form quench cracks of steels. Figure 10.60 shows a crack directly associated with quenching stresses. Quenching cracks are usually intergranular. Steels with larger austenitic grain size and lower M_s temperatures are more prone to quench cracking. It is important to consider that the fast cooling caused by a quench medium is not the only cause of cracking during quenching (Ref 36). The presence of thick oxide layers inside the crack or evidence of decarburization in the crack edges will indicate that the crack is not a recent quench crack. After quenching (Fig. 10.61 and 10.62) there are no conditions under which these would happen, even if the part has been tempered. When the cooling is not sufficiently uniform, with the occurrence of volumes of stagnant or low circulation of quenchant, high stresses may also develop and cause cracks that otherwise would not form. In this case, microstructure and hardness heterogeneity may be the cause. A more complete discussion, illustrated with many examples of cracks observed in quenched parts, can be found in Ref 35. Stress concentrations are also important causes of failure during quenching. The design of a part to be quenched must avoid sharp transitions in the cross section as well as guarantee that all transitions do not have sharp corners. Machining or grinding marks can also originate cracks, as they act as stress raisers. For many large parts, it is standard to have premachining for quenching (where much material is removed, holes that will be present in the final part are premachined, etc.) and then a lighter final machining operation.

10.4 Tempering

Martensitic microstructures obtained directly from quenching usually have high residual stresses and insufficient ductility and toughness for use in most applications. Further heat treatment is required to properly condition the mi-

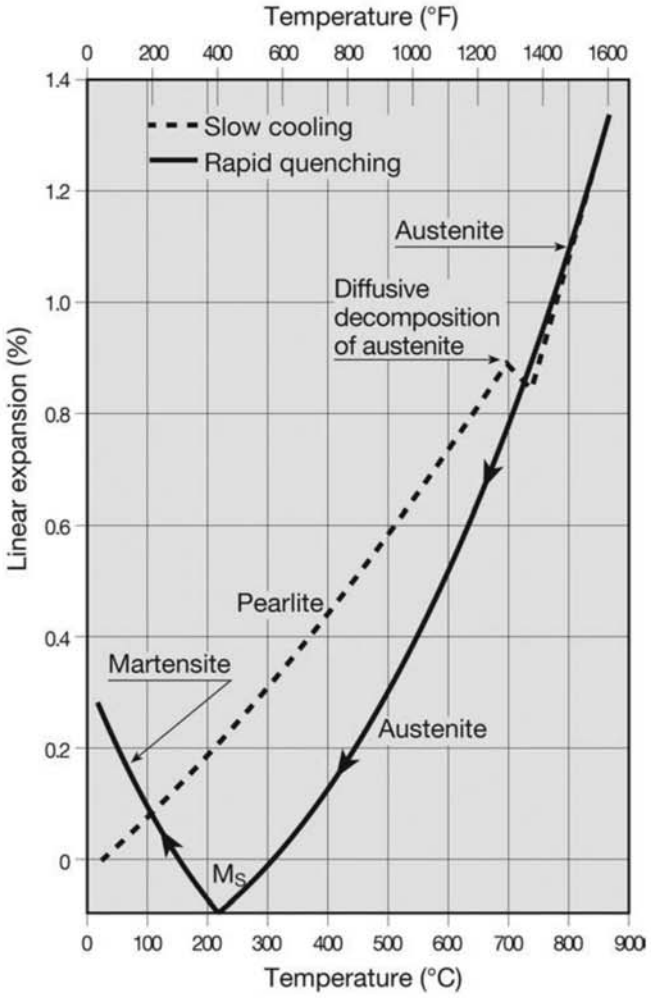

Fig. 10.57 Dilatometry measurements of the linear expansion (length change) of a steel slowly and rapidly cooled. During slow cooling the volume change associated with austenite decomposition happens at high temperatures, when the material is very ductile and has lower yield strength. Stresses are easily relieved through deformation. Upon subsequent cooling there is thermal contraction. When quenching, austenite contracts (due to thermal expansion) until the material reaches the M_s temperature. At this point, the expansion associated with the martensitic transformation starts. In this temperature range, the material has higher yield strength, and the untempered martensite has low ductility. Source: Ref 3

crostructure, relieving stresses and increasing ductility and toughness. This heat treatment is called tempering. Tempering involves heating to temperatures below A_{c1} to increase ductility and toughness, reduce strength and hardness to the desired levels, and reduce or eliminate residual stresses.

10.4.1 Transformations on Tempering

Martensite, the desired constituent of quenched steel, is metastable. Heating, even without entering the intercritical zone, favors transformation toward phases closer to equilibrium until finally microstructures composed of

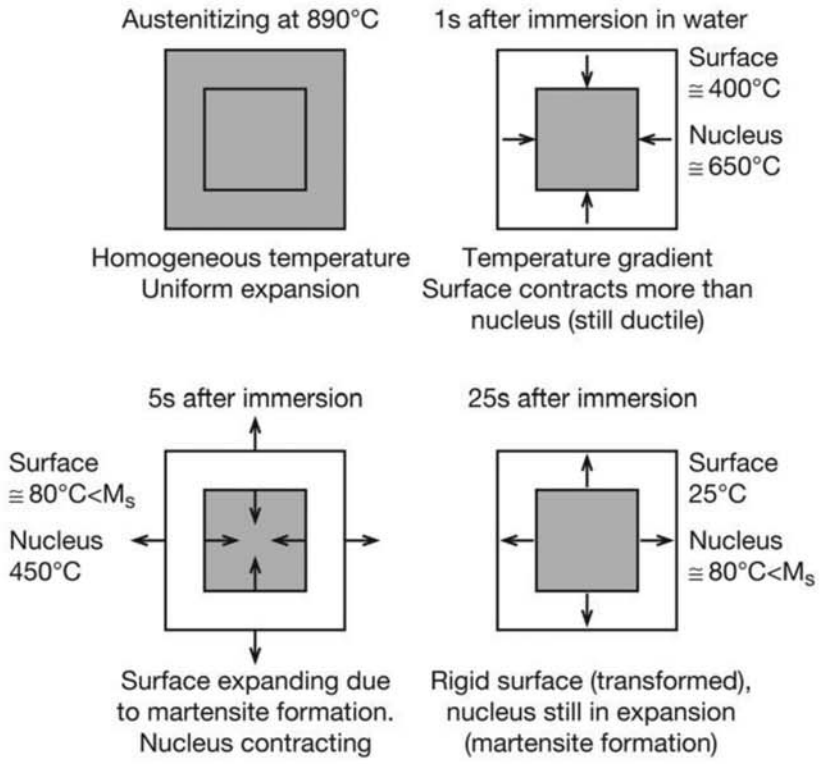

Fig. 10.58 Schematic representation of the development of stresses during the water quenching of a steel block. Source: Ref 34

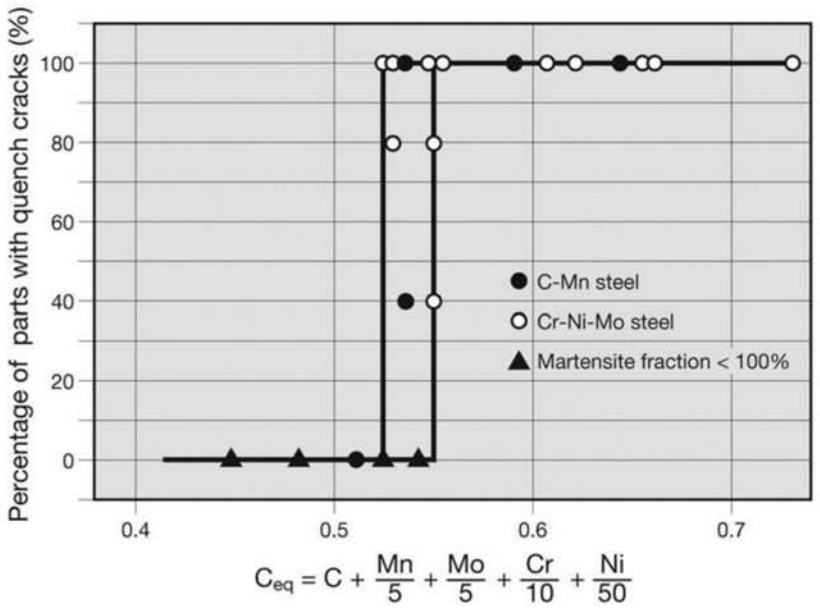

Fig. 10.59 Quenching crack susceptibility as a function of the "equivalent carbon" used as a measure for hardenability. Source: Ref 13

ferrite and carbides (either cementite or carbides of the alloying elements, depending on the steel composition) are reached. The various stages of the tempering process are quite complex. During these changes, the steel goes through structures that have extremely interesting combinations of properties. Figure 10.63 presents the changes in mechanical properties caused by tempering, using two different steels as examples. The overall trend of the

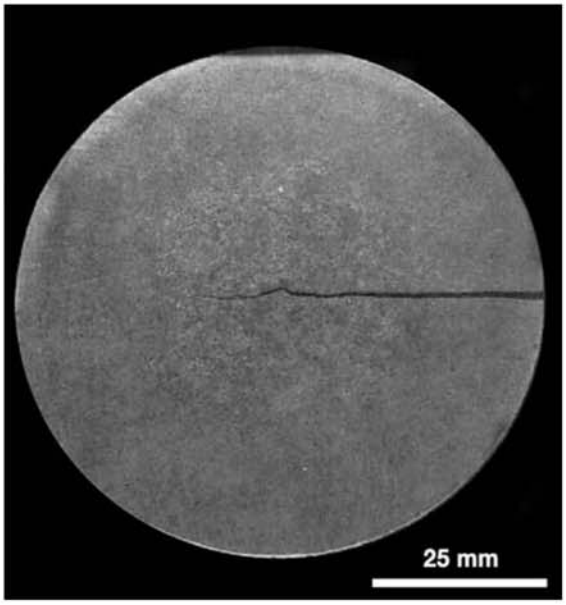

Fig. 10.60 Crack caused by quenching stresses in an AISI 4340 cylindrical bar. Reprinted with permission from ASM. Source: Ref 35

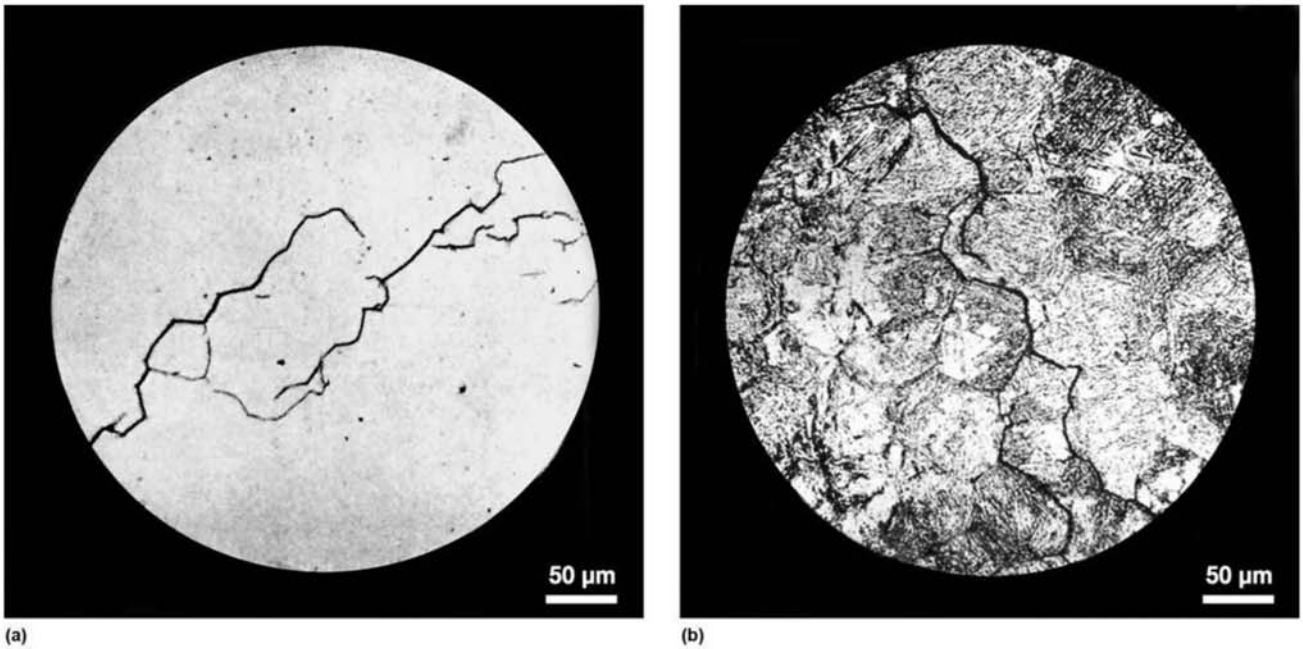

Fig. 10.61 Crack in quenched steel (a) without etching (b). Etchant: aqua regia. Crack follows the prior austenitic grain boundaries.

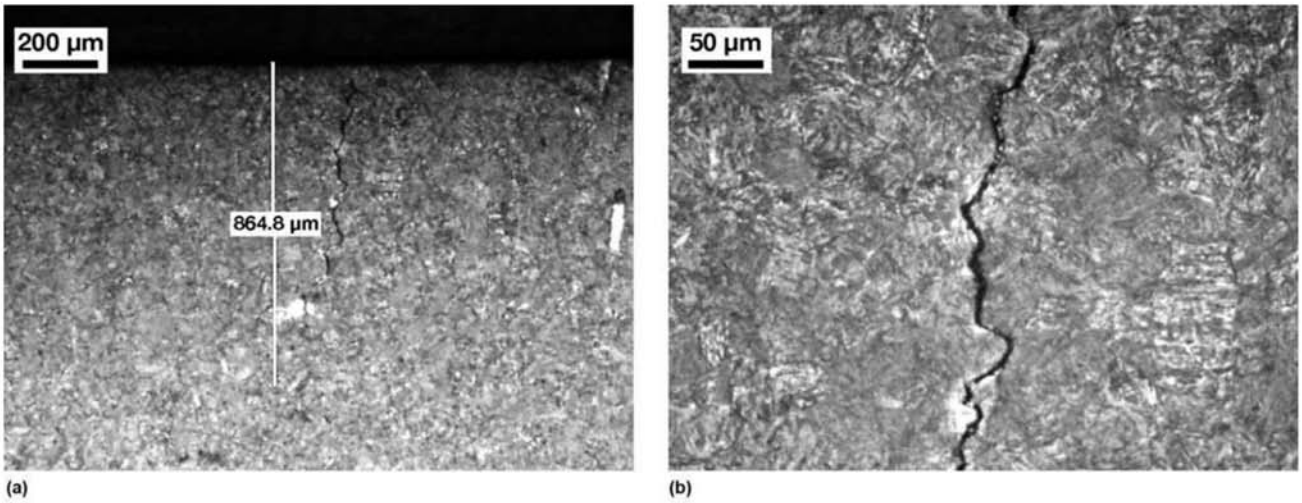

Fig. 10.62 Quench crack in prior austenitic grain boundaries. During heating for quenching there was excessive austenitic grain growth. Etchant: nital 2%. Courtesy of M.M. Souza, Neumayer-Tekfor, Jundiaí, Brazil.

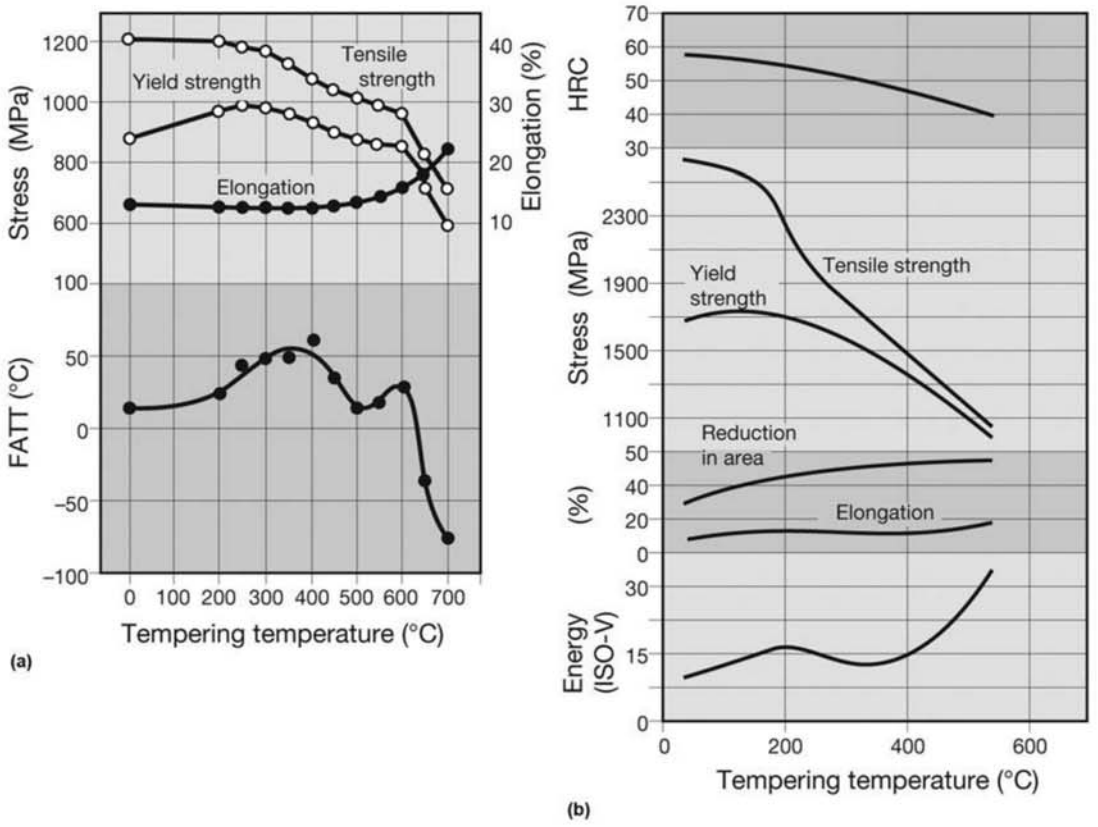

Fig. 10.63 (a) Effect of tempering on the mechanical properties of a steel containing C = 0.12%, Si = 0.3%, Mn = 0.83%, Cu = 0.3%, Ni = 1.1%, Cr = 0.53%, Mo = 0.49%, V = 0.03%, Al = 0.03%. FATT is the fracture appearance transition temperature (50% ductile, 50% brittle). The lower the FATT, the higher the material toughness. (b) Effect of tempering on the mechanical properties of AISI 4340. Source: Ref 13 and 42

properties during increasing tempering is toward hardness and strength reduction and ductility increase. In some cases (in particular in tool steels), hardness may increase in a certain range of tempering temperatures. This is called secondary hardening. On the other hand, it is extremely difficult to make general statements concerning the effect of tempering on toughness. Although the general trend is that the increase of tempering temperature should lead to increased toughness, this does not happen in a uniform (or monotonic) way. In some temperature ranges, toughness-decreasing phenomena (embrittlement) may be observed. The phenomena that give rise to these toughness reductions are especially important because they usually do not manifest themselves in other properties or in easily identifiable microstructural changes. From the metallurgical point of view, the transformations happening during martensite tempering can be described in a sequence of stages (Ref 2, 13, 23, 37):

1. Redistribution of the carbon atoms up to around 100 °C (210 °F).
2. Precipitation of carbides in the range of approximately 100 to 300 °C (210 to 570 °F). Besides the ε (epsilon) carbides, in steels with higher carbon content, cementite or cementite combined with χ (chi) carbides may precipitate. In some steels, alloying elements that make carbide formation more difficult, such as silicon, are added to achieve tempering at relatively low temperatures, and combinations of high strength and reasonable toughness.
3. Retained austenite in medium and high carbon steels decomposes in the temperature range of around 200 to 300°C (390 to 570 °F) (the mechanism normally involves the precipitation of carbides in the austenite, reducing its carbon content and making possible the transformation to martensite on cooling from the tempering temperature).
4. Above around 300 °C (570 °F), recovery and recrystallization of martensite (with the rearrangement and annihilation of dislocations) begins, combined with the growth and spheroidization of the cementite particles. These processes lead to strength and hardness reduction (see Chapter 12, “Mechanical Work of Steels: Cold Working”).
5. In the range of approximately 500 to 650 °C (930 to 1200 °F) in the case of steels containing carbide-forming elements, the precipitation of the carbides of these elements (such as V_4C_3, Mo_2C, etc.) may occur, causing an increase of strength and hardness (secondary hardening).

The major part of these processes occur in a scale that is not amenable to detailed observation via optical microscope. The main effect of tempering that can be observed in optical metallography is the increase in the rate at which the structure is etched as carbides are precipitated and later the presence of coalesced carbides, when tempering is too long.

Microstructural Evolution in Optical Metallography

As martensite is tempered and fine carbides precipitate, the rate at which the microstructure is etched increases. At the same time, the acicular feature of the microstructure becomes less well defined with tempering. Figure 10.64

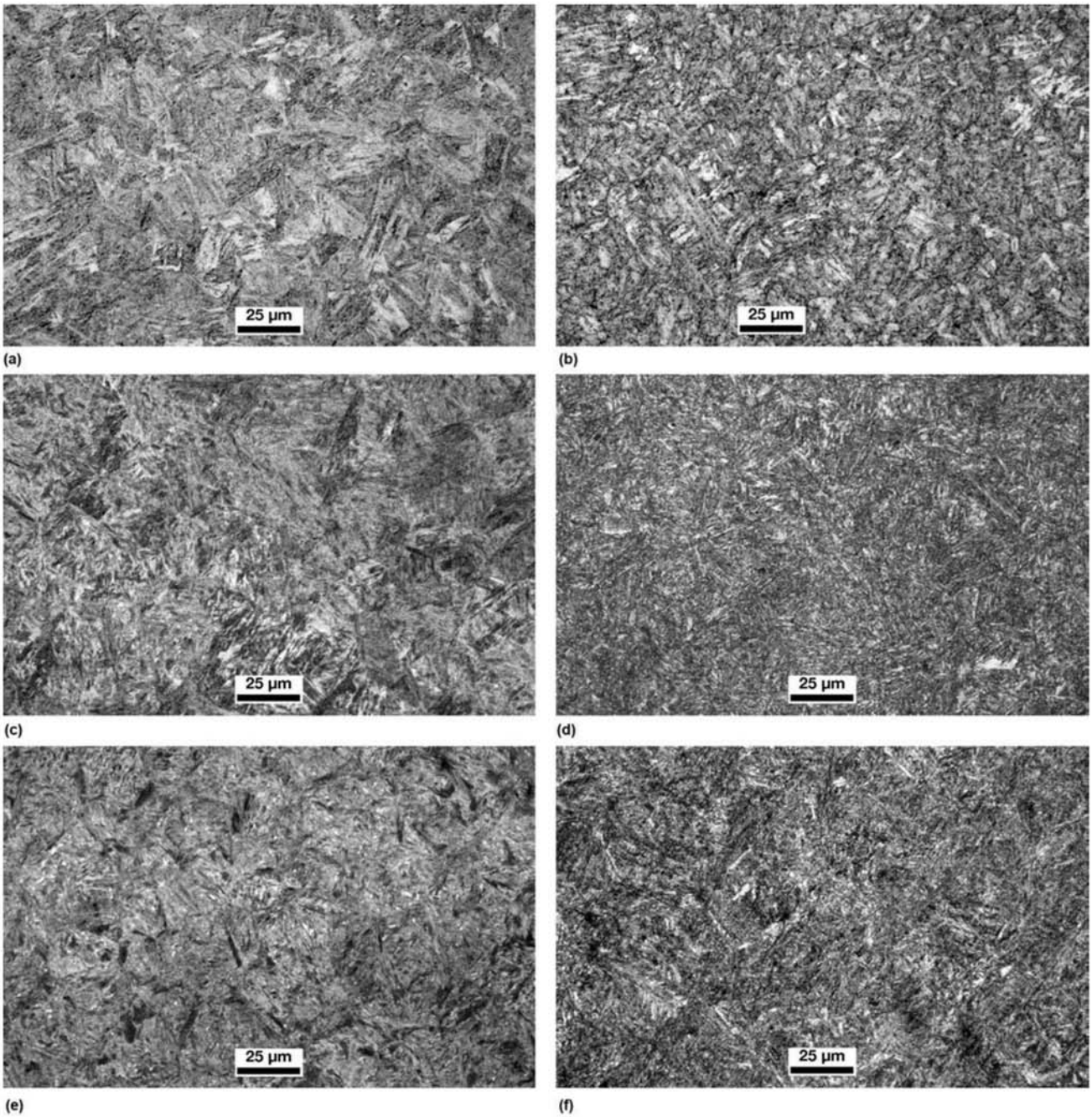

Fig. 10.64 Effect of tempering temperature on the microstructure of steels with the basic composition AISI 43xx and different carbon contents. The increase in tempering temperature reduces the acicular aspect of the microstructure. The difference in martensite morphology as a function of carbon content can also be noticed in the samples tempered at 200 °C (390 °F). (a) AISI 4320, 200 °C (390 °F), courtesy of L. Sandor. (b) AISI 4320, 600 °C (1110 °F). (c) AISI 4340, 200 °C (390 °F). (d) AISI 4340, 600°C (1110 °F). (e) AISI 4360, 200°C (390 °F). (f) AISI 4360, 600°C (1110 °F). Courtesy of L. Sandor. Source: Ref 38. (continued)

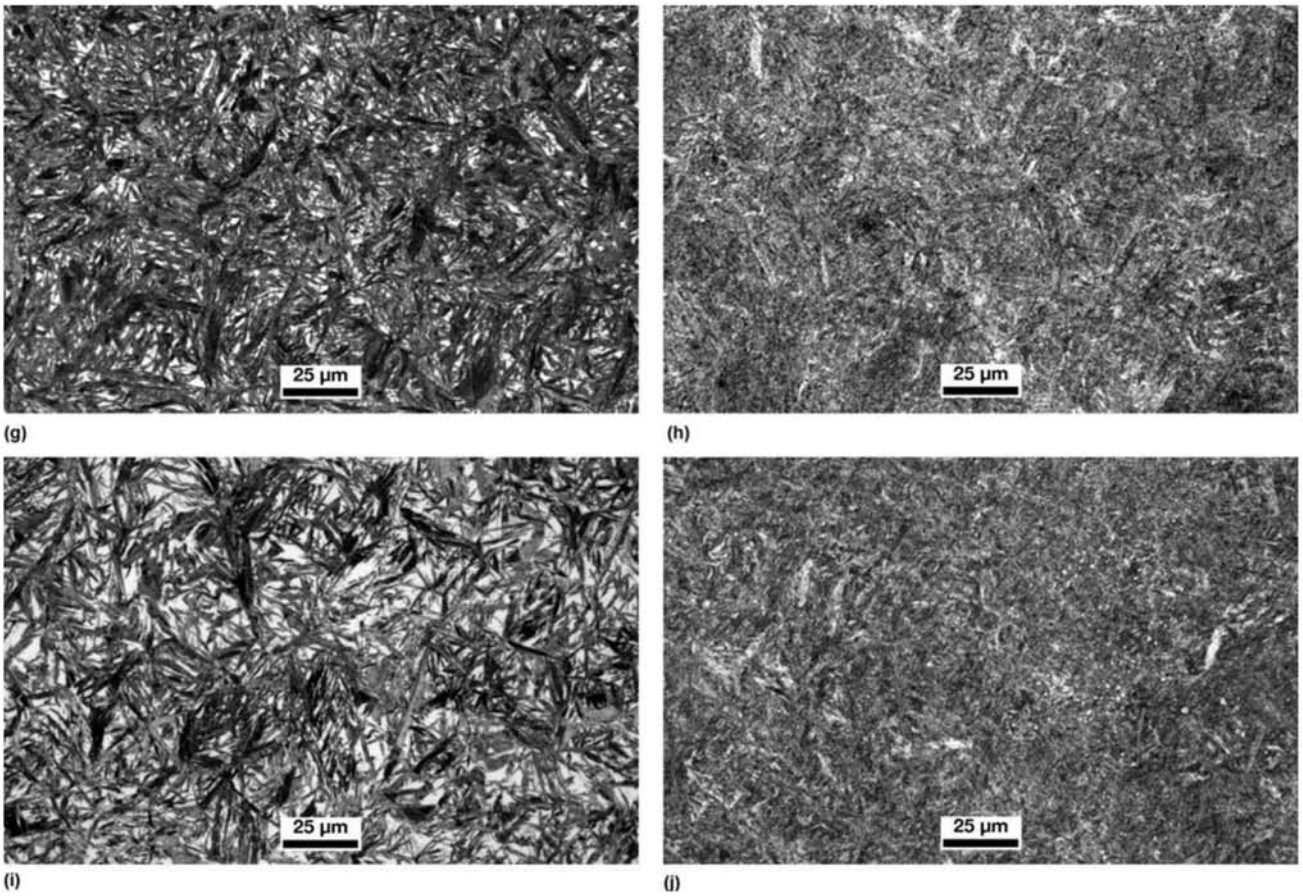

Fig. 10.64 (continued) Effect of tempering temperature on the microstructure of steels with the basic composition AISI 43xx and different carbon contents. The increase in tempering temperature reduces the acicular aspect of the microstructure. The difference in martensite morphology as a function of carbon content can also be noticed in the samples tempered at 200 °C (390 °F). (g) AISI 4380, 200°C (390 °F). (h) AISI 4380, 600°C (1110 °F). (i) AISI 43100, 200°C (390 °F). (j) AISI 43100, 600°C (1110 °F). Source: Ref 38

compares the microstructure of various AISI 43xx steels with different carbon contents, tempered at low and high temperatures.

Because tempering is a thermally activated phenomenon, the comparative effect of time and temperature can be defined through analysis based on the Arrhenius equation. The Holloman-Jaffe parameter (Ref 39) was developed with this purpose.

Thus, combinations of time (in h) and temperature (in K) resulting in the same value of the parameter should cause the same tempering effect in the steel. It is important to keep in mind that an Arrhenius approach can only be applied when there is no change in the thermally activated mechanisms occurring. Thus, this parameter should not be applied at very different temperatures or at temperature ranges that include the embrittlement range.

$$P = T(\mathrm{K})[C_{HJ} + \log(t(h))] \qquad \text{(Eq 1)}$$

P is the Holloman-Jaffe parameter
C_{HJ} is the constant of the Holloman-Jaffe equation

$$C_{HJ} = 20$$

or

$$C_{HJ} = 21.53 - (5.8 \times \%C)$$

Inoue (Ref 40) proposed a formulation that allows the effects of time along any tempering cycle to be added (integrated) as long as temperatures are between 400 and 700 °C (750 and 1290 °F) and times in the range of 0.1 and 1000 h. The proposed formulation is applicable to carbon and low alloy (including "engineering") steels. A parameter calculated as $\lambda = \log C$ represents the effect of a given time of tempering (in h) at a certain temperature (in K). The parameter C can be added during each cycle. Thus:

$$\lambda = \log C = \log t - \left(\frac{Q}{2.3RT}\right) + K \qquad \text{(Eq 2)}$$

where

$$Q = 12 + 5.23 \times \%C + 2.39 \times \%Cr + 27.6 \times \%Mo\left(in\frac{J}{mol}\right)$$

$$R = 8.314\frac{J}{mol}$$

$$K = 50$$

The additivity of the parameter *C* implies that the effect of a combination of *n* cycles can be obtained adding:

$$C_{total} = C_1 + C_2 + \ldots + C_n \qquad \text{(Eq 3)}$$

or

$$[\lambda]_{total} = \log(10^{(\lambda_1)} + 10^{(\lambda_2)} + \ldots 10^{(\lambda_n)} \qquad \text{(Eq 4)}$$

This kind of evaluation is especially useful when various tempering cycles are used or when the effects of tempering cycles and stress relief treatments are to be compared. Figure 10.65, for instance, presents the microstructural changes in a quenched and tempered steel subjected to stress-relief annealing for different times at a temperature that is probably higher than the tempering temperature.

10.4.2 Temper Embrittlement

In general, the decrease of hardness and strength is monotonic with the increase of tempering temperature. The exception occurs during the secondary hardening of tool steels, when the precipitation of fine alloy carbides causes precipitation hardening and increases in hardness and strength (Ref 2, 34). On the other hand, the effect of tempering temperature on toughness is much more complex, as the examples in Fig. 10.63 indicate. Among the various embrittling phenomena that might occur during tempering, two are highlighted here. The most common one is illustrated in Fig. 10.66(a) and hap-

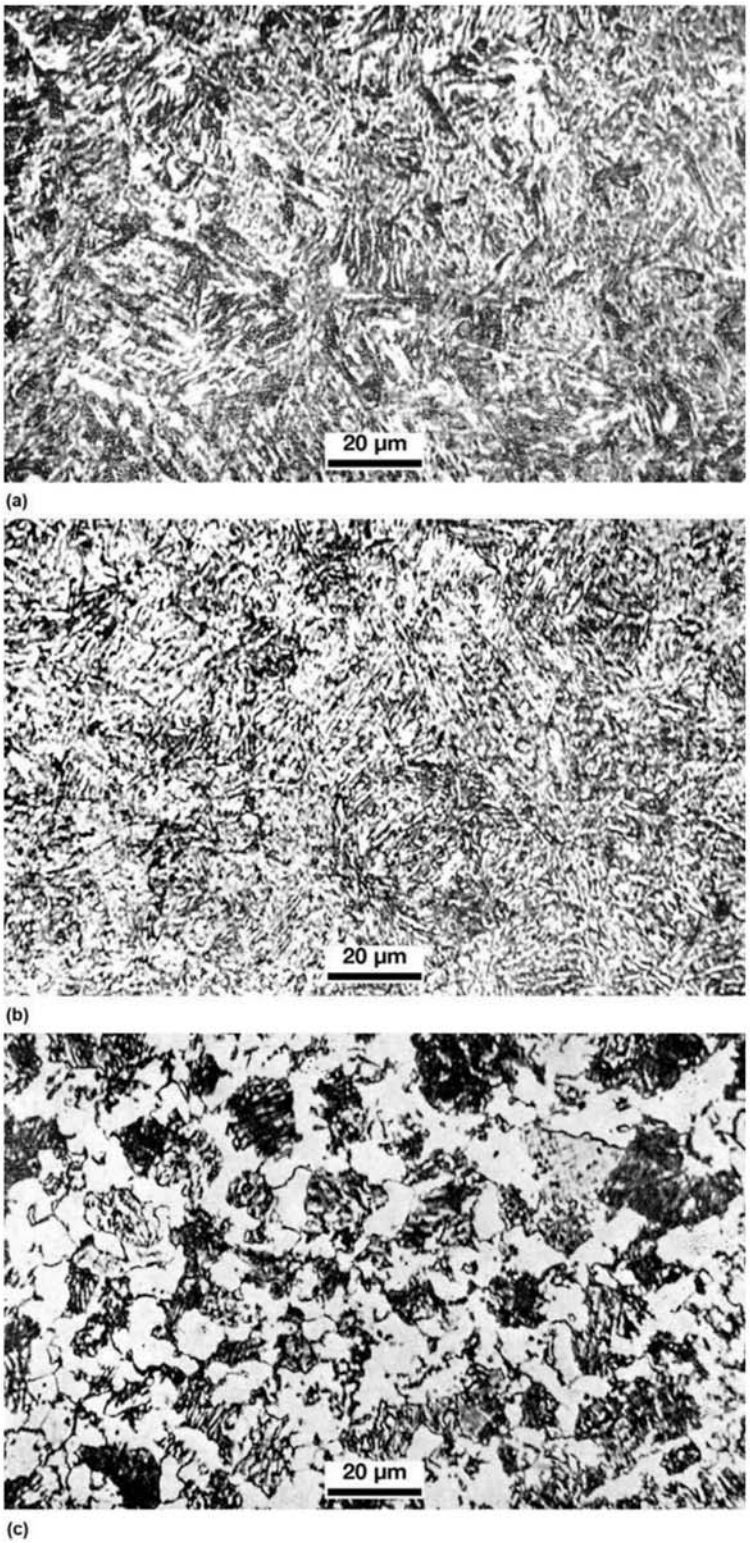

Fig. 10.65 Steel containing C = 0.5% water quenched and tempered at (a) 200 °C (390 °F): tempered martensite, well-defined acicular structure. (b) 400 °C (750 °F): tempered martensite, acicular structure less defined due to the changes happening during tempering. (c) 750 °C (1380 °F). This is an intercritical treatment. At this temperature, in equilibrium, the austenite volume fraction is about 85% and the ferrite volume fraction 15%. After cooling from the "tempering," the microstructure is composed of ferrite, dispersed carbides, and pearlite, transformed from the austenite formed in the intercritical treatment.

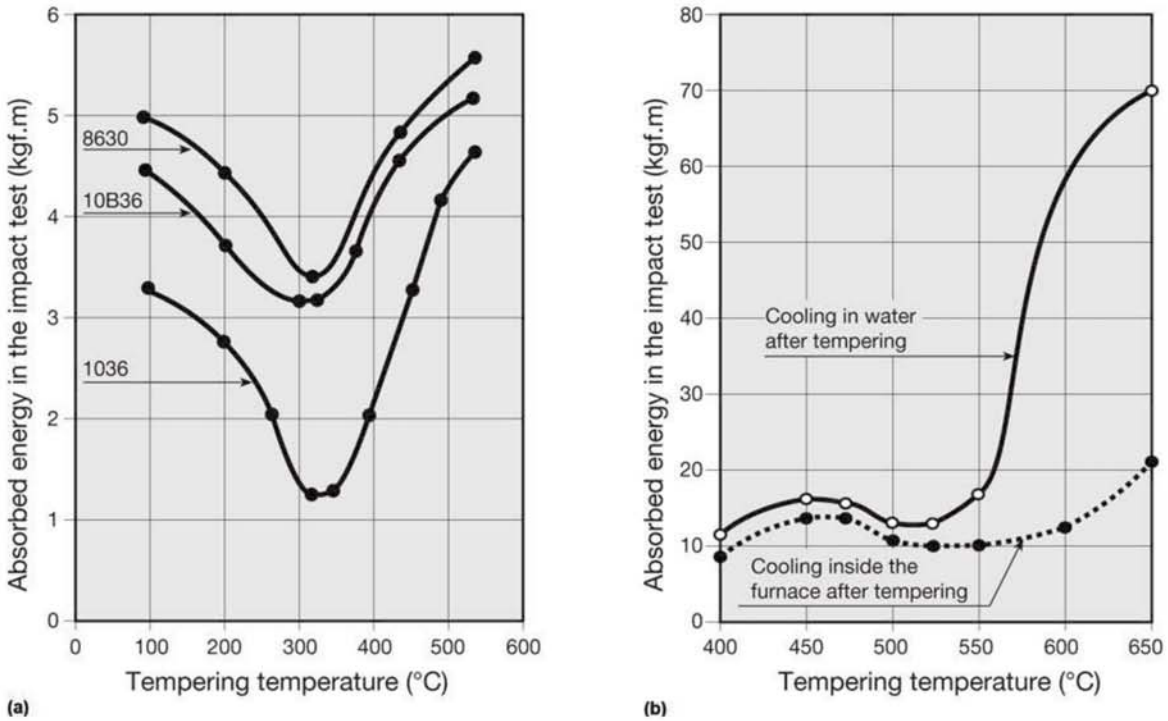

Fig. 10.66 Two types of temper embrittlement, measured by the drop in absorbed energy in impact test. (a) The most common type, observed in many engineering steels (some examples indicated on the curves). (b) Embrittlement observed in some special high alloy steels such as the one presented in the graph (C = 0.35%, Ni = 3.44%, and Cr = 1.05%). Source: Ref 41

pens in a large number of engineering steels. In general, this range of tempering temperatures is avoided, except for steels specifically designed to prevent this type of embrittlement. Some steels present a second embrittlement phenomenon, associated to the holding in the temperature range around 500 °C (930 °F). In order to avoid the possibility of embrittlement between 250 and 500 °C (480 and 930 °F) these steels are normally tempered well above 500 °C, and are rapidly cooled from tempering, to minimize the steel permanence in the temperature range that conducts to brittleness, as indicated in Fig. 10.66 (b). Otherwise, the steel will display brittleness. The other types of brittleness that can be experienced by quenched and tempered steels are discussed elsewhere, for instance in Ref 23, 42, 43.

10.4.3 Retained Austenite and Double Tempering

As the steel carbon content increases, M_s and M_f temperatures are lowered. This increases the possibility of austenite retention at the temperature at the end of quenching. During subsequent tempering, carbides may precipitate in the retained austenite, decreasing its carbon content and thus increasing its M_s and M_f temperatures. When cooling from the tempering cycle, this lower carbon–containing austenite may transform to fresh (untempered) martensite. This fresh martensite needs to be tempered to guarantee adequate properties of the steel.

Double tempering treatments are specified for many tool steels and high carbon content steels to guarantee toughness and dimensional stability. Characterizing the presence of retained austenite is not always easy. Besides x-ray diffraction techniques, which in principle are able to identify phases with a volume fraction above 5%, as-quenched hardness can be used as an indication of the presence of retained austenite. However, interrupting the quenching and tempering cycle to perform hardness measurements may risk the part integrity because the time between the treatments must be kept to a minimum due to the quenching stresses in the part. Metallographic techniques also make it possible to identify the presence of retained austenite. In some cases, color etchants are especially indicated, as illustrated in Chapter 13, "Advanced Steels for Forming Operations," in this book. Electron backscatter diffraction (EBSD) is also effective for determining the presence and location of retained austenite, although the sample preparation is delicate, and presently analysis time involves some hours in the SEM (Ref 44).

10.4.4 Subzero Treatment

As discussed earlier, steels with high carbon content may have a significant volume fraction of retained austenite at the end of conventional quenching (to room temperature) because their M_f temperature is quite low. During the application of these parts, retained austenite may undergo deformation-induced martensitic transformation, causing distortion and even cracking. For this reason, high carbon steels used for tools, calipers, bearings, and so on may undergo subzero treatments (see Fig. 9.19, in Chapter 9, "Conventional Heat Treatments—Usual Constituents and Their Formation," in this book). Retained austenite may also have an important effect on fatigue resistance and is a problem to be considered in steels that are surface carburized. Figure 10.67 shows the effect of sequential subzero treatments followed by

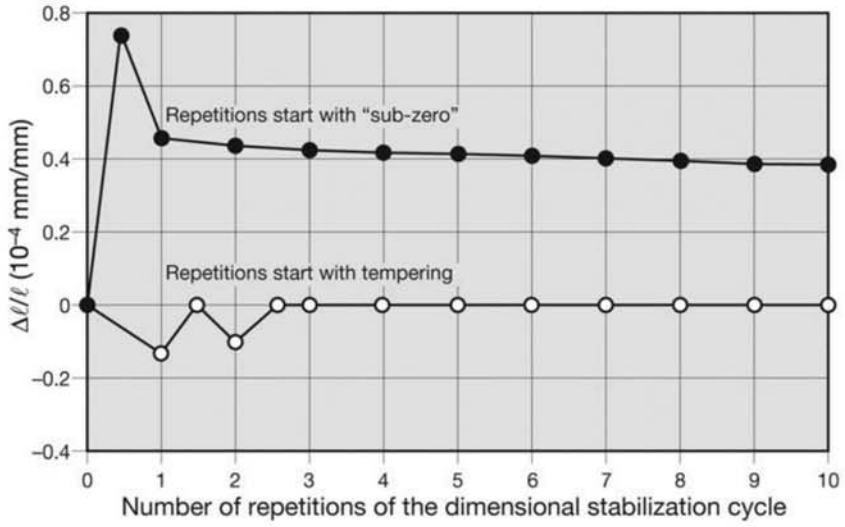

Fig. 10.67 Effect of the repetition of treatment cycles involving subzero treatment and tempering (or tempering and subzero treatment) on the dimensional stability of tool steel calipers martempered (see the section 10.6 "Martempering" in this chapter). Source: Ref 41

tempering on the dimensional stability of a tool steel caliper. The best results were achieved when the first subzero treatment followed a first tempering heat treatment, rather than when it immediately followed the quenching. It is also important to remember that the longer the time retained austenite is kept at room temperature, the less effective will be the subzero treatment in transforming it to martensite because there appears to be some austenite "stabilization" with time at room temperature.

10.4.5 Tempering Colors

When a ground, polished, or sanded steel surface is heated in the presence of air, a layer of oxide is formed. At low temperatures, this layer is very thin and diffracts light in such a way that the part appears to be of a certain color. This coloring effect, which happens in the approximate range of 220 to 320 °C (430 to 445 °F) for carbon steels, depends on layer thickness, which is a function of the temperature reached. This allows one to roughly evaluate the temperature the part was exposed to, because after the part is cooled, the color remains on the surface. Table 10.3 presents the approximate relation between the temperature and the corresponding color of the oxide layer. These are called "tempering colors" and are sometimes used in shops where quenching followed by low-temperature tempering is performed. This is no substitute for temperature measurement and assurance of furnace homogeneity and efficient heat transfer.

10.5 Selective Quenching

When it is desired to create hard areas in specific locations of parts, selective quenching can be applied. Railroad wheels, for instance, are subjected to localized quenching of their rim region. This treatment guarantees the transformation to a favorable microstructure on the region of the rim that contacts the rail and generates a compressive state of stresses, making it difficult for surface fatigue cracks to grow (see Chapter 15, "Engineered Special Bar Quality Steel (Engineered Steels)," in this book). Flame or induction hardening are the standard ways of performing localized heating for selective quenching. This austenitizes the surface region of the part, which is then subjected to quenching. Usually induction heating results in better process control and more precise control of the thermal cycle the parts are subjected to. Figures

Table 10.3 Tempering colors

Straw	220 °C	430 °F
Dark yellow	240 °C	465 °F
Red brown	260 °C	500 °F
Violet	280 °C	535 °F
Blue	300 °C	570 °F
Gray blue	320 °C	610 °F

10.68–10.70 present part of a bearing made of 100Cr6 steel (similar to AISI 52100) with a surface region hardened by selective quenching. Before this treatment, the material was spheroidized to ensure a tough core. The surface treatment involved rapid localized heating followed by localized quenching. Figures 10.71 and 10.72 present two examples of pins subjected to surface hardening and the corresponding structure.

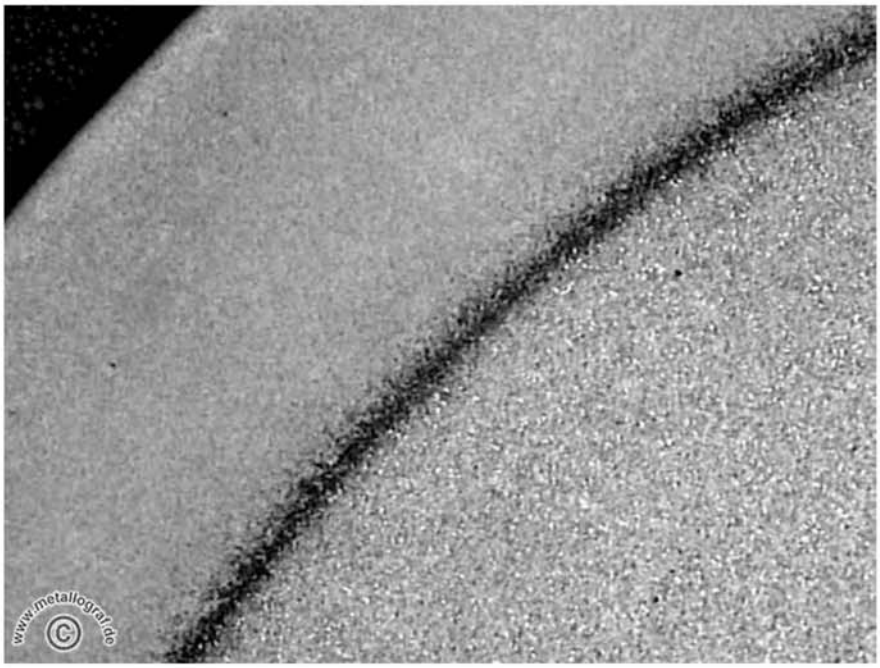

Fig. 10.68 Bearing part in steel 100Cr6 (similar to AISI 52100) subjected to selective quenching. The hardened layer is 2.25 mm (0.09 in.) thick. The core is spheroidized. Etchant: nital 3%. Courtesy of D. Lober. Source: Ref 26

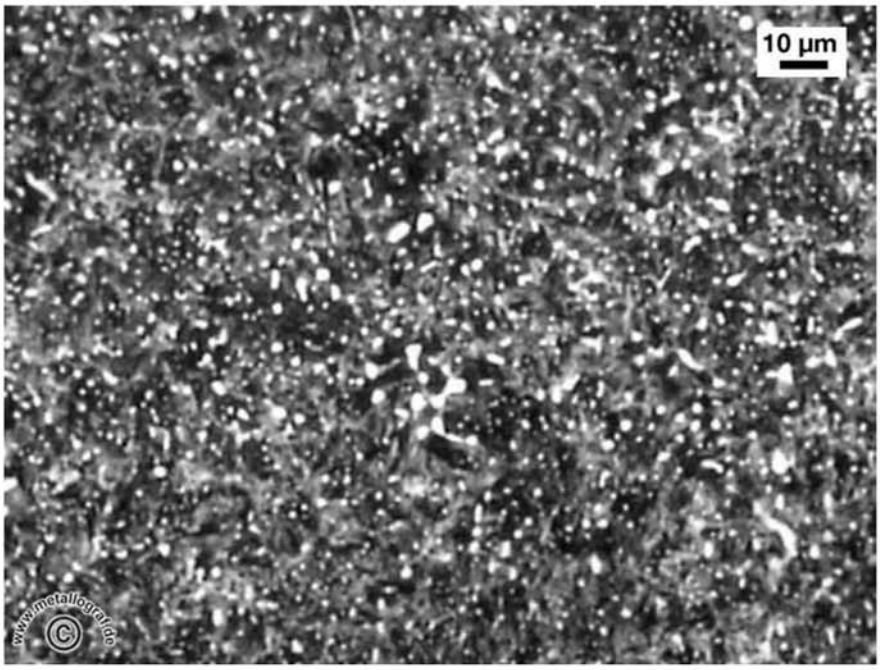

Fig. 10.69 Superficial region of the bearing part in Fig. 10.68. Martensite with spheroidized carbides. Etchant: nital 3%. Courtesy of D. Lober. Source: Ref 26

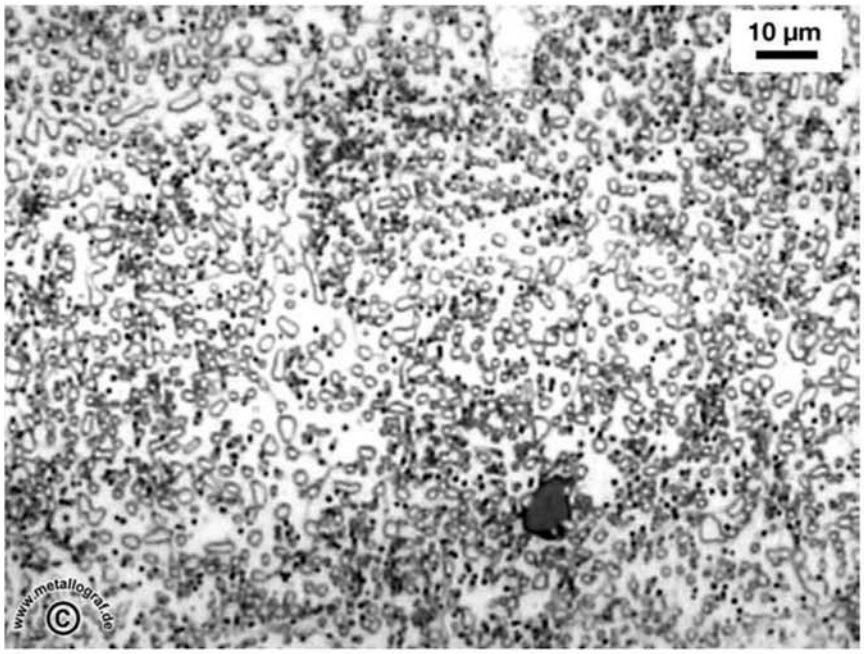

Fig. 10.70 Central region of the bearing part in Fig. 10.68. Spheroidized microstructure. Carbides in a ferritic matrix. Etchant: nital 3%. Courtesy of D. Lober. Source: Ref 26

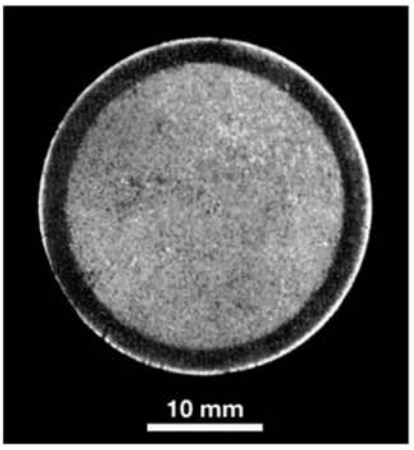

Fig. 10.71 Cross section of pin selectively hardened using induction heating. Etchant: iodine.

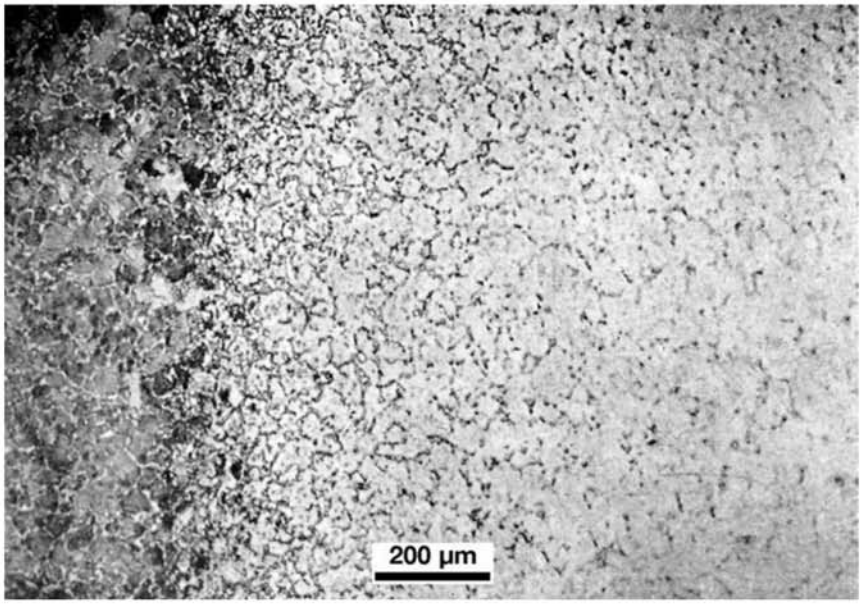

Fig. 10.72 Higher magnification of the quenched layer in the pin of Fig. 10.71. The part surface is close to the right region of the image. In this region, the microstructure is martensite. As the microstructure is observed closer to the core of the part, ferrite can be seen and a region where intercritical treatment happened can be observed.

Manual tools are frequently subjected to selective quenching to guarantee a tough body in combination with a hard and wear-resistant working surface. Figure 10.73 shows the example of a manual sickle subjected to selective quenching, and Fig. 10.74 shows the flat end of a pick subjected to the same type of treatment.

Another interesting example of selective quenching is the production of manual hoes. The blades of these hoes combine two interesting technologies: the blade is bimetallic, made by forge welding of two steels with different carbon contents, as shown in Fig. 10.75–10.77. The blades are then subjected to selective quenching: they are heated up to around 800 °C (1470 °F) (depending on the steel composition) and then partially immersed in water, as shown in Fig. 10.75(a). With this treatment, the quenched region remains all in the higher carbon steel. The region made of low carbon steel does not suffer any hardening because not only is the carbon content too low (0.1–0.2%) but the cooling rate is insufficient for martensite formation.

The hoe blade is subjected to a tempering treatment to increase the toughness of the hardened edge. In these cases the forging welding (and the accompanying changes in chemical composition) are superimposed on the gradient of cooling rates applied in the selective quenching, resulting in a variety of microstructures along the blade. The edge is hard and abrasion resistant, and the rest of the blade has good toughness, an important combination of properties in many tools such as punches, chisels, and hammers. An alterna-

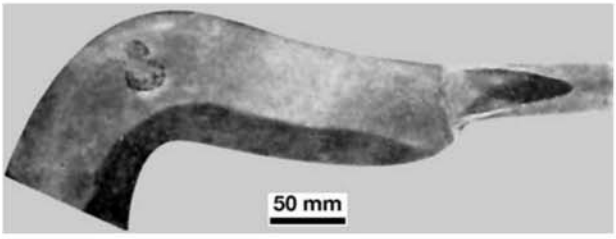

Fig. 10.73 Side face of a sickle polished and etched with iodine etchant. Quenched zone with uniform depth.

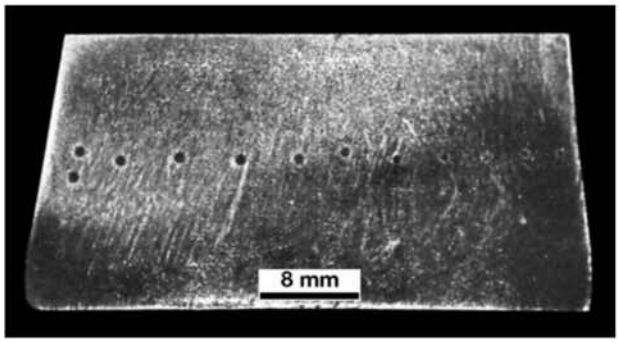

Fig. 10.74 Surface of the flat end of a steel pick. The dark region was subjected to selective quenching. The quenching extension is not regular. This was probably caused by nonuniform heating of the region to be quenched. The Rockwell hardness impressions on the part confirm that the dark region was hardened. Etchant: iodine.

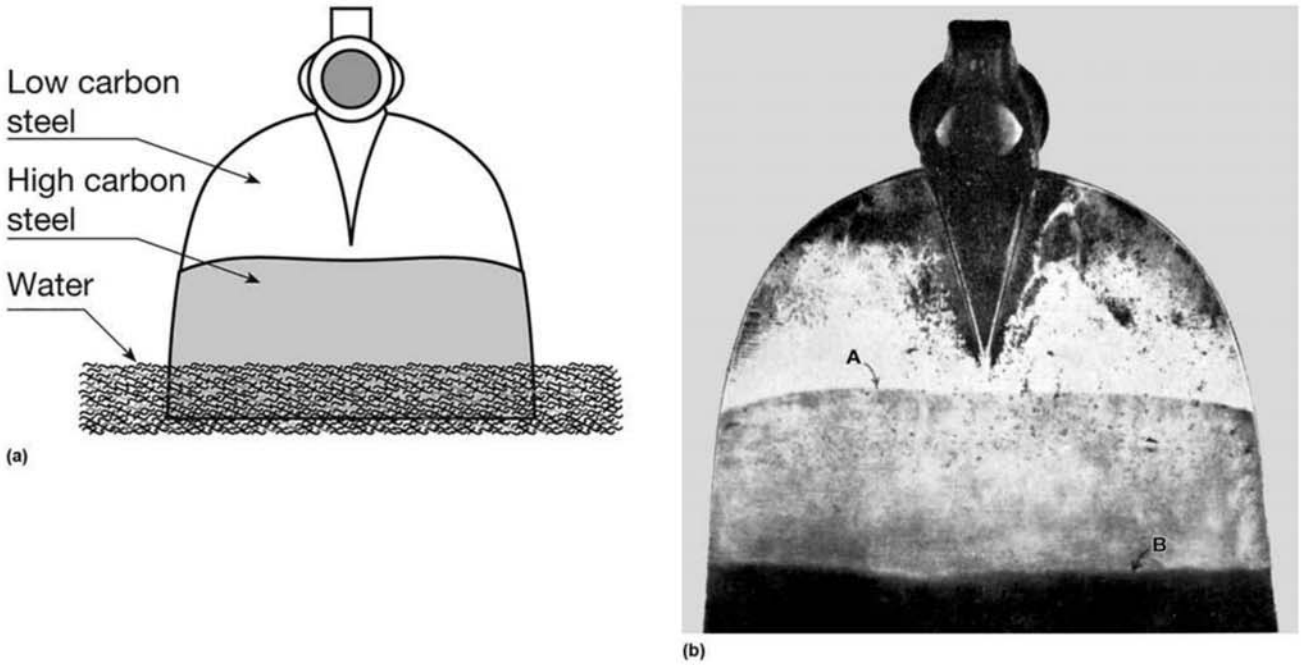

Fig. 10.75 (a) Manufacturing schematic of a forge welded hoe blade and its selective quenching. (b) Macrograph. Line A indicates the forge weld line of the two steels. Line B indicates the hardened region, as shown in panel (a). As in many cases this used to be an artisanal process, the transition between the two steels may fall outside of the hardened zone (as indicated in Fig. 10.76) or inside the hardened zone (Fig. 10.77).

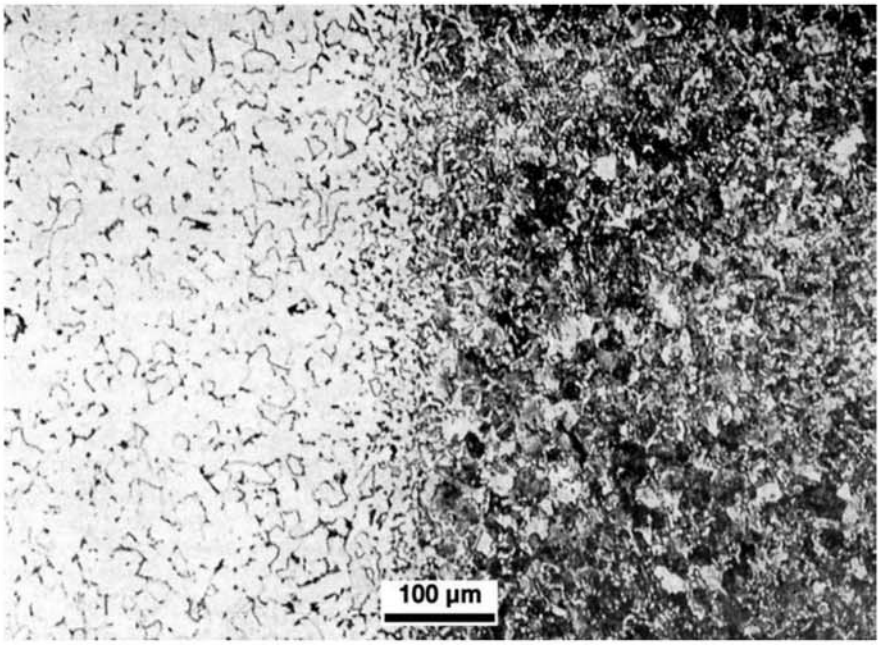

Fig. 10.76 Forge weld region of a steel hoe blade. High carbon steel (to the right) welded to low carbon steel (to the left). Region not quenched. Microstructure is pearlite in the right side and ferrite and pearlite in the left side. Etchant: nital.

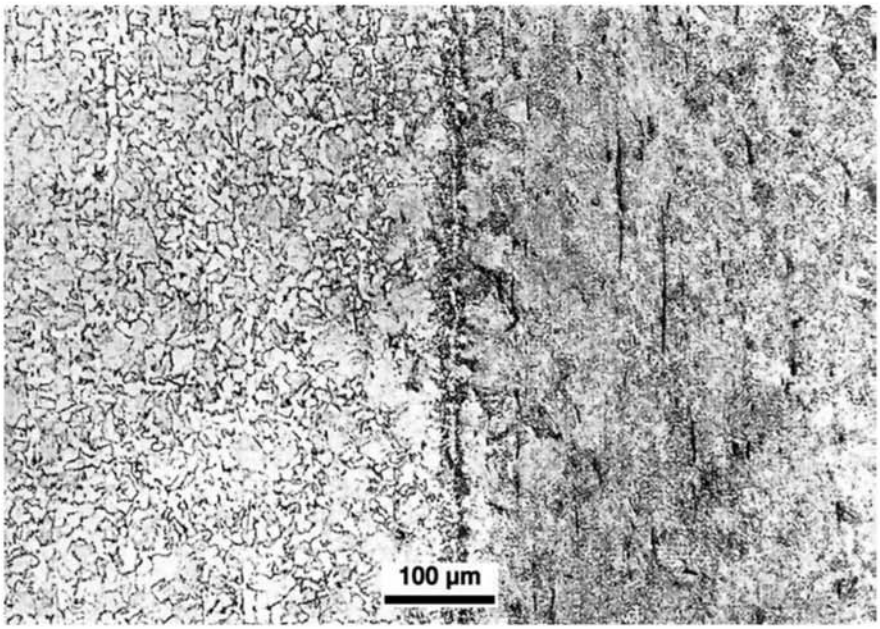

Fig. 10.77 Forge weld region of a steel hoe blade. High carbon steel (to the right) welded to low carbon steel (to the left). Quenched region. Martensite and elongated nonmetallic inclusions (to the right) and ferrite, acicular ferrite and martensite (to the left). Etchant: nital.

tive way to achieve this gradient of properties is with selective tempering, in which the extremity of the part that is to reach higher toughness is tempered at higher temperatures than the extremity where abrasion resistance is desired. The manufacturing process of forge welded tools has been important in the past because it made possible the refurbishing of worn tools (in small scale). Saw blades are also produced using forge welding or pressure welding. The simplest process involves fusion welding the segment of tool steel where the saw teeth will be machined to the lower alloy steel for the back side of the blade. Alternatively, using pressure and temperature, it is possible to pressure weld two segments of tool steels to the sides of the saw blade where most of the wear will concentrate. These manufacturing methods are schematically presented in Fig. 10.78.

10.6 Martempering

As discussed in the section "Quench Cracks," the superposition of thermal stresses and stresses associated with the martensitic transformation are responsible for the incidence of cracks and quenching distortion. In steels that have sufficiently high hardenability, a quenching operation involving a temperature homogenization stage before reaching M_s can be performed, as shown in Fig. 10.79. During martempering, the parts can be intermediately cooled into a furnace held at, for instance, 350 °C (660 °F) for a short time, just sufficient to equalize the temperatures on the surface and in the center of the part while the steel is still fully austenitic. Then cooling proceeds, forming martensite with less risk of cracking and excessive distortion. Notwithstanding the name of the treatment, tempering is still required after martempering.

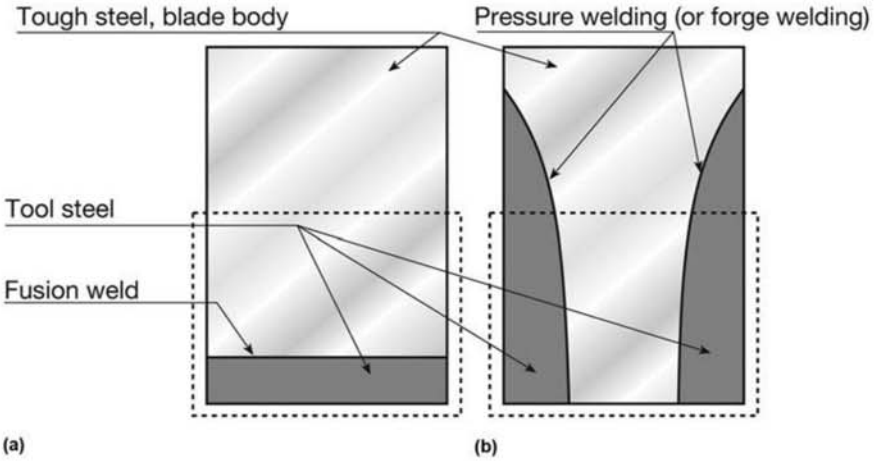

Fig. 10.78 Schematic cross section of two bimetallic saw blades. (a) The tool steel (high-speed steel) is fusion welded to a cheaper, higher toughness steel that will make up the body of the saw band. (b) The high-speed steel is forge welded (using pressure and temperature) to the tough steel, resulting in a configuration in which surfaces that have contact to the part to be sawed are made of high-speed steel.

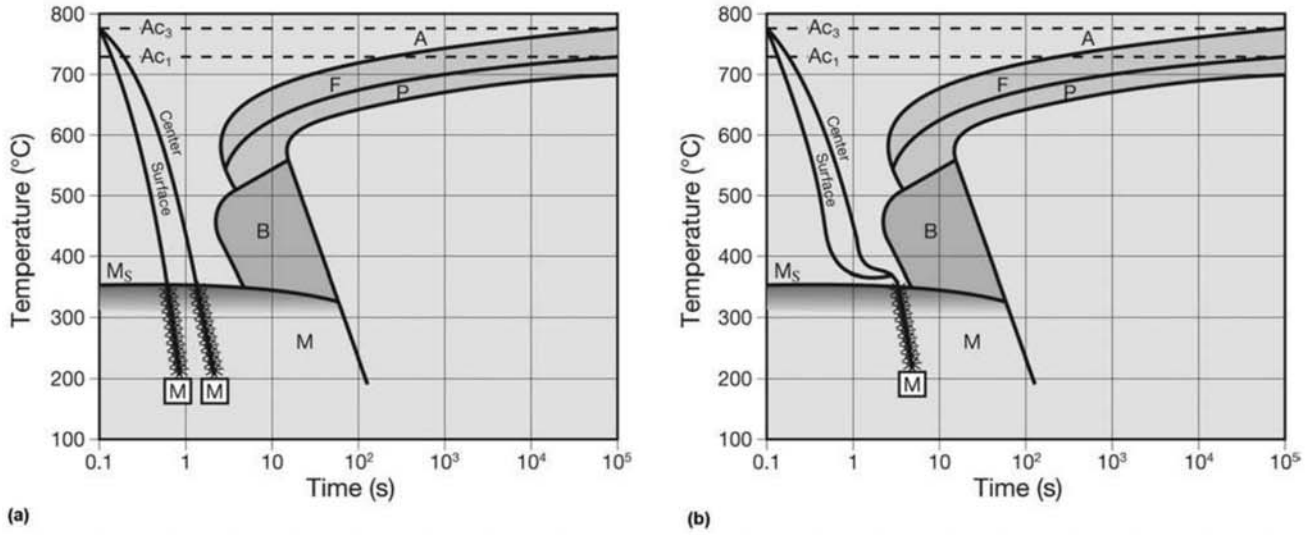

Fig. 10.79 During quenching (a), surface and core of the part will reach the M_s temperature at different times, increasing the stresses in quenching. During martempering (b), a short isothermal intermediate hold makes it possible to homogenize the temperature of the part before it reaches M_s, substantially reducing the quenching stresses. B = bainite, M = martensite, F = ferrite, P = pearlite, A = austenite.

10.7 Austempering

Austempering is a heat treatment conducive for bainite formation, in general, as indicated in Fig. 10.80. Examples of microstructures obtained with austempering are presented in Chapter 13, "Advanced Steels for Forming Operations," in this book.

10.8 Patenting

Patenting is a treatment usually applied to wires and rods during their manufacture, particularly to eutectoid compositions (Fig. 10.81). It is mainly composed of an austenitizing cycle followed by either air cooling or isothermal holding at a temperature below Ae_1. The main objective is usually to produce a fine pearlite structure.

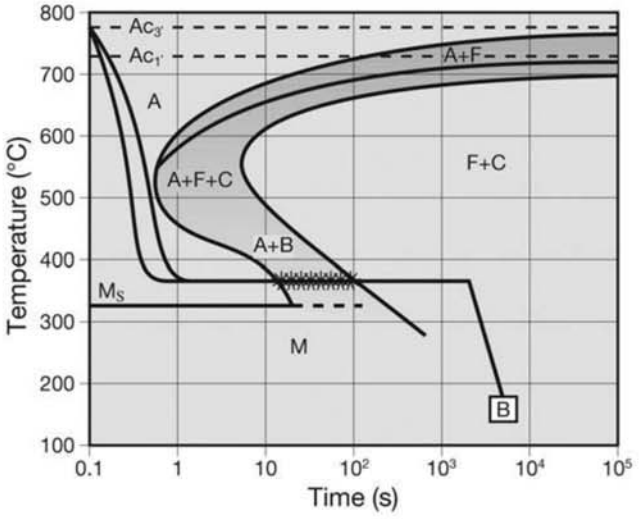

Fig. 10.80 Austempering is an isothermal heat treatment resulting most times in bainitic structures. After austempering, tempering is not required. B = bainite, M = martensite, F = ferrite, P = pearlite, A = austenite.

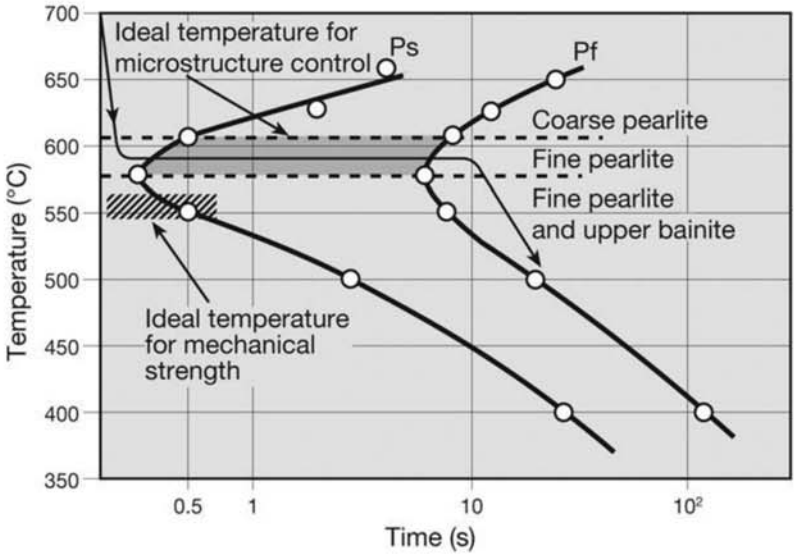

Fig. 10.81 Thermal cycle of patenting treatment. Ps = pearlite transformation start, Pf = pearlite transformation end. Source: Ref 23

10.9 Thermochemical Treatments

A large variety of thermochemical treatments can be applied to steels when it is desired to produce significant changes to the surface properties. These treatments are chosen usually when a part with a combination of a high toughness nucleus and a surface with high wear resistance is desired.

Gears and camshafts are some examples of parts in which the ideal combination of properties is achieved by altering the chemical composition of steel surface and then performing a heat treatment. Most thermochemical treat-

ments involve adding carbon and/or nitrogen to the surface layer of the part. These being interstitial solutes, their diffusion into the solid steel is relatively fast, making these treatments viable. Some treatments in which boron is introduced into the part surface are also used. Some steels are especially adequate for thermochemical treatments. The phrase "case hardening" is frequently used to encompass all these treatments.

The most common thermochemical treatments are:

- Carburizing, in which carbon is introduced in the steel surface in the austenitic range, usually at temperatures above 900 °C (1650 °F).
- Nitriding, in which nitrogen is introduced in the steel surface, usually at temperatures in the range of 500 to 590 °C (930 to 1095 °F).
- Carbonitriding, derived from carburizing, where carbon and nitrogen are introduced in the steel surface at temperatures above Ac_1, usually in the range of 800 to 900 °C (1470 to 1650 °F).
- Nitrocarburizing, in which carbon and nitrogen are introduced in the range of temperatures in which ferrite is stable, as in nitriding.

Common to all these processes is that as the interstitial element is introduced in the part, through the surface, it diffuses and forms a diffusion layer under the part surface. The depth and profile of this layer are important in defining its behavior.

Many industrial arrangements and conditions are available to perform these treatments, particularly with respect to the media used to provide and transport carbon and nitrogen. Solid, liquid, and gaseous media can be used. Presently, liquid and gaseous media are preferred, due to the highest rate of reaction. More details about the specific aspects of these treatments is available in Ref 3.

10.9.1 Carburizing

Carburizing steels generally have a carbon content in the range of 0.15% to 0.25%. Steels such as AISI 5120, 8620, 4118, 4620, and 4023 are some of the most commonly used steels for carburized gears, because it is possible to quench them in oil after carburizing. AISI 9310 and 4320 may be used in applications subjected to higher stresses. The carbon content at the surface is usually adjusted to a value in the range of 0.8% to 1% (Figure 10.82).

Two important aspects have a great influence on how carbon enters and distributes itself in the part. First is the type of medium used for carburizing. Second is the process of carbon diffusion in steel itself. Carburizing may be performed using gaseous, liquid, or solid media. Plasma carburizing is also used. The chemical potential of carbon in the carburizing medium defines the maximum carbon potential in the system and thus the carbon content on the part surface, which will be close or at equilibrium with the carburizing medium.

Diffusion of carbon inside the part is influenced not only by the carbon potential at the part surface, but also by temperature and steel composition. While the classical approach to calculate diffusion in carbon during carburizing is the use of standard analytical solutions (Ref 3), software is available that

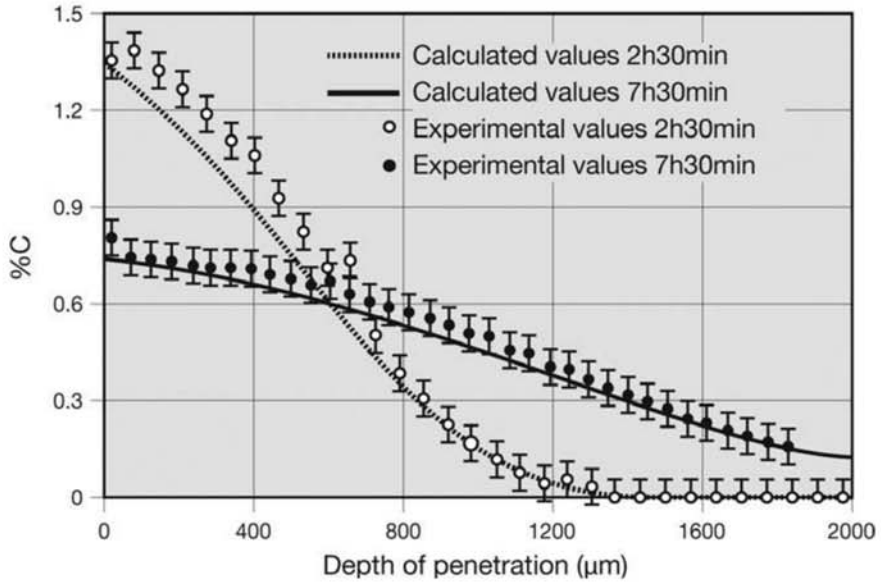

Fig. 10.82 Carbon content as a function of depth under the part surface in a steel containing Cr = 1% carburized for 2 h, 30 min (gas with 80% N_2 20% CH_4) followed by water quenching. The carbon content profile in the same steel subjected to an additional 5 h of homogenization heat treatment (called "diffusion"). Experimental values are compared to values calculated with DICTRA software. Source: Ref 45

can calculate diffusion, taking into consideration the effects of the various alloying elements in steel (Ref 46).

10.9.2 Solid Medium Carburizing—Pack Carburizing

Traditionally, carburizing has been developed using solid carburizing media. The slow kinetics of the process and the difficulties with precise control of the results are two factors that limit the application of this process. In any case, it is relevant to understand the processes defining the steel microstructure, because this has been the basis for the development of the other variants.

Carburizing is performed above the intercritical region, where steel has a high carbon solubility. Even with the source of carbon being a solid, it is evident that carbon must be transported to the steel via the atmosphere formed around the part, as it is surrounded by the solid "packing" material. The reaction $CO_2 + C = 2CO$ is critical for defining the chemical potential of carbon. The usual packing materials were mixtures of ground charcoal and carbonates. The carbonates act as catalyzers, increasing the proportion of CO in the gas to values very close to equilibrium. A classic carburizing mixture was composed of 40% barium carbonate and 60% charcoal. Because carburizing with solid media or pack carburizing material is a slow process that may require holding the part above the intercritical zone (900 to 1000 °C, or 1650 to 1830 °F) for hours, austenitic grain growth normally happens, as shown in Fig. 10.83. Thus, after pack carburizing, a heat treatment that refines the austenitic grain size is required. Normalizing was the process of choice. After normalizing, the external layer of the part may harden (air cooling can be sufficient to

form martensite in these high carbon compositions) as shown in Fig. 10.84. Figure 10.85 schematically shows that the quenching temperature has been sufficient to harden the carburized region due to its high carbon content, but did not affect the part core, which has low carbon content. This way, the part core maintains its toughness. An alternate to the normalizing followed by quenching option is double quenching. The first quenching is performed from around 900 °C (1650 °F), followed by a second quenching treatment, from a lower temperature (770 °C, or 1420 °F, for instance). In this case, the part core may transform to a finer structure with better toughness. The treatment is finalized with a tempering around 180 °C (355 °F) for stress relief. Tem-

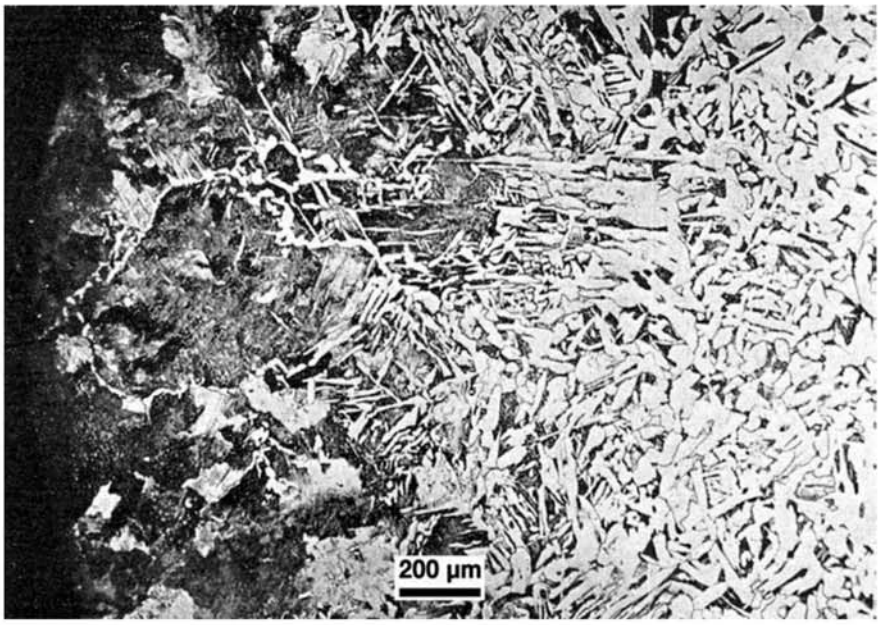

Fig. 10.83 Cross section, close to the surface of a low carbon steel bar pack carburized. Observe the increase in the carbon content and austenitic grain size at the surface (left), which resulted in the formation of acicular constituents during cooling. Etchant: nital.

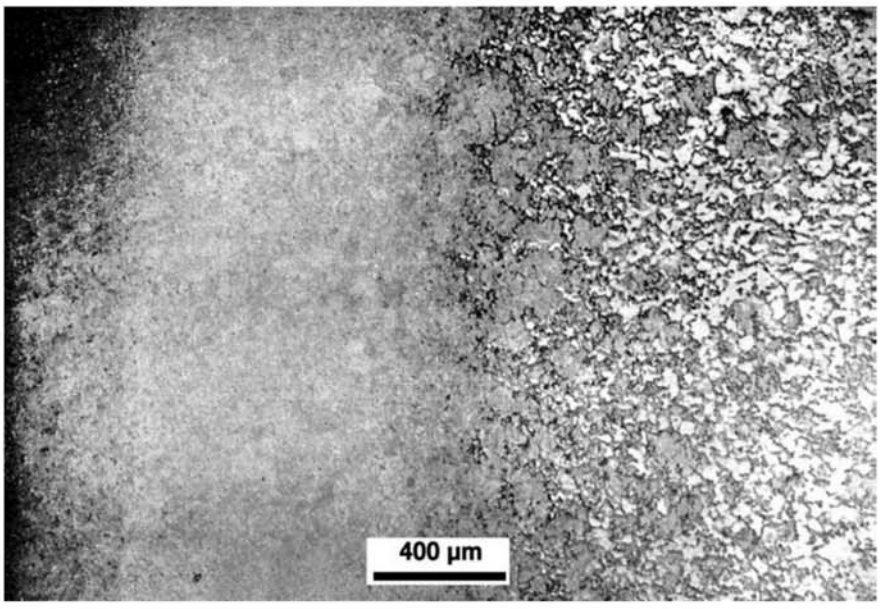

Fig. 10.84 Cross section, close to the surface of a low carbon steel bar pack carburized after normalizing and tempering (from 770 °C, or 1420 °F). The carburized region, on the left, is martensitic. Etchant: nital.

pering of carburized parts is, by necessity, performed at low temperatures so as not to significantly decrease the surface hardness. The carburized layer thickness depends on the processing time. Figure 10.86 presents the effect of carburizing time on the thickness of the carburized layer, measured using macrographic examination.

Adjusting the chemical potential of carbon during pack carburizing is extremely difficult. Excessive carburizing is an important risk in this process. In this case, a network of cementite can be formed, leading to cracks during

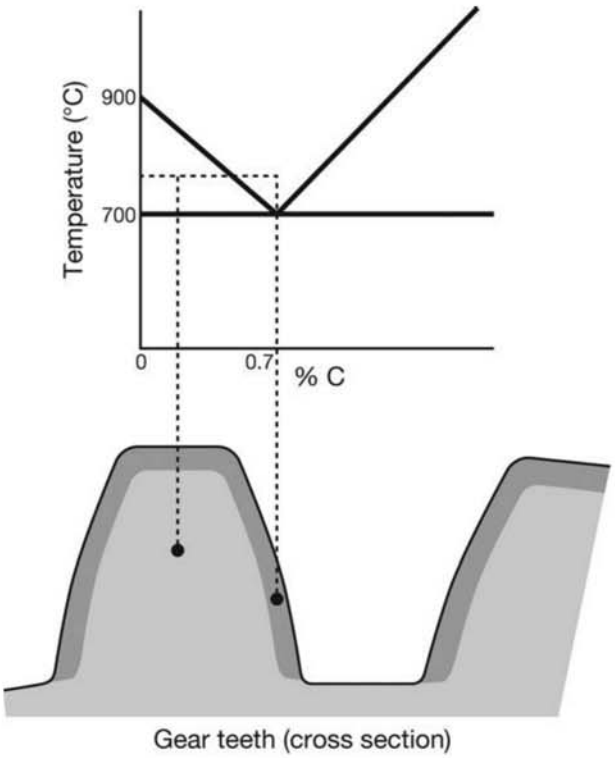

Fig. 10.85 Schematic diagram of the region of the part that has been austenitized for quenching in the example of Fig. 10.84. The carburized region has transformed completely to austenite, while the nucleus of the part is subjected to an intercritical treatment.

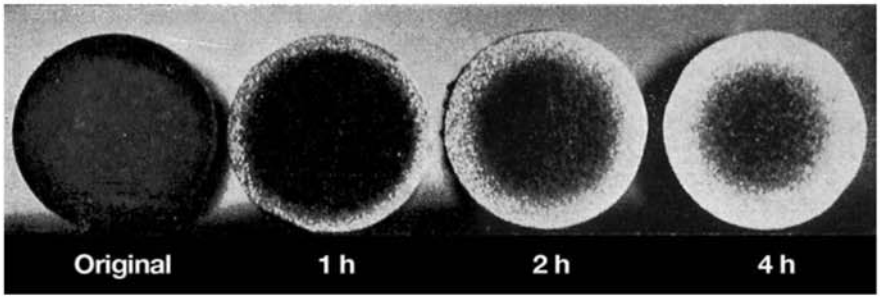

Fig. 10.86 Depth of penetration of pack carburizing as a function of treatment time. Transversal cross sections, etched with nital and illuminated with oblique lighting.

quenching and/or during final surface finishing. When steep carbon content gradients are formed, there is also the risk of carburized layer spalling. Metallographic examination can be used to evaluate depth and homogeneity of the carburized layer, as shown in Fig. 10.87 and 10.88. The carburized layer is also evident in fractographic examination (Fig. 10.89).

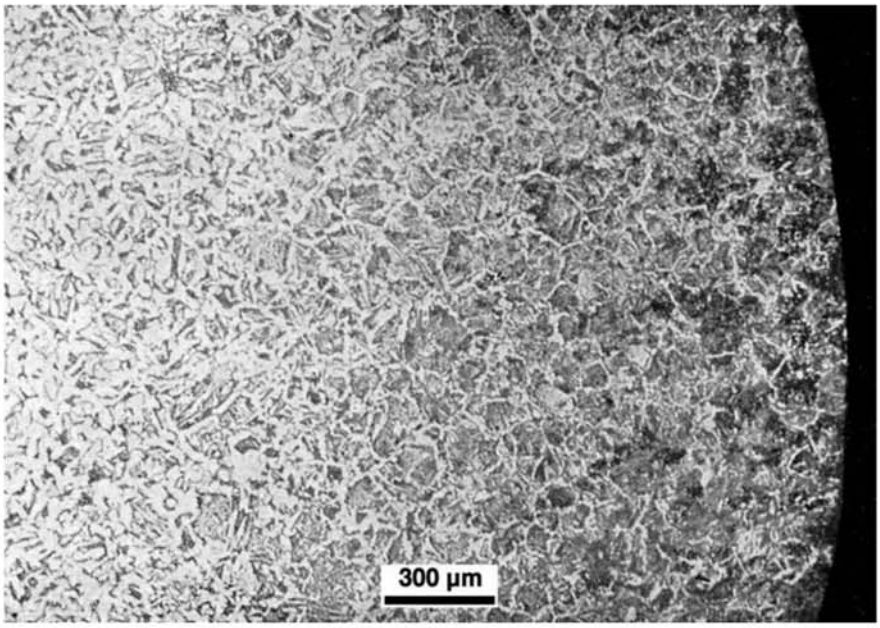

Fig. 10.87 Carburized region treated for 4 h at 1000 °C (1830 °F), not yet quenched. The variation in carbon content along the section is uniform. Etchant: nital.

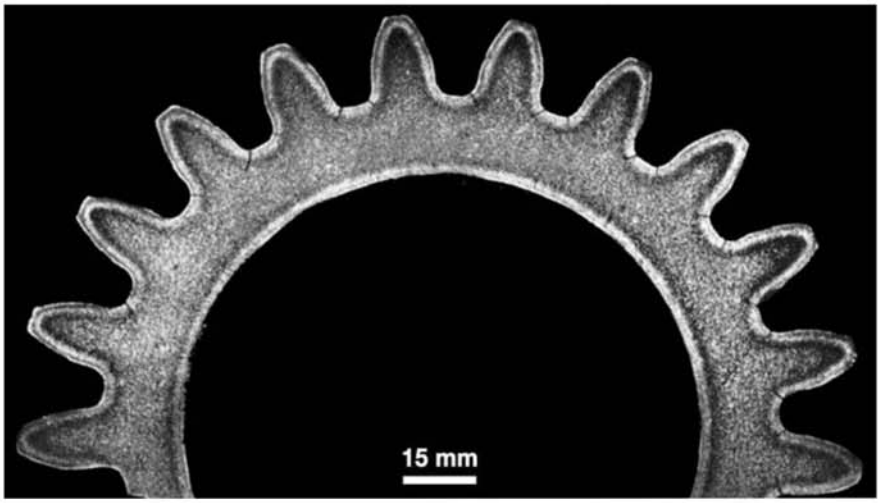

Fig. 10.88 Transverse cross section of a carburized gear. The carburization treatment was applied to the teeth and the internal surface. The macrograph shows the thickness of the carburized layer and its homogeneity. Cracks at the root of the teeth are also visible. The rest of the steel structure is homogeneous. Etchant: iodine.

10.9.3 Carburizing in Gaseous Media

The most widely used carburizing technique involves using a gaseous medium. In this case, previous surface cleaning is very important to ensure uniform results. The control of the carbon chemical potential usually involves gases that are a mixture of CO, CO_2, H_2, H_2O, and CH_4. Not only the carbon but also the oxygen potential must be properly controlled in the process to avoid excessive oxidation. To guarantee a good carbon distribution in the part, it is standard to perform a treatment for carbon diffusion, after the carburizing treatment but still in the austenitic phase field. The results are always similar to those indicated in Fig. 10.82. Figure 10.90 presents the structure of a part

Fig. 10.89 Fracture of a carburized gear in AISI 8620 steel. The fracture happened in the radial plane. To the right, fracture initiation at the root of one of the gear teeth (some secondary initiation also toward the gear hub). The fracture aspect changes highlight the carburized region indicated on a single position with two arrows (the carburized layer with high hardness is about 3 mm, or 0.1 in., thick). Courtesy of MRS Logística S.A., Rio de Janeiro, RJ, Brazil.

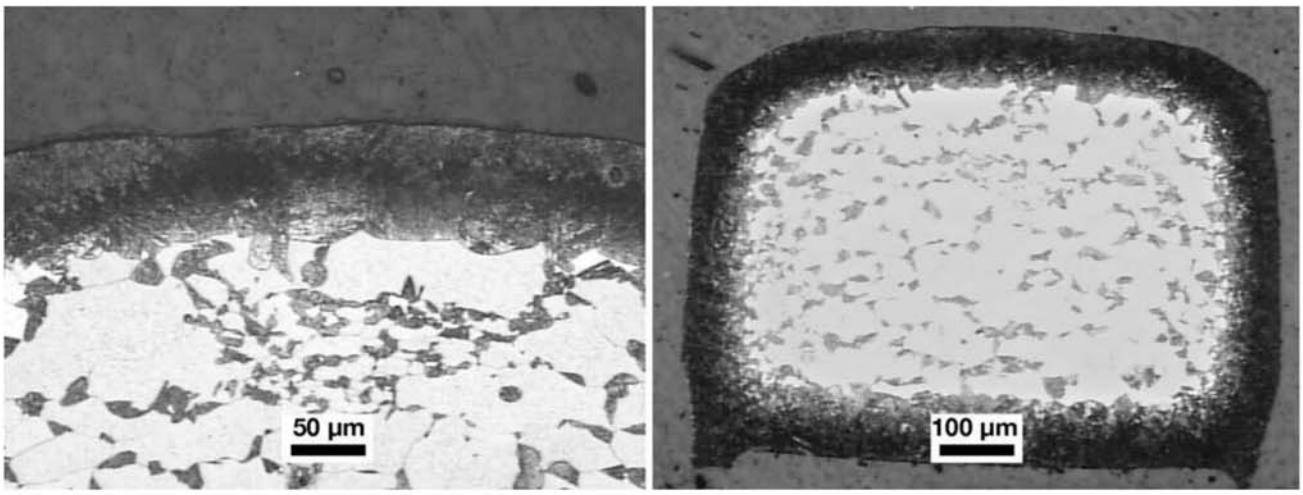

Fig. 10.90 AISI 5120 steel carburized in controlled atmosphere at 920 °C (1670 °F)/1 h cooled to 850 °C (1560 °F) and held for 2 h (diffusion treatment) and quenched in oil at 50–60 °C (120–140 °F), followed by tempering at 180 °C (355 °F) for 2 h. Courtesy of L. Queiroz and L.T. Sandor.

subjected to gas carburizing. The microstructure of carburized parts must be analyzed, considering that in quenching variations in cooling rates are superimposed on variations in chemical compositions, as indicated in Fig. 10.91. Figures 10.92 and 10.93 present parts that were carbonitrided using cyaniding, a treatment that uses a cyanide salt bath to introduce carbon and nitrogen into the steel. Special safety concerns must be addressed when consider-

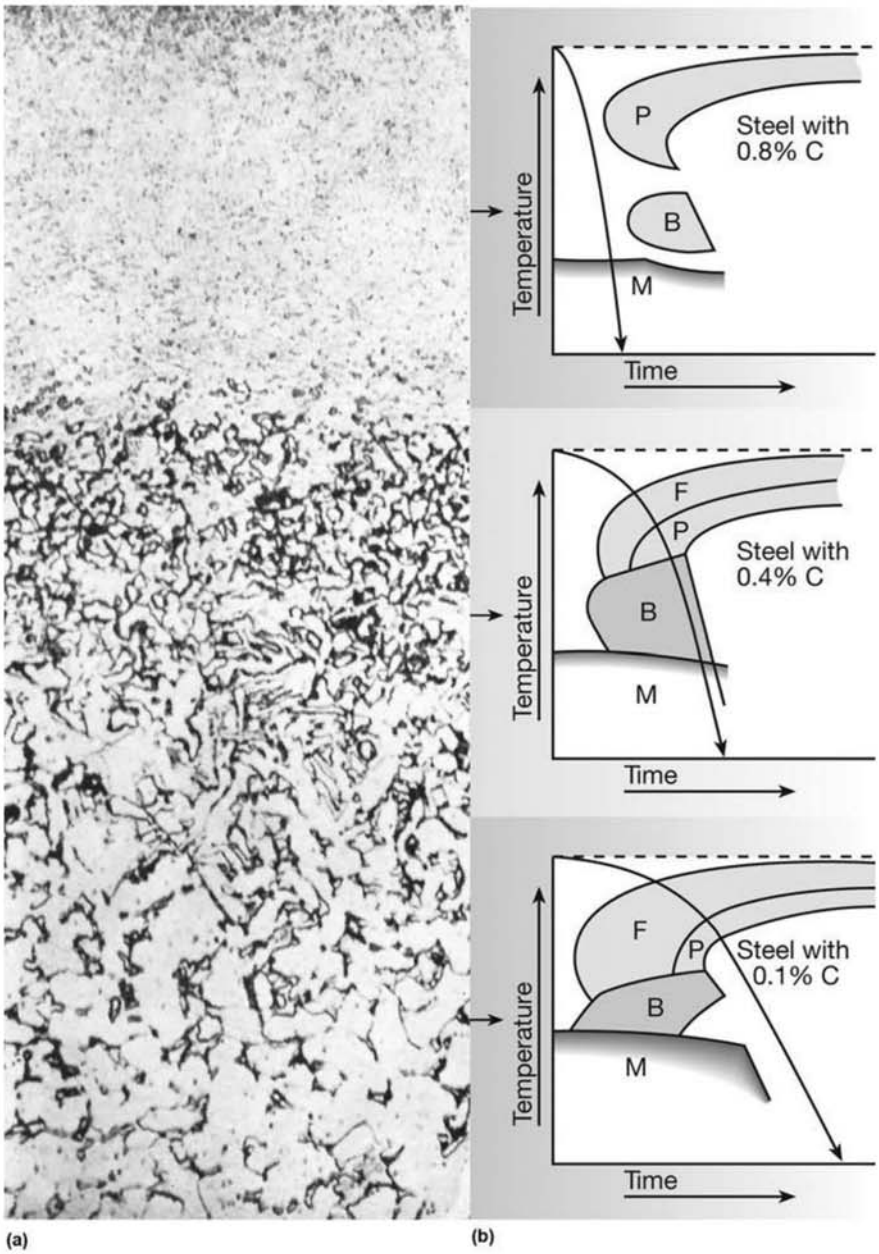

Fig. 10.91 (a) The microstructure of a carburized and quenched steel varies from the surface for two reasons: (1) carbon content decreases and (2) cooling rate decreases. (b) CCT curves for each chemical composition are sketched, with the applicable cooling curve superimposed. B = bainite, M = martensite, F = ferrite, P = pearlite. Etchant: nital.

ing these treatments. Because cyaniding is accomplished by submerging the parts in a molten salt bath that contains cyanides at temperatures in the range of 850 to 900 °C (1560 to 1650 °F), health and safety of the personnel involved are paramount concerns. Figure 10.94 presents an example of AISI 4340 steel quenched, tempered, and nitrided.

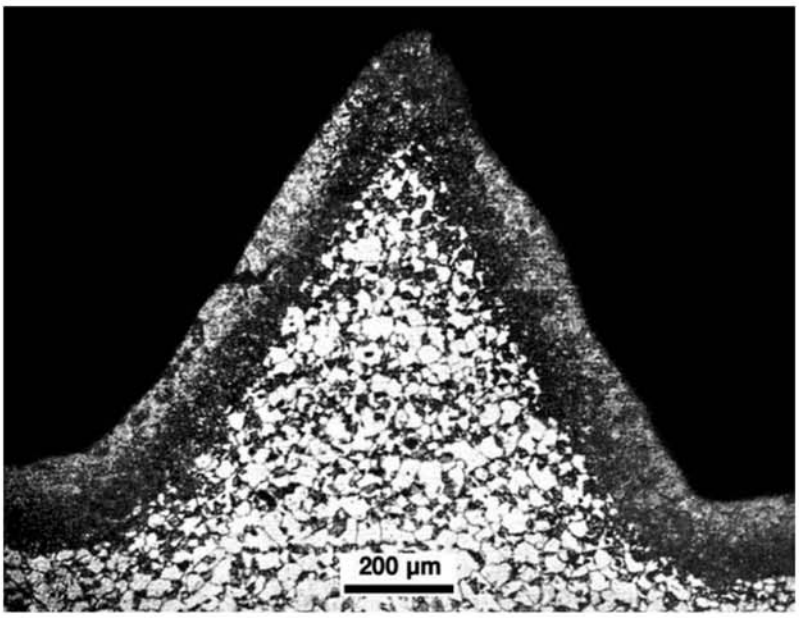

Fig. 10.92 Fastener thread cyanided (nitrogen and carbon introduced from a cyanide salt bath). The case thickness can be observed. Etchant: nital.

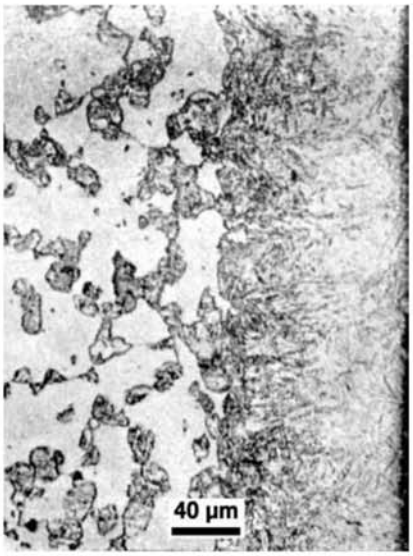

Fig. 10.93 Example of a cyanided layer, without a transition zone. Martensite in the region close to the part surface (to the right). In the part center, martensite and ferrite. Etchant: nital.

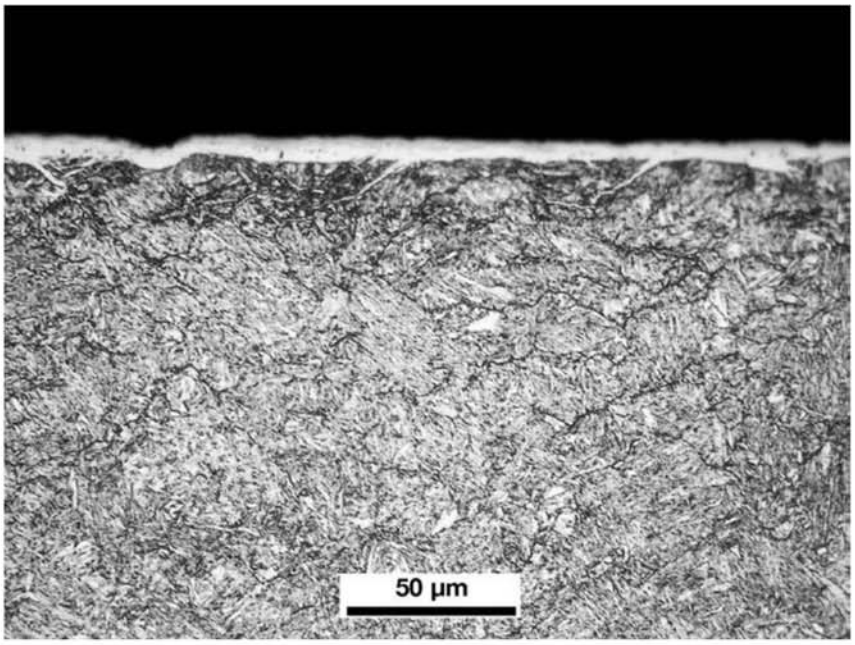

Fig. 10.94 Cross section transverse to the surface of a part made of AISI 4340 steel quenched, tempered, and nitrided. The white layer, rich in high-hardness nitride, can be observed (see Ref 3.) Courtesy of A. Zeemann, Tecmetal, RJ, Brazil.

The formation of a layer close to the part surface, rich in compounds (usually nitrides) is common in nitrided parts. This is usually called a "white layer."

Nitrocarburizing has many industrial applications (Ref 2). It is particularly used to increase the resistance to thermal fatigue and corrosion and to improve tribological properties of steels that will be used in hot working. In a study performed with the steel JIS S40C (similar to AISI 1040) Ref 47 performed the characterization of the structures formed. Figure 10.95 presents two examples of this characterization.

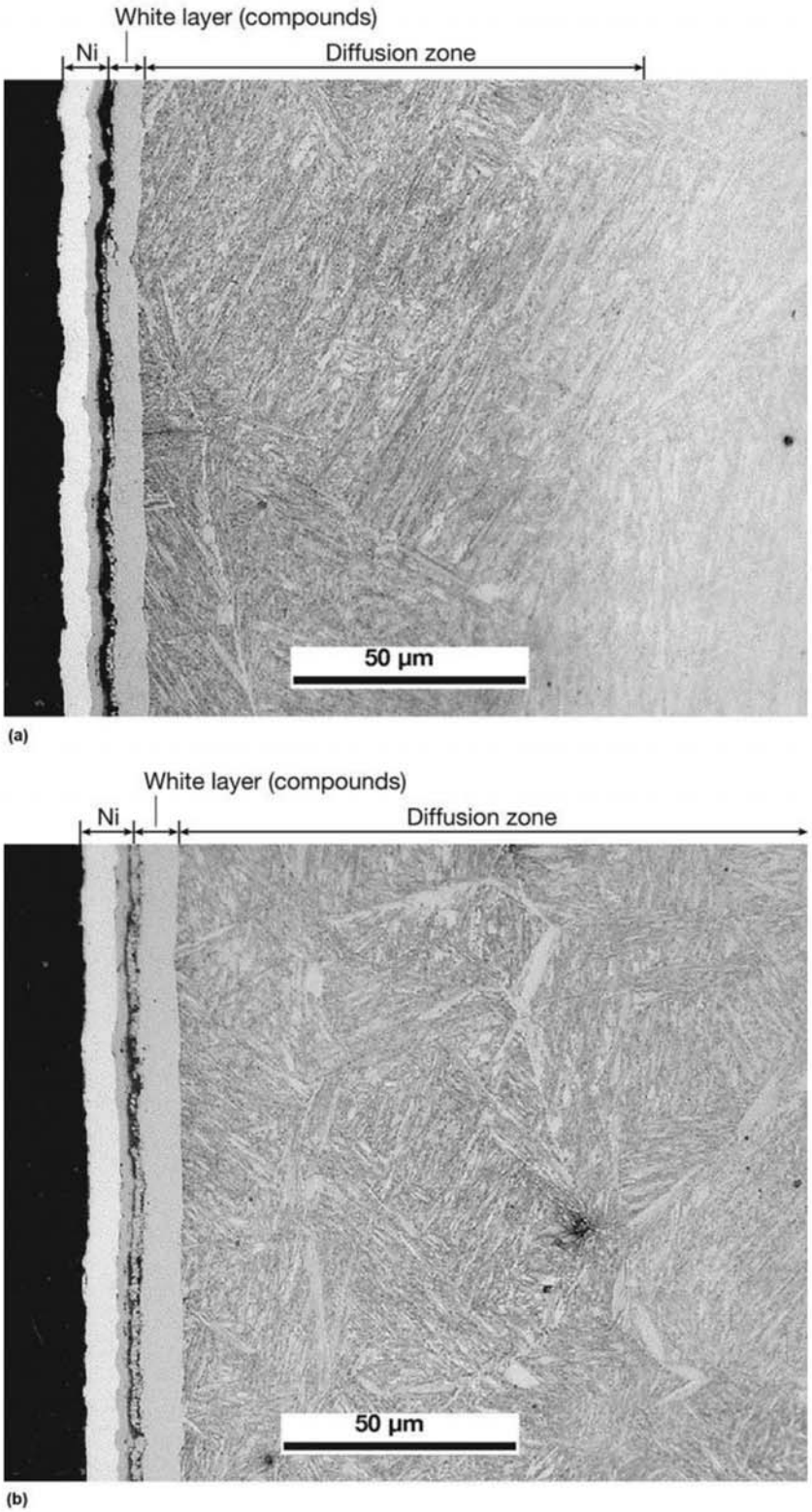

Fig. 10.95 Steel nitrocarburized at 550 °C (1020 °F) for 5 h. The surface was coated with a chemically deposited layer of hard nickel to preserve it for metallographic examination (indicated as Ni in the figure). The "white layer" is where the formation of high hardness nitrides occur. Tempered martensite. In the research that originated this sample, it was observed that the increase in steel chromium content increases the hardness of the diffusion zone due to the precipitation of CrN (observed in TEM), notwithstanding the fact that the diffusion layer has been reduced, as shown in (a). Reprinted from Denki-Seiko, courtesy of Daido Steel, Japan. Source: Ref 47

REFERENCES

1. API, API Spec 6A/ISO 10423—Specification for Wellhead and Christmas Tree Equipment, 19th edition, AP, 2004
2. ASTM, A941-13b Standard Terminology Relating to Steel, Stainless Steel, Related Alloys, and Ferroalloys, ASTM, 2013
3. J.L. Dossett and G.E. Totten, eds., *ASM Handbook Volume 4A Steel Heat Treating Fundamentals and Processes*, ASM International, 2013
4. S.W. Banovic, C.N. McCowan, and W.E. Luecke, *NIST NCSTAR 1-3E (Draft) For Public Comment Federal Building and Fire Safety Investigation of the World Trade Center Disaster Physical Properties of Structural Steels* (Draft), NIST2005
5. J.W. McEnerney and P. Dong, Recommended practices for local heating of welds in pressure vessels, Welding Research Council Bulletin, WRC, 2000
6. A.R. Troiano, The role of hydrogen and other interstitials in the behavior of metals, *Trans. ASM*, Vol 52 (1960), p 54–79, 1960
7. ISO, ISO 3763:1976(en), reapproved 2012, *Wrought Steels—Macroscopic Methods for Assessing the Content of Non-metallic Inclusions*, ISO, 2012
8. H. Schummann, K. Cyrener, W. Molle, H. Oettel, J. Ohser, and L. Steyer, *Metallographie*, Deutscher Verlag fur Grundstoffindustrie—Wiley-VCH, 1990
9. Fruehan, R. (ed.) *Making, Shaping, and Treating of Steel, Steelmaking and Refining Volume*, 11th edition, AISE Steel Foundation, 1998
10. A.W. Dana Jr., F.J. Shortsleeve, and A.R. Troiano, Relation of flake formation in steels to hydrogen microstructure and stress, *J. Metals Trans. AIME* (August 1955), p 895–905
11. T.E. Scott and A.R. Troiano, Hydrogen and segregates in flaking, *J. Metals* (September 1959), p 619–22
12. E. Fromm and G. Hoerz, Hydrogen, nitrogen, oxygen and carbon in metals, *Int. Met. Rev.*, Vol 5, No. 6 (1980), p 269–310
13. H. Ohtani, Processing—conventional heat treatments, In: *Materials Science and Technology-Constitution and Properties of Steels*, F.B. Pickering, ed., Wiley-VCH, 1996
14. F.L. Carvalho, *Influência do tamanho de grão austenítico na resistência à corrosão sob tensão de aços para aplicação Sour Service*, Masters thesis, UFMG, 2007
15. SAE, *SAE J419—Methods of Measuring Decarburization*, SAE International, 1983
16. ASM, *ASM Handbook 1. Properties and Selection—Irons, Steels and High-Performance Alloys*, 10th edition, Vol 1, ASM, 1990
17. K.E. Thelning, *Steel and Its Heat Treatment—Bofors Handbook*, Butterworths, 1975

18. ASM, *Atlas of Isothermal Transformation and Cooling Transformation Diagrams*, ASM International, 1977
19. Bosch, *Umwandlungsvorgänge und Gefügeausbildung bei rascher Temperaturänderung*, Bosch Norm N67W 2.2 (substituted), 1973
20. E.C. Bain and H.W. Paxton, *Alloying Elements in Steel*, ASM, 1966
21. ASM International, *SteCal 3.0* (CD-ROM), ASM, 2004
22. ASTM, ASTM A255–10(2014), *Standard Test Methods for Determining Hardenability of Steel*, ASTM, 2014
23. G. Krauss, *Steels: Processing, Structure and Performance*, ASM International, 2005
24. http://www.doitpoms.ac.uk/vidlib/videos/html/jet.html (accessed October 10, 2016)
25. http://www.doitpoms.ac.uk/tlplib/jominy/sim2.php (accessed October 10, 2016)
26. D. Lober, Informations about steel for metallographer, http://www.metallograf.de/jominy-eng/jominy.htm (accessed October 12, 2016)
27. R. Blondeau, P. Maynier, and J. Dollet, Prevision de la dureté et de la résistance des aciers au carbone et faiblement alliés d'après leur structure et leur composition, *Mém. Sci. Rev. Metall.*, Vol 70, No. 12 (1973), p 883–92
28. S. S. Babu, *Acicular Ferrite and Bainite in Steels*, Ph.D. thesis, University of Cambridge, 1992
29. http://calculations.ewi.org/vjp/secure/tttcctplots.asp (accessed October 12, 2016)
30. A. Sauveur, *Metallography and Heat Treatment of Iron and Steel*, 4th edition, McGraw-Hill, 1935
31. B.L. Bramfitt and J.G. Speer, A perspective on the morphology of bainite, *Metall. Trans. A*, Vol 21A (1990), p 817–29
32. C.S. Smith, Microstructure, *Trans. ASM*, Vol 45 (1953), p 533–75
33. M. Hillert, The nature of bainite, *ISIJ Int.*, Vol 35, No. 9 (1995), p 1134–40
34. G.A. Roberts, G. Krauss, R. Kennedy, and G. Roberts, *Tool Steels*, 5th edition, ASM, 1998
35. R.R. Blackwood, L.M. Jarvis, D.G. Hoffman, and G.E. Totten, Conditions leading to quench cracking other than severity of quench, In: *18th Heat Treating Society Conference Proceedings*. ASM International, 1998
36. L.C.F. DeCanale, G.E. Totten, R.R. Blackwood, L.M. Jarvis, and D.G. Hoffman, An overwiew of non-quench related problems often attributed to the quenchant and quenching process, In: *59 Congresso Anual da Associação Brasileira de Metalurgia e Materiais*, ABM, 2004

37. R.W.K. Honeycombe, *Steels: Microstructure and Properties*, Edward Arnold, 1981

38. L.T. Sandor, *Influência do teor de carbono na propagação de trinca e na tenacidade à fratura em camada cementada em aços de alta resistência mecânica*, PhD dissertation, UNICAMP, 2008

39. J.H. Holloman and L.D. Jaffe, Time-temperature relations in tempering steels, *Trans. AIME*, Vol 162 (1945), p 223–49

40. T. Inoue, A new tempering parameter and its application to the integration of tempering effect of continuous heat cycle, *Testsu-to-Hagane* Vol 66, No 10. (1980), p 1532–41 (74–89)

41. Nagoya International Training Center, *Precautions against Failure of Heat Treatment*, Japan International Cooperation Agency, 1974

42. G. Krauss, Deformation and fracture in martensitic carbon steels tempered at low temperatures, *Metall. Mat. Trans. B*, Vol 32B, No. 2 (2001), p 205–21

43. A. Reguly, T.R. Strohaecker, G. Krauss, and D.K. Matlock, Quench embrittlement of hardened 5160 steel as a function of austenitizing temperature, *Metall. Ma. Trans. A*, Vol 35A (2004), p 153–62

44. S. Zaefferer, P. Romano, and F. Friedel, EBSD as a tool to identify and quantify bainite and ferrite in low-alloyed Al-TRIP steels, *J. Microsc.*, Vol 230, No. 3 (2008), p 499–508

45. T. Turpin, J. Dulcy, and M. Gantois, Carbon diffusion and phase transformations during gas carburizing of high-alloyed stainless steels: experimental study and theoretical modeling, *Metall. Mat. Trans. A*, Vol 36A (2005), p 2751–60

46. A. Borgenstam, A. Engstrom, L. Hoglund, and J. Agren, DICTRA, a tool for simulation of diffusional transformations in alloys, *J. Phase Equil.*, Vol 21, No. 3 (2000), p 269–80

47. N. Yokoi, Y. Hiraoka, and K. Inoue, TEM observation of microstructure in diffusion layer nitrocarburized hot work die steel, *Denki-Seiko*, Vol 78, No. 4 (2007), p 315–22

Metallography of Steels—Interpretation of Structure and the Effects of Processing
Hubertus Colpaert
Updated and Translated by André Luiz V. da Costa e Silva

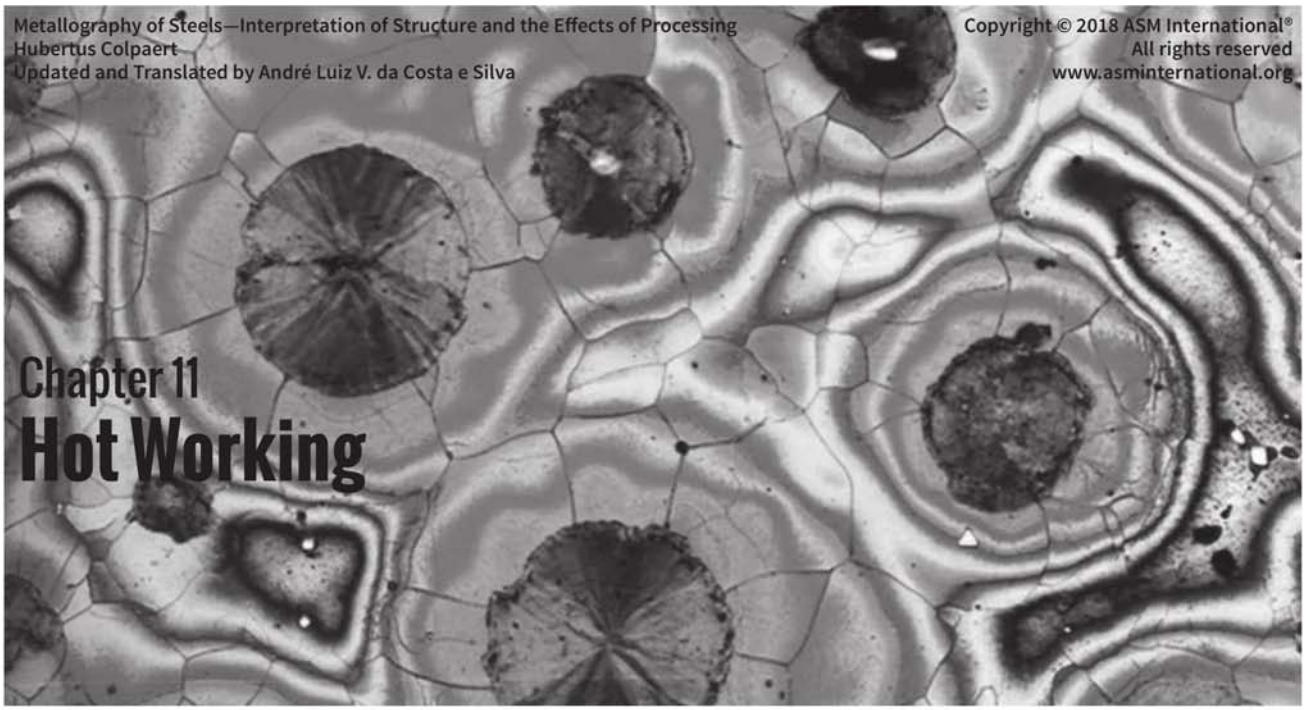

Chapter 11
Hot Working

Steels are subjected to mechanical working (or forming) for two main reasons:

- To change shape and dimensions
- To alter structure, at different scales

The temperature at which mechanical work is performed is an important variable, as are the deformation rate and the prevailing stress state during the forming process.

It is normal to divide working (or forming) into hot and cold working, notwithstanding the fact that in latter decades "warm working" processes have been cited and used more often as important alternatives in steel processing.

11.1 Hot Working and Cold Working

Process temperature is the variable that allows the most consistent classification of steel mechanical working in terms of the product characteristics.

In metallurgy, the distinction between hot and cold is not set by a single, absolute temperature. In simplified terms, working is considered to be performed "cold" when it is performed at conditions in which the deformation energy is stored in the material, recovery and recrystallization processes not being active. Hot working processes, on the other hand, are distinguished by significant structural changes in the material that eliminate a large part of the deformation energy via recovery and recrystallization. A limit frequently used as a reference to distinguish hot and cold work is $0.5T_m$, where T_m is the melting point of the metal being worked, in Kelvin. In an attempt to better define what would be "warm working," some authors have adopted the range of $0.3T_m$ to $0.5T_m$ to define this operation. Beside the important structural differences, two other important aspects differentiate cold and hot work: forming steel at high temperatures usually results in surface oxidation and distortion related to temperature change. Thus, cold worked products will generally

have better surface finish and can be produced to narrower dimensional tolerances. Essentially all steel products that are subjected to mechanical work are subjected at least to hot working. Cold worked products are usually obtained from semi-finished products that have been previously hot worked. For this reason, hot working is discussed before cold working, which is detailed in the next chapter.

11.2 Main Effects of Hot Working

11.2.1 Effects on Mechanical Strength

Generally, hot working is the first step in forming ingots and products from continuous casting. Increasing the working temperature results in a decrease in the yield stress and mechanical strength of the material, thus reducing the forces and energy required to cause deformation (Fig. 11.1). For this reason, the power needs in the forming equipment are lower than those required if working was not performed at high temperature.

11.2.2 Closing Cavities

Working at high temperatures will promote diffusion. This enhances the reduction of chemical heterogeneities caused by solidification segregation in the ingot. Furthermore, small pores and cavities naturally occurring during the solidification processes may be eliminated by "forge welding" as long as an adequate stress state is present, together with sufficient time and temperature for the defect "healing" (Fig. 11.2).

A Lower Quality "Wrought Iron"—A Historical Note

The possibility of forge welding—welding by pressure and temperature—of steel parts has been explored in many historical processes for steel production, as discussed in Chapter 2, "Processes in Steel Production," in this book. Besides the Catalan forge and the puddling process, in which forge welding is an integral part, a lower quality product, produced from pieces of iron from puddling and pieces of low carbon iron, consolidated by hot forg-

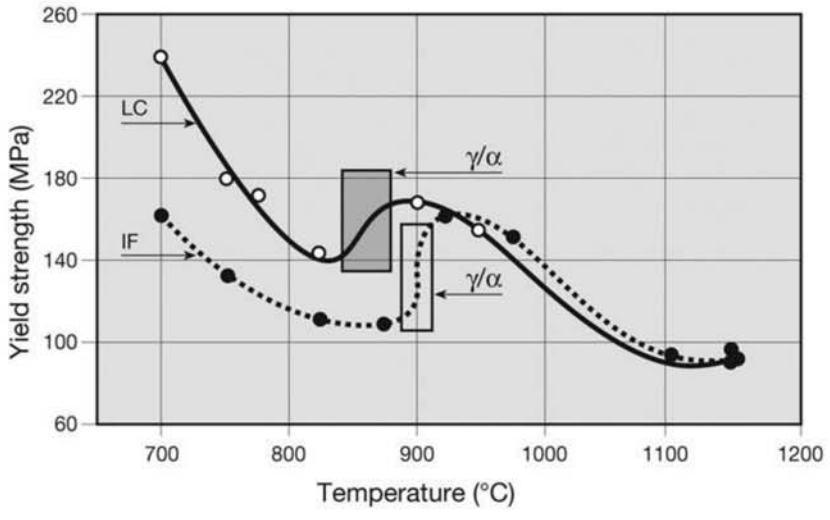

Fig. 11.1 Changes in the yield stress of a low carbon steel (LC) and an interstitial free (IF) steel. The region corresponding to the phase transformation is indicated. Source: Ref 1

ing, has been used in the past to produce engineering parts, as shown in Fig. 11.3. This has been called "package iron" in some countries.

It is important to remember that forge welding in itself does not lead to lower quality parts. The famous Japanese swords *nippon-tô* (Ref 3) or *katana*, for instance, are manufactured by the controlled forge welding of pieces of high-purity steel (*tamahagane*) produced in a reduction furnace (*tatara*) (Ref 4). The parts produced by forge welding many pieces of high-purity steel were successively folded and forged, resulting in a material with exceptional properties, hard to achieve today using other processing routes. Finally, a "plate" of higher carbon steel, which would form the cutting edge and the outer surfaces of the sword, was folded around a core of a high-toughness lower carbon piece that constituted the blade core. The heat treatment was performed in a differential way to provide maximum hardness to the edge and peak toughness for the whole blade. Yoshindo Yoshihara is a Japanese master sword maker who uses the exact technique described in Ref 4. Many videos detailing the technique are available online. (A detailed documentary is available in Ref 5.)

11.2.3 Change of Shape and Distribution of Segregates

The change in shape of the product associated with the reduction of its dimensions perpendicular to the direction of deformation (the thickness direction, in the case of flat rolled products, and the radial direction in simply produced cylindrical products, for instance) also results in the decrease of the distance between the dendrite arms that originated from the solidification process (see Chapter 8, "Solidification, Segregation, and Nonmetallic Inclusions," in this book). Orientations in a part can be defined based on the highest deformation direction: longitudinal, transverse, or normal; or based

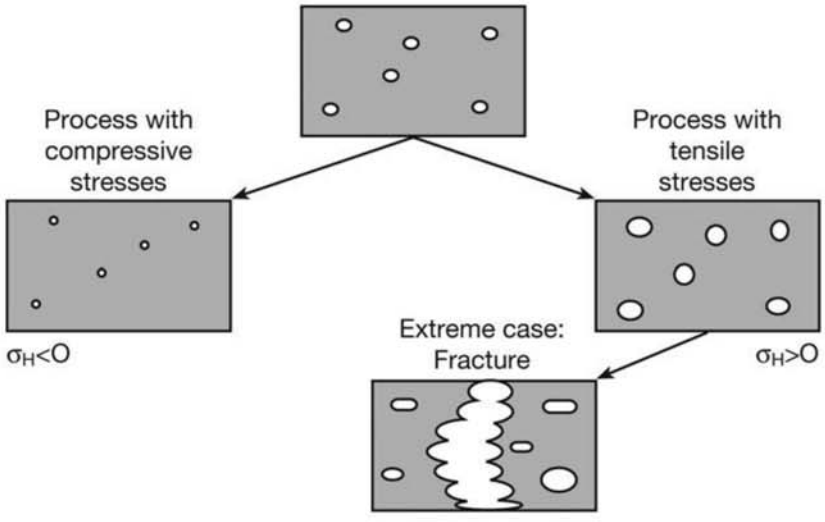

Fig. 11.2 The effect of deformation on "cavities" present in the material. Hydrostatic compressive stresses (σ_H) are essential to cause the consolidation and elimination of "cavities" (pores, shrinkage cavity, etc.). Unfavorable stress states may even lead to rupture during forming. Source: Ref 2

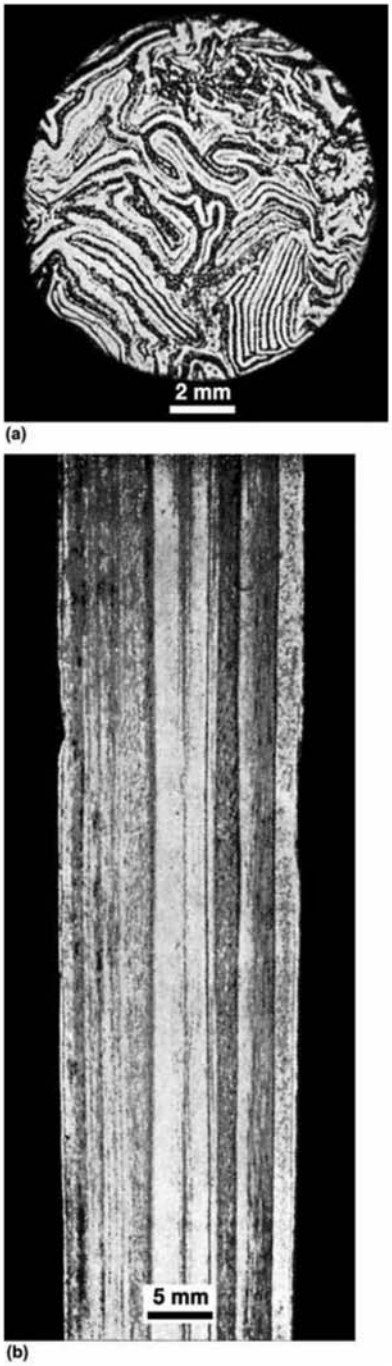

Fig. 11.3 A low-quality wrought iron made from puddling iron and pieces of used iron. (a) Transverse cross section trough of a product made of thin plates of iron wrought together. (b) Longitudinal section of a round bar. Etchant: iodine.

on the part geometry: axial, radial, and tangential, for instance. To correlate these ways of defining orientations in a part, one must know the details of the deformation schedule used to form the part. The reduction of the distance between dendrite arms also favors the product chemical composition homogenization, by diffusion. For this reason, the degree of reduction or the degree of deformation in the hot working processes is particularly important. Figures 11.4 and 11.5 present the changes in dendritic structure as the material is subjected to increased degrees of hot working.

The strong orientation that microsegregated regions take during solidification end up giving the material a structure that on the macroscopic scale resembles "fibers" oriented in the direction of the larger elongation the material suffered during work, as shown in Fig. 11.4. It is thus common to discuss the fibers in a material and how they are altered in forming processes or during subsequent machining operation. The effect of deformation is much clearer in a longitudinal section (containing the direction of main deformation) than in the transverse section, as can be observed in Fig. 11.4 and 11.5.

From a macroscopic viewpoint, the effect of deformation on the segregation characteristics of ingots and continuous casting products can also be clearly observed, as shown in Fig. 11.6 to 11.18.

11.2.4 The Effect on the Insoluble Phases—Nonmetallic Inclusions and Stable Carbides, Carbonitrides, and Nitrides

Phases that are not soluble in the steel matrix at the hot-working temperature (for instance, primary carbides in high-speed steels) and nonmetallic inclusions have their shape and distribution altered by hot working, contribut-

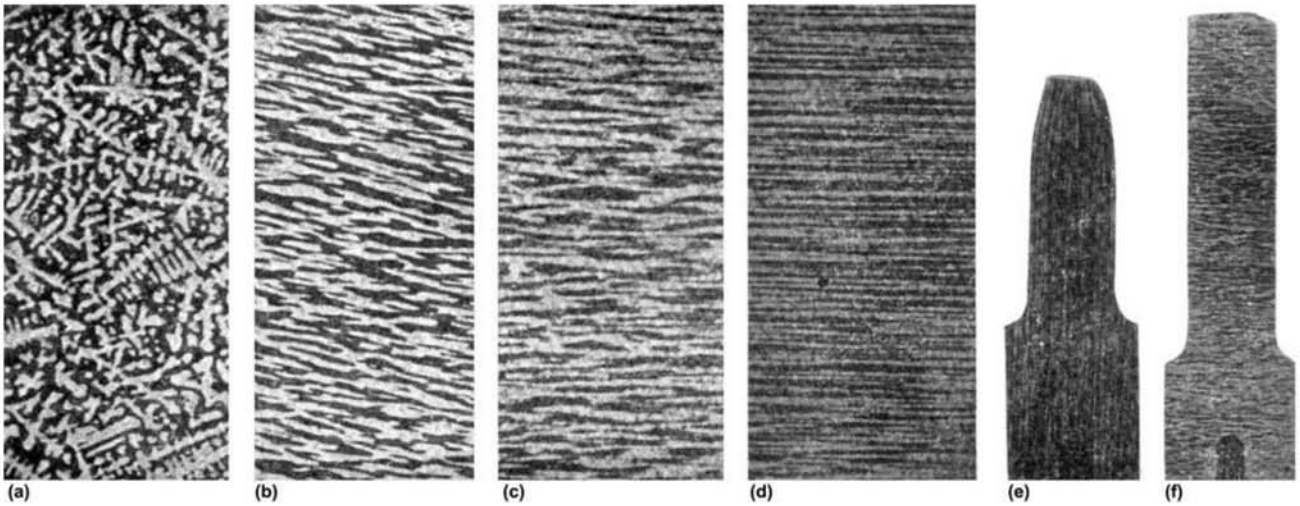

Fig. 11.4 The effect of hot working on the macrostructure of a steel. (a) Dendritic structure in the original ingot. (b) Cross section after a reduction by hot working to 1/5 of the cross-sectional area. (c) Cross section after a reduction by hot working to 1/30 of the cross-sectional area. (d) Cross section after a reduction by hot working to 1/150 of the cross-sectional area. (e) A longitudinal section through a longitudinal tensile specimen taken from the material shown in (d). (f) A longitudinal section through a transverse tensile specimen from the same material. Source: Ref 6

ing to the formation of a structure that retains the "memory" of the hot working to which the part was subjected.

Nonmetallic Inclusions

In the case of nonmetallic inclusions, the ability of these insoluble phases to deform or not at the temperatures of hot working can be measured through the relative plasticity between steel and inclusion, as proposed in Ref 8, shown in Fig. 11.19. When the relative plasticity has a value of 1, the inclusion

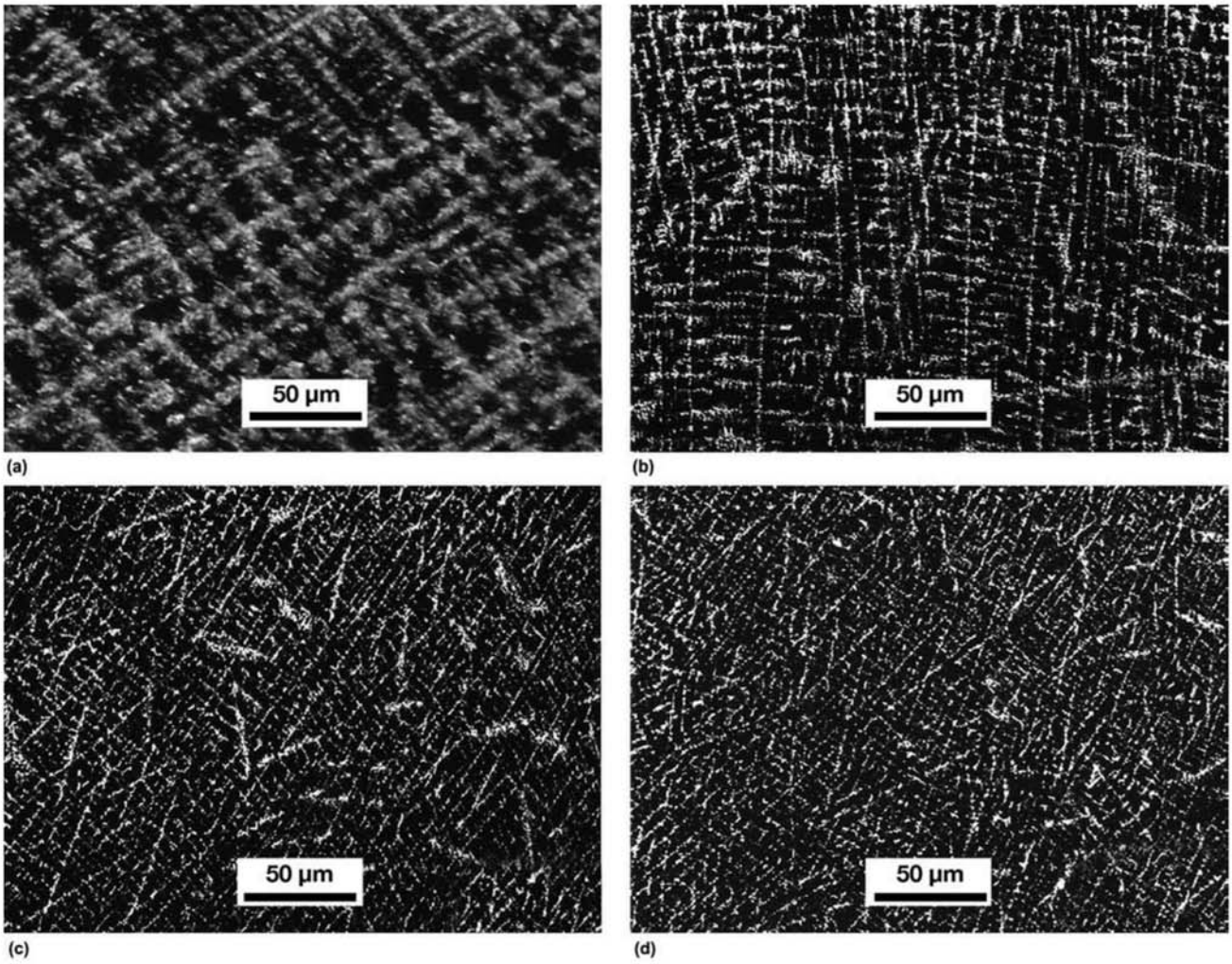

Fig. 11.5 Transverse cross sections of round bars of AISI 10V45 steel rolled from a continuous cast billet of 178 × 178 mm (7 × 7 in.) cross section. The deformation ratio during rolling was measured as the ratio between the initial and final cross-sectional areas (a) 7:1, (b) 10:1, (c) 27:1, and (d) 49:1. Some remaining image of the dendritic structure of the billet can still be observed. Etchant: hot etching with a water solution of picric acid with a surfactant agent (sodium tridecyl benzene sulfonate), proportions not informed (reactant is similar to Bechet-Beaujard). As in the case of Oberhoffer etchant (Fig. 8.38, in Chapter 8, "Solidification, Segregation, and Nonmetallic Inclusions," in this book) this etchant does not reveal the ferrite and pearlite microstructure but the variations in chemical composition in the sample. Reproduced with permission from Springer Science and Business Media. Source: Ref 7

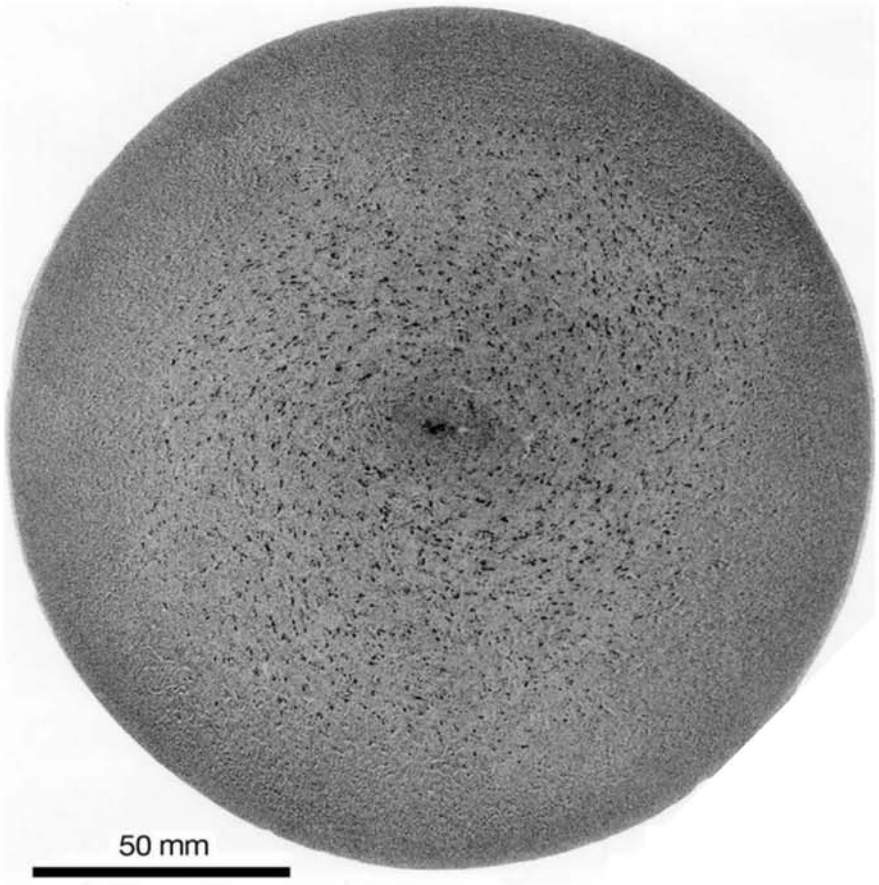

Fig. 11.6 Transverse cross section of a forged rail axis. Segregated regions originated from the "A" segregates in the original ingot can be seen (in the transverse section they appear as dark "dots"). The outer region (around 30 mm, or 1.2 in.) is homogeneous, and there are practically no indications of the previous dendrites in the macrograph. As one moves to the center of the forging (where the solidification times were longer in the ingot, and where sometimes the deformation is lower), residues of the dendritic structure can be seen. Etchant: hot hydrochloric acid. Courtesy of M. Talarico, N. Oliveira, CETEC, Belo Horizonte, MG, Brazil.

deforms the same amount as the steel matrix. When this value is 0, the inclusion does not deform during working at the indicated temperature.

The effect of hot working on the morphology of the nonmetallic inclusions will be directly dependent on their initial shape and distribution and on their plasticity, together with the temperature and deformation cycle to which the material is subjected. The various results possible are schematically presented in Fig. 11.20. Nonmetallic inclusions have a large effect in various important properties of steel products. They normally occur in sizes and volume fractions that can influence steel properties:

- Properties associated to the ductile fracture process
  a. Ductility
  b. Elongation and reduction of area (in tensile test)

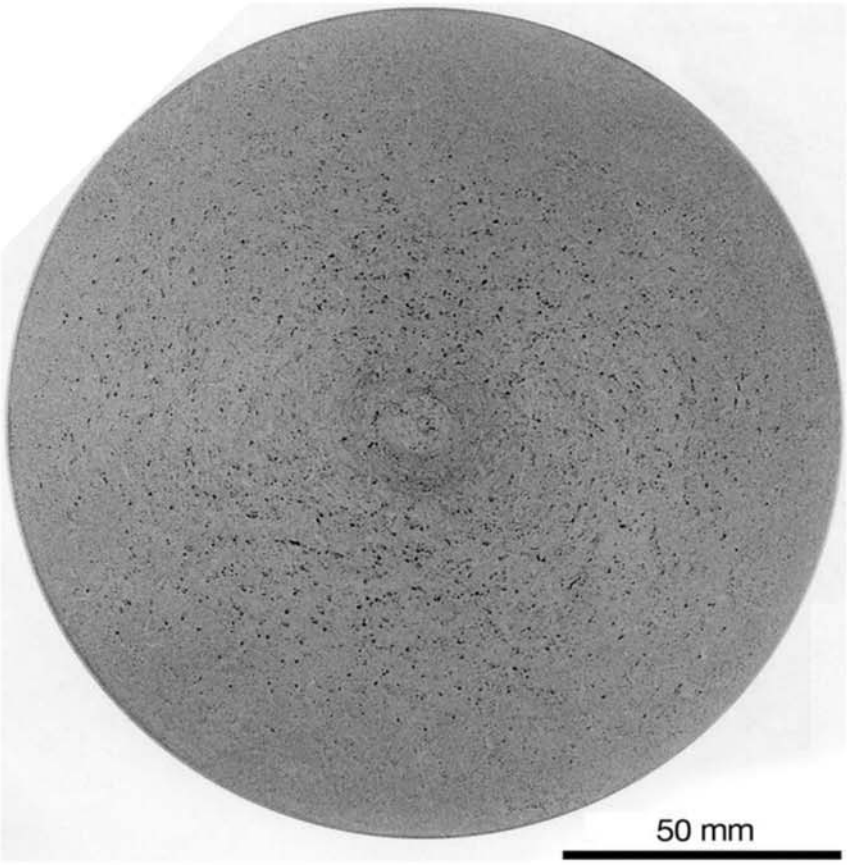

Fig. 11.7 Transverse cross section of a forged rail axis. The segregated areas originated from the "A" segregates are less pronounced than in Fig. 11.6. These comparisons can only be performed if the parts are prepared and etched in exactly the same conditions. Etchant: hot hydrochloric acid. Courtesy of M. Talarico, N. Oliveira, CETEC, Belo Horizonte, MG, Brazil.

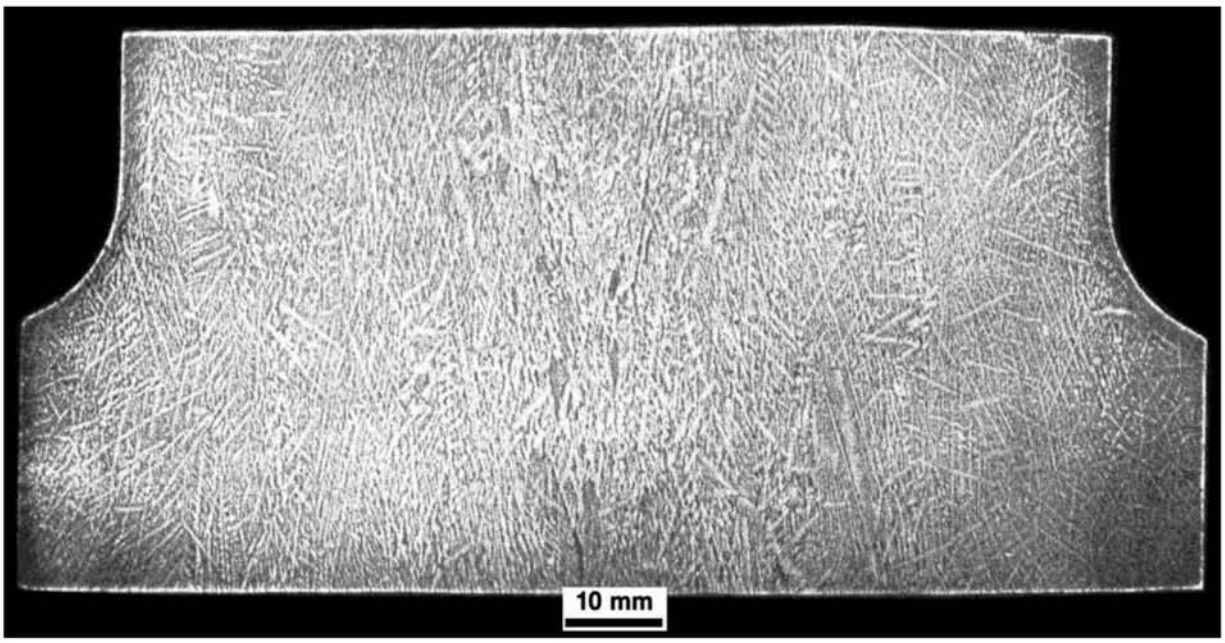

Fig. 11.8 Longitudinal cross section of a forged rail axis in the region where there is a transition in axis diameter (the wheel would be assembled in the region shown in the lower part of the figure). Large dendrites only lightly altered by deformation can be seen. This indicates that the degree of deformation during hot working was probably not sufficient to produce the desired changes in the part structure. The longitudinal section (parallel to the direction of larger deformation during hot working) is normally the most adequate to evaluate the degree of deformation. Etchant: iodine.

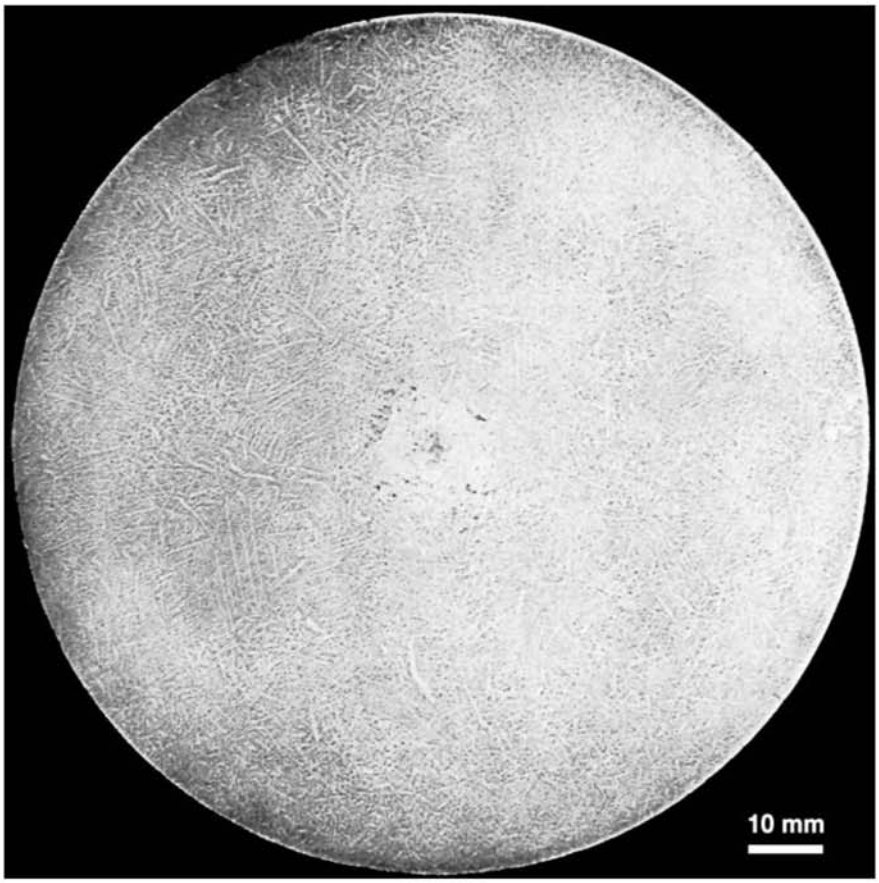

Fig. 11.9 Transverse cross section of the forged rail axis shown in Fig. 11.8. Dendritic structure with little segregation in central region (compare with Fig. 11.6 and 11.7, and consider the axis diameters). Etchant: iodine.

c. Toughness in the region of ductile fracture and ductile to brittle transition temperature

- Fatigue resistance
- Ability to be polished
- Corrosion resistance

Furthermore, nonmetallic inclusions are decisive in defining the extent of the anisotropy in these properties. The effect of nonmetallic inclusions on the properties related to ductile fracture, for instance, is well characterized and depends mostly on the fraction of the cross section transverse to the loading that is occupied by these particles as shown in Fig. 11.21. Manganese sulfide, a classical inclusion in steel, is plastic at hot working temperatures and elongates (Fig. 11.22–11.24). Calcium treatment of the liquid steel can be used to decrease the plasticity of the sulfides still left in the steel by making them richer in calcium (Fig. 11.25).

The increase in understanding the effect of nonmetallic inclusions on the various properties of steel has led to the development of what is currently

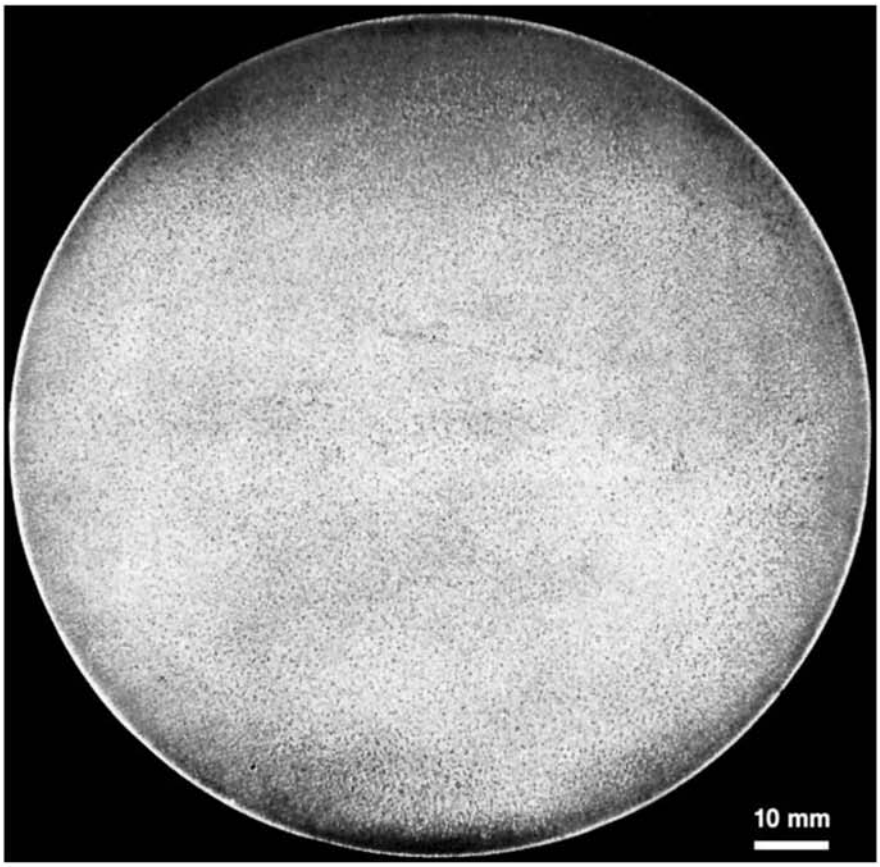

Fig. 11.10 Transverse cross section of a tram axis. Homogeneous macrostructure. Neither segregation nor dendrites are observed. Etchant: iodine.

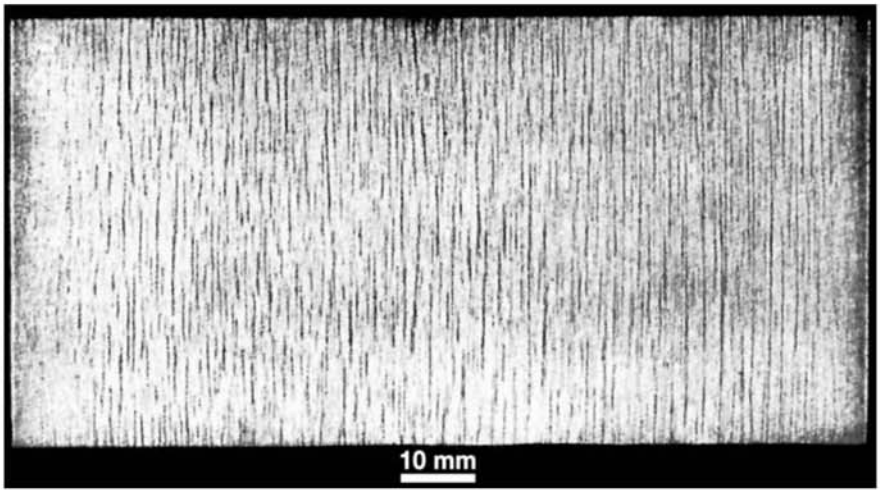

Fig. 11.11 Longitudinal cross section of the axis of Fig. 11.10. The segregation has been aligned by hot working, creating the aspect of fibers. This indicates a high degree of deformation in hot working. Etchant: iodine.

Fig. 11.12 Cross section transverse to a forged plate of WStE355 steel (C ≅ 0.20%, Mn ≅ 1.1%) with a thickness of 250 mm (10 in.). This plate was forged from a conventional ingot (the surfaces of the plate are on the top and bottom of the image). Notwithstanding the bad sample preparation for the macrographic examination (circular marks from the final machining operation can be seen), one can clearly see the segregates originated from the "A" segregates in the original ingot. These are located at about 1/4 thickness. Etchant: hot hydrochloric acid.

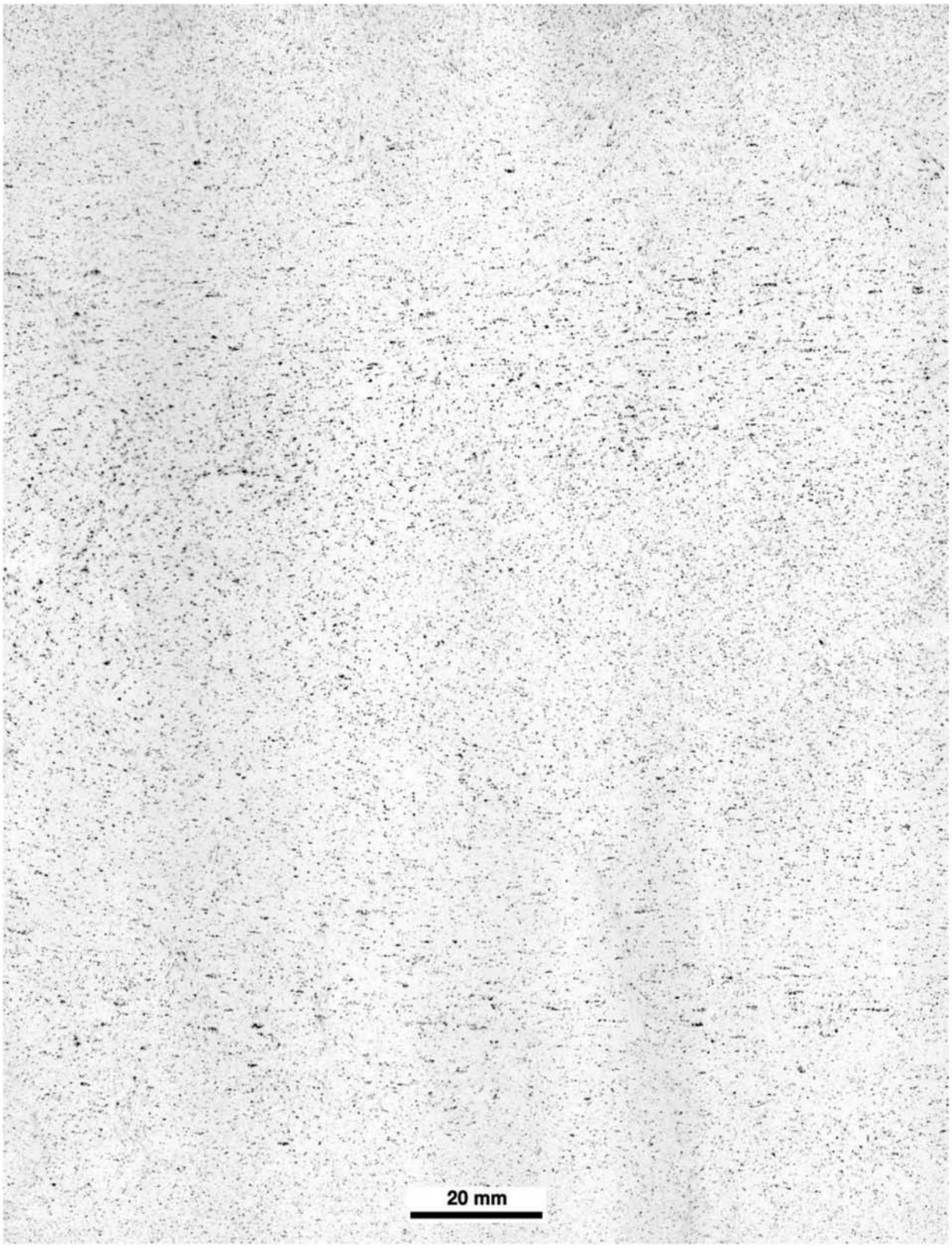

Fig. 11.13 Sulfur print from the same region as Fig. 11.12. The "A" segregates are visible in the print. The higher homogeneity of the product in the region between the surface and the "A" segregates when compared to the region between these segregates and the central region of the plate is evident.

Fig. 11.14 Cross section equivalent to that of Fig. 11.12 in a forging with the same dimensions and made of the same steel obtained from an ingot processed by electroslag remelting (ESR). No macro-segregation is visible. Etchant: hot hydrochloric acid.

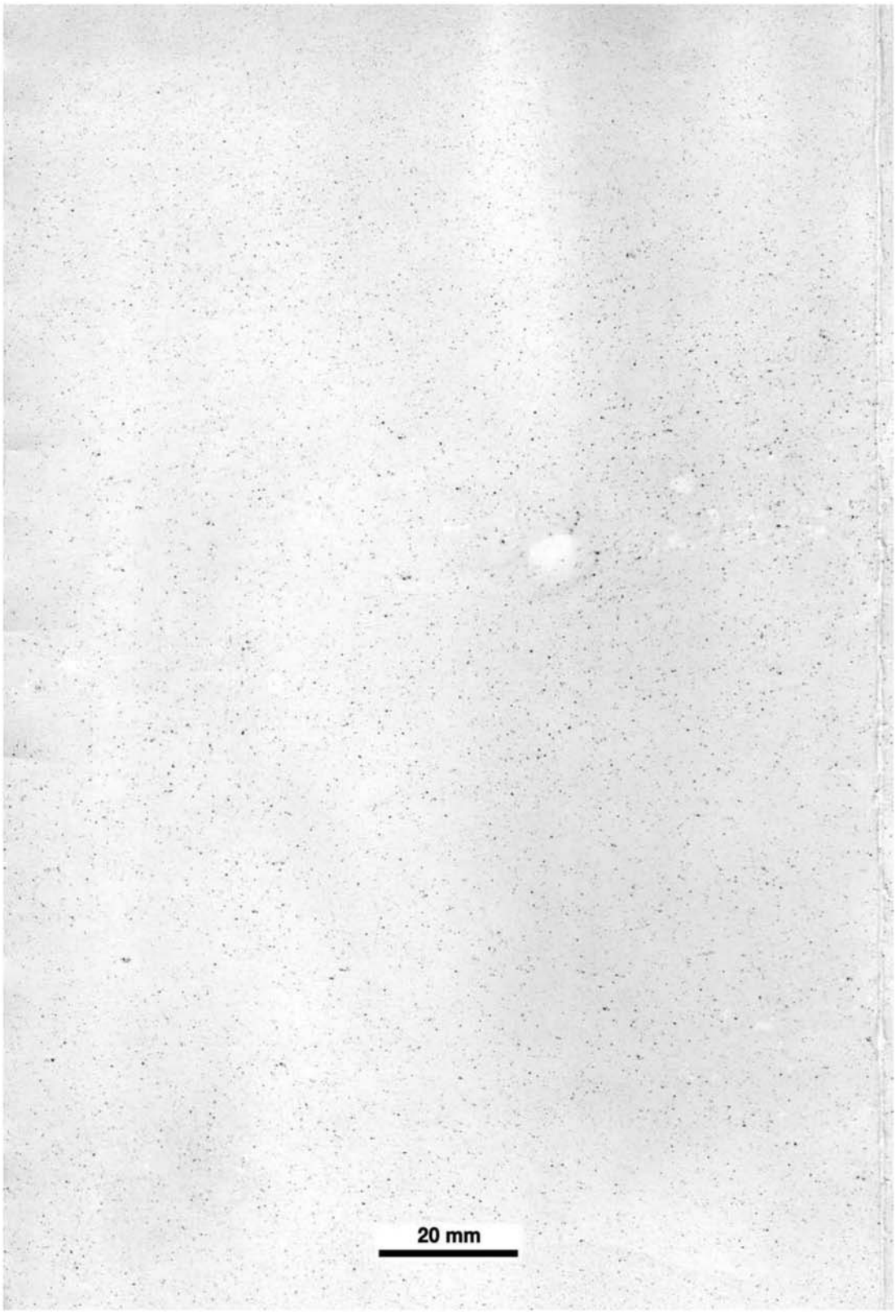

Fig. 11.15 Sulfur print from the same region as Fig. 11.14. The cross section is homogeneous with small dark dots uniformly spread (enhanced by the high-contrast digitizing of the print).

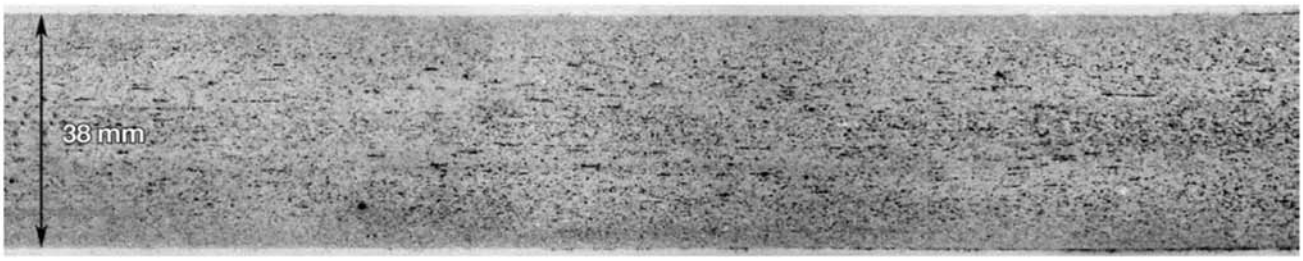

Fig. 11.16 Sulfur print of a thick rolled plate of structural steel WStE355. Section transverse to the main rolling direction, region corresponding to the top of the conventional ingot used to roll the plate, in mid-width. Some concentration of sulfides can be seen, elongated in the transverse direction of the plate.

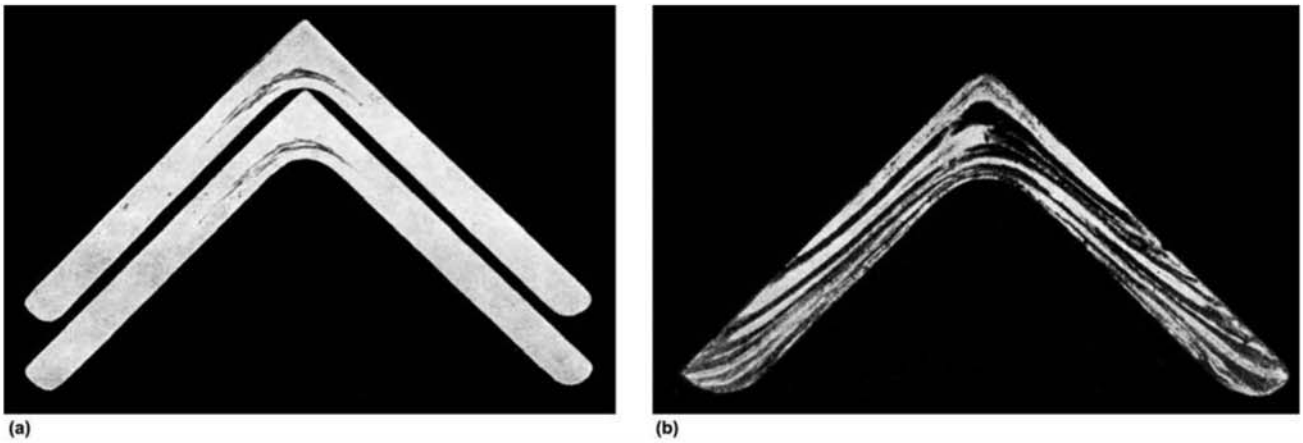

Fig. 11.17 (a) Cross section of rolled structural profiles with "residual pipe" (the bottom of the pipe—solidification contraction—in the conventional ingot was not completely eliminated from the rolled product). No etching. (b) Cross section of a structural profile rolled from iron obtained by puddling. Although this material has not been produced for a long time, the image is of historical value to compare with modern products.

known as "inclusion engineering" (Ref 11, 12, 13). Depending on the desired properties or type of product, the steelmaking and refining processes are adjusted to form the less deleterious (or even beneficial) nonmetallic inclusions for the desired properties. In long products, such as spring wire and tire cord wire, it may be desired to form high-plasticity inclusions to guarantee optimized performance, for instance, in fatigue or during the wire drawing process. (Ref 13, 14). Figures 11.26 to 11.31, for instance, show how composition of the complex oxides in nonmetallic inclusions alter their plasticity, resulting in inclusions that either elongate or break while working the wire rod. Free-cutting steels were one of the first applications in which the positive effect of controlling of nonmetallic inclusions was observed. Dispersed particles in the ductile steel matrix will help break the turnings generated during machining and may even have lubricating properties. The final effect is increased tool life, faster and easier machining, and frequently improved surface finish. Figure 11.32 presents some alternatives for free-cutting stainless steels developed by Ref 15, 16.

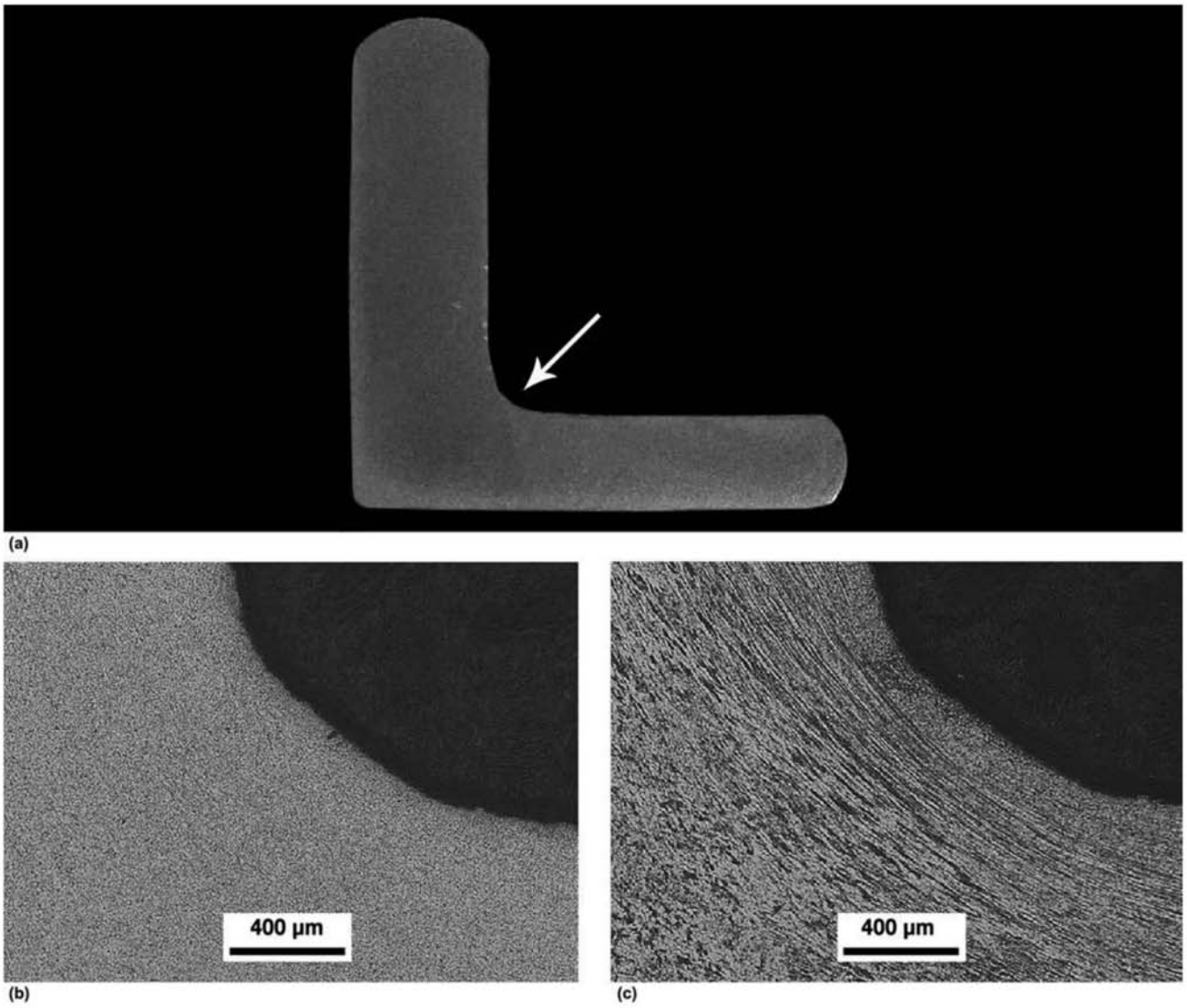

Fig. 11.18 Transverse cross section of a rolled structural profile. (a) Homogeneous macrostructure. Etchant: hot hydrochloric acid. The arrow indicates the internal radius of the rolled angle presented in detail in (b) and (c). (b) Microstructure of the internal radius. Etchant: nital 2%. (c) "Fibers" in the internal radius of the rolled angle. A high degree of deformation close to the internal radius can be observed. Etchant: Béchet-Beaujard. Courtesy of ArcelorMittal Aços Longos, Juiz de Fora, MG, Brazil.

Quantifying Nonmetallic Inclusions

As the importance of nonmetallic inclusions for the properties of steels became better and better established and inclusion engineering processes are developed, the need for precise and accurate methods to quantify nonmetallic inclusions becomes evident for the prediction of the performance and conrol of the steelmaking and refining processes. The simplest procedure for the quantification of nonmetallic inclusions is ASTM E45 (Ref 17) standard. One of the most common methods involves comparing metallographic sections to

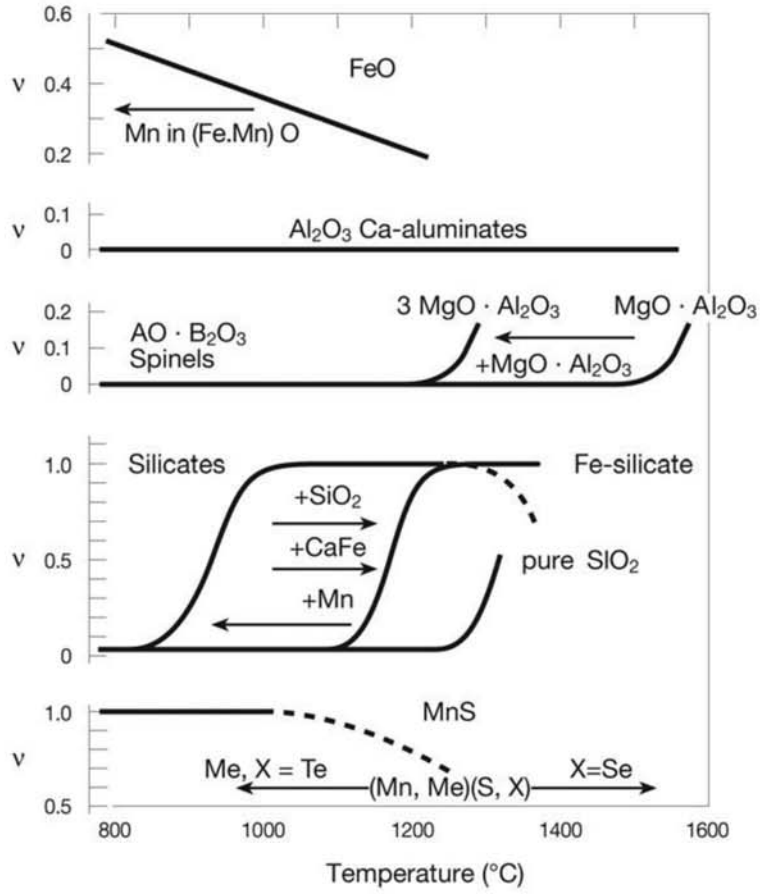

Fig. 11.19 The influence of temperature on the relative plasticity of various typical nonmetallic inclusions in steels. Relative plasticity ν is measured as ν = nonmetallic inclusion plasticity/steel plasticity. Source: Ref 8

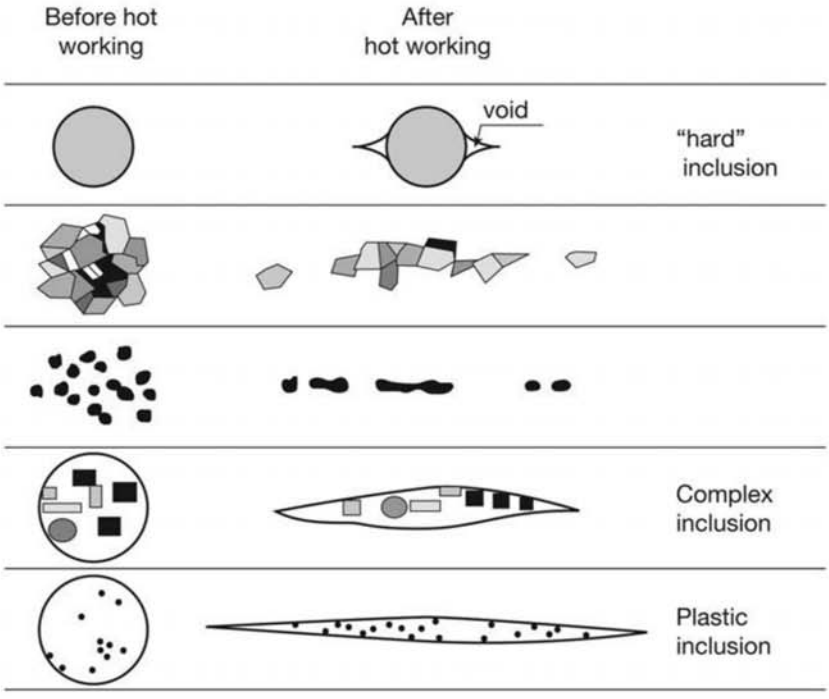

Fig. 11.20 The effect of the relative plasticity of nonmetallic inclusions on their deformation with respect to the steel. Plastic inclusions will elongate as a result of hot working. Hard inclusions may remain unchanged or break and redistribute in the product.

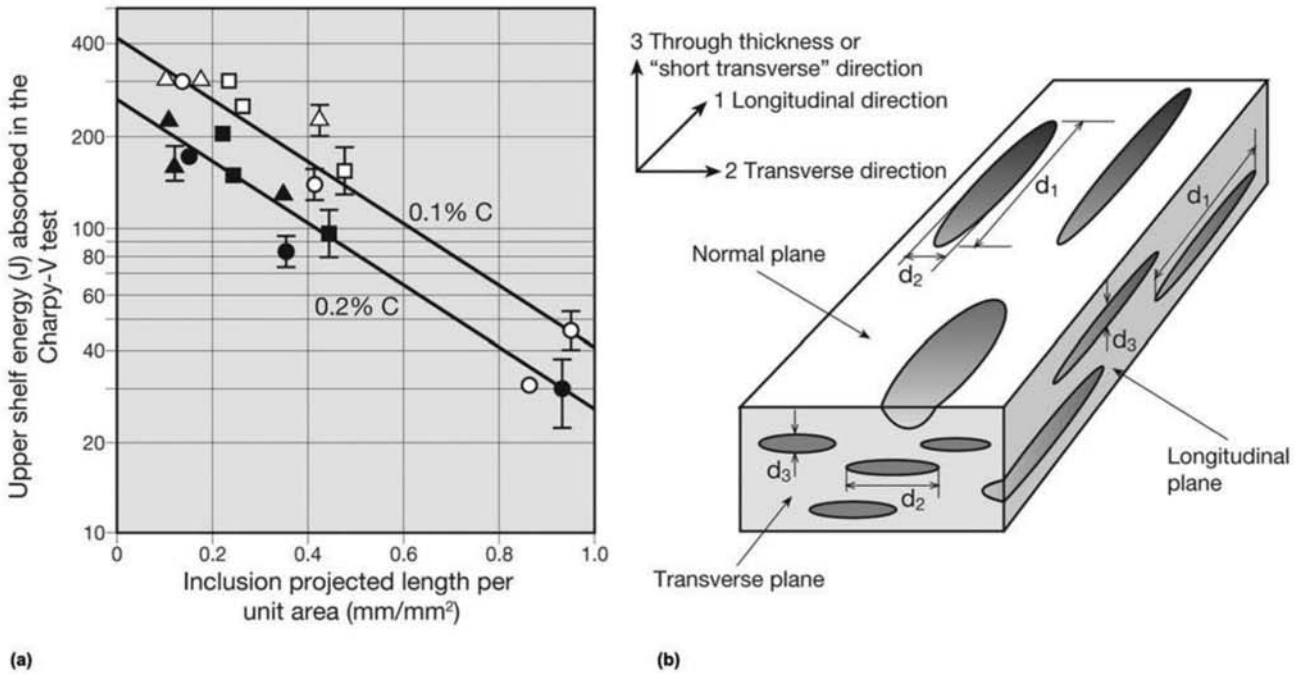

Fig. 11.21 (a) Effect of the inclusion projected length on the tested area on the energy absorbed in the upper shelf of Charpy-V impact tests for a C-Mn structural steel for different specimen orientations. (b) Nomenclature adopted for planes and directions used in the characterization shown in (a). Data obtained with sulfides. Source: Ref 9

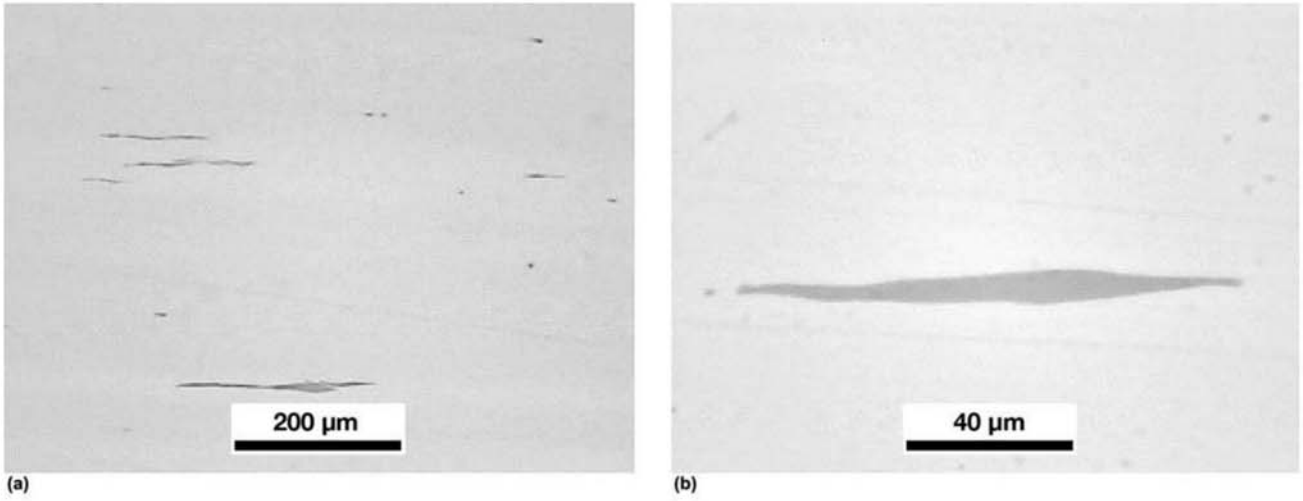

Fig. 11.22 Manganese sulfide inclusions elongated in the longitudinal directions (parallel to the direction of larger elongation during hot working) in stainless steel AISI 304. Not etched. Courtesy of Villares Metals S.A. Sumaré, SP, Brazil.

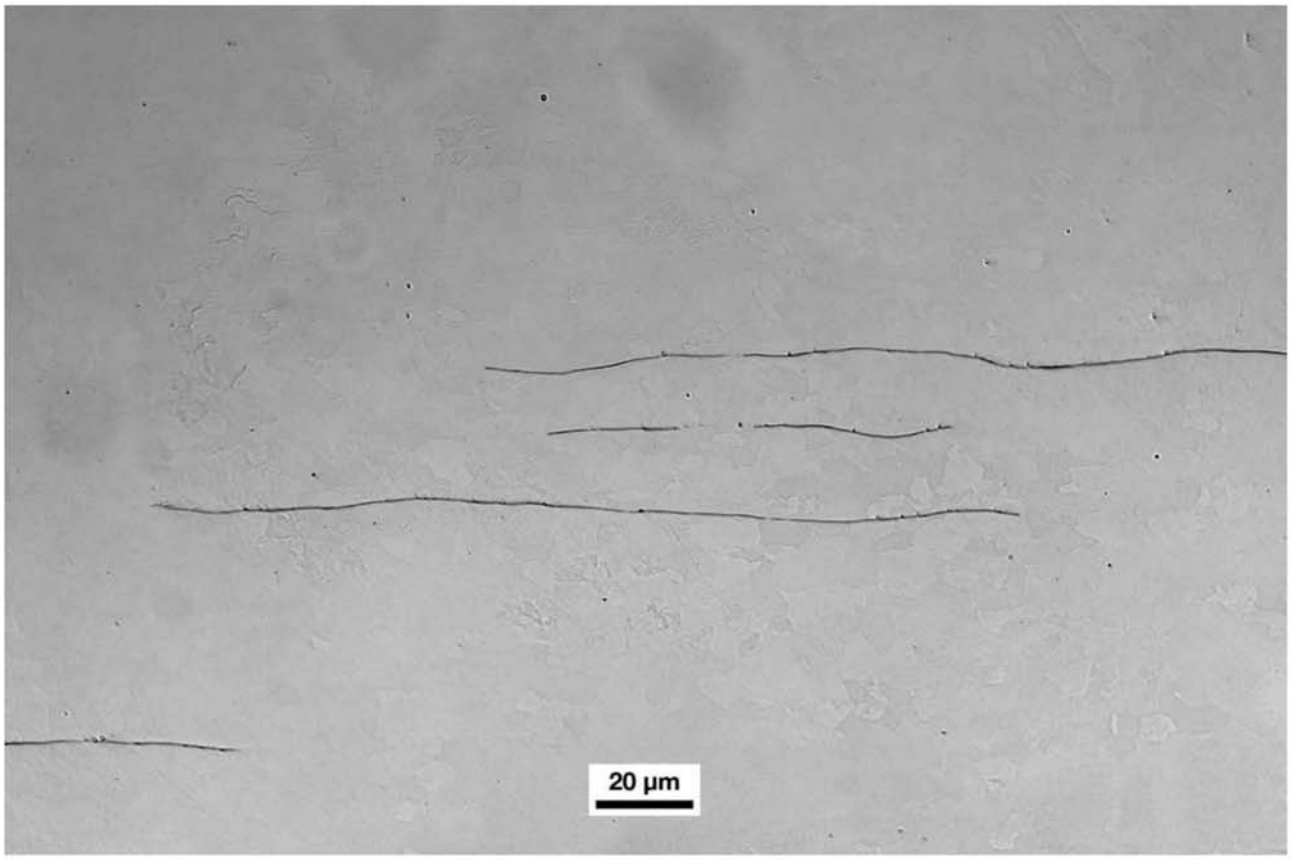

Fig. 11.23 Manganese sulfide inclusions elongated in the longitudinal directions (parallel to the direction of larger elongation during hot working) in a plate of structural steel. Not etched. Courtesy NIST (National Institute of Standards and Technology), Gaithersburg, MD, USA. Source: Ref 10

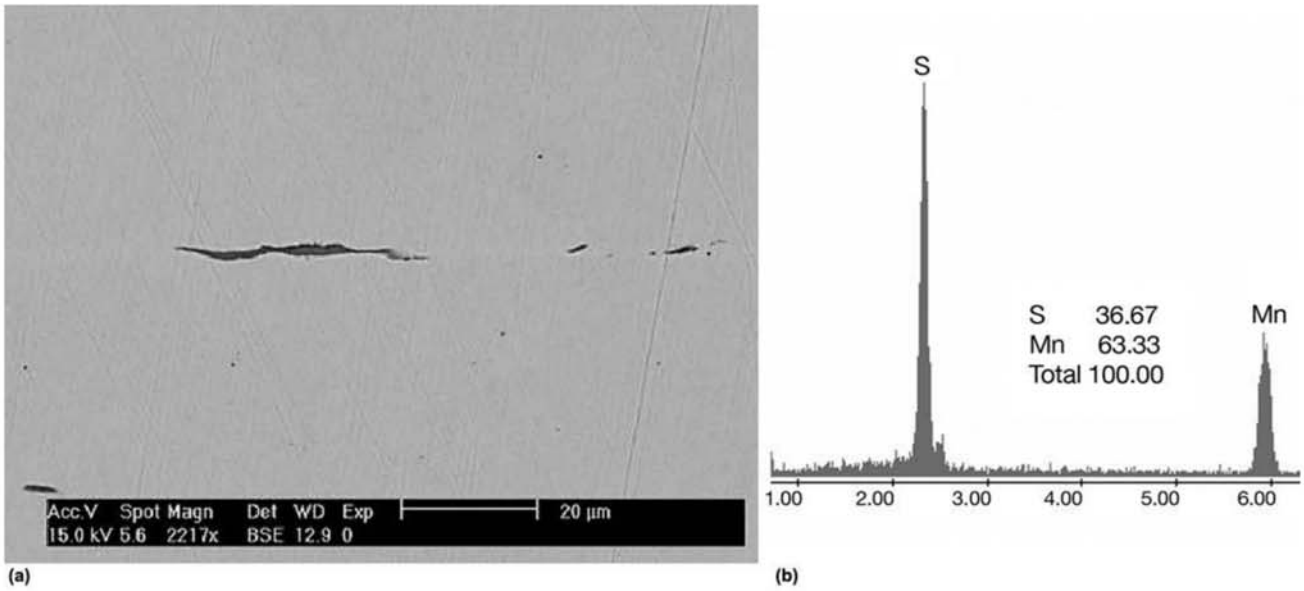

Fig. 11.24 (a) Longitudinal cross section of wire rod, presenting elongated manganese sulfide nonmetallic inclusion. The hot working was concluded at 900 °C (1650 °F). Not etched. SEM, BE. (b) EDS x-ray spectrum of the inclusion presented in (a).

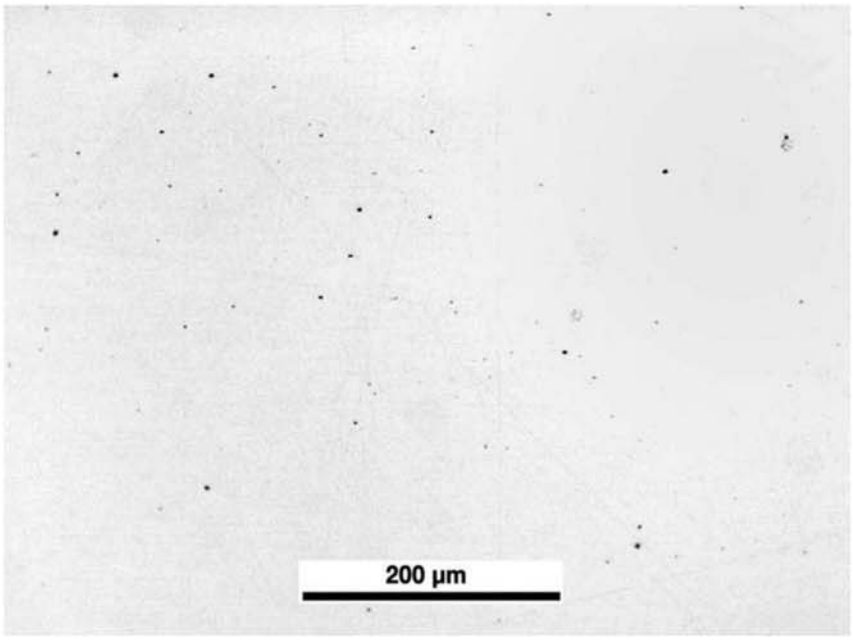

Fig. 11.25 Longitudinal cross section of a hot rolled plate of medium carbon steel, treated with calcium in the liquid state to achieve inclusion globularization. In this case, the inclusions are classified as globular oxides according to ASTM E45, severity 1.5, fine series. Courtesy of ArcelorMittal Tubarão, ES, Brazil.

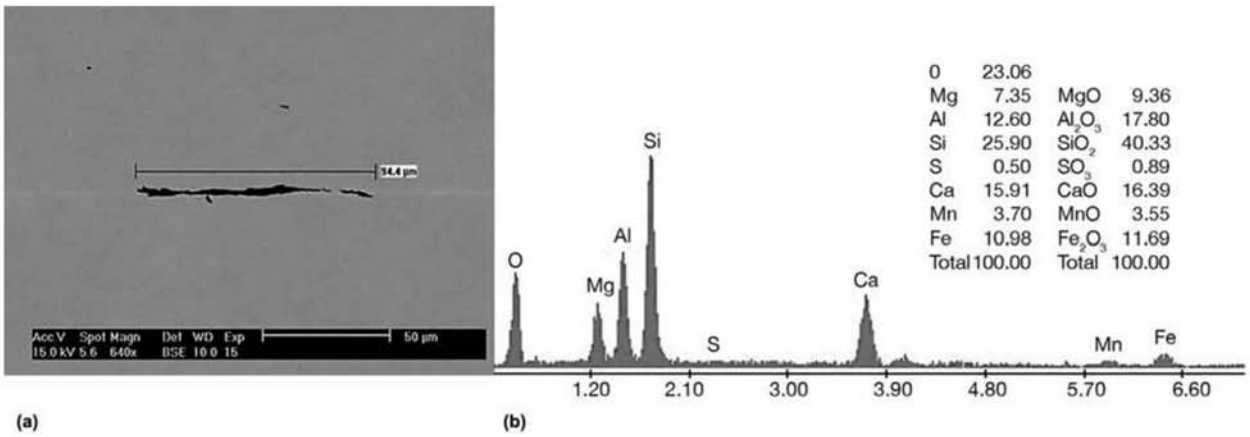

Fig. 11.26 (a) Longitudinal cross section of a wire rod presenting an elongated silicate inclusion. Hot working was concluded at 900 °C (1650 °F). Not etched. SEM, BE. (b) EDS x-ray spectrum of the inclusion presented in (a).

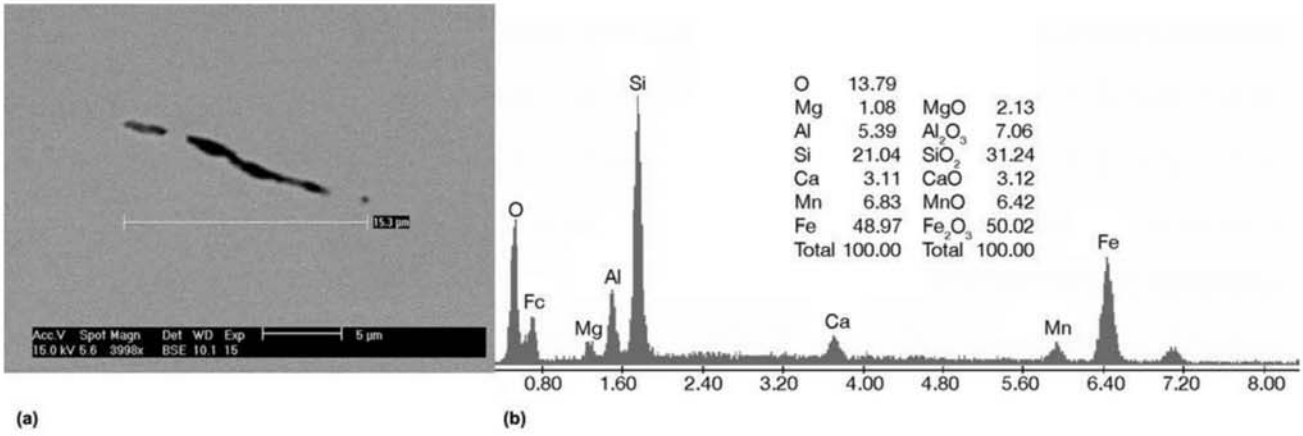

Fig. 11.27 (a) Longitudinal cross section of a wire rod presenting an elongated silicate inclusion. Hot working was concluded at 1000 °C (1830 °F). Not etched. SEM, BE. (b) EDS x-ray spectrum of the inclusion presented in (a).

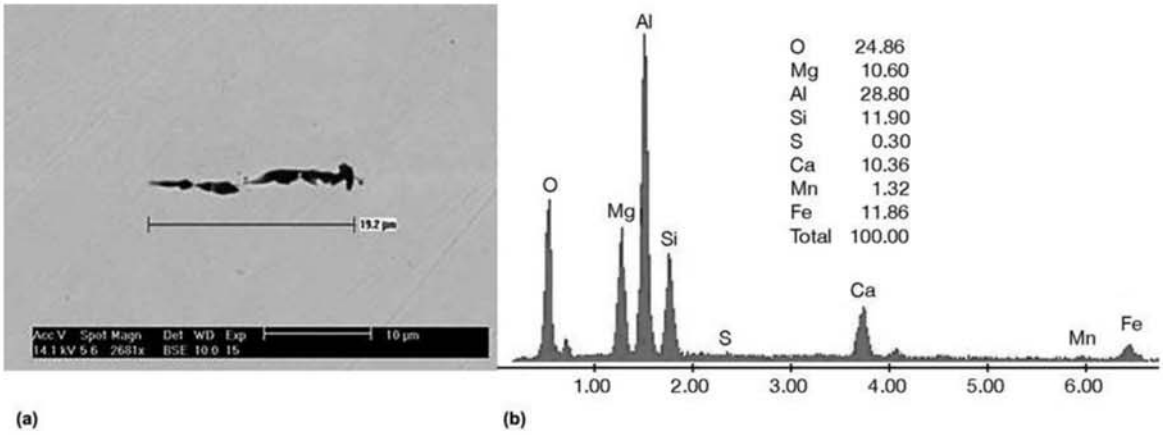

Fig. 11.28 (a) Longitudinal cross section of a wire rod presenting a broken nonmetallic inclusion. Hot working was concluded at 900 °C (1650 °F). Not etched, SEM, BE. (b) EDS x-ray spectrum of the inclusion presented in (a).

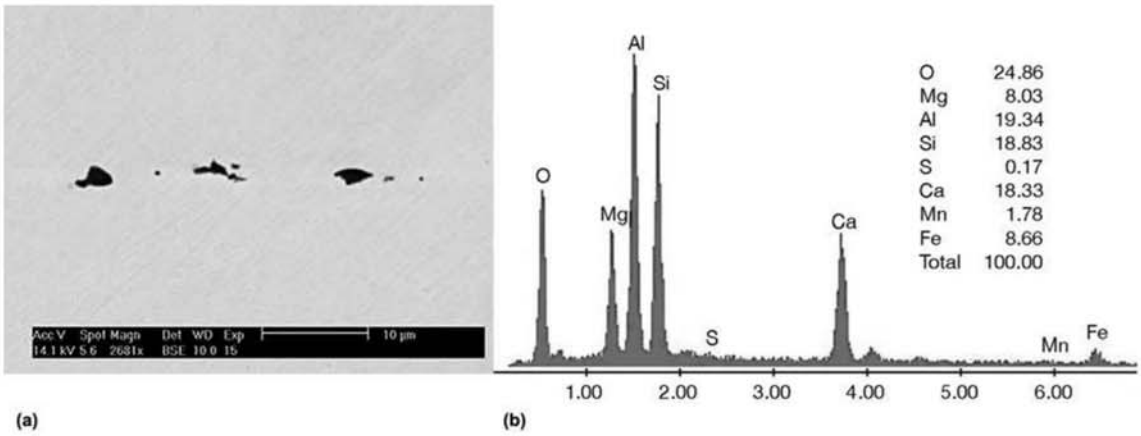

Fig. 11.29 (a) Longitudinal cross section of a wire rod presenting a broken nonmetallic inclusion. Hot working was concluded at 900 °C (1650 °F). Not etched, SEM, BE. (b) EDS x-ray spectrum of the inclusion presented in (a).

standardized charts. However, many normal steelmaking products are not amenable to a useful quantification on inclusions using this technique because of their high internal cleanliness. When using automatic methods for the quantification, ASTM E1245 (Ref 18) is the recommended practice. For the estimation of the largest nonmetallic inclusion in a given volume of steel, an important property for evaluations related to fatigue life, ASTM E2283 (Ref 19) can be employed. Currently, extensive research is ongoing for reliable, reproducible, accurate, and fast methods for quantifying nonmetallic inclusions in steel, as discussed in Ref 20 and 21. In the case of free-cutting steels, with a significant volume fraction of second-phase particles, ASTM E1245 (Ref 18) has specific recommendations.

Insoluble Carbides and Nitrides

When the amounts of carbide- and nitride-forming elements and carbon (or nitrogen) contents are sufficiently high, structures can be obtained in

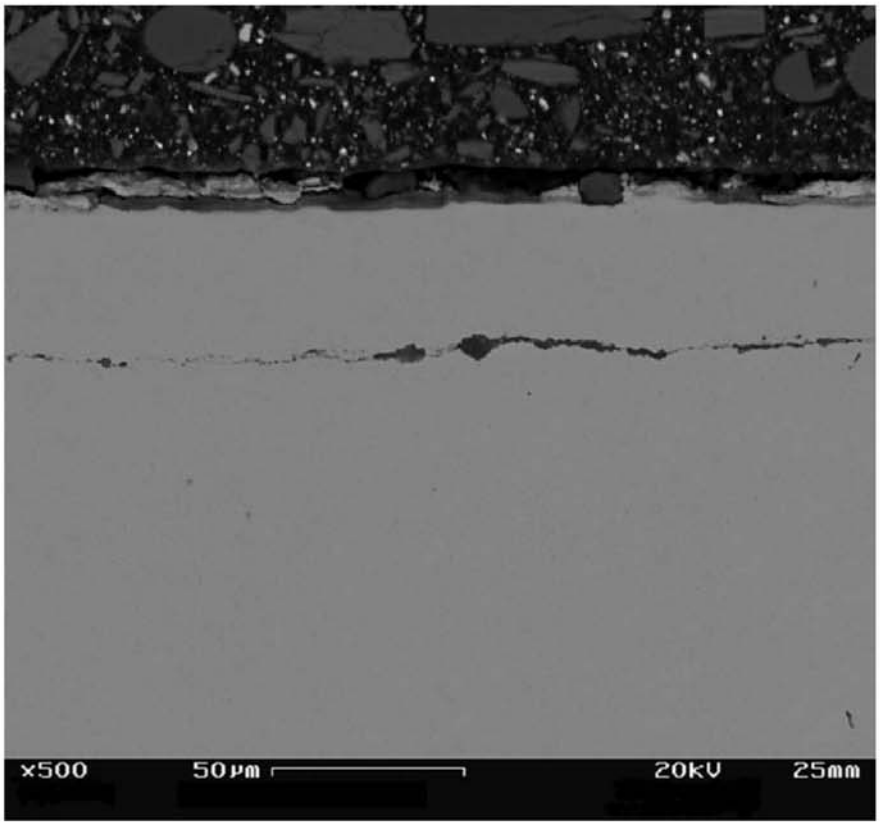

Fig. 11.30 Longitudinal cross section of a plate presenting a long alumina inclusion, broken and redistributed during the hot working. The inclusion is around 30 µm below the plate surface. Not etched.

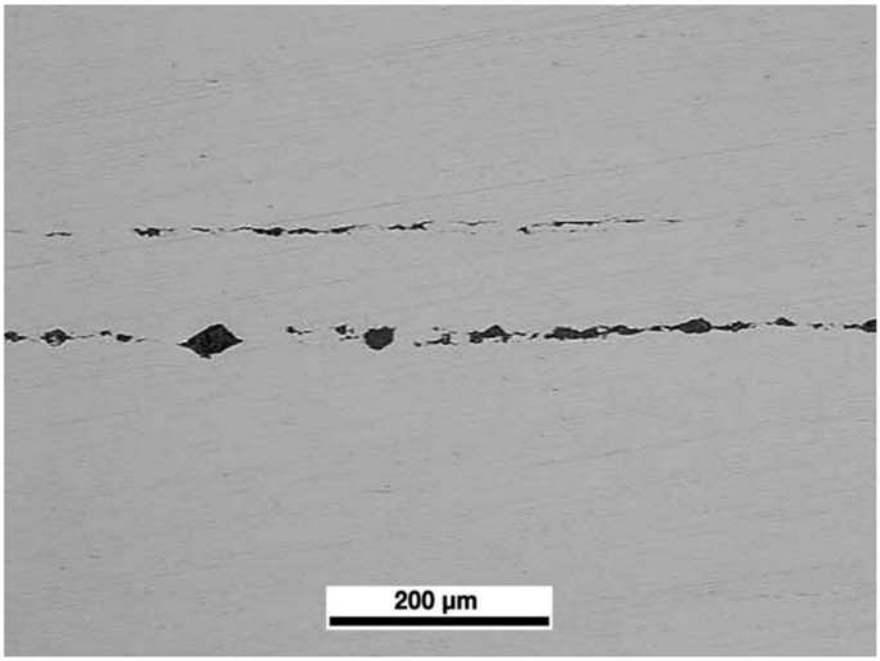

Fig. 11.31 Longitudinal cross section of a plate presenting a long alumina inclusion, broken and redistributed during the hot working. Not etched.

which carbides and/or nitrides are stable all the way up to the melting point of the steel. Hence, these phases cannot be completely dissolved. Figure 11.33 presents an examples of polygonal titanium nitride particles that precipitated from the steel in the liquid phase. These phases are yellowish (or golden) when observed with white light, without etching in an optical microscope. When carbide networks are formed during solidification, a situation not uncommon in some high alloy tool steels, such as high-speed steels, hot working will cause the redistribution of these particles, increasing the steel

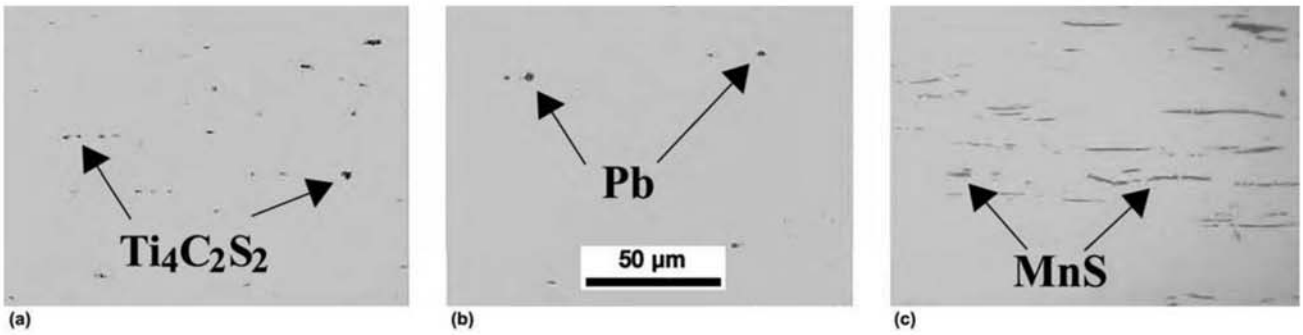

Fig. 11.32 Shape of different types of nonmetallic inclusion produced in stainless steels to improve machinability. Steel has been hot worked and heat treated. (a) Cr = 13%, Si = 1%, Al = 0.3% + Ti, C, S; (b) Cr = 13%, Si = 1%, Al = 0.3% + Pb; and (c) Cr = 18%, Si = 1%, Mo = 0.5%, S = 0.3% + Mn. The best machinability results were obtained with steel (a). Not etched. Courtesy of K. Ishida, Tohoku University, Japan; see also Ref 16

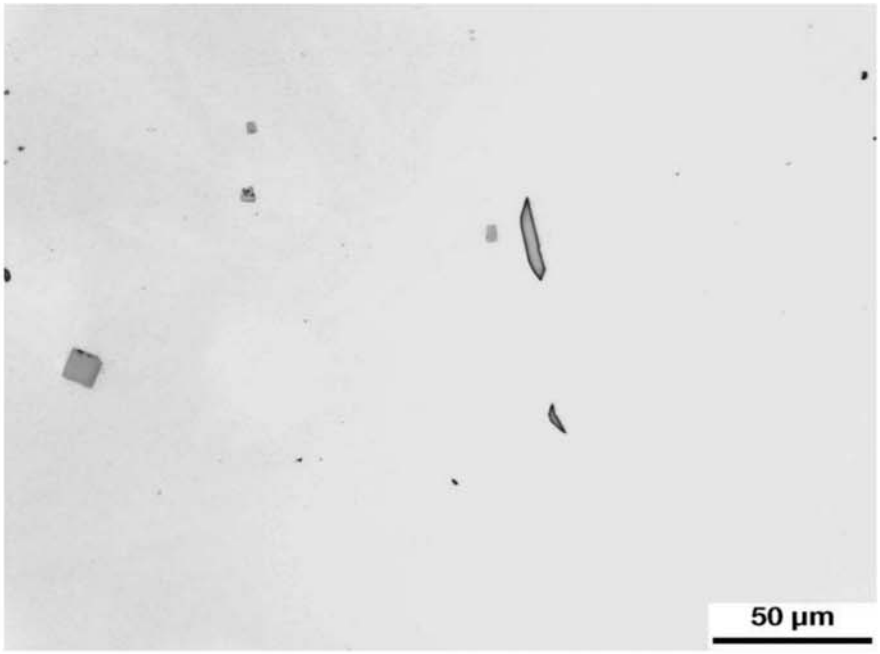

Fig. 11.33 Polygonal, nondeformed, titanium nitride inclusions (or titanium carbonitride) and deformed delta ferrite in a martensitic stainless steel W. Nr. 1.4418 (X 4CrNiMo 16 5 1) hot worked. Etchant: NaOH. Courtesy of Villares Metals S.A. Sumaré, SP, Brazil.

homogeneity, as shown in Fig. 11.34. The heterogeneity of the as-cast starting material has a large influence over what it is possible to obtain via hot working, as exemplified in Fig. 11.35. When the steels have a large volume fracture of insoluble carbides, and the maximum of structural homogeneity is desired, powder metallurgy processing is an interesting alternative, as shown in Fig. 11.35(c) and in the comparison presented in Fig. 11.36. Because the powders are usually atomized, the solidification happens with structures that are much finer than those obtained from ingots. This makes it possible to obtain uniform carbide dispersions and outstanding performance during the use of the tool (Ref 22, 23).

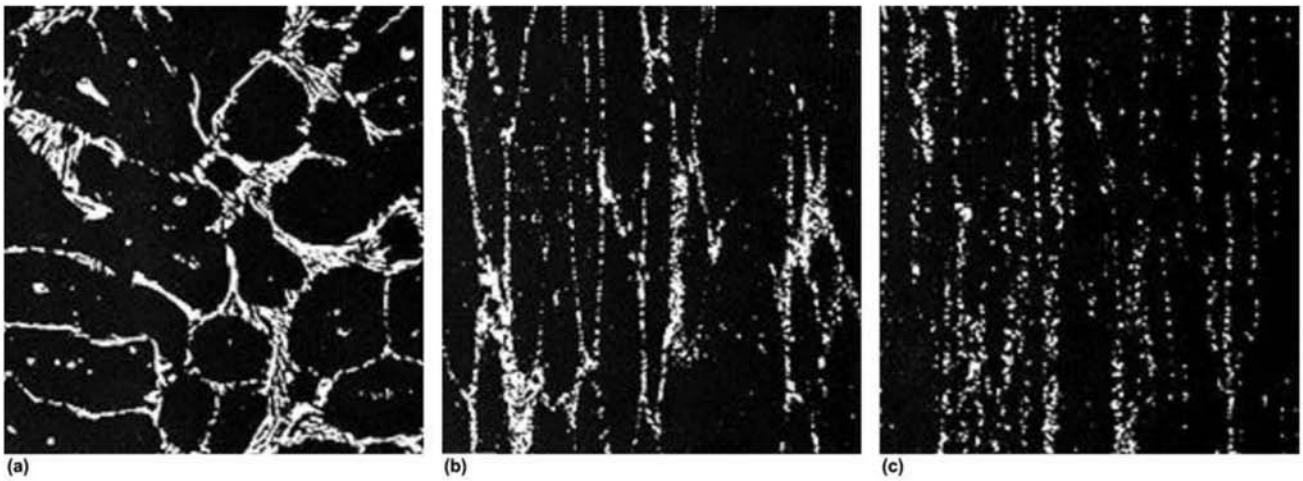

Fig. 11.34 The effect of hot working on the distribution of carbides in a high-speed steel. (a) As-cast material, with eutectic colonies, presenting carbides. (b) Carbides have been fragmented and redistributed as an effect of hot working. (c) Carbide distribution improves with the increase in deformation. Reprinted with permission. Source: Ref 22

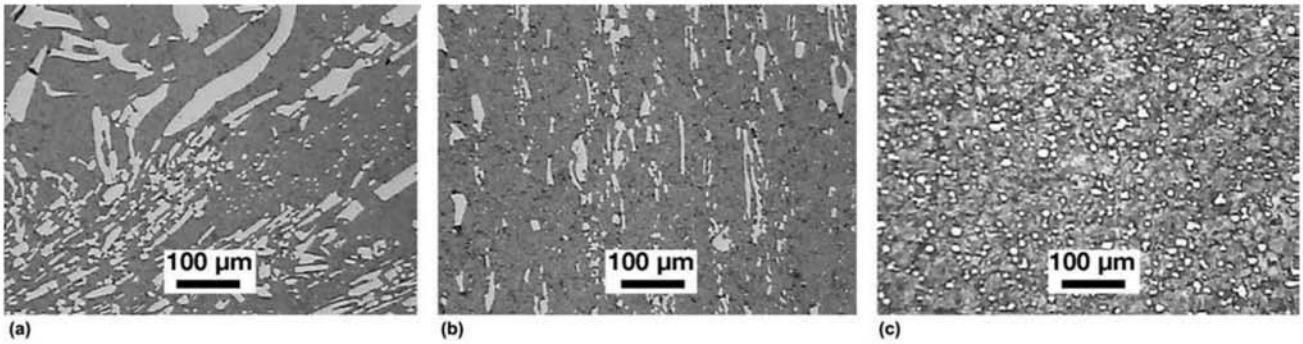

Fig. 11.35 ASTM A681–D2, tool steel for cold working. Annealed to 250 HB. Carbides in a ferritic matrix. (a) Conventional ingot, 830 mm (33 in.) diameter subjected to forging reduction via hot working of 5.6:1 (measured as the ratio of cross sections before and after work). (b) An ingot produced by electroslag remelting (ESR), with the same starting diameter and the same degree of hot working. In (a) and (b) the fragmentation and redistributions of the carbides caused by hot working can be observed. (c) Same steel produced by powder metallurgy and hot rolled. Uniform distribution of carbides. Etchant: nital 4%. Courtesy of Villares Metals S.A., Sumaré, SP, Brazil.

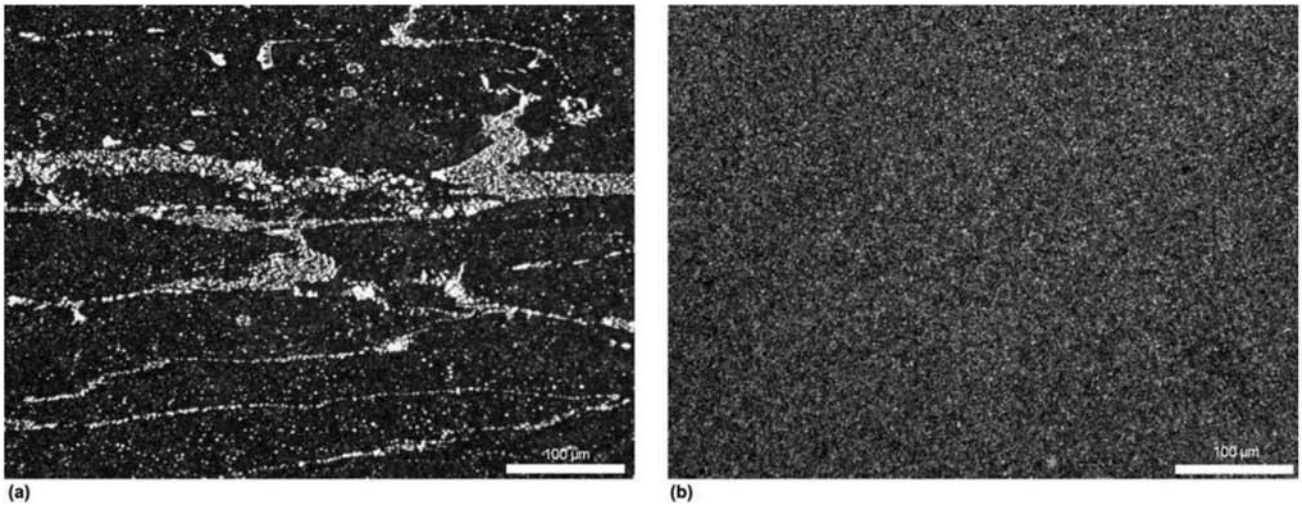

Fig. 11.36 M2 high-speed tool steel (a) cast in a conventional ingot and hot worked. Carbides are fragmented and distributed in an aligned microstructure (comparable to Fig. 11.34c). (b) Produced by powder metallurgy and hot rolled. Uniform distribution of carbides. Etchant: nital 4%. Courtesy of Villares Metals S.A., Sumaré, SP, Brazil.

11.2.5 Effects on the Macroscopic Properties

The combination of changes on the distribution of segregates and inclusions and the potential for weld forging the voids and microporosity formed during solidification represent significant macrostructural changes that reflect directly on the properties of the material, as shown in Fig. 11.37. It is important to note that the less heterogeneous and more dense the initial product to be forged, the less dramatic the beneficial effect of hot working. The comparison of the results obtained with conventional ingots (Fig. 11.37) and those with ingots produced via remelting processes clearly shows that (Fig. 11.38). The combination of the experimental results presented in Fig. 11.37 and 11.38 and the effects of working on the austenitic grain size (discussed below) have led to the definition of a general rule (sometimes adopted in standards) of requiring a 4:1 minimum degree of reduction of the transverse cross section to guarantee satisfactory properties in the forged material. Although this is indeed a good reference value, one must keep in mind two facts:

- If the original ingot product has low quality and low soundness, this degree of reduction in hot working might be insufficient
- The degree of deformation calculated using the changes of product dimensions is not a guarantee of uniform deformation through the whole cross section of the product

In the case of open die forging, for instance, it is possible to forge relatively large parts in low-capacity presses (low pressure or low applied force) causing little or no deformation in the center of the part. This is due to the fact that the depth of deformation penetration depends directly on the size of the forging "bite," which in turn is limited by the press capacity. Thus, it is convenient

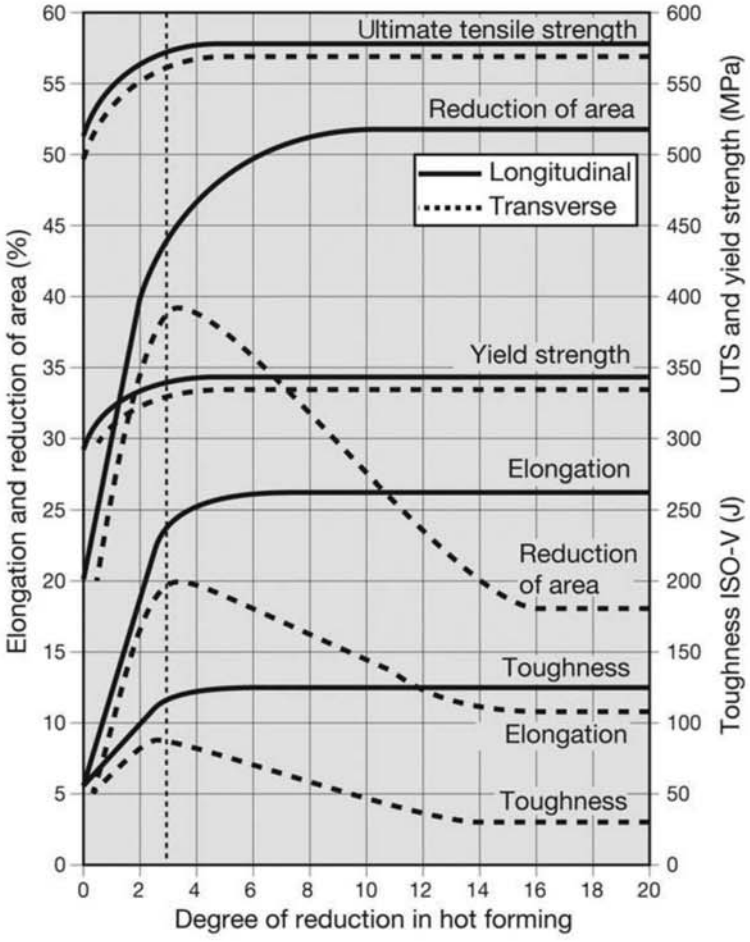

Fig. 11.37 The effect of the degree of deformation during hot forging (measured as the ratio of transverse cross sections before and after hot forging) on the properties of a Ni-Cr steel produced through conventional ingot casting. Source: Ref 24

in the case of new suppliers or the supply of new part designs to proceed to a qualification (or "first article approval") performing macrographic examinations that can demonstrate the extension of forging deformation. In the case of flat or long products produced by rolling, the degree of deformation is usually large enough that these considerations are not so important. In the case of thicker plates, however, produced from continuously cast slabs which usually range from 200 to 250 mm (8 to 10 in.) in thickness, it is convenient to consider this possibility. Finally, for high-homogeneity products, which are essentially free of voids (Fig. 11.38), this degree of deformation may not be needed. A deformation of 3:1 may be more than sufficient provided the quality that can be confirmed through tests and examination. However, qualification should not be overlooked, since the calculated deformation may be misleading, due to heterogeneous distribution of deformation in the part, for instance, in the case for rolled rings (Fig. 11.39 and 11.40).

11.2.6 Microstructural Changes

During hot working, grain size and microstructure can be altered through recrystallization. The main mechanism producing microstructural changes during hot working is recrystallization. When the deformation energy stored

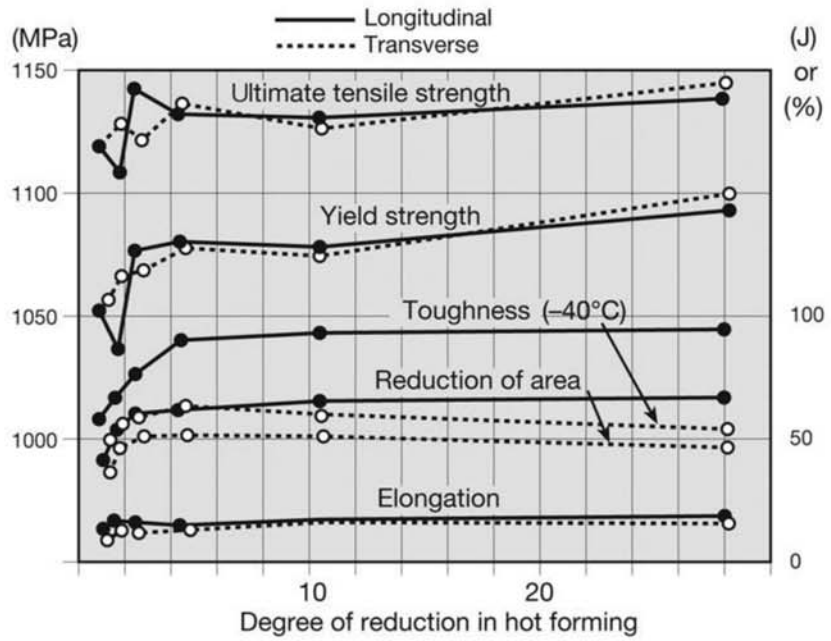

Fig. 11.38 The evolution of the mechanical properties of a Ni-Cr-Mo-V steel electroslag remelted as a function of the degree of hot working (compare with Fig. 11.37, obtained with a conventional ingot). Source: Ref 25

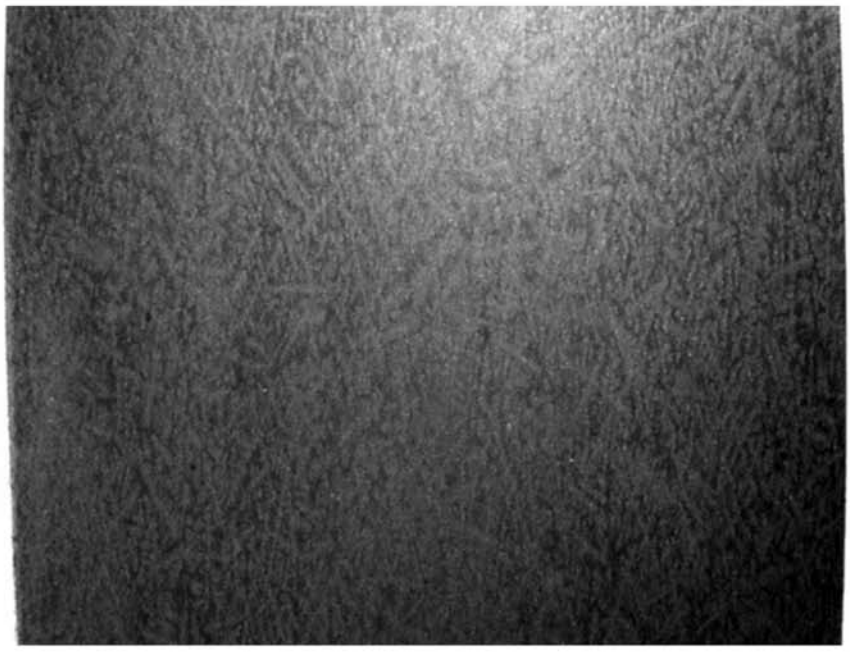

Fig. 11.39 Longitudinal cross section of a rolled ring of AISI 8630 Mod steel produced by hot forging. (forging reduction 2:1), followed by ring rolling (total approximate deformation during hot working 4:1). Dendritic structure. The regions close to the cylindrical surfaces (left and right of the macrograph) present evidence of hot working as the dendrites have been deformed. The center of the ring cross section has suffered essentially no deformation. Etchant: hot hydrochloric acid.

in the material reaches a certain level, which is essentially a function of the material and the temperature, new nondeformed grains can be nucleated. This process is called recrystallization. Besides essentially eliminating the increased resistance associated with work hardening, recrystallization creates new grains (Fig. 11.41 and 11.42). The effect of this process is, on average, a

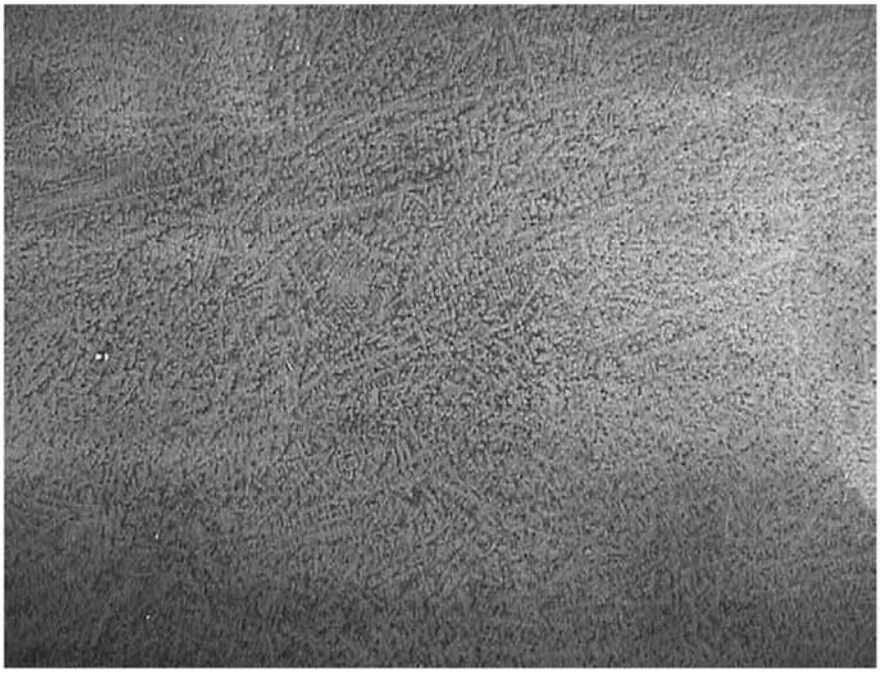

Fig. 11.40 Transverse cross section of the ring presented in Fig. 11.39. Dendritic structure. Some changes in the as-cast structure, produced by the hot working, can be seen in the region to the right of the macrograph (ring surface). Etchant: hot hydrochloric acid.

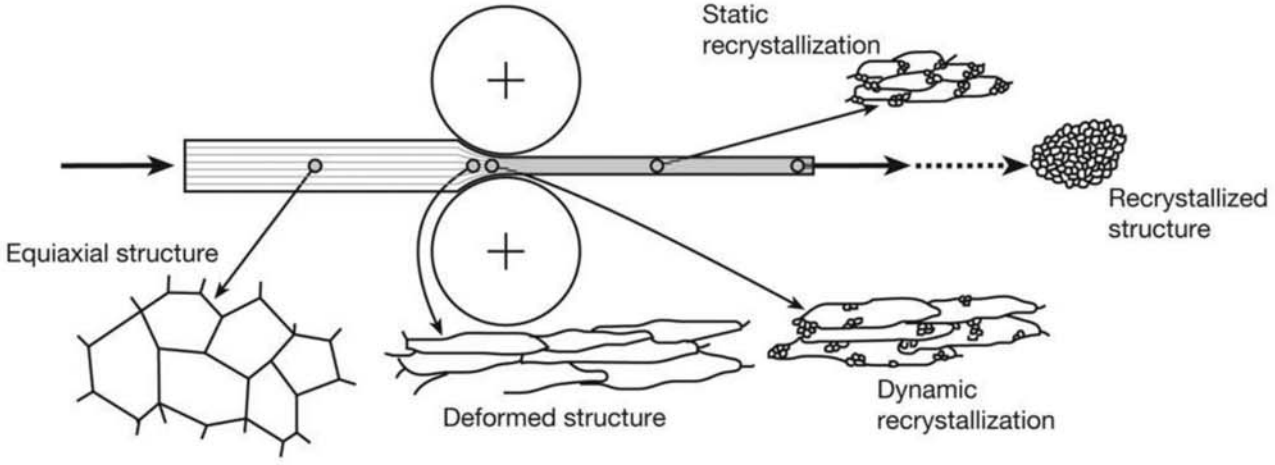

Fig. 11.41 Schematic presentation of the microstructure evolution during hot working (hot rolling in the example). Two possibilities are illustrated; when the recrystallization starts while the material is still suffering hot working, it is called dynamic recrystallization. Static recrystallization occurs when some time elapses after the hot working step.

decrease of the austenitic grain size of the material when compared with the as-cast starting material, as shown in Fig. 11.43. The sequence of images in Fig. 11.44 and 11.45 shows the evolution of the microstructure of a plate of AISI 1045 steel subjected to 4:1 deformation during forging under different heat treatment conditions. The increase in structural homogeneity caused by hot working is evident.

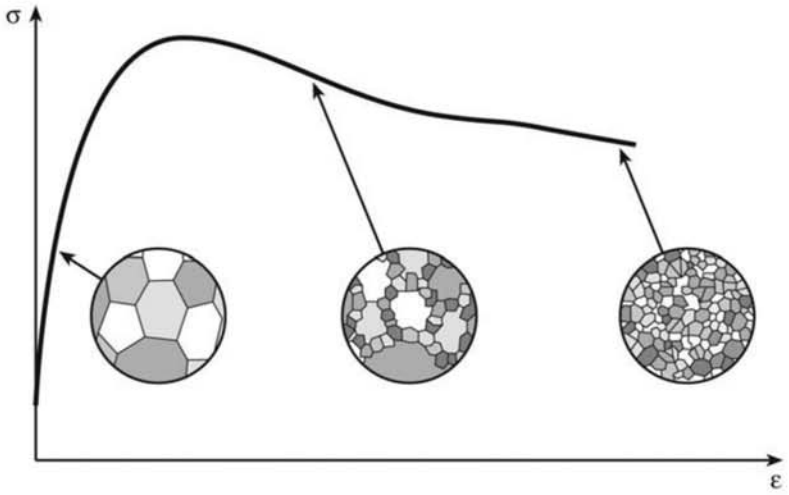

Fig. 11.42 Schematic presentation of the stress-strain curve of a material when dynamic recrystallization happens. Recrystallization eliminates work hardening and keeps the load needed to cause plastic deformation at reasonable levels during the stages of the hot working process.

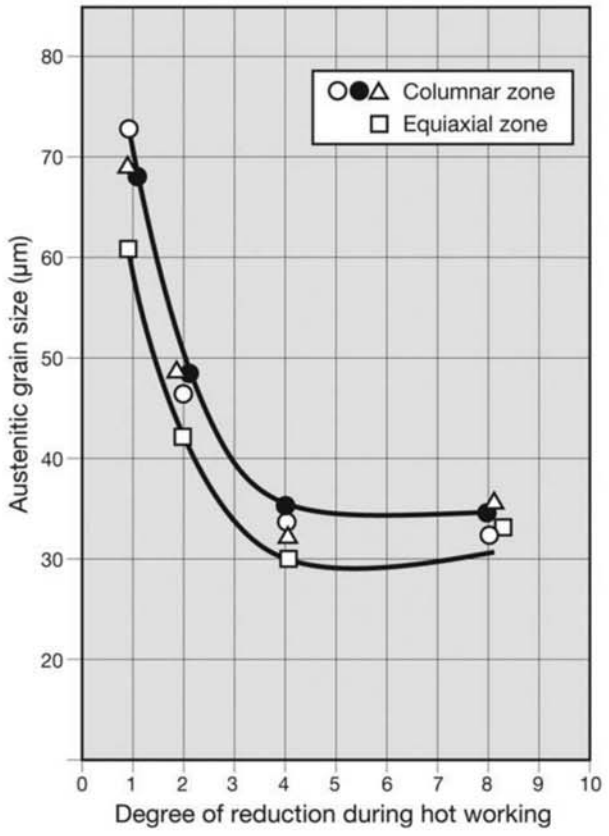

Fig. 11.43 The influence of the degree of deformation during hot working on the average austenitic grain size for two original ingot structures. Steel containing C = 0.11%, Mn = 0.62%, Ni = 3.7%, Cr = 0.25%, and Mo = 0.18%. Source: Ref 26

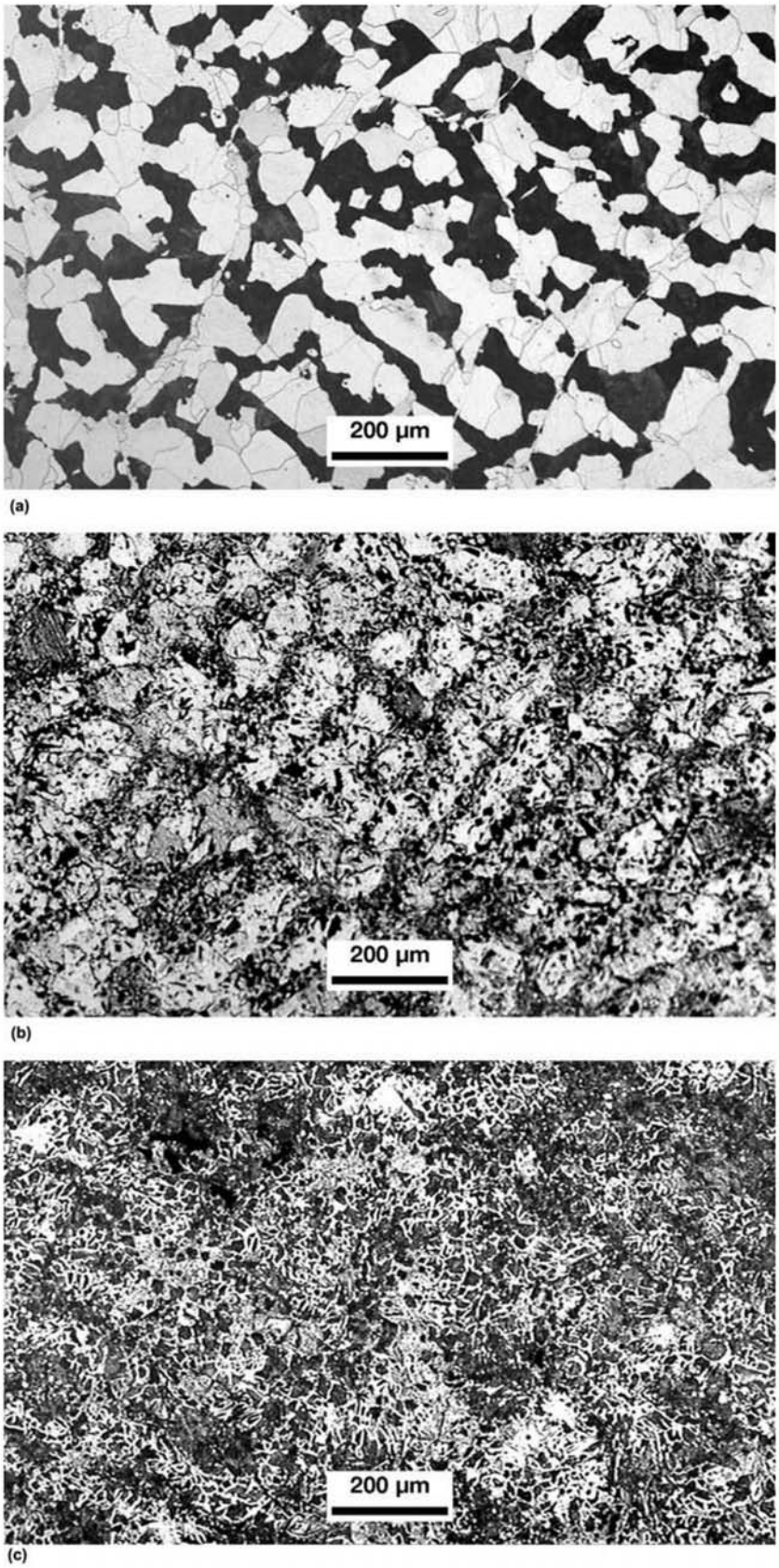

Fig. 11.44 Three positions in a plate of AISI 1045 steel produced via continuous casting, as-cast. Though the microstructures are composed of ferrite and pearlite, the structural heterogeneity when comparing the three images is evident, esspecially in (b) and (c), where segregation becomes evident due to its effect on the microstructure formed. Courtesy of ArcelorMittal Tubarão, ES, Brazil.

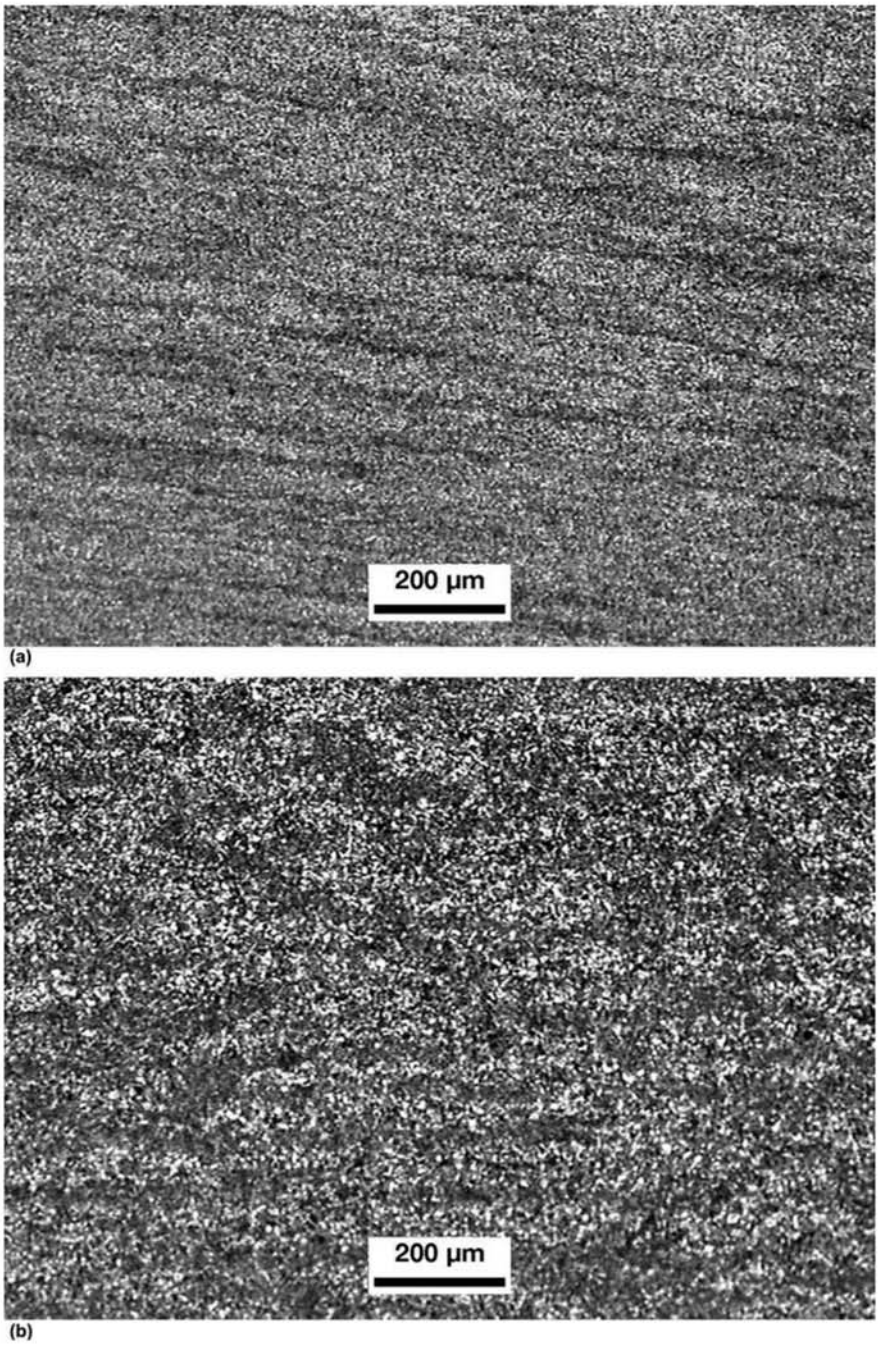

Fig. 11.45 The same AISI 1045 steel from Fig. 11.44 forged with a 4:1 deformation reduction. (a) Normalized. (b) Annealed. Ferrite and pearlite. Some alignment of the microstructure can be observed, particularly in (b) (See section "Banding," in this chapter). Etchant: nital. Courtesy of ArcelorMittal Tubarão, ES, Brazil.

Thermomechanical Treatments

Traditionally, hot working processes were designed only to alter the shape and make the changes discussed earlier, not to directly produce the desired mechanical properties at the end of the final cooling stage. After the hot working process was concluded, heat treatment was performed. This is still the conventional route for producing steels through hot working. In order to shorten processing times (when just-in-time production techniques became important, at the end of the last century), there was an effort to develop forming processes that would achieve structures that could directly attain the desired properties at the end of the process. The first such process was called controlled rolling. Presently, the family of processes that have this objective are called thermomechanical processes.

Figure 11.46 compares two generic types of thermal cycles for forming processes. In the thermomechanical cycle, the concern with producing an austenitic structure capable of transforming to the desired microstructure during final cooling is evident. Furthermore, cooling is performed in a controlled way to optimize the processes occurring during austenite decomposition. Some examples of the application of these processes are presented in Chapter 14, "Structural Steels and Steels for Pressure Vessels, Piping, and Boilers," in this book.

11.2.7 Banding

Some of the structures typical of hot working are studied to a greater extent than others. A particularly interesting case is that of banded structures, as exemplified in Fig. 11.47. Banding normally presents itself through the for-

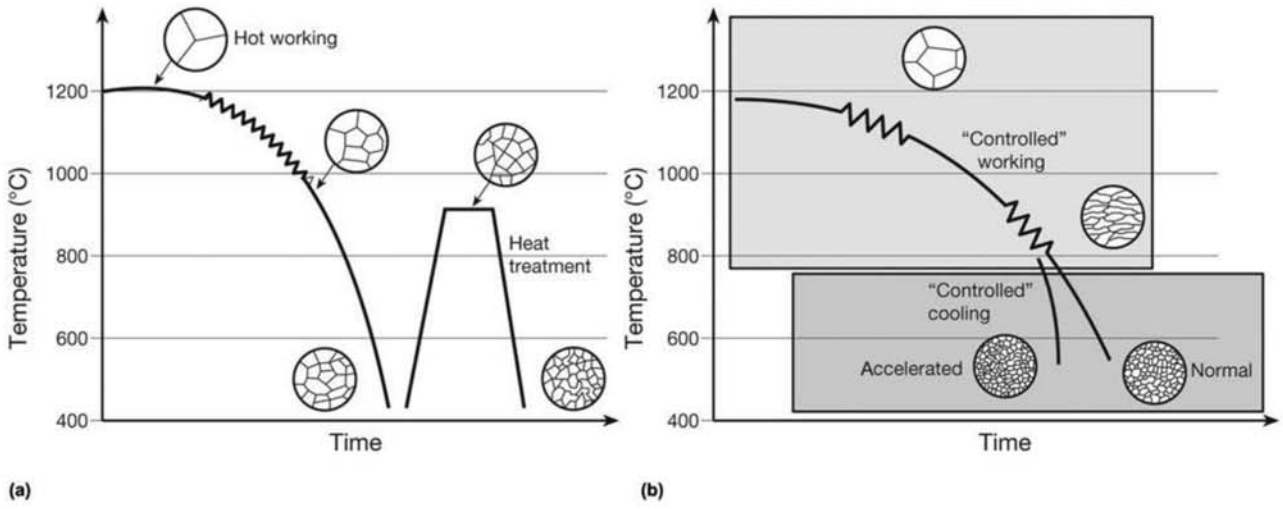

Fig. 11.46 Hot working with phase transformation on cooling. (a) Conventional: while the structure is controlled during hot working following adequate combinations of temperature and deformation, the final properties of the part are defined in a heat treatment performed afterward. (b) Thermomechanical treatment. The controlled forming leads to a reduced austenitic grain size. This small grain size favors the nucleation of the final constituents of the steel microstructure. With controlled cooling after forming, the need for a further heat treatment may be completely eliminated.

mation of alternating bands of pearlite and ferrite or other constituents with a significant variation in the carbon content. The phenomenon is especially interesting because carbon is an interstitial solute that diffuses rapidly and thus is easily homogenized during austenitization treatments. However, normalizing or annealing heat treatments are unable to eliminate banding (Fig. 11.48). Conversely, heat treatments involving rapid cooling from the austenitic single-phase region can eliminate or dramatically reduce the occurrence of banding (Ref 27, 28) as the example presented in Fig. 11.49 shows. Banding is a phenomenon associated with the segregation of substitutional elements,

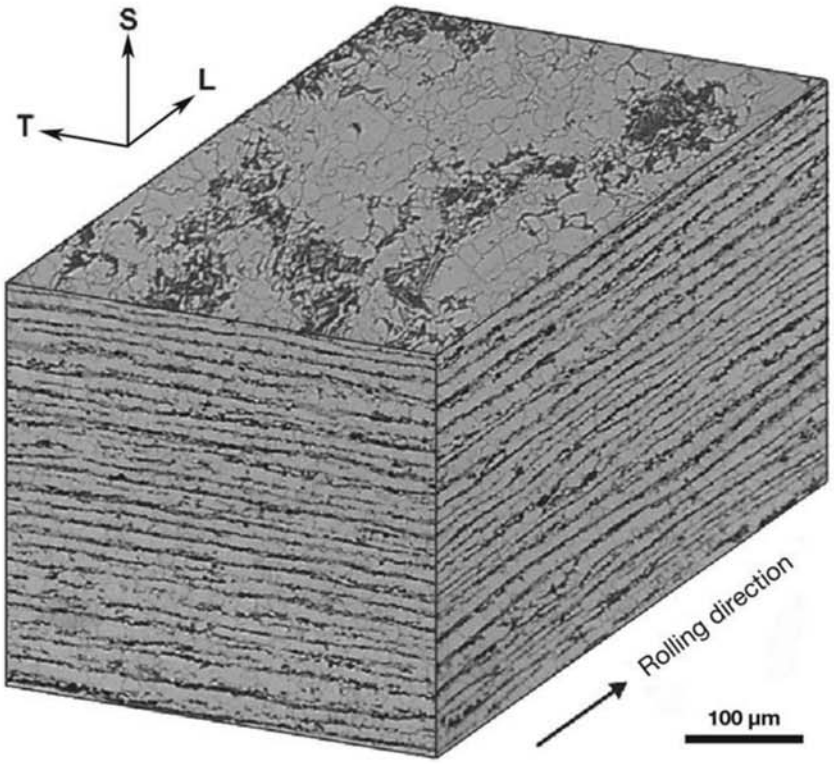

Fig. 11.47 Composite image from three micrographs with orthogonal orientations from a banded low carbon steel plate. Ferrite and pearlite. L = longitudinal, T = transverse, S = short transverse. Courtesy of H. Badheshia, University of Cambridge.

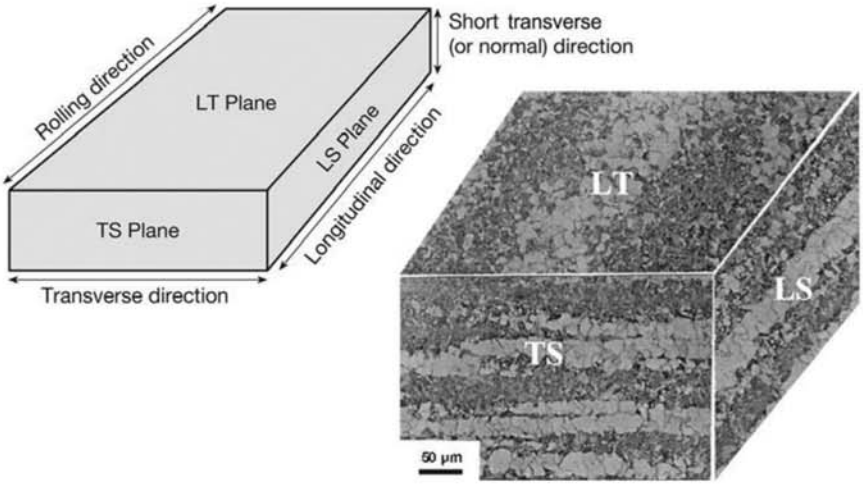

Fig. 11.48 Composite image from three micrographs with orthogonal orientations from a plate of HY-100 steel, slow cooled from the austenitic region. Banded structure. Ferrite, acicular ferrite, bainite, and martensite. L = longitudinal, T = transverse, S = short transverse. Etchant: nital 2%. Reproduced with permission from Springer Science and Business Media. Source: Ref 27

as shown in Fig. 11.50. When steel is austenitized, the segregation of substitutional elements cannot be eliminated, because these are slow diffusing elements. Thus, different regions of the steel (bands) have different chemical compositions and therefore have different behavior during austenite decomposition. Austenite decompositions starts in the regions that are leaner in

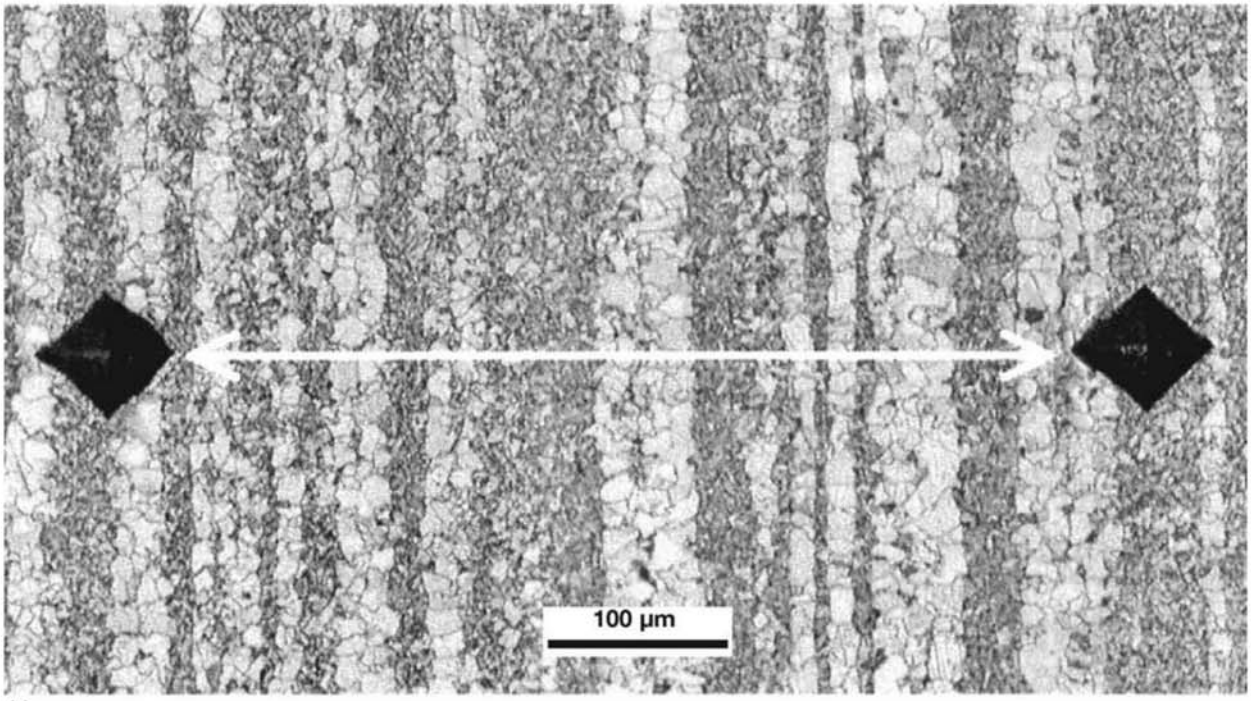

(a)

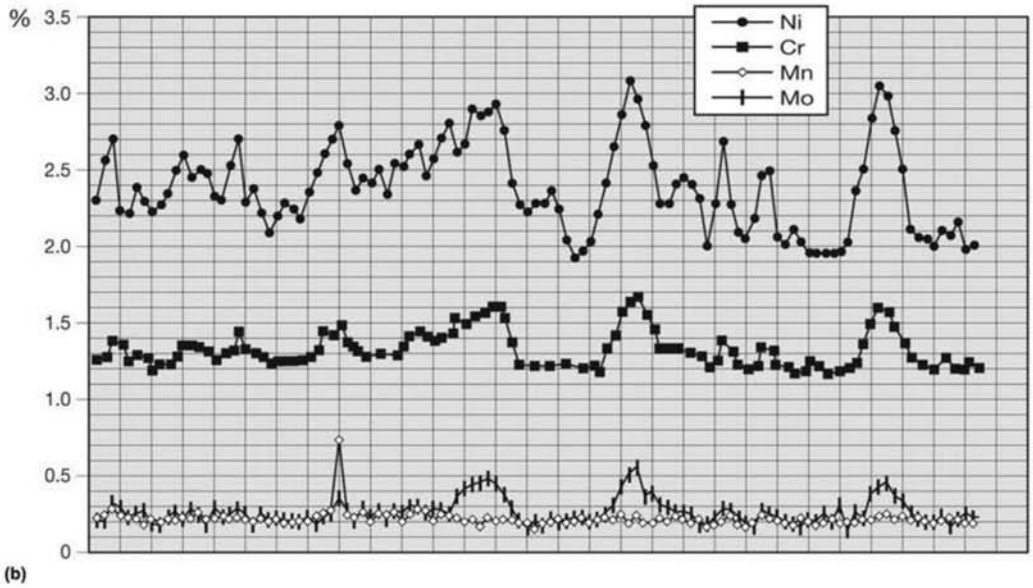

(b)

Fig. 11.49 Cross section of the plane identified as LS in the HY-100 steel plate shown in Fig. 11.48, slow cooled. The hardness prints indicate the location where the microprobe (WDS) analysis started and ended. Chemical analysis (WDS), shown in (b). Heat analysis: C = 0.16%, Mn = 0.26%, P = 0.008%, S = 0.009%, Si = 0.22%, Ni = 2.62%, Cr = 1.32%, Mo = 0.25%. Reprinted with permission from Springer Science and Business Media. Source: Ref 27

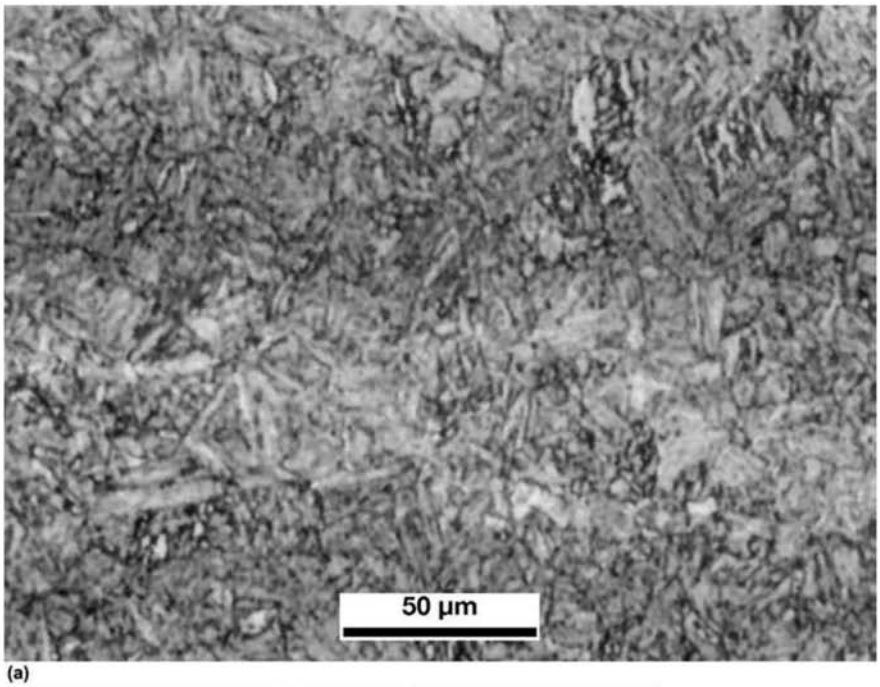

(a)

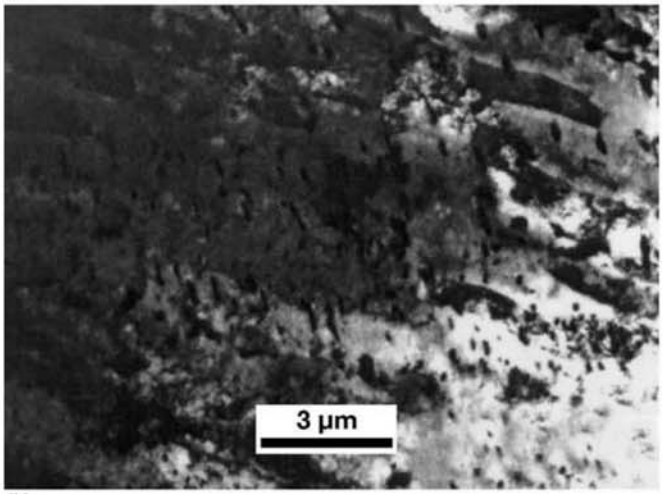

(b)

Fig. 11.50 Cross section of the plane identified as TS in the hot rolled HY-100 steel presented in Fig. 11.48, quenched and tempered. (a) Very little evidence of segregation can be noticed. Etchant: nital 2%. (b) TEM of selected region of the sample: tempered martensite. Reproduced with permission from Springer Science and Business Media. Source: Ref 27

austenite-stabilizing elements (or, conversely, richer in elements that are ferrite stabilizers). If the steel is cooled at a sufficiently slow rate to allow carbon diffusion, this element will be rejected from the regions that transform first to ferrite (due to the low carbon solubility in this phase) and will concentrate on the regions that remain austenitic. When these regions transform, they will be sufficiently carbon-rich to form constituents that are significantly different from what would be expected as the average microstructure of the steel. In

particular, these regions commonly transform to pearlite in low and medium carbon structural steels, either normalized or air-cooled after hot rolling.

However, if the cooling is fast, there may not be sufficient time for carbon to redistribute during austenite decomposition and the only evidence of segregation that can be obtained is related to the response to chemical etching and the eventual difference in hardenability between the less segregated and the more segregated areas. Essentially all substitutional elements will cause banding. Evidently, those elements that segregate with more intensity during solidification will have a larger potential to produce banding. For this reason, phosphorous was considered the element responsible for banding for many years.

11.2.8 Other Evidence of Segregation Appearing in Steel Products

The main structural effects associated with microsegregation in steel are banding and the appearance of fibers in the hot worked material. As the size of the as-cast product (ingot or plate) increases, and when larger-scale segregates occur, the heterogeneities can become even more evident. Examining products using cross sections in the longitudinal direction is not always viable, making it harder to characterize these segregates. The occurrence of these segregates (and segregation itself) is a feature of solidification performed on an industrial scale. As larger parts are needed, the starting ingots must be also larger, resulting in an overall increase of segregation-related issues. The acceptability of these heterogeneities is directly related to the performance of the parts in question. Various studies have been performed to evaluate the effects of segregated regions on the properties of finished parts (Ref 7, 27, 29, 30). It is not reasonable to expect that parts produced from large ingots (larger than around 25 t, for instance) will have the same homogeneity achieved when forging parts from small ingots (smaller than around 5 t, for instance) or that of a highly deformed product that originated from a continuously cast plate or bloom (Fig. 11.51).

Figure 11.52 presents the results of a study conducted by the International Atomic Energy Agency (IAEA) to evaluate the toughness of the materials used as primary components in nuclear power plants (Ref 30). The forgings manufactured for these applications are at the limit of modern ingot casting and open-die forging technology in view of their sizes and applicable quality requirements. The structural variation from surface to center in the forging is evident, as is its effect on the variation of the mechanical properties. It is up to the designer using these parts to consider these property variations and define adequate sampling positions for the performance of qualification (first article approval) and acceptance tests of these products. Figure 11.53 presents a replica of the result of a surface crack examination performed by magnetic particles (MT) on the weld edges to be welded in a thick plate of structural steel WStE355. The replica was produced using transparent adhesive tape to retain the magnetic particles after magnetization and performance of the MT exam. When the same region was examined using dye penetrant technique, no indications were present in the region. These nondestructive evaluations were followed by metallographic examinations to determine the cause of the indications in the MT exam. The results are shown in Fig. 11.53.

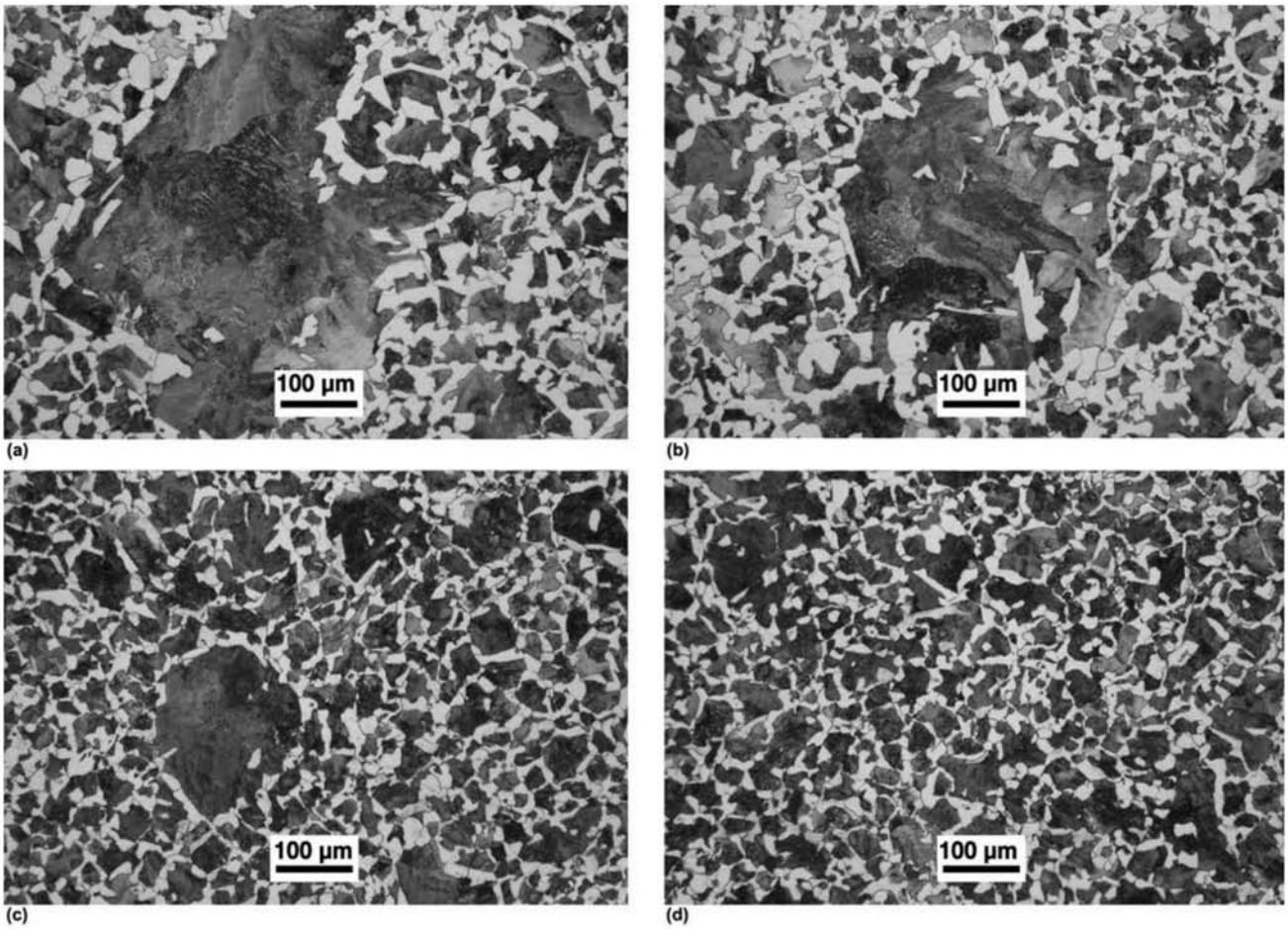

Fig. 11.51 A bar of AISI 1045 forged from a 29 t ingot to a 700 mm (28 in. diameter) cylinder. Normalized. (a) and (b) samples from the bar region closer to the ingot top, (c) and (d) samples from the bar region closer to the foot of the ingot. Micrographs (a) and (b) shown heterogeneity on the size of the pearlite colonies and micro-regions with a larger volumetric fraction of pearlite. Micrograph (c) shows some heterogeneity in the pearlite colony size. Mechanical tests (tensile and Charpy-V) of this material in specimens with comparable microstructures did not indicate deviations in the mechanical properties associated with these micrographic features.

These indications caused by microstructural heterogeneities are called ghost indications. It is only possible to be sure that they are not relevant discontinuities when a complete metallographic evaluation is performed, as shown in this case.

11.3 Forming Finished Parts

Cold and hot working processes are also used to produce parts very close to the shape and dimensions of the desired final products. Rolling rails (Chapter 15, "Engineered Special Bar Quality Steel (Engineered Steel)," in this book) and profiles are some typical examples. Rolling threads in fasteners, normally done by cold working, is discussed in Chapter 12, "Mechanical Work of Steels: Cold Working," in this book. Closed die forging is one of the most common processes used to manufacture steel parts with dimensions very close to the finished parts. In this section, cold and hot closed die forging are discussed.

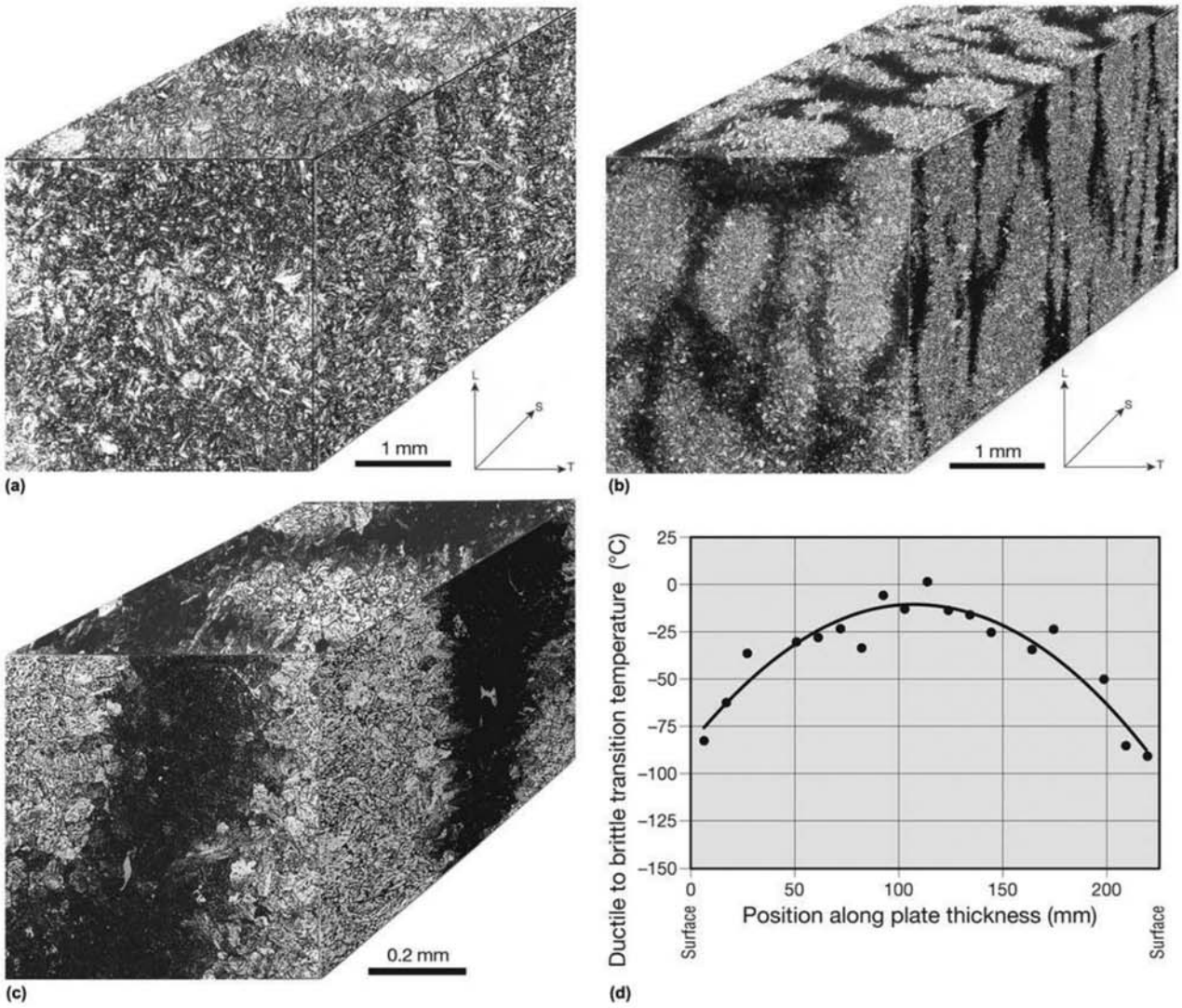

Fig. 11.52 The structures at the surface (a) and at the center (b) and (c) of a thick plate (225 mm, or 9 in., thickness) in quenched and tempered ASME/ASTM A533B Class 1 steel manufactured for nuclear applications. The increase in segregation from the surface to the center is evident, even after forging and rolling. Reproduced with permission from Elsevier. In (d) the measured values for the ductile-brittle transition temperature through the thickness are presented (the criteria for transition was defined as 41J absorbed in the ISO-V test). Images supplied by H.-W. Viehrig, FZR, Dresden, Germany. Source: Ref 30

11.3.1 Closed Die Forging

Cold or hot forming operations in which the solid material is forced to "flow" through plastic deformations inside a die or cavity with the shape of the desired part (Ref 31) are called closed die forging operations. Closed die forging can be performed with flash or be flashless. The most common process is performed with flash, in which excess material is expelled by the forging operation from the forging cavity as part of the process design. Flash will

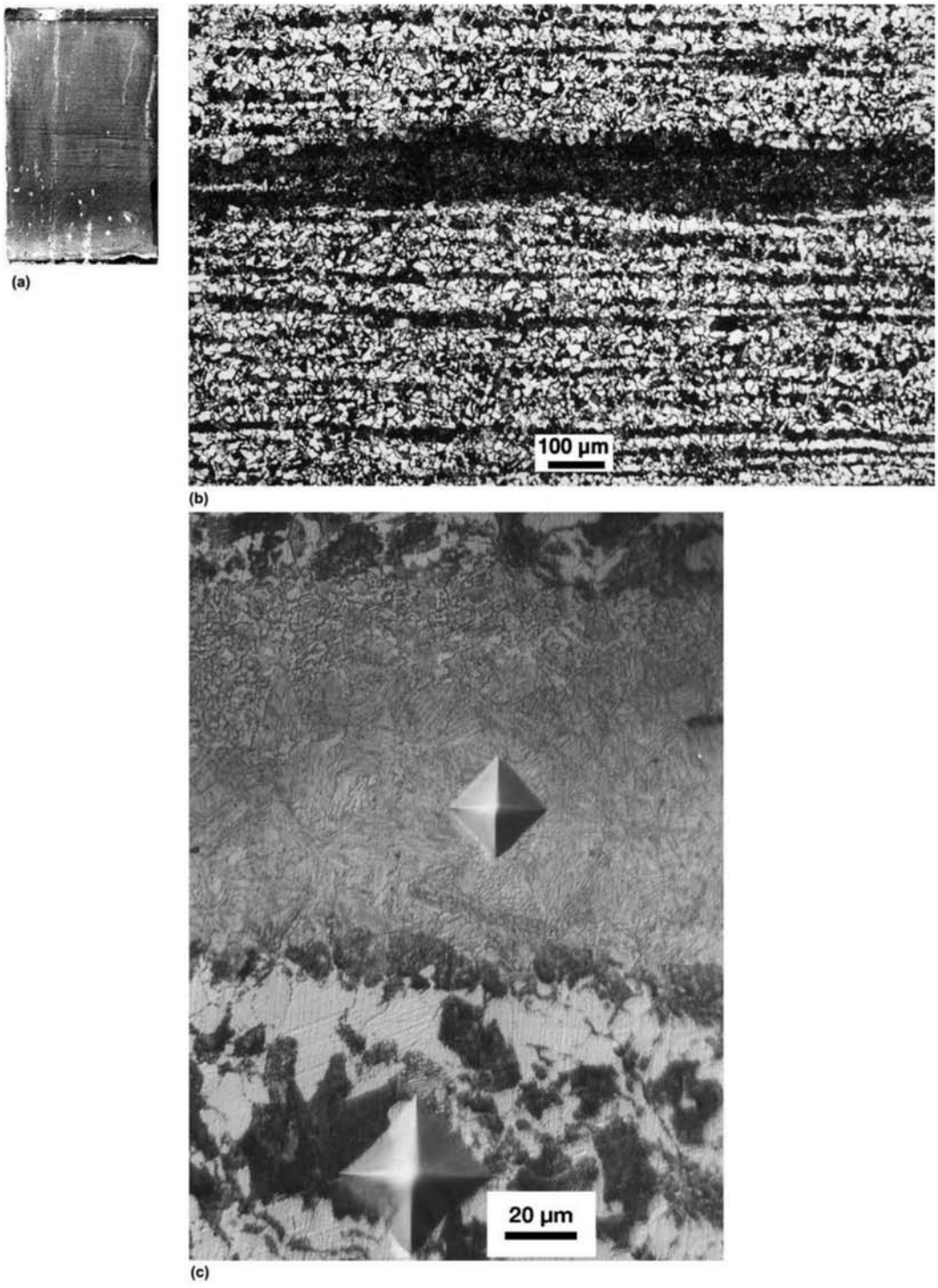

Fig. 11.53 (a) Replica, produced with transparent adhesive tape of the magnetic particle (MT) examination of the weld edges of a plate of structural steel WStE355. The plate is 38 mm (1.5 in.) thick. The indications are elongated in the direction of rolling. (b) Micrograph of the region of the indications. Banded structure with a large, wide dark band in the region corresponding to the indication. (c) Detail of the region of image (b). Lighter etching than in image (b) makes it possible to observe the presence of bainite and acicular ferrite. The hardness impressions (produced with the same load) indicate that the segregated region that caused the MT indication has significantly higher hardness than the rest of the steel. Using EMPA (WDS) manganese segregation was identified: (Mn average = 1.0% Mn segregate = 1.8%). Etchant: nital 2%.

unavoidably cause an interruption or cut in the fibers of the material. To ensure that the flash line will not be a weak point in the forging, particularly with regard to fatigue resistance, it is very important to consider its location with respect to the mechanical loading of the part. Eventually, additional measures that can improve the fatigue resistance of these regions, such as the control of part roughness or shot-peening, should be considered (Ref 32, 33). Furthermore, the fact that the fibers concentrate inclusions and microsegregation should be considered in the design of these forgings. If the degree of deformation during die forging is too high, it is possible that this concentration may result in unfavorable conditions in the further processing of the part, such as machining, heat treatment, and surface treatment. In some special cases, it may be necessary to prevent an excessive concentration of fibers in critical regions of the component. Presently, the use of finite element models is common to predict the flow lines and the extent of deformation expected during forging (Ref 33). Figures 11.54 and 11.55 present examples of the distribution of fibers in closed die forgings.

11.4.1 Laps and Cracks

11.4 Defects in Hot Working

During hot working, mechanical defects such as laps or folds are prone to occur if care is not taken with tooling design and process operations. Unless these defects are properly identified and removed, they can give rise to defects in the product during further heat treatment or application of the material. Figures 11.56 to 11.60 present examples of these defects. The presence of oxides and the occurrence of decarburization inside these laps and cracks are good indications that the parts have been exposed to oxidizing atmospheres

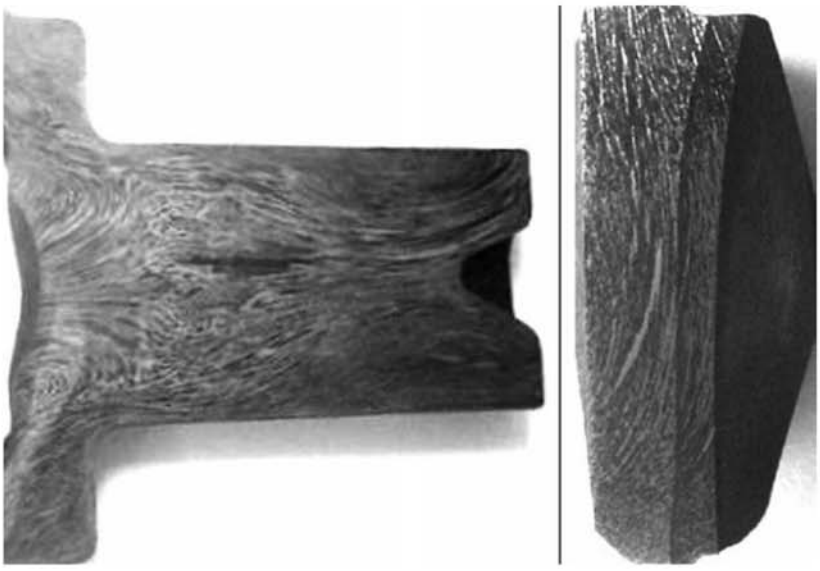

Fig. 11.54 Cross sections of parts produced by closed die forging. Fiber orientation is clearly visible. The fibers are not cut, indicating a good forging design. For improved visualization of the fibers after etching with hot hydrochloric acid, the visibility of the fibers is enhanced either by the careful application of rubber stamp ink or aniline. Courtesy of M.M. Souza, Neumayer-Tekfor, Jundiaí, SP, Brazil.

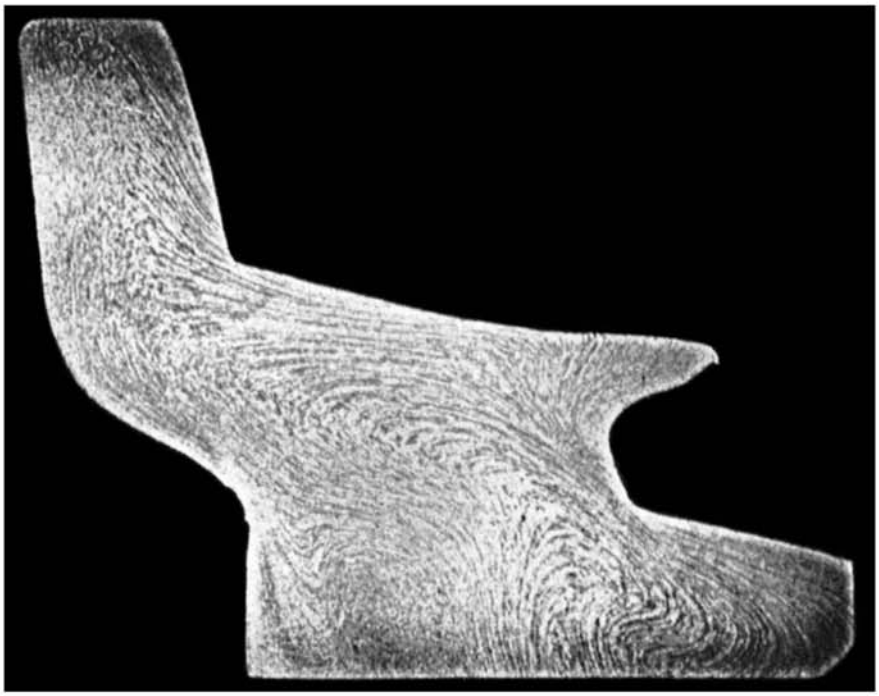

Fig. 11.55 Part of the longitudinal cross section of a tractor roll, closed die forged. The presence of fibers with narrow spacing indicates that the material used for the forging operation was a rolled or forged bar. The curves in the fibers indicate that the part was produced by closed die forging. Etchant: iodine.

at high temperatures when the defects were already present. This helps separate defects that occur prior to heat treatment from heat treatment cracks (Chapter 9, "Conventional Heat Treatment—Usual Constituents and Their Formation," in this book).

11.4.2 Overheated or "Burned" Material

Excessive heating is a problem with a higher potential of happening during hot working than during heat treatment. The temperatures at which hot forming starts can be significantly high. Furthermore at the beginning of the hot working stage, ingots and products of continuous casting present the maximum level of segregation. The combination of segregation and high temperatures can lead to heating very close to or above the solidus temperature. Even if temperatures at which the liquid phase becomes stable are not reached, very high rates of oxidation can be experienced, particularly at grain boundaries. Depending on the fuels used in the heating furnaces, this can occur through surface contamination by sulfur or, less commonly, by heavy metals. In general, the material is called "burned" when melting or oxidation occurs in the austenitic grain boundaries. This material generally cannot be recovered via heat treatments and normally must be scrapped (Ref 7, 34, 35). Overheating can reveal itself in many ways and is associated to different phenomena. One of the mechanisms of overheating during hot working is the dis-

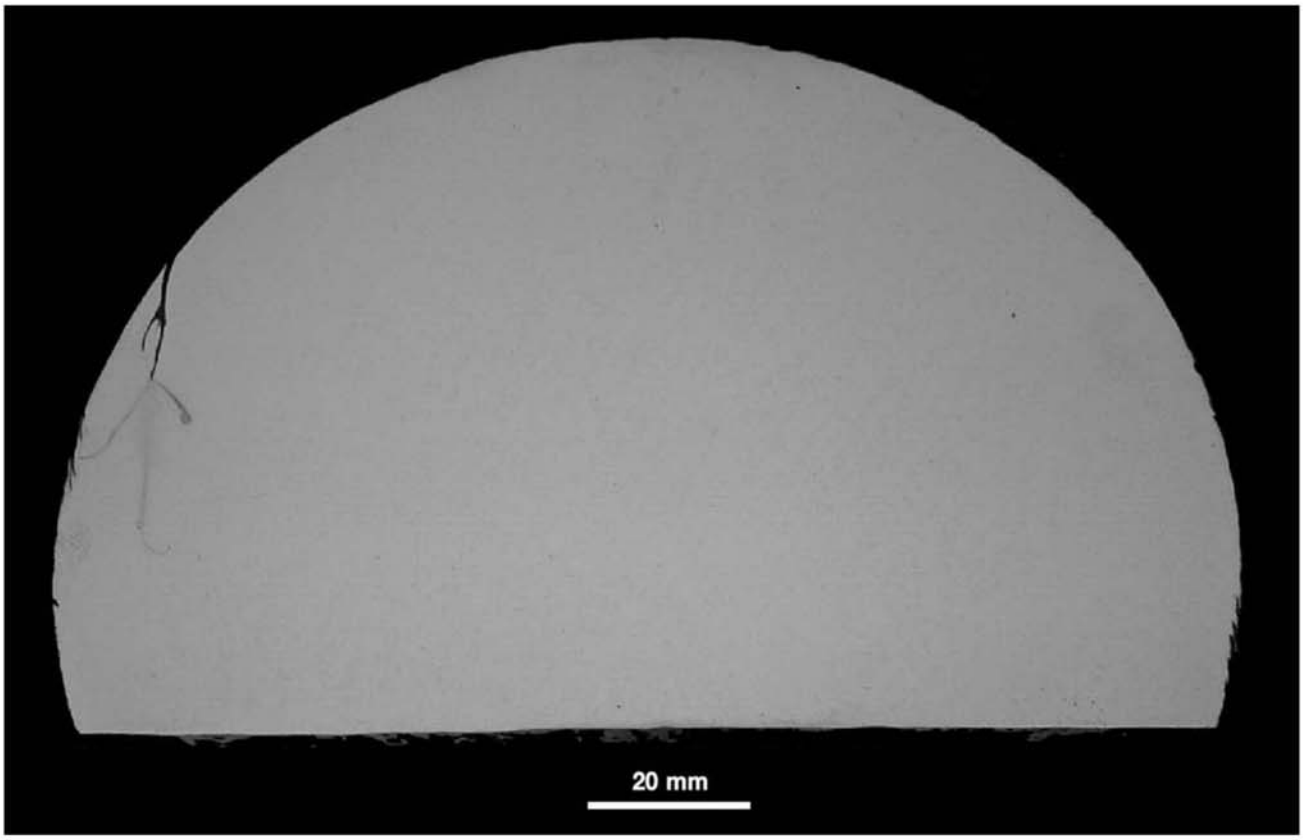

Fig. 11.56 Forging lap in a bar of ASTM A564 UNS 17400 (17-4PH) stainless steel. Transverse cross section. (There is an etching stain close to the lap caused by liquid retained inside the lap during the preparation process). Etchant: 2000 ml H_2O + 300 ml H_2O_2 + 350 ml HCl + 50 ml HNO_3. The hydrogen peroxide causes heating. Additional heating is not necessary. Etching time 15 min. Courtesy of Villares Metals S.A., Sumaré, SP, Brazil.

solution and reprecipitation of manganese sulfides. When the sulfide reprecipitates in austenitic grain boundaries, it normally causes embrittlement (Ref 7). The occurrence of excessive austenitic grain growth due to excessive local heating is also frequently called overheating. In the case of hypereutectoid steels with primary carbides, overheating may occur through dissolution and reprecipitation of these very stable carbides as a network. Steel containing a stable network of carbides has very low hot workability (Fig. 11.61). Figures 11.62 through 11.67 present some examples of burned material.

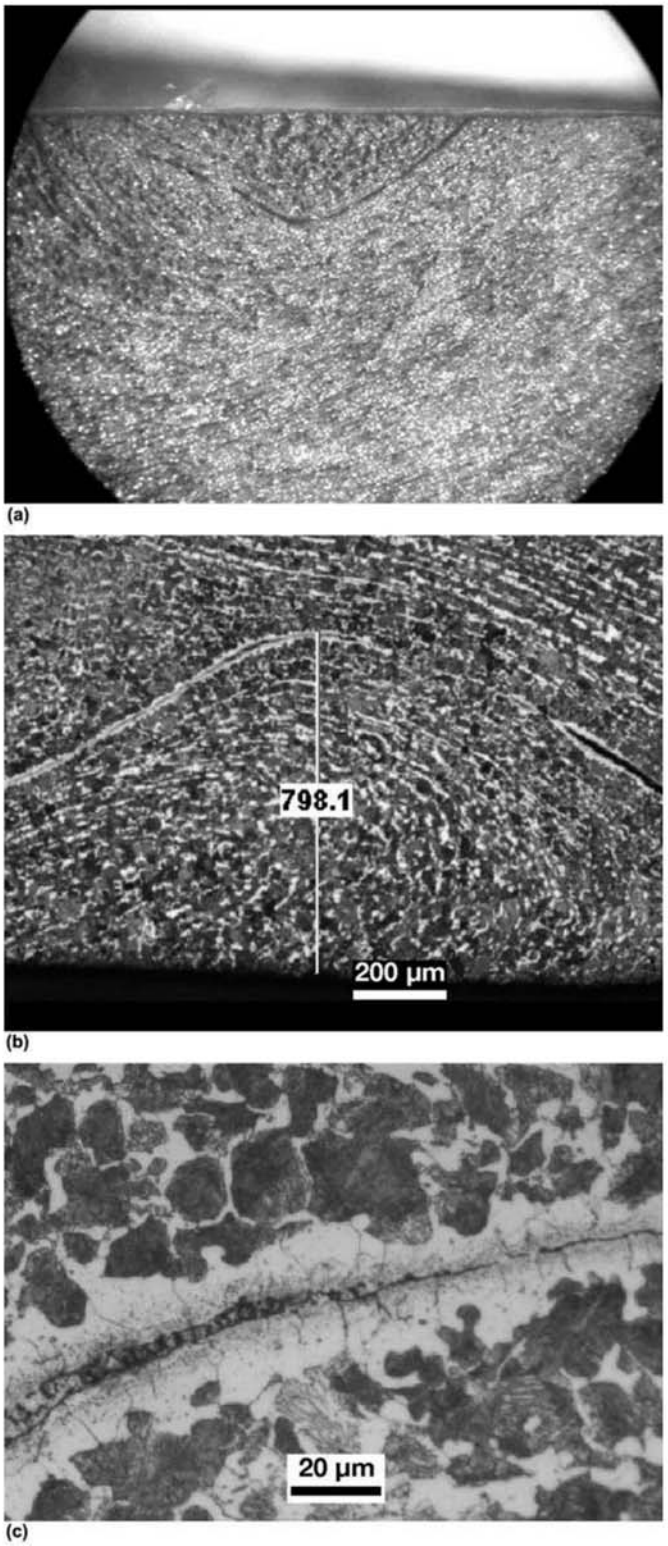

Fig. 11.57 Forging lap. (a) Macrograph. (b) Ferrite, pearlite. Decarburization and oxides inside the discontinuity. Etchant: nital 2%. (c) Extensive decarburization and presence of oxides in the discontinuity. Etchant: nital 2%. Courtesy of M.M. Souza, Neumayer-Tekfor, Jundiaí, SP, Brazil.

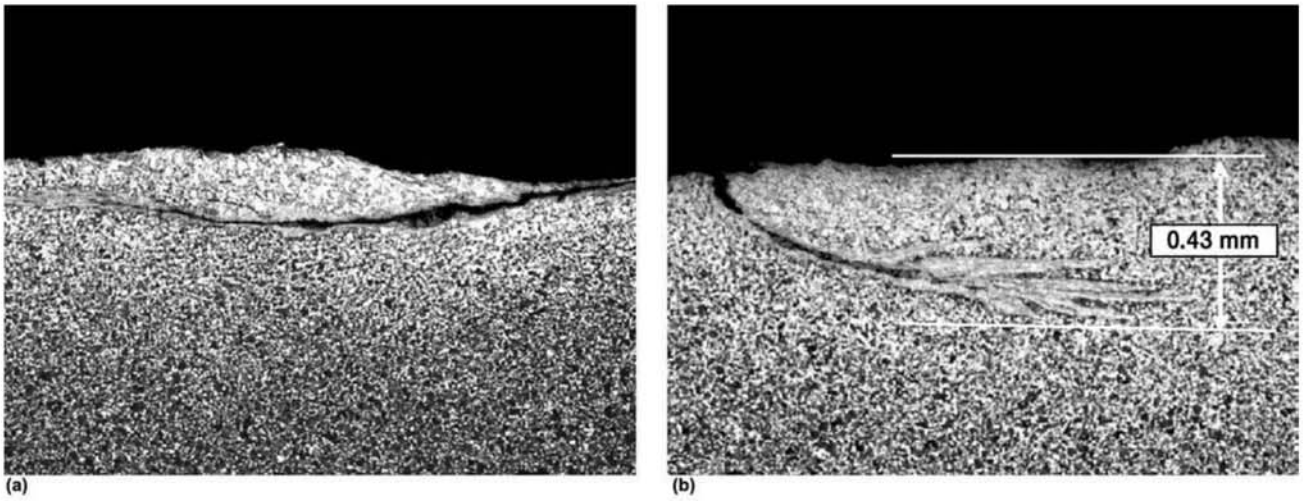

Fig. 11.58 Forging laps detected by surface crack examinations. Extensive decarburization of the lap region can be noticed when observing the reduction of the pearlite volume fraction. Etchant: nital 2%. Courtesy of M.M. Souza, Neumayer-Tekfor, Jundiaí, SP, Brazil.

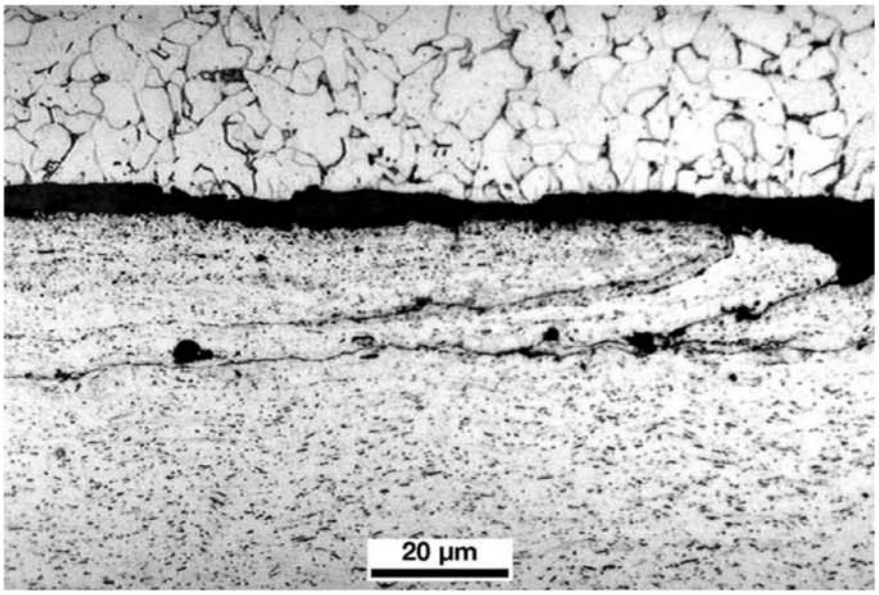

Fig. 11.59 Surface lap in hot rolled product, containing oxide particles inside the lap. For the metallography, the sample was mounted in contact with another plate (top, in the figure) to preserve the surface area to avoid rounding it during grinding and polishing.

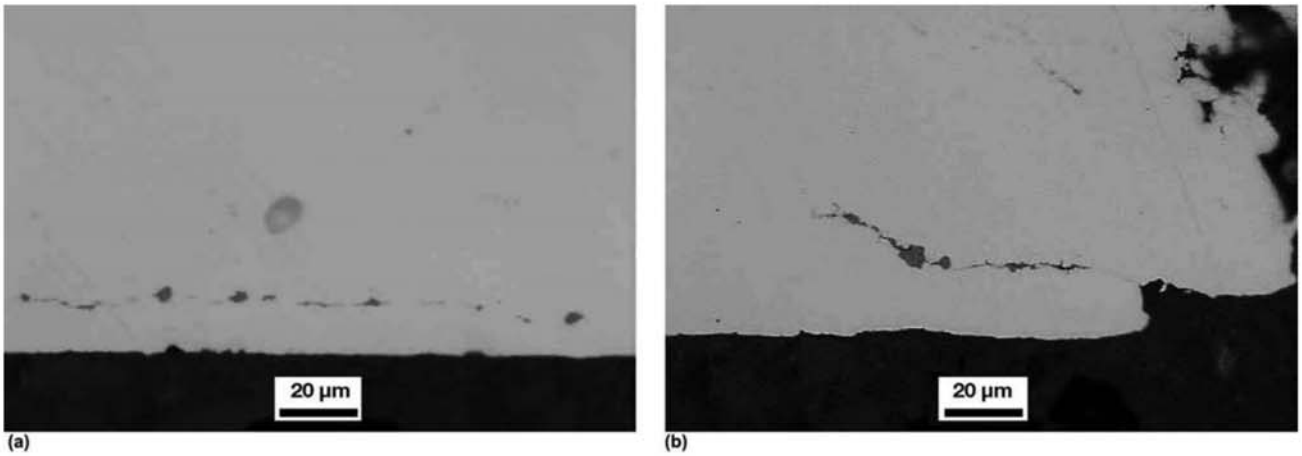

Fig. 11.60 Longitudinal cross section of a cold rolled product. Subsuperficial oxides are visible. Possible cause is encrustation of the hot work scale.

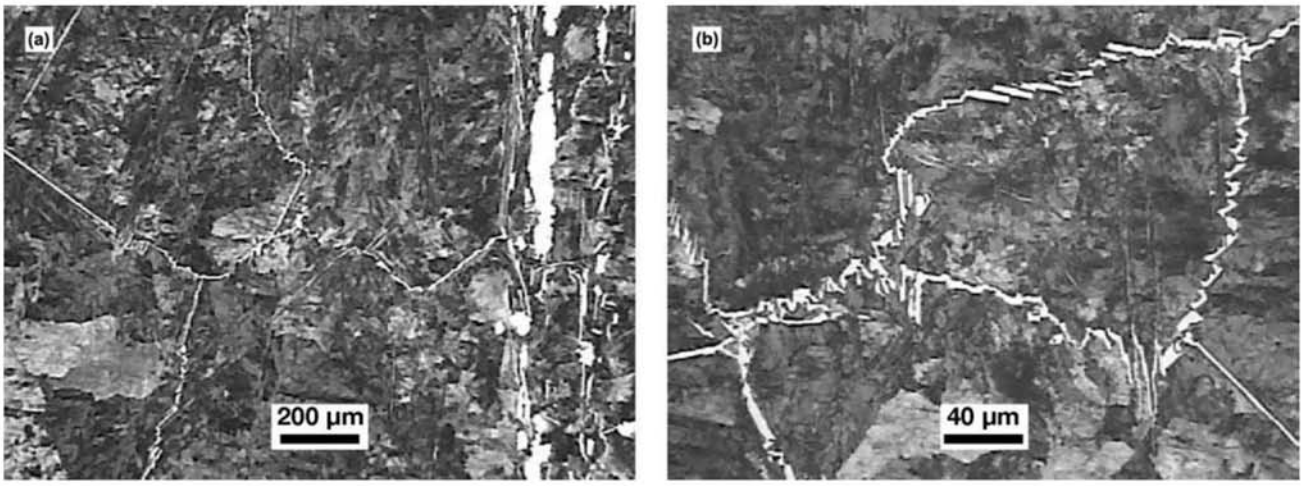

Fig. 11.61 Tool steel containing C = 1.60%, Mn = 0.90%, Cr = 1.50%, Mo = 0.55%, Ni = 0.70%, and W = 0.20% overheated. (a) Coarse primary carbides (right, in the image) pearlite matrix with carbides in network on the previous austenitic grain boundaries. (b) Detail of the complex carbides morphology in the prior austenitic grain boundaries and fine pearlite inside the grains. Etchant: nital 4%. Courtesy of Villares Metals S.A., SP, Brazil.

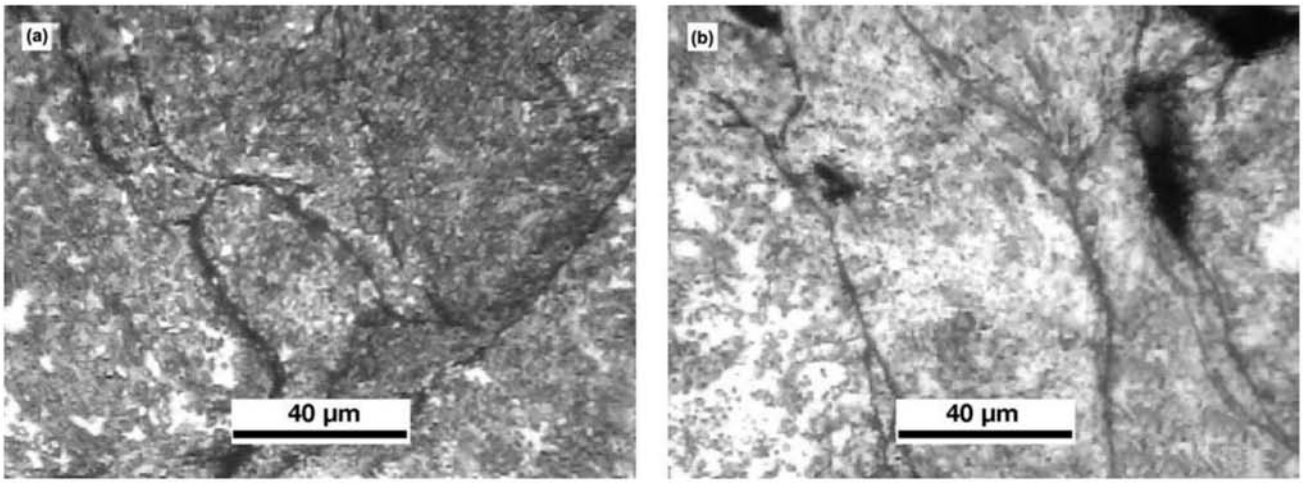

Fig. 11.62 (a) Shock-resistant steel ASTM A681-S7 overheated during forging (burned). Presence of oxides and evidence of start of melting (incipient fusion) at the grain boundaries. Etchant: nital 4%. (b) Hot working tool steel DIN W.Nr. 1.2885-X32 CrMoCoV 3-3-3 overheated (burned). Etchant: nital 4%. Courtesy of Villares Metals S.A., SP, Brazil.

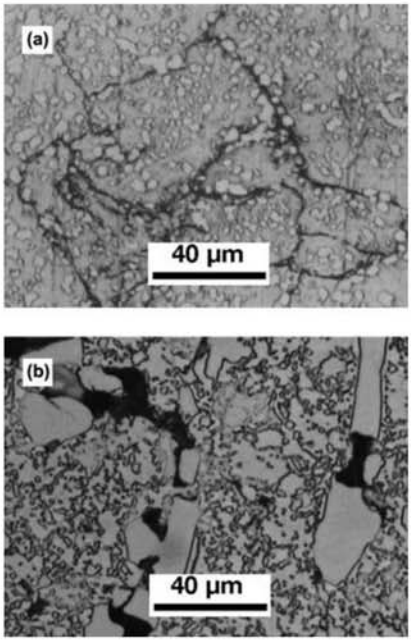

Fig. 11.63 (a) Martensitic stainless steel ASTM A 182-420 overheated (burned) during forging. Etchant: Villela. (b) ASTM A681-D2 tool steel overheated (burned) during heating for hot working. Separations at the grain boundaries in regions adjacent to chromium carbides. Etchant: nital 4%. Courtesy of Villares Metals S.A., SP, Brazil.

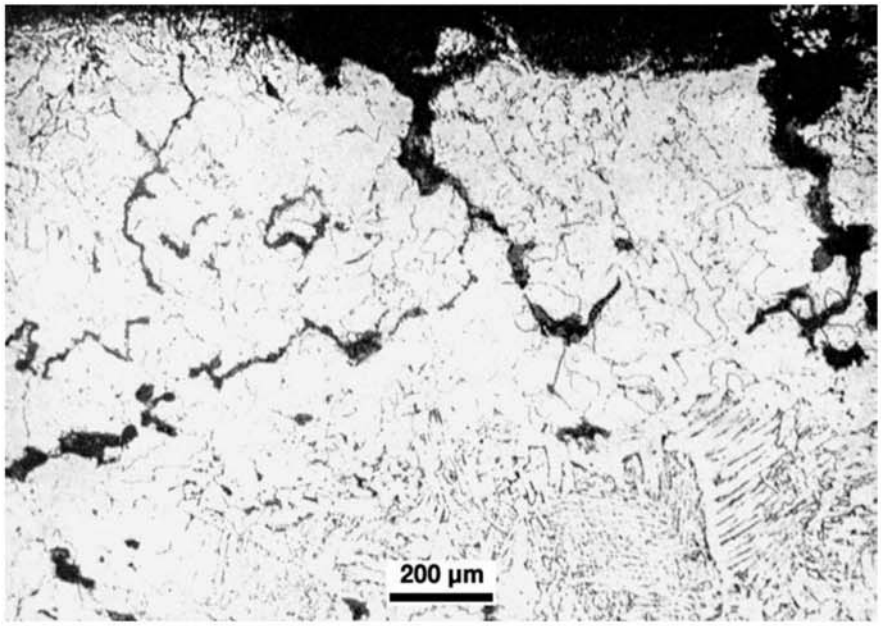

Fig. 11.64 Transverse cross section close to the surface of a bar of steel overheated and burned. Intense decarburization and oxidation of the grain boundaries. Etchant: nital.

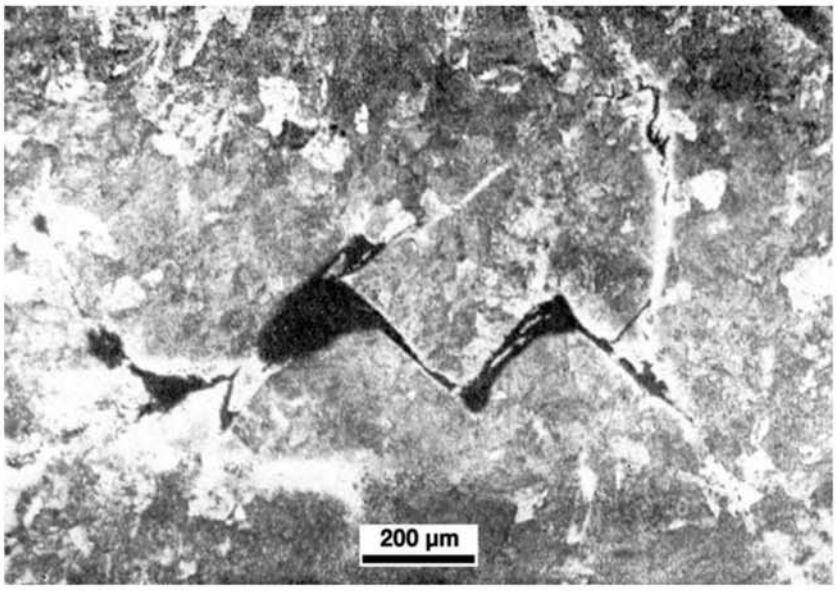

Fig. 11.65 Transverse cross section of a bar of a steel containing C = 0.84% and P = 0.03%. Zig-zag cracks formed during forging in regions with indications of a "burned" structure (larger dark areas). Etchant: nital.

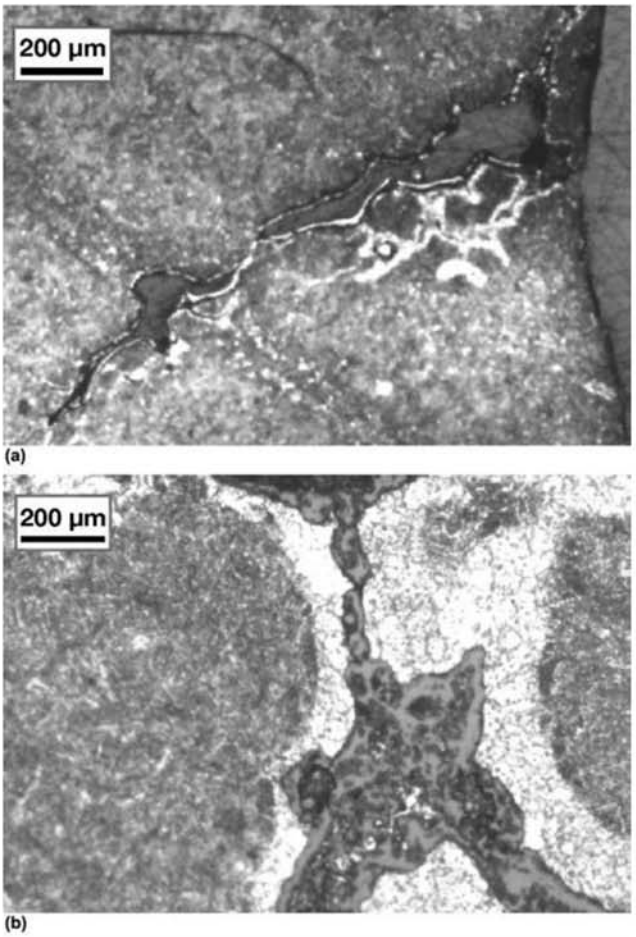

Fig. 11.66 Steel that was burned during heating for hot forming. Intergranular oxidation, decarburization, and incipient melting (observe the shape of the oxides and the crack). Courtesy of M.M. Souza, Neumayer-Tekfor, Jundiaí, SP, Brazil.

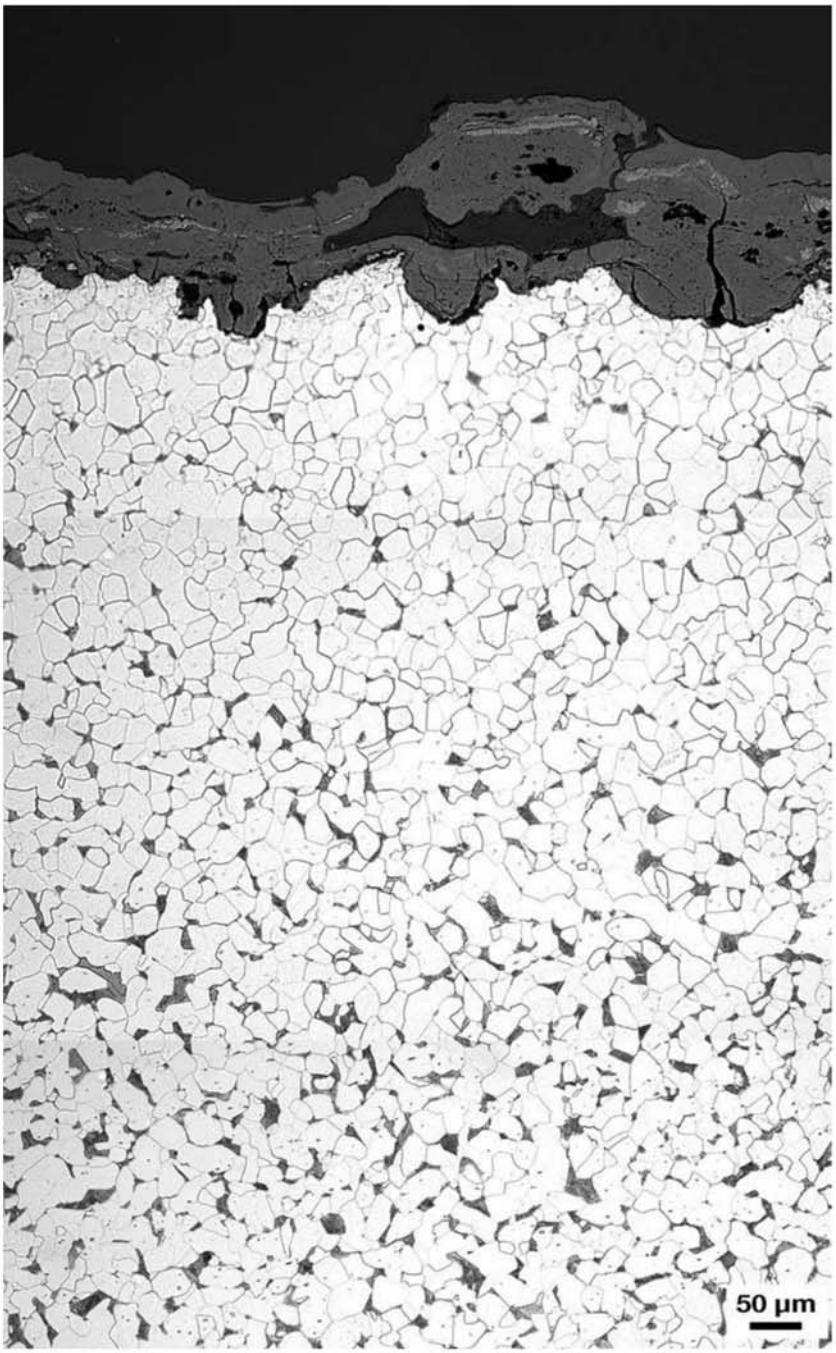

Fig. 11.67 Cross section of a structural steel plate (ferrite and pearlite) that was exposed to a building fire. Oxidation with the formation of a thick layer of oxides in the plate surface, and a region that suffered partial decarburization. The kinetics of the oxidation and the decarburization process, as well as the composition of the oxides formed depend on the process temperature and the atmosphere presence. Notice the difference with respect to material that has been "burned" during hot working, shown in previous figures. Etchant: nital 2% and picral 4%. Courtesy of National Institute of Standards and Technology (NIST), Gaithersburg, MD, USA. Source: Ref 10

REFERENCES

1. A. Tomiz and R. Kaspar, Deep-Drawable Thin-Gauge Hot Strip of Steel as a Substitution for Cold Strip, *ISIJ Int.*, Vol 40 (No. 9), 2000, p 927–31
2. A. Costa e Silva and P.R. Mei, *Aços e ligas especiais*, 3rd ed., Blucher, 2010 (in Portuguese)
3. E.C. Bain, Nippon-To and Introduction to Old Swords of Japan. *J. Iron Steel Inst.*, April 1962, p 265–82
4. T. Inoue, The Japanese Sword—The Material, Manufacturing and Computer Simulation of Quenching Process, *Mat. Sci. Res. Int.*, Vol 3 (No. 4), 1997, p 193–203
5. National Geographic Magazine documentary, https://www.youtube.com/watch?v=53vdwxN9WeQ (accessed November 11, 2016)
6. A. Sauveur, *Metallography and Heat Treatment of Iron and Steel*, 4th ed., McGraw-Hill, 1935
7. G. Krauss, Solidification, Segregation, and Banding in Carbon and Alloy Steels, *Metall. Mat. Trans. B*, Vol 34B (No. 6), 2003, p 781
8. R. Kiessling, *Non-Metallic Inclusions in Steels*, Iron and Steel Institute, 1968
9. W.A. Spitzig, Effect of Sulfides and Sulfide Morphology on Anisotropy of Tensile Ductility and Toughness of Hot-Rolled C-Mn Steels, *Metall. Trans. A*, Vol 14A, 1983, p 471–84
10. S.W. Banovic, C.N. McCowan, and W.E. Luecke, NIST NCSTAR 1-3E (draft) for public comment federal building and fire safety investigation of the World Trade Center disaster physical properties of structural steels (draft), NIST, 2005
11. S. Mizoguchi, "A Study on Segregation and Oxide Inclusions for the Control of Steel Properties," PhD thesis, University of Tokyo, 1996
12. Y. Ueshima, H. Yuyama, S. Mizoguchi, and H. Kajioka, Effect of Oxide Inclusions on MnS Precipitation in Low Carbon Steel, *Tetsu-to-Hagane*, Vol 75 (No. 3), 1989, p 501–8
13. A. Costa e Silva, Thermodynamic Aspects of Inclusion Engineering in Steels, *Thermodynamics of Alloys TOFA 2006*, Beijing, full paper published as A. Costa e Silva, Thermodynamic Aspects of Inclusion Engineering in Steels, *Rare Metals*, Vol 25 (No.5), 2006, p 412–9
14. T. Onoe, S. Ito, K. Ogawa, T. Mimura, H. Matsumoto, and S. Maeda, Shape Control of Inclusions for Steel Tire Cord (Development in Ladle Arc Refining), *Trans. ISIJ*, Vol 27, 1987, p B249
15. K. Oikawa, H. Mitsui, T. Ebata, T. Takiguchi, T. Shimizu, K. Iishikawa, T. Noda, M. Okabe, and K. Ishida, A New Pb-Free Machinable Ferritic Stainless Steel, *ISIJ Int.*, Vol 42 (No. 7), 2002, p 806–7
16. K. Oikawa, S. Sumi, and K. Ishida, Morphology Control of MnS Inclusions in Steel during Dolidification by the Addition of Ti and Al, *Zeit. Metall.*, Vol 90 (No. 1), 1999, p 13–18

17. ASTM, *ASTM E45-05 Standard Test Methods for Determining the Inclusion Content of Steel*, American Society for Testing of Materials, 2005
18. ASTM, *ASTM E1245-03 Standard Practice for Determining the Inclusion or Second-Phase Constituent Content of Metals by Automatic Image Analysis*, American Society for Testing and Materials, 2003
19. ASTM, *ASTM E2283 Standard Practice for Extreme Value Analysis of Nonmetallic Inclusions in Steel and Other Microstructural Features*, American Society for Testing of Materials, 2004
20. L. Zhang and B.G. Thomas, State of the Art in Evaluation and Control of Steel Cleanliness, *ISIJ Int.*, Vol 43 (No. 3), 2003, p 271–91
21. I.M.V. Caminha, I.D.C. Abud, J.L.D. Nascimento, and A.A. Costa e Silva, Avaliação preliminar de métodos para estimativa do tamanho máximo de inclusão não-metálica em aço de alta limpeza, In: 62º Congresso da ABM, Associação Brasileira de Metalurgia e Materiais, 2007
22. M. Hillert, *Metallographic Atlas*, Materials Education Council (MEC), Pennsylvania State University, 1991; http://www.met.kth.se/ia/ (accessed November 4, 2016)
23. G. Roberts, G. Krauss, and R. Kennedy, R, *Tool Steels*, 5th ed., ASM International, 1998
24. A. Brossi, Untersuchung über den einfluss des schmiedens auf die mechanischen eigenschaften bei freiformschmiedestücken, International Forgersmasters Conference, 1952
25. A. Suzuki et al., Manufacturing of Large and Integral-Type Steel Forgings for Nuclear Steam Supply System Components, International Forgersmasters Conference. 1981, paper 1.7
26. H. Ohtani, Processing—Conventional Heat Treatments, *Materials Science and Technology—Constitution and Properties of Steels*, F.B. Pickering, Ed., Wiley-VCH, 1996
27. D. Chae, D.A. Koss, A.L. Wilson, and P.R. Howell, The Effect of Microstructural Banding on Failure Initiation of HY-100 Steel, *Metall. Mat. Trans. A*, Vol 31A (2000), p 995–1005
28. T.F. Majka, D.K. Matlock, and G. Krauss, Development of Microstructural Banding in Low-Alloy Steels with Simulated Mn Segregation, *Metall. Mat. Trans. A*, Vol 33A (No. 6), 2002, p 1627–37
29. H.B. Gayley, Relationship between Turbine Rotor and Disk Metallurgical Characteristics and Stress-Corrosion Cracking Behavior, Final Report, Report 50490, EPRI, 1986
30. H.W. Viehrig, J. Boehmert, and J. Dzugan, Some Issues by Using the Master Curve Concept, *Nucl. Engin. Des.*, Vol 212, 2002, p 115–24
31. M. Shirgaokar, Forging Processes: Variables and Descriptions, *Cold and Hot Forging Fundamentals and Applications*, T. Altan, G. Ngaile, and G. Shen, Eds., ASM International, 2004
32. J.L.A. Autran and M.M. Souza, Viabilidade Econômica e Precisão de Forjamento a Frio de Peças Funcionais de Médio Porte, XII Seminário Nacional de Forjamento, 1992

33. M.M. Souza, Private communication, 2007
34. G.E. Hale and J. Nutting, Overheating of Low-Alloy Steels, *Int. Met. Rev.*, Vol 29, 1984, p 273–98
35. G. Krauss, *Steels: Processing, Structure and Performance*, ASM International, 2005

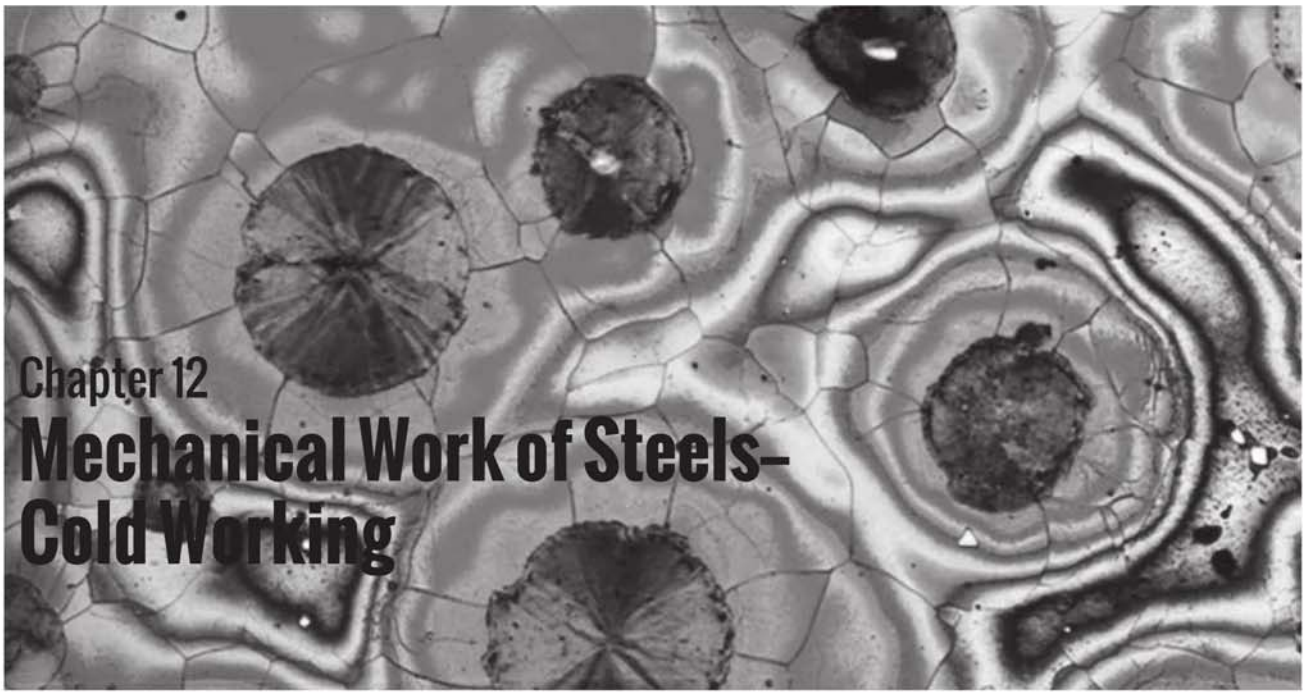

Chapter 12
Mechanical Work of Steels–Cold Working

Steels are subjected to mechanical work for two main reasons:

- To change shape and dimensions
- To alter the structure, in different scales

As discussed in Chapter 11, "Hot Working," in this book, the distinction between cold and hot working in metallurgy is not characterized by a unique temperature. In a simplified way, working is considered "cold" when it happens at temperatures in which the deformation energy is stored in the material, so recovery and recrystallization processes do not occur. An approximate limit to separate hot and cold work frequently used is 0.5 T_m, where T_m is the melting point of the metal, in K.

12.1 Cold Work

The main strengthening mechanisms of iron and its alloys are (Ref 1):

- Work hardening
- Solid solution hardening
- Grain size control
- Dispersion or precipitation hardening

The change of the volume fraction of phases is also an important tool in controlling the strength of steels and cast irons.

Work hardening consists of an increase of the dislocation density in the material through cold working. Examples of the other mechanisms are presented in the following chapters of this book.

12.1.1 Stress-Strain Curve in the Tensile Test

The simplest way to evaluate the mechanical behavior of a steel is through a uniaxial tensile test. In the most common form of this test, force is applied

to a specimen of known cross section and controlled in such a way that the deformation rate is kept approximately constant.

The usual way of presenting the results of such a test is using an engineering stress-strain curve, instead of presenting the real stresses and real strains during the test. Thus, the vertical axis (stress) represents the engineering stress, that is, the load (P) at any point of the test, divided by the area of the initial cross section of the specimen (A_0). Thus, $\sigma_E = \frac{P}{A_0}$. In the horizontal axis, the engineering strain is usually presented as $\varepsilon_E = \Delta l / l_0$, where l_0 is the initial specimen length, as shown in Fig. 12.1 and 12.2. As the material is loaded, an initial stage occurs in which the deformation is directly proportional to the applied stress. In this stage, deformation is nonpermanent: if the load is removed, deformation disappears and the specimen returns to its initial dimensions. This is called the elastic range of the material, and the proportionality constant that relates stress and strain is called the elastic modulus, E. Thus $\sigma_E = E\varepsilon_E$. The elastic, reversible deformation happens because of the increase in the interatomic distances in the material. During this stage of elastic deformation, the material volume is not conserved. Beyond a certain stress level, permanent deformation (plastic deformation) starts to occur and the measured deformation is the sum of the elastic and plastic deformations. When this happens, the proportionality between stress and strains ceases to exist. The point at which plastic deformation starts is called yield point or yield stress or yield strength (the latter is the accepted term accord-

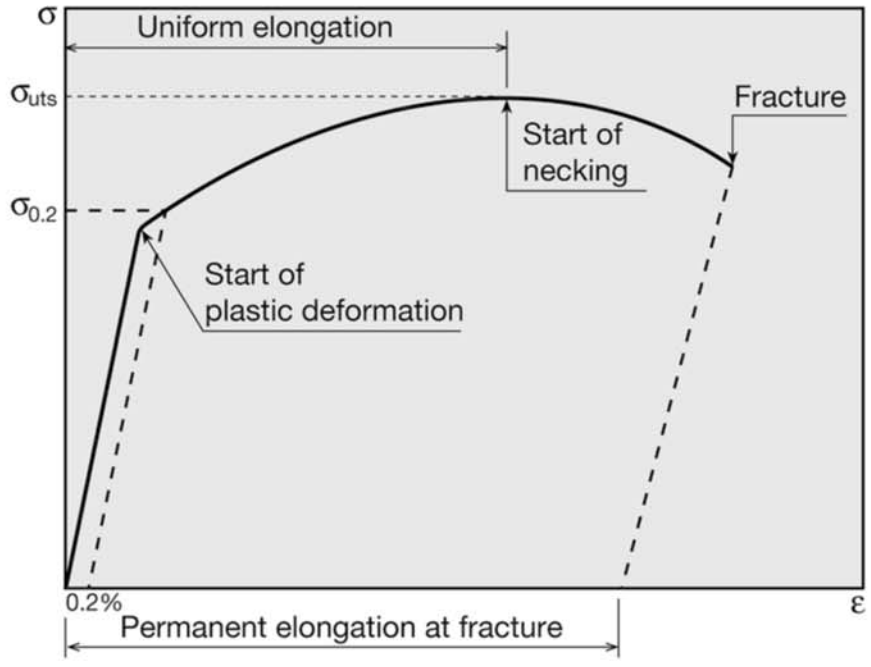

Fig. 12.1 Engineering stress-strain curve for a steel that does not show discontinuous yield. After plastic deformation starts, the force required to continue deformation increases (and thus so does the engineering stress) up to the start of the specimen "necking." After this point, work hardening is no longer evident in the engineering stress-strain curve.

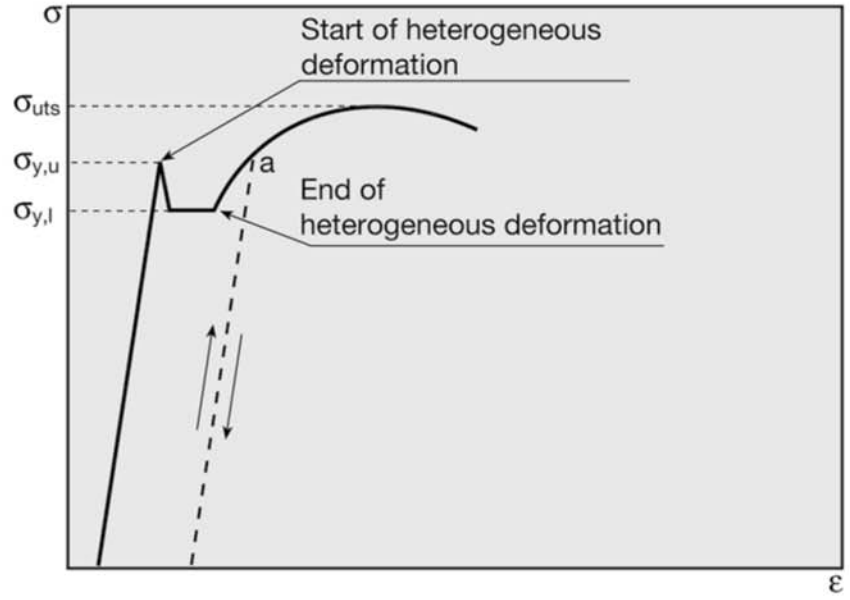

Fig. 12.2 Engineering stress-strain curve for a steel that shows discontinuous yielding. The region of discontinuous yielding is shown. During the heterogeneous deformation that occurs with discontinuous yielding, Lüders bands are formed (Fig. 12.3 and 12.4). If at point *a* the load is removed and immediately reapplied, the discontinuous deformation does not happen again.

ing to ASTM E6). The start of plastic deformation may or may not happen smoothly. When the transition from pure elastic to elastic plus plastic deformation is not sharp, it is not easy to identify the exact point where it starts. In these cases, it is normal to define the yield point as a value corresponding to a conventional value of plastic deformation, usually 0.2% (this is called an "offset yield strength"), as shown in Fig. 12.1. As plastic deformation starts, the stress needed to continue deforming the material increases. This phenomenon is related to the increase in dislocation density associated with deformation and their interaction and is called work hardening. When engineering stress and strain are used, the stress-strain curve goes through a maximum, called tensile strength (or ultimate tensile strength, UTS) related to the maximum force measured during the tensile test. In this type of plot, one may get the incorrect impression that work hardening would stop at this point. Analyzing the real stress and the real strain will eliminate this erroneous impression.

When the start of plastic deformation occurs with a sharp transition, it is called discontinuous yielding (according to ASTM E6), as shown in Fig. 12.2. Sharp or discontinuous yield is mostly associated with the interaction between dislocations and interstitial solutes, such as carbon and nitrogen. The interaction between their stress fields leads, when there is sufficient mobility for the interstitial atoms, to a concentration of these solutes in the region just below the dislocation line. These are called Cottrell atmospheres, after Sir Alan Cottrell (1919–2012).

When the upper yield stress is reached, dislocations can separate from these "atmospheres" and deformation becomes easier in these regions, de-

creasing the stress needed to continue deformation. Thus, deformation happens in a heterogeneous way, giving rise to the formation of surface marks such as Lüders bands, as shown in Fig. 12.3 and 12.4 (see Ref 2 for a video). The areas that suffered more plastic deformation are etched by the reactant in a deeper way than those that have not yet deformed or have suffered less deformation. Light deformation, in particular in low-carbon steels, may sometimes lead to dark streaks crossing each other in the etched surface, as shown in the figures (Fry's etchant is recommended for etching in these cases). Once heterogeneous deformation is concluded, the material starts work hardening.

True Stress and True Strain

The values of displacement and force measured during an "engineering" tensile test may be converted into the actual stress and strain in the specimen, called true stress and true strain, if the following is considered.

The true strain at any moment is given by the differential:

$$d\varepsilon_R = \frac{dl_R}{l_R} \qquad \text{(Eq. 1)}$$

where *R* indicates "real" or true variables (length and deformation).

This relationship may be integrated, resulting in:

$$\mu_R = \frac{\ln l_R}{l_0} \qquad \text{(Eq. 2)}$$

Thus,

$$\mu_R = \frac{\ln(l_0 + \Delta l)}{l_0} = \ln(1 + \mu_E) \qquad \text{(Eq. 3)}$$

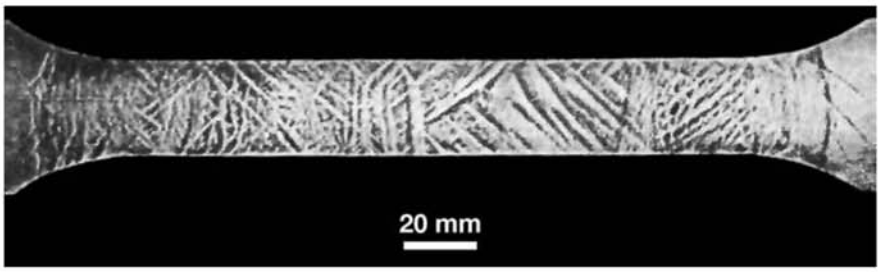

Fig. 12.3 Macrograph of tensile specimen. Lüders bands are visible on the surface. Etchant: Fry.

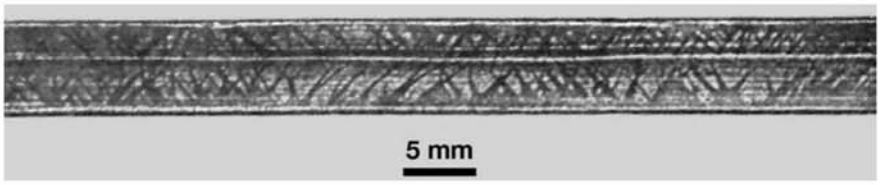

Fig. 12.4 Macrograph of the longitudinal section of a low carbon steel bar presenting Lüders bands. Etchant: Fry.

where ε_E denotes "engineering" deformation.

Furthermore, since volume is conserved during plastic deformation, the following relationship is valid at any moment:

$$A_0 l_0 = A_R l_R \quad \text{(Eq. 4)}$$

Thus:

$$\sigma_R = \frac{P}{A_R} = \frac{P}{A_0}\frac{l_R}{l_0} = \sigma_E \frac{(l_R - l_0) + l_0}{l_0} = \sigma_E(1+\varepsilon_E) \quad \text{(Eq. 5)}$$

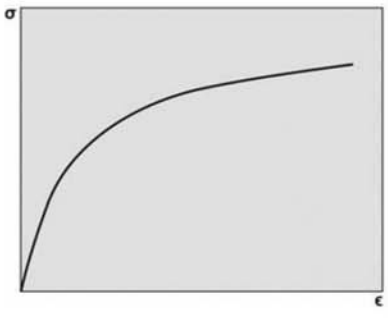

Fig. 12.5 A typical true stress versus true strain curve. No maximum occurs when necking starts. The material continues to work harden all the way until rupture.

A true stress versus true strain curve shows continuous increase in stress with deformation, clearly showing that work hardening does not end before the rupture of the specimen (Fig. 12.5). A large number of metallic materials can have their true stress versus true strain tensile behavior fitted to an equation of the type:

$$\sigma_R = k\varepsilon_R^n \quad \text{(Eq. 6)}$$

where n is defined as the work hardening exponent, an important property when measuring the deformation ability or formability of metals. Another important property in characterizing the performace of metas in forming operations is the anisotropy coefficient. The measurements needed to determine this coefficient, which relates longitudinal, transverse, and through thickness deformations, cannot be derived through simple mathematical relationships from an engineering tensile test and must be obtained using extensometric measurements during the test.

12.1.2 The Effects of Deformation on Structure

Although in the tensile test the most common measurement of deformation is elongation, this form of measuring deformation is not always the most adequate for industrial forming processes. In simple forming processes, deformation is frequently measured as a degree of deformation or percentage deformation, calculated as the ratio between the starting (A_s) and final (A_f) cross sections of the material, as indicated in the following equation:

$$\%\text{Deformation} = \left(\frac{A_s - A_f}{A_S}\right) \times 100 \quad \text{(Eq. 7)}$$

In rolling, where the width frequently suffers little alteration, this can be approximated using the material thickness:

$$\%\text{Deformation} = \left(\frac{t_s - t_f}{t_S}\right) \times 100 \quad \text{(Eq. 8)}$$

With cold work, mechanical strength (measured either by yield strength or ultimate tensile strength) increases and ductility (measured by elongation, reduction of area, or fracture toughness) normally decreases, as illustrated in Fig. 12.6.

It is important to keep in mind that the values of yield strength and tensile strength that can be obtained in work-hardened materials exceed the tensile

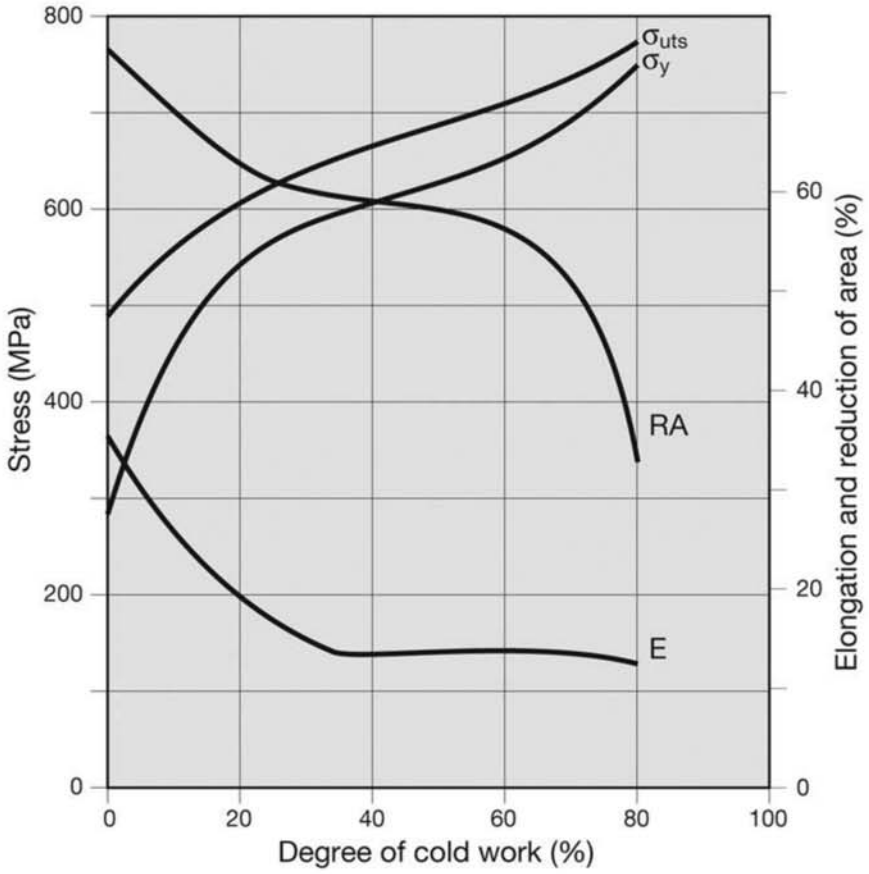

Fig. 12.6 Mechanical properties measured in tensile test for a steel containing C = 0.13–0.15%, Mn = 0.6–0.9% as a function of the degree of cold work. RA = reduction of area; E = elongation. Source: Ref 3

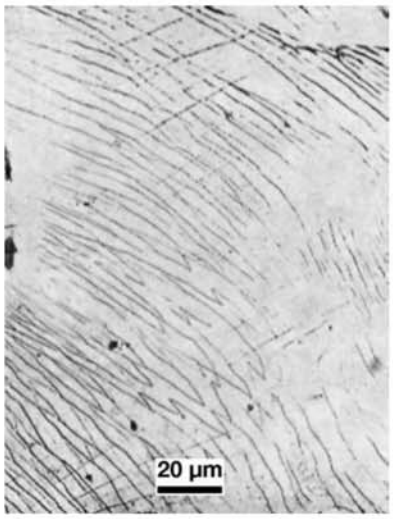

Fig. 12.7 Slip lines inside deformed ferrite grains. Etchant: aqua regia.

strength measurements in the (engineering) tensile test of the material before work hardening. This apparent contradiction is caused by the fact that the ultimate strength of a specimen tested in the not-cold-worked condition is measured with respect to the specimen initial cross section and is not the true stress reached when necking begins.

Ferrite deforms mostly by slip (Fig. 12.7). Twinning marks can be observed in ferrite when very high deformation rates (caused by shock or impact) are used, as shown in Fig. 12.8. Austenite deforms mostly by slip (Fig. 12.9). In a polycrystalline material, slip deformation does not happen to the same extent in all grains. Some grains have orientations with respect to the load that are more favorable to slip than others are. The first effect of cold work is the occurrence of heterogeneous deformation (in steel that show discontinuous yield), usually accompanied by the occurrence of slip bands in some grains. It is possible to show that the most favourable grains will store more deformation energy (Ref 5, 6). As deformation proceeds, grain shape (Fig. 12.10) and orientation change, causing anisotropy associated with the crystal orientation of the grains in this material. This anisotropy is normally characterized by a crystallographic texture (see the section "Crystallographic Texture" in this chapter). The grains elongate more and more (Fig. 12.11) to a point where,

Fig. 12.8 Twins produced inside ferrite grains by shock loading the material at high impact velocities. (Neumann lines; Ref 4) in a very low carbon steel. Etchant: nital. Neumann lines are named after the German scientist Franz Ernst Neumann (1798–1895), who observed these twins in meteorites. He is also known for the Neumann-Kopp rule for heat capacities.

since the stored energy inside the grains is very significant, chemical etching may not lead to a distinction between the grain interior and the grain boundaries (see the discussion and figures in the section "Following Recrystallization Using Microscopy").

Cementite, when dispersed in ferrite, may fracture and redistribute in an elongated pattern in the ferritic matrix (see the section "Following Recrystallization Using Microscopy"). Pearlite is also subject to reorientation with cold work, as discussed and shown in figures in the sections "Following Recrystallization Using Microscopy" and "Electrical Steels." Extremely strong wires, such as those used for tire reinforcement, can be obtained with controlled deformation of pearlite (Fig. 12.12). Wire-drawing decreases the lamellae spacing in pearlite (starting pearlite lamellar spacing should be small, see Chapter 10, "Conventional Heat Treatment: Basic Concepts," in this book) and changes the orientation of the platelets to parallel to the wire axis in such a way that very reasonable ductility can be preserved. The hardening potential of these structures is presented in Fig. 12.13.

12.2 The Effects of Subcritical Annealing in Steels for Forming

Figure 12.14 schematically presents the changes occurring in steels during subcritical annealing. In some cases, the effects on the mechanical properties are not easy to measure (Fig. 12.15). Some of the structural changes, particularly those happening during the stage called recovery, require observation on a very fine scale. The use of equipment such as the transmission electron microscope is necessary to properly observe and evaluate these changes. Figure 12.16 presents the evolution of the microstructure of an extra low carbon steel that following 90% reduction by cold rolling after hot rolling was annealed at different temperatures. Among the changes occurring during

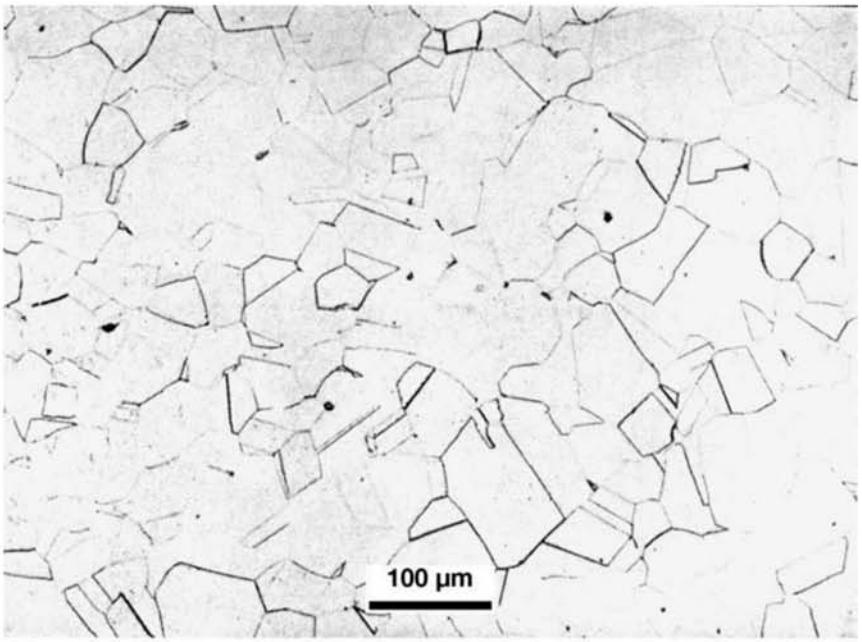

(a)

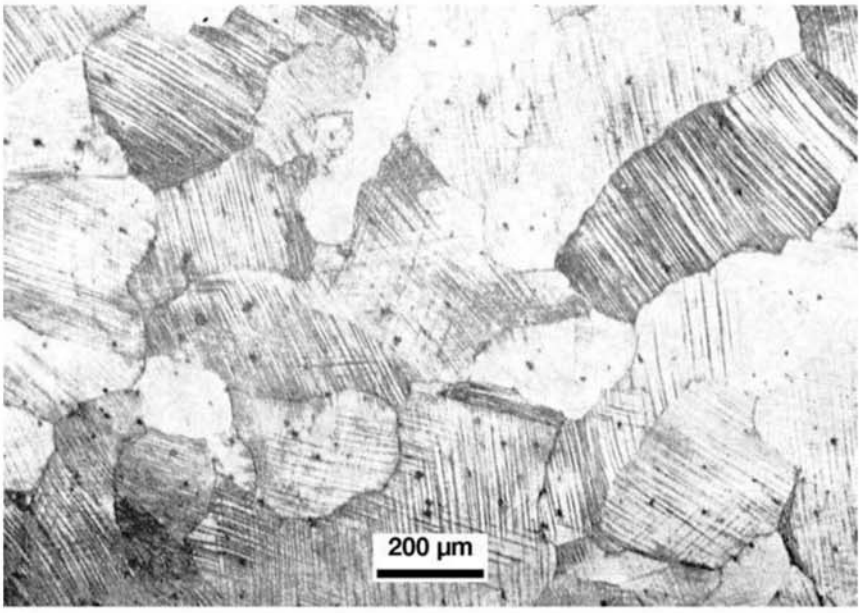

(b)

Fig. 12.9 (a) Austenitic manganese steel. Polygonal austenitic grains and some non-metallic inclusions. Undeformed. Etchant: nital and picral. (b) Austenitic manganese steel lightly cold worked. The slip lines show with relative ease in a clear pattern in this type of steel. Etchant: nital.

the subcritical annealings performed after cold rolling, only recrystallization can be followed by conventional metallography. Souza (Ref 11) used the image quality index in electron backscatter diffraction (EBSD) to follow processes taking place during annealing. Because the deformed regions have high densities of dislocations, the deformed structure has a lower image

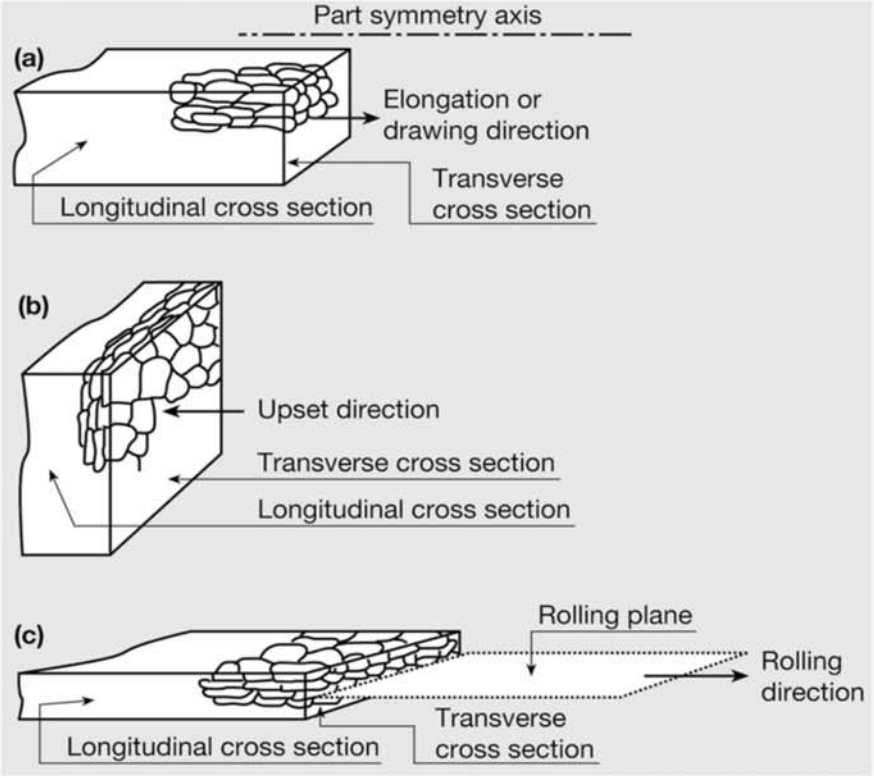

Fig. 12.10 Cold working polycrystalline materials will generate anisotropy of the grain shape: their elongation in the deformation direction is evident. Anisotropy increases with cold work. For small deformations (< approx. 10%), this anisotropy may not be observable in the metallographic examination.

quality index in EBSD, as shown in Fig. 12.17 (see also Ref 10). Thus, cold working in combination with different annealing treatments makes it possible to explore an extensive range of mechanical properties, making this an extremely interesting tool for the production of sheet steels for different applications, as shown in Fig. 12.18.

12.3 Crystallographic Texture (Ref 13)

In Chapter 3, "Introduction to the Metallographic Technique," in this book, the fact that metals are generally polycrystalline, that is, made up by a number of crystals, is presented. The size of the grains in steel normally used in engineering applications is in the range between 10 μm and 1 mm. In the case of hot- or cold-worked materials, the range is narrower, usually somewhere between 10 μm and 100 μm. Thus, a typical tensile specimen may contain around 10^{10} grains or individual crystals (Ref 14). Because the grains have a given crystal structure, it is possible to identify a certain orientation for each crystal with respect to a fixed reference. In general, this reference is tied to the external shape of the steel part or product. When the grain orientations are concentrated around a defined orientation, the material is said to present a crystallographic texture. This preferred orientation of grains can be generated in different ways. The generation of texture by cold work (and subsequent annealing) is briefly discussed here.

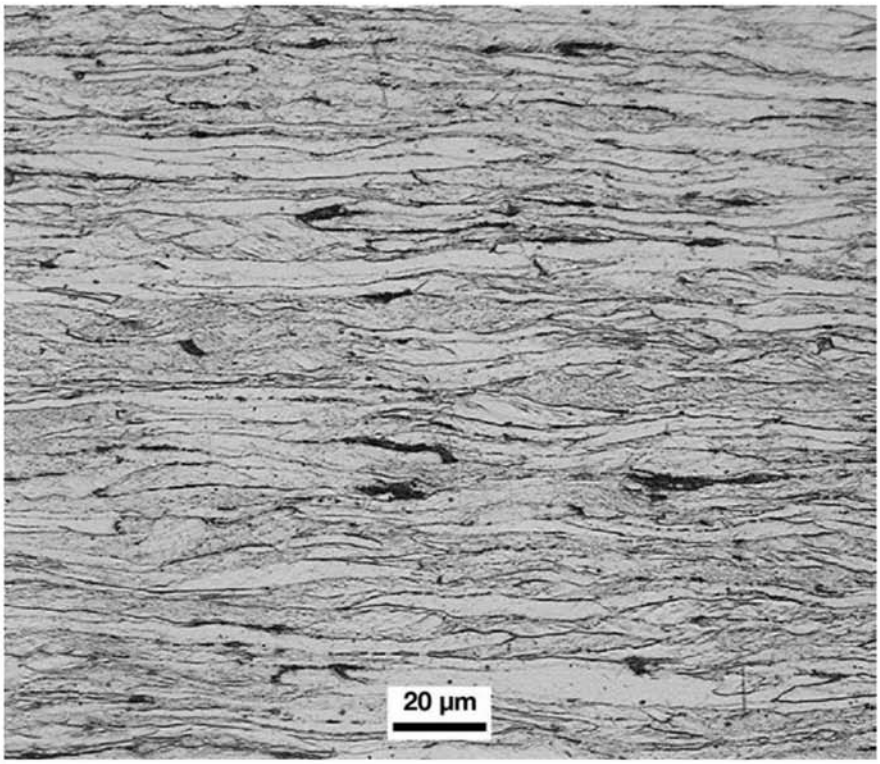

Fig. 12.11 Low carbon steel sheet C = 0.06%, Mn = 0.55%, after cold working, in the work hardened state, prior to annealing. Very elongated grains of ferrite and cementite. Hardness: 95 HRB.

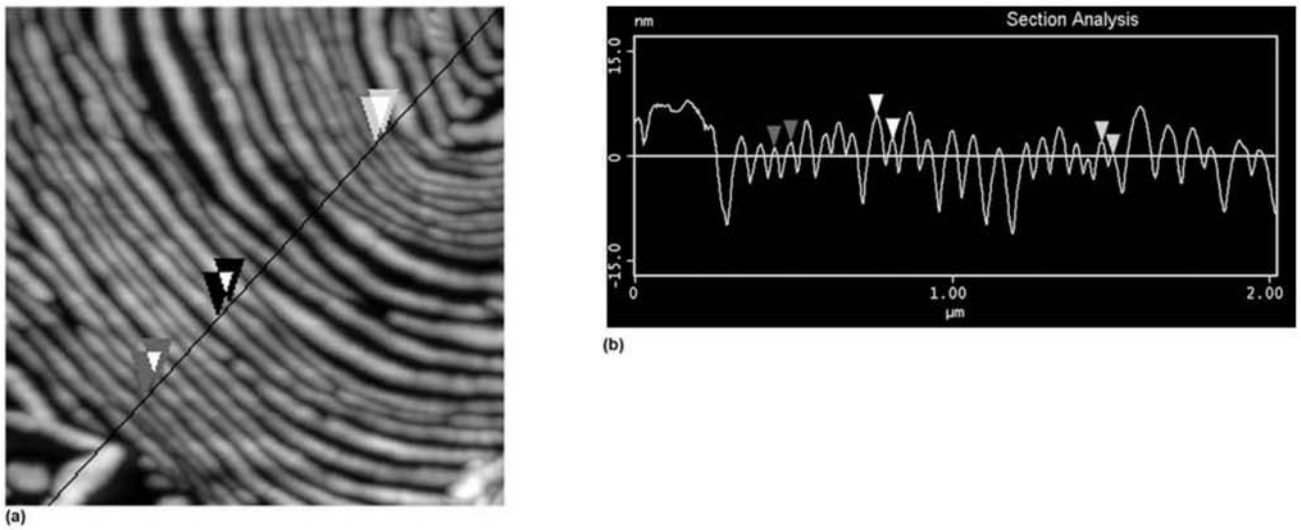

Fig. 12.12 Pearlite highly deformed during wire drawing. (a) Atomic force microscopy image. (b) Relief along the line indicated in (a) and some measurements of the lamellae spacing after wire drawing. Etchant: nital 2%. See also Ref 7. Courtesy of M. S. Andrade, CETEC, Belo Horizonte, MG, Brazil.

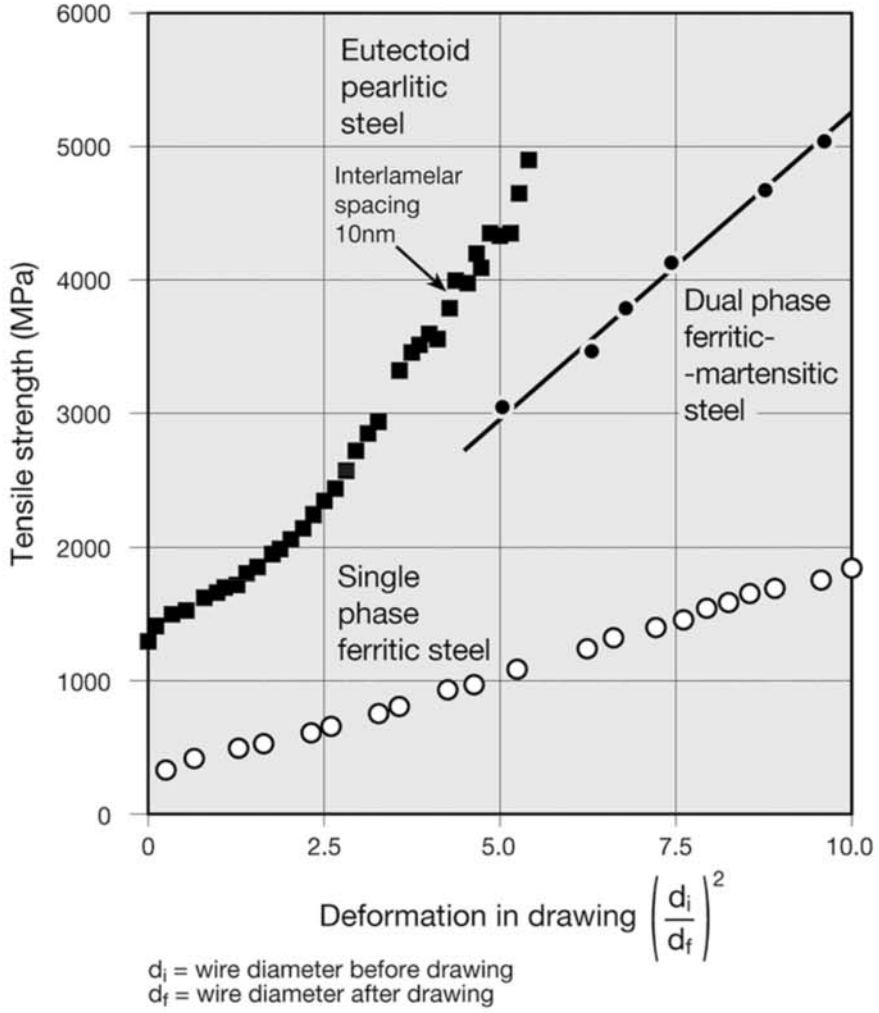

Fig. 12.13 Relationship between cold work in wire drawing and tensile strength for different steel microstructures. The potential for strength increase with cold working of pearlitic steels is evident. Source: Ref 8

12.3.1 Identifying Crystallographic Textures

In general, the texture of a material is made of components. A component of a texture is defined by a given specific orientation, around which the various crystals align themselves. In the case of flat products, the crystallographic plane parallel to the rolling surface is normally used to specify the components. Thus, if the plane in the face of the cube in a BCC or FCC crystal (family of planes identified as {001}, including the (001), (010) . . . planes) is parallel to the rolled sheet surface, this texture will contain the identifier {001} in its name. Furthermore, if a direction aligned to the rolling direction (for instance, the direction that corresponds to a face diagonal in these cubic structures is identified as <110> and includes the directions [011], [110], etc.) the texture will be described as {001}<110>. In the case of products with axial symmetry (wires, rods, etc.), the "fiber" texture is characterized by the crystallographic direction that is aligned to the product axis.

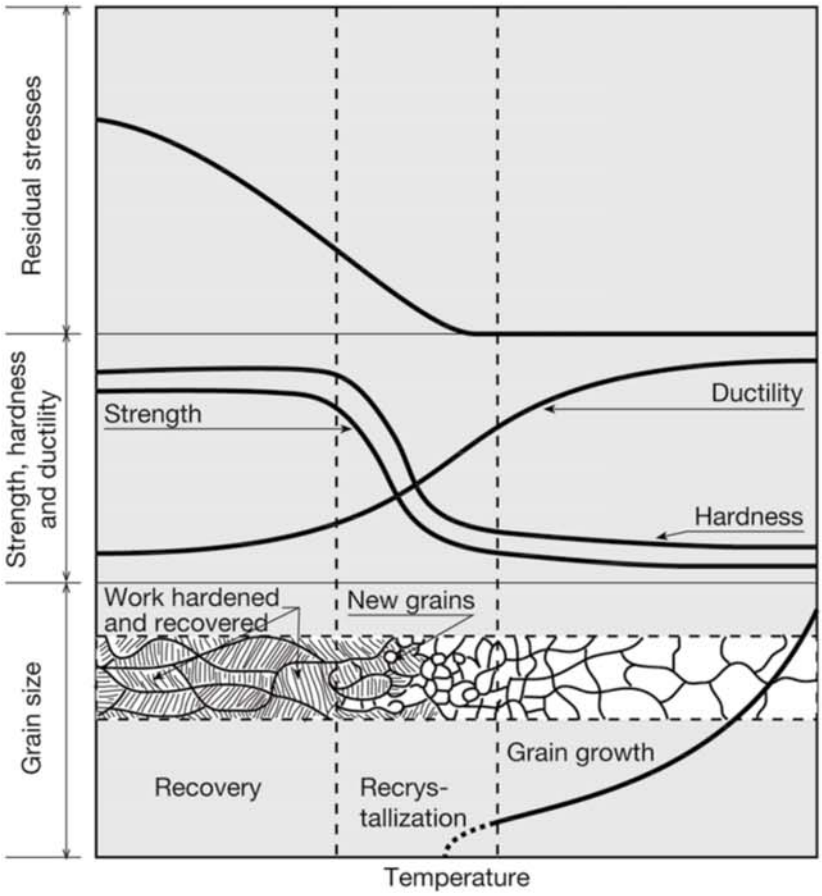

Fig. 12.14 Schematic presentation of the effect of the subcritical annealing temperature on the structural changes in cold-worked steel. The grains in the recovery region are still deformed. The new grains formed on recrystallization are not deformed. Source: Ref 9

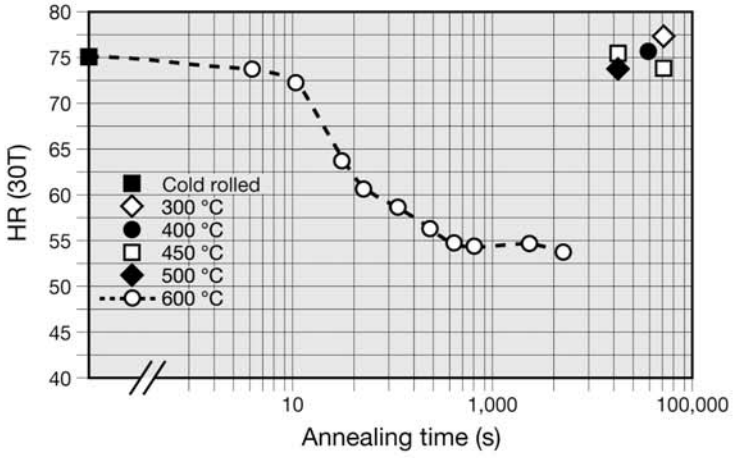

Fig. 12.15 The effect of annealing time and temperature on a low carbon steel hardness (C = 0.03%, Mn = 0.19%, Al = 0.13%) cold worked 84%, via cold rolling. For temperatures under 500 °C (930 °F), hardness is essentially independent from the structural changes for a long treatment time (approx. 13.6 h). Source: Ref 10

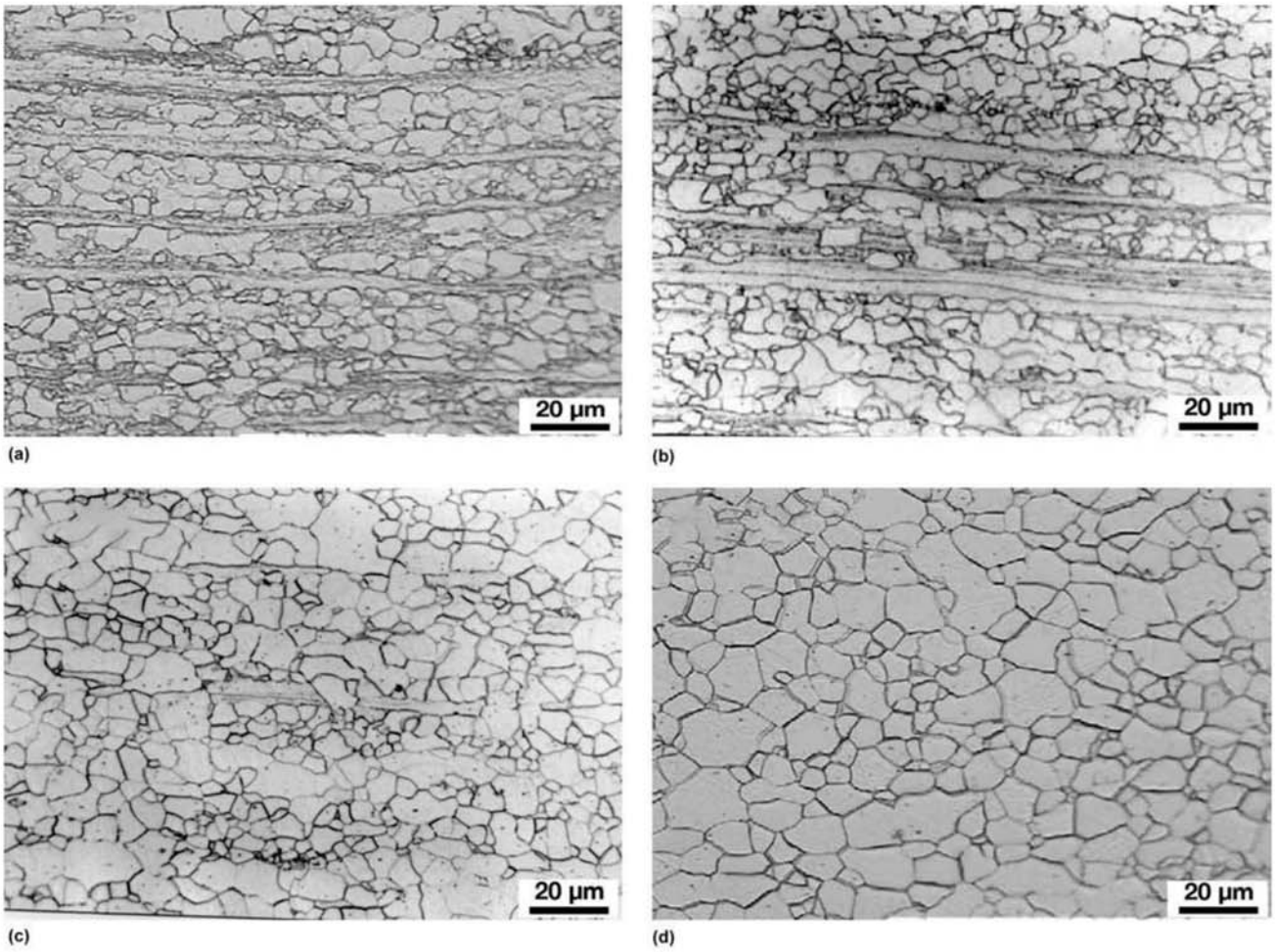

Fig. 12.16 The evolution of the microstructure of an extra low carbon steel (C = 0.011%, Mn = 0.193%) cold worked (90% reduction), annealed at different temperatures: (a) 540 °C (1000 °F), (b) 560 °C (1040 °F), (c) 580 °C (1075 °F), (d) 600 °C (1110 °F). (Remark: the α–γ transformation in this steel starts around 800 °C, or 1470 °F). Courtesy of C. S. Viana, EEIMVR-UFF, Volta Redonda, RJ, Brazil. Source: Ref 11

12.3.2 The Importance of Texture in Forming Operations

Steel texture can be very important in many applications. Steels for electrical applications (Ref 15), and steels for forming operations are some important examples. In the case of flat products for mechanical forming operations, texture is especially important to ensure homogeneous deformation in the plane of the sheet, with a minimum of thickness reduction, as shown in Fig. 12.19 and 12.20. Steels intended to be subjected to mechanical forming, are in general, processed in a way that will generate adequate textures for forming. The most common method involves subcritical annealing treatments, which may be preceeded by cold working.

12.3.3 Texture and Electron Backscattered Diffraction

Electron backscattered diffraction (EBSD) (Chapter 6, "Metallographic Technique: Electron Miscroscopy and Other Advanced Techniques," in this

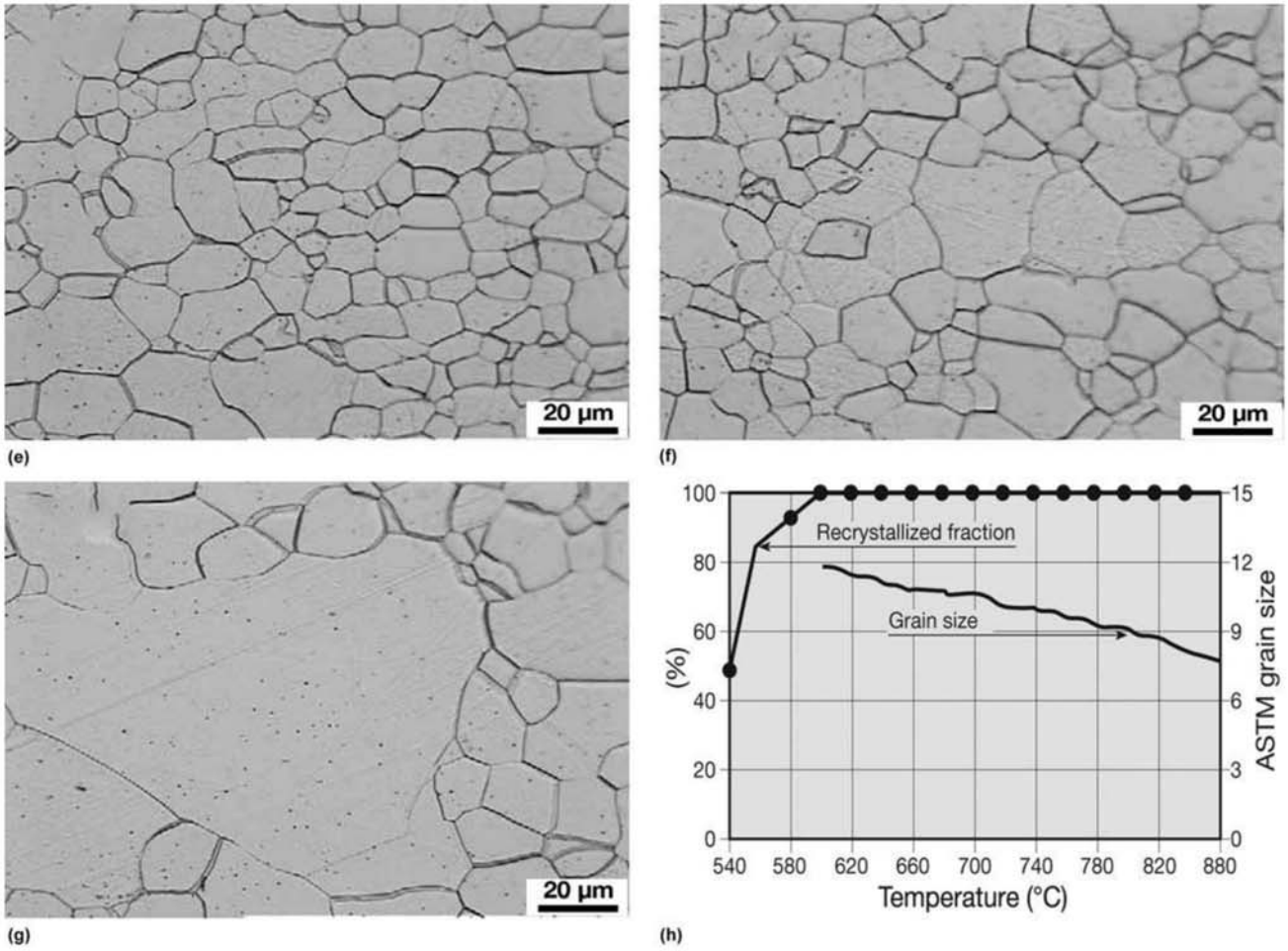

Fig. 12.16 (continued) (e) 680 °C (1255 °F), (f) 720 °C (1330 °F), (g) 760 °C (1400 °F). (h) The evolution of the ferritic grain size and the recrystallized fraction. (Remark: the α–γ transformation in this steel starts around 800 °C, or 1470 °F). Courtesy of C. S. Viana, EEIMVR-UFF, Volta Redonda, RJ, Brazil. Source: Ref 11

book) is especially useful in evaluating and measuring crystallographic orientations. EBSD makes it possible to evaluate the misorientation between different grains in the material (thus identifying, for instance, the presence of special grain boundaries). It also helps one evaluate the crystallographic orientation of the grains with respect to the shape of the product (in particular with relation to the direction of major working), characterizing and quantifying the presence of crystallographic texture (Ref 16). Figure 12.21 shows the results of EBSD measurements of a steel that was cold worked and subcritically annealed at 540 °C (1000 °F). The nonrecrystallized regions (see also Fig. 12.16a) have essentially the same crystallographic orientation {001}<uvw>, where <uvw> is a family of crystallographic directions and have low-angle grain boundaries. The recrystallized regions present a higher occurrence of the {111}<uvw> texture. This is the most desirable texture in flat products for forming. In Fig. 12.22, after annealing the same steel at 760 °C (1400 °F), the predominance of the {111}<uvw> orientation is observed. Indeed, at this temperature, when Ref 11 performed quantititative texture determination, a

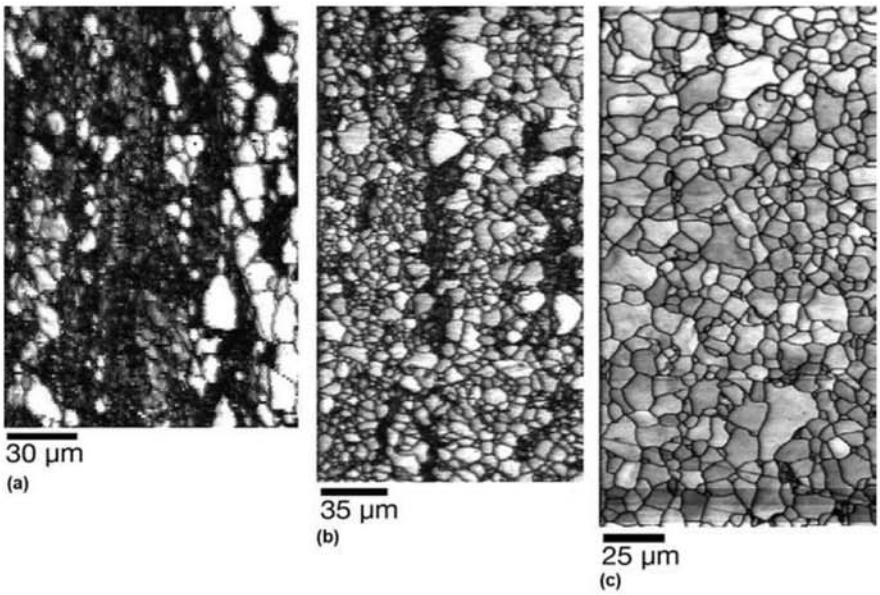

Fig. 12.17 EBSD image quality image for the samples in Fig. 12.16. After reduction of 90% through cold roling and annealing at (a) 540 °C (1000 °F), (b) 560 °C (1040 °F), and (c) 580 °C (1075 °F). Darker areas indicate lower image quality index, corresponding to the nonrecrystallized areas, still work hardened. Courtesy of C.S. Viana, EEIMVR-UFF, Volta Redonda, RJ, Brazil. Source: Ref 11

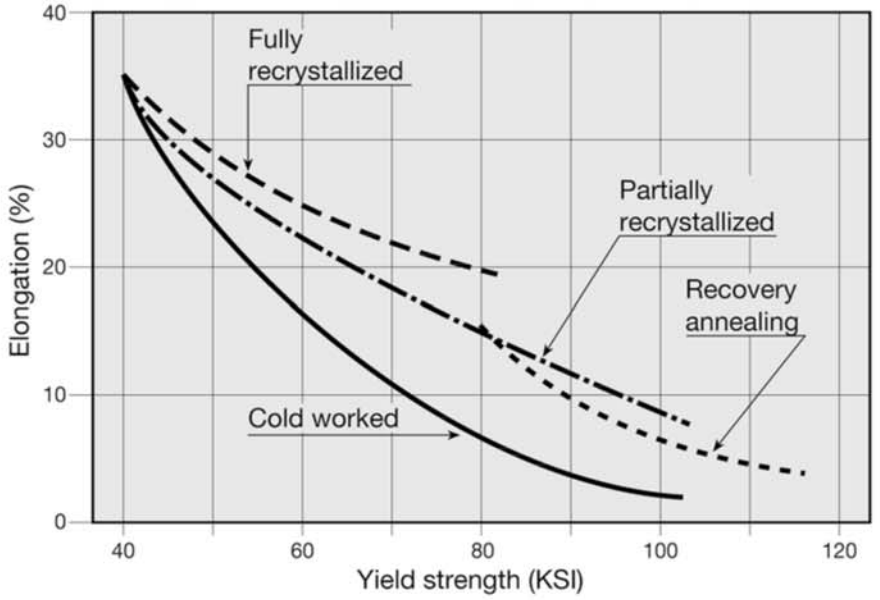

Fig. 12.18 The effect of cold work and subcritical annealing on the properties of low carbon steels. Source: Ref 12

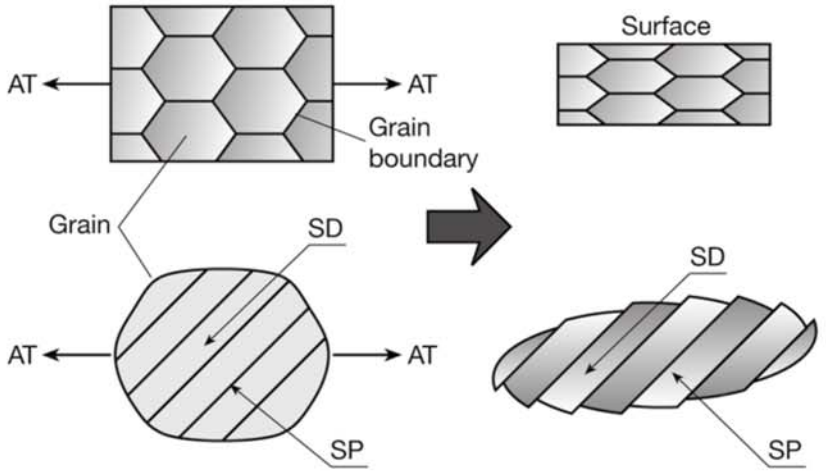

Fig. 12.19 The orientation of the slip planes (SP) and the active slip directions (SD) when the material is subjected to axial tension (AT) will the define the anisotropy of the deformation, as shown in Fig. 12.20.

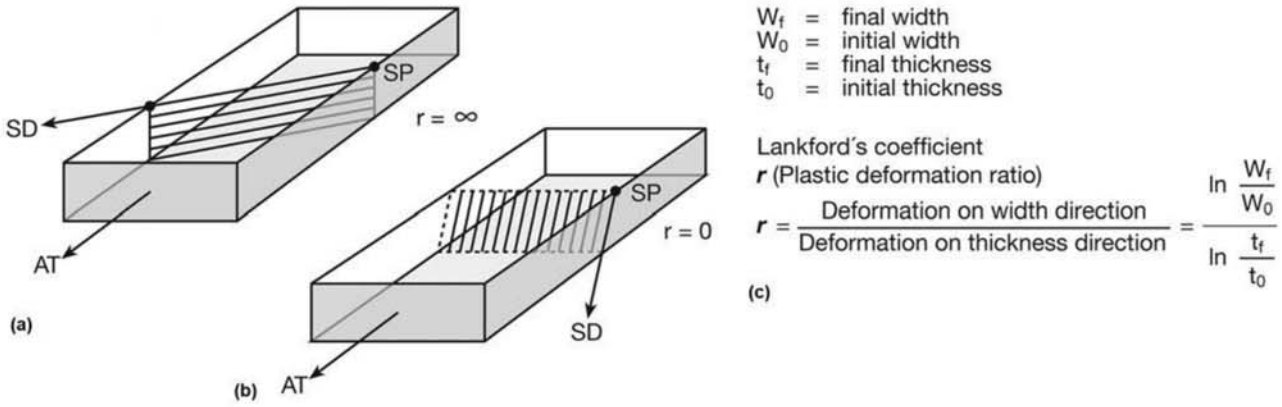

Fig. 12.20 Two limiting cases of anisotropy in plastic deformation, considering (for simplicity) a single active slip system, characterized by slip planes (SP) and slip directions (SD). When subjected to axial tension (AT) in (a) the material will undergo reduction of the width without any reduction of thickness. In (b) there will be reduction of thickness without any reduction in width. (c) Anisotropy is measured, in general, by *r*. Real steels have values of *r* between 0 and 3, depending on the preferential orientation of their grains (crystallographic orientation).

higher volume fraction of ferrite with the {111}<uvw> orientation was determined.

12.4 Following Recrystallization Using Microscopy

Although recovery cannot be followed by optical microscopy, it is possible to follow clearly the progress of recrystallization using this technique. Thus, for instance, the recrystallization of the heavily cold-worked sheet in Fig. 12.11 is followed through Fig. 12.23 and 12.24. Figures 12.25 to 12.31 also show sheets with different recrystallized volume fractions of ferrite. In these images, the redistribution of cementite caused by cold working can also be observed.

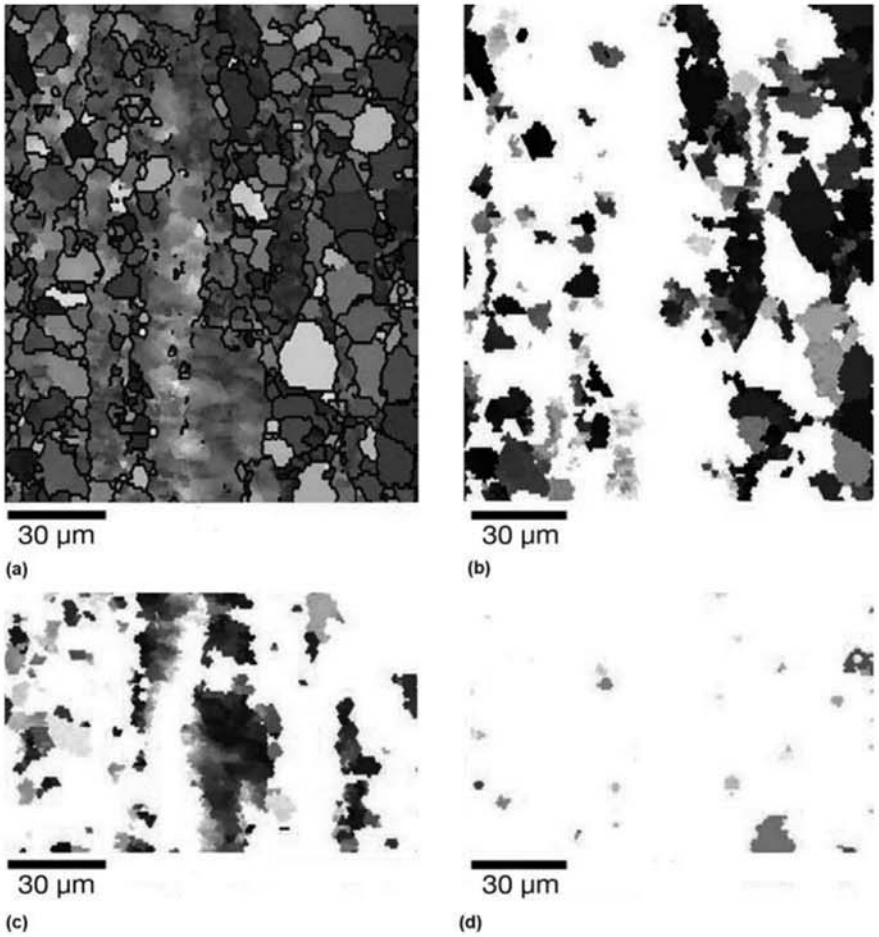

Fig. 12.21 EBSD orientation map (orientation imaging microscopy, or OIM: for a good tutorial see Ref 16) of the extra low carbon steel in Fig. 12.16 annealed at 540 °C (1000 °F). (a) Orientation map, reproduced in grayscale. (Generally orientation maps are done in color, so that the orientation of each individual grain can be clearly identified.) The dark lines are high-angle grain boundaries. One can generate individual maps for each orientation (or color). (b) {111}<uvw> orientation; (c) {001}<uvw> orientation; and (d) {101}<uvw> orientation. The predominance of the {111}<uvw> orientation in the recrystallized regions and of {001}<uvw> in the work-hardened regions can be clearly seen. Courtesy of C.S. Viana, EEIMVR-UFF, Volta Redonda, RJ, Brazil. Source: Ref 11

Techniques such as transmission electron microscopy (Fig. 12.31) make possible a much more detailed observation of the structural differences between work-hardened and recrystallized grains. The structural evolution indicated in Fig. 12.16 shows that for a given degree of cold work, reaching a fine ferritic grain size depends on the choice of the subcritical annealing temperature. Processing parameters, as well as the presence or absence of precipitates, are very important in reaching a fine and uniform microstructure, such as that presented in Fig. 12.32. In some cases, combinations of cold working and heat treatment that cause little nucleation during recrystalliza-

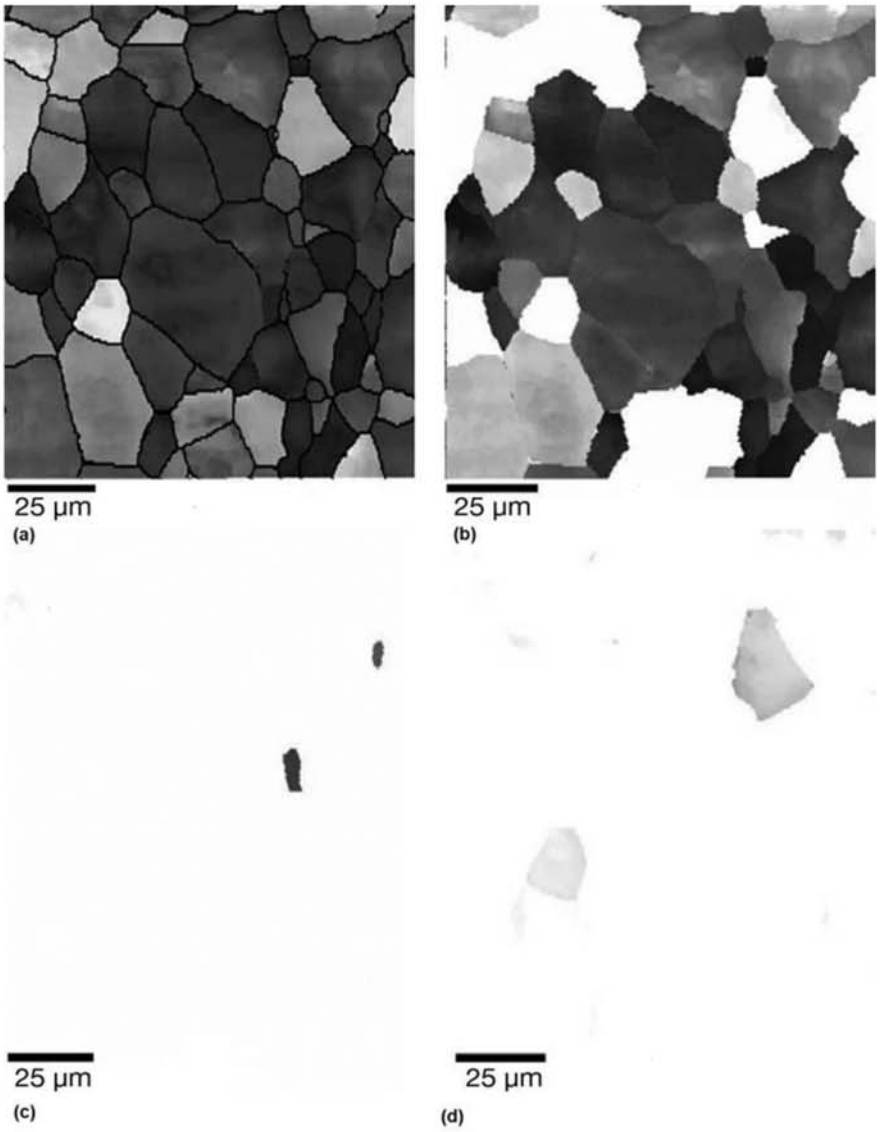

Fig. 12.22 EBSD orientation map (OIM) of the extra low carbon steel in Fig. 12.16, annealed at 760 °C (1400 °F). (a) Orientation map, reproduced in grayscale. The dark lines are high-angle grain boundaries. One can generate individual maps for each orientation (or color). (b) {111}<uvw> orientation; (c) {001}<uvw> orientation; (d) {101}<uvw> orientation. The predominance of the {111}<uvw> is observed. Courtesy of C.S. Viana, EEIMVR-UFF, Volta Redonda, RJ, Brazil. Source: Ref 11

tion may lead to very large grain sizes. Figure 12.33 shows the effects of deformation on recrystallization for the same heat treatment. As the hardness impression generates a deformation gradient in the material, from a large deformation close to the surface to no deformation away from the impression, it is possible to identify a region where deformation is just enough to cause recrystallization but with a low nucleation rate. At the end of recrystallization, this region will have a coarse grain size.

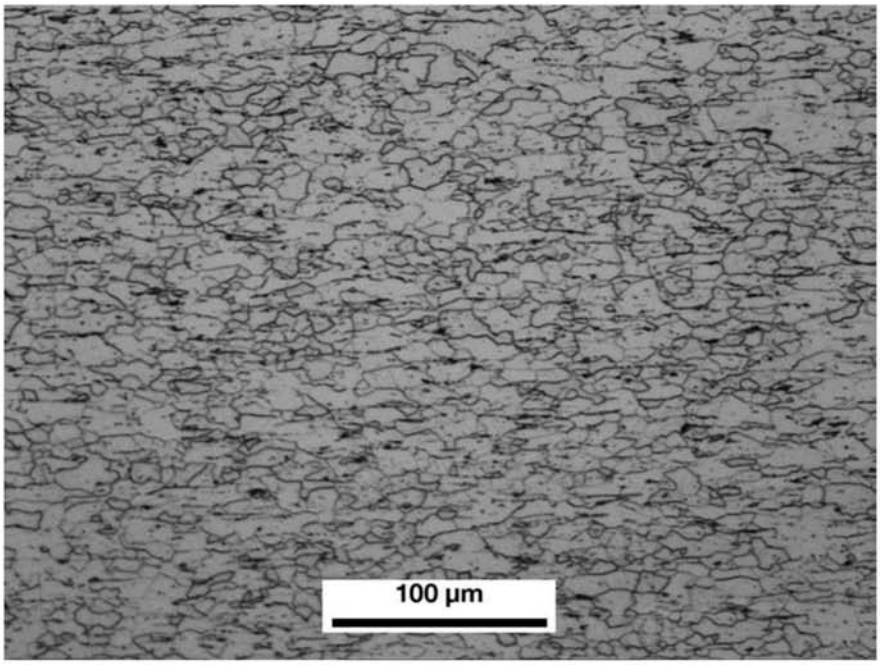

Fig. 12.23 Same steel as Fig. 12.11 (C = 0.06%, Mn = 0.55%) during the recrystallization process. Mostly equiaxial ferrite and aligned cementite. Heat-treated at 600 °C (1110 °F), hardness: 60 HRB. Etchant: nital 2%.

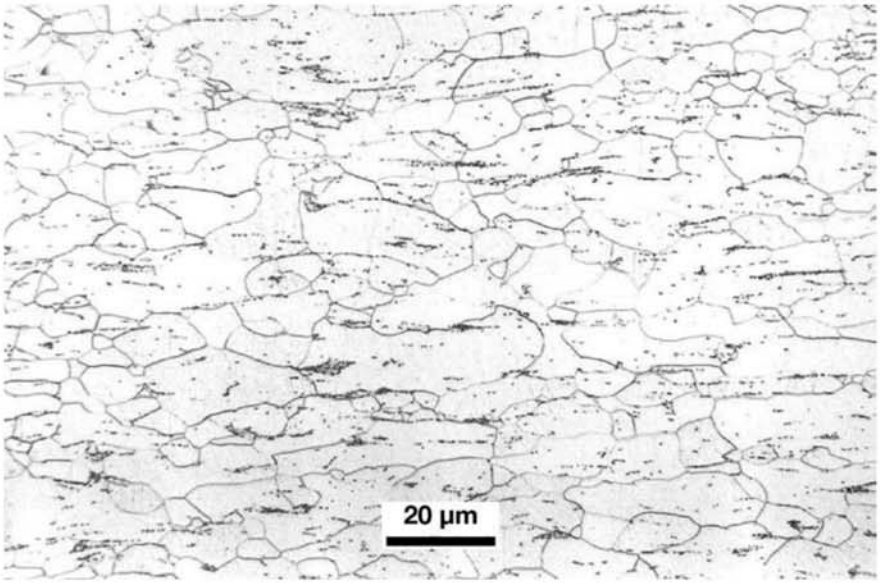

Fig. 12.24 Same steel as Fig. 12.11 (C = 0.06%, Mn = 0.55%) after completing the recrystallization. Equiaxial ferrite and coarse cementite in fragmented aligned pieces. Heat-treated at a 660 °C (1220 °F), hardness: 55 HRB. Etchant: nital 2%.

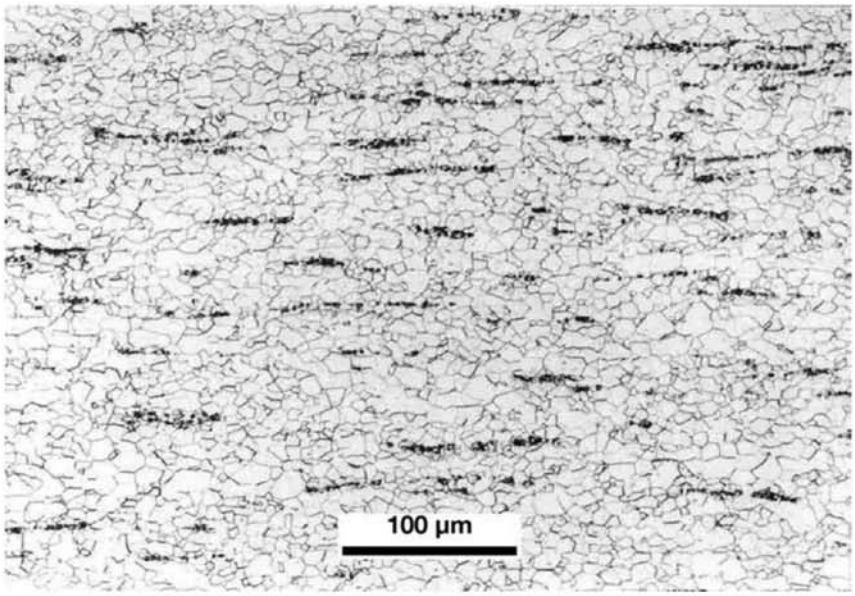

Fig. 12.25 Annealed sheet of steel (C = 0.05%, Mn = 0.30%). Polygonal ferritic grains and coarse cementite in fragmented aligned pieces. Ferrite grain size = 11.0 ASTM. Etchant: nital 2%.

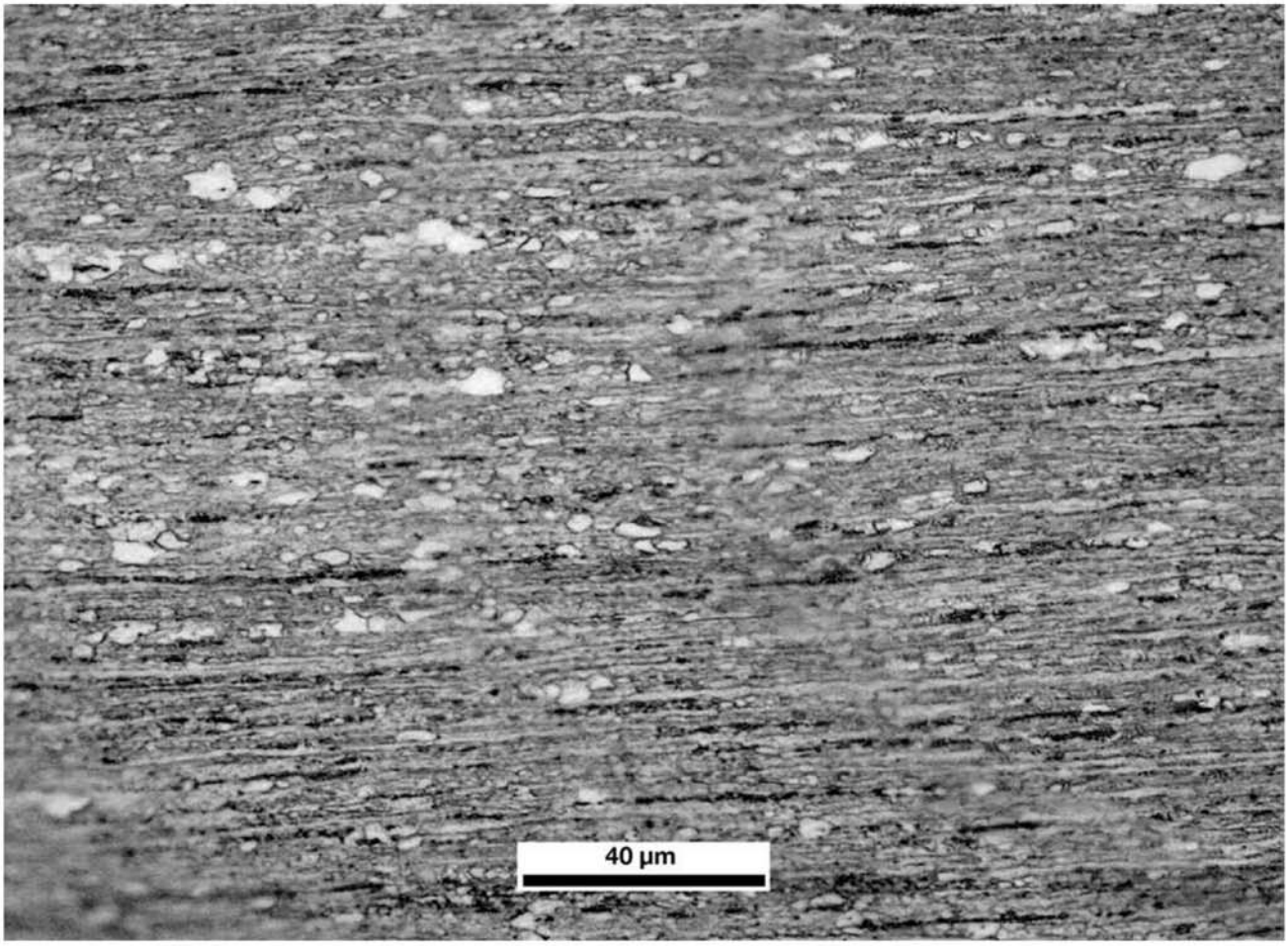

Fig. 12.26 Sheet of low carbon steel (C = 0.046%, Mn = 0.3%) cold worked and partially recrystallized (recrystallized fraction approx. 10%). Etchant: nital 2%.

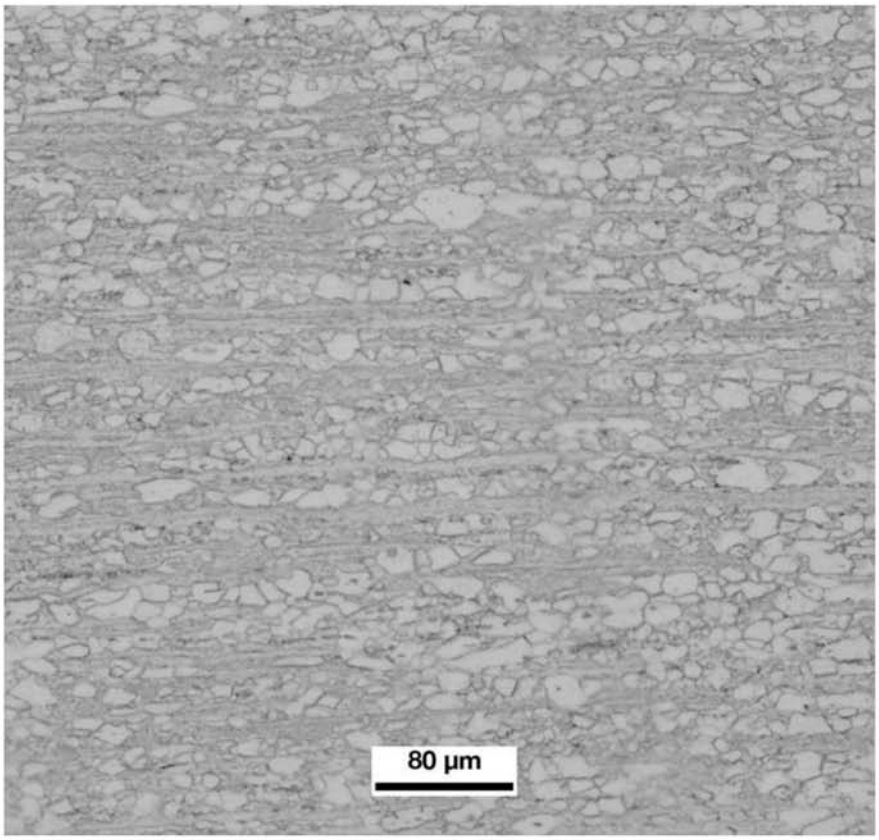

Fig. 12.27 Sheet of low carbon steel (C = 0.048%, Mn = 0.32%) cold worked and partially recrystallized (recrystallized fraction approx. 50%). Etchant: nital 2%.

The fact that any plastic deformation introduced by a surface impression (or by any other means) will cause structural changes under the surface, as shown in Fig. 12.33, has interesting practical implications. Figure 12.34 presents a steel part in which relief marking was made by punching, at room temperature. Even when the visible relief marks are eliminated by grinding, a cold-worked region remains, under the marks. A metallographic etching can reveal the previous marks. This technique is used in forensic investigations. In Fig. 12.35 the longitudinal section of a lightly cold-worked reinforcing bar is presented. The elongation of the grains along the longitudinal direction is visible. Chapter 14, "Structural Steels and Steels for Pressure Vessels, Piping, and Boilers," Fig. 14.37(e), in this book, presents the cross section of the same reinforcing bar, and the deformation is not visible in this section.

Figures 12.36 and 12.37 compare the microstructures of AISI 1006 wires as cold drawn and annealed. The striking differences in the microstructure reflect on the mechanical properties and hence on the materials application. In some hot rolled flat products, a final cold rolling pass can be used, called "skin pass." A small cold reduction is applied, improving surface finish, dimensional tolerances, and even producing some changes in mechanical properties. Figure 12.38 presents the cross section of a low-carbon sheet subjected to a skin pass.

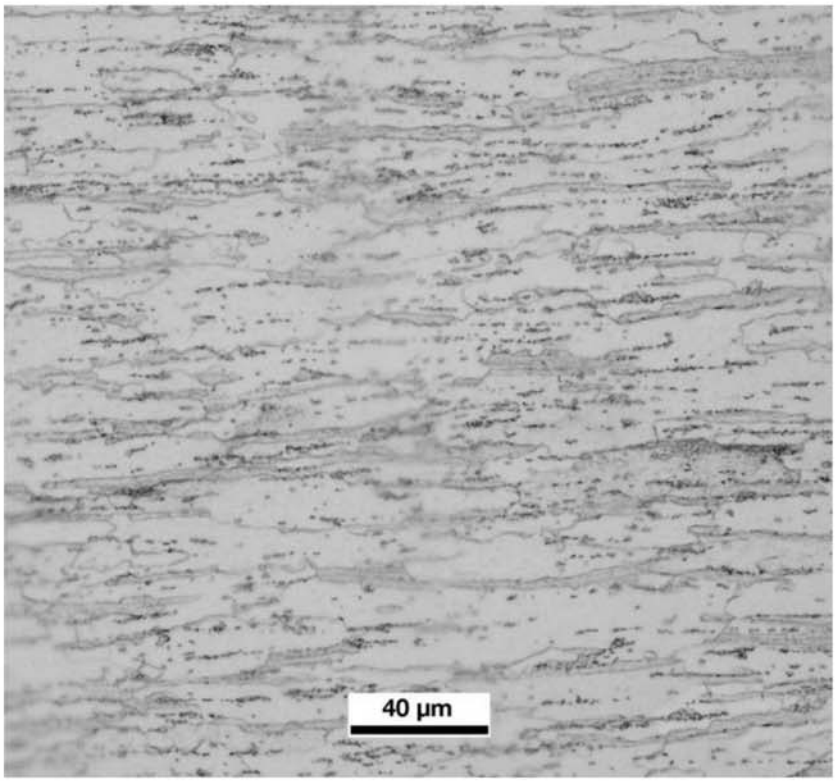

Fig. 12.28 Sheet of low carbon steel (C = 0.065%, Mn = 0.3%) cold worked and partially recrystallized (recrystallized fraction approx. 70%). Fine globular cementite aligned in the matrix. Etchant: nital 2%.

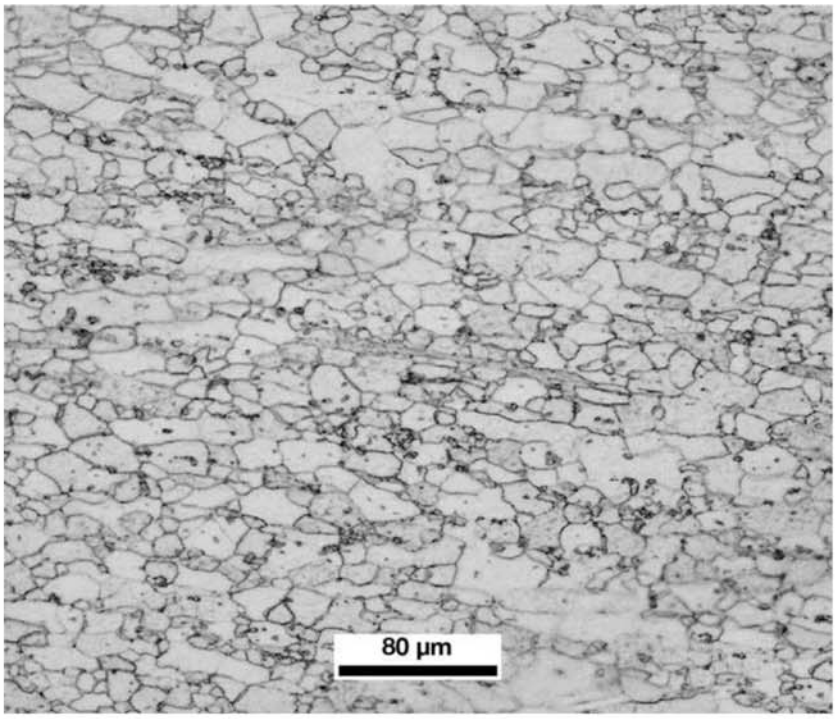

Fig. 12.29 Sheet of low carbon steel (C = 0.044%, Mn = 0.28%) cold worked and partially recrystallized (recrystallized fraction approx. 95%). Polygonal ferrite grains with lamellar cementite precipitated on grain boundaries. Some aligned cementite is still present. Ferrite grain size: 12.0 ASTM. Etchant: nital.

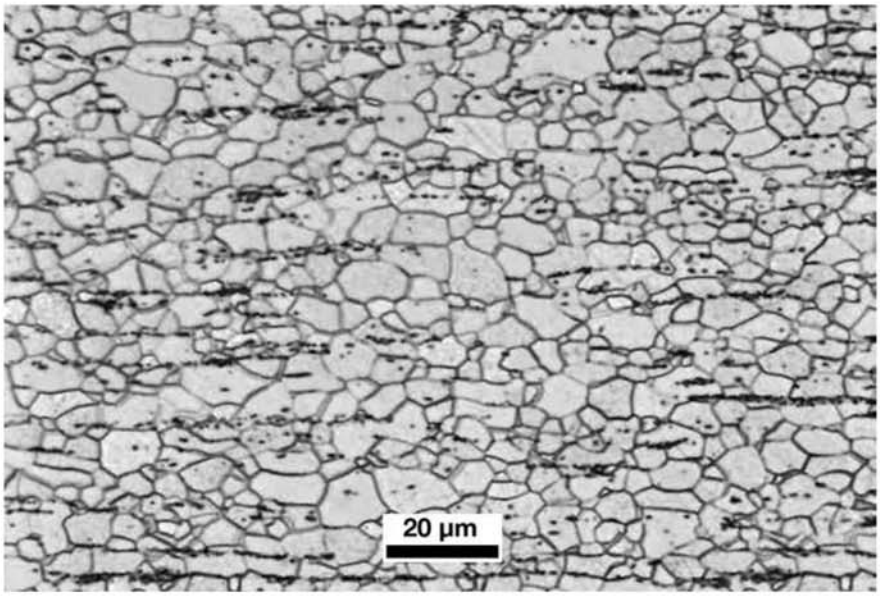

Fig. 12.30 Sheet of low carbon steel with 0.28 mm (0.01 in.) thickness produced via single-reduction cold work and continuous annealing. Temper T61 ASTM A623-11 (HR30TS 57-65); approximate values in tensile test: yield strength: 430 MPa (62 ksi); tensile strength: 470 MPa (68 ksi); elongation: 12%. Polygonal ferrite with globular cementite aligned in the matrix. Ferritic grain size: 12.0 ASTM. Etchant: nital.

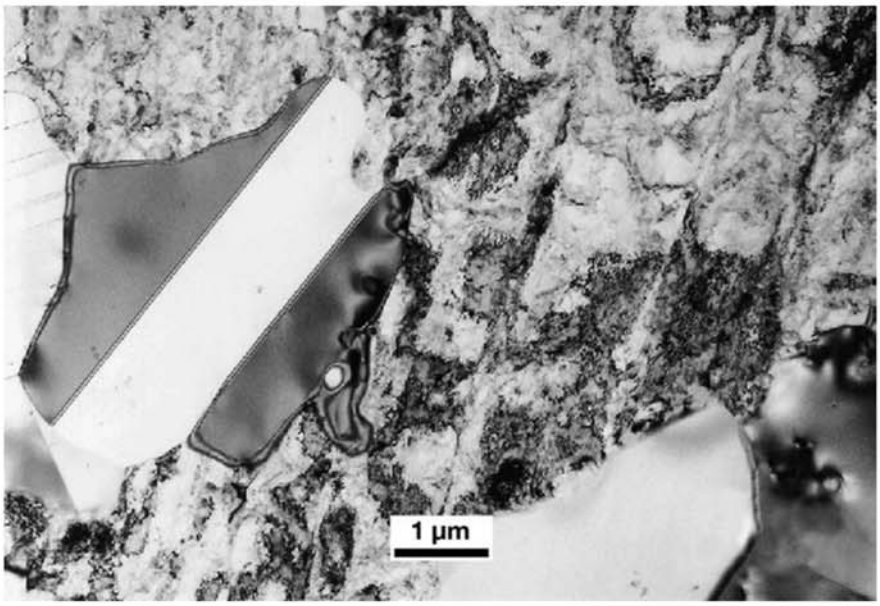

Fig. 12.31 AISI 302 stainless steel cold rolled and recrystallization annealed for 1 h at 704 °C (1300 °F). Recrystallized grains with low dislocation density surrounded by a matrix still work hardened, with high dislocation density. The recrystallized grain to the left of the image has an annealing twin (parallel bands, with contrast). TEM, 200 kV. Reproduced with permission from DoITPoMS, University of Cambridge, Cambridge, England.

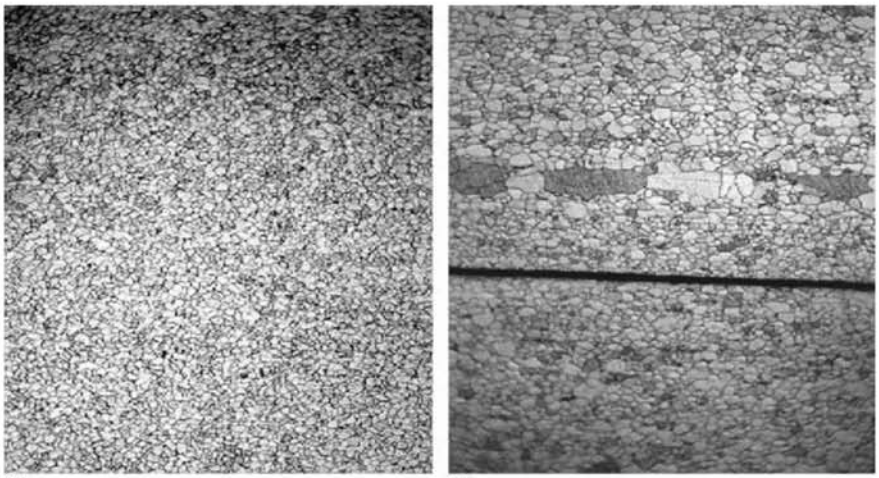

Fig. 12.32 (a) Longitudinal cross section of a thin sheet of low carbon steel for extra deep drawing (EDDS ASTM A1008/A1008M–16) continuously annealed after cold working, with uniform ferritic grain size. (b) Another heat of the same steel, subjected to the same processing but presenting heterogeneous grain size, with abnormal grain growth. To preserve the surfaces of the thin sheets, two sheets were mounted together. The black line in the center of the image corresponds to the region where the two sheet surfaces are in contact. Etchant: nital. Source: Ref 17

Fig. 12.33 Cross section of a piece of steel annealed after the performance of a Brinell hardness impression. The size of the recrystallized grains depends on the nucleation density, which depends on the degree of deformation. Outside the region delimited by very large grains, deformation was not sufficient to nucleate new grains. Magnification not provided. Courtesy M. Hillert. Source: Ref 18

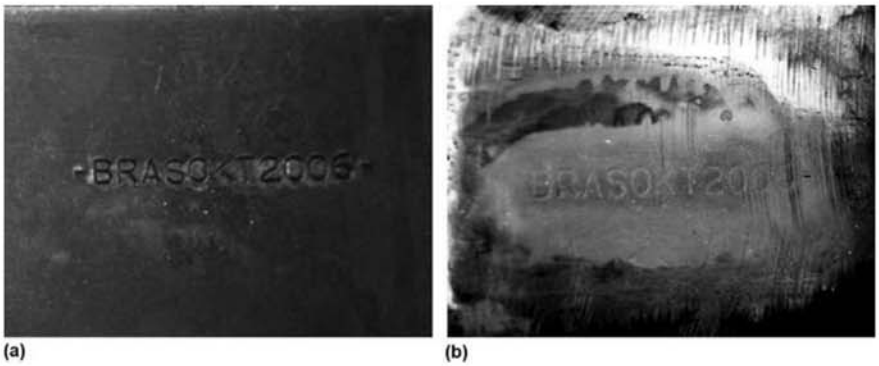

Fig. 12.34 (a) In a steel part, punching was used to mark in relief BRASOKT 2006. The marking was completely removed by grinding. In (b) after metallographic preparation and etching with Fry's etchant, the cold deformation associated with the marking is revealed. Courtesy of A. Martiny and A. Pinto, IME, Rio de Janeiro, Brazil.

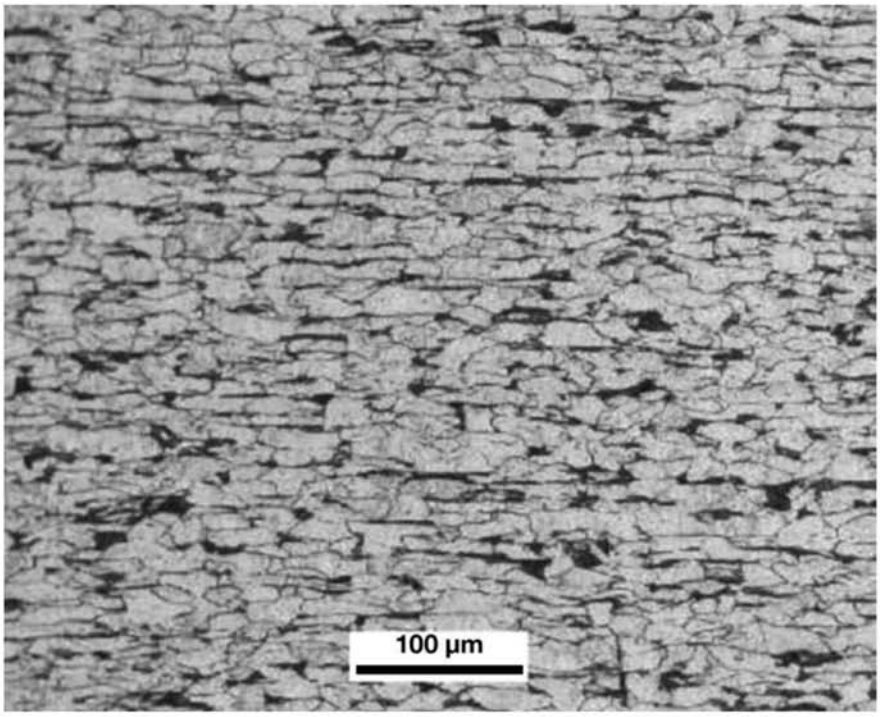

Fig. 12.35 Longitudinal cross section of a reinforcing bar (rebar) for concrete made to 600 MPa (87 ksi) minimum yield strength specification, with 6 mm (0.25 in.) diameter, lightly work hardened during wire drawing (reduction of 30%). Pearlite and ferrite. Along the longitudinal section, it is possible to observe the deformation of ferrite that resulted from the drawing operation. Etchant: nital 2%. Courtesy of ArcelorMittal Aços Longos, Juiz de Fora, MG, Brazil.

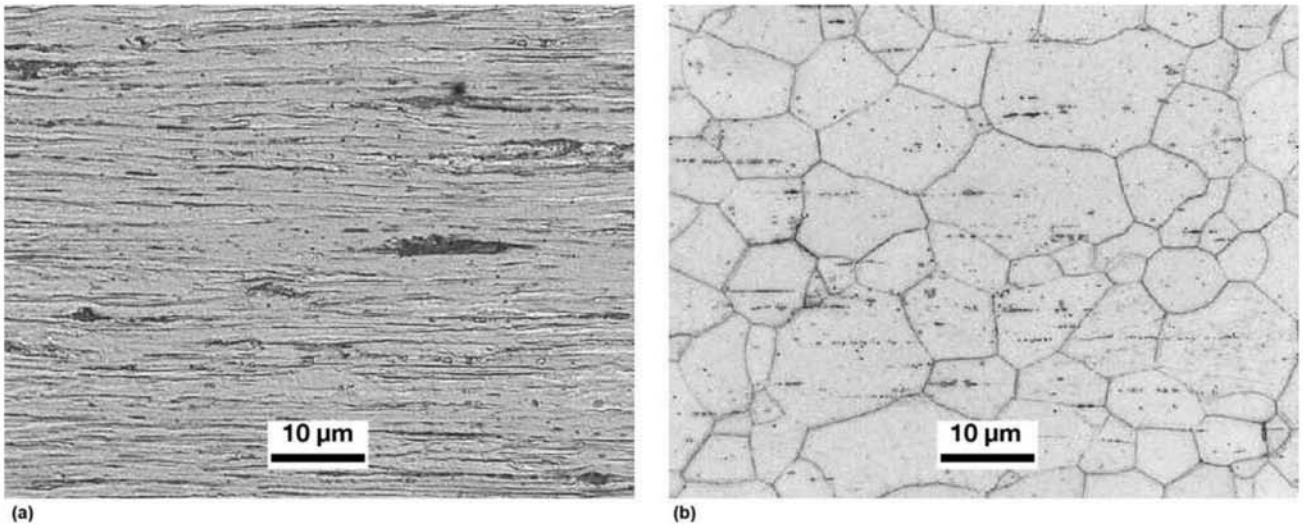

Fig. 12.36 Longitudinal cross section of a AISI 1006 steel wire with diameter of 1.15 mm (0.05 in.) (a) As drawn (cold worked). (b) Annealed. Etchant: nital 2%. Courtesy of ArcelorMittal Aços Longos, Juiz de Fora, MG, Brazil.

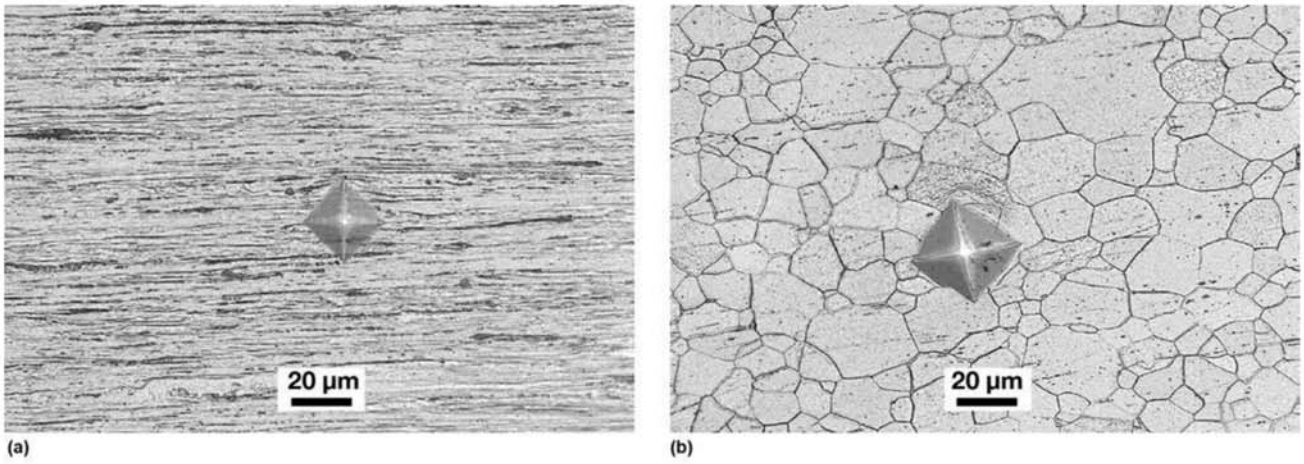

Fig. 12.37 Longitudinal cross section of a AISI 1006 steel wire cold drawn from 5.5 to 1.15 mm (0.2 to 0.06 in.) diameter. (a) As drawn (cold worked), hardness 249 HV 100 gf. (b) Annealed, hardness 135 HV 100 gf. The hardness impressions, performed with the same load, are visible in the micrographs. Etchant: nital 2%. Courtesy of ArcelorMittal Aços Longos, Juiz de Fora, MG, Brazil.

12.5 Medium-Carbon Steels

Figures 12.39 and 12.40 present the effects of cold work on steels with medium carbon content.

12.6 Electrical Steels

Silicon grain oriented electric steel (GOES) is used in transformers. According to Ref 19, this steel presents a strong (110)[001] s crystallographic texture (Ref 20), obtained via abnormal grain growth. Grains as large as 10 mm (0.4 in.) in sheets with 0.3 mm (0.01 in.) thickness are not uncommon. GOES is not as frequently used as the non–grain oriented electric steel (NGOES), widely used

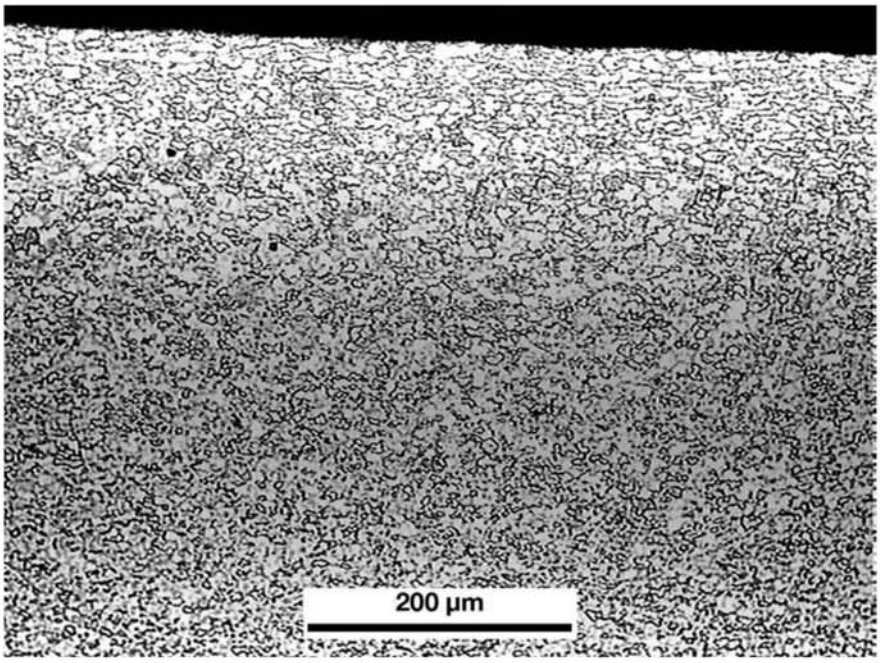

Fig. 12.38 AISI 1006 steel hot rolled, pickled, and subjected to a skin pass cold work (a small cold reduction of the surface to guarantee good surface quality and precise thickness). Equiaxial ferrite and pearlite inside the plate. On the surface region, the ferrite grains are elongated. Etchant: nital. Courtesy of ArcelorMittal Tubarão, ES, Brazil.

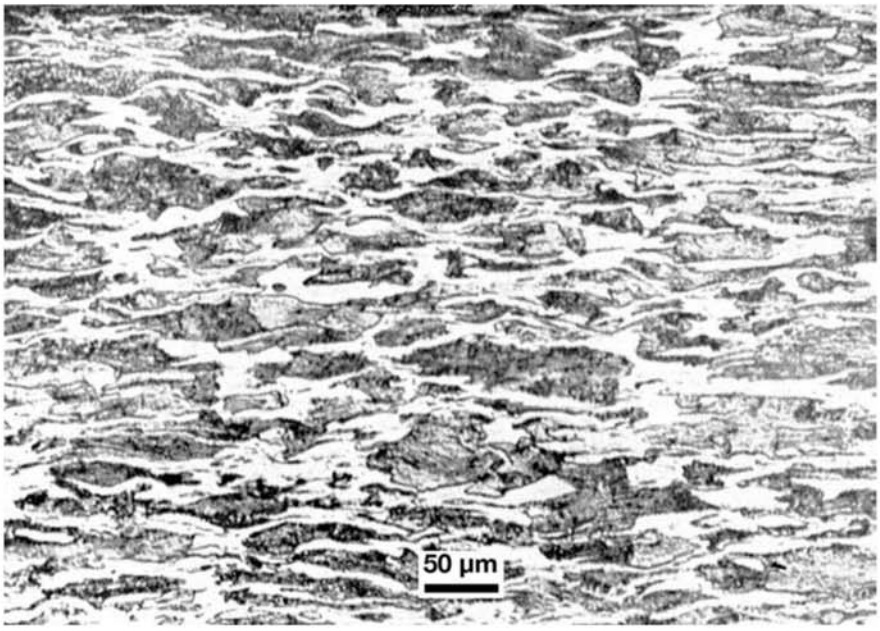

Fig. 12.39 Longitudinal cross section of a medium carbon steel heavily cold worked. Deformed ferrite and pearlite. Etchant: nital.

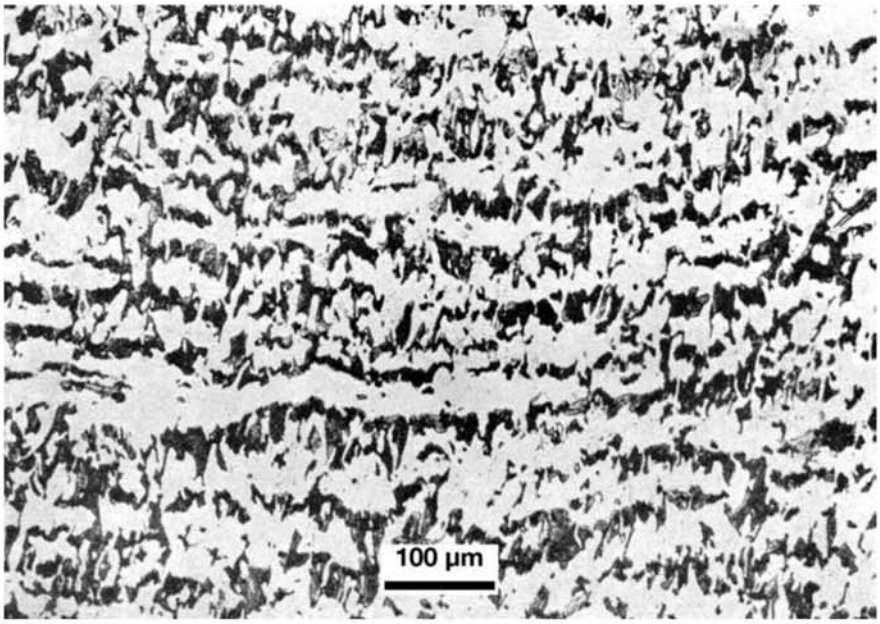

Fig. 12.40 Transverse cross section of a medium carbon steel bar axially compressed (vertical direction in the image). Cold deformation of ferrite and pearlite can be seen. Etchant: nital.

in electric motors. Even the NGOES has a considerable texture, because processing aims at maximizing the number of grains with the [100] direction parallel to the sheet surface. Two processes are used to obtain the ideal grain size of around 150 µm. "Fully processed" steels have enough silicon in their composition to completely avoid austenite formation. In these steels, normal grain growth happens during annealing. In "semi-processed" steels, the silicon content is lower. In these steels, grain growth is achieved through recrystallization after a small cold forming (around 6%). The two classes of NGOES are easily distinguished via optical microscopy: grain boundaries in normal grain growth are either planar or have a single curvature. Semi-processed steels, on the other hand, exhibit multiple curvatures in the grain boundaries as a result of the different recrystrallization fronts of large grains that grow from cold-worked ones meeting at various points, as shown in Fig. 12.41 (Ref 21). To ensure a high magnetic permeability and low hysteresis losses, these steels have a carbon content lower than 30 ppm, the minimum achievable amount of nonmetallic inclusions, and minimum dislocation density, since these features hinder the movement of the walls of the magnetic domains. Figure 12.42 presents an example of the distribution, shape, and size of the manganese sulfide inclusions in these steels. Figure 12.43 presents the structure of a "warm rolled" electric steel in which the elongated aspect and the work hardening of the grains is evident.

12.7 Warm Working—Working in the Intercritical Region

Figures 12.44 and 12.45 present the aspect of material worked in the intercritical region, where the heterogeneity of deformation can be observed, at least for smaller deformations. Working in the intercritical region, however, can also lead to interesting results and is currently being considered an option for

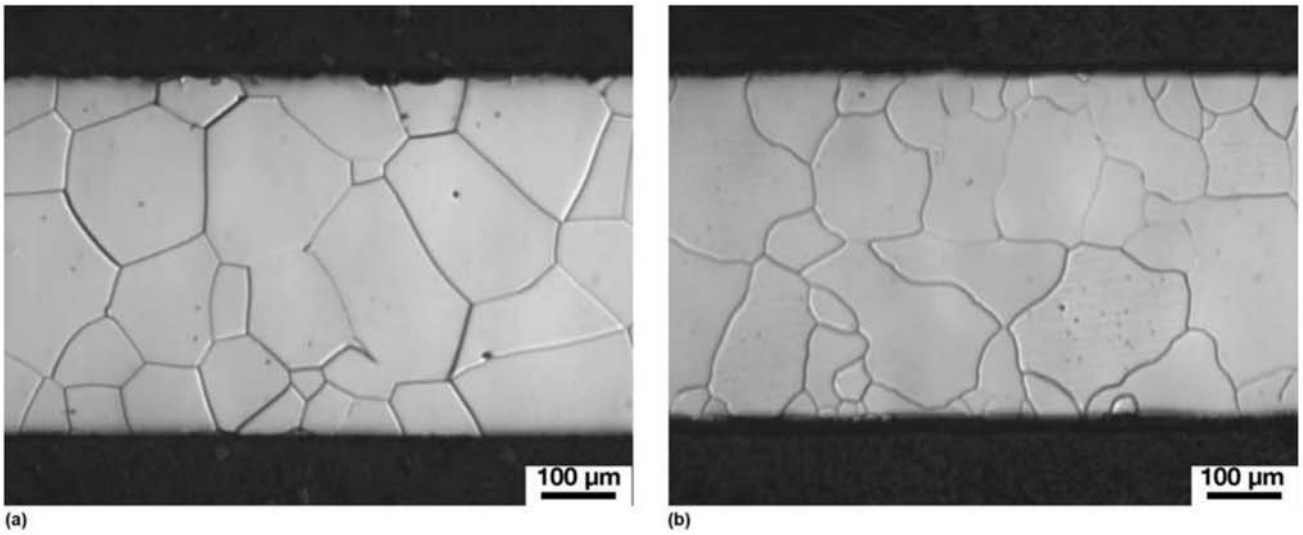

Fig. 12.41 Longitudinal cross section of non–grain oriented electric steel (NGOES). (a) Sheet with 0.5 mm (0.02 in.) thickness of electric steel with Si = 3%, "fully processed." (b) Sheet with 0.5 mm thickness of electric steel with Si = 0.5%, "semi-processed." Etchant: nital 2%. Courtesy F. Landgraf, USP, São Paulo, SP, Brazil. Source: Ref 21

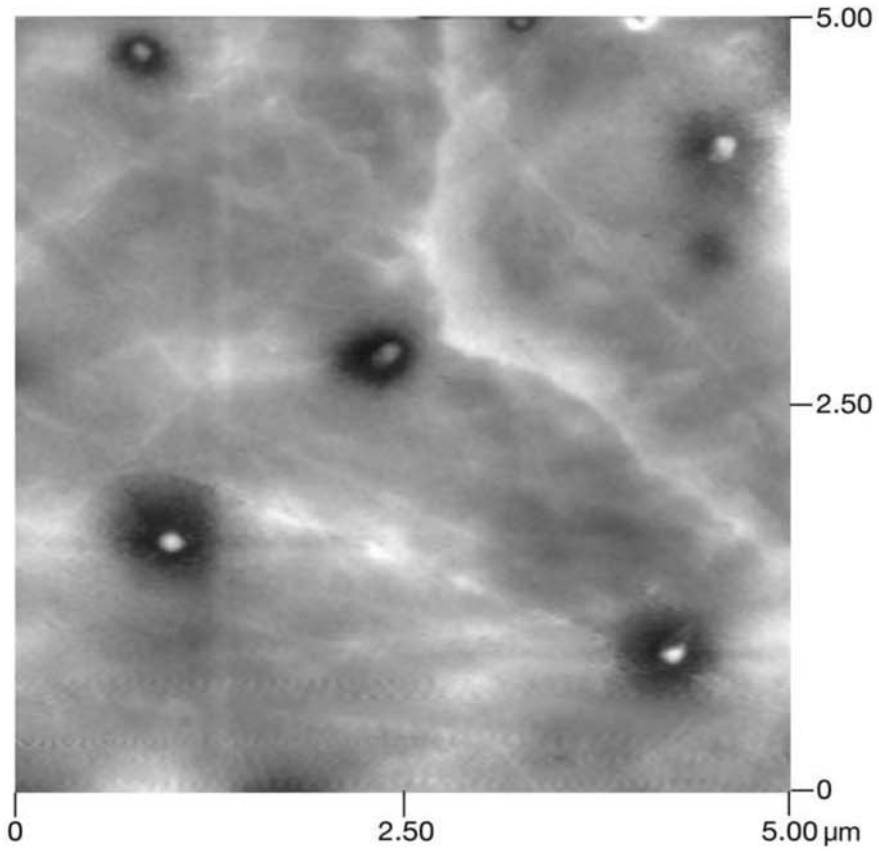

Fig. 12.42 Atomic force microscopy image of a high silicon electric steel showing the size, shape, and distribution of manganese sulfide inclusions in this steel. The inclusions are smaller than 250 nm. See also Ref 7. Courtesy of M.S. Andrade, CETEC, Belo Horizonte, MG, Brazil.

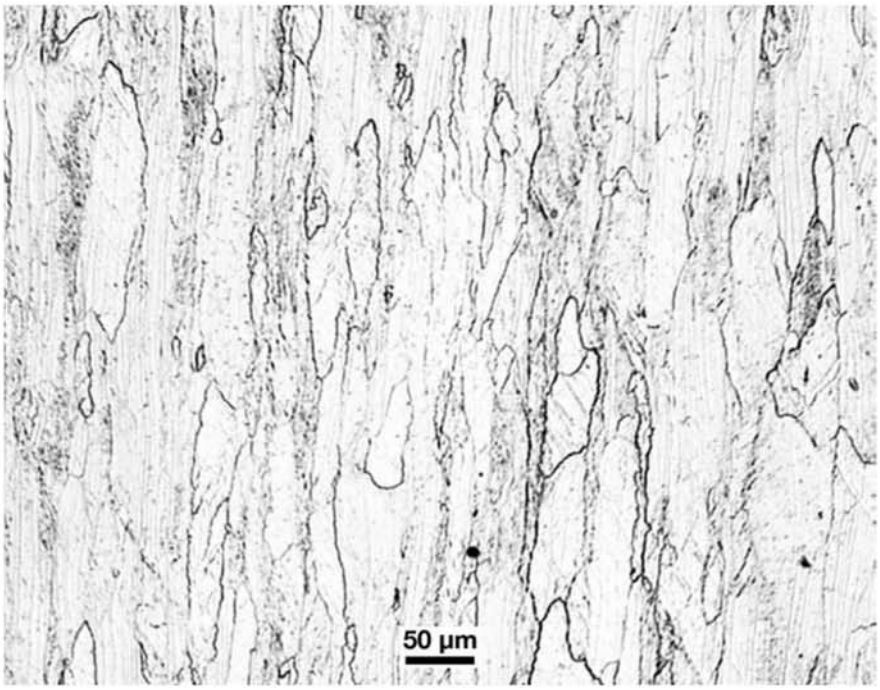

Fig. 12.43 Electric steel (high silicon) warm rolled with elongated grains of ferrite. (The annealed structure is presented in Fig. 7.6, Chapter 7, "Equilibrium Phases and Constituents in the Fe-C System," in this book). Courtesy of C. Capdevila Montes, Centro Nacional de Investigaciones Metalúrgicas—CENIM-CSIC, grupo Materialia, Madrid, Spain.

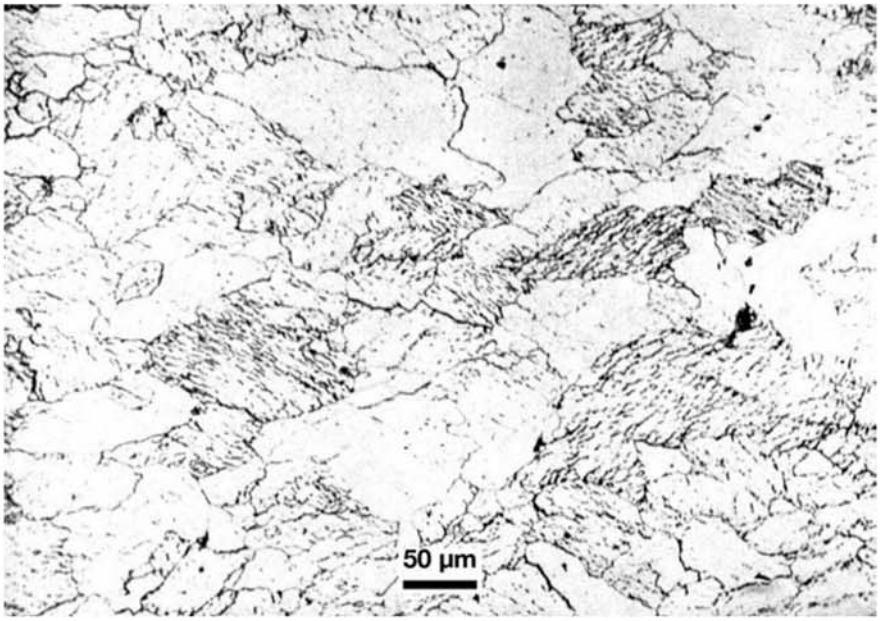

Fig. 12.44 Extra low carbon steel deformed under compression between 750 and 800 °C (1380 and 1470 °F). The ferrite grains present polygonal lines, only visible after etching. Etchant: nital.

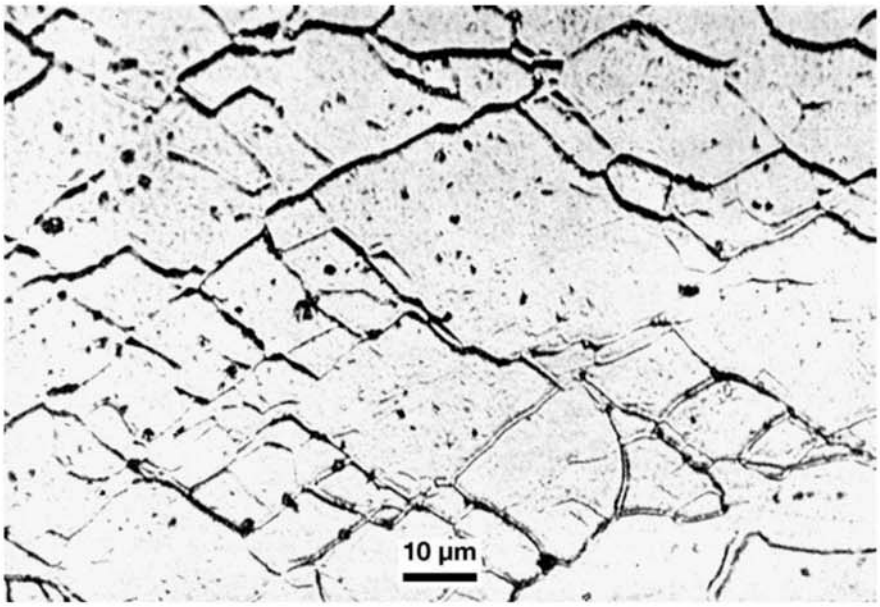

Fig. 12.45 Detail of the microstructure in Fig. 12.44.

the production of ultrafine grained steels. Figure 12.46 presents results for warm forming of low-carbon steel, followed by annealing (Ref 23).

12.8 Cold Forming of Parts—Fasteners as Examples

Besides the forming of products from steel sheet and foil, the main process for the manufacture of food and drink packages, vehicle body parts, and many other components, parts can be cold forged or cold formed, whenever the material has sufficient ductility, and its strength and dimensions are compatible with the forming equipment. Compared to hot working, cold working offers the following main advantages: better dimensional tolerances of the formed product, better surface finish (including the absence of oxides, "scale"). Some interesting examples of complexities and potential difficulties of cold forming are seen in the manufacture of fasteners. Figure 12.47, for instance, shows the formation of the head of a fastener for the automotive industry. Because each volume of material suffers a different deformation (in terms of the degree of deformation and the deformation orientation), fibers are deformed by the material flow during forming (see Chapter 11, "Hot Working"). There is a wealth of experience accumulated about the effects of material flow during forming (and the consequences on the deformation of previously existing "fibers") on the performance of formed parts. In general, it is well established that the lines or fibers should not be cut or interrupted or emerge at the surface of the part, providing crack starters for various failure processes, including a significant reduction in fatigue resistance. Threads in fasteners are frequently made by a cold forming process called "rolling." Rolled threads (Fig. 12.48a and c) use thread rolling dies (either flat or cylindrical). Rolling threads causes no interruption in the fibers of the material and should not give rise to common surface irregularities that can be experienced in machined threads (Fig. 12.48b and d and Fig. 12.49).

Figure 12.50 shows a fatigue crack started at a thread root in a AISI 303 stainless steel (free-cutting steel with high volume fraction of nonmetallic in-

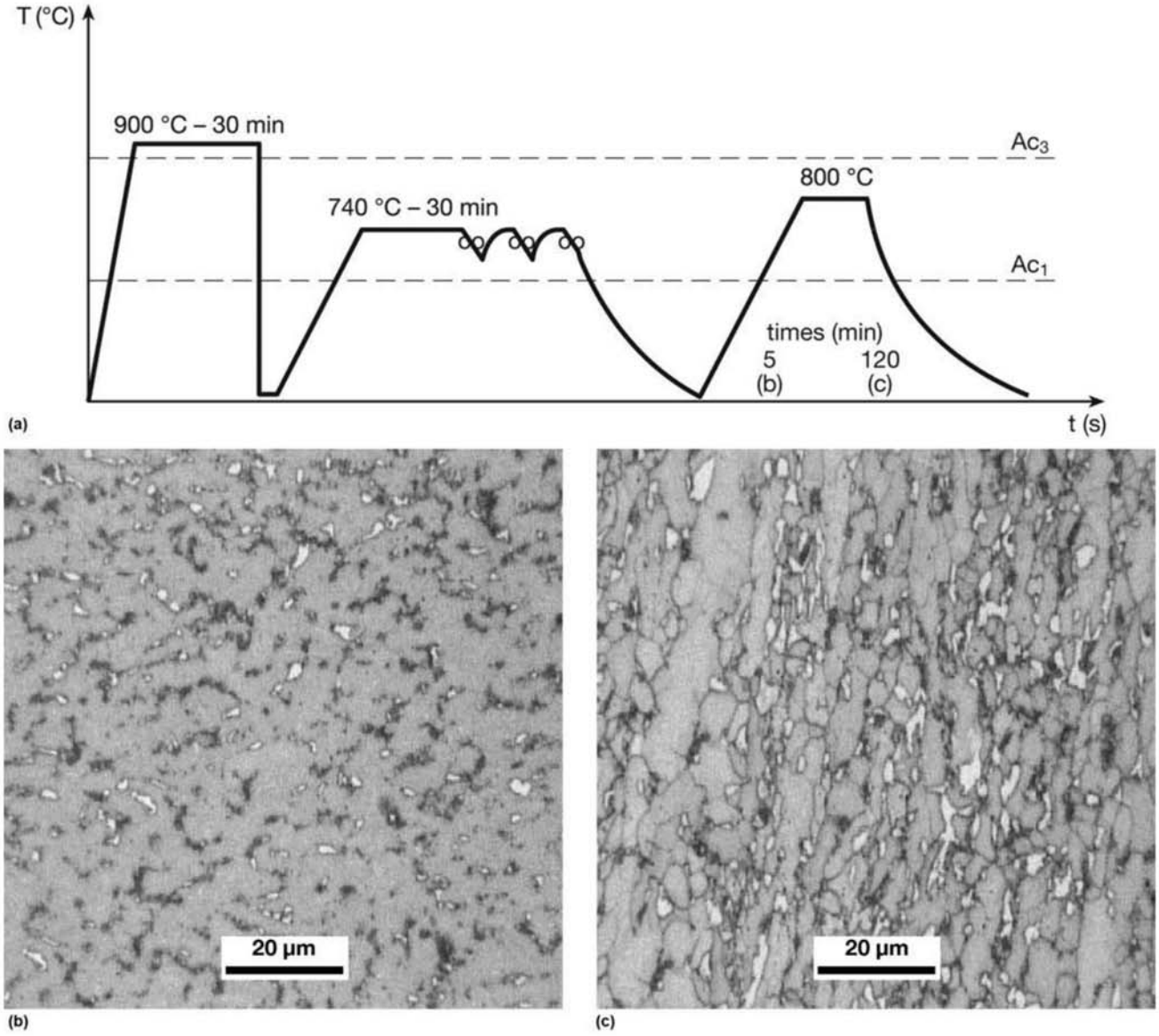

Fig. 12.46 (a) Thermal cycle for warm working. The steel containing C = 0.11%, Mn = 1.41%, Si = 0.29%, Nb = 0.028% was quenched from 900 °C (1650 °F), then, rolled between 740 and 700 °C (1365 and 1290 °F) until a reduction of 50% was achieved. Material annealed at 800 °C (1470 °F) for (b) 5 min (ferrite grain size: 2.05 μm) and (c) 120 min, ferrite grain size: 3.48 μm. The gray regions are ferrite. Pearlite and carbides appear dark and the MA constituent appears light. Etchant: LePera. Courtesy of D. Santos, UFMG, Belo Horizonte, MG, Brazil. Source: Ref 22

clusions). The crack happened after a vibration test. The causes of the failure (Ref 23) were: (a) the use of machined threads instead of rolled threads; (b) the poor quality of the thread surface finish; (c) the use of a steel with a lower strength than appropriate for the applications; and (d) the use of a free-cutting steel for an application in which vibration with high cyclic stresses were expected.

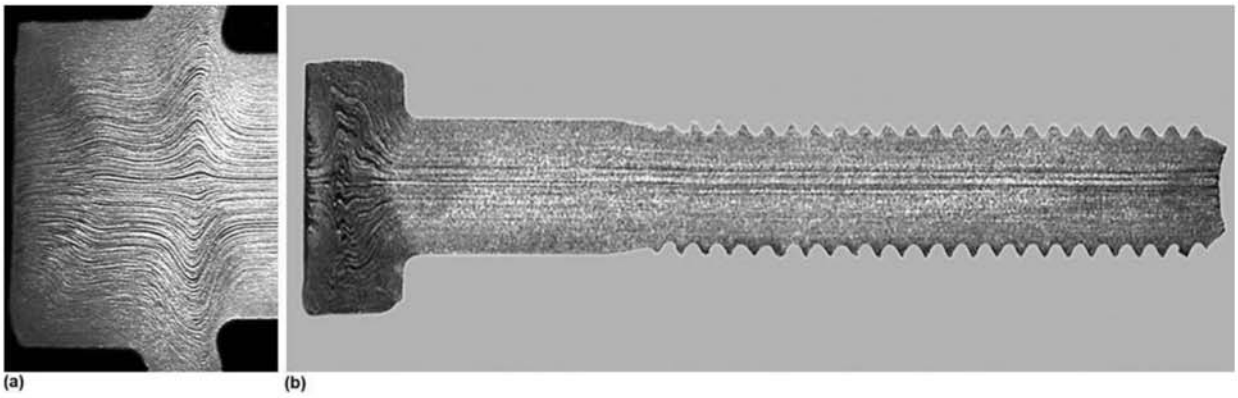

Fig. 12.47 Longitudinal cross section of fasteners cold formed from a hot-worked wire rod. The "fibers" of the original material can be seen, as well as the orientation change caused by deformation. (a) Detail of the head of a special fastener. (b) M5x30 bolt. Etchant: hot 30% hydrochloric acid. Courtesy of FIBAM Cia. Industrial, São Bernardo do Campo, SP, Brazil.

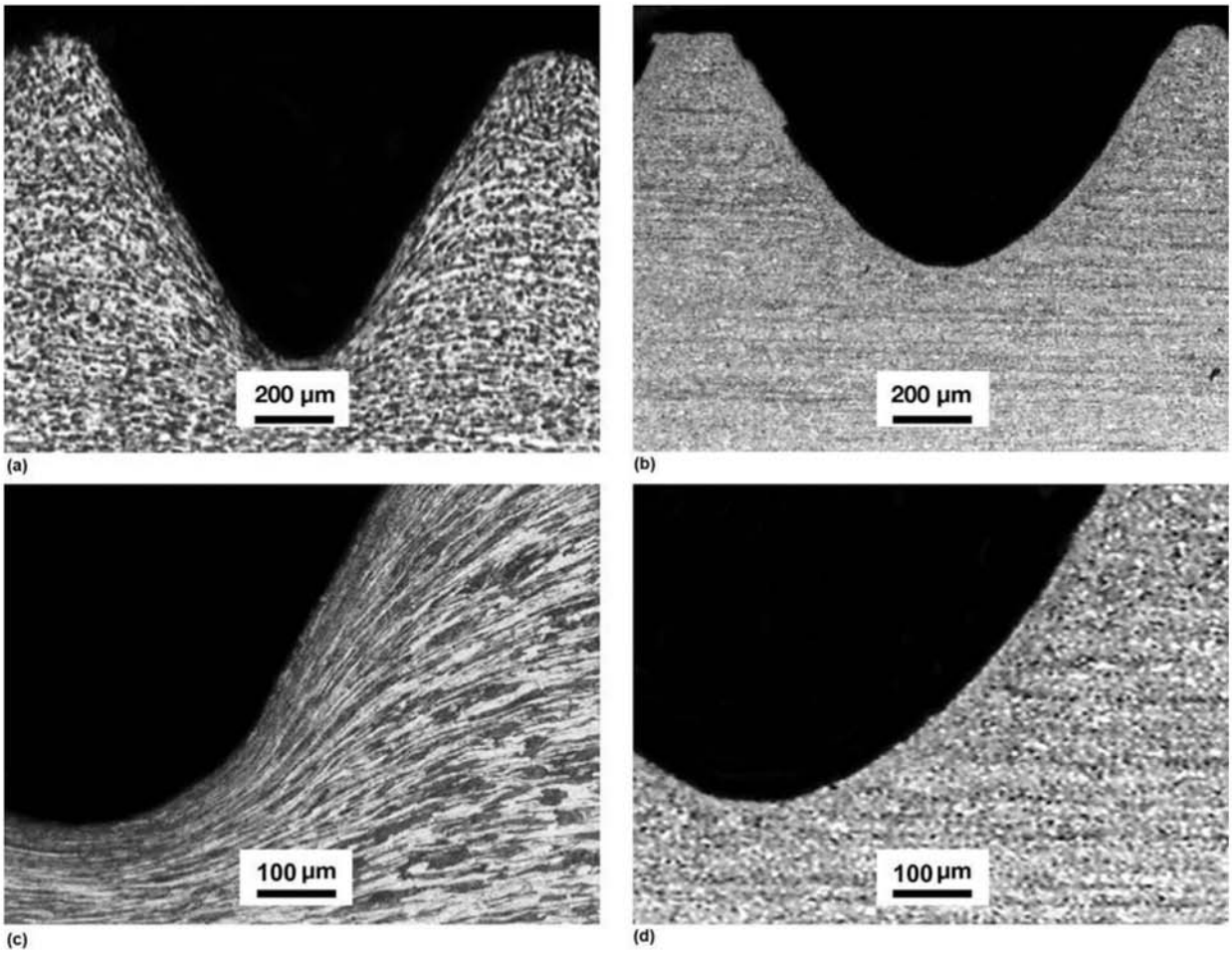

Fig. 12.48 Longitudinal cross section of the threaded region of M5 fasteners. (a) and (c) Rolled thread. (b) and (d) Machined (or cut) thread. The deformation of the "fibers" of the original material causes a large reduction of the fiber spacing close to the thread roots in the case of rolled threads. In (b), surface irregularities caused by machining can be seen. Etchant: nital 3%. Courtesy of FIBAM Cia. Industrial, São Bernardo do Campo, SP, Brazil.

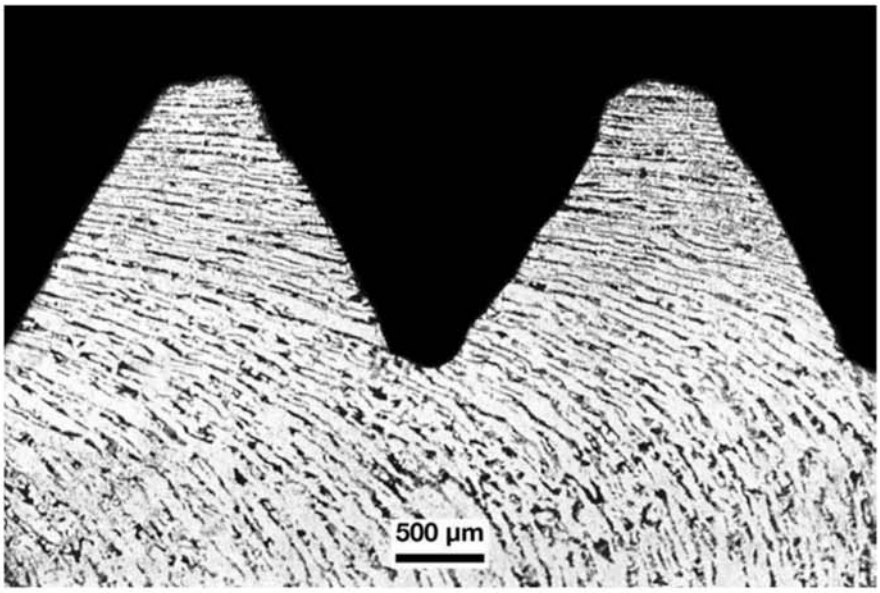

Fig. 12.49 Longitudinal cross section of a nut, close to the thread. The alignment of the structure, which is deformed, indicates that the central hole of the nut was made by punching (in the image, from right to left). Afterward, the thread was machined (cut). Etchant: nital.

12.8.1 Laps in Threads

Thread rolling may lead to the appearance of laps (Fig. 12.51). In some standards for fasteners, a certain extent of laps is acceptable, up to a certain position, and if they are not close to the thread root (see, for instance, ISO 6157-1 in Ref 24 or ASTM F788 in Ref 25).

12.8.2 Nails

Nails are usually cold formed from wires, as shown in Fig. 12.52.

12.9 Defects in Cold Forming

Deformation conditions are generally more stringent in cold working than in hot working. Thus, the incidence of fracture during forming must be taken in consideration. In addition, smaller dimension products are frequently more conveniently produced by cold forming. In these cases, nonmetallic inclusions with inadequate dimensions and plasticity may have serious effects on the material behavior, as shown in Fig. 12.53 to 12.58. It is evident from these figures that nonmetallic inclusions are an important source of failure during forming of products with small dimensions, such as wires, filaments for cords, foil and thin sheet, and the products obtained from these semi-finished materials. In addition, the combination of proper microstructure and correct cold forming are essential to the control of the cold work product properties. Figure 12.59, for example, shows the "delamination" fracture of a filament of eutectoid steel cold worked. These filaments are frequently used to manufacture cords. The desired mode of failure is transverse to the filament cross section, not as shown in the figure. The conditions leading to this type of failure are discussed in Ref 26.

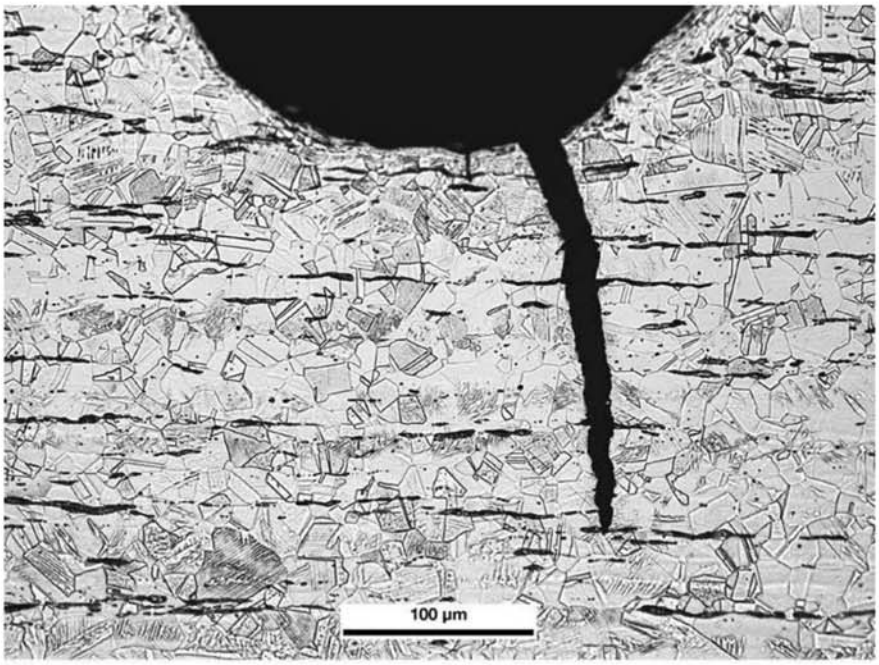

(a)

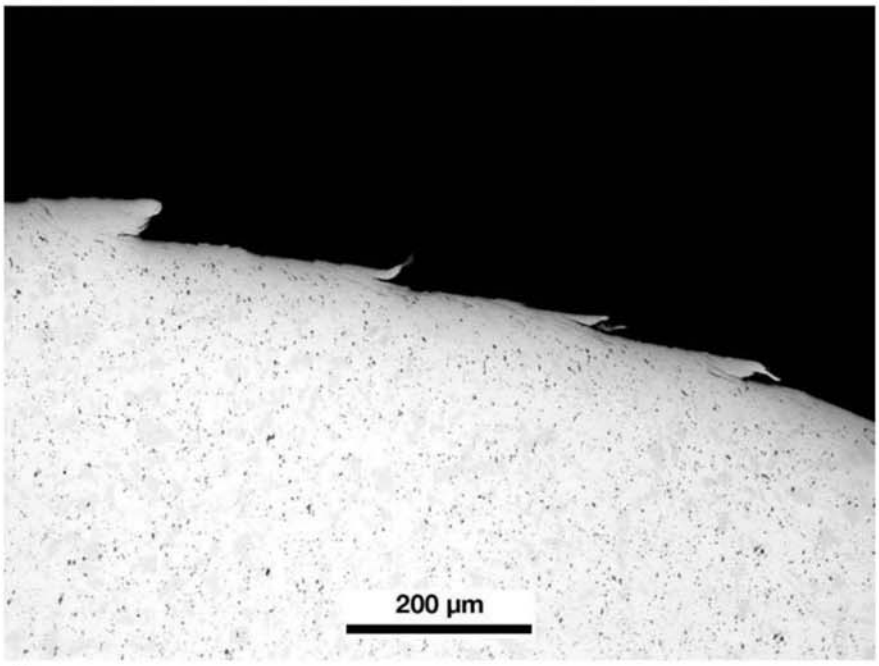

(b)

Fig. 12.50 (a) Longitudinal cross section of a bolt machined from AISI 303 stainless steel, subjected to vibration testing. Fatigue cracks are present in the thread root. Large quantity of sulfides (nonmetallic inclusions), since this is a free cutting steel. The structure corresponds to solubilizing or solubilizing annealing (see Chapter 16, "Stainless Steels," in this book). (b) Transverse cross section of the bolt, showing the poor quality of the surface finish of the machining operation. Courtesy of D. Susan, reproduced with permission from Cambridge University Press. Source: Ref 23

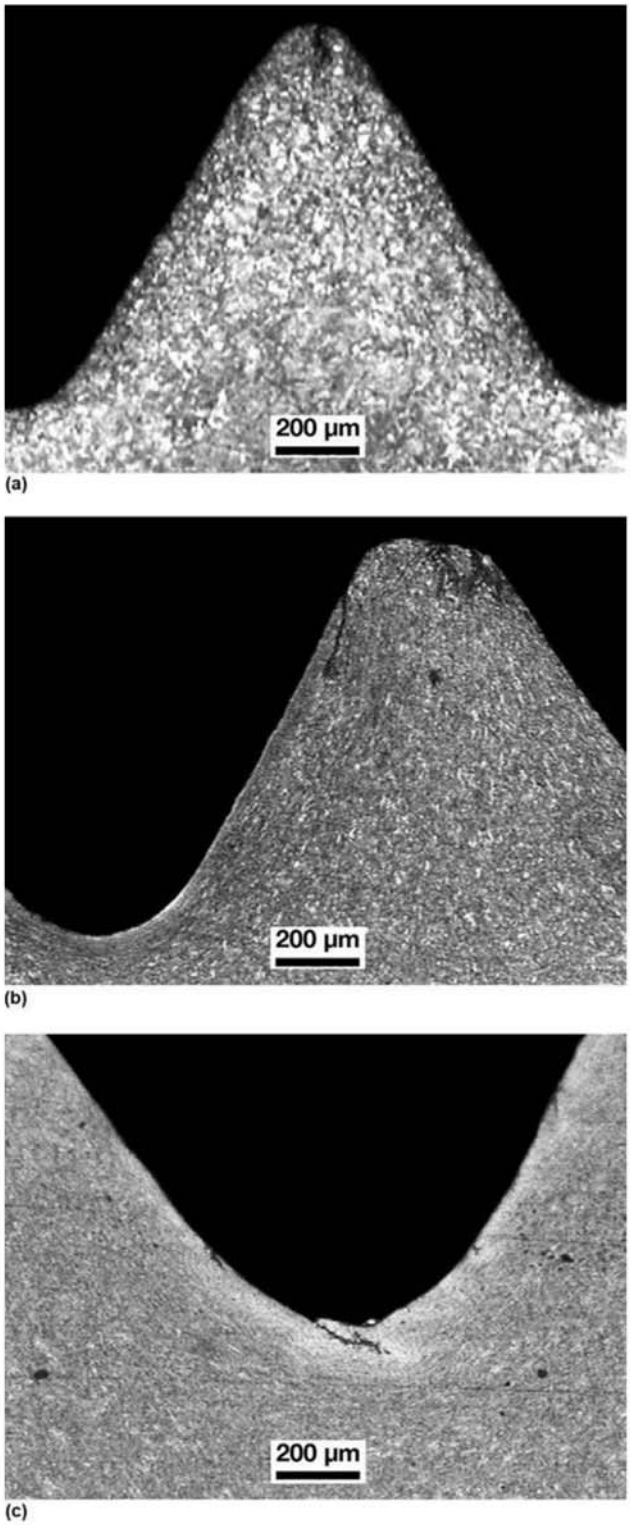

Fig. 12.51 Longitudinal cross section of fasteners presenting rolling folds or laps in different extents and locations. (a) Lap in the thread crest. (b) Lap close to the thread crest. (c) Lap in the thread root.

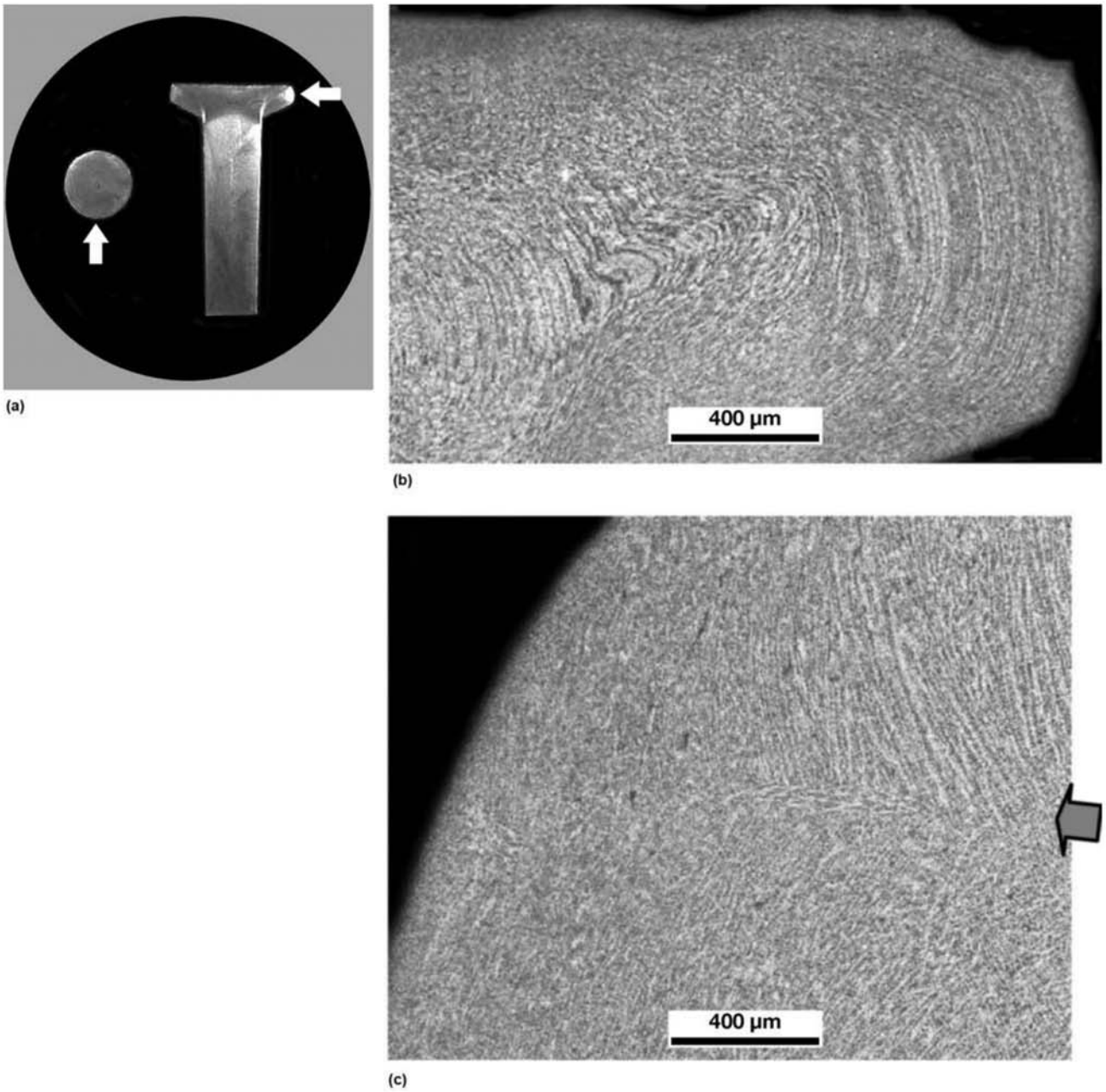

Fig. 12.52 (a) Metallographic assembly for the examination of a nail. (b) Longitudinal cross section of the nail, showing the edge of the nail head where the "fibers" have been deformed by the forming operation. (c) Transverse cross section of the body of the nail: the fiber orientation gives information about the original dendritic structure. The point where the original dendrites met at the edge of the continuous casting billet that originated the nail can still be seen. Etchant: Béchet-Beaujard. Courtesy of ArcelorMittal Aços Longos, Juiz de Fora, MG, Brazil.

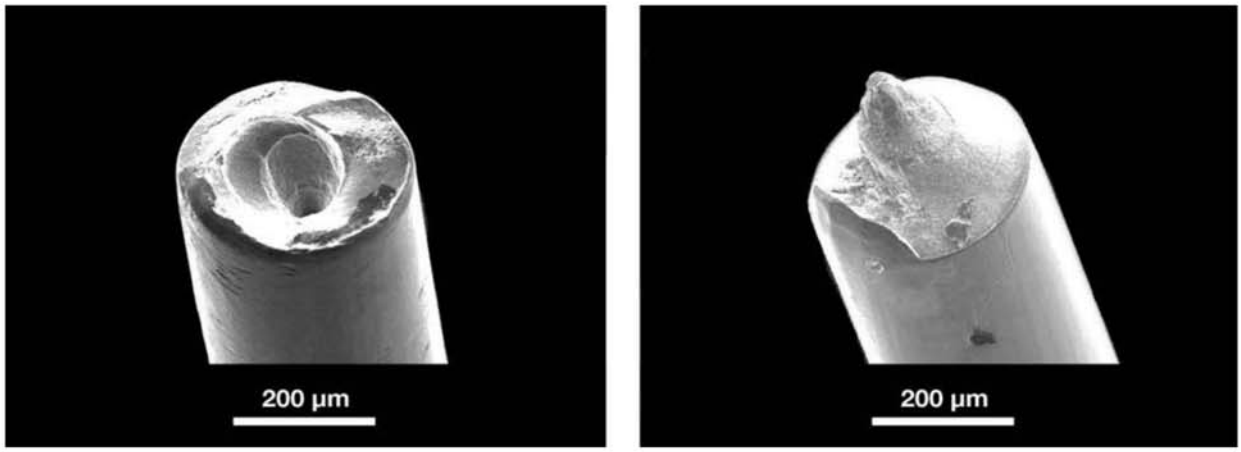

Fig. 12.53 Some examples of eutectoid steel filaments (for cord making) with cup and cone fracture that occurred during wire drawing (SEM, SE).

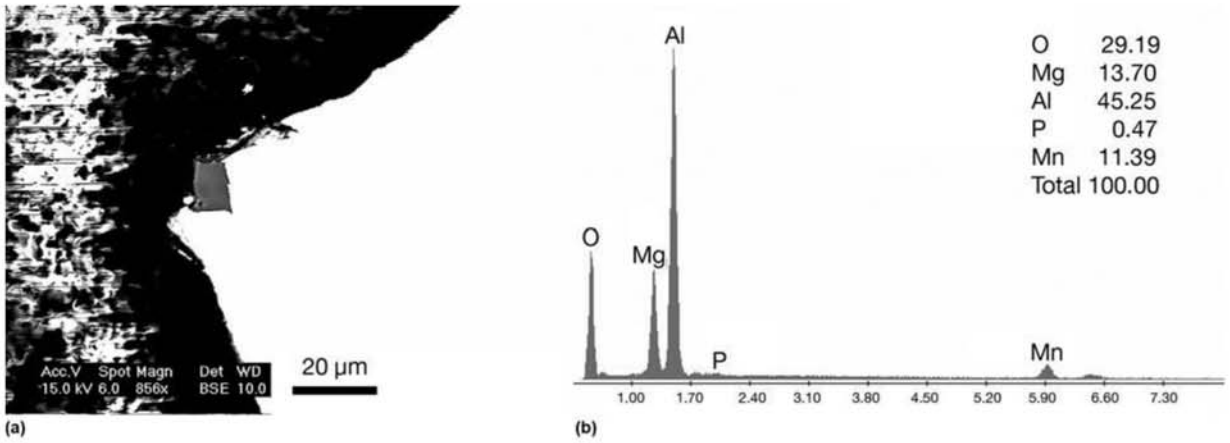

Fig. 12.54 (a) Longitudinal cross section of a cold drawn filament of eutectoid steel (as shown in Fig. 12.53) showing cup and cone fracture. A polygonal nonmetallic inclusion that has not been deformed during hot working (see Chapter 11, "Hot Working," in this book) can be seen. SEM, BE. (b) Energy spectrum of the inclusion in (a) obtained by EDS. Results indicate this is probably a spinel inclusion ($MgAl_2O_4$).

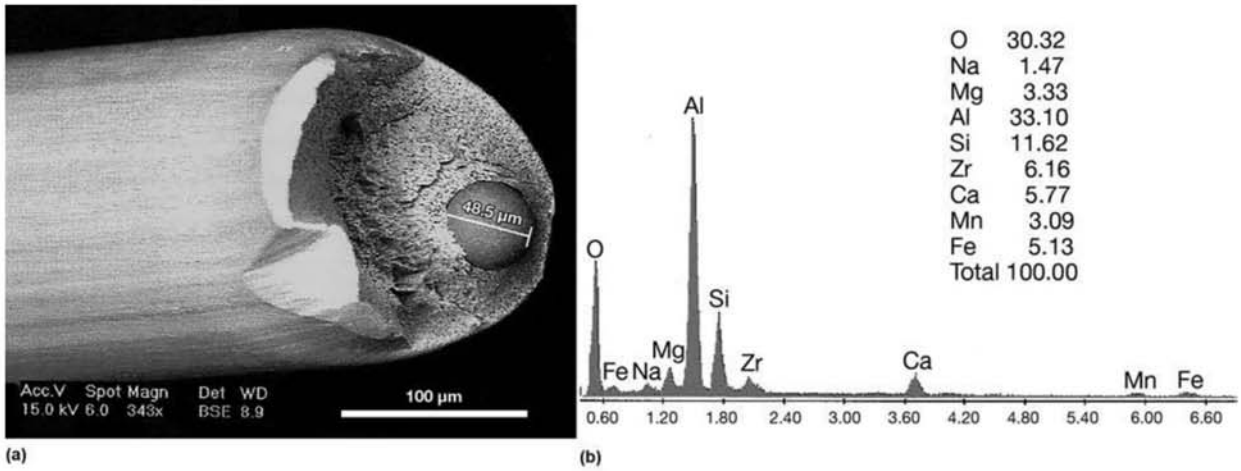

Fig. 12.55 (a) Fracture of a cold drawn eutectoid steel filament showing a large nonmetallic inclusion. SEM, BE. (b) Energy spectrum of the inclusion in (a) obtained by EDS.

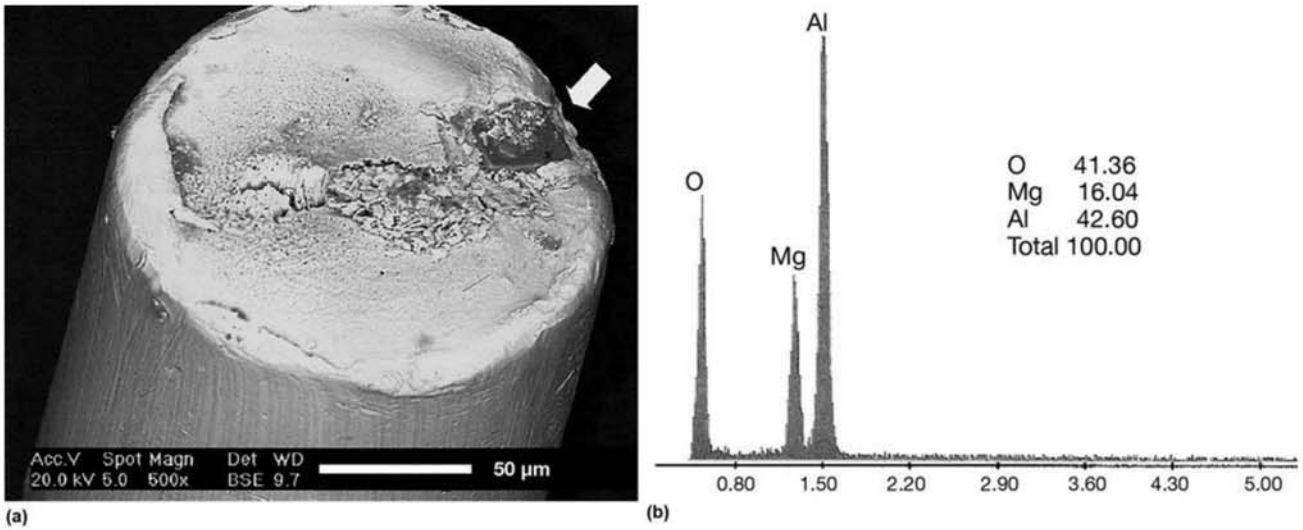

Fig. 12.56 (a) Fracture of a cold drawn eutectoid steel filament showing a large nonmetallic inclusion. SEM, BE. A polygonal nonmetallic inclusion that has not been deformed during hot working (see Chapter 11, "Hot Working") can be seen. SEM, BE. (b) Energy spectrum of the inclusion in (a) obtained by EDS. Results indicate this is probably a spinel inclusion ($MgAl_2O_4$).

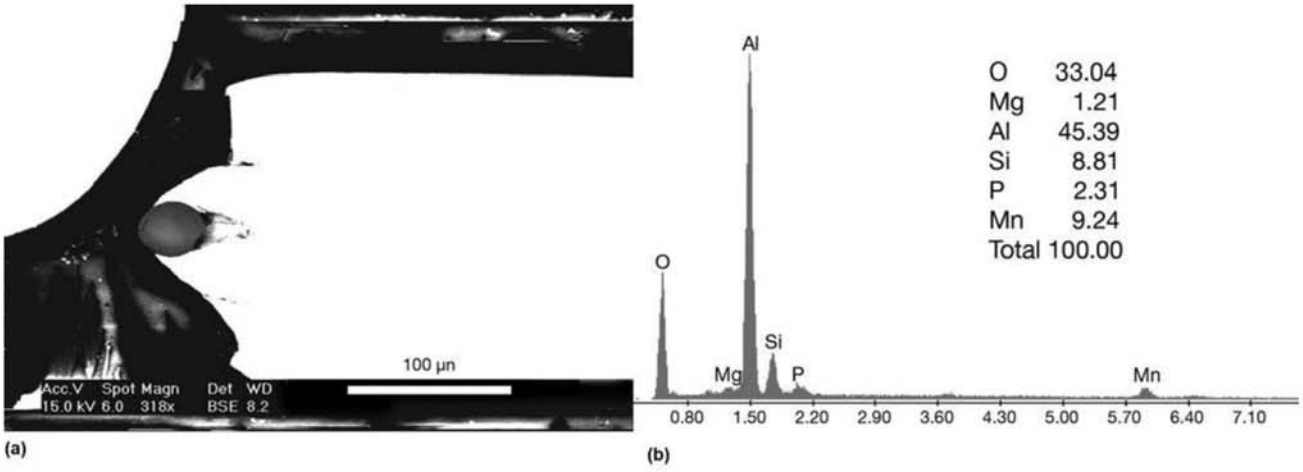

Fig. 12.57 (a) Longitudinal cross section of the cold drawn filament of eutectoid steel shown in Fig. 12.53. Large nonmetallic inclusion is present. SEM, BE. (b) Energy spectrum of the inclusion in (a) obtained by EDS.

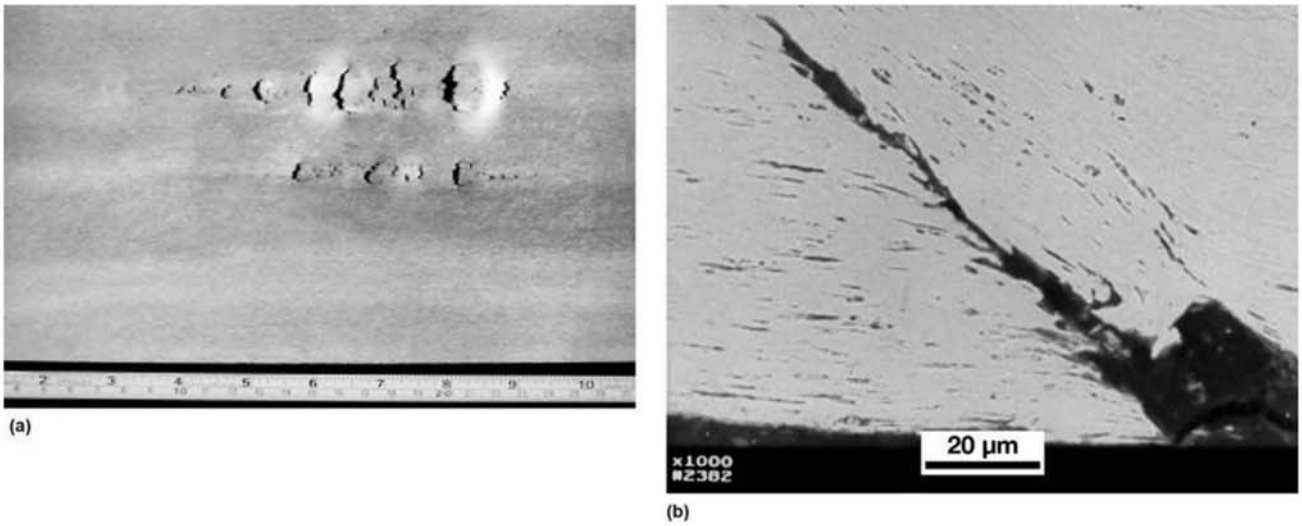

Fig. 12.58 (a) Defect that gave rise to the rupture, during cold rolling of a thin sheet of steel. (b) Longitudinal cross section of the sheet, tangential to the edge of one of the defects. The surface of the sheet is at the bottom of the image. The dark line is the crack, slightly opened in this region. The dark spots are Al_2O_3 inclusions, concentrated in this region of the product. Inclusions were identified using EDS. SEM, BE, no etching.

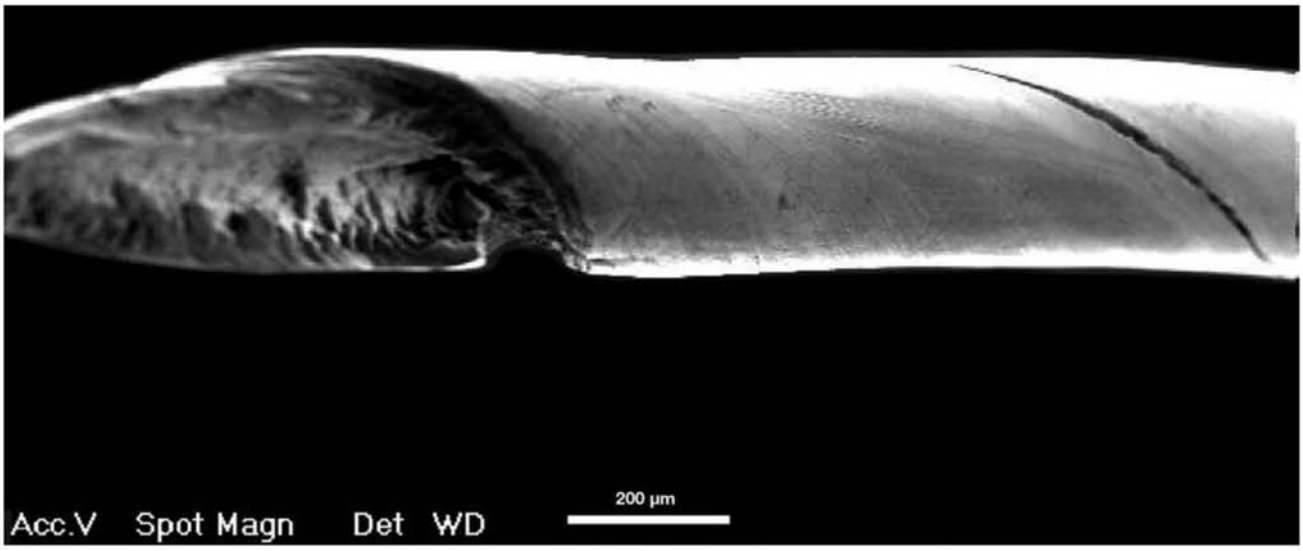

Fig. 12.59 Delamination fracture in a cold worked filament of eutectoid steel, used to manufacture twisted steel cords.

REFERENCES

1. R.W.K. Honeycombe, *Steels: Microstructure and Properties*, Edward Arnold, 1981
2. M. Meiers and A. Broumas, Lüders Bands in Steels, https://vimeo.com/4586024 (accessed November 13, 2016)
3. G.E. Dieter, *Mechanical Metallurgy*, McGraw-Hill, 1961, and M.A. Meyers and K.K. Chawla, *Mechanical Behavior of Materials*, 2nd ed., Cambridge University Press, 2008
4. W. Nicodemi, C. Mapelli, R. Venturini, and R. Riva, Metallurgical Investigations on Two Sword Blades of 7th and 3rd Century BC Found in Central Italy, *ISIJ Int.*, Vol 45 (No. 9), 2005, p 1358–67
5. S.F. Castro, J. Gallego, F.J.G. Landgraf, and H.J. Kestenbach, Efeito da orientação cristalográfica sobre a laminação de encruamento em aços elétricos, *Tecnol. Metal. Mat.*, Vol 2 (No 3), 2006, p 53, http://www.tecnologiammm.com.br/doi/10.4322/tmm.00203011 (acessed November 15, 2016)
6. N. Rajmohan, Y. Hayakawa, J.A. Szpunar, and J.H. Root. Neutron Diffraction Method for Stored Energy Measurement in Interstitial Free Steel, *Acta Mater.*, Vol 45 (No. 6), 1997, p 2485–94
7. M.S. Andrade, J.M.C. Vilela, and O.A. Gomes, Microscopia de Varredura por Sonda Mecânica, *Metal. Mat.*, Vol 58 (No. 518), 2002, p 123–25
8. H. Tashiro, The Challenge for Maximum Tensile Strength Steel Cord, *Nippon Steel Tech. Rep.*, Vol 80, 1999, p 6–8
9. S. Kalpakjian, *Manufacturing Processes for Engineering Materials*, Addison-Wesley, 1984
10. A. Martínez-de-Guerenu, F. Arizti, M. Díaz-Fuentes, and I. Gutiéerrez, Recovery during Annealing in a Cold Rolled Low Carbon Steel. Part I: Kinetics and Microstructural Characterization, *Acta Mater.*, Vol 42, 2004, p 3657–64
11. E.G. Souza, "Textura de recristalização de um aço extra-baixo, carbono ao boro," Masters thesis, IME, 2004
12. R.P. Krupitzer et al., *Progress in HSLA Steels in Automotive Applications*, SAE Paper 770162, 1977
13. A. Haldar, S. Suwas, and D. Bhattacharjee, eds., *Microstructure and Texture in Steels and Other Materials*, Springer, 2009
14. C.S.C. Viana and A.S. Paula, Texturas de deformação, In: *Textura e relações de orientação*, A.P. Tschiptschin et al., eds., IPEN, 2003, p 35–54
15. M.F. de Campos, F.J. Landgraf, I.G. Falleiros, G.C. Fronzaglia, and H. Kahn, Texture Evolution during the Processing of Electrical Steels with 0.5% Si and 1.25% Si, *ISIJ Int.*, Vol 44 (No. 10), 2004, p 1733–37
16. Stanford University, Introduction to Orientation Imaging Microscopy, https://snsf.stanford.edu/equipment/eim/SEM/OIMIntro.html (accessed November 15, 2016)

17. R.T. Renó, B.O. Monteiro, C.A.L. Novaes, and A. Costa e Silva, Granulação grosseira em aço baixo carbono acalmado ao alumínio com temperatura de bobinamento elevada, *54º Congresso Anual da ABM*, ABM, 1999
18. M. Hillert, *Metallographic Atlas*, Materials Education Council (MEC), Pennsylvania State University, 1991
19. F. Landgraf, Private communication, 2007
20. M. Matsuo, Texture Control in the Production of Grain Oriented Silicon Steels, *ISIJ Int.*, Vol 29 (No. 10), 1989, p 809–27
21. F.J.G. Landgraf, R. Takanohashi, and M.F. Campos, Tamanho de grão e textura de aços elétricos de grão não-orientado, *Textura e relações de orientação*, A.P. Tschiptschin et al., eds., IPEN, 2003, p 211–46
22. H.R. Silva, G.G. Lourenço, L.H.R. Braga, P.C.M. Rodrigues, and D.B. Santos, Encruamento e tenacidade do aço Nb-Ti de grão ultrafino, *62º Congresso Anual da ABM*, ABM, 2007
23. D.F. Susan, A.C. Kilgo, and N.B. McKenzie, Fatigue Failures of Fasteners: Optical Metallography and SEM Fractography, *Proceeding of Microscopy and Microanalysis*, Cambridge University Press, 2006
24. ISO, ISO 6157-1 Fasteners—Surface Discontinuities—Part 1: Bolts, Screws and Studs for General Requirements, ISO, 1988
25. "Standard Specification for Surface Discontinuities of Bolts, Screws, and Studs, Inch and Metric Series," F788–13, ASTM, 2013
26. G. Krauss, *Steels: Processing, Structure and Performance*, ASM International, 2005

Metallography of Steels—Interpretation of Structure and the Effects of Processing
Hubertus Colpaert
Updated and Translated by André Luiz V. da Costa e Silva

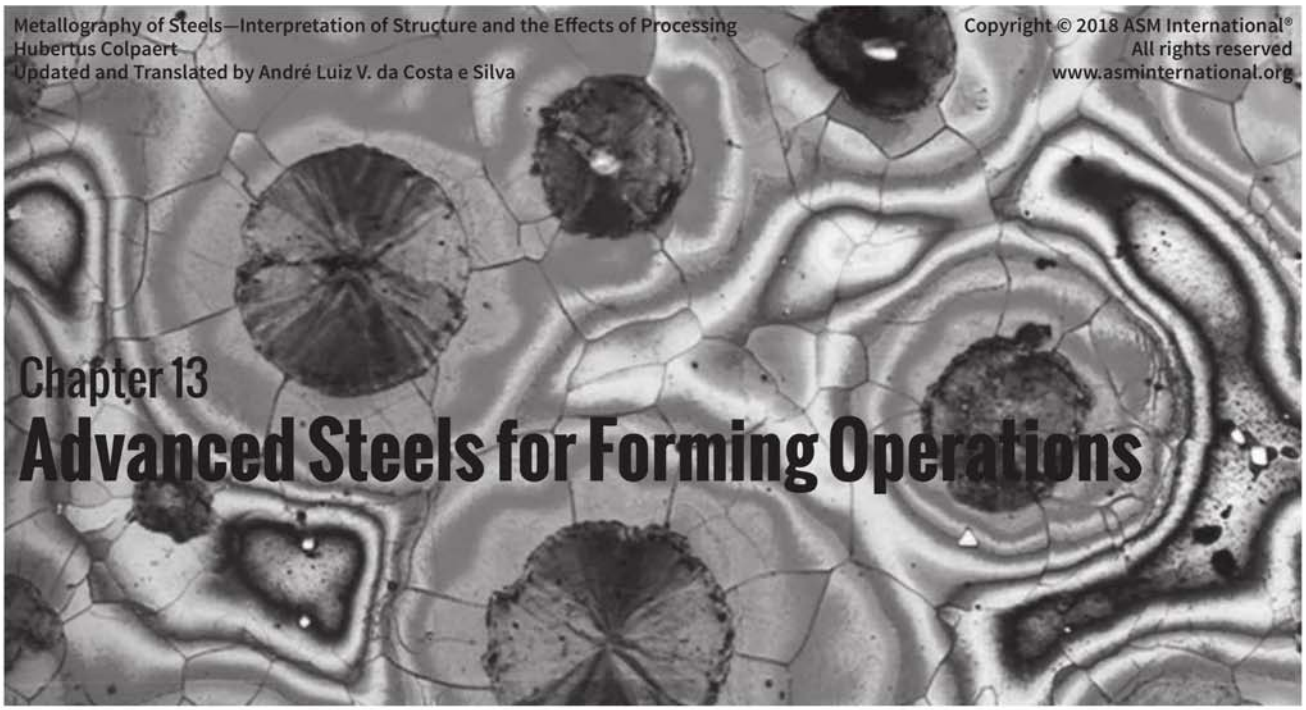

Chapter 13
Advanced Steels for Forming Operations

Steels can be classified according to different criteria. The most common classifications are based on (a) chemical composition (carbon steels, low-alloy steels, etc.) (b) intended application (structural steels, engineering steels, tool steels, etc.) and (c) microstructural applications (austenitic steels, dual-phase steels, etc.). It is clear that no classification system can be considered complete, and it is also reasonable that the same steel may be classified in different ways, depending on which point of view is central to the classification system used. The past decades have seen considerable progress in the development of metallic materials, particularly those for application in parts that are produced by forming flat products. This processing route allows the production of large quantities of material with extremely competitive costs. The automotive and the packaging industries are two examples in which steel has faced strong competition from alternative materials in recent decades. In these industries, steels adequate for forming operations are especially important. To maintain its competitiveness, the steel industry has developed various products that are classified generally as "advanced high-strength steels," as shown in Fig. 13.1 (Ref 1, 2). A large number of these steels are developed and used for body and closure parts in the automotive industry, and formability is a critical property. (In the recent past, these parts were all cold formed, and hence it would be more adequate to mention "cold formability" here. Presently, there is a strong impetus for the development of warm and hot forming steels that can reach their final properties directly at the end of the forming operation, just like the cold forming steels but improving the process and reducing costs.) With the growing demand for the reduction of weight and increase in safety in automotive vehicles, one can expect that these steels will have a rising importance in this industry.

Figure 13.2 presents a general overview of the steels used for forming in the automotive industry, classified by their ultimate strength and elongation in the tensile test. The criteria for the selecting of steels for forming are, however, more complex than the consideration of just these properties. The per-

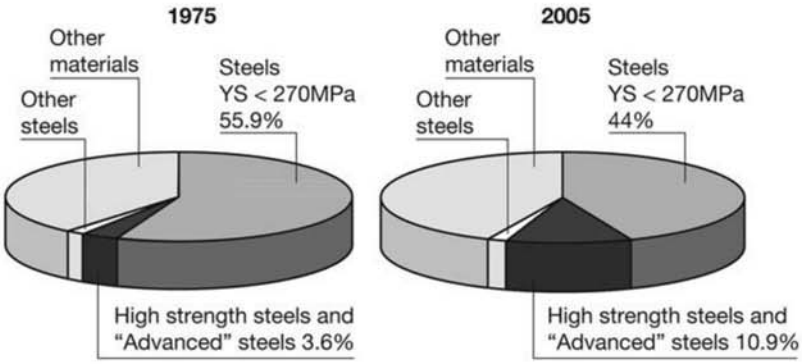

Fig. 13.1 The use of different materials in automotive applications in the United States in 1975 and 2005. Steel share in weight percentage remains approximately unchanged, due to the constant development of improved steels. Steels with yield strength under 270 MPa (40 ksi) have been arbitrarily grouped together as "common" steels. Source: Ref 1

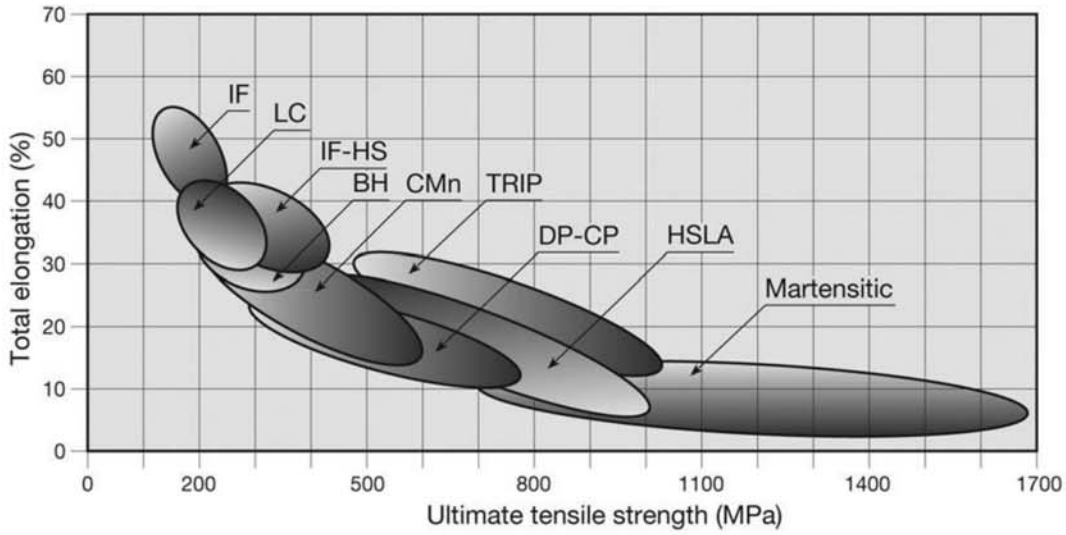

Fig. 13.2 Range of properties of steels grouped according to their ultimate strength and ductility (measured by elongation) for some steels used for formed parts in automotive industry. IF: interstitial free; LC: low carbon; IF-HS: interstitial-free high-strength IF steels; BH: bake hardening; CMn: C-Mn structural steels; HSLA: high-strength low alloy steels; DP: dual phase; CP: complex phase; TRIP: transformation-induced plasticity. Source: Ref 2

formance of steel in some cold forming operations is better described by technological properties: in the case of deep drawing operations, for instance, the normal anisotropy ratio (or strain ratio or Lankford value) is the most critical property, whereas in stretch forming operations the work hardening coefficient is the property that better correlates to the forming performance (Ref 3, 4). Properly selecting a steel for a part or designing a formed part from available steels are complex processes (Ref 2, 3).

13.1 Low and Extra-Low Carbon Steels (Interstitial-Free)

The majority of steels used for packaging can be classified as low or extra-low (such as interstitial-free (IF) steels) carbon steels. Similar steels have extensive application in the automotive industry. Most of these steels have ferritic microstructures, with a small volume fraction of cementite or, in some cases, pearlite, as discussed in Chapter 12, "Mechanical Work of Steels: Cold Working," in this book. Steel for packaging is normally used in the cold worked condition, as presented in Chapter 12.

13.2 High-Strength Low Alloy and Carbon-Manganese Structural Steels

The main structural features of high-strength low alloy (HSLA) steels and carbon-manganese structural steels (C-Mn) are discussed in Chapter 14, "Structural Steels and Steels for Pressure Vessels, Piping, and Boilers," in this book.

13.3 Dual-Phase and Complex-Phase (or Multiphase) Steels

A combination of ferrite with other metastable phases can lead to an interesting combination of formability and strength. Achieving the desired structure, and thus properties, with dual-phase and multiphase steels depends on an intercritical heat treatment. In this treatment, austenite is formed and enriched in carbon. Despite the fact that intercritical heat treatments do not always reach thermodynamic equilibrium, the illustration in Fig. 13.3 is useful for understanding the principles for achieving multiphase structures with steels that have substantially low carbon content. The microstructures resulting from these treatments are normally composed of a continuous matrix of ferrite, which guarantees ductility and formability, and reinforcing "is-

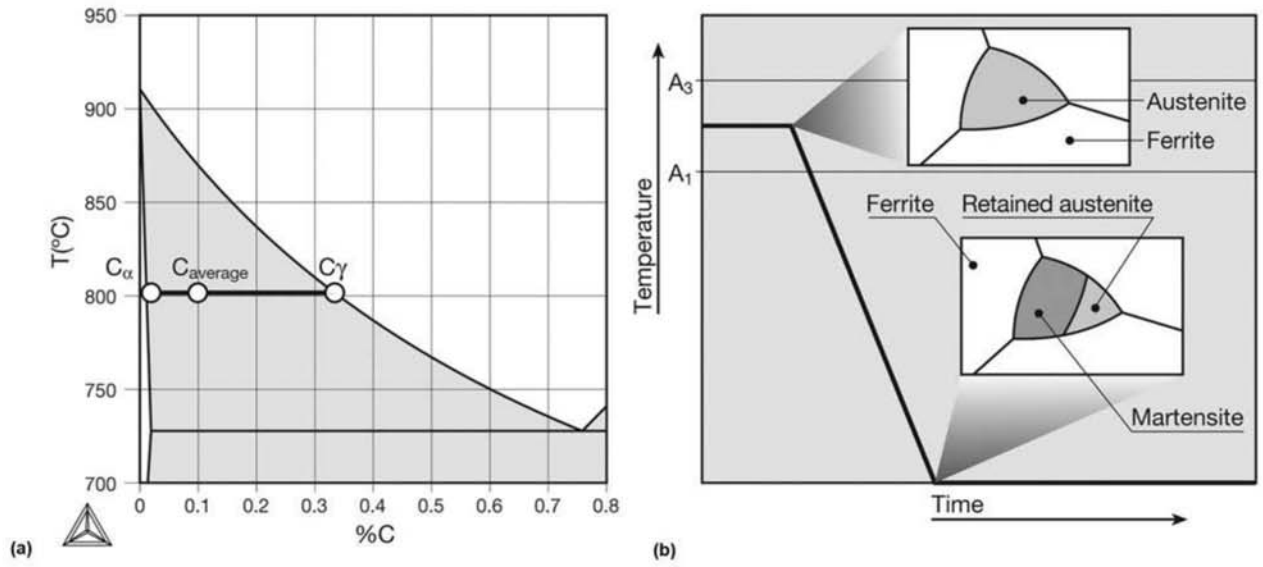

Fig. 13.3 (a) During treatment in the critical region of dual-phase and multiphase steels, carbon enriched austenite is formed (figure shows the equilibrium condition for a Fe-C alloy). (b) On cooling, austenite transforms partially to martensite. Depending on its chemical composition, some austenite is retained, as schematically illustrated.

lands" of martensite and/or martensite-austenite (MA). Depending on the processing variables (temperature and time), the austenitic regions may transform to more complex combinations of a variety of phases, resulting in "multiphase" or complex-phase steels. Figures 13.4 to 13.6 present examples of the microstructure of dual-phase steels. Figures 13.7 to 13.10 present examples of the microstructure of multiphase steels revealed with different etchants.

The processing conditions and the transformations that occur, both during the intercritical treatment and during cooling, are very important to the achievement of the desired results: a steel with high ductility and formability and considerable mechanical strength. Thus, it is normal to evaluate through modeling and experiments the effect of different processing parameters on the microstructure. Identifying the different constituents in these microstructures is an interesting challenge, and a variety of etchants are used, with complementary objectives, as discussed next.

Caballero (Ref 6) investigated the effect of the processing parameters on the microstructure of a dual-phase steel (DP 750, with a yield strength of 750 MPa, or 110 ksi). The steel was hot rolled. The hot rolling was concluded at 900 °C (1650 °F). After hot rolling, various cooling rates and coiling temperatures were tested. The hot coiling temperature is an important parameter in hot rolling flat steel because from the coiling on, the cooling rate of the material decreases sharply. Figure 13.11 presents the microstructure of a hot rolled sample, cooled at 7 °C/s (13 °F/s) and coiled at 650 °C (1200 °F). This is the

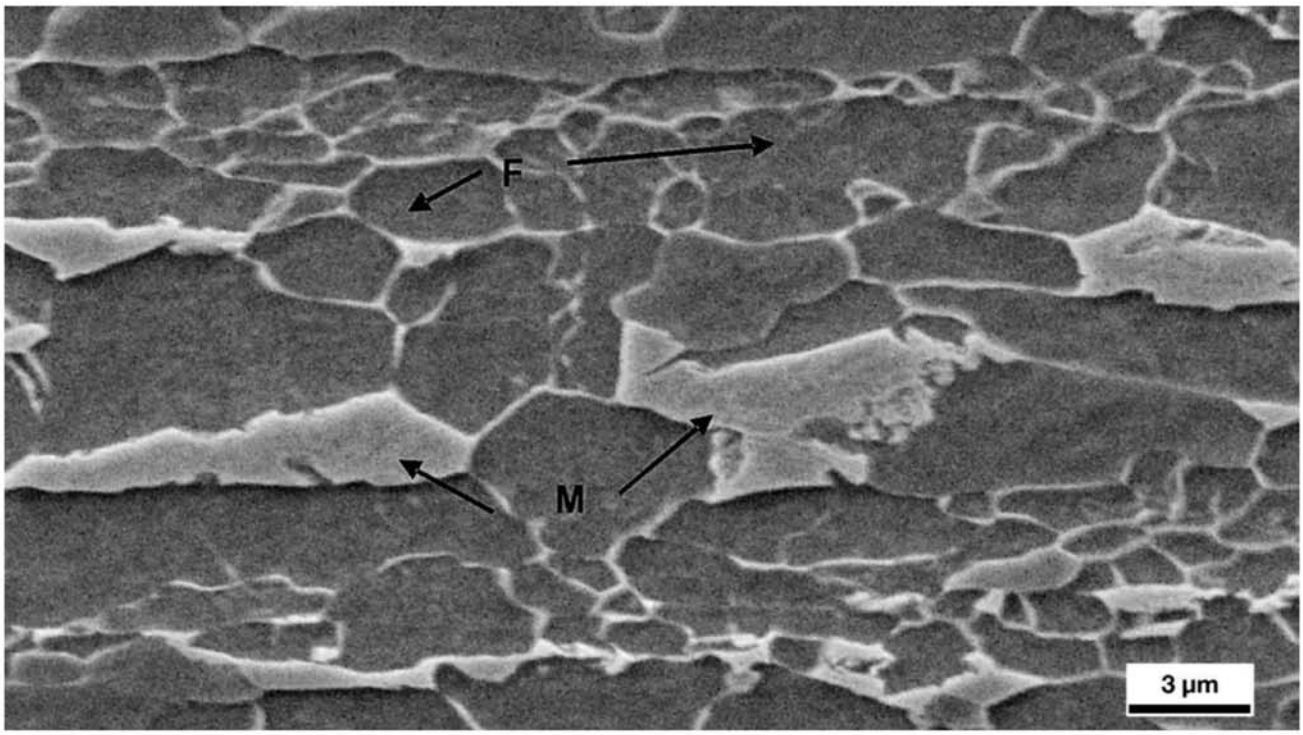

Fig. 13.4 Transverse cross section of a dual-phase steel containing C = 0.09%, Mn = 1%, and Nb = 0.03%. Ferrite (F) and martensite (M). Ferrite grain size: 5 µm. Etchant: nital. SEM, SE. Courtesy of ArcelorMittal Tubarão, ES, Brazil.

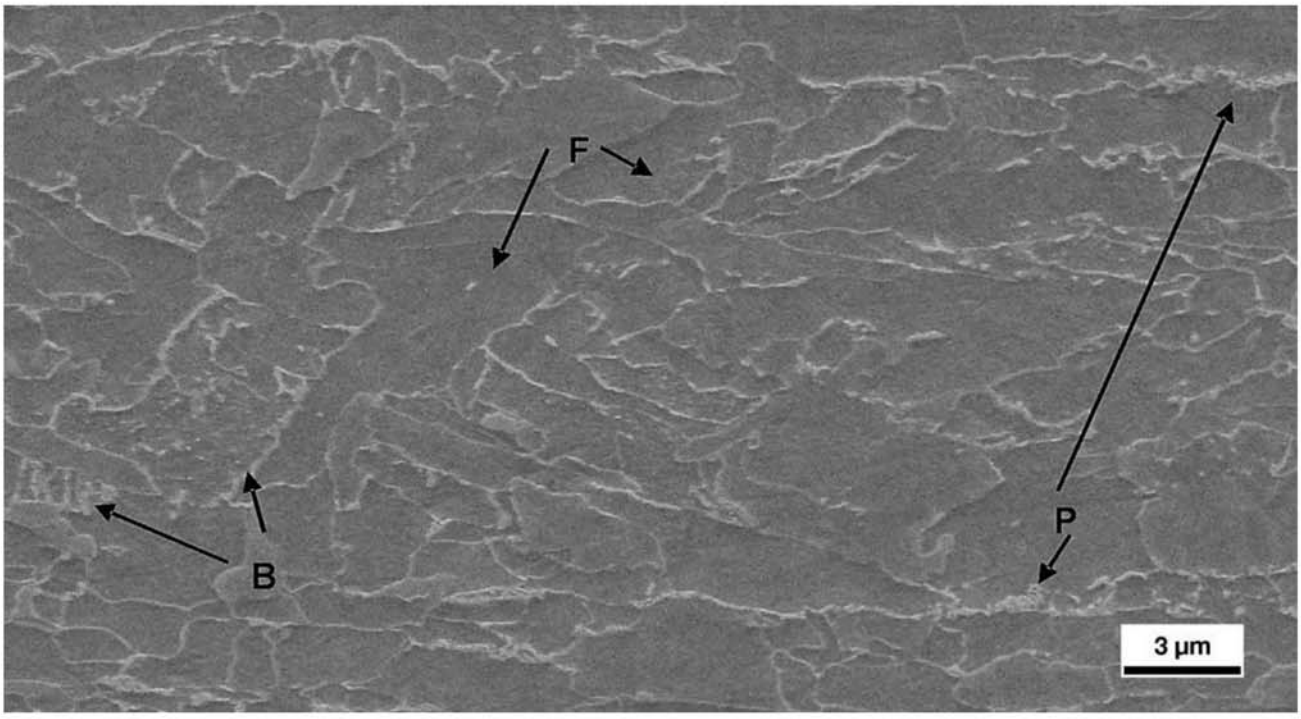

Fig. 13.5 Transverse cross section of a dual-phase steel containing C = 0.09%, Mn = 1%, and Nb = 0.03%. Ferrite (F) and bainite (B), with some pearlite (P). Ferrite grain size: 3 μm. Etchant: nital. SEM, SE. Courtesy of ArcelorMittal Tubarão, ES, Brazil.

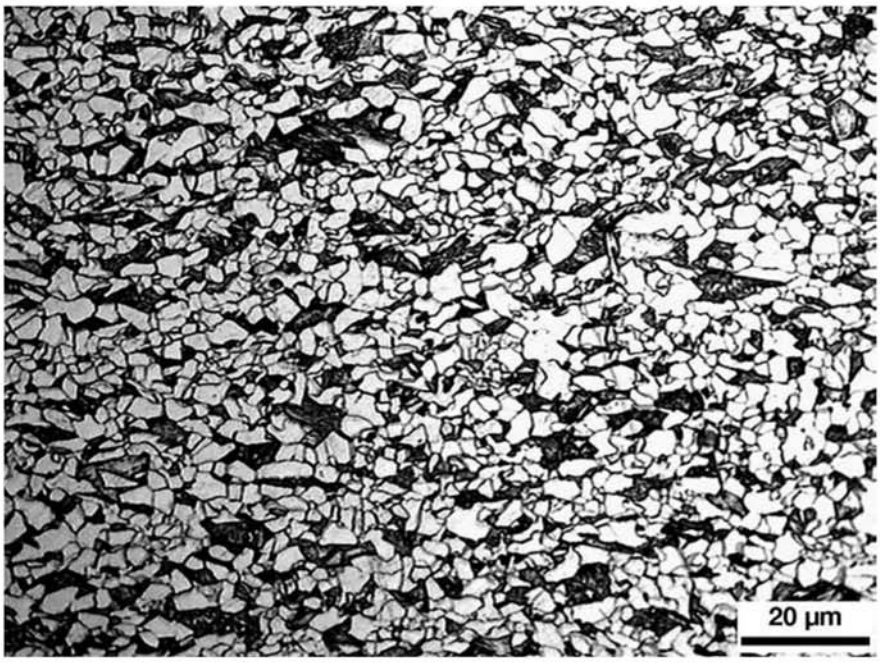

Fig. 13.6 Dual-phase steel. Ferrite and some martensite areas with retained austenite. Etchant: nital 4% followed picral 4%. Courtesy of ArcelorMittal Tubarão, ES, Brazil.

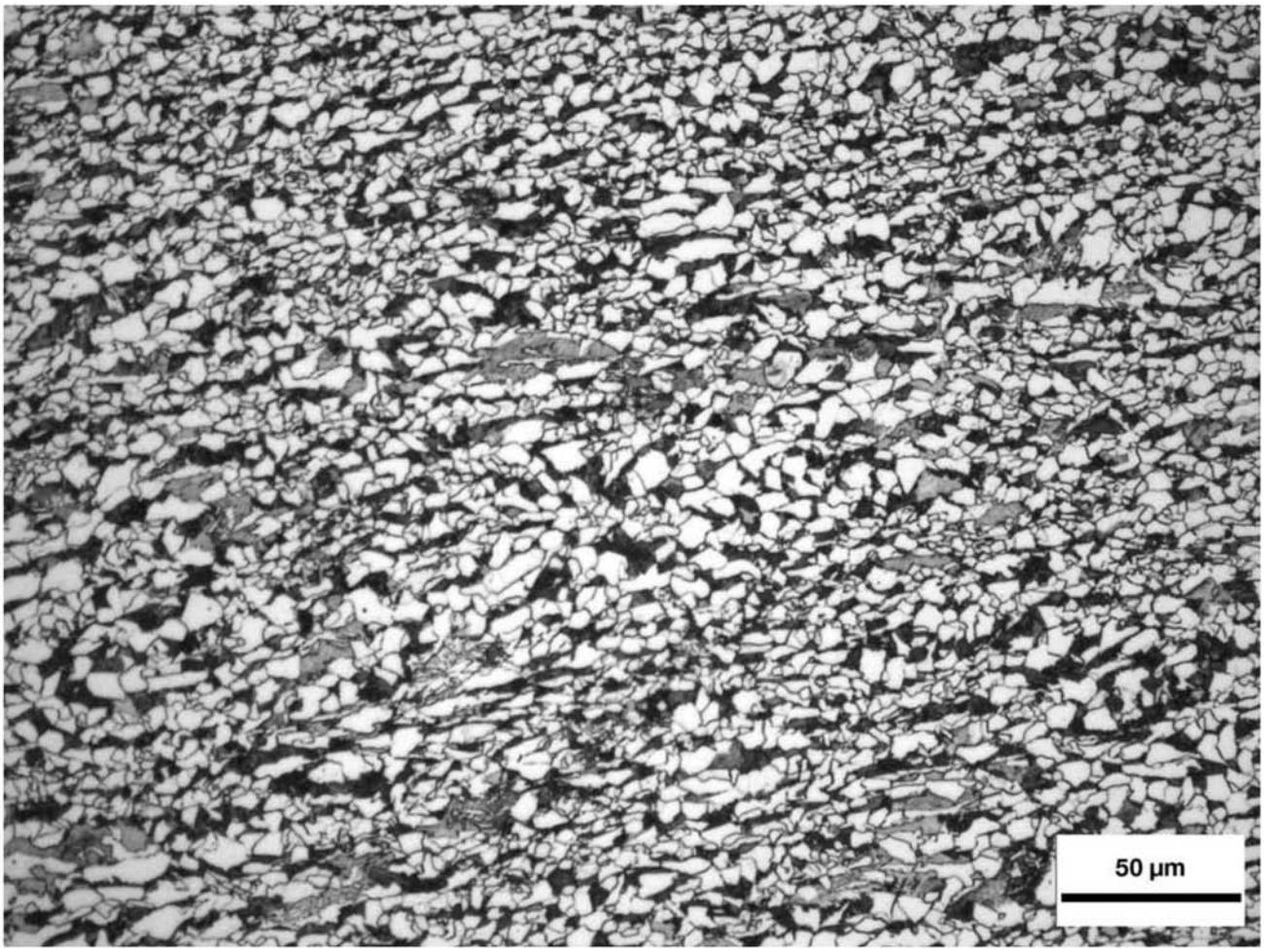

Fig. 13.7 Hot rolled multiphase steel C = 0.2%, Mn = 1.5%, Si = 1.5%. Ferrite, pearlite, and the constituents shown in Fig. 13.8. Etchant: nital 3%. Courtesy of C. S. Viana, EEIMVR-UFF, Volta Redonda, RJ, Brazil. Source: Ref 5

slowest cooled sample among all samples prepared by these authors. The sheets produced with different combinations of cooling rates and coiling temperatures were then cold rolled with 68% reduction. Figure 13.12 presents the effect of the cooling rate at the end of rolling on the steel microstructure (although in the samples taken after cold rolling it is possible to observe significant microstructural differences caused by the hot rolling and the subsequent cooling). The grain size is significantly smaller with the increase in the cooling rate, and instead of the formation of pearlite, martensite and bainite are formed at the higher cooling rates.

The effect of intercritical annealing after cold rolling has also been investigated. For the same initial condition (hot rolling, coiling condition, and cold rolling) the effect of intercritical austenitizing time and temperature were investigated. The effect of the different etchants usually used in these evaluations can also be observed. Figure 13.13 presents the $\alpha \rightarrow \gamma$ transformation temperatures in equilibrium obtained by experimental measurements during heating for the steel under study. For treatments performed at 750 °C

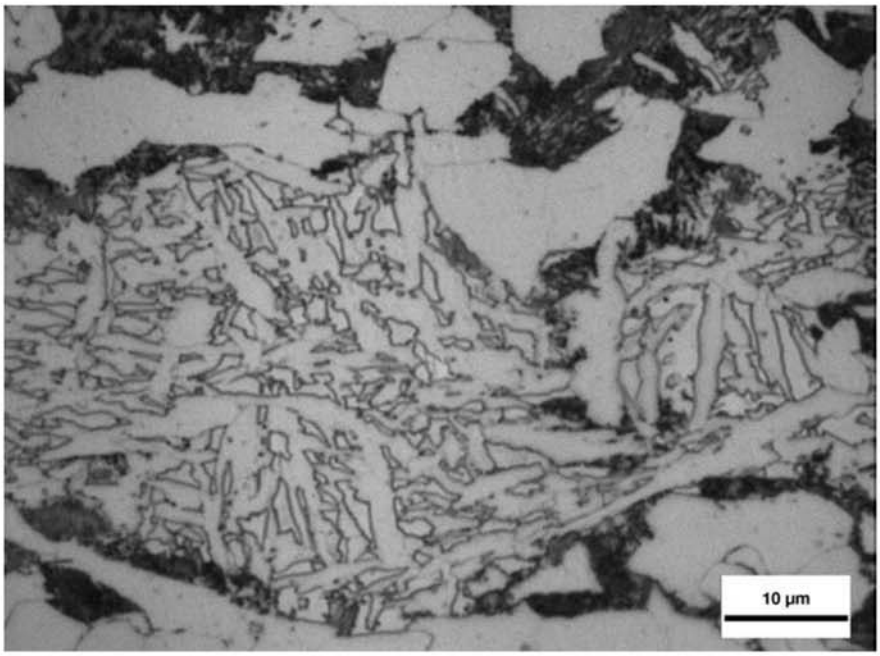

(a)

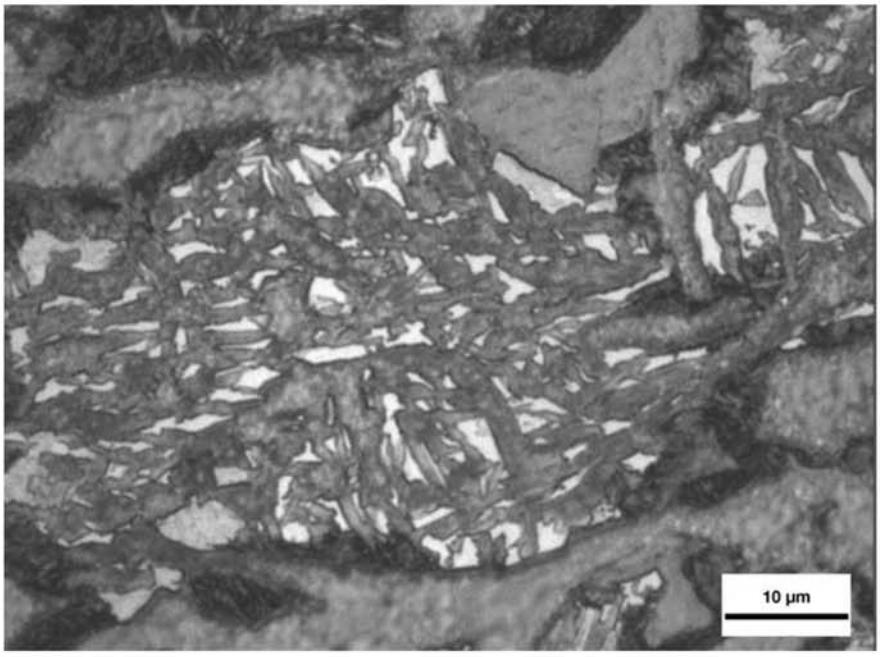

(b)

Fig. 13.8 Multiphase region of the steel shown in Fig. 13.7 with two different etching techniques. (a) Etched with potassium metabisulfite (800 mg potassium metabisulfite + 100 ml distilled water). Ferrite (light), pearlite (dark), and acicular constituent with intermediate white areas. (b) Etched with LePera etchant: ferrite (greenish blue, here light gray), bainite or bainitic ferrite (brown, here darker gray), pearlite (dark), and martensite-austenite (MA) regions (white). Courtesy of C. S. Viana, EEIMVR-UFF, Volta Redonda, RJ, Brazil. Source: Ref 5

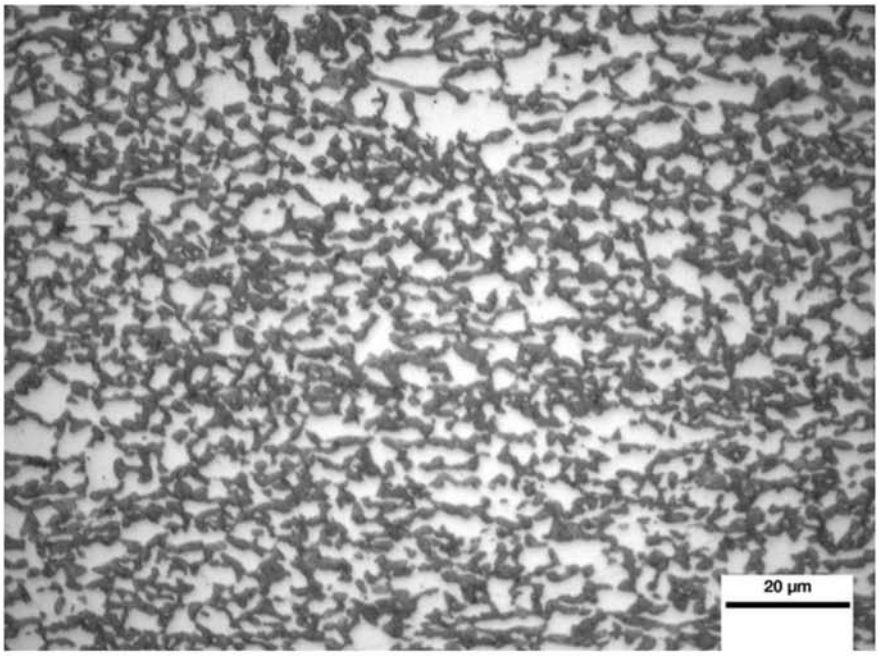

Fig. 13.9 Same steel from Fig. 13.7 (C = 0.2%, Mn = 1.5%, Si = 1.5%) treated inside the critical region (750 °C, or 1380 °F, for 15 min) followed by quenching. Two-phase microstructure. Ferrite (light) surrounded by martensite in the areas that have transformed to austenite during the treatment inside the critical region. Etchant: potassium metabisulfite. Courtesy of C. S. Viana, EEIMVR-UFF, Volta Redonda, RJ, Brazil. Source: Ref 5

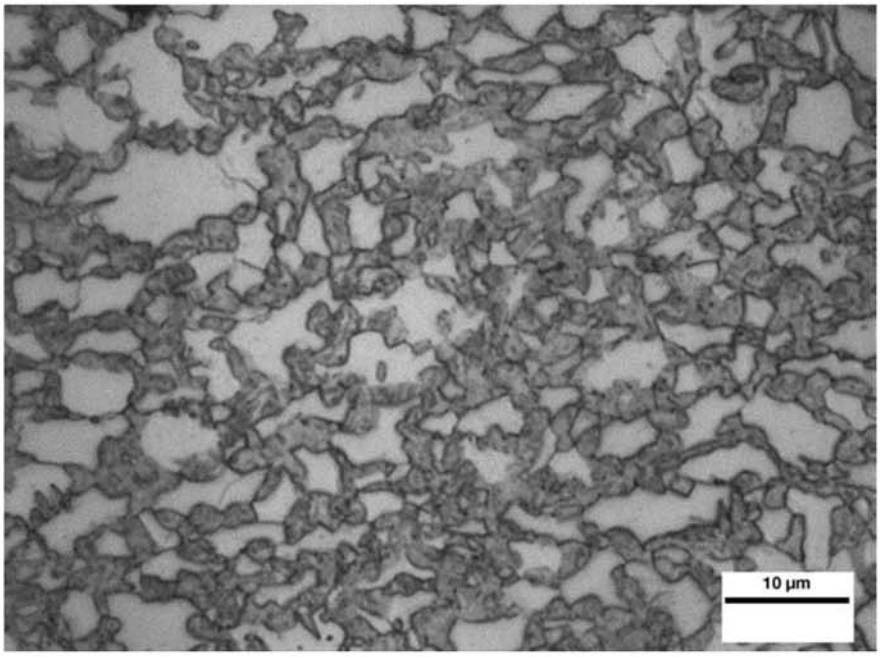

Fig. 13.10 Detail from Fig. 13.9. Ferrite (light) and martensite. The martensite areas are easier to observe. In this case, in the optical microscope retained austenite cannot be identified. Etchant: nital 3%. Courtesy of C. S. Viana, EEIMVR-UFF, Volta Redonda, RJ, Brazil. Source: Ref 5

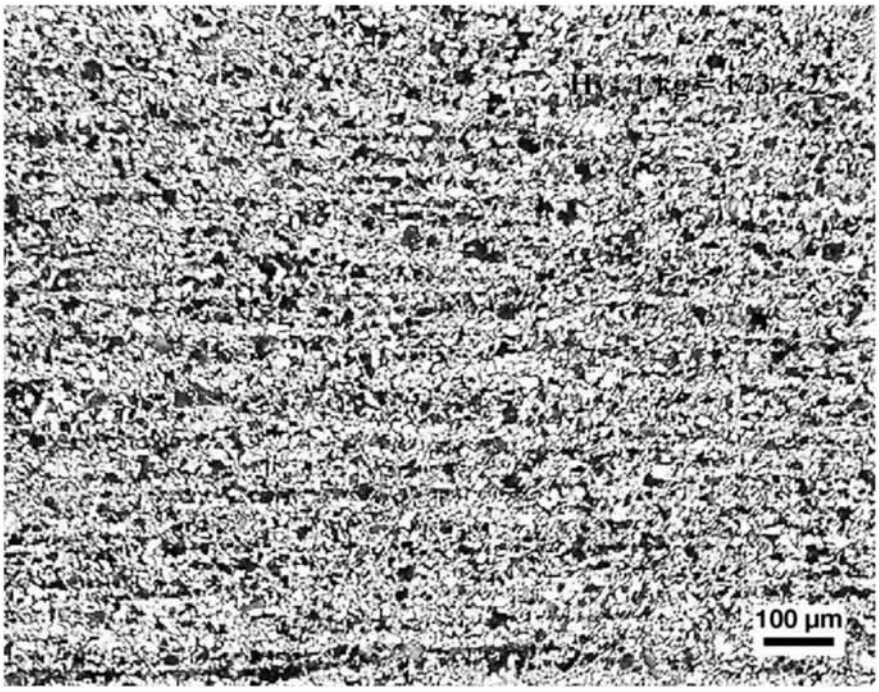

Fig. 13.11 Longitudinal cross section of a sheet of steel containing C = 0.15%, Mn = 1.9%, Si = 0.2%, Cr = 0.2% hot rolled (rolling ended at 900 °C, or 1650 °F) cooled at 7 °C/s (13 °F/s), and coiled at 650 °C (1200 °F). Ferrite and pearlite. Slight banding. Hardness HV 173. Etchant: nital. Courtesy of F. G. Caballero, CENIM-CSIC, Grupo Materialia, Madrid, Spain.

(1380 °F) (Fig. 13.14a–c) LePera etchant was used. When LePera etchant is used and the color micrograph is converted to a grayscale image, martensite appears light, ferrite appears gray, and the carbides or pearlite appear dark. From these treatments, it can be seen that a sample that has been austenitized for 1 s contains ferrite and pearlite with a small amount of light martensite spots (Fig. 13.14a). This indicates that there has been little transformation into austenite during this short holding time. For longer holding times at temperature, it is possible to see increasing amounts of martensite in the cooled samples, indicating the formation of an increasing amount of austenite during the intercritical treatment. A similar behavior is observed when the treatment is performed at 800 °C (1470 °F). The etchant based on sodium metabisulfite proposed by Ref 7 provides a good contrast between ferrite and martensite. In Fig. 13.14(e), ferrite, pearlite, and martensite resulting from the austenite formed during treatment can be observed. The fraction of nontransformed ferrite in Fig. 13.14(f) is quite small, as indicated by the results of quantitative measurements presented in Fig. 13.15. It is important to observe that when the samples contain more than about 60% martensite, the contrast between ferrite and martensite caused by LePera etchant starts to degrade (Ref 6). In these cases, the etchants based on sodium metabisulfite may become interesting alternatives. Finally, when the treatment is performed at 850 °C (1560 °F) (Fig. 13.14g–i), ferrite is only observed after very short heat treatment times. Austenitizing at this temperature is rapid and reaches full

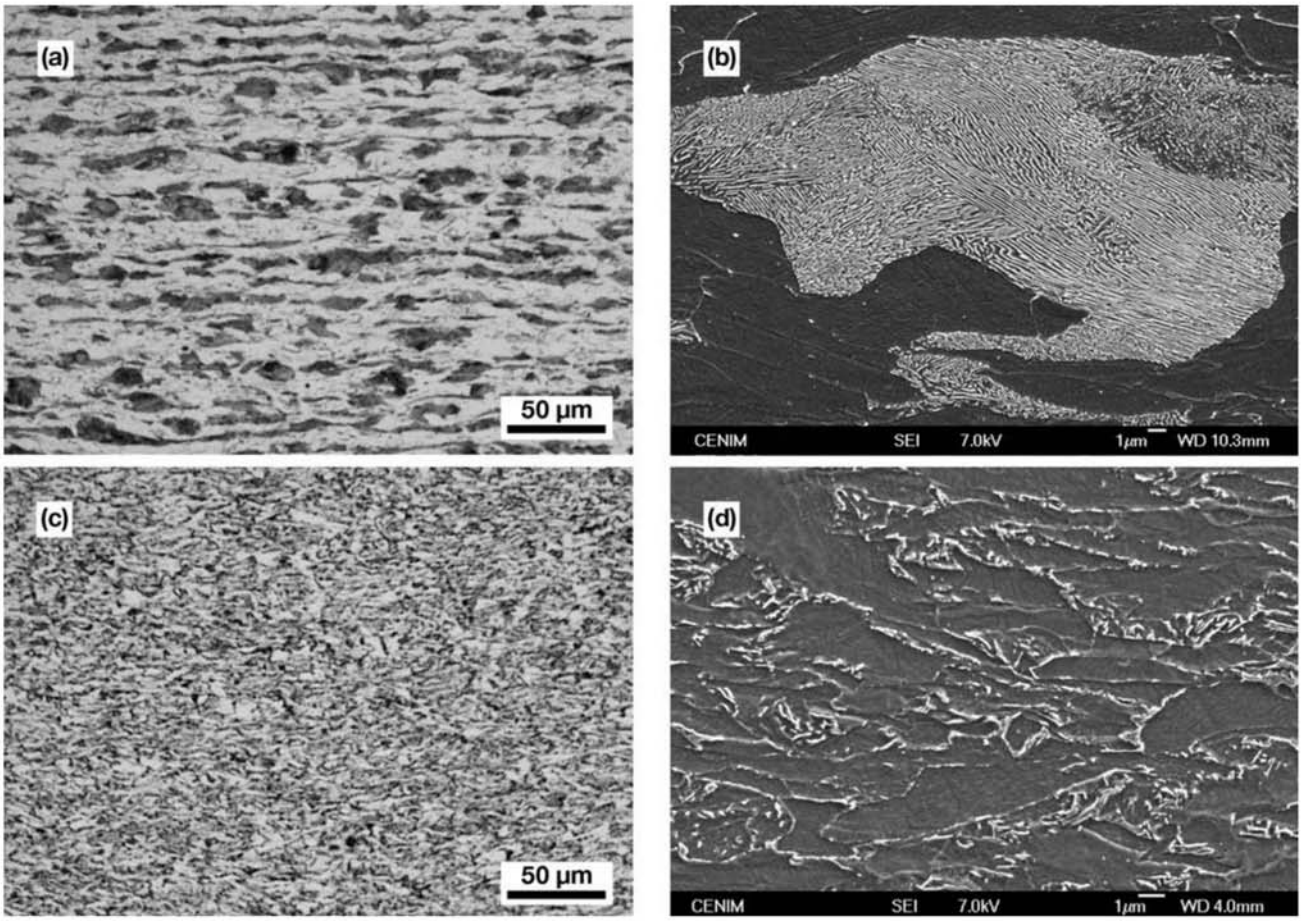

Fig. 13.12 Longitudinal cross section of the same steel from Fig. 13.11. (a) and (b) Hot rolled, cooled 7 °C/s (13 °F/s) and coiled at 650 °C (1200 °F), followed by cold rolling. (c) and (d) Hot rolled, cooled at 60 °C/s (110 °F/s) and coiled at 500 °C (930 °F), followed by cold rolling. The microstructure of the slow-cooled material in (a) and (b) presents cold worked ferrite and pearlite. The microstructure of the material subjected to faster cooling in (c) and (d) present ferrite and bainite or martensite, cold worked. Etchant: nital. (b) and (d) SEM, SE. Courtesy of F. G. Caballero, CENIM-CSIC, Grupo Materialia, Madrid, Spain.

transformation. Nital etching produces good results with these microstructures composed by martensite (and a small volume fraction of ferrite, in the case of Fig. 13.14(g), 1 s treatment). The metallographic techniques used for these steels are also applied in characterizing the microstructure of other steels that, when processed, may reach similar conditions. In the case of rapid cooling from the critical region, or when the decomposition of austenite is incomplete in low-carbon steels, structures very similar to those of multiphase steels can be observed. This is shown in Fig. 13.16 to 13.18.

13.4 Transformation-Induced Plasticity Steels

Not only quenching can induce martensitic transformation: mechanical deformation can also induce the transformation of austenite into martensite. This phenomenon is relatively common in some austenitic stainless steels (Chapter 16, "Stainless Steels," in this book). Two effects are observed in this case: the total uniform plastic deformation that can be reached is increased by the additional deformation associated with the phase transformation, and

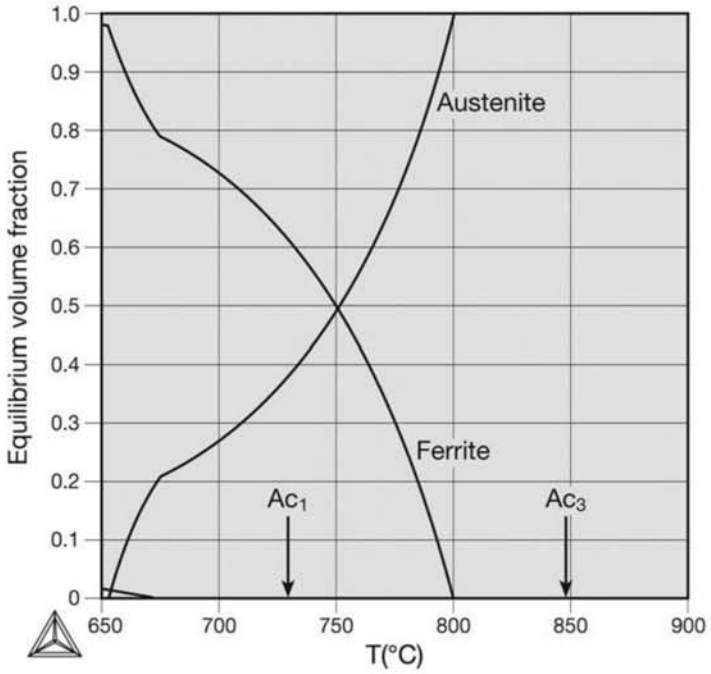

Fig. 13.13 Equilibrium austenite volume fraction for the dual-phase steel in Fig. 13.11. The experimentally measured Ac_1 and Ac_3 are included. For 7 °C and 60 °C/s (13 °F and 110 °F/s) the transformation temperatures did not change significantly. Source: Ref 6

in the case of austenitic steels, the materials begin to show ferromagnetic behavior, caused by the presence of martensite. This enhancement in the deformation ability is exploited in one class of advanced steels for forming, called transformation-induced plasticity (TRIP) steels. In these steels, the amount and chemical composition of the retained austenite are adjusted so that the martensitic transformation occurs during the forming operation. Figure 13.19 presents the usual thermomechanical treatment cycles for TRIP and dual-phase steels. The main difference between the cycles is the austempering process the TRIP steel undergoes after being treated in the critical region. Part of the austenite formed during the treatment inside the critical region transforms to bainite. Besides "granular" retained austenite, retained austenite is also found between the bainite plates (or bainitic ferrite, since the silicon contents are frequently high enough to delay or prevent carbide precipitation during bainite formation). The different steps described in Fig. 13.19 may be optimized if one can control the cooling conditions after hot rolling so that the critical region is traversed in conditions adequate to obtain the desired structure, without the need for a new austenitizing treatment. During development of TRIP steels, it is very important to properly characterize and quantify the regions of the microstructure where martensite, bainite, and granular retained austenite are present (Fig. 13.20). Girault, et al. (Ref 9) proposed some ways of improving the visualization of these constituents in these steels, as shown in Fig. 13.20 to 13.23. TRIP steel microstructures are generally complex, and properly characterizing them normally requires a combination of techniques from optical microscopy and SEM to x-ray diffrac-

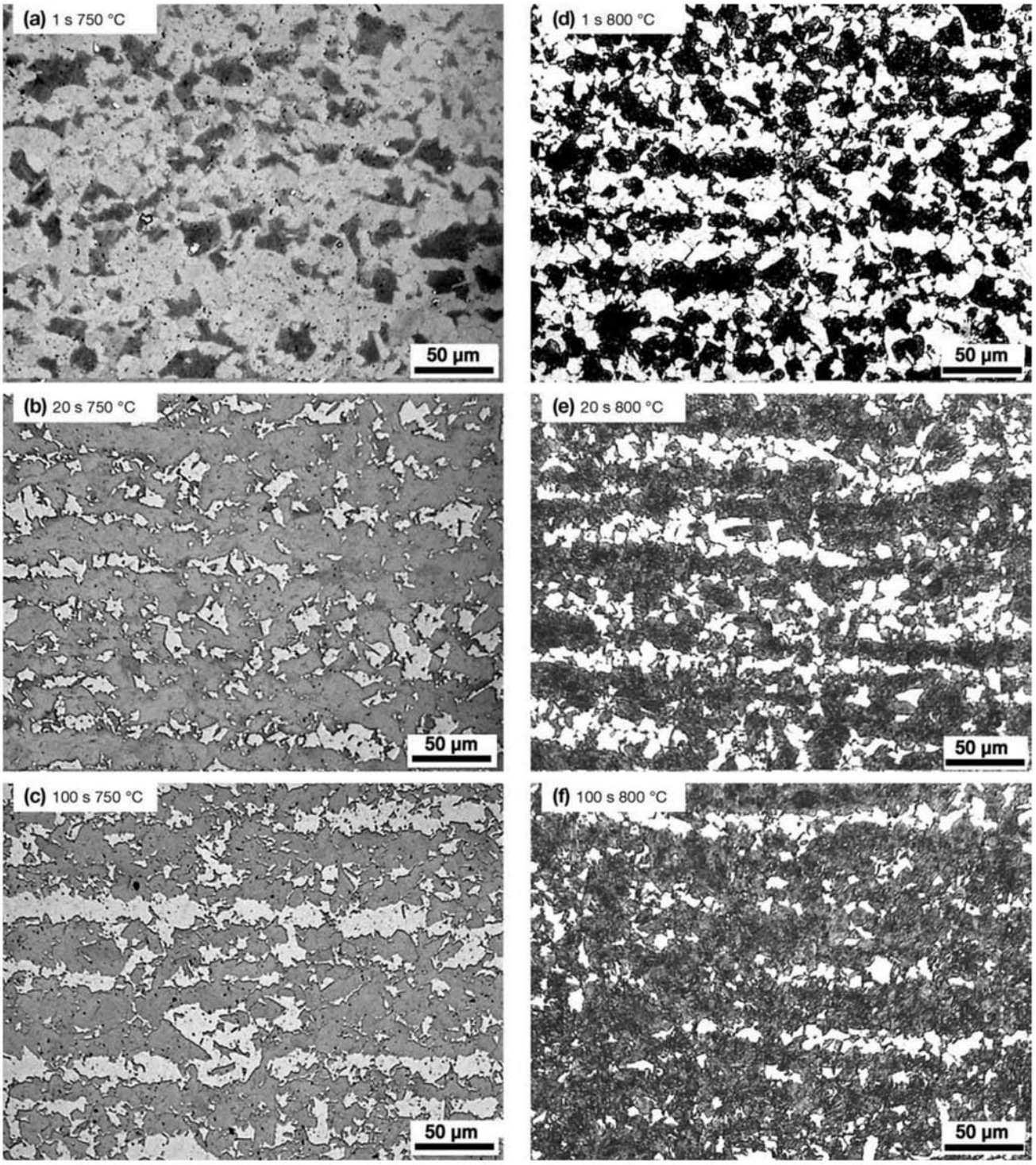

Fig. 13.14 Microstructural evolution of a dual phase steel hot rolled, cold worked, and subjected to austenitization inside the critical zone for the times and temperatures indicated in (a), (b), and (c). Etchant: LePera. Martensite: light; ferrite: gray; pearlite: dark. (d), (e), and (f). Etchant: Datta and Gokhale (Ref 7) (20 g sodium metabisulfite in 100 ml water). Ferrite: light; pearlite: dark. (g), (h), and (i): Etchant: nital. See text for discussion; for further details, see Ref 6. Courtesy of F. G. Caballero, (CENIM-CSIC), Madrid, Spain.

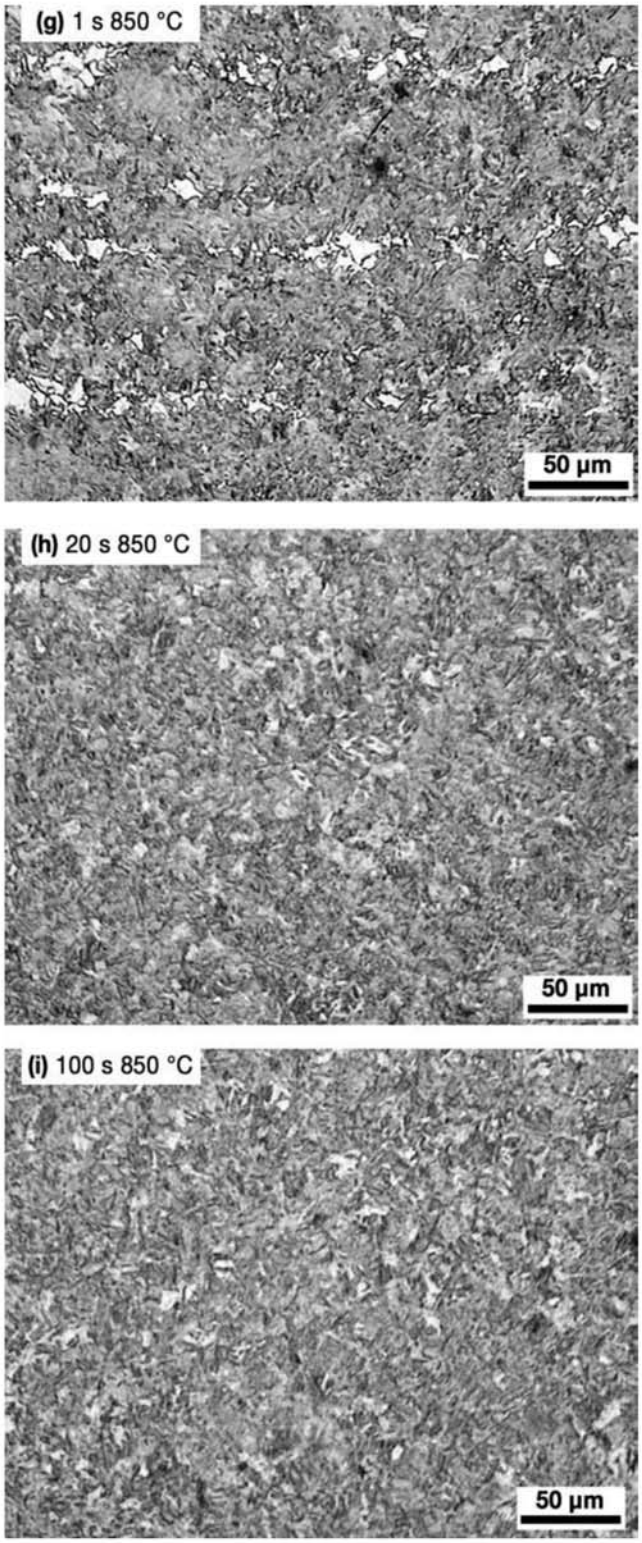

Fig. 13.14 (continued) Microstructural evolution of a dual phase steel hot rolled, cold worked, and subjected to austenitization inside the critical zone for the times and temperatures indicated in (a), (b), and (c). Etchant: LePera. Martensite: light; ferrite: gray; pearlite: dark. (d), (e), and (f). Etchant: Datta and Gokhale (Ref 7) (20 g sodium metabisulfite in 100 ml water). Ferrite: light; pearlite: dark. (g), (h), and (i): Etchant: nital. See text for discussion; for further details, see Ref 6. Courtesy of F. G. Caballero, (CENIM-CSIC), Madrid, Spain.

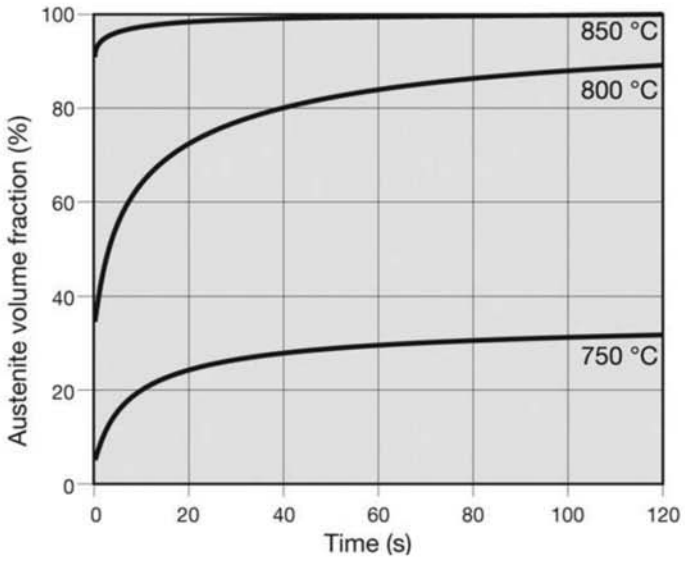

Fig. 13.15 Volume fraction of austenite formed during the treatments inside the critical zone indicated in Fig. 13.14, as determined by quantitative metallography. Source: Ref 6

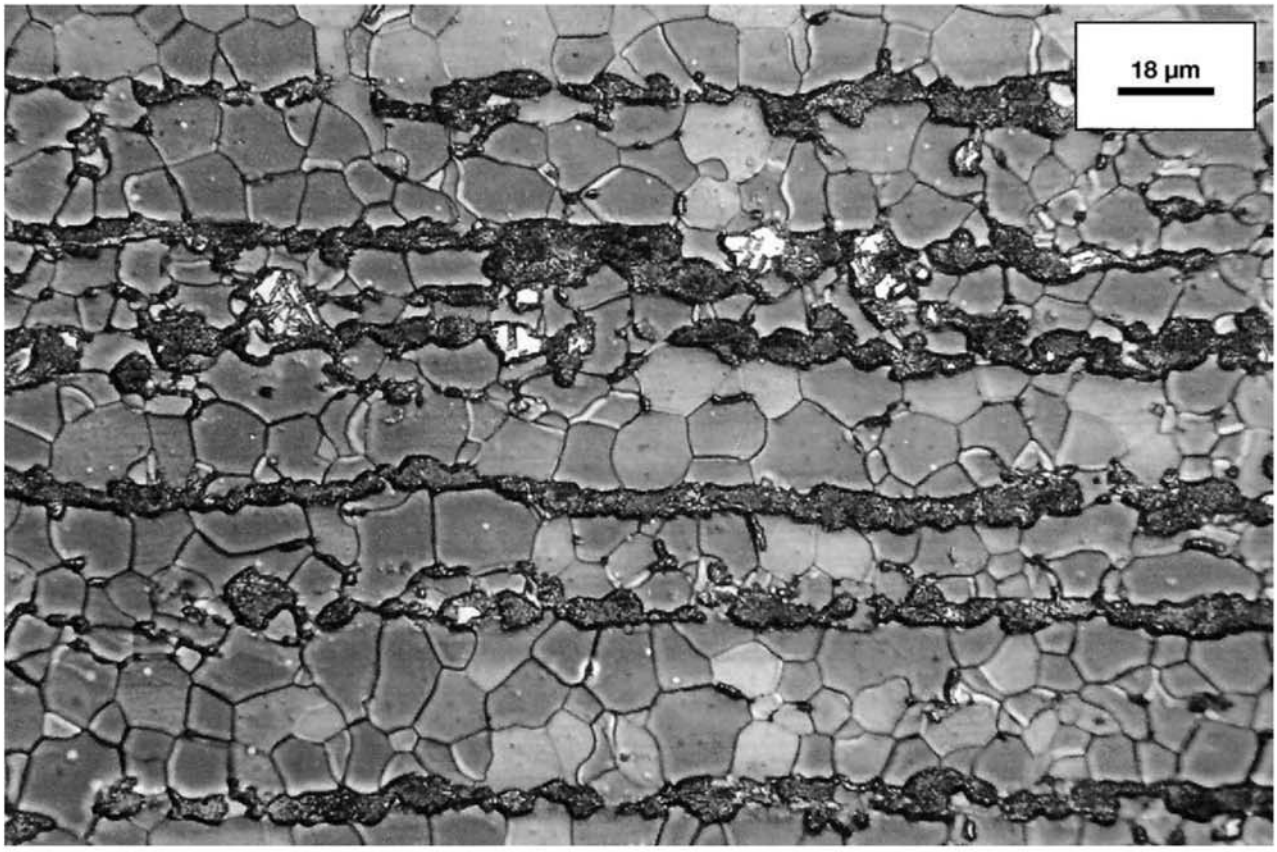

Fig. 13.16 Longitudinal cross section of a steel wire containing C = 0.06–0.15%, Si = 0.80–1.15%, Mn = 1.40–1.85% (AWS A5.18 ER 70S-6). Equiaxed ferrite (gray) and banded pearlite (dark). Islands of martensite-austenite (MA) appear white. Sample was austenitized at 900 °C (1650 °F), cooled to 650 °C (1200 °F), at 1.0 °C/s (2 °F/s), and quenched in flowing helium. The carbon enrichment in the white areas, together with the austenite decomposition, was sufficient for the formation of MA on quenching. Etchant: LePera. Optical microscope, polarized light. Courtesy of M. S. Andrade, CETEC, MG, Brazil.

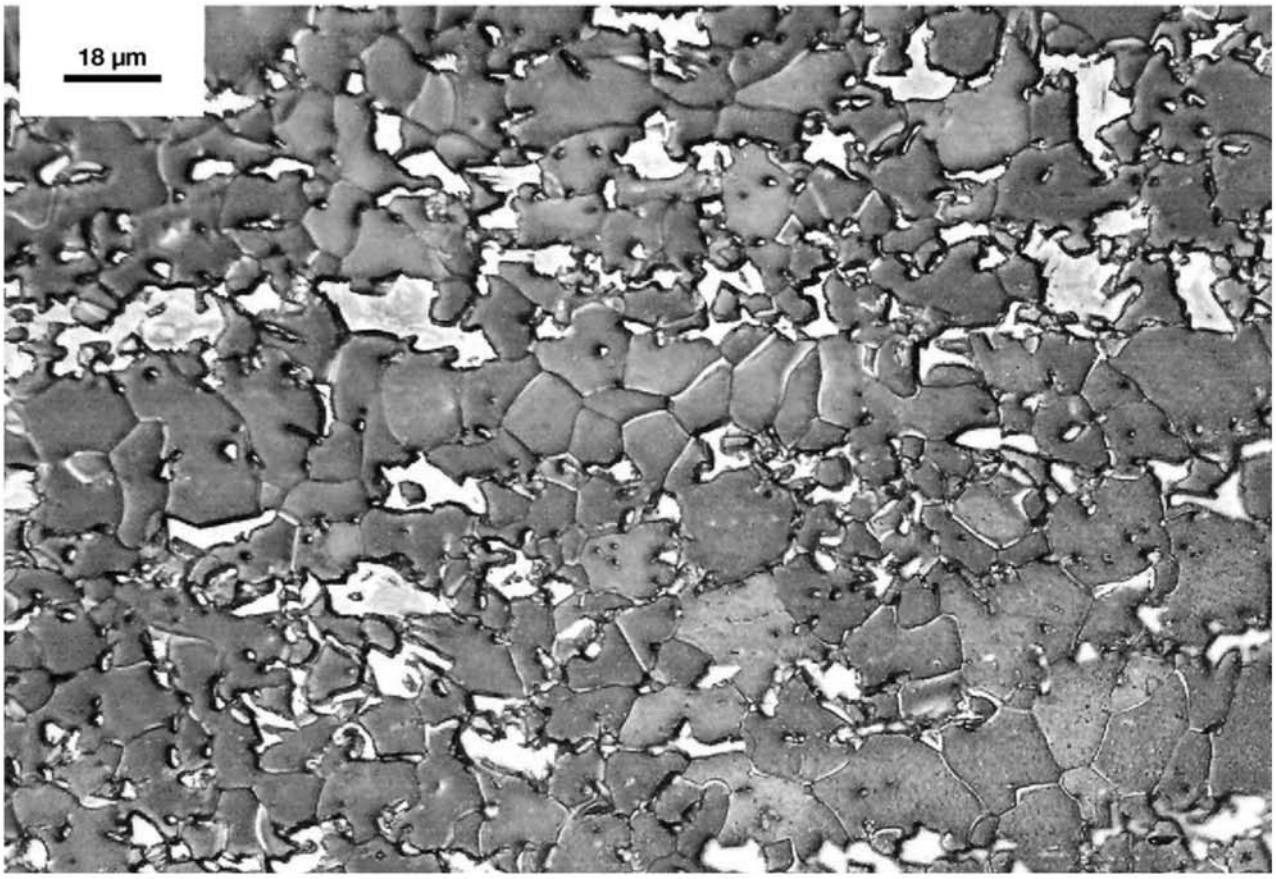

Fig. 13.17 The same wire from Fig. 13.16 austenitized at 900 °C (1650 °F), cooled to 700 °C (1290 °F), at 0.8 °C/s (1.5 °F/s), and quenched in flowing helium. Equiaxed ferrite (gray) and retained austenite (white). Quenching started before the start of the pearlite formation. Etchant: LePera. Courtesy of M. S. Andrade, CETEC, MG, Brazil.

tion and sometimes TEM to properly identify the phases and constituents. Figure 13.24 presents transmission electron micrographs of "classical" bainite, when carbides precipitate; of bainitic ferrite in which there is sufficient addition of silicon to prevent the precipitation of carbides; and of auto-tempered martensite. Auto-tempering is a feature of low-carbon martensites, in which the M_s temperature is sufficiently high that after martensite is formed, carbon still has sufficient mobility to precipitate the carbides typically present on tempering. Thus, at the end of the cooling stage ("quenching"), martensite is already partially tempered (Ref 11). Distinguishing between these constituents is not always an easy task, especially in the size and volume fraction ranges that may occur in dual-phase and TRIP steels. An interesting alternative used to highlight the constituents in TRIP steels, in particular to differentiate martensite from austenite, is the procedure described in Ref 12 in which a sequence of etchants is used together with a blue filter in the optical microscope, with the results shown in Fig. 13.25. Whereas the application of twinning-induced plasticity (TWIP) steels remains somewhat limited (mostly because of the cost of alloying), because compositions in the 17–24% Mn range, fully austenitic, are common, these are very promising materials.

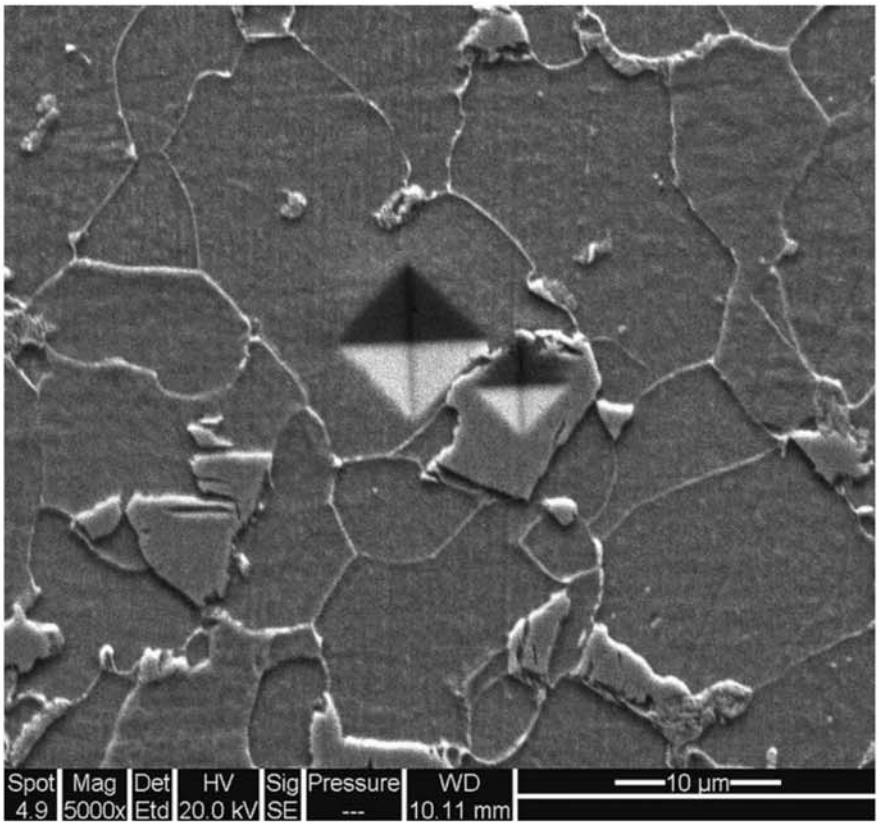

Fig. 13.18 Multiphase steel. Equiaxed ferrite (at a slightly lower level in the image) and regions of martensite-austenite (MA). The hardness impressions show the difference in mechanical behavior of the constituents. In some regions, some structural aspects of the MA areas can be observed. (Note that the hardness values would not be valid due to the proximity of the impressions—the objective was to show the difference semi-quantitatively). Etchant: nital. SEM, SE.

During deformation, deformation twins are formed. This results in a high work-hardening coefficient together with very high ultimate strength, as shown in Fig. 13.26.

13.5 Ferritic-Bainitic Steels

Ferritic-bainitic steels have an especially good performance in forming operations where edge stretching is needed. This property is usually measured via hole expansion tests. These steels have properties intermediate between DP and TRIP steels in Fig. 13.2. The microstructure of a ferritic-bainitic steel is presented in Fig. 13.27.

13.6 Steels Subjected to Quenching and Partitioning Heat Treatment

In recent years, the quenching and partitioning (Q&P) technique has been developed as an alternative route to obtaining microstructures containing controlled amounts of retained austenite (Ref 13, 14). In this technique, a steel with an adequate chemical composition is rapidly cooled (quenching stage of the treatment) to a temperature between M_s and M_f, as shown in Fig. 13.28. Thus a certain volume fraction of martensite is formed, with the same carbon

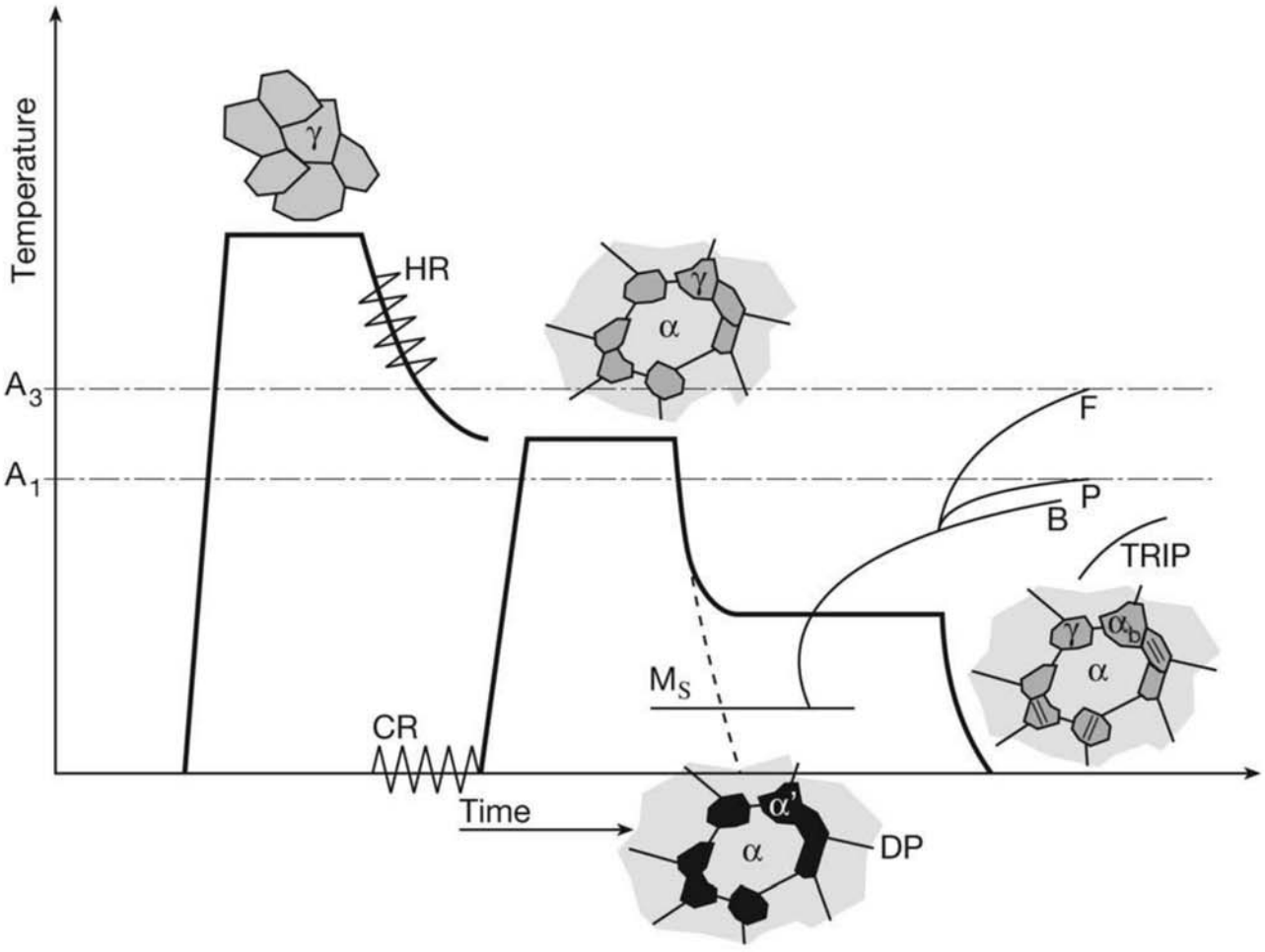

Fig. 13.19 Schematic presentation of simplified thermomechanical treatment schemes for dual-phase (DP) and transformation-induced plasticity (TRIP) steels. One of the routes involves finishing hot rolling (HR) and coiling the steel. This is followed by cold rolling to condition the austenite formation during the austenitizing inside the critical zone. In another method, the steel is subjected to controlled cooling after hot rolling to promote the formation of ferrite inside the critical zone. DP steels are rapidly cooled after the treatment inside the critical zone, forming martensite (α'). TRIP steels are cooled to the austempering temperature, as indicated in the figure, forming bainite (α_b). It is also possible to control the cooling condition after hot rolling and produce TRIP steels directly from the hot rolling. Note: the time scale in the CCT curve superimposed in the right side of the figure starts at the end of the treatment inside the critical zone. Source: Ref 8

content as the original austenite. The material is then subjected to a heat treatment somewhat similar to austempering but aimed at allowing carbon to diffuse from martensite to the retained austenite. This happens because martensite and austenite are not yet in thermodynamic equilibrium after quenching. During this new stage of the heat treatment in which carbon partitions (the partitioning stage), martensite carbon content is decreased and austenite is enriched in carbon. When the material is cooled after the partitioning stage, new martensite is formed from an austenite that is now richer in carbon than the average steel composition. A part of the austenite usually does not transform and remains as retained austenite, since the M_f for the

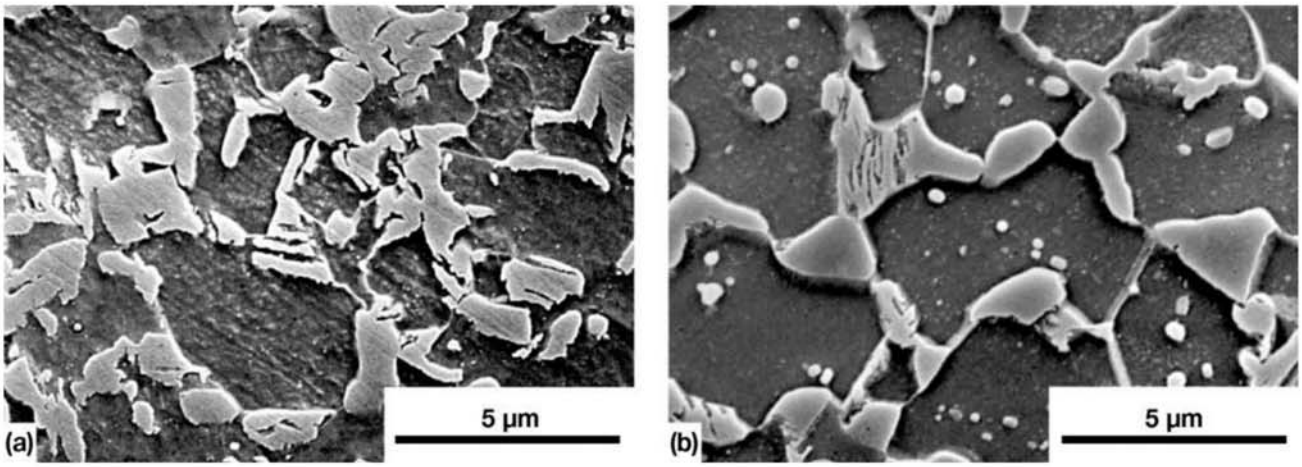

Fig. 13.20 Transformation-induced plasticity (TRIP) steels heat-treated in the critical region followed by quenching and austempering. Ferrite grains surrounded by areas of martensite with retained austenite (MA). It is not possible to properly distinguish these areas when etching with nital. MA areas are essentially not etched. Etchant: nital: (a) C = 0.11%, Mn = 1.53%, Si = 1.5%, (b) C = 0.27%, Mn = 1.4%, Si = 1.4%. Reproduced from Ref 9 with permission from Elsevier.

carbon enriched austenite is normally lower than room temperature. The combination of mechanical properties that can be achieved with this treatment (particularly toughness, strength, and formability) seem extremely promising for a number of applications (Ref 14). Besides the processing route presented in Fig. 13.28, other heat treatment cycles are being evaluated. Figure 13.29 presents the microstructure of an AISI 9260 steel quenched to 190 °C (375 °F) and then subjected to partitioning at the same temperature. When this steel is directly quenched to room temperature, the retained austenite fraction is less than 2%. In the Q&P treatment described, more than 6% austenite has been retained, as desired. Q&P treatments can also be applied starting from inside the critical region. Figure 13.30 presents a TRIP steel in which a Q&P treatment was performed after the austenitization in the critical region, instead of the conventional treatment. The structure obtained this way presented superior properties to those obtained in the classical austempering of these steels.

13.7 Coatings

Steels for forming are frequently coated, mostly for corrosion protection. The two most common families of coatings are zinc-based coatings (Ref 16) (galvanizing, *galvanneal*, *Galvalume*®; Galvalume is an internationally registered trademark of BIEC International, Inc., for coatings containing 55% Al-Zn) and tin-based coatings (tin plate). Zinc and zinc-based alloy coatings have thicknesses that make possible their evaluation and control using cross-section metallographies. Tin coatings are generally so thin that their evaluation is performed with examination normal to the coated surface, that is, direct evaluation. After electrolytic deposition, they normally go through a melting treatment followed by rapid cooling. Figure 13.31 shows the transverse section of a product that has been coated with a zinc alloy by hot dipping (galvanized product). On the other hand, galvanneal coating involves a heat treatment after the immersion coating, resulting in an alloyed coating that contains

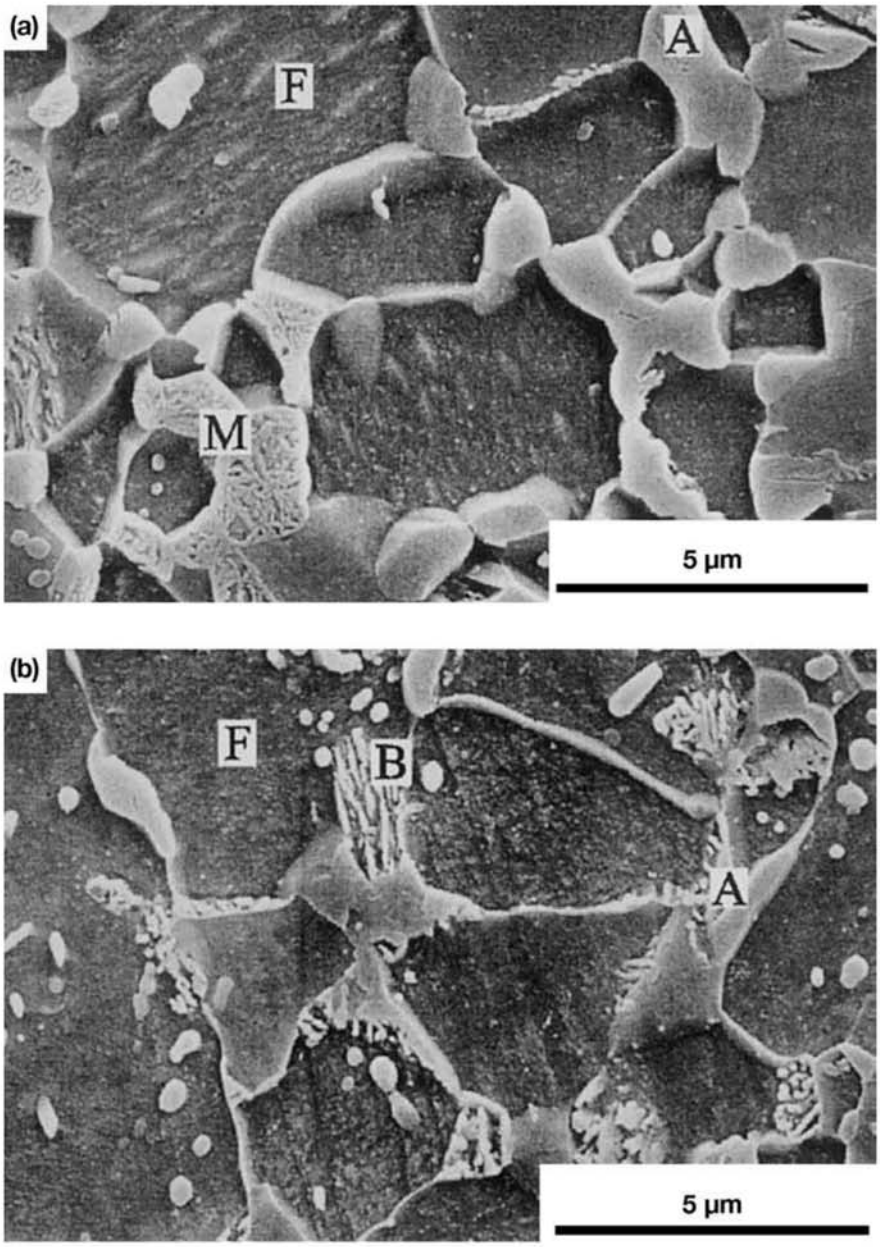

Fig. 13.21 (a) Multiphase transformation-induced plasticity (TRIP) steel containing C = 0.11%, Mn = 1.53%, Si = 1.5% heat-treated in the critical region followed by quenching and austempering. Ferrite grains surrounded by areas of bainite and martensite with retained austenite (MA). The structure of the MA areas is revealed by a rapid tempering at 200 °C (390 °F) for 2 h (Ref 9). (a) Treatment inside the critical zone at 750 °C (1380 °F) for 4 min followed by quenching and austempering at 375 °C (705 °F) for 3 min. Ferrite (F), martensite (M), and retained austenite (A). Etchant: nital. (b) Austempered for 15 min. A larger fraction of austenite has transformed, with the formation of bainite (B). Etchant: nital. Originally published in Ref 10, reproduced with permission from ISIJ, Japan.

Fe-Zn intermetallic phases. Figure 13.32 presents the sequence of reactions occurring during the simulation of a galvanneal treatment at 500 °C (930 °F). Metallographic preparation for this type of observation requires polishing without water lubrication to avoid stains during the etching, with a reactant specific for this purpose prepared the following way: stock solution: 25 ml

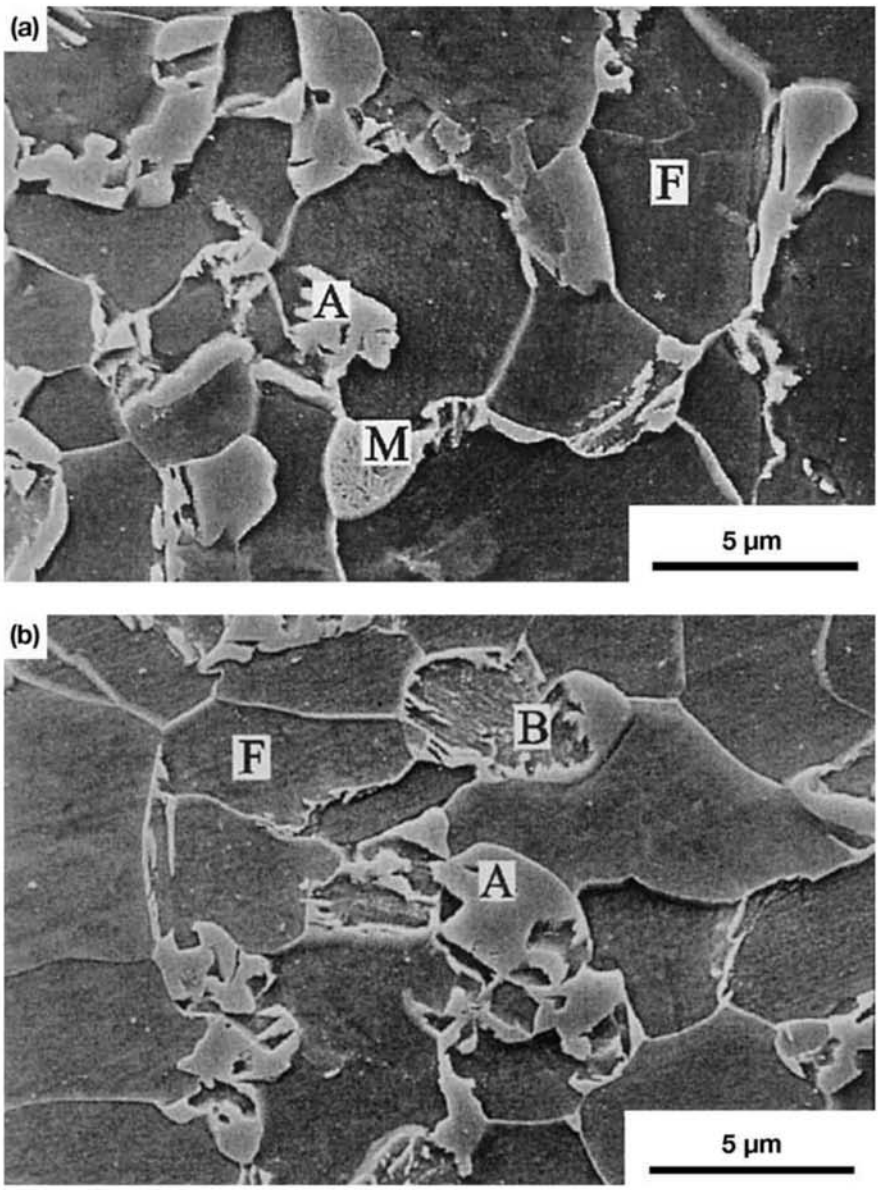

Fig. 13.22 Multiphase transformation-induced plasticity (TRIP) steel containing C = 0.11%, Mn = 1.55%, Si = 0.59%, Al = 1.5% heat-treated in the critical region followed by quenching and austempering. Ferrite grains surrounded by areas of martensite with retained austenite (MA). The structure of the MA areas is revealed by a rapid tempering at 200 °C (390 °F) for 2 h (Ref 9). Intercritical treatment at 750 °C (1380 °F) for 4 min followed by quenching and austempering at 375 °C (705 °F) (a) for 1 min (b) for 5 min. Ferrite (F), bainite (B), and retained austenite (A). SEM, SE. Etchant: nital. Originally published in Ref 10, reproduced with permission from ISIJ, Japan.

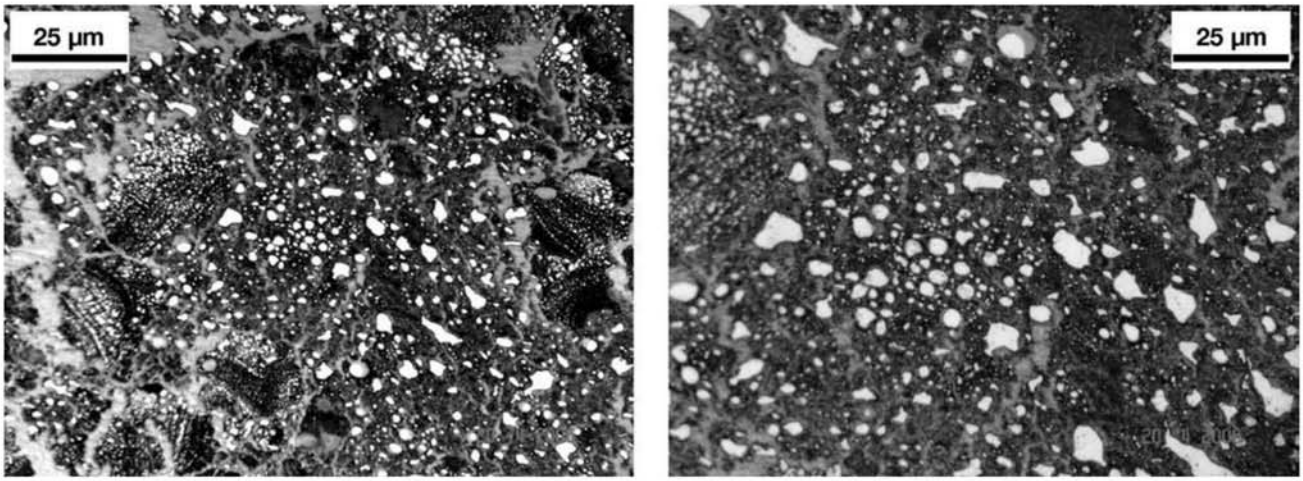

Fig. 13.23 Longitudinal cross section of a specimen of transformation-induced plasticity (TRIP) steel produced via hot rolling with controlled cooling, subjected to tensile test. Ferritic matrix, bainite (dark areas), and martensite with retained austenite in light areas. Etchant: LePera. The hardness of the light areas is around 550 HV. Courtesy of ArcelorMittal Tubarão, ES, Brazil.

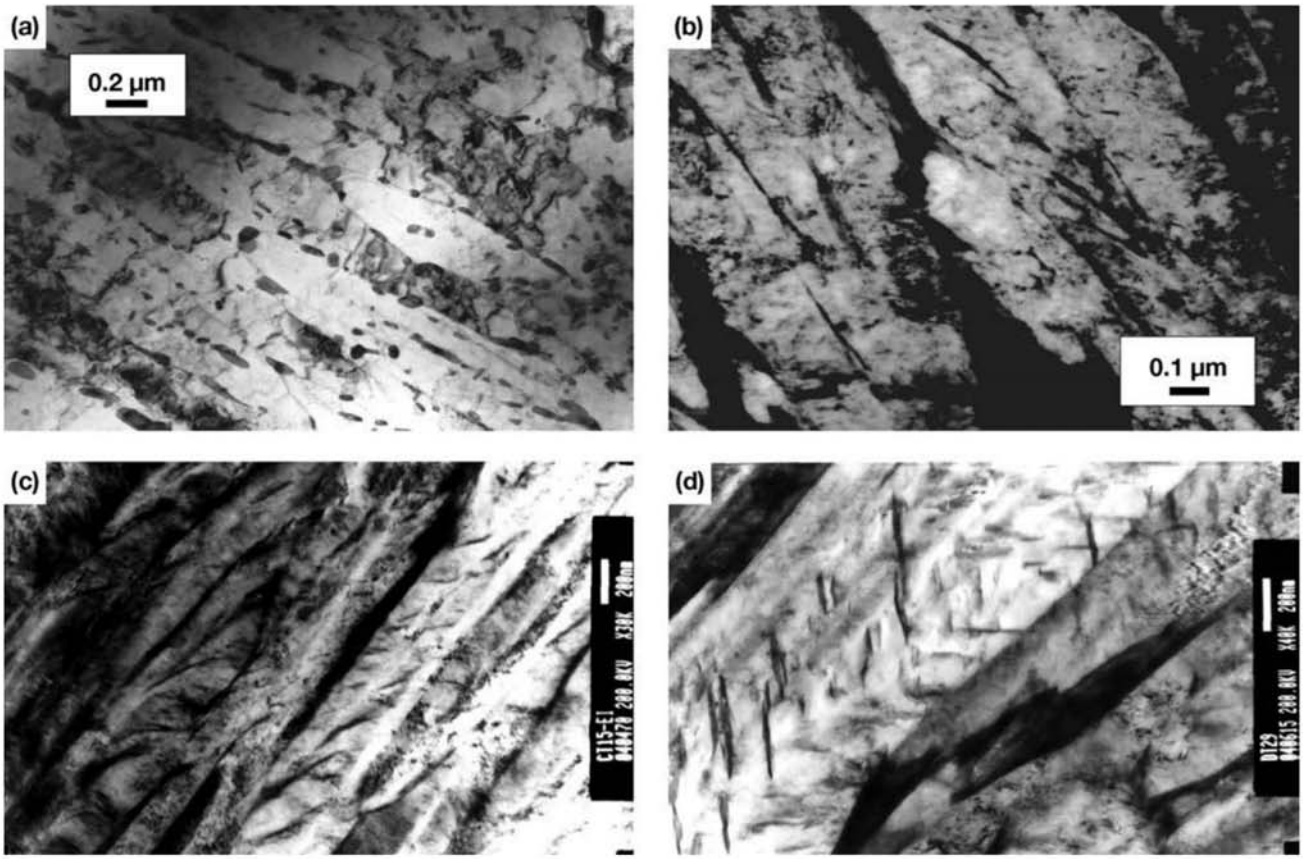

Fig. 13.24 (a) "Conventional" bainite formed in continuous cooling. Parallel plates, forming "packets." Precipitated carbides can be observed. (b) and (c) Bainitic ferrite: parallel plates, without the presence of carbides. Between the plates, there is usually retained austenite. (d) Auto-tempered martensite: carbides precipitate with crystallographic relationship with respect to the martensite plates. Courtesy of F.G. Caballero, (CENIM-CSIC), Grupo Materialia, Madrid, Spain.

picral 4%, around five drops of benzalkonium chloride, 25 ml nital 2%, and 150 ml ethanol. Dilute the stock solution 1:3 in ethanol before use (Ref 18).

Galvalume coatings have around 55% aluminum and 1.5% silicon. Figure 13.33 presents an optical micrograph of this coating without etching. This type of observation (without etching) is not sufficient to define beyond controversy, the type of zinc-based coating. Figure 13.34 presents Galvalume coating observed using SEM, when its characteristics become evident. Aluminum dendrites, a zinc-rich interdendritic region, and a fine dispersion of silicon particles form the coating. Solidification follows the expected sequence from the Al-Zn-Si phase diagram (Ref 16). Figure 13.35 presents surface views of tin plates.

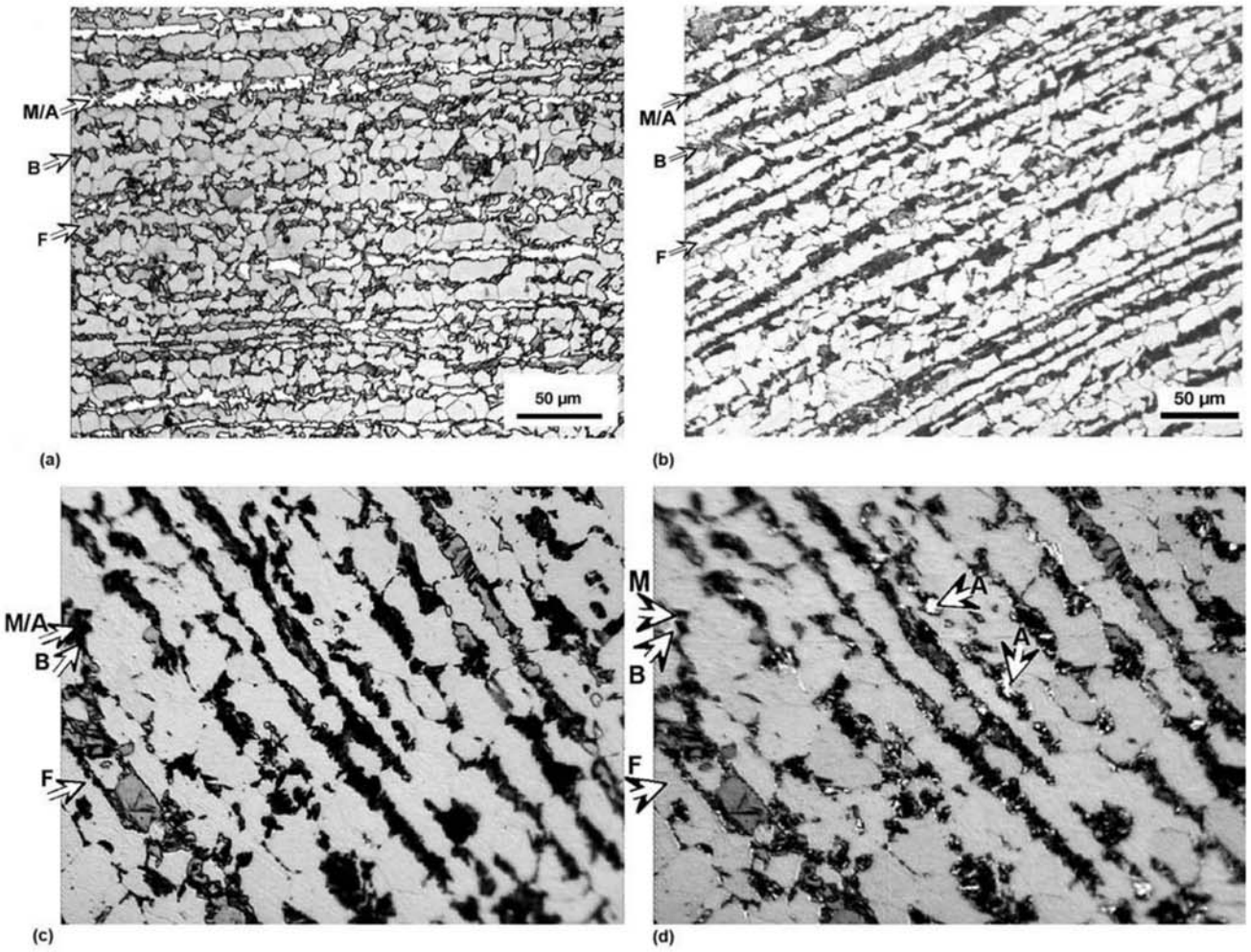

Fig. 13.25 Transformation-induced plasticity (TRIP) steel: ferrite, martensite-austenite (MA) areas, and bainite, with different responses to etching. (a) Etchant: LePera (converted to grayscale): bluish ferrite (medium gray), brown bainite (dark gray), MA areas (light). (b) Etchant: nital: ferrite (light), MA and B gray. MA and B can be identified only by differences in morphology. (c) Nital 2% (10 s) followed by 10% solution of sodium metabisulfite in water (30 s). (d) The same etching observed with a blue filter changes austenite into light, making it possible to distinguish austenite from martensite (dark). Courtesy of C. Capdevila Montes, CENIM-CSIC, Grupo Materialia, Madrid, Spain.

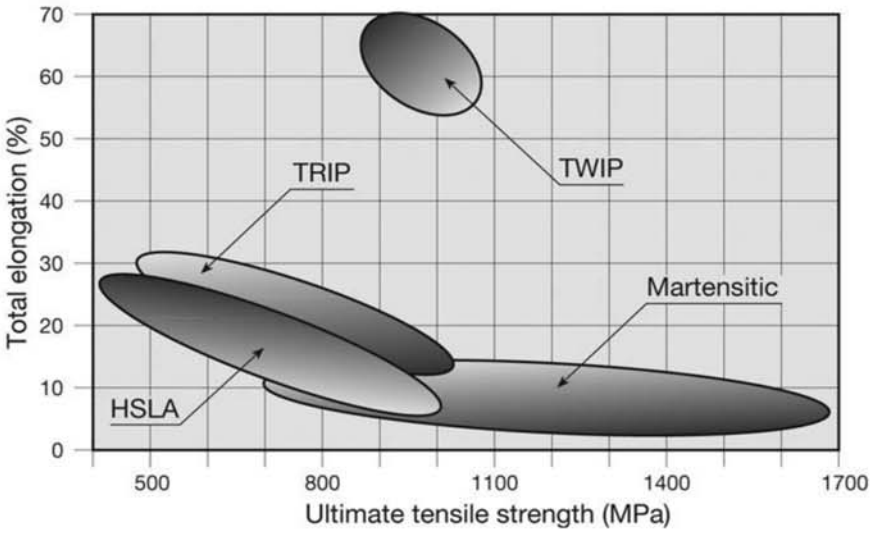

Fig. 13.26 Steels with twinning-induced plasticity (TWIP) have an extraordinary potential for applications where high deformations are considered with high work-hardening coefficient and high mechanical strength.

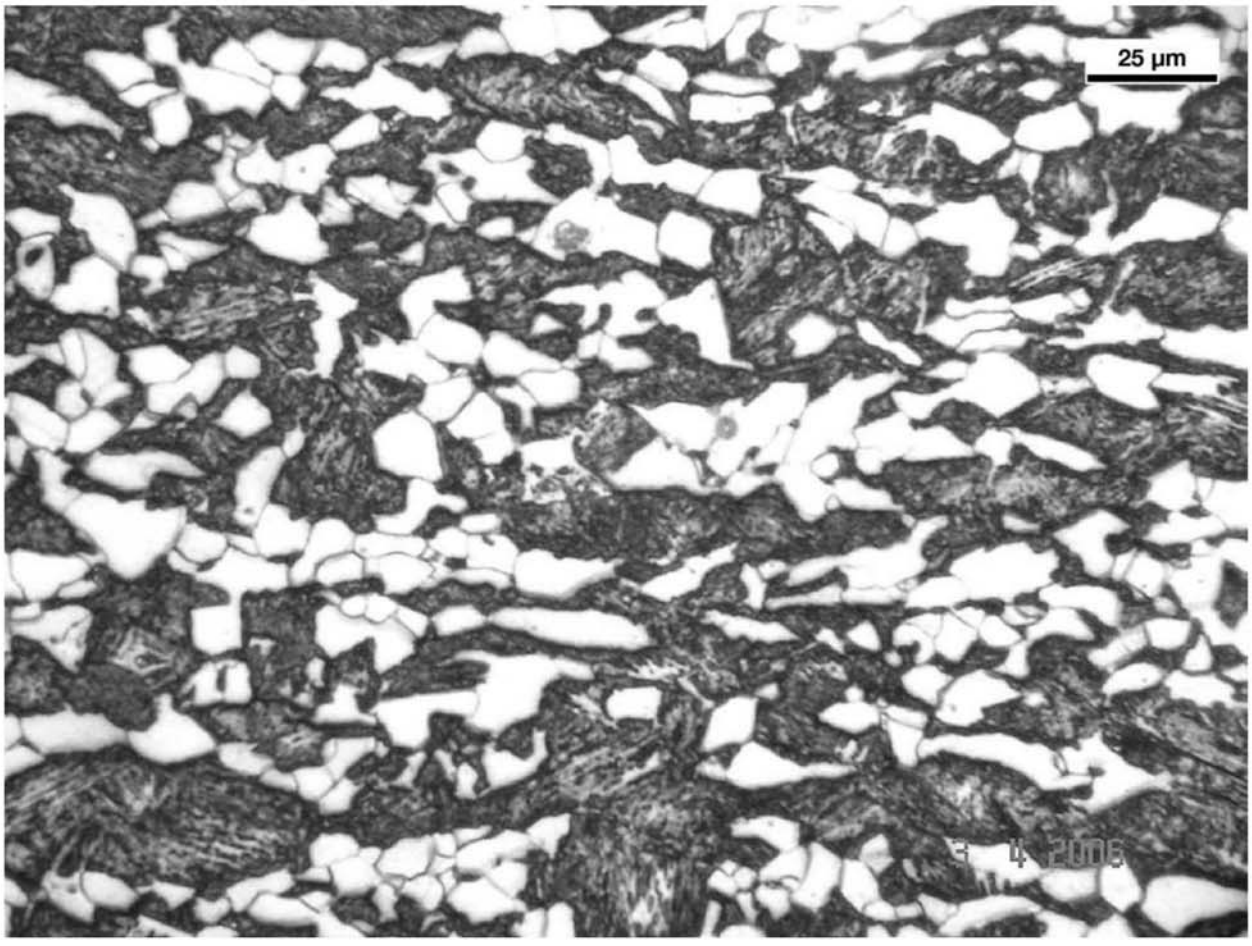

Fig. 13.27 Longitudinal cross section of a ferritic-bainitic steel. Equiaxed ferrite appears light. Compare with Fig. 13.8. Etchant: LePera, modified. In this case, two solutions are prepared: Part I: 1 g sodium metabisulfite in 100 ml distilled water. Part II: 4 g picric acid in 100 ml ethanol. Keep reactants at 0 °C (32 °F). After ultrasonic cleaning on the sample, perform a short time etching (≅ 30 s) with 2% nital to develop grain boundaries. Mix approx. 60% Part I and 40% Part II. Etch for ≅ 30–40 s. Stop etching with ethanol. Bainite appears dark, ferrite tan, and martensite white. Courtesy of ArcelorMittal Tubarão, ES, Brazil.

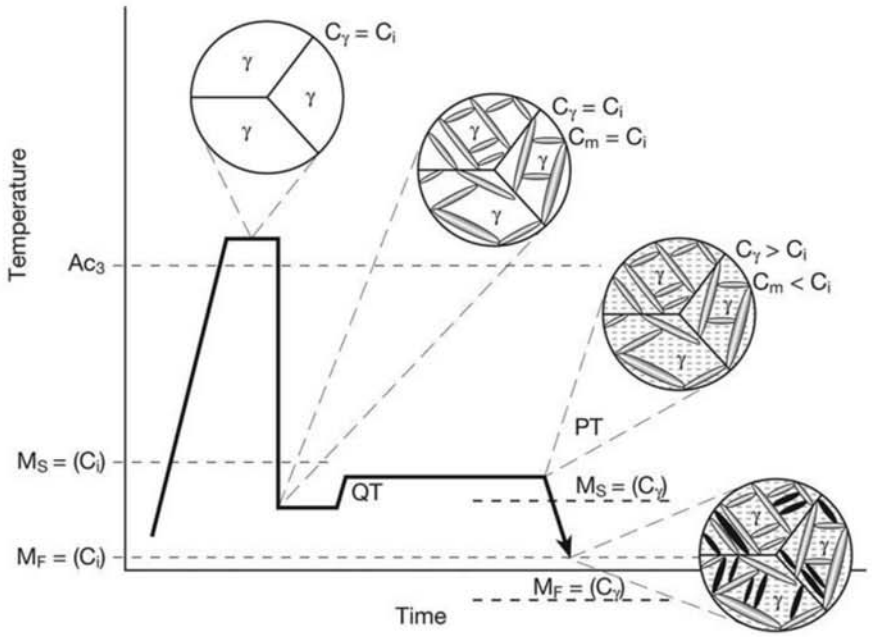

Fig. 13.28 The quenching and partitioning (Q&P) cycle to produce structures with retained austenite, schematically presented. C_i, C_γ, C_m are the carbon content, respectively, in the starting steel (average) in austenite and in martensite. QT= quenching stage, PT= partitioning stage. The effect of the carbon content on the M_s and M_f temperatures is also indicated. Source: Ref 14

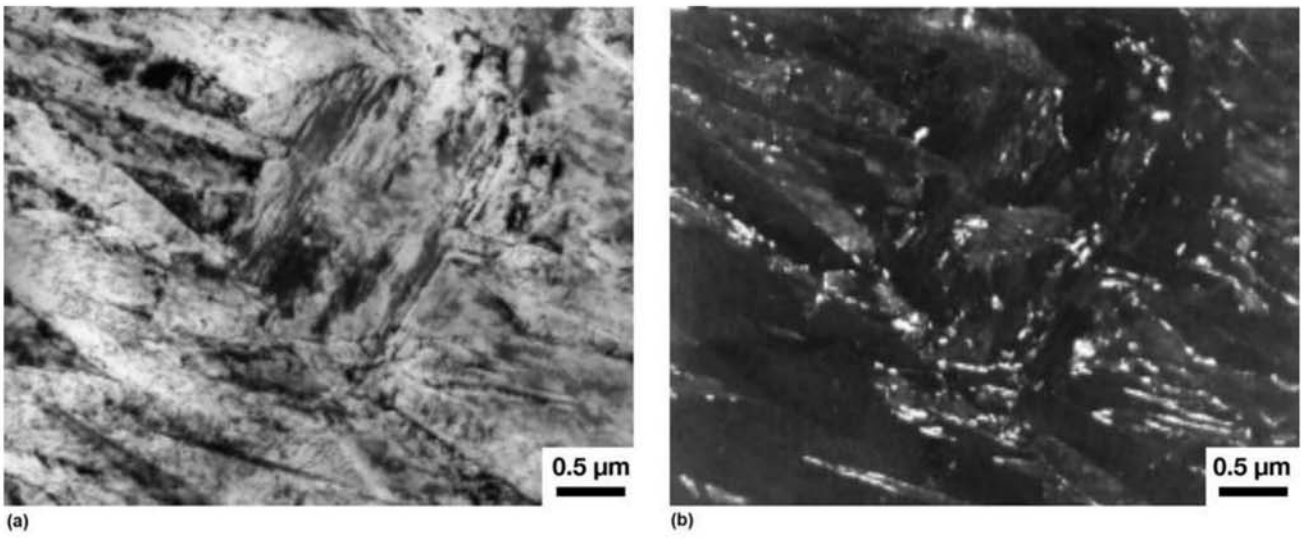

Fig. 13.29 AISI 9260 steel quenched to 190 °C (375 °F) and held at this temperature for 120 s. (This is a Q&P treatment in which the partitioning stage happens at the same temperature as the end of the quenching stage.) (a) Martensite with substructure, visible in TEM, bright field. (b) "Dark field" condition in which only electrons diffracted by austenite are used to form the image in the TEM (austenite thus appears light in the image. (For more details on this technique, see Ref 15.) Courtesy of J. Speer, reproduced with permission from Ref 14.

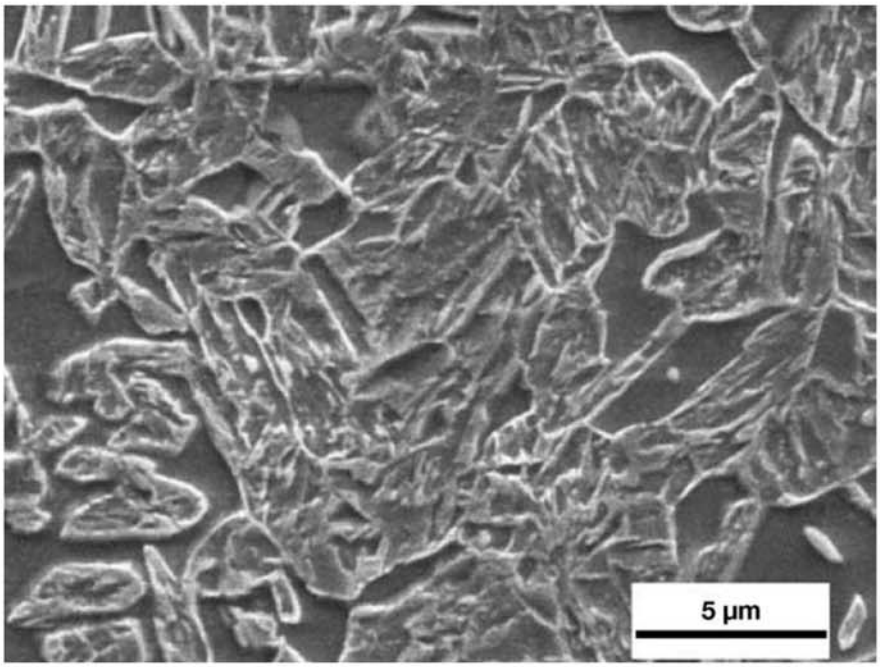

Fig. 13.30 High-silicon transformation-induced plasticity (TRIP) steel with 8.4% volume fraction of austenite, subjected to intercritical austenitization (temperature corresponding to 75% γ + 25% α) followed by quenching to 200 °C (390 °F) and partitioning at 400 °C (750 °F) for 10 s. The ferrite remaining from the treatment inside the critical region appears as larger grains with no internal relief produced by the etching. The regions that were austenite have partially transformed to martensite. Retained austenite is present. SEM, SE. Etchant: nital 2%. Courtesy of J. Speer, reproduced from Ref 14 with permission.

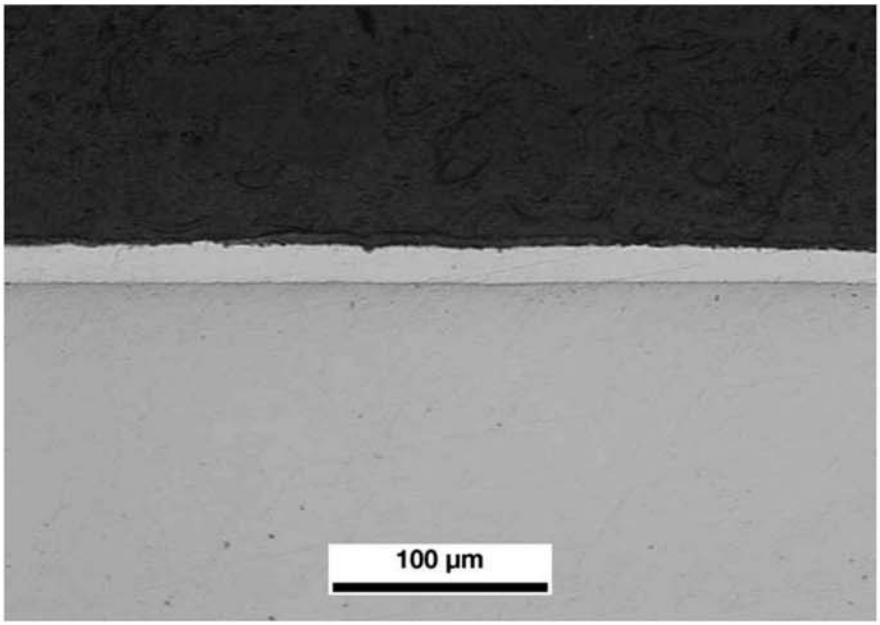

Fig. 13.31 Cross section of steel sheet galvanized by immersion. No etching.

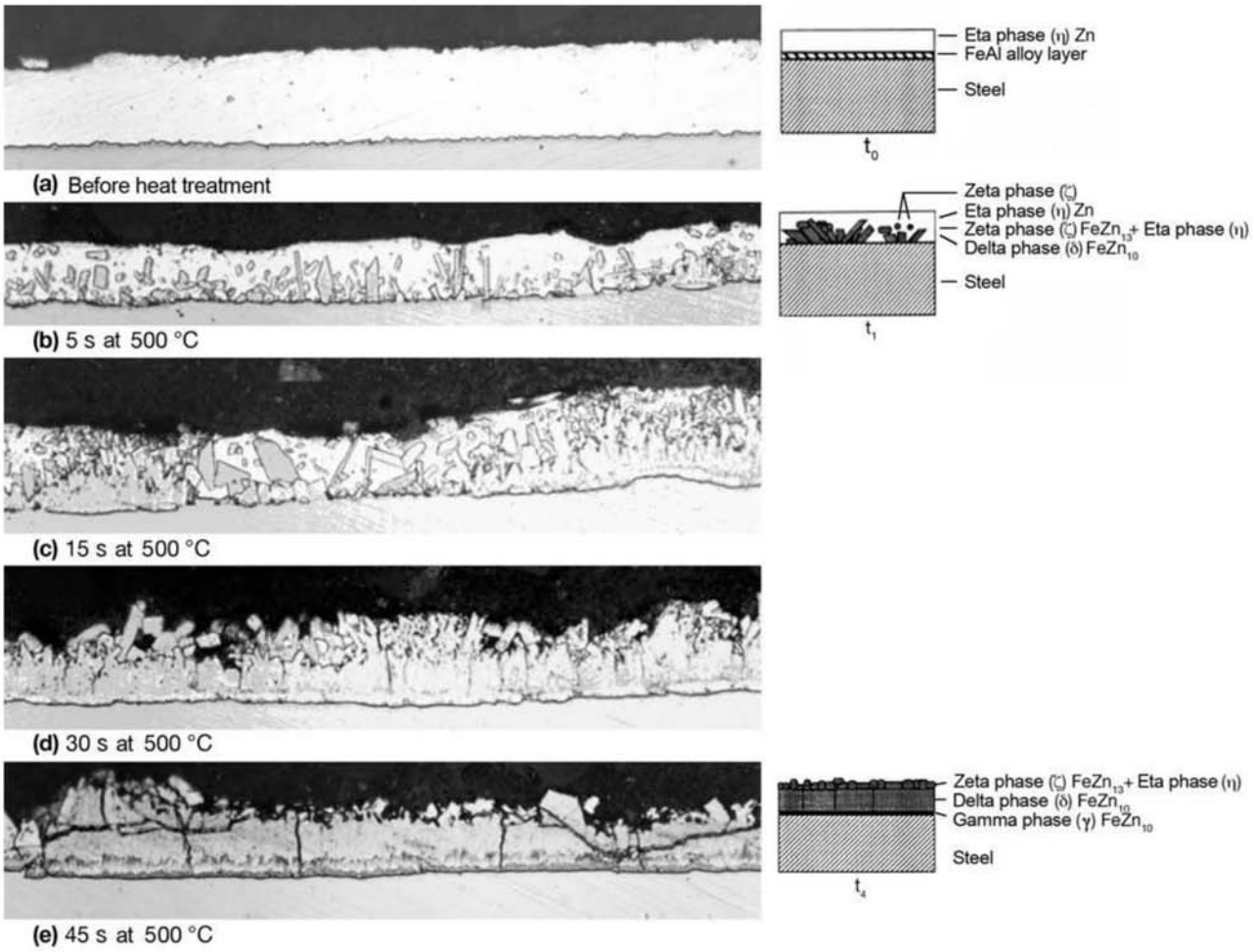

Fig. 13.32 Effects of a simulated heat treatment at 500 °C (930 °F) on the iron enrichment of the galvanneal coating. As treatment time increases the zinc layer, (eta phase) is converted into intermetallic compounds present in the Fe-Zn binary system. The various possible compounds are described in detail in Ref 16 and 17. In (c), closer to the left-hand side, an *outburst* can be observed. Courtesy of C. R. Xavier and P. R. Rios, EEIMVR-UFF, Volta Redonda, RJ, Brazil. Source: Ref 17

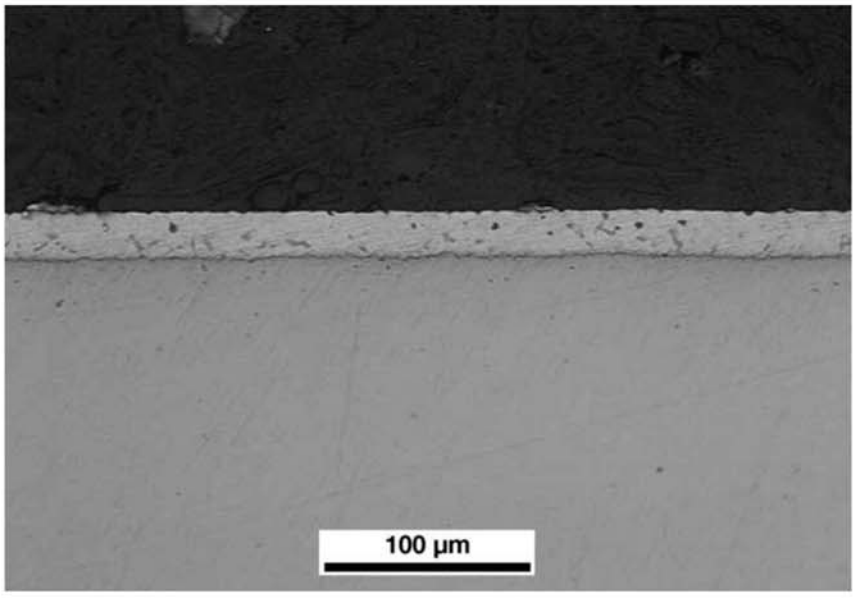

Fig. 13.33 Cross section of a steel sheet coated by galvalume. No etching.

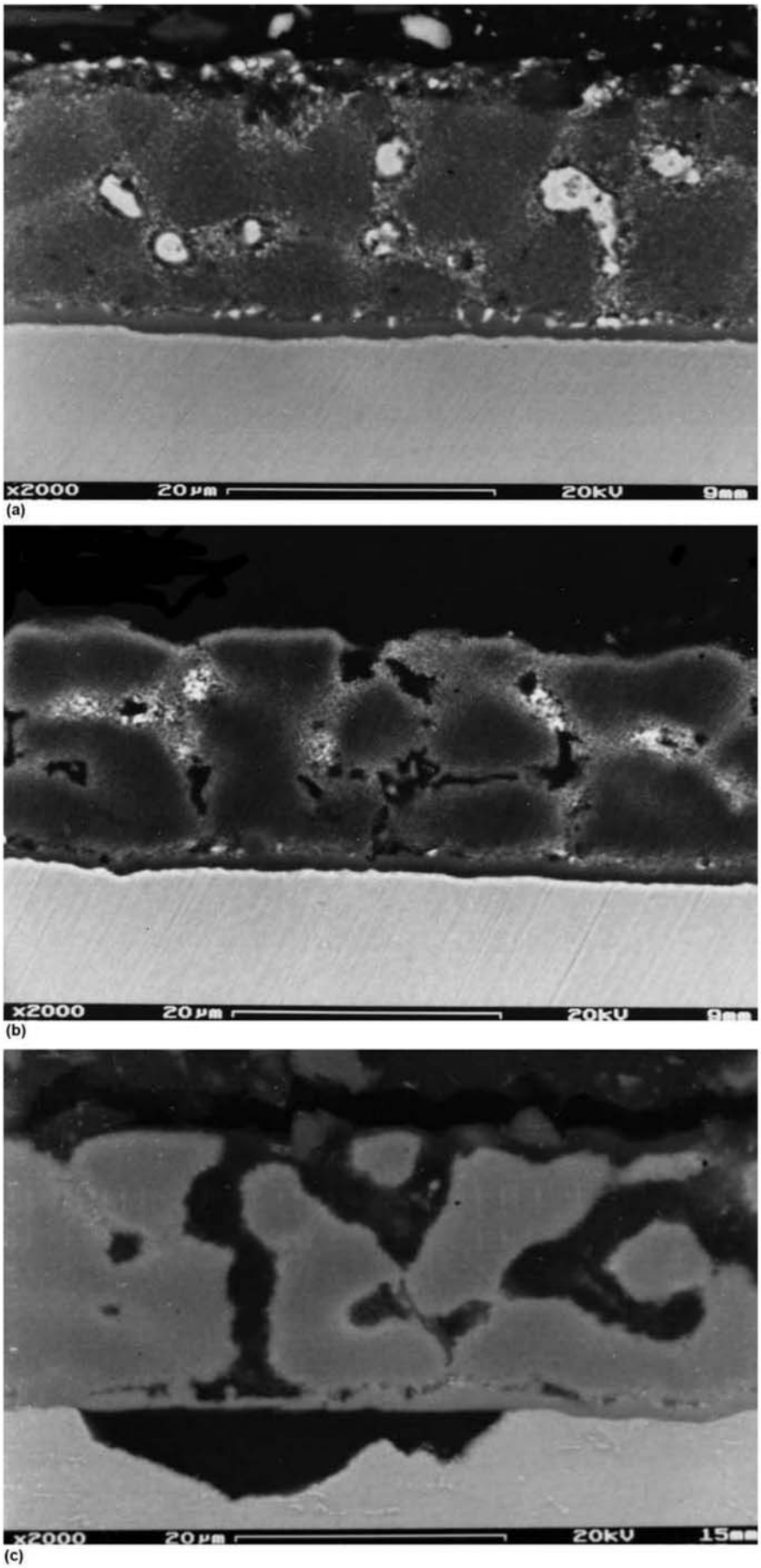

Fig. 13.34 (a) Cross section of a sheet coated by Galvalume. The aluminum-rich dendrites are darker. The interdendritic regions rich in zinc are lighter in SE mode in the SEM. (b) Transverse cross section of a steel sheet coated with Galvalume, partially corroded. The zinc-rich regions have been preferentially corroded. SEM, SE. (c) Transverse cross section of a steel sheet coated by Galvalume partially corroded. The zinc-rich regions are preferentially corroded. Corrosion has reached the steel after creating a continuous path between the external surface of the coating and the steel substrate, caused by the corrosion of the interdendritic areas. SEM, SE. Courtesy of T. Nogueira and P. R. Rios, EEIMVR-RFF, Volta Redonda, RJ, Brazil. Reproduced from Ref 19 with authorization from ISIJ, Japan.

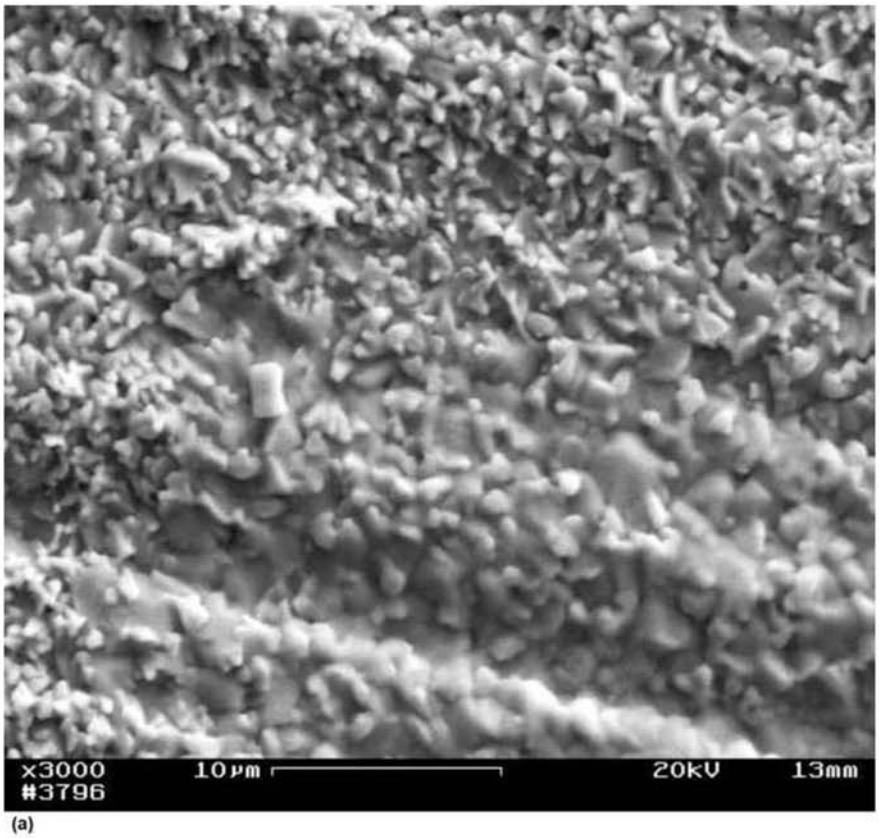

(a)

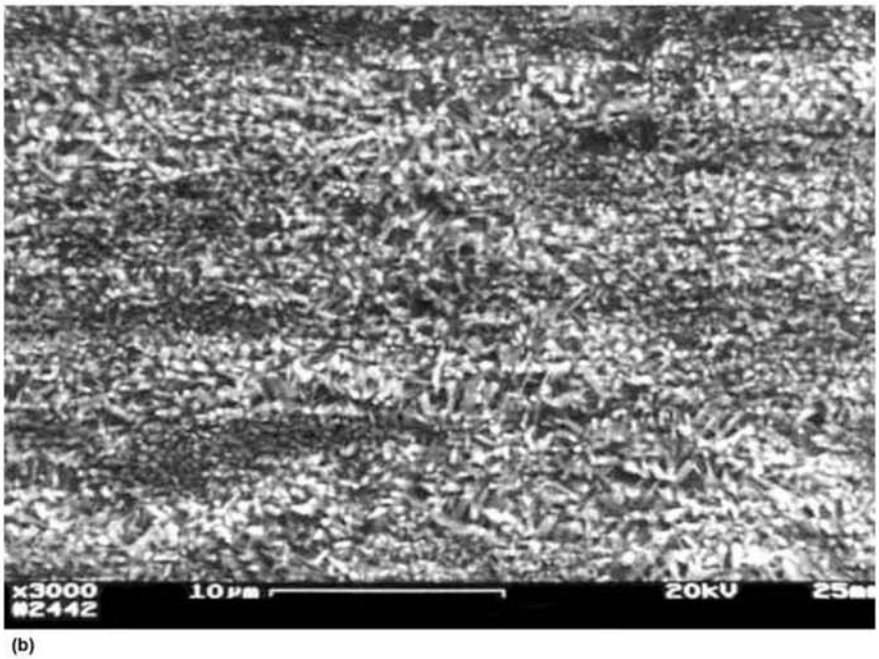

(b)

Fig. 13.35 Tin coating. (a) Tinfoil surface after electrolytical coating with $FeSn_2$ before the melting of the coating. (b) Finished coating, where the fusion treatment and rapid cooling have already been performed.

REFERENCES

1. R. A. Schultz, Metallic Material Trends for North American Light Vehicles, *Great Designs in Steel 2007*, Ducker Worldwide, AISI, 2007
2. *Advanced High-Strength Steels Application Guidelines*, S. Keeler and M. Kimchi, eds., Vol 5, WorldAutoSteel, 2015, http://www.worldautosteel.org/projects/advanced-high-strength-steel-application-guidelines/ (accessed November 25, 2016)
3. D.T. Llewellyn and R.C. Hudd, *Steels: Metallurgy and Applications*, Butterworth-Heinemann, 1998
4. I. Kozasu, Processing—Thermomechanical Controlled Processing, *Materials Science and Technology—Constitution and Properties of Steels*, F.B. Pickering, Ed., Wiley-VCH, 1996
5. P. Rodrigues, Caracterização Microestrutural de Aços Multifásicos ao Silício e Manganês, Projeto Final de Graduação, Volta Redonda, RJ Brazil, EEIMVR-UFF, 2007
6. F.G. Caballero, A. Garcia-Junceda, C. Capdevila, and C.G. Andrés, Evolution of Microstructural Banding during the Manufacturing Process of Dual Phase Steels, *Mat. Trans. JIM*, Vol 47 (No. 9) 2006, p 2269–76
7. D.P. Datta and A.M. Gokhale, Austenitization Kinetics of pearlite and ferrite aggregates in a low carbon steel containing 0.15 wt pct C, *Metall. Trans.* A, Vol 12A (1981), p 443–50
8. P.J. Jacques, Transformation-Induced Plasticity for High-Strength Formable Steels, *Curr. Opin. Solid State Mat. Sci.*, Vol 8, 2004, p 259–65
9. E. Girault, P. Jacques, P. Harlet, K. Mols, J.V. Humbeeck, E. Aernoudt, and F. Delannay, Metallographic Methods for Revealing the Multiphase Microstructure of TRIP-Assisted Steels, *Mat. Charact.*, Vol 40, 1998, p 111–18
10. P.J. Jacques, E. Girault, A. Mertens, B. Verlinden, J.v. Humbeeck, and F. Delannay, The Developments of Cold-Rolled TRIP-Assisted Multiphase Steels. Al-Alloyed TRIP-Assisted Multiphase Steels, *ISIJ Int.*, Vol 41 (No. 9), 2001, p 1068–74
11. G. Krauss, *Steels: Processing, Structure and Performance*, ASM International, 2005
12. T.D. Cock, J.P. Ferrer, C. Capdevila, F.G. Caballero, V. López, and C. García de Andrés, Austenite Retention in Low Al/Si Multiphase Steels, *Scripta Materialia*, Vol 55, 2006, p 441–43
13. J.G. Speer, D.V. Edmonds, F.C. Rizzo, and D.K. Matlock, Partitioning of Carbon from Supersaturated Plates of Ferrite, with Application to Steel Processing and Fundamentals of the Bainite Transformation, *Curr. Opin. Solid State Mat. Sci.*, Vol 8, 2004, p 219–37
14. J.G. Speer, F.C.R. Assunção, D.K. Matlock, and D.V. Edmonds, The "Quenching and Partitioning" Process: Background and Recent Progress, *Mat. Res.*, Vol 8 (No. 4), 2005, p 417–23

15. Image nodes in TEM—dark field Images, http://www.microscopy.ethz.ch/TEM_DF.htm or Transmission electron microscopy at http://labs.mete.metu.edu.tr/tem/TEMtext/TEMtext.html (accessed December 13, 2016)
16. A.R. Marder, The Metallurgy of Zinc-Coated Steel, *Prog. Mat. Sci.*, Vol 45, 2000, p 191–271
17. C.E. Jordan and A.R. Marder, A Model for Galvanneal Morphology Development, *The Physical Metallurgy of Zinc Coated Steel*, A.R. Marder, Ed., TMS, 1994
18. C.R. Xavier, *Simulação do revestimento galvanneal*, Master's thesis, EEIMVR–UFF, Volta Redonda, RJ, Brazil, 1996
19. T.M.C. Nogueira, A.S. Cruz, and P.R. Rios, Application of a Direct Current Anodic Voltammetric Technique to a 55mass%Al-Zn Coated Steel Sheet Before and After an Annealing Heat Treatment, *ISIJ Int.*, Vol 39 (No. 3), 1999, p 295–97

Metallography of Steels—Interpretation of Structure and the Effects of Processing
Hubertus Colpaert
Updated and Translated by André Luiz V. da Costa e Silva

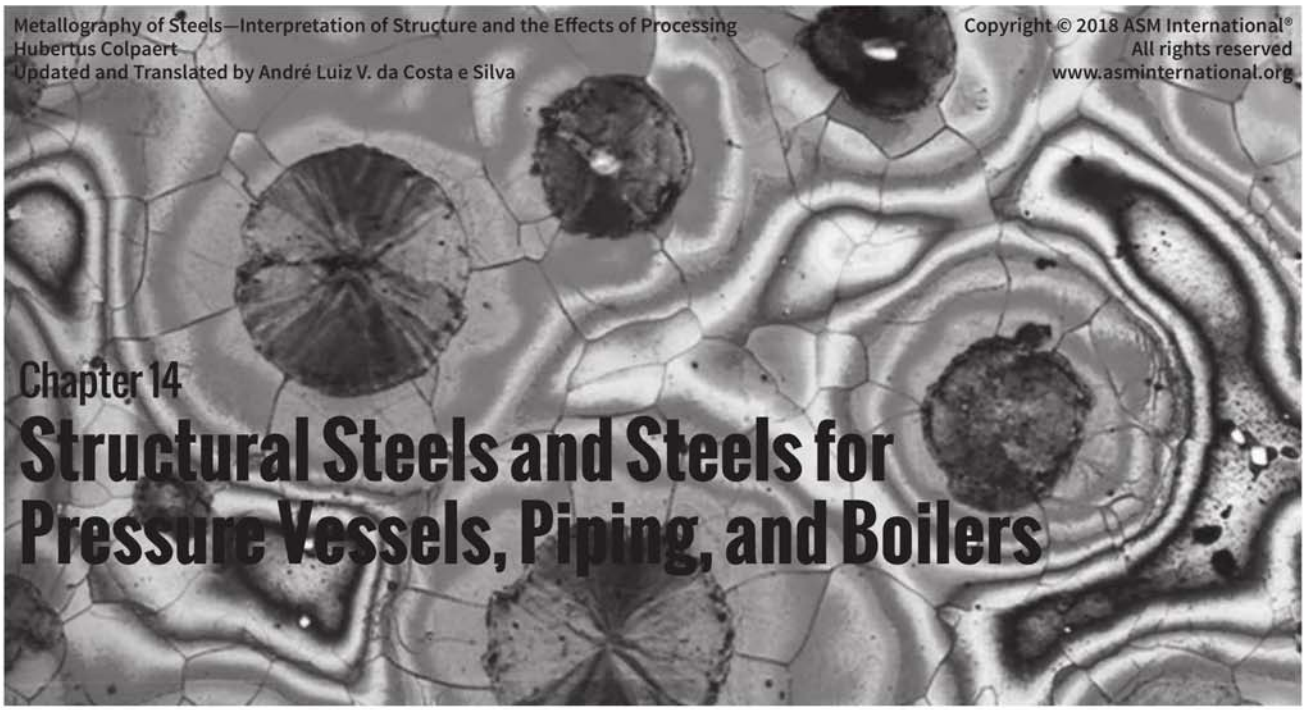

Chapter 14

Structural Steels and Steels for Pressure Vessels, Piping, and Boilers

The classification "structural steels" basically covers steels for concrete reinforcement (rebar), bars and tubes (for static structural applications), and plates and profiles for structural applications.

On the other hand, a large portion of the steels used to build industrial equipment such as boilers, pressure vessels, and piping are very similar to structural steels, particularly when the envisioned application temperatures are lower than about 350 °C (660 °F). (Below this temperature, creep is normally not a relevant issue for steels.) For this reason, steels for these applications are also discussed in this chapter.

For applications at higher temperatures, when creep resistance and microstructural stability are critical properties, the design conditions are different, as briefly discussed in the section 14.6 "Welding of Structural Steels—Metallographic Aspects" in this chapter.

Classically structural steels are medium to low carbon steels (C < 0.25%), manganese alloyed with controlled phosphorus and sulfur contents. The development of high-strength low-alloy (HSLA) steels since their inception in the late 1950s has been extensive, aiming at achieving adequate properties at minimum cost and making it possible to achieve significant reductions in the carbon content, thus reducing solidification segregation and improving weldability and toughness in these steels. Most of these new compositions are also designed with thermomechanical treatments in mind, instead of the classical route of hot working followed by heat treatment. Furthermore, special applications require medium or low alloyed steels similar to engineering steels. This is the case for such as steels for nuclear reactor pressure vessels, high-pressure vessels, submarine hulls, and so on.

A large part of the world's use of steel encompasses structural steels. Their use increases dramatically with a significant expansion in infrastructure and construction. Structural steels are usually rolled products in view of the large amount that must be produced. They may also be produced by forging or casting, when the advantages of neat net shape processing are desired. In the past, rimming and semi-killed steels used to be selected for the less demand-

ing applications, as these types of deoxidation were much more economical. With the widespread introduction of continuous casting, these types of steels have essentially disappeared (see Chapter 8, "Solidification, Segregation, and Nonmetallic Inclusions," in this book).

The main requirements placed on structural steels are (see also Ref 1):

- High yield strength: most modern design codes and standards are built around the use of yield strength as the basic property for design considering static loads. The "classical" concept widespread in the past that a low elastic ratio (yield strength/ultimate strength) would be needed to prevent plastic instability is being replaced with the judicious use of yield strength to prevent generalized plastic deformation. Many codes still impose limitations on the elastic ratio as an indirect way of guaranteeing toughness, in particular when the ductile failure of the structure is a critical consideration for the equipment (pipelines, for instance).
- High toughness: preventing rapid or catastrophic failure of steel structures has been the focus of special attention, at least since World War II. Toughness control is essential to avoid rapid failure (brittlen).
- Good weldability: the changes in the material on a welded joint should be minimal, ideally with minimum operational limitations for the welding processes. This is an important feature to make possible rapid, simple and reliable construction, as well as flame cutting, which is of great advantage from the economic point of view.
- Good formability: in many cases, it is necessary to form parts (bending, pressing, spinning, rolling of shells, etc.) to fabricate the desired structure.
- Minimum cost.

14.1 Fine-Grained Structural Steels

The simplest products in this category of steels are those that have the desired mechanical properties directly in the "as rolled" condition without further heat treatment and without special care during rolling that would characterize it as thermomechanical processing or controlled rolling. The ASTM A36 (Ref 2) standard is probably the classical example of this type of steel. It is by no means the only standard, and there are many similar specifications. This turns out to be a common problem when one wants to determine the specification to which a certain steel was manufactured. Although one can characterize the chemical composition, mechanical properties, and microstructure, this information is not normally sufficient to define a single standard the steel would meet, but many possibilities. This is the case of the steels presented in Fig. 14.1 (and in more detail in Fig. 14.2 and 14.3). It is normal for steelmakers to use a single heat of steel to fulfill orders that are specified according to different standards but have compatible or equivalent properties.

14.2 Quenched and Tempered Structural Steels

Quenched and tempered structural steels are a good alternative for those specifications requiring the higher end of the spectrum of mechanical properties, above those presented in Fig. 14.1. The investments required to manufacture quenched and tempered flat products, however, limit their production to a small number of plants in a limited number of countries. Controlled rolling followed or not by accelerated cooling, is frequently a more economi-

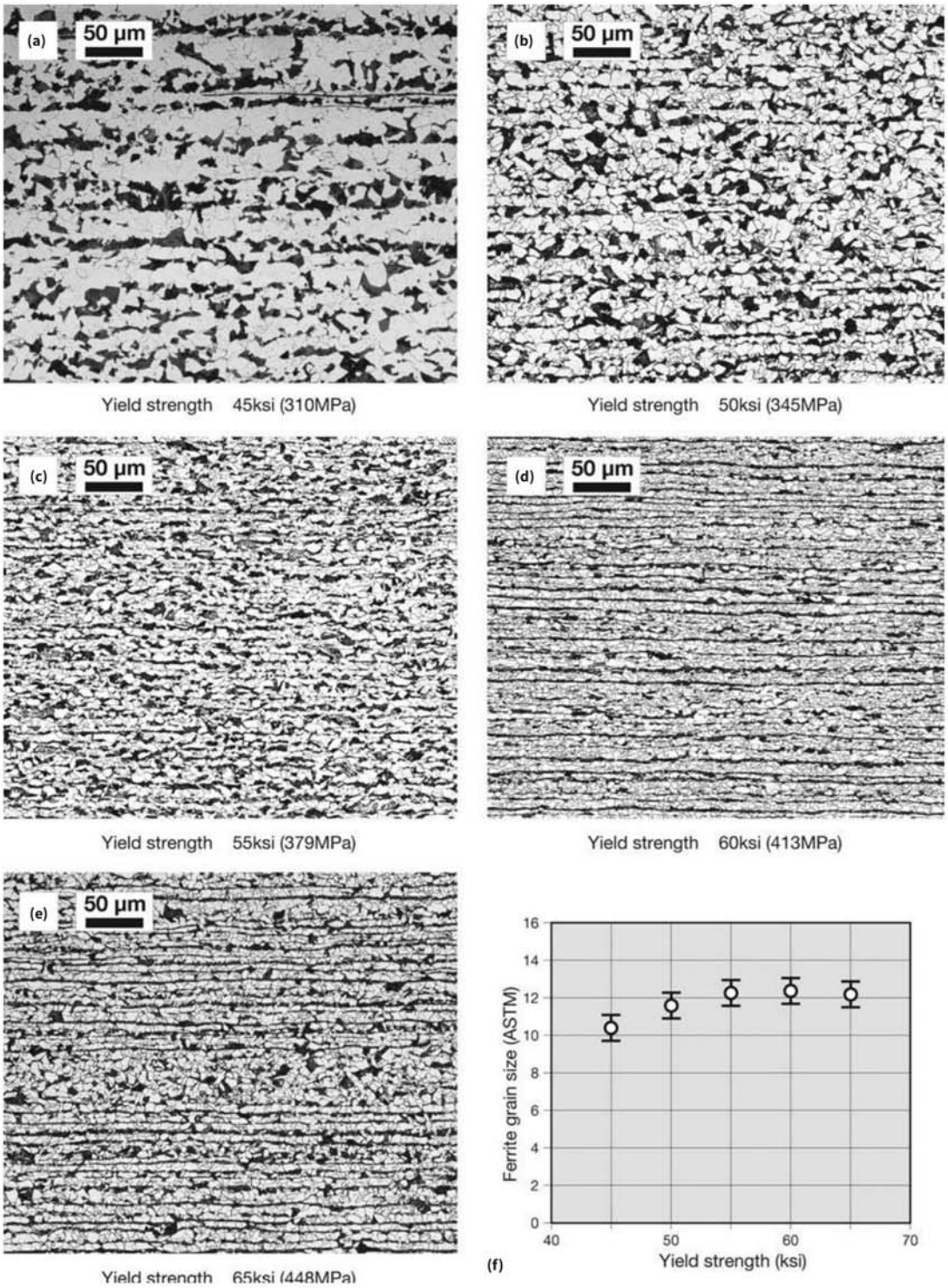

Fig. 14.1 Longitudinal cross sections near mid-thickness of hot rolled structural steel plates with various yield strengths in the range between 310 and 450 MPa (45 and 65 ksi). Equiaxial ferrite and fine pearlite. The volume fraction of pearlite is in the range of 25–30% for all plates. The measured ferritic grain size is presented in (f). The samples in (d) and (e) present significant banding (Chapter 11, "Hot Working," section "Banding," in this book). The original evaluation of banding in these steels was performed according to ASTM E1268 (Ref 3). The banded material has finer pearlite (the difference cannot be observed with the magnification used in these figures). Etchant: nital 2% and picral 4%. Courtesy of National Institute of Standards and Technology. Source: Ref 4

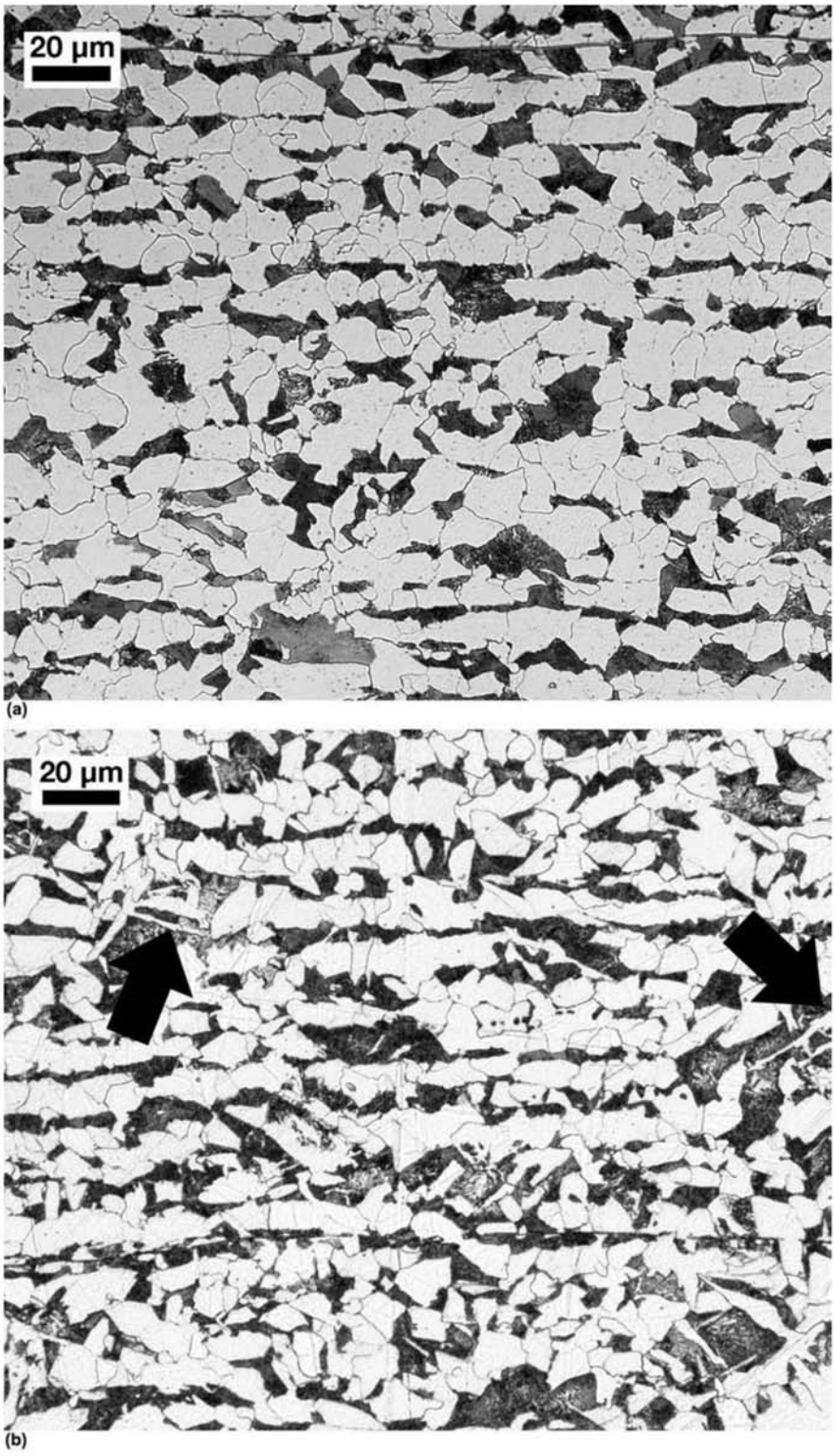

Fig. 14.2 (a) Higher magnification of details of microstructure presented in Fig. 14.1. (b) (Yield strength 345 MPa, or 50 ksi). Equiaxial (or polygonal) ferrite and fine pearlite. Some Widmonstäten or acicular ferrite is present in (b) (indicated by arrows). Some variation in the ferritic grain size. In the upper part of the image in (a), elongated manganese sulfide inclusions. Etchant: nital 2% and picral 4%. Courtesy of National Institute of Standards and Technology, Gaithersburg. (b) Higher magnification of details of microstructure 415 MPa (60 ksi) (similar to the steel presented in Fig. 14.1d). Besides equiaxial (or polygonal) ferrite and fine pearlite, some Widmanstätten (or acicular) ferrite is observed (indicated by arrows). Etchant: nital 2% and picral 4%. Courtesy of National Institute of Standards and Technology. Source: Ref 4

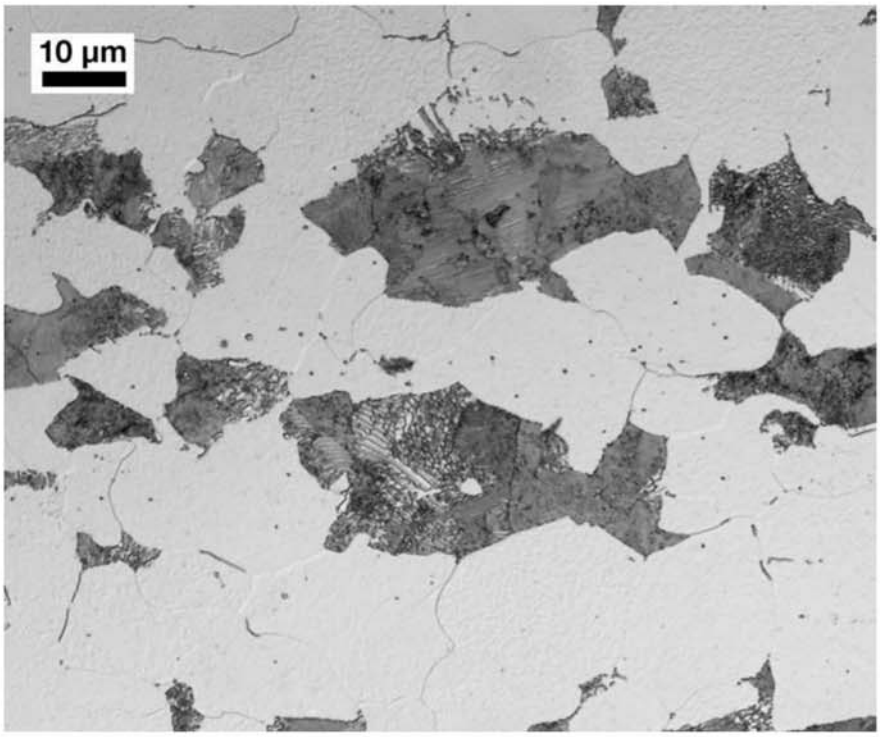

Fig. 14.3 Higher magnification of pearlite in hot rolled steels of Fig. 14.1 (steel with yield strength of 310 MPa, or 45 ksi). Pearlite with lamellar spacing that can be resolved in the optical microscope. The apparent lamellar spacing of pearlite in micrographs depends on the angle between the polished section and the lamellae in each pearlite colony. Etchant: nital 2% and picral 4%. Courtesy of National Institute of Standards and Technology. Source: Ref 4

cally viable option for the production of higher strength structural steels. Figure 14.4 presents the structure of different plates, supposedly supplied by the same steelmaker, in the quenched and tempered condition, to the requirement of different strength classes. Although the steel in Fig. 14.4(a) presents a martensite free structure, possibly composed of acicular ferrite (or bainite) and carbide, the higher strength classes all have very similar microstructures, apparently preferentially composed of low carbon tempered martensite. They probably differ only on the tempering temperature. As the acicular aspect of the microstructure becomes less evident and the presence of carbides becomes better defined (both evidence of more tempering) the steel strength decreases, as expected.

14.3 Controlled Rolled (Thermomechanical Treatment) Structural Steels

Judicious use of a combination of microalloying elements that form stable precipitates at high temperatures and may control austenitic grain size by pinning and the presence of elements in solution such as niobium, which retard austenite recrystallization, are the core of modern controlled rolled steel composition design and processing (Ref 5–7).

The effectiveness of the use of elements that are able to form stable precipitates and control austenitic grain growth in combination with a controlled thermomechanical cycle is demonstrated in Fig. 14.5 and 14.6, which summa-

rize results from Ref 8 when processing tubes. Various additions of vanadium, niobium, and titanium have been made to a steel with an approximate basic chemical composition of C = 0.15%, Mn = 1.5%, and Si = 0.45%. After the definition of the hot rolling cycle deformation and temperature parameters, the main investigation focused on the intermediate cooling, performed between the two-step hot rolling of the tubes. During this intermediate cooling, carbonitrides of the microalloying elements (V, Nb, and Ti) may precipitate, further hindering austenite grain growth in the final hot rolling step, which is followed

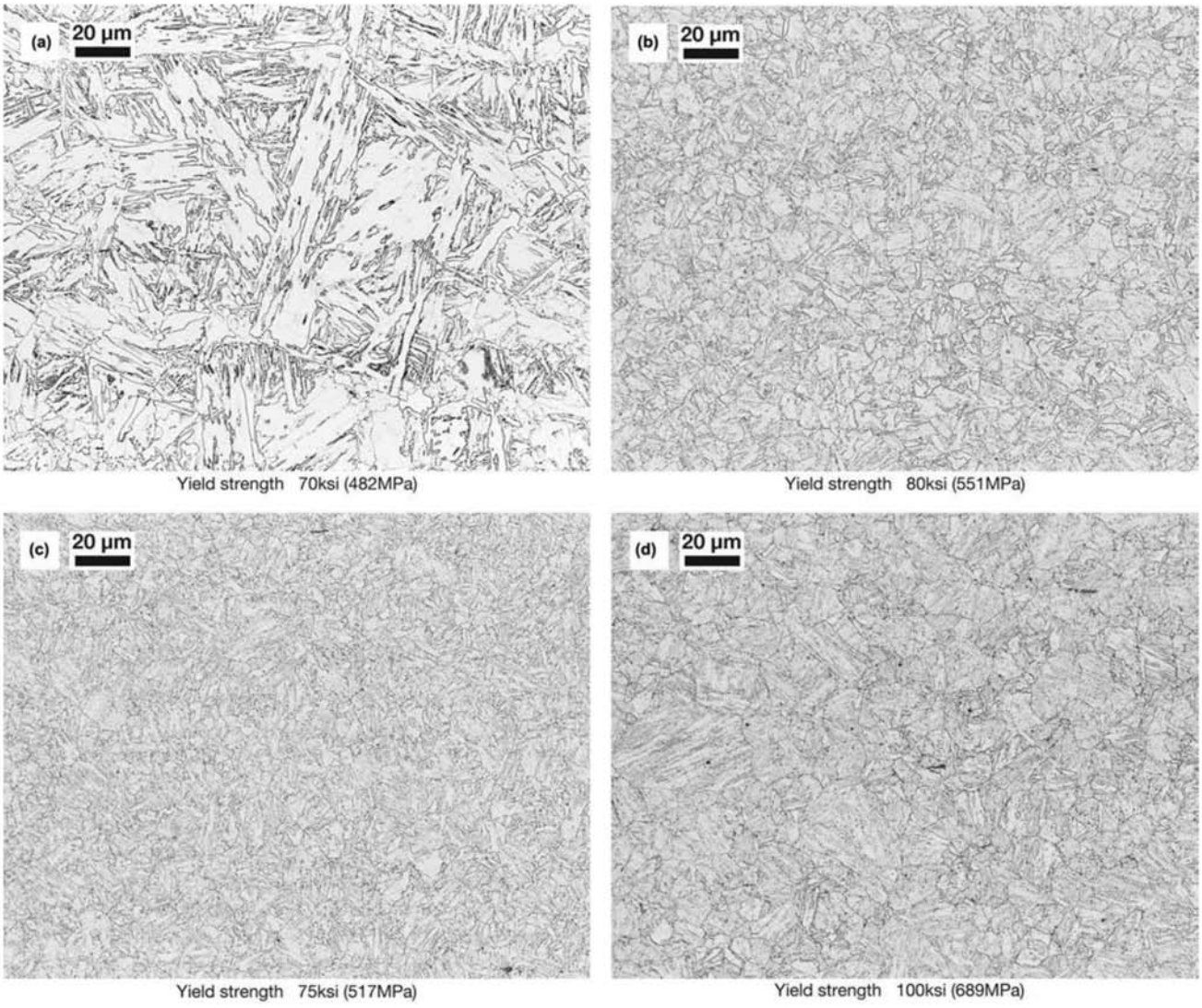

Fig. 14.4 Longitudinal cross sections near mid-thickness of hot rolled structural steel plates quenched and tempered to different yield strengths in the range of 480 to 700 MPa (70 to 100 ksi). (a) Widmanstätten ferrite or tempered bainite with carbides. Martensite was not formed in this steel. (b), (c), and (d) present tempered martensite. Prior austenite grain boundaries are visible. As the strength increases, the "acicular" feature of the microstructure is better defined. With higher magnification, some carbides were observed in the prior grain boundaries and between the martensite laths. The presence of carbides is more evident in the lower strength steels in this series. Because all plates are expected to come from the same steelmaker, it is probable that the single difference between the different strength plates is the tempering temperature. Etchant: nital 2% and picral 4%. Courtesy of National Institute of Standards and Technology. Source: Ref 4

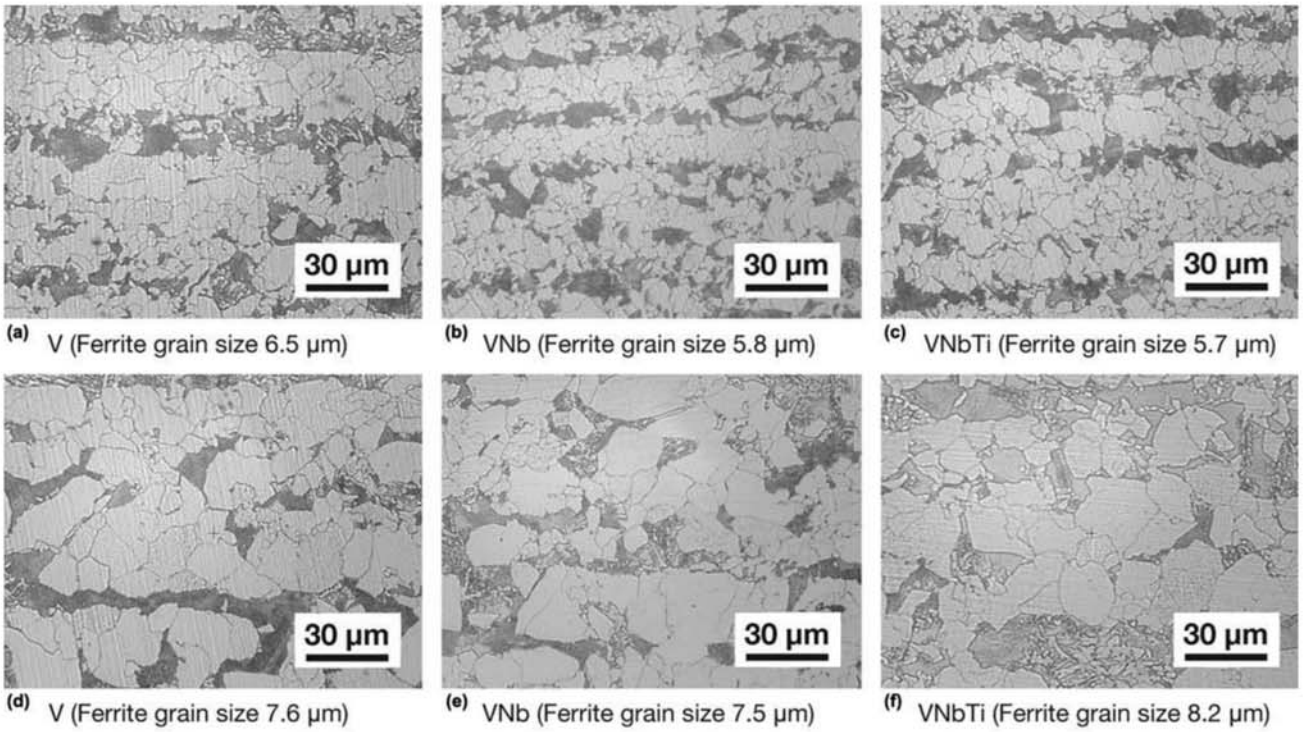

Fig. 14.5 Microstructures obtained with the use of thermomechanical processing in seamless tubes with a basic composition of approx. C = 0.15%, Mn = 1.5%, Si = 0.45% and microalloying additions of vanadium, niobium, and titanium, as indicated in the figures. Samples (a) to (c) present structures from steels that have been cooled until the complete transformation of austenite after the first stage of hot rolling and reheated for the final hot rolling of the tube. The ferritic grain size is indicated in each image. Samples (d) to (f) present microstructures of steels that did not suffer intermediate cooling and austenite transformation. Fig. 14.6 presents the effect of these microstructures on the material toughness. In all samples, polygonal ferrite and pearlite are observed. In samples (e) and (f), some acicular constituents, probably acicular ferrite, are present. Courtesy of R. N. Carvalho. Source: Ref 8

by cooling without any further heat treatment. The effect of changing the parameters of this processing cycle on the ferritic grain size of the final product is clear. Evidently, this depends on a favorable distribution of precipitate size, measured by TEM (Ref 8) and controlling the amount of dissolved precipitates. The effect of the ferritic grain size refinement on the steel toughness is clearly shown in Fig. 14.6. Gorni, Xavier et al. (Ref 9) studied the austenite decomposition kinetics in various microalloyed steels, determining their CCT diagrams and the final microstructures. Figure 14.7 presents the CCT curve for one of the steels in that investigation, and Fig. 14.8 shows two examples of the microstructures observed in their work.

The ability to reach the various strength levels of API 5L standard (Ref 10) is one of the most interesting proving grounds for the development of steel subjected to thermomechanical processing. The reason is clear when one considers the impact of steel strength on the final cost of a pipeline. Mechanical steel strength defines the wall thickness of the tubes and thus the weight of steel that must be used and the costs associated with the logistics of transporting and laying these tubes in place. When pipelines are hundreds or even thousands of kilometers long, these compound costs are extremely significant. API 5L standard is quite flexible with respect to the steel chemical com-

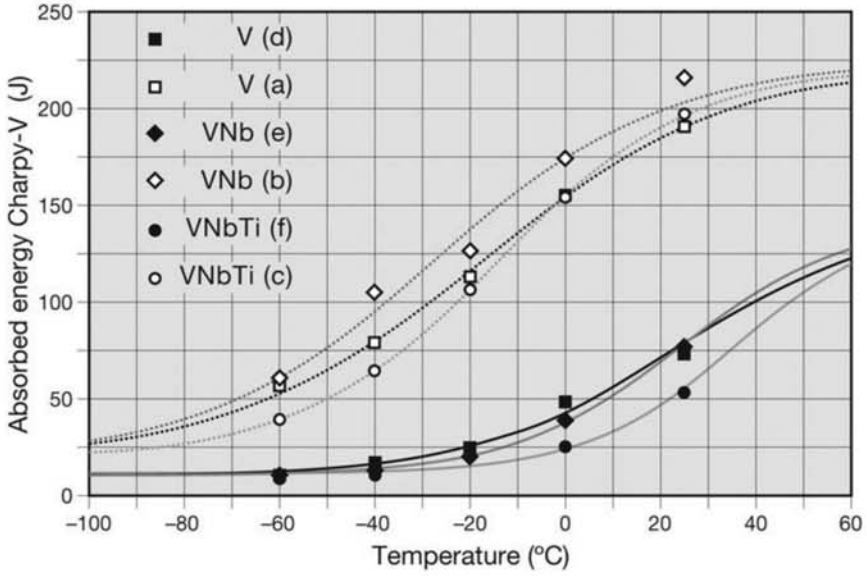

Fig. 14.6 Absorbed energy in impact test of the steels presented in Fig. 14.5. The effect of controlled thermomechanical treatment is evident. Source: Ref 8

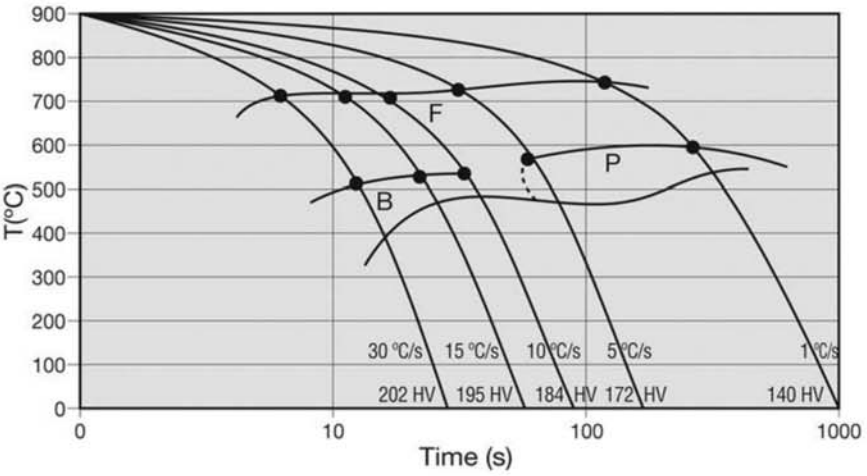

Fig. 14.7 CCT curve of a microalloyed steel containing C = 0.07%, Mn = 1.32%, Si = 0.13%, Al = 0.013%, Nb = 0.036%, and N = 0.0013%. Austenitizing: 900 °C (1650 °F), 360 s. In each cooling curve, the final hardness is also indicated. B = bainite, F = ferrite, P = pearlite. Source: Ref 9

position, but is quite strict when it comes to mechanical properties, carbon equivalent (relevant to the weldability), and some chemical elements, particularly the residuals. This has been one of the first standards to accept the application of steels subjected to thermomechanical processing (instead of requiring a defined heat treatment cycle) in pressure retaining applications, where safety is of paramount importance. As a result, a wide range of microstructures have been developed, usually with close collaboration between steelmaker and tube maker, to reach the different strength grades.

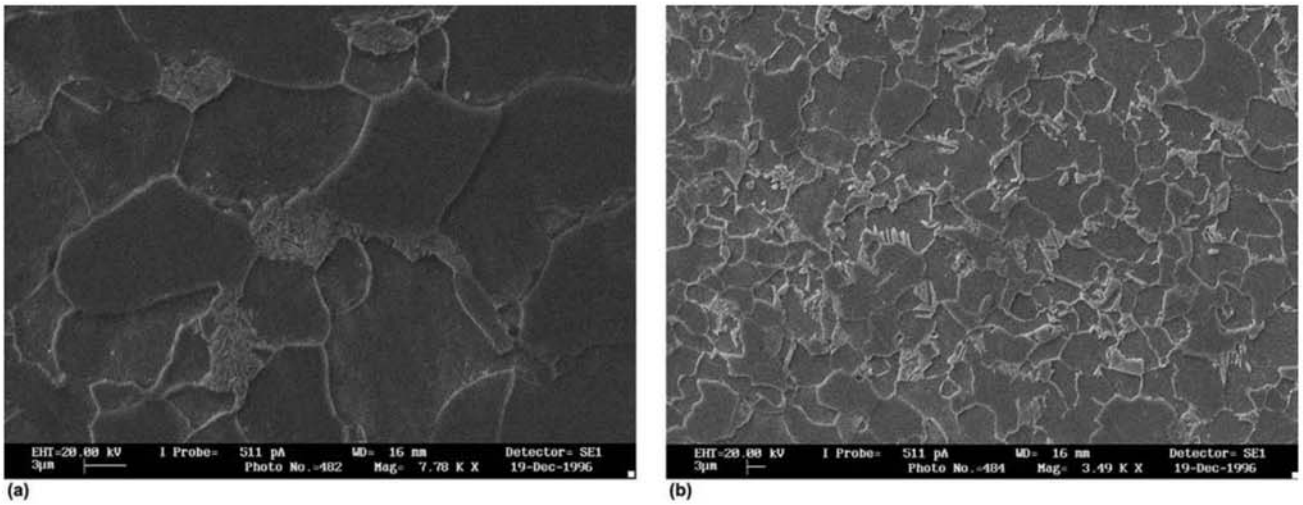

Fig. 14.8 Microstructures of the steel used for the determination of the CCT curve in Fig. 14.7. (a) Cooled at 5 °C/s (9 °F/s); equiaxial ferrite and fine pearlite; (b) cooled at 15 °C/s (27 °F/s); finer equiaxial ferrite, acicular ferrite, bainitic ferrite, and some massive ferrite. Etchant: nital 2%. SEM, SE. Courtesy of A. Gorni. Source: Ref 9

The combination of the target chemical composition and the exact thermomechanical cycle parameters to reach the desired structure is normally developed by each steelmaker based on available equipment, desired wall thickness, and expertise. As a rule, this is internal information and is rarely published to a complete extent. Some examples of these microstructures are presented in Fig. 14.9 to 14.11. The technological limit for these steels in 2008 was grade X120. This meant a yield strength of 827 MPa (120 ksi), with excellent weldability and toughness. In the case of the structure shown in Fig. 14.12, the absorbed energy at −40 °C (−40 °F) ISO-V test was 258J for the "lower bainite" structure and 167J for the structure composed of "upper bainite" and martensite-austenite (MA). These are significant toughness levels. Although there is still some restriction from the tube makers' point of view with respect to boron microalloying (due to concerns with weldability behavior and reproducibility of properties), the use of this element offer promising avenues, as shown in Fig. 14.12.

14.4 Steel for Concrete Reinforcement

The market for concrete reinforcement steel is very competitive. The basic standard for the supply of common reinforcement bar is ASTM A615 (Ref 13). This standard has few requirements related to chemistry and is mostly based on the specification of requirements for mechanical properties. For this reason, it advises the user about possible restrictions on weldability. When more restricted chemistry or a narrower range of properties is desired, ASTM A706 (Ref 14) may be used. Although most reinforcement bar is supplied in the hot-rolled condition or subjected to controlled cooling (as discussed further in this section), cold working is permitted in ASTM and other standards around the world. Cold-worked steels may suffer reduction of strength when welded, however, and this fact is noted in many international standards, including the ACI code (Ref 15). In ASTM standards, grades are designated by their minimum yield strength in ksi. Tendons for prestressed concrete are usually more

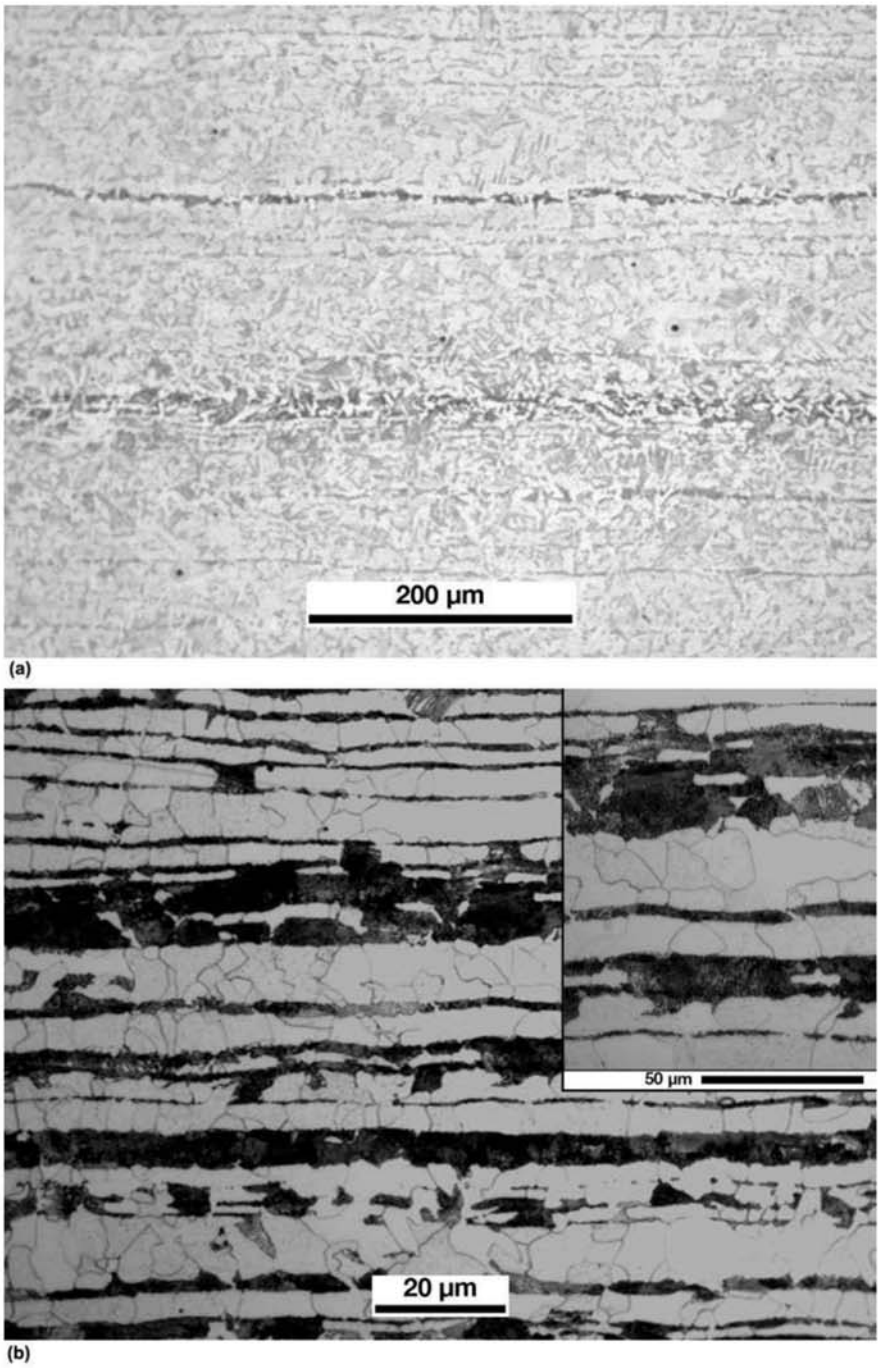

Fig. 14.9 Plates of (a) API X56 and (b) API X65 steels, produced through controlled rolling. Mid-thickness, longitudinal cross section. (a) Ferrite (both equiaxial and acicular), pearlite, and some banding. Elongated sulfides are visible. (b) Ferrite and fine pearlite, banded structure. Elongated sulfides are visible. (Compare to Fig. 14.1e). Courtesy of ArcelorMittal Tubarão, ES, Brazil.

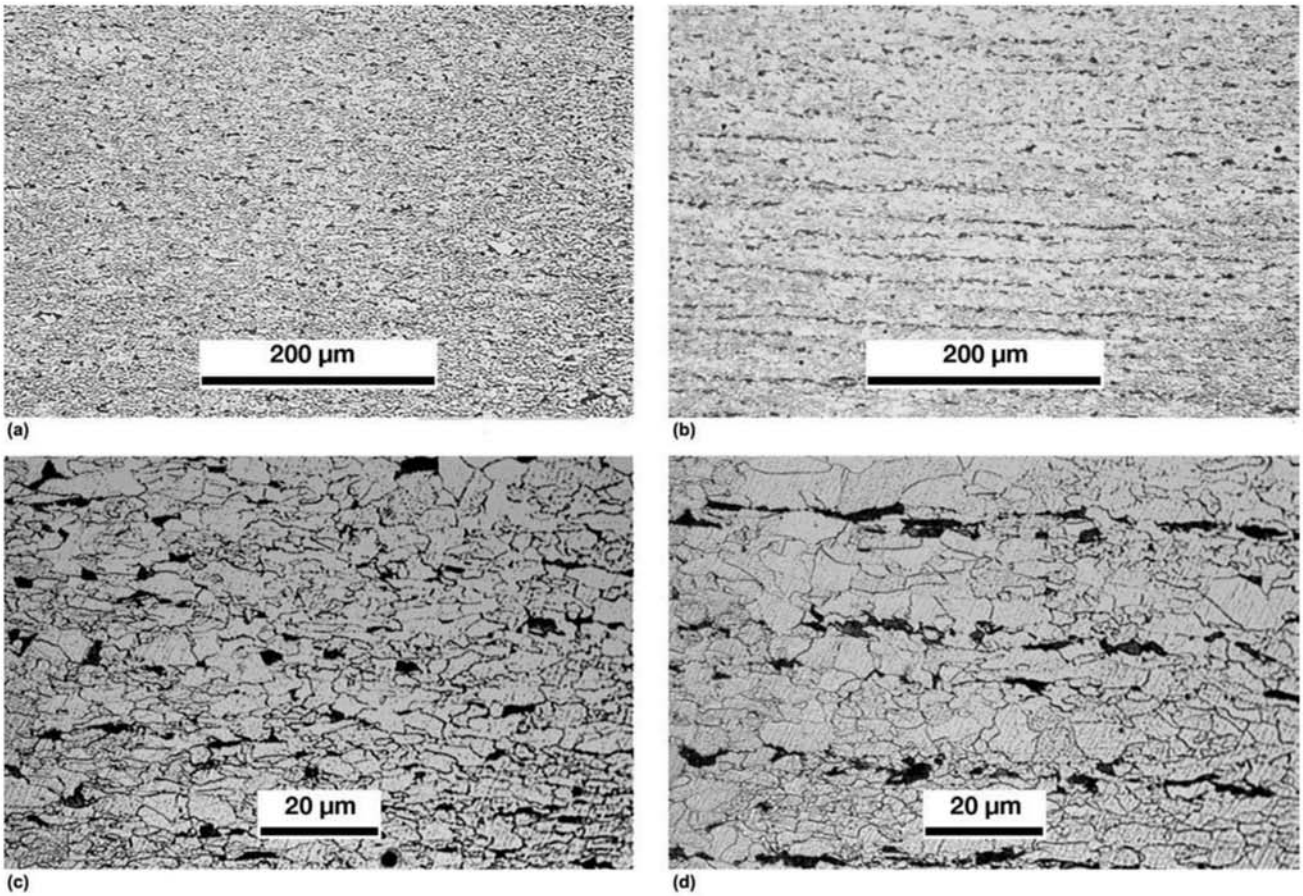

Fig. 14.10 Plates of API X70, steel, produced through controlled rolling. Longitudinal cross section. (a) and (c), at 1/4 thickness (t/4 position). (b) and (d) mid-thickness (t/2 position). Ferrite (ferritic grain size ASTM 11) and fine pearlite. Some banding. Courtesy of ArcelorMittal Tubarão, ES, Brazil.

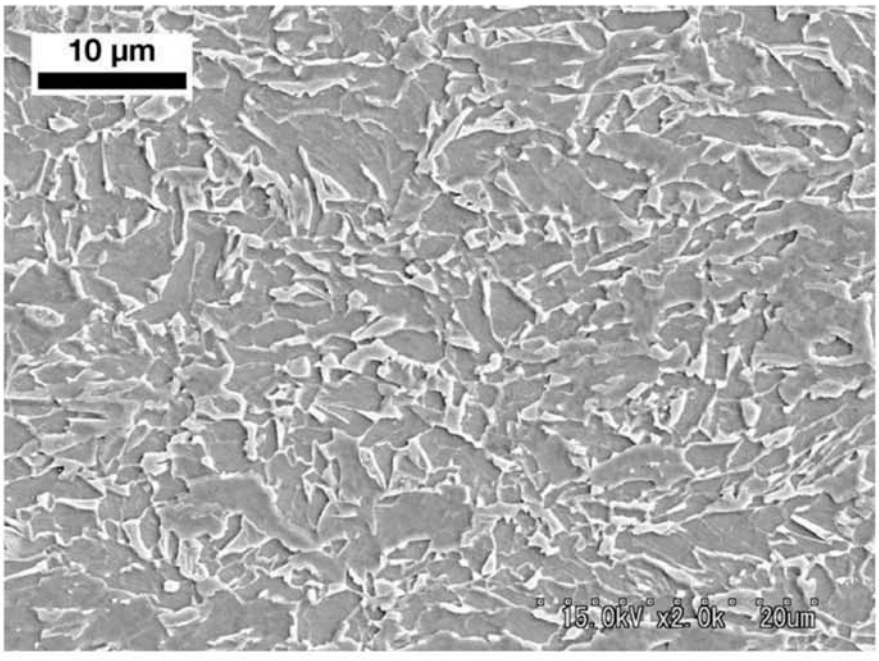

Fig. 14.11 Dual-phase API X100 steel for piping produced through controlled rolling. C = 0.06%, Mn = 1.96%, Nb = 0.04%, Ti = 0.01%, + Ni, Cu, Mo. Granular ferrite and bainite (martensite and retained austenite are also present). Courtesy of Nippon Steel Corporation. Source: Ref 11

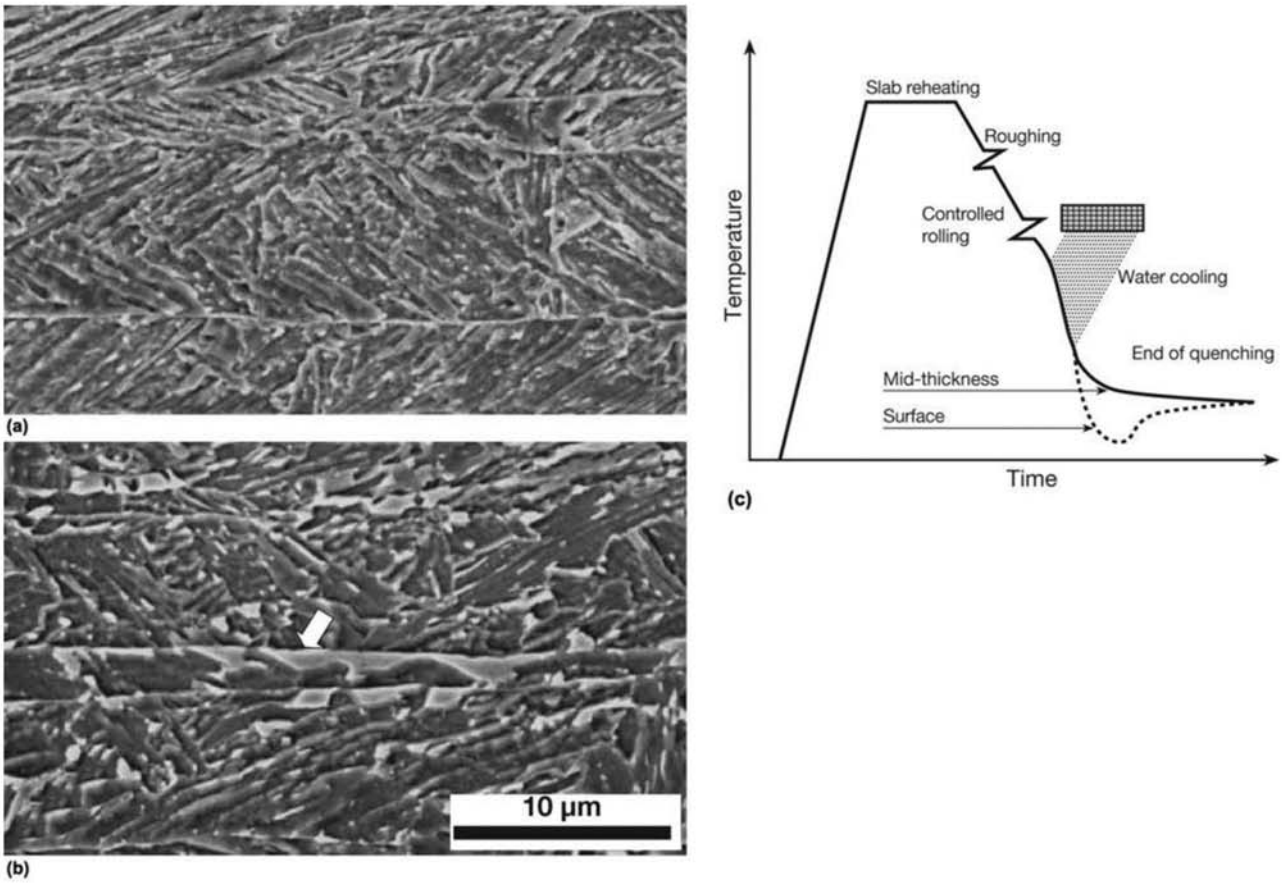

Fig. 14.12 Experimental API X120 steel produced by controlled rolling in accordance with the cycle presented in (c). Steel containing C ≅ 0.05%, Mn ≅ 1.95%, Mo ≅ 0.33%, B = 12 ppm and other additions, including titanium to prevent the formation of boron nitride. (a) Lower bainite. Quenching finished at 453 °C (845 °F). (b) Upper bainite and MA areas (martensite and retained austenite), indicated by arrows. Courtesy of Nippon Steel Corporation. Source: Ref 12

sophisticated products than regular reinforcing bars and are specified in a set of different standards, such as Ref 16.

Although not forbidden, it is advisable to refrain from welding reinforcing bars for which no explicit weldability guarantee is given (Ref 15). Steel mills strive to optimize chemical composition and processing to achieve the required strength and ductility (usually including bending tests), with the economics of processing in mind. In the case of steels that are to be welded, further care with respect to chemical composition and avoidance of cold working should be taken. Accelerated cooling is frequently used and its effect on weldability should also be considered. Figures 14.13 and 14.14 show the transverse cross section of two reinforcing bars manufactured to meet a minimum yield strength of 500 MPa (73 ksi) (for comparison, Grade 75 of ASTM A615 has a specified minimum yield strength of 520 MPa, or 75 ksi) produced using accelerated cooling. Tempcore, a trademark of the CRM Group (Ref 17) and Stelmor, a trademark of Primetals Technologies, are good examples of accelerated cooling processes. Figure 14.15 is a schematic diagram of the accelerated cooling cycle used in the Tempcore process. The rolling temperature is adjusted to guarantee a uniform and approximately constant tempera-

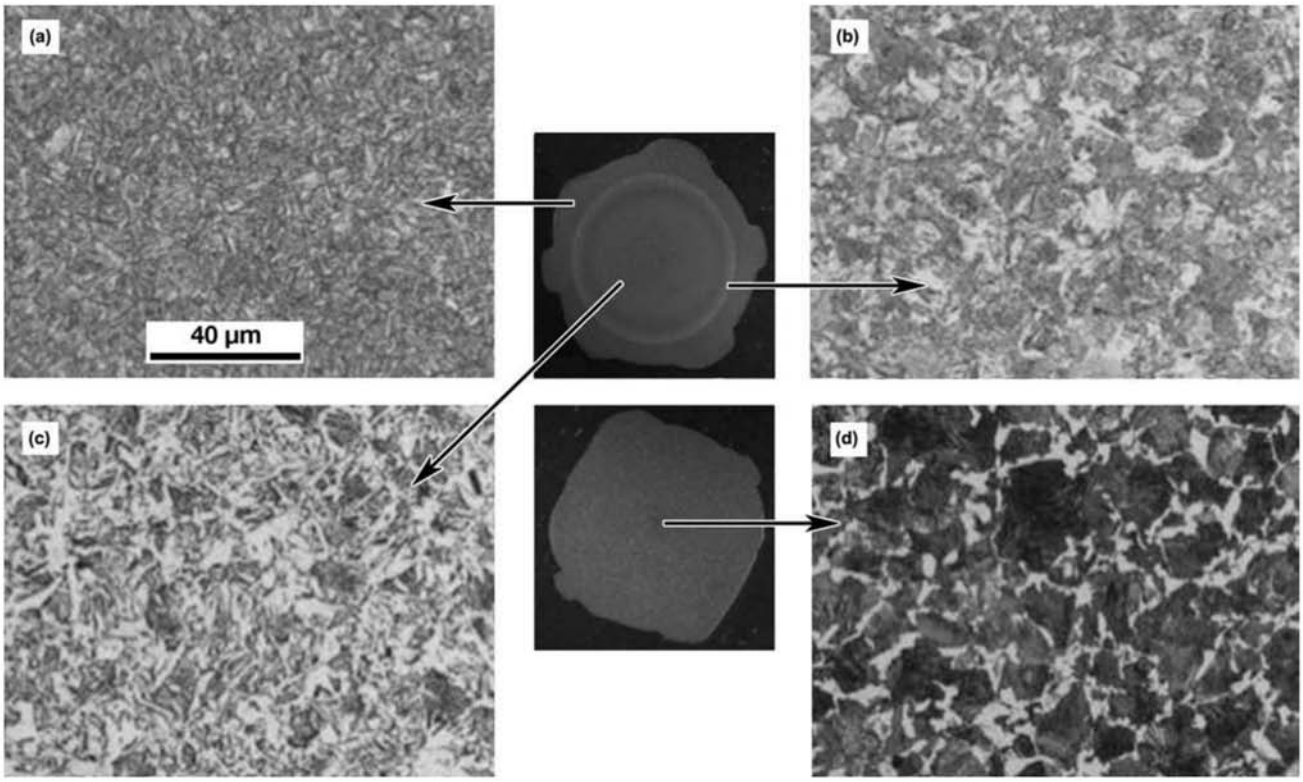

Fig. 14.13 Transverse cross section of reinforcing bar with minimum yield strength of 500 MPa (73 ksi). Top: macrograph of a bar subjected to accelerated cooling (see Fig. 14.15) after hot rolling. Corresponding micrographs: (a) tempered martensite, (b) pearlite and ferrite, (c) pearlite and ferrite. Bottom: macrograph of a bar subjected to forced air cooling (similar to Stelmor process). (d) Pearlite and ferrite. Etchant: nital 2%. Courtesy of ArcelorMittal Aços Longos, Juiz de Fora, MG, Brazil.

ture at the end of the hot rolling train. Then, the bar enters a cooling station using water as the quenching medium. This rapid cooling, indicated as the "first stage" in Fig. 14.15, leads to the formation of a martensite layer in the bar surface. When the bar leaves the water cooling, part of its core is still untransformed austenite, and part is martensite mixed with untransformed austenite. From this point on, as the bar core cools, the surface reheats, tempering the martensite in the surface layer, and the rest of the bar transforms. An alternative process involves forced air-cooling (Stelmor, for instance). In this type of process, at the end of hot rolling, the bar enters a water cooling station that brings it to temperatures around 900 °C (1650 °F), still fully austenitic. Then the steel undergoes accelerated cooling in a continuous bed where a forced flow of air is introduced. Besides changing the constituents of the microstructure, the accelerated cooling makes possible the increase of the volume fraction of pearlite beyond that predicted by the equilibrium phase diagram. Thus, accelerated cooling—even with forced air flow—makes it possible to establish conditions that form pearlite-rich microstructures with compositions away from the eutectoid composition. Figure 14.16 shows that there is a region in the Fe-C phase diagram in which it is possible to have austenite simultaneously saturated in ferrite and cementite. This is the thermodynamic condition necessary for pearlite formation. This region expands as the temperature is lowered, that is, as austenite transformation is slowed

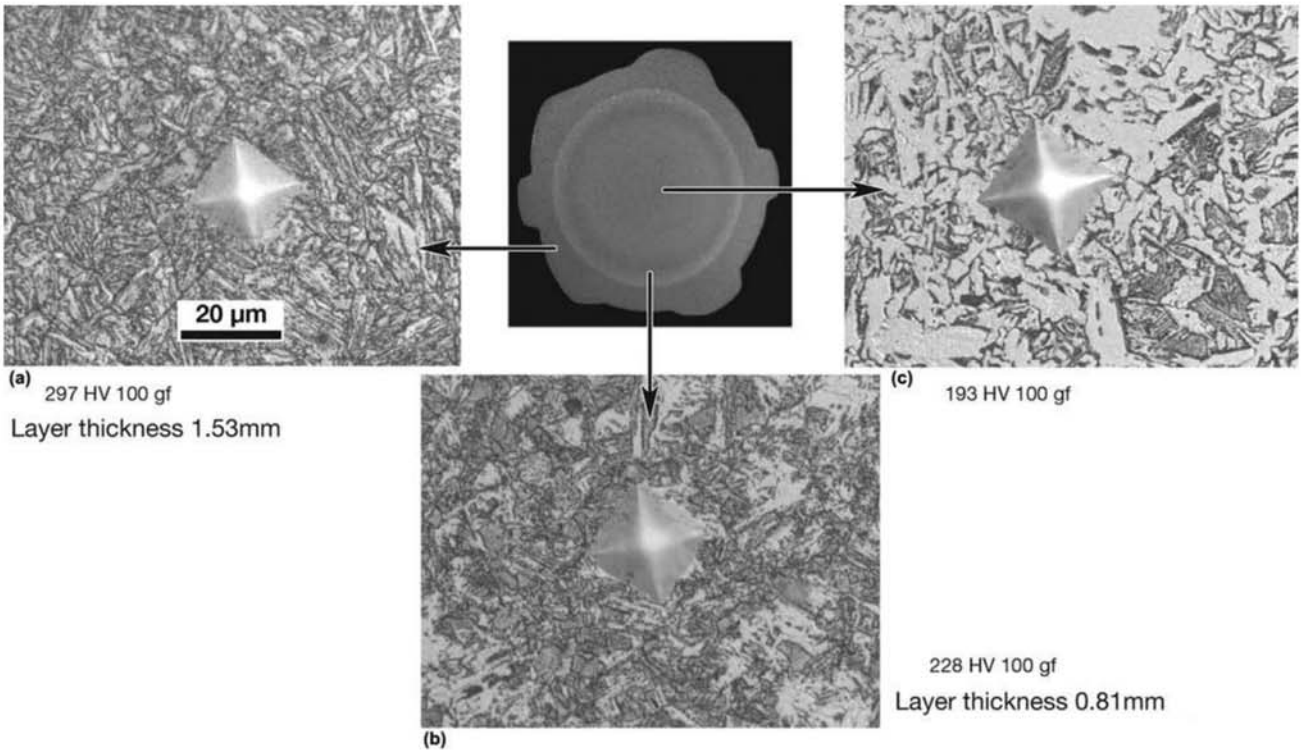

Fig. 14.14 Transverse cross section of reinforcing bar with minimum yield strength of 500 MPa (73 ksi) produced using accelerated cooling (see Fig. 14.15) after hot rolling. (a) Tempered martensite, (b) tempered martensite and acicular ferrite, (c) pearlite and acicular ferrite. The thickness and hardness of each layer with typical microstructure is also indicated. Vickers 100 gf impressions can be observed. Etchant: nital 2%. Courtesy of ArcelorMittal Aços Longos, Juiz de Fora, MG, Brazil.

on cooling. The result is that when the CCT curves of hypo-eutectoid steels are examined, it is possible to identify a cooling rate beyond which austenite can decompose directly into pearlite, without the formation of pro-eutectoid ferrite. Steels that are cooled close to this critical rate will have increased volume fractions of pearlite compared with the values expected from lever-rule calculations in equilibrium conditions.

Figure 14.17 compares the microstructure of an annealed AISI 1045 steel (annealed close to equilibrium and thus with the pearlite volume fraction close to the calculated value using the lever rule) with that obtained with the same steel subjected to accelerated cooling in a forced air cooling bed. The increase in the volume fraction of pearlite is evident. This results in significant increase in the tensile yield and ultimate strengths. Welding reinforcing steels is becoming more relevant. Thus, weldability is very important. Welding is important not only during construction, as there has also been a significant increase in the use of prewelded reinforced bar mats or welded wire mesh (see the section 14.6 "Welding of Structural Steels—Metallographic Aspects").

Steels for Thick-Wall Pressure Vessels (High-Pressure Vessels)

In many applications where high pressures are present, it is necessary to combine steels with higher strengths than usual structural steels with considerable wall thickness. In these cases, the choice is usually to use heat-

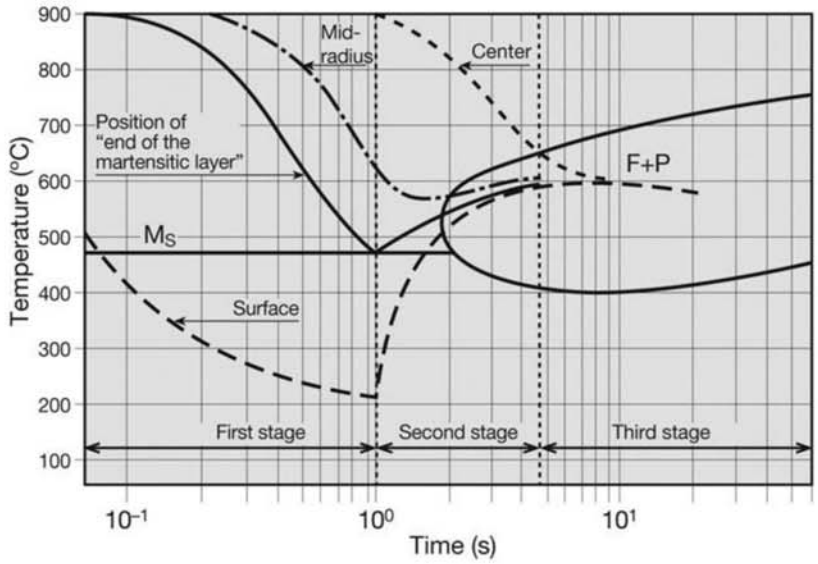

Fig. 14.15 Cooling curves of different positions on the radius of a bar subjected to accelerated cooling superimposed on the CCT curve (schematic) of the steel. Up to the end of the first stage of cooling, the bar surface cools significantly below the steel M_s temperature. The curve identified as position of "end of the martensitic layer" represents a point in the bar that at the end of the first stage of cooling will reach the M_s temperature exactly. Thus, martensite is not formed at this point. Because the center of the bar is subjected to slower cooling, it is still at high temperatures when the surface layer has already transformed. The second stage of cooling is characterized by surface reheating (that tempers the martensite that has formed in the first stage). From this point, the cooling rates are such that ferrite (F) (acicular or not) and pearlite (P) may form. Source: Ref 18

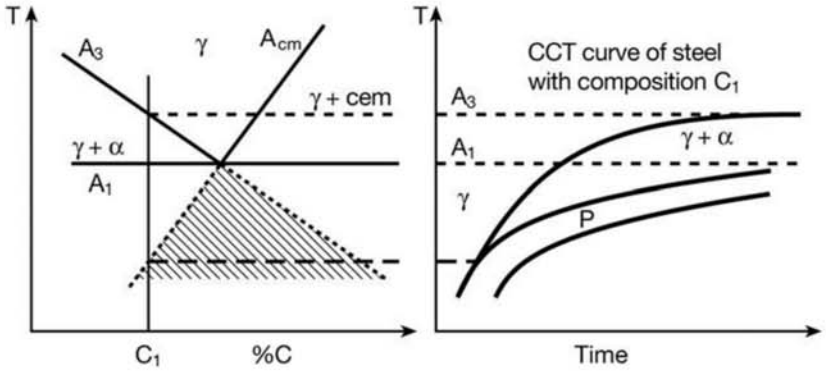

Fig. 14.16 Left: schematic Fe-C phase diagram. Right: CCT curve corresponding to the steel with composition C_1 indicated in the diagram in the left. The dashed region in the equilibrium phase diagram indicates the conditions of temperature and chemical composition in which austenite would be supersaturated in ferrite and cementite (region delimited by the metastable extension of the A_3 and A_{cm} lines below the A_1 line). Austenite in this region can decompose to pearlite. The CCT curve indicates that beyond a critical cooling rate, the formation of pro-eutectoid ferrite can be prevented, forming only pearlite. The closer to this critical cooling rate, the lower the volume fraction of pro-eutectoid ferrite. Source: Ref 19

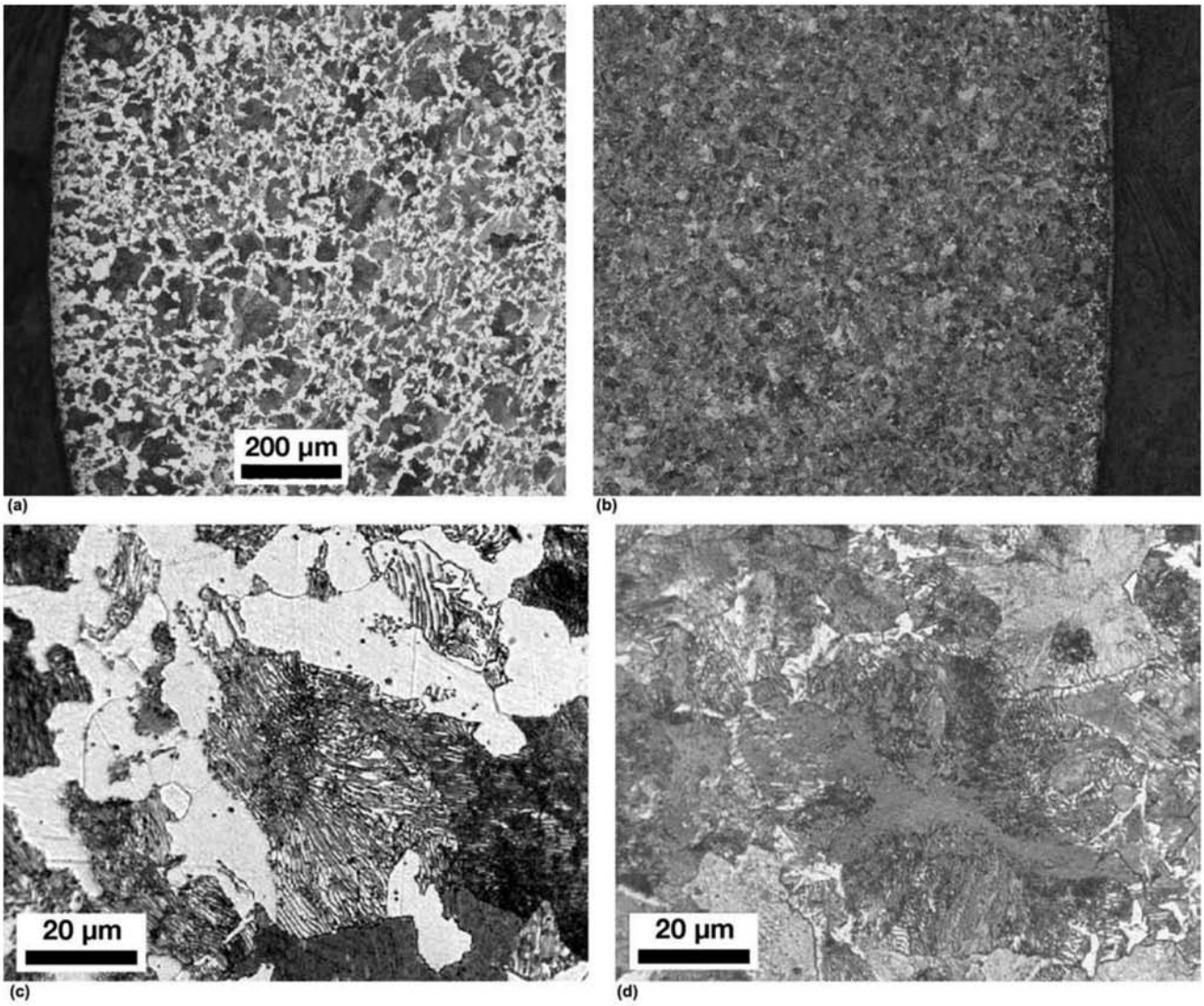

Fig. 14.17 Transverse cross section of wire rod of AISI 1045 steel annealed (a) and (c) and subjected to forced air accelerated cooling (Stelmor) from the austenitic region (b) and (d). Lever-rule calculations are applicable only to cooling near equilibrium, which is the case of the annealed steel. Etchant: nital 2%. Courtesy of ArcelorMittal Aços Longos, Juiz de Fora, MG, Brazil

treatable steels with a balanced chemical composition to achieve good hardenability (martensitic or bainitic) with moderate to low carbon contents to guarantee weldability. Steels such as AISI 8630 Modified, frequently used in the subsea oil industry, have good hardenability and thus can transform to martensitic structures even in heavy wall parts. In this case, the chemical composition was developed to achieve good hardenability with limited additions of nickel, because NACE International has recommended a 1% Ni limit for steels used for applications where the presence of H_2S may lead to stress corrosion (Ref 20). Steel specified according to ASTM A508 Gr.3 (forgings) or ASTM A533 Cl.1 (plates) (both with properties and chemical composition similar to the German Steel 20MnMoNi55 and the French steel 16 MND 5) is widely used in thick-wall pressure vessels and heat exchangers in nuclear power plants. Figure 14.18 presents the CCT curve for this steel, and Fig.

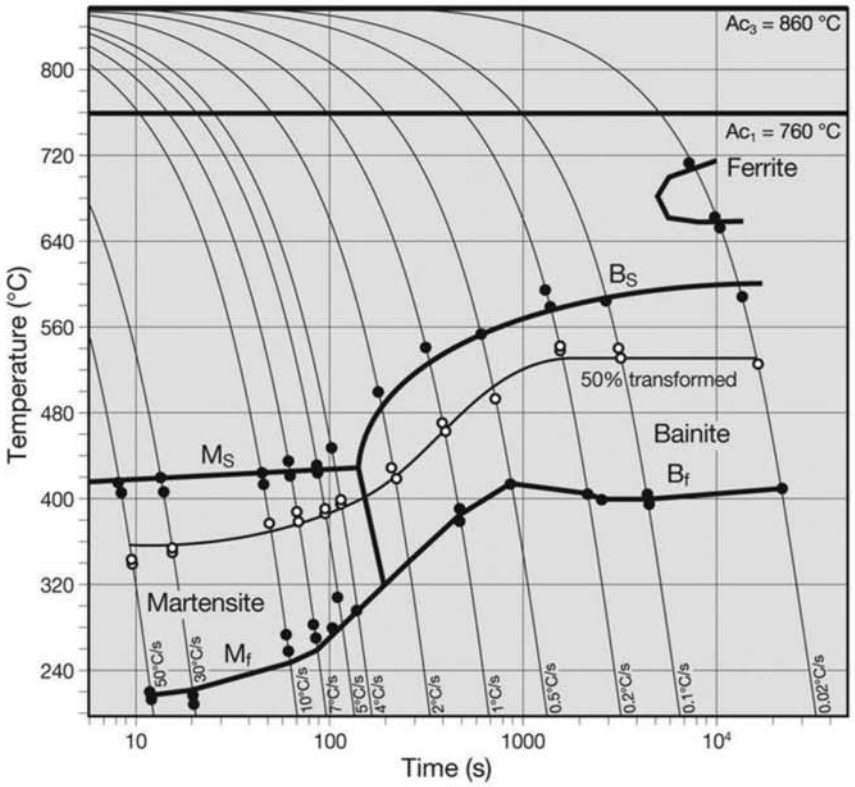

Fig. 14.18 CCT curve for ASTM A533 Cl.1 steel containing C = 0.2%, Mn = 1.8%, Mo = 0.49%, Ni = 0.83%, Cr = 0.15%. Austenitization at 1100 °C (2010 °F) for 30 min. The cooling rates are indicated on the diagram. The corresponding microstructures are shown in Fig. 14.19. Courtesy of B. Marini (CEA, France). Source: Ref 21, 22

14.19 shows the various microstructures obtained with this steel at different cooling rates (Ref 21, 22). A fully bainitic structure will be formed in the center of plates ranging from around 100 mm (4 in.) thickness (2 °C/s, or 4 °F/s) to 490 mm (19 in.) thickness (0.1 °C/s, or 0.2°F/s) when the usual water quenching treatment is used. Figure 14.20 presents microstructures of a 220 mm (9 in.) plate, water quenched and tempered, used for the manufacture of a primary circuit component in a nuclear power plant. The variation of structures from the surface to the center of the plate, in accordance with Fig. 14.18, is evident. At this magnification, the additional differences in structure, caused by segregation and highlighted in Fig. 11.52 (Chapter 11, "Hot Working," in this book), are not visible. The microstructure in the center of the plate corresponds to that of a somewhat slower cooling than predicted for this plate when comparing with those of Fig. 14.19 (calculated cooling rates are indicated in the caption of Fig. 14.20). This difference may be caused by different austenite grain size when quenching or by less efficient cooling than expected in industrial conditions.

Microstructure is very important for the achievement of the right combination of toughness and strength, essential for these applications. Kim, Lee, and Lee (Ref 24) evaluated crack paths during impact tests at –100 °C (–150 °F) of these steels. They have observed that prior-austenitic grain boundaries

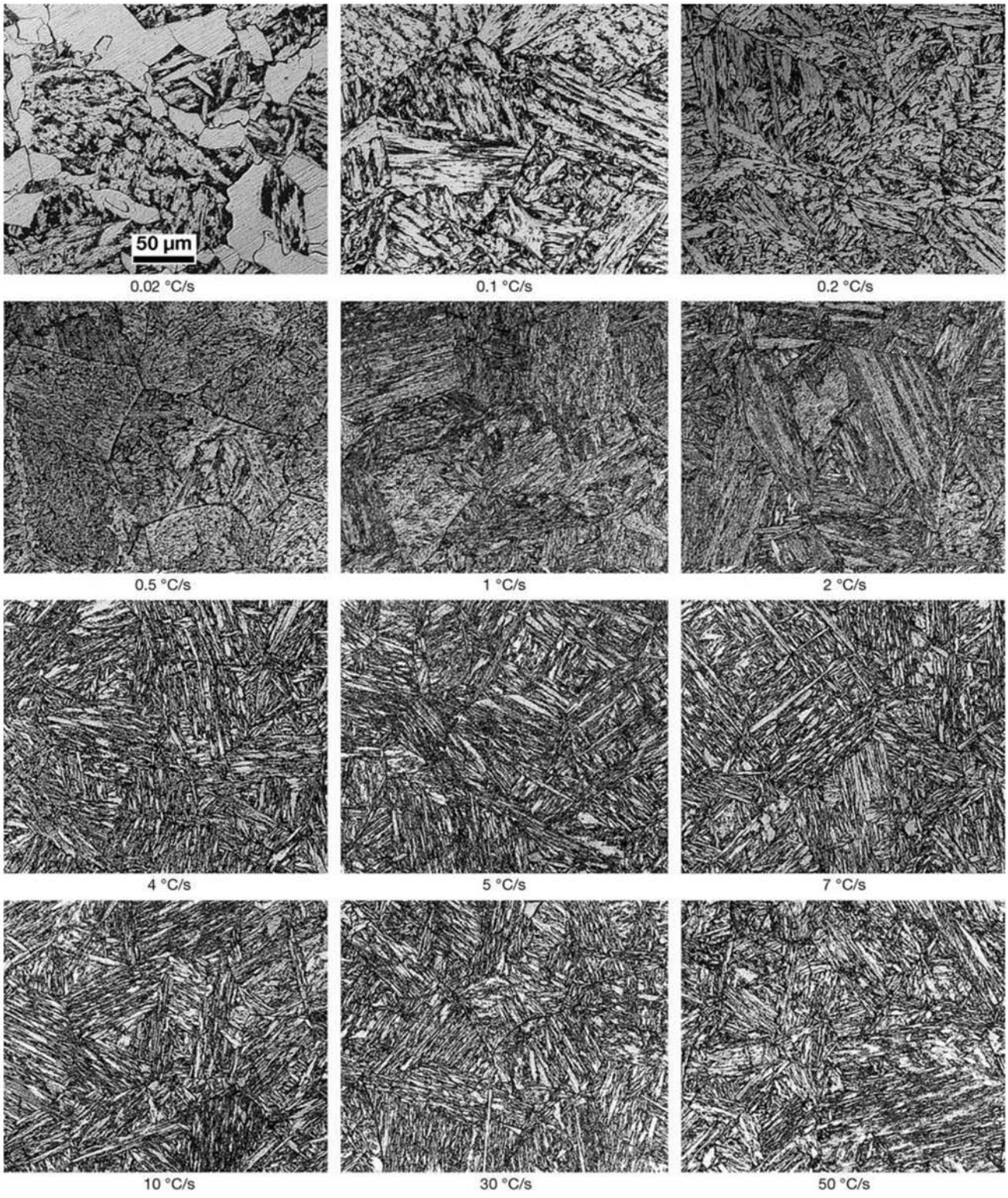

Fig. 14.19 Microstructures of ASTM A533 Cl.1 (CCT curve in Fig. 14.18). The cooling rates from the austenite region are indicated. It is possible to distinguish martensitic microstructure (laths, from 4 to 50 °C/s, or 7 to 90 °F/s) from bainitic structures (0.1 to 2 °C/s, or 0.2 to 4 °F/s). With a rate of 0.02 °C/s (0.04 °F/s) polygonal ferrite and bainite are formed. Etchant: nital 2%. Courtesy of B. Marini (CEA, France). Source: Ref 21, 22

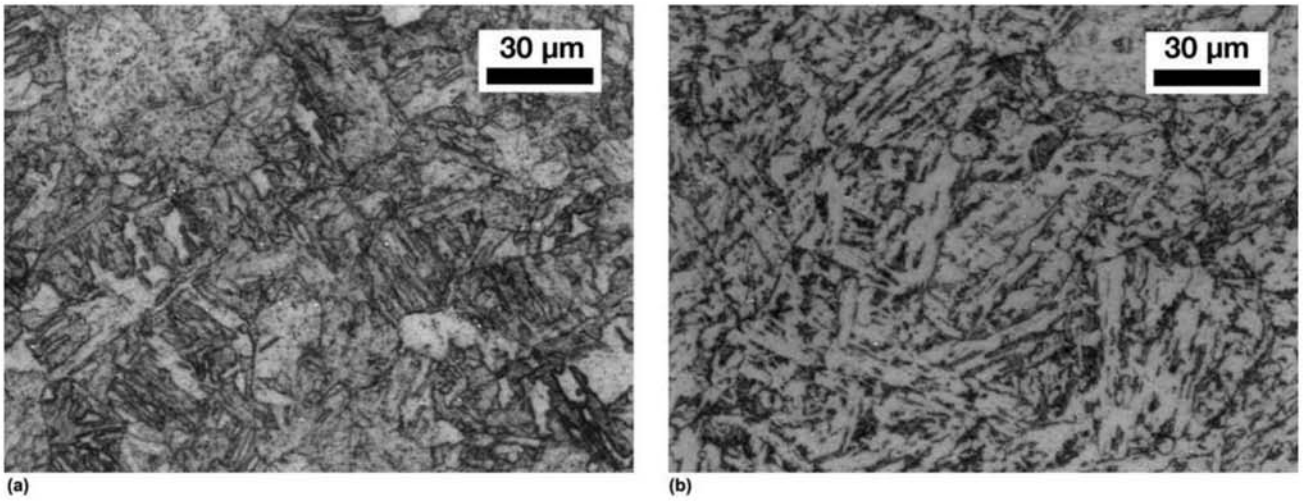

Fig. 14.20 20MnMoNi55 steel plate with 220 mm (9 in.) thickness austenitized at 900 °C (1650 °F) for 8.5 h, water quenched and tempered at 635 °C (1175 °F) for 6.5 h. (a) Microstructure 15 mm (0.6 in.) under the plate surface (cooling rate ≅ 7 °C/s, or 13 °F/s), martensite. (b) Microstructure at mid-thickness (cooling rate ≅ 0.48 °C/s, or 0.9°F/s), bainite. Etchant: nital. Courtesy of M. M. Moraes. Source: Ref 23

and bainite packet boundaries deflect or even stop cracks, as shown in Fig. 14.21. To protect the fracture surface during sample preparation and make possible the examination of the microstructures right under the fracture surface, they chemically deposited a layer of nickel on the fracture surface.

14.5 Steels for High-Temperature Pressure Vessels

Steels with the target composition 2.25 Cr 1 Mo (ASTM A336 F22) are also used in structural applications where thick parts with homogeneously high strength is desired. These steels have a significant bainitic hardenability, as shown in the CCT diagram in Fig. 14.22. These steels were initially designed and are most widely used in high-temperature applications, up to 650 °C (1200 °F) (Ref 1, 26). The most usual supply conditions for high-temperature application of F22 or T22 (ASTM A213) in pressure vessels and piping are summarized in Table 14.1. When high-temperature applications are considered, it is essential to adhere exactly to the recommended heat treatment cycles specified in the standards, because the proper microstructure is essential for the application. Measuring room-temperature properties and observing the microstructure at the optical microscope level are no guarantee of proper behavior during long time use at high temperatures. For room-temperature and lower-temperature applications, alternative heat treatment cycles that will lead to the desired strength and toughness combination can be used. Figure 14.23 shows usual microstructures of 2.25 Cr 1 Mo in different heat treatment conditions, as listed in Table 14.1. The creep resistance of the different microstructures depends on the applied stress. For relatively low stresses, the material with ferrite-pearlite microstructure shows the longest lifetime under stress. For higher stresses, quenched and tempered material presents better behavior. The microstructure of these steels suffers changes during long time service at high temperatures. Some of the carbides dissolve while other, more stable carbides will precipitate and coalesce. Furthermore, the bainite substructure will undergo recovery. Figure 14.24 presents the microstructure of

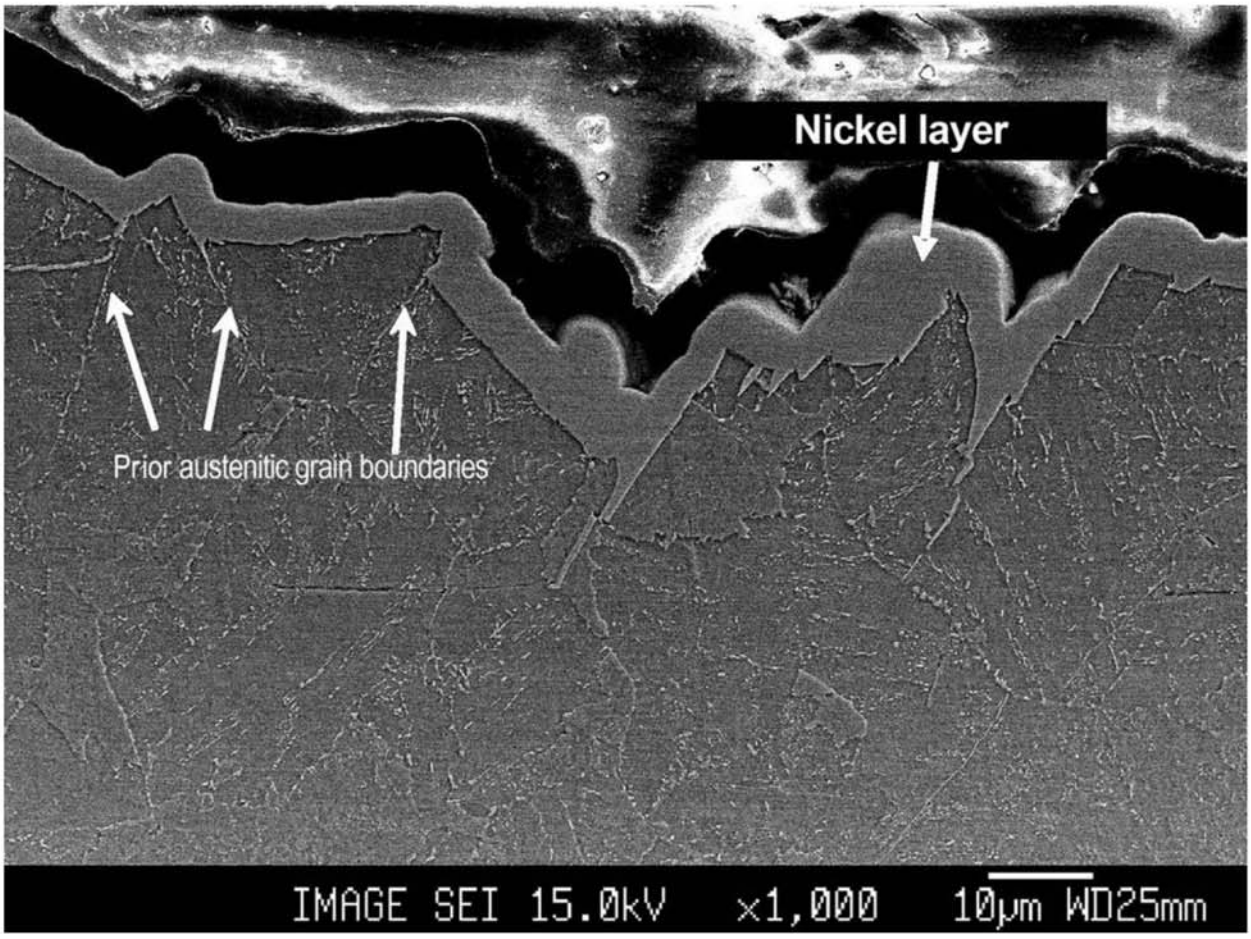

Fig. 14.21 Cross section transverse to the fracture surface of ISO-V impact specimen tested at –100 °C (–150 °F), steel ASTM A533 Cl.1. The fracture changes direction at the prior-austenitic grain boundaries. To make possible the observation of the region close to the fracture surface without damage, a layer of nickel 3–5 μm thick was deposited on this surface by a chemical process. SEM, SE. Courtesy of S. Lee, Pohang University of Science and Technology, South Korea.

F22 steel quenched and tempered for applications at room to moderate temperature, where creep resistance is not an important factor. This steel usage has increased because large and complex parts may be quenched with very good results, even in media with lower quenching severity, in view of its extreme bainitic hardenability. While the mechanical properties that can be reached with the commercially available steels are quite satisfactory (Ref 18, 26), this becomes an area of great interest for applications in advanced nuclear reactors, when materials that are not subjected to neutron activation are needed. The 9 Cr steels have been developed to increase their creep resistance and various alloying elements have been considered and evaluated to design "low activation" steels. Many of the microstructural changes observed in the development of these steels are only noticeable with TEM observation. Figure 14.25 shows some of the variations of the 9 Cr steels as summarized and presented in Ref 27. Figure 14.26 shows that one of the mechanisms that leads to loss of creep resistance in these steels is the coalescence of martensite laths, due to the movement of their interfaces at high temperature. Ta-

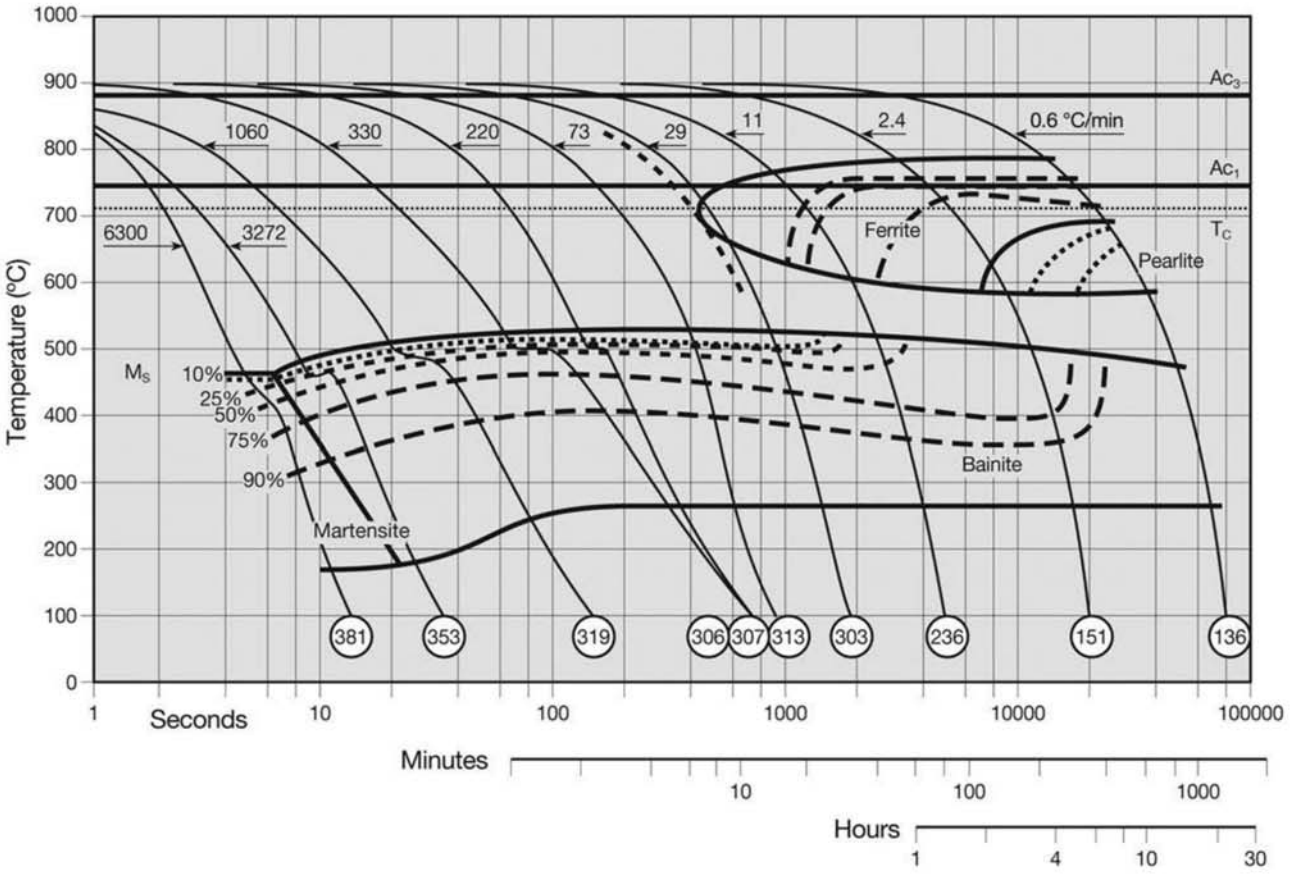

Fig. 14.22 CCT curve for F22 (2.25 Cr 1 Mo) steel. Circled numbers are as-quenched HV hardness values. Martensite formation is almost impossible in this steel. However, there is a very wide range of cooling rates that lead to bainite formation. Source: Ref 25

Table 14.1 Some usual heat treatment conditions for the supply of 2.25 Cr 1 Mo steel for high-temperature applications

Heat treatment condition and applicable standard	Thermal cycle
Annealed (JIS STBA 24)	930 °C (1705 °F), cooling to 720 °C (1330 °F) followed by air cooling
Normalized and tempered (JIS SCMV 4NT)	930 °C (1705 °F), air cooling followed by 740 °C (1365 °F), air cooling, followed by tempering at 700 °C (1290 °F), cooling inside the furnace
Quenched and tempered (ASTM A542)	930 °C (1705 °F), water quenched, followed by double tempering: 630 °C (1165 °F), air cooling and 600 °C (1110 °F), air cooling

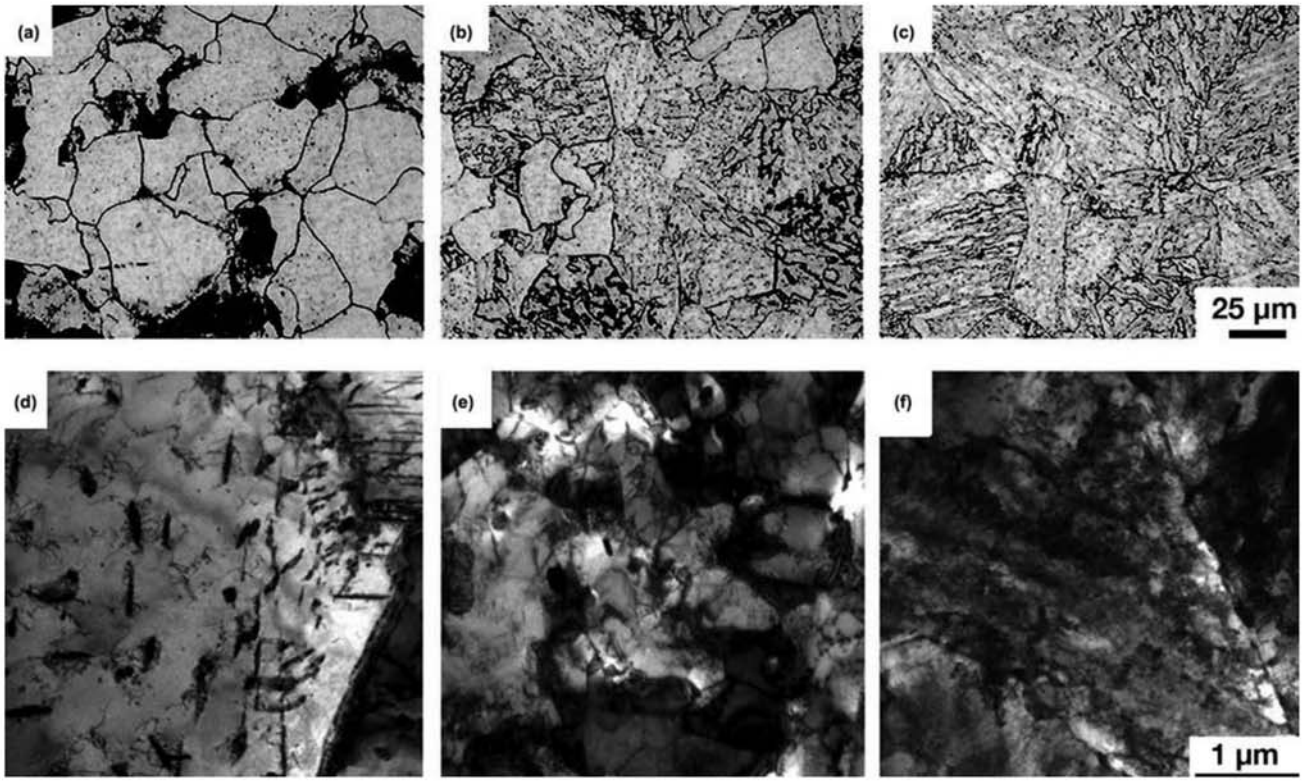

Fig. 14.23 Typical microstructures for the usual supply conditions for 2.25 Cr 1 Mo steel. Grade JIS STBA24. (a) Annealed, ferrite and pearlite. (b) Bainite and ferrite. (c) Bainite. (d) Carbides dispersed in ferrite. Grade JIS SCMV 4NT. (e) Dislocation substructure and small carbides. Grade ASTM A542. (f) Dislocation substructure and small carbides in bainite. (a), (b), and (c) Etchant: nital. (d), (e), and (f): TEM. Courtesy of F. Abe, National Institute for Materials Science (NIMS), Japan.

14.6 Welding of Structural Steels—Metallographic Aspects

neike, Abe, and Sawada (Ref 28) dramatically increased the creep strength of these steels by lowering the carbon content and promoting the formation of a fine dispersion of carbides in the lath boundaries to prevent their movement.

The study of the phase transformations happening during welding and their control through the selection of welding processes and parameters is beyond the scope of this book. There are excellent texts on the subject, such as Ref 29. Thus, the objective of this section is to present and discuss some of the important and interesting effects of welding on the micro and macrostructure of steels. When a heat source (such as the welding electrode) moves along a piece of material, it generates distinct time-temperature profiles in each position of the part. Rosenthal (Ref 30) proposed the first mathematical solutions for this problem. In his approach, the heat source is surrounded by a steady-state temperature field, when observed in the reference frame moving with the source. When this stationary solution is converted to the reference frame of the part being welded, time-temperature profiles can be derived for each point in the part. Figure 14.27 presents the temperature distribution around a moving heat source, the thermal cycles calculated for some

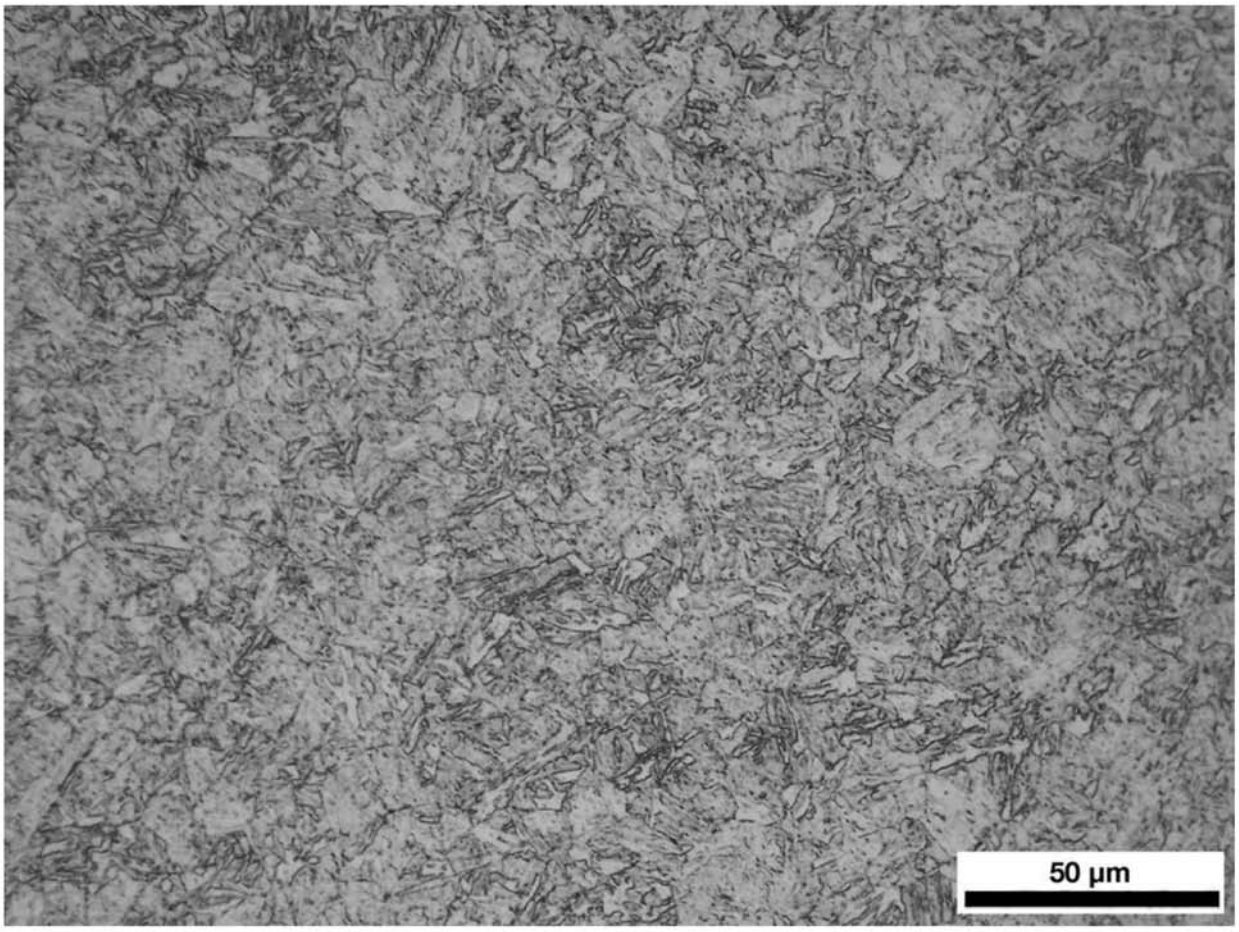

Fig. 14.24 F22 steel quenched and tempered to 22 HRC hardness. Bainite. Courtesy of A. Zeemann, Tecmetal, Rio de Janeiro, Brazil.

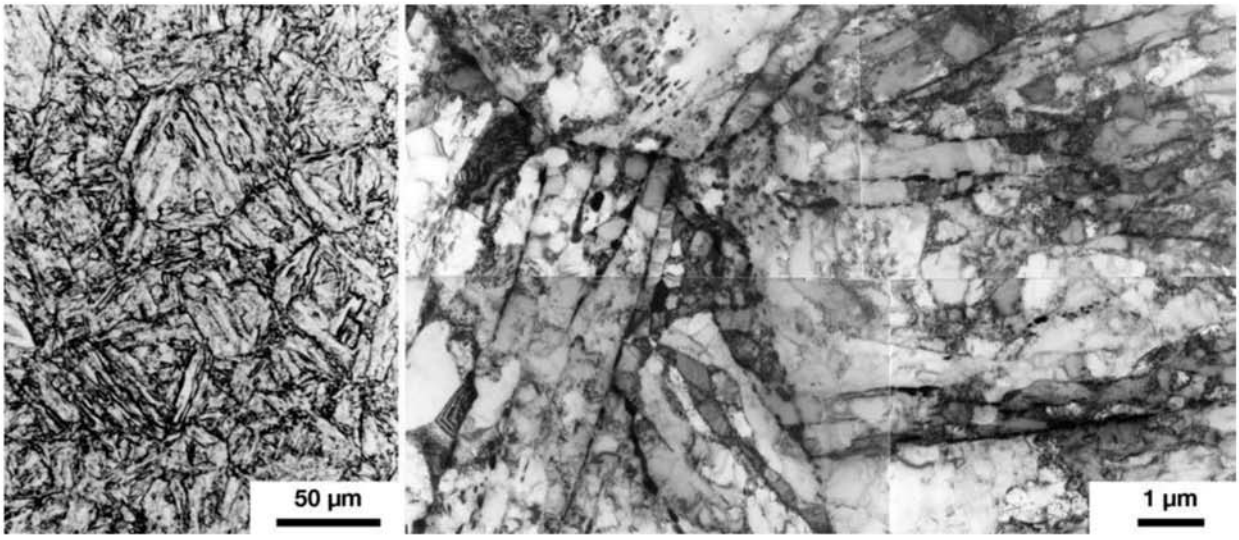

Fig. 14.25 (a) Optical and (b) TEM. Steel for high-temperature application containing C = 0.1%, Cr = 9%, W = 2%, quenched and tempered. Martensite laths in packets. Dislocations and subgrains inside the laths. Carbides precipitated mostly at the lath interfaces. Courtesy of F. Abe, National Institute for Materials Science (NIMS), Japan.

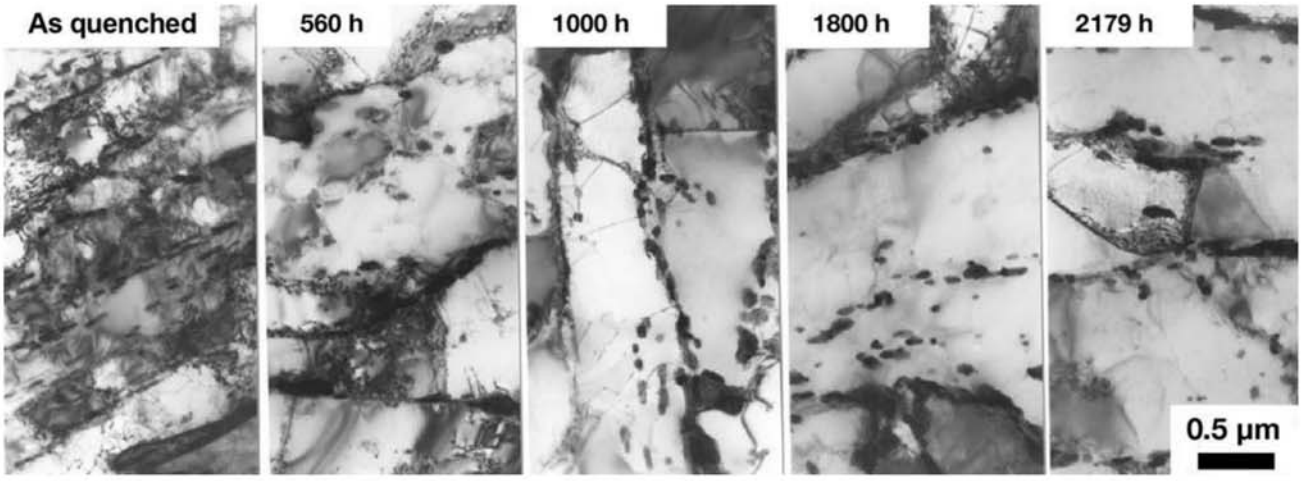

Fig. 14.26 The steel shown in Fig. 14.25 after creep testing at 600 °C (1110 °F) and 118 MPa (17 ksi). Time to rupture was 2179 h. It is possible to follow the microstructure evolution with time, during use under these conditions: recovery, in particular close to the prior austenitic grain boundaries, eliminating substructure and martensite dislocations and the formation of precipitate, probably $Cr_{23}C_6$. Courtesy of F. Abe, National Institute for Materials Science (NIMS), Japan.

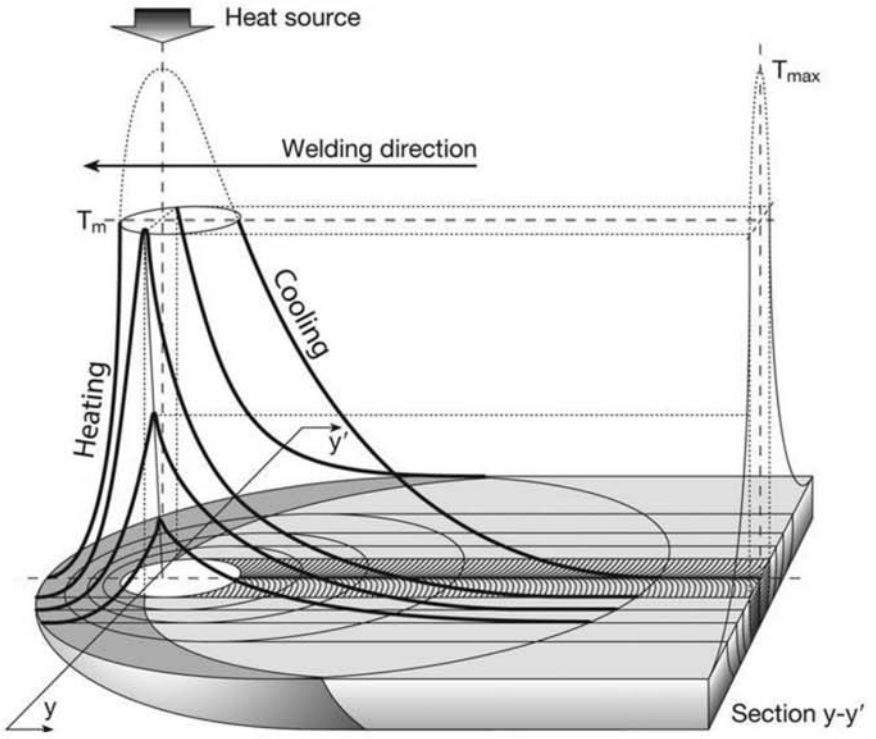

Fig. 14.27 Temperature distribution around a moving heat source (such as the welding electrode in a weld joint). The thick lines parallel to the weld axis present the thermal cycles (temperature (T) versus time (t)) for points at well-defined distances to the weld axis. Section y-y' records the maximum temperatures reached by points at a given distance from the weld axis.

points around this source as well as a "cross section" where the maximum temperature reached at each distance from the weld centerline is recorded. Thus it is possible to know the thermal cycle to which each point in the welded joint has been subjected. The thermal profiles in the plane transverse to the weld direction (section y-y' in Fig. 14.27) may then be superimposed on an equilibrium phase diagram to evaluate the possible effects associated with

the maximum temperature to which each point of the material was exposed, as shown in Fig. 14.28.

Figure 14.29 presents the metallographic structure of a weld joint in a structural steel, indicating the various important regions in this joint. Larger magnification images of the various regions of the joint are presented in Fig. 14.30. As in welding, flame, electrode, or plasma cutting (or any other heat source) will create a heat-affected zone in the material, as shown in Fig. 14.31.

Because weldability is a fundamental requirement for structural steels, studying the transformations associated with welding thermal cycles and predicting the resulting microstructures and properties are extremely important research areas in metallurgy, where metallographic analysis is an essential tool. It is normal to perform thermal cycle simulations to evaluate the effects on the material to be welded. Besides giving better control of the experimental conditions, this method makes it possible to produce larger sam-

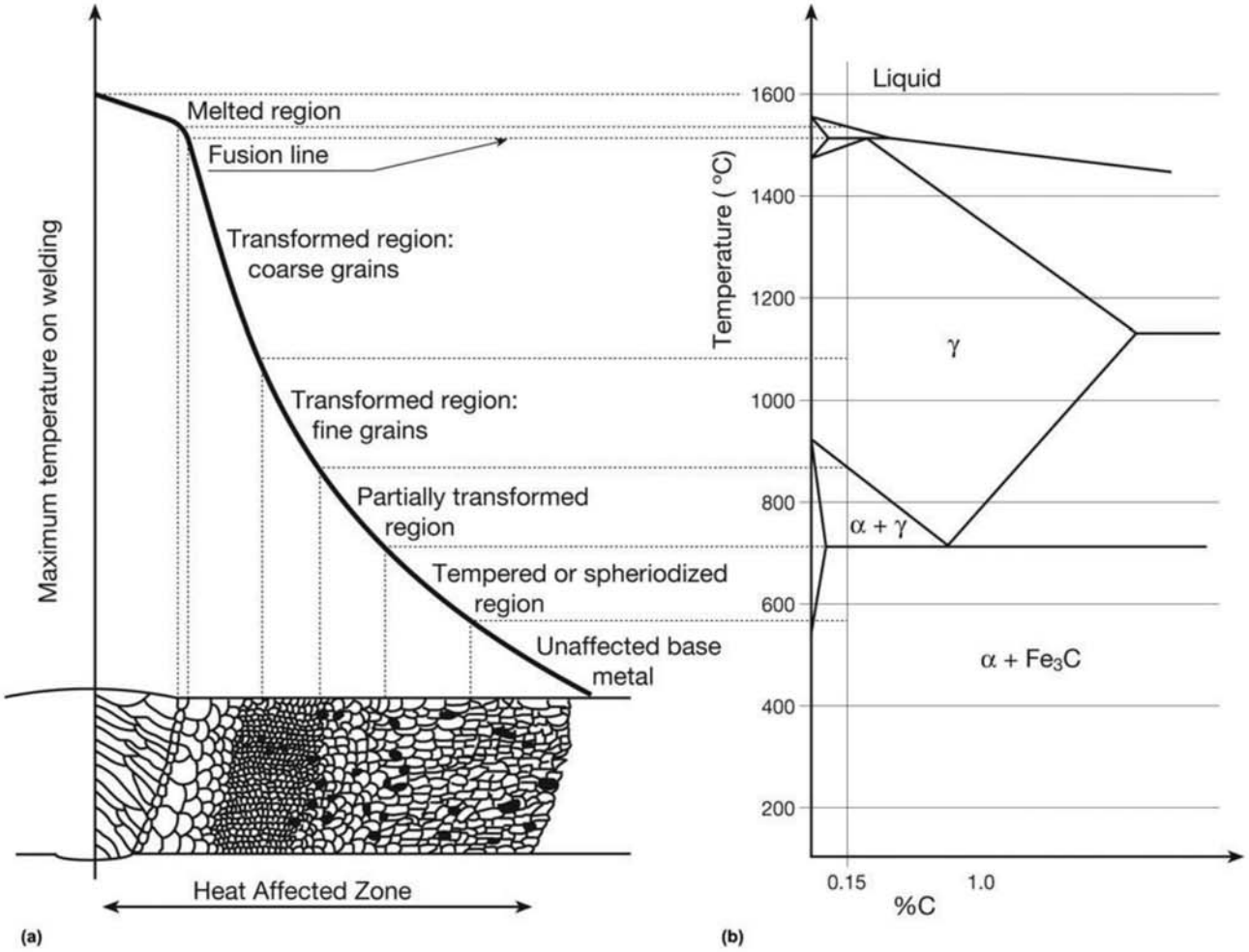

Fig. 14.28 (a) Schematic presentation of the maximum temperature reached in the weld joint as a function of the distance from the weld axis (compare to section y-y' in Fig. 14.27). (b) Fe-C equilibrium phase diagram indicating the effects of the maximum welding temperatures on the phases in equilibrium and the possible effects on the microstructure for an arbitrarily chosen carbon content of 0.15%. Phase diagram not to scale.

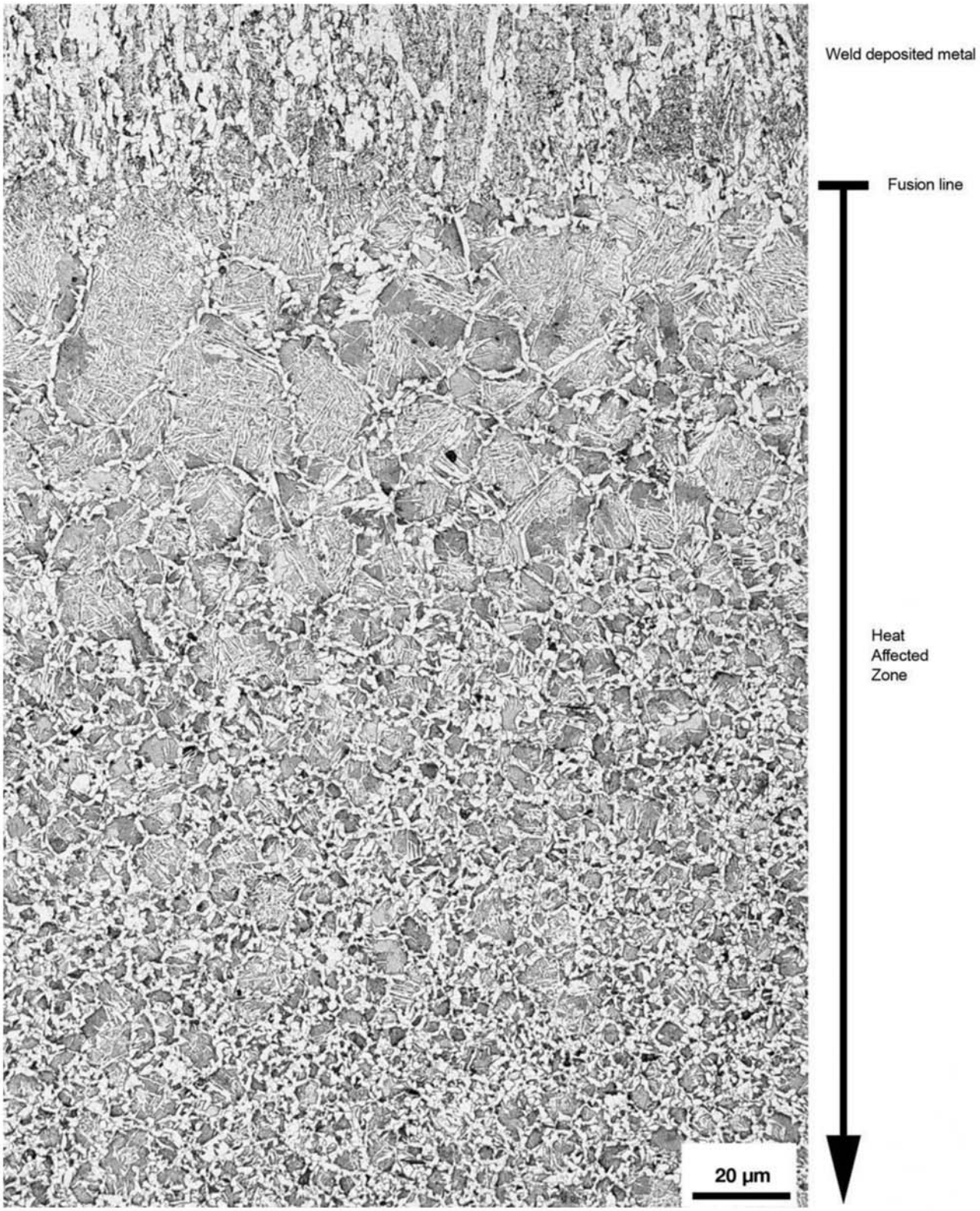

Fig. 14.29 Transverse cross section to a weld in structural steel with yield strength of 379 MPa (55 ksi) (see Fig. 14.1). At the top of the image is the weld-deposited metal. The base of the image shows the region of grain refinement. Compare to Fig. 14.28. Etchant: nital 2% and picral 4%. Courtesy of National Institute of Standards and Technology. Source: Ref 4

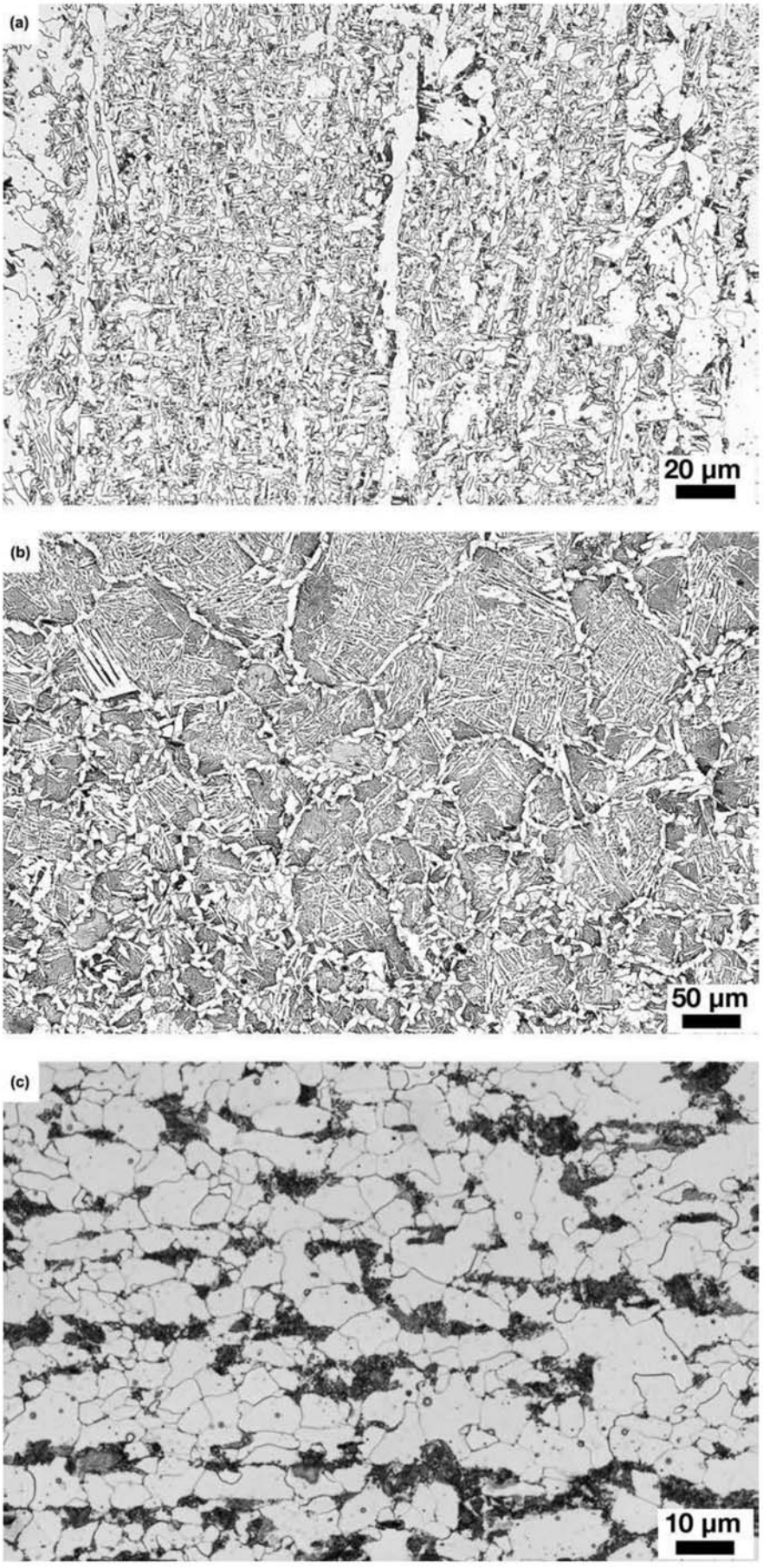

Fig. 14.30 Higher magnification images of the regions of the welded joint presented in Fig. 14.29. (a) Weld-deposited metal. Ferrite veins and acicular ferrite with carbides. (b) Coarse-grained region, close to the fusion line. Allotriomorphic ferrite in prior austenitic grain boundaries, Widmanstätten and acicular ferrite, possibly bainite (complete characterization not included on the source). (c) Region where the carbides in pearlite have suffered slight spheroidization: ferrite and slightly spheroidized pearlite. Etchant: nital 2% and picral 4%. Courtesy of National Institute of Standards and Technology. Source: Ref 4

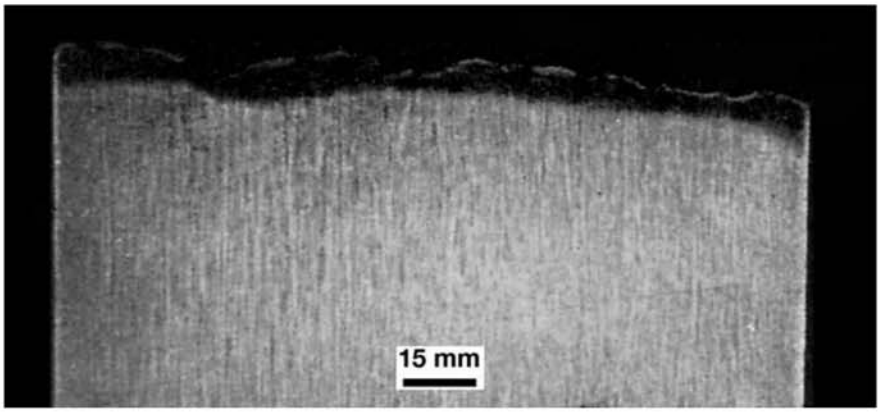

Fig. 14.31 Longitudinal cross section of a rolled bar subjected to transverse cut by flame. "Fibers" are apparent in the material. The dark region is the heat-affected zone caused by the flame cutting. Etchant: iodine.

ples with the same microstructure as in a welded joint; in an actual welded joint, the volume of material exposed to each specific thermal cycle is small and sampling it can be challenging.

Achieving a combination of high strength and good toughness is usually the main challenge in welding structural steels. Two main mechanisms are generally effective to increase the toughness of the heat affected zone of structural steels: (a) controlling the austenitic grain growth, particularly in the regions that are exposed to higher temperatures, and (b) nucleating ferrite inside the austenitic grains (intragranular ferrite) to decrease the crack mean free path on the microstructure and force cracks to change propagation planes. These processes increase the absorbed energy in the fracture process (Ref 31).

Aihara, Shigesato et al. (Ref 32) simulated various thermal cycles in a structural steel to evaluate under which conditions the nucleation of intragranular ferrite is favored, as a result of the modification of the nonmetallic inclusions present in the steel. The cycles they studied are presented in Fig. 14.32, and the different microstructures they obtained using a C-Mn structural steel are presented in Fig. 14.33.

Figure 14.34 presents the intragranular ferrite volume fraction measured in Ref 32. Higher temperatures and shorter times at an intermediate holding temperature caused the formation of a larger volume fraction of intragranular ferrite. The researchers attributed this effect to the inclusions rich in manganese sulfide (MnS). Careful measurements indicated that the austenite surrounding these inclusions is locally impoverished in manganese. Because manganese is an austenite stabilizer, the local decrease in the concentration of this element will favor the nucleation of ferrite. At the higher temperatures in the study (1250 °C, or 2280 °F), manganese would rapidly homogenize in austenite after the precipitation of the sulfide, thus eliminating the depletion in manganese and its favorable effect. By the same reasoning, long times at 1100 °C (2010 °F) lead to austenite homogenization and decrease or suppress the effect when the steel reaches the temperature range where ferrite forms (see Chapter 9, "Conventional Heat Treatments—Usual Constituents and Their Formation," in this book).

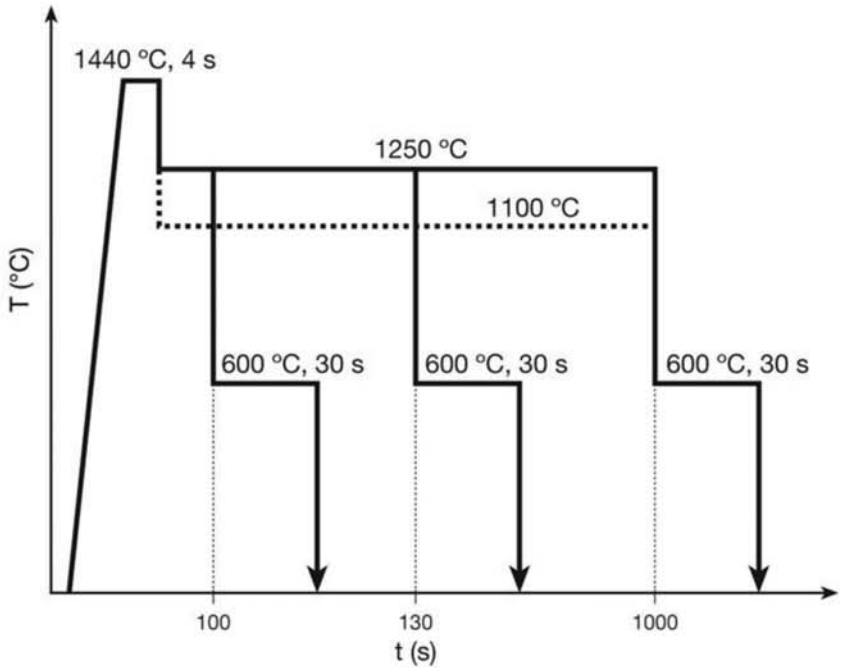

Fig. 14.32 Thermal cycles used to simulate welding and evaluate the formation of intragranular ferrite in structural steel welds. In all cases, the maximum temperature during the cycle was kept constant. After the peak temperature, the steel is quenched to an intermediate temperature and is kept at this temperature for different times. Then, the steel is quenched to 600 °C (1110 °F) and held at this temperature for 30 s to complete the transformation to ferrite. Source: Ref 32

Welded Long Products—Bar Mats and Welded Wire Mesh

Welding is a very efficient process for the rapid manufacture of mats, meshes, and trusses. It also makes possible the preassembly of reinforcing bar structures for reinforced concrete building, saving significant time and labor in the construction. To guarantee that the welds will have satisfactory properties, it is essential to control the characteristics of the material to be welded, in particular chemical composition (normally expressed through a "carbon equivalent" expression and a limiting value) as well as the thermal cycle (or thermomechanical cycle, in the case of electric fusion welding). The metallography of two applications of electric fusion welding are presented in Fig. 14.35 and 14.36. Figure 14.37 presents the structure of a MIG-MAG weld connecting reinforcing bar with minimum yield strength of 600 MPa (87 ksi).

Thick-Wall Pressure Vessel Welding

The welding of ASTM A533 Cl.1 steels and similar (see the section, "Steels for Thick-Wall Pressure Vessels (High-Pressure Vessels)," in this chapter) has been the subject of extensive study in view of its importance for the safety of nuclear pressure vessels, including pressurized and boiling water reactors. Because these welds frequently involve very thick sections, technology that reduces the volume of deposited weld metal can lead to significant economy in the production stage and because of the reduced volume of weld to be in-

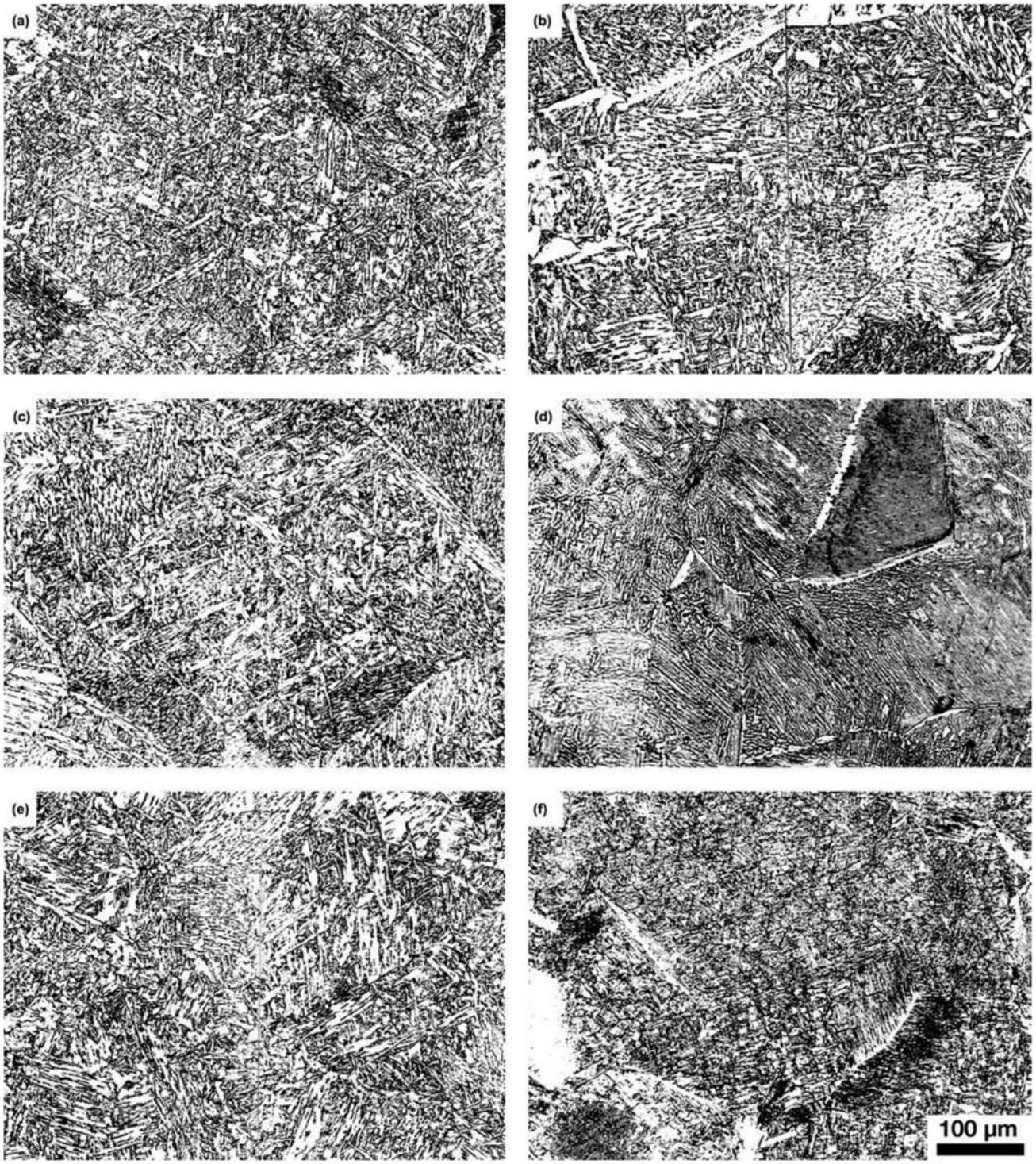

Fig. 14.33 Steel containing C = 0.08%, Mn = 1.47%, Ti = 120 ppm, Al = 0.026%, N = 40 ppm, subjected to the welding simulation according to the cycles in Fig. 14.32. Intermediate temperature 1100 °C (2010 °F): (a) 100 s, (b) 300 s, (c) 1000 s. Intermediate temperature 1250 °C (2280 °F): (d) 100 s, (e) 300 s, (f) 1000 s. Etchant: nital 2%. See Fig. 14.34 for the quantification of intragranular ferrite volume fraction in the samples. Courtesy of Nippon Steel Corporation. Source: Ref 32, 33

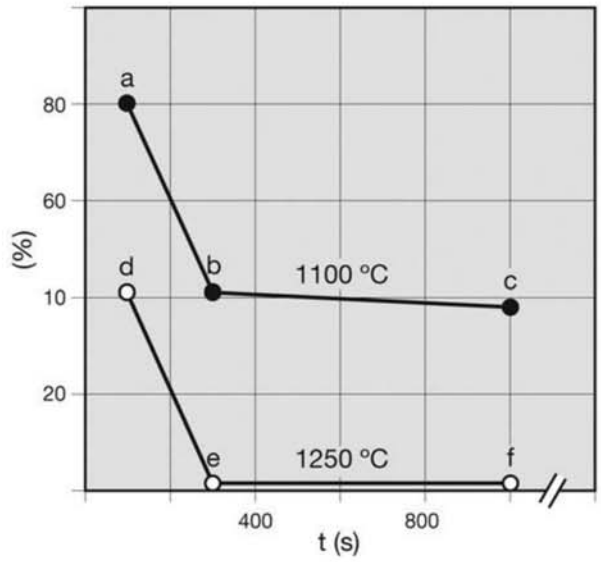

Fig. 14.34 Intragranular ferrite volume fraction in the samples shown in Fig. 14.33. Each point is identified with the same letter used to identify the micrographs in Fig. 14.33. Source: Ref 32

service requiring inspection. Figure 14.38 presents the cross section of a submerged arc weld (SAW) in thick plates of 20MnMoNi55 steel. The sequence and positioning of each pass over the previous one is of great importance. The thermal cycle imposed by subsequent passes produces structural refinement in the coarse-grained region of previous passes. It is normal to finish the weld in these steels with so-called temper beads, final passes deposited in a precise position that will refine the structure of the last layer of weld. Temper beads are usually ground off after welding. In some cases, if the proper welding sequence is done with sufficient care, postweld heat treatment may be skipped (Ref 34): this is of great importance when repairing finished or operating components. Figure 14.39 presents the narrow gap (NG) variation of SAW in a similar condition to Fig. 14.38. The reduction of the volume of deposited weld metal is evident. Furthermore, the effect of subsequent passes on previous ones is more effective than in normal SAW, and the welding causes less distortion (Ref 23). The microstructures observed in the weld joint of Fig. 14.39 were classified in accordance with the IIW method (Chapter 9, "Conventional Heat Treatments—Usual Constituents and Their Formation," section "9.3.2 Metallographic Classifications of Ferrite," in this book). Figure 14.40 presents some examples of the microstructures in this weld and the classification of the constituents. When a pass is deposited over the base metal, there is a region close to the fusion line that reaches temperatures sufficiently high to experience austenitic grain growth (Ref 35, 36) (see Fig. 14.28b). The ideal pass sequence is such that most of the coarse grain region of a pass is reaustenitized at a lower temperature by the subsequent passes. This depends mostly on the chamfer angle, weld penetration and superposition of each pass. Figures 14.41 and 14.42 show this effect in the SAW-NG weld of Fig. 14.39. In this case, the effect of the thermal cycle is more relevant than the heterogeneities associated with the base material

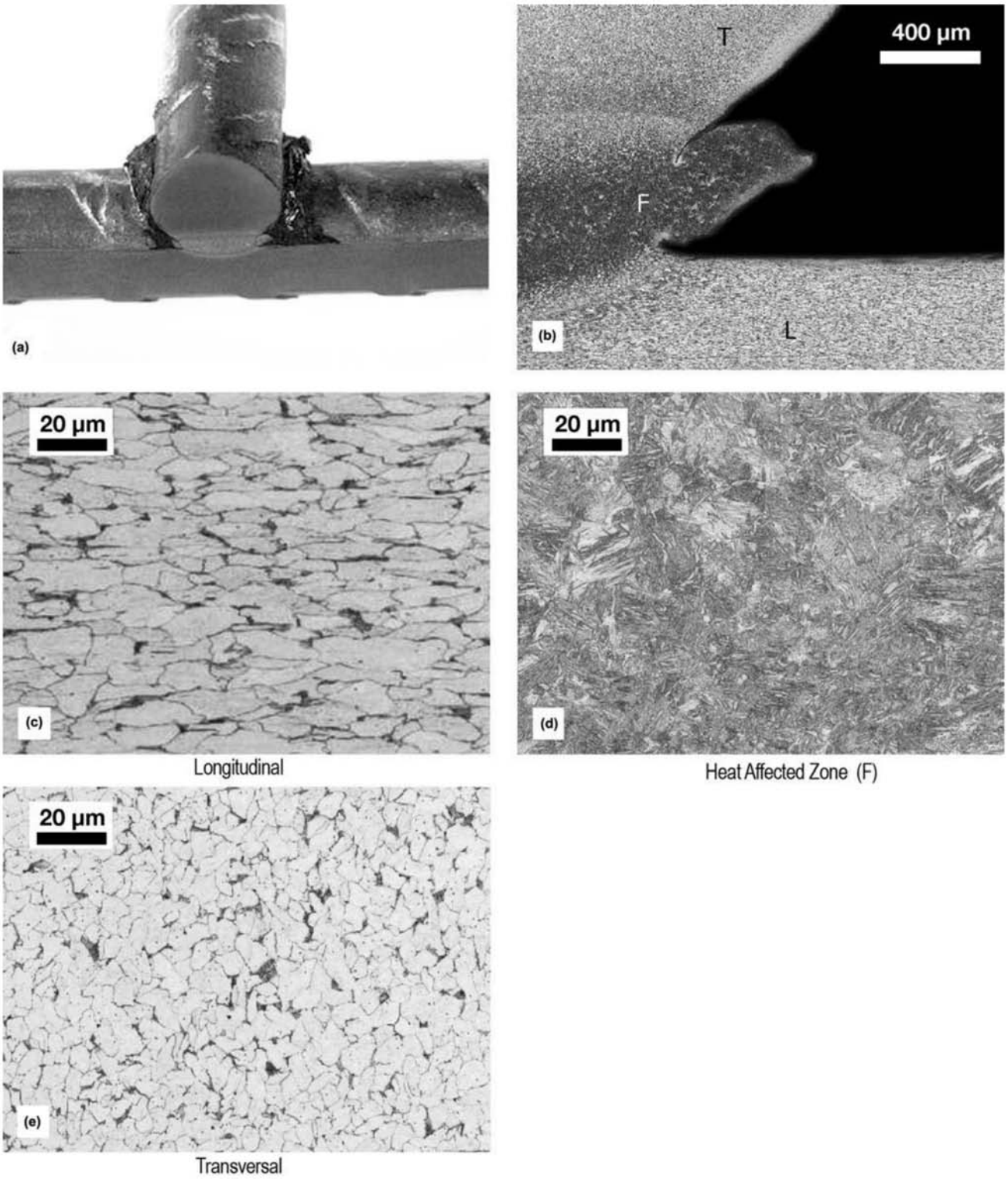

Fig. 14.35 Welded mesh of reinforcement bar with minimum yield strength of 600 MPa (87 ksi) welded by electric fusion. (a) Arrangement of the reinforcement bars, partially cut, etched. (b) Higher magnification of the section presented in (a). Transverse cross section of the top rebar and longitudinal section in the bottom rebar. Fusion zone, flash protruding out of the weld, and the heat-affected zones can be seen in both bars. (c) Region marked as "L" in (b). Longitudinal cross section of the bottom bar. Deformed ferrite and pearlite. (d) Fusion zone, acicular microstructure. (e) Region marked as T in (b). Transverse cross section of the top bar. Ferrite and pearlite. The cold forming, visible in the longitudinal section, is not perceptible in the cross section, as discussed in Chapter 12, "Mechanical Work of Steels: Cold Working," in this book. Etchant: nital 2%. Courtesy of ArcelorMittal Aços Longos, Juiz de Fora, MG, Brazil.

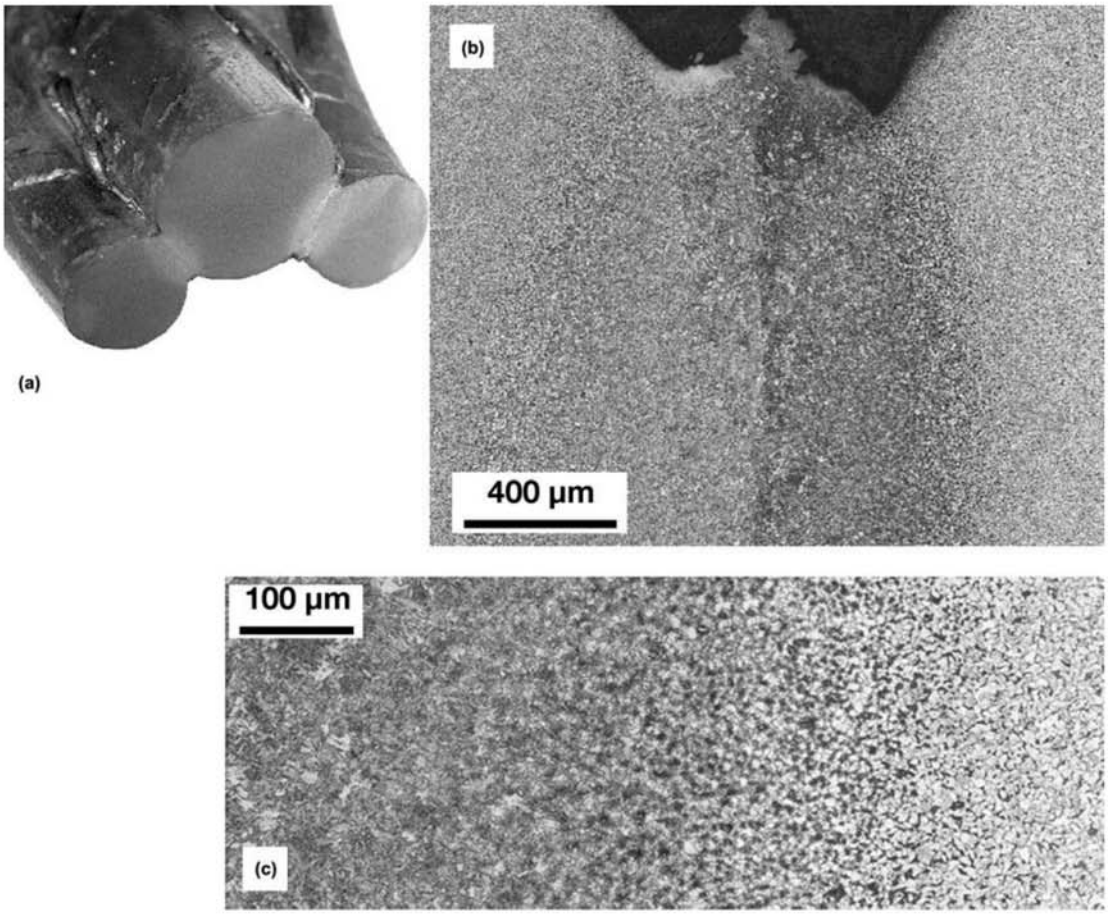

Fig. 14.36 Portion of a truss made of reinforcing bar with minimum yield strength of 600 MPa (87 ksi) welded by electric fusion. (a) Arrangement of the reinforcement bars, partially cut, etched. (b) Higher magnification of the section presented in (a). Cross section taken transverse to the weld and to the bars. Fusion zone, flash protruding out of the weld, and heat-affected zones in both bars. (c) From left to right, acicular martensite, ferrite, and partially spheroidized pearlite and base material not affected by the thermal cycle. Courtesy of ArcelorMittal Aços Longos, Juiz de Fora, MG, Brazil.

segregation. When welding material in which segregation is expected, as in this case, the procedure must be adjusted so that even under these conditions, satisfactory results are consistently achieved.

Metallography is also useful when analyzing and identifying the causes of defects found, for instance, by non-destructive techniques. Figure 14.43 presents the metallographic characterization of a simple defect in the transition zone of a weld-deposited corrosion-resistant cladding.

Some Other Welding Related Aspects

In some cases, welding large parts may be an interesting alternative, because of limitations in the production of very large forgings or the simpler field assembly. One of the processes used is electroslag welding. This process has an extremely high heat input and usually results in a large molten pool and wide heat-affected zone. This can cause distortion and cracks if care is

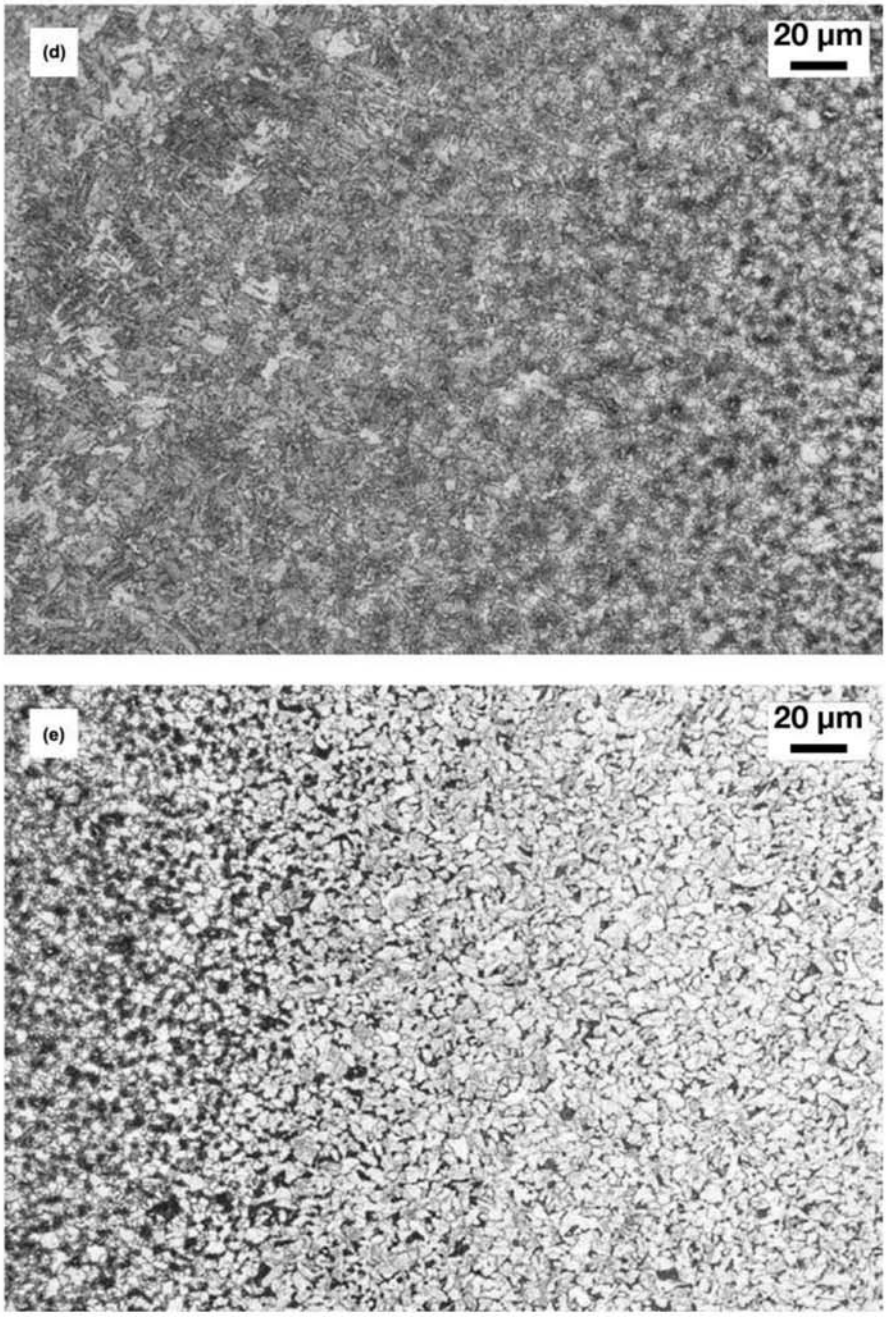

Fig. 14.36 (continued) (d) Higher magnification of the heat-affected zone: acicular ferrite, ferrite, and partially spheroidized pearlite. (e) Ferrite and partially spheroidized pearlite and base material not affected by the thermal cycle. Etchant: nital 2%. Courtesy of ArcelorMittal Aços Longos, Juiz de Fora, MG, Brazil.

not exercised. Furthermore, to obtain a good microstructure and adequate properties, a new heat treatment after welding is frequently required. In some cases, the welding may be done prior to hot working. Figure 14.44 presents an example of an experimental weld, joining two forged blocks of AISI 1045 steel using electroslag welding. The final block was to be used as forging stock for a large part.

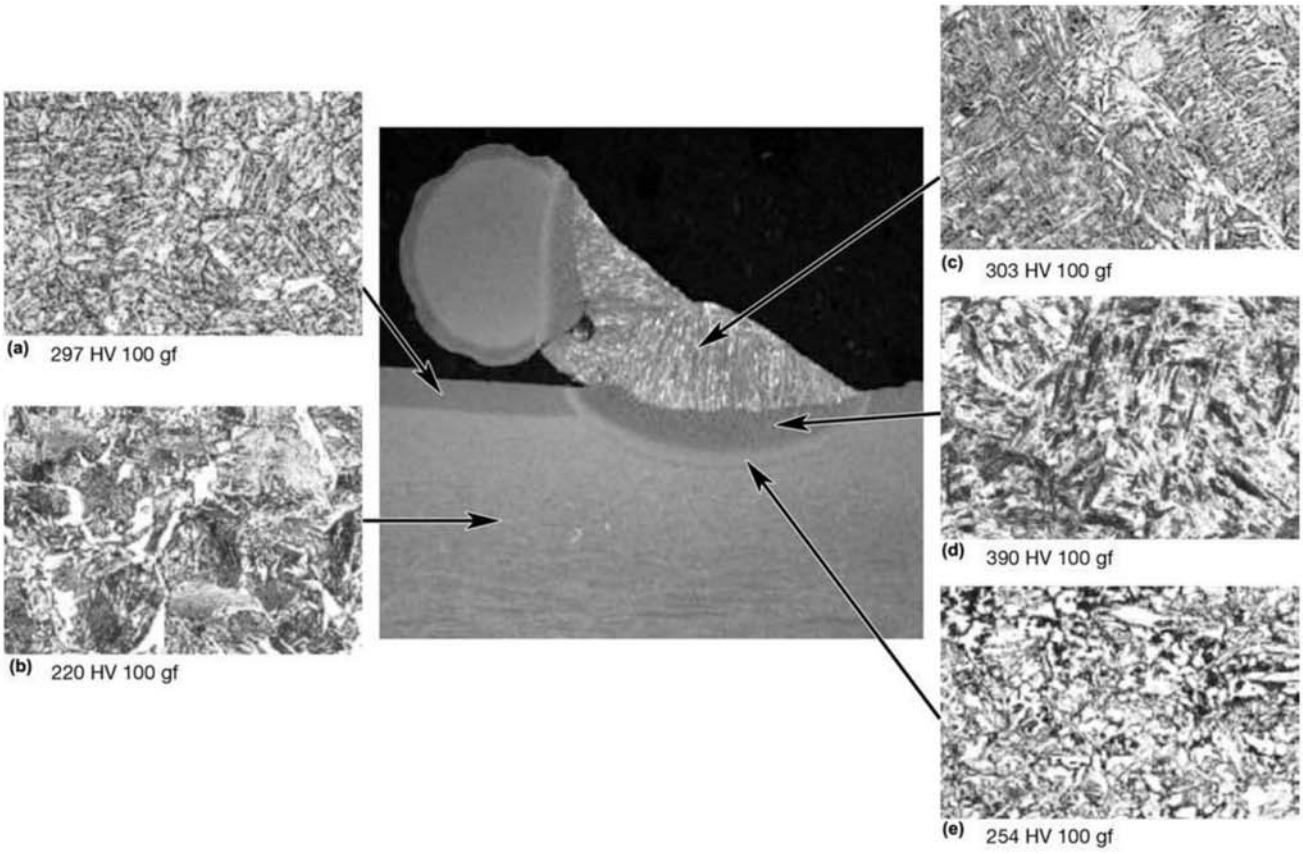

Fig. 14.37 MIG-MAG weld joining two bars of steel with a specified minimum yield strength of 500 MPa (73 ksi) of 6.3 and 16 mm (0.25 and 0.63 in.) diameters. Bars produced by the Tempcore process. Hardness in each region of the microstructure is indicated. (a) Layer of tempered martensite. (b) Core, composed of ferrite and pearlite. (c) Weld-deposited metal: acicular ferrite. Heat-affected zone. (d) Coarse martensite. (e) Transition zone with equiaxial and acicular ferrite and pearlite. Etchant: nital 2%. Courtesy of ArcelorMittal Aços Longos, Juiz de Fora, MG, Brazil.

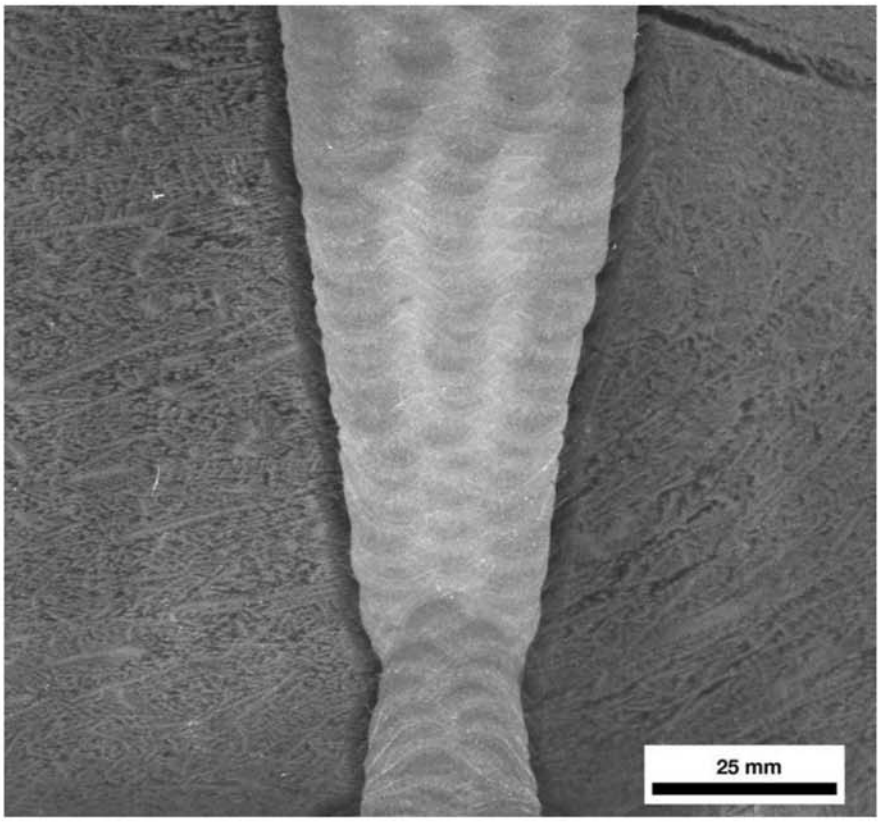

Fig. 14.38 Macrograph transverse to a SAW welded joint of 20MnMoNi55 steel. In the base metal, dendritic segregation (see Chapter 8, "Solidification, Segregation, and Nonmetallic Inclusions," in this book) is still visible. The segregation is aligned nearly perpendicular to the fusion line. The pass disposition is clearly visible, as is the effect of each pass on the previous ones. The heat-affected zone in the base metal is slightly darker. The weld root has been removed and welding was completed from the opposite side (lower portion of the image). Etchant: nital 10%. Courtesy of M. M. Moraes. Source: Ref 23

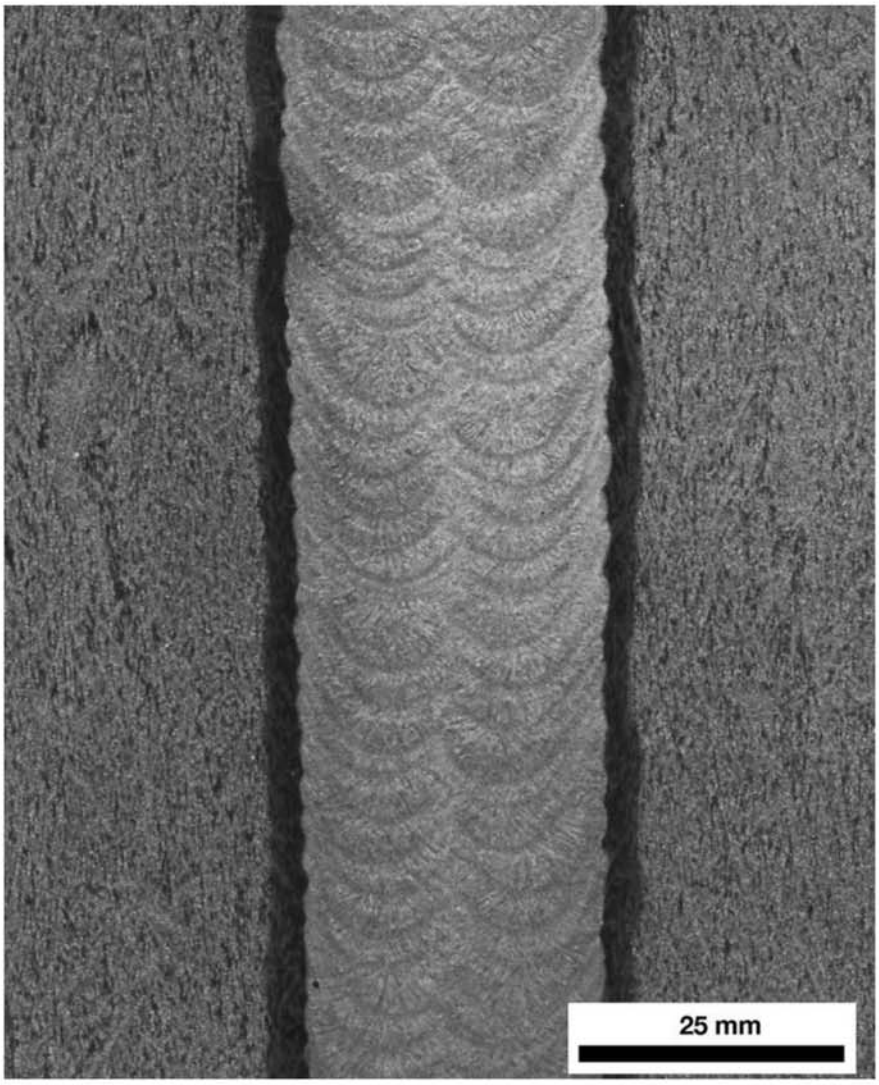

Fig. 14.39 Macrograph transverse to a SAW-NG welded joint of 20MnMoNi55 steel. In the base metal, dendritic segregation (see Chapter 8, "Solidification, Segregation, and Nonmetallic Inclusions," in this book) is still visible. The segregation is aligned nearly parallel to the fusion line. The pass disposition is clearly visible, as is the effect of each pass on the previous ones. The heat-affected zone in the base metal is slightly darker. Etchant: nital 10%. Courtesy of M. M. Moraes. Source: Ref 23

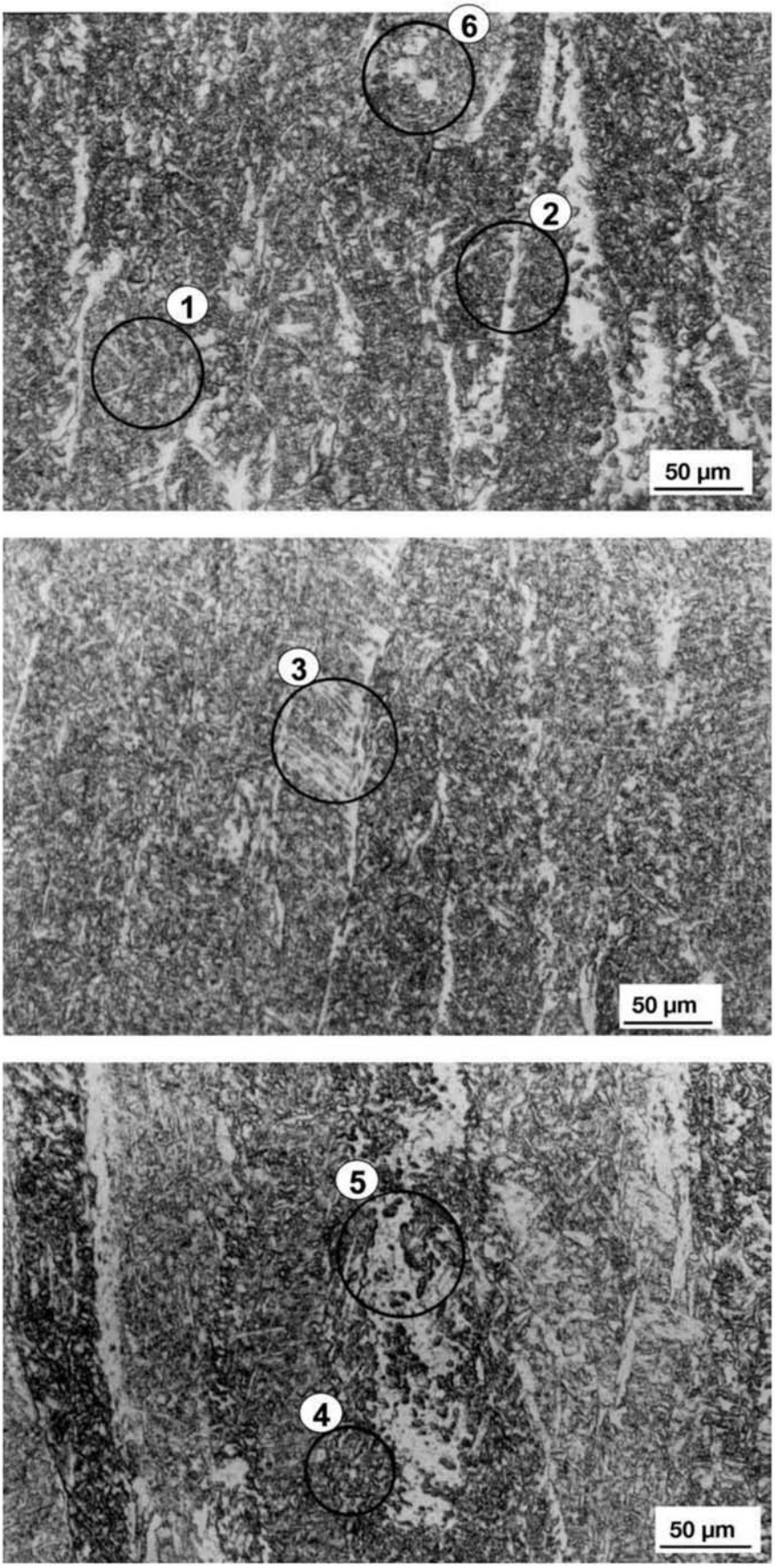

Fig. 14.40 Microstructure of the weld metal deposited by SAW using S3Ni-Mo1 wire (DIN EN ISO 14171-A S3Ni1Mo similar to AWS A5.23 EF3, EF3N uncoppered) and OP41TT flux. Weld subjected to stress relief heat treatment. (1) Acicular ferrite. (2) Grain boundary ferrite. (3) Ferrite with aligned second phase. (4) Ferrite-carbide aggregate. (5) Ferrite with nonaligned second phase. (6) Intragranular polygonal ferrite. Mechanical properties of all weld metal tensile specimen: yield strength: 556 MPa (81 ksi); ultimate tensile strength: 646 MPa (94 ksi), elongation: 22.4%, reduction of area: 69%. Courtesy of M. M. Moraes. Source: Ref 23

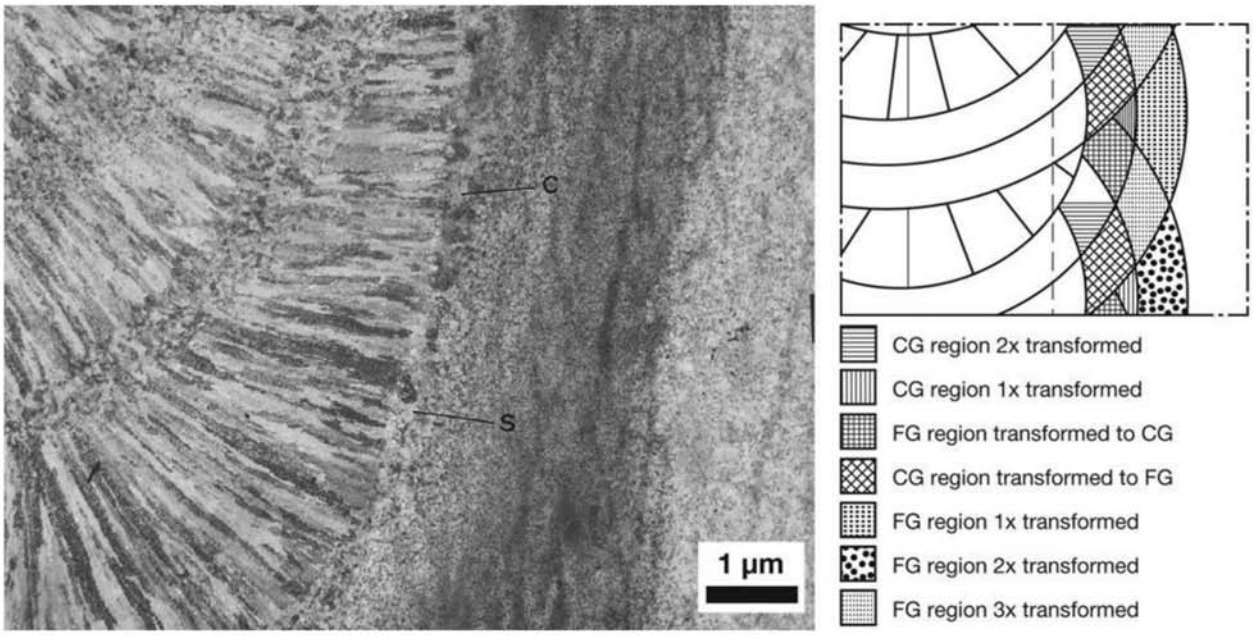

Fig. 14.41 (a) Higher magnification of fusion line and heat-affected zone of SAW-NG weld of 20MnMoNi55 (Fig. 14.39). From the top left to the right, three welding beads can be observed. It is possible to observe the columnar region in each of the beads as well as the refined microstructure in the bead transition, caused by the proper pass sequence. In the base metal, segregation can be observed, particularly in the heat-affected zone. Close to the fusion line, in the base metal, two regions are indicated: (S) a region free from segregation in the base metal and (C) a segregated region. (b) Schematic presentation of the coarse-grain regions (CG) in a given bead that are refined to form fine austenitic grains (FG) by the following passes. Etchant: nital 2%. Courtesy of M. M. Moraes. Source: Ref 23

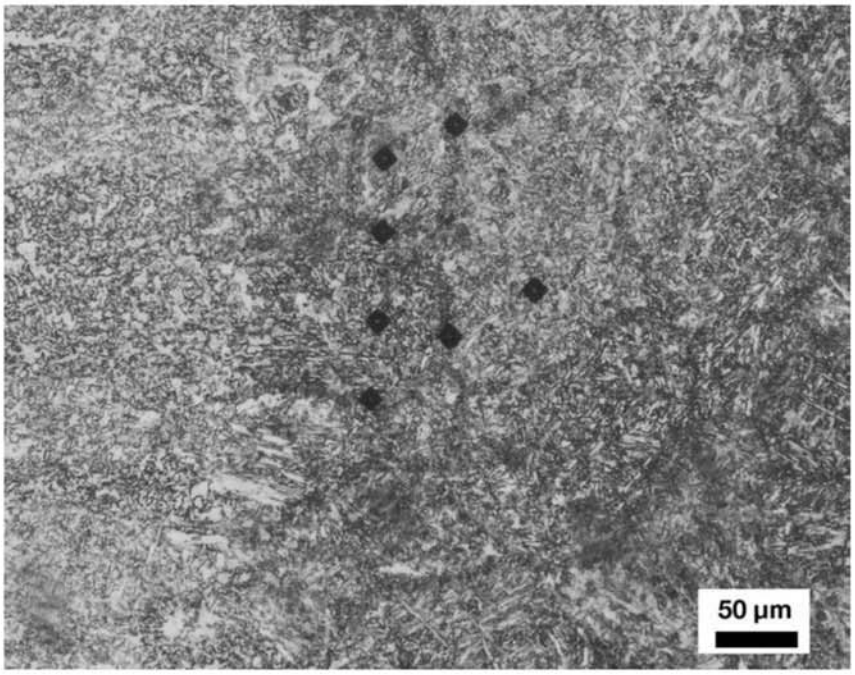

Fig. 14.42 Coarse-grained area in a segregated region from Fig. 14.41. The segregated regions, darker in the image, have bainite and in some cases MA in their microstructure. The nonsegregated regions present bainitic microstructure. Hardness in the segregated regions has reached 401 HV while the maximum observed outside of the segregated regions was 327 HV. Etchant: nital 2%. Courtesy of M. M. Moraes. Source: Ref 23

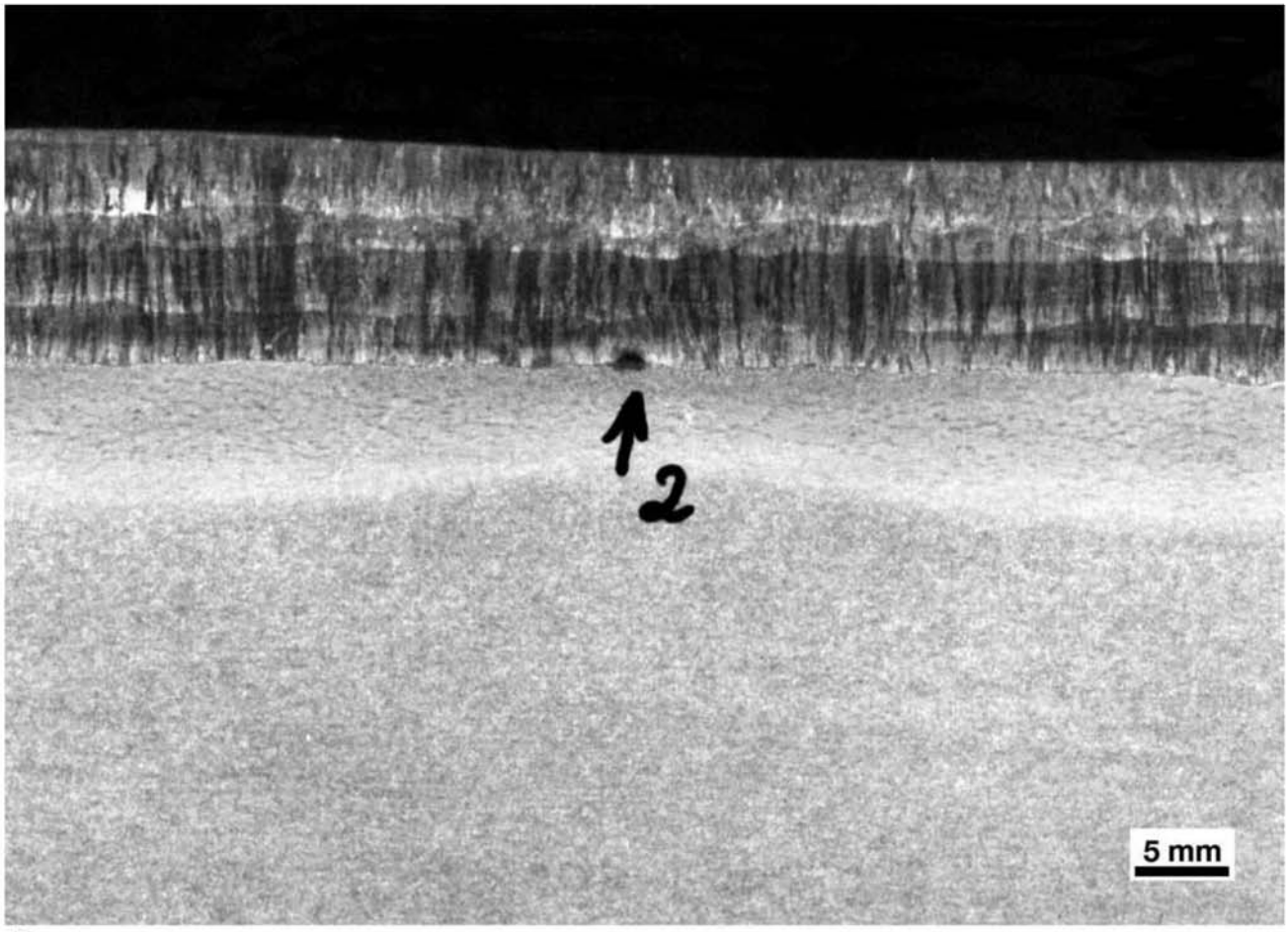

(a)

(b)

Fig. 14.43 (a) Austenitic stainless steel cladding weld deposited over a substrate of 20MnMoNi55 steel. Heat-affected zone is visible, as is the columnar structure in the weld-deposited material, in multiple layers. The arrow indicates a slag inclusion defect, detected during ultrasonic examination of the cladding. (b) Higher magnification of the slag inclusion in the fusion line between 20MnMoNi55 steel and the stainless weld deposit. The segregation in the base metal as well as the as-cast structure of the weld-deposited metal can be observed. Courtesy of NUCLEP, RJ, Brazil.

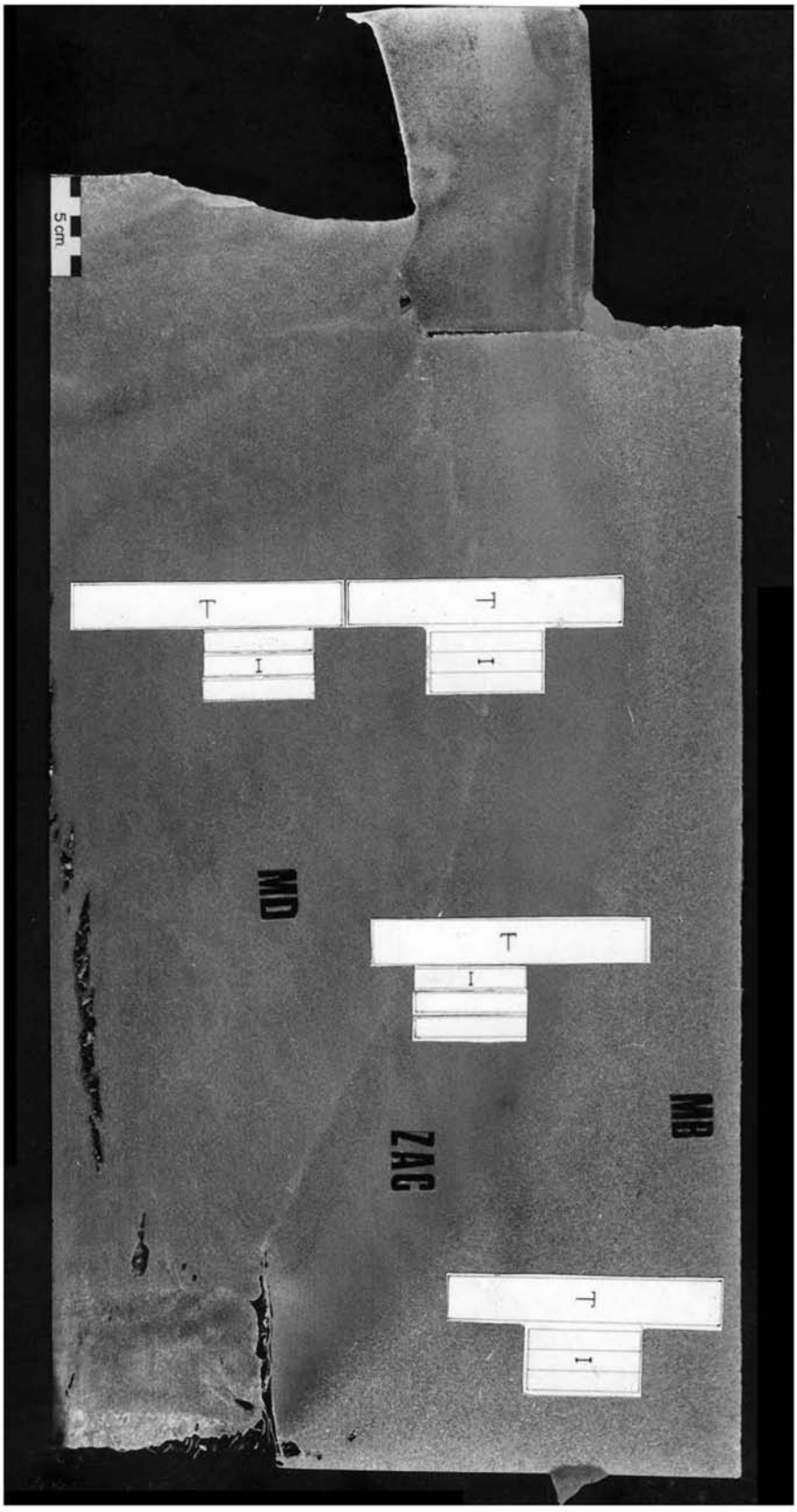

Fig. 14.44 Transverse cross section of an experimental electroslag weld of two forged blocks of AISI 1045 steel. The weld was sectioned along the axis of the weld deposit (MD), so only a single block of base metal (MB) can be seen. Hot tears close to the weld axis can be observed. Porosity close to the starting block (at the bottom of the weld) is also observed. Penetration and heat-affected zone (ZAC) are large in this process. The heat-affected zone extends for more than 50 mm (2 in.). The location of test specimens to evaluate the process are indicated. Etchant: hot hydrochloric acid.

REFERENCES

1. *Properties and Selection—Irons, Steels and High-Performance Alloys*, Vol 1, *ASM Handbook*, 10th edition,ASM International, 1990
2. "Specification for Carbon Structural Steel," A36-12, ASTM International, 2012
3. "Practice for Assessing the Degree of Banding or Orientation of Microstructures," E1268-01, ASTM International, 2016
4. S.W. Banovic, C.N. McCowan, and W.E. Luecke, "For Public Comment Federal Building and Fire Safety Investigation of the World Trade Center Disaster Physical Properties of Structural Steels," NCSTAR 1-3E (Draft), NIST, 2005
5. T.N. Baker, Microalloyed Steels, *Ironmak. Steelmak.*, Vol 43 (No. 4), April 2016, p 264–307
6. S. Vervynckt, K. Verbeken, B. Lopez, and J.J. Jonas, Modern HSLA Steels and Role of Non-Recrystallisation Temperature, *Int. Mat. Rev.*, Vol 57 (No. 4), July 2012, p 187–207
7. A.J. Deardo, Niobium in Modern Steels, *Int. Mat. Rev.*, Vol 48 (No. 6), December 2003, p 371–402
8. R.N. Carvalho, *Aspectos da precipitação e da recristalização na laminação contínua de tubos sem costura*, PhD thesis, UFMG, 2007
9. A.A. Gorni, M.D. Xavier, H. Goldenstein, and A.P. Tschiptschin, Transformação da austenita em aços microligados com microestrutura ferrítica-bainítica, In: *62° Congresso Anual da ABM International, July 23–27, 2007, Vitória, ES, Brazil*, ABM, 2007
10. API, ANSI/API Spec 5L Specification for Line Pipe, 44th edition, American Petroleum Institute, 2007
11. Y. Terada, H. Tamehiro, H. Morimoto, T. Hara, E. Tsuru, H. Asahi, M. Sugiyama, N. Doi, M. Murata, and N. Ayukawa, X100 Linepipe with Excellent HAZ Toughness and Deformability, *Proceedings of the 22nd International Conference OMAE, ASME*, ASME OMAE2003-37392, 2003
12. H. Asahi, A. Hara, E. Tsuru, H. Morimoto, S. Ohkita, M. Sugiyama, N. Maruyama, K. Shinada, K. Koyama, Y. Terada, et al., Development of Ultrahigh-Strength Linepipe, X120, *Nippon Steel Tech. Rep.*, Vol 90, July 2004, p 82–87
13. "Standard Specification for Deformed and Plain Carbon-Steel Bars for Concrete Reinforcement," A615/A615M-16, ASTM International, 2016
14. "Standard Specification for Deformed and Plain Low-Alloy Steel Bars for Concrete Reinforcement," A706/A706M-16, ASTM International, 2016
15. American Concrete Institute, Building Code Requirements for Structural Concrete (ACI 318-95) and Commentary (ACI 318R-95), ACI, 1995
16. "Standard Specification for Low-Relaxation, Seven-Wire Steel Strand for Prestressed Concrete," A416/A416M 16, ASTM International

17. M. Economopoulos, Y Respen, G. Lessel, and G. Steffes, Application of the Tempcore Process to the Fabrication of High Yield Strength Concrete-Reinforcing Bars, *CRM Rev.*, Vol 45, 1975, p 1–17

18. D.T. Llewellyn and R.C. Hudd, *Steels: Metallurgy and Applications*, Butterworth-Heinemann, 1998

19. D.A. Porter and K.E. Easterling, *Phase Transformations in Metals and Alloys*, 2nd edition, Chapman & Hall, 1992

20. "Petroleum and Natural Gas Industries—Materials for Use in H_2S-Containing Environments in Oil and Gas Production, MR0175/ISO 15156, NACE International, 2003

21. S. Raoul, Rupture ntergranulaire fragile d'un acier faiblement allié induite par la ségrégation d'impuretés aux joints de grains: Influence de la microstructure [Intergranular brittle fracture of a low alloy steel induced by grain boundary segregation of impurities: Influence of the microstructure], Rapport CEA-R-5874 Université Paris-Sud XI, 1999

22. S. Raoul, B. Marini, and A. Pineau, Effect of Microstructure on the Susceptibility of a 533 Steel to Temper Embrittlement, *J. Nuc. Mat.*, Vol 257, 1998, p 199–205

23. M.M. Moraes, *A soldagem do aço DIN 20MnMoNi55 pelo processo arco submerso em chanfro estreito* [Welding the Steel DIN 20MnMoNi55 Using the Narrow Gap Process], M.Sc. thesis, Engenharia Metalúrgica, COPPE-UFRJ, 1987

24. S. Kim, S. Lee, and B.S. Lee, Effects of Grain Size on Fracture Toughness in Transition Temperature Region of Mn-Mo-Ni Low-Alloy Steels, *Mat. Sci. Engin. A*,Vol A359, 2003, p 198–209

25. W.W. Cias, *Phase Transformation Kinetics and Hardenability of Medium Carbon Alloy Steels*, Climax Molybdenum, 1972

26. "Application of 2 1/4Cr-1Mo Steel for Thick-Wall Pressure Vessels," G. Sangdahl and M. Semchyshen., Eds., STP 755, ASTM International, 1982

27. F. Abe, Bainitic and Martensitic Creep-Resistant Steels, *Curr. Opin. Solid State Mat. Sci.*, Vol 8, 2004, p 305–11

28. M. Taneike, F. Abe, and K. Sawada, Creep-Strengthening of Steel at High Temperatures Using Nano-Sized Carbonitride Dispersions, *Nature*, Vol 424, July 17, 2003, p 294–96

29. K. Easterling, *Introduction to the Physical Metallurgy of Welding*, Butterworths, 1982

30. D. Rosenthal, The Theory of Moving Source of Heat and Its Application to Metal Transfer, *Trans. ASME*, Vol 68 (No. 11), 1946, p 849–66

31. H.K.D.H. Bhadeshia, *Bainite in Steels*, 2nd edition, Institute of Materials, 2001

32. S. Aihara, G. Shigesato, M. Sugiyama, and R. Uemori, Microstructural Control of Weld Heat-Affected Zone of Steel by Mn Depletion Around Non-Metallic Inclusions, *Nippon Steel Tech. Rep.*, Vol 91, 2005, p 43–48

33. G. Shigesato, M. Sugiyama, S. Aihara, R. Uemori, and Y. Tomita, *Tetsu-to-hagane*, Vol 87 (No. 2), 2001, p 23–30

34. "Alternative Welding Methods, XI Rules for Inservice Inspection of Nuclear Power Plant Components," IWA-4600, Boiler & Pressure Vessel Code 2015 edition, ASME, 2015

35. M.F. Ashby and K.E. Easterling, A First Report on Diagrams for Grain Growth in Welds, *Acta Metall.*, Vol 30 (No. 11), 1982, p 1969–78

36. J.C. Ion, K.E. Easterling, and M.F. Ashby, A Second Report on Diagrams of Microstructure and Hardness for Heat-Affected Zones in Welds, *Acta Metall.*, Vol 32 (No. 11), 1984, p 1949–62

Metallography of Steels—Interpretation of Structure and the Effects of Processing
Hubertus Colpaert
Updated and Translated by André Luiz V. da Costa e Silva

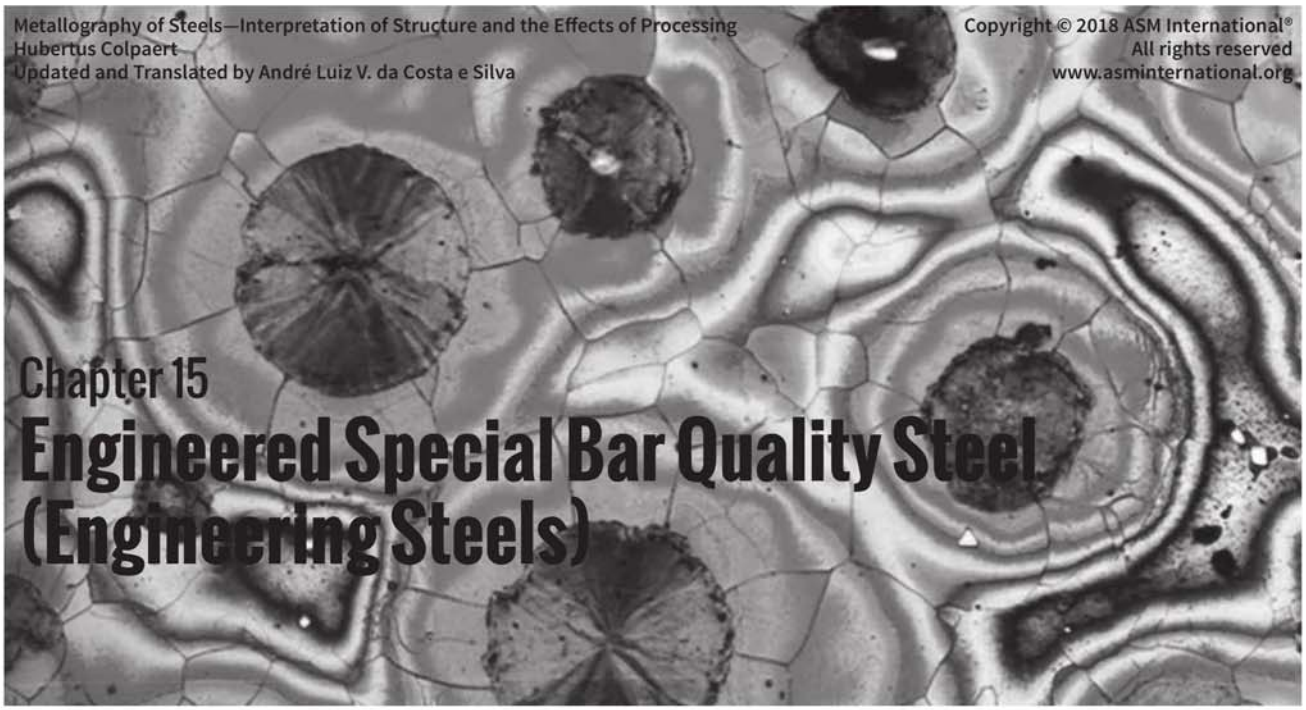

Chapter 15
Engineered Special Bar Quality Steel (Engineering Steels)

The classification of engineering steels or, commonly known in the United States as special bar quality (SBQ) steels, was presented in Chapter 10 "Conventional Heat Treatment—Basic Concepts," in this book. These steels are selected based on their hardenability and are normally used in the quenched and tempered condition. In this condition, with microstructures mostly composed of tempered martensite, the most relevant differences in the microstructure are caused by carbon content, tempering temperature, and prior austenitic grain size.

In this chapter, some typical microstructures of quenched and tempered products from the most common steels in this classification are presented. Significant differences should not be expected when examining the microstructure of other SBQ or engineering steels except, of course, those associated with differences in hardenability. For a given part, geometry , size, and the depth at which each microstructure will occur evidently depends on the hardenability of the steel and the chosen quenching medium. Engineering steels that are sometimes classified as "medium to high carbon steels" instead of SBQ are also discussed in this chapter. These are mostly steels for rails and train wheels.

This is not to say all these steels are the same in other aspects. When it comes to steel cleanness, soundness, and degree of segregation, SBQ steels are above "merchant bar" quality, tbut hey can cover a wide range of "quality" steel. Just specifying a steel grade and final hardness (directly related to the quenched and tempered (Q&T) properties) leaves the part performance undefined. Fatigue resistance and resistance to hydrogen embrittlement, for instance, are as much dependent on the amount and type of nonmetallic inclusions in the steel as on the level of segregation in the product.

15.1 Quenched and Tempered Steels

15.1.1 The Effect of Carbon Content and Tempering Temperature

Sandor (Ref 1) studied the effect of carburizing on the mechanical properties of AISI 4320. That work made an extensive evaluation of the microstruc-

ture of steel with the same base composition (AISI 43xx) but different carbon contents. The steels were produced under very well-controlled conditions: they were vacuum melted and forged and heat-treated in a research laboratory.

For a sequence of steels with increasing carbon content and the basic composition of AISI 43xx, Fig. 15.1 shows the microstructures obtained after quenching and tempering at 200 °C (390 °F). With increasing tempering temperature or time, all martensitic structures will approach a dispersion of carbides in ferrite, so the differences between these various steels are better observed with low tempering temperatures, as shown in Fig. 15.1.

As carbon content increases, various microstructural changes can be observed in the images in Fig. 15.1. The martensite morphology in lower carbon

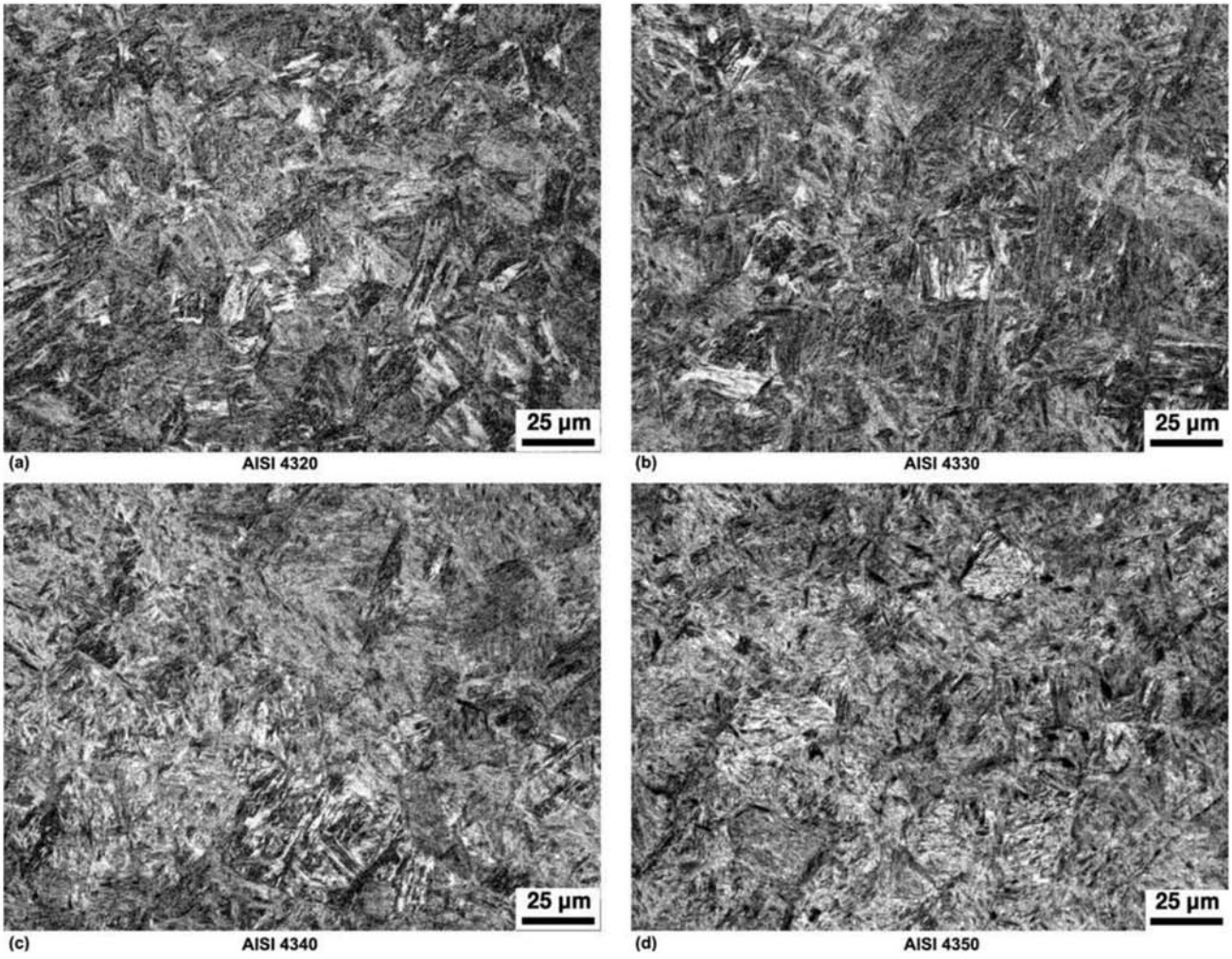

Fig. 15.1 (a) AISI 4320, (b) AISI 4330, (c) AISI 4340, (d) AISI 4350, (e) AISI 4360, (f) AISI 4380, (g) AISI 4390, and (h) AISI 43100 steels with different carbon contents quenched and tempered at 200 °C (390 °F). The microstructure is composed of tempered martensite. Starting with AISI 4380 steel (f), it is possible to see in the optical micrographs the presence of retained austenite (light-colored areas that might have been partially transformed to martensite on cooling after tempering). It is possible to observe the martensite morphology change, too (see Chapter 9, "Conventional Heat Treatments: Usual Constituents and Their Formation," in this book). Etchant: nital. Courtesy of L.T. Sandor. Source: Ref 1

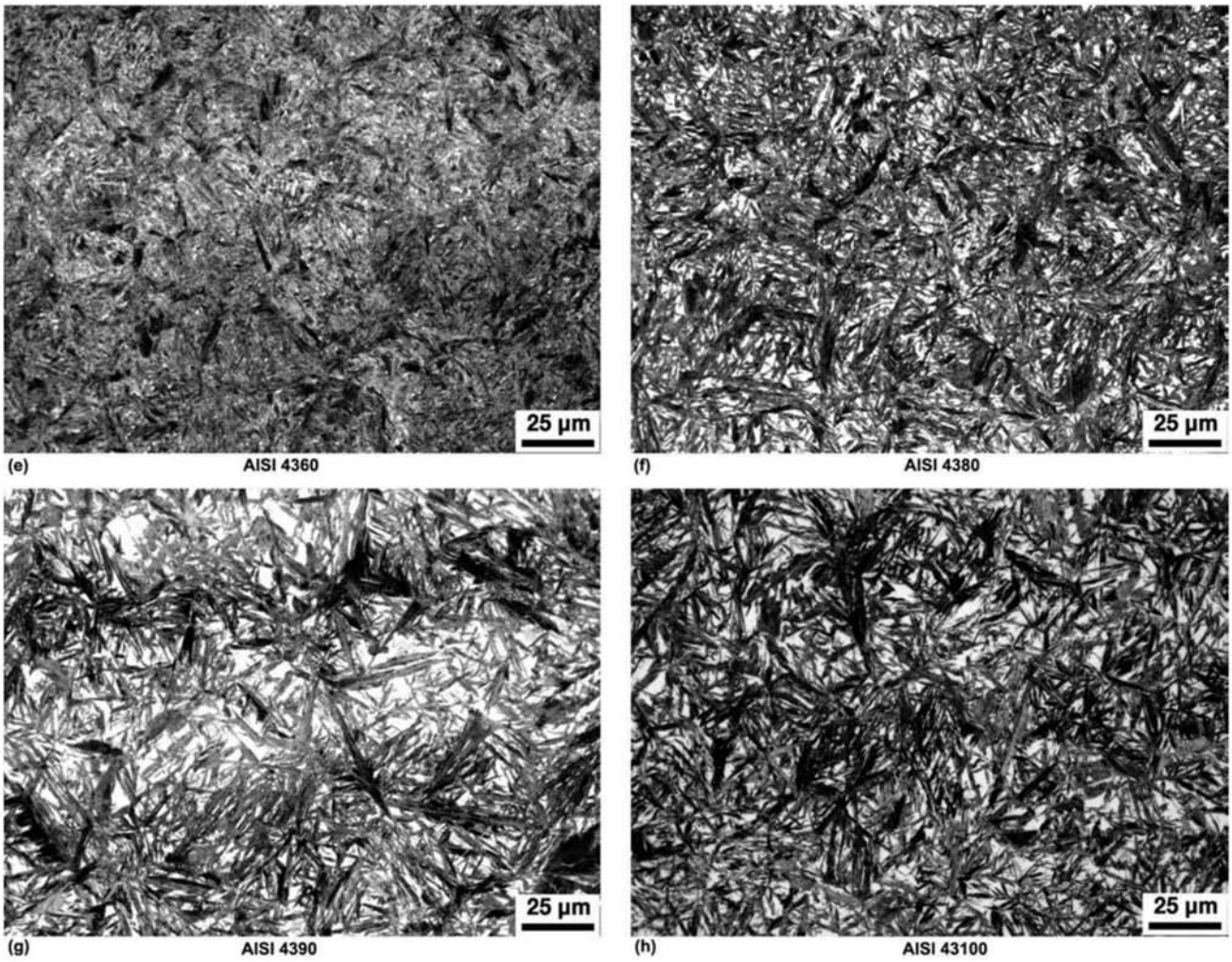

Fig. 15.1 (continued) (a) AISI 4320, (b) AISI 4330, (c) AISI 4340, (d) AISI 4350, (e) AISI 4360, (f) AISI 4380, (g) AISI 4390, and (h) AISI 43100 steels with different carbon contents quenched and tempered at 200 °C (390 °F). The microstructure is composed of tempered martensite. Starting with AISI 4380 steel (f), it is possible to see in the optical micrographs the presence of retained austenite (light-colored areas that might have been partially transformed to martensite on cooling after tempering). It is possible to observe the martensite morphology change, too (see Chapter 9, "Conventional Heat Treatments: Usual Constituents and Their Formation," in this book). Etchant: nital. Courtesy of L.T. Sandor. Source: Ref 1

steels is different from that in high carbon steels, as discussed in Chapter 9, "Conventional Heat Treatments: Usual Constituents and Their Formation," in this book. In steels with carbon content above approximately 0.8%, light areas are clearly visible between the martensite plates. As the M_f temperature of these steels is lower than room temperature (Chapter 10, "Conventional Heat Treatment: Basic Concepts"), austenite is not completely transformed on quenching, and after quenching there is a significant volume fraction of retained austenite. Tempering at 200 °C (392 °F) may cause the precipitation of some carbides in this austenite, reducing its carbon content and making possible the formation of fresh martensite on cooling from the tempering temperature. Because this martensite is not tempered at this point, it etches

in a different way from tempered martensite and may look light, inside areas of austenite that is still retained.

Double tempering is always recommended for higher carbon content steels for this reason. In the AISI 4390 and 43100 steels, it is possible to see some banding of the structure. This is not a particular feature of these steels; instead, it is related to the sampled regions and the actual microstructure, which helps make visible the segregation due to either the apparent difference in martensite volume fraction or the response to etching.

The increase of the tempering temperature tends to make it harder to notice, at least with optical microscopy, the microstructural differences among steels with different carbon contents (Fig. 15.2) if other influences, mostly the effect of carbon in hardenability, are eliminated. In the present experiments, all steels have been quenched sufficiently fast to exceed the critical rate for the formation of martensite.

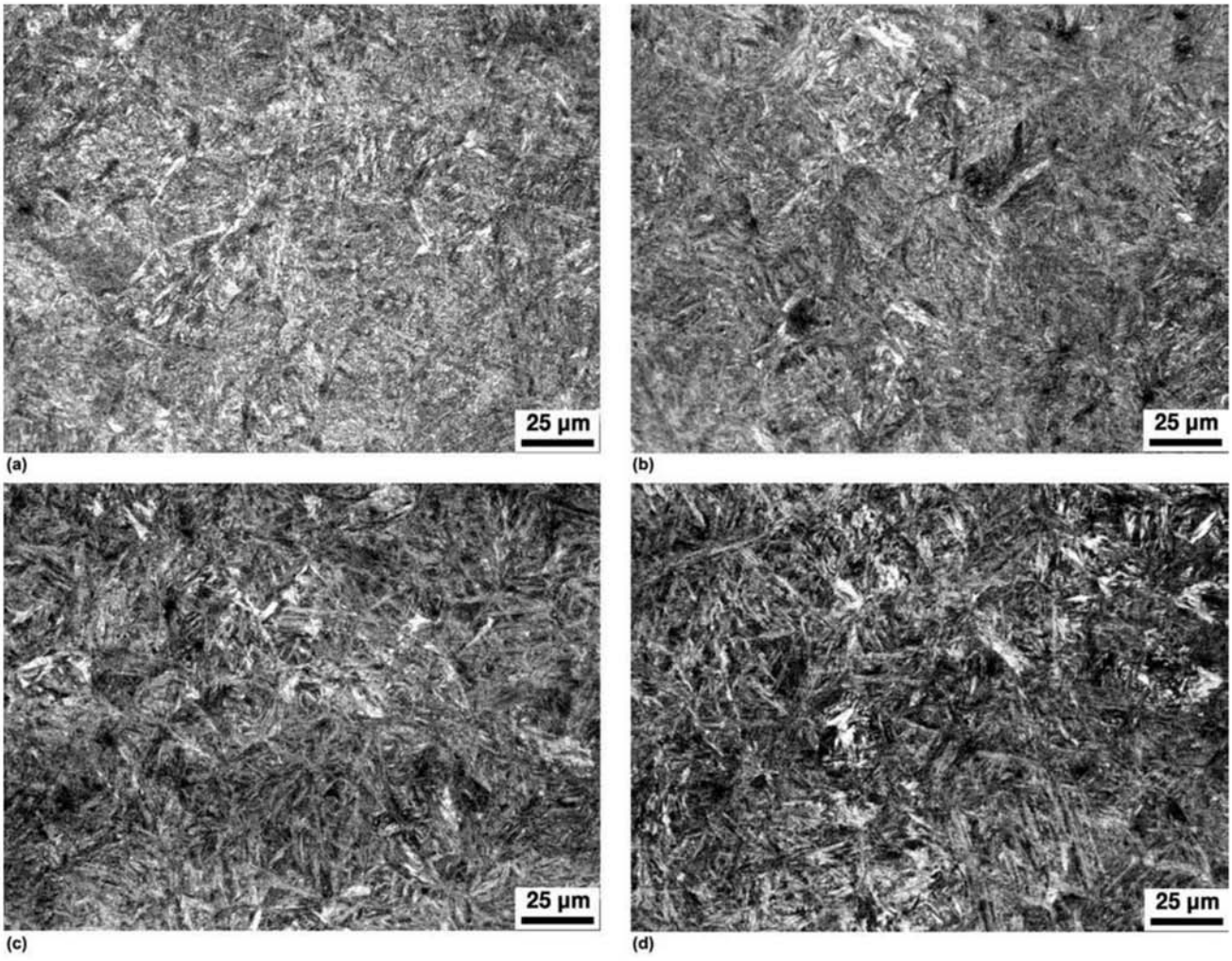

Fig. 15.2 AISI 4360 (a), 4370 (b), 4380 (c), and 4390 (d) steels, quenched and tempered at 300 °C (570 °F). Comparing this image with Fig. 15.1, one can observe that the increase in tempering temperature makes less evident the microstructural differences of the quenched structures. Etchant: nital. Courtesy of L.T. Sandor. Source: Ref 1

Figure 15.3 demonstrates the difficulty in detecting the microstructure feature changes in steels tempered at higher temperatures or for long times. When the structure obtained by tempering AISI 43100 steel at 600 °C (1110 °F) is compared with that used as an example for AISI 4340 in Chapter 10, "Conventional Heat Treatment—Basic Concepts," especially Fig. 10.64 in this book, the difficulty in detecting the most relevant differences, using only optical microscopy, is evident. It is not uncommon to obtain complex microstructures, which are hard to characterize with an optical microscope, when examining quenched and tempered engineering steels. As in the case of multiphase steels (Chapter 13, "Advanced Steels for Forming Operations," in this book), the use of different etchants to get complementary information can also be successfully applied to quenched and tempered steels. Figure 15.4 presents a sample of 300M steel cooled at a rate of approximately 10 K/s. In Fig. 15.4(a), nital etching did not make it possible to properly characterize the acicular constituents (martensite and bainite) nor to differentiate ferrite from retained austenite eventually present. Etching with sodium metabisulfite (Fig. 15.4b) highlights the areas of retained austenite, as all other phases are colored by this reactant. If the color etching is properly developed, it may be possible to eliminate doubts between the presence of bainite and martensite.

An additional tool to distinguish between ferrite, bainite, and martensite is electron backscatter diffraction (EBSD), as discussed in Chapter 9, "Conventional Heat Treatments—Usual Constituents and Their Formation," in the section "Upper and Lower Bainite" in this book.

15.1.2 AISI 52100 Steel

Steels containing around 1% C and 1.5% Cr (such as AISI 52100 or DIN 100Cr6) are widely used in bearings. A fully martensitic microstructure is frequently used, resulting in high strength combined with high fatigue resistance—ideal properties for bearing applications.

When operating in high-humidity environments, AISI 52100 with a martensitic structure may suffer stress corrosion caused by hydrogen (Ref 2). In these cases, it may be convenient to use a microstructure based on lower bainite that will have better fatigue resistance in the presence of water. Luzginova, Zhaoa, and Sietsma (Ref 2) performed a detailed evaluation of the phase transformations in the process of producing bainitic AISI 52100.

To promote spheroidization of the microstructure before the isothermal treatments aimed at forming bainite (austempering), the "as-received" steel (Fig. 15.5) has been subjected to intercritical annealing. The parameters used for this treatment are indicated in Fig. 15.6. Bearing steels are often supplied in the condition obtained with homogenization and annealing heat treatment. The microstructure obtained with the intercritical annealing aimed at spheroidization is presented in Fig. 15.7. One sample has been quenched directly after austenitization (stages 3 and 4 in the cycle presented in Fig. 15.6a) and its microstructure is presented in Fig. 15.8. Part of the cementite has dissolved in austenite. The austenite has transformed to martensite during quenching.

Figure 15.9 presents the results of the various austempering processes evaluated in accordance with the cycles presented in Fig. 15.6, as well as the volume fraction of lower bainite formed. In these microstructures, the aus-

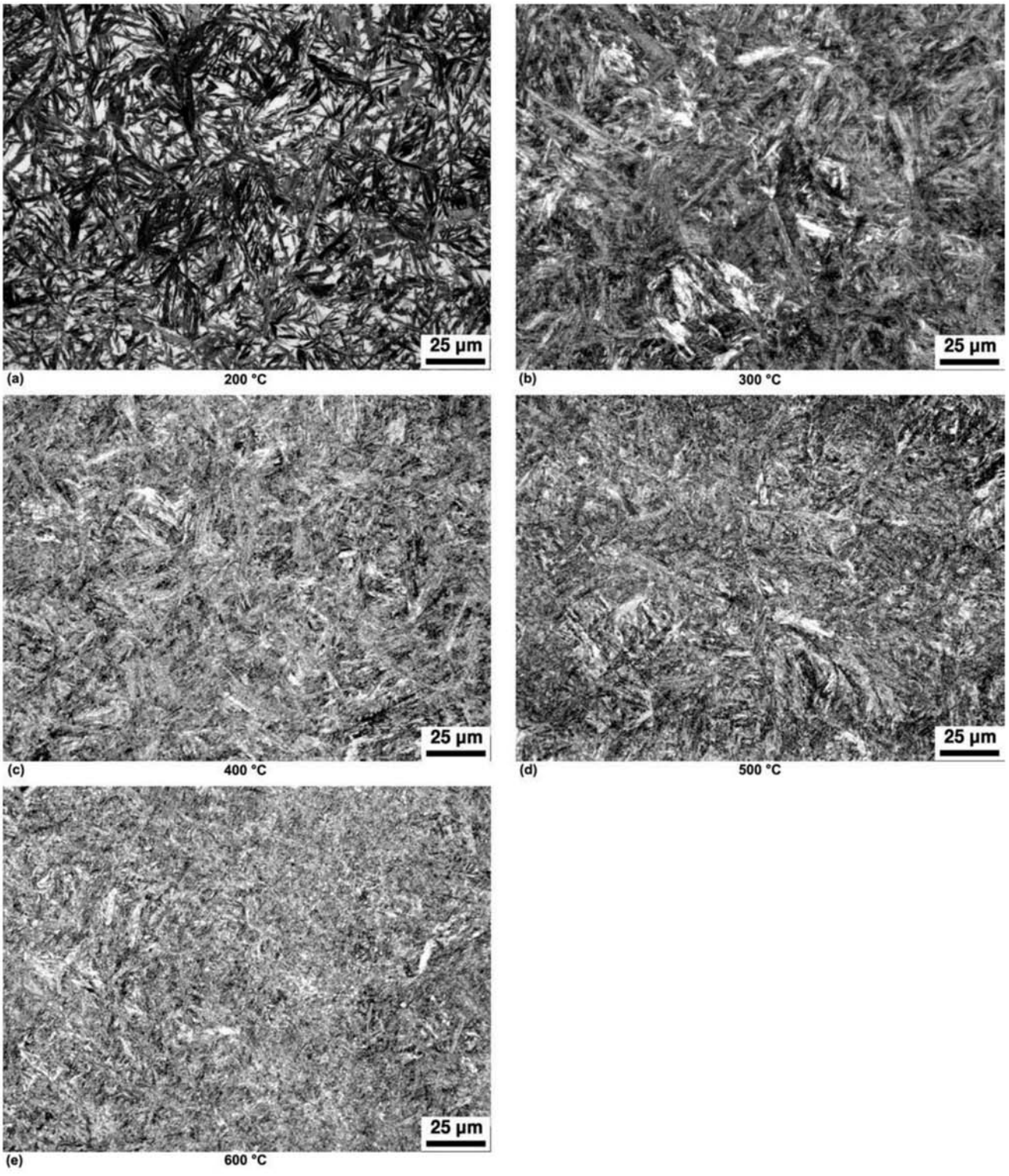

Fig. 15.3 AISI 43100 steel quenched and tempered at different temperatures:(a) 200 °C (390 °F), (b) 300 °C (570 °F), (c) 400 °C (750 °F), (d) 500 °C (930 °F), (e) 600 °C (1110 °F). Etchant: nital. Courtesy of L.T. Sandor. Source: Ref 1

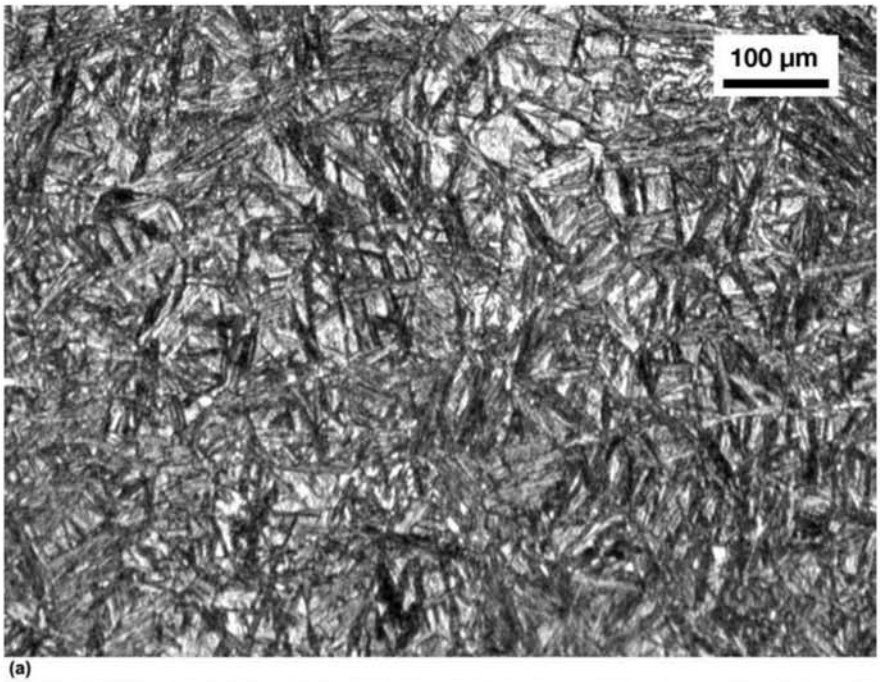

(a)

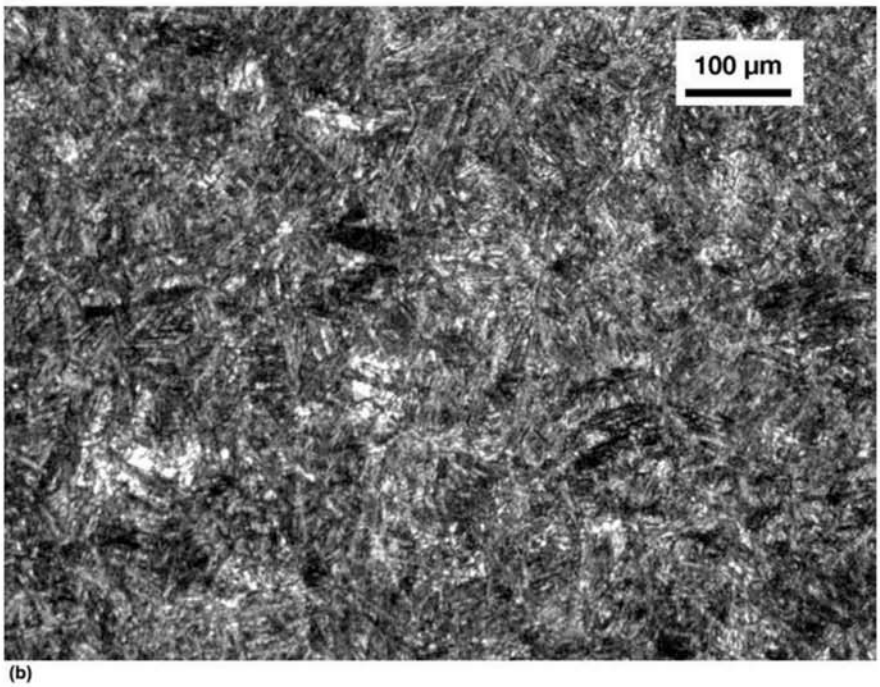

(b)

Fig. 15.4 (a) 300M steel quenched at approximately 10 K/s. Bainite, martensite, and areas of ferrite and/or retained austenite. Etchant: nital 2%. (b) 300M steel quenched at approximately 10 K/s in a different region. Bainite, martensite, and ferrite or pearlite are colored by the etchant. The areas of retained austenite are light colored. By properly adjusting the etching conditions, it is possible to identify bainite and martensite by their different colorations after etching. Etchant: sodium metabisulfite 10% in water. Courtesy of A.J. Abdalla and R.M. Anazawa, IEAv/CTA, S.J. dos Campos, SP, Brazil.

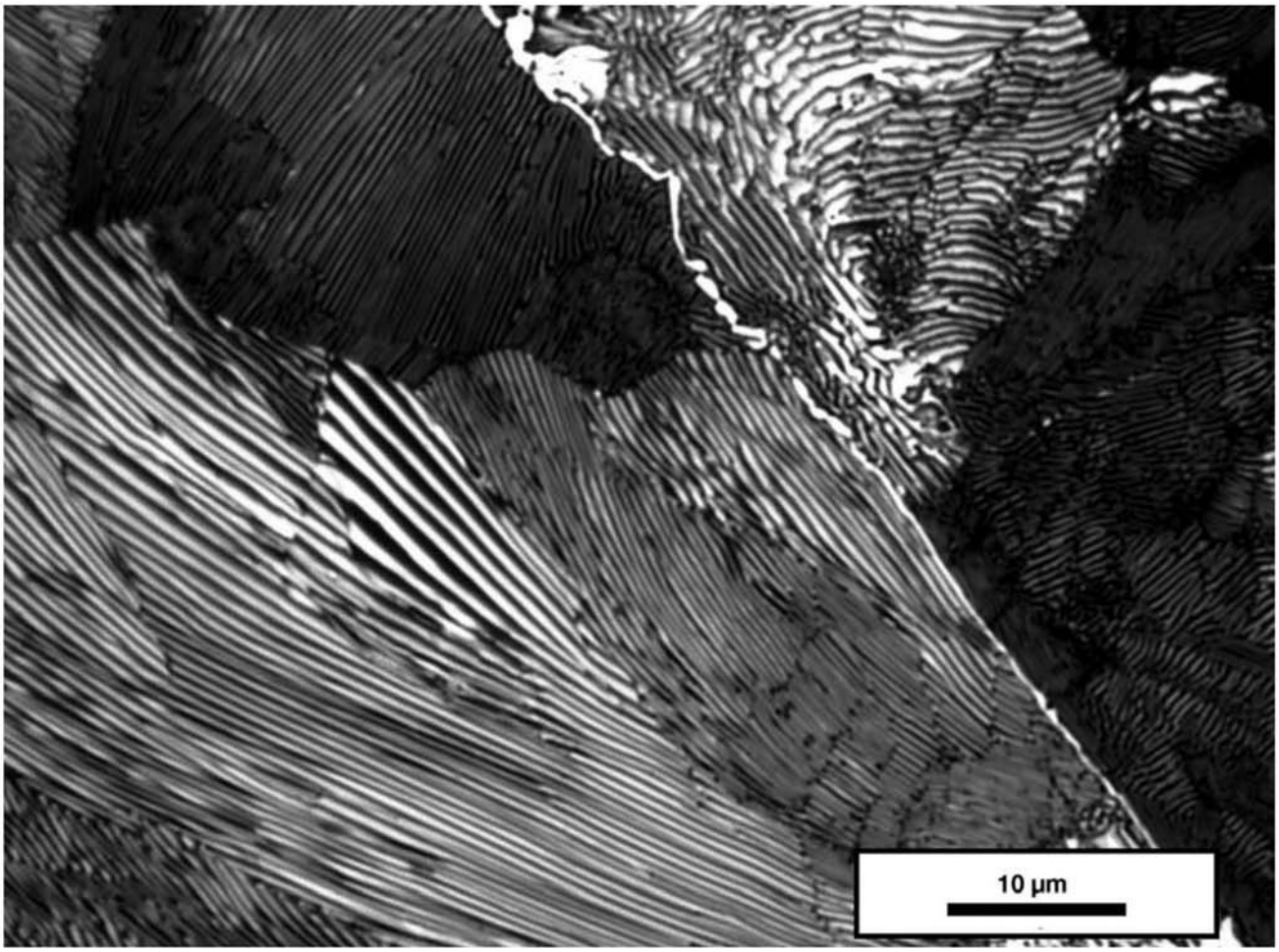

Fig. 15.5 AISI 52100 steel hot rolled and annealed at 820 °C (1510 °F) for 2 h followed by slow cooling (10 °C/h, or 18 °F/h) to 690 °C (1275 °F), followed by air cooling. Pearlite with a network of cementite in the prior-austenitic grain boundaries. Stage (1) in Fig. 15.5(a). Etchant: pre-etching with nital 5% followed by Klemm etchant: 50 ml saturated solution of sodium thyosulfate in water and 1 g sodium bisulfide. Klemm etchant colors ferrite, increasing the image contrast. Courtesy of N. Luzginova and J. Sietsma, Delft University of Technology, Delft, Netherlands

tenite that did not transform to bainite in the austempering is present in two forms: (a) in grains, that transform to martensite (and some retained austenite) upon cooling after the austempering and (b) in films between the laths of lower bainite. These films are not visible using optical microscopy. To properly follow the transformation and experimentally determine the volume fraction of retained austenite, besides using metallography, Ref 2 used x-ray diffraction (XRD) and dilatometry during the austempering process, as shown in Fig. 15.10.

As bainite is formed, austenite also suffers changes in its chemical composition. These changes are extremely important in various steels, such as transformation-induced plasticity (TRIP) steels and those that are subjected to quenching and partitioning (Q&P) heat treatment, both discussed in Chapter 13, “Advanced Steels for Forming Operations,” in this book.

One of the accepted theories related to bainite is that carbon may diffuse from bainite or from bainitic ferrite to austenite, thus enriching the austenite

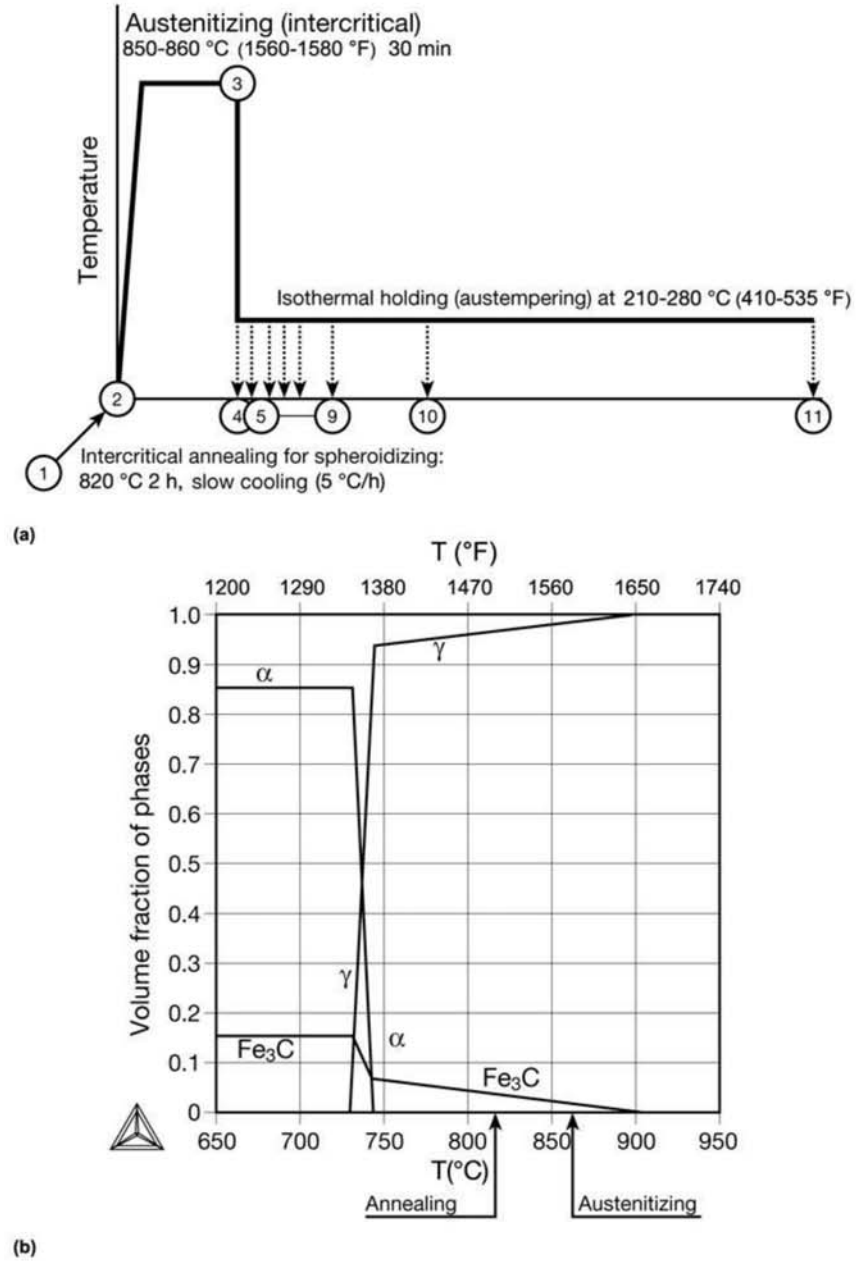

Fig. 15.6 (a) Thermal cycle used in the heat treatment of AISI 52100 steel to obtain lower bainite structure. Adapted from Ref 2. (b) Volume fraction of the phases in equilibrium for the composition considered for the AISI 52100 steel.

in carbon (Ref 3, 4). This process is important in silicon-alloyed steels, for instance. In these steels, carbide precipitation in bainite is strongly inhibited, and the chemical potential of carbon in fresh bainite may be much higher than that in austenite (as a general rule, in iron-based structures, for a given carbon content, the carbon chemical potential is much higher in BCC and BCT structures than in FCC). This difference in chemical potential would cause the carbon partition from bainite to austenite. Figure 15.11 presents the values of

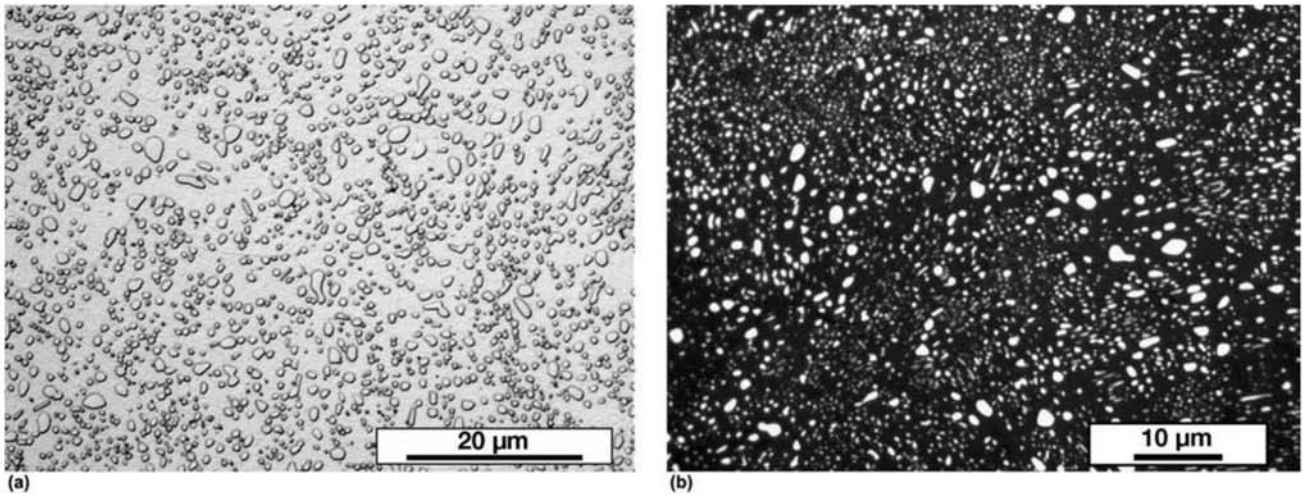

Fig. 15.7 AISI 52100 steel spheroidized starting from the microstructure presented in Fig. 15.6 subjected to the cycle described in Fig. 15.6(a), stage 2 in the cycle. Volume fraction of spheroidized cementite is 15% (compare with the calculated values in Fig. 15.6b). (a) Etchant: nital. (b) Etchant: pre-etching with nital 5% followed by Klemm etchant. Ferrite has been colored, increasing the contrast between phases. Courtesy of N. Luzginova and J. Sietsma, Delft University of Technology, Delft, Netherlands.

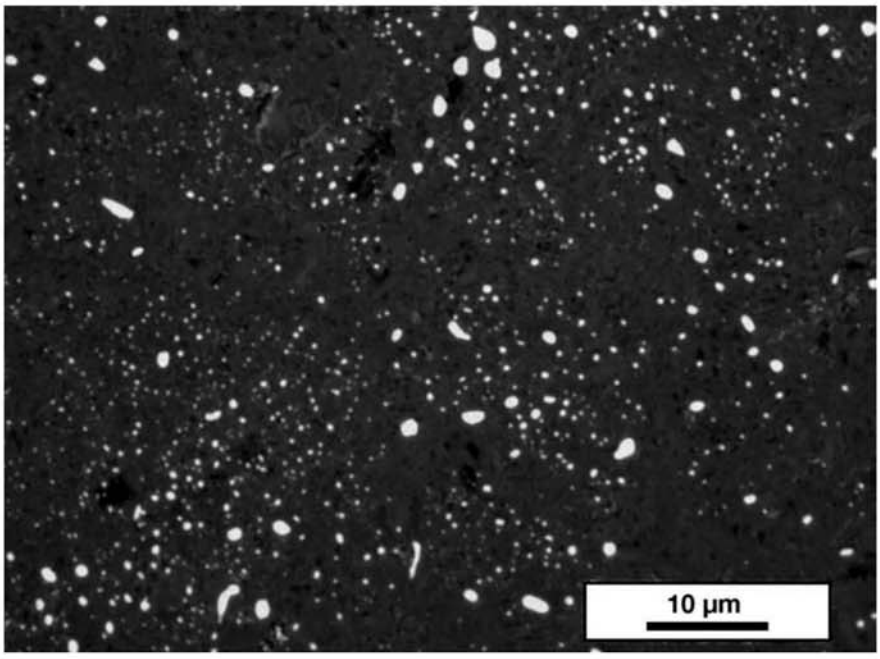

Fig. 15.8 AISI 52100 steel quenched from intercritical austenitizing (850–860 °C, or 1560–1580 °F, for 30 min). Approximately 5% of spheroidized cementite (compare with the calculated value in Fig. 15.6b) in a matrix of austenite that has partially transformed to martensite (dark in the figure). Retained austenite in this steel is formed as films between the martensite plates and is not easily identified in optical microscopy. Courtesy of N. Luzginova and J. Sietsma, Delft University of Technology, Delft, Netherlands.

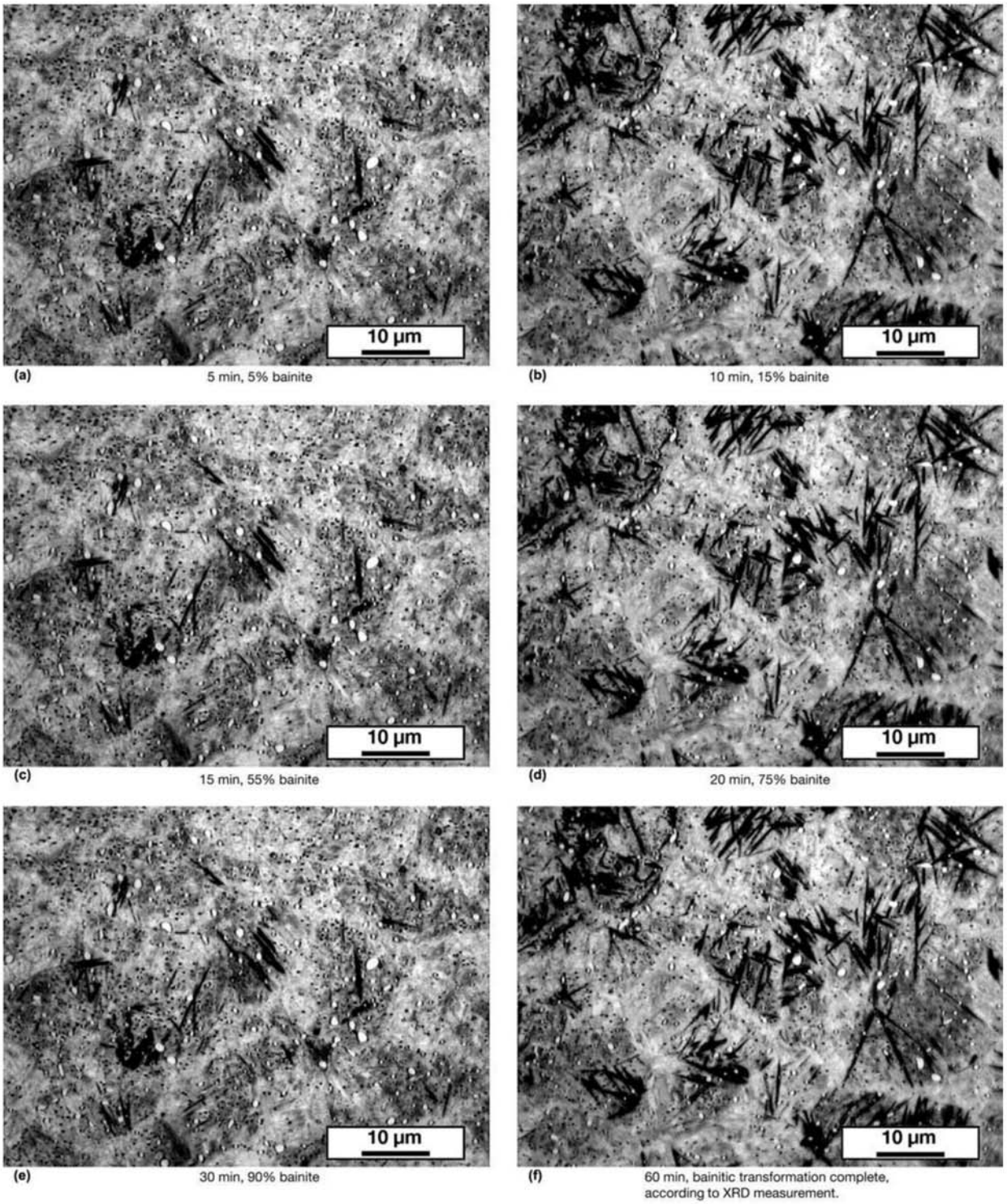

Fig. 15.9 The evolution of the microstructure of AISI 52100 steel as a function of the isothermal holding time, in accordance with the austempering cycles presented in Fig. 15.6(a). Lower bainite is present as dark needles; the cementite that did not dissolve during austenitization shows as white globules. The untransformed austenite at the end of the austempering holding time transforms into martensite and retained austenite in the postaustempering cooling, giving rise to the "light" matrix, more easily observed in the samples subjected to holding times shorter than 15 min. In this matrix, the darker region is richer in martensite—some "needles" can be seen. Etchant: picral 4%. Courtesy of N. Luzginova and J. Sietsma, Delft University of Technology, Delft, Netherlands.

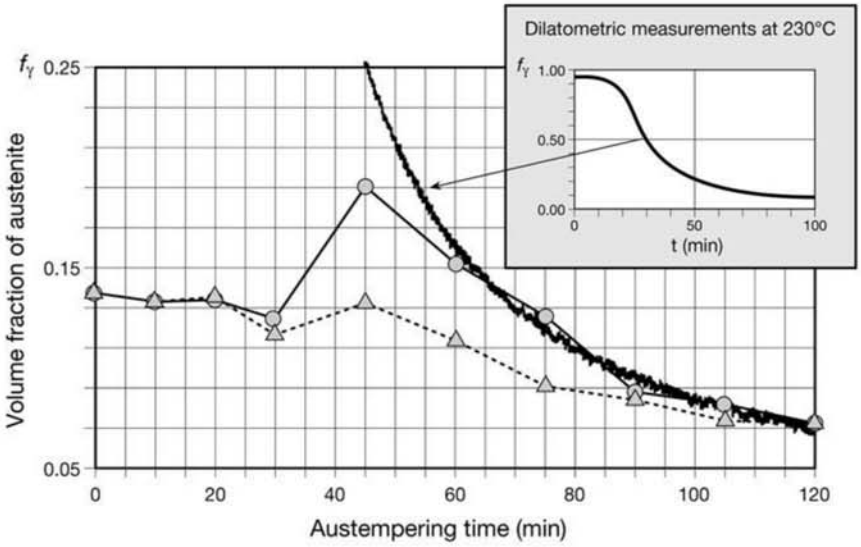

Fig. 15.10 Austenite volume fraction $f\gamma$ as a function of austempering holding time. The solid line represents the values of the austenite volume fraction at 230 °C (445 °F) determined through dilatometry. The circles represent the values of the volume fraction of austenite at room temperature, measured using x-ray diffraction after the cooling subsequent to the end of the austempering holding time. Triangles represent the calculated values; see text for a discussion of the calculation method. Source: Ref 2

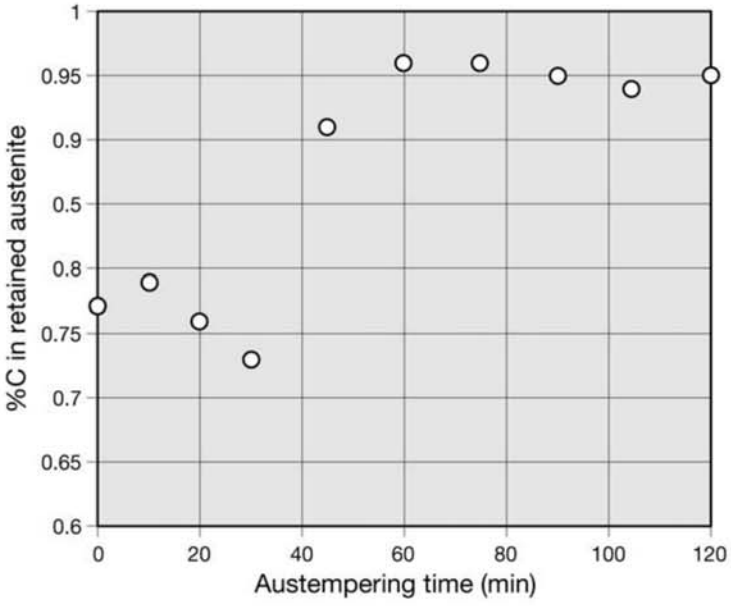

Fig. 15.11 Carbon content of the retained austenite as a function of the austempering holding time, determined using x-ray diffraction measurements. Source: Ref 2

carbon content measured in austenite (using XRD) as a function of the austempering time (Ref 2). Based on the volume fractions of austenite at the end of austempering (measured by dilatometry, see inset in Fig. 15.10) and on the carbon content of this austenite, Ref 2 calculated the volume fraction of austenite that should be present at room temperature, using the following methodology:

Using the DRX measurements, the carbon content of austenite has been calculated (Fig. 15.11). M_s temperature was estimated using Andrews equation (see Table 9.1, Chapter 9, "Conventional Heat Treatments—Usual Constituents and Their Formation," in this book). Using Koistinen-Marburger equation (Chapter 9) it was then possible to calculate the volume fraction of retained austenite at room temperature using Eq 15.1.

$$f_{\gamma,\text{retained}} = f_{\gamma,\,230\ ^\circ\text{C}} \exp(-C_1[M_S - T_{\text{Room}}]) \quad \text{(Eq 15.1)}$$

where C_1 is a constant. The values calculated this way are presented in Fig. 15.10 and show good correlation when compared with experimental results.

AISI 4145 Steel

AISI 4145 steel is a common choice for drill columns in oil fields. It is normally used in the quenched and tempered condition. When necessary, these columns are friction welded, with good results. Figures 15.12 to 15.14 present examples of typical microstructures of this steel in the quenched and tempered condition.

AISI 8630 Modified (8630Mod) Steel

As mentioned in Chapter 14, "Structural Steels and Steels for Pressure Vessels, Piping, and Boilers," in this book, the chemical composition of AISI 8630

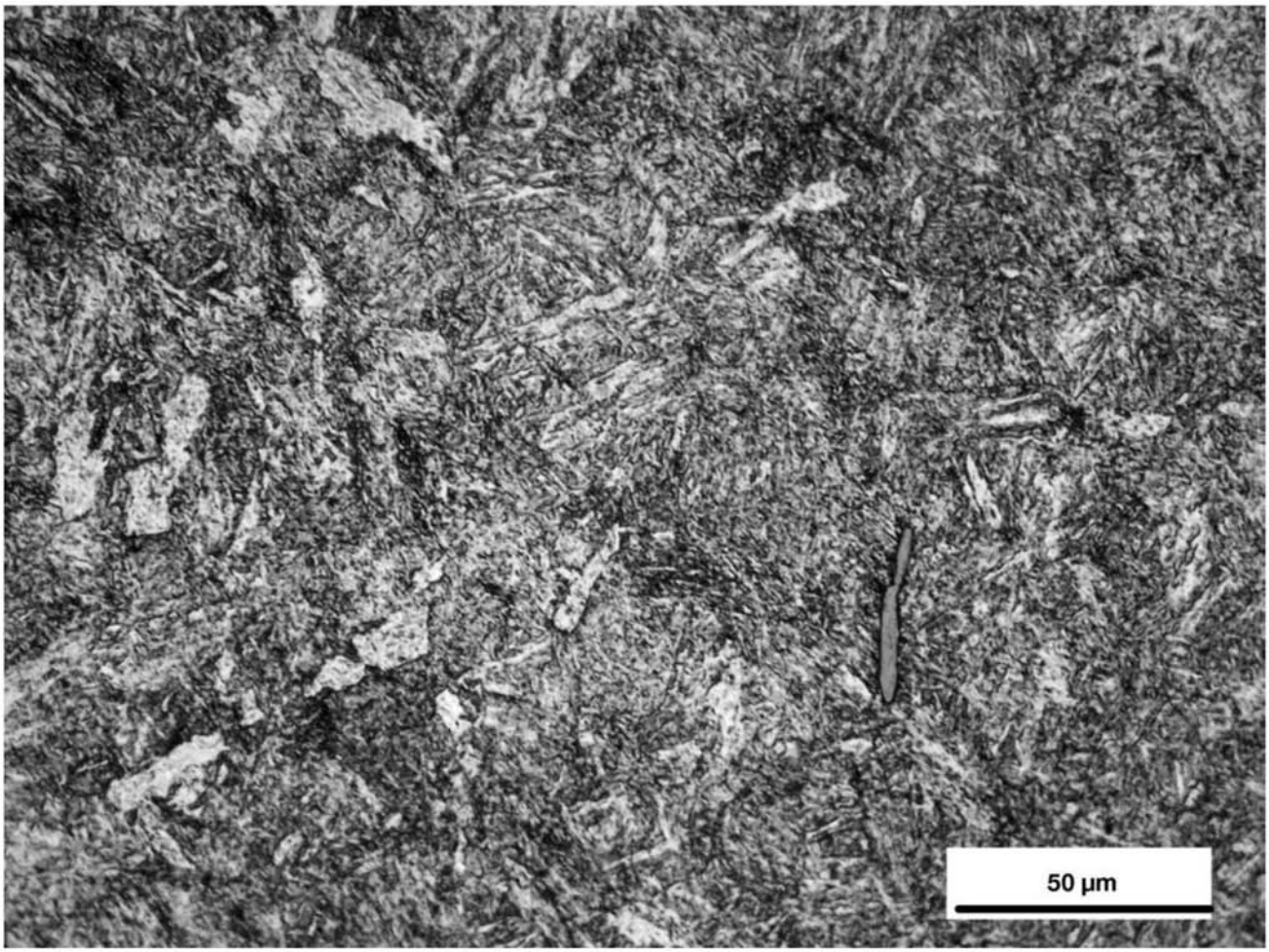

Fig. 15.12 AISI 4145 steel quenched and tempered. Tempered martensite. Hardness 32 HRC. An elongated manganese sulfide nonmetallic inclusion is also visible. Courtesy of A. Zeemann, Tecmetal, RJ, Brazil.

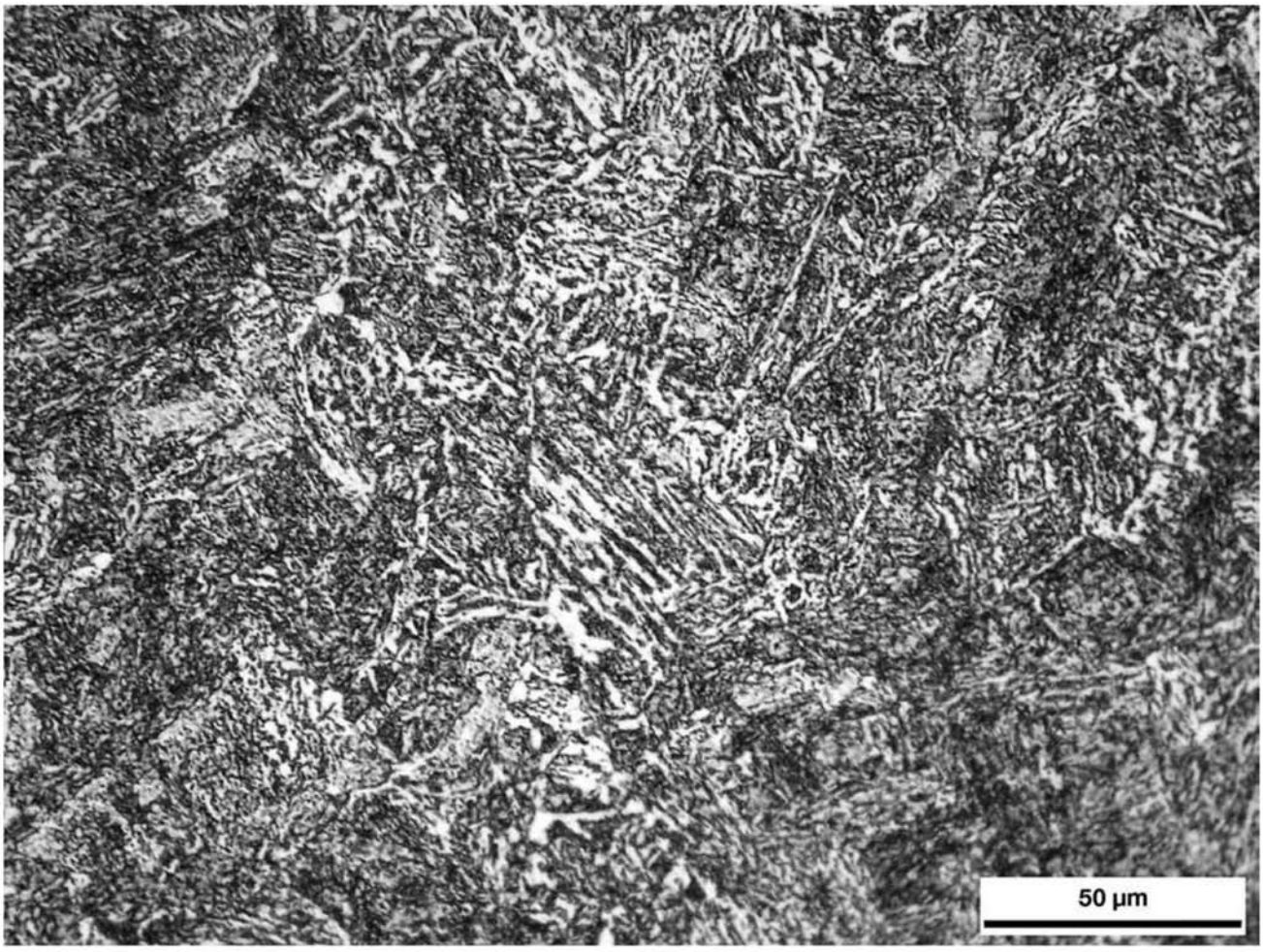

Fig. 15.13 AISI 4145 steel quenched and tempered. Tempered martensite and bainite. Hardness 30 HRC. Courtesy of A. Zeemann, Tecmetal, RJ, Brazil.

has been modified to increase hardenability while fulfilling the requirements for stress corrosion resistance defined by NACE MR0175 (Ref 5). Thus, Ni is kept under 1% and the chemical composition is balanced (the content of some elements are outside of the range of compositions of conventional AISI 8630) to reach hardenability and a good strength-to-hardness relationship. With this steel in the quenched and tempered condition it is possible to produce thick forgings with yield strength above 585 MPa (85 ksi) and hardness under 22 HRC, as required by Ref 5. Figure 15.15 shows an example of the structure of a forging for subsea wellhead equipment made from this steel.

15.2 Coatings

Some coatings, beyond those presented for structural steels, may also be applied to engineered steels and stainless steels. Coatings such as nickel-phosphorous (Ni-P) or chemically deposited nickel are hard deposits that can be applied without significant reaction with the steel substrate.

Figure 15.16 presents the cross section of a Ni-P coating applied on an oil field part. The coating is used to avoid scratches and other surface damage that may interfere with the part functionality.

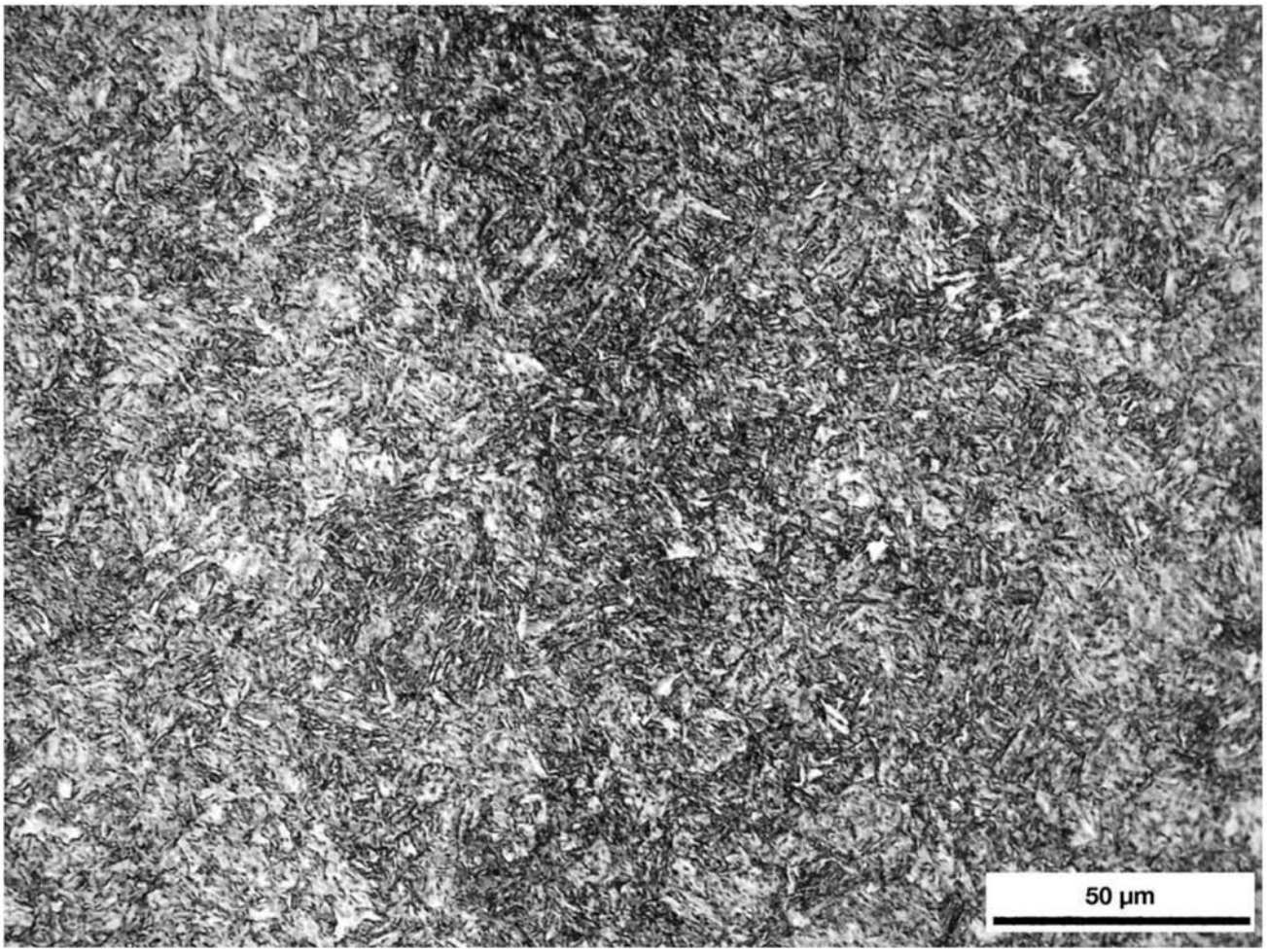

Fig. 15.14 AISI 4145 steel quenched and tempered. Tempered martensite and bainite. Hardness 33 HRC. Courtesy of A. Zeemann, Tecmetal, RJ, Brazil.

Some materials with very high resistance to scratching or to corrosion, such as carbides, may be thermally spray deposited or applied by processes similar to metallization, as shown in Fig. 15.17.

Phosphate coatings are frequently used to help in the mechanical processing of steel. These coatings can have a lubricating effect, reducing the friction between the tools and the parts, for instance. However, if the phosphate is not properly removed from the part surface before heat treatment, it may decompose in a reducing atmosphere, causing the introduction of phosphorous into the part surface. This phosphorous may diffuse into the surface layer of the part (Ref 6), causing a ferritic layer to form on the part surface (Fig. 15.18) (because phosphorous is a ferrite stabilizer) or even embrittling the superficial layer of the material.

15.3 Medium and High-Carbon Steels

These steels are frequently not included in the classification of engineering steels and often are not SBQ steels. In some applications, the use of high and medium carbon can be advantageous. Steels such as AISI 1050 and 1060, for instance, are used in agricultural equipment (e.g., plough wheels) and grind-

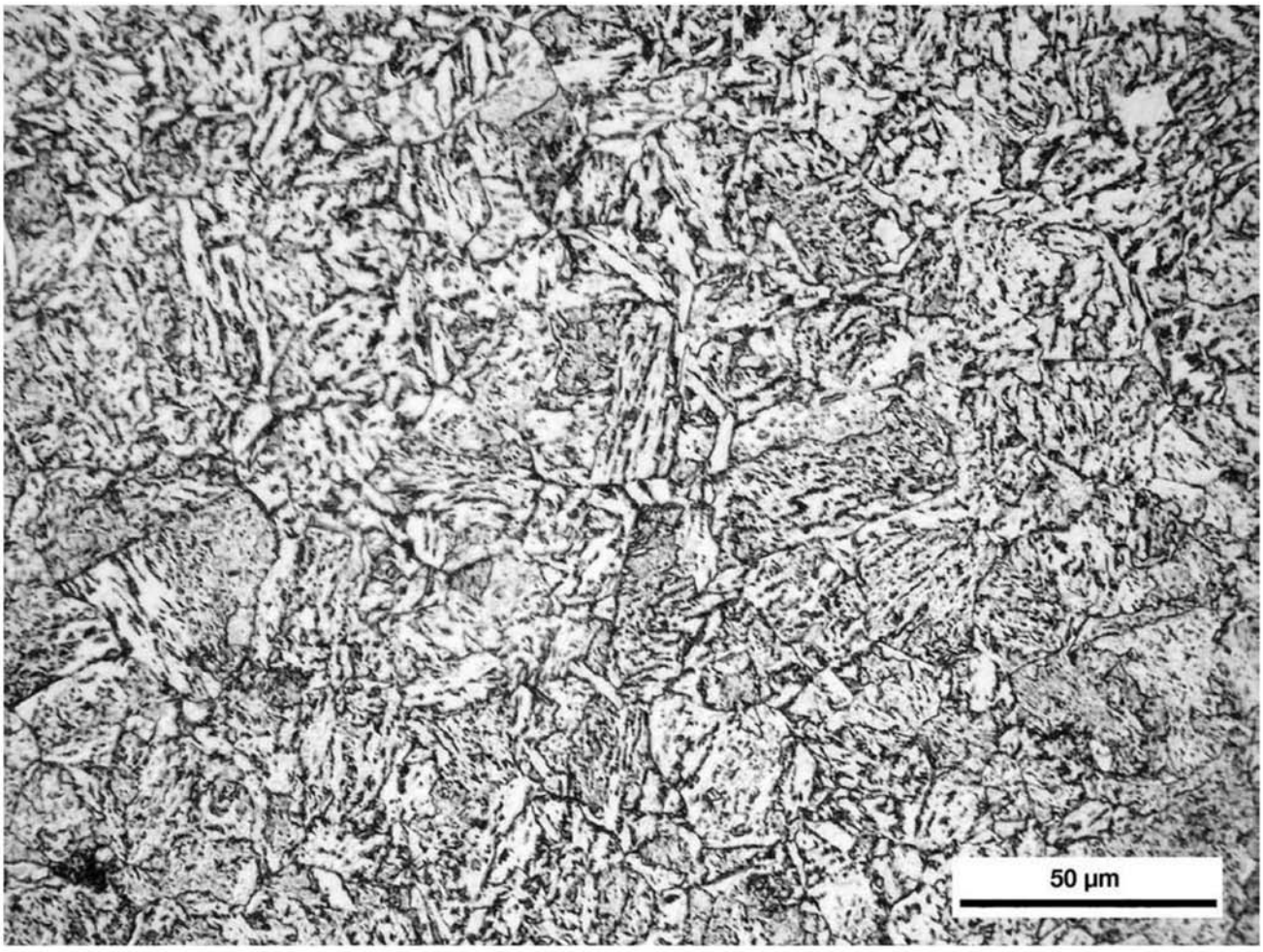

Fig. 15.15 AISI 8630 Mod. steel, quenched and tempered, bainitic structure. Hardness 240 HB. Courtesy of A. Zeemann, Tecmetal, RJ, Brazil.

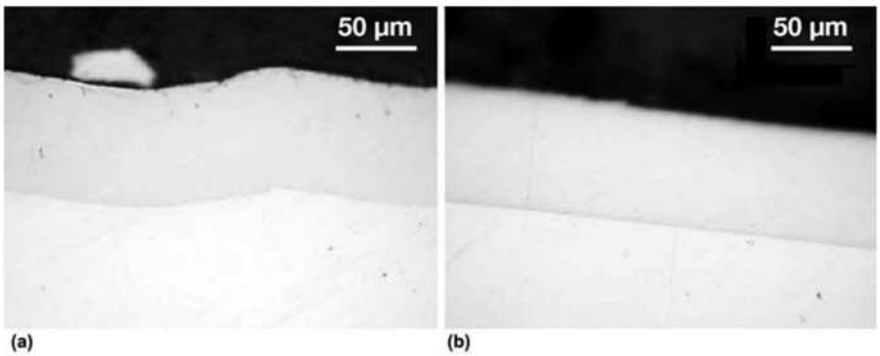

Fig. 15.16 Ni-P layer deposited by chemical process on the surface of a part of F6NM stainless steel (see Chapter 16, "Stainless Steels," in this book) (a) and (b). This coating is deposited for surface protection and to avoid scratches or other superficial damage that may interfere with the part performance, such as sealing. Courtesy of A. Zeemann, Tecmetal, RJ, Brazil.

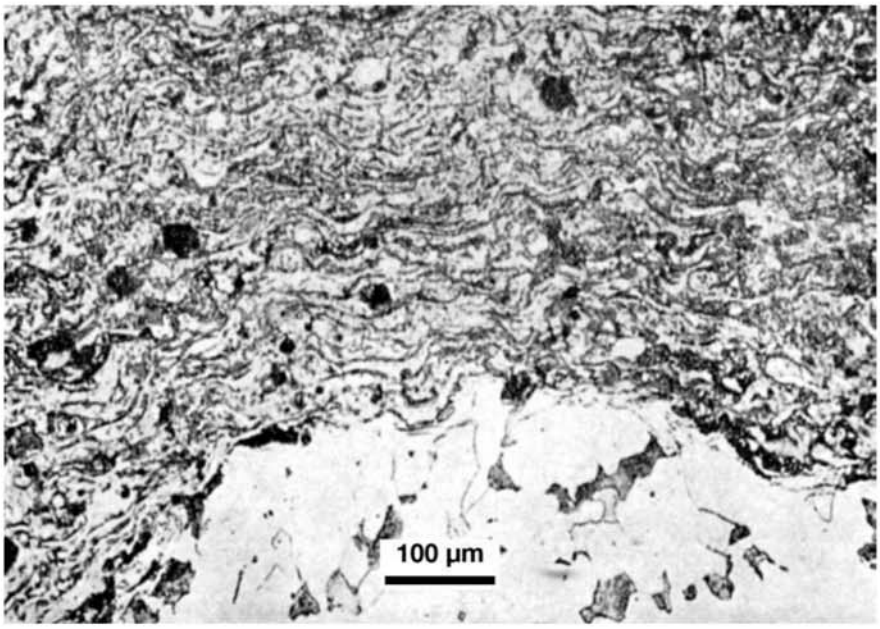

Fig. 15.17 Typical aspect of the transverse cross section of a material deposited using thermal spray. The particles of the pulverized material deform when reaching the substrate and create the appearance of irregular layers. In the lower part of the image, the substrate can be seen, here, a low-carbon steel.

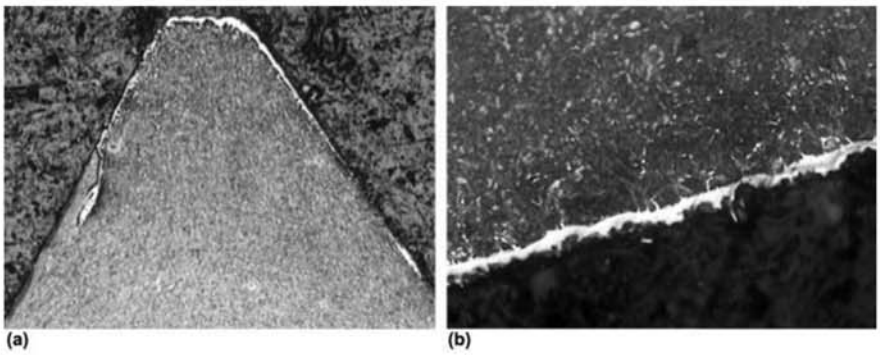

Fig. 15.18 Ferrite layer formed on the surface of a thread of a bolt due to deficient removal of the phosphate layer that was applied to the bolt before the heat treatment; a lap can also be observed (a). (b) Higher magnification view of the thread surface. Courtesy of FIBAM Industrial, SP, Brazil.

ing tools. Eutectoid and hyper-eutectoid steels are among those that give the best results when used in rails and railroad wheels, particularly for heavy haul services.

AISI 1050 and 1060 Steels

Figures 15.19 to 15.22 present microstructures of AISI 1050 and 1060 after controlled rolling and hot rolling followed by normalizing. In these heat treatment conditions, these steels present good wear resistance and high strength.

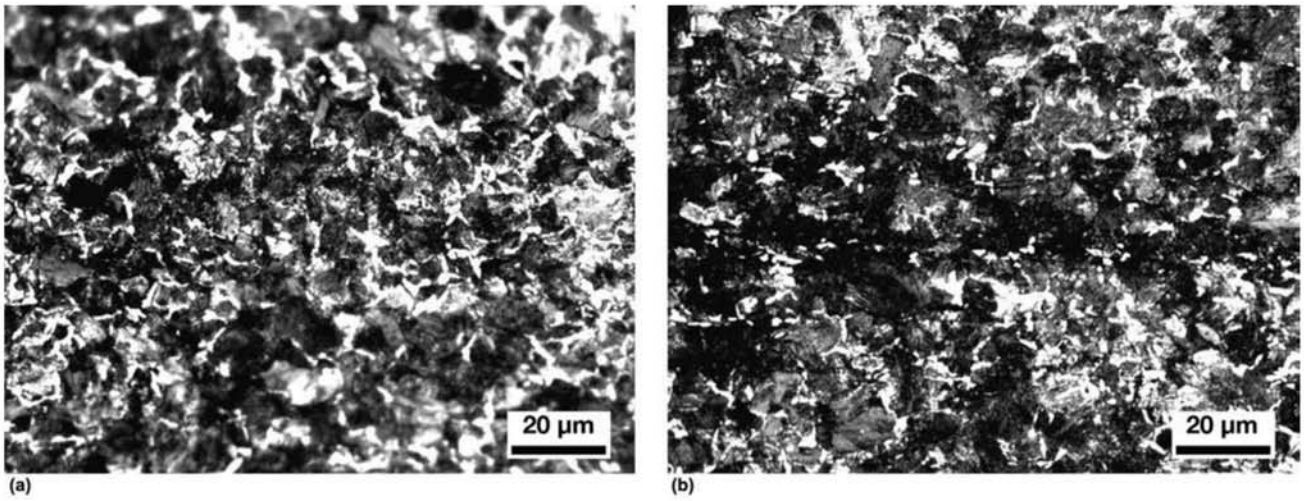

Fig. 15.19 AISI 1050 steel plate, normalized. (a) Surface; (b) mid-thickness. Pro-eutectoid ferrite and pearlite. Etchant: nital 2%. Courtesy of ArcelorMittal Tubarão, ES, Brazil.

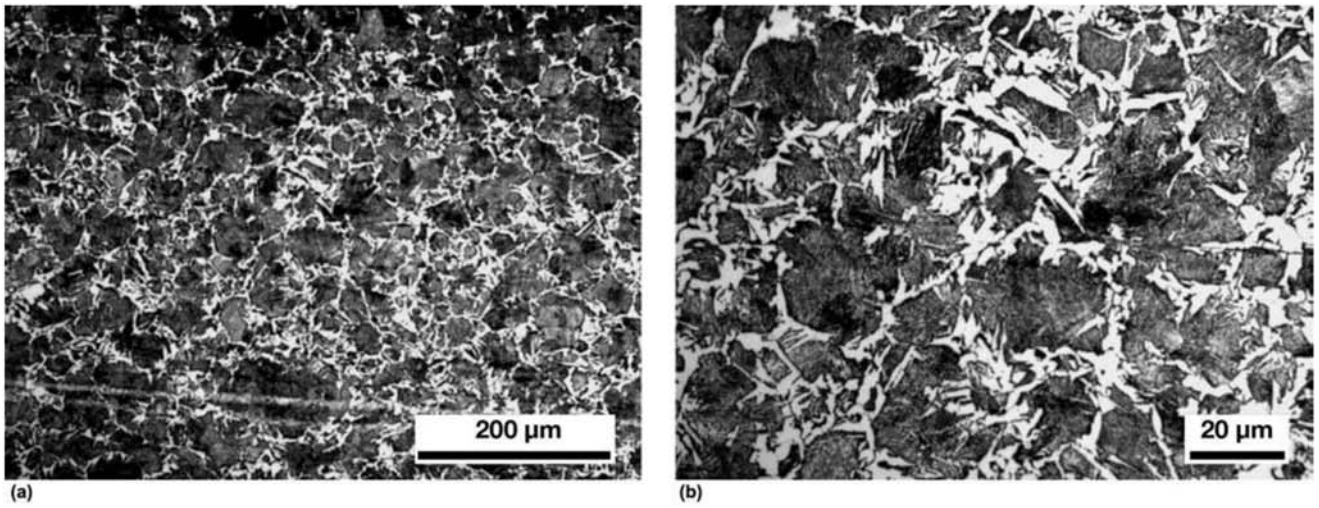

Fig. 15.20 AISI 1060 steel plate, controlled rolled. (a) One quarter thickness position; (b) mid-thickness. Pro-eutectoid ferrite and pearlite. Some acicular ferrite. Etchant: nital 2%. Courtesy of ArcelorMittal Tubarão, ES, Brazil.

Figure 15.23 presents the microstructure of annealed AISI 1050 steel. The pearlite lamellae spacing and the volume fraction of pro-eutectoid ferrite are larger than in the normalized condition.

Railway axles are frequently produced using steels similar to AISI 1050. Although this selection is adequate from the point of view of the expected performance, some care must be exercised during use. The high hardness and hardenability of these steels make welding very difficult or impossible. For this reason, they are normally not welded. When it is essential to weld these steels, carefully designed weld procedures, including preheating and postweld controlled cooling and postweld heat treatment are usually required. When these precautions are not followed, premature failure may occur, as shown in Fig. 15.24. Figure 15.25 presents the site of the fatigue crack initiation indicated in Fig. 15.24 displaying two planes: one plane

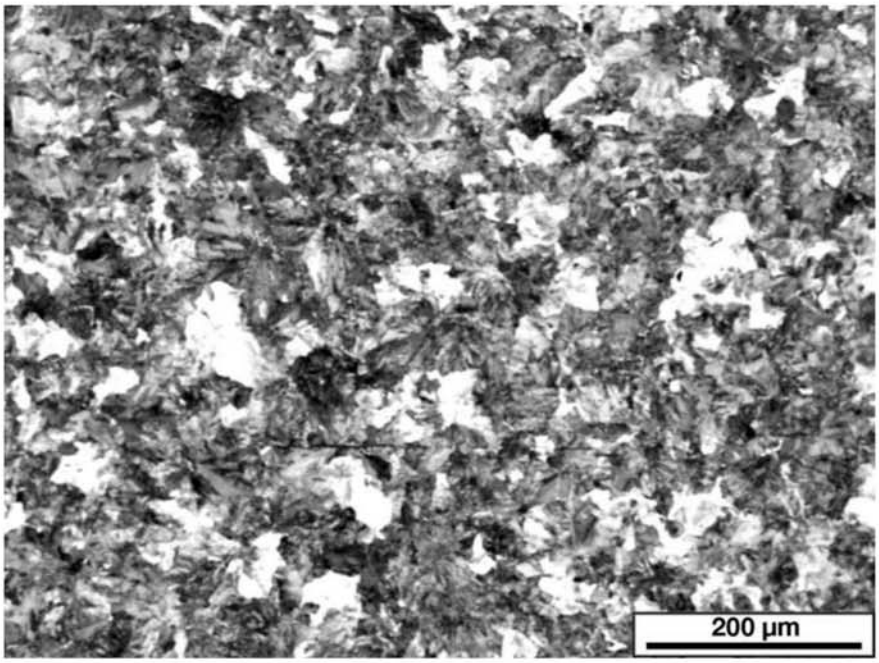

Fig. 15.21 Steel containing C = 0.64% and Mn = 0.82% for shear knives, subjected to controlled rolling. Fine pearlite with little pro-eutectoid ferrite. The accelerated cooling at the end of the rolling process has prevented the formation of pro-eutectoid ferrite (for this manganese content, the eutectoid composition is close 0.73% C).

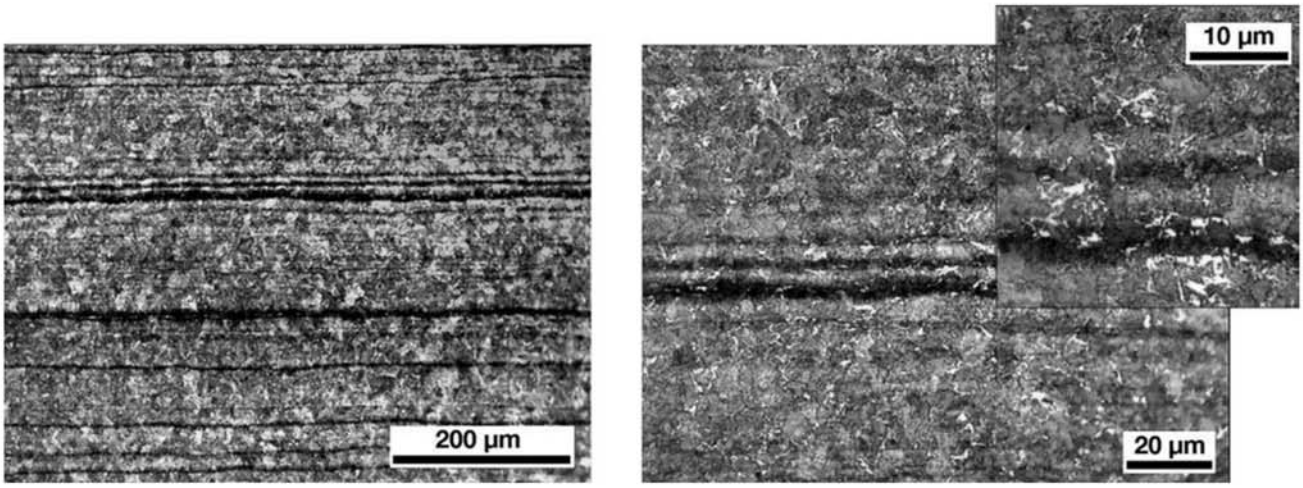

Fig. 15.22 Longitudinal cross section at mid-thickness of a plate of AISI 1060 steel, as hot rolled. Central segregation. Notice that due to the volume fraction of ferrite and pearlite in medium and high carbon steels, banding is seldom noticeable. Fine pearlite with some pro-eutectoid ferrite. Etchant: picral 4%. Courtesy of ArcelorMittal Tubarão, ES, Brazil.

contains the axial and radial directions of the axle and has been prepared for metallographic examination. It is evident from the observation of this figure that welding was performed in this region, as the fusion line and heat affected zones are visible. Micrographic observation (Fig. 15.26) confirms this.

Steels with Chemical Composition Near the Eutectoid

Railroad car wheels are manufactured by forging (Fig. 15.27) or casting in permanent graphite molds (Fig. 15.28) according to a patented process. Most wheels are subjected to a heat treatment in which after austenitizing, the

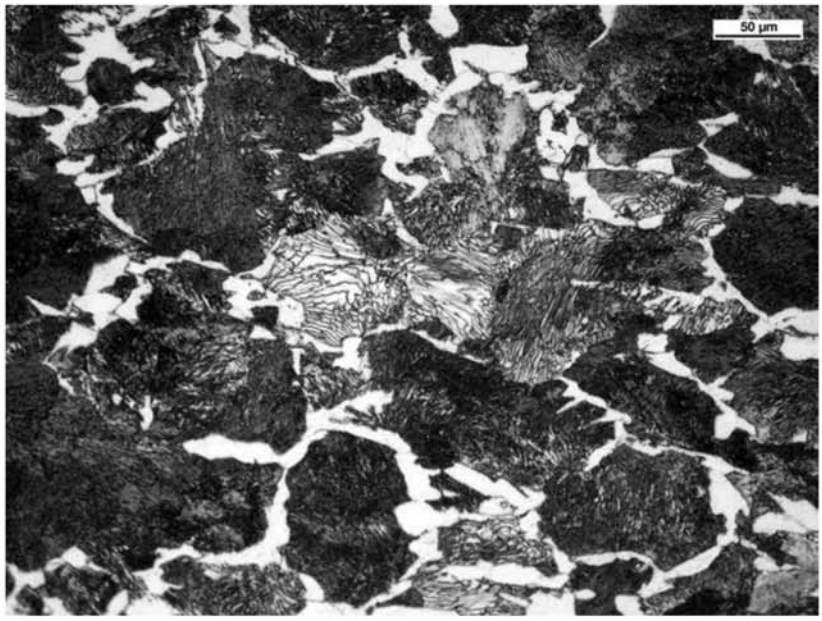

Fig. 15.23 Annealed AISI 1050 steel. Pro-eutectoid ferrite and pearlite. Courtesy of A. Zeeman, Tecmetal, RJ, Brazil.

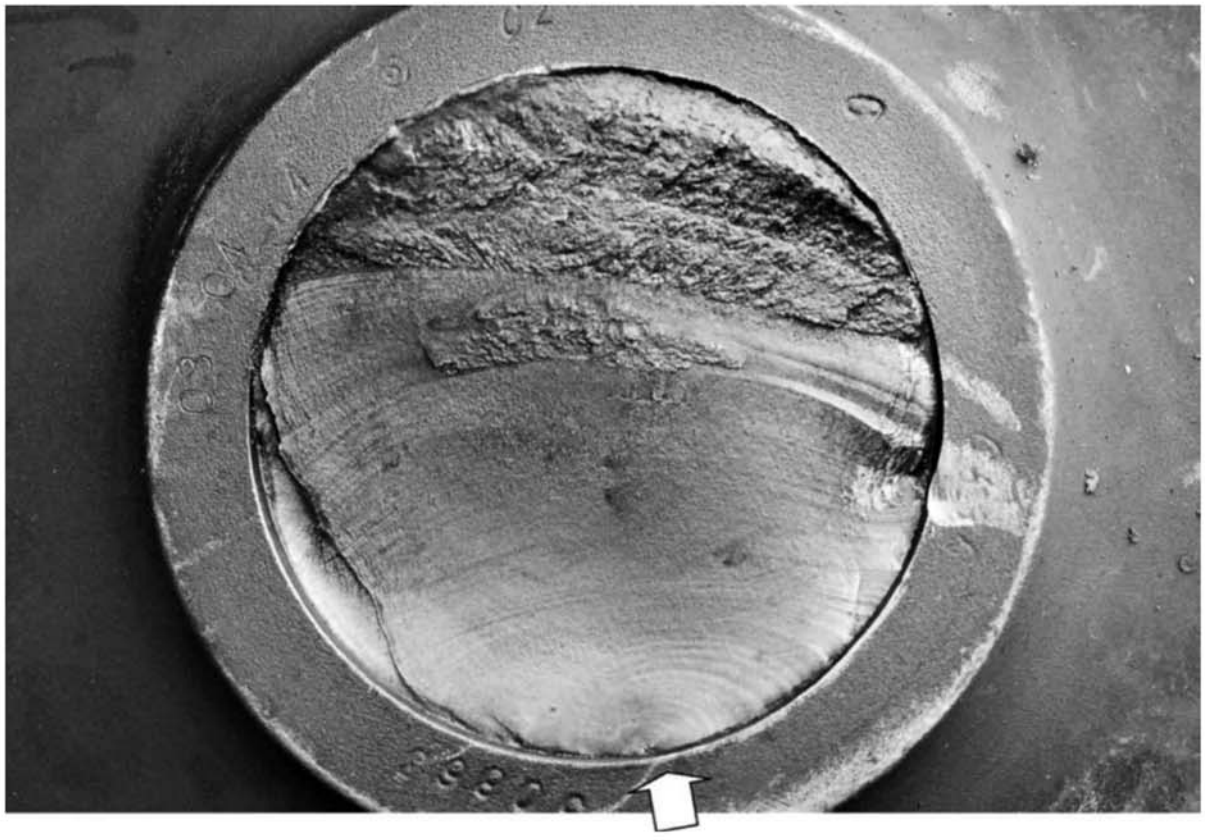

Fig. 15.24 Fatigue failure in a forged railway axle. The wheel is still mounted in the axle. The fracture started at the radius transition corresponding to the area of the axis where the wheel is assembled. The arrow indicates the initiation. Beach marks indicate that the crack propagated by fatigue. The region on the top of the image fractured due to lack of cross section to resist the applied stresses. Courtesy of MRS Logística S.A., RJ, Brazil.

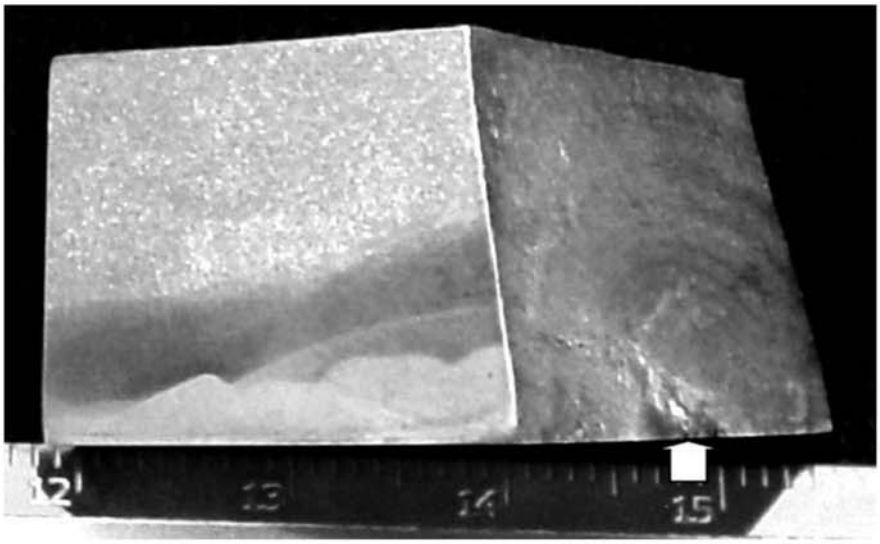

Fig. 15.25 Region where the fatigue fracture of Fig. 15.24 started (right side) and a cross section in the axial-radial plane of the axis of Fig. 15.24. The macrograph performed on the cut surface (left side) indicate the presence of a weld repair, with the weld-deposited metal in the lower part of the image, a wide heat-affected zone (around 5 mm, or 0.2 in.) and unaffected material. Scale is in mm. Courtesy of MRS Logística S.A., RJ, Brazil.

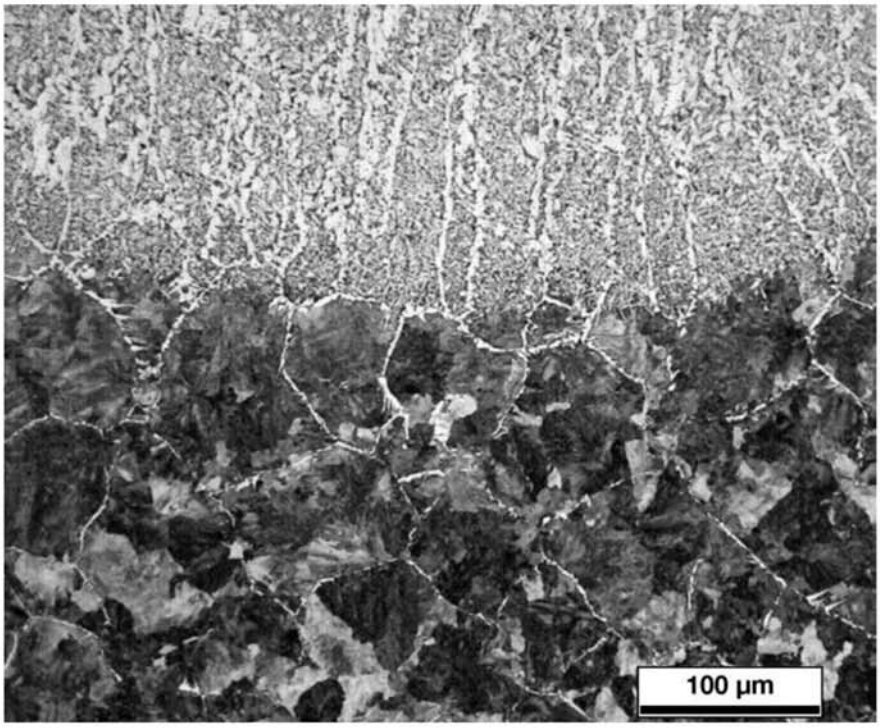

Fig. 15.26 Region of the axle close to the point where the fatigue crack started, shown in the macrograph of Fig. 15.25. Weld deposited metal (upper region of the image), heat affected zone in base metal similar to AISI 1050 (lower region of the image). Metallography by I. C. Abud, INT, Brazil. Courtesy of MRS Logística S.A., RJ, Brazil

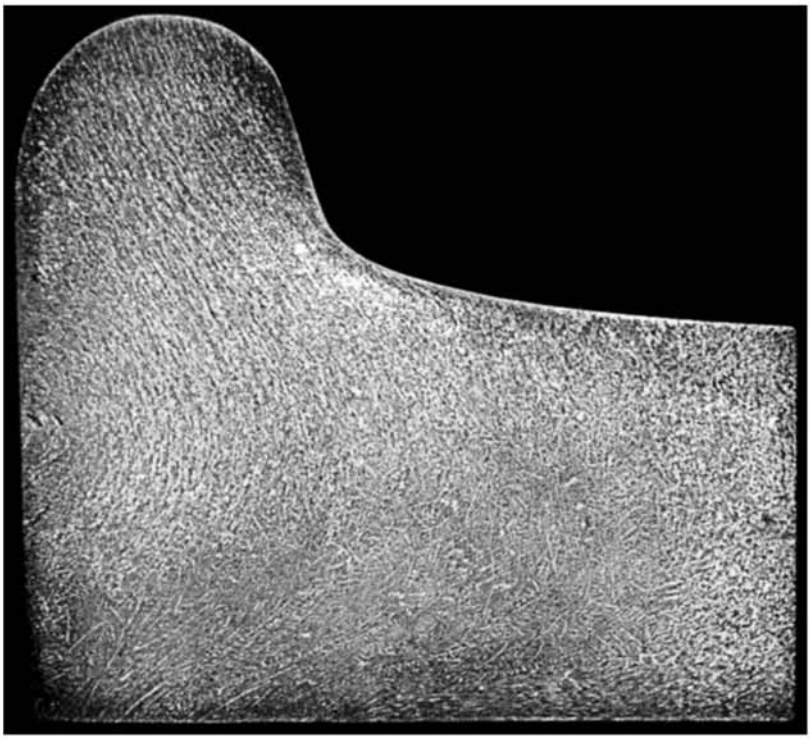

Fig. 15.27 Macrograph of part of the radial plane of a railway wheel produced using hot working (fibers characteristic of hot working are visible). Etchant: iodine.

Fig. 15.28 Macrograph of part of the radial plane of a railway wheel produced by permanent mold casting. The dendritic structure is visible. The wheel tread, the flange, and part of the wheel side are darker due to accelerated cooling during the heat treatment. Etchant: hot hydrochloric. Courtesy of MRS Logística S.A., RJ, Brazil.

wheel rotates so that the rim is water quenched by a set of jets arranged in a circle (Fig. 15.29). This quenching results in the formation of fine pearlite in the rim region and a compressive stress state in the wheel's tangential direction, close to the rim surface. This is very important to prevent the propagation of fatigue cracks in the radial plane of the wheel, which could lead to catastrophic failures.

The chemical compositions and the heat treatment conditions are carefully adjusted to guarantee very fine pearlite in the rim region, as shown in Fig. 15.30 and 15.31.

On the other hand, the loads on rails are increasing every year in heavy haul railways, particularly where the railroad has curves or is sloped. Among the notable failure mechanisms (Ref 7), contact fatigue is becoming especially important and the rail microstructure and its maintenance must be optimized to control this phenomenon. Internal cleanliness is very important, too, since fracture may initiate in nonmetallic inclusions below the rail surface (Fig. 15.32) (Ref 8). Very good results are obtained with uniform fine pearlite microstructures (Ref 9, 10) and by using of steels with a very low level of total oxygen to minimize the amount of oxide nonmetallic inclusions. Bainitic structure rails have also been the subject of interest in recent decades.

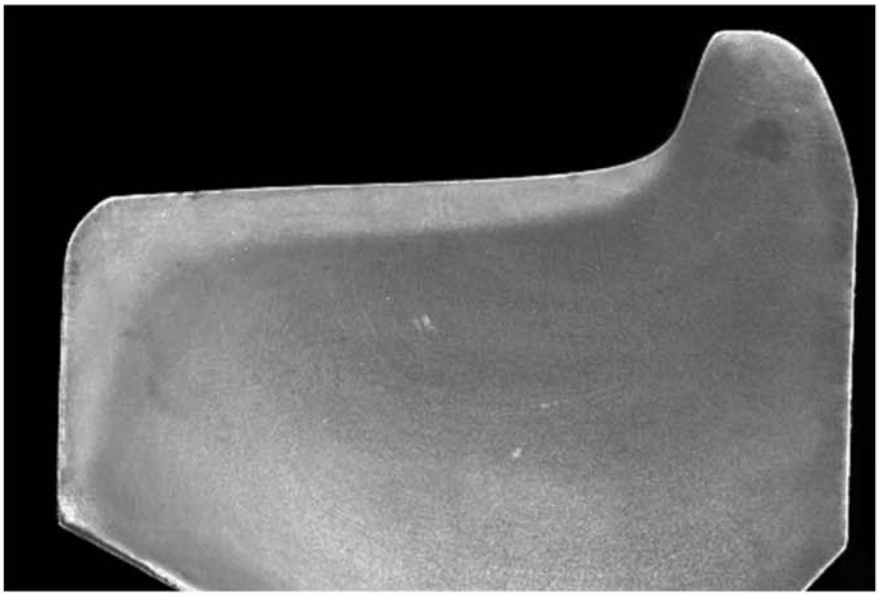

Fig. 15.29 Macrograph of the radial plane of a railway wheel. The etching with nital 4% shows the region subjected to accelerated cooling (lighter, under the illumination conditions used) that does not reach the wheel flange, in this case. This etchant is not adequate for the observation of segregation. For this reason, it cannot be used to determine the manufacturing process used for this wheel. Courtesy of MRS Logística S.A., RJ, Brazil.

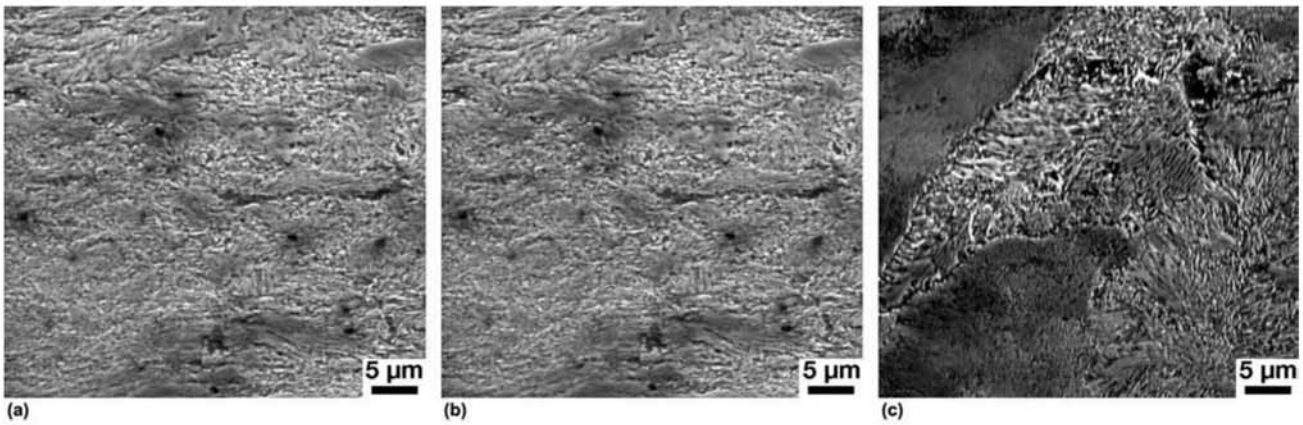

Fig. 15.30 Railway wheel. Steel has a chemical composition very close to the eutectoid. Close to the tread, (a) deformed fine pearlite, (b) deformed fine pearlite and pro-eutectoid ferrite. (c) Away from the tread, still in the region subjected to accelerated cooling. Fine pearlite. Etchant: nital. SEM, SE. Courtesy of MRS Logística S.A., RJ, Brazil.

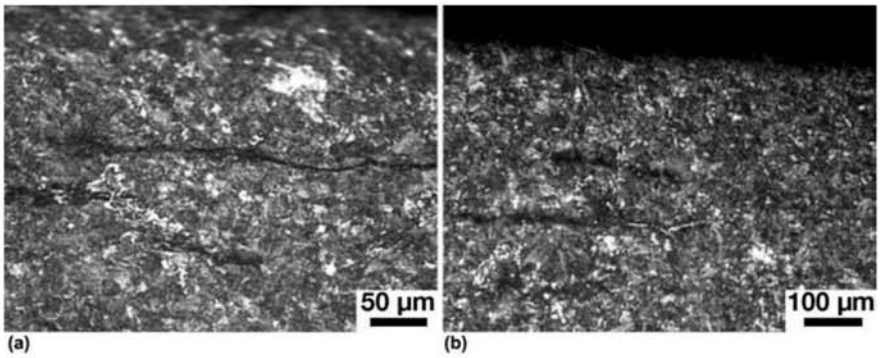

Fig. 15.31 Radial section of a railway wheel. Region immediately below the tread. Fine pearlite. Etchant: nital 2%. Cracks caused by contact fatigue. Courtesy of MRS Logística S.A., RJ, Brazil.

Fig. 15.32 Fatigue failure of a rail. Initiation close to rail head. Courtesy of MRS Logística S.A., RJ, Brazil.

Figure 15.33 presents a macrograph of the transverse cross section of a rail with a hardness of HB 400. The microstructure of this rail can be seen in Fig. 15.34 and 15.35: it is composed of very fine pearlite colonies without any proeutectoid constituents. The heterogeneities in the rolled rails can be observed in macrographs and sulfur prints (Fig. 15.36 and 15.37). Electromagnetic stirring during the continuous casting of the billets to be rolled into rails has proven to be effective in minimizing segregation and thus enhancing the homogeneity of the structure of the final rolled product. Figure 15.38 presents the transverse cross section of rolled blocks after rough rolling of billets produced with and without electromagnetic stirring during continuous casting (compare with the results presented in Fig. 8.54, Chapter 8, "Solidification, Segregation, and Nonmetallic Inclusions," in this book). Figure 15.39 presents the transverse cross sections of rails rolled with different stirring conditions in the continuous casters. The effect of the magnetic stirring on segregation is evident.

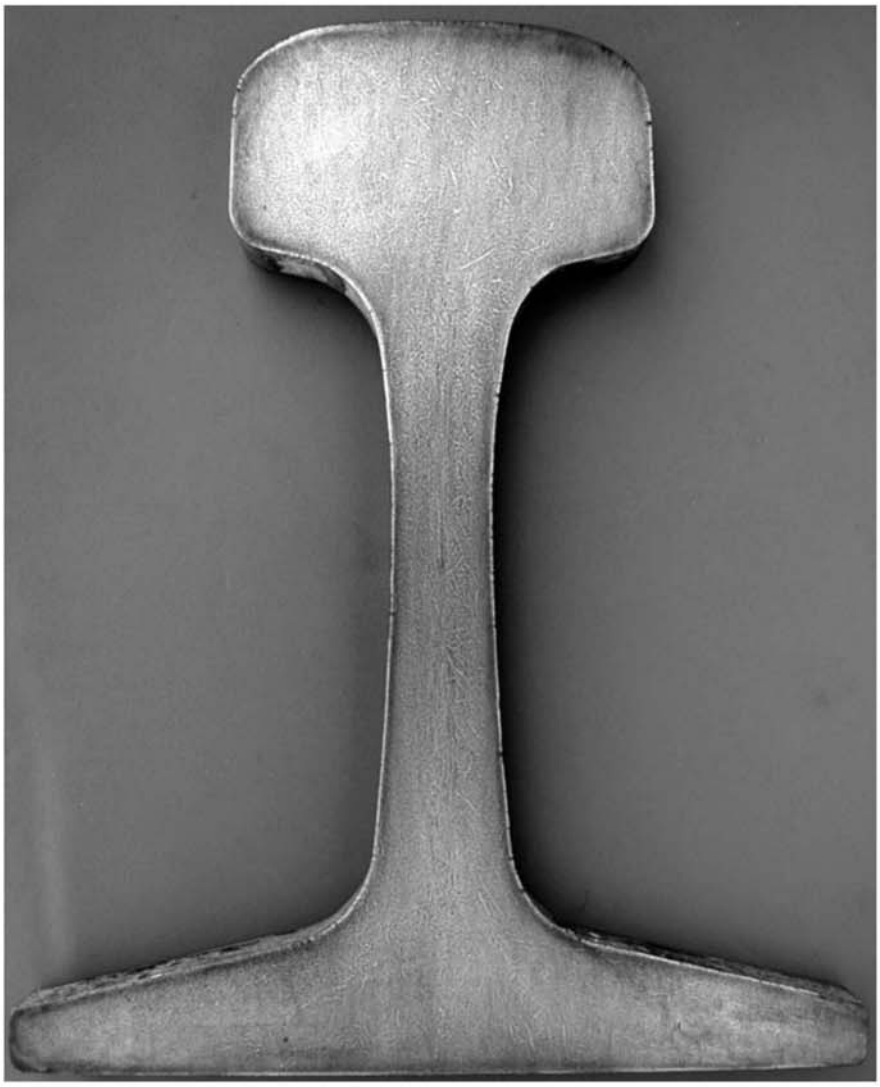

Fig. 15.33 Transverse cross section on a hyper-eutectoid rail with approximate hardness of HB 400. The rail was hot rolled, but some residues of the dendritic structure are still visible. The transverse cross section (as discussed in Chapter 12, "Mechanical Work of Steels: Cold Working," in this book) usually presents less evidence of working than the longitudinal section. Metallography by I. C. Abud, INT, Brazil. Courtesy of MRS Logística S.A., RJ, Brazil.

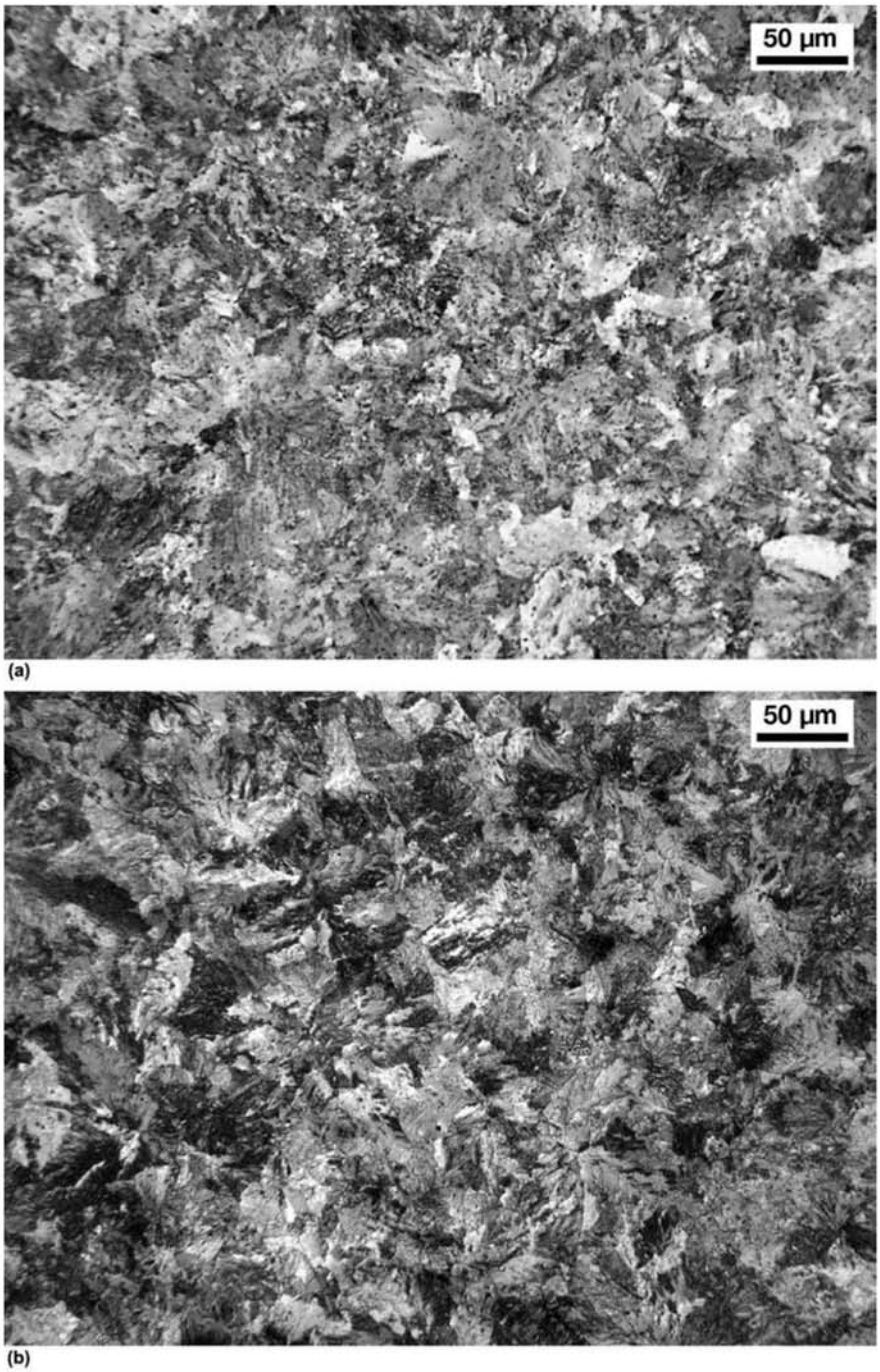

Fig. 15.34 Transverse cross section close to the head of the rail shown in Fig. 15.33. Fine pearlite and absence of pro-eutectoid constituents. (a) Etchant: nital + picral (1:1) (with 0.5 g benzalkonium chloride) (b) Etchant: Marshall (Part I: 8 g oxalic acid + 5 ml sulfuric acid + 100 ml distilled water. Dilute Part I in 100 ml hydrogen peroxide (30%) just before using.) Metallography by I. C. Abud, INT, Brazil. Courtesy of MRS Logística S.A., RJ, Brazil.

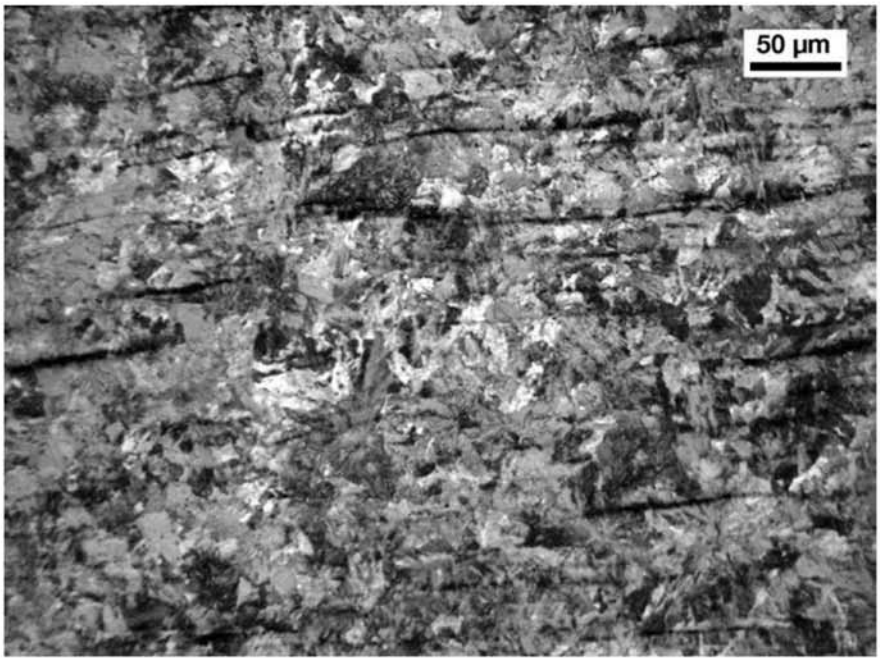

Fig. 15.35 Transverse cross section at the center of the web of the rail in Fig. 15.32. Fine pearlite, absence of pro-eutectoid constituents. Nonmetallic inclusions aligned according to deformation direction. Etchant: Marshall. Metallography by I. C. Abud, INT, Brazil. Courtesy of MRS Logística S.A., RJ, Brazil.

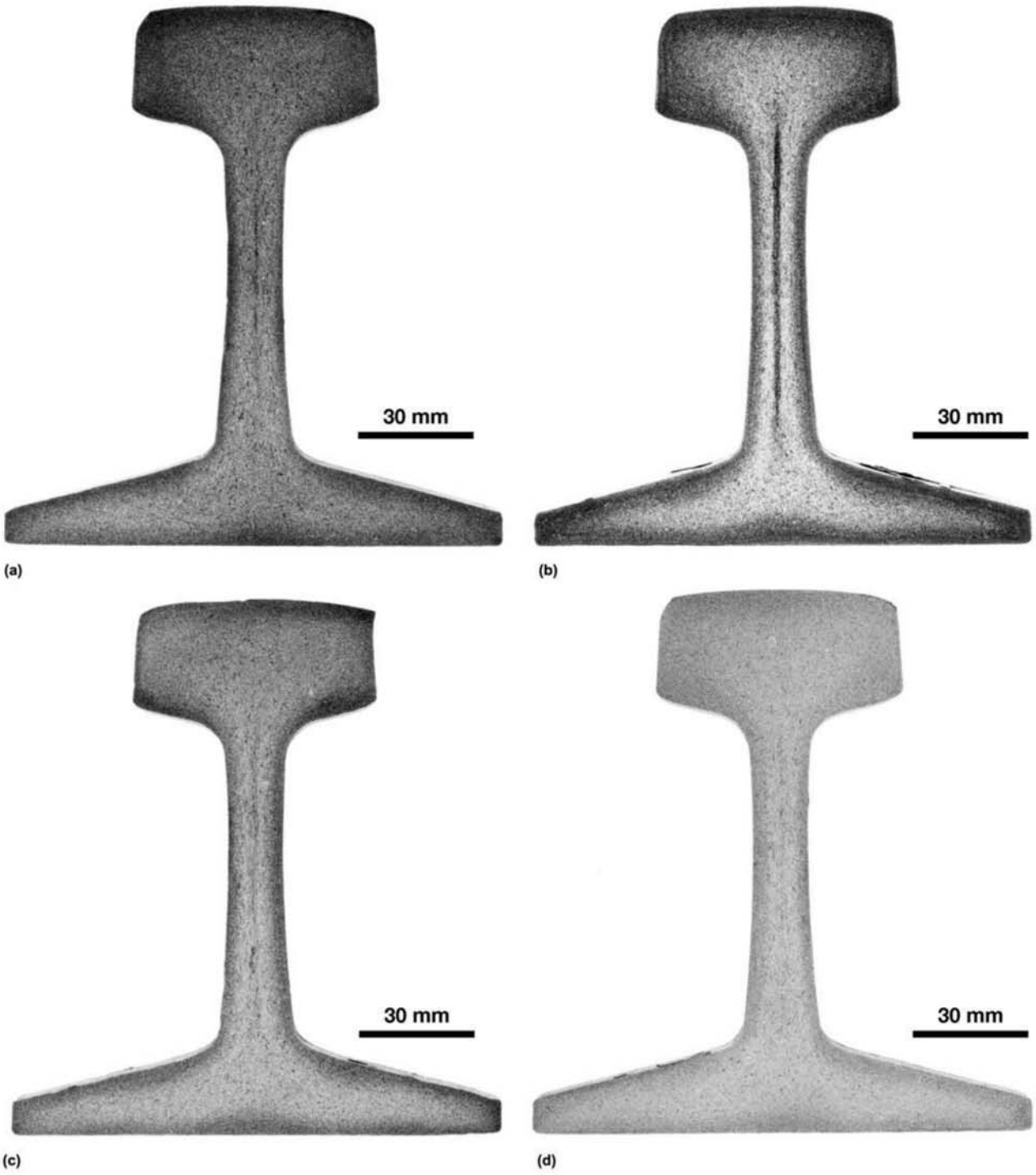

Fig. 15.36 Transverse cross sections of rails with different levels of segregation at the center of the web. Etchant: hot hydrochloric acid. Courtesy of M. Oliveira and M. Talarico, CETEC, MG, Brazil.

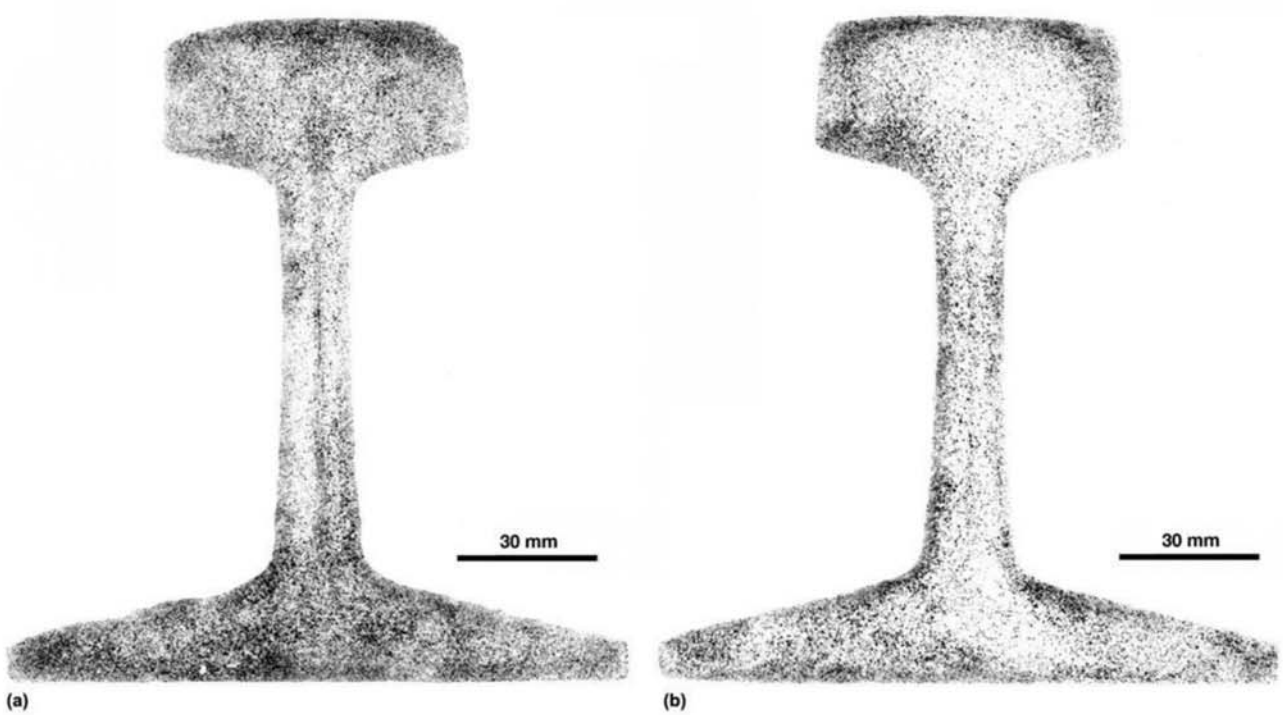

Fig. 15.37 Sulfur prints of transverse cross sections of rails. Modern rail steels have chemical compositions and sulfur levels that give little information in sulfur prints. Print (a) corresponds to the macrograph of Fig. 15.36(b). Print (b) corresponds to the macrograph of Fig. 15.36(c). Courtesy of M. Oliveira and M. Talarico, CETEC, MG, Brazil.

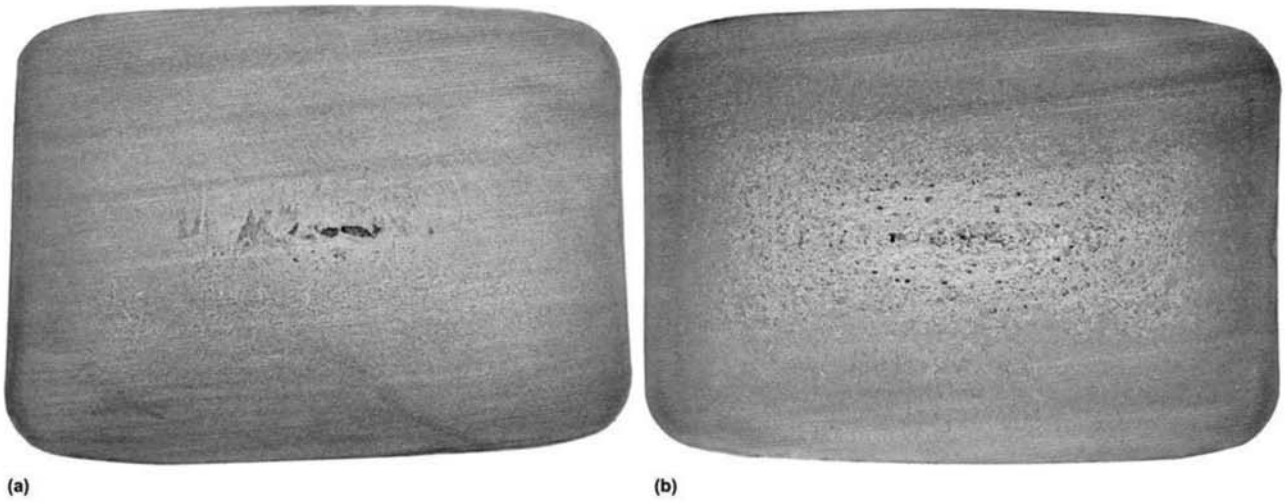

Fig. 15.38 Transverse cross sections of blooms rolled from continuous casting billets. The bloom is an intermediate stage during rolling of rails. (a) No magnetic stirring in continuous casting. (b) With magnetic stirring in continuous casting. Porosity and segregation are dispersed and the region of equiaxial structure increase with stirring, resulting in a more homogeneous product. Etchant: hot hydrochloric acid.

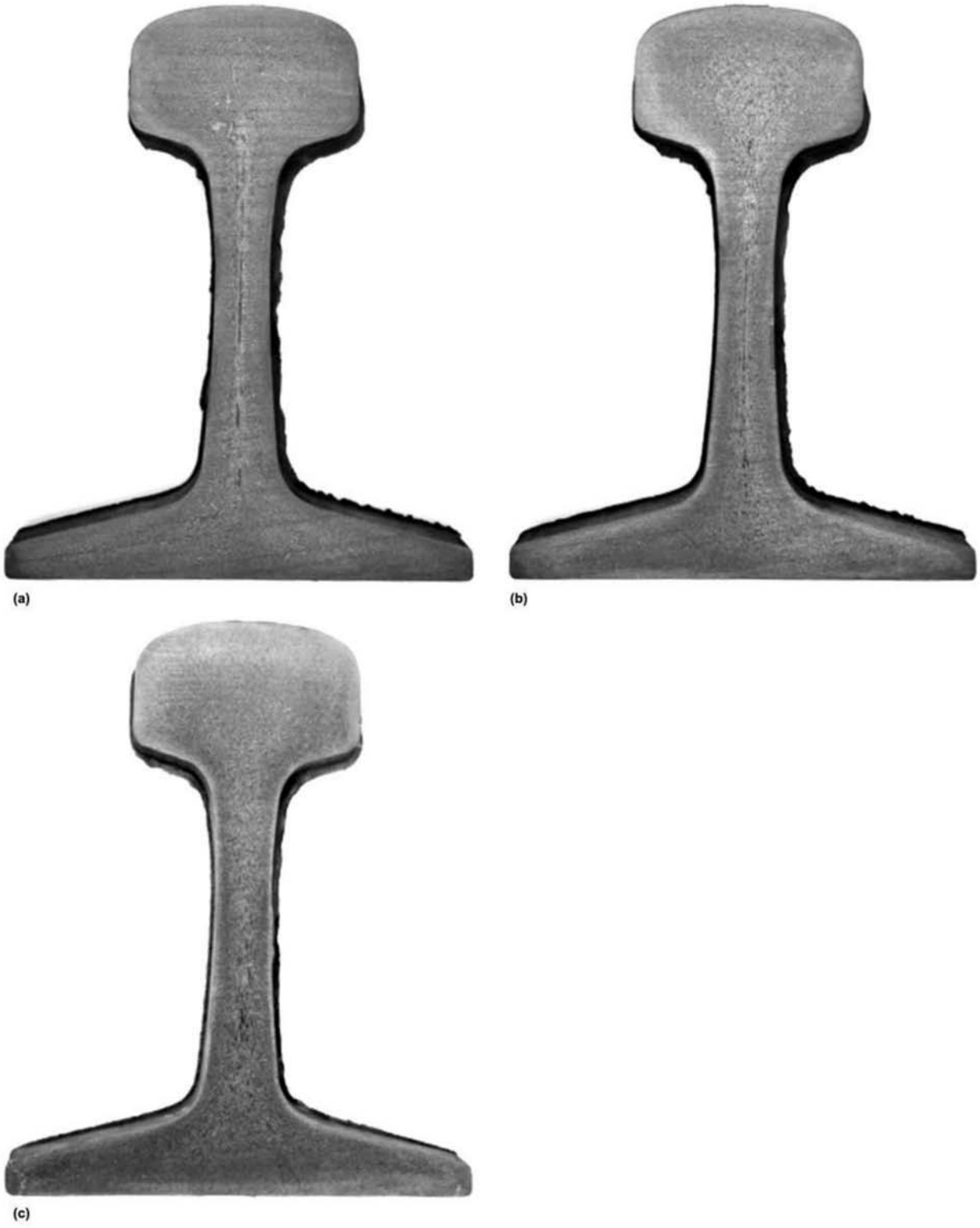

Fig. 15.39 Transverse cross sections of rails manufactured from billets cast under different conditions. (a) Billet cast without stirring. Segregation is evident, particularly in the web region. (b) Billet cast with stirring. Segregation is reduced. (c) Billet cast with stirring, causing rotational movement of the liquid inside the strand. Increased homogeneity. The macrograph shows almost no segregation.

REFERENCES

1. L.T. Sandor, *Influência do teor de carbono na propagação de trinca por fadiga e na tenacidade à fratura em camada cementada em aços de alta resistência mecânica*, Ph.D thesis, UNICAMP, SP, Brazil, 2008
2. N. Luzginova, L. Zhaoa, and J. Sietsma, Evolution and Thermal Stability of Retained Austenite in SAE 52100 Bainitic Steel, *Mat. Sci. Engin. A*, Vol 448, 2007, p 104–10
3. J.G. Speer, F.C.R. Assunção, D.K. Matlock, and D.V. Edmonds, The Quenching and Partitioning Process: Background and Recent Progress, *Mat. Res.*, Vol 8 (No. 4), 2005, p 417–23
4. J.G. Speer, D.V. Edmonds, F.C. Rizzo, and D.K. Matlock, Partitioning of Carbon from Supersaturated Plates of Ferrite, with Application to Steel Processing and Fundamentals of the Bainite Transformation. *Curr. Opin. Solid State Mat. Sci.*, Vol 8, 2004, p 219–37
5. "Petroleum and Natural Gas Industries—Materials for Use in H_2S-Containing Environments in Oil and Gas Production," MR0175/ISO 15156, NACE, 2003
6. Z. Panossian, *Fosfatização de metais ferrosos*, IPT, unpublished results, 2003
7. U. Zerbst, K. Mädler, and H. Hintze, Fracture Mechanics in Railway Applications, *Engin. Fract. Mech.*, Vol 72, 2005, p 163–94
8. E.A. Shur, N.Y. Bychkova, and S.M. Trushevsky, Physical Metallurgy Aspects of Rolling Contact Fatigue of Rail Steels, *Wear*, Vol 258, 2005, p 1165–71
9. J.E. Garnham, J.H. Beynon, and K.J. Sawley, Rolling Contact Fatigue of Three Pearlitic Rail Steels, *Wear*, Vol 192 (No. 1–2), 1996, p. 94–111
10. H. Yokoyama, S. Mitao, M. Takemasa, Development of High-Strength Pearlitic Steel Rail (SP Rail) with Excellent Wear and Damage Resistance, *NKK Tech. Rev.*, Vol 86, 2002, p 1–7

Metallography of Steels—Interpretation of Structure and the Effects of Processing
Hubertus Colpaert
Updated and Translated by André Luiz V. da Costa e Silva

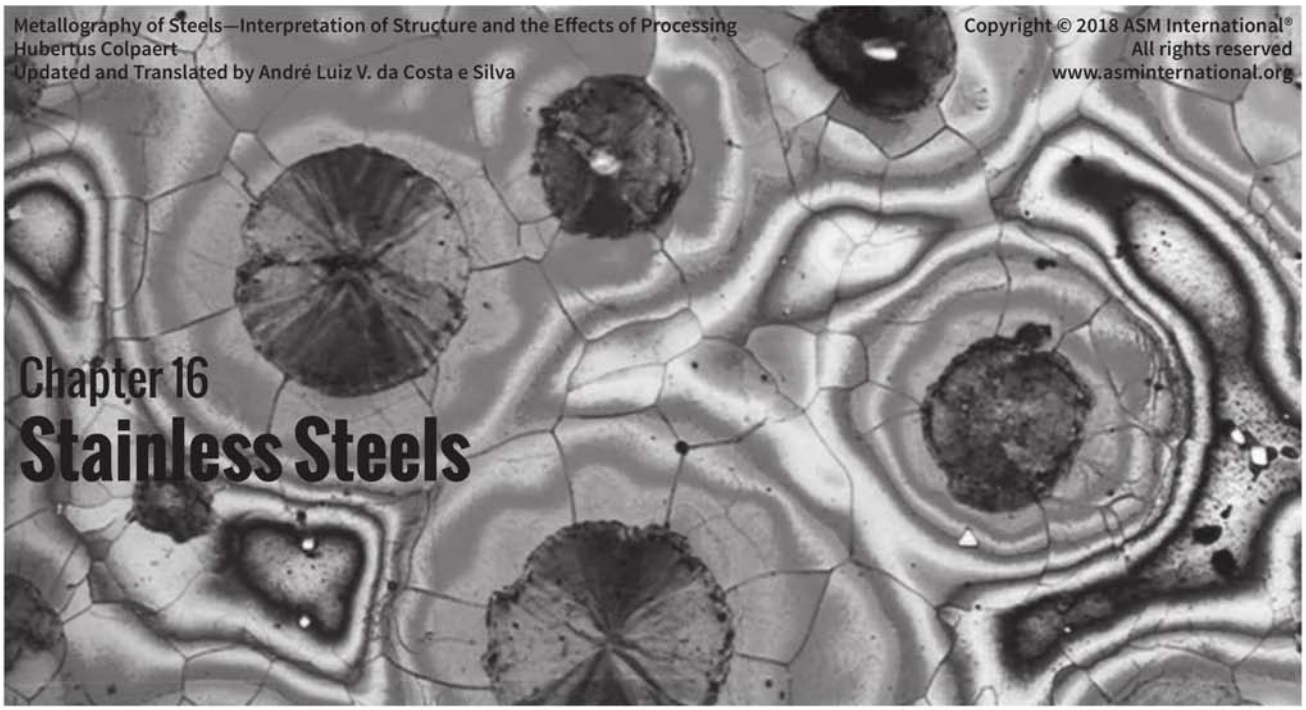

Chapter 16
Stainless Steels

Steels with chromium contents above 12% show high resistance to oxidation and corrosion and are generally designated as stainless steels. These steels are important in engineering in view of their resistance to oxidation and corrosion, mechanical properties at elevated temperatures, and toughness (for austenitic stainless steels).

The most common compositions of stainless steels (for instance, 12% Cr, 18% Cr + 8% Ni, etc.) were developed mostly by accident at the beginning of the 20th century. Since then, the development of new compositions has evolved into a systematic and scientifically sound process. As the microstructure of these steels has a dominant effect over their properties, they are usually classified based on their room temperature microstructure. The effect of different alloying elements on the phases expected in the microstructure of stainless steels can be observed through the use of phase diagrams, even though most of these steels are used in microstructural conditions that are not in thermodynamic equilibrium.

Stainless steels are normally grouped in five categories (Ref 1 has a more detailed discussion):

- Martensitic: these are iron-chromium (11–18%) alloys with carbon content usually above 0.1%. The most common martensitic stainless steel is AISI 410. In recent years, however, "supermartensitic" steels have been developed and are widely used in piping and pressure vessels. These steels usually have carbon contents below 0.1% and very well-controlled levels of residual elements. These compositions cross the austenitic field in the phase equilibrium diagram, and are thus hardenable by quenching heat treatment. They are magnetic. Also included in this family of steels are AISI 403; 410; 414; 416; 420; 431; 440A, B, and C; and 501.
- Ferritic: these are iron-chromium alloys that are essentially ferritic (BCC) at all temperatures up to the melting point and do not harden by

quenching heat treatment. They usually have higher chromium content but lower carbon content than the martensitic stainless steels. The most common alloys in this family are AISI 405, 430, 430F, 446, 502.

- Austenitic: these are basically iron, chromium (16–30%), nickel (8–35%) alloys in which the microstructure after commercial heat treatment is predominantly composed of austenite (FCC). They are normally nonmagnetic. In this family, common grades are AISI 301, 302, 304, 304L, 308, 310, 316, 316L, 317, 321, and 347. The carbon content of these steels is generally below 0.08%.
- Ferritic-austenitic (duplex): microstructures with approximately equal volume fractions of ferrite and austenite are obtained by balancing the content of iron, chromium (18–27%), nickel (4–7%), molybdenum (1–4%), and other elements, particularly nitrogen. These alloys have interesting properties for many applications. In this group, common grades are AISI 329 and UNS S32304 and S31803. The cast steels in ASTM A890 grades 1A, 1B, 1C, 2A, 3A, 4A, 5A, and 6A, and the DIN-EN steels such as W.Nr. 1.4468, 1.4517, and 1.4471 are also important compositions in this group.
- Precipitation hardening (PH): alloys of iron, chromium (12–17%), nickel (4–8%), and molybdenum (0–2%) containing alloying additions that make possible the precipitation hardening of the low carbon martensite through the formation of intermetallic compounds (aluminum, copper, titanium, and niobium are common additions for this purpose).

16.1 Relationships Between Chemical Composition and Structure

Microstructure has a dominant effect on the performance of stainless steels and directly depends on chemical composition and heat treatment conditions. Because the systems involved are complex and have many components (as a general rule, at a minimum the effects of chromium, carbon, and nickel on phase equilibria must be considered in the simplest stainless steels), simplified relations between phases present and chemical composition have been developed and are widely used.

One of the representations of these relations is the Schaeffler and Delong diagram (Ref 2, 3). All elements that behave as BCC stabilizers are included in the calculation of a "chromium equivalent," and all elements that stabilize FCC are included in a "nickel equivalent" factor:

$$\%\,Cr_{equivalent} = \%\,Cr + 1.5 \times \%\,Si + \%\,Mo$$
$$\%\,Ni_{equivalent} = \%\,Ni + 30 \times (\%\,C + \%\,N) + 0.5 \times (\%\,Mn + \%\,Cu + \%\,Co)$$

Notwithstanding the fact that this diagram was originally developed to forecast the ferrite (BCC) content in weld-deposited metal, it supplies a useful first approximation of the main phases to be expected in rolled or forged material. Estimates of below 10% ferrite in rolled and forged products may be in error because these materials are generally closer to equilibrium conditions than are welds and castings.

For cast materials, other formulas may be more useful for the calculation of Cr equivalent and Ni equivalent, and different graphs may be better fitted for predicting ferrite content in the microstructure (Ref 4).

Figure 16.1 presents the Schaeffler diagram with the approximate range of compositions for each family of stainless steels.

16.2 Martensitic Stainless Steels

Martensitic stainless steels may be considered in some aspects equivalent to engineering steels for quenching and tempering (carbon or alloy steels). The main difference is evidently the high chromium content. This leads to extremely high hardenability, a significant lowering of the M_s temperature, and a decrease of softening on tempering.

Martensitic stainless steels are usually austenitized at relatively high temperatures (925–1070 °C, or 1700–1960 °F) to completely dissolve carbides and guarantee the uniformity of the austenite before quenching. Controlling austenitic grain size is extremely important to ensure reasonable toughness and this, combined with the need for high austenitizing temperatures, is one of the challenges in alloy design and processing in this family of steels.

The basic composition in this family is AISI 410. Alloying additions are made to this basic composition to modify its properties. Figures 16.2 to 16.5 present microstructures of this steel.

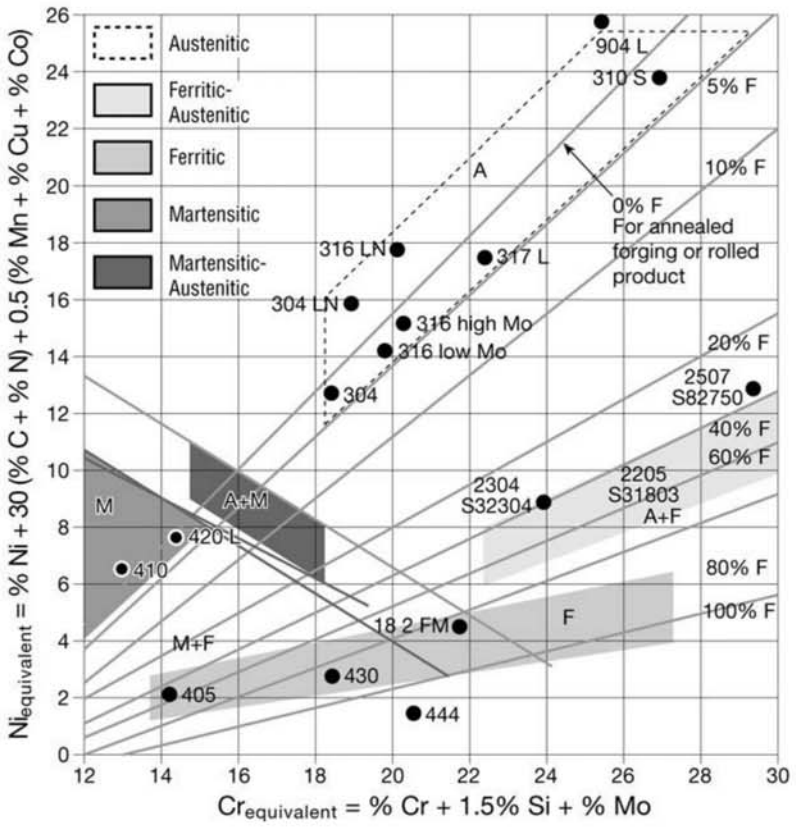

Fig. 16.1 Schaeffler diagram. The regions corresponding to the most common stainless steel families are indicated.

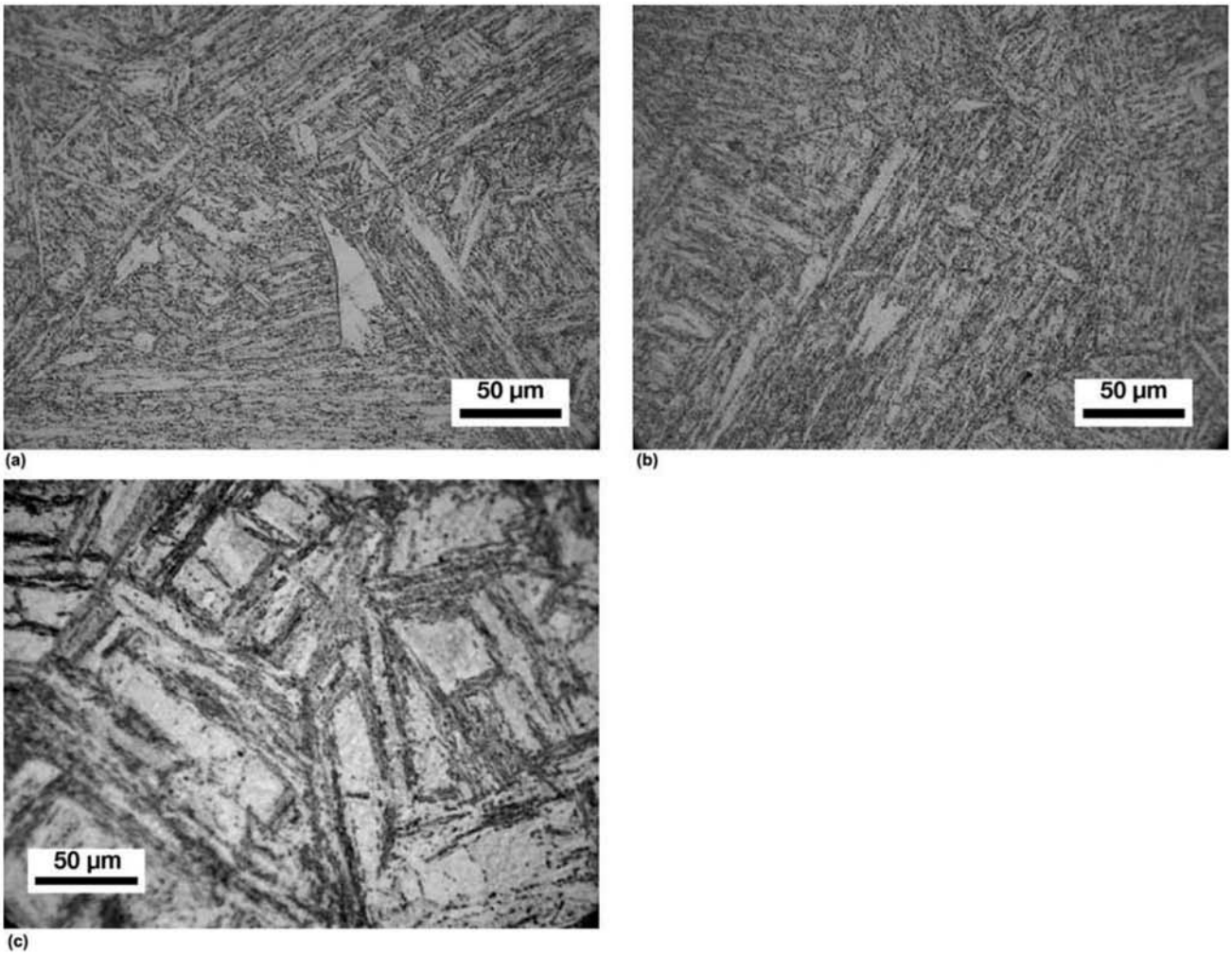

Fig. 16.2 AISI 410 martensitic stainless steel quenched and tempered. (a) and (b) Tempered martensite. (c) Tempered martensite with grain boundaries decorated with fine precipitates. This precipitation can be clearly seen in SEM examination. Etchant: Kalling. Courtesy of A. Zeemann, Tecmetal, Rio de Janeiro, Brazil.

Lower carbon martensitic stainless steels, such as F6NM (Fig. 16.6 and 16.7), derived from the ASTM casting CA6NM, find wide applications in equipment in the oil industry in view of its good weldability (Ref 5) and beneficial combination of mechanical properties and corrosion resistance (Ref 6, 7).

16.3 Ferritic Stainless Steels

The classic definition of ferritic stainless steels encompasses steels with a composition such that it does not cross the austenitic field in the Fe-Cr phase diagram. More exactly, this analysis should be performed at least on the ternary diagram Fe-Cr-C, since carbon is a strong austenite stabilizer. Their structure is composed essentially of ferrite at all temperatures to the melting point (see Fig. 16.8). Surprisingly, most steels classified as ferritic do not fulfill this definition. AISI 430 (0.1% C max, 17% Cr, the most popular of the ferritic stainless steels) may present 30–50% austenite if heated above 800 °C (1470 °F). During cooling, austenite may transform into martensite. For this reason, the as-cast structure of this steel is usually a mixture of ferrite and

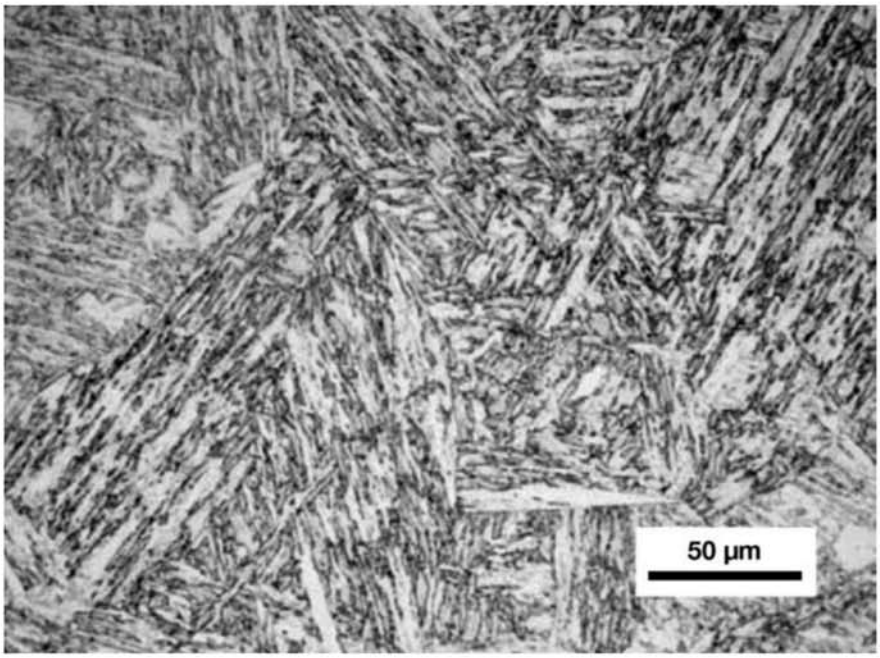

Fig. 16.3 AISI 410 martensitic stainless steel quenched and tempered. (Double tempering at 730 and 690 °C, or 1345 and 1275 °F). Tempered martensite. Approximate hardness: 220 HB. Etchant: Kalling. Courtesy of A. Zeemann, Tecmetal, Rio de Janeiro, Brazil.

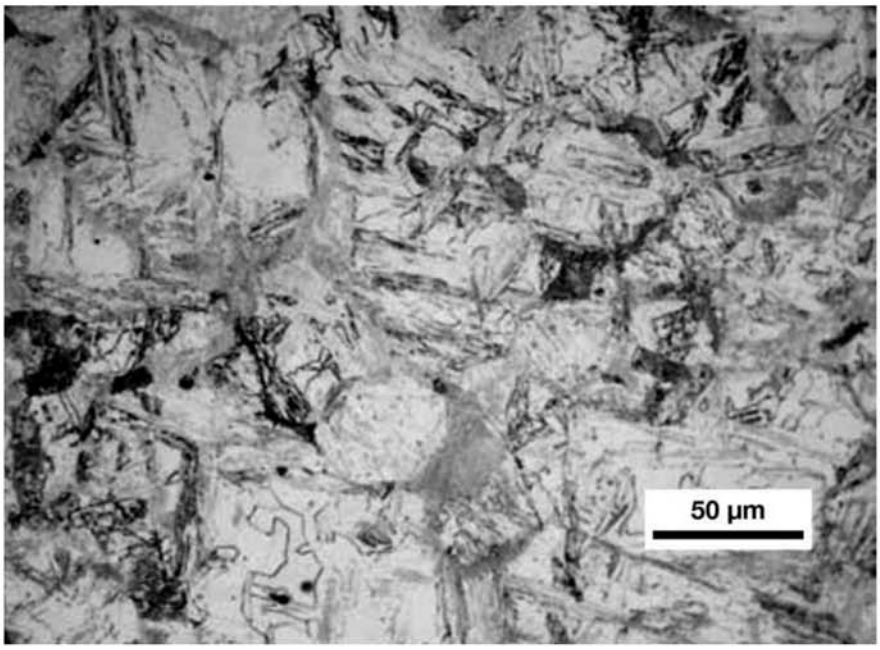

Fig. 16.4 AISI 410 martensitic stainless steel quenched and tempered (excessive tempering). Tempered martensite. Approximate hardness: 185 HB. Etchant: Kalling. Courtesy of A. Zeemann, Tecmetal, Rio de Janeiro, Brazil.

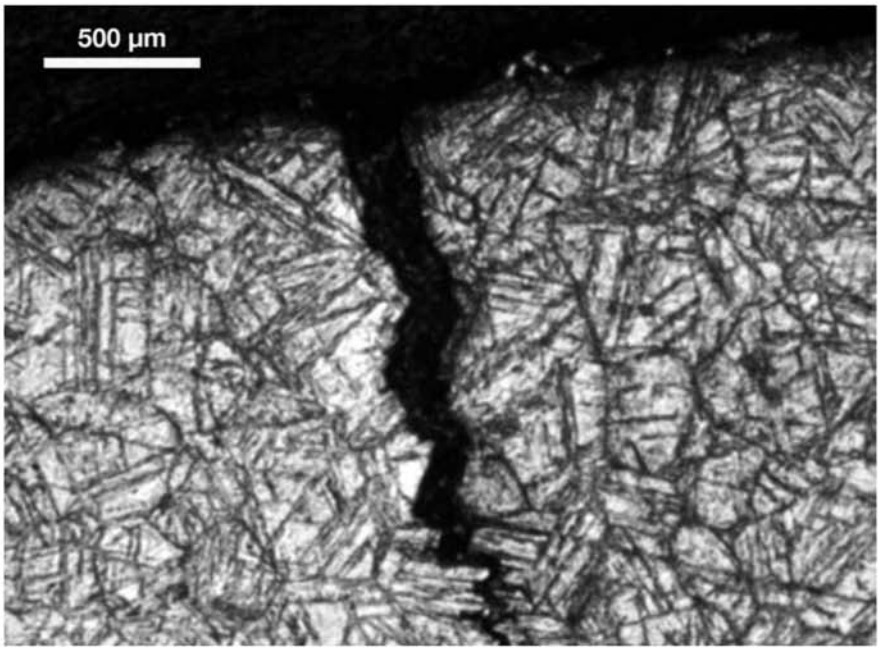

Fig. 16.5 Crack following prior austenitic grain boundaries in AISI 410 steel subjected to corrosion testing according to NACE TM 0177 standard. Courtesy of A. Zeemann, Tecmetal, Rio de Janeiro, Brazil.

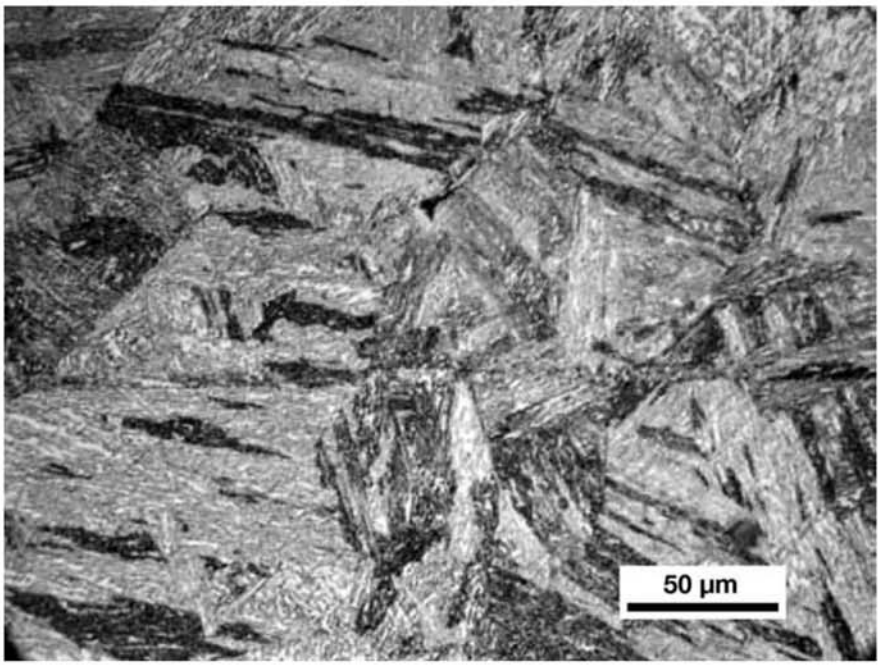

Fig. 16.6 F6NM stainless steels containing C = 0.025%, Cr = 12.6%, Ni = 3.9%, and Mo = 0.5%, quenched and tempered. Tempered martensite. Etchant: Kalling. Courtesy of A. Zeemann, Tecmetal, Rio de Janeiro, Brazil.

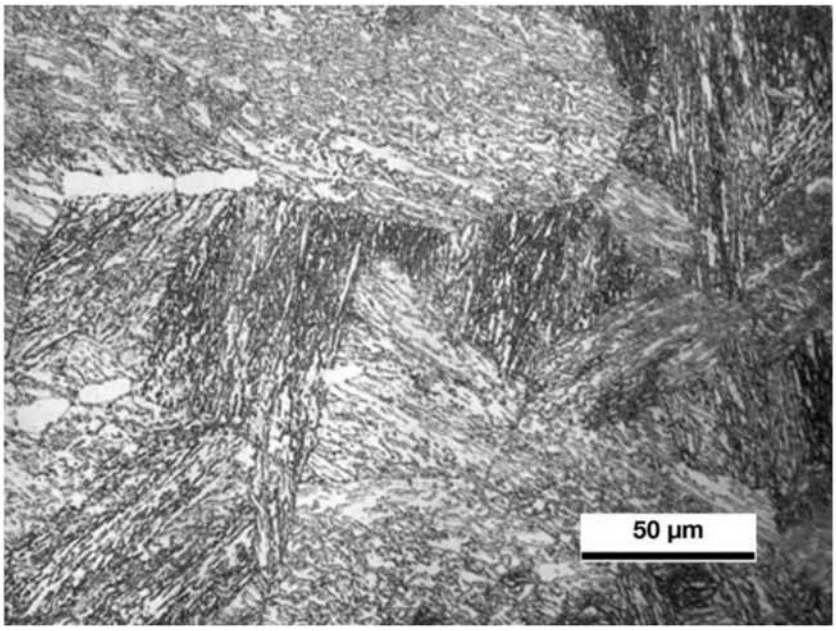

Fig. 16.7 Quenched and tempered F6NM stainless steel. Delta ferrite islands in a matrix of tempered martensite. Etchant: Kalling. Courtesy of A. Zeemann, Tecmetal, Rio de Janeiro, Brazil.

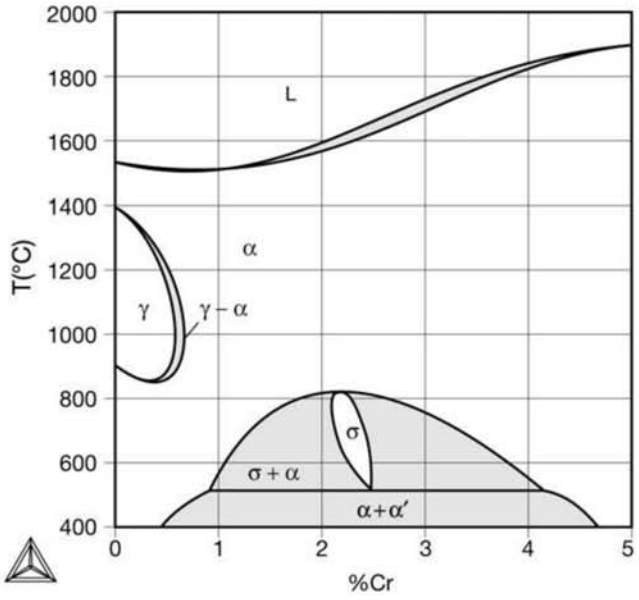

Fig. 16.8 Fe-Cr phase equilibrium diagram. In the Fe-C diagram, the two single-phase fields where BCC (ferrite) occurs are named α (alpha) and δ (delta), due to a rule in the construction of phase diagrams according to which two isolated single-phase fields must be identified by different Greek letters. It is evident that there can be no structural difference between "the two" ferrites (α and δ). Furthermore, the BCC phase field must have a single name. Thus, it is common to treat the ferrite that forms in stainless steels (in particular in austenitic and duplex steels) as "delta ferrite". Although they are equilibrium phases, the formation of α' and σ (sigma) are slow processes, and stainless steels are always processed in ways that should prevent their formation.

austenite. Even the high chromium stainless steels (such as AISI 446, 27% Cr) may present some austenite at high temperatures. Figures 16.9 and 16.10 present examples of microstructures of ferritic stainless steels.

16.4 Austenitic Stainless Steels

These are the most common of the stainless steels. They have very good corrosion resistance, high toughness, and good weldability. The austenitic (FCC) structure is stabilized to room temperature with the addition of nickel and other elements that have similar effects on iron, such as manganese. The FCC structure makes them especially interesting for cryogenic applications (be-

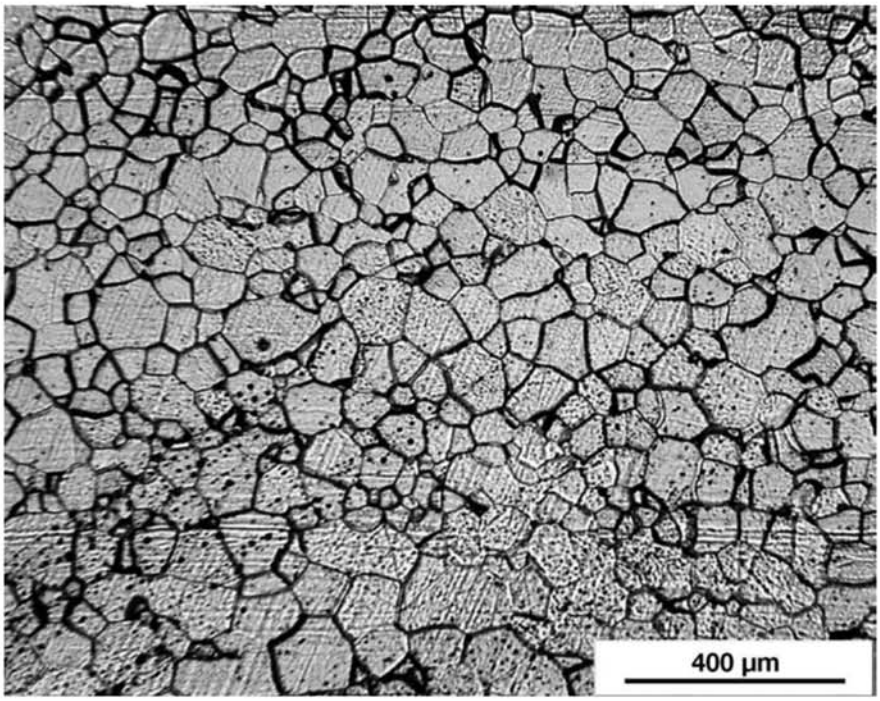

Fig. 16.9 AISI 409A steel cold rolled with 85% reduction and annealed at 850 °C (1560 °F). Equiaxial ferrite. Etchant: Vilella. Courtesy of C. S. Viana, EEIMVR-UFF. Volta Redonda, RJ, Brazil. Source: Ref 8

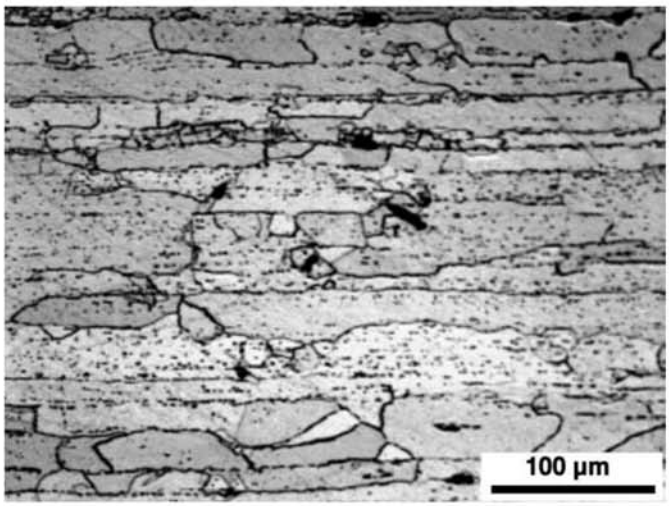

Fig. 16.10 AIS 430A steel hot rolled. Elongated ferrite grains. Presence of fine precipitates, possibly carbides. Etchant: Vilella. Courtesy of C. S. Viana, EEIMVR-UFF. Volta Redonda, RJ, Brazil. Source: Ref 8

cause this structure does not have a ductile-to-brittle transition) and high-temperature applications, in view of their resistance to softening and hot deformation.

In these steels, austenite does not suffer significant decomposition on cooling after hot working. Thus, the austenitic structure resulting from the

hot working operation is essentially the final one. The usual treatment for forgings and rolled products is solubilizing or solution annealing. This treatment is performed to dissolve carbides that compromise their corrosion resistance (see the section 16.7 "Intercrystalline or Intergranular Corrosion" in this chapter). Shape and size of the austenitic grains are not affected by this heat treatment (unless the material has suffered cold work). Thus, in the case of forgings and rolled products of larger dimensions, the final microstructure is not easily modified through heat treatment. Grain size, for instance, is usually defined by judiciously combining deformation and temperature in the last stages of hot working. The presence of twins is very common in austenitic grains in the annealed condition. Figures 16.11 to 16.15 present examples of the microstructure of austenitic stainless steels.

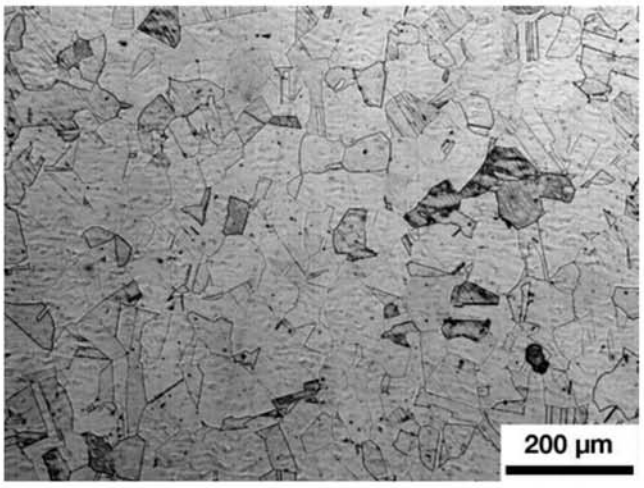

Fig. 16.11 AISI 304 austenitic stainless steel annealed at 1050 °C (1920 °F) and water quenched. Austenite. Etchant: oxalic acid. Courtesy of Villares Metals S.A., Sumaré, SP, Brazil.

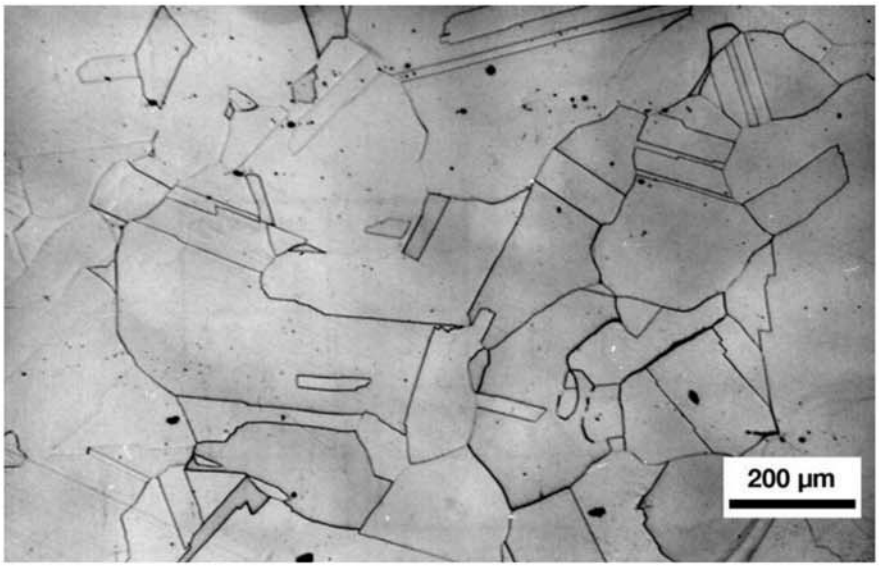

Fig. 16.12 W. Nr. 1.4439 austenitic stainless steel, forged, annealed for solubilization, and quenched. Austenite with grain size ASTM 2–4.

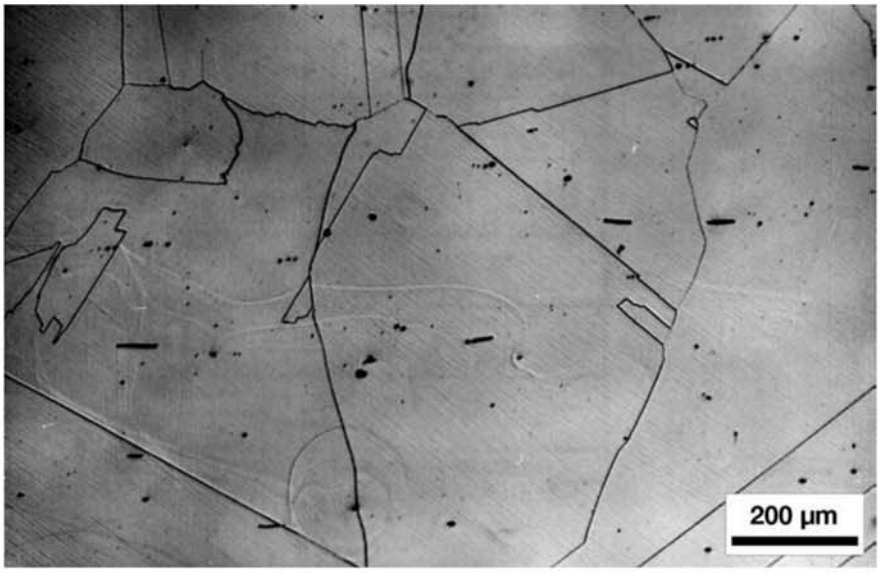

Fig. 16.13 W. Nr. 1.4439 austenitic stainless steel, forged, annealed for solubilization, and quenched. Austenite with grain size ASTM 0–1. Large grain sizes in austenitic stainless steels may lead to yield strength below specified limits and difficulties (or impossibility) in performing ultrasonic examination.

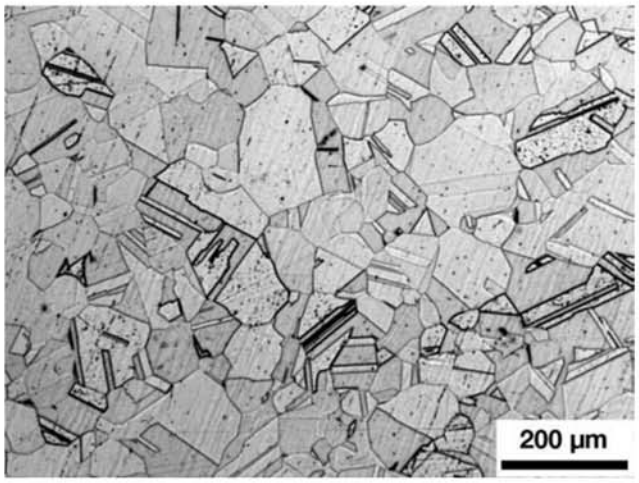

Fig. 16.14 AISI 304 forged, annealed for solubilization, and quenched. Austenite with large grains. The dark points are sigma phase precipitates (identified via SEM). Etchant: oxalic acid. Courtesy of Villares Metals S.A., Sumaré, SP, Brazil.

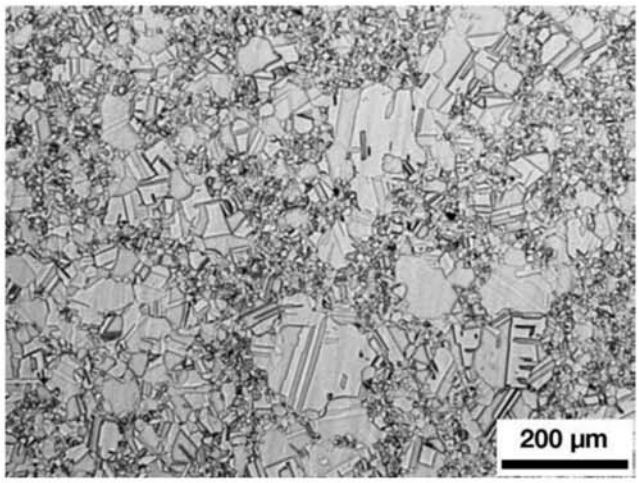

Fig. 16.15 AISI 310 annealed for solubilization at 1050 °C (1920 °F) and quenched. Austenite with heterogeneous grain size. Etchant: glyceregia. Courtesy of Villares Metals S.A., Sumaré, SP, Brazil.

The solidification sequence of austenitic (and duplex ferritic-austenitic) stainless steels is very important in the casting stage of the production (ingots, blooms, or cast parts) and when welding these steels. When the different ranges of specified chemical compositions for the various austenitic stainless steels are marked on the Schaeffler diagram (Fig. 16.1), it is evident that some possible compositions will fall in the range where some ferrite is present. This indicates that some austenitic stainless steel products may

have, in their microstructure, some fraction of delta ferrite. This is not an indication of deviations in the permitted chemical composition. It is interesting to note that when ferrite is present, the part will be weakly magnetic, instead of nonmagnetic, as a fully austenitic structure would be. The fact that a magnet will "stick" to some austenitic steel parts is in itself no cause for rejection of the part, unless (a) the specification determines that ferrite must be completely absent, or (b) the steel is of the "NM" type (nonmagnetic) in its specification. Furthermore, some austenitic stainless steels undergo strain-induced martensitic transformation. Thus, magnets may stick to parts made of austenitic stainless steels after they are formed.

Because solidification is seldom accompanied by perfect redistribution of the substitutional solutes (which are present in large amounts in these steels), solidification segregation (Chapter 8, "Solidification, Segregation, and Nonmetallic Inclusions," in this book) may also cause ferrite to form. Finally, some compositions may undergo solidification with a liquid to ferrite transformation; later, during hot working and annealing, this ferrite may completely dissolve. Figure 16.16 presents a summary of the possible solidification modes of austenitic stainless steels. The FA mode is normally preferred, since ferrite is formed from the liquid, thus avoiding or reducing the risk of hot tearing (or hot cracking) (see Ref 11, 12). An example is presented in Fig. 16.17.

When one evaluates the transformations in the FA and F mode, it is not always easy to understand the solidification sequence of these steels just by examining their as-cast structures. Experimental diagrams, such as the one given in Fig. 16.18, and computational thermodynamic calculations, can be helpful in understanding the phenomena involved. Mathematical models for

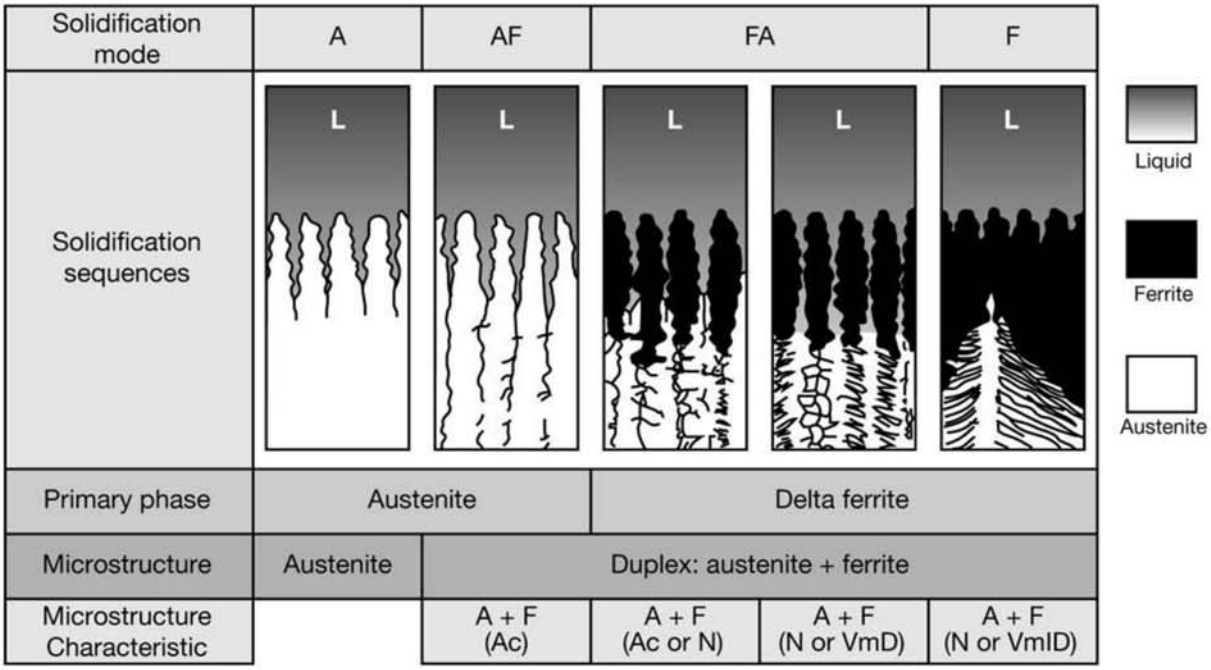

Fig. 16.16 Solidification sequences typical of austenitic stainless steels. Besides the primary phase forming from the liquid, the important morphological aspects of the as-cast product are also indicated. A = austenite, F = ferrite, Ac = acicular, N = lacy or network, Vm = vermicular or skeleton, D = dendritic, ID = interdendritic. Source: Ref 9 and 10

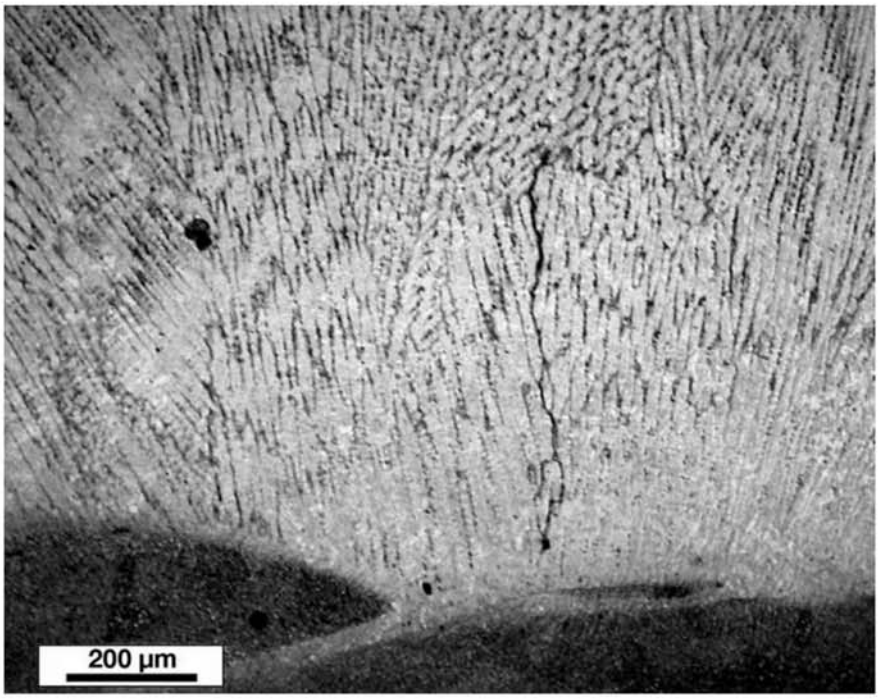

Fig. 16.17 Example of a hot crack in the heat-affected zone of a dissimilar metals weld (an engineering steel—Chapter 15, "Engineered Special Bar Quality Steel (Engineered Steels)," in this book—and a stainless steel). The crack propagates through the last region to solidify. The crack morphology is similar to those observed in the solidification of austenitic castings with bad selection of chemical composition. (In this case, the weld metal composition was excessively changed by diluting the engineering steel in the lower part of the image, generating conditions favorable to cracking). Excellent visualizations of the formation of hot cracks during solidification are available at: http://www.tms.org/pubs/journals/JOM/0201/Grasso/Grasso-0201.html.

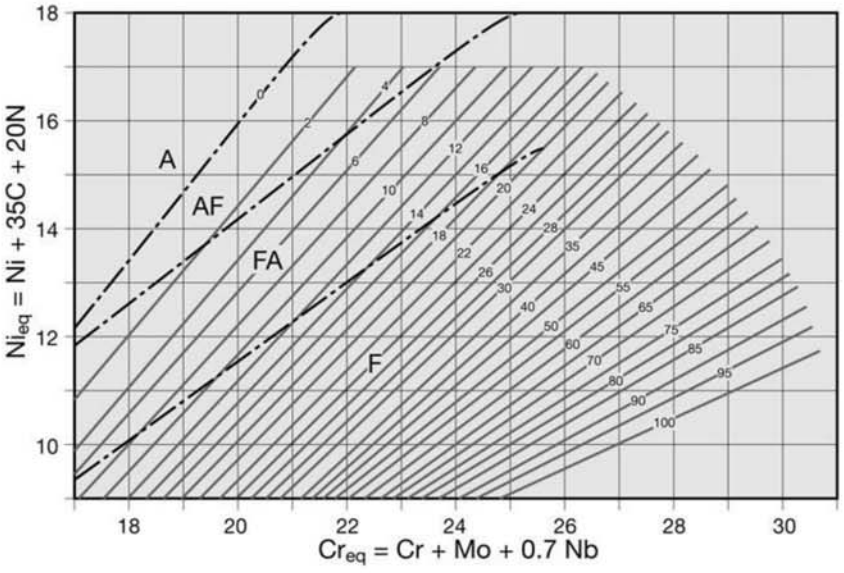

Fig. 16.18 Constitution diagram by Siewert, McCowan, and Olson for the estimation of the solidification mode of stainless steel castings, adapted from Ref 13. The numbers on the lines in the regions where ferrite is present are the volumetric fraction of ferrite (FN) in the steel. The letters indicate the solidification model in accordance with Fig. 16.16.

this purpose have been developed, and the work at Oak Ridge National Laboratory (Ref 14) is especially interesting. The results of the model developed in Ref 14 are accessible online (see Ref 14 for the link).

Figure 16.19 presents the two morphologies of ferrite observed in the FA solidification mode of these steels. There is significant discussion in the literature about the effect of these microstructures on the mechanical properties and corrosion resistance of the weld-deposited metal (Ref 9). Figure 16.20 shows the presence of vermicular ferrite in an ingot of AISI 316L steel (see the lower magnification micrograph, Fig. 8.53) and Fig. 16.21, presents the same in AISI 304 steel. It is quite evident that a quick analysis might suggest—wrongly—that the material has solidified as austenite, ferrite having formed in the interdendritic spaces. Careful experiments such as those performed in Ref 9 and 17, for instance, have clarified that the solidification sequences are indeed those described in Fig. 16.16. In Fig. 16.22, one can observe how the primary ferrite dendrites transform to austenite as the steel cools down. A transverse cross section of this sample would result in a micrograph close to those of Fig. 16.20 and 16.21.

According to Ref 9, the crystallographic relationship observed in Ref 16 in Fig. 16.20 results from the preferential growth both of ferrite and austenite

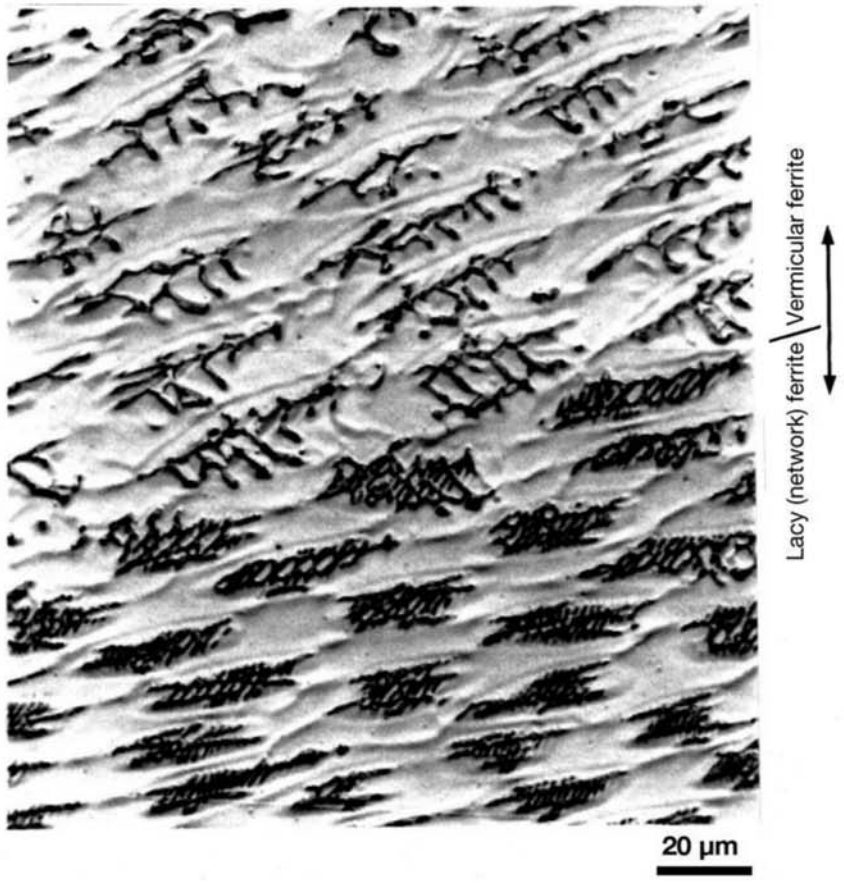

Fig. 16.19 Typical structures of austenitic stainless steels that solidified in the FA mode. Vermicular ferrite and lacy (network) ferrite. Reproduced from Ref 11 and 15. Courtesy of Nippon Steel Corporation.

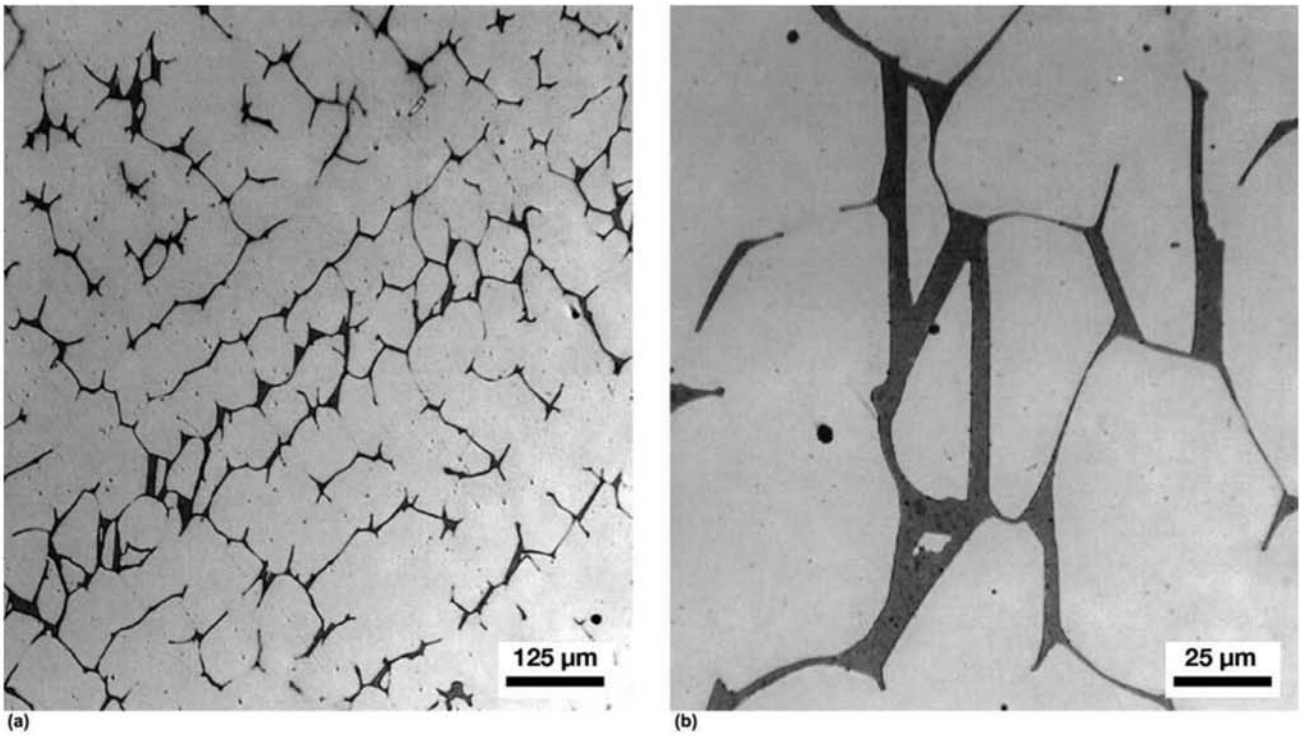

Fig. 16.20 AISI 316L steel, as-cast (see Fig. 8.51, Chapter 8, "Solidification, Segregation, and Nonmetallic Inclusions," in this book). (a) Austenite (light) with ferrite (vermicular). (b) Higher-magnification image of similar region. The straight δ–γ boundaries suggest some preferred crystallographic orientation between the phases. Electrolytic etched with 60% (vol) HNO_3 solution. Reproduced from Ref 16 with permission from Springer Science and Business Media.

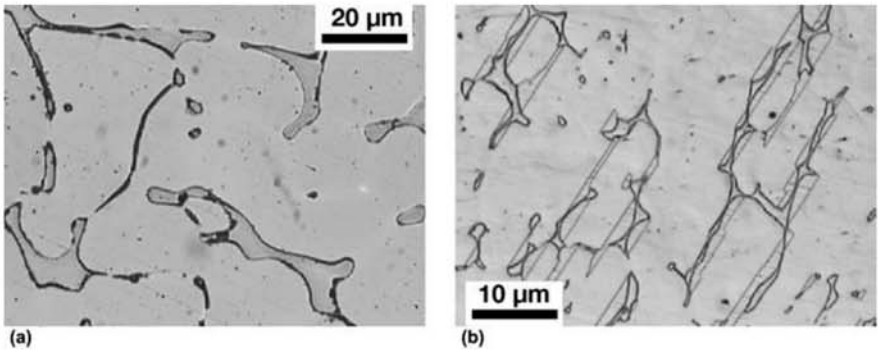

Fig. 16.21 AISI 304 steel, as-cast ingot. Delta ferrite in an austenitic matrix. (a) Etchant: oxalic acid. (b) Etchant: glyceregia. Courtesy of Villares Metals S.A., Sumaré, SP, Brazil.

with the <100> crystal direction (the direction of an edge of the cube of the unit cell) parallel in the two phases. This is the preferred orientation for rapid dendritic growth for both phases. In some cases, complete planes are parallel, giving rise to the observed interfaces. To test this hypothesis, researchers cast stainless steel ingots with and without nitrogen and titanium additions.

In steel having a sufficient content of titanium and nitrogen, titanium nitride (TiN) was formed. This nitride has a crystal structure that is an efficient nucleating agent in stainless steels (Ref 11). When the nucleation of ferrite was favored by the presence of TiN, copious nucleation of ferrite occurred,

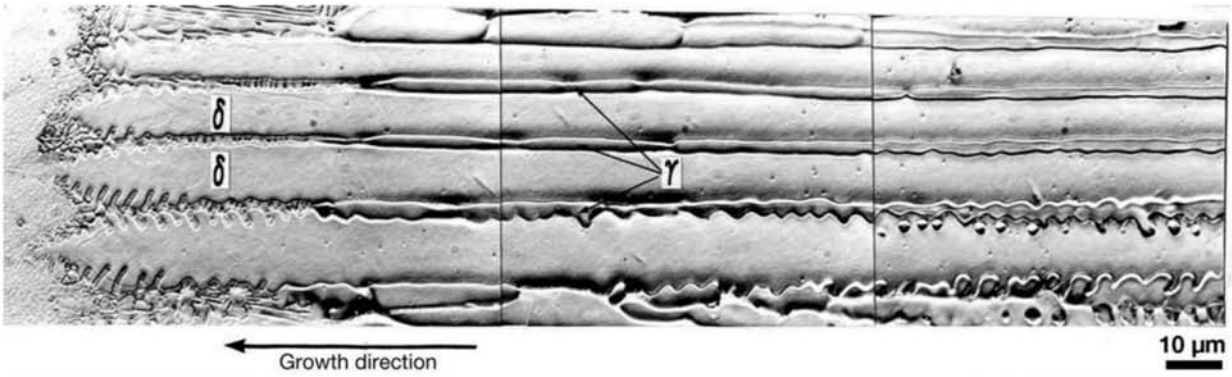

Fig. 16.22 Microstructural evolution of a weld metal containing Cr = 19% and Ni = 11% during solidification. Solidification was performed by quenching in liquid tin. Left of the image: the steel that was liquid when quenched. The dendrites grow as ferrite (δ) from the liquid. Later, austenite (γ) is formed, consuming the ferrite. Solidification sequence FA (Fig. 16.16), showing an increase in the volume fraction of austenite as the metal solidifies. Reproduced from Ref 9 and 17.

and the morphology of the phases formed in solidification changed. On a macroscopic view, however, growth was still columnar, as shown in Fig. 16.23.

Austenitic stainless steel castings have their structure well described by these models, as shown in Fig. 16.24. As in the case of other steels, hot working will homogenize the microstructure. Thus, the fraction of ferrite in the microstructure approaches the thermodynamic equilibrium values at the process temperature, as shown in Fig. 16.25.

16.5 Duplex Stainless Steels (Ferritic-Austenitic)

Duplex ferritic-austenitic stainless steels have microstructures that are formed by approximately equal volume fractions of austenite and ferrite. These steels have a favorable combination of the properties of both classes: considerable strength, good toughness, excellent corrosion resistance in many media, and outstanding stress corrosion and fatigue resistance. They are susceptible to hydrogen embrittlement, so their use in conditions where hydrogen charging is possible (such as cathodic protection) must be carefully evaluated (Ref 19).

This microstructure and combination of properties is normally achieved by increasing the chromium and molybdenum contents and by a significant increase in the nitrogen content. Whereas the three elements increase corrosion resistance, nitrogen, as an interstitial solute, has a very favorable effect on strength. These modifications in the chemical composition, however, stabilize deleterious phases such as sigma (σ) and other intermetallic phases such as chi (χ) (approx. Fe30Cr18Mo4).

Hence, besides the usual care to avoid the precipitation of carbides after annealing, attention must be paid to the potential of precipitation of embrittling intermetallic phases such as sigma (σ) and chi (χ) that also compromise corrosion resistance in duplex steels. As a rule, the higher the content of alloying elements that stabilize these phases, the faster the precipitation kinetics of the intermetallic phases, as indicated in Fig. 16.26 and 16.27.

Avoiding the precipitation of these compounds is an important challenge, particularly in welding procedures for these alloys. In case of doubt, one of the tests prescribed in ASTM A923 should be included in the testing specification to make sure these phases are absent. The metallographic method A has

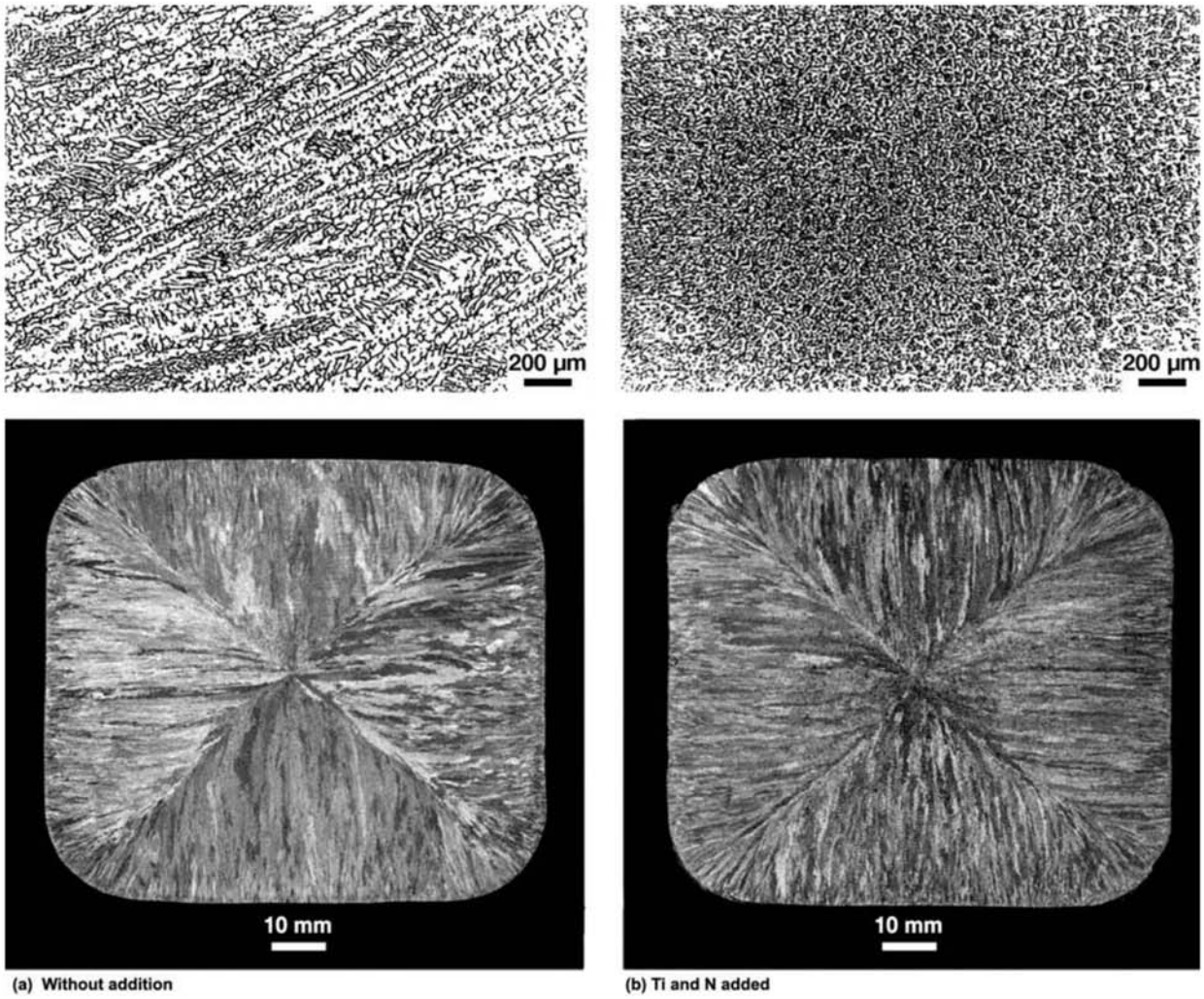

Fig. 16.23 The effect of the presence of TiN on ferrite nucleation in austenitic stainless steel. (a) No TiN addition, typical vermicular structure of ferrite (the micrograph is taken in a plane parallel to the primary axis of the dendrites). (b) Ti and N addition. Equiaxed grains of ferrite nucleated on TiN. Secondary austenite solidified as columnar dendrites. Reproduced from Ref 11 and 18. Courtesy of Nippon Steel Corporation.

been shown as quite efficient for the determination of the presence of sigma phase, also in austenitic stainless steels (Ref 22). On the other hand, when mechanical tests are selected, this ASTM standard also proposes well-defined criteria for the acceptance of the commercial duplex stainless steels. The balance between the chemical composition and the annealing (solubilizing) heat treatment temperature is critical to achieve the desired volume fraction of austenite and ferrite and to guarantee the complete solubilization of all precipitates. Rapid cooling to avoid precipitation must follow annealing. Figures 16.28 to 16.30 present structures of wrought duplex stainless steels. The detailed characterization of the structure evolution during hot working of these steels can be found in Ref 24.

The microstructures of cast duplex stainless steels combine the complexity of duplex steels with the usual deviations from thermodynamic equilib-

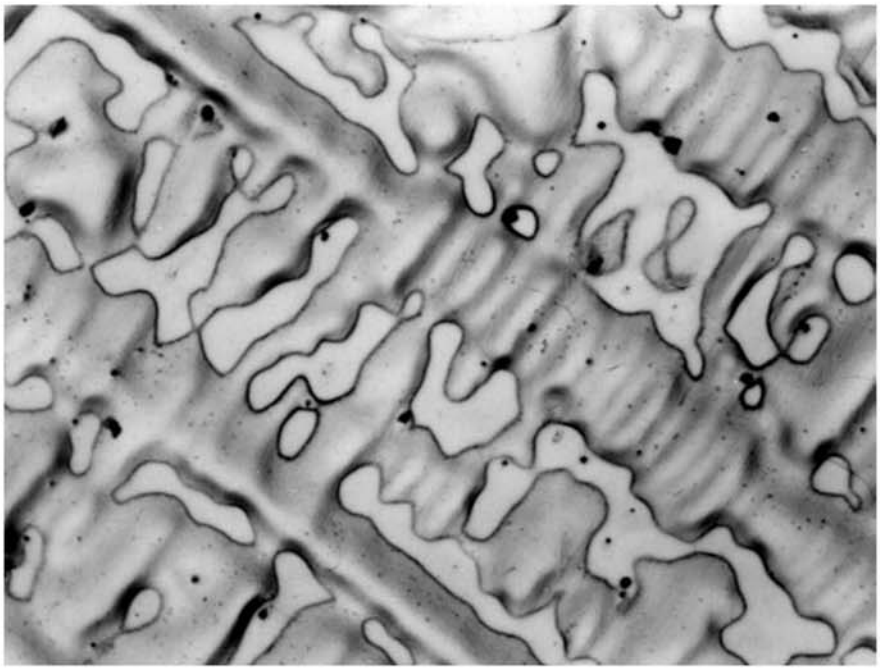

Fig. 16.24 Microstructure of a casting of steel W. Nr. 1.4439 in the annealed state. Austenitic matrix with lighter areas of ferrite (delta). Some interfaces between the ferrite and the austenite are deeper etched, which seems to indicate carbide precipitation. Etchant: villela + 5% HCl + 6% HNO_3. Source: Ref 19

rium found in as-cast structures, as Fig. 16.31 exemplifies. When the steel chemical composition is known, computational thermodynamics is a useful tool in the prediction of the equilibrium phases in the steel, as presented in Fig. 16.32. The various microstructures obtained when heat treating a steel with the chemical composition used for the calculations presented in Fig. 16.32 are shown in Fig. 16.33 to 16.37. Similar results are obtained with other duplex alloys as indicated by the calculations presented in Fig. 16.38 (for ASTM A890/A890M, Grade 1C) and shown in Fig. 16.39.The same changes evidently happen in forgings or rolled products. Figure 16.40, for instance, shows the decomposition of ferrite in austenite and sigma phase (σ). The morphology of the phases originating from the casting process clearly differentiate them from the shape of the phases formed during ferrite decomposition.

16.6 Precipitation Hardening Stainless Steels

Precipitation hardening (PH) stainless steels are classified in three groups: martensitic, austenitic, and semi-austenitic. These steels may be considered as a development from the classical 18-8 austenitic stainless steels. During the development of the martensitic PH steels, the main changes were the decrease of the nickel content and the addition of other elements (mostly copper) to promote the formation of precipitates. Overall, the martensitic PH steels combine the corrosion resistance equivalent to classic austenitic stainless steels (such as AISI 304) with elevated mechanical properties, comparable to those of the martensitic stainless steels. The typical heat treatment for these steels is solubilization followed by aging. During solubilization, the in-

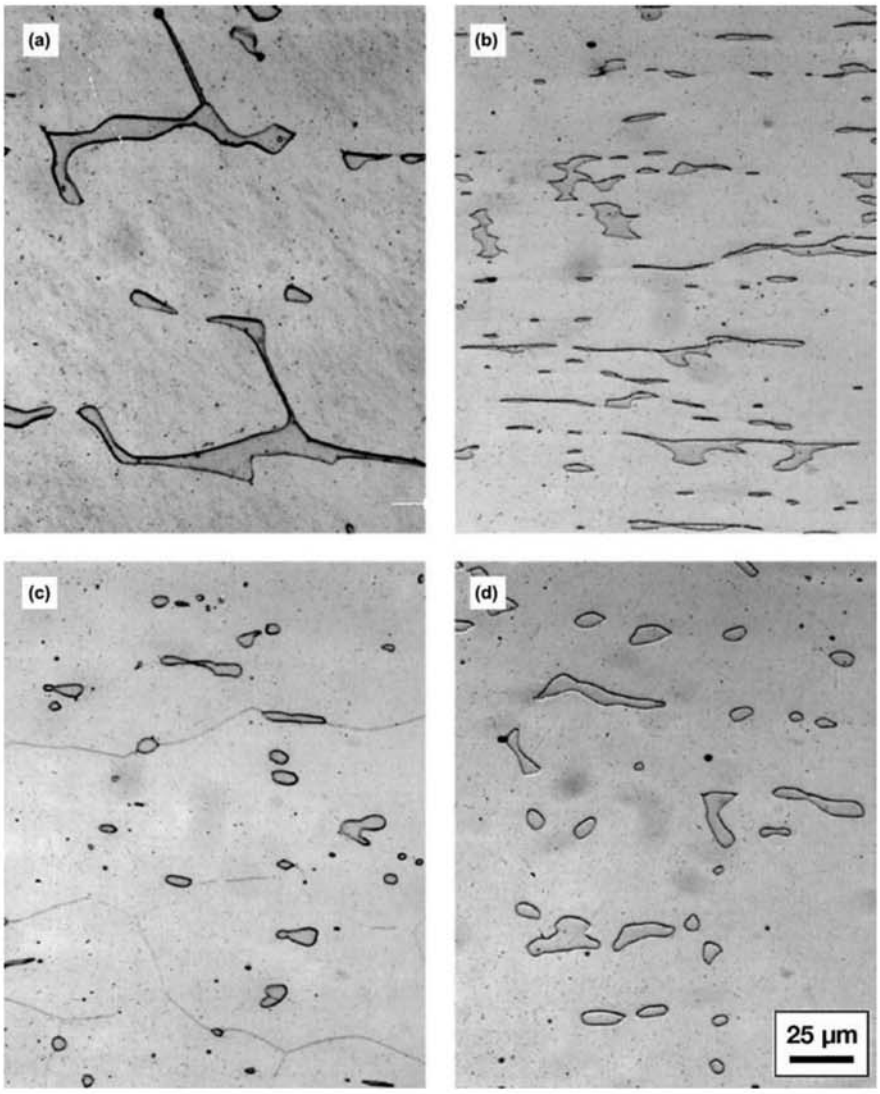

Fig. 16.25 Initial stages of the microstructural homogenization and ferrite dissolution during hot working of the AISI 316 austenitic stainless steel shown in Fig. 16.20 at 1150 °C (2100 °F). (a) Real deformation (ε) = 0, time (t) = 3600 s, (b) ε = 1, t = 2 s, (c) ε = 1, t = 3600 s, (d) ε = 0.1, t = 3600 s. With ε = 1, t = 3600 s, both at 1100 and at 1150 °C (2010 and 2100 °F), Ref 16 observed the dissolution of around 90% of the ferrite and 100% austenite recrystallization. Austenitic grain boundaries are visible in (c). Reproduced with permission from Springer Science and Business Media. Source: Ref 16

termetallic compounds based on copper, niobium, or aluminum are dissolved on the austenitic matrix. The steel is then cooled at a sufficiently high rate to avoid the reprecipitation of the compounds. For martensitic PH steels, the resulting microstructure after the cooling that follows solubilizing is essentially martensitic. Because the carbon content in these alloys is quite low, this is a low-hardness martensite. The steels actually harden during the precipitation treatment, when the intermetallic compounds precipitate in the martensitic matrix. Thus, in the solubilized condition these steels are easily machined (even being martensitic). Because aging is done at relatively low tempera-

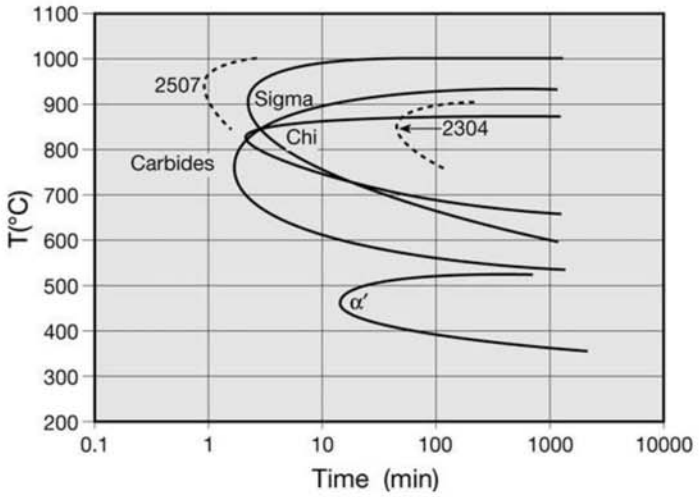

Fig. 16.26 Isothermal transformation curve for the precipitation in W. Nr. 1.4462 (2505/UNS S31803) steel after annealing at 1050 °C (1920 °F). The curves indicate the time required, at each temperature, for the start of the precipitation of the phase indicated (carbides, sigma, chi, or α'). Dotted lines indicate the start of the precipitation of intermetallic compounds in two other typical duplex stainless steel compositions (2507/UNS S31803 and 2304/UNS S32304). Precipitation is faster in steels containing more chromium and/or molybdenum (2507/UNS S32750).

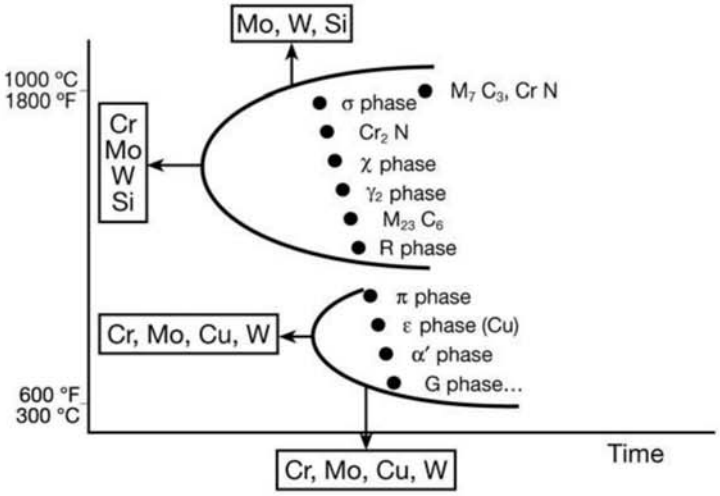

Fig. 16.27 Schematic TTT curves for the possible precipitates in duplex stainless steels and the effect of alloying elements on the precipitation kinetics of these phases. Source: Ref 21

tures, the dimensional changes are small; distortion, cracks, and decarburization, frequently associated with hardening heat treatments, are essentially eliminated. The aging (precipitation) cycles used have different effects on the final properties of the steels. Holding time and temperature are important. The precipitates are very fine so as to effectively harden the material, and evaluating the aging process is normally not easy through conventional me-

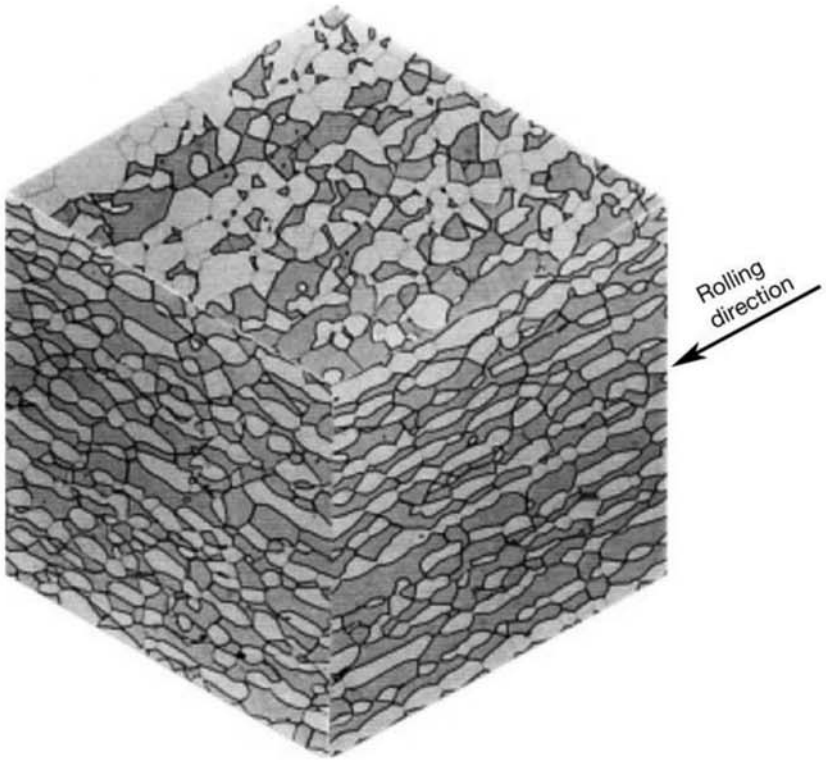

Fig. 16.28 Microstructure of UNS S31803 duplex stainless steel plate rolled and annealed for 30 min at 1050 °C (1920 °F), followed by quenching. Ferrite (dark) and austenite islands (light). The mechanical forming was done inside the two-phase field. Electrolytic etching with 30% (vol) HNO_3 solution. Courtesy of A. Ramirez, The Ohio State University. Source: Ref 23

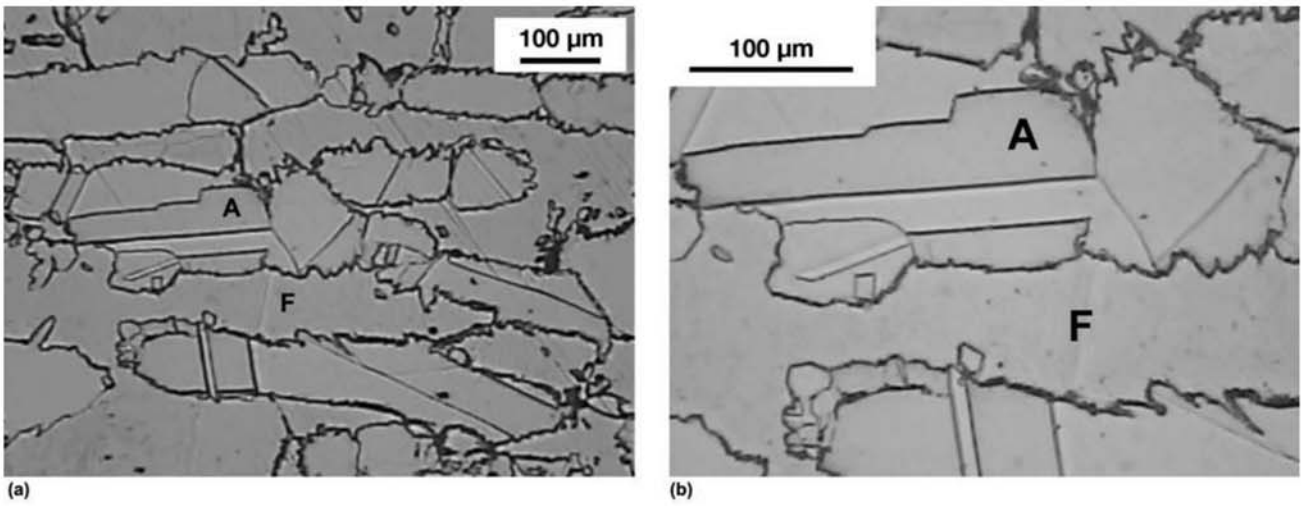

Fig. 16.29 (a) Forged bar of ASTM A182 grade F53 (UNS S 32750, DIN W. Nr. 1.4410) steel air cooled from 1000 °C (1830 °F). As forged structure. Austenite (Light gray) and ferrite (gray) are indicated as A and F in the figures. (b) Higher magnification of a region of panel (a): austenite contains twins, in general, making it easier to identify this phase. The grain boundaries have a jagged aspect because the recrystallization and grain growth occurring during hot work were interrupted by the air quenching. Etchant: glyceregia. Courtesy of Villares Metals S.A., Sumaré, SP, Brazil.

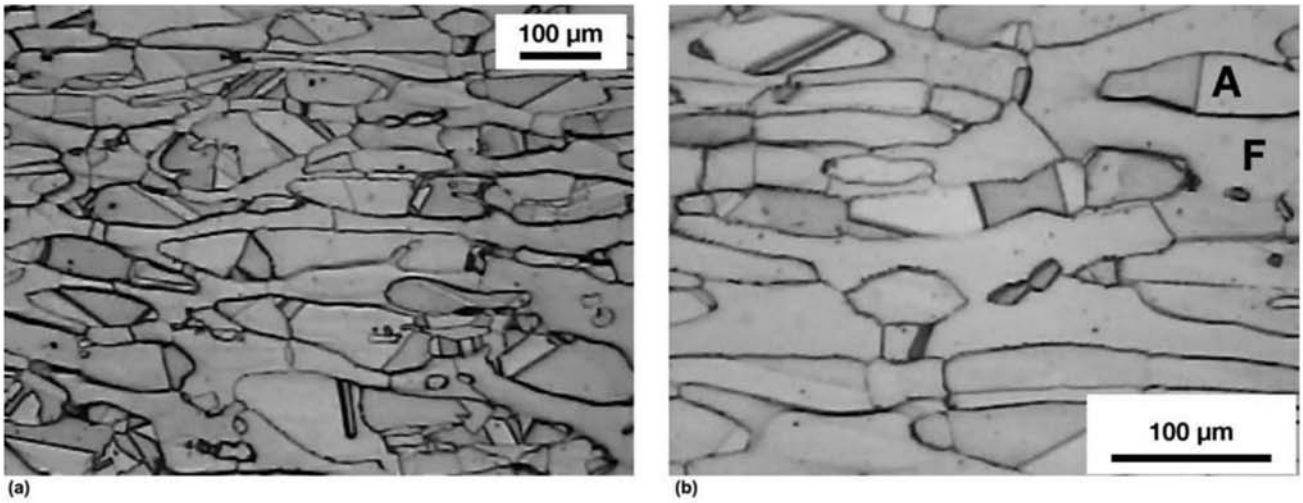

Fig. 16.30 (a) The duplex steel shown in Fig. 16.29 (ASTM A182 grade F53) after annealing at 1120 °C (2050 °F) for 8 h followed by water quenching (b) Higher magnification of a region of (a). (A = austenite, F = ferrite). Courtesy of Villares Metals S.A., Sumaré, SP, Brazil.

Fig. 16.31 As-cast ASTM A890/A890M Grade 6A duplex stainless steel. The composition has been adjusted for FA solidification. Austenite (light, dendritic) and interdendritic ferrite. Etchant: Beraha II. Courtesy of M. Martins. (See also Ref 25).

tallography. Figures 16.41 and 16.42 present examples of optical micrographs of PH steels.

16.7 Intercrystalline or Intergranular Corrosion

Certain elements may segregate to grain boundaries at certain temperatures. Furthermore, grain boundaries are higher energy regions; for this reason, they are preferential sites for the nucleation of second phases. In some cases, this may make the grain boundaries of stainless steels too reactive, giving rise to intercrystalline or intergranular corrosion. Both ferritic and austenitic

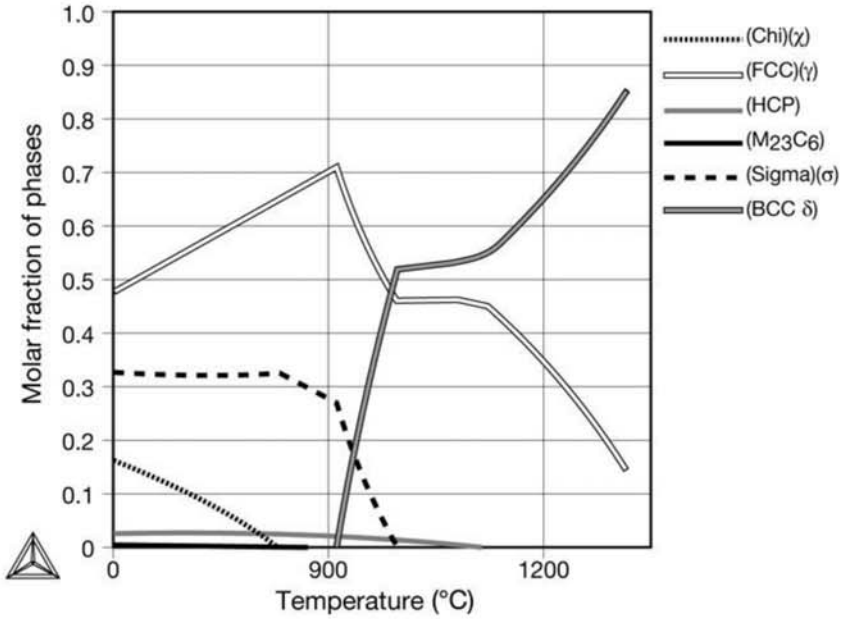

Fig. 16.32 Molar fraction of phases in equilibrium as a function of temperature for an ASTM A890/A890M, Grade 6A duplex stainless steel. Solubilization annealing is usually performed around 1100 °C (2010 °F). Below approximately 1000 °C (1830 °F), ferrite decomposes in austenite and sigma (σ). Below approximately 830 °C (1525 °F) chi (χ) becomes stable. (Calculated for a specific chemical composition in the range of Grade 6A. The temperatures and phase fractions evidently depend on the exact chemical composition.)

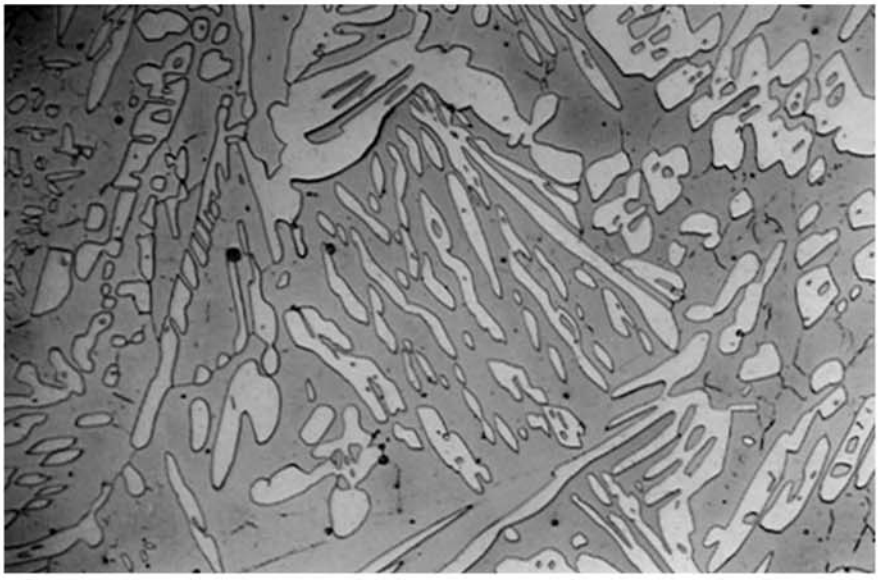

Fig. 16.33 ASTM A890/A890M Grade 6A cast duplex stainless steel annealed at 1100 °C (2010 °F) and quenched. Austenite (light) and ferrite. The annealing temperature defines the volume fraction of the phases present, for each specific chemical composition. Etchant: Beraha II. Courtesy of M. Martins. Source: Ref 26

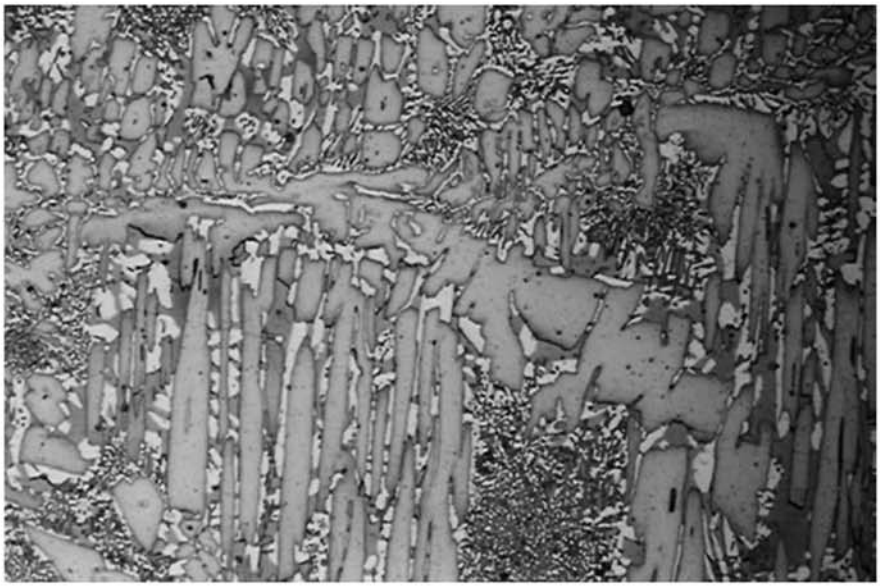

Fig. 16.34 ASTM A890/A890M Grade 6A cast duplex stainless steel annealed at 980 °C (1795 °F) and quenched. Austenite (light) and ferrite. At this temperature, ferrite decomposes into austenite and sigma phase (σ). Thus, there are two types (and sizes) of austenite: large grains, formed prior to the ferrite decomposition, and finer grains, between the larger ones, formed as a product of the ferrite decomposition reaction. (See also Fig. 16.37, SEM evaluation). Etchant: Beraha II. Courtesy of M. Martins. Source: Ref 26

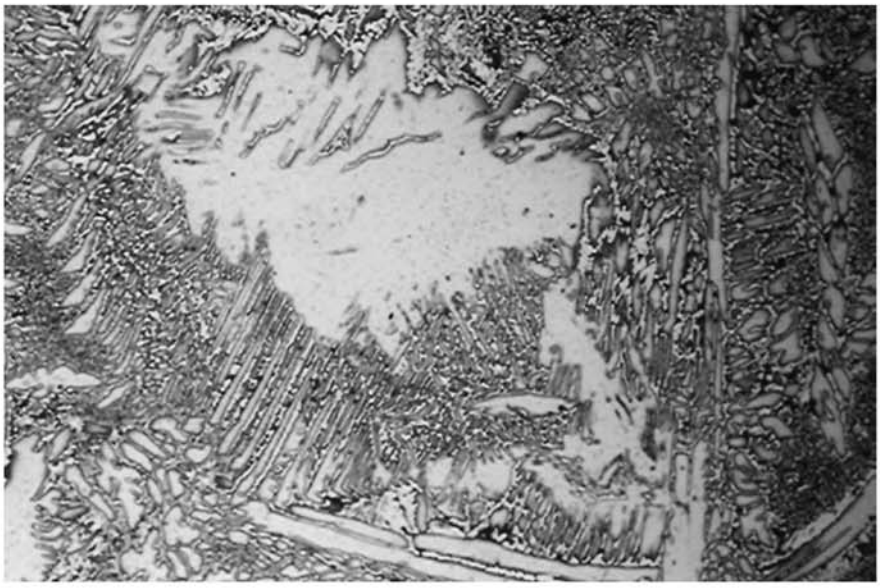

Fig. 16.35 ASTM A890/A890M Grade 6A cast duplex stainless steel annealed at 960 °C (1760 °F) and quenched. Austenite (light) and ferrite. At this temperature, ferrite decomposes into austenite and sigma phase (σ). Etchant: Beraha II. Courtesy of M. Martins. Source: Ref 26

Fig. 16.36 ASTM A890/A890M Grade 6A cast duplex stainless steel annealed at 900 °C (1650 °F) and quenched. Austenite (light) and ferrite. At this temperature, ferrite decomposes into austenite and sigma phase (σ). Ferrite is almost absent. (See Figure 16.37, SEM evaluation). Etchant: Beraha II. Courtesy of M. Martins. Source: Ref 26

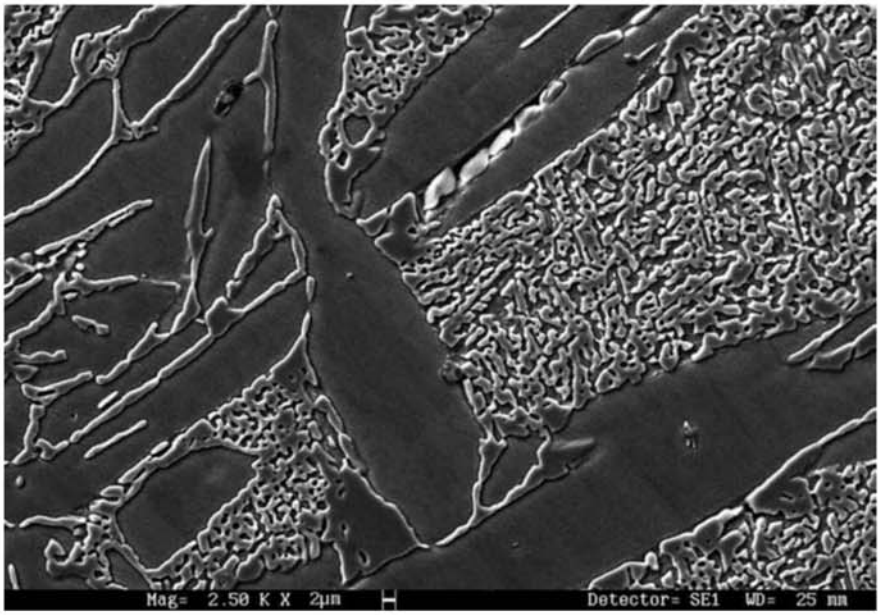

Fig. 16.37 ASTM A890/A890M Grade 6A cast duplex stainless steel aged at 920 °C (1690 °F). Austenite and sigma (σ). The larger grains are austenite and the fine structure between the austenite grains is composed of austenite and sigma (σ), probably formed by cooperative growth similar to a eutectoid. SEM, SE. Courtesy of M. Martins. Source: Ref 26

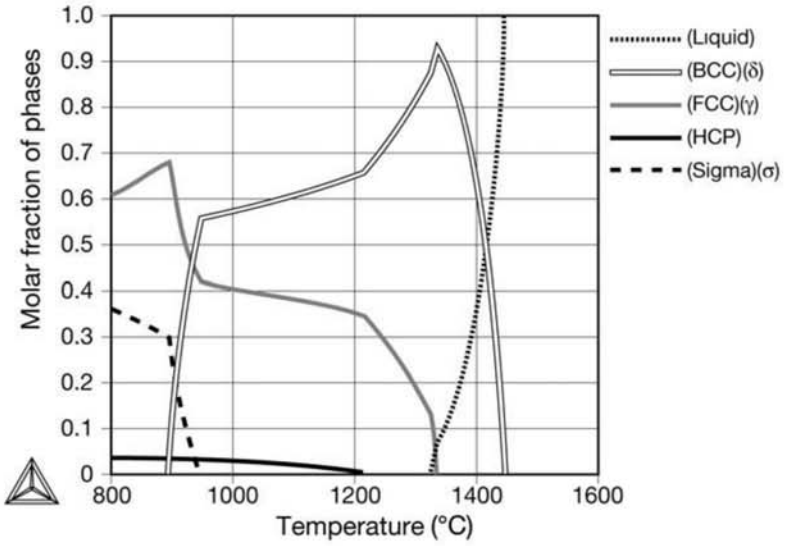

Fig. 16.38 Molar fraction of phases in equilibrium as a function of temperature for an ASTM A890/A890M Grade 1C duplex stainless steel. Solubilization annealing is normally performed above 1000 °C (1830 °F). Below approximately 950 °C (1740 °F) ferrite decomposes into austenite and sigma (σ). (Calculated for a specific chemical composition in the range of Grade 1C. The temperatures and phase fractions evidently depend on the exact chemical composition.)

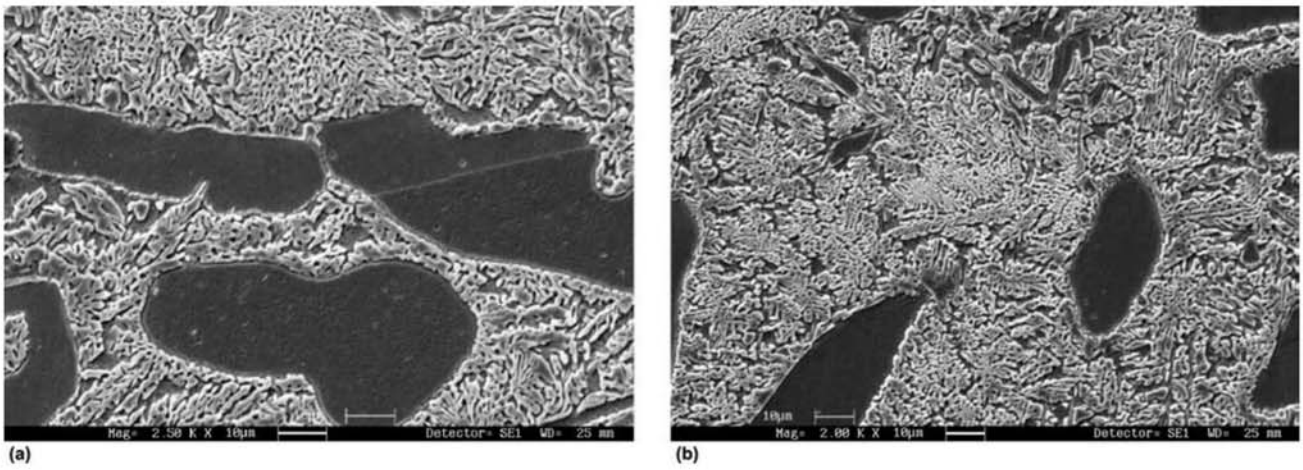

Fig. 16.39 ASTM A890/ A890M Grade 1C duplex stainless steel (as calculated in Fig. 16.38) subjected to an isothermal hold at 880 °C (1615 °F). SEM, SE. Larger austenite grains and finer structure composed of austenite and sigma (σ). Courtesy of M. Martins. Source: Ref 26

stainless steels are susceptible to this type of corrosion. The condition of this susceptibility is normally known as sensitization. It is believed that the main mechanism responsible for sensitization is the precipitation of chromium carbides ($M_{23}C_6$). The formation of these carbides will deplete the surrounding matrix in chromium, lowering the passivation of these regions, as schematically presented in Fig. 16.43. The kinetics of sensitization is quite similar to

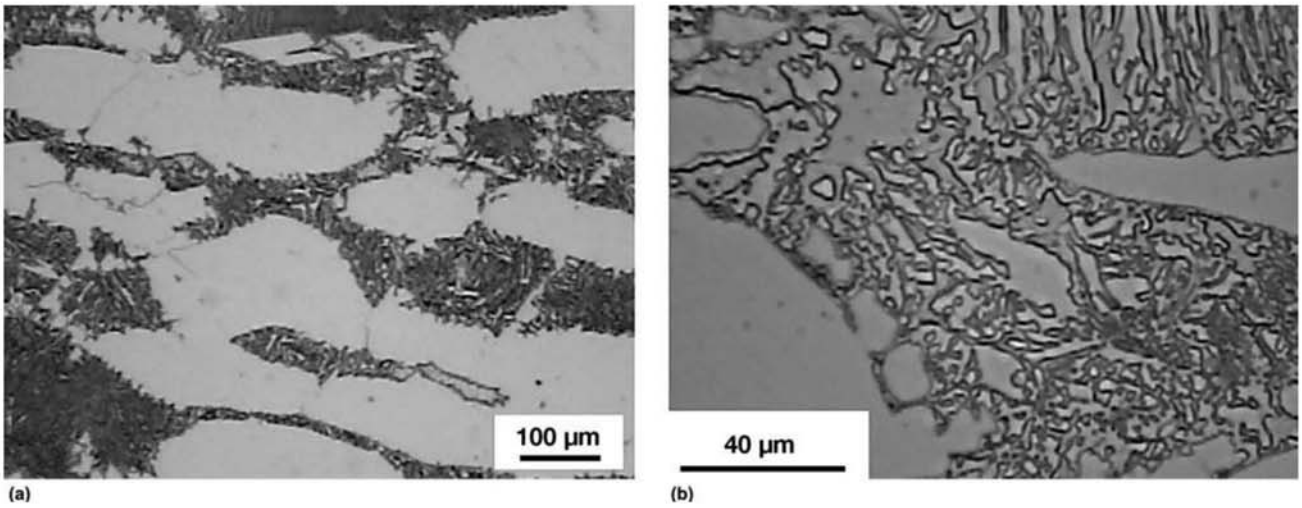

Fig. 16.40 (a) The duplex stainless steel presented in Fig. 16.30 after a 12 h treatment at 750 °C (1380 °F). All ferrite has decomposed into austenite and sigma (σ). Larger austenite grains and finer structure composed of austenite and sigma (including some sigma at larger austenite grain boundaries). These phases were formed by the decomposition of ferrite as discussed in the previous examples. (b) Higher magnification of panel (a). The decomposition microstructure is clearer at larger magnification. Courtesy of Villares Metals S.A., Sumaré, SP, Brazil.

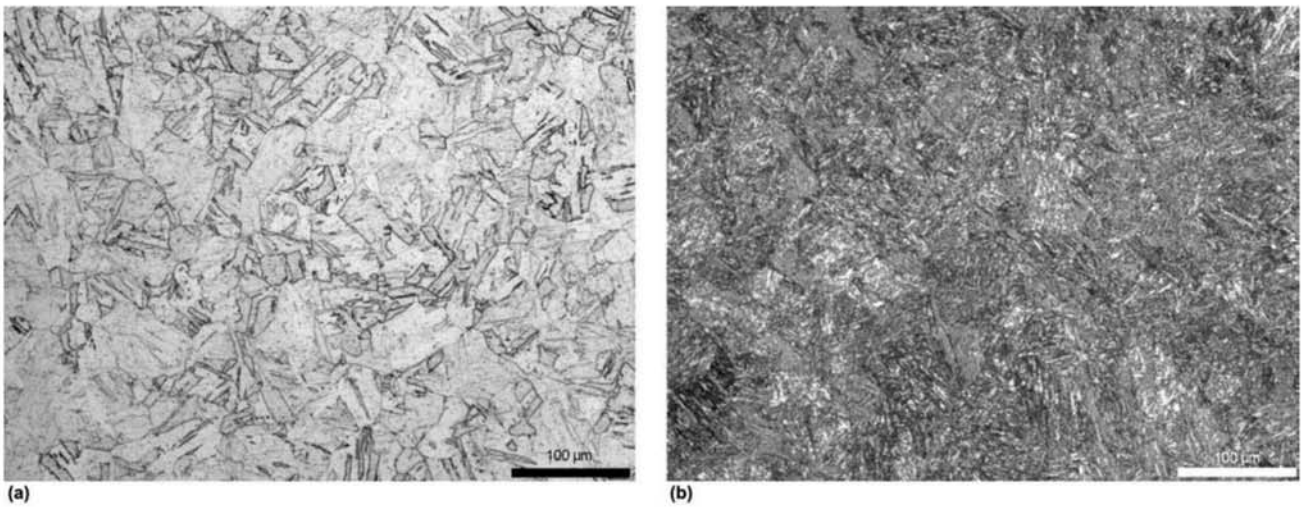

Fig. 16.41 ASTM A564 UNS 17400, SAE/AISI 630 (17-4PH) precipitation hardening stainless steel. (a) Solubilized at 1040 °C (1905 °F) for 1 h followed by water quenching. Low carbon martensite (maximum specified carbon content is 0.07%). (b) Solubilized and aged at 590 °C (1095 °F) for 4 h, air-cooled. Courtesy of Villares Metals S.A., Sumaré, SP, Brazil.

the kinetics of chromium carbide precipitation. An example is given in Fig. 16.44.

Two measures are commonly adopted to reduce or avoid sensitization. These are the use of stabilizing elements (titanium or niobium, which form carbides that are much more stable than chromium carbides) and the drastic reduction of the carbon content of the steel (austenitic steels in the L series typically have C < 0.03%). In some cases, the loss of strength associated with the very low carbon content may be compensated for by increasing the nitro-

gen content. The techniques used to evaluate the presence of sensitization are described in the various methods given in the standard ASTM A262. Figure 16.45 shows the metallographic evaluation of results of approved and rejected tests performed according to this standard. Welding processes may subject stainless steels to thermal cycles that lead to sensitization. A classic manifestation of this phenomenon is the so-called knife line corrosion, where a line parallel to the weld fusion line in the base material is exposed to a thermal cycle, leading to the precipitation of chromium carbides and sensitization, as shown in Fig. 16.46.

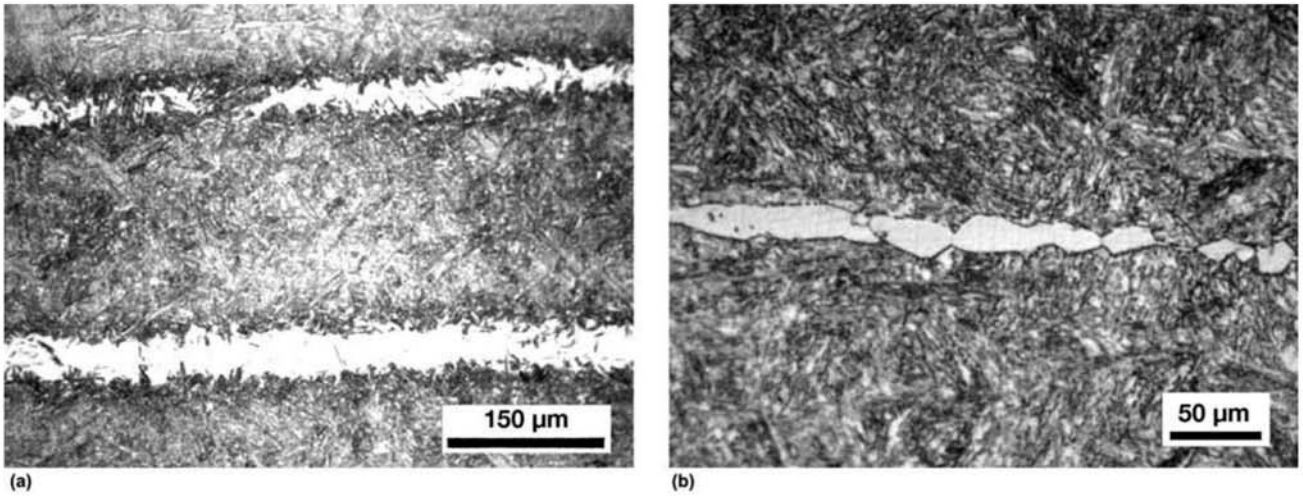

Fig. 16.42 Longitudinal cross sections of a 100 mm (4 in.) diameter bar of 17-4PH precipitation hardening stainless steel. (a) Martensite with presence of segregated areas containing retained austenite. (b) Presence of delta ferrite. In some oil industry specifications, these conditions are cause for rejection. Etchant: Kalling. Courtesy of A. Zeemann, Tecmetal, Rio de Janeiro, Brazil.

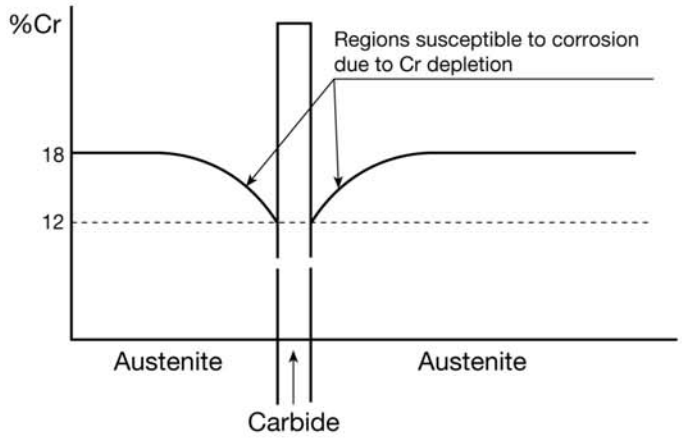

Fig. 16.43 Schematic presentation of the precipitation of chromium carbide causing sensitization and decreasing the corrosion resistance of the grain boundary region.

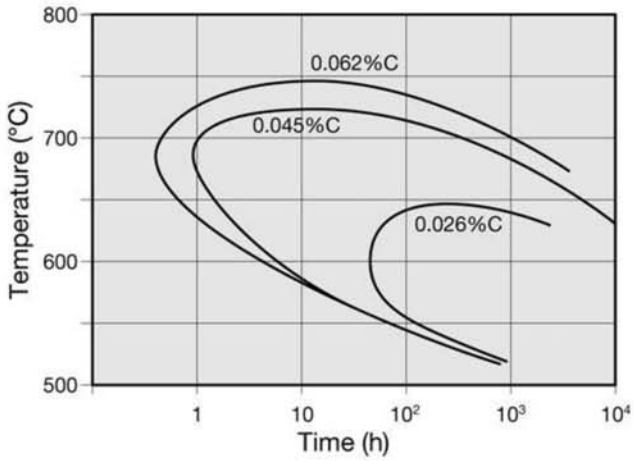

Fig. 16.44 Isothermal treatment time at indicated temperature necessary to cause sensitization and rejection in the test according to Method E of ASTM A262 standard for the evaluation of resistance to intergranular corrosion. Results for AISI 304 steel with different carbon contents, annealed at 1050 °C (1920 °F) followed by water quenching.

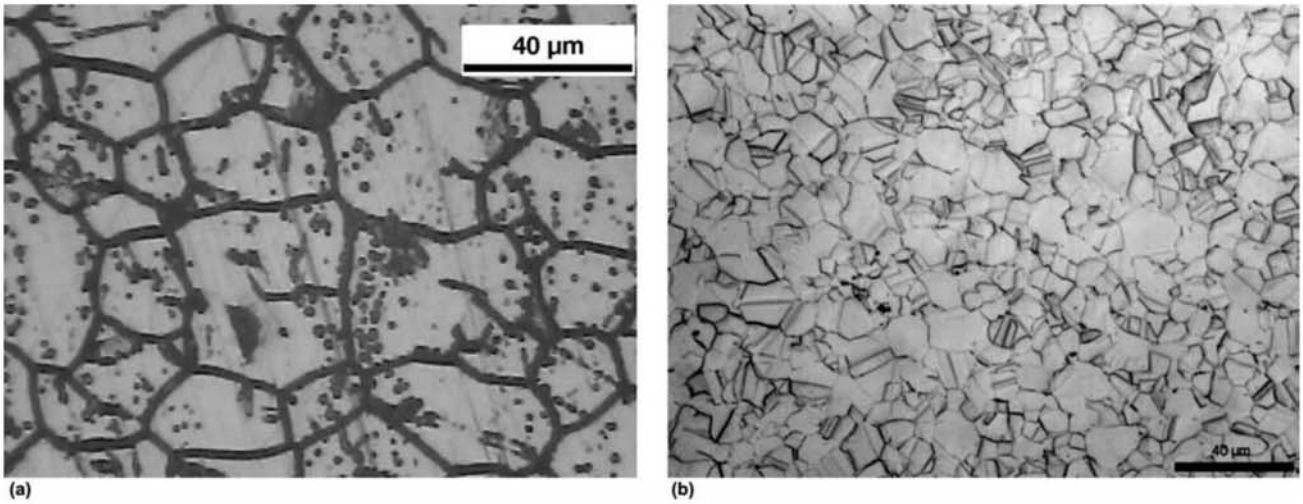

Fig. 16.45 (a) AISI 310 austenitic stainless steel annealed at 1060 °C (1940 °F) for 1 h followed by water quenching and a simulated sensitization treatment at 675°C (1245 °F) for 1 h, followed by air-cooling. Etchant: electrolytic oxalic acid at 10% current density of 1 A/cm². Rejected according to ASTM A262 due to intergranular corrosion. (b) AISI 321 austenitic stainless steel annealed at 1060°C (1940 °F) for 1 h followed by water quenching and a simulated sensitization treatment at 675 °C (1245 °F) for 1 h followed by air cooling. Etchant: same as in panel (a). This stabilized austenitic stainless steel was approved in the ASTM A262 test because of absence of intergranular corrosion. Courtesy of Villares Metals S.A., Sumaré, SP, Brazil.

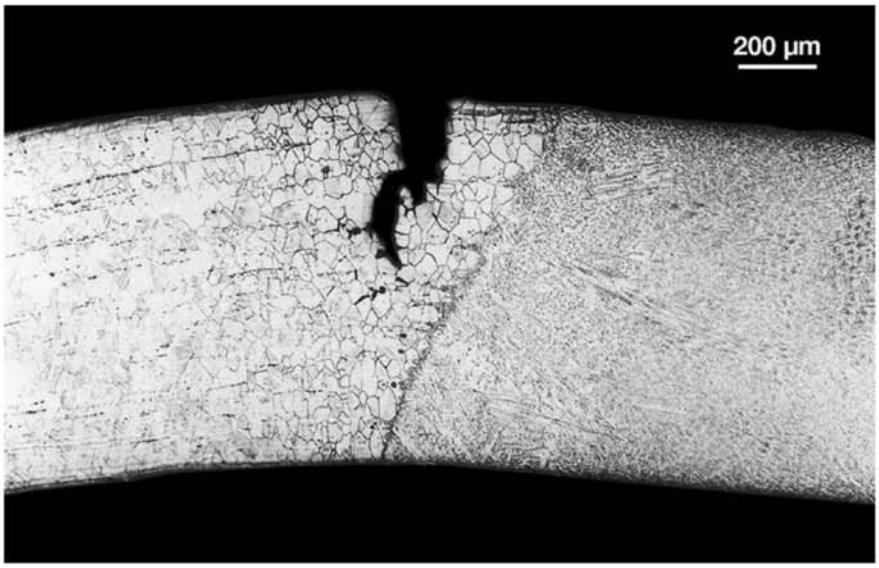

Fig. 16.46 Longitudinal cross section of a specimen of W. Nr. 1.4550 (similar to AISI 347L) austenitic stainless steel welded and subjected to intergranular corrosion test according to DIN 50914 standard (standard replaced by DIN EN ISO 3651-2, both equivalent to ASTM A262 E). The region subjected to tensile stresses during bending (upper portion of the image) has cracked in the heat-affected zone after about 15° of bending. Courtesy of M. Moraes, NUCLEP, RJ, Brazil.

REFERENCES

1. ASM, *Stainless Steels,* ASM Specialty Handbook, J.R. Davis, Ed., ASM International, 1994
2. A.L. Schaeffler, Constitution Diagram for Stainless Steel Weld Metal, *Metal Prog*., 1949, v. 56 (11), p 680–680B
3. W.T. DeLong, Ferrite in Austenitic Stainless Steel Weld Metal, *Welding J.*, Vol 53 (No. 7), 1974, p 273–86
4. "Standard Practice for Steel Casting, Austenitic Alloy, Estimating Ferrite Content Thereof," A800-14, ASTM, 2014
5. T.G. Gooch, P. Woollin, and A.G. Haynes, Welding Metallurgy of Low Carbon 13% Chromium Martensitic Steels, *Supermartensitic Stainless Steels 99 Proceedings*, Belgian Welding Institute, May 27–28, 1999
6. P.E. Kvaale and S. Olsen, Experience with Supermartensitic Stainless Steels in Flowline Applications, *Stainless Steel World 99 Conference*, KCI Publishing, 1999
7. O.M. Akselsen, G. Rorvik, P.E. Kvaale, and C. vanderEijk, Microstructure-Property Relationships in HAZ of New 13% Cr Martensitic Stainless Steels, *Welding Res. Suppl.*, May 2004, p 160–67
8. D.M. Carramanhos, *Texturas de deformação e recristalização de aços inoxidáveis ferríticos dos tipos AISI 430 e 409* (Deformation and Recrystallization Textures of Ferritic Stainless Steels Type 430 and 409), M. Sc. thesis, Instituto Militar de Engenharia, 2006
9. *The Making, Shaping and Treating of Steel, Casting Volume,* 11th edition, A. Cramb, ed., AISE, 2003
10. M.C. Flemings, Solidification, *Advanced Physical Chemistry for Process Metallurgy, N. Sano et al., eds.*, Academic Press, 1997, p 151–82
11. H. Inoue and T. Koseki, Clarification of Solidification Behaviors in Austenitic Stainless Steels Based on Welding Process, *Nippon Steel Tech. Rep.*, Vol 95, January 2007, p 62–70
12. J.C. Lippold W.A. Basleak III, and I. Varol, Heat-Affected Zone Liquation Cracking in Austenitic and Duplex Stainless Steels, *Welding Res. Suppl*., January 1992, p 1–14
13. T.A. Siewert, C.N. McCowan, and D.L. Olson, Ferrite Number Prediction to 100FN in Stainless Steel Weld Metal, *Welding J. Suppl.*, 1988, p 289–98
14. S.S. Babu, J.M. Vitek, Y.S. Iskander, S.A. David, New Model for Prediction of Ferrite Number of Stainless Steel Welds, *Sci. Technol. Weld. Join.*, Vol 2 (No. 6), 1997, p 279–85
15. H. Inoue, T. Koseki, S. Ohkita, and M. Fuji, *Sci. Technol. Weld. Join.*, Vol 5, 2000, p 385–96
16. M.C. Mataya, E.R. Nilsson, E.L. Brown, and G. Krauss, Hot Working and Recrystallization of As-Cast 316L, *Metall. Mat. Trans. A*, Vol 34A, 2003, p 1683–703

17. H. Inoue, T. Koseki, S. Ohkita, and M. Fuji, *Quart. J. Japan Weld. Soc.*, Vol 15, 1997, p 88–89

18. H. Inoue and T. Koseki, *Proceedings of the 7th International Conference on Trends in Welding Research*, Georgia, USA, ASM International, 2005

19. M. Martins, private communication, 2007

20. Det Norske Veritas, Recommended practice Det Norske Veritas DNV-RP-F112, Design of Duplex Stainless Steel for Subsea Equipment Exposed to Cathodic Protection, October 2008

21. J.A. Charles, Super Duplex Stainless Steel: Structure and Properties, *2nd Duplex Stainless Steels,* 1991, Beaune Borcogne, France.

22. X. Tang, Sigma Phase Characterization in AISI 316 Stainless Steel. *Microsc. Microanal.*, Vol 11, Suppl 2, 2005, p 78–79

23. A.J. Ramirez, *Estudo da precipitação de nitreto de cromo e fase sigma por simulação térmica da zona afetada pelo calor na soldagem multipasse de aços inoxidáveis duplex* (Study of the Precipitation of Chromium Nitride and Sigma Phase via Thermal Simulation of the Multipass Welding of Duplex Stainless Steels), M.Sc. thesis, Escola Politécnica-USP, 1997

23. A. Iza-Mendia, A. Pinol-Juez, J.J. Urcola, and I. Gutierrez, Microstructural and Mechanical Behavior of a Duplex Stainless Steel under Hot Working Conditions, *Metall. Mat. Trans. A*, Vol 29A, 1998, p 2975–86

25. M. Martins and L.C. Casteletti, Heat Treatment Temperature Influence on ASTM A890 GR 6A Super Duplex Stainless Steel Microstructure, *Mat. Charact.*, Vol 55, 2005, p 225–33

26. M. Martins, *Caracterização microestrutural-mecânica e resistência à corrosão do aço inoxidável super dúplex ASTM A890/A890M Grau 6A* (Microstructural and Mechanical Characterization and Corrosion Resistance of the Superduplex Stainless Steel ASTM A890/A890M Grade 6A), Ph.D. dissertation., Universidade de São Paulo, 2006

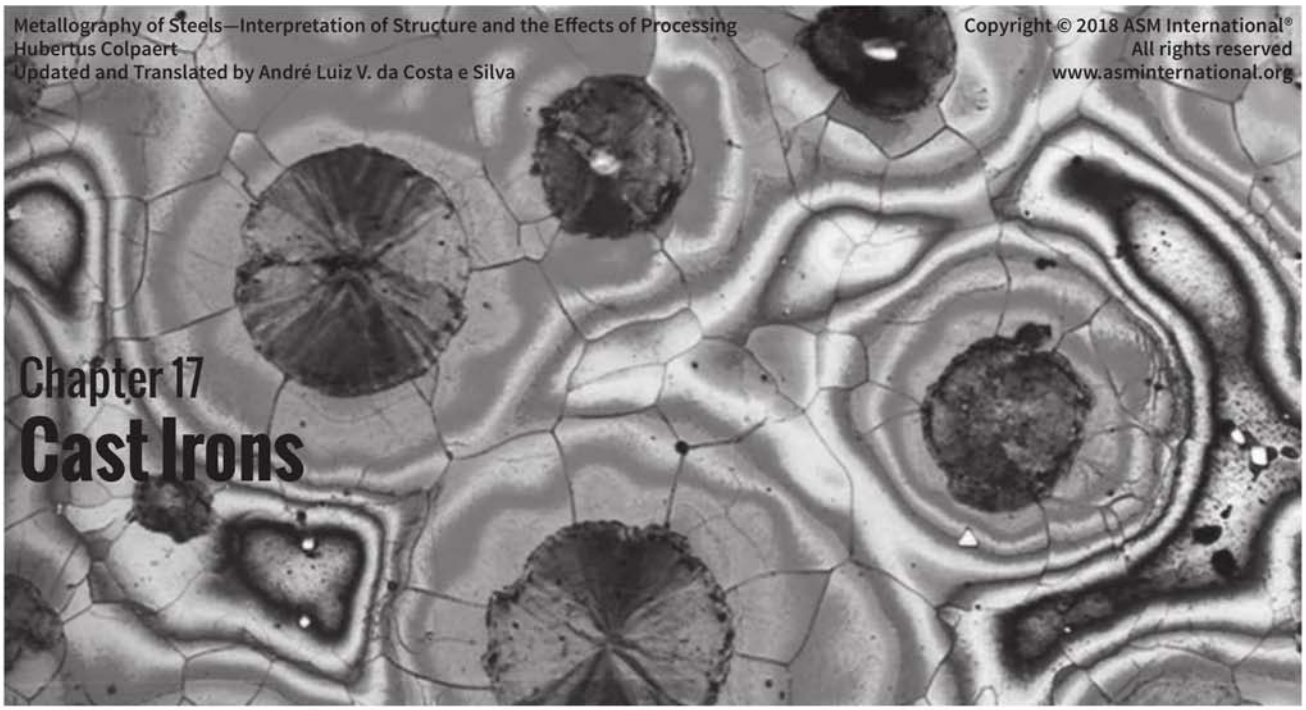

Chapter 17
Cast Irons

Cast irons are iron-based alloys with chemical compositions close to that of the eutectic point in the iron-carbon phase diagram (see Fig. 17.1). The classical definition distinguishes cast irons from steel using the maximum solubility limit of carbon in austenite in the presence of graphite or cementite, around 2%. With higher carbon contents, either graphite or primary carbides are formed during solidification. As the carbon content is increased from the

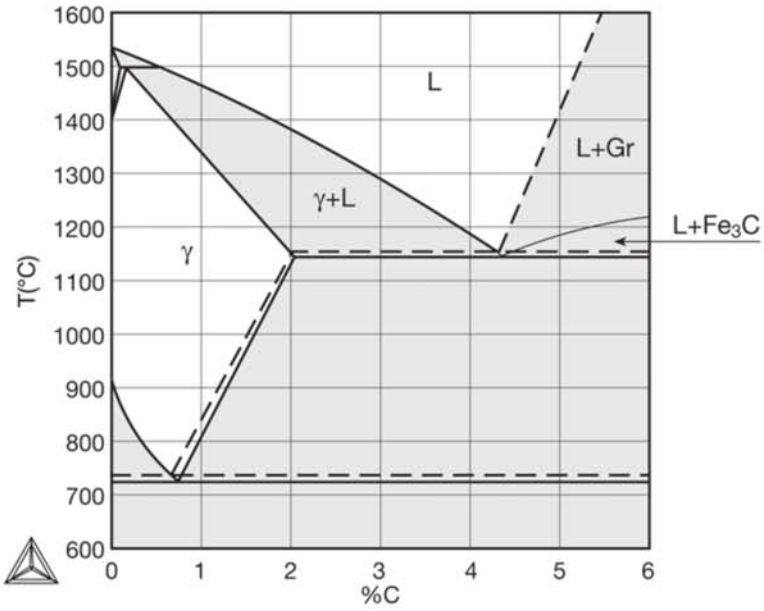

Fig. 17.1 Iron-carbon phase diagram. Dashed lines: equilibrium with graphite. Solid lines: metastable equilibrium with cementite. Some phase equilibria are not affected by the presence of either graphite or cementite. Gr: graphite; L: liquid; (gamma) γ: austenite.

composition range of steels, the *liquidus* temperature decreases, and it is thus easier to cast these alloys. On the other hand, the presence of significant amounts of primary carbides or graphite normally restricts the formability of these alloys. According to Ref 1, the oldest record of a cast iron part is a Chinese lion statue dating from around 500 BCE, whereas in Europe this alloy was introduced between the 13th and 15th centuries CE. The water pipes in Versailles in France (1664) (Ref 2) and the Coalbrookdale bridge in England (Ref 3) are important examples of the historical relevance of this material.

For many years, the use of cast irons was restricted due to its limited ductility and toughness. The search for a material that combined the toughness of steel and the ease of fabrication through casting led to the development of malleable cast irons (see the section "Malleable Cast Irons" in this chapter), in which a long heat treatment leads graphite formation in a reasonably tough microstructure. The cost of the process, however, creates a significant limitation. The development of nodular cast iron (see the section "17.5 Nodular Cast Iron or Ductile Cast Iron" in this chapter), either in 1940 per Ref 1 or 1948 according to Ref 4, brought a new stimulus to the cast iron industry, dramatically expanding the range of successful applications of this material. From a microstructural point of view, the effect of carbon dissolved in the solid phases of iron is completely equivalent to what has been discussed for steels in the previous chapters. However, the considerable excess of carbon in the alloy may be present in cast irons in three different forms:

- Dissolved in the solid phases of iron
- As cementite (or alloyed carbides)
- As graphite

Industrial experience with cast irons significantly precedes knowledge of the iron-carbon equilibrium phase diagram as well as knowledge of the constituents and microstructures that could be associated with compositions in the iron-carbon system. It is sufficient to recall that, as discussed in Chapter 8, "Solidification, Segregation, and Nonmetallic Inclusions," in this book, Ledebur, the pioneer in the studies of the Fe-C eutectic, performed his studies around 1880–90, when cast irons were already widely used in commercial applications. This has led to a significant development of empirical classifications for these alloys.

The most common way of classifying cast irons is related to the aspect of its fracture. When carbon is combined in cementite, the fracture has a crystalline character and a light aspect. These alloys are called white cast irons. Alloys containing graphite in their structure present dark, grayish fractures and are called gray cast irons.

For many years, it was not possible to affect how graphite precipitates during solidification. More recently, ways of influencing the morphology of graphite have been developed, enlarging the range of possible graphite variations and increasing the possibilities of controlling the properties of alloys with graphite in their microstructure. In these cases, solidification is the most important stage in achieving the desired structure, as partially discussed in Chapter 8, "Solidification, Segregation, and Nonmetallic Inclusions."

When microscopy and metallography were developed, the classification of cast irons based on their microstructure became possible.

Cast irons containing graphite are primarily classified by the shape of the graphite. Thus, there are cast irons with lamellar, nodular, or vermicular (or compacted) graphite. Within each shape classification, the way the graphite is distributed in the product and its size are important metallographic features and are routinely characterized. Furthermore, the matrix microstructure of cast irons can also be used for their classification. Apart from graphite, cast iron microstructures present the same constituents as steels.

Table 17.1 presents the various types of commercial cast iron, the shape of their graphite (when present), the possible microstructures, and the method of obtaining these structures.

Though cast irons with less than 4.3% C (the eutectic composition in the stable Fe-C phase diagram) are commonly classified as hypoeutectic and those above this composition are classified as hypereutectic, cast irons generally have at least one more alloying element, silicon being the most common. Besides silicon and carbon, the most common elements in cast irons are manganese, sulfur, and phosphorus. These elements change the eutectic composition and temperature and may alter the solidification sequence of the alloys. It is common to adopt formulas to calculate the carbon equivalent (CE) to forecast the solidification behavior of cast irons. A simple formula used to calculate the "carbon equivalent" is given as (Ref 4):

$$CE = \%C + \frac{1}{3}(\%Si + \%P)$$

This formula makes possible a preliminary assessment of the position of the alloy composition with respect to the eutectic composition (hypo or

Table 17.1 Types of cast iron and their structural characteristics

Usual name	Carbon rich phase	Matrix	Final structure obtained through
Gray cast irons	Lamellar or flake graphite	P, F	Solidification
Nodular cast iron or ductile cast iron	Nodular graphite	F, P, A	Solidification or heat treatment
Compacted graphite iron, GGI, or vermicular graphite iron, VG or GGV	Compacted or vermicular graphite	F, P	Solidification
White cast irons	Cementite	P, M	Solidification and heat treatment (stress relief and/or finishing austenite decomposiiton)
Malleable cast irons	…	F, P	Heat treatment
Austempered nodular cast iron or austermpered ductile iron	Nodular graphite	B, austempering	Heat treatment

Note: A = austenite, F = ferrite, P = pearlite, M = martensite, B = bainite. Source: Ref 5

hyper). Besides the empirical validation of the formula, thermodynamic data support it (Ref 6).

17.1 White Cast Irons and Gray Cast Irons

When cooling steels after solidification and heat treatments, if carbon exceeds the solubility in the phases of iron, it usually precipitates as a carbide, the metastable cementite being the most common. The occurrence of the stable equilibrium phase in the Fe-C system, graphite, very rarely occurs in steels.

Conversely, in the case of cast irons, starting from solidification, the system influences which one of the carbon-rich phases will form, and the situation is more complex than in the case of steels. In general, two factors influence the formation of the carbon-rich phase in cast irons:

- Cooling rate
- Chemical composition

17.1.1 The Effect of the Cooling Rate

Slower cooling favors equilibrium and hence the formation of graphite during solidification. Higher cooling rates lead to metastable solidification and the formation of cementite.

The cooling rate in casting is usually defined by the part dimensions and the casting mold material. As a rule, large parts will cool at slower rates. Molding sands with lower thermal conductivity may also lead to lower cooling rates. On the other hand, metallic molds lead to high cooling rates.

A common test is the casting of wedges in which the thickness and hence the cooling rate vary continuously. The thinner regions of the wedge may solidify in a metastable way (white cast iron). As the wedge thickness increases, gray cast iron may be formed, as shown in Fig. 17.2. The wedge test is standardized in accordance with ASTM A367 (Ref 7).

Many empirical and semi-empirical formulas relate chemical composition and the critical cooling rate in the wedge test. Some of these are reviewed in Ref 8.

Not only does the cooling rate affect the solidification mode, it also has an influence on the final microstructure. Figure 17.3 presents one example of the hardness profile along a wedge cast per ASTM A367 standard, similar to the one presented in Fig. 17.2. The different microstructures formed along the wedge, due to the different cooling rates, give rise to a range of different properties and types of cast irons discussed in this chapter. One of the explanations put forward to explain the effect of the cooling rate on the casting mode is that it would affect the eutectic temperatures for the stable and metastable eutectic transformations. The increase in the cooling rate would lower both eutectic temperatures. However, one can expect that the cooling rate may differently influence each of the eutectic temperatures, and there would be a cooling rate beyond which the metastable eutectic temperature would be higher than the stable eutectic temperature, and this would justify the beginning of the formation of cementite, as shown in Fig. 17.4. For this reason, thermal analysis is frequently used as a development and quality control tool in the cast iron industry. The solidification structure can be predicted and controlled with the information provided by this method, as shown schematically in Fig. 17.5. Furthermore, superheating the cast metal also reduces the

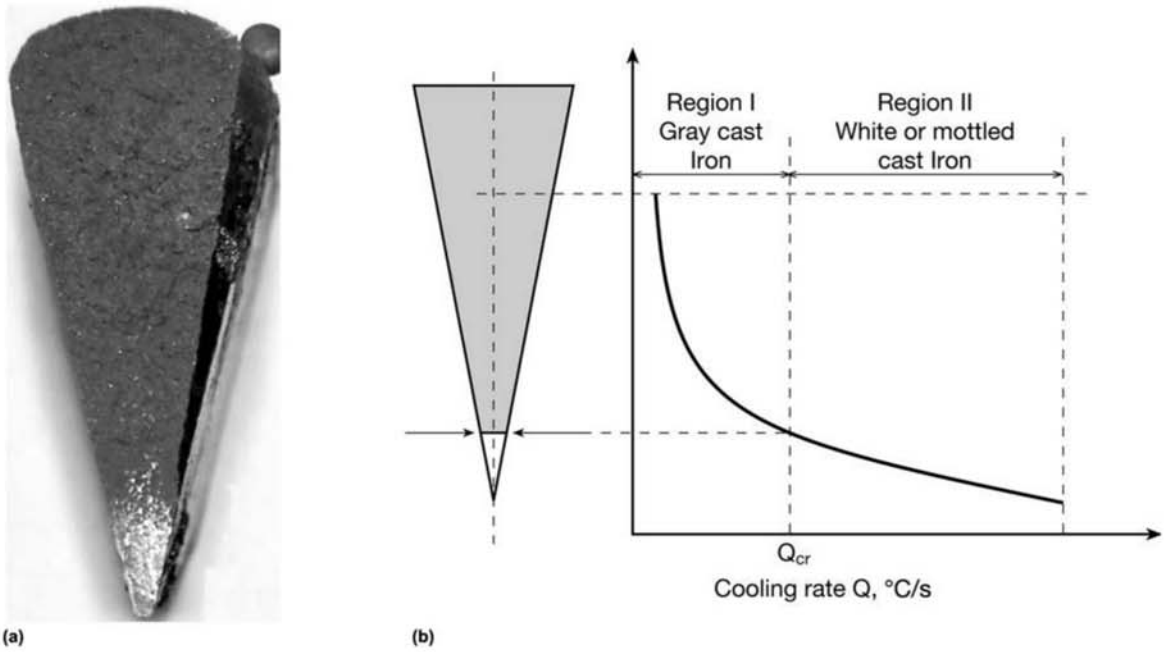

Fig. 17.2. (a) Appearance of the fracture of a cast iron wedge. The region near the final extremity presents a white fracture. Most of the wedge has a gray structure. Courtesy of C.H. Lopes, BR Metals Fundições Ltda, Barra do Piraí, RJ, Brazil. (b) Schematic relationship between the cooling rate and position in the wedge. Q is the cooling rate at a given position of the wedge.

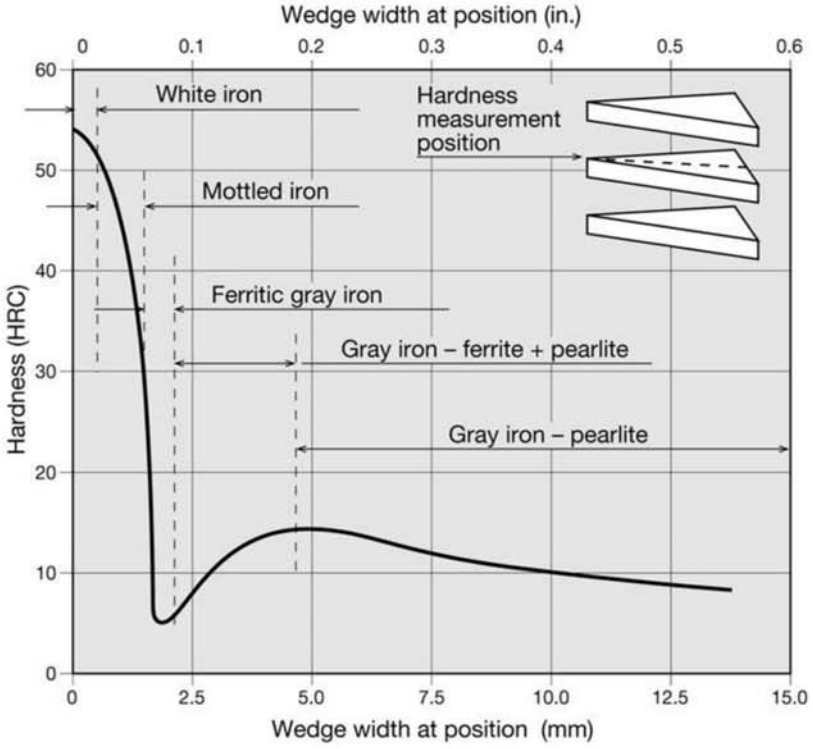

Fig. 17.3 Hardness along a wedge cast according to the ASTM A367 standard. The variations in microstructure along the wedge caused by the different cooling rates obtained give rise to different types of cast irons discussed in this chapter. Source: Ref 5

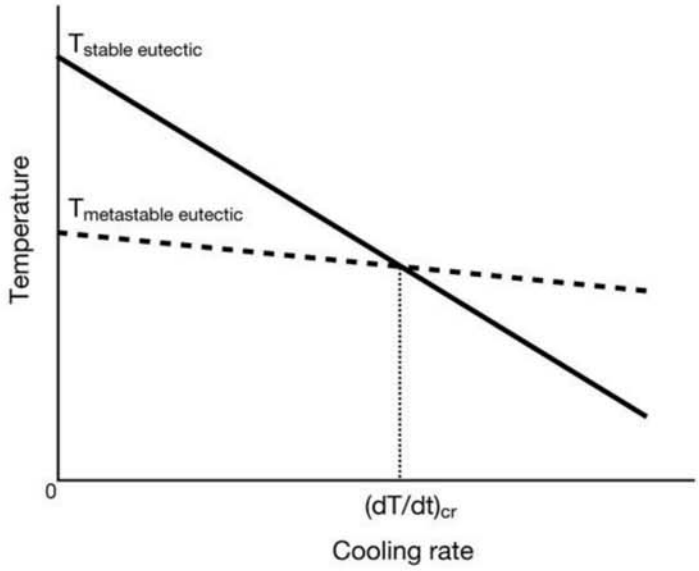

Fig. 17.4 Schematic graph indicating the effect of the cooling rate on the solidification temperature of the stable and the metastable eutectics in cast irons. Although both temperatures decrease with an increasing cooling rate, at lower cooling rates the equilibrium eutectic is favored, and at rates above a certain critical value, the metastable eutectic is preferred. Source: Ref 1

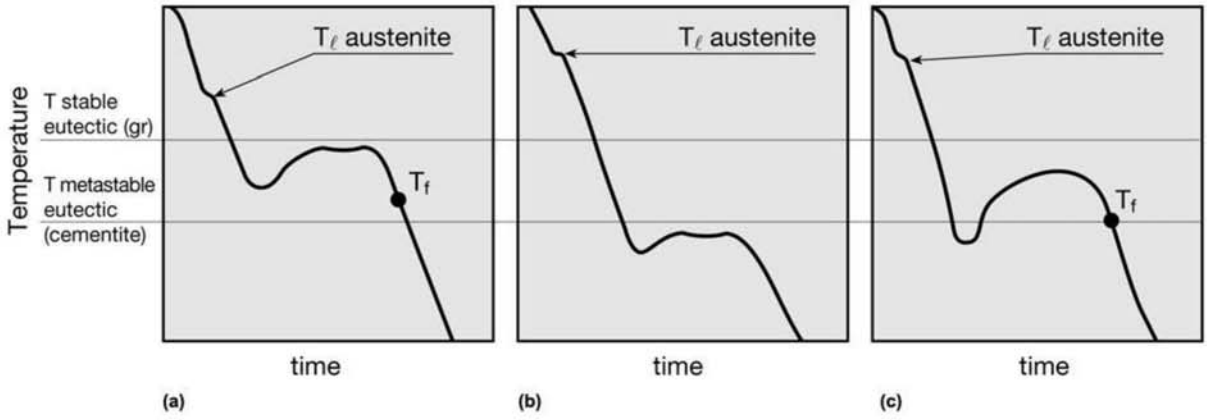

Fig. 17.5 Cooling curves (schematic) of (a) gray cast iron, (b) white cast iron, and (c) mottled cast iron. In addition to the stable and metastable eutectic temperatures, the temperatures at the start of the solidification of the pro-eutetic austenite (T_ℓ) and the end of solidification (T_f) are indicated. Note: T_f for the white cast iron was not indicated in Ref 9 (see also Fig. 17.22). Source: Ref 9

cooling rate. However, this factor has an important influence on other results of the casting process (mold erosion, for instance) and cannot be changed just to influence graphite formation.

17.1.2 The Effect of Chemical Composition

The effect of chemical composition on the formation of graphite or cementite is mainly related to their effect on the stability of cementite. Any general-

izing description of the effect of alloying elements on steels and cast irons is risky, in view of the complexity of the effects, the interaction between the elements, and the effects of other variables on the microstructure. Thus, the following discussion is to be understood as a general orientation on the main effects to be expected. Because carbon and silicon are the two most important elements, the overall view presented in Fig. 17.6 is useful to outline—in a general way—the composition ranges of each type of commercial cast iron.

Carbon

Carbon content in industrial cast irons is usually in the range of 2.0% to 4.0%. With values in the lower end of this range, white cast iron is the most common result. As the carbon content increases, the conditions for graphite formation and hence gray cast iron (or other type of graphitic iron) improve. In white cast irons, hardness increases along with carbon content, since the amount of cementite in the structure increases.

Silicon

After carbon, silicon is the most important alloying element in the composition of common cast irons. As discussed in Chapter 13, "Advanced Steels for

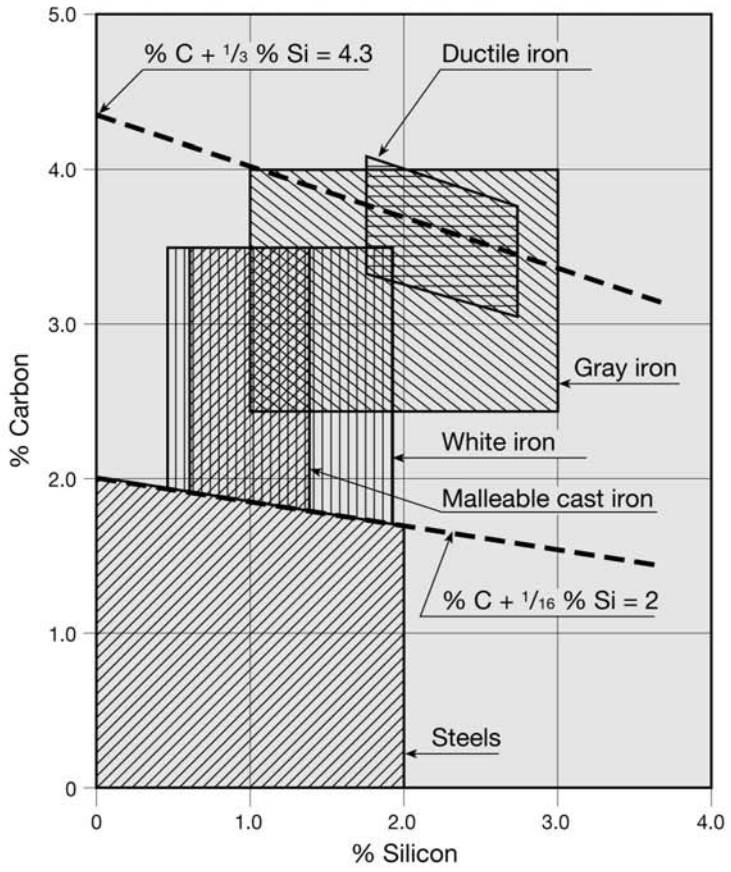

Fig. 17.6 Ranges of carbon and silicon contents typical of the most common cast irons. These limits are approximate and given only as guidance. A region representing the typical range of chemical composition of steels is also indicated. Source: Ref 5

Forming Operations," in this book, silicon reduces the stability of cementite. Thus, it also favors the decomposition of cementite into ferrite and graphite. As can be seen in Fig. 17.6, the addition of silicon is important when cast irons containing graphite are desired. With low silicon content, cast iron usually presents a white fracture. To obtain cast irons containing graphite but with higher mechanical strength, both the carbon and silicon contents must be limited to avoid the formation of ferrite and coarse pearlite. The effect of silicon on the eutectic composition can be evaluated using the expression for carbon equivalent, presented earlier in this chapter. However, silicon affects many other important phase equilibria in the Fe-C-Si system. Figure 17.7 presents the eutectic region of the Fe-C-Si phase diagram. It is possible to evaluate the effect of silicon on the various equilibria in the system. A two-dimensional projection of this diagram is shown in Fig. 17.8.

Manganese

Manganese makes cementite decomposition more difficult because it dissolves in this phase. In manganese-containing iron-based alloys, cementite can be described as $(Fe, Mn)_3C$. When the manganese content is high, it may counteract the effects of silicon and render the cast iron white. However, its main effect in common cast irons is to counteract possible negative effects of sulfur, forming MnS, as in steels.

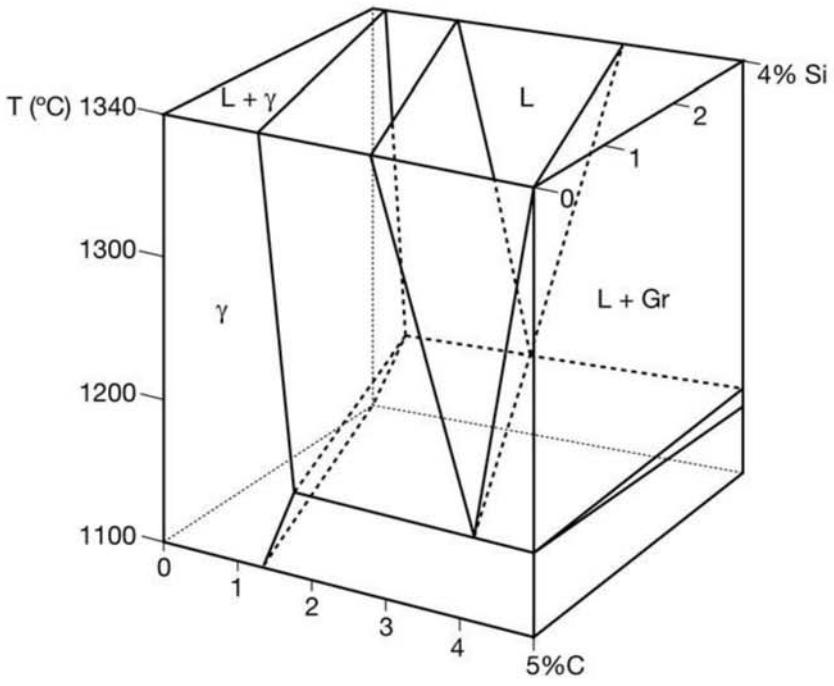

Fig. 17.7 A portion of the Fe-C-Si diagram in the region of the graphite containing eutectic. Gr: graphite; L: liquid; gamma, γ: austenite. The effect of increasing the silicon content on the important equilibria is evident. The increase of the silicon content causes the reduction of carbon content in the eutectic, the reduction of the solubility of carbon in austenite, the reduction of carbon solubility in the liquid. The projection of this figure in the % C-T plane is shown in Fig. 17.8.

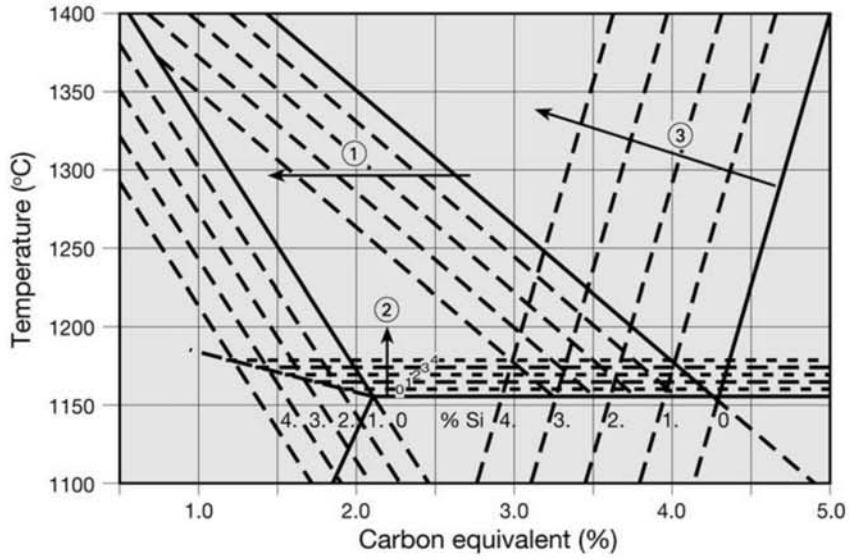

Fig. 17.8 Stable iron-carbon phase diagram indicating the approximate effect of silicon additions on the diagram. Silicon decreases the carbon solubility in austenite (arrow 1), increases the eutectic temperature (arrow 2), and favors the precipitation of graphite (arrow 3).

Sulfur

Cast iron may contain significantly higher amounts of sulfur than does steel. Sulfur has an important role in defining the morphology of graphite in cast iron (see the section "Nodular Cast Iron or Ductile Cast Iron" in this chapter). The correct adjustment of the levels of sulfur and manganese in gray cast irons is important to guarantee the desired mechanical properties (see the section "Sulfur and Sulfides" in this chapter).

Phosphorus

When in normal to low concentrations, phosphorus contributes to graphite formation but does not play a significant role in the process. In high concentrations, phosphorus embrittles the material and acts as a cementite stabilizer. Phosphorus decreases the liquid metal viscosity, increasing fluidity, making it possible to cast thinner sections and have better replication of mold details. However, the potential for negative effects on mechanical properties must always be considered when using phosphorus for this purpose. The embrittling behavior of phosphorus in steels is a little less critical in the cast irons that have low toughness due their microstructure, such as gray cast irons (Ref 10). Thus phosphorus contents significantly higher than those accepted in steels are common in some cast irons, particularly in gray cast irons. In the case of nodular cast irons, phosphorus is an undesirable residual, as in steels. Phosphorus can form a phosphide with iron (Fe_3P), and binary or ternary eutectics may be formed. Steadite is an example of a phosphorus-induced binary eutectic (ferrite, Fe_3P) in iron (see the section "Phosphorus-Containing Eutectics" in this chapter). Cast iron parts with high wear resistance have been produced using high-phosphorus gray cast irons (Ref 11, 12).

Table 17.2 summarizes the effect of the main alloying elements in cast iron on graphite formation. There are a large number of models in the literature combining the effects of chemical composition and cooling rate on graphite formation. Figure 17.9 presents a common diagram used for this, originally developed by Laplanche.

Table 17.2 Graphitizing potential of various elements in cast iron

Elements with positive graphitization potential	
Carbon Tin Phosphorous Silicon Aluminum Copper Nickel	Increasing graphitization potential ↑
Iron	
Elements with negative graphitization potential (favor carbide formation)	Stronger trend toward carbides ↓
Manganese Chromium Molybdenum Vanadium	

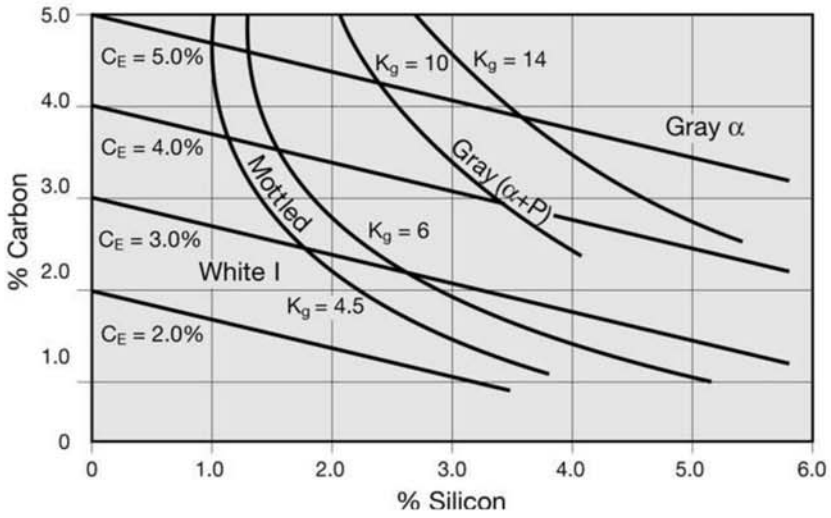

Fig. 17.9 Diagram indicating the expected microstructure as a function of carbon and silicon content, carbon equivalent (CE = % C + 1/3 (% Si + % P)) and cooling rate, expressed as the casting wall thickness (*R*), which is part of the graphitization constant equation $K_g = C\ (Si + \log R)$. Source: Ref 13

17.2 White Cast Irons

White cast irons have high hardness and wear resistance, but very low ductility and toughness. Their use is normally restricted to applications in which very high hardness and wear resistance are needed and toughness is not an important concern. Wear parts in mills used to grind minerals are frequently produced in white cast irons.

Solidification and processing conditions in white cast irons are such that graphite is not formed and the metastable equilibrium with cementite (Fe_3C) prevails.

Although a proper evaluation of the microstructural constitution and its evolution during solidification must take into consideration the transformations in the Fe-C-Si system, a very simplified overview using the metastable Fe-C phase diagram can be helpful in forming a basic understanding of the possible microstructures of these alloys. In general, three types of structures can be identified in white cast irons, using the composition of the eutectic liquid as the reference point: hypoeutectic, hypereutectic, and eutectic alloys.

17.2.1 Hypoeutectic White Cast Irons

In a hypoeutectic composition, the first phase to form from the liquid will be austenite, when the *liquidus* line of the phase diagram (Fig. 17.10) is reached on cooling. Under normal solidification conditions, austenite will grow in the shape of dendrites (see Chapter 8, "Solidification, Segregation, and Nonmetallic Inclusions"). As temperature is further reduced, the volume fraction of austenite increases while that of liquid decreases. On a binary phase diagram and in the absence of segregation, these values could be calculated using the lever rule.

The liquid gets enriched in carbon up to the composition of the eutectic liquid. At this point, cooperative growth of austenite and cementite starts, forming the eutectic constituent called ledeburite (see the section "The Eutectic Reaction" in Chapter 8, "Solidification, Segregation, and Nonmetallic Inclusions").

Hillert and Rao (Ref 14) proposed a model for the formation of ledeburite, presented in Fig. 17.11. Cementite plates are nucleated in the carbon-rich liquid between the austenite dendrites. This nucleation of cementite causes the nucleation of austenite plates parallel to them. In the second stage of the reaction, austenite and cementite start to grow in a cooperative way, with austenite having a rod-like morphology in a matrix of cementite. Under directional solidification conditions, Ref 15 observed that in Fe-C alloys with low to moderate growth rates, the eutectic has the shape of plates. In Fe-C-Si alloys, the morphology of the eutectic is rod-like. In Fe-C alloys, increasing the growth rate favors a rod-like morphology. The observation in the micrographs discussed below is consistent with the initial formation of plate-like eutectics followed by a eutectic with rod-like austenite in a cementite matrix. During controlled solidification experiments with cast iron, Ref 16 noted that with higher cooling rates (and thus increased undercooling), it is possible to favor the formation of the plate-like eutectic (as indicated on the left side of Fig. 17.11). This morphology is sometimes found in chilled regions of castings. They also observed that at slightly under 1130 °C (2065 °F), the structure of the casting was composed of austenite dendrites surrounded by the eutectic, as discussed above.

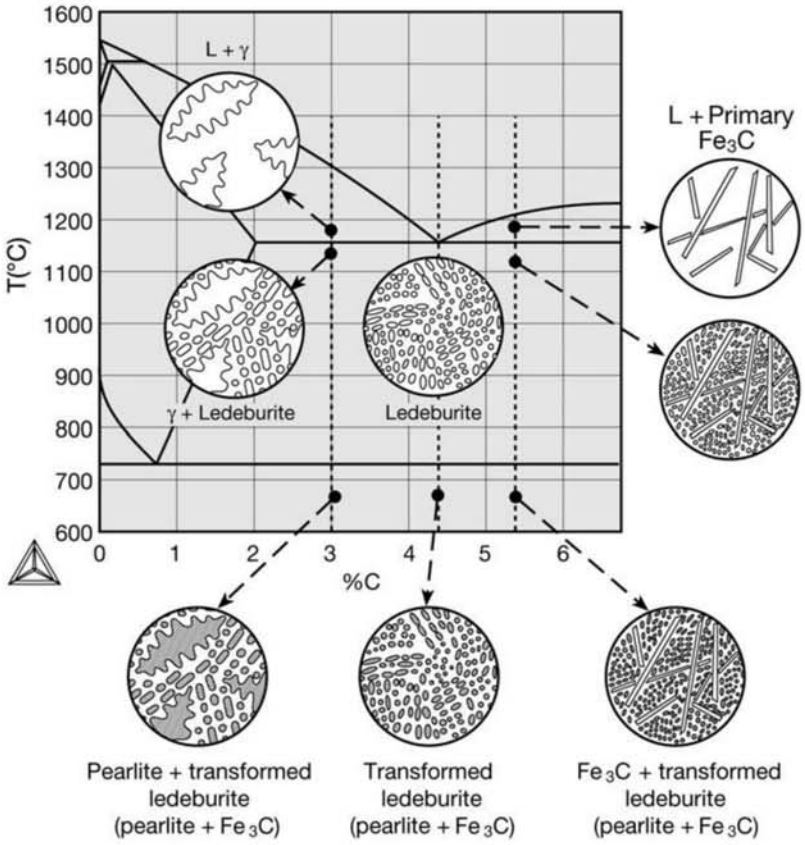

Fig. 17.10 Iron-carbon metastable equilibrium phase diagram. L: liquid; gamma, γ: austenite. The microstructural evolution of three types of white cast iron is presented in a simplified way on this diagram: hypoeutectic cast iron (3% C), eutectic cast iron (4.3% C), and hypereutectic cast iron (5.4% C) (hypereutectic white cast irons may solidify without forming pro-eutectic cementite). Even though alloying elements alter the diagram and the composition of phases in equilibrium, using the binary phase diagram is helpful in a first attempt at understanding the microstructures of these materials.

As the cooling proceeds, the solubility of carbon in austenite decreases and the excess carbon precipitates as cementite in the austenite–cementite interfaces of the eutectic. This process continues to around 723 °C (1335 °F), when the austenite carbon content should reach the eutectoid composition, around 0.77% C. As discussed in Chapter 7, "Equilibrium Phases and Constituents in the Fe-C System," and Chapter 9, "Conventional Heat Treatments: Usual Constituents and Their Formation," in this book, this austenite, if cooled at a slow rate, will transform to pearlite. Thus, austenite, in both the primary dendrites and ledeburite, will transform to pearlite. Transformed ledeburite will thus be formed by rod-like or plate-like pearlite in a cementite matrix, as shown in Fig. 17.12 and 17.13. In some points of the casting, isolated areas of cementite may be found due to austenite solidification in the eutectic reaction over the primary austenite dendrites. These small areas of cementite are part of a divorced eutectic, that is, ledeburite without the accompanying austenite rods.

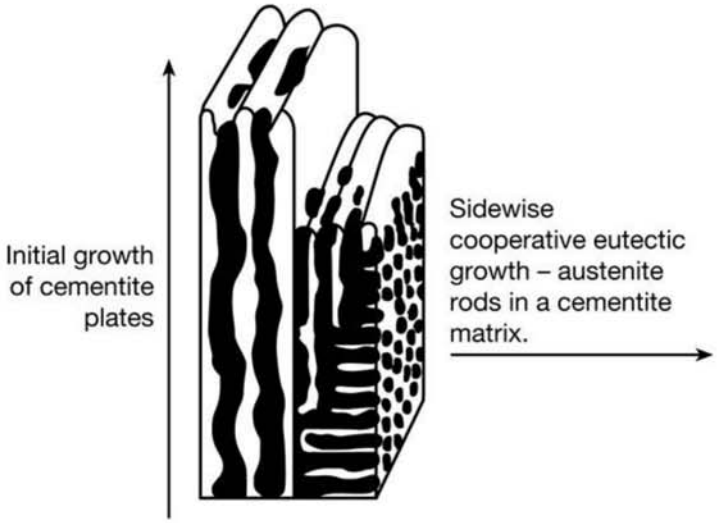

Fig. 17.11 Schematic presentation of the model of ledeburite formation proposed in Ref 12. The initial growth of cementite plates (light, in the drawing) does not occur cooperatively with the austenite (dark, in the drawing). Then conditions for cooperative growth are established, causing lateral growth in the form of austenite rods in cementite plates. Cementite maintains a preferential growth orientation based on its crystal structure.

Continuing the simplified analysis of the white cast irons on the Fe-C metastable diagram, the application of the lever rule at the eutectic temperature indicates that ledeburite will start forming when the carbon content is above 2%, and its fraction will increase as carbon concentration increases up to the point where it is the single constituent in the microstructure at 4.3% carbon, the eutectic liquid composition (see Fig. 17.10 and the section "Eutectic White Cast Irons" in this chapter). Low carbon compositions may not form ledeburite (Fig. 17.14). For higher carbon contents, in hypereutectic cast irons (see the section "Hypereutectic White Cast Irons"), the fraction of ledeburite starts to decrease as the carbon content increases until, at 6.7% carbon (25% atom percent, i.e., Fe_3C) the alloy has cementite as its single constituent. As discussed in Chapter 8, "Solidification, Segregation, and Nonmetallic Inclusions," the increase in cooling rate during solidification leads to the decrease of the dendrite arm spacing. Comparison of Fig. 17.12 and 17.15 also clearly show this effect for white cast irons. The spacing of rods or plates in the eutectic structure also decreases as the cooling rate increases. Park and Verhoeven (Ref 15) proposed some quantitative relationships between these variables for unidirectionally solidified white cast irons. These relationships can be useful when attempting to quantify the effect of processing variables on the microstructure of these alloys.

17.2.2 Hypereutectic White Cast Irons

In some extreme cases in hypereutectic white cast irons, cementite can form as a primary phase in the shape of plates, as indicated in Fig. 17.10. As cooling proceeds, the carbon content of the liquid decreases until the eutec-

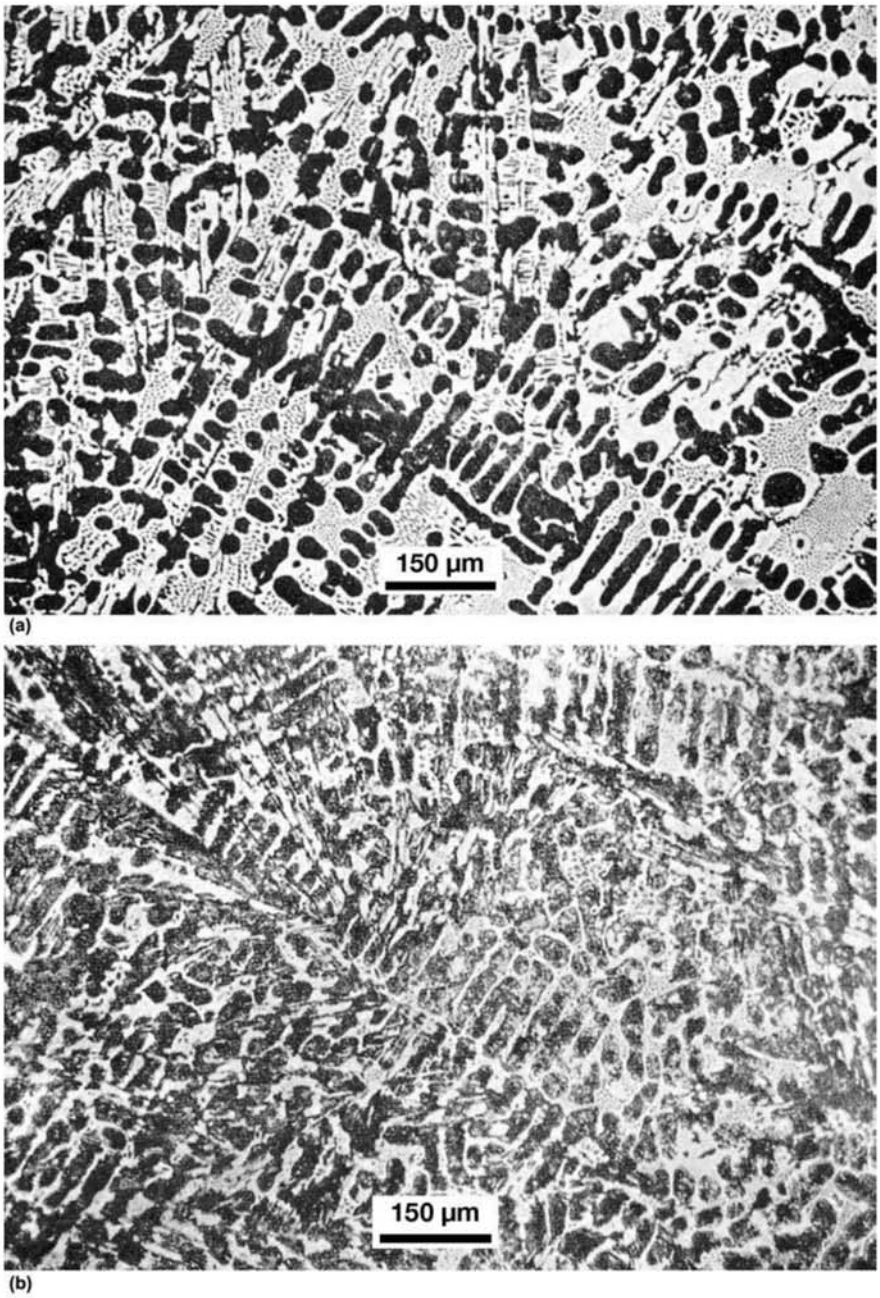

Fig. 17.12 (a) Hypoeutectic white cast iron. Austenite dendrites were transformed into pearlite (dark). The transformed ledeburite, among the dendrites, is composed of cementite (white) and pearlite (dark, small dots). Etchant: nital. (b) Another hypoeutectic white cast iron. Austenite dendrites were transformed into pearlite (dark). The transformed ledeburite, between the dendrites, is composed of cementite (white) and pearlite (dark, small dots). Etchant: picral. The different etching behavior of nital and picral on ferrite and cementite, mentioned in Chapter 5, "Metallographic Technique: Micrography," in this book, is evident.

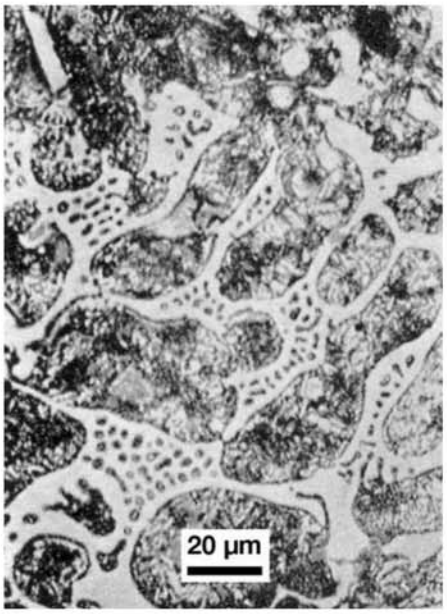

Fig. 17.13 Larger magnification view of the structure presented in Fig. 17.12(b). Transformed ledeburite between the austenite dendrites. Austenite has transformed to pearlite. Etchant: picral.

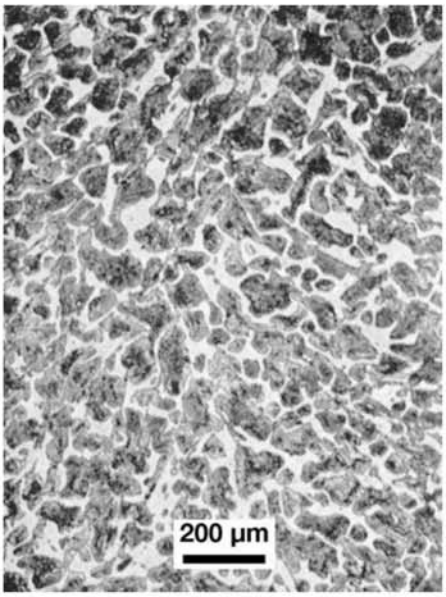

Fig. 17.14 Iron-carbon alloy with approximately C = 2%. Ledeburite is not formed. Pro-eutectoid cementite in a considerable volume fraction in the prior austenitic grain boundaries. Pearlite. Etchant: picral.

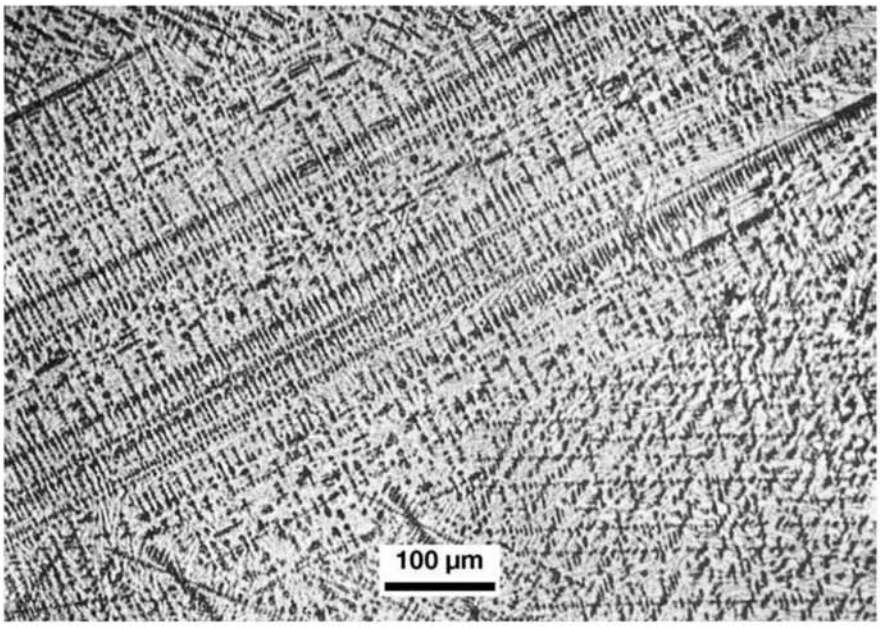

Fig. 17.15 Hypoeutectic white cast iron rapidly cooled during solidification. Small interdendritic arm spacing. Etchant: picral.

tic composition of 4.3% is reached at 1130 °C (2065 °F). Should primary cementite have formed, it will suffer no further transformation on cooling to room temperature, but the ledeburite that will be formed surrounding it will undergo the transformations described in the previous section. Thus, at room temperature, the microstructure of these cast irons will be composed of elongated (plate) cementite surrounded by ledeburite (Fig. 17.16 and 17.17). Figure 17.18 shows the possibility of using a different etchant to further highlight cementite.

17.2.3 Eutectic White Cast Irons

The eutectic white cast irons—following the simplified analysis on the metastable Fe-C phase diagram—would start solidifying at 1130 °C (2065 °F) and the temperature would remain constant until the end of solidification. (The cooling rate will influence the solidification starting temperature, see the section "The Effect of the Cooling Rate" in this chapter.) The microstructure would be completely ledeburitic (Fig. 17.19 and 17.20).

17.3 Gray Cast Irons

When the chemical composition and the cooling conditions are such that the equilibrium eutectic occurs during solidification, graphite is formed. The most common morphology of graphite in this eutectic is lamellar, as shown in Fig. 17.21. Graphite is an interesting constituent in iron-based products because it has unique properties:

- While the density of the solid phases of iron, cementite, and even most complex carbides formed by usual alloying elements in steel and irons is in the range of 7–8 g/cm^3—the carbides of heavy elements such as

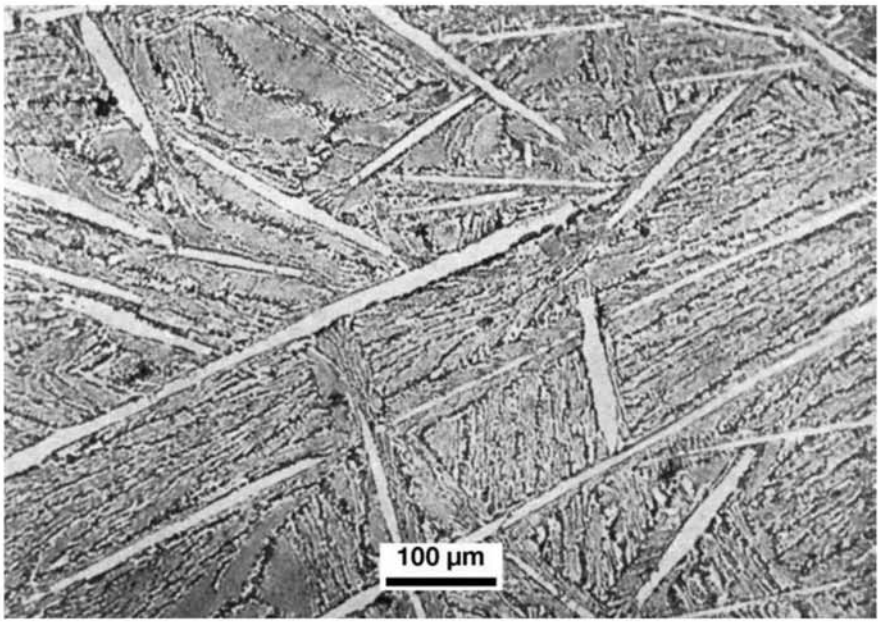

Fig. 17.16 Hypoeutectic white cast iron. Long cementite crystals in a matrix of transformed ledeburite. Etchant: picral.

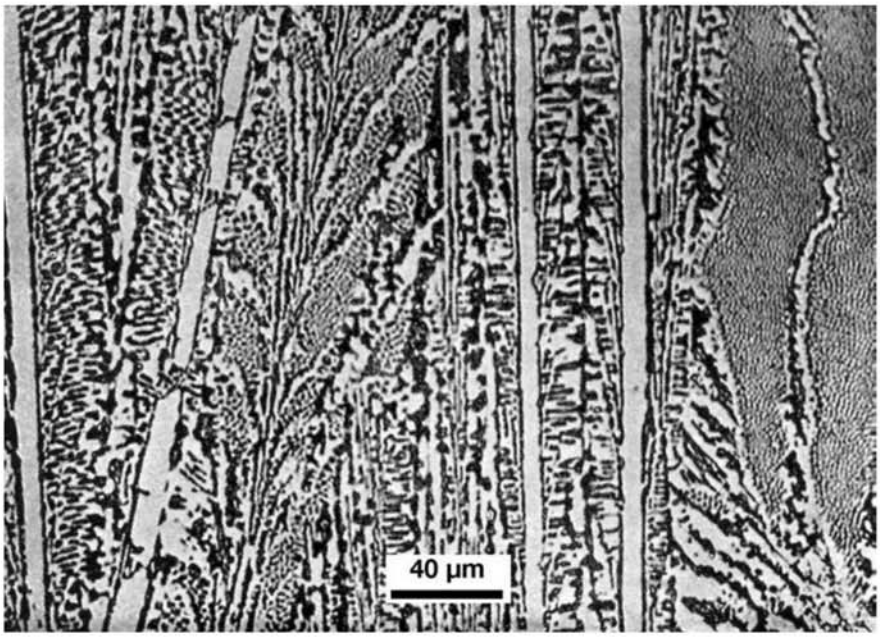

Fig. 17.17 Larger magnification view of the structure of the white cast iron presented in Fig. 17.16. Etchant: picral.

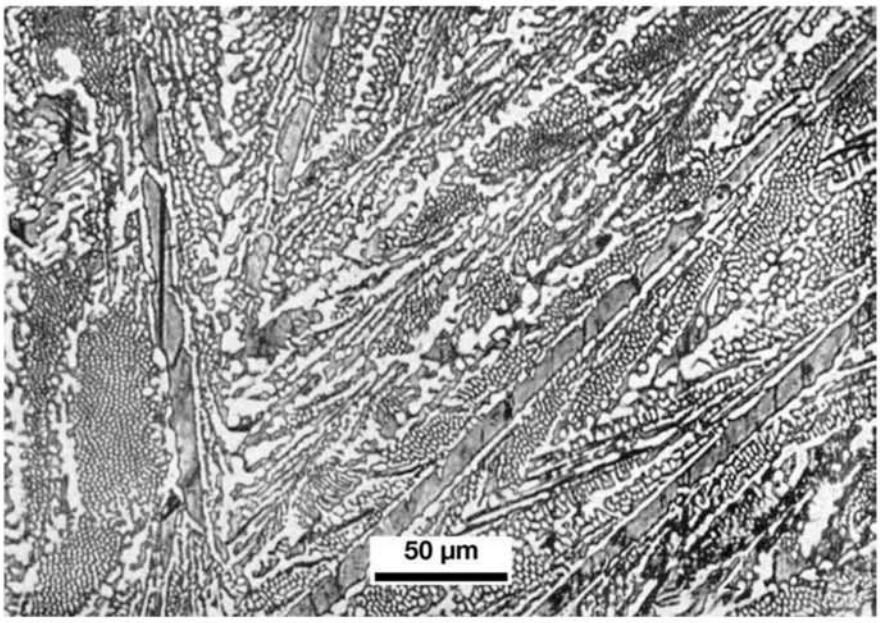

Fig. 17.18 Hypereutectic white cast iron. Etching with sodium picrate colors cementite gray (both pro-eutectic cementite and the cementite in ledeburite). Etchant: sodium picrate solution.

molybdenum and tungsten being important exceptions—the density of graphite is approximately 2.27 g/cm^3.

- The thermal conductivity of BCC iron (ferrite) at room temperature is a function of chemical composition but varies in the range of 30–80

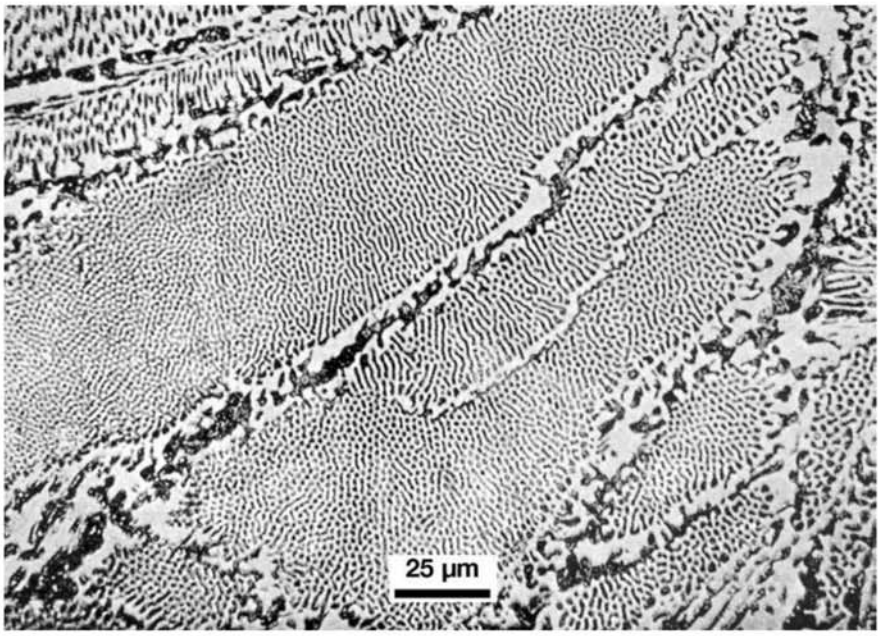

Fig. 17.19 Transformed ledeburite in the eutectic region of a white cast iron. Small areas of pearlite in a cementite matrix. Etchant: picral.

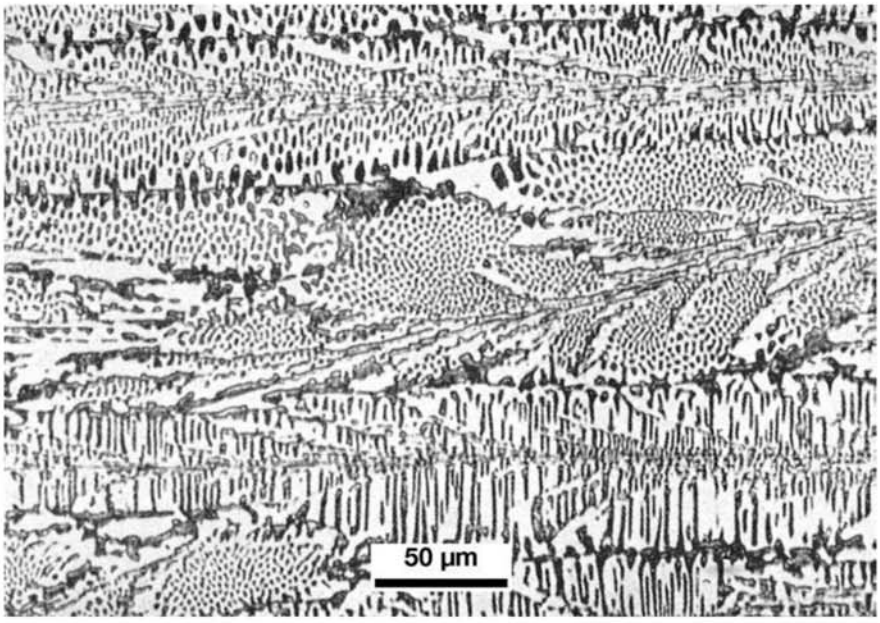

Fig. 17.20 Ledeburite. Depending on the growth direction of ledeburite and on the orientation of the plane of the metallographic section, different morphological aspects of the austenite (already transformed to pearlite) distribution in the cementite matrix can be observed. (Compare with the schematic presentation of Fig. 17.11.)

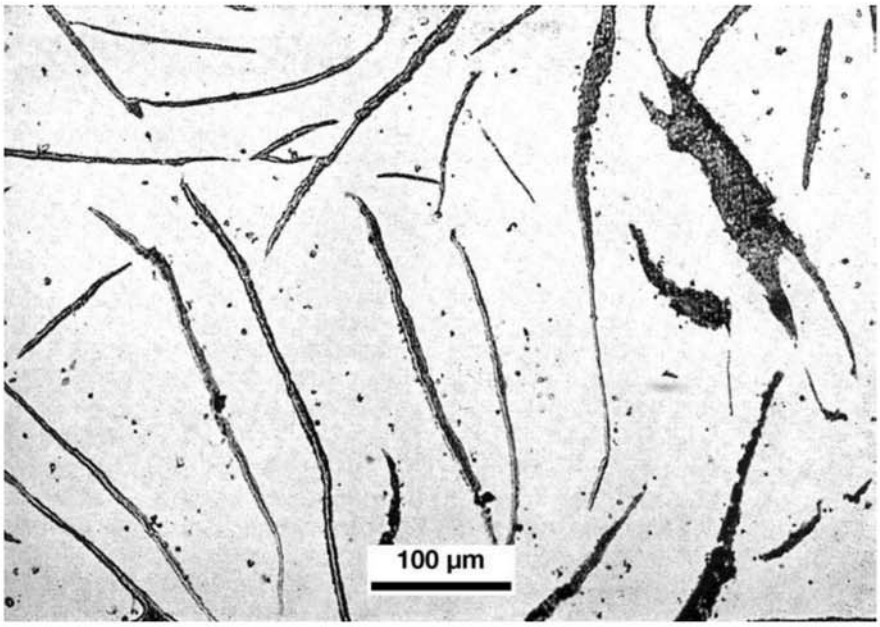

Fig. 17.21 Gray cast iron with large graphite flakes. Nonmetallic inclusions can also be observed. Not etched.

W/mK, whereas that of graphite, which is strongly dependent on orientation with respect to its crystal structure, varies in the range of 10–2,000 W/mK (Ref 17).

As a result of these properties:

- Phase transformations that involve graphite formation may be accompanied by significant volume change. This can even result in expansion during some stages of solidification.
- Cast iron may have outstanding thermal conductivity, as shown in Table 17.3. This is a very useful property in applications such as engine blocks or braking systems for vehicles.
- Graphite presence in the microstructure can result in significant vibration damping due to the relative movement between graphite and the matrix. As a result, the use of cast iron can have significant advantages over steel in many applications.
- Graphite acts as a lubricant during machining operations. It also promotes chip fracture, making some of these alloys extremely easy to machine and capable of achieving very good surface finish.

However, the way graphite is distributed, its shape (morphology), and its relative and absolute dimensions in the microstructure are critical features that define the properties it imparts to the cast irons.

Silicon additions are important to ensure graphite stability, as discussed in the previous sections. Figure 17.8, a projection in the %C-T plane of the Fe-C-Si ternary phase diagram, summarizes the main effects of silicon.

Table 17.3 Thermal conductivity of some cast irons

Cast iron type	Specified tensile strength, MPa (ksi)	Thermal conductivity at 100 °C (W/mK)
Gray	150 (22)	65.6
	300 (44)	47.7
	400 (58)	45.3
Ductile	400 (58)	38.5
	600 (87)	32.9
Malleable	350 (51)	40.4
	600 (87)	34.3

Thus, silicon additions:

- Decrease the carbon solubility in austenite, keeping more carbon in the liquid phase.
- Increase the temperature at which the stable eutectic (austenite-graphite, see Fig. 17.7) occurs.
- Increase the range of stability of graphite, favoring its formation.

Furthermore, the composition of the liquid at the eutectic is moved to lower carbon content. The microstructure evolution of cast irons in which graphite precipitation occurs is quite complex. Evidence of this is the fact that nodular cast irons (see the section 17.5 "Nodular Cast Iron or Ductile Cast Iron" in this chapter) were only developed around the middle of the 20th century.

Figure 17.22 presents a thermal analysis curve of a gray cast iron and the accompanying evolution of the microstructure (compare with Fig. 17.5). The austenite-graphite eutectic is formed as cells that initially can grow without restrictions into the liquid. In these cells, graphite's most common morphology is lamellar. The growth continues until these cells consume all the liquid. Evidently the more abundant the nucleation of the cells, the smaller the cells will be and a better distribution of graphite in the microstructure will be achieved.

17.3.1 Metallographic Sample Preparation: Graphite

Two points require special attention when preparing metallographic samples of cast irons containing graphite. First, because graphite is brittle and

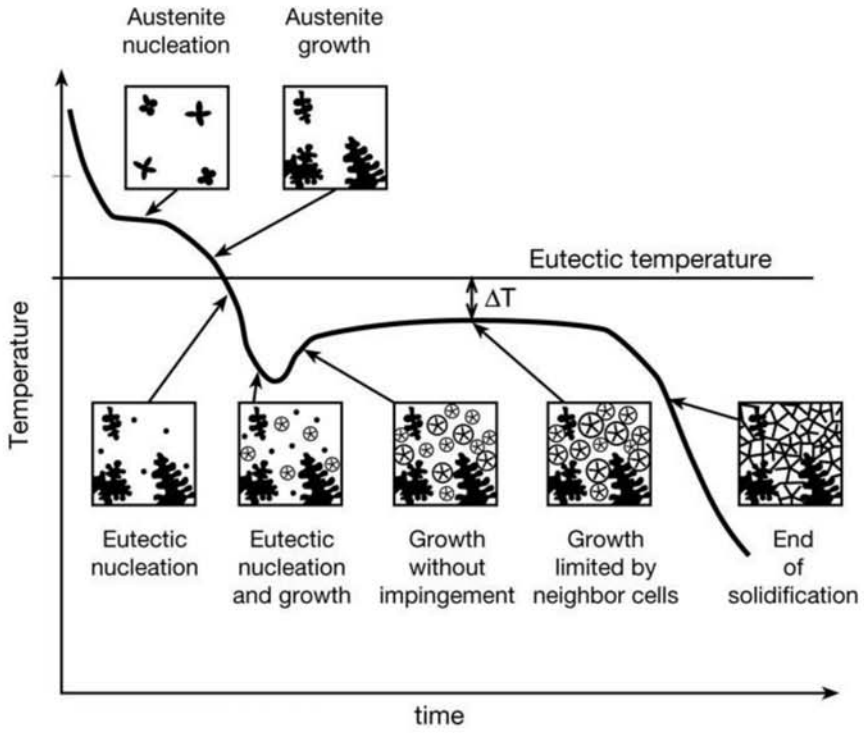

Fig. 17.22 Schematic microstructural evolution of a gray cast iron during solidification superimposed on a thermal analysis curve. Some undercooling below the eutectic temperature is needed for nucleation to start. Eutectic solidification happens essentially at constant temperature. The microstructures could also be located on a phase diagram similarly to what was done in Fig. 17.10 for white cast irons. Source: Ref 19

can be pulled out of the matrix with relative ease, fracture and pull-out of the graphite may occur during sample preparation, particularly during grinding. If this damage happens during the first stages of grinding, it may be impossible to remove enough material in the subsequent stages to recover the quality of the surface and obtain a good representative metallographic sample. The proper combination of pressure on the specimen, grinding time, and grinding material is essential to avoid graphite being pulled out of the sample. While one of the suggestions is that fresh, unused grinding paper should always be used (Ref 13), other authors suggest that better results are achieved with worn grinding paper (Ref 20) to avoid graphite pull-out. Reference 12 and 13 suggest a limited number of steps in grinding and polishing and using automatic polishing to guarantee adequate control of the pressure on the specimen. Besides this problem, it is not unusual to observe deformation of the matrix—in particular ferritic matrixes—at the interface with the graphite, causing the matrix to partially cover the edges of the graphite. When using diamond paste for polishing, a last step with alumina suspension may be useful in eliminating this problem (Ref 12). Following the progress of the sample preparation with microscopic observation is important, particularly during the stages of practice development, to guarantee that the best results will be reached consistently.

17.3.2 Types of Graphitization

When analyzing the Fe-C equilibrium phase diagram, it can be observed that graphite, when present in cast irons, can form:

- During solidification, either as a pro-eutectic phase, in the case of hypereutectic cast irons, or in the austenite-graphite eutectic.
- From austenite, as the temperature decreases below the eutectic temperature and the solubility of carbon in austenite is reduced.
- During the decomposition of austenite in ferrite and graphite (at the eutectoid) when the chemical composition is such that cementite is not stable and thus pearlite does not form.
- From the cementite in pearlite, when there is graphitization at temperatures around 700 °C (1290 °F).

In addition, for malleable cast irons, graphite may form due to the decomposition (graphitization) of cementite originally formed in a white cast iron.

In the case of pro-eutectic precipitation, from the liquid, and during the eutectic reaction, the presence of nuclei for graphite formation is a critical factor in defining morphology, distribution, and size of the graphite formed.

While graphite shape and distribution is of paramount important for the behavior of cast irons, the metallographic examination of graphite is an especially interesting example of the loss of information that accompanies the two-dimensional sectioning, with planes, of a three-dimensional structure, as discussed in Chapter 3, "Introduction to Metallographic Technique," in this book.

Figure 17.23(a) presents the aspect of lamellar graphite in a gray cast iron subjected to deep etching, so that the matrix is completely dissolved and graphite is preserved. Figure 17.23(b) presents a three-dimensional reconstruction of lamellar graphite, performed through the composition of successive parallel plane sectioning performed using FIB (see Chapter 6, "Metallographic Technique: Electron Microscopy and Other Advanced Techniques," in this book) (Ref 21–24). Other results are presented in the next sections when other graphite morphologies are discussed. ASTM standard A 247 (Ref 25) and ISO standard 945 (Ref 26) are frequently adopted to classify the morphology and measure the size of graphite in cast irons. The graphite usually seen in gray cast irons, flake graphite, is classified as Type VII graphite. Type VII graphite can be further classified in one of five distributions, as presented in Fig. 17.24–17.29. These figures should not be used as a substitute to the comparison charts provided by ASTM and/or ISO, which are the official standards for graphite classification. The standard also classifies, for each graphite morphology, the graphite size, as the examples in Fig. 17.30 and 17.31 show. Shape, size, and distribution of graphite have a paramount influence on the behavior of cast irons. Mechanical, electrical, magnetic, and thermal properties, among others, are directly dependent on these features of the graphite and evidently on its volume fraction in the structure. Different quantitative metallographic and stereological techniques have been applied in attempts to better characterize graphite and better correlate its measured characteristics with the material properties. The various possible techniques that can be used are discussed in detail in Ref 27.

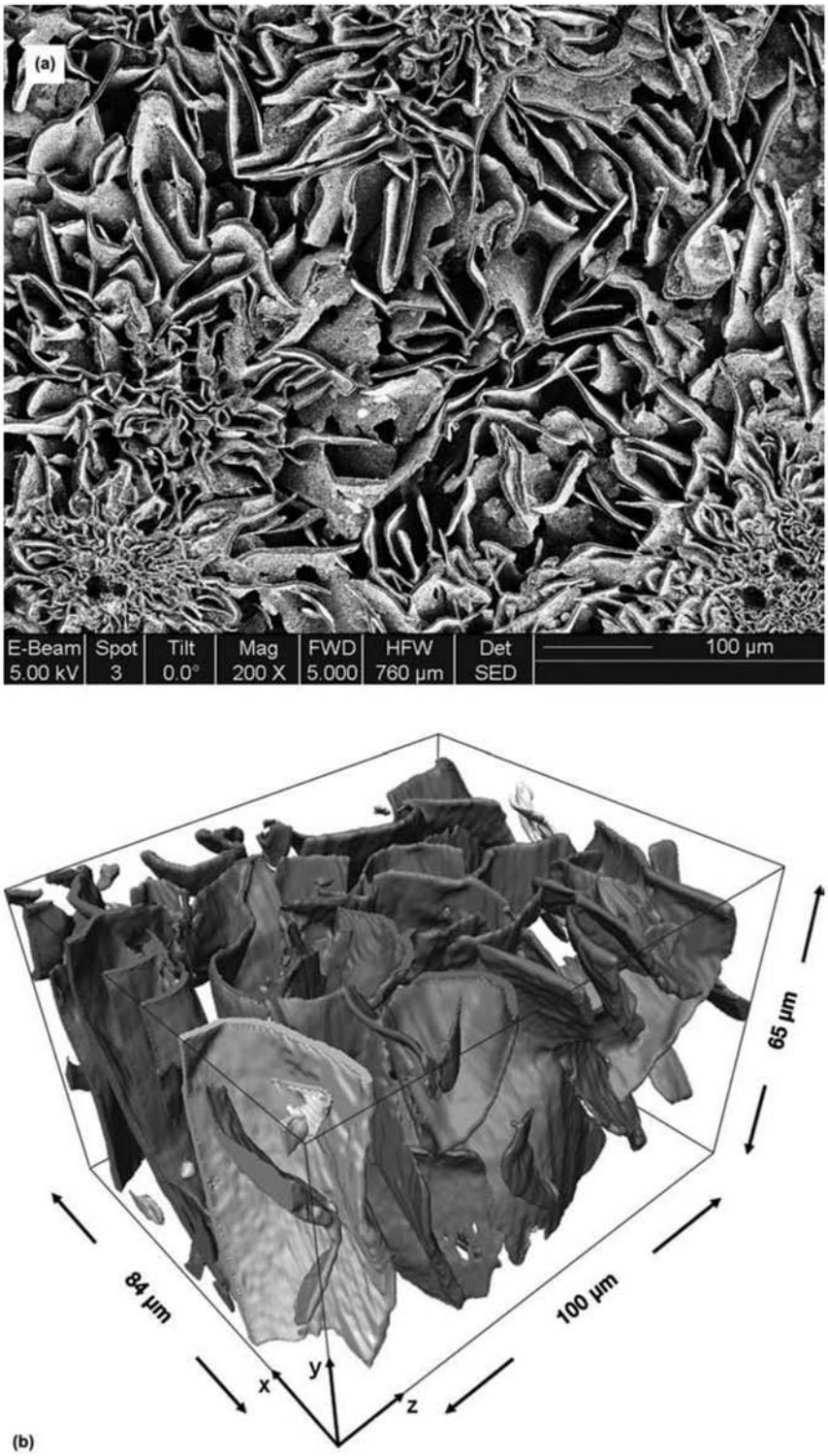

Fig. 17.23 (a) Lamellar graphite in gray cast iron, subjected to deep etching to completely dissolve the metal matrix. Etchant: nital 10%, 2 h LSEM, SE. (b) Tridimensional reconstruction of lamellar graphite in gray cast iron. Section done by focused ion beam (FIB) and images obtained by SE in SEM. Courtesy of A. Velichko and F. Mücklich, Universität des Saarlandes, Saarbrücken, Germany.

Graphite in the austenite-graphite eutectic is mainly heterogeneously nucleated on various substrates such as graphite (that may be already present in the liquid), ferro-silicon alloy, oxides, nitrides, and calcium silicide (Ref 19). Nucleation has a critical role in defining the shape and amount of graphite formed, and the use of inoculants is fundamental. "A" distribution graphite, with a random distribution of lamellae of uniform size is generally associated

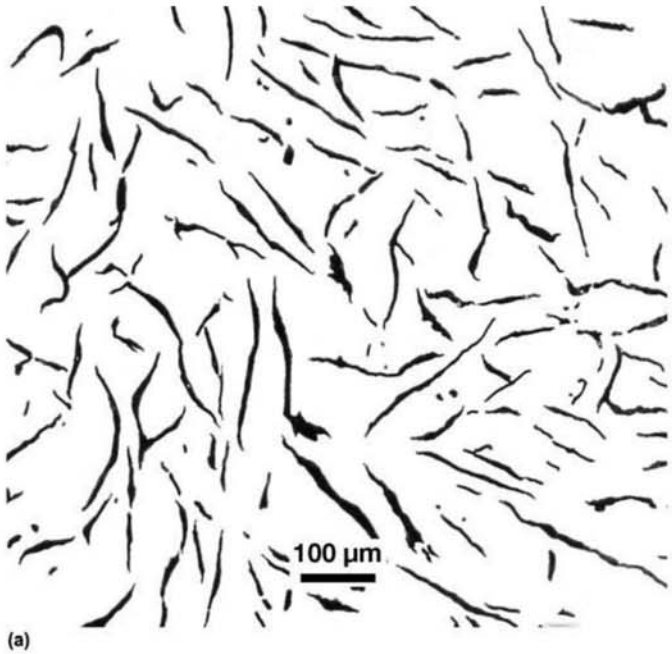

Fig. 17.24 (a) Type VII, Distribution A graphite (ASTM A247). Flakes with random orientation, curved and sometimes presenting bifurcations. (b) Type VII, Distribution A graphite in a gray cast iron. Not etched.

with the best mechanical properties for gray irons and is the preferred type for engineering applications. It is formed in inoculated cast irons cooled at moderate rates. This distribution of graphite is associated with significant nucleation and solidification close to the equilibrium eutectic temperature (hence, low to moderate undercooling). Distribution "B" of graphite is associated with low nucleation. For this reason, the eutectic cells are larger. The lamellae are initially fine and increase in size as growth continues (Ref 18).

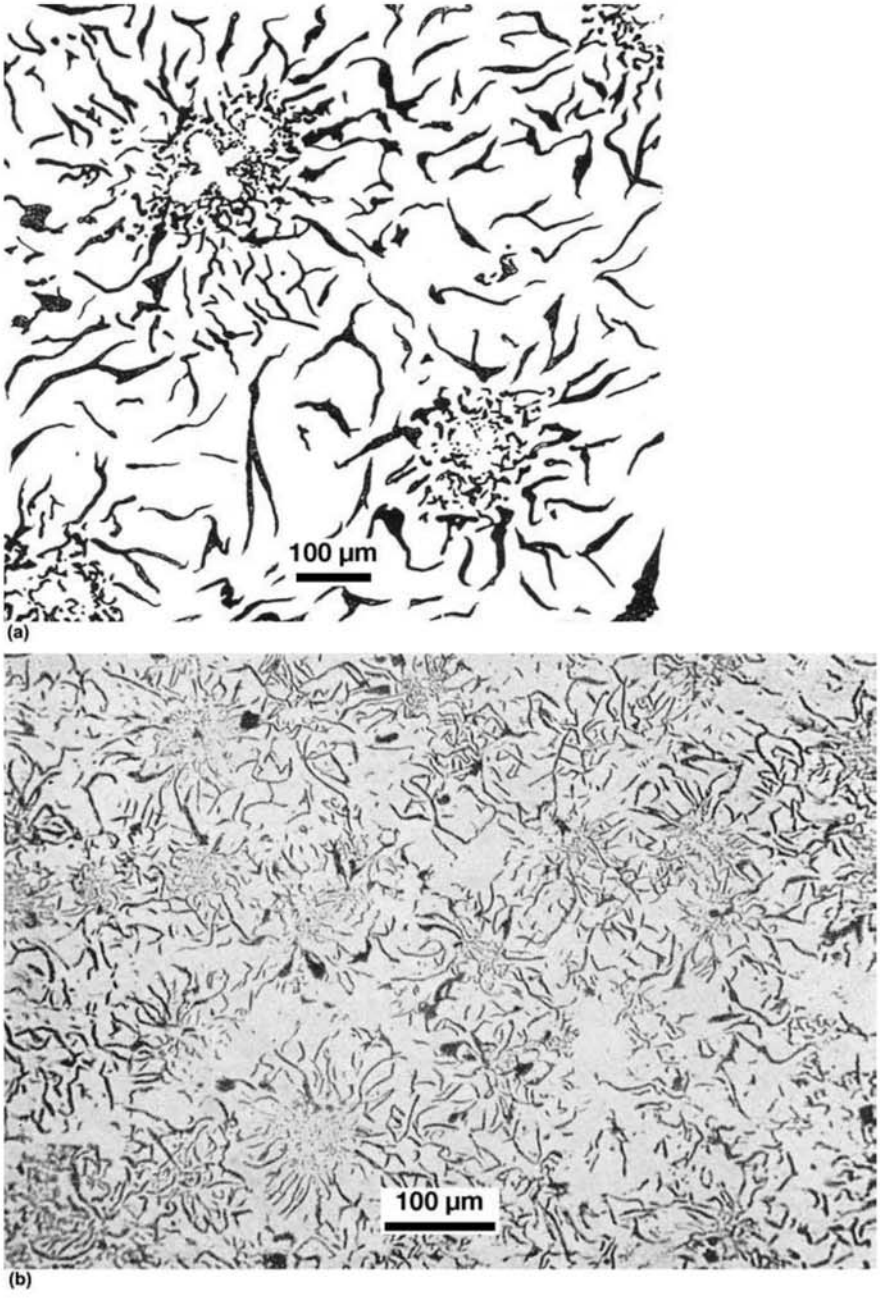

Fig. 17.25 (a) Type VII, Distribution B graphite (ASTM A247). Flakes with radial distribution around nuclei with eutectic aspect (see also Fig. 8.24). (b) Type VII, Distribution B graphite in a gray cast iron. Not etched.

Graphite with "C" distribution is present mostly in hypereutectic cast irons, when there is primary nucleation of graphite. According to Ref 18, this type of graphite may compromise mechanical strength and cause defects in machined surfaces. Graphite with morphologies classified as "D" and "E" are fine and usually formed in rapid cooling with insufficient nucleation. Although fine graphite can have a positive influence on mechanical strength, it may compromise the ability to form a pearlitic microstructure (Ref 18).

Fig. 17.26 (a) Type VII, Distribution C graphite (ASTM A247). Large flakes, almost straight. Small normal flakes in between the large flakes. (b) Type VII, Distribution C graphite in a gray cast iron. Not etched.

Fig. 17.27 Type VII, Distribution C graphite in a gray cast iron. Not etched.

Reference 28 reviewed the various models proposed to describe the microstructural evolution of cast irons. The first important difficulty in the modeling is related to the fact that, notwithstanding that the eutectic in gray cast irons grows in austenite-graphite cells, measuring the spacing between these phases indicates that cast iron does not follow the behavior of the so-called regular eutectics and presents significantly larger spacings than would be expected of a regular eutectic. Figure 17.32 presents a model for the growth of eutectic cells that are presented in the schematic representations in Fig. 17.22. Stefanescu (Ref 28) attributes to Ref 29 the first successful model for the description of gray cast iron solidification. Oldheld (Ref 29) assumed that nucleation happens for all possible nuclei at a given undercooling. This way it is possible to relate the cell density in the eutectic with the solidification undercooling through the expression given in Eq 1:

$$N_e = A_e(\Delta T)^{n_e}$$

$$A_e = 7.12 \times \frac{10^{-3}\text{nuclei}}{\text{mm}^3\,\text{K}} \qquad \text{(Eq. 1)}$$

$$n_e = 2$$

where

N_e = cell density
A_e = constant
n_e = exponent

The parameters in Eq 1 were determined empirically for one nucleation condition. With this model, Ref 29 started developing mathematical modeling of cast iron solidification and opened the way for using thermal analysis

as a valuable tool in the control of microstructure of these castings. Further studies have confirmed that the effect of nucleants may be expressed by Eq 1, as shown in Fig. 17.33.

17.3.3 The Microstructure of Gray Cast Irons

Depending on the silicon content, as previously discussed, the carbon content of the liquid at the austenite-graphite eutectic changes from the value in

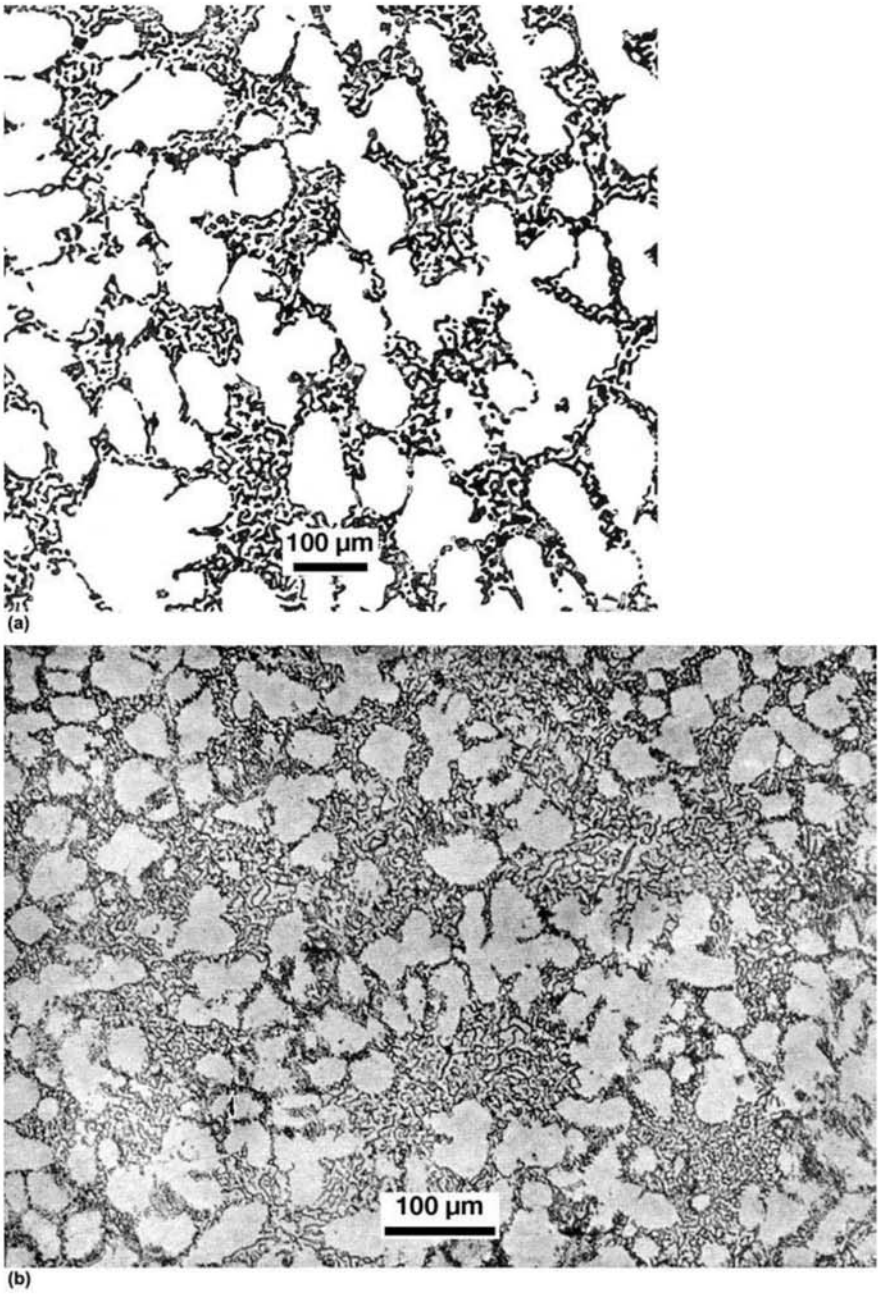

Fig. 17.28 (a) Type VII, Distribution D graphite (ASTM A247). Small, short flakes in the interdendritic spaces, eutectic morphology (see also Fig. 8.24). (b) Type VII, Distribution D graphite in a gray cast iron. Not etched.

the Fe-C system of 4.3%. Thus, it is possible to use lower carbon contents and still cast gray hypereutectic cast irons. Because gray cast irons undergo graphitization even after solidification, the dendritic structure is not always clearly visible, as in the case of white cast irons. In some cases, however, it is possible to identify vestiges of the dendritic structure, as shown in Fig. 17.34 and 17.35.

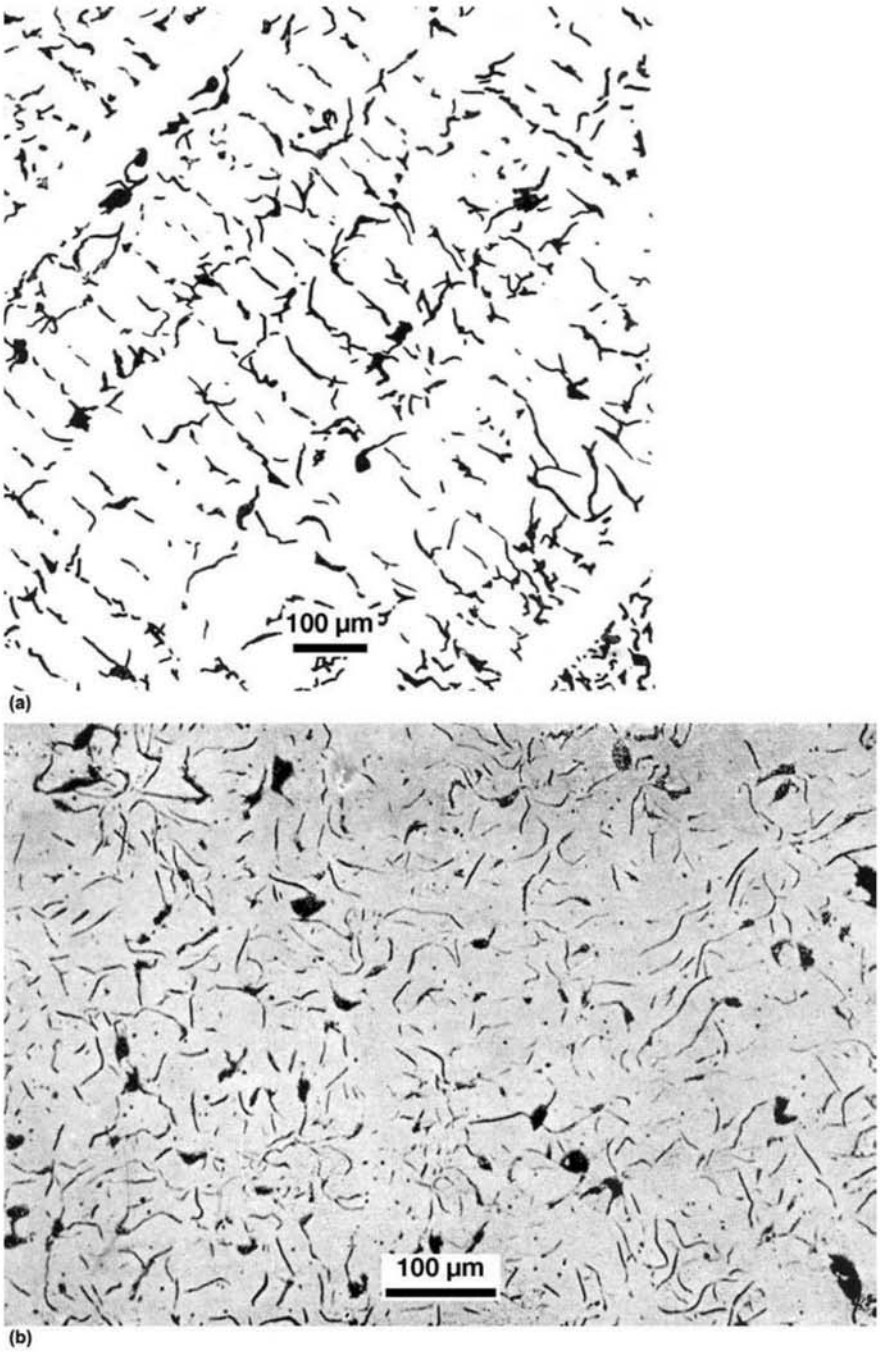

Fig. 17.29 (a) Type VII, Distribution E graphite (ASTM A247). Flakes oriented according to the interdendritic spaces. (b) Gray cast iron with Type VII, Distribution E graphite. Not etched.

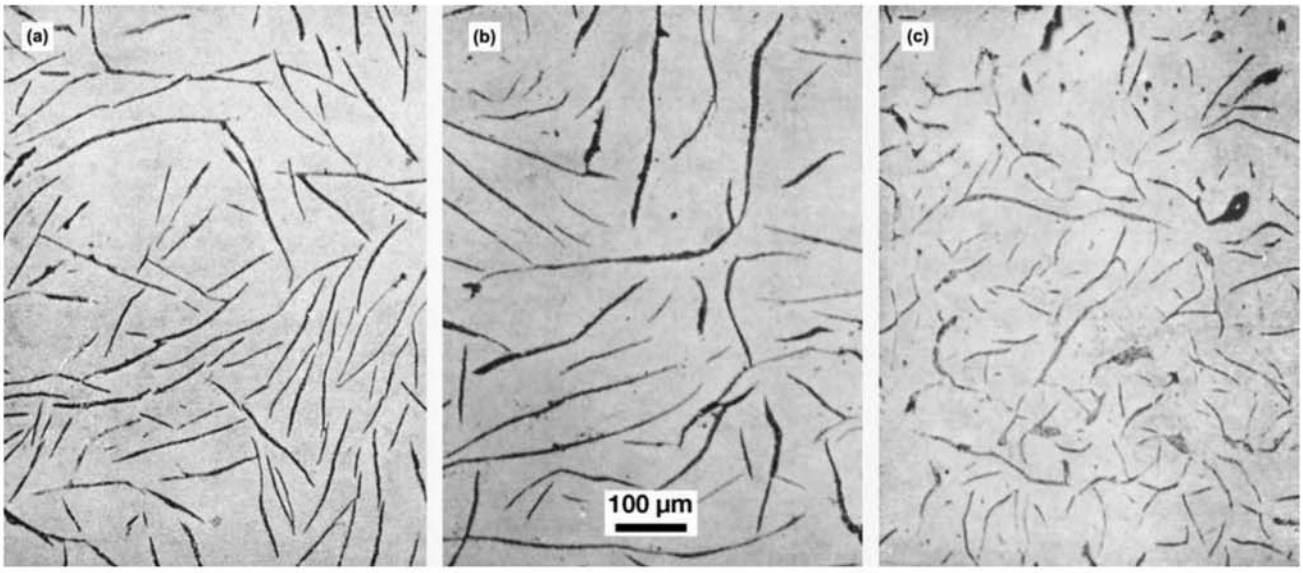

Fig. 17.30 Gray cast iron. Example of various size classes flakes (ASTM A247), (a) 3, (b) 2, (c) 4. Not etched.

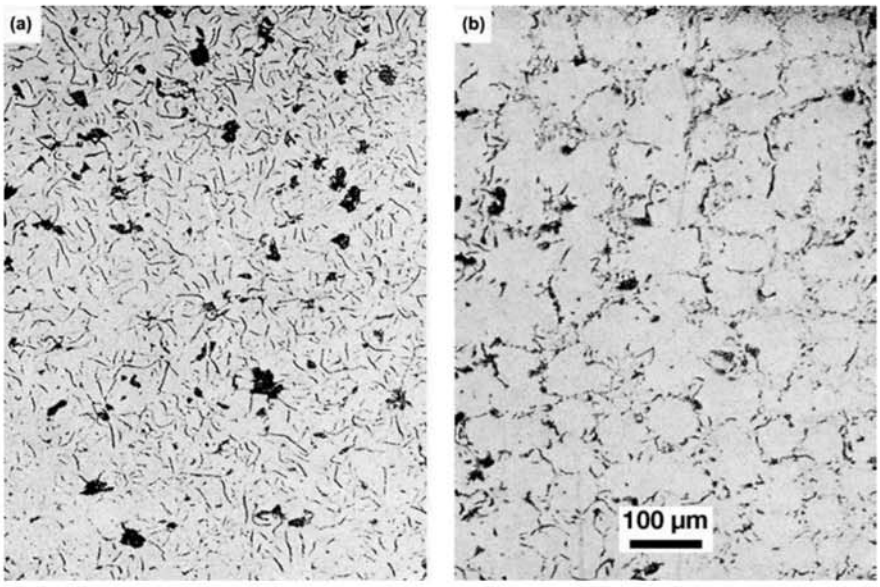

Fig. 17.31 Gray cast iron. Examples of flakes of various size classes (ASTM A247) (a) 6 (b) 8. Not etched.

Rivera et al. (Ref 30 and 31) developed a combination of heat treatment and metallographic techniques that make possible the clear visualization of these dendrites. When eutectic formation happens at the end of the solidification (in the case of high phosphorus cast irons), it is easier to observe the dendritic nature of the structure of gray cast irons (Ref 11). The matrix in gray cast irons may be ferritic, ferritic-pearlitic (Fig. 17.36 and 17.37), or pearlitic (Fig. 17.38), and they may even be quenched and tempered to form a martensitic matrix. The matrixes of these cast irons show no difference from steels with the same microstructures. The results that can be obtained when the

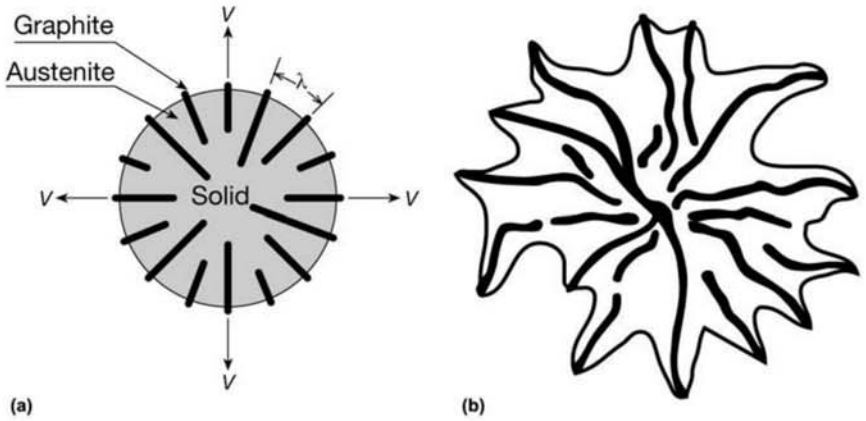

Fig. 17.32 (a) Simplified model for cell growth during the solidification of gray cast irons. V: growth velocity; λ: lamelae spacing. In the case of cast irons, by contrast with regular eutectics, the liquid-graphite and liquid-austenite interfaces are not at the same temperature. Source: Ref 26. (b) Schematic representation of an austenite-graphite cell or colony growing during solidification of cast iron, based on the metallographic observations of Hultgren. Source: Ref 14. See also Fig. 17.22.

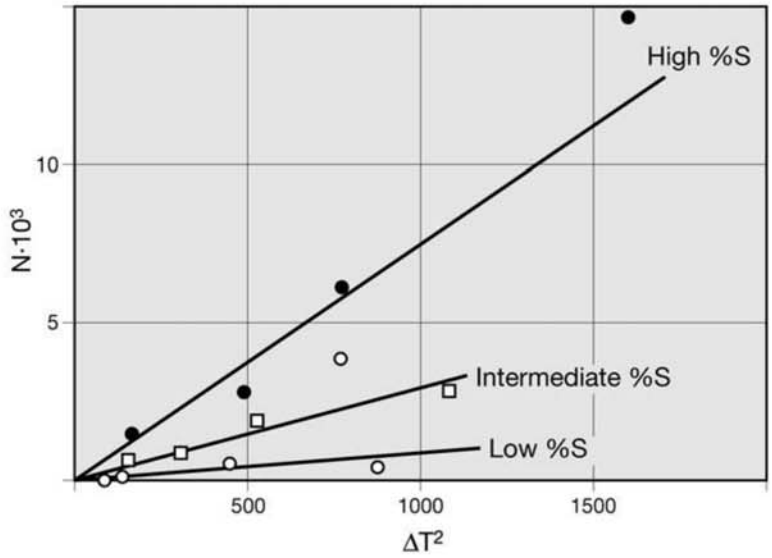

Fig. 17.33 Relationship between the number of grains or eutectic colonies in a gray cast iron and the undercooling in solidification, for different nucleation conditions. A_e, the growth constant described in Eq 1, depends on the sulfur content of the liquid in this case. Source: Ref 27

matrix of cast irons are heat treated are essentially the same as those obtained with steels. It is important to keep in mind that, depending on the temperature and holding time of these heat treatments, additional carbon from the graphite may dissolve into the austenite, altering the resulting aspect of the microstructure (refer to later discussion of Fig. 17.39 and 17.40). Segrega-

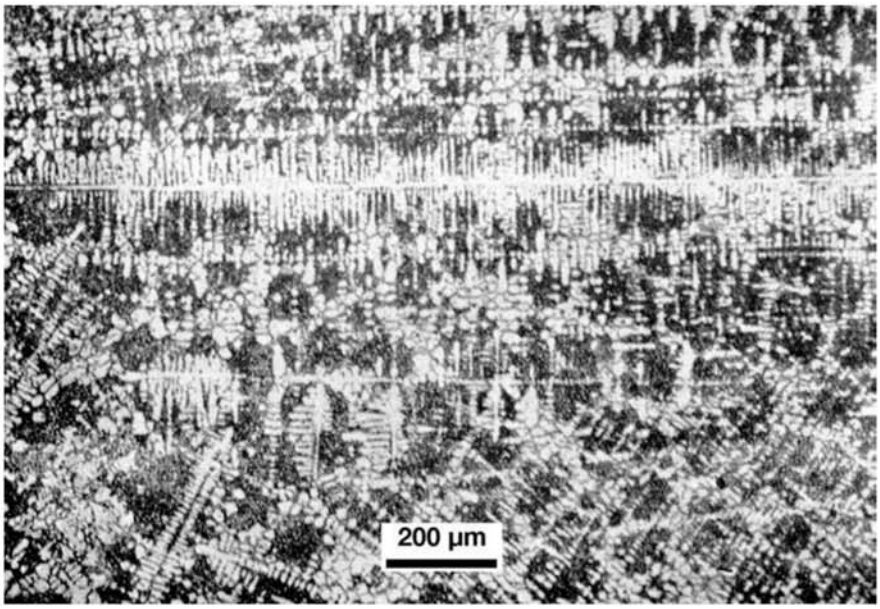

Fig. 17.34 Gray cast iron with ferrite dendrites. Ferrite is formed due to graphitization during cooling in the solid state. Distribution D graphite. Etchant: picral.

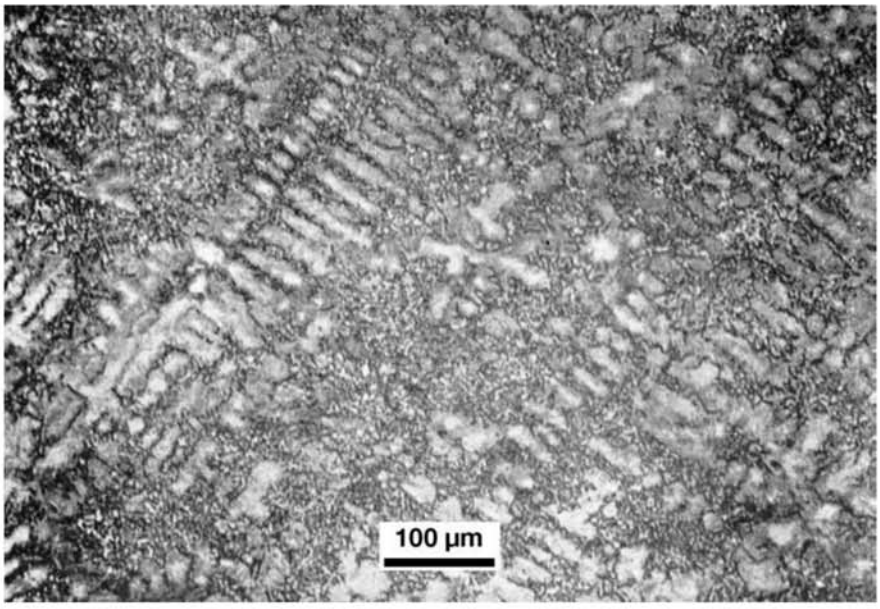

Fig. 17.35 Gray cast iron with pearlite dendrites. Distribution D graphite. Etchant: picral.

tion and deviations in heat treatment can lead to variations in microstructures (Fig. 17.41 and 17.42). Austempering, nowadays a heat treatment frequently applied to nodular cast irons (see the section 17.5.1 "Austempered Nodular Cast Iron or Austempered Ductile Iron" in this chapter), is also applied to gray cast iron, resulting in the product called austempered gray iron

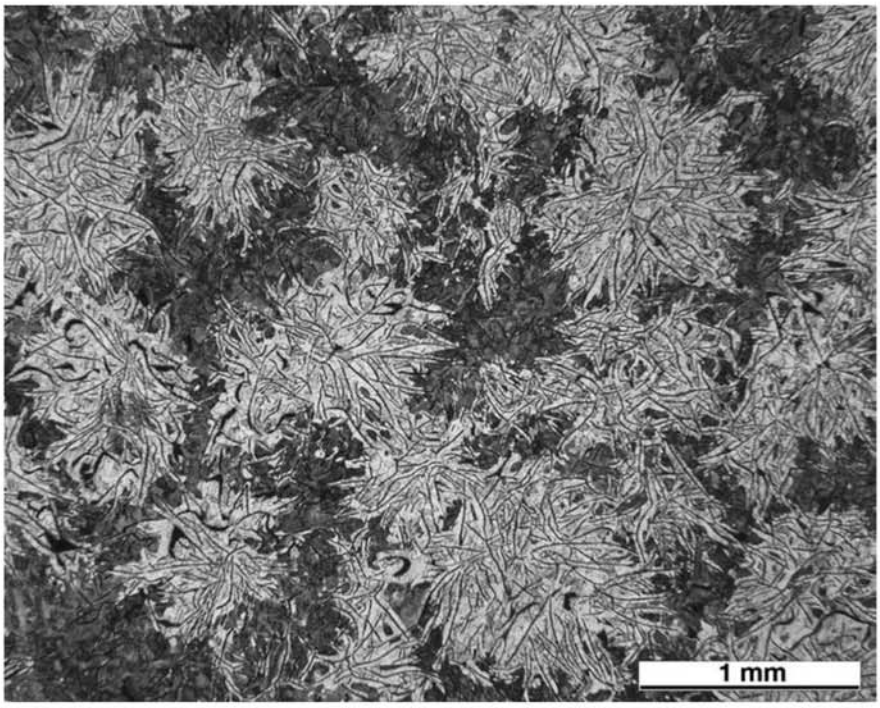

Fig. 17.36 Gray cast iron. Lamellar graphite. Ferrite and pearlite. The eutectic colonies presented in the sketch of Fig. 17.32 (b) can be seen. Courtesy of J. Sertucha, Azterlan, Centro de Investigacion Metalurgica, Durango, Bizkaia, Spain.

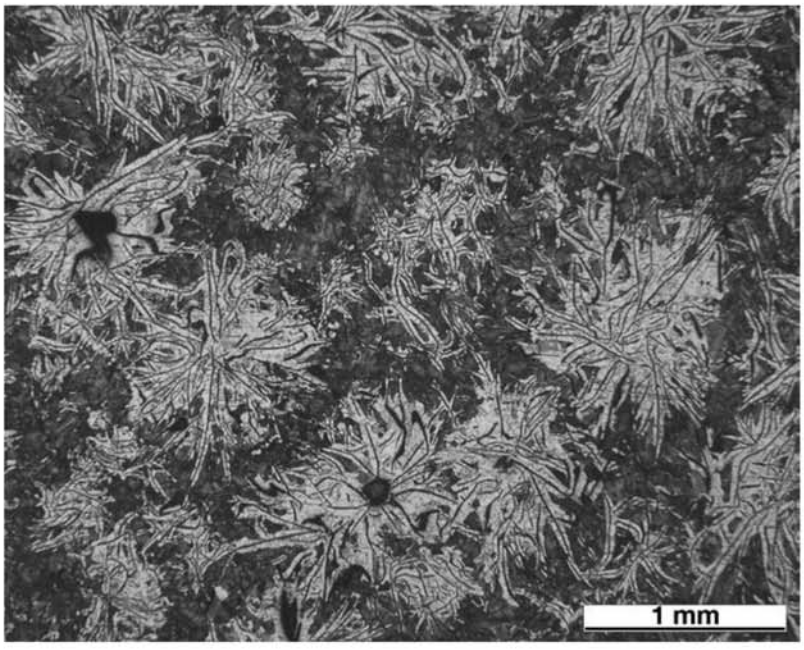

Fig. 17.37 Gray cast iron. Lamellar graphite. Ferrite and pearlite. The eutectic colonies presented in the sketch of Fig. 17.32 (b) can be seen. Courtesy of J. Sertucha, Azterlan, Centro de Investigacion Metalurgica, Durango, Bizkaia, Spain.

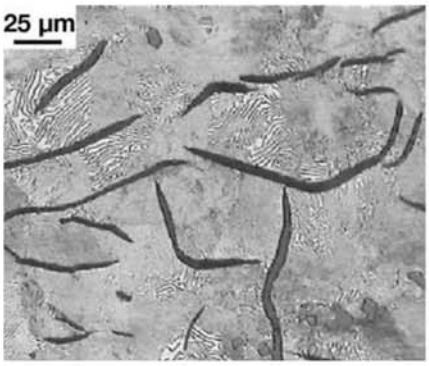

Fig. 17.38 Gray cast iron with 250 MPa (36 ksi) minimum tensile strength (ASTM A48, Class No. 250B). Graphite flakes and pearlitic matrix. Some small manganese sulfide inclusions (gray particles, at the lower right corner of the image, for instance) that enhance machinability. Etchant: nital. Courtesy of W. Guesser, Tupy Fundições, SC, Brazil.

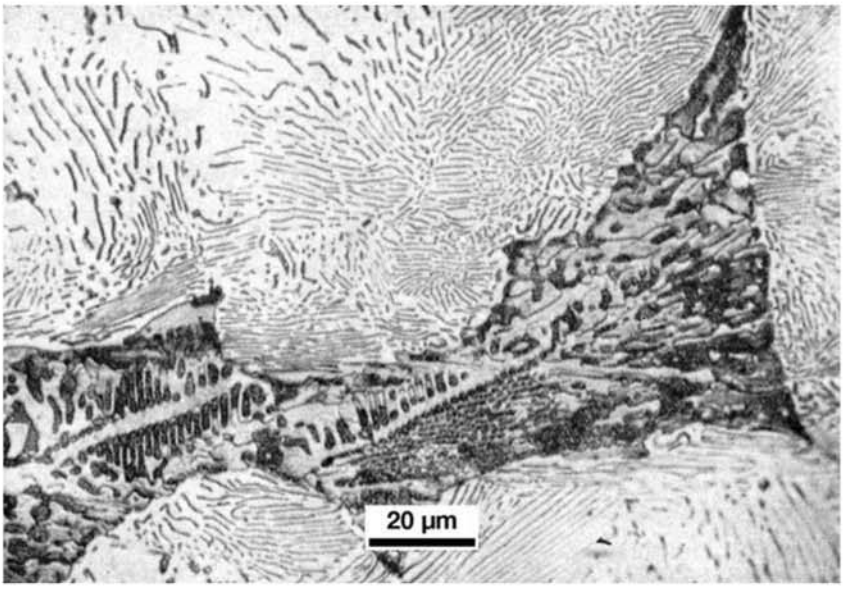

Fig. 17.39 Ternary eutectic in a hypereutectic gray cast iron C = 3.83%, Si = 2.25%, P = 0.46%. Etchant: sodium picrate.

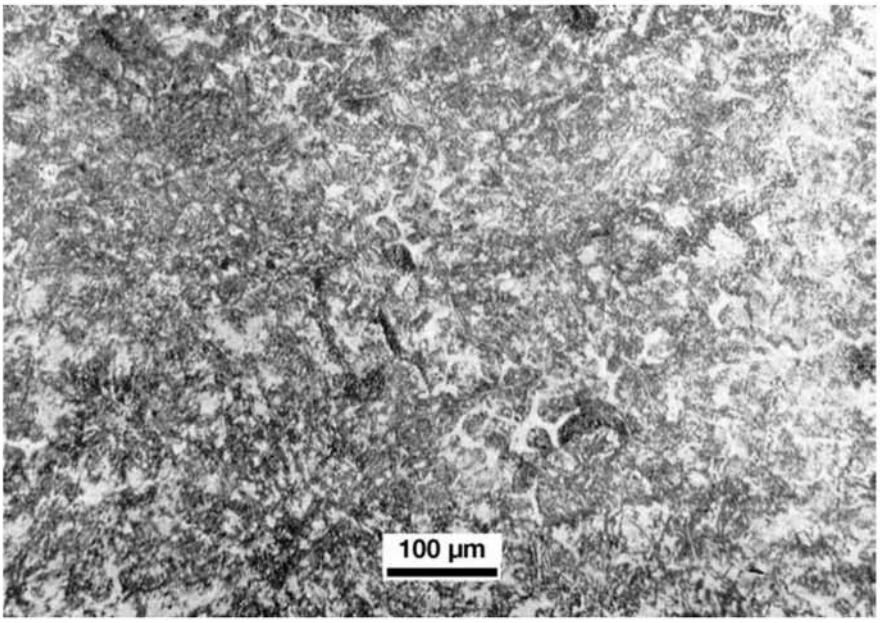

Fig. 17.40 Gray cast iron C = 3.18%, Si = 2.5%, P = 0.62%. As cast. Graphite flakes and fine microstructure composed of pearlite and interdendritic areas with steadite. Etchant: picral

(AGI) or, sometimes, "acicular cast iron." Very favorable combinations of properties for many applications can be achieved with this structure—for instance, an excellent combination of damping and strength. Notwithstanding the microstructural similarities with steels, the transformation kinetics is sometimes different and the presence of phosphorus can give rise in cast

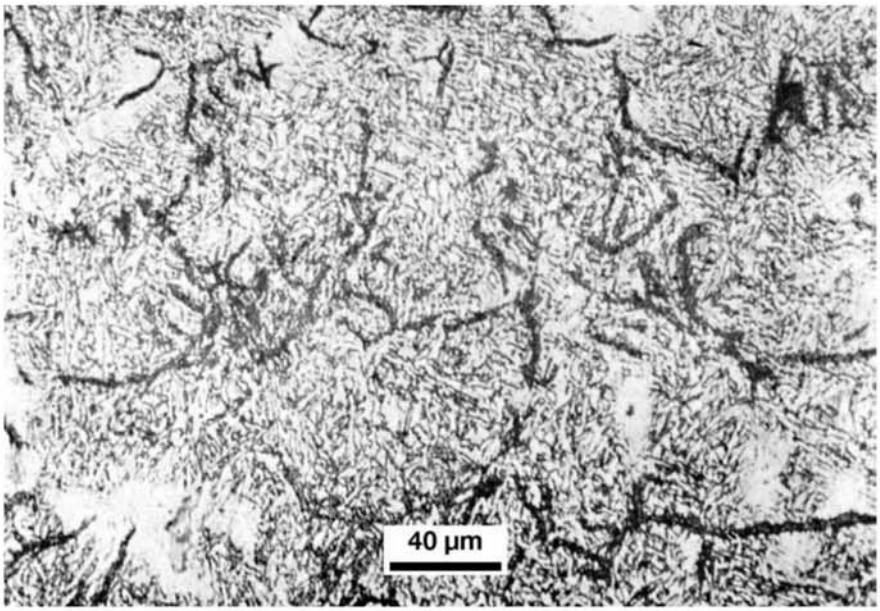

Fig. 17.41 Gray cast iron with acicular structure. Graphite flakes in a matrix of bainitic ferrite and retained austenite. ASTM A644 defines as "ausferrite" "a cast iron matrix microstructure, produced by a controlled thermal process, which consists of predominantly acicular ferrite and high carbon austenite." The heterogeneities (lighter areas) are evidence of solidification segregation. Etchant: picral

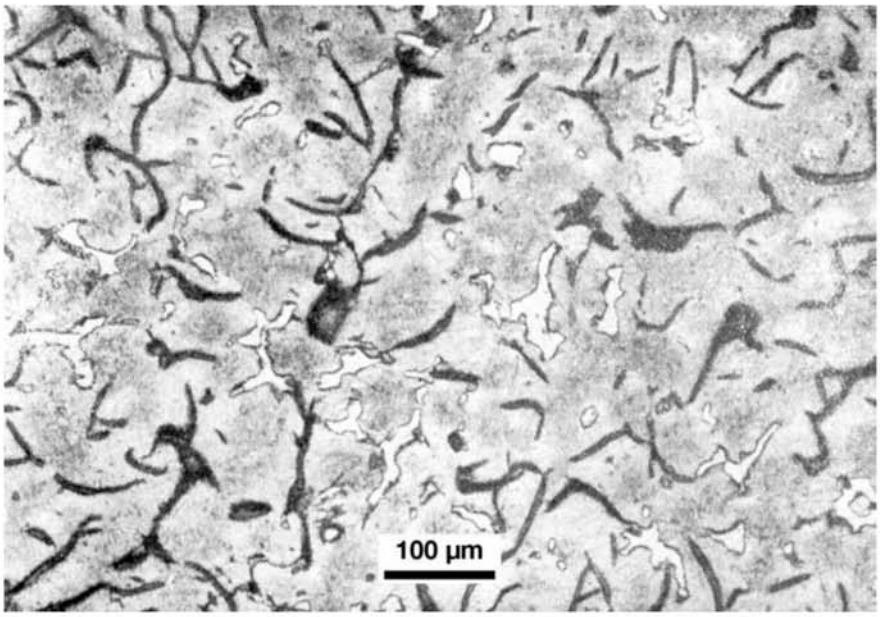

Fig. 17.42 Gray cast iron with acicular structure. Deviation during heat treatment. Complex carbides (containing Mo) that were not properly dissolved in the austenitization stage of the austempering are visible. Graphite flakes in a matrix of ausferrite (see Fig. 17.41 for ausferrite definition according to ASTM A644).

irons to the formation of constituents that are not normally observed in steels, as discussed in the next section.

Phosphorus-Containing Eutectics

The Fe-P system presents a eutectic between ferrite and iron-phosphide (Fe_3P) as discussed before. This eutectic occurs at approximately 1050 °C (1920 °F) with a liquid containing about 9.7% P. Sauveur (Ref 32) proposed that this eutectic should be named steadite, as it was first characterized and described by John Edward Stead (1851–1923), a chemist and one of the first British iron and steel researchers (Ref 33).

In the Fe-C-P system, which is more relevant in the study of cast irons, a ternary eutectic is formed. The cast iron literature also sometimes names this ternary eutectic steadite, which leads to confusion. Figure 17.43 presents the *liquidus* surface projection of the Fe-C-P equilibrium phase diagram and the composition of the ternary eutectic. As cast irons seldom solidify in equilibrium, literature indicates that steadite and the ternary eutectic may be observed in commercial alloys. The ternary eutectic is constituted of 31% Fe_3C, 42% Fe_3P, and 27% iron (austenite). Phosphorus eutectics are hard, with hardness in the 400–600 HB range. There are some indications that solidification may occur via a metastable eutectic that would involve a different iron phosphide, Fe_2P (Ref 10). Although in the past several theories were advanced proposing that cementite (Fe_3C) and iron phosphide (Fe_3P) could present extensive miscibility, this is not very likely, as they have different crystal structures (Ref 34). These eutectics and phosphides have a very important role in cast

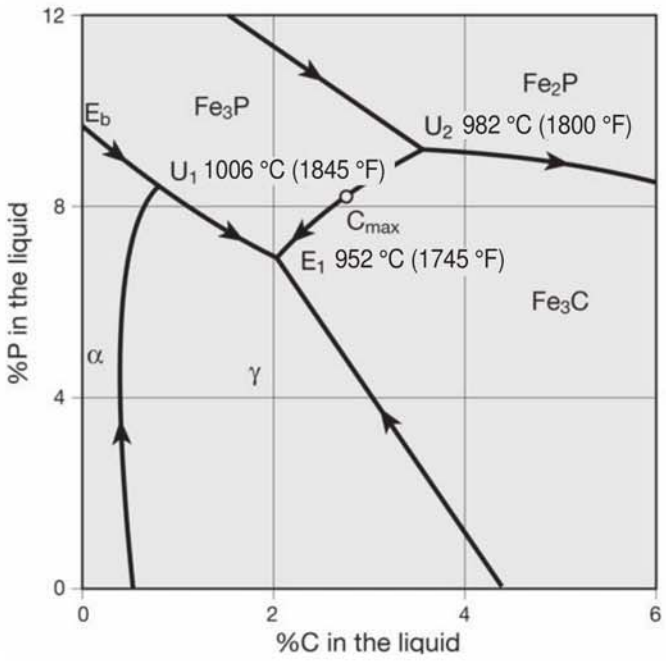

Fig. 17.43 *Liquidus* surface projection in the iron rich corner of the Fe-C-P phase diagram. The binary eutectic α-Fe_3P (steadite) is indicated as E_b. The ternary eutectic is indicated as E_1. Source: Ref 32

irons where wear resistance is an essential feature, such as rail car braking pads. According to Ref 12, these phosphorus containing eutectics may occur in two different ways in cast irons: the ternary and the pseudo-binary eutectic forms. The ternary eutectic, composed of ferrite (after austenite decomposition), iron phosphide and cementite, is a fine grained eutectic. Figure 17.39 presents a eutectic with this aspect. Usual etchants (such as nital and picral) cannot fully clarify the participation of each constituent in the eutectic. The small points inside the eutectic are usually ferrite. The light part of the eutectic is composed of the phosphide and cementite, which are not clearly separated by these etchants. Reference 12 suggests the use of Murakami etchant to identify the phosphide, since this phase is colored preferentially by this etchant (Ref 10, 11). Murakami etchant, composed of 10 g potassium ferricyanide ($K_3Fe(CN)_6$), 10 g potassium hydroxide (KOH), and 100 mL distilled water, should be used at 50 °C (120 °F) for 3 min to color the iron phosphide. To properly identify ferrite in the eutectic, including the layer frequently formed surrounding the eutectic, Ref 10 and 11 recommend the alkaline sodium picrate reactant, composed of 25 g sodium hydroxide (NaOH), 2 g picric acid, and 75 mL distilled water, to be used in the 60–100 °C (140–210 °F) range, for 1–3 min. This will color both cementite and the phosphide, leaving ferrite without coloring (Fig. 17.44) or over-etching with Murakami etchant (Fig. 17.45). Beraha etchant may also be useful in identifying the phases in the eutectic, since it will color the three phases differently (Fig. 17.46) (Ref 12).

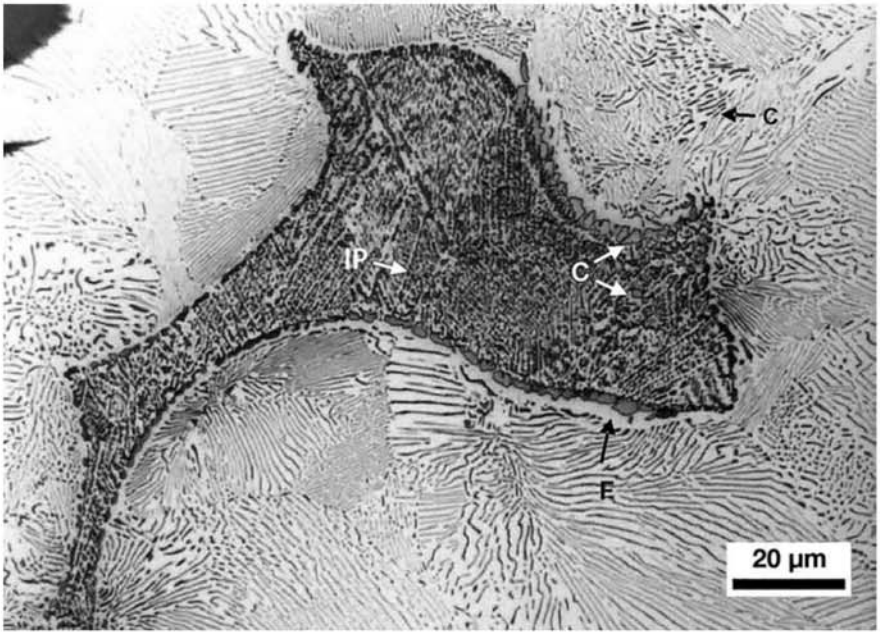

Fig. 17.44 Ternary Fe-C-P eutectic in a gray cast iron etched with alkaline sodium picrate. This etchant would normally tint only cementite (C), leaving ferrite and the phosphide unaltered. In this case, the sample was slightly overetched and the iron phosphide (IP) was tinted (dark yellow in the original image) while the cementite was tinted (blue and dark brown in the original image). Ferrite (F) was not affected by etching. With this technique, all constituents of the eutectic can be revealed. Courtesy of J.M. Radzikowska, Foundry Research Institute, Krakow, Poland.

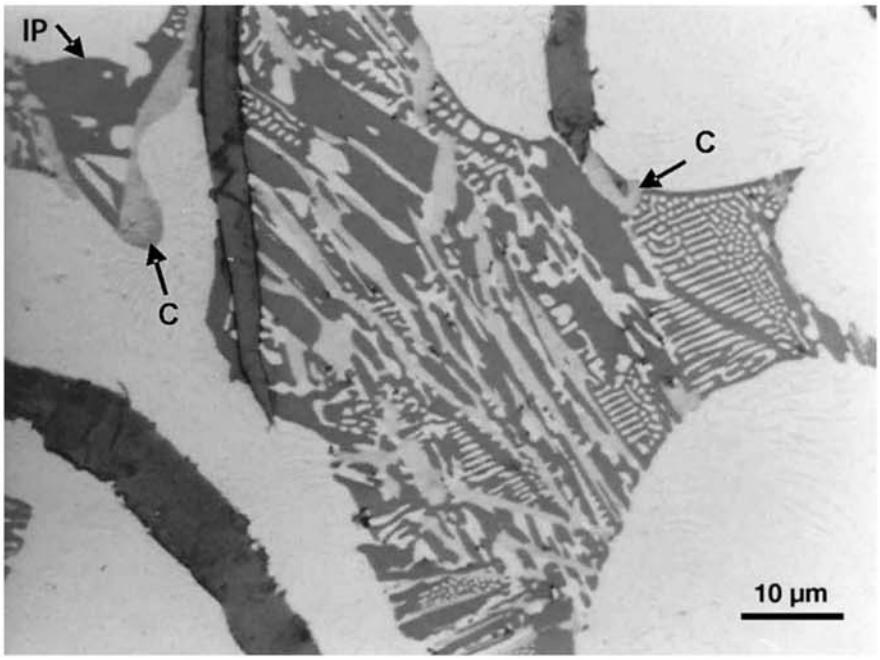

Fig. 17.45 Ternary Fe-C-P eutectic in a gray cast iron etched with hot Murakami etchant. This etchant would normally tint only iron phosphide (IP) and not ferrite and cementite. In this case, the sample was slightly overetched so that the eutectic cementite (C) was lightly tinted (light yellow in the original image). Ferrite was not affected by the etching. With this technique, all constituents of the eutectic can be revealed. Courtesy of J.M. Radzikowska, Foundry Research Institute, Krakow, Poland.

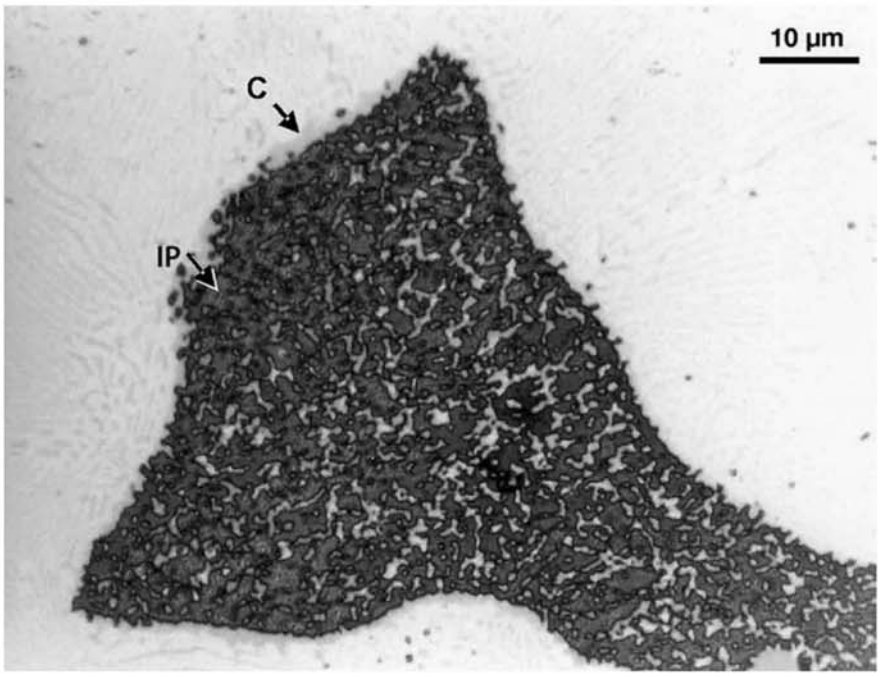

Fig. 17.46 Ternary Fe-C-P eutectic in a pearlitic gray cast iron etched with Beraha etchant. The etching has tinted the iron phosphide (IP) and cementite (C) and had no effect on ferrite. Courtesy of J.M. Radzikowska, Foundry Research Institute, Krakow, Poland.

The pseudo binary eutectic is composed only of ferrite and a phosphide. In general, it has a "herring bone" aspect, as shown in Figs 17.39, 17.47, and 17.48.

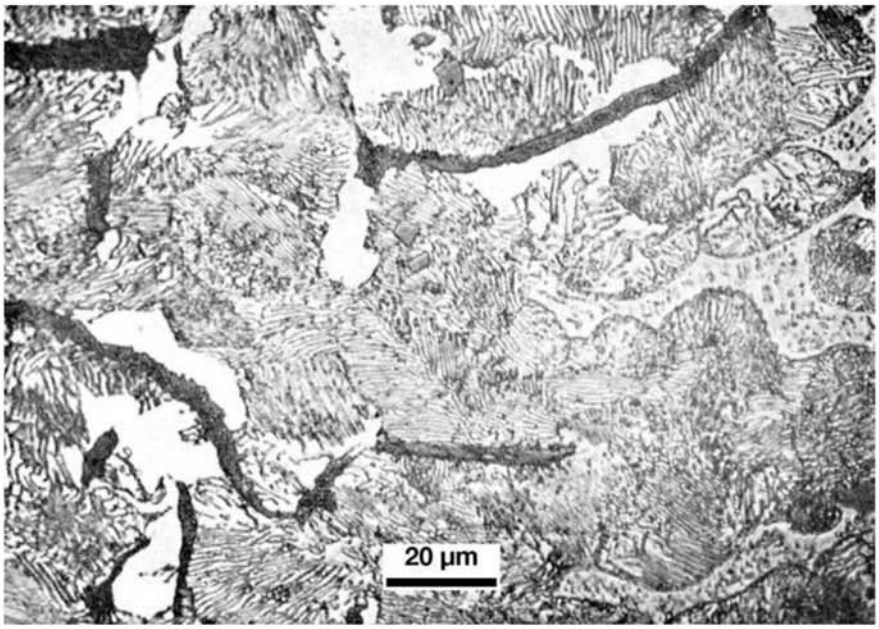

Fig. 17.47 The same gray cast iron presented in Fig. 17.45. Ferrite, pearlite, graphite, and steadite and manganese sulfide nonmetallic inclusions. Etchant: picral.

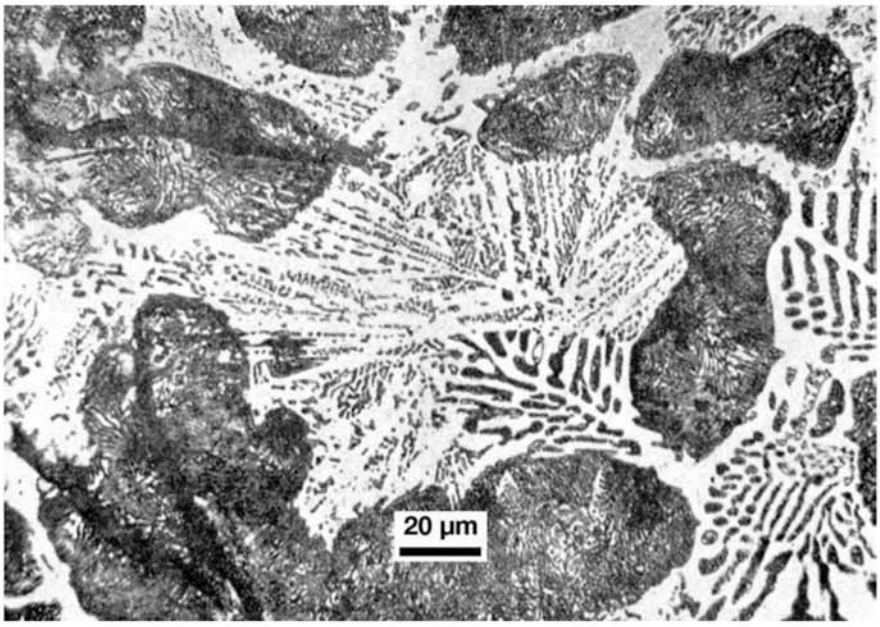

Fig. 17.48 Gray cast iron with 2% P, annealed. Phosphorus-rich eutectic. The etching makes it impossible to completely differentiate the phases present in the eutectic. Etchant: picral.

17.3.4 Some Examples of Gray Cast Iron Microstructures

Figures 17.49 to 17.58 present selected additional examples of gray cast iron microstructures.

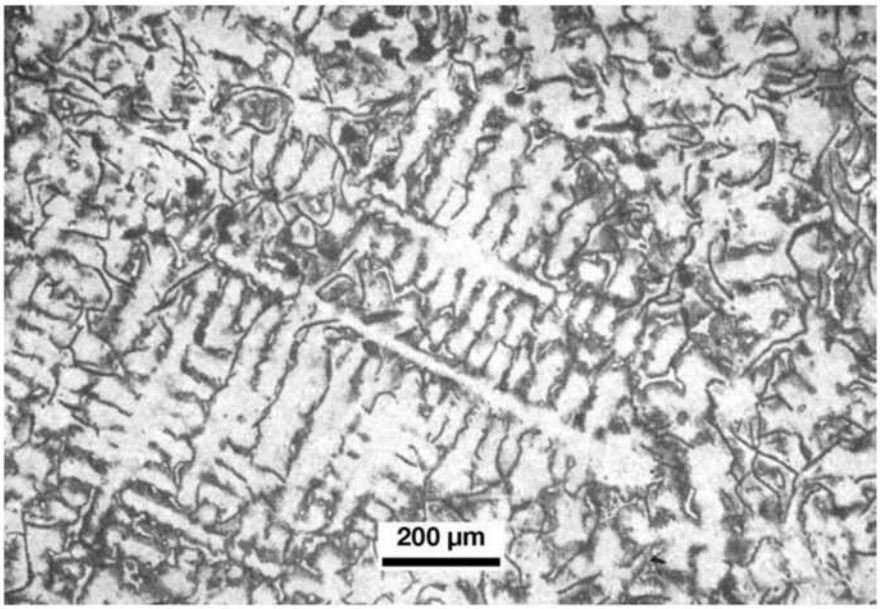

Fig. 17.49 Gray cast iron with ferritic dendrites. Graphite Distribution E. Pearlite and steadite are present in the interdendritic regions. Etchant: picral.

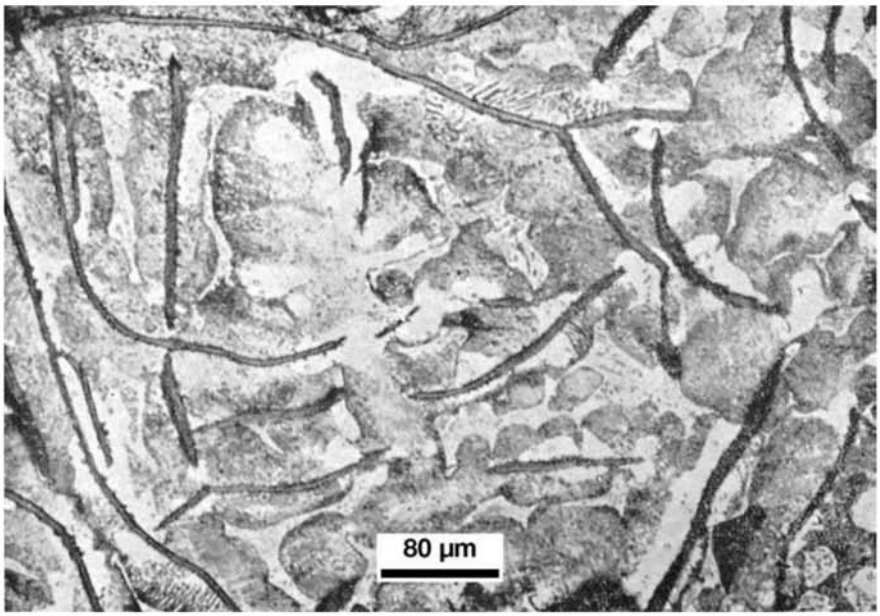

Fig. 17.50 Gray cast iron with a hypoetectoid matrix. Ferrite, pearlite, graphite, and steadite. Etchant: picral.

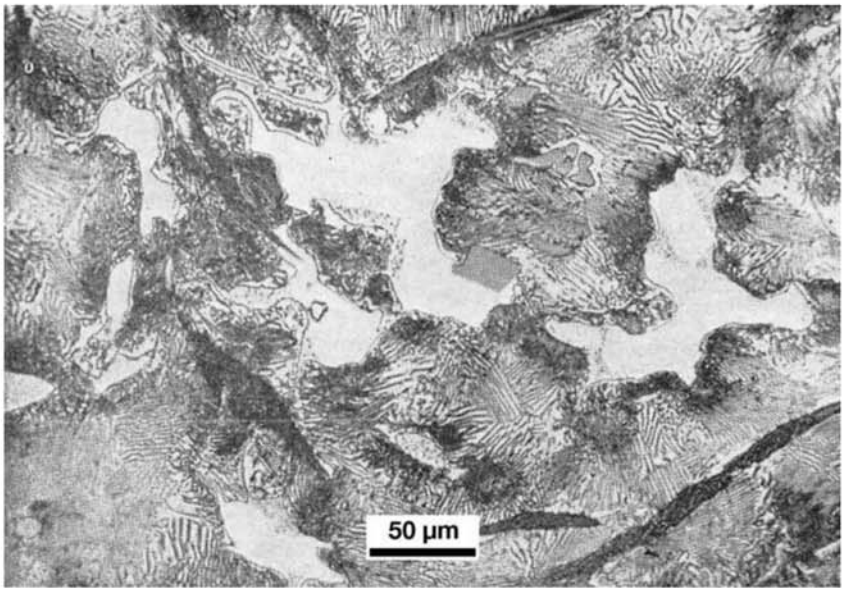

Fig. 17.51 Gray cast iron. Hypereutectoid matrix. Pearlite, graphite, cementite, phosphorus eutectic, and nonmetallic inclusions. Etchant: picral.

Fig. 17.52 Gray cast iron. Graphite and steadite in a ferritic matrix. Etchant: picral.

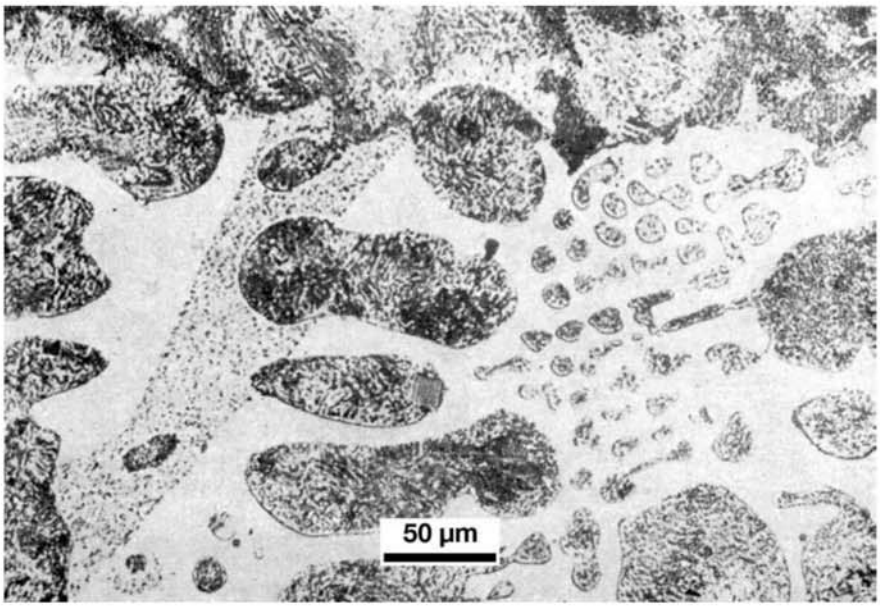

Fig. 17.53 Chilled cast iron. Mottled region. Partially spheroidized pearlite, cementite, and phosphorus-rich eutectic. The region presenting a dotted feature, to the left, with a straight boundary is the phosphorus eutectic. To the right, a ledeburitic region. The white matrix is cementite. Etchant: picral.

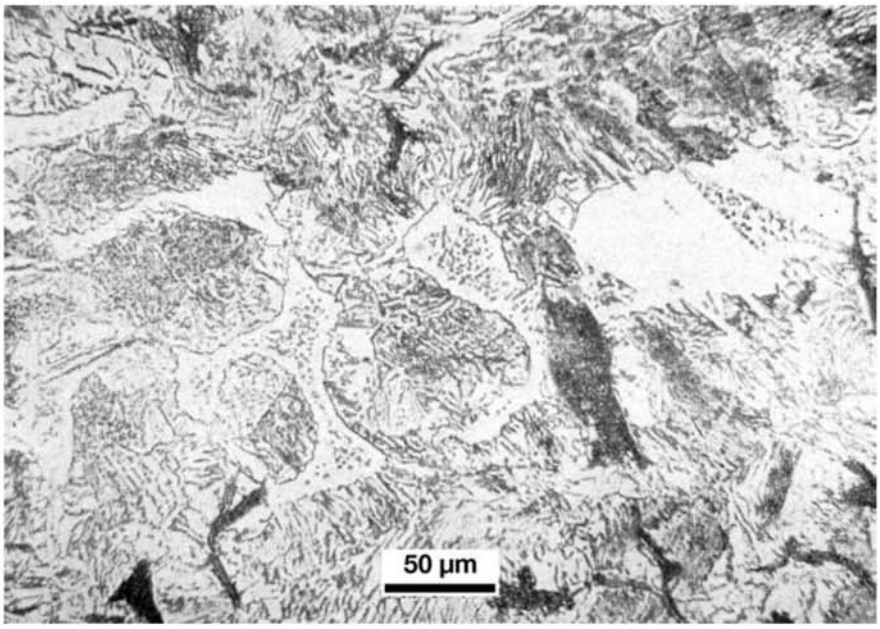

Fig. 17.54 Gray cast iron. Graphite, steadite (dotted regions) and cementite in a pearlitic matrix. Steadite presents a white edge. The constituent in this edge can be identified using color etchants (see the section "Phosphorus-Containing Eutectics" in this chapter). Etchant: picral.

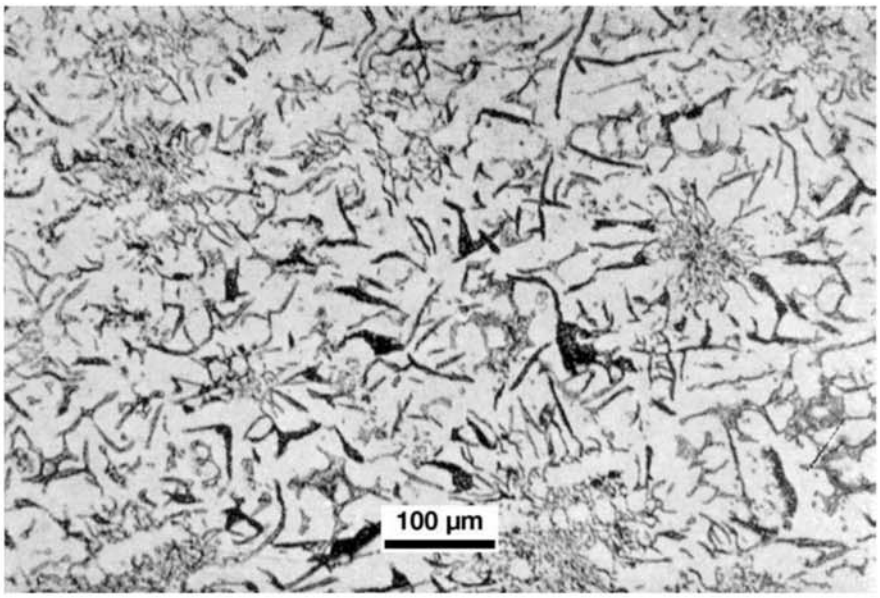

Fig. 17.55 The cast iron in Fig. 17.40, annealed. The matrix transformed into ferrite. Graphite is more clearly observed. Distributions A, B, and D. Some regions containing steadite. Etchant: picral.

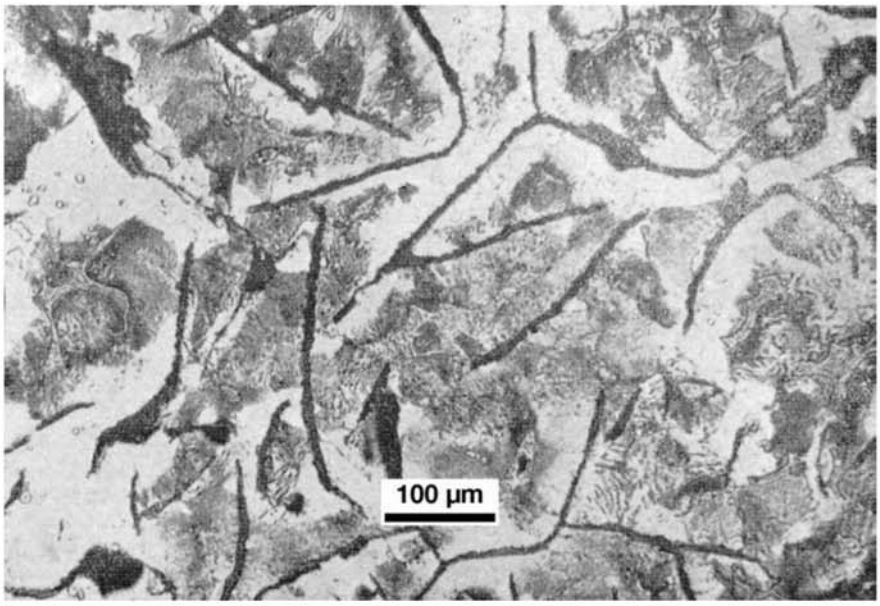

Fig. 17.56 Gray cast iron, as cast. C = 3.25%, Si = 1.82%, P = 0.48%. Pearlite, ferrite, lamellar graphite, and steadite. Hardness: 108 HB. Etchant: picral.

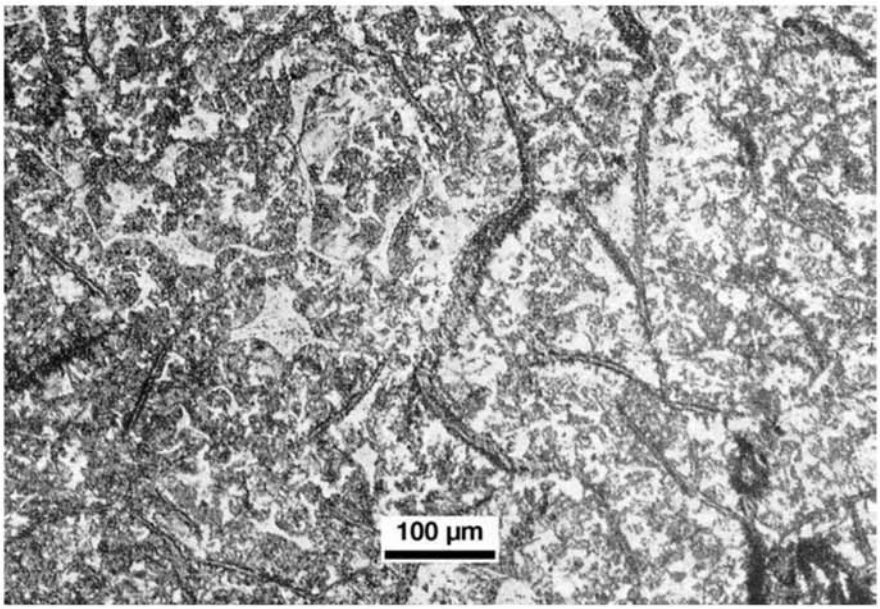

Fig. 17.57 The cast iron of Fig. 17.56, annealed. Part of the graphite carbon has dissolved in the austenite, resulting, after annealing, in a larger volume fraction of pearlite than in the as-cast condition. Hardness: 147 HB. Etchant: picral.

17.3.5 Sulfur and Sulfides

Sulfur effects in cast irons are frequently controlled by adjusting manganese and sulfur content (Ref 35) according to empirical relationships such as:

$$\%Mn = 1.7 \times (\%S) + 0.3\% \qquad \text{(Eq. 2)}$$

where the 1.7 factor is the ratio of manganese to sulfur atomic mass.

Another useful tool is the solubility product of manganese sulfide. This can be used to make sure that this sulfide does not precipitate above the *liquidus* temperature of the cast iron, as shown in Fig. 17.59. Figure 17.60 show manganese sulfide inclusions in a gray cast iron.

17.3.6 The Oxidation of Gray Cast Iron

When gray cast iron oxidizes, there can be an increase in volume, sometimes called swelling. Oxygen combines with carbon in the graphite to form CO or CO_2 and leaves voids in the spaces previously occupied by graphite. When these new internal surfaces are exposed to the air, they oxidize, and oxide formation may cause a significant increase in volume (Fig. 17.61). This problem can be especially important in the production of malleable iron, when graphite formation on the part surface may lead to surface defects associated to oxidation of the graphite during the heat treatment (see the section "Blackheart Malleable Cast Iron" in this chapter).

Fig. 17.58 Gray cast iron with hypoeutectoid matrix, annealed for 5 min at 1000 °C (1830 °F). Lamellar graphite, ferrite, and phosphorus eutectic surrounded by pearlite.

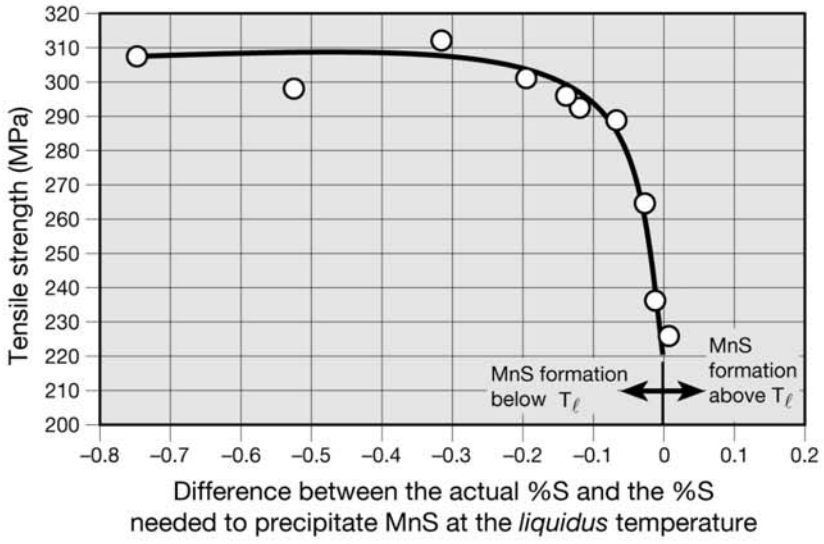

Fig. 17.59 The effect of the difference between the actual sulfur content of a gray cast iron and that needed to cause the precipitation of MnS at the liquidus temperature of the alloy. T_ℓ is the *liquidus* temperature. All experiments performed with S = 0.12% and C_{eq} = 3.8% with different manganese contents. Source: Ref 35

Fig. 17.60 Gray cast iron. Graphite and polyhedral manganese sulfide in the interdendritic spaces. Not etched.

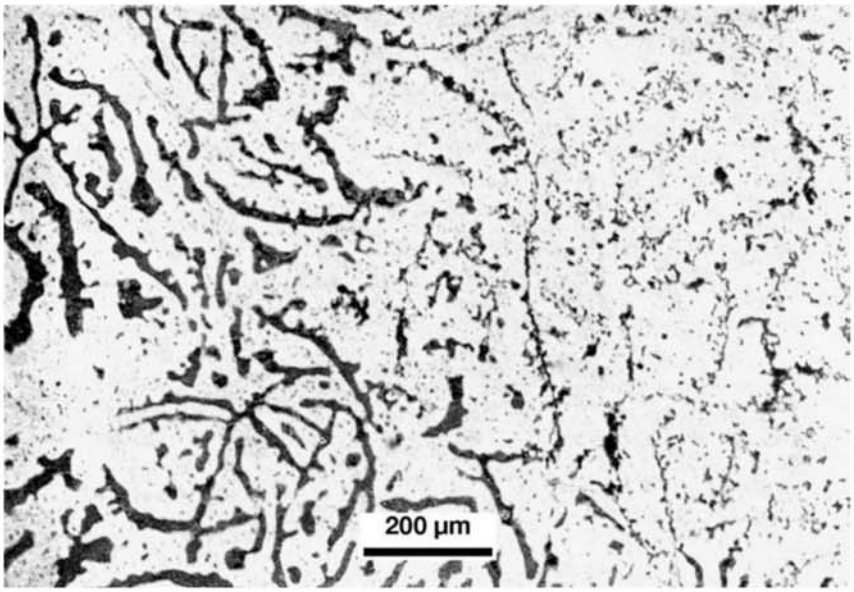

Fig. 17.61 "Burned" (oxidized) gray cast iron. Oxidation happened from the left to the right of the image. In the image right side, the disappearance of the graphite flakes can be noticed. On the left, it is possible to see the empty spaces caused by graphite oxidation already filled with oxide.

17.4 Mottled and Chilled Cast Irons

For cooling conditions and compositions intermediate to those that lead to white cast irons and graphite-containing cast irons, complex microstructures are obtained, where both carbides and graphite can be formed during solidification. Accelerated cooling obtained with a high conductivity mold material ("chilling") such as a metal (usually cast iron itself) is especially well suited to

cause the formation of these structures. When a mix structure is formed, the fracture aspect is intermediate between white and gray cast irons, presenting numerous dark areas on a light background in a "mottled" pattern, as presented in Fig. 17.62.

When the microstructure is observed, it is possible to characterize the regions with structures typical of gray and white iron, as shown in Fig. 17.63 to 17.66. The material obtained this way has an interesting balance between the

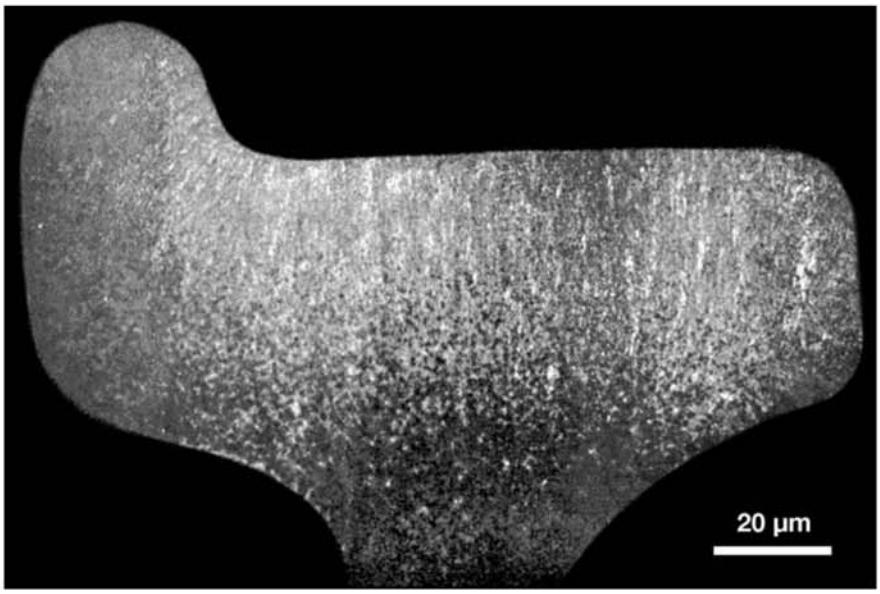

Fig. 17.62 Appearance of the fracture surface of an old railroad wheel, made from chilled cast iron. It is possible to clearly see the white regions (close to the tread and flange), gray regions (away from the tread, close to the central region), and the intermediate mottled region.

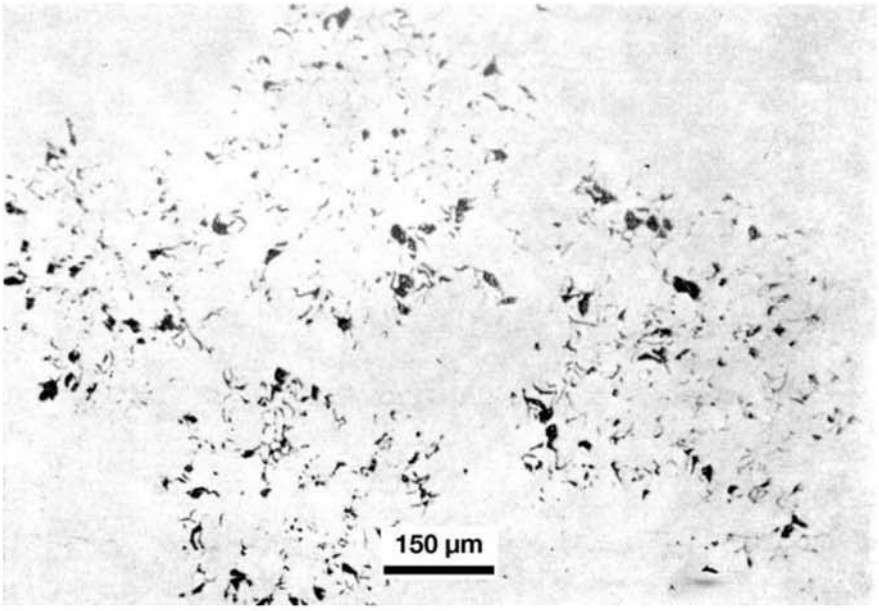

Fig. 17.63 Mottled cast iron. Regions with graphite clusters (gray areas) and regions without graphite (white regions). Not etched.

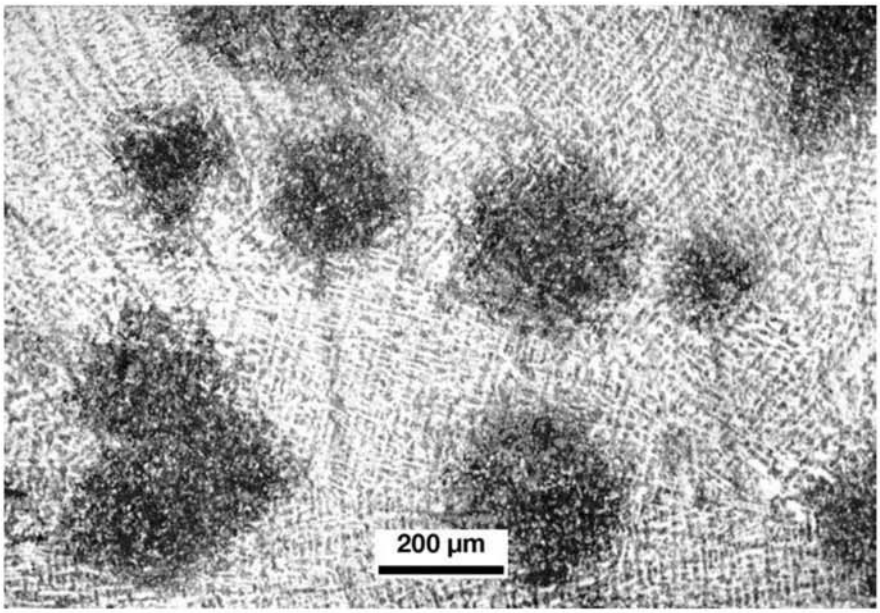

Fig. 17.64 Mottled gray iron. Dark areas are regions of gray cast irons (the contours are not as clear as in Fig. 17.63). The rest of the cross section is white cast iron. Etchant: picral.

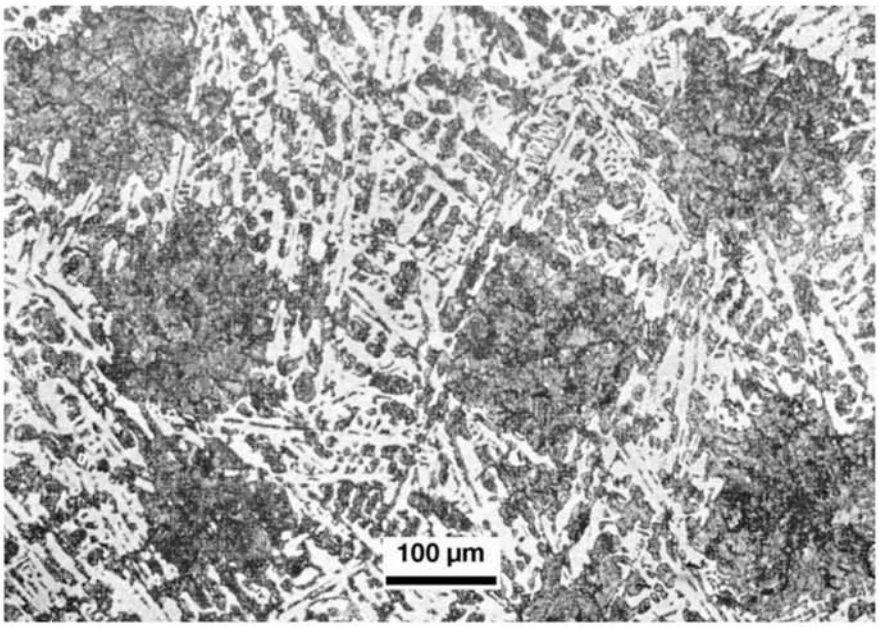

Fig. 17.65 Mottled cast iron. Dark areas are gray cast iron. The rest of the cross section is white cast iron. Etchant: picral.

high hardness and wear resistance of white cast iron and toughness and high thermal conductivity and damping capacity of gray cast iron, as the application example in Fig. 17.67 indicates. When chilled parts are produced, it is possible to obtain regions in the chilled surfaces with the microstructure of

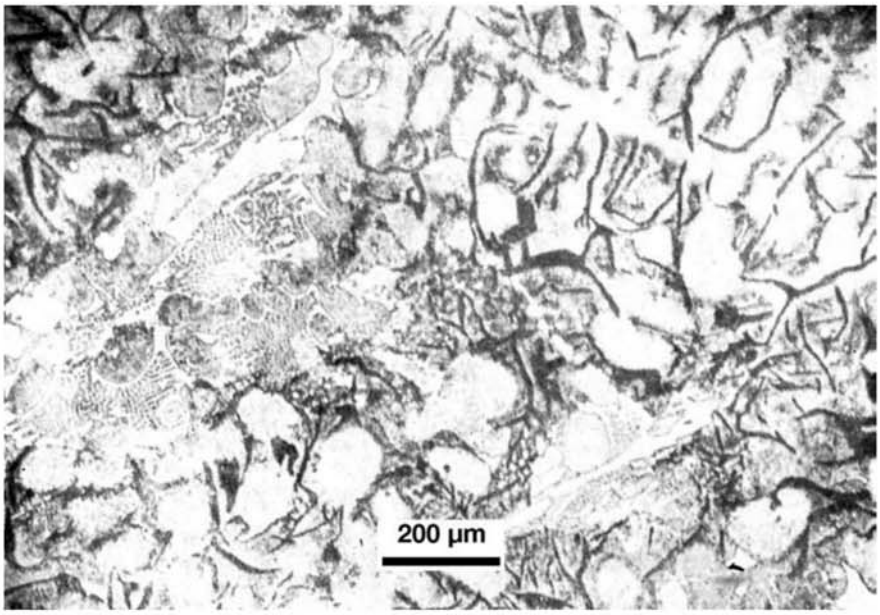

Fig. 17.66 Mottled cast iron. Dendrites transformed into pearlite. Distribution E graphite. Areas of ledeburite and cementite. Etchant: picral.

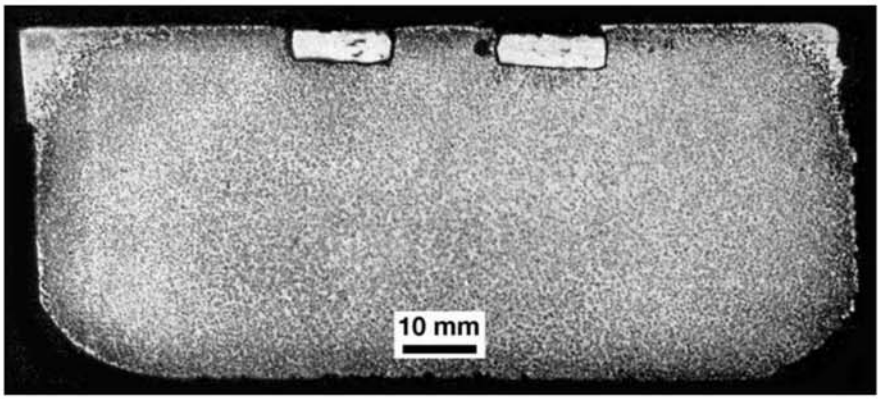

Fig. 17.67 Transverse cross section of an old brake pad, made of mottled cast iron. The edges of the pad, in the upper part of the image, have cooled faster than the rest of the part and have a white cast iron structure. The macrograph also shows the presence of two low-carbon steel bars that are inserts in the casting and have the purpose of preventing shattering by releasing large pieces of the brake pad in case of fracture. Etchant: iodine.

white cast iron and thus high hardness and wear resistance and, at the same time, have the core region of the part with a graphitic microstructure less brittle and with higher thermal conductivity and damping. Figures 17.68 and 17.69 show examples of parts produced by chilling in which the transition in the microstructure is evident. In the case of rolling cylinders, the technology has evolved dramatically with respect to simply using chilling: cylinders in which different metal compositions are used for the surface and for the core

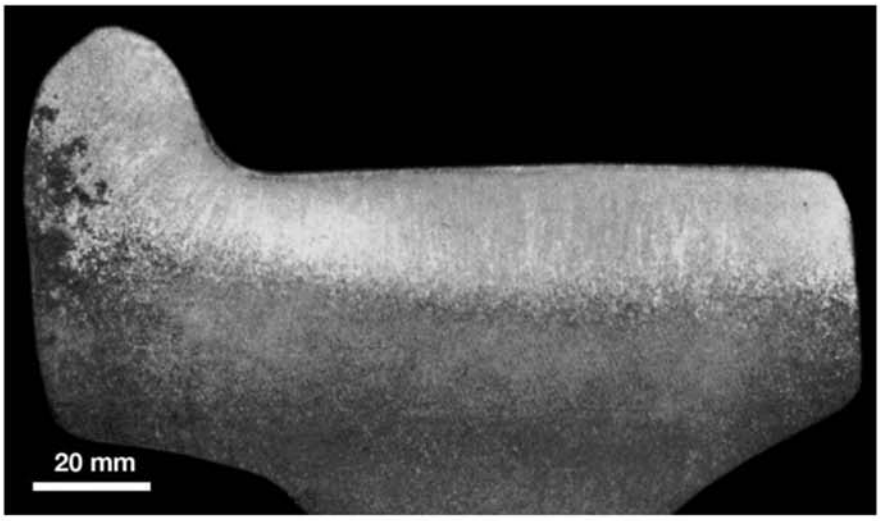

Fig. 17.68 Cross section of a wheel in chilled cast iron. The chilled layer is thinner than that in Fig. 17.62. To the left (inner portion of the flange), some casting defects can be seen. The wheel has been cast with its axis in the vertical position and the flange in the upper portion of the mold, where the defects happened. Etchant: iodine.

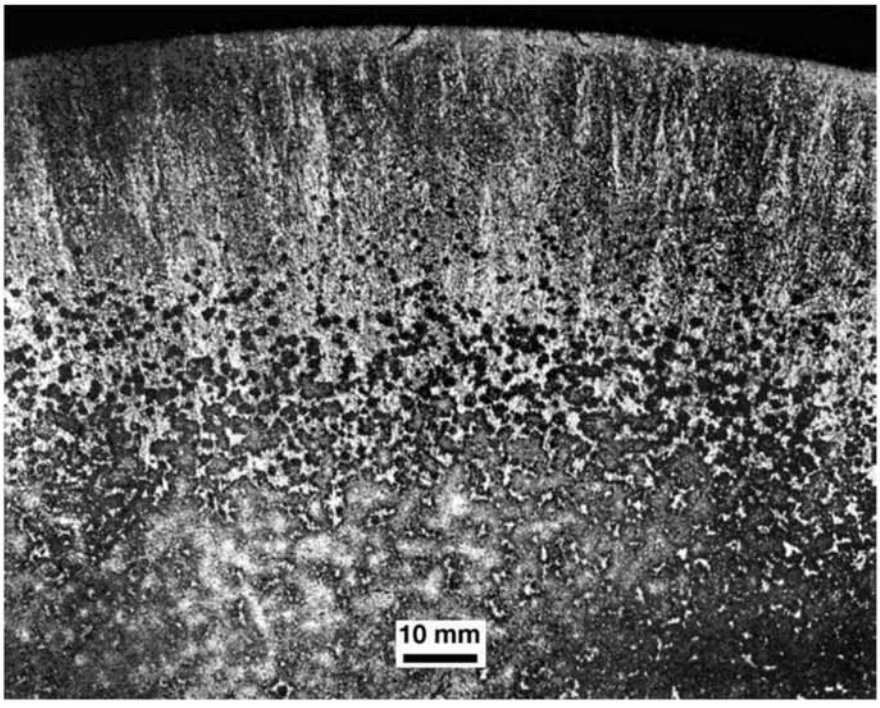

Fig. 17.69 Transverse cross section of a rolling mill roll. The cylinder surface (upper portion of the image) has been chilled. White cast iron region close to the roll surface, gray core, and mottled transition region. Etchant: iodine.

have been developed (Ref 36, 37), and wide applications have been found in steels, too. Chilling is also used for nodular cast irons (Fig. 17.70 to 17.73). Parts such as camshafts for engines, for instance, may be produced using either gray or chilled nodular cast iron (Ref 38).

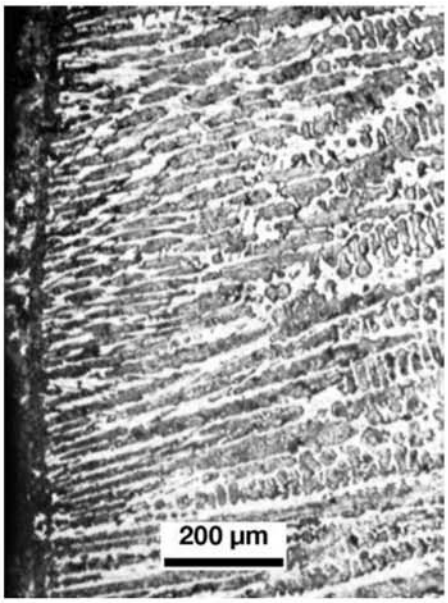

Fig. 17.70 Region close to the surface in a hypoeutectic white cast iron part. The rapid extraction of heat through the surface has led to the growth of dendrites in a direction normal to the surface, forming a columnar zone. Etchant: nital.

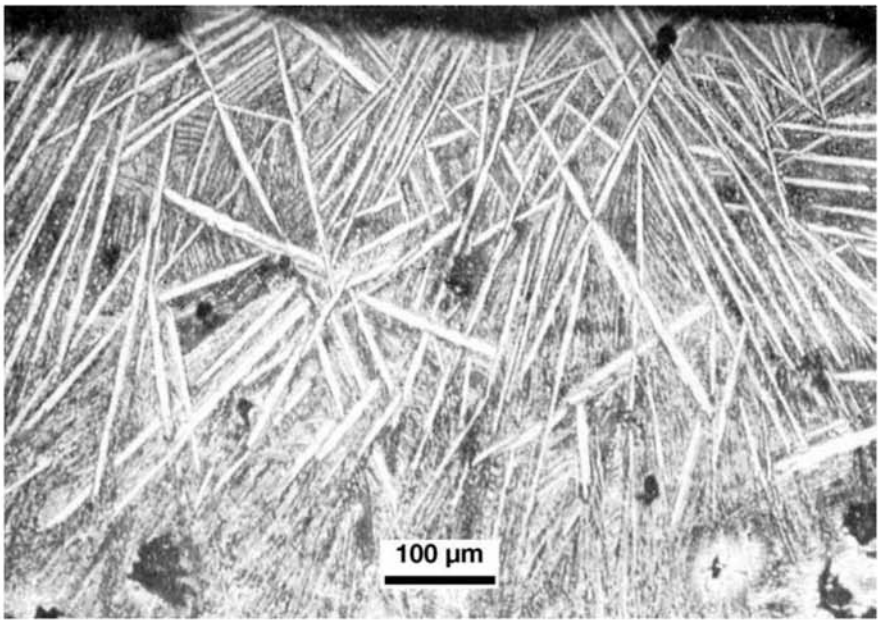

Fig. 17.71 Chilled region close to the surface of a hypereutectic gray cast iron, with a mottled aspect. Some white needles of cementite on a background of ledeburite. Dark regions are areas where graphite precipitation has happened.

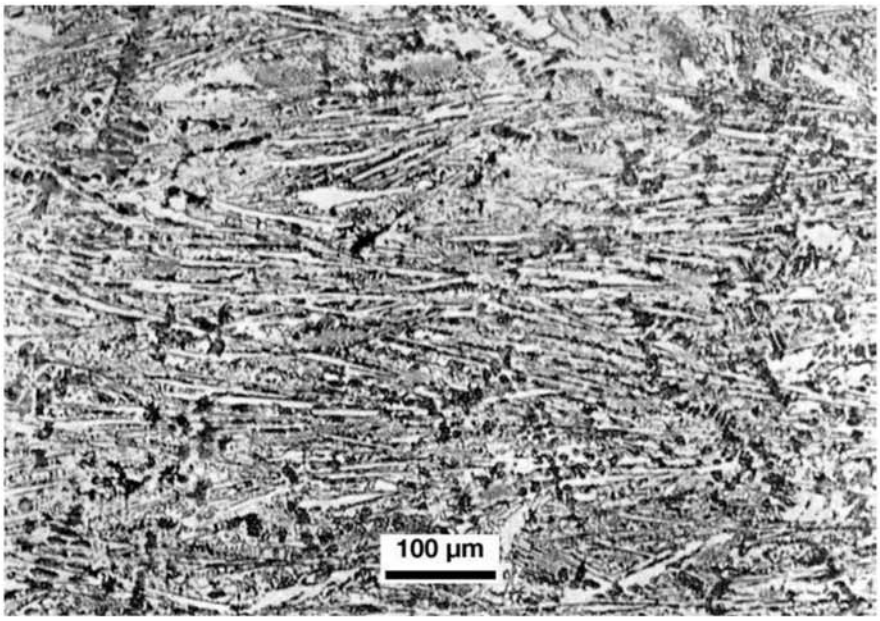

Fig. 17.72 Chilled region close to the surface of a hypoeutectic gray cast iron. Elongated cementite (similar to the plate eutectic, see the section "17.2 White Cast Irons" in this chapter) in a ledeburitic matrix. Some remains of dendrites of austenite that transformed to pearlite can be seen. Etchant: picral.

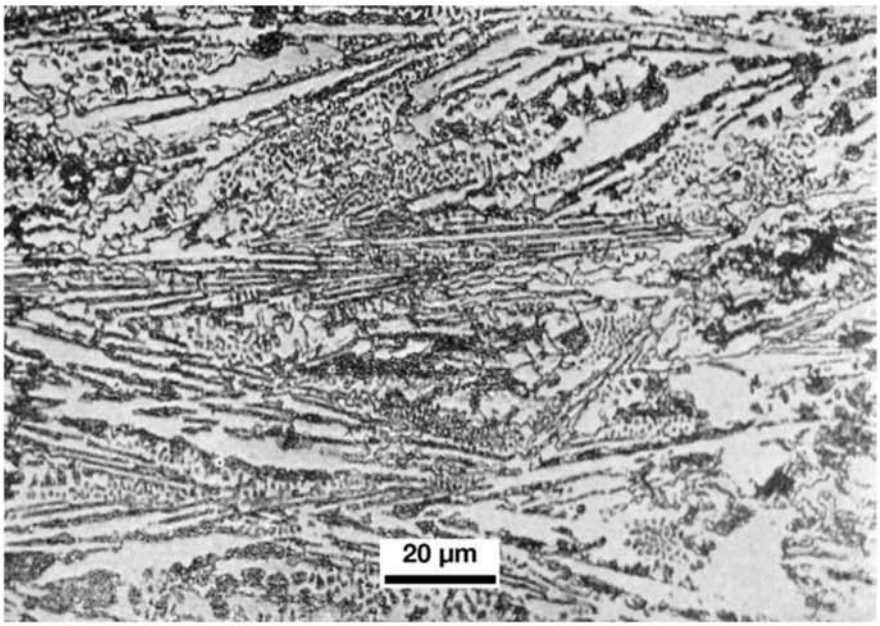

Fig. 17.73 Region close to the chilled surface of a hypoeutectic gray cast iron. Elongated cementite (similar to the plate eutectic; see the section "17.2 White Cast Irons" in this chapter) and ledeburite. Graphite is visible in the center of the image. Etchant: picral.

17.5 Nodular Cast Iron or Ductile Cast Iron

Nodular cast iron (or ductile cast iron) makes it possible to combine interesting properties of cast irons and steels. The main feature of these alloys is the combination of chemical composition adjustment and liquid metal inoculation to favor graphite formation in nodules, instead of flakes. Magnesium and cerium play a critical role in this function, as shown in Fig. 17.74. The overall process of preparing and casting a heat of nodular cast iron may encompass several stages of chemical composition control to achieve the desired objectives, as summarized in the flowchart in Fig. 17.75.

The entire process must be properly controlled to ensure the efficiency of the spheroidizing process and inoculation. In some cases, for high-performance parts, complete nodularization is confirmed by measuring the velocity of ultrasonic waves in the parts, since this property is directly dependent on the degree of nodularization (Ref 39), as shown in Fig. 17.76. The extent of nodularization influences many properties of the nodular cast iron, as indicated in Fig. 17.77.

Because the boiling point of magnesium is low (1090 °C, or 1995 °F, significantly lower than the melting point of iron or the processing temperatures during melting operations to produce cast iron), many industrial techniques have been developed to achieve a satisfactory and consistent yield of this important addition. Some elements can interfere negatively with nodularization (aluminum, titanium, lead, and tin), and additions of cerium and calcium are especially effective in neutralizing this interference effect (Ref 18). Although the nucleation phenomena are extremely important to achieve adequate properties in cast irons and a series of important mechanisms and nucleation sources have been observed in cast irons, much evidence points to superficial phenomena controlling the morphology with which graphite forms in solidifying cast iron (Ref 4). Apparently, elements that have a signifi-

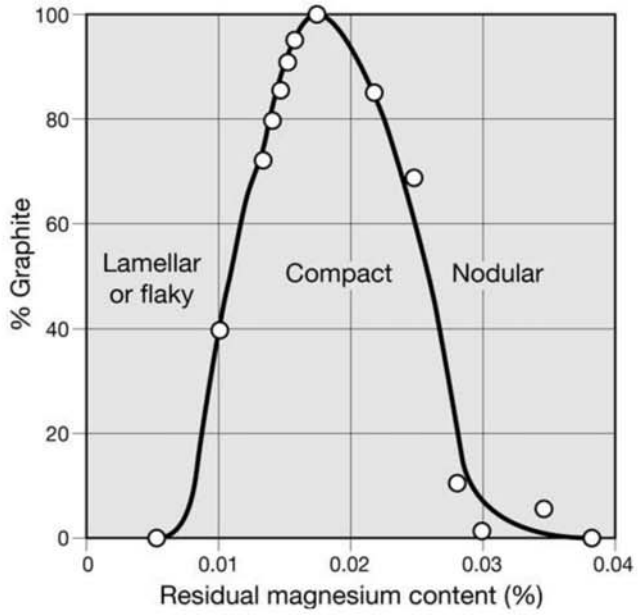

Fig. 17.74 The effect of magnesium content on the graphite morphology in cast iron. Source: Ref 1

cant effect on the surface tension of iron, mainly oxygen, sulfur, selenium, and tellurium, will locate themselves preferentially at the interfaces between the basal plane of graphite—which has a hexagonal structure—and the liquid, favoring the growth of graphite along the prismatic planes and thus favoring the formation of lamellar graphite (Ref 4, 41). This mechanism can explain many of the key features of the process graphite nucleation. Fading, the gradual reduction of the effect of the nodularizing elements, can be shown to be related to this effect, since vacuum processed cast irons, in which oxygen and sulfur have been removed, solidified nodularly (Ref 41). Thus, interestingly, though it took many centuries to develop nodular cast iron, nodular graphite would be the "normal" solidification morphology, while the lamellar morphology happens only due to the presence of surface active impurities.

The morphology of spheroidized graphite is presented in Fig. 17.78. Not all nodules are perfect spheres or have a smooth interface with the metal matrix. The evaluation of the fracture surface is also useful for understanding the structure and distribution of graphite, as seen in Fig. 17.79. The appearance of nodular graphite on a classical metallographic cross section is presented in Fig. 17.80.

Incomplete nodularization or deviations during the nodularization process can be seen in Fig. 17.81. As briefly discussed in Chapter 8, "Solidification, Segregation, and Nonmetallic Inclusions," the solidification of nodular cast irons is a complex process. Because graphite is surrounded by austenite, growth can only proceed with carbon diffusing through the solid phase, even during solidification. Solidification is always accompanied by segregation, and some special etching techniques make it possible to reveal it during metallography, as shown in Fig. 17.82. Presently the metallurgy of nodular cast irons has evolved in a way in which different matrixes, very similar to those of steels, can be obtained through adequate heat treatment procedures.

Nodular or ductile cast irons are usually specified with a combination of the minimum ultimate tensile strength and the minimum total elongation in the tensile test (in %). Some chemical composition limits are also frequently defined. As a rule, nodular cast irons have sulfur and phosphorus limits much lower than those of other cast irons. Compositions such as C = 3.7%, Si = 2.5%, Mn = 0.3%, P = 0.01%, and S = 0.01% are representative, even though most specifications limit the maximum phosphorus content at 0.08%. Sulfur must be kept at low levels to avoid reactions with magnesium, either increasing its consumption or compromising nodularization.

Ferritic matrix cast irons (Fig. 17.83) present structures closest to thermodynamic equilibrium among cast irons. Even though in the past ferritic matrix cast irons used to be produced via heat treatment, the search for more efficient and economic production routes has led to the understanding of how it is possible to achieve a ferritic microstructure directly in the "as-cast" condition through the proper balancing of chemical composition. It is important to control at least the contents of copper, manganese, and tin, elements that favor the formation of pearlite, besides evidently the silicon content (Ref 42, 43). When either carbides or pearlite are present in the as-cast condition, it may be necessary to use heat treatments to achieve a ferritic microstructure. The decision on the most suitable heat treatment depends on whether primary carbides or just pearlite are present in the as-cast structure. A usual heat treatment to form ferritic microstructure from a structure containing

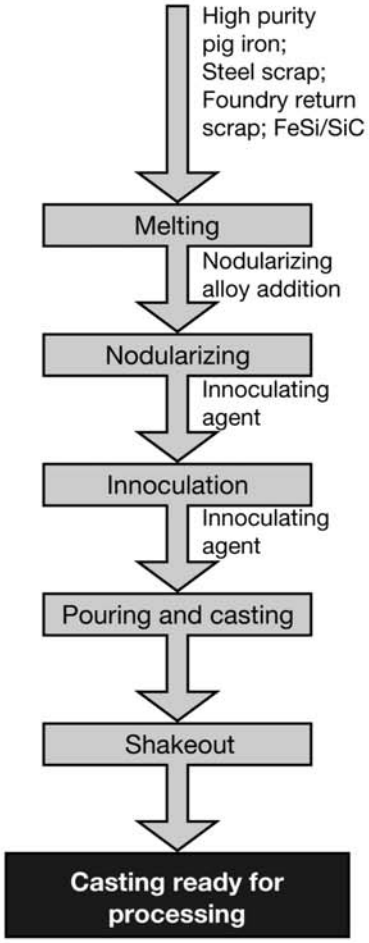

Fig. 17.75 A sample flowchart to produce ductile (nodular) cast iron. Source: Ref 4

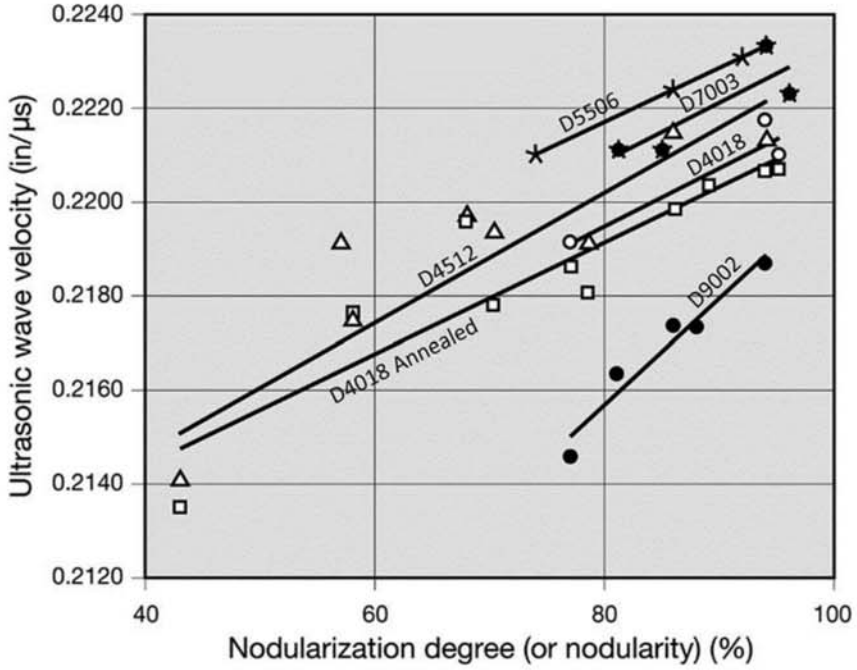

Fig. 17.76 The effect of the extent of nodularization (or "nodularity," acc. ASTM A247) measured by quantitative metallography on the sound velocity in different grades of ductile cast irons according to SAE J434 standard. Besides nodularity, microstructure also has an influence of the sound propagation velocity. Source: Ref 40

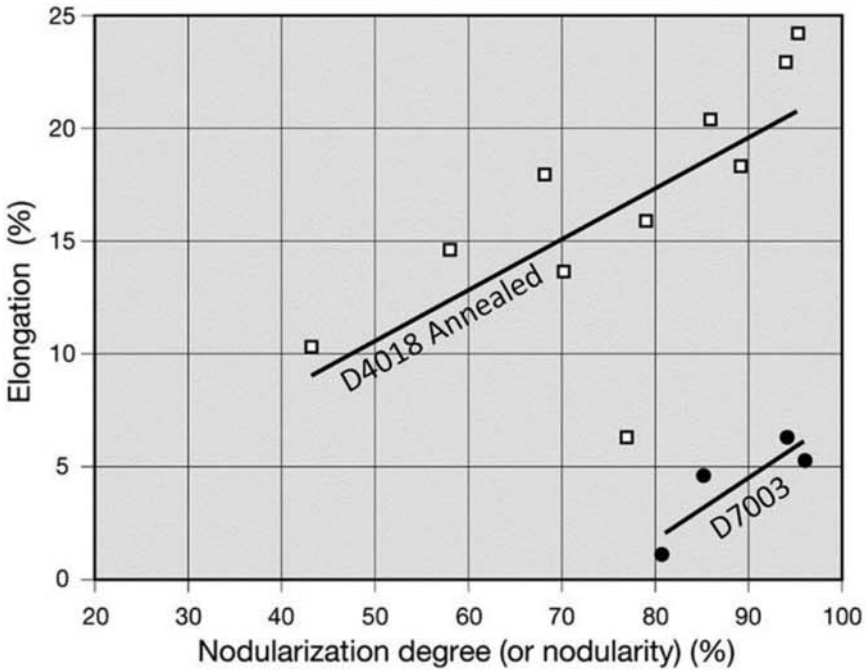

Fig. 17.77 The effect of the extent of nodularization measure by quantitative metallography on the elongation measure on tensile test for two grades of ductile cast irons according to the SAE J434 standard. Source: Ref 40

eutectic carbides consists of austenitizing at 900–925 °C (1650–1700 °F) for 3 to 5 h, followed by slow cooling (20–35 °C/h, or 35–65 °F/h) in the transformation range (800–710 °C, or 1470–1310 °F), followed by furnace cooling (50–100 °C/h, or 90–180 °F/h) up to around 200 °C (390 °F).

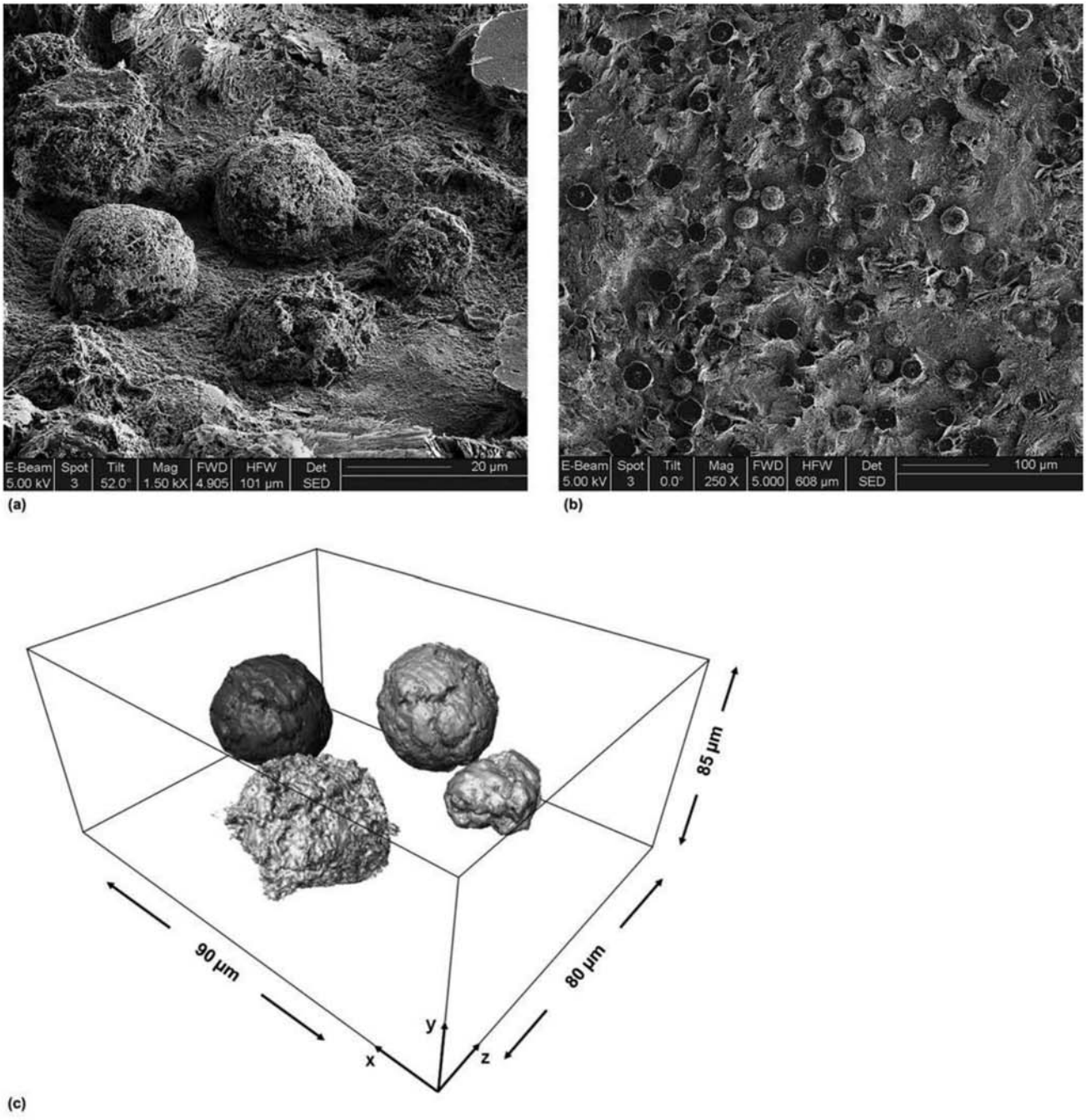

Fig. 17.78 (a) and (b) Aspect of nodular graphite in ductile cast iron subjected to deep etching. Some of the nodules have been sectioned in the original metallography, before deep etching. SE, SEM. (c) Tridimensional reconstruction of nodular graphite in ductile cast iron. Cuts were made by focused ion beam (FIB) and the images obtained with SE, SEM. Courtesy of A. Velichko and F. Mücklich, Universität des Saarlandes, Saarbrücken, Germany.

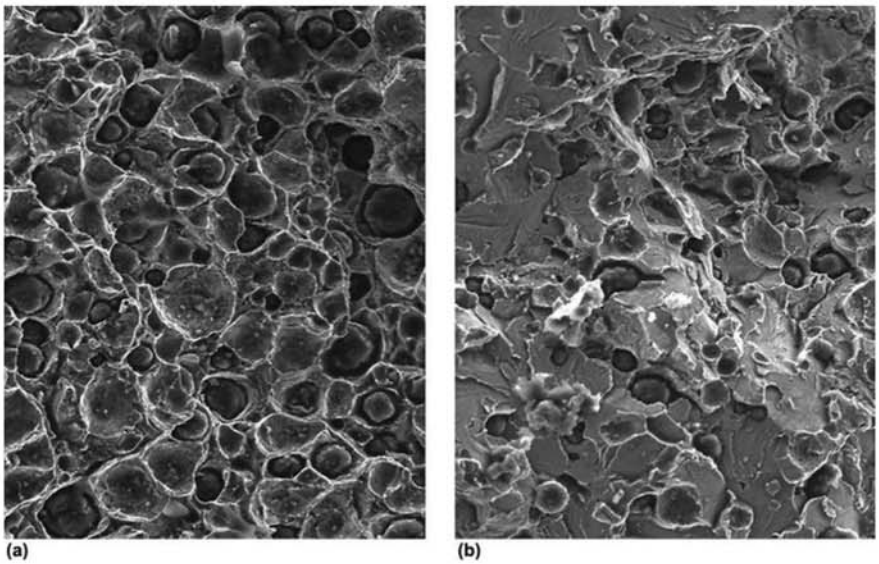

Fig. 17.79 (a) Ductile fracture and (b) brittle fracture in ductile cast iron. SE, SEM. Not etched. The aspect of graphite and its role in the fracture process are evident. Courtesy of J. Sertucha, Azterlan, Centro de Investigacion Metalurgica, Durango, Bizkaia, Spain.

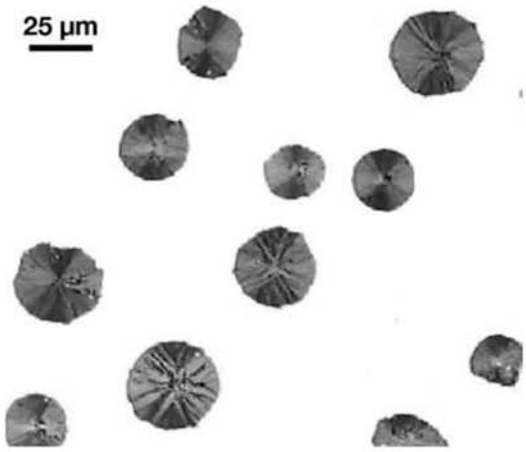

Fig. 17.80 Ductile cast iron. Graphite nodules. Not etched. Courtesy of W. Guesser, Tupy Fundições, Joinville, SC, Brazil.

Microstructures combining ferrite and pearlite make it possible to reach a wide range of mechanical properties, as indicated in Table 17.4. During solidification cooling or during heat treatment, at a certain temperature range the structure of the cast iron will be formed by austenite and graphite. During cooling, more graphite may be formed as the carbon solubility in austenite decreases. Austenite decomposition, on the other hand, may start at the eutectoid transformation temperature, as shown in the diagram of Fig. 17.84.

There are two main factors that contribute to the preferential formation of ferrite close to the graphite nodules. During solidification, silicon is concen-

trated close to the nodules (i.e., it undergoes negative segregation) as indicated in Fig. 17.82, and manganese segregates to the last regions of the metal to solidify. As silicon increases the eutectoid transformation temperature and manganese decreases it, regions close to the nodules will reach the transformation earlier (at higher temperatures) than the rest of the metal (Ref 44), in a way not much different from that explaining banding formation, discussed in the section, "Banding," in Chapter 11, "Hot Working," in this book. Furthermore, the austenite-graphite interface is a heterogeneous nucleation site. When the temperature decreases to the metastable eutectoid (involving cementite) transformation temperature, conditions for pearlite formation as established. There are good mathematical models that can describe this transformation mechanism, confirmed experimentally (see, for instance, Ref 44, 45). Figure 17.85 presents examples of nodular cast irons with a ferrite-pearlite matrix. Before the development of austempered cast irons, alloys

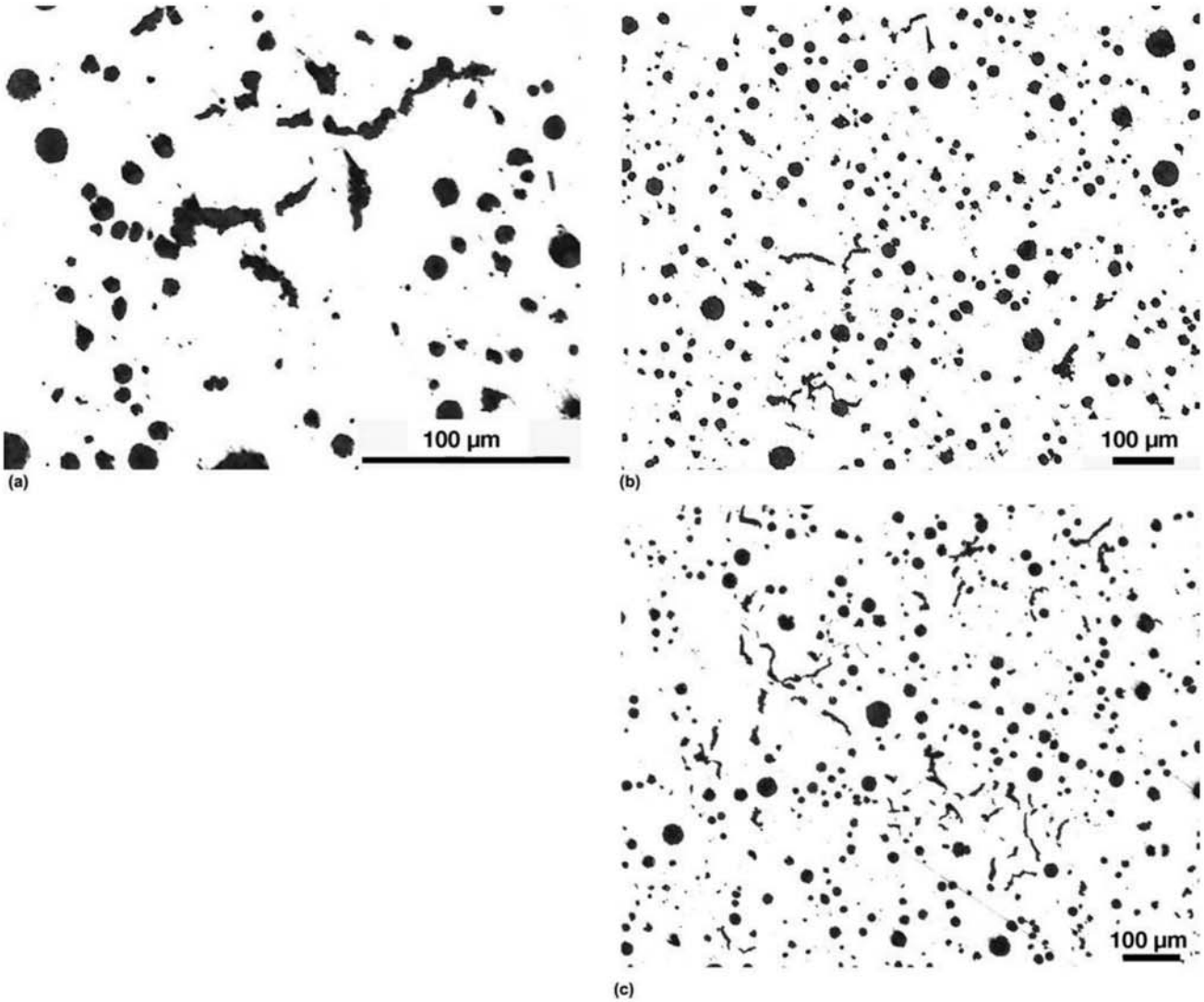

Fig. 17.81 (a–c) Some examples of nodularization failures (or incomplete nodularization). Not etched. Courtesy of J. Sertucha, Azterlan, Centro de Investigacion Metalurgica, Durango, Bizkaia, Spain.

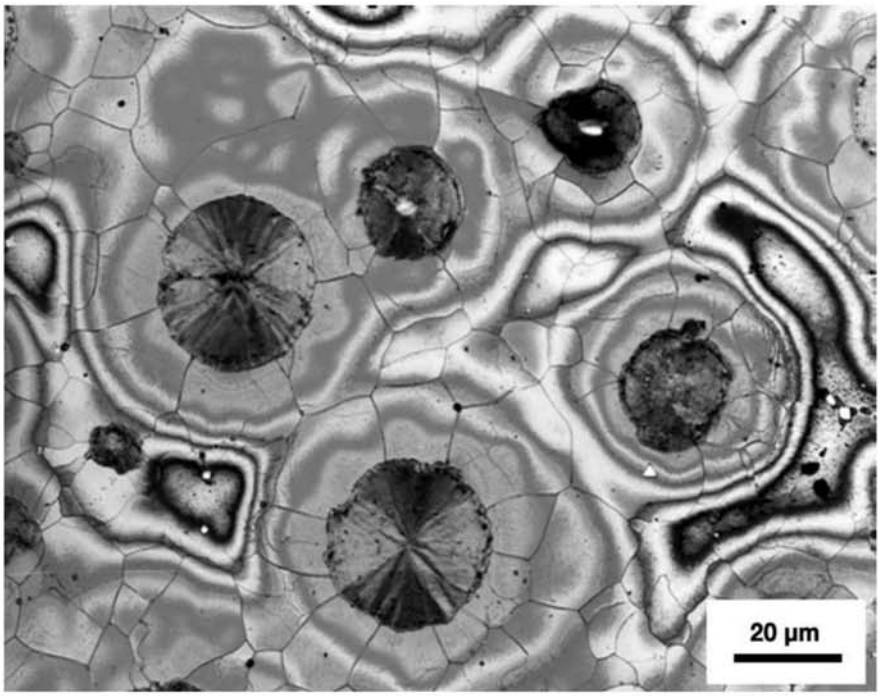

Fig. 17.82 Ductile cast iron, annealed (3.9% C, 2.9% Si, 0.32% Mn, 0.06% P, 0.037% Mg, 1.5% Ni, 0.57% Cu). The etchant reveals silicon segregation. Silicon content decreases as the distance from the graphite nodule increases. The etchant is composed of 28 g sodium hydroxide (NaOH), 4 g picric acid, 1 g potassium metabisulfite in 100 mL distilled water. The etchant is used hot, close to its boiling point; etching time 30–60 min. Courtesy of J. Radzikowska, Foundry Research Institute, Krakow, Poland.

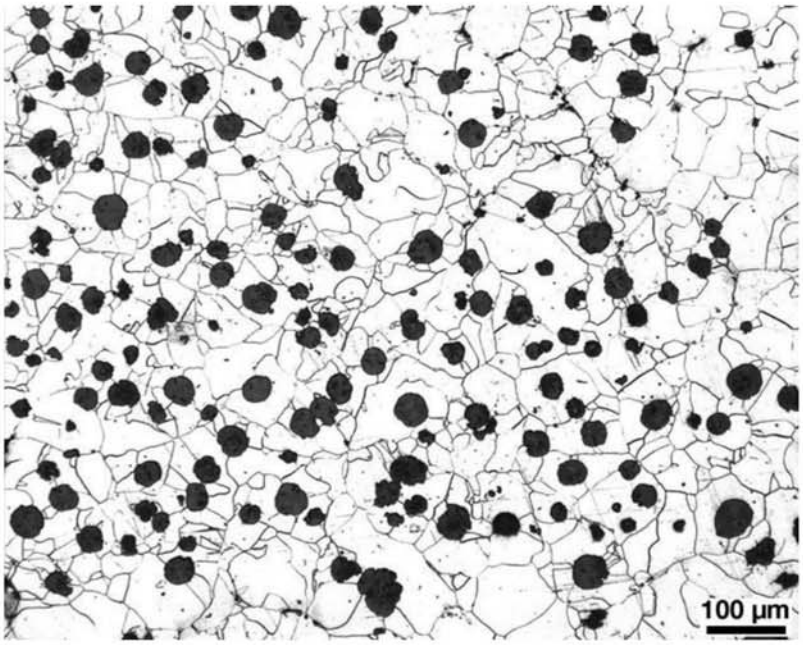

Fig. 17.83 Ductile cast iron with ferritic matrix. Etchant: nital. Courtesy of J. Sertucha, Azterlan, Centro de Investigacion Metalurgica, Durango, Bizkaia, Spain.

Table 17.4 Minimum specified properties for ductile cast iron and typical microstructures

Standard	Grade, defined by level of properties			
ISO 1083 and EN 1563, tensile strength (MPa), elongation (%)	350-22	450-10		
	400-18	500-7	700-2	900-2
	400-15	600-3		
ASTM A536, tensile strength (ksi), elongation (%)	60-40-18	70-50-05		
	60-42-10	80-55-06	100-70-03	…
	65-45-12	80-60-03		
	Typical microstructures			
	Ferrite	Ferrite plus pearlite	Pearlite	Tempered martensite

Source: Ref 18

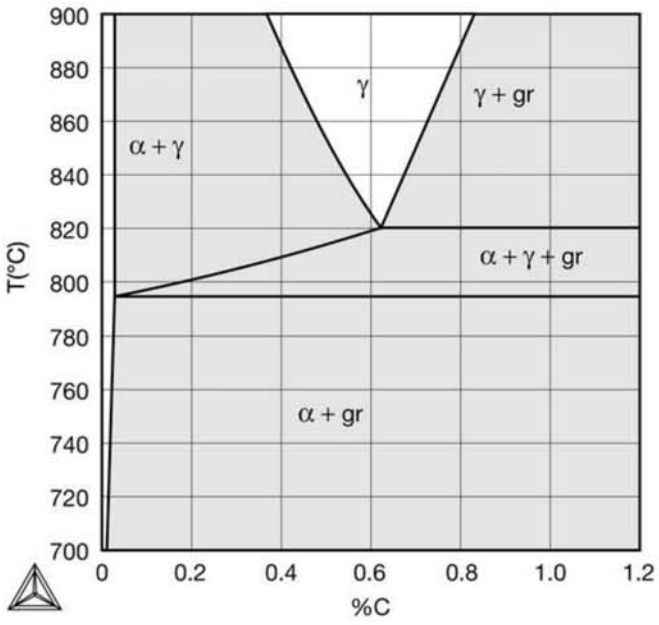

Fig. 17.84 Isopleth section (section with constant silicon content) at 2.5% Si of the Fe-C-Si phase diagram. Gr: graphite, α: ferrite, γ: austenite. Silicon increases the eutectoid equilibrium temperature. During cooling, austenite in equilibrium with graphite may start transforming to ferrite upon reaching the eutectoid temperature.

with a fully pearlitic and tempered martensite matrix (Fig. 17.86) were the classical options for high-strength parts. Pearlitic matrixes can be achieved with a normalization treatment with the proper adjustment of chemical composition, particularly elements such as copper and tin.

17.5.1 Austempered Nodular Cast Iron or Austempered Ductile Iron

Austempered nodular cast iron, normally known as austempered ductile iron (ADI), presents an excellent combination of strength, toughness, and wear and fatigue resistance that makes it a material of great interest for many engineering applications, including many in the automotive industry. These properties are associated with the interesting microstructures that can be formed with austempering. The high silicon content in these alloys prevents carbide formation carbides during austempering so that the microstructures formed are composed of bainite (or bainitic ferrite), retained austenite and graphite. This is similar to the effect of silicon used in TRIP steels, as discussed in Chapter 13, "Advanced Steels for Forming Operations." in this book. With these alloys, it is possible to reach mechanical strengths that are up to twice as great than those of conventional cast irons, as shown in Table 17.5.

The duration of the austempering treatment is selected so that the isothermal transformation to bainite (or bainitic ferrite) and retained austenite is completed but carbide formation, which could occur with longer times, is avoided (Ref 46). The temperatures used in the austempering cycle are adjusted according to the desired microstructure and accompanying properties. Figures 17.87–17.91 present some examples of the microstructure of austempered ductile iron.

17.5.2 Porosity in Ductile Cast Iron

Preventing pipe and porosity associated with solidification shrinkage is normally simpler when designing castings for cast iron parts rather than cast steel parts, but nodular cast irons may present porosity problems due to their solidification mode. Ductile iron solidifies, in general, without the formation of a solid shell and of a well-defined solidification front, as in the case of gray cast irons (Fig. 17.92). Thus, casting design must take this fact in consideration to avoid the formation of microcavities such as those shown in Fig. 17.93.

17.6 Compacted Graphite Iron (CGI) or Vermicular Graphite Iron (VG or GGV)

In Fig. 17.74 it is possible to observe that the transition from lamellar graphite (typical of gray cast iron) to spheroidized graphite (typical of ductile cast iron) is not sharp. An intermediate graphite morphology, called compacted graphite, occurs in between the two extreme morphologies. Not unexpectedly, the properties obtained in compacted graphite cast iron are also intermediate between those of gray and ductile cast iron. In particular, it is possible to reach a good combination of strength and toughness and maintain a high thermal conductivity. An example of the application of this type of cast iron is in the casting of diesel engine blocks (Ref 47). The morphology of compacted (or vermicular, the preferred term in non-English-speaking countries) graphite is complex and hard to characterize properly. Figure 17.94 presents the tridi-

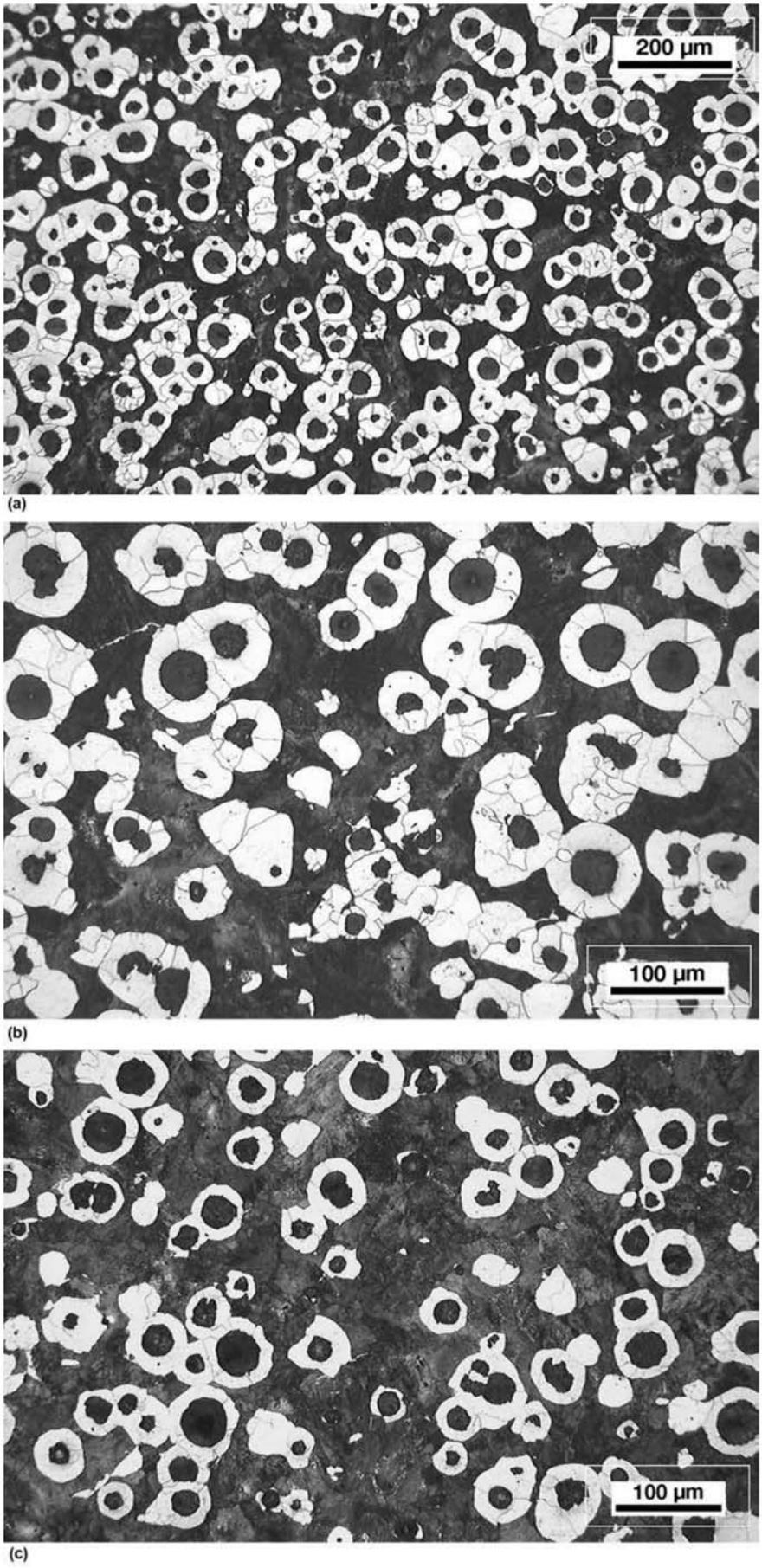

Fig. 17.85 Ductile cast irons with ferrite plus pearlite matrixes, with different volume fractions of ferrite. The ferrite is formed preferentially around the graphite nodules. Decreasing the ferrite volume fraction increases the strength, as in the case of steels. Courtesy of J. Sertucha, Azterlan, Centro de Investigacion Metalurgica, Durango, Bizkaia, Spain.

mensional aspect of this type of graphite. Figure 17.95 presents an example of a metallographic section of compacted graphite cast iron. The difficulty of imagining the structure presented in Fig. 17.94 from these two-dimensional

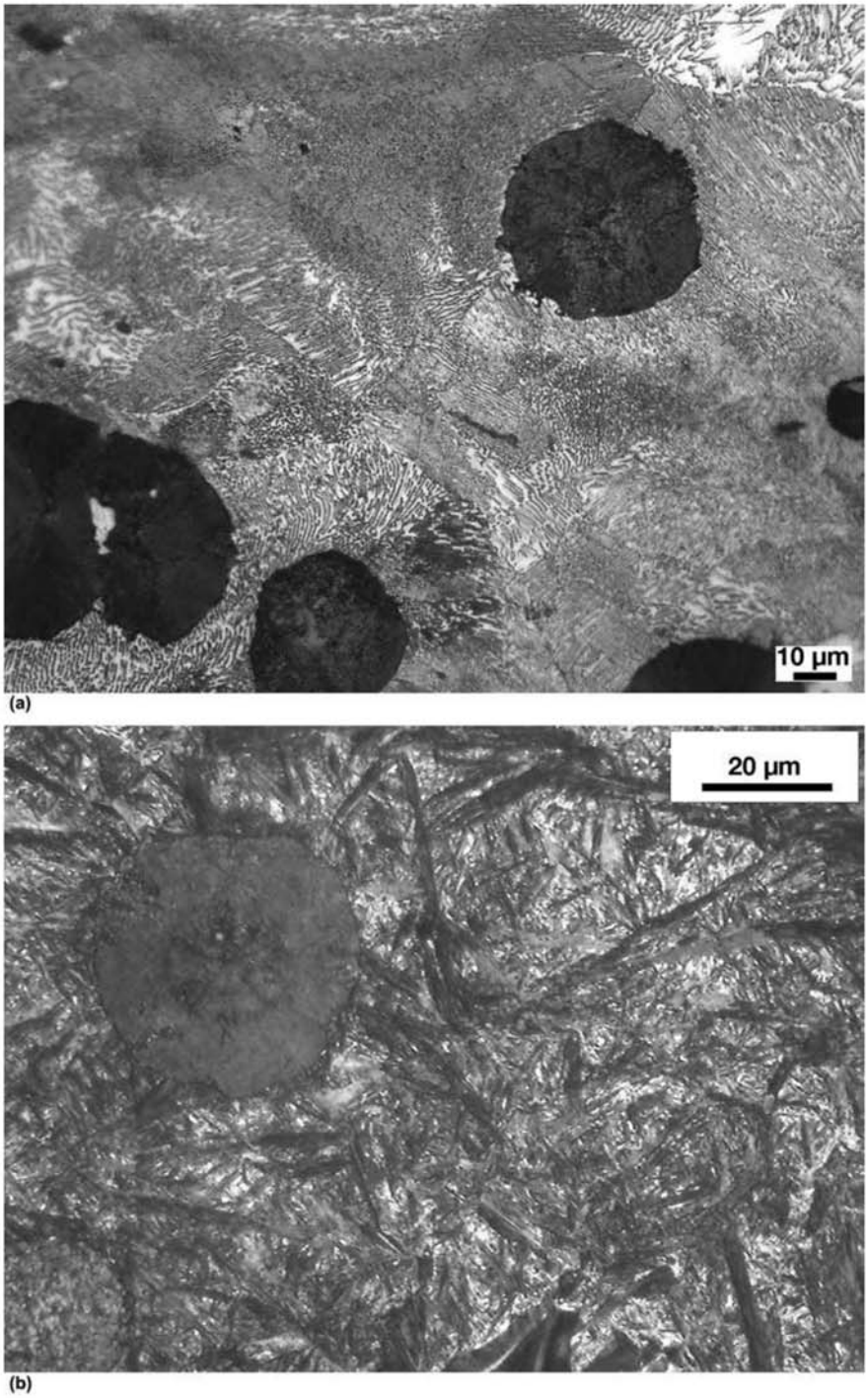

Fig. 17.86 Ductile cast iron with (a) pearlitic and (b) martensitic matrix. Etchant: nital. Courtesy of J. Sertucha, Azterlan, Centro de Investigacion Metalurgica, Durango, Bizkaia, Spain.

Table 17.5 Minimum specified mechanical properties for austempered ductile cast iron in accordance with ASTM A897

Grade ASTM A897	Tensile strength, MPa (ksi)	Yield strength, MPa (ksi)	Elongation, %	Toughness, Charpy V, J
1	850 (125)	550 (80)	10	100
2	1050 (150)	700 (100)	7	80
3	1200 (175)	850 (125)	4	60
4	1400 (200)	1100 (160)	1	35
5	1600 (230)	1300 (190)	…	…

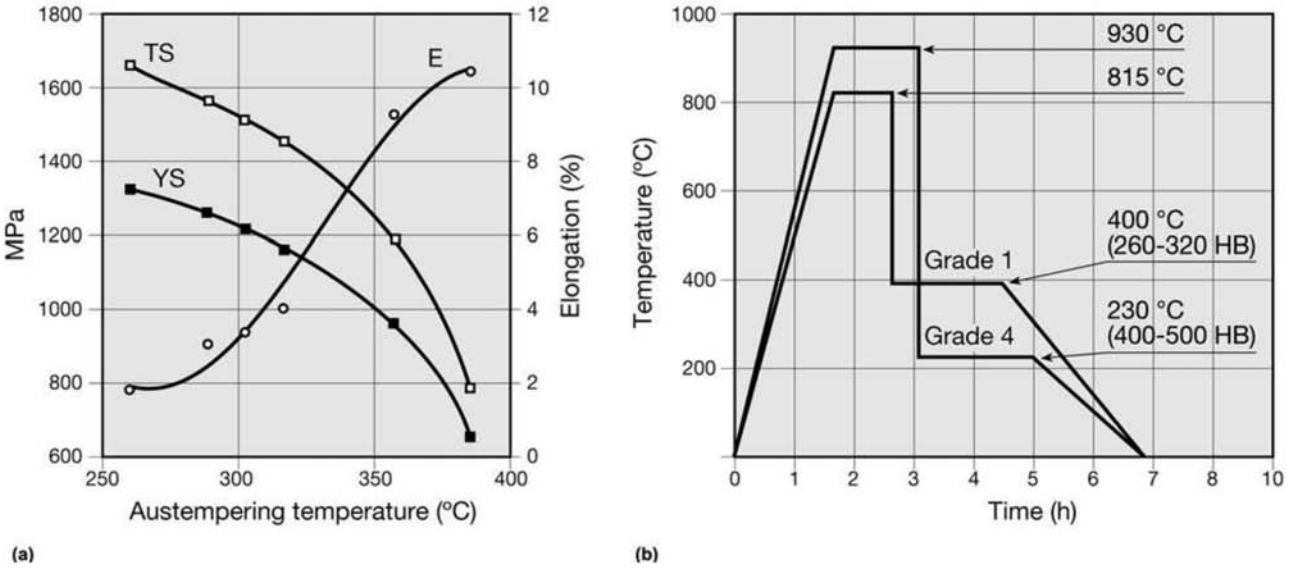

Fig. 17.87 (a) Effect of austempering temperature on the tensile properties of a ductile cast iron. Source: Ref 46. TS: tensile strength, YS: yield strength, E: elongation. (b) Examples of austempering cycles used with ductile iron to achieve different combinations of properties. The grades listed are those of ASTM A897. Source: Ref 18

cross sections is evident and highlights the importance of the three-dimensional reconstruction techniques, particularly when one attempts to derive quantitative relationships between the microstructure and properties.

17.7 Malleable Cast Irons

The first successful attempt at producing tougher cast irons is attributed to René-Antoine Ferchault de Réaumur (1683–1757) (Ref 48) a French scientist better known for a temperature scale named after him. In the decade of 1720-1730, Réaumur (Ref 18) developed what is presently known as whiteheart cast

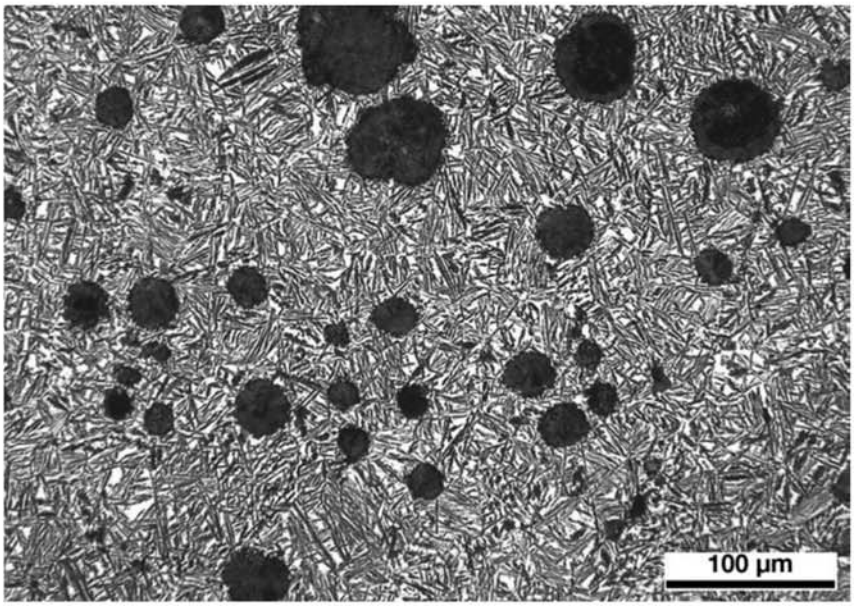

Fig. 17.88 Austempered ductile iron. Bainitic matrix (bainitic ferrite) and retained austenite (white areas). Structure known as ausferrite. Graphite nodules. Etchant: nital. Courtesy of J. Sertucha, Azterlan, Centro de Investigacion Metalurgica, Durango, Bizkaia, Spain.

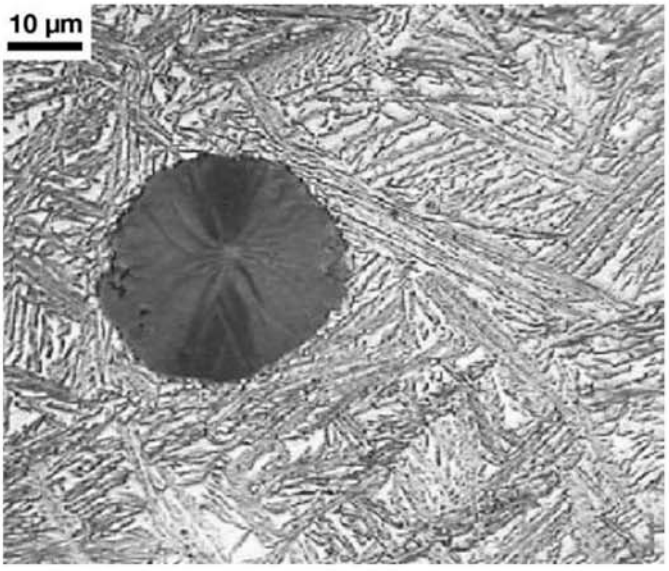

Fig. 17.89 Austempered ductile iron. Graphite, bainitic ferrite formed during austempering and retained austenite. Structure known as ausferrite. Etchant: nital. Courtesy of W. Guesser, Tupy Fundições, Joinville, SC, Brazil.

iron. In 1821, Seth Boyden developed and patented in the United States blackheart cast iron (Ref 49). Malleable cast irons, as a rule, solidify without graphite and are subjected to some form of heat treatment to transform carbides into graphite. The way the casting and the heat treatment is performed impacts on the final product and defines the differences between the two products.

17.7.1 Whiteheart Malleable Cast Iron

When producing whiteheart malleable iron, most common in Europe (Ref 50), the alloy is cast as a white cast iron, containing cementite in the eutectic

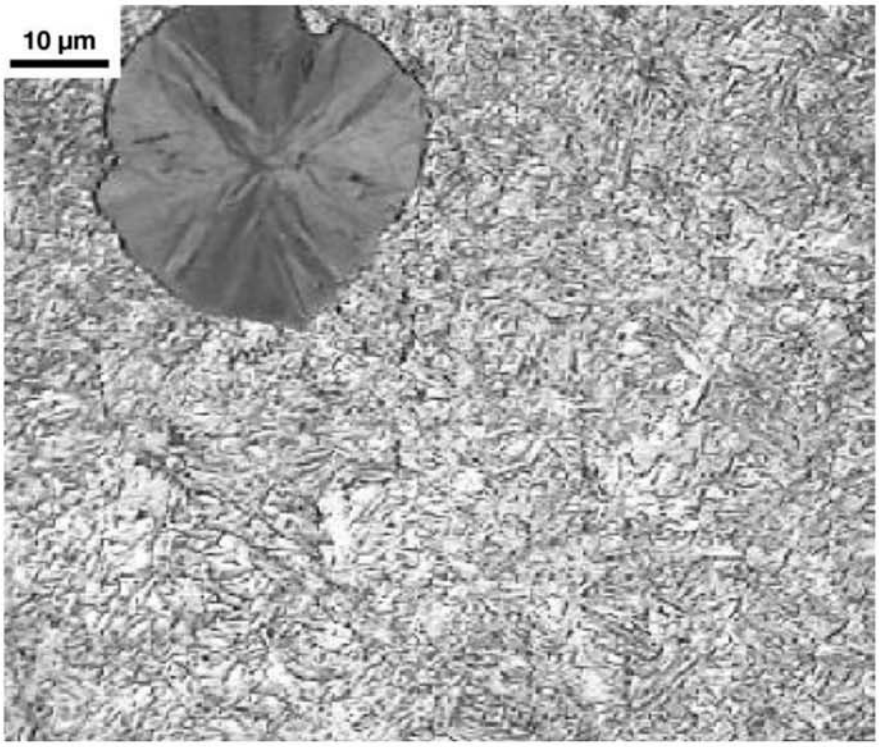

Fig. 17.90 Ductile cast iron subjected to surface hardening. Graphite, martensite, and retained austenite. Camshaft. HRC 56. Etchant: nital. Courtesy of W. Guesser, Tupy Fundições, Joinville, SC, Brazil.

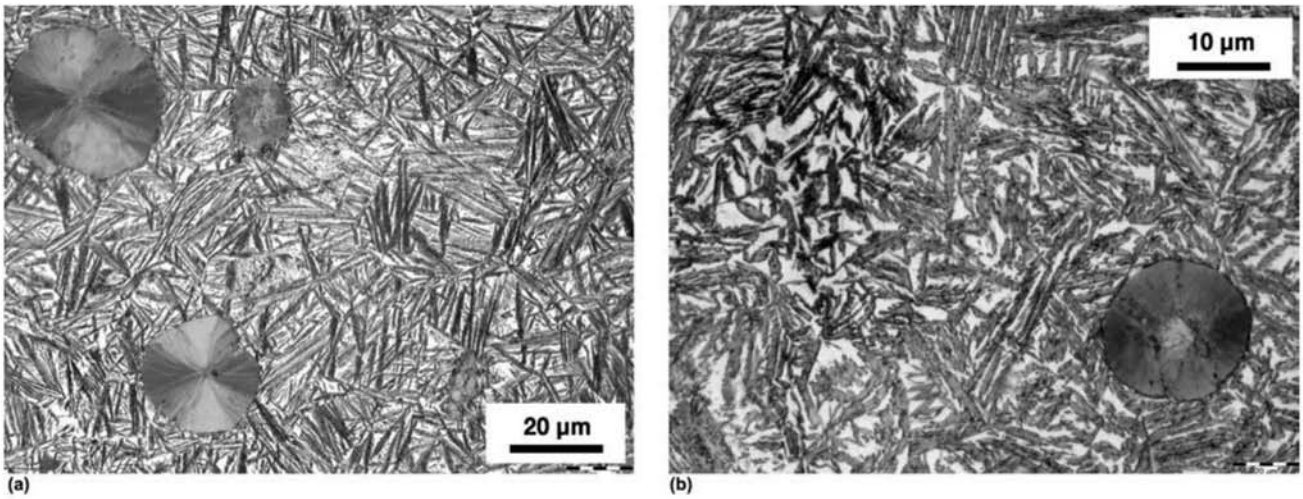

Fig. 17.91 (a,b) Austempered ductile cast iron. Beraha etchant is effective in the metallography of these alloys.

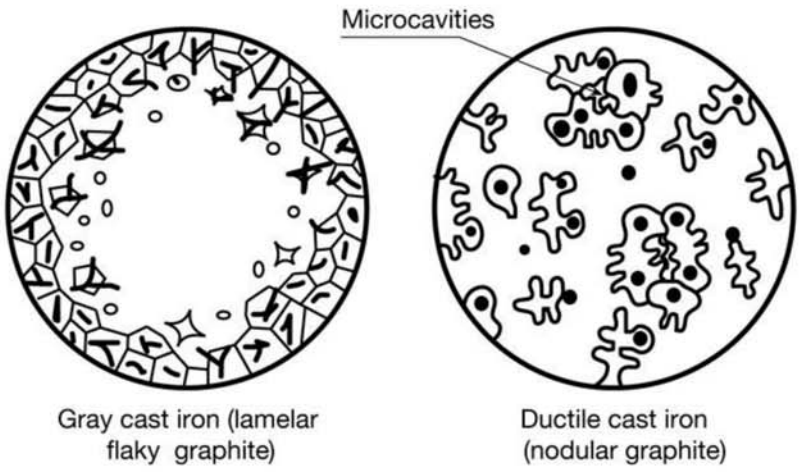

Fig. 17.92 Schematic representation of the solidification in a gray cast iron and in a ductile cast iron. Whereas the first solidifies with the formation of a solid shell, the second does not develop a well-defined solidification front. This may make microfeeding complicated and may originate porosity. Source: Ref 1

(ledeburite) and in pearlite. Later, the alloy is subjected to heat treatment. Thin parts decarburize totally, whereas larger parts present only a decarburized layer. The carbide decomposes to what is called temper graphite. It is possible to have different microstructures, such as a surface layer of ferrite, then mixtures of pearlite, ferrite, and temper graphite in different proportions. The material finds wide application in connections in Europe. Their fracture usually has a light aspect in the central region of the part, hence the name "whiteheart." They are most frequently used for parts with small thickness. Table 17.6 presents the usual range of composition for whiteheart malleable cast iron.

The annealing process used is a combination of decarburization and graphitization. An oxidizing medium is used. Packing in oxide or salt baths or oxidizing atmospheres have been used, at temperatures around 1070 °C (1960 °F). In Europe, this material is supplied in accordance with ISO 5922 (Ref 18, 51). Figures 17.96 to 17.100 show examples of microstructures of whiteheart malleable cast iron.

17.7.2 Blackheart Malleable Cast Iron

Even though the mandatory heat treatment after casting increases production costs, blackheart malleable cast iron is still an important alloy, even after the development of ductile iron. Ductile iron (see the section "17.5 Nodular Cast Iron or Ductile Cast Iron," in this chapter) is the best option when (Ref 5):

- Parts of larger dimensions are required, because to produce malleable iron, the whole cross section of the casting must be initially white cast iron)
- Casting shrinkage is an important aspect

On the other hand, malleable cast iron is preferred in the following cases (Ref 5):

- For small thickness castings
- For parts that will undergo cold forming, coining, or cutting
- When optimum machinability is desired

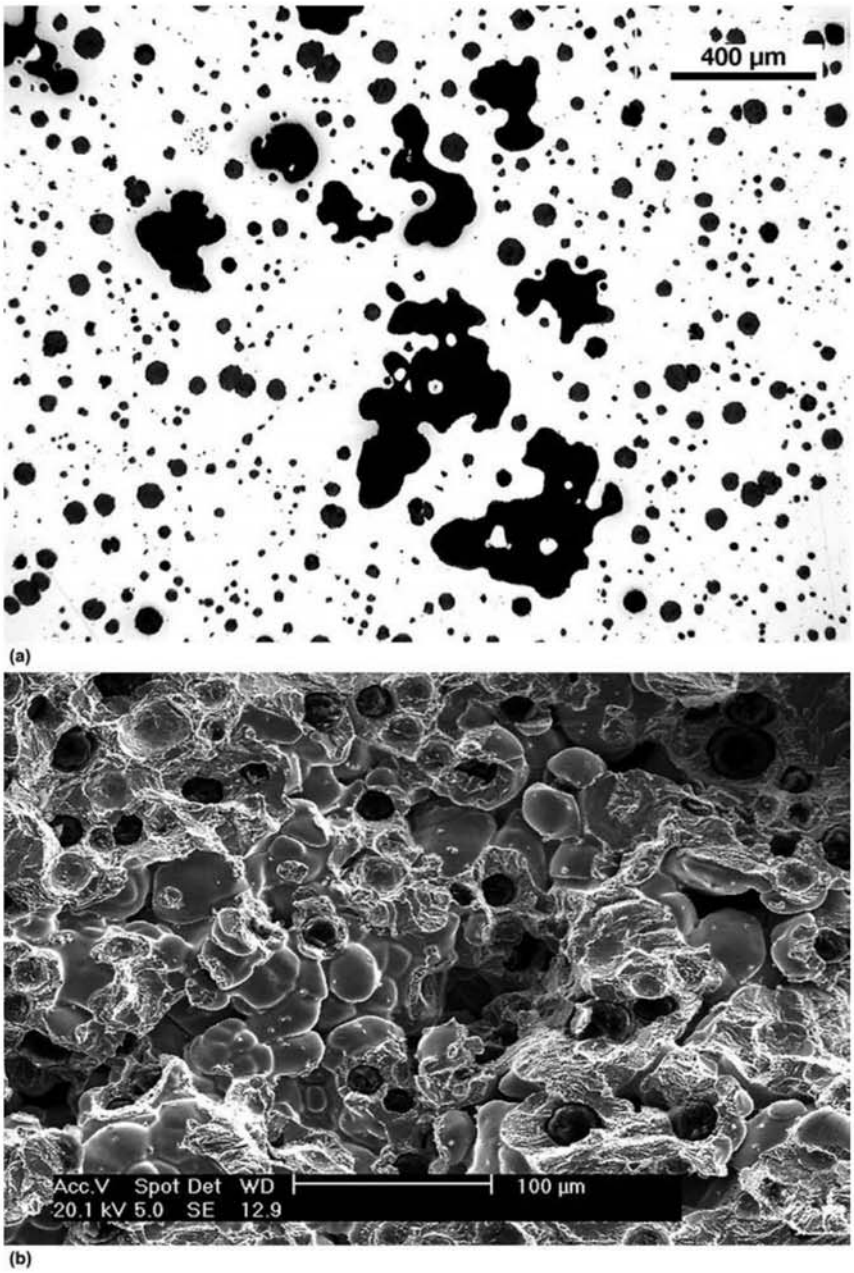

Fig. 17.93 Microporosity in ductile cast iron. (a) Not etched. (b) SE, SEM. Graphite nodules and the dendritic structure can be seen. Courtesy of J. Sertucha, Azterlan, Centro de Investigacion Metalurgica, Durango, Bizkaia, Spain.

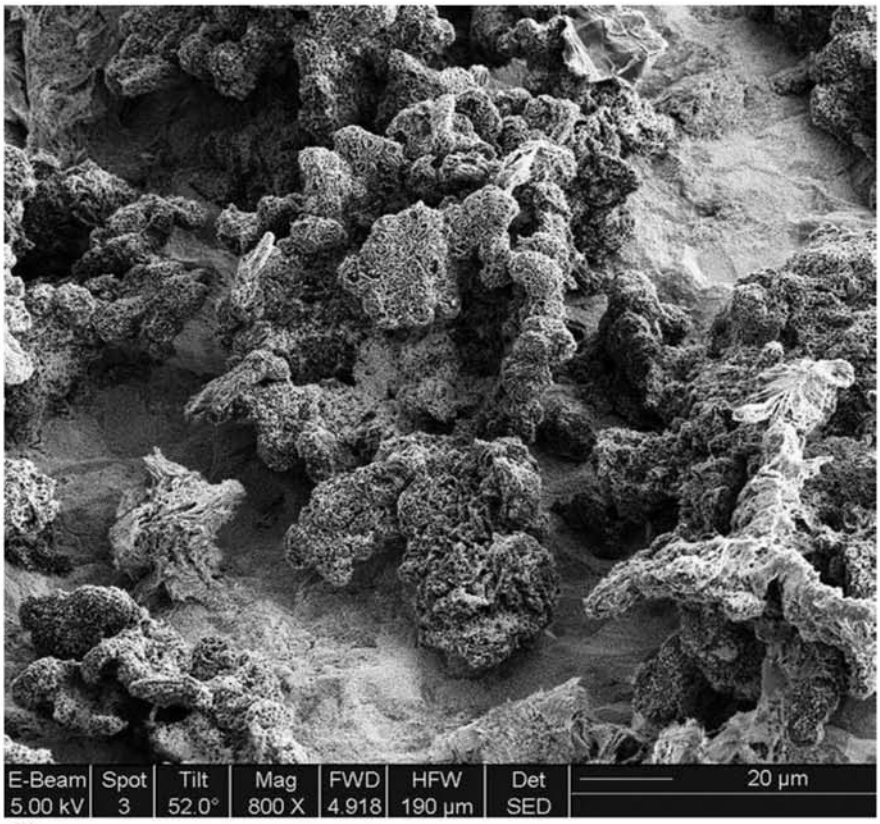

Fig. 17.94 (a) Vermicular or compact graphite in cast iron deep etched to completely dissolve the matrix. Etchant: nital 10%, 2 h. (b) Tridimensional reconstruction of vermicular (or compact) graphite in cast iron. Sectioning done by focused ion beam (FIB) and images by SE, SEM. Courtesy of A. Velichko and F. Mücklich, Universität des Saarlandes, Saarbrucken, Germany.

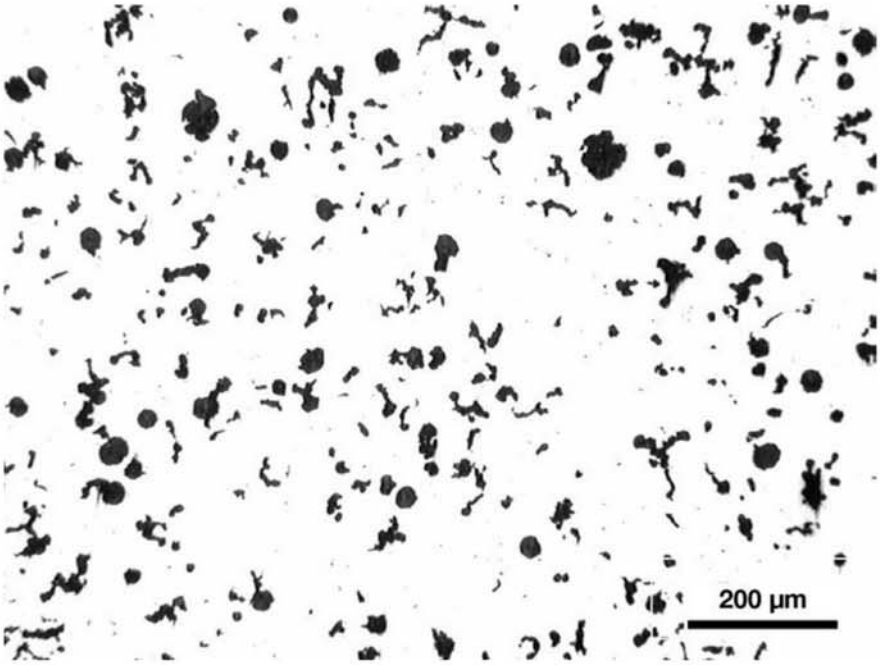

Fig. 17.95 Compact graphite in cast iron. Courtesy of J. Sertucha, Azterlan, Centro de Investigacion Metalurgica, Durango, Bizkaia, Spain.

Table 17.6 Typical compositions range for whiteheart malleable cast iron

Element	Before annealing, %	After annealing, %
Carbon	3.0–3.7	0.5–2.0
Silicon	0.4–0.8	0.4–0.7
Manganese	0.1–0.4	0.1–0.4
Sulfur	0.3, max	0.3, max
Phosphorus	0.1, max	0.1, max

Source: Ref 18

- When toughness at low temperature is required
- For parts with high wear resistance (martensitic malleable iron)

Malleable cast iron parts are supplied according to ASTM A197 (Ref 52). ISO 5922 (Ref 51) also covers blackheart malleable cast irons.

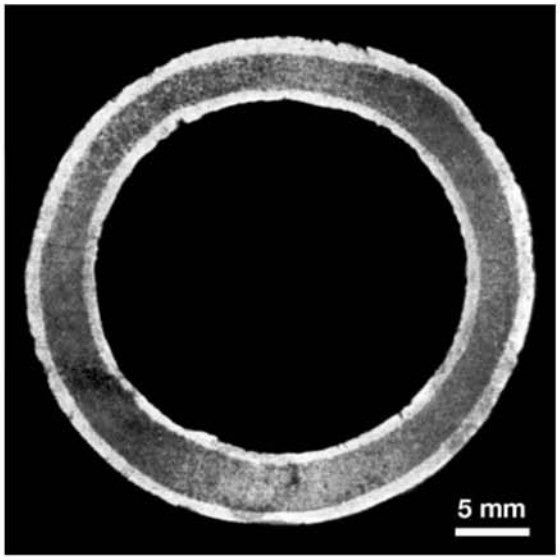

Fig. 17.96 Cross section of a connection made of cast iron that was transformed into malleable iron by decarburization (whiteheart malleable iron). The white region close to the surface is composed of ferrite (complete decarburization) and the darker region, closer to the center, is composed of ferrite and pearlite. Etchant: iodine.

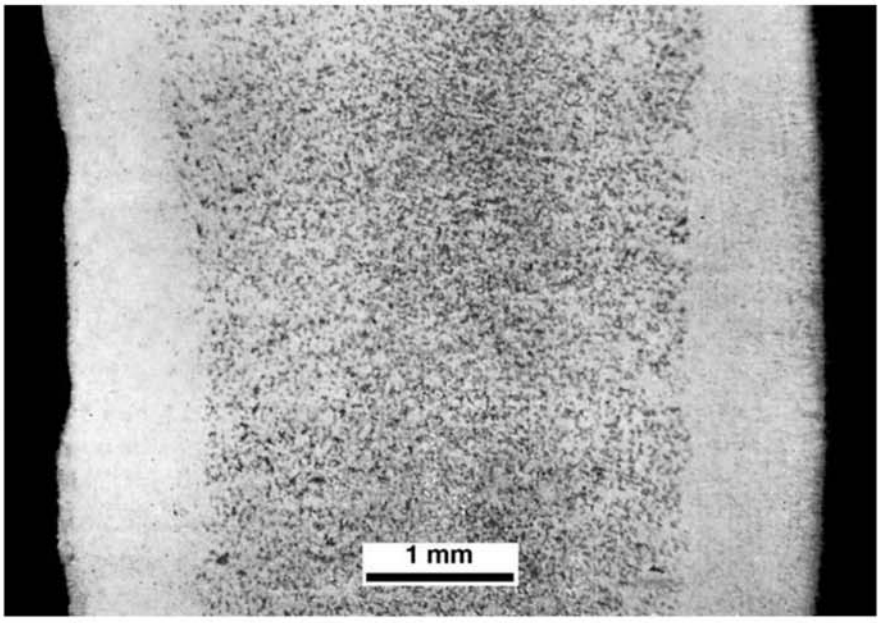

Fig. 17.97 Higher magnification of the structure of the part presented in Fig. 17.96. Etchant: picral.

Blackheart malleable cast iron is cast in conditions where the complete cross section solidifies as a white cast iron. Then it is subjected to a heat treatment where the cementite decomposes to temper graphite. Adjusting chemical composition and heat treatment parameters is important to reach the proper distribution and size of the temper graphite formed. Temper

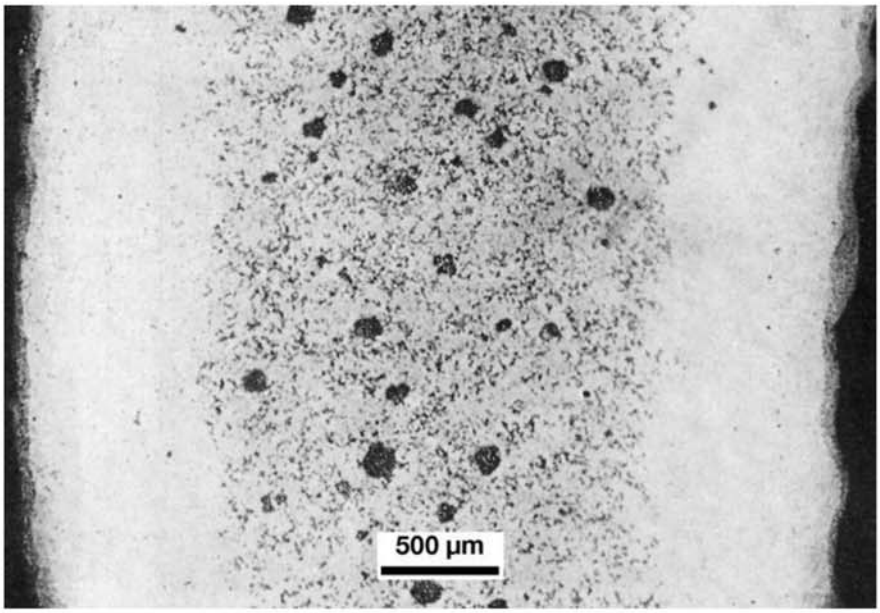

Fig. 17.98 Cross section of a part of whiteheart malleable iron produced by box decarburization using an oxidizing medium as decarburizing agent. Oxidized surface region, followed by fully decarburized ferritic layer. In the center region, temper graphite in a matrix of ferrite and pearlite. Etchant: picral.

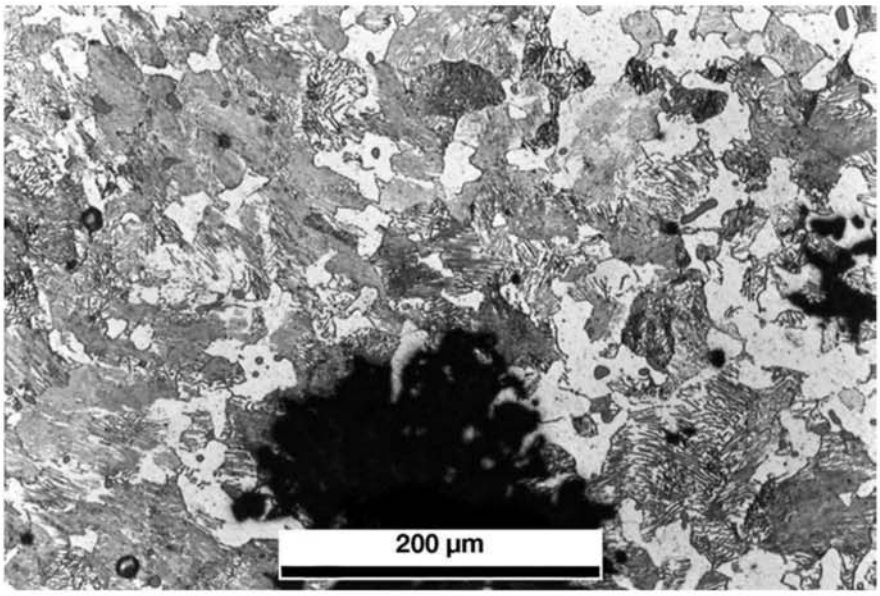

Fig. 17.99 Whiteheart malleable cast iron. Region that did not suffer decarburization. Ferrite, pearlite, and graphite. Sulfides can also be seen (gray tone). Courtesy of DoIT-PoMS, Department of Materials Science and Metallurgy, University of Cambridge.

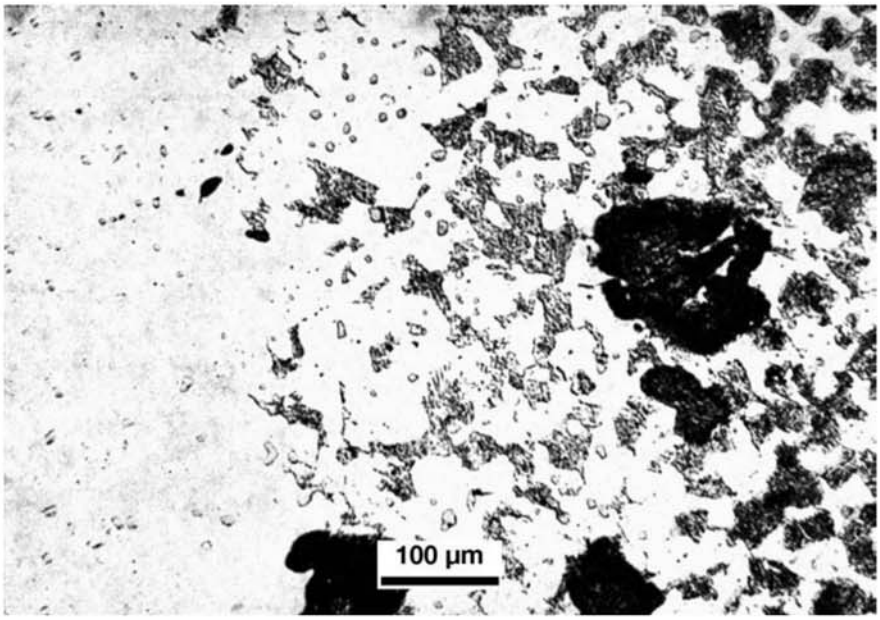

Fig. 17.100 Whiteheart malleable cast iron. Region between center and surface. To the left side of the image: ferrite. To the right side of the image: pearlite and temper graphite. The volume fraction of pearlite increases from left to right. Etchant: picral.

graphite is compact but less regular than the nodules formed in ductile iron, as indicated in Fig. 17.101 and 17.102. Classification and quantification of graphite in these cast irons is complex, and significant errors may be caused when a single nodule is intercepted more than once by a sampling plane. This results in discrepancies between the values of N_A (number of particles per area) and N_V (number of particles per volume) when they are measured using independent techniques. Conversely, larger sections through some particles can cause then to be mistakenly classified as nodular graphite (Ref 21). References 21 and 27 propose some ways to correct these problems when using quantitative metallography.

One of the practical difficulties in designing these alloys is that the chemical composition has to be adjusted so that no graphite is formed during solidification, but it must also be possible for graphitization to happen within a reasonable length of time during heat treatment (Ref 5).

Heat Treatment of Blackheart Malleable Iron

The heat treatment of blackheart malleable iron starts with a first cycle aimed at graphitization. This is performed at temperatures in the 900–970 °C (1650–1780 °F) range. Properly balanced compositions can be graphitized in 3.5 h; depending on the conditions of the starting casting and its chemical composition, times as long as 20 h may be required. After the graphitization stage, the thermal cycle should define the matrix microstructure. If ferrite is desired, a thermal cycle like the one presented in Fig. 17.103 is adequate. After 8–15 h at around 950 °C (1740 °F) the parts are cooled at 40–50 °C/h (70–90 °F/h) to 760 °C (1400 °F). From this temperature onward, cooling must be very slow to guarantee that ferrite formation is accompanied by the diffusion of

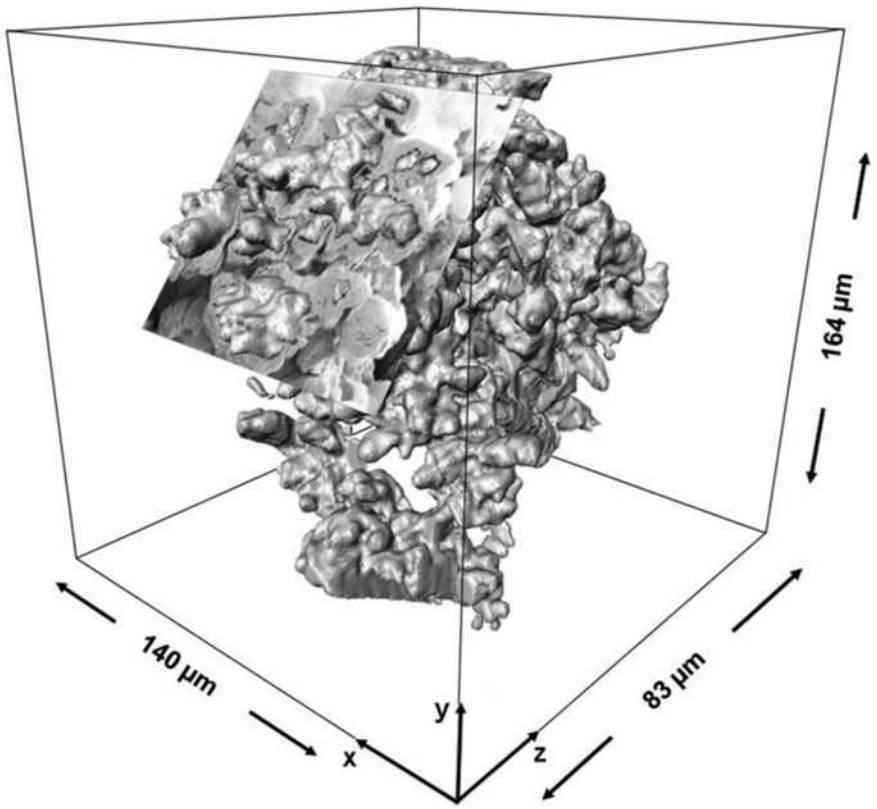

Fig. 17.101 Tridimensional reconstruction of temper graphite in malleable cast iron. Sectioning performed by focused ion beam (FIB) and images SE, SEM. Depending on the sectioning plane, it is possible to generate nonconnected cuts in the plane from a single graphite particle. Courtesy of A. Velichko and F. Mücklich, Universität des Saarlandes, Saarbrucken, Germany.

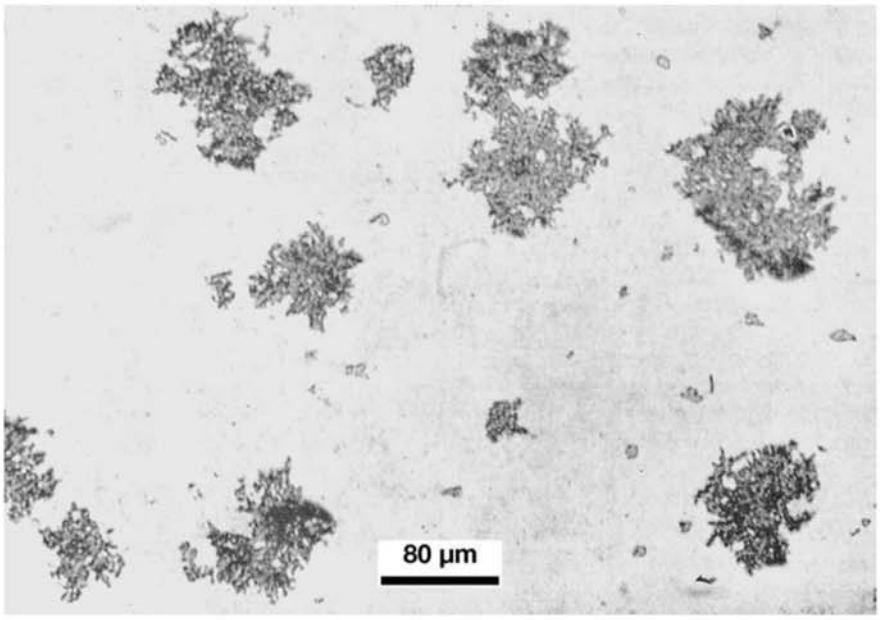

Fig. 17.102 Blackheart malleable iron. Temper graphite. Not etched.

carbon to the graphite nuclei. Rates of 3–10 °C/h (5–18 °F/h) up to 660–690 °C (1220–1275 °F), when the transformation is completed, are used (Ref 5, 53).

Figures 17.104 to 17.106 present microstructures of blackheart malleable ferritic cast iron. In view of the very long heat treatments, controlled atmospheres are essential to avoid surface decarburization. Atmospheres composed of CO/CO_2 mixtures with controlled dew points are used (Ref 5).

When graphite formation occurs during solidification, the flakes may oxidize during the heat treatment, resulting in microstructures with a defective surface region, as shown in Fig. 17.107 and 17.108. When the atmosphere is too rich in CO, the decomposition of cementite close to the part surface may be hindered, resulting in a surface layer of pearlite (Fig. 17.109).

When corrosion resistance is important, malleable cast iron may be galvanized, a common treatment for connections and similar parts (Fig. 17.110).

Other types of deviation might occur during the malleabilization treatment, as exemplified in Fig. 17.111. When higher strength is desired, malleable cast irons maybe heat treated to form a pearlite matrix or even a martensitic matrix, using cycles as indicated in Fig. 17.112. Depending on the original casting and the heat treatment cycle, malleabilization may lead to excessive ramification of the temper graphite, as shown in Fig. 17.113. Figure 17.114 presents an example of a malleable cast iron with a pearlitic matrix.

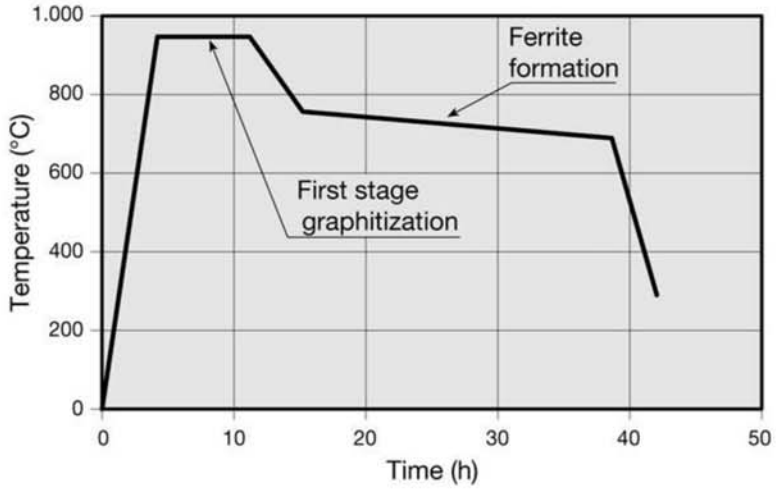

Fig. 17.103 Typical heat treatment cycle to obtain ferritic blackheart malleable iron. The first stage, in which cementite is transformed into graphite, may take as long as 8 h. The subsequent cooling in the austenitic range should cause graphite precipitation, avoiding supersaturation of the austenite with carbon. Finally, slow cooling in the intercritical region makes possible the growth of ferrite and the rejection of carbon to austenite, followed by its precipitation as graphite.

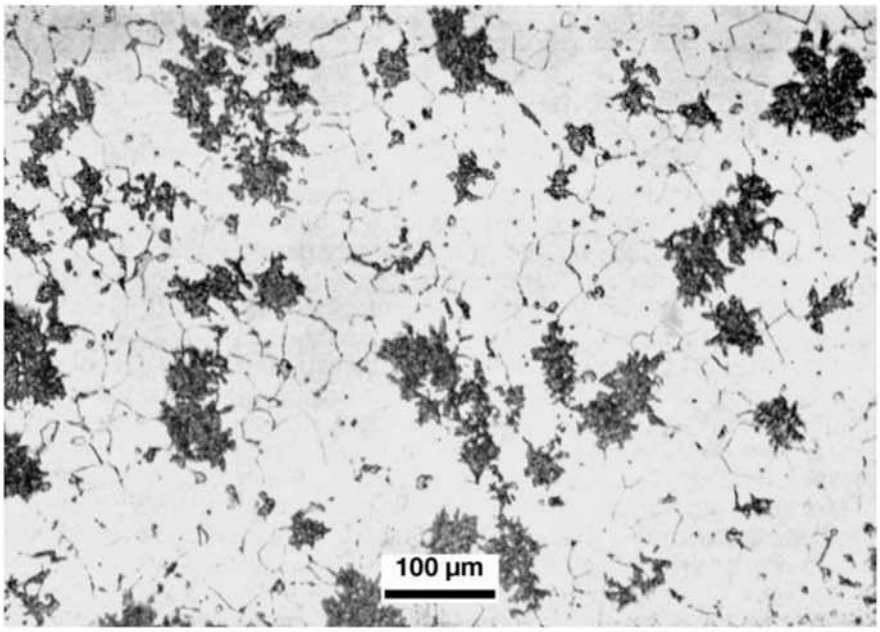

Fig. 17.104 Blackheart malleable iron. Temper graphite in a ferrite matrix. Etchant: picral.

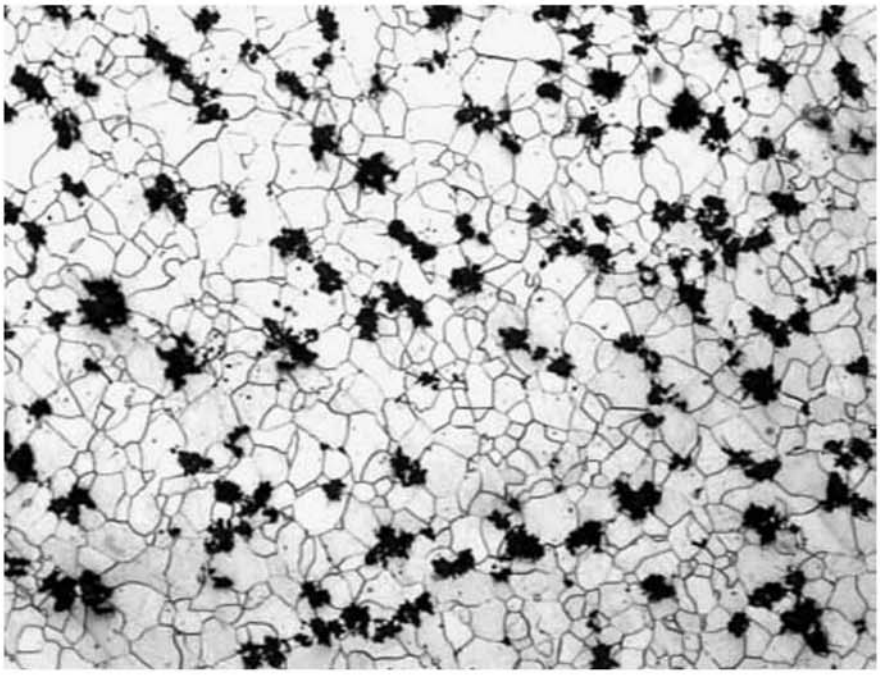

Fig. 17.105 Ferritic blackheart malleable iron. Temper graphite formed during annealing in a ferrite matrix. Etchant: nital. Courtesy of J. Sertucha, Azterlan, Centro de Investigacion Metalurgica, Durango, Bizkaia, Spain.

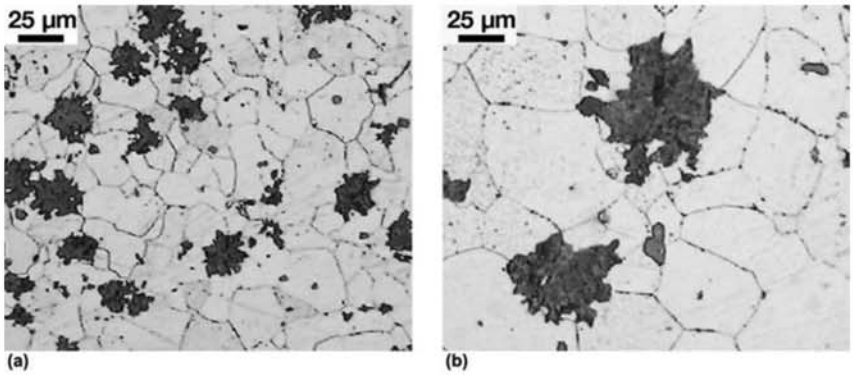

Fig. 17.106 Ferritic blackheart malleable iron. Temper graphite formed during annealing in a ferrite matrix. Some manganese sulfide inclusions are present. Etchant: nital. Courtesy of W. Guesser, Tupy Fundições, Joinville, SC, Brazil.

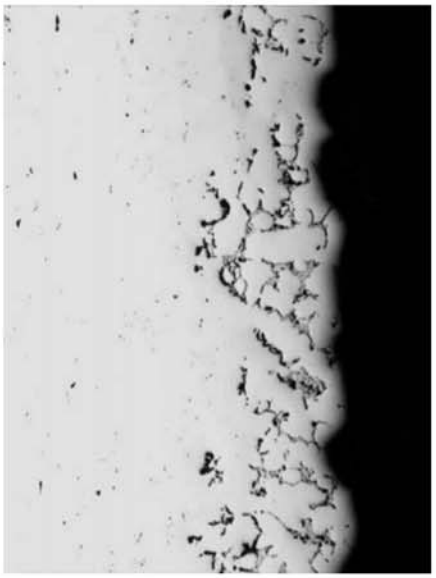

Fig. 17.107 Malleable cast iron, as cast (before the malleabilization heat treatment). The region close to the surface (to the right of the image) shows the formation of graphite due either to deviation in chemical composition or changes caused by the mold material. Courtesy of J. Sertucha, Azterlan, Centro de Investigacion Metalurgica, Durango, Bizkaia, Spain.

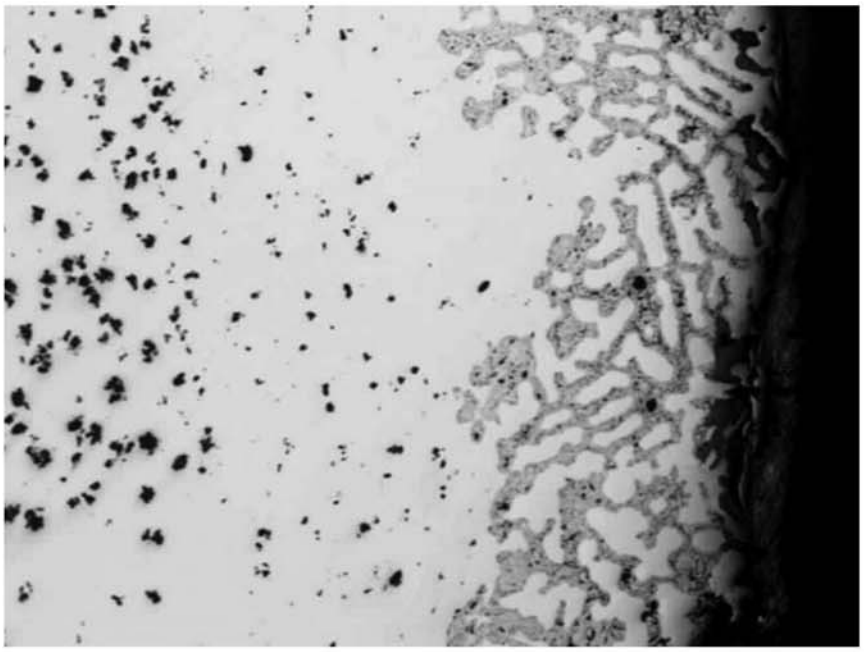

Fig. 17.108 Malleable cast iron that contained graphite close to the part surface in the as-cast condition. Extensive oxidation in the subsurface region (see the section "17.3.6 The Oxidation of Gray Cast Iron" in this chapter). Courtesy of J. Sertucha, Azterlan, Centro de Investigacion Metalurgica, Durango, Bizkaia, Spain.

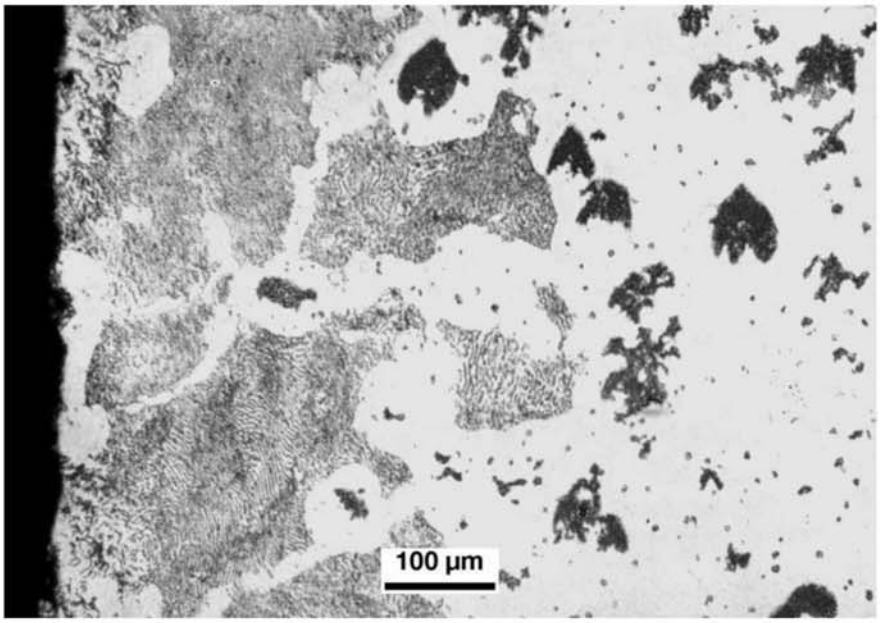

Fig. 17.109 Blackheart malleable iron heat treated in conditions in which a "frame" of pearlite is formed. Etchant: picral. This part has been heat treated using a nonreactive solid packing instead of inert controlled atmosphere. In this case, as shown, both silicon oxidation and decarburization can happen in the region very close to the part surface.

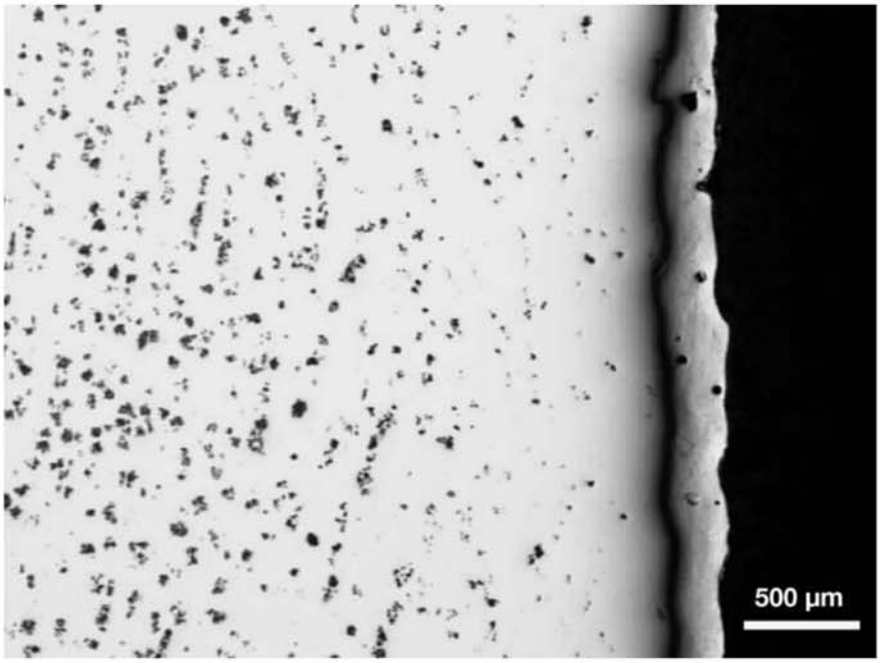

Fig. 17.110 Galvanized blackheart malleable iron (the zinc layer is to the right of the image). Not etched. Courtesy of J. Sertucha, Azterlan, Centro de Investigacion Metalurgica, Durango, Bizkaia, Spain.

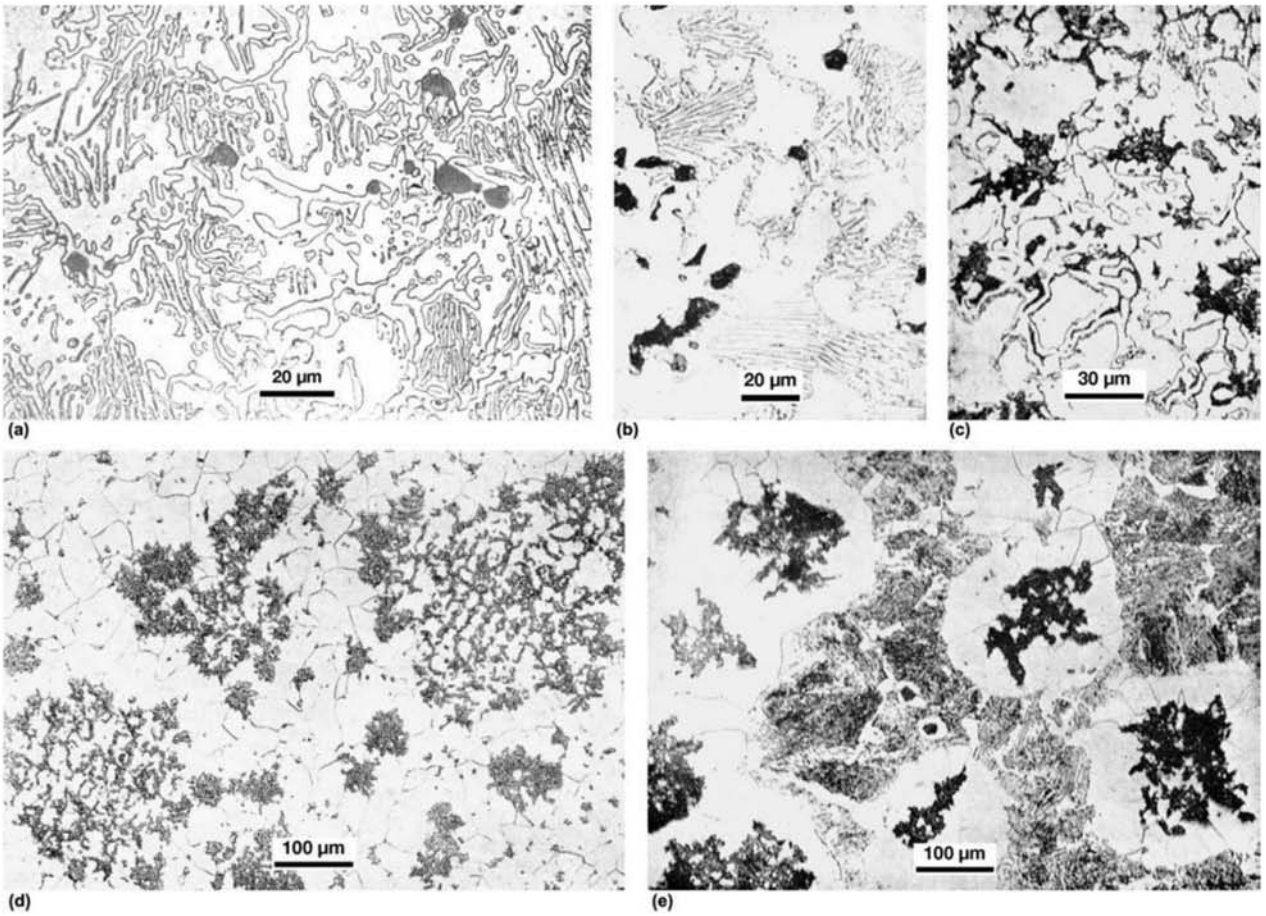

Fig. 17.111 Incomplete malleabilization treatment. (a) The cementite in pearlite has been spheroidized and coalesced, and large areas of ledeburite can be seen. Some manganese sulfide inclusions are present. Graphite has not been formed. (b) Pearlite is beginning to decompose and form temper graphite. (c) Graphite formation inside areas of cementite, still present in the microstructure. (d) Graphite formed is not compact in shape. (e) Blackheart malleable cast iron. (Compare to ductile cast iron structures, in the section "17.5 Nodular Cast Iron or Ductile Cast Iron" in this chapter, and Fig. 17.85). Etchant: picral.

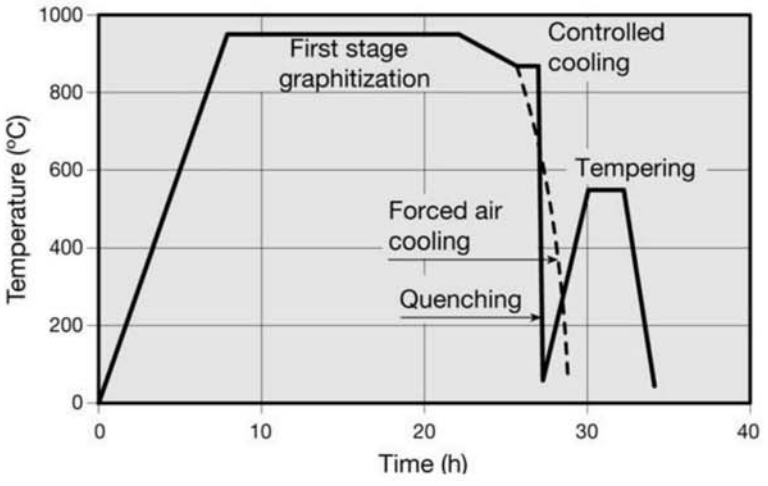

Fig. 17.112 Two possible heat treatment cycles to produce blackheart malleable iron having either pearlite or pearlite + martensite structures. After graphitization, controlled cooling takes the austenite to approximately 870 °C (1600 °F). (a) Still or forced air cooling, or (b) homogenization, quenching, and tempering.

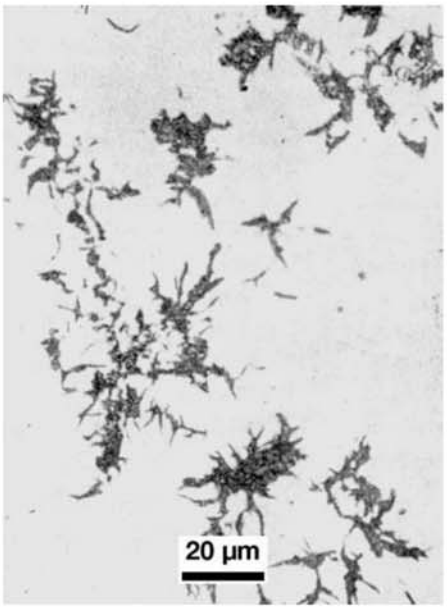

Fig. 17.113 White cast iron, produced by chilling, and annealed. Graphite is present.

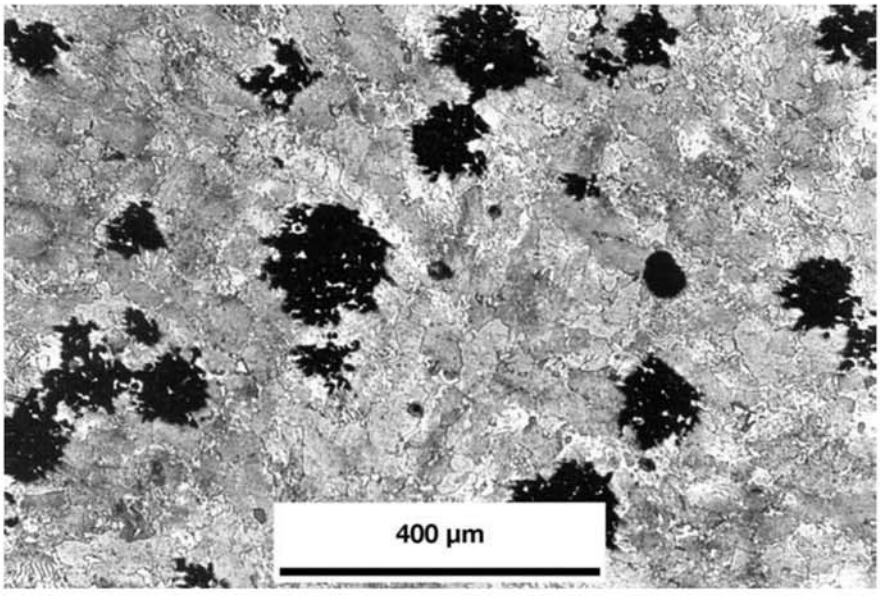

Fig. 17.114 Pearlitic blackheart malleable cast iron. Temper graphite in a pearlite matrix. Small regions of ferrite. Courtesy of DoIT-PoMS, Department of Materials Science and Metallurgy, University of Cambridge.

REFERENCES

1. D.M. Stefanescu, Solidification and modeling of cast iron—a short history of the defining moments, *Mat. Sc. Engin. A*, Vol 413–14, 2005, p 322–33
2. See http://www.sewerhistory.org/grfx/components/pipe-iron1.htm (accessed April 3, 2017)
3. See http://www.ironbridge.org.uk/collections/the-iron-bridge/ (accessed April 3, 2017)
4. C. Labrecque and M. Gagne, Review: Ductile Iron: Fifty Years of Continuous Development. *Can. Metall. Q.*,Vol 26 (No. 4), 1998, p 232–67
5. *Properties and Selection—Irons, Steels and High-Performance Alloys*, Vol 1, ASM Handbook, 10th ed., ASM International, 1990
6. R.C. Creese and G.W. Healy, Metallurgical Thermodynamics and the Carbon Equivalent Expression*, Metall. Trans. B*, Vol 16B, 1985, p 169–70
7. "Standard Test Methods of Chill Testing of Cast Iron," A367-11, ASTM, 2011
8. E. Frás, M. Górny, and H.F. López, The Transition from Gray to White Cast Iron during Solidification: Part III. Thermal Analysis*, Metall. Mat. Trans. A*, Vol 36A, 2005, p 3093–101
9. D. Maijer, S.L. Cockcroft, and W. Patt, Mathematical Modeling of Microstructural Development in Hypoeutectic Cast Iron, *Metall. Mat. Trans. A*, Vol 30A, 1999, p 2147–58
10. F. Mampaey, Solidification Mode and Feeding Behavior of Phosphorus Alloyed Gray Cast Iron, *AFS Trans.*, Paper 03-164(05), 2003, p 1–17
11. H.R. Abbasi, M. Bazdar, and A. Halvaee, Effect of Phosphorus as an Alloying Element on Microstructure and Mechanical Properties of Pearlitic Gray Cast Iron, *Mat. Sci. Engin. A*, Vol A444, 2007, p 314–17
12. J.M. Radzikowska, Effect of Specimen Preparation on Evaluation of Cast Iron Microstructures, *Mat. Character.*, Vol 54, 2005, p 287–304
13. *Metallography and Microstructures*, Vol 9, *ASM Handbook*, 10th ed., ASM International, 1990
14. M. Hillert and V.V.S. Rao, *The Solidification of Metals*, Iron and Steel Institute Publication n. 110, ISI, 1968
15. J.S. Park and J.D. Verhoeven, Directional Solidification of White Cast Iron, *Metall. Mat. Trans. A*, Vol 27A, 1996, p 2328
16. A. Mazur, M.M. Gasik, and V.I. Mazur, Thermal Analysis of Eutectic Reactions of White Cast Irons, *Scand. J. Metall.*, Vol 34, 2005, p 245–49
17. J. Helsing and G. Grimvall, Thermal Conductivity of Cast Iron: Models and Analysis of Experiments, *J. Appl. Phys.*, Vol 70 (No. 3), 1991, p 1198–206
18. J.R. Brown, *Foseco Ferrous Foundryman's Handbook*, Butterworth-Heinemann, 2000

19. D. Goettsch and J. Dantzig, Modeling Microstructure Development in Gray Cast Irons, *Metall. Mat. Trans. A*, Vol 25, 1994, p 1063–79

20. L. Dillinger, L. Polishing, *LECO MET TIPS #13*, 2002, https://www.leco.com/support/application-support-metallographic/metallographic-tips-2?task=document.viewdoc&id=281 (accessed April 6, 2017)

21. A. Velichko, C. Holzapfel, and F. Mücklich, 3D Characterization of Graphite Morphologies in Cast Iron, *Adv. Engin. Mat.*, Vol 9 (No. 1–2), 2007, p 39–45

22. A. Velichko and F. Mücklich, 3D-Analysis of Complex Microstructures: Quantification and Classification by FIB/SEM—Nanotomography, *G.I.T. Imag. Microsc.*, Vol 3, 2007, p 40–42

23. A. Velichko, C. Holzapfel, A. Siefers, K. Schladitz, and F. Mücklich, Unambiguous Classification of Complex Microstructures by Their Three-Dimensional Parameters Applied to Graphite in Cast Iron, *Acta Mat.*, Vol 56 (No. 9), 2008, p 1981–90

24. A. Velichko, *Quantitative 3D Characterization of Graphite Morphologies in Cast Iron Using FIB Microstructure Tomography*, doctoral dissertation, Universität des Saarlandes, 2008

25. "Standard Test Method for Evaluating the Microstructure of Graphite in Iron Castings," A247-16a, ASTM, 2016

26. "Microstructure of Cast Irons—Part 1: Graphite Classification by Visual Analysis," 945-1:2008/Cor 1:2010, ISO, 2008; and "Microstructure of Cast Irons—Part 2: Graphite Classification by Image Analysis," TR 945-2:2011, ISO, 2010

27. A. Velichko and F. Mücklich, Shape analysis and classification of irregular graphite morphology in cast iron, *Prakt. Metallogr.*, Vol 43 (No. 4), 2006, p 192–208

28. D.M. Stefanescu, Modeling of Cast Iron Solidification—The Defining Moments, *Metall. Mat. Trans. A*, Vol 38A, 2005, p 1433–47

29. W. Oldfield, A Quantitative Approach to Casting Solidification—Freezing of Cast Iron, *Trans. ASM*, Vol 59, 1966, p 945

30. G.L. Rivera, R.E. Boeri, and J.A. Sikora, Solidification of Gray Cast Iron, *Scripta Mat.*, Vol 50 (No. 3), 2004, p 331–35

31. G. Rivera, P. Calvillo, R. Boeri, Y. Houbaert, and J. Sikora, Examination of the Solidification Macrostructure of Spheroidal and Flake Graphite Cast Irons Using DAAS and ESBD, *Mat. Charact.*, Vol 59 (No. 9), 2008, p 1342–48

32. A. Sauveur, *Metallography and Heat Treatment of Iron and Steel*, 4th ed., McGraw-Hill, 1935

33. John Edward Stead, *Grace's Guide to British Industrial History*, http://www.gracesguide.co.uk/John_Edward_Stead (accessed on April 7, 2017)

34. V. Raghavan, C-Fe-P (Carbon-Iron-Phosphorus), *J. Phase Equil. Diff.*, Vol 25, 2004, p 541–42

35. G.M. Goodrich, T.G. Oakwood, and R.B. Gundlach, How do Manganese, Sulfur Levels Affect Gray Iron Properties?, *Mod. Cast.*, Vol 96, 2006, p 42–44

36. C.G. Schon and A. Sinatora, Hot Rolling Mill Roll Microstructure Interpretation: A Computational Thermodynamics Study, *J. Phase Equil.*,- Vol 22 (No. 4), 2001, p 470–4

37. A. Rivaróli Jr., R.R. Xavier, C.E.R. Santos, M.A. Carvalho, and A. Sinatora, Desenvolvimento de cilindros em aço rápido para a laminação de não-planos, In: 40 Seminário de Laminação—*Processos e Produtos Laminados e Revestidos*, ABM, 2003

38. Mahle, Camshaft, passenger car, http://www.mahle.com/mahle/en/products-and-services/passenger-cars/valve-train/camshafts/index.jsp#castcamshafts (accessed April 7, 2017)

39. M. Willcox, Ultrasonic Velocity Measurements Used to Assess the Quality of Iron Castings, *Insight NDT*, 2000, http://insightndt.com/papers/technical/t012.pdf (accessed December 2007)

40. R.B. Gundlach, DIS (Ductile Iron Society) Research Project n. 37: *Nodularity, its Measurement and its Correlation with the Mechanical Properties of Ductile Iron*, Stork Climax Research Services for Ductile Iron Society, 2006 http://www.ductile.org/member/researchactivity/proj37.pdf (accessed June 2008)

41. D.D. Double and A. Hellawell, The Nucleation and Growth of Graphite—The Modification of Cast Iron, *Acta Metall. Mat.*, Vol 43 (No. 6), 1995, p 2435–42

42. J.A. Brzostek and W.L. Guesser, Producing As-Cast Ferritic Nodular Iron for Safety Applications, *Proceedings of the 65th World Foundry Congress*, Gyeongju, Korea, 2002

43. I. Riposan, M. Chisamera, and S. Stan, Factors Influencing Microstructure and Mechanical Properties of As Cast and Heat Treated 400-18 Grade Ductile Cast Iron, *Int. J. Cast Met. Res.*, Vol 20 (No. 2), 2007, p 64–67

44. M. Wessén and I.L. Svensson, Modeling of Ferrite Growth in Nodular Cast Iron, *Metall. Mat. Trans. A*, Vol 26ª, 1996, p 2209–20

45. J. Lacaze, Transformação Eutectóide direta e inversa em ferros fundidos, *Metal. Mat. ABM*, Vol 57 (No. 516), 2001, p 697–99

46. P.P. Rao and S.K. Putatunda, Influence of Microstructure on Fracture Toughness of Austempered Ductile Iron, *Metall. Mat. Trans. A*, Vol 28A, 1997, p 1457–70

47. W. Guesser, Ferro fundido com grafita compacta, *Metal. Mat.*, June 2002, p 403–5

48. Wikipedia, René Antoine Ferchault de Réaumur, 2007, http://en.wikipedia.org/wiki/Ren%C3%A9_Antoine_Ferchault_de_R%C3%A9aumur

49. Wikipedia, Seth Boyden, 2007, https://en.wikipedia.org/wiki/Seth_Boyden

50. Whiteheart Malleable Iron Connections, http://malleableironfittings.com/iron-foundry/white-heart-malleable-iron/, http://www.gfps.com/traisen/en/products_and_solutions/products_traisen/malleable-cast-iron-fittings_traisen.html (accessed April 9, 2017)
51. "Malleable Cast Iron," 5922:2005, ISO, confirmed 2014
52. "Standard Specification for Cupola Malleable Iron," A197/A197M-00(20015), ASTM, 2015
53. F. Tupy, *Conexões Tupy—Catálogo*

Metallography of Steels—Interpretation of Structure and the Effects of Processing
Hubertus Colpaert
Updated and Translated by André Luiz V. da Costa e Silva

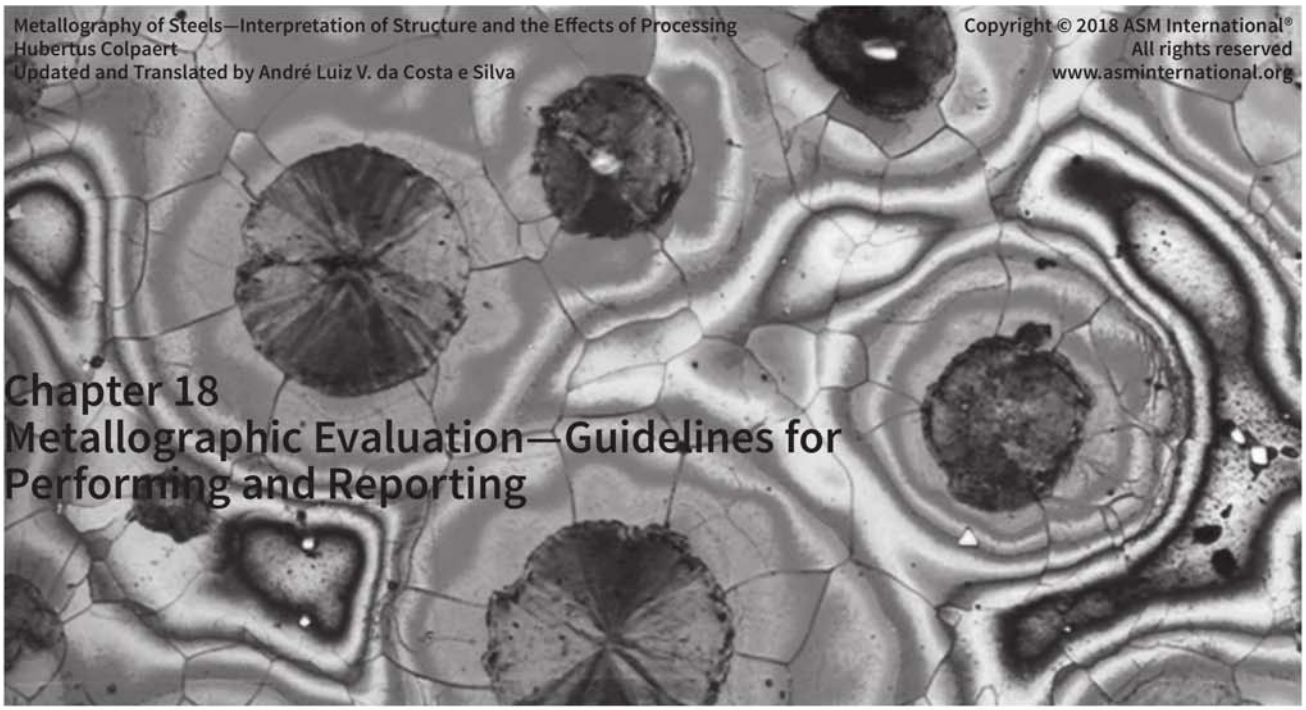

Chapter 18
Metallographic Evaluation—Guidelines for Performing and Reporting

Metallographic evaluation is a valuable tool in metal characterization, particularly for steels and cast irons. To guarantee that useful and reliable results are generated using this technique, care in planning a performance methodology is essential. Likewise, care and attention to the presentation of the results are essential to ensure that the results can be properly understood and used.

In this chapter, basic guidelines on points that deserve attention in the performance of metallographic exams, regardless of the technique in question, are presented. Basic suggestions on how to report the results of these investigations are also given. The main objective of these suggestions is to make sure that once prepared, reports will be clear and properly understood by the reader and no doubts are left about the results obtained.

18.1 The Objectives of Metallographic Evaluation

In general, a steel or a cast iron is subjected to metallographic evaluation with one of the following objectives in mind:

- To measure a micro- or macrostructural feature of an item
- To test a hypothesis related to the behavior or performance of an item
- To investigate structure-related causes of a given behavior or performance of an item

It is very important to clearly understand the differences between these objectives so that the metallographic evaluation will be properly performed and reported. In all cases measurements are performed, and it is important to clearly distinguish if the final objective of the evaluation is simply to measure a given feature or to test a certain hypothesis on this feature. Furthermore, while metallographic investigations end up testing hypotheses, it is essential to start with an open framework instead of directly starting the investigation with a single hypothesis in mind to be tested, as this dramatically limits the possibilities of an investigation.

The characteristics of each type of evaluation and its specific aspects are discussed next.

18.2 The Measurement of Micro- or Macrostructural Features

18.2.1 Management Systems and the Competence of Laboratories

Performing measurements is fundamental to the understanding of any phenomenon. A growing concern about the reliability of measurements performed in different laboratories has led to consolidating several concepts and guidelines mostly related to management systems and to testing methods in laboratories. ISO standard 17025 (Ref 1) sets general requirements for the competence of testing and calibration laboratories, regardless of their size or the extent of tests or calibrations performed. ISO 17025 defines "quality assurance" requirements like those of ISO 9001 (Ref 2). In addition, ISO 17025 defines technical requirements concerning the methodologies to be used for testing and calibrations. These requirements cover the basic care that any laboratory must have to be considered competent performing a given measurement.

It is interesting to note that for a long time, laboratories that were focused on research—either academic or technological—attempted to dismiss the need for quality assurance methods and well-defined and reproducible methods when performing tests, alleging that research is a creative activity and quality assurance methodology could only be introduced when activities were consolidated as routine, typically the opposite of what would be expected from research activity.

It has since been well established that reliability in the results of measurements performed during research or development can only be guaranteed if the tests, exams, and measurements are performed with proper basic concerns for traceability, proper identification, correct calibration, and proper recording—typical concerns addressed by an adequate quality management system.

Although it is evident that the creative process inherent to research and development cannot be described in a written procedure or standard, the measurements that demonstrate the results reached during tests and exams, fundamental to research and development in engineering and technological activities, can only be useful if performed within a framework that ensures reliability, typical of a quality management system, as described by the standards mentioned above.

18.2.2 The Measurement Method

When one wants to measure a micro- or macrostructural feature, the first decision concerns the method to be used. If the evaluation is to be done in accordance with a defined (by the client, for instance) standard or specification, the method should be defined in this document and strictly followed.

Many methods established in standards and specifications have an essentially comparative character or are used to indirectly inform users about a different feature of the material. It is thus of fundamental importance that the conditions defined in the standard are completely adhered to, even if the per-

son performing the analysis believes there is a better or more efficient way to measure the feature in question.

Conversely, if the method is not defined a priori, it is important to completely and clearly define it before the start of the test activities (such as sample removal). In this case, there are essentially two options:

- The selection of a national, international, or widely accepted standard for the performance of the evaluation. In the absence of those, methods defined by well-reputed technical organizations, published in reputable journals, or even prescribed by the equipment manufacturer may be acceptable.
- The definition of an internal methodology, suitable to the evaluation in question.

When methods prescribed by standards are used, it is important that the laboratory ensures that it is prepared to properly perform the tests in accordance with that method. When methods that are not prescribed in standards must be used, method validation is of paramount importance. According to ISO 17025, "validation is the confirmation by examination and the provision of objective evidence that the particular requirements for a specific intended use are fulfilled." It is thus essential to confirm, in a reliable, traceable, and properly documented way, that the method provides the desired results whenever it is used.

These concepts are not just applicable to laboratories looking for accreditation according to ISO 10725:. Instead, they should be viewed as common sense and a practical road map for any laboratory that intends to generate reliable results, regardless of whether they will be part of an undergraduate research project, a thesis or dissertation, a forensic technical report, quality control documentation, or a report of a development project.

It should be evident that the section titled "Methods" or "Materials and Methods" in a publication "should provide sufficient information to allow replication of the results" (see, for instance Ref 3). However, the trend of accepting reduced information on materials and methods observed in recent decades in many reputable journals is making the independent verification of published results more difficult, a condition that has been a fundamental requirement in scientific publications for centuries.

Although in a limited number of cases commercial confidentiality may be the alleged cause for not properly revealing materials and methods, it is debatable if these results should be published as research or protected as patents or similar.

In the following sections, some of the aspects that must be considered before the start of any measurement process and that are critical to the correct performance of metallographic analysis are presented.

Sampling

Steels and cast irons present heterogeneities originating from various sources, as discussed at length in the previous chapters in this book. Metallographic examination must thus carefully consider the position and orienta-

tion of the portion of the material to be sampled. Depending on the technique used, the region that will be observed and analyzed may be as small as hundreds of square micrometers. Evidently, how representative this sample is of the part features is a highly relevant question.

When developing a test method or when studying a standardized method, it is important to clearly identify all the aspects related to sampling and, once they are identified or defined, strictly follow them. Should the standardized method fail to properly define any of the relevant sampling details (position, orientation, depth in the product, heat treatment condition, acceptable techniques for removing and preparing the sample, etc.) it is essential to define them as well. Should the analysis be performed for a third party (the client), it is fundamental to obtain agreement to these decisions. Table 18.1 presents some of the more important aspects to be considered when sampling steel or cast irons and some examples of the sampling criteria used.

The discussion in previous chapters made clear that the results of metallographic examination will be strongly dependent on sampling decisions. Two simple examples are:

- The amount and type of nonmetallic inclusions observed is strongly influenced by:
  - Position of the sample with respect to the solidification process (top or bottom of an ingot, see Chapter 8, "Solidification, Segregation, and Nonmetallic Inclusions," in this book)
  - Thermomechanical treatments performed (the effect of hot working on nonmetallic inclusions, for instance, see Chapter 11, "Hot Working," in this book)
  - Detailed position in the part—surface, mid-radius, or center results in bars or plates are significantly different
  - Orientation of the sampling plane with respect to working. The relative area occupied by nonmetallic inclusions and the aspect ratio of the inclusions are directly dependent on the orientation of the plane selected for observation in a wrought product (see Chapter 11).
- Microstructure
  - In engineering steels, for instance, the volume fraction of martensite formed depends on the cooling rate and hence on the position of the part and the distance from the sampled position to the free surfaces during quenching (see Chapter 10, "Conventional Heat Treatment: Basic Concepts," in this book)
  - In structural steels (see Chapter 14, "Structural Steels and Steels for Pressure Vessels, Piping, and Boilers," in this book), the microstructure is also strongly affected by cooling conditions and hence the sampling position is critical
  - When the material is cold worked, evaluation on a transverse plane may not show it (see Chapter 12, "Mechanical Work of Steels: Cold Working," and Chapter 14 in this book), whereas this feature is easily observed on a longitudinal plane

Table 18.1 Some of the main aspects considered when sampling steel or cast iron products and examples of sample criteria used

Feature of the sampling process	Examples of sampling criteria
Number of samples with respect to the amount of liquid metal produced (in a heat)	• One sample per heat • One sample per remelting (ESR or VAR) heat • One sample per casting ladle • One sample of cast metal per hour of operating the casting process
Sampling position with respect to the solidification product	• Sample at the position corresponding to the ingot top, in the part • Sample the top and bottom of a continuous cast plate • Sample the first and last continuous cast plate in a heat • Sample a "keel block" produced with the same metal as the part and cast as defined in applicable standard • One sample at the top and bottom or remelted ingot (ESR or VAR)
Heat treatment or thermomechanical treatment condition	• Sample the continuous casting plate or billet before any working • Sample after final heat treatment of part • Sample with simulated heat treatment • Sample of the wire rod to be used to manufacture the items
Position of sample in part (discards)	• Mid-thickness ($t/2$) at least t distance from any free surface during heat treatment • Mid-thickness ($t/2$) and at the center of the product width, at least t distance from any free surface during heat treatment • At $t/4$ position (or $r/2$) and at least $t/4$ or $r/2$ from any free surface during heat treatment
Orientation of the plane to be sampled (or of the specimen to be subjected to mechanical testing)	• Working related definitions –Longitudinal: parallel to the major working direction –Transverse: transverse to the major working direction –Short transverse (or normal): transverse to the major working direction and normal to the formed surface • Geometric definitions –Axial, radial, tangential

Traceability of Identification

The rigorous control of all information that would completely reconstruct the sampling process is a critical point in any metallographic analysis. It is essential to preserve, in all steps of sample preparation, all information related to exactly where the sample was taken from, which sample surface is closer or farther to the surface, is the longitudinal direction in the sample (one must remember that to properly characterize the examined plane, the information about *two* directions is needed!), and so on.

If any of this information is lost, the reliability of the examination and its results is seriously compromised. Because samples tend to change in shape and size during preparations for various reasons, such as size reduction as sample preparation proceeds and surface wear by grinding, polishing, etching, and so on, it is essential to conceive a clear and organized identification system for samples and specimens that will make it possible, beyond any doubt, to recover all information about the origin of the sample. Combining ink marking (that may be defaced by cleaning procedures, chemical etchants, etc.) and mechanical marking with stamps or engraving pens (which can damage the samples by changing them, for instance, by deformation) must be conceived, as well as a failsafe code using letters and numbers that will condense the information to account for the limited size of the final specimen. The ease of access to digital photography makes it a very useful recording tool for sampling steps that are not routine or for a clearly understandable record of the sample procedure and a clear relation of the sample to the sampled part. Once again, the system must be conceived in advance, without improvisation, and rigorous discipline is necessary to make sure all steps are correctly followed and recorded. Otherwise, confidence about the exact origin of the sample and how it relates to the part will be weakened or even lost. Unfortunately, it is just too common that once a laboratory is questioned in detail about sample position, orientation, which face was closer to the part surface, and so on, lack of proper controls becomes evident.

Stages in the Method

Most metallographic examination methods include a series of sequential steps of sampling, sample preparation, etching, evaluation, measurement, recording, and preparation of the report. In general each step is relatively simple, but it is not uncommon that some step is overlooked, even by technicians very experienced in the exam according to the method under consideration. The best way of avoiding this source of errors is advance preparation and the use of a checklist to control and register the performance of every step of the method and preclude overlooking and skipping a step.

18.2.3 Calibration

The first step in properly understanding any phenomenon involves measuring a quantity that can be related to it. Lord Kelvin expressed this with great insight (Ref 4) when he stated that one cannot claim to understand any phenomenon unless the observations can be expressed in numbers or quantities. A basic condition for the performance of meaningful quantitative mea-

surements is proper calibration of the measuring system. Length is one of the most common quantities measured in metallography, and doing so requires calibrations that are traceable to primary and international standards. There is a common confusion, particularly in academic research laboratories, involving the quality and age of the instruments with accuracy and associated uncertainties and the need for calibration. Whereas an instrument may have outstanding reproducibility and very little dispersion in the measurement results, this is no guarantee that the value measure is indeed correct: this is only possible by following the proper standard for calibration.

One of the most important variables in metallography, on which essentially all other measurements depend, is the magnification of the instrument employed in the examination. In the case of optical microscopes, ASTM E1951 (Ref 5) defines the applicable calibration procedures. It is important to emphasize once again that there is no assurance that a brand-new microscope will be properly calibrated, unless it is accompanied by a valid calibration certificate. For scanning electron microscopes, ASTM E766 (Ref 6) gives orientation about the calibration procedures. The most relevant deviations that can be observed in SEMs have been demonstrated in a systematic manner in Ref 7, which should be read by anyone responsible for an SEM. Thus, to generate reliable measurements, any optical or electron microscope must be subjected to periodic calibrations to ensure that measured dimensions can be relied on.

Furthermore, the use of microanalytical techniques, even the so-called standardless techniques, cannot dispense with an adequate calibration system for all the used instruments, to avoid the risk of generating results that are not dependable.

Uncertainties (Ref 8, 9)

When a measurement is performed, the result is an estimate of the measurand (the quantity to be measured). Uncertainty is a parameter associated with the result of a measurement and can be correlated with dispersion of the values that can reasonably be attributed to the measurand (Ref 9). Presently, the information on the uncertainty of a given measurement is a very important parameter, widely used to evaluate the results reported. Present practice is very well described in a NIST document (Ref 8) and involves identifying, for a given measurement process, all sources of measurement uncertainties and quantifying them, using either statistical methods or other practices. The combined value of all uncertainties allows one to understand the total uncertainty of a given measurement and identify the main factors that play a role in this uncertainty. A good example of the evaluation of uncertainty in quantitative metallography is given Ref 10. The complete evaluation of the uncertainty of all methods used in a laboratory is also a requirement of ISSO 17025.

Digital Treatment of Images

As computational techniques and digital photography have evolved, it has become common practice to acquire images digitally and use processing tools to treat these images. This is done with commercial software or sometimes with software developed in house.

Notwithstanding the fact that these techniques are becoming widespread, it is necessary that the user have a firm knowledge of the transformations caused in the images by the applications of the tools. Furthermore, it is essential that one evaluates to what extent these techniques may alter the information contained in the original image. A good discussion of the questions involved in the digital processing of images can be found in Ref 11 and 12.

In some fields of science, the problems associated with the changes caused by digital imagery have already been identified and are receiving careful attention. A large part of the changes induced by digital tools do not damage the image or cause relevant changes: cropping and improving contrast, gamma, and brightness to increase the visibility of sample features are common transformations and are generally acceptable. The effects of changes in brightness and contrast on image segmentation for quantitative metallography is an example of a case where even those "simple" changes may cause relevant modifications.

In some cases, however, attempts at making some features of the images more evident may eliminate valuable information or raise suspicion of image manipulation (Ref 13). Some journals, for instance, have already defined explicit rules about the type and extent of permissible digital manipulation of images (e.g., *Journal of Cell Biology*) (Ref 14). In general, transformations that affect the whole image (changes in brightness and contrast, for instance) are accepted if they are clearly indicated, whereas transformations that produce localized changes in images are considered unacceptable.

Furthermore, essentially all automatic equipment that performs quantitative metallography examinations rely on applying transformations on the acquired image to make possible the measurement of the desired feature. When a standard exists that defines the techniques to be used, as, for instance, in the case of the image segmentation methods for counting nonmetallic inclusions according to ASTM E1245, adopting the standardized method guarantees at least using a method that has been previously validated (see the section "18.2.2 The Measurement Method," in this chapter). When, on the other hand, other mathematical transformations and/or image transformation methods are used, it is important to completely understand the effects of the relevant variables in the method on the results of the measurement and the associated uncertainty.

18.3 Testing a Hypothesis

The second classical application of metallographic examination is as a tool in the testing of a hypothesis. While the scientific method uses a systematic formulation of hypothesis tests, it is not rare that insufficient time and attention are dedicated to clearly define this stage of the investigation in an explicit and recorded way. As a result, the hypothesis is not always expressed in a sufficiently clear and explicit formulation, nor are the criteria for its acceptance or rejection clearly defined. This may mislead investigators and result in mistaken conclusions about the relationships between processing, structural characteristics and properties, or performance of the material.

Some simple examples of hypotheses that can be formulated with respect to steels and tested using metallographic techniques are:

- The austenitizing temperature of a given steel in a certain process has an effect on the final ferritic grain size of the product.

- There is a correlation between the ferritic grain size of a given steel and its yield strength.
- For a given steel, there is a correlation between the volume fraction of phases present and its hardness.

In the case of cast irons, some examples of hypotheses that could be tested are:

- Adding a certain amount of a given inoculant results in the formation of a certain type of graphite.
- The thickness of the critical section, below which a given cast iron composition will solidify as a white iron, depends on the sulfur content in the alloy.

In many instances, tests or research projects involve testing hypotheses. Based on theoretical knowledge or previous experience, the researcher supposes that a certain process (and hence structural) change will result in a specific effect (usually the desired effect, the final objective of the project). Once the hypothesis is formulated, it is necessary to define:

- Which tests will be used to test if the hypothesis is true or not
- Which criterion will be used to judge the test results and then decide on the acceptance or rejection of the hypothesis

In the first stage, care should be taken in the design of the experiments to guarantee that the effect of the variable one wants to study will indeed be evaluated. The number of variables interfering on micro- and macrostructure of steels and cast irons is so vast that it is usually impossible to isolate a single variable during the performance of tests. Design of experiments (DoE) techniques are useful to eliminate or understand the effect of other variables and the interaction between the effects of different variables.

The second stage is especially important because it is extremely difficult for a researcher not to develop some bias toward a certain result of the test of hypothesis. Should the hypothesis be formulated by the researcher him- or herself, it is difficult to avoid the expectation that the results will confirm it. Unfortunately, this attitude might lead to the absence of an independent, unbiased analysis of the results. From the conceptual standpoint, the best way of proving a hypothesis is to strongly endeavor to prove it wrong. A very challenging philosophical discussion contrasts Francis Bacon (to whom the scientific method is attributed) and Karl Popper (1902–1994). Popper argued that truth should be sought by elimination instead of verification. The basic argument is that the elimination (by proving the negative of the hypothesis) is indisputable, whereas the confirmation, using induction based on observations and tests, will never be completely unchallengeable (according to Popper). Indeed, if many tests cannot discredit a hypothesis, the chances that it is truthful are very large.

However, this approach is seldom found in investigations to test hypotheses. In any case, before starting the tests some questions must be unequivocally answered:

- What will be the criterion for the acceptance or rejection of the result of a given test? It is not uncommon to see tests considered invalid or "outliers" for poorly defined reasons. This appears to be more frequent, unfortunately, when the results disagree with the hypothesis that is being tested.
- Which will be the criterion for the judgment of the hypothesis? The quantitative results obtained with metallographic examination come, as previously discussed, from small volumes of material and are subjected to the inherent variations associated with the structural variability in materials. A statistical criterion must normally be established to compare values, taking into account not only averages but also their statistical dispersions.

Once the basic conditions of the test of hypothesis are defined, the performance of the actual tests and exams can be started, as discussed in the section "18.2 The Measurement of Micro- or Macrostructural Features," in this chapter.

18.4 The Investigation

Performing an investigation adds a new complexity to the problem of testing a hypothesis, described in the previous section, "18.3 Testing a Hypothesis." In an investigation, in principle, one wants to identify the reason for a certain observation: frequently, a deviation with respect to expected performance, during processing or during use (in this case, a "failure").

The first and probably more critical step in this process involves collecting sufficient information to enable the formulation of the various hypotheses to be tested. The achievement of a satisfactory result when testing a hypothesis in a normal procedure can be considered satisfactory regardless of proving or negating the formulated hypothesis. In the case of an investigation, however, the work cannot be considered properly concluded if a cause for the observation cannot be identified.

The most likely risk in an investigation is thus not getting to formulate the proper hypothesis. Evidently, in many cases the data available to the investigator are not sufficient to formulate the right hypothesis, and even if the correct one can be formulated, sometimes it is not possible to properly test it. In any case, a basic rule in an investigation is that the collection of data and factual information should be done, to the maximum extent possible, without any preconceived hypothesis. The sooner in an investigation that a hypothesis is formed, the more likely is the information collection to be limited or biased and thus, the chances of reaching a correct and satisfactory conclusion are reduced.

Figure 15.24 in this book presented the example of a fracture of a railroad axle. In the image, the wheel is still mounted on the axle and one can observe that the fracture occurred in a plane essentially transverse to the axle longitudinal axis and very close to the internal face of the wheel.

A considerable number of metallographic evaluations were performed in samples removed from the region where the fracture started, in an attempt at identifying the probable causes of the failure. The selected techniques focused on fractographic examination of the initiation point and SEM examination of the fracture surface in this location in an attempt to find significant discontinuities that could have caused the crack to start. Another technique

focused on the visual examination of the external surface of the axle, in search of stress raisers caused, for instance, by machining, as shown in Fig. 18.1.

Only when an examination aimed at quantifying the nonmetallic inclusion population and distribution was carried out close to the axle surface (caused by the observations of Fig. 18.1) was a weld repair in the fracture initiation region detected. Railroad axles are not supposed to be welded or weld repaired (this is forbidden in the applicable specification), as they are similar to forged AISI 1050 steel, so the hypothesis that the axis could have been welded had initially been unconsciously discarded. A macrographic examination of the region close to fracture—that would have immediately revealed the weld—was not included in the original investigation testing plan and was only performed afterward, as shown in Fig. 15.25 in this book. Even though the root cause of the failure was correctly identified in the end, this example is didactic, demonstrating that what is perceived as unexpected is frequently

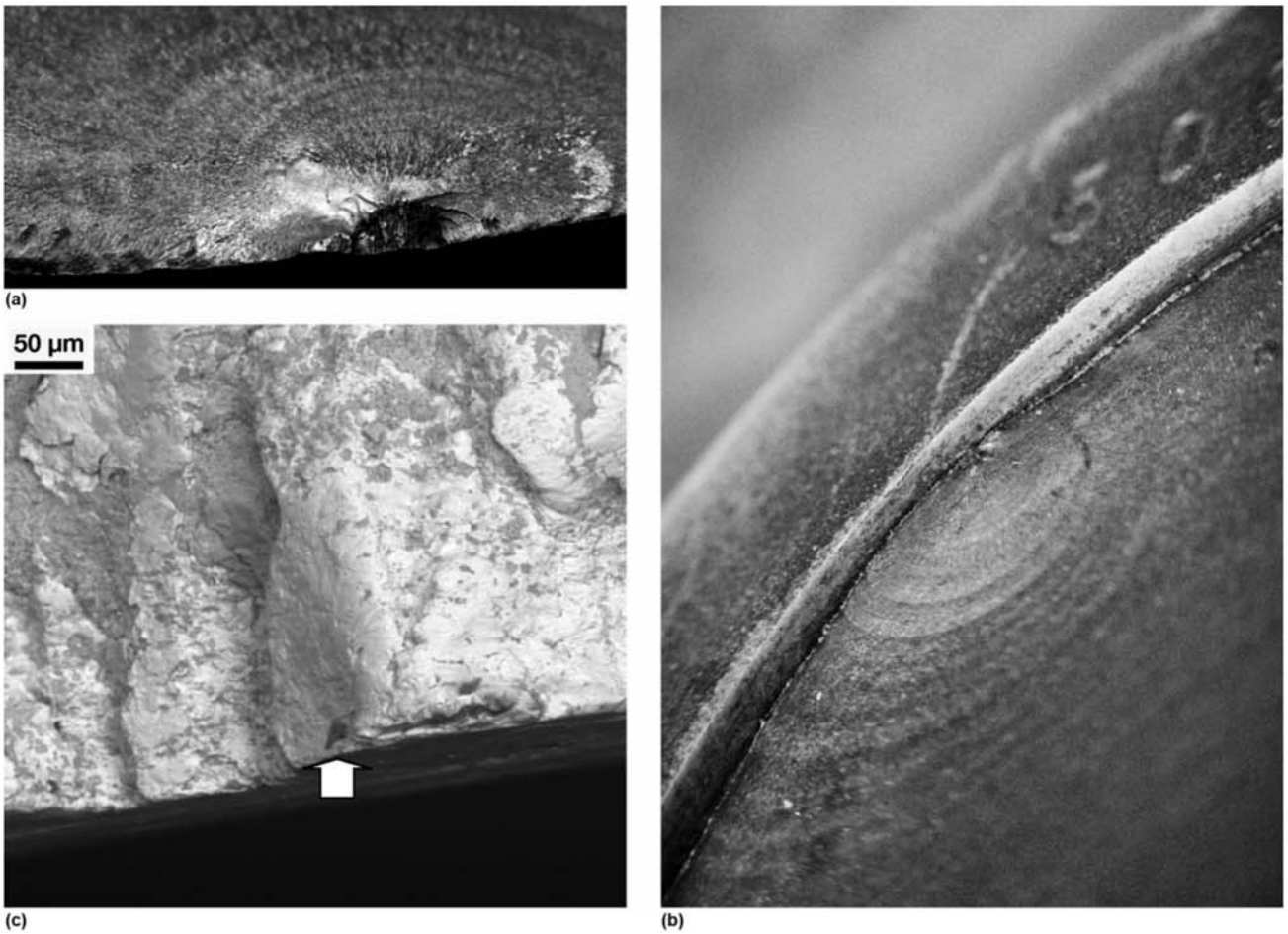

Fig. 18.1 The region where the fatigue fracture of the axle presented in Fig. 15.24 (Chapter 15, "Engineered Special Bar Quality Steel (Engineered Steels)," in this book) started. (a) The radial aspect of the marks inside the defect that started the fatigue failure. (b) A view of the region where fatigue started, including the axle surface. No serious surface irregularities are present. (c) SEM (BE) image of the region where the fracture started. The arrow indicates an oxide inclusion close to the surface of the axle. Courtesy of MRS Logística S.A., RJ, Brazil.

excluded from the analysis, many times in an unconscious way, and this may lead to lack of success.

Evidently, the collection of all factual information about the axle and its failure should have been more carefully planned before performing the tests, to guarantee the collection of all relevant data by using a well-defined plan, even if part of it, by the end, proved to have been irrelevant.

18.5 The Report

Oral communication differs from written communication for at least two important reasons:

- The only way written communication occurs is through the text, tables, and figures presented. Further explanations and clarifications, as well as other common techniques in oral communication to better clarify ideas, are not possible.
- Written communication can be carefully organized, reviewed, and improved until the writer is satisfied that the best way of conveying the ideas has been reached. In oral communication, this is not possible, but the speaker can resort to additional clarifications, questions, gestures, and so on.

Although the first aspect poses significant difficulties, the second one more than compensates for them. The fact that a report can be read many times, subjected to criticism from an independent reader and further polished and improved is certainly a great advantage of written communication. It requires patience and significant effort, however. It is essential that whoever must prepare reports, gets used to taking advantage of the possibilities that come with organization and revision. The writing process thus must be performed considering the assumption that revisions, rereading, and reading by independent readers are part of the process. Furthermore, one must assume that these stages will be repeated until one is certain that the text, tables and images convey the desired information in the most clear and efficient way.

There are some well-defined models for the sequence of topics in a technical report. The adoption of these models is not always mandatory (theses, dissertations, and papers in some journals are exceptions, since these frequently have mandatory models). However, practice indicates that these are the most efficient ways of writing reports and frequently result in clearer and more objective reports. In general, the sequence indicated in Table 18.2 is sufficient to produce clear and objective reports. In the following items, some additional remarks to this table are presented. Reports may range from those describing a single test performed in accordance with a well-defined standard to the results of a complex investigation in which many hypotheses are evaluated and tests are performed to support (or discard) one (or more) hypotheses or even to more extensive work such as theses or dissertations, where not only tests are reported but one attempts to construct and organize the knowledge with the support of previous articles and critical investigation. Thus, each section of a report may have a different length, depth, and complexity, depending on what is being reported.

Table 18.2 A recommended itemization for a technical report or academic work

Section of the report	Content
Objectives	Defines, in a clear and concise way, what will be reported. Ideally, it should be written in a single paragraph.
Abstract	In the case of academic work, the section "Objectives" is usually replaced by a summary or abstract where all the content of the work is presented in a summarized and concise way, highlighting: objective, main results and main conclusions. The reader frequently decides whether or not to read an academic work based on the abstract content and qualities (clear, concise, objective).
Introduction	Puts the problem in context. Normally presents the facts that led to the analysis and closes by clearly defining the problem that will be the focus of the report. In the case of academic works it normally also includes some justification on the relevance of the work.
Relevant information or prior information	When the analysis to be reported takes into consideration additional information besides the tests that will be presented in the report, a specific section should be present where all this information is described.
Literature review or literature survey	In academic work, the prior information is usually the available literature on the subject. Anything that is not germane to the theme or issue in question should not be included in the literature review, regardless of how interesting it might be. Similarly no information from previous articles that will be used in the report should be omitted from this section. Suspense and surprise are not parts of a technical report.
Materials and methods or experimental	In this section all the techniques used in the tests and exams performed should be described. In principle, this description should enable the replication of the reported results. Thus, all data related to sampling, sample preparation, test method, etc. should be clearly described. Similarly, if there is any relevant information that the reader may be unaware of, this should be explicitly presented in this section.
Results	The results of the tests and exams are presented in this section. In academic publications it is usual to include, in this section, the discussion of the results, based on the previous knowledge (literature review) highlighting what agrees and what is not in agreement with previous knowledge and what is new. This section is frequently named "Results and Discussion."
Conclusions	This section presents the conclusions of the work. It is important to clearly separate conclusions and (if present) speculations. In academic work the speculations are frequently included in the previous section ("Results and Discussion"). In technical reports, when the results and data cannot support a certain conclusion beyond doubt (a common situation in failure analysis) it is important to make clear to the reader the limits between facts and speculation, even if the speculation is based on facts and evidence.
References or bibliography	The sources of information used in a report must be clearly identified to the reader. Here, also, it is essential to guarantee that the reader will be able to independently locate the sources and confirm the information included in the report.

18.5.1 The Literature Review

In the literature review section, when present, it is not enough to list the "previous articles"—the results of previous work that are relevant to the work being reported. It is essential to critically evaluate them, comparing them and presenting discrepancies, inconsistencies, and methodological deficiencies or stressing the consistency of the results and indicating knowledge that is lacking and should be researched. A good literature review should convince the reader that the work to be presented needs to be done and will indeed expand knowledge or at least solve some controversy. One must also resist the temptation of including interesting and important points that are not germane to the work in question.

18.5.2 The "Materials and Methods" or "Experimental Technique" Section

In an academic, scientific, or technological report, the objective of this section is to provide sufficient information to allow replication of the results.

In other types of reports, this section has an additional role. It confirms to the client or reader that given methods or standards previously defined were adopted. Thus, while this section may appear an unnecessary repetition to some, it represents:

- The formal statement that the defined requirement for the performance of the tests or exams have been followed
- A confirmation that sufficient attention was paid to all critical variables defined in the test method selected

18.5.3 The Results

The results determined and their uncertainties (or "error bars") for each measurement performed must be clearly presented. When reporting measured or calculated values nowadays, it is common to extract the values directly from the display of electronic instruments, calculators, or computer software. It is important to recall that in view of the precision or uncertainties of the measurement systems, the results should be presented with a certain number of significant digits. Some standards, such as ASTM A370, define the procedure for the rounding of test data and the number of significant digits to be used. In other cases, it is important to carefully consider how many significant digits should be used based on the uncertainty of the method.

18.5.4 The Conclusions

All conclusions presented in the report should be clearly supported by results included in the report.

REFERENCES

1. "General Requirements for the Competence of Testing and Calibration Laboratories," IEC 17025:2005, ISO, 2005
2. "Quality Management Systems—Requirements," 9001, ISO, 2015
3. AAAS, Science, Instructions for preparing an initial manuscript (ref for science journals), http://www.sciencemag.org/authors/instructions-preparing-initial-manuscript, (accessed April 2017)
4. W. Thompson, Lord Kelvin, *Popular Lectures and Addresses*, Macmillan, 1891
5. "Standard Guide for Calibrating Reticles and Light Microscope Magnifications," E1951-14 A, ASTM, 2014
6. "Standard Practice for Calibrating the Magnification of a Scanning Electron Microscope," E766-14e1, ASTM, 2014
7. M.T. Postek and D.C. Joy, Submicrometer Microelectronics Dimensional Metrology: Scanning Electron Microscopy, *J. Res. Natl. Bur. Stand*., Vol 92, 1987, p 205–28
8. B.N. Taylor and C.E. Kuyatt, Guidelines for Evaluating and Expressing the Uncertainty of NIST Measurement Results, NIST Technical Note 1297, 1994 edition, https://www.nist.gov/sites/default/files/documents/pml/pubs/ tn1297/tn1297s.pdf (accessed April 2017)
9. BIPM, International Vocabulary of Metrology—Basic and General Concepts and Associated Terms (VIM), 3rd ed., 2008 version with minor corrections, *JCGM*, Vol 200, 2012, http://www.bipm.org/en/publications/guides/vim.html (accessed April 2017)
10. P.R.M. Vieira and S. Paciornik, Uncertainty Evaluation of Metallographic Measurements by Image Analysis and Thermodynamic Modeling, *Mat. Charact.*, Vol 47 (No. 3–4), 2001, p 219–26
11. S. Paciornik, Análise de imagens e microscopia digital, *Metal. Mat.*, Vol 58 (No. 518), 2002, p 121–23
12. S. Paciornik and M.H.P. Maurício, Digital Imaging, *Metallography and Microstructures*, Vol 9, *ASM Handbook*, G.V. Voort, ed., ASM International, 2004, p 368–402
13. H. Pearson, CSI: Cell Biology, *Nature*, Vol 434, 2005, p 952–53
14. M. Rossner and K.M. Yamada, What's in a Picture? The Temptation of Image Manipulation, *J. Cell Biol.*, Vol 166, 2004, p 11–15

Index

B

C

D

E

F

G

H

I

J

K

L

M

N

O

P

S

T

U

V

W

X / Y